TR Attachments

Test Reports

- Attachment TR1: Cast-in-place Specimen Test Report
  - Final report for experimental results from cast-in-place specimen
- Attachment TR2: Grouted Duct Specimen Test Report
  - Final report for experimental results from grouted duct specimen
- Attachment TR3: Cap Pocket Full Ductility Specimen Test Report
  - Final report for experimental results from cap pocket full ductility specimen
- Attachment TR4: Cap Pocket Limited Ductility Specimen Test Report
  - Final report for experimental results from cap pocket limited ductility specimen
- Attachment TR5: Hybrid Specimens Test Report
  - Final report for experimental results from hybrid specimens
- Attachment TR6: Integral Specimen Test Report
  - Final report for experimental results from integral specimen

California State University, Sacramento
College of Engineering and Computer Science
Research Report

EMULATIVE PRECAST BENT CAP CONNECTIONS FOR SEISMIC REGIONS: COMPONENT TESTS— CAST-IN-PLACE SPECIMEN (UNIT 1)

Eric E. Matsumoto, Ph.D., P.E.

November 19, 2009

Final Report for: NCHRP 12-74, Development of Precast Bent Cap Systems for Seismic Regions

ECS Report Number: ECS-CSUS-2009-01

College of Engineering and Computer Science

California State University, Sacramento

Sacramento, California 95819-6023

California State University, Sacramento
College of Engineering and Computer Science
Research Report

EMULATIVE PRECAST BENT CAP CONNECTIONS FOR SEISMIC REGIONS: COMPONENT TESTS— CAST-IN-PLACE SPECIMEN (UNIT 1)

Eric E. Matsumoto, Ph.D., P.E.
Associate Professor, Structural Engineering

November 19, 2009

Final Report for: NCHRP 12-74, Development of Precast Bent Cap Systems for Seismic Regions
ECS Report Number: ECS-CSUS-2009-01

College of Engineering and Computer Science
California State University, Sacramento
Sacramento, California 95819-6023

Please cite this report as follows:

Matsumoto, Eric. E., *Emulative Precast Bent Cap Connections for Seismic Regions: Component Tests—Cast-in-place Specimen (Unit 1)*, ECS Report No. ECS-CSUS-2009-01, California State University, Sacramento, CA (November 2009) 89 pp.

DISCLAIMER

The research presented in this report was conducted as part of the National Cooperative Highway Research Program, Project 12-74, Development of Precast Bent Cap Systems for Seismic Regions. The opinions and conclusions expressed or implied in the report are solely those of the author. They are not necessarily those of the Transportation Research Board, the National Research Council, the Federal Highway Administration, the American Association of State Highway and Transportation Officials, or the individual states participating in the National Cooperative Highway Research Program.

ACKNOWLEDGEMENT OF SPONSORSHIP

This work was sponsored by the American Association of State Highway and Transportation Officials, in cooperation with the Federal Highway Administration, and was conducted in the National Cooperative Highway Research Program, which is administered by the Transportation Research Board of the National Research Council.

OTHER ACKNOWLEDGEMENTS

The author gratefully acknowledges the significant contributions from many graduate and undergraduate students, as well as laboratory technicians at California State University, Sacramento. Of particular note are David Van Zanen, P.E., Jeremy Wright, P.E., Arvind Gopalakrishna, Andy Wilson, Jim Ster, and Brett Anthony. The author also gratefully acknowledges contributions from the NCHRP 12-74 Team, including Dr. Jose I. Restrepo and Matthew Tobolski of UCSD, Mary Lou Ralls, P.E., of Ralls-Newman LLC, and Steve Mislinski, P.E, of AECOM/LAN Engineering. Finally, the author gratefully acknowledges the many contributions of Glen Underwood and Don Clark of Clark Pacific, West Sacramento, CA for fabrication support.

EXECUTIVE SUMMARY

This report, Emulative Precast Bent Cap Connections for Seismic Regions: Component Tests—Cast-in-place Specimen (Unit 1), is the first in the series of four reports summarizing the California State University, Sacramento (CSUS) component tests supporting National Cooperative Highway Research Program (NCHRP) Project 12-74, "Development of Precast Bent Cap Systems for Seismic Regions". CSUS is investigating two emulative connections—cap pocket and grouted duct—for nonintegral precast bent caps.

CSUS designed a Cast-in-place (CIP) prototype bridge and emulative component specimens in accordance with the 2006 Recommended LRFD Guidelines for the Seismic Design of Highway Bridges (2006 LRFD RSGS), which contains less conservative joint reinforcement requirements—including a smaller area of vertical stirrups within the joint and smaller area of bent cap longitudinal reinforcement—than the 2009 AASHTO Guide Specifications for LRFD Seismic Bridge Design (2009 LRFD SGS). For a major seismic event, the CIP prototype bridge was designed and detailed to exhibit ductile plastic hinging in the column adjacent to the capacity-protected bent cap and joint. The CIP control specimen was designed using a 42% scale of the central portion of the prototype bridge and was expected to perform similarly to the prototype bridge.

Specimen response was dominated by plastic hinging of the column adjacent to the bent cap. Post-test inspection revealed that the core remained primarily intact with several column bars buckling and fracturing at ultimate. The specimen exhibited excellent ductility to a large drift of 5.9%, which corresponded to a nominal displacement ductility of 10. The load-displacement response indicated stable hysteretic behavior without appreciable strength degradation.

Displacement decomposition confirmed the dominance of plastic hinging. For example, at 3.6% drift (μ6), the flexural components (fixed end rotation and column flexure) accounted for 90% of the column displacement. The contribution of joint shear to overall displacement was minor, not exceeding 10%. This was confirmed by visual observations of joint crack widths limited to 0.025 in. Column bars were well anchored

within the joint, with bar slip contributing less than 4% on average to fixed end rotation. Principal tensile stresses significantly exceeded $3.5\sqrt{f_c'}$ and justified the use of additional joint reinforcement required for development of a force transfer mechanism. The test specimen, designed per 2006 LRFD RSGS, did not require stirrups inside the joint; however, two joint stirrups were included for construction, providing an area 65% of that required by the 2009 LRFD SGS ($0.135A_{st}$). Strain records confirmed plastic hinging, effective hoop confinement in the column and joint, and strain penetration with bar yield 6 in into the joint. Bent cap bars reached only 46% of yield, even though the specimen design did not include the additional bent cap longitudinal reinforcement ($0.245A_{st}$) required by 2009 LRFD SGS. Stirrup strain outside the joint remained well below yield, but the north construction stirrup within the joint yielded, indicating its contribution to the stable joint performance and the importance of vertical stirrups inside the joint.

Despite the less conservative design basis compared to the 2009 LRFD SGS, the CIP specimen satisfied the performance goal of the design, exhibiting extensive plastic hinging of the column, limited joint distress, and essentially elastic behavior of the bent cap. The CIP specimen also provided an appropriate benchmark (control) for comparison with the precast grouted duct and cap pocket specimens. In addition, test results can be reliably used as a supporting basis for developing design and construction specifications for seismic precast bent cap systems.

TABLE OF CONTENTS

Page

List of Tables

Chapter 1

Chapter 2

Chapter 3

List of Figures

Chapter 1

Chapter 2

Chapter 3

1.0 Introduction

1.1 Background

1.1.1 Overview

Thousands of bridges throughout the United States have been classified as structurally deficient or functionally obsolete and many are in need of immediate repair or replacement. To replace or rehabilitate these structures with minimal traffic interruption, Accelerated Bridge Construction (ABC) techniques have been sought. The use of precast concrete bent caps is one approach to accelerate construction, as it removes much of the work from the critical path. Other advantages of precast bent caps include: reduction in environmental impact due to decreased onsite construction time and removal of environmentally hazardous operations to less intrusive locations; increased quality as bent caps are fabricated in a more controlled environment; improved safety for construction workers and the traveling public due to reduced exposure to hazardous conditions; and improved overall economy. [1]

Precast bent caps such as that shown in Figure 1-1 have been used to meet a variety of project objectives. Considerable research has been conducted to develop constructible details with reliable performance. [2-4] However, implementation in seismic regions has been limited due to: 1) uncertainty in performance of connections between the bent cap and columns (or piles) for nonintegral systems and between the superstructure and bent cap for integral systems, especially in assuring adequate ductility, strength, and stiffness; 2) lack of specifications for design and construction; and 3) potential congestion of connections in higher seismic regions. [5]

1.1.2 Integral and Nonintegral Precast Bent Cap Systems

Precast bent cap systems can be classified as either integral or nonintegral depending on superstructure-to-substructure connectivity. When the superstructure is connected to the supporting bent cap by a cast-in-place (CIP) pour, closure pour, post-tensioning and/or other means, longitudinal moment continuity exists. This integral connection creates longitudinal framing action and thereby provides redundancy in the load path, and, in some cases, can reduce the displacement demand and demand on the

foundation. Nonintegral connections are typically produced by supporting the superstructure on bearings on top of the bent cap. The bent cap-to-column connection provides a moment connection in the transverse direction, but moment transfer does not develop between the superstructure and substructure in the longitudinal direction. Thus, the longitudinal strength and stiffness of the bridge are based on cantilever response of the supporting columns and soil-structure interaction at the abutments. Because of their simplicity, nonintegral bent cap systems are expected to be more widely implemented than integral systems, especially in regions of low to moderate seismicity, where such a system can provide suitable performance. For higher seismicities, nonintegral systems may still provide an economical solution for shorter span bridges, although additional provisions such as CIP diaphragms and additional seat width must be incorporated into the design.

1.1.3 Emulative Precast Bent Cap Systems

Precast connections are typically described as being either emulative or hybrid, depending on the use of "wet" or "dry" connections, respectively. Wet connections use CIP concrete or grout to connect precast elements, whereas dry connections often employ mechanical devices for connection. Many seismic regions around the world such as the United States, Japan, and New Zealand have used emulative connections, which are designed to produce a system performance that is similar to (or "emulates") that developed by monolithic, CIP construction. Certain emulative systems using partially-precast construction offer some of the advantages of precast construction such as increased speed of erection and are designed to produce emulative response through the use of limited on-site concrete pours. [6]

Bridges using emulative connections are expected to form plastic hinges in the columns and redistribute forces to other members like CIP systems do. In addition, the lateral force-lateral displacement response of an emulative system is expected to exhibit full hysteresis loops and stable energy dissipation, as shown in Figure 1-2. This response is characteristic of significant energy dissipation and hysteretic damping assumed in the underlying seismic design philosophy for CIP bridges. As dissipation and damping

occurs through column plastic hinging in an earthquake, life safety is ensured. Emulative performance is commonly preferred for seismic regions, despite the potential for large inelastic deformations that can lead to significant residual displacements and regions of severe, and sometimes non-repairable, damage post-earthquake. [7]

1.2 NCHRP 12-74 Research Objective

To address the uncertainties associated with seismic behavior of precast bent cap systems and the lack of specifications, the National Cooperative Highway Research Program (NCHRP) funded Project 12-74, Development of Precast Bent Cap Systems for Seismic Regions, to develop design methodologies, design and construction specifications, design examples, and semi-standard details for seismic precast bent cap systems using emulative and hybrid connections for nonintegral and integral systems. [5, 7]

1.3 CSUS Research Objective and Approach

The California State University, Sacramento (CSUS) research objective is to develop design methodologies, design and construction specifications, design examples, and semi-standard details for nonintegral emulative precast bent caps. As reported in Reference 5, two emulative connections types—grouted duct and cap pocket—were selected for development based on a review of past connection usages and consideration of expected seismic performance, durability, constructability, and cost.

Nine tasks are included in NCHRP 12-74 to reach the overall research objectives. [7] As part of Task 6—Conduct of Analytical and Experimental Work—CSUS conducted tests and associated analysis to investigate grouted duct and cap pocket connections. Table 1-1 shows the Test Matrix for CSUS component tests, including a brief summary of the four test specimens (units).

1.4 Scope of Report

This report is the first in a series of four reports that summarize the experimental and analytical efforts for each CSUS test unit. This report includes the following chapters:

1.0 Introduction: Background, statement of NCHRP research objective, CSUS research objective and approach, and scope of report.

2.0 Specimen Design, Fabrication, and Testing: Summary of prototype and specimen design, fabrication and testing, including key aspects of fabrication processes and issues, as well as specimen material properties, test setup, loading sequence, instrumentation and pretest predictions.

3.0 Specimen Response and Analysis: Experimental observations, hysteretic response, column curvature response, displacement decomposition, joint response, and strain records.

4.0 Summary and Conclusions.

1.5 Tables

Table 1-1. CSUS Component Test Matrix for Bent Cap-Column Connections

Test Unit	Brief Description
1. Cast-in-place (CIP)	Control specimen for comparison to precast connections, with bent cap and column detailing intended to achieve full ductility
2. Grouted Duct Connection (GD)	Individual ducts cast in bent cap to connect each column bar, with bent cap and column detailing intended to achieve full ductility
3. Cap Pocket Full Ductility (CPFD)	Single pipe cast in bent cap to connect all column bars, with bent cap and column detailing intended to achieve full ductility
4. Cap Pocket Limited Ductility (CPLD)	Single pipe cast in bent cap to connect all column bars, with bent cap and column detailing intended to achieve limited ductility

1.6 Figures

Figure 1-1. Precast concrete bent cap system used in crossing of State Highway 36 over Lake Belton, Texas [2]

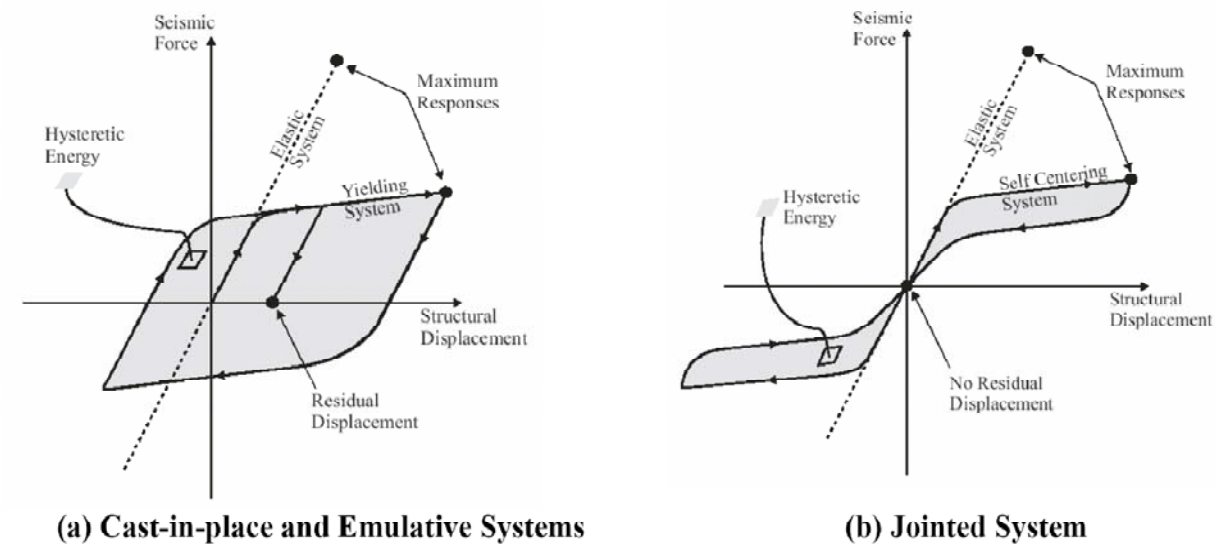

Figure 1-2. Hysteretic Response for Cast-in-place, Emulative and Jointed Systems [7]

2.0 Specimen Design, Fabrication, and Testing

2.1 Design

In coordination with the NCHRP 12-74 Panel, the prototype structure was selected as a two-span, nonintegral bridge with a three-column CIP bent supporting precast, prestressed girders, intended to represent a typical highway overcrossing located in an urban region. Design of the component specimens is based on a representative portion of the center column and bent cap of the bridge. The full design for the prototype and specimen are reported in Reference 8. This section summarizes key features of the prototype and specimen design.

2.1.1 Prototype Bridge

CSUS designed the CIP prototype bridge (and emulative component specimens) in accordance with the AASHTO LRFD Bridge Design Specifications, Third Edition, 2004, with 2006 Interims (2006 LRFD BDS) and the 2006 Recommended LRFD Guidelines for the Seismic Design of Highway Bridges (2006 LRFD RSGS) prepared as part of NCHRP 20-07 Task 193 and provided to the Research Team by the Panel. [9, 10] It is important to note that the 2006 LRFD RSGS was superseded by the 2007 Proposed AASHTO Guide Specifications for LRFD Seismic Bridge Design (2007 LRFD PSGS) and later updated to the current 2009 AASHTO Guide Specifications for LRFD Seismic Bridge Design (2009 LRFD SGS). [11, 12] In addition, the 2006 LRFD RSGS contains different—and in some aspects more liberal (i.e., less conservative)—joint reinforcement requirements than the current 2009 LRFD SGS. For example, in contrast the 2006 LRFD RSGS, the 2009 LRFD SGS specifies vertical joint stirrups both inside and outside the joint region, a larger total area of joint stirrups, as well as a significant increase in bent cap longitudinal reinforcement.

For a major seismic event, the CIP bridge is designed and detailed to exhibit ductile plastic hinging in the column adjacent to the bent cap (and footing). Prototype bridge drawings are shown in Figures 2-1 through 2-5.

Initial member sizing was based on input from design engineers and refined through application of the 2006 LRFD BDS. Seismic analysis and design were

performed to finalize column and cap beam sections. The prototype structure was considered non-essential and designed for the associated life-safety performance objectives defined in 2006 LRFD RSGS. Because the system is nonintegral, the specified earthquake resisting system in the longitudinal direction consisted of cantilever response of the columns with plastic hinge formation at the base of columns. One-way soil springs were used to account for seismic resistance of the abutment backfill. Transverse earthquake resistance was provided by the three-column bent with plastic hinge formation occurring at both top and bottom of the columns. The design acceleration response spectrum (ARS) curve incorporated 5% damping and was developed using a 1.0-sec acceleration of 0.8 g, a 0.2-sec acceleration of 1.5 g and coefficients for Site Class D soil. The resulting peak rock acceleration was 0.6 g. The ARS curve is representative of a site located in a high seismic region such as Southern California. Based on the design earthquake response spectral acceleration coefficient at a 1.0-sec period, S_{D1}, larger than 0.50, the structure was classified as Seismic Design Category (SDC) D. This category required a demand analysis, displacement capacity pushover analysis, capacity design, and SDC D detailing.

Elastic dynamic analysis was performed according to 2006 LRFD RSGS to estimate seismic displacement demands. The columns were assumed to be fixed at the base, and foundation design was not performed. Moment-curvature analysis was conducted to estimate the effective stiffness of columns. Seismic demands were determined using the program SEISAB (2006). [13] Results from the seismic analysis indicated a first mode (longitudinal) period of 1.27 sec and associated displacement demand of 15.1 in. The second mode (transverse) period was 0.58 sec, with a displacement demand of 5.3 in, including magnification to account for underestimation of demand for shorter period structures. Shear keys at the abutments were designed to fail during the design seismic event.

In the longitudinal direction, the displacement Demand to Capacity ratio, D/C, was 0.85. For determining transverse capacity, overturning effects were considered using an iterative procedure to refine the estimated column plastic moment capacities based on

column axial loads obtained from the pushover analysis. The program, XSection, was used to perform moment-curvature analysis, and the program WFrame was used for pushover analysis, including overturning effects and bent cap flexibility. [14, 15] The transverse displacement D/C ratio was 0.57. Ductility demand ratios were approximately 5.0 for both the longitudinal and transverse directions, well below the limit of 8.0 (multicolumn bents). The prototype structure thus satisfied the requirements for displacement and ductility. P-delta effects were checked per 2006 LRFD RSGS.

Capacity protection design principles were also applied. Flexural and shear demands on the bent cap were based on force levels associated with the columns reaching their overstrength capacity. The bent cap design considered axial load effects due to transverse response in combination with gravity loads and overstrength demands imposed by columns. According to 2006 LRFD RSGS, the bent cap was required to remain "nominally elastic." Bent cap transverse reinforcement outside of the joint region was designed according to LRFD provisions based on the modified compression field theory and considered seismic plus gravity loading. Column transverse reinforcement was designed to resist overstrength demands due to transverse response.

The joint region of the bent cap was designed based on transverse response using the external force transfer mechanism assumed in the 2006 LRFD RSGS. As shown in Figure 2-3, joint design included vertical stirrups with horizontal cross ties in the region adjacent to the column (not within the joint), joint transverse reinforcement (hoops), extension of column bars close to the top of the bent cap, and side face reinforcement. In addition, two 2-leg construction stirrups were used within the joint region. However, the prototype bridge did not incorporate the more conservative joint reinforcement requirements of the 2009 LRFD SGS, such as placement of the required area of stirrups inside the joint or the additional area of longitudinal bent cap reinforcement.

2.1.2 Test Specimen

The CIP test specimen was designed using a 42% scale of the central portion of the prototype bridge, as shown in Figure 2-6. This scale factor was based on scaling a 48-in diameter column to 20 in (20/48=0.42). As the prototype bridge would be expected

to exhibit ductile plastic hinging in the column region adjacent to the bent cap due to transverse response, the scaled CIP control specimen—loaded in the transverse direction under quasi-static force control and displacement control sequences—was expected to perform similarly.

The specimen dimensions and reinforcement allowed for accurate examination of the behavior of the scaled beam-column joint region and reasonably matched points of contraflexure of the prototype. Loading on the specimen was designed to replicate scaled forces adjacent to the joint as closely as possible for an accurate assessment of the joint behavior. Prototype moments at the face of the joint were accurately reproduced from the specimen design, based on the use of an axial force on the column equal to 38 kips. Although the axial force produced a smaller column compressive stress than the prototype, such a condition increased the principal tensile stresses in the joint, thereby producing a more severe (i.e., conservative) joint condition that was useful for examining joint performance. For the push direction, the negative moment side of the specimen joint is not expected to reach yield. (Note: 2006 LRFD RSGS does not explicitly prevent the flexural reinforcement of the capacity protected bent cap from reaching yield, although some engineers design to prevent yield). On the positive moment side, even smaller bar stresses exist. For the pull direction, a less severe condition exists at the joint due to support conditions that produce an axial compression in the bent cap, compared to no axial force for the push direction. The column overstrength moments for the specimen and prototype also matched well.

The size of the longitudinal reinforcement for the specimen (#5's) was based on the application of scaling laws to the prototype, although the percentage was increased 14% (1.38% for prototype and 1.58% for specimen) due to scaling from #11 to #5 bars. Although 14 column bars instead of 16 could have been used in the specimen, the same number of bars was selected for the specimen and prototype to help achieve an accurate scaling of the plastic moment at a smaller specimen axial stress, as well as to examine constructability for the precast connections, such as duct spacing and potential congestion in the bent cap for the grouted duct connection. The transverse reinforcement size was

based on scaling laws, and spacing was based on displacement ductility capacity and an equal volumetric reinforcing ratio. Because the diameter of a #3 (0.375 in) is larger than the diameter of a #6 times the scale factor (0.31 in), a larger hoop spacing was used for the specimen (2 in o.c.) than dictated by scaling laws (1.25 in o.c.); however, this spacing was considered acceptably small. Transverse reinforcement was governed by required hoop spacing for ductility rather than by shear.

Dead load plus seismic governed the bent cap flexural reinforcement in the prototype. This reinforcement was scaled for use in the bent cap and resulted in properly scaled flexural capacity at the joint face. Bent cap transverse reinforcement used #3's as a reasonable scale for the #6's in the prototype and was designed per AASHTO LRFD to prevent shear failure. Capacity protection of the bent cap was also verified for the specimen. A large ratio (over 2.5) was achieved, due in part to the liberal 2006 LRFD RSGS definition of essentially elastic flexural capacity for the bent cap, M_{ne}, that specified the use of a large concrete compressive strain (0.005) and corresponding steel strain over 0.05.

Both the prototype and specimen required the "additional" joint shear reinforcement, with principal tensile stresses much larger than the estimated tensile cracking strength of $3.5\sqrt{f_c'}$. However, the principal tensile stress for the specimen, $p_{t,specimen}$, was 539 psi, or 1.66 $p_{t,prototype}$. This more severe condition, due to relatively smaller column load, larger cap and column tension, and imperfect scaling of dimensions, was considered more desirable for examining joint behavior. In addition, hoop spacing within the specimen joint was purposely maximized to a spacing of 5 in, close to the maximum permissible per 2006 LRFD RSGS.

Table 2-1 provides a detailed comparison of the column, bent cap, and joint reinforcement for the CIP prototype and CIP specimen. Ratios of the specimen reinforcement to the similitude (or design) ratio are shown to be reasonably close to 1.0.

2.2 Fabrication

2.2.1 Specimen

The specimen consisted of the bent cap and column shown in Figures 2-7 through 2-9. The bent cap used a 25 in x 25 in cross section, 12-#5's (0.65%) for flexural reinforcement, and #3's at 6 in for transverse (shear) reinforcement. The 20-in column included 16-#5's (1.58%) and #3 hoops at 2 in within the plastic hinge region. Joint reinforcement included three sets of 4-leg #3 stirrups at 5 in (with two sets of #3 cross ties through the depth) adjacent to each side of the joint, #3's at 5 in hoop reinforcement, and an embedment of column bars equal to the joint depth less 3 in. Figure 2-9 shows a somewhat congested, but constructible, joint region during fabrication. The two 2-leg stirrups shown in Figures 2-8 and 2-9 were intentionally placed in the joint to represent construction stirrups sometimes used for support of the rebar cage during fabrication or limit states other than seismic.

2.2.2 Material Properties

Concrete and reinforcing steel used in the bent cap and column were tested to determine material properties. Sampling, preparing, and testing of specimens were generally performed in accordance with governing ASTM standards.

2.2.2.1 Portland Cement Concrete

The bent cap and column were constructed with normal weight concrete using the concrete mix proportions shown in Table 2-2. The mix design was expected to achieve a 28-day compressive strength of 4000 psi based on a water-cement ratio of approximately 0.49. A 3/8-inch maximum coarse aggregate size was used in the concrete mix in accordance with specimen scaling. Standard 6x12 in cylinders were cast from the concrete batch used for the specimen fabrication. Concrete cylinders were cured for the same length of time and in the same conditions as the concrete specimens.

Compression and tensile (split cylinder) tests were conducted in the CSUS Structural Laboratory. Concrete cylinders were produced for each casting and tested over a range of days including test day.

The design and actual properties of the concrete are shown in Table 2-3, and representative concrete compressive strength gain curves are shown in Figure 2-10. It is noted that the column achieved larger test-day strengths than the bent cap. Post-test analysis accounted for differences in strength.

2.2.2.2 Reinforcing Steel

The column and bent cap longitudinal reinforcing steel consisted of ASTM A706 Grade 60 deformed #5 rebar, and the column hoops and stirrups consisted of ASTM A615 Grade 60 (weldable) #3's. Uniaxial tensile tests were conducted on samples from the rebar lot; specimens were prepared in accordance with ASTM requirements. Yield and tensile strengths are shown in Table 2-4 for the different bar sizes. Figure 2-11 shows stress-strain plots for specimen reinforcing bars. The rebar displays expected strength and ductility. Although limitation in the data collection limited the exact determination of yield strength, it is reasonably bounded within a narrow range. The extensometer was removed prior to bar fracture.

2.2.3 Fabrication and Issues

All CSUS specimens were fabricated with the assistance of Clark Pacific (West Sacramento, CA plant). The fabrication and assembly of the specimens were intended to replicate as much as possible the expected field process, and thereby examine constructability issues.

Therefore, all specimens were built in the upright position, including the CIP control specimen. For the CIP specimen, this required building special elevated forms in the precast yard for casting the bent cap on top of the column, as well as inverting the entire T-shaped specimen in the yard for transportation.

The construction sequence for the CIP specimen included the following (Figures 2-12 through 2-18):

1. Fabricate rebar cages for the bent cap and column, including strain gages, at CSUS.
2. Transport rebar cages to Clark Pacific, prepare the column form, and cast the column.

3. Prepare the bent cap form on an elevated platform around the column.
4. Place the rebar cage into the form and cast the bent cap monolithically with the column in an upright position.
5. Invert specimen at Clark Pacific and transport specimen to CSUS and install in test area.

There were no significant issues during fabrication. The specimen was fabricated accurately according to the drawings. Table 2-5 summarizes significant specimen as-builts for column bars and hoops.

2.3 Testing

2.3.1 Test Setup

The specimen test setup, shown in Figure 2-19, includes the following:

- Simply supported bent cap, with an equivalent pin support at the north end with vertical and lateral restraint (right side as shown) and an equivalent roller at the south end with vertical support only (left side as shown). This simple setup allowed accurate establishment of specimen forces. Although scaled modeling of the moment gradient along the cap was not required, accurate conditions adjacent to the faces of the joint were required and modeled in appropriate proportion to resist the column moment. [8, 16] The test setup ensured accurate conditions at each end of the joint so that the force transfer mechanism in the joint could be investigated.
- Inverted specimen, with a column stub. This allowed biaxial loading of the specimen, using a vertical actuator to apply scaled gravity load and the horizontal actuator to induce seismic response.
- Different axial force conditions in the bent cap for the push and pull directions. The push direction is considered more critical, as the axial force causes tension at the joint face, in contrast to the compression for the pull direction. However, the magnitude of axial force remained relatively small during testing.

2.3.2 Loading Sequence

The vertical and horizontal hydraulic actuators were used to apply specified force control and displacement control sequences to the specimen, as shown in Figures 2-20 and 2-21. The stages of loading are briefly summarized as follows:

1. Vertical Load: A monotonic increasing concentrated vertical load representing gravity load was applied to the top of the column stub to a maximum load of 38 kips. Force control was used to maintain the vertical load throughout the horizontal loading sequence. A very slight change in vertical load developed during testing.
2. Horizontal Load: After the vertical load was applied, a horizontal load or displacement, representing seismic-induced load or displacement, was applied in two sequences: Force Control, followed by Displacement Control.

   Force Control: An increasing horizontal load was applied to the side of the column stub using one cycle per load level (Figure 2-20). A cycle consisted of both a push and pull at the specified load. Load was held at select cycle peaks for marking, photographing and documenting. The Force Control sequence was discontinued after an approximate determination of first yield of column longitudinal bars in the push and pull directions.

   Establishment of Effective Yield: Column strain gages and displacement measurements were intended to be used to calculate the system effective yield displacement, Δ_{YE}, and thus displacement ductility demand, μ_D, for the Displacement Control sequence. Although loss of some gages made the establishment of first yield experimentally approximate, an experimental yield displacement reasonably close to the predicted yield displacement was established. The following equation specifies the relationship between the experimental first yield displacement of the system, Δ_Y, and the system effective yield displacement, Δ_{YE}, used for establishing the displacement control sequence:

$$\Delta_{YE} = \frac{M_{YE}}{M_{Y\exp}} \Delta_Y$$

where M_{YE} is the theoretical moment at effective yield based on moment-curvature analysis, and M_{Yexp} is the experimental first yield moment (experimental force at the first yield times the distance between the actuator and soffit). The ratio of M_{YE}/M_{YEexp} was approximately 1.4.

Displacement Control: Displacements were applied quasi-statically to the column stub in 3 cycles: two cycles at the target displacement ductility, followed by one cycle at the displacement ductility of the prior level (see Figure 2-21). Application of reversed cyclic displacements permitted examination of hysteretic loop stability. Displacement ductility demand, as multiples of system effective yield displacement, was applied at the following levels, or until the residual capacity of the specimen dropped below 30% of the maximum load: μ1, μ1.5, μ2, μ3, μ4, μ6, μ8, μ10. (Note: μ1 = nominal (target) displacement ductility of 1.0, μ2 = nominal displacement ductility of 2.0, etc.) The CIP specimen maintained capacity to μ10; however, the stroke capacity was limited in the pull direction to μ8; therefore, four cycles of equal displacement were used for the final stage of loading, prior to application of a monotonic push to failure. Data reduction accounted for the slight additional lateral load applied to the specimen due to the inclination of the vertical actuator under cyclic displacements.

2.3.3 Instrumentation

Extensive instrumentation was used for the test specimen, including internal gages (strain gages mounted on bent cap and column rebar) and external gages (linear potentiometers mounted on the column, joint, and cap). Figures 2-22 through 2-25 show the instrumentation drawings, which define gage locations, and Figure 2-26 through 2-28 show various photos of the instrumentation attached to the specimen. Strain gage as-builts accompany the original drawings to show differences in final gage locations.

Strain gages on column longitudinal bars and hoops were intended to provide evidence of level and distribution of column flexure, including plastic hinging and strain penetration. Strain gages on bent cap longitudinal bars and stirrups, including in the joint region, were expected to provide evidence of joint distress and a force transfer mechanism through and adjacent to the joint.

Linear potentiometers provide column displacement, column curvature, panel deformation, joint rotation, bar slip, and specimen rigid body motion. Column curvature required the use of two linear potentiometers, one on each side of the column, to determine curvature. Four sets were used to divide the column into four curvature cells. Table 2-6 summarizes column curvature cell as-builts. Two sets of panel deformation gages were used to examine joint panel deformation. On the east side of the specimen, five linear potentiometers were used, whereas on the west side a simplified measurement with two linear potentiometers was used. To limit the number of gages, bent cap curvature was not explicitly examined, but the bent cap was assumed to remain essentially elastic; however, strain gages were used to monitor strain levels in the bent cap flexural reinforcement.

In addition to active instrumentation, specimen response was documented using digital photos, crack markings and measurements, video recording, and hand notes.

2.3.4 Pretest Predictions

2.3.4.1 Stages of Cracking

Four stages of initial specimen cracking were examined: 1) initial bent cap cracking in flexure due to gravity loads (specimen self weight plus the vertical actuator force, P_V; 2) initial bent cap cracking in flexure with the additional horizontal actuator force, P_H; 3) initial column flexural cracking; and 4) initial joint cracking.

Table 2-7 summarizes the predicted values of vertical and horizontal actuator loads for the stages of cracking. Bent cap flexural cracking is not expected under specimen self weight and the maximum applied vertical load, P_V, of 38 kips. However, the addition of a minor horizontal load, P_H, of 8 kips is expected to generate the first flexural crack. Column cracking is anticipated at a slightly larger horizontal load of 14

kips. Finally, joint shear cracking is not expected until P_H reaches a large value of 48 kips. It should be noted that prediction of cracking load is considered an estimate, as it depends on the highly variable tensile strength of concrete.

2.3.4.2 Lateral Load-Lateral Displacement Envelope

An envelope of the lateral load-lateral displacement response of the column was predicted before testing, as shown in Figure 2-29. Deflection at each stage was taken as the sum of the column displacements due to column elastic deflection to yield, column plastic deflection, column shear, and bent cap flexibility.

Flexural component contributions were calculated using moment-curvature results from the sectional analysis software which used stress-strain models for the concrete and steel based on actual material tests of the concrete and steel used in the specimen. An effective yield curvature based on a bilinear moment-curvature response with best fit secondary stiffness was used to define the member effective yield displacement, Δ_{ye}. Various levels of displacement ductility were established as a multiple of the effective yield displacement of the system, Δ_{YE}.

2.3.4.3 Moment-Curvature Envelope

An envelope of the normalized moment-curvature response of the column was also predicted, using the sectional analysis software, XTRACT, as shown in Figure 2-30. [17] Note that the curvature is normalized by multiplying curvature by the column diameter; moment was not modified.

2.4 Tables

Table 2-1. Comparison of Reinforcement for CIP Prototype and CIP Specimen

CIP		Prototype Design	Similitude [or Design] Requirement	Test Specimen	Specimen to Similitude [or Design] Ratio
Column					
Longitudinal Reinforcement					
Bar Size (diameter, in)		#11 (1.41)	0.59	#5 (0.63)	1.06
No. of bars		16	14	16	1.14
f_y	ksi	66.0	—	64.5	—
ρ		0.0138	0.0138	0.0158	1.14
M_n^*	K·ft	3760	272	222	0.82
M_n/D_c^3	K·ft/ft^3	58.7	58.7	48.0	0.80
Transverse Reinforcement					
Bar Size (diameter, in)		#6 (0.75)	0.31	#3 (0.38)	1.20
Spacing	in	3.0	[1.8]	2.0	[1.11]
f_y	ksi	66.0	—	68.2	—
ρ		0.0139	0.0139	0.0125	0.90
Bent Cap					
Longitudinal Reinforcement					
Bar Size (diameter, in)		#11 (1.41)	0.59	#5 (0.63)	1.06
No. of bars		12	—	12	—
f_y	ksi	66.0	—	64.5	—
ρ		0.0051	0.0051	0.0065	1.27
M_n^*	K·ft	6680	483	454	0.94
M_n/bh^2	K·ft/ft^3	44.2	44.2	50.2	1.14
Transverse Reinforcement					
Bar Size (diameter, in)		#6 (0.75)	0.31	#3 (0.38)	1.20
Spacing	in	12.0	[8.4]	6.0	[0.71]
f_y	ksi	66.0	—	68.2	—
Joint					
Inside Joint					
Transverse Reinforcement (ρ_s)					
Bar Size (diameter, in)		#6 (0.75)	—	#3 (0.38)	—
Spacing	in	3.0	—	5.0	—
ρ_s/ρ_{min}		5.56†	—	1.22	—
f_y	ksi	66.0	—	68.2	—
Side Face Reinforcement (A_s^{sf})					
No. of bars - Bar Size		8 - #6	—	4 - #3	—
A_s/A_{cap}	in^2/ in^2	0.19	[0.10]	0.12	[1.20]
f_y	ksi	60.0	—	68.2	—
Construction Stirrups					
No. of bars - Bar Size		2 2-leg – #6	—	2 2-leg - #3	—
Area	in^2	1.76	—	0.44	—
f_y	ksi	66.0	—	68.2	—
Adjacent to Joint					
Vertical Stirrups (A_s^{jv})					
No. of bars - Bar Size		5 4-leg - #6	—	3 4-leg - #3	—
Spacing	in	6.0	—	5.0	—
A_s^{jv}/A_{st}	in^2/ in^2	0.35	[0.20]	0.27	[1.33]
f_y	ksi	66.0	—	68.2	—
Horizontal Ties (A_s^{jh})					
No. of bars - Bar Size		4 - #6	—	2 - #3	—
Spacing	in	12.0	—	8.0	—
A_s^{jh}/A_{st}	in^2/ in^2	0.35	[0.10]	0.13	[1.33]
f_y	ksi	66.0	—	68.2	—

Note: Prototype and Specimen Design per 2006 LRFD RSGS [10]

* Nominal moment @ ε_c=0.003

† Represents extension of column hoops into joint

Table 2-2. Concrete Mix Proportions

Material Designation	(Based on Saturated Surface Dry)		
	Quantity	Weight (lbs)	Volume (ft^3)
ASTM C 150 – Type I/II		564	2.87
ASTM C 33 – 3/8"		1,826	10.92
ASTM C 33 – Concrete Sand		1,217	7.39
ASTM C 494 - Superplasticizer	45 oz	3	0.05
Water	W/C=0.49	276	4.43
Total Air Content	5.00%		1.35
TOTAL		3,886	27.0

Table 2-3. Concrete Properties

Parameter	Design	Actual
Slump	5½" +/- 2½"	< 3 in, cap and column
Unit Weight	143.9 pcf	N/A
Compressive Strength	4000 psi (28 day)	Cap: 4553 psi (137 days) Column: 6178 psi (194 days)
Tensile Strength (Split Cylinder)	N/A	Cap: 361 psi ($5.35\sqrt{f_c^{'}}$, 138 days) Column: 452 psi ($5.75\sqrt{f_c^{'}}$, 195 days)
Modulus of Elasticity	N/A	Cap: 3811 ksi (137 days) Column: 4033 ksi (194 days)

Table 2-4. Yield and Tensile Strength of Reinforcing Bars

Rebar Size	Type	Yield Strength (ksi)	Tensile Strength (ksi)
#3	Bent cap stirrups; Column hoops	68.2	95.5
#5	Bent cap longitudinal; Column longitudinal	64.5	90.0

*Due to testing limitations, yield strength was taken as value of first data point indicating strain hardening. Actual value of yield strength may be slightly lower than listed value.

Table 2-5. Significant Column As-builts

Description	Drawing	As-built
Length of column reinforcement embedded into bent cap, l_{ac}	22 in	23 in +/- 1/2 in (average)
Column hoop spacing within plastic hinge	2 in	2 in +/- 1/2 in
First column hoop below top of column	≤1 in	1.56 in (ave); varied due to interference with threaded rod

Table 2-6. Column Curvature Cell As-builts

Cell Number	Drawing		CIP	
	Cell Height (in)	Cell Width (in)	Cell Height (in)	Cell Width (in)
Cell 1	3.5	26	3.67	26.79
Cell 2	3.0	26	3.00	26.04
Cell 3	4.0	26	4.14	26.01
Cell 4	9.5	26	9.25	26.07

Table 2-7. Predicted Stages of Specimen Cracking

Stage	Load (kips)	
	P_V	P_H
Bent Cap—Flexural	None	-
	38.0	8.4
Column—Flexural	38.0	14.0
Joint Shear	38.0	48.3

2.5 Figures

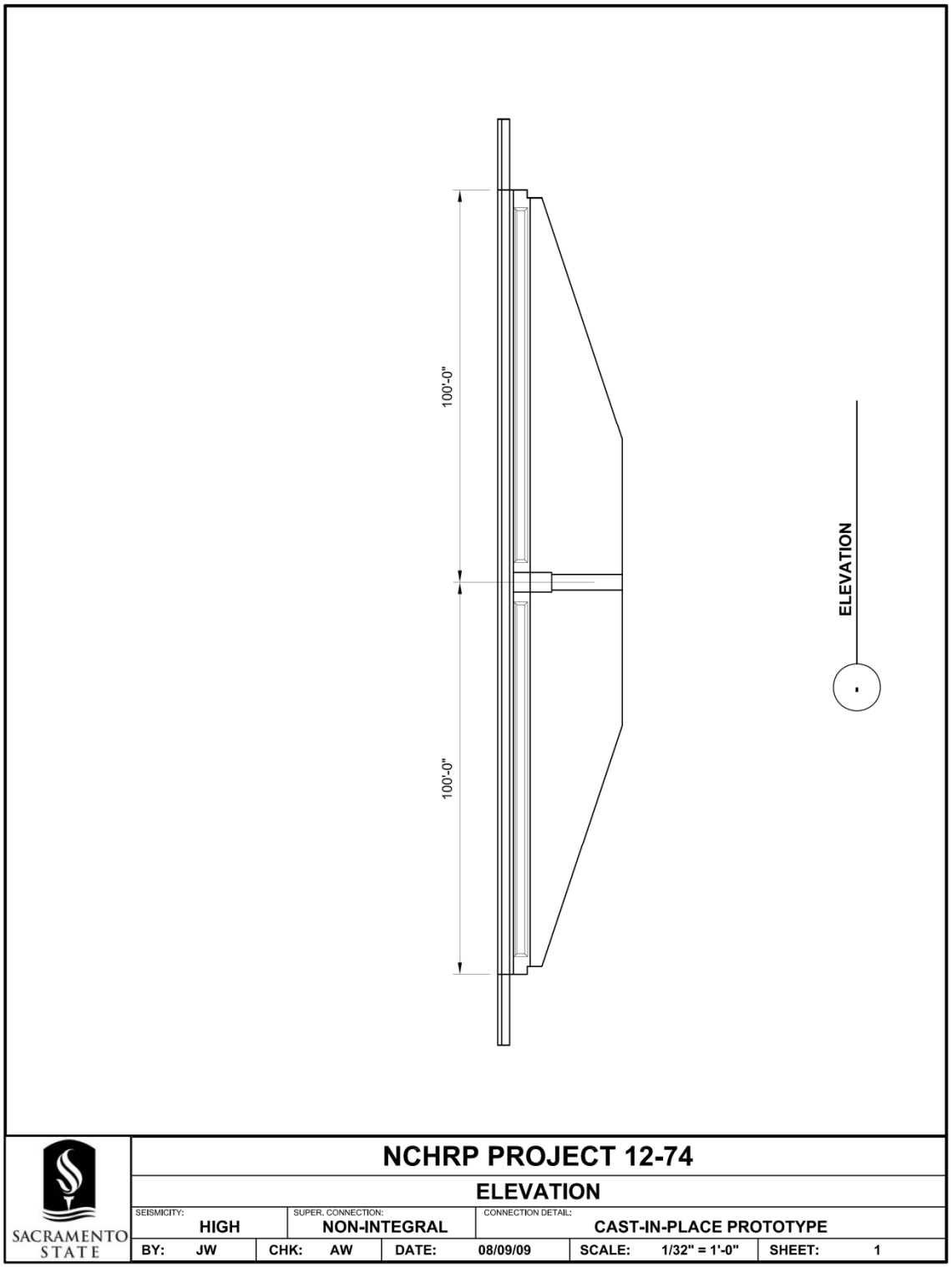

Figure 2-1. Prototype 2-Span Bridge with Nonintegral Bent Cap—Elevation

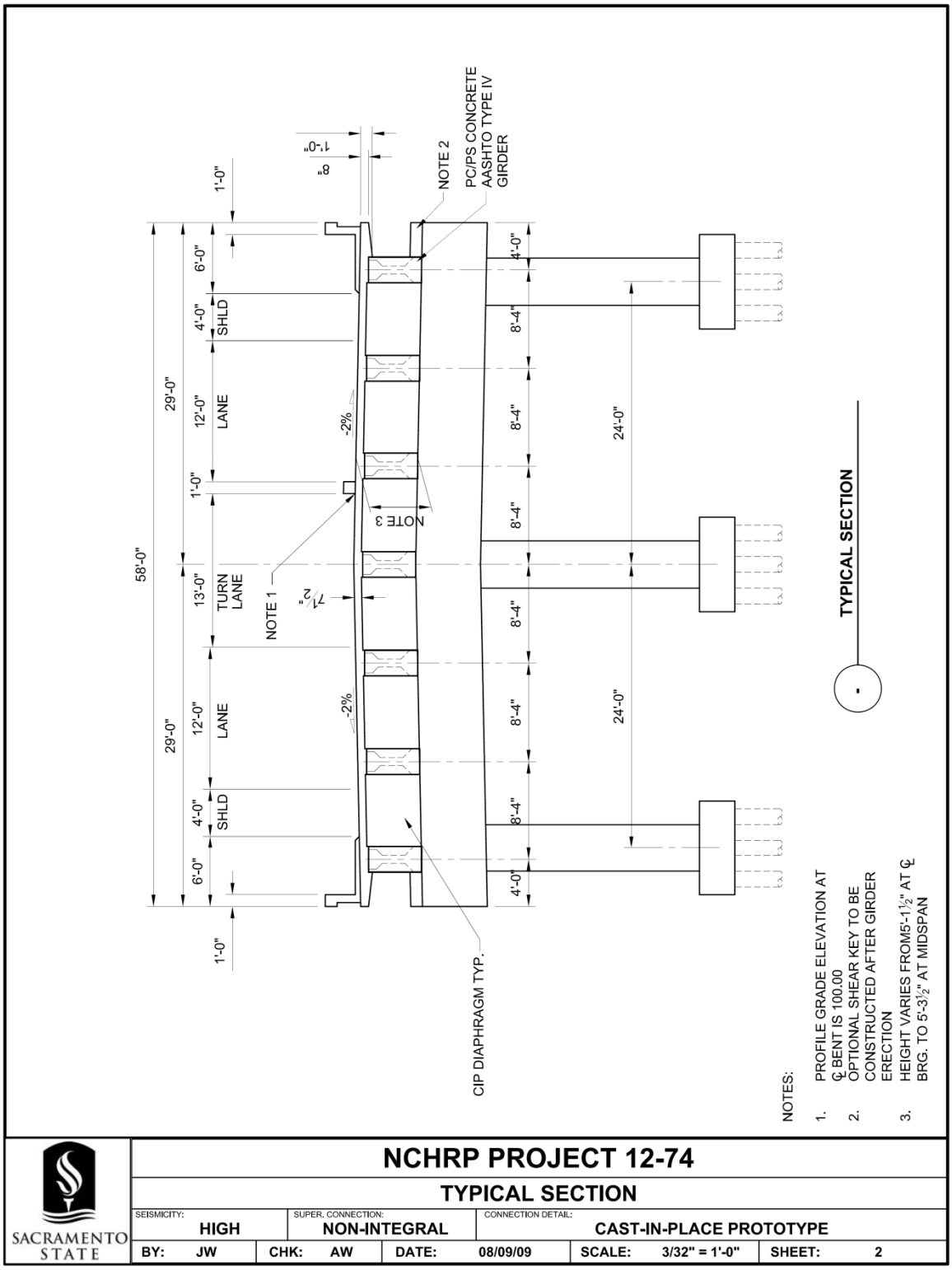

Figure 2-2. Prototype Bridge—Typical Section

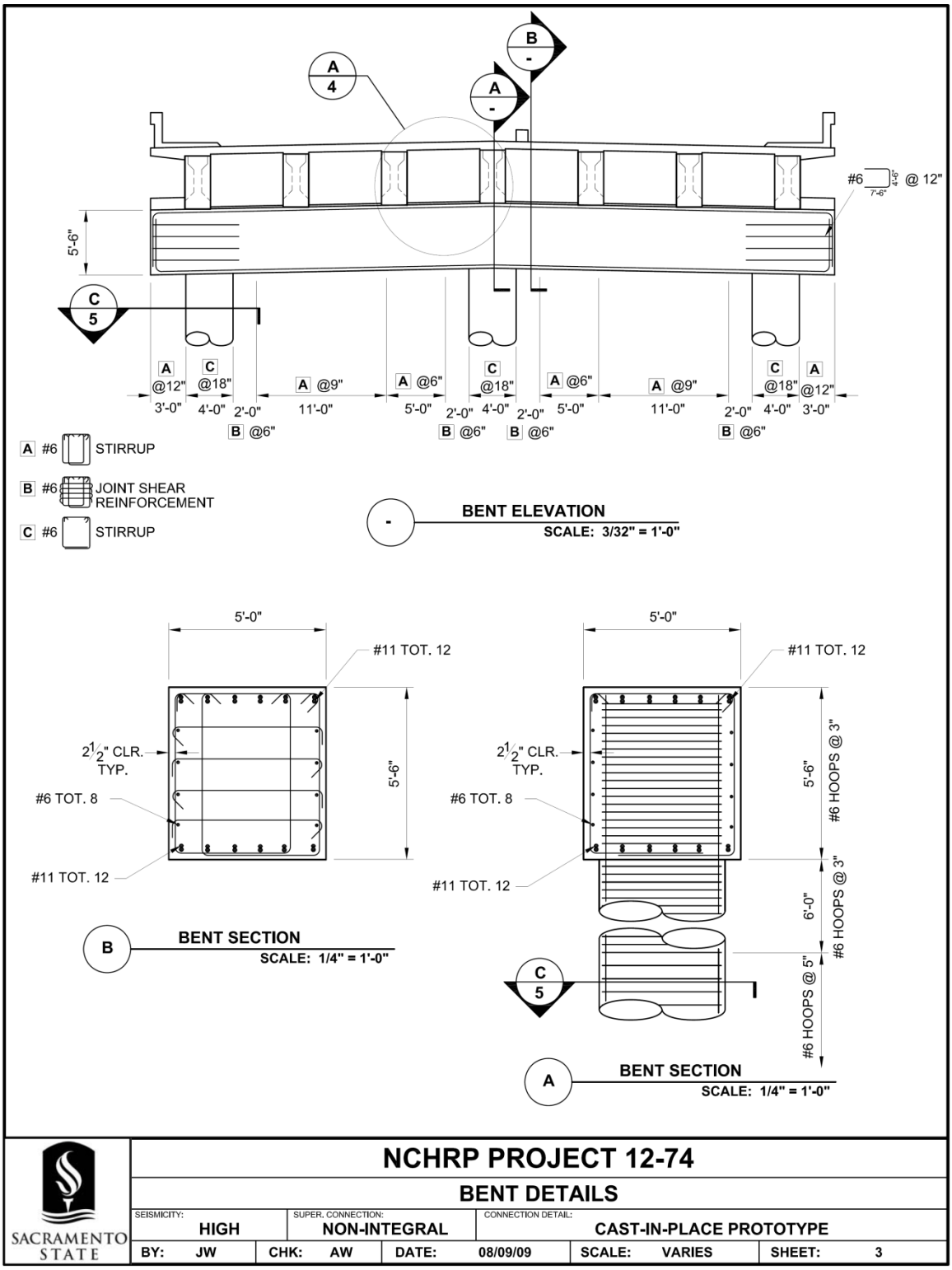

Figure 2-3. Prototype Bridge—Bent Details, Part 1

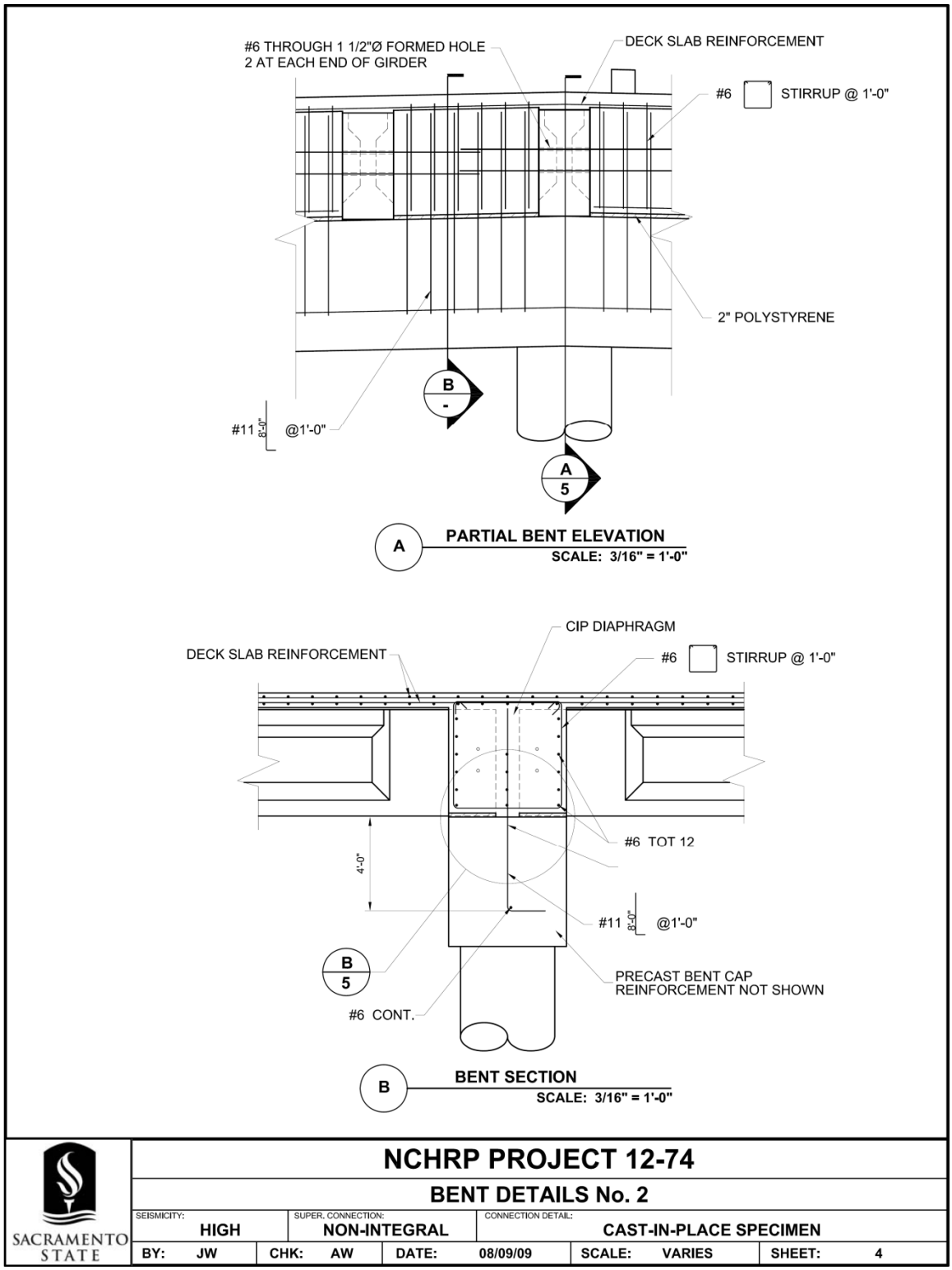

Figure 2-4. Prototype Bridge—Bent Details, Part 2

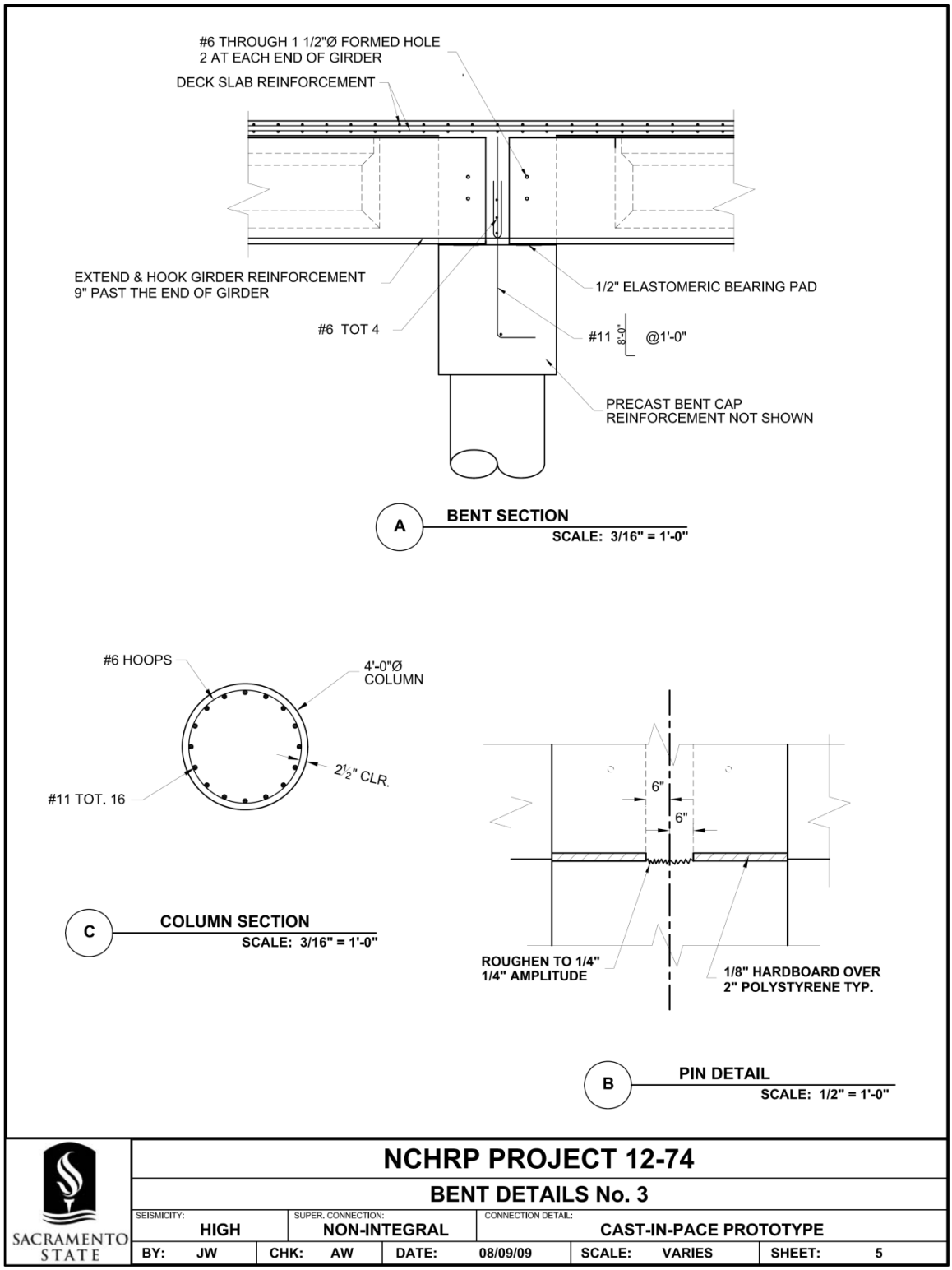

Figure 2-5. Prototype Bridge—Bent Details, Part 3

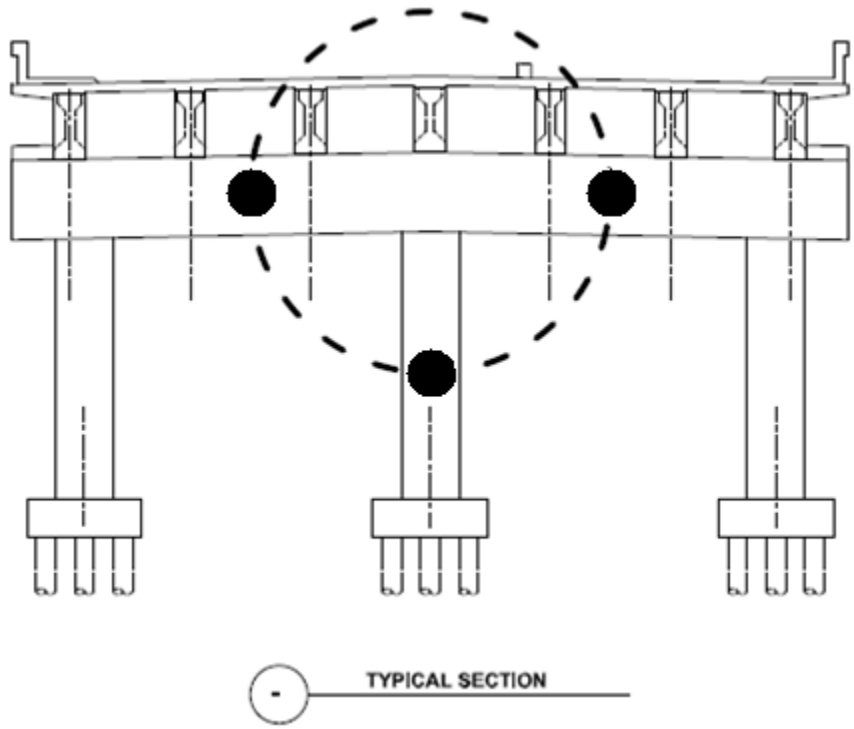

Figure 2-6. Portion of Prototype Used for Specimen Design

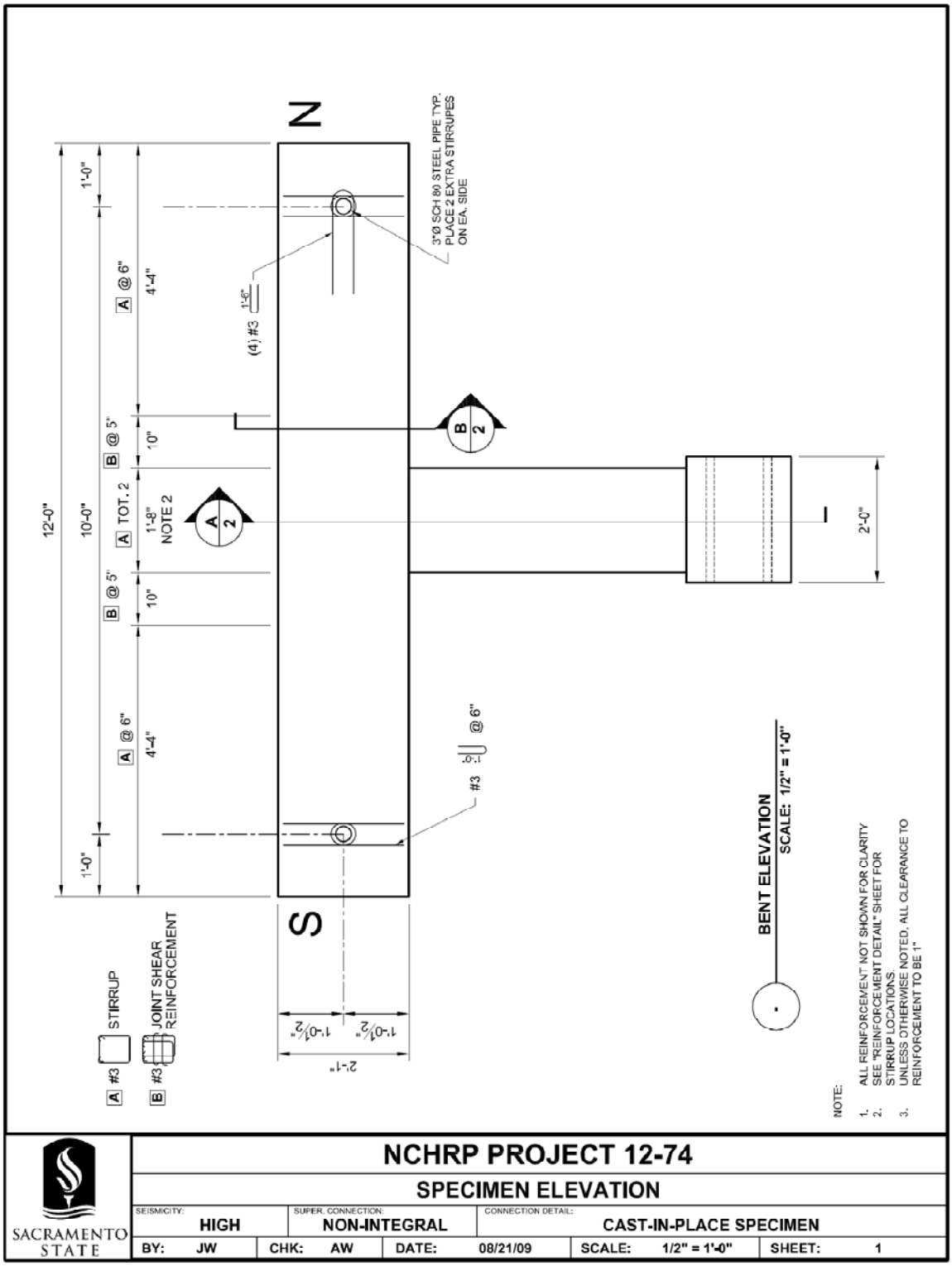

Figure 2-7. Cast-in-Place Specimen Design—Elevation

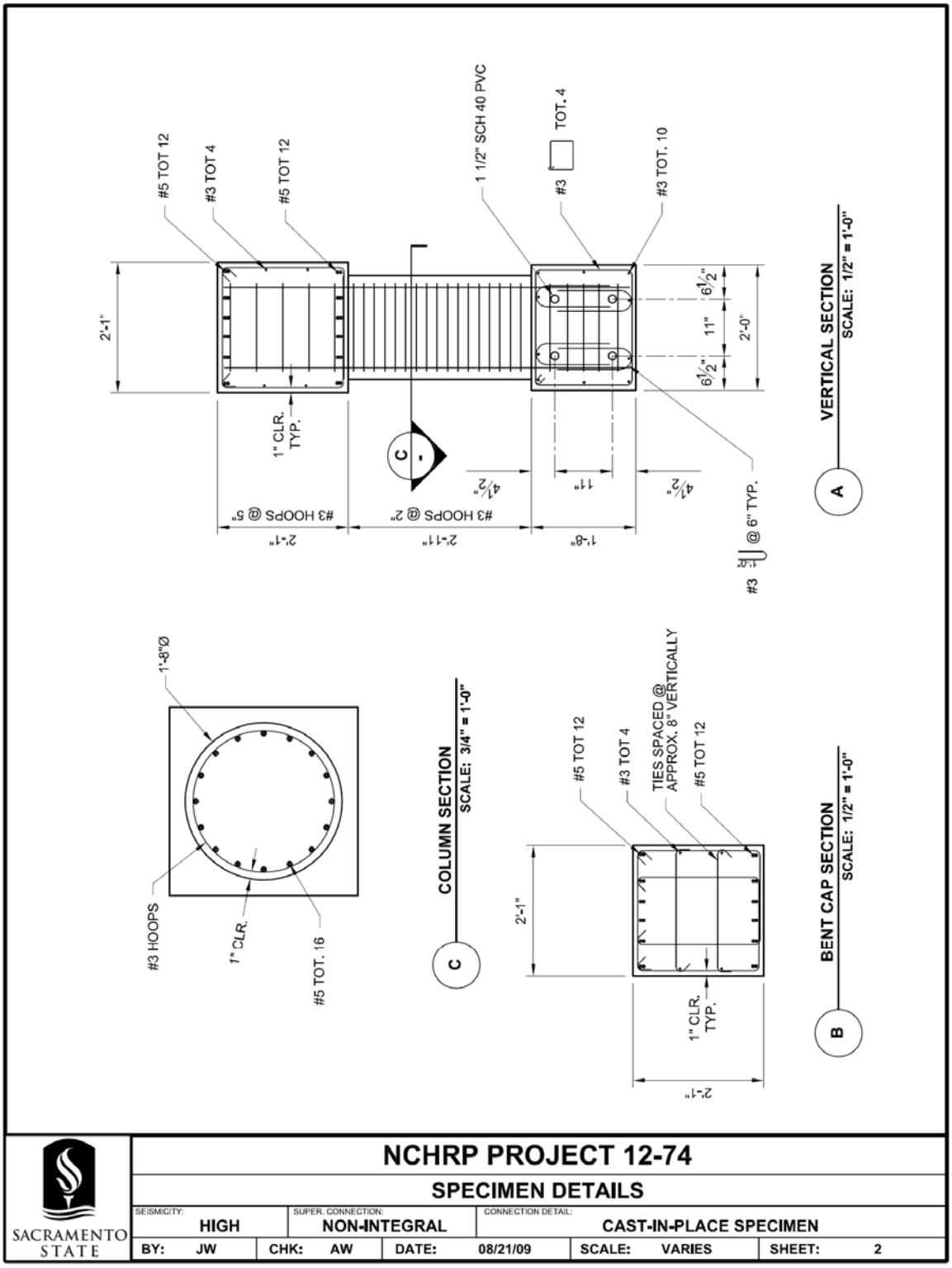

Figure 2-8. Cast-in-Place Specimen Design—Bent Cap and Column Sections

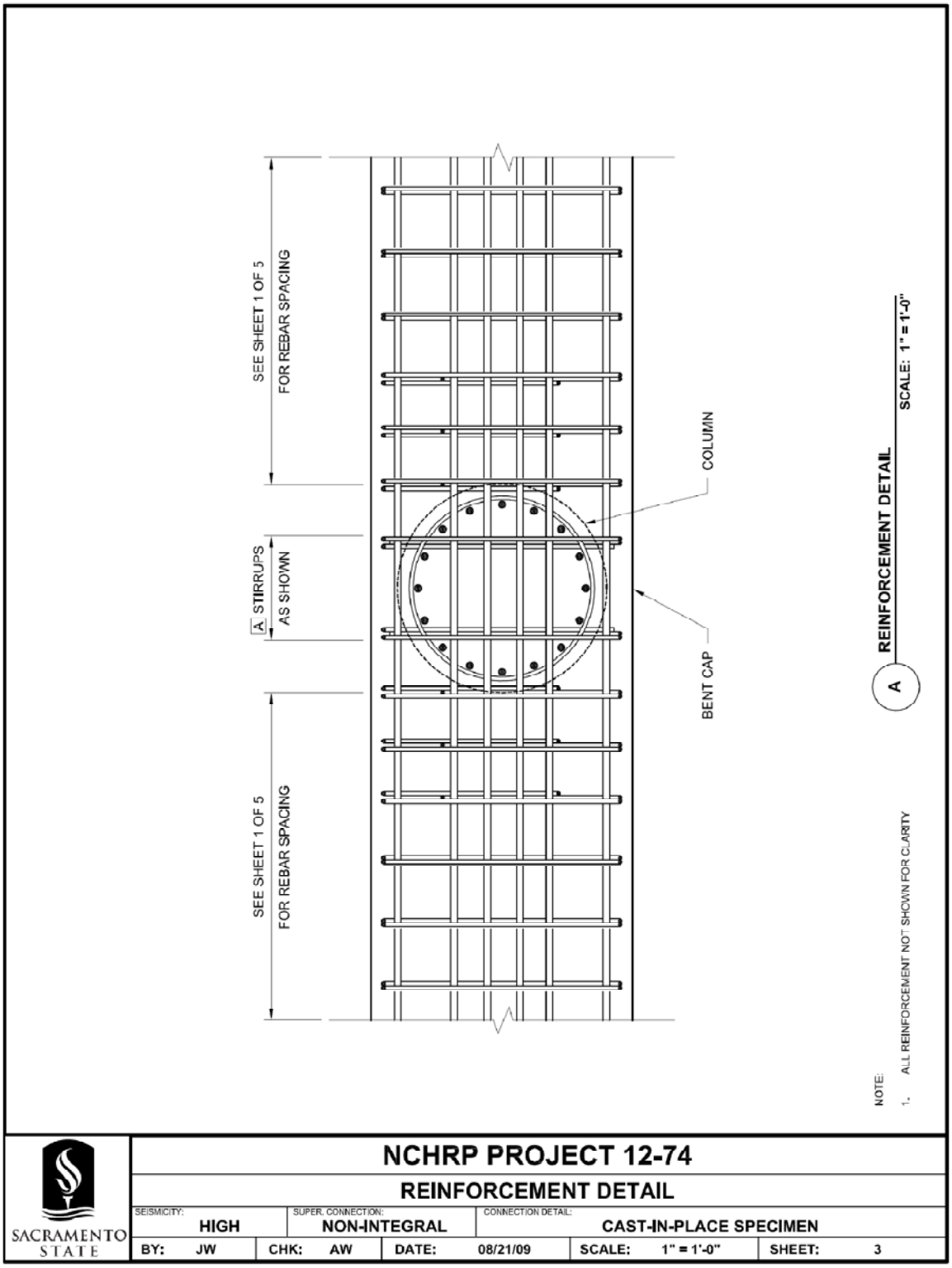

Figure 2-9. Cast-in-Place Specimen Design—Bent Cap Reinforcement Detail

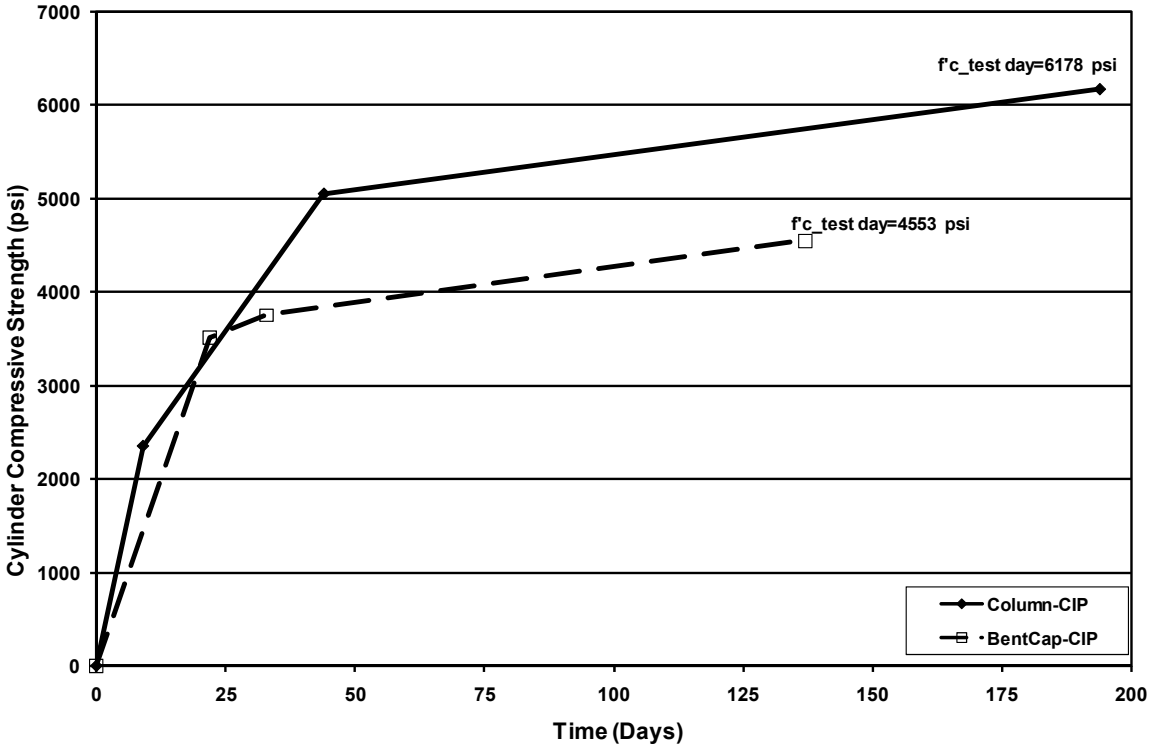

Figure 2-10. Concrete Cylinder Compressive Strength vs. Time

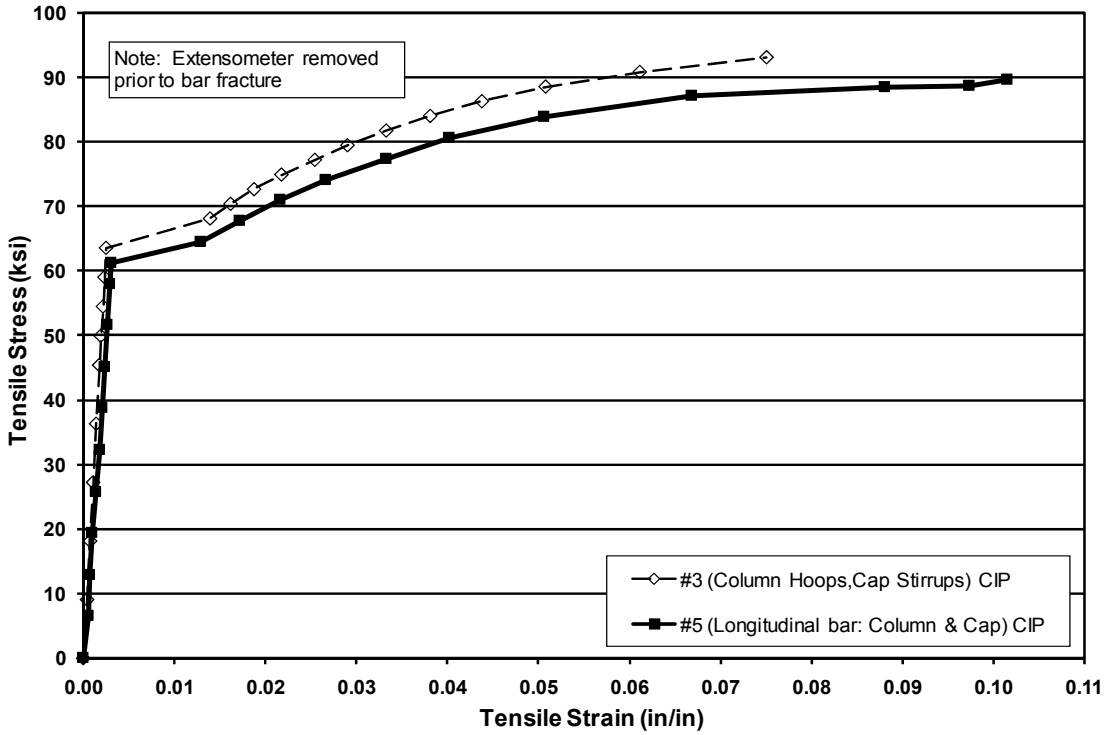

Figure 2-11. Tensile Stress-Strain for Reinforcing Bars

Figure 2-12. Assembly of Column Rebar Cage

Figure 2-13. Assembly of Bent Cap Form above Column

Figure 2-14. Lowering Bent Cap Rebar Cage into Elevated Formwork

Figure 2-15. Bent Cap Rebar Cage in Form during Fabrication

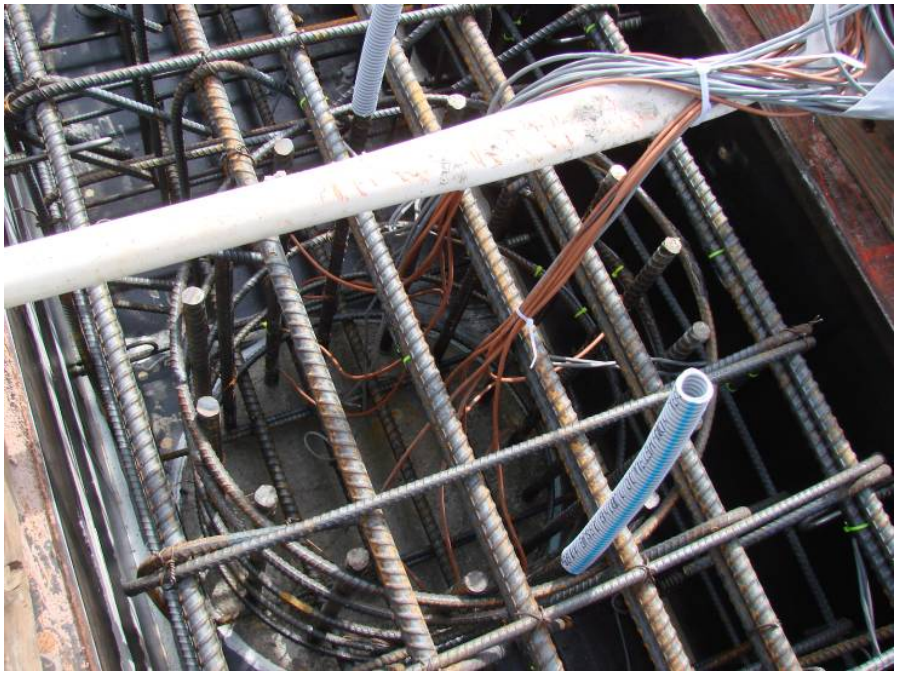

Figure 2-16. Joint Region of Bent Cap during Fabrication

Figure 2-17. Casting of Bent Cap

Figure 2-18. Inverting the Specimen at Clark Pacific

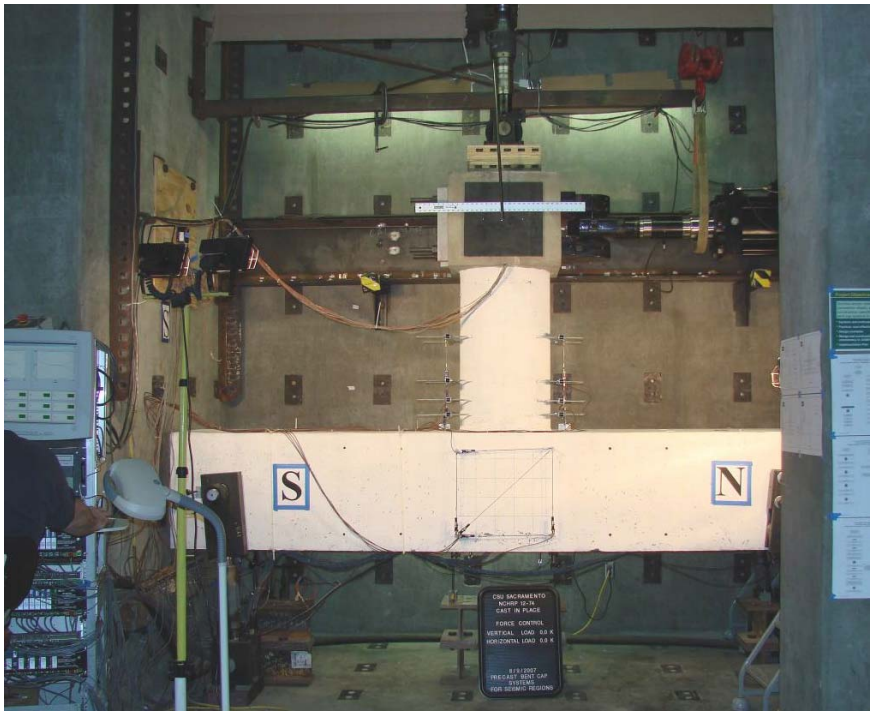

Figure 2-19. Specimen in Preparation for Testing

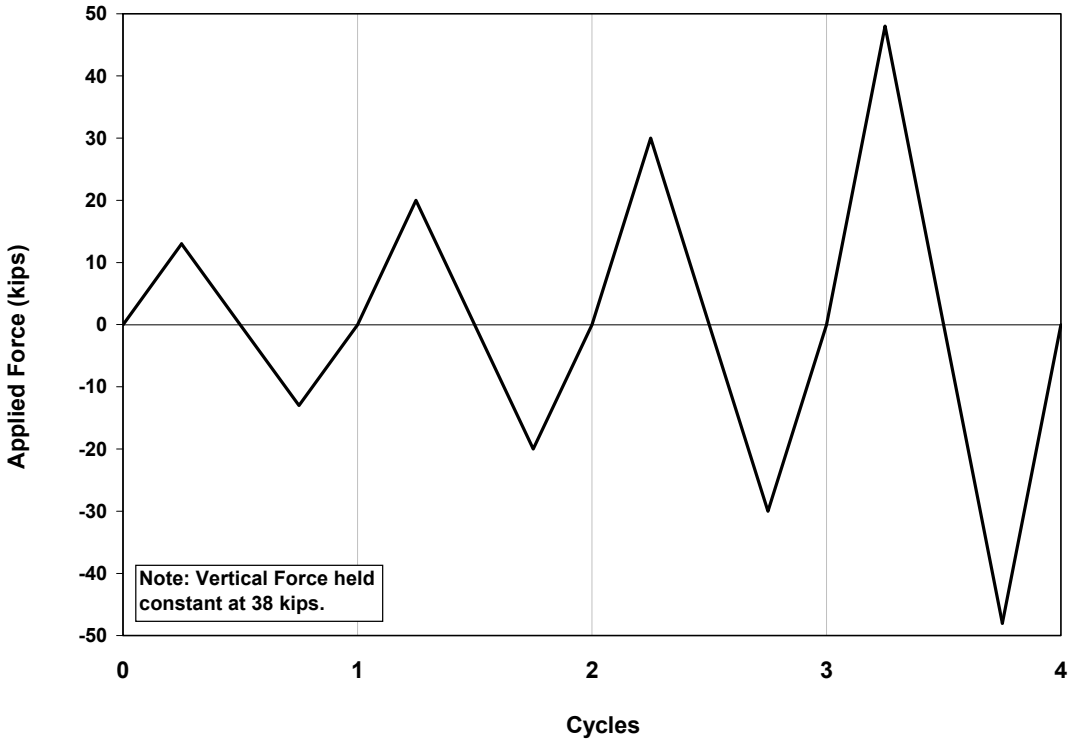

Figure 2-20. Force Control Sequence

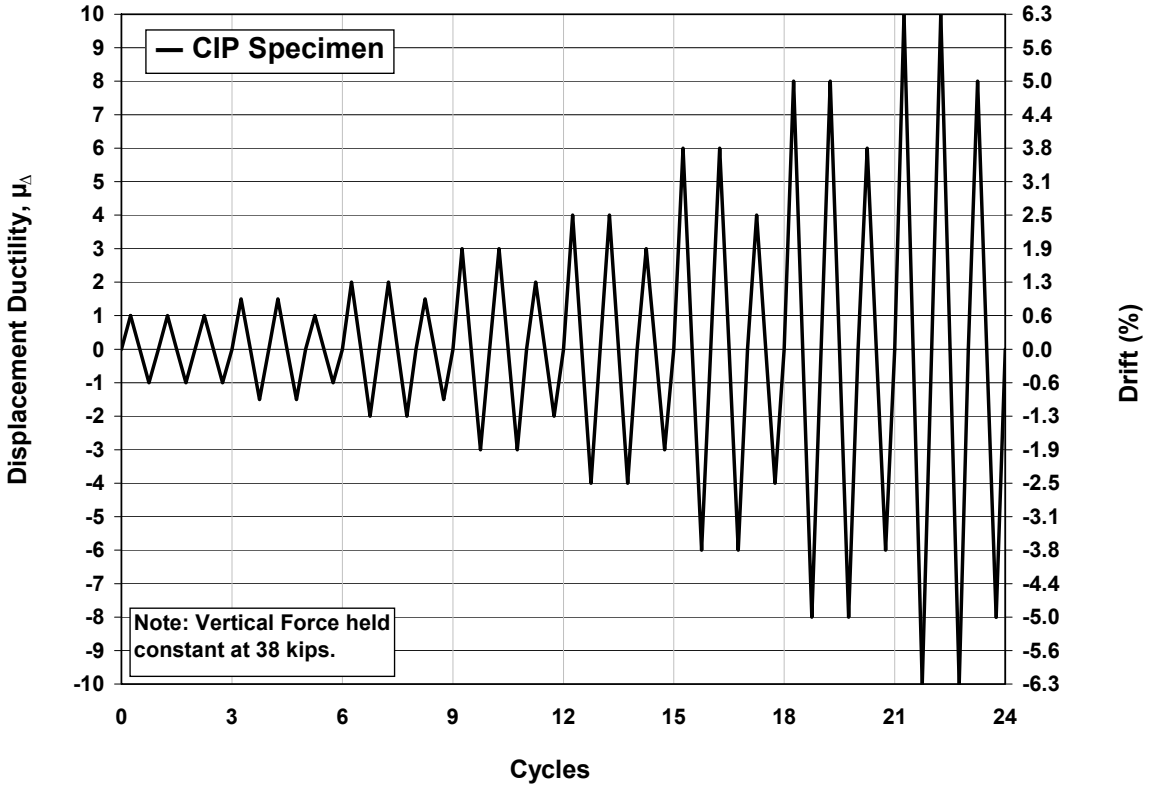

Figure 2-21. Displacement Control Sequence

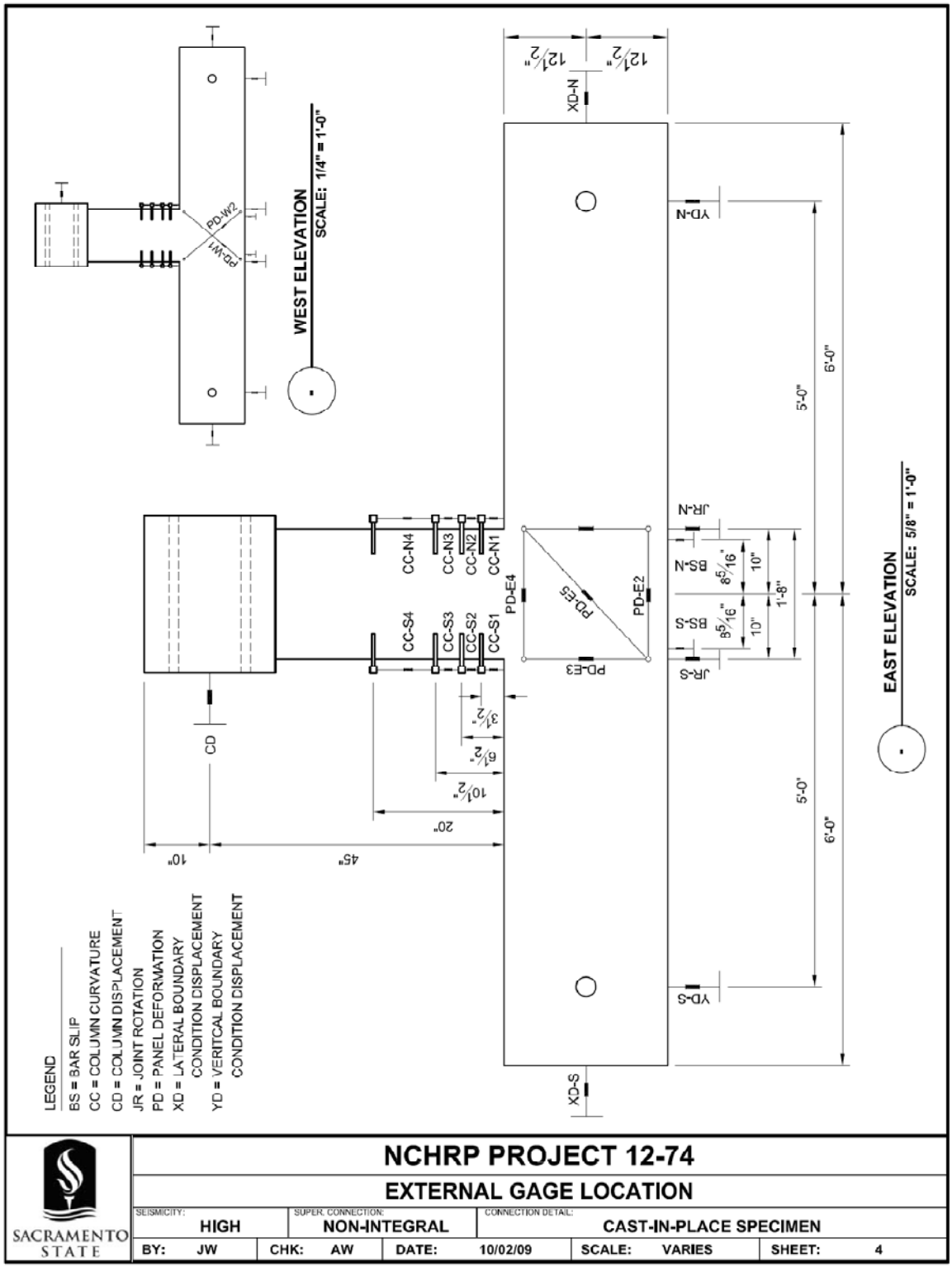

Figure 2-22. Instrumentation Drawings—External Gage ID

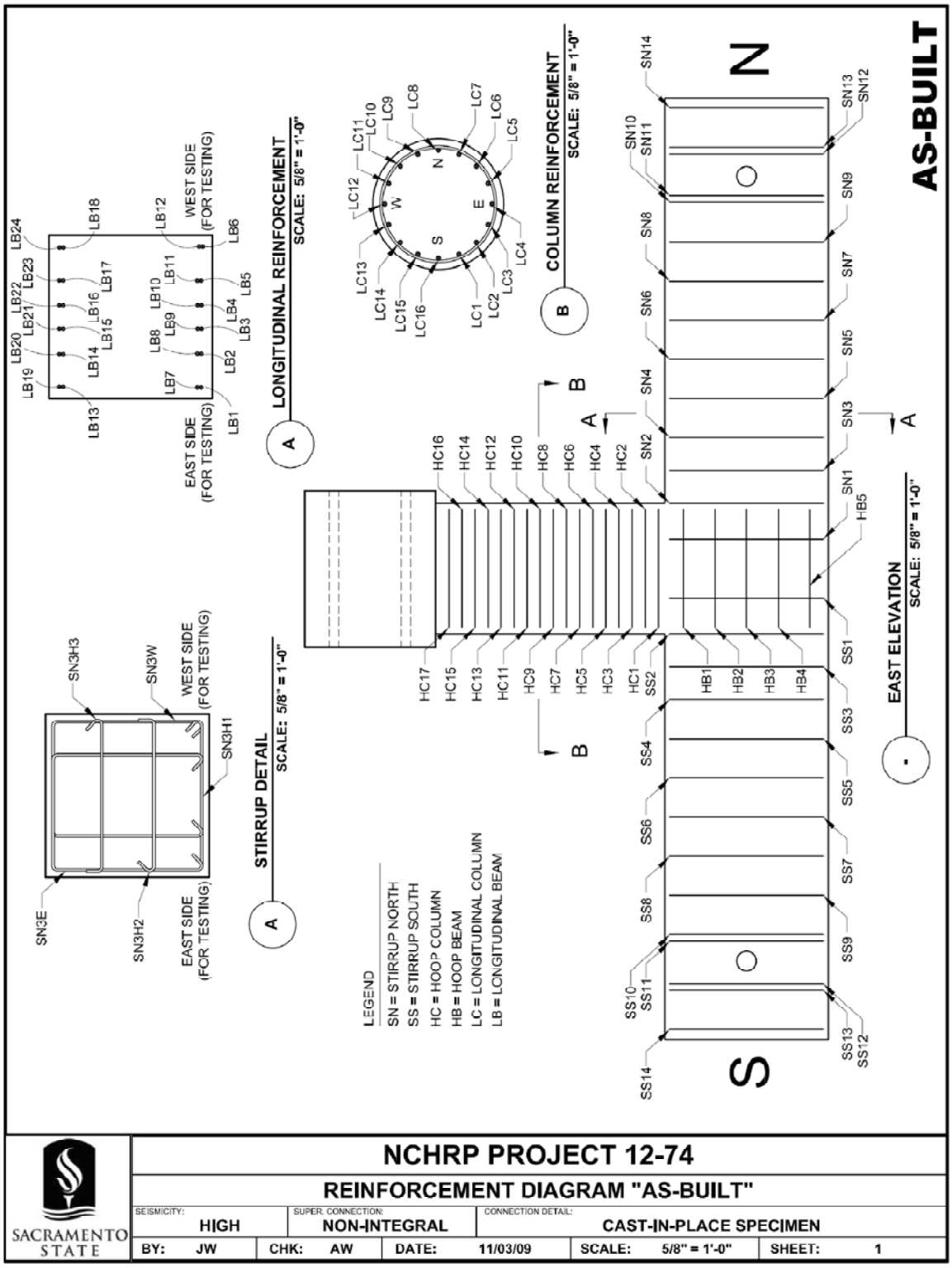

Figure 2-23. Instrumentation Drawings—Reinforcing Bar ID (As-built)

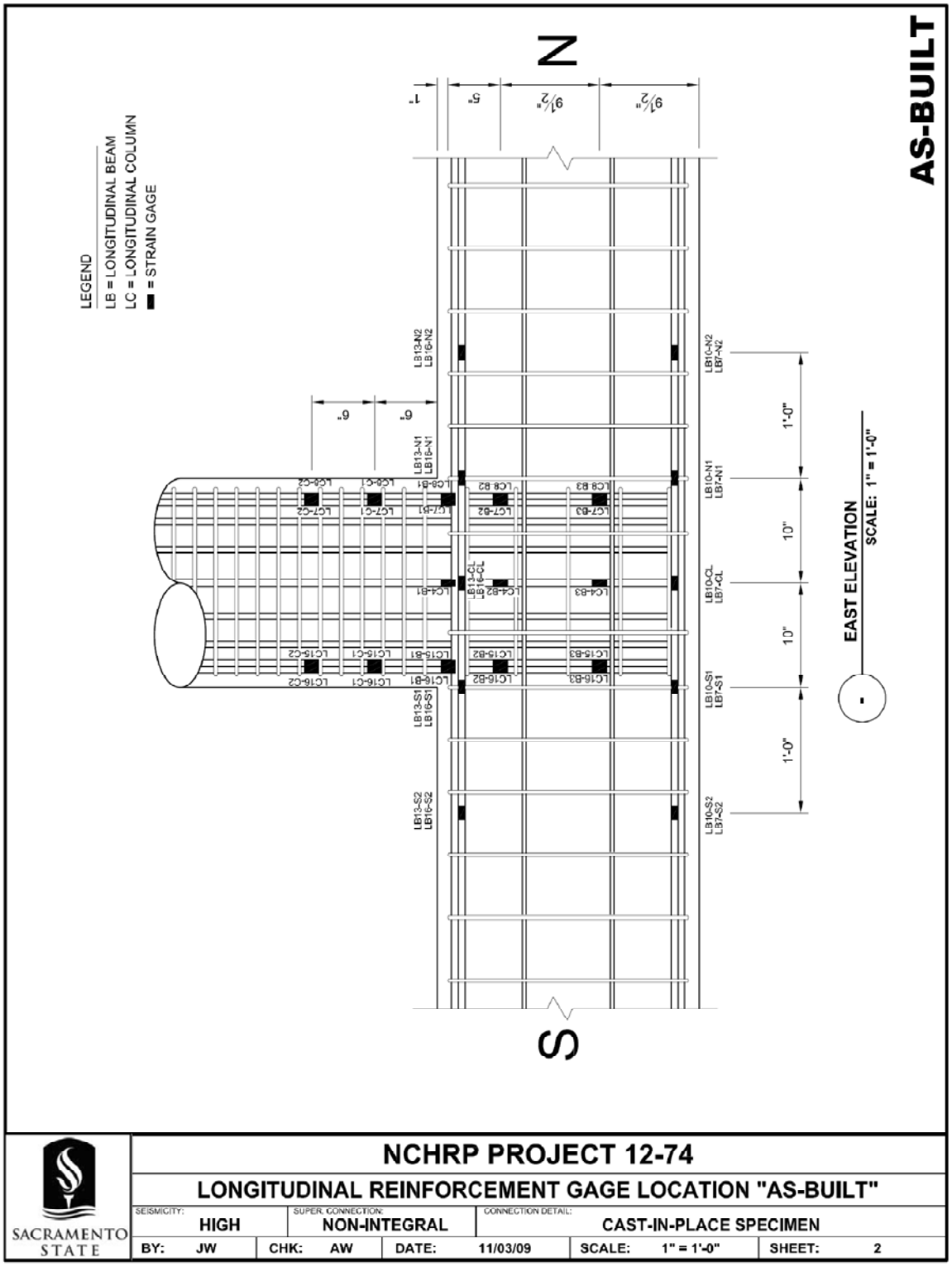

Figure 2-24. Instrumentation Drawings— Longitudinal Reinforcement Strain Gage Locations (As-built)

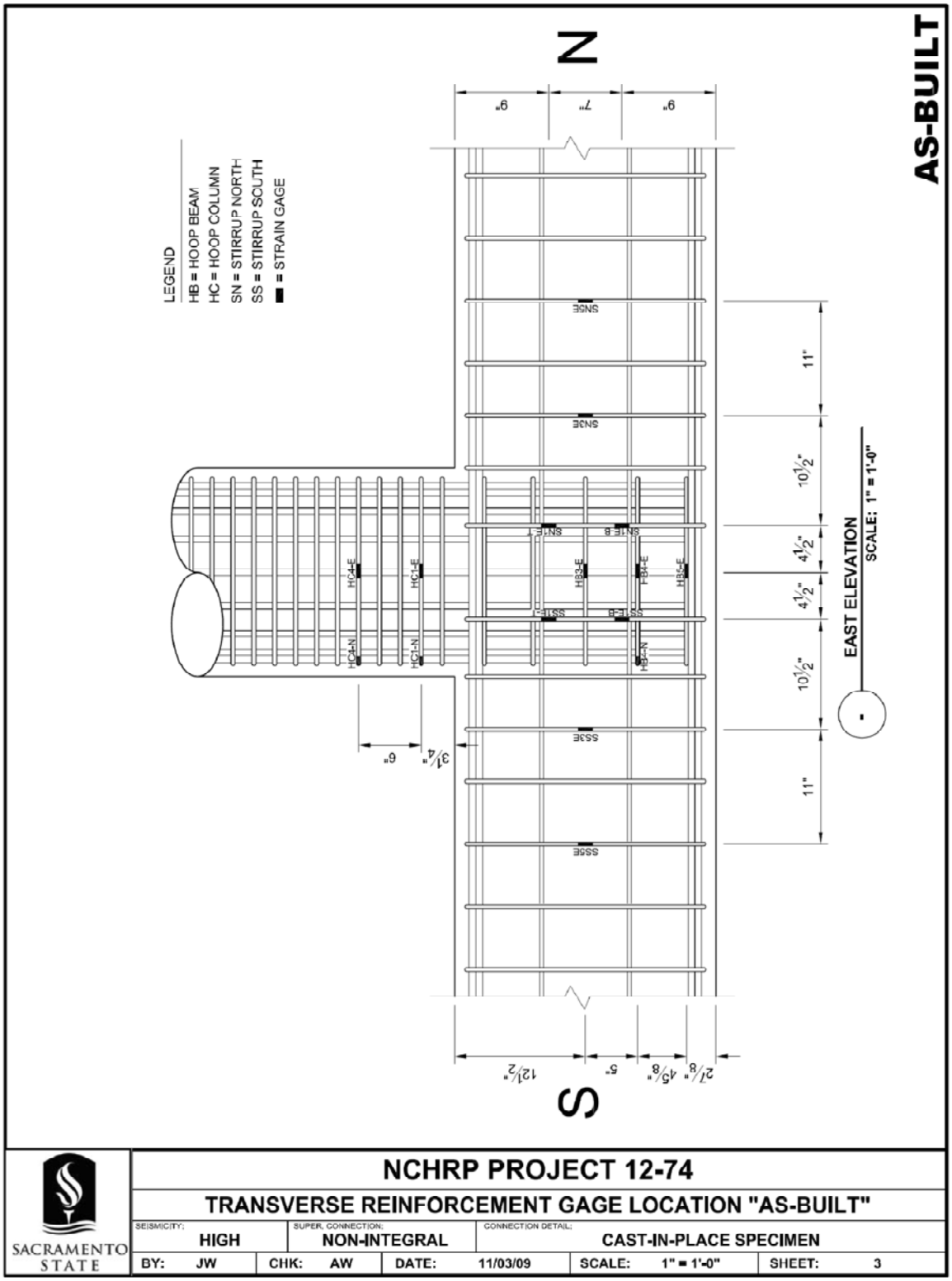

Figure 2-25. Instrumentation Drawings— Transverse Reinforcement Strain Gage Locations (As-built)

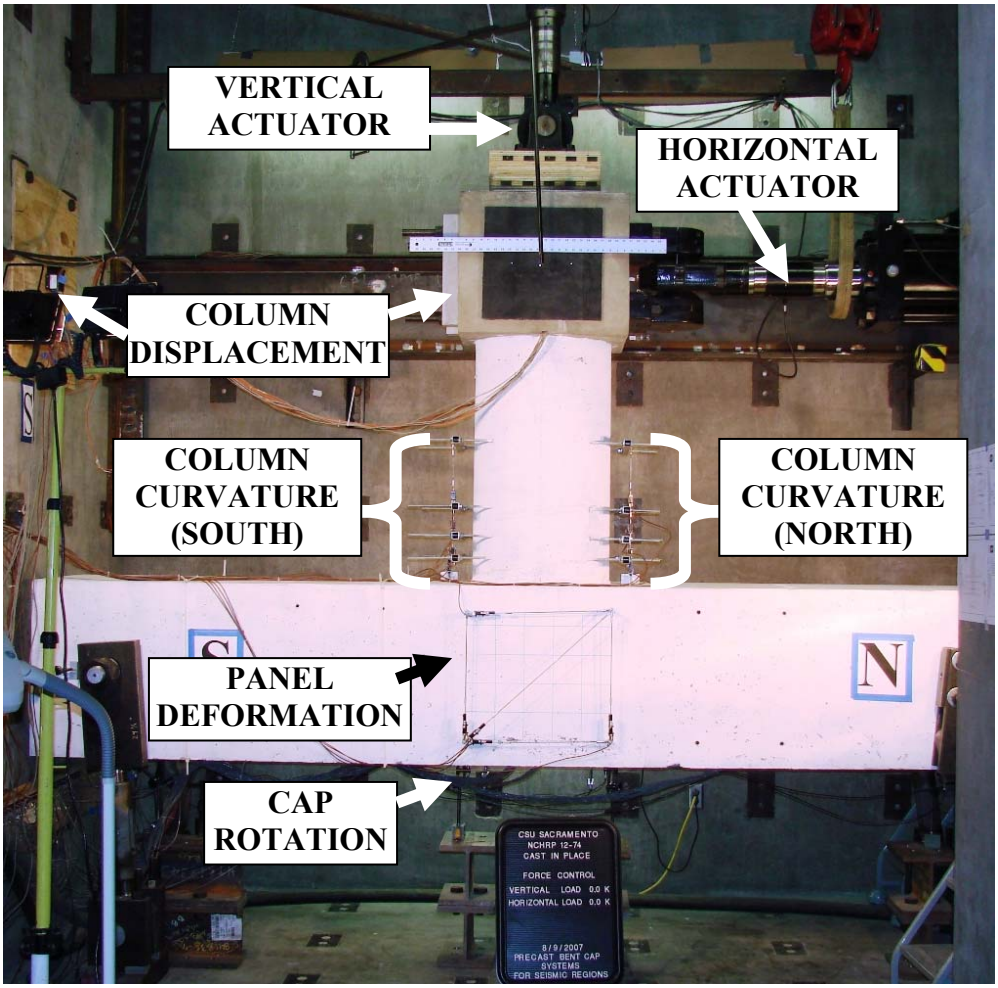

Figure 2-26. Instrumentation Photos—Overall View

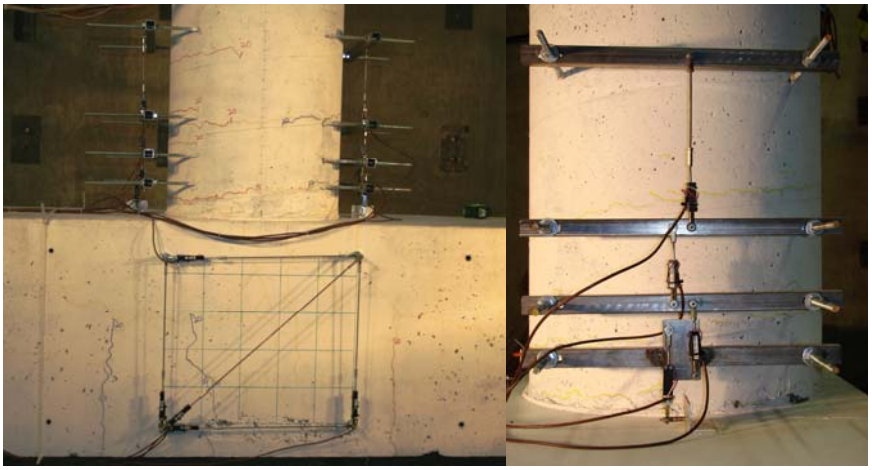
Figure 2-27. Instrumentation Photos—Panel Deformation and Column Curvature

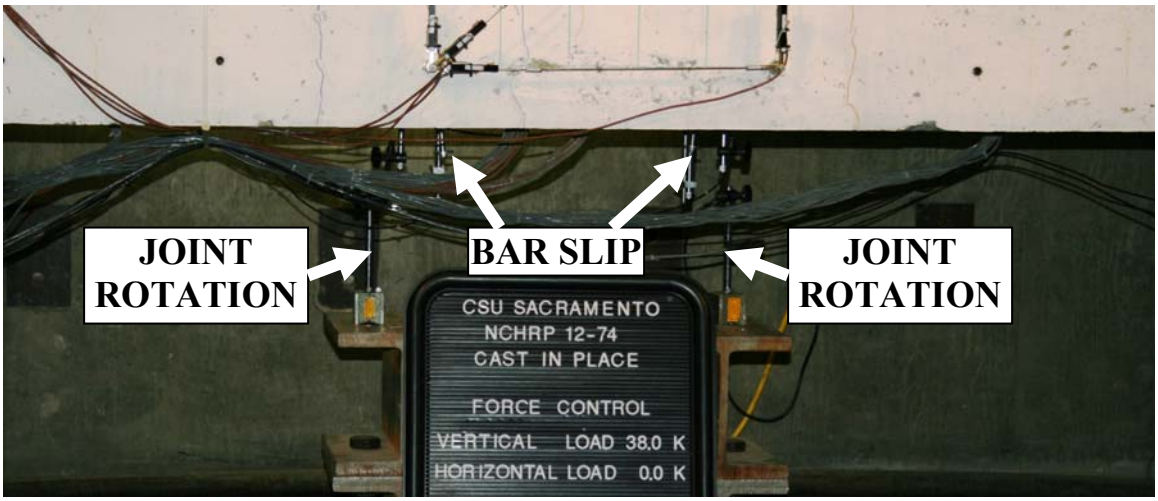

Figure 2-28. Instrumentation Photos— Joint Rotation and Bar Slip

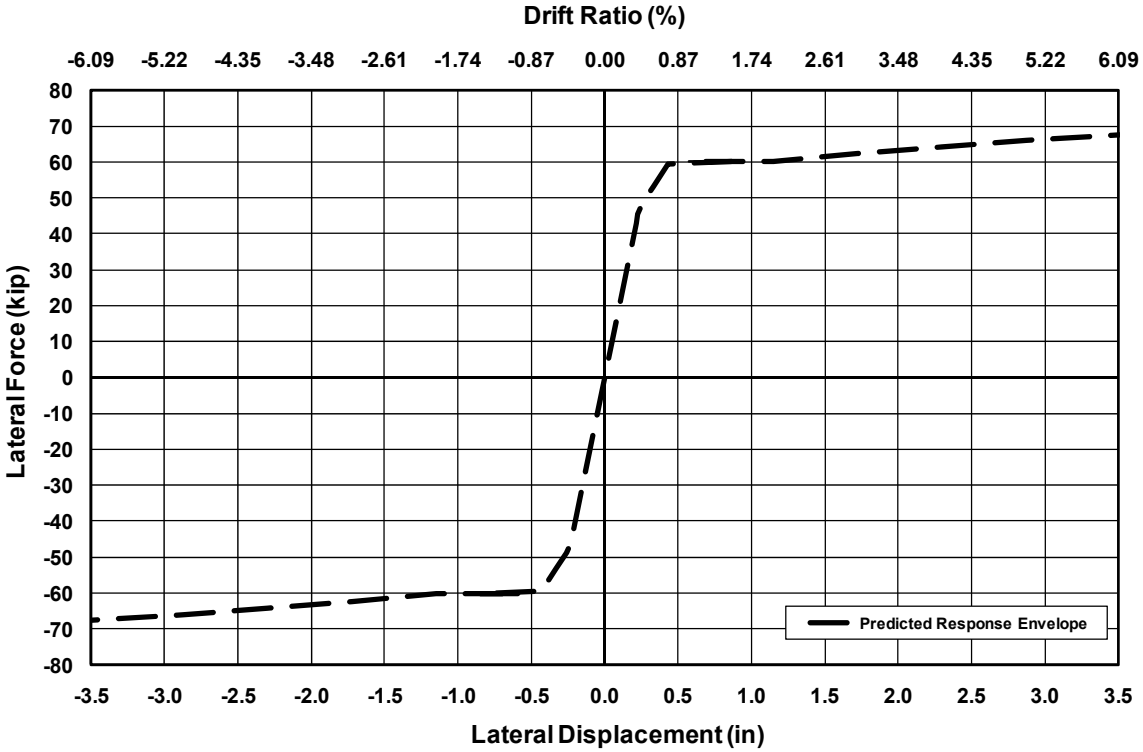

Figure 2-29. Predicted Lateral Force vs. Lateral Displacement Envelope

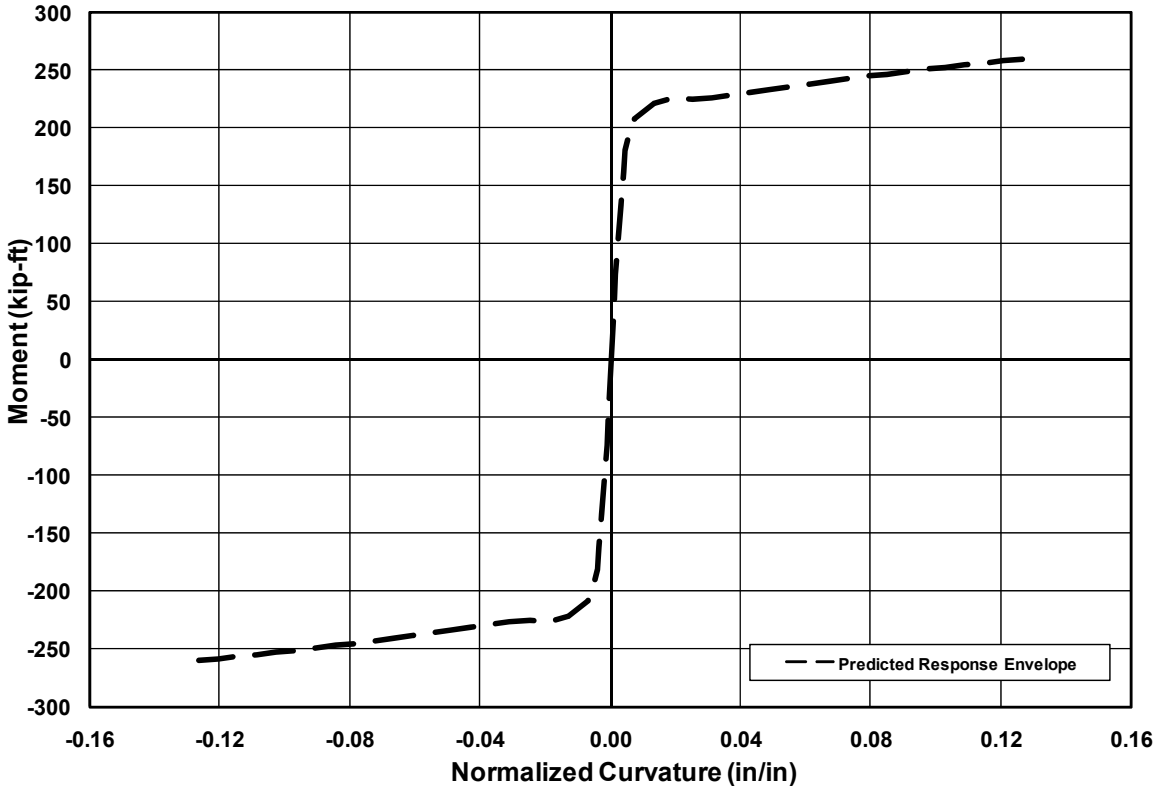

Figure 2-30. Predicted Normalized Moment-Curvature Envelope

3.0 Specimen Response and Analysis

3.1 Experimental Observations

This section summarizes experimental observations made during testing, based on visual inspection and digital photos. Photos of the specimen include color-coded markings adjacent to cracks, as follows:

- Yellow: Pre-existing cracks
- Brown: Cracks that formed or extended under vertical actuator loading
- Blue: Cracks that formed or extended under push direction loading
- Red: Cracks that formed or extended under pull direction loading

Markings also included: 1) load level or displacement ductility level; 2) transverse mark perpendicular to marking to identify end of crack. Crack widths were measured while the specimen load or displacement was held nearly constant.

In reporting specimen response, displacement is given in terms of both displacement ductility, μ, and drift ratio. (Note: "drift ratio" and "drift" are used interchangeably.) Drift ratio is defined as the column displacement divided by the column height, as a percent. This is a more consistent basis for comparison of specimen response. System ductility levels are also reported but, though reasonable, should be considered representative or nominal (i.e., approximate) due to the approximate determination of first yield previously mentioned. Table 3-1 summarizes the associated values of force, displacement, displacement ductility, and drift ratio for Force Control and Displacement Control stages (push and pull, Cycle 1).

3.1.1 Stages of Cracking

The specimen was observed for crack formation and growth under loading sequences. Few pre-existing cracks were noted. Table 3-2 compares the predicted and actual stages of specimen cracking under Force Control and shows initial cracking very close to the predicted loads. Cracks first formed under push direction loading and crack widths did not exceed 0.009 in. Figure 3-1 shows the specimen crack pattern at the end of the Force Control sequence (48 kips).

3.1.2 Select Observations

Specimen response was dominated by plastic hinging of the column adjacent to the bent cap, as intended by the specimen design. This is clearly shown in Figures 3-2 through 3-5, which document response for increasing drift ratios (μ2 to μ8). In contrast to the significant column flexural (and shear) cracks associated with increasing lateral load, relatively minor joint and bent cap cracks developed. This corresponded well with the capacity protection philosophy implemented in design. Hysteretic response is discussed in further detail in subsequent sections.

The following additional observations were made:

- Initial joint cracking that occurred at 48 kips (both push and pull directions, under force control) exhibited cracking in the upper half of the joint. However, cracking through the center of the joint developed at 2.3% drift (μ4, push) and 3.3% drift (μ6, pull). Cracks were wider in top half of the joint during testing. Figures 3-1 through 3-5 show this progressive development.
- Initial radial splitting crack in the top surface of the bent cap (as tested) extended from the column bar at 0.7% drift (μ1) and further development of these cracks occurred at 1.2% drift (μ2). Splitting cracks also developed vertically along column longitudinal bars. See Figure 3-6.
- Initial spalling of the column occurred at 1.8% drift (μ3), with progressive spalling at higher drifts. At ultimate, significant spalling occurred along a length of 8.5 in at the plastic hinging region (or a length equal to 43% of the column diameter). See Figures 3-7 and 3-8.
- Flexural cracks developed in the bent cap, but remained relatively minor during testing.
- The specimen exhibited a significant reduction in strength at a drift ratio of 5.9% (μ10). This decrease in strength was associated with the onset of column bar buckling. The specimen was ultimately pushed monotonically to failure, with 3 bars fracturing (Figure 3-9).

- Post-test inspection revealed that the core remained primarily intact but with concrete crushing localized over 1-2 in of the extreme compression zone. Several column bars buckled at both column faces in push and pull directions. The specimen exhibited excellent ductility due to confinement in the plastic hinge region based on properly designed and accurately placed hoops. The joint cracking pattern post-test is shown in Figure 3-10.

3.2 Hysteretic Response

3.2.1 Column Load-Displacement Response

The lateral force-lateral displacement (hysteretic) response of the column is used to characterize the fundamental performance of the specimen. Figure 3-11 shows the load-displacement response, together with the response envelope and predictions. The primary aspects of the response were:

- Plastic hinging of the column enabling the specimen to undergo a very large drift ratio of 5.9% (μ10)
- Stable hysteretic behavior with loops of increasing area without appreciable strength degradation through a drift of 5.9% (μ10)
- Maximum loading of approximately 55.9 kips reached and maintained to a drift of 3.6% (μ6)
- Strength degradation of 15% at a drift of 5.9% (μ10), associated with the onset of column bar buckling

A comparison of the response envelope to the predicted envelope shows a good correlation. Although the specimen capacity was slightly smaller than predicted, the specimen maintained 89% of its capacity through the first cycle at a drift of 5.9% (μ10, push). Due to limited actuator stroke, a displacement corresponding to a drift of only 4.6% (μ8) was applied in the pull direction.

The hysteretic response also portrayed appropriate stiffness, strength, ductility and other features such as crack distribution and width representative of CIP response observed for a beam-column connection test. The dominance of ductile plastic hinging in the column and minimal damage in the capacity-protected joint and bent cap satisfied the

performance goal for the CIP control specimen. Thus, the specimen provides an appropriate baseline for comparison with the precast specimens.

Column displacement data was corrected to remove rigid body translation and rotation.

3.2.2 Equivalent Viscous Damping

Determination of the equivalent viscous damping ratio provides a quantitative means to establish the energy dissipating characteristic of the specimen for eventual comparison to the precast connections. The equivalent viscous damping ratio, ξ, represents the energy dissipation per cycle, determined as follows:

$$\xi = (2/\pi)(A_L/A_R)$$

where:

A_L =Area of hysteretic loop for a complete cycle (push and pull);

A_R =Area of rectangle bounded by maximum loads and displacements of a complete hysteretic loop.

Figure 3-12 plots the equivalent viscous damping ratio, ξ, versus drift ratio, including the first two cycles for each drift ratio. ξ increased significantly with increasing drift ratio, reaching approximately 27% (first cycle, 5.9% drift). This level is reasonable for ductile response of a reinforced concrete beam-column connection. ξ increased slightly between the first and second cycles at the larger drift ratios.

3.3 Column Curvature Response

3.3.1 Moment-Curvature

Figures 3-13 and 3-14 plot normalized moment-curvature responses for the first two curvature cells up the column, together with the predictions. Predicted and measured response envelopes are shown to compare reasonably. Cell 1 curvature is shown to be more extensive than Cell 2, even though Cell 1 data was limited to $\mu 6$ and Cell 2 data was plotted to $\mu 8$ (data at a larger μ was considered unreliable due to disturbed curvature rods related to column damage). This is indicative of the greater plastic hinging occurring at the bottom of the column (as tested), adjacent to the soffit. The Cell 1 maximum

curvature was approximately 23 times the effective yield curvature (estimated), representative of extensive curvature ductility.

The moment at the midheight of the cell was used for plotting, except that strain penetration was accounted for Cell 1. In addition, data was corrected for joint rotation to provide a matching basis to the predictions. Note that the curvature was normalized by multiplying curvature by the column diameter; moment was not modified.

3.3.2 Curvature over Height

Figures 3-15 and 3-16 show the normalized curvature profile over the column height for the Force Control and Displacement Control sequences, respectively. These profiles demonstrate the concentration of plasticity adjacent to the soffit, as well as the spread of plastic hinging up the column under Displacement Control. Based on an estimated first yield normalized curvature of approximately 0.0036 in/in, it is evident that under the final loading cycle of Force Control (48 kips) yielding occurred, and much more significant inelastic response developed over an increasing height under Displacement Control.

It should be noted that the North linear potentiometer for Cell 3 exhibited unusual behavior in push direction. This is observed in the Force Control curvature profile for Cell 3 (push). In addition, for Displacement Control, some data required additional zeroing.

3.4 Displacement Decomposition

Displacement decomposition refers to the separation of the column displacement into the various components that contribute to the overall lateral displacement of the column. Components include column flexure, fixed end rotation (due to plastic hinging and bar slip), column shear, bent cap flexibility, and joint shear. Decomposition quantifies the magnitude of each component, and is determined for analytical predictions and experimental measurements for comparison purposes. Figure 3-17 shows a schematic representation of the displacement components, including applicable equations.

Some limitations exist when comparing predicted and measured displacements. For example, in the test program the column shear displacement was not measured but was estimated analytically, and the joint shear displacement was not determined analytically but was measured. This leads to some approximation.

Properly designed cast-in-place and emulative bridge bents are expected to display flexural plastic hinging, which result in flexural displacement components dominating the displacement at increasing drift or displacement ductility levels. The total experimental flexural component is taken as the sum of the fixed end rotation plus column flexure. Fixed end rotation represents displacement due to plastic hinging within the first curvature cell plus displacement due to bar slip. However, because the plastic hinging length extended beyond the first curvature cell, plastic hinging response also contributed to the column flexure component. Thus, the total predicted flexural displacement is compared to the sum of column flexure and fixed end rotation.

To match the assumption of ideal pin and roller support conditions, rigid body translation and rotation of the specimen were removed from the raw data during data reduction.

3.4.1 Overview

Table 3-3 summarizes the displacement decomposition for the first push and pull cycles for drift ratios from 0.7% to 5.9%. For each drift ratio, results are tabulated in two columns. The first column includes two sections: 1) the top section summarizes the column displacement (CD) and the corresponding drift and force; and 2) the bottom section lists the displacement components determined from measurements, as shown in Figure 3-17, and the sum of the components (Component Total, CT). At the bottom of the table is the CT/CD ratio, indicating what portion of actual displacement is represented by the measured components.

The second column shows the analytically predicted displacement components. Although the load-displacement envelope was predicted pretest, the actual displacements imposed on the specimen were not well defined pretest, as these are dependent on the establishment of first yield, which was approximate. Thus, the second column shows

predicted displacement components that sum up the imposed displacement in the test (i.e., CT/CD=1.0). In addition, predicted displacements are based on actual material properties. This approach allows actual and predicted displacement components to be appropriately compared, as shown in the third column (Actual/Predicted ratio).

Some approximation is expected in predicted and measured values. Joint shear was not predicted and column shear was predicted but not measured. The difference between CT and CD represents column displacement due to column shear, joint shear and potential inaccuracies in measurements. Joint shear was not expected to represent a large percentage of the total measured displacement in full ductility specimens. Although prediction of column shear is considered approximate, inclusion of this component in predictions allows a more realistic comparison in Actual/Predicted ratios: omission of column shear in predictions would require its portion to be incorrectly assigned to column flexure and bent cap rotation, biasing ratios. Significant column shear cracking is clearly shown in Figures 3-1 through 3-8. To some extent, these approximations tend to offset one another; however, some error is introduced in the process.

3.4.2 Fixed End Rotation, Column Flexure, and Bent Cap Flexibility

As shown in Table 3-3 for the push direction, the CT/CD ratios ranged from 0.77 to 0.86 (0.82 average) through a drift of 4.6% (μ8, push). This suggests that the displacement components were reasonably determined. (At a drift approaching 5.9% (μ10), some instrumentation was unreliable and removed.) The Actual/Predicted ratios for flexure ranged between 0.78 and 0.89, which indicate reasonably accurate predictions for flexure. Bent cap flexibility was less accurately predicted; however, joint rotation was underestimated in predictions. In addition, as shown in Figure 3-18, the bent cap flexibility contribution to overall displacement was much smaller than column flexure. Similar overall trends are evident in Table 3-3 for the pull direction.

Figure 3-19 plots the displacement decomposition component values for the push and pull directions. The height of each bar segment shows the relative contribution of a component. In correlation with experimental observations of the specimen, flexural components (fixed end rotation and column flexure) dominated the response and

increased significantly with increasing drift. Bent cap flexibility provided a smaller contribution with joint shear clearly being the smallest contributor.

Figure 3-20 plots the displacement decomposition components as a percentage of the total component displacement (CT). For example, at a push drift of 0.9% (μ1.5), the combined flexural components (fixed end rotation and column flexure) accounted for 79% of CT (column elastic plus plastic deformation was predicted to represent 76%). However, at 3.6% drift (μ6), the flexural components accounted for 90% of CT (vs. prediction of 86%). This corresponded well with the observed dominance of plastic hinging in the column. The contribution of column shear to column displacement was not directly measured, and significant shear cracks did develop in the column; thus, predictions are considered approximate, as previously mentioned.

As shown in Figure 3-19, the bent cap flexibility (joint rotation) component increased in magnitude with drift (and bent cap cracking). Figure 3-20 shows its relative contribution to CT decreased with increasing drift, from 18% at 0.7% drift to 6% at 5.9% drift.

It should be noted that the values in Table 3-3 for the first displacement ductility level are labeled as FC48 rather than μ1 because this first stage uses data from the final stage of Force Control (48 kips). This was required since the specimen was loaded under Force Control to a force and displacement larger than that expected for effective yield (determined from analysis).

3.4.3 Joint Shear

Figures 3-19 and 3-20 confirm the minor contribution of joint shear, with the joint shear displacement not exceeding a 10% contribution to CT. Joint shear was the smallest measured contributor to column displacement.

3.4.4 Bar Slip

Table 3-4 summarizes bar slip and compares bar slip to fixed end rotation. By definition, fixed end rotation includes the effect of bar slip on rotation. As shown in the table, bar slip was minor, contributing less than 4% on average to the displacement component attributable to fixed end rotation. Due to bar anchorage forces, splitting

cracks formed in the bent cap and column, and the top surface of the bent cap (as tested) exhibited splitting cracks and local spalling; however, bar slip was minor overall, indicating that column bars were well anchored within the joint.

3.5 Joint Response

This section summarizes joint response in terms of joint shear stress, principal stresses and angle, joint cracking and joint deformation.

3.5.1 Joint Shear Stress, Principal Stresses, and Principal Angle

The average joint shear stress, plotted in Figure 3-21, exhibits a similar hysteretic trend as the load-displacement plot and relatively small stresses. Figure 3-22 shows the joint shear stress vs. shear strain, including appropriate stiffness and limited softening at increasing drift ratios. Shear stress and shear strain are calculated as shown in the List of Equations and, strictly speaking, refer to average (or nominal) values applicable to the joint region.

Shear stresses, which did not exceed $5\sqrt{f_c'}$, were used in determining the principal stresses and principal angle shown in Figures 3-23 through 3-25. Figure 3-23 shows that the principal tensile stress was limited to $5.4\sqrt{f_c'}$, less than half of the 2006 LRFD RSGS limit of $12\sqrt{f_c'}$, but about 50% larger than $3.5\sqrt{f_c'}$, the level at which more extensive (additional) joint reinforcement is required for development of the force transfer mechanism. Figure 3-24 indicates that the principal compressive stress was limited to approximately $0.09f_c'$, slightly more than a third of the 2006 LRFD RSGS limit of $0.25f_c'$. These values correspond well with the intentions of the design and the observed joint performance.

Figure 3-25 plots the angle of principal plane in the joint, which is shown to be approximately 40-45 degrees from horizontal, with the push direction shown to be slightly smaller. These values correlate well with the expected response.

3.5.2 Joint Cracking

Consistent with the level of joint stresses reported, joint cracking occurred but crack widths were relatively minor. Figure 3-5 shows the crack pattern in the joint at 4.6% drift (μ8, push) and Figure 3-10 shows the pattern post-test. Some flexural cracks

were evident, and diagonal cracks in the middle to upper portion of the joint were consistent with the principal angles reported in the previous section. Table 3-5 summarizes the maximum measured surface crack widths in the joint region at the various drift and lateral force levels. The maximum crack width was 0.025 in, which occurred at a drift ratio of 4.6% (μ8, push) and a force slightly lower than the maximum applied force. No surface spalling developed on the side faces of the bent cap.

3.5.3 Joint Rotation and Deformation

Joint rotation and panel deformation were measured during the test. Figure 3-26 shows joint rotation magnitude, which was limited to less than 0.002 rad (0.11 deg). This was approximately twice that assumed in predictions; however, predictions were based on an estimate of the cracked bent cap section.

The deformation of the joint was measured using linear potentiometers in the region of the joint. The maximum change in panel area was very small, limited to less than 0.2%. This corresponds with the limited joint cracking and joint stresses.

3.6 Strain Records

This section uses strain profiles and tables to present select results from specimen strain records. Profiles show the strain levels for a series of strain gages at specific regions of the specimen and for specific load or ductility (drift) levels. Profiles include strain for: 1) column longitudinal rebar (locations along the column and into the joint); 2) hoops in the column and joint; and 3) stirrups in the bent cap and joint. A table is provided for the bent cap longitudinal rebar (locations along the bent cap, including through the joint). Figures 2-23 through 2-25 show the associated instrumentation drawings with strain gages.

Some gages reliably recorded large strains well in excess of yield, while others produced unreliable data typically after bar yield. Plots reflect only data considered reliable.

Only select strain gage records are discussed. These strain records and others will be further analyzed and addressed through future efforts.

3.6.1 Column Longitudinal Rebar

Figure 3-27 shows the strain profile for the extreme column bar on the north side of the specimen for both Force Control and Displacement Control. As expected, the column strains were largest in the plastic hinging region and dropped off at distances above (column) and below (joint). Significant strain penetration was evident, including bar yield at 6 in into the joint.

3.6.2 Hoops in Column and Joint

Figure 3-28 shows strain profile for the hoops in the column and joint on the east side (as tested). A larger number of gages were used for the east side, where out-of-plane transverse tension can produce larger hoop strains than in plane of loading (north/south). However, due to the significant spacing between gages, profile lines are not shown connecting strain values.

Hoop strains in the plastic hinging regions were largest, with yield reached at μ2 at the soffit, reflecting the confining effect of the hoop. Strains were lower at the three locations within the joint. At 18 in into the joint, the east hoop displayed a strain of 63% of yield. At approximately 12 in into the joint, the hoop strain remained very low, but increased to 42% of yield at μ8.

3.6.3 Bent Cap Longitudinal Rebar

Table 3-6 lists bent cap longitudinal bar strain (top and bottom bars) for the first cycle of three nominal displacement ductilities of Displacement Control (μ2, μ4, μ6) during which the maximum load was reached. Table 3-6 shows that strain levels for bottom and top bars were largest within the joint (S1, CL, and N1 positions) and that the strain level did not exceed 46% of yield. Strain patterns reasonably matched expected distribution per an assumed force transfer model similar to that of Reference 18. It should be noted that the test specimens, designed per 2006 LRFD RSGS, did not include the significant additional area of bent cap longitudinal reinforcement ($0.245A_{st}$) required by 2009 LRFD SGS.

3.6.4 Stirrups in Bent Cap and Joint

Figures 3-29 through 3-32 show the strain profiles for stirrups within the bent cap and joint. Two 2-leg stirrups were placed within the joint for constructability reasons, as explained in Section 2.2.1. Two strain gages were placed on the east leg of each stirrup, at approximately the 1/3 and 2/3 points along the stirrups (Figure 2-25). Since stirrups in the regions adjacent to the joint used gages at the mid-height of the stirrup, two sets of plots are shown: 1) mid-height gages on stirrups outside the joint together with the top gage on the joint stirrups (Figures 3-29 and 3-30); and 2) mid-height gages on stirrups outside the joint together with the bottom gage on the joint stirrups (Figures 3-31 and 3-32).

Figure 3-29 shows a minor strain level in the stirrups both outside the joint and inside the joint (top location) under Force Control. Slightly larger strains developed outside the joint on the north end, in compression. Under Displacement Control (Figure 3-30), the stirrup within the joint on the south side reached 47% of yield in compression and only 11% of yield in tension at the north side joint stirrup and at the north most stirrup outside the joint.

In contrast, Figures 3-31 and 3-32 show the strain distribution in the joint for the bottom strain gage location. Under Force Control, both joint stirrups exhibited a strain of 18% of yield; however, under Displacement Control, the joint stirrup on the north end clearly yielded. The high level of strain for this construction stirrup indicates the importance of its contribution to joint performance. Stirrups outside the joint remained at a low level not exceeding 17% of yield.

It should be noted that although test specimens designed per 2006 LRFD RSGS did not require stirrups inside the joint, the 2007 LRFD PSGS and 2009 LRFD SGS require an area of $0.135A_{st}$ for vertical stirrups within the joint. The two joint stirrups, with an area of $0.089A_{st}$ and included for construction, provided an area approximately 66% of that required by the 2009 LRFD SGS.

3.7 Tables

Table 3-1. Associated Values of Force, Displacement, Ductility, and Drift Ratio

Push (Cycle 1)					
Stage	Force (kips)	Disp. (in)	Displacement Ductility, μ		Drift %
			Actual	Nominal	
Force Control	13.0	0.034	-	-	0.06
	20.0	0.072	-	-	0.13
	30.1	0.154	-	-	0.27
	48.4	0.397	-	-	0.69
Displacement Control	40.0	0.406	1.13	1.0	0.71
	49.4	0.533	1.49	1.5	0.93
	53.3	0.684	1.91	2.0	1.19
	55.6	1.014	2.83	3.0	1.76
	54.6	1.345	3.75	4.0	2.34
	55.9	2.070	5.77	6.0	3.60
	53.2	2.638	7.36	8.0	4.59
	50.0	3.383	9.43	10.0	5.88
Pull (Cycle 1)					
Stage	Force (kips)	Disp. (in)	Displacement Ductility, μ		Drift %
			Actual	Nominal	
Force Control	-13.3	-0.031	-	-	-0.05
	-20.3	-0.080	-	-	-0.14
	-30.4	-0.158	-	-	-0.27
	-48.7	-0.419	-	-	-0.73
Displacement Control	-32.7	-0.293	0.82	1.0	-0.51
	-44.5	-0.413	1.15	1.5	-0.72
	-50.6	-0.545	1.52	2.0	-0.95
	-53.6	-0.877	2.45	3.0	-1.53
	-54.9	-1.239	3.46	4.0	-2.15
	-57.2	-1.921	5.36	6.0	-3.34
	-55.7	-2.538	7.08	8.0	-4.41
	-45.2	-2.633	7.34	10.0	-4.58

Table 3-2. Predicted vs. Actual Stages of Specimen Cracking

Stage	P_V (kips)		P_H (kips)	
	Predicted	Actual	Predicted	Actual
Bent Cap—Flexural	None	None	-	-
	38	38	8.9	13.0
Column—Flexural	38	38	14.0	20.0
Joint Shear	38	38	36.5	48.0

Table 3-3. Displacement Decomposition (1st Push and Pull Cycles)

Displacement Decomposition—Cast-in-Place (1st Push Cycle)

		Actual	Predicted	Act/Pred	Actual	Predicted	Act/Pred	Actual	Predicted	Act/Pred	Actual	Predicted	Act/Pred
Displacement Ductility	**(μ)**	**FC48****	**-**	**-**	**1.5**	**-**	**-**	**2.0**	**-**	**-**	**3.0**	**-**	**-**
Col Displacement [CD]	**(in)**	0.397	0.397	1.00	0.533	0.533	1.00	0.684	0.684	1.00	1.014	1.014	1.00
Drift	**(%)**	0.69	-	-	0.93	-	-	1.19	-	-	1.76	-	-
Force	**(kip)**	48.4	57.4	0.84	49.4	59.9	0.82	53.3	60.1	0.89	55.6	60.2	0.92
Column Flexure	**(in)**	0.067	0.298	0.78	0.081	0.404	0.86	0.119	0.536	0.89	0.217	0.840	0.89
Fixed End Rotation	**(in)**	0.166			0.267			0.356			0.527		
Column Shear	**(in)**	*	0.047	*	*	0.076	*	*	0.094	*	*	0.120	*
Bent Cap Flexibility	**(in)**	0.059	0.051	1.15	0.071	0.054	1.33	0.083	0.054	1.54	0.095	0.054	1.75
Joint Shear	**(in)**	0.029	*	*	0.020	*	*	0.025	*	*	0.032	*	*
Component Total [CT]	**(in)**	0.321	0.397		0.439	0.533		0.583	0.684		0.871	1.014	
CT/CD		0.81	1.00		0.82	1.00		0.85	1.00		0.86	1.00	
		Actual	**Predicted**	**Act/Pred**	**Actual**	**Predicted**	**Act/Pred**	**Actual**	**Predicted**	**Act/Pred**	**Actual**	**Predicted**	**Act/Pred**
Displacement Ductility	**(μ)**	**4.0**	**-**	**-**	**6.0**	**-**	**-**	**8.0**	**-**	**-**	**10.0**	**-**	**-**
Col Displacement [CD]	**(in)**	1.345	1.345	1.00	2.070	2.070	1.00	2.638	2.638	1.00	3.383	3.383	1.00
Drift	**(%)**	2.34	-	-	3.60	-	-	4.59	-	-	5.88	-	-
Force	**(kip)**	54.6	61.0	0.90	55.9	63.5	0.88	53.2	65.2	0.82	50.0	67.2	0.74
Column Flexure	**(in)**	0.245	1.139	0.86	0.436	1.771	0.84	0.572	2.266	0.82	0.549	2.915	0.70
Fixed End Rotation	**(in)**	0.736			1.052			1.281			1.482		
Column Shear	**(in)**	*	0.151	*	*	0.242	*	*	0.313	*	*	0.407	*
Bent Cap Flexibility	**(in)**	0.101	0.055	1.85	0.116	0.057	2.03	0.127	0.059	2.18	0.132	0.060	2.18
Joint Shear	**(in)**	0.038	*	*	0.049	*	*	0.057	*	*	0.063	*	*
Component Total [CT]	**(in)**	1.121	1.345		1.653	2.070		2.037	2.637		2.226	3.382	
CT/CD		0.83	1.00		0.80	1.00		0.77	1.00		0.66	1.00	

Note: *Column shear displacement not measured; Joint shear displacement not predicted. During μ10 (pull), actuator stroke limited full displacement. **Specimen loaded >μ1.0 under Force Control (48 kips); 48-kip data reported.

Displacement Decomposition—Cast-in-Place (1st Pull Cycle)

		Actual	Predicted	Act/Pred	Actual	Predicted	Act/Pred	Actual	Predicted	Act/Pred	Actual	Predicted	Act/Pred
Displacement Ductility	**(μ)**	**FC48****	**-**	**-**	**1.5**	**-**	**-**	**2.0**	**-**	**-**	**3.0**	**-**	**-**
Col Displacement [CD]	**(in)**	-0.419	-0.419	1.00	-0.413	-0.413	1.00	-0.545	-0.545	1.00	-0.877	-0.877	1.00
Drift	**(%)**	-0.73	-	-	-0.72	-	-	-0.95	-	-	-1.53	-	-
Force	**(kip)**	-48.7	-58.7	0.83	-44.5	-58.3	0.76	-50.6	-60.0	0.84	-53.6	-60.1	0.89
Column Flexure	**(in)**	-0.086	-0.311	0.85	-0.076	-0.307	0.77	-0.099	-0.414	0.82	-0.194	-0.709	0.85
Fixed End Rotation	**(in)**	-0.179			-0.161			-0.240			-0.406		
Column Shear	**(in)**	*	-0.055	*	*	-0.053	*	*	-0.077	*	*	-0.114	*
Bent Cap Flexibility	**(in)**	-0.052	-0.052	1.00	-0.062	-0.052	1.18	-0.070	-0.054	1.30	-0.079	-0.054	1.45
Joint Shear	**(in)**	-0.008	*	*	-0.026	*	*	-0.034	*	*	-0.037	*	*
Component Total [CT]	**(in)**	-0.325	-0.418		-0.325	-0.412		-0.443	-0.545		-0.716	-0.877	
CT/CD		0.77	1.00		0.79	1.00		0.81	1.00		0.82	1.00	
		Actual	**Predicted**	**Act/Pred**	**Actual**	**Predicted**	**Act/Pred**	**Actual**	**Predicted**	**Act/Pred**	**Actual**	**Predicted**	**Act/Pred**
Displacement Ductility	**(μ)**	**4.0**	**-**	**-**	**6.0**	**-**	**-**	**8.0**	**-**	**-**	**10.0**	**-**	**-**
Col Displacement [CD]	**(in)**	-1.239	-1.239	1.00	-1.921	-1.921	1.00	-2.538	-2.538	1.00	-2.633	-2.633	1.00
Drift	**(%)**	-2.16	-	-	-3.34	-	-	-4.41	-	-	-4.58	-	-
Force	**(kip)**	-54.9	-60.6	0.91	-57.2	-63.0	0.91	-55.7	-64.9	0.86	-45.2	-65.2	0.69
Column Flexure	**(in)**	-0.281	-1.047	0.83	-0.437	-1.641	0.86	-0.617	-2.178	0.83	-0.801	-2.262	0.96
Fixed End Rotation	**(in)**	-0.593			-0.971			-1.197			-1.376		
Column Shear	**(in)**	*	-0.138	*	*	-0.224	*	*	-0.300	*	*	-0.312	*
Bent Cap Flexibility	**(in)**	-0.084	-0.054	1.55	-0.097	-0.057	1.72	-0.107	-0.058	1.84	-0.106	-0.059	1.81
Joint Shear	**(in)**	-0.040	*	*	-0.049	*	*	-0.055	*	*	-0.054	*	*
Component Total [CT]	**(in)**	-0.998	-1.239		-1.555	-1.921		-1.977	-2.537		-2.337	-2.633	
CT/CD		0.80	1.00		0.81	1.00		0.78	1.00		0.89	1.00	

Note: *Column shear displacement not measured; Joint shear displacement not predicted. During μ10 (pull), actuator stroke limited full displacement. **Specimen loaded >μ1.0 under Force Control (48 kips); 48-kip data reported.

Table 3-4. Displacement Components—Bar Slip and Fixed End Rotation

Drift Ratio (%)	Displacement Ductility (μ)	Force (kips)	Bar Slip, BS (in)	Fixed End Rotation, FER (in)	BS/FER
0.69	FC48	48.4	0.008	0.166	0.049
0.93	1.5	49.4	0.014	0.267	0.051
1.19	2.0	53.3	0.014	0.356	0.038
1.76	3.0	55.6	0.016	0.527	0.031
2.34	4.0	54.6	0.016	0.736	0.022
3.60	6.0	55.9	0.022	1.052	0.021
4.59	8.0	53.2	0.030	1.281	0.023
5.88	10.0	50.0	0.035	1.482	0.024

Table 3-5. Maximum Measured Crack Width on Joint Surface

Drift Ratio (%) Push (Pull)	Displacement Ductility (μ)	Force (kips) Push (Pull)	Crack Width (0.001 in) Push (Pull)
0.69 (0.73)	FC48	48.4 (48.7)	2 (7)
0.93 (0.72)	1.5	49.4 (44.5)	2 (7)
1.19 (0.95)	2.0	53.3 (50.6)	5 (9)
1.76 (1.53)	3.0	55.6 (53.6)	7 (NA)
2.34 (2.15)	4.0	54.6 (54.9)	10 (NA)
3.60 (3.34)	6.0	55.9 (57.2)	13 (NA)
4.59 (4.41)	8.0	53.2 (55.7)	25 (NA)

Table 3-6. Bent Cap Longitudinal Bar Strain

Top Bar		S2		S1		CL		N1		N2	
		Push	Pull	Push	Pull	Push	Pull	Push	Pull	Push	Pull
CIP (LB13)	μ2	-218	118	146	252	—	—	267	-208	—	—
	μ4	-194	141	80	228	—	—	168	-392	—	—
	μ6	-229	116	30	302	—	—	53	-581	—	—
	$\varepsilon_{max}/\varepsilon_y$	-0.10	0.06	0.07	0.14	—	—	0.12	-0.26	—	—

Bottom Bar		S2		S1		CL		N1		N2	
		Push	Pull	Push	Pull	Push	Pull	Push	Pull	Push	Pull
CIP (LB10)	μ2	823	-108	968	68	891	221	259	755	78	535
	μ4	867	-135	875	132	947	334	349	876	59	587
	μ6	890	-164	1,021	157	961	434	449	1,018	35	685
	$\varepsilon_{max}/\varepsilon_y$	0.40	-0.07	0.46	0.07	0.43	0.20	0.20	0.46	0.04	0.31

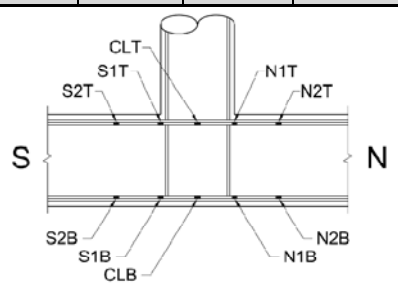

Note: Reference Table 3-1 for associated drift and force levels.
— Not available

3.8 Figures

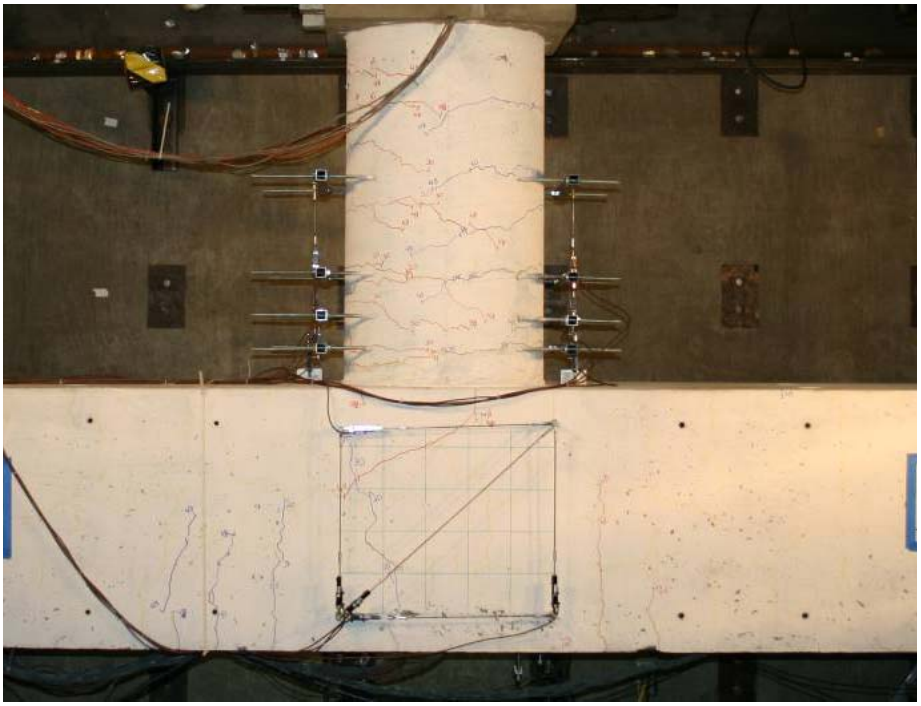

Figure 3-1. Specimen Crack Pattern at End of Force Control Sequence (48 kips)

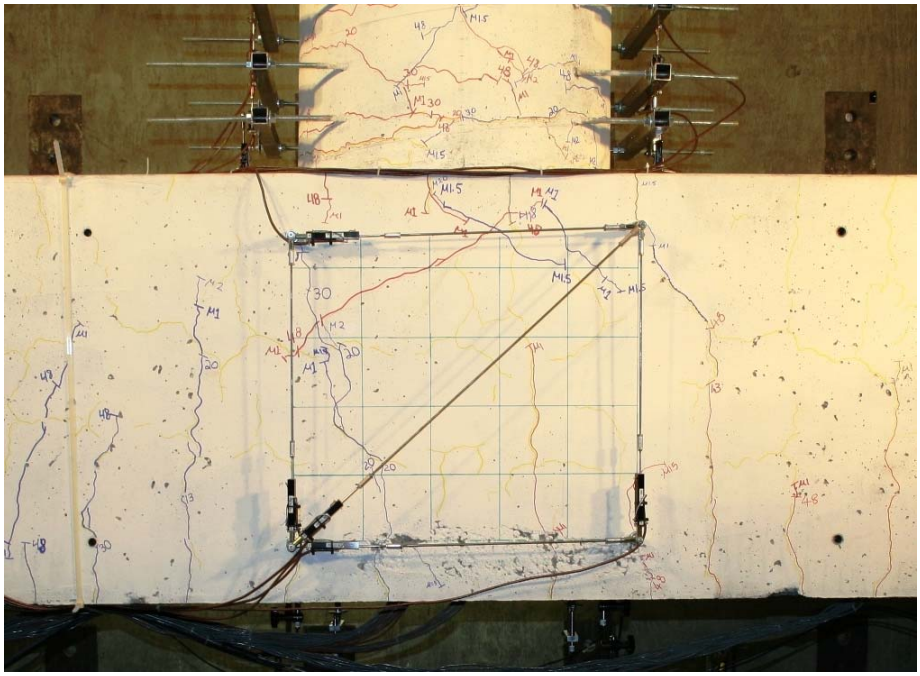

Figure 3-2. Specimen Response at 1.2% Drift Ratio (μ2)

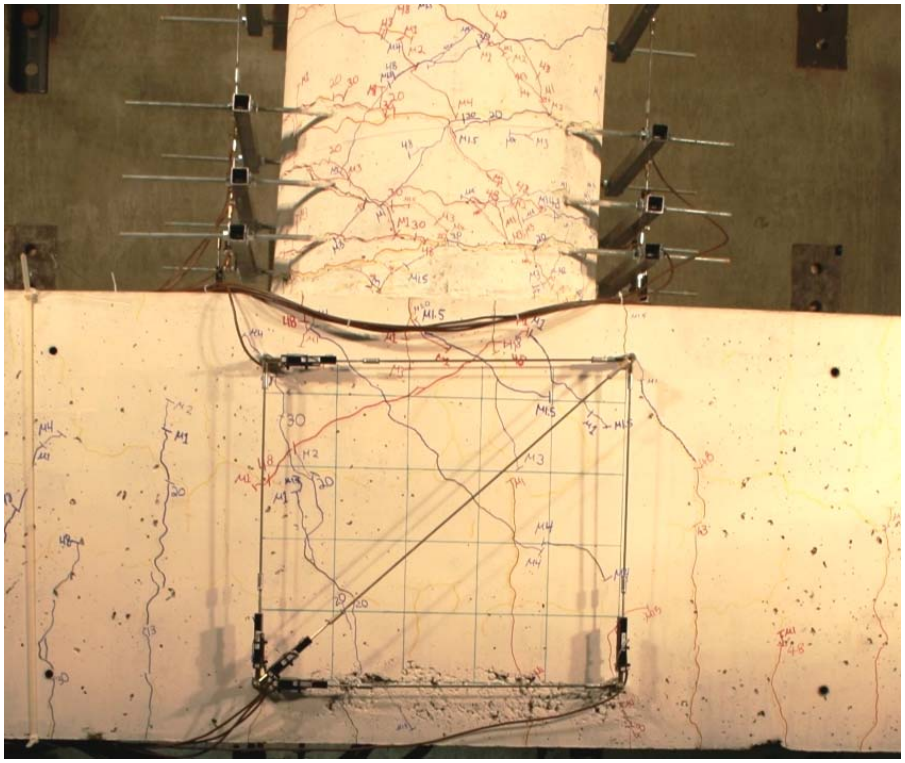

Figure 3-3. Specimen Response at 2.3% Drift Ratio (μ4)

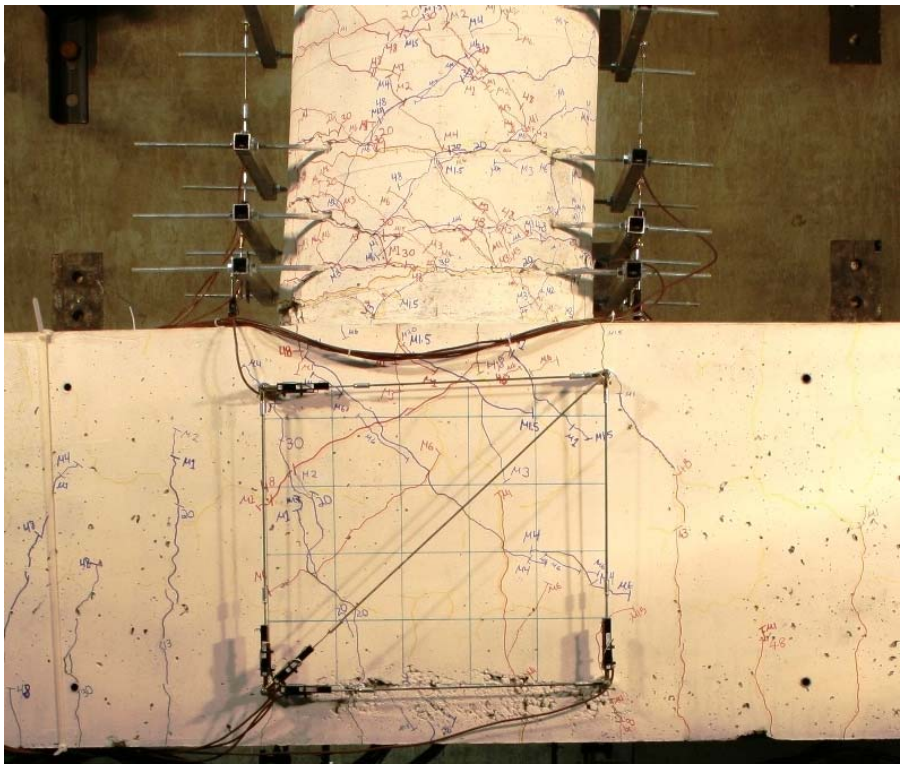

Figure 3-4. Specimen Response at 3.6% Drift Ratio (μ6)

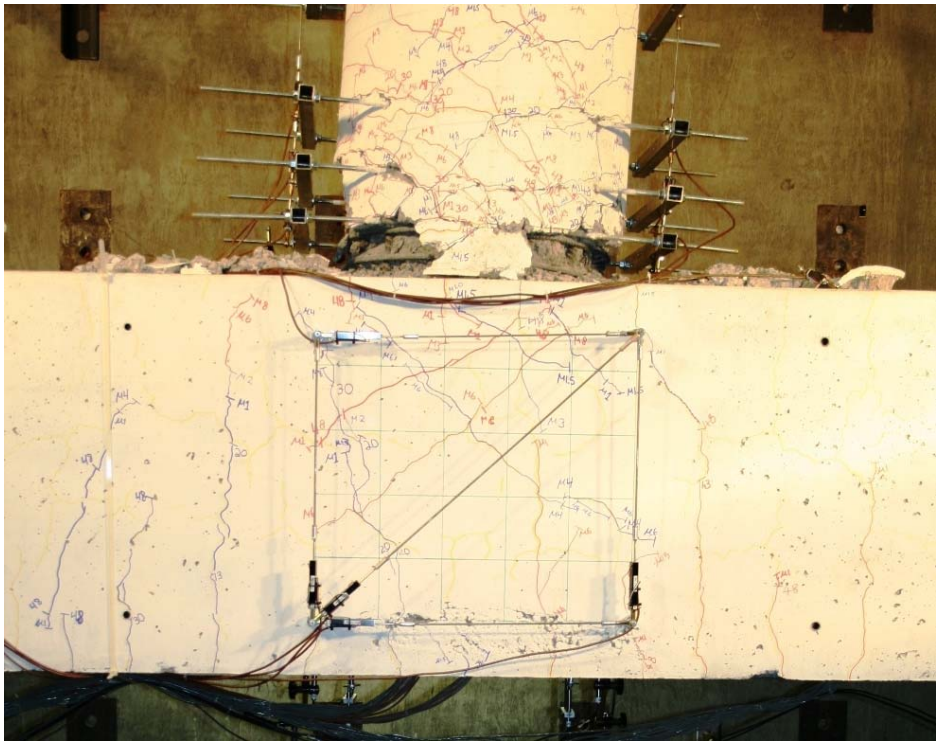

Figure 3-5. Specimen Response at 4.6% Drift Ratio (μ8)

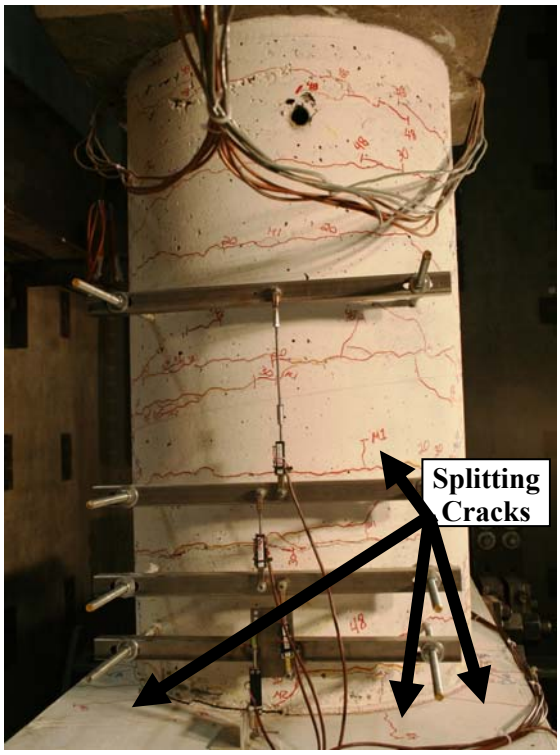

Figure 3-6. Splitting Cracks along Column at 1.2% Drift Ratio (μ2)

Figure 3-7. Initial Column Spalling at 1.8% Drift Ratio (μ3)

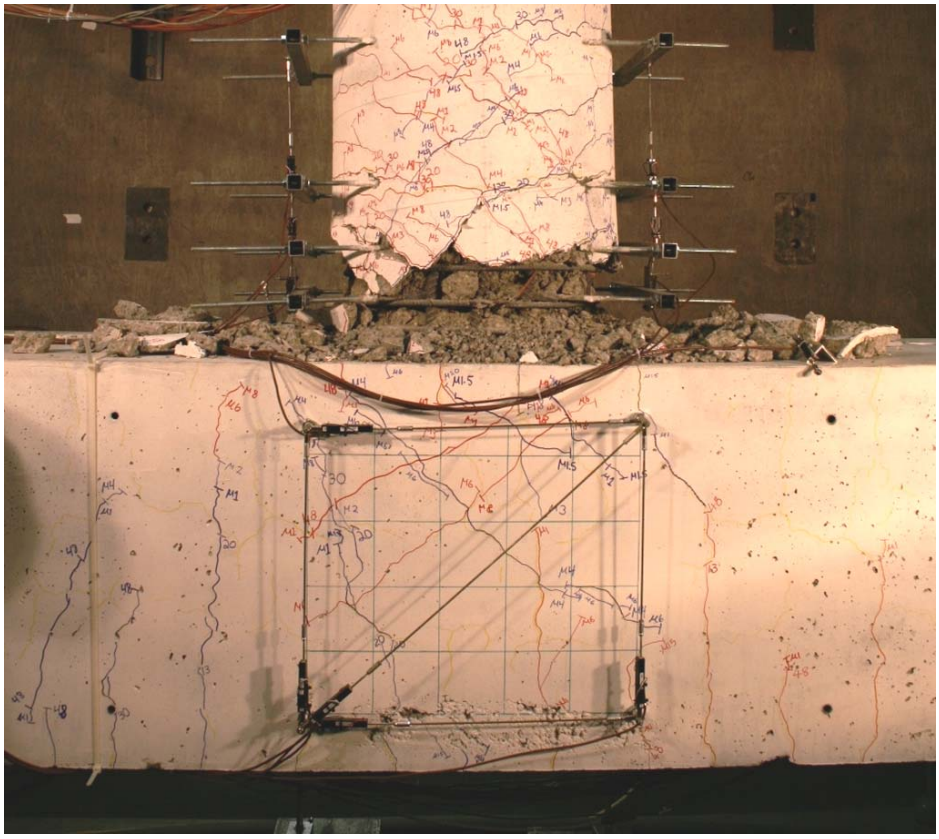

Figure 3-8. Specimen Response at 5.9% Drift Ratio (μ10)

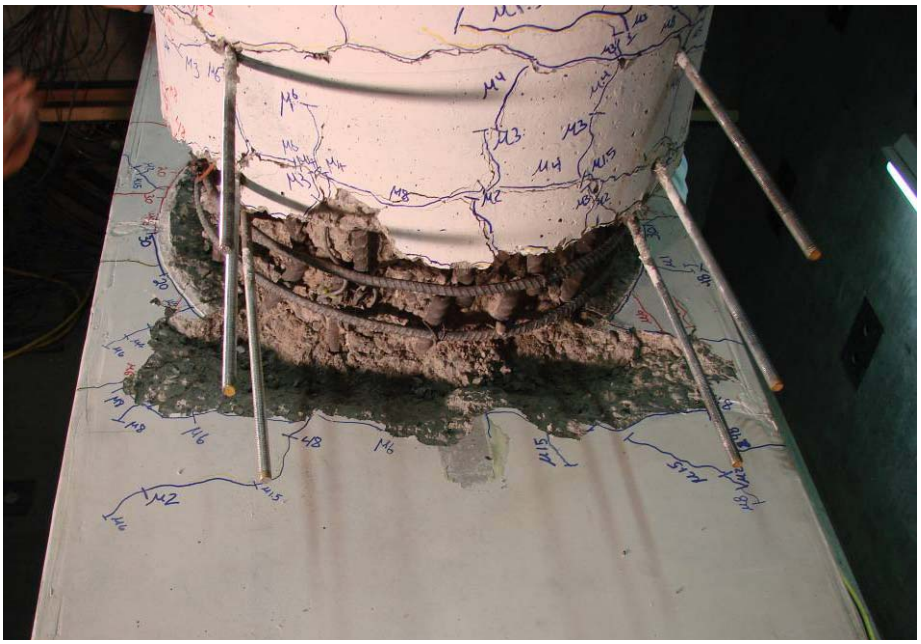

Figure 3-9. Fractured Bars and Crushed Concrete in Plastic Hinge Region (North)

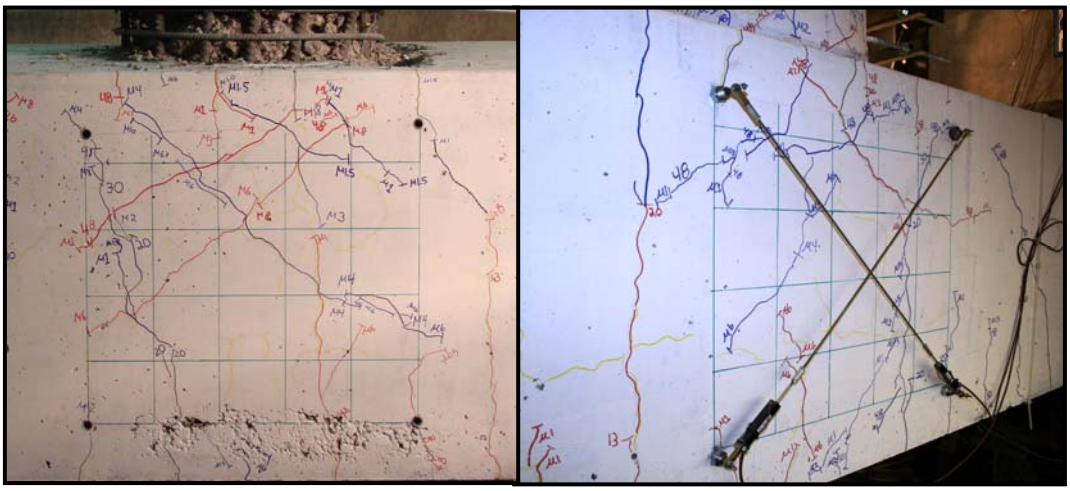

A. East Side B. West Side

Figure 3-10. Joint Region Cracking Post-Test

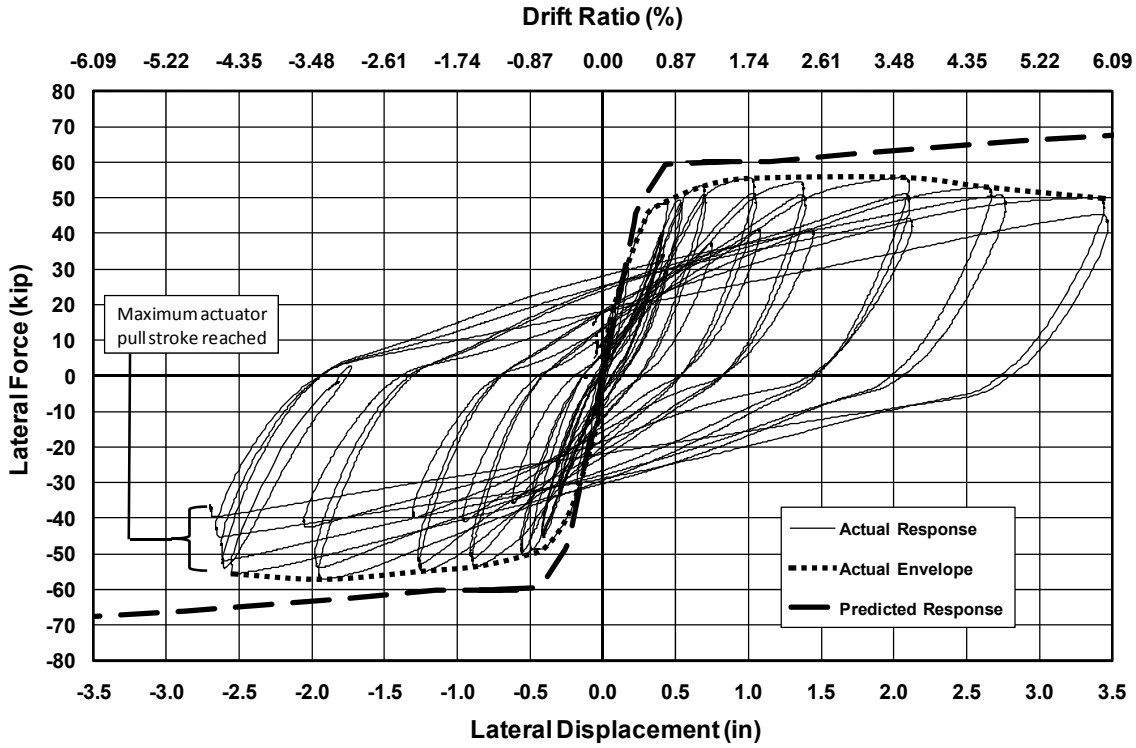

Figure 3-11. Lateral Force vs. Lateral Displacement

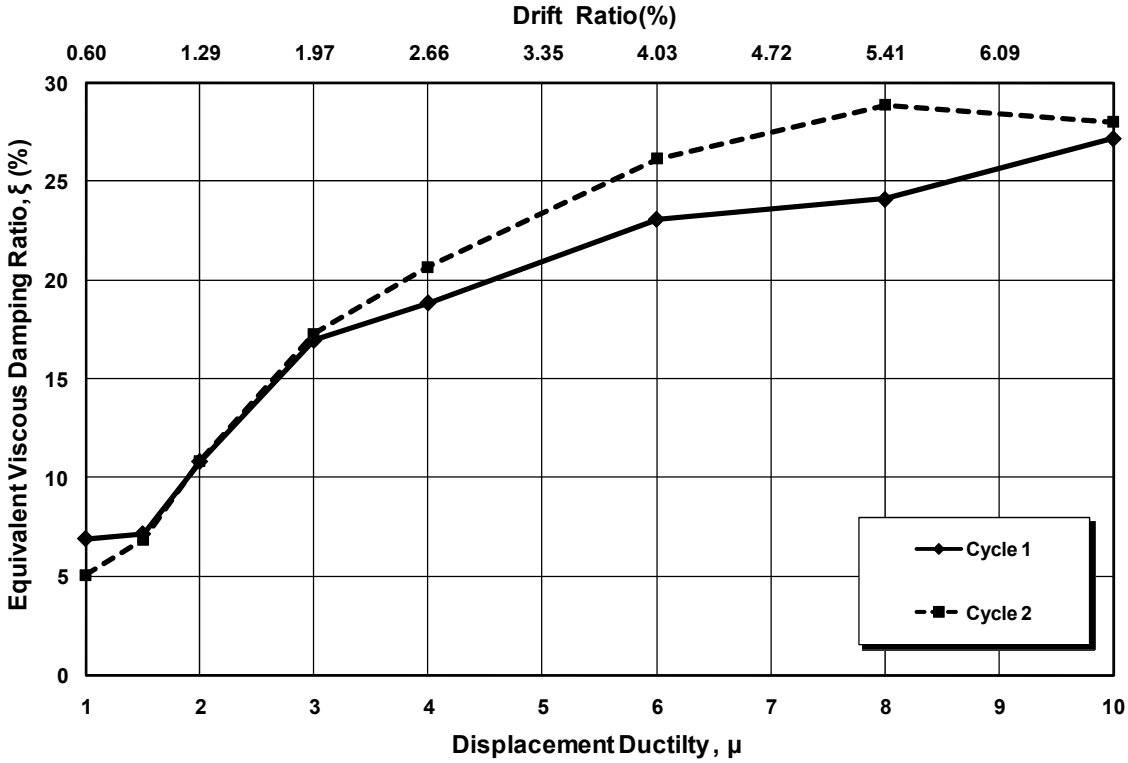

Figure 3-12. Equivalent Viscous Damping Ratio vs. Drift Ratio

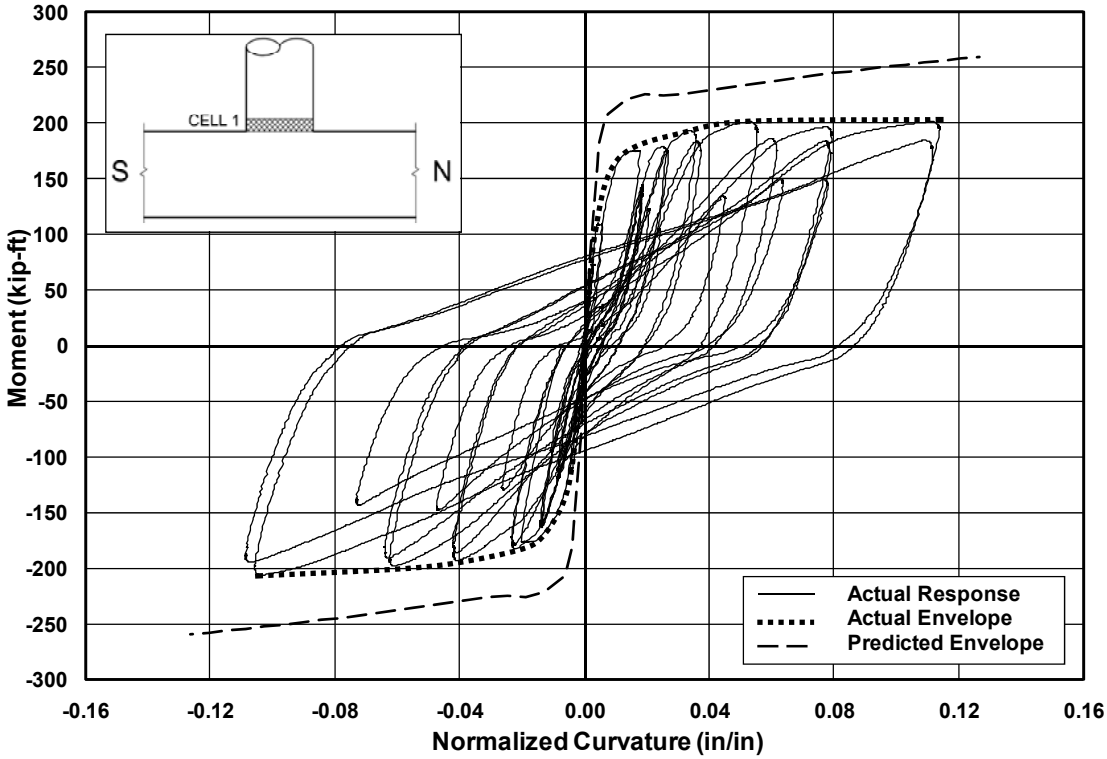

Figure 3-13. Normalized Moment-Curvature Response—Cell 1

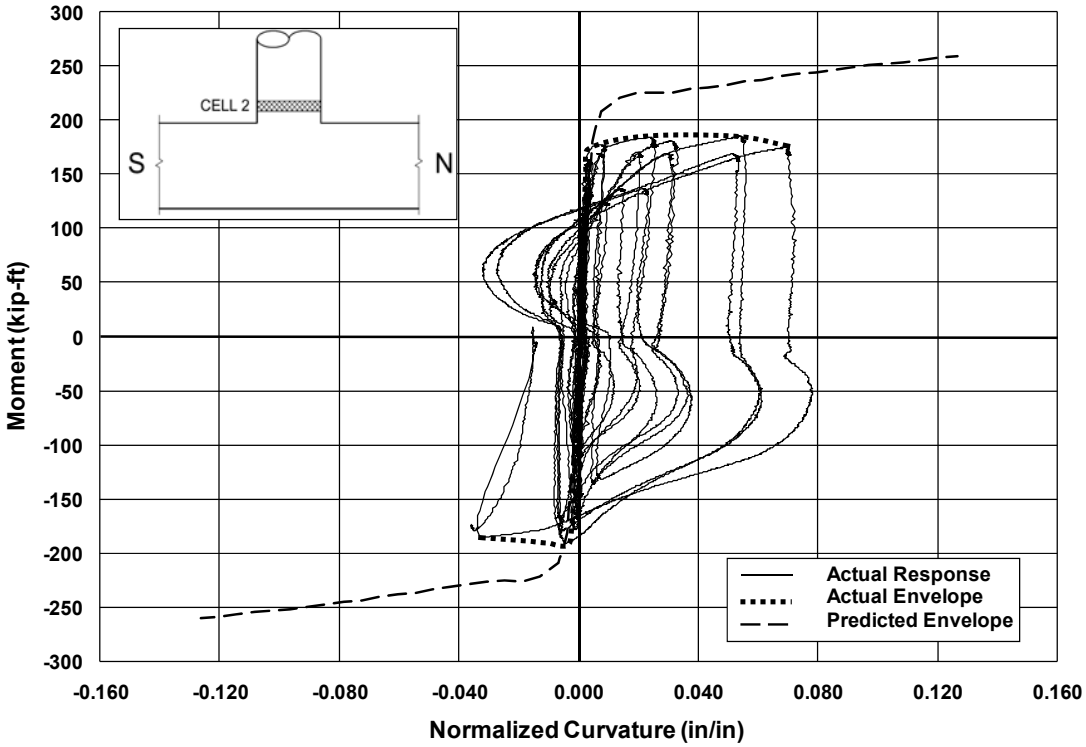

Figure 3-14. Normalized Moment-Curvature Response—Cell 2

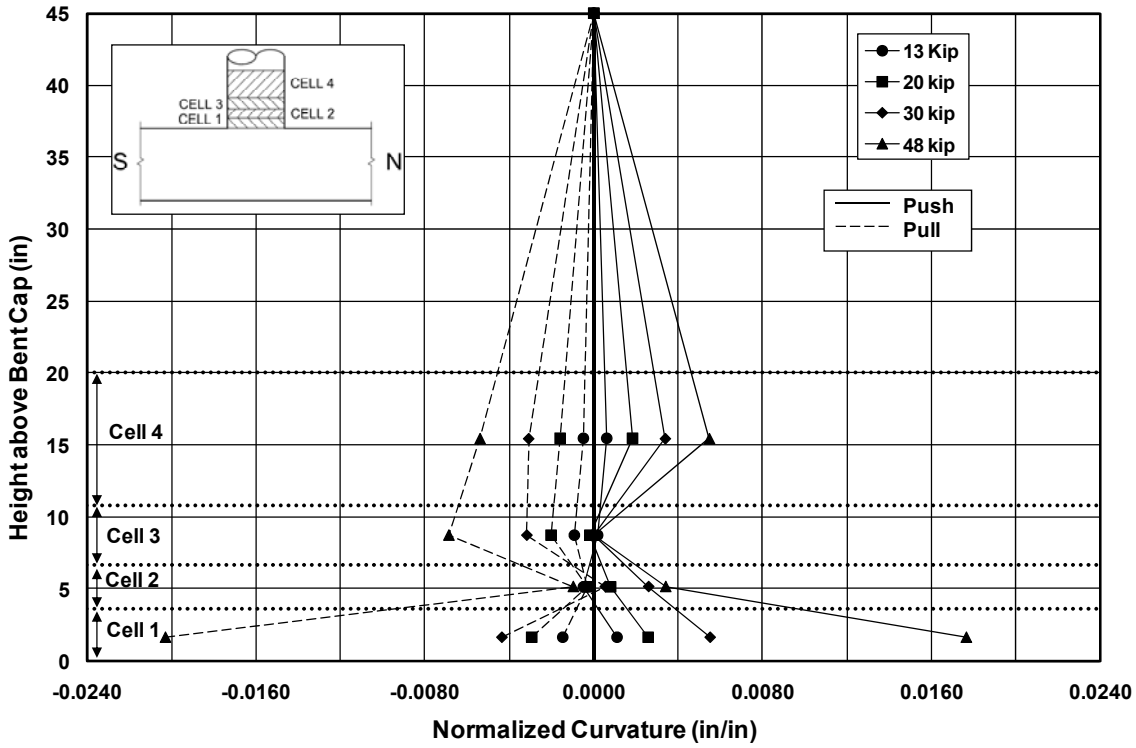

Figure 3-15. Curvature Profile—Force Control

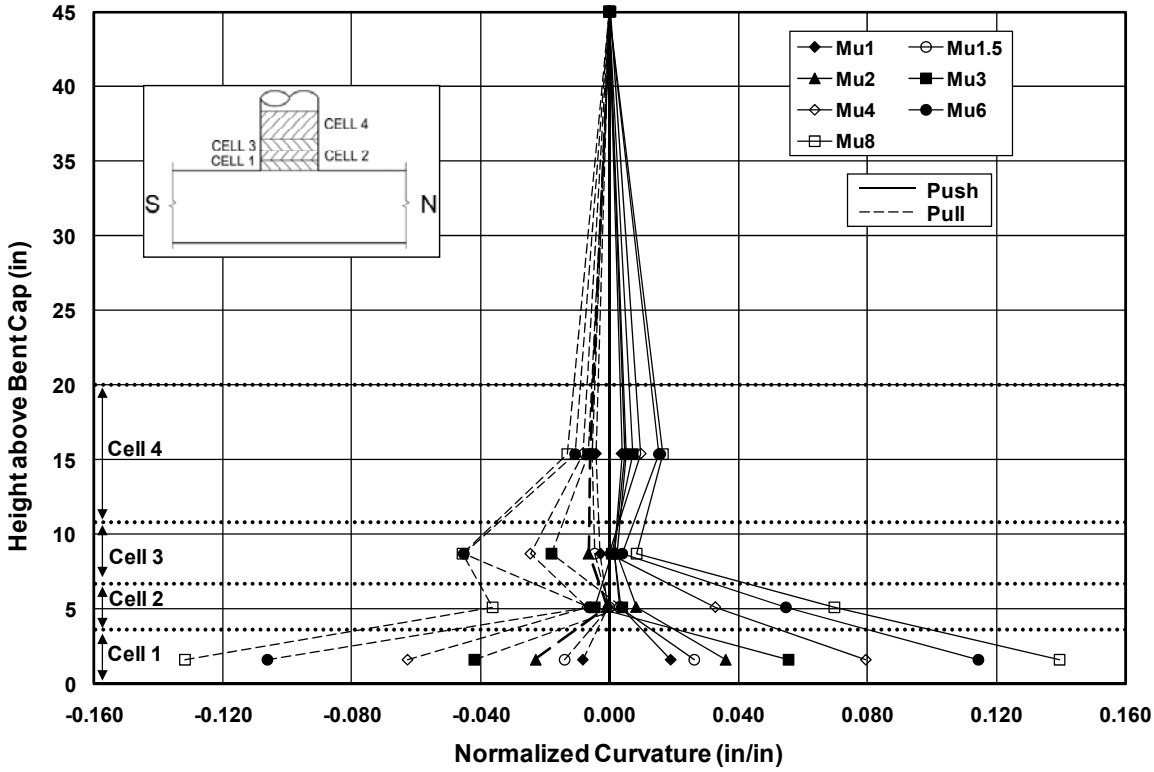

Figure 3-16. Curvature Profile—Displacement Control

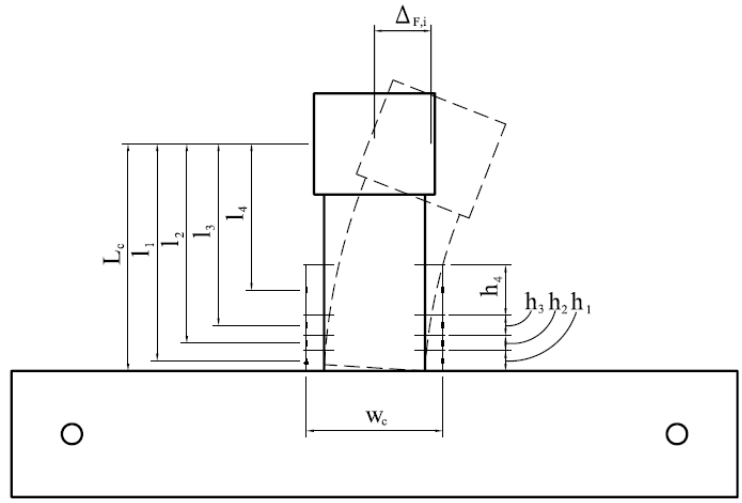

$$\Delta_{F,i} = l_i \frac{(\delta h_{i,n} - \delta h_{i,s})}{w_c}$$

$$\Delta_{F,1} = (l_1 + l'_g) \frac{(\delta h_{i,n} - \delta h_{i,s})}{w_c}$$

$$l'_g = h_1 + (0.022 \ f_y \ d_{bl})$$

A. Column Flexure and Fixed End Rotation (Cell 1)

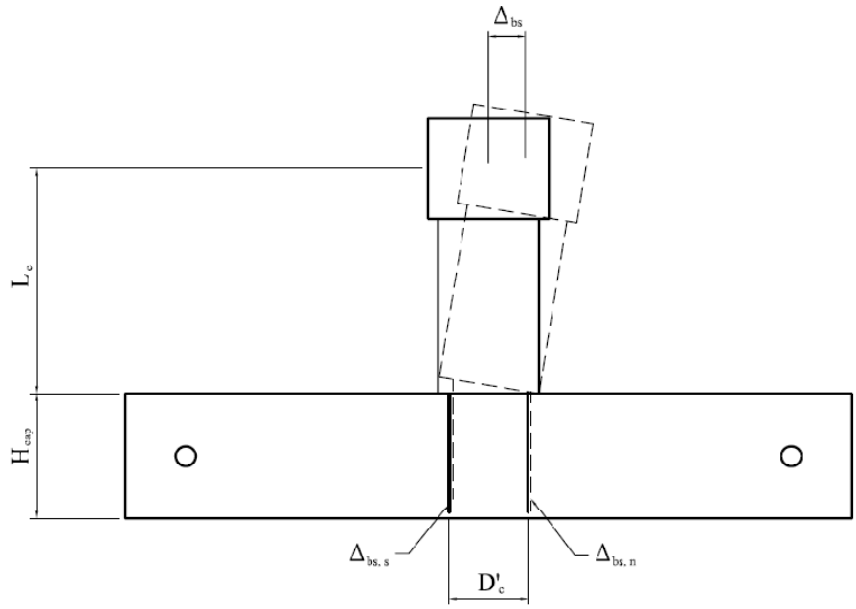

$$\Delta_{bs} = \left(\frac{\Delta_{bs,s} - \Delta_{bs,n}}{D'_c}\right)(L_c + H_{cap})$$

B. Bar Slip

Figure 3-17. Schematic Representation of Column Displacement Components

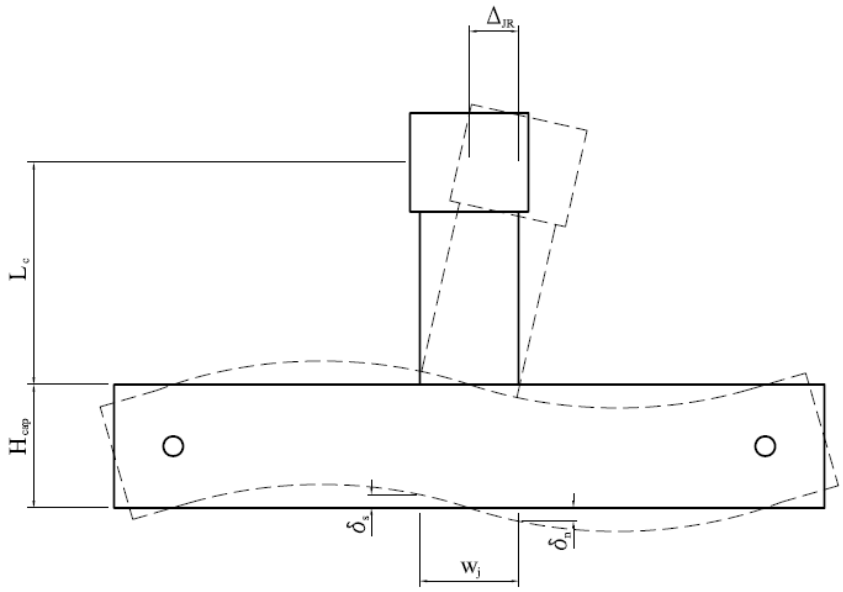

$$\Delta_{JR} = \frac{(\delta_n - \delta_s)}{w_j} (L_c + H_{cap})$$

C. Bent Cap Rotation

Figure 3-17. Schematic Representation of Column Displacement Components (Cont.)

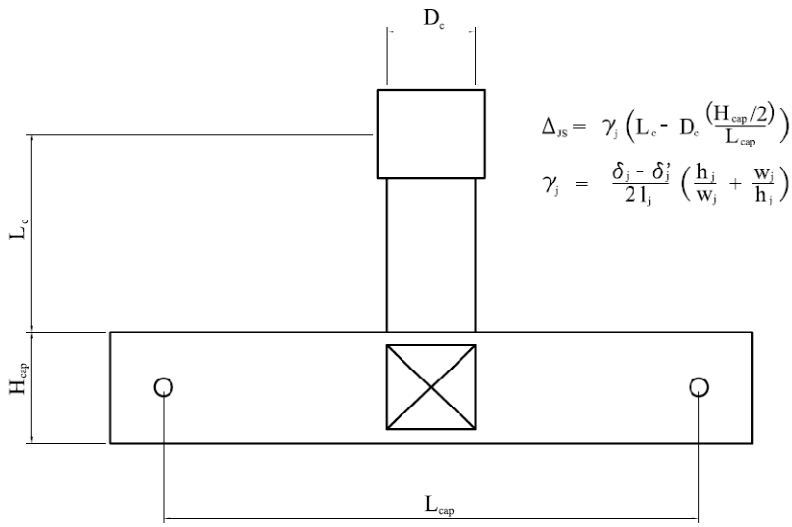

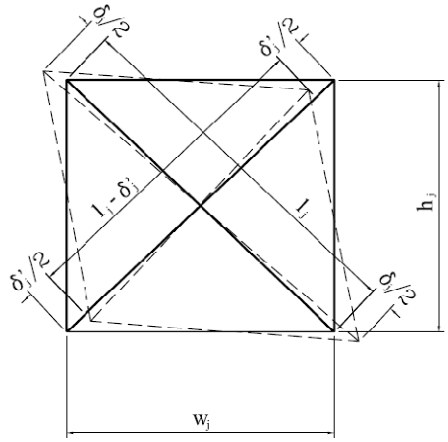

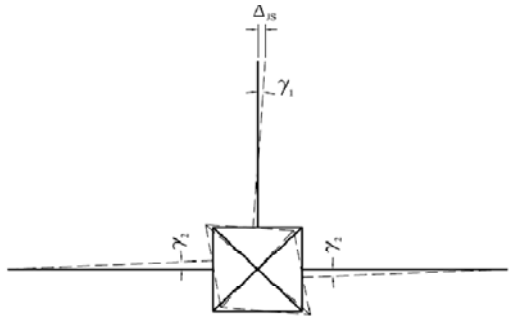

$$\gamma_j = \gamma_1 + \gamma_2$$

D. Joint Shear

Figure 3-17. Schematic Representation of Column Displacement Components (Cont.)

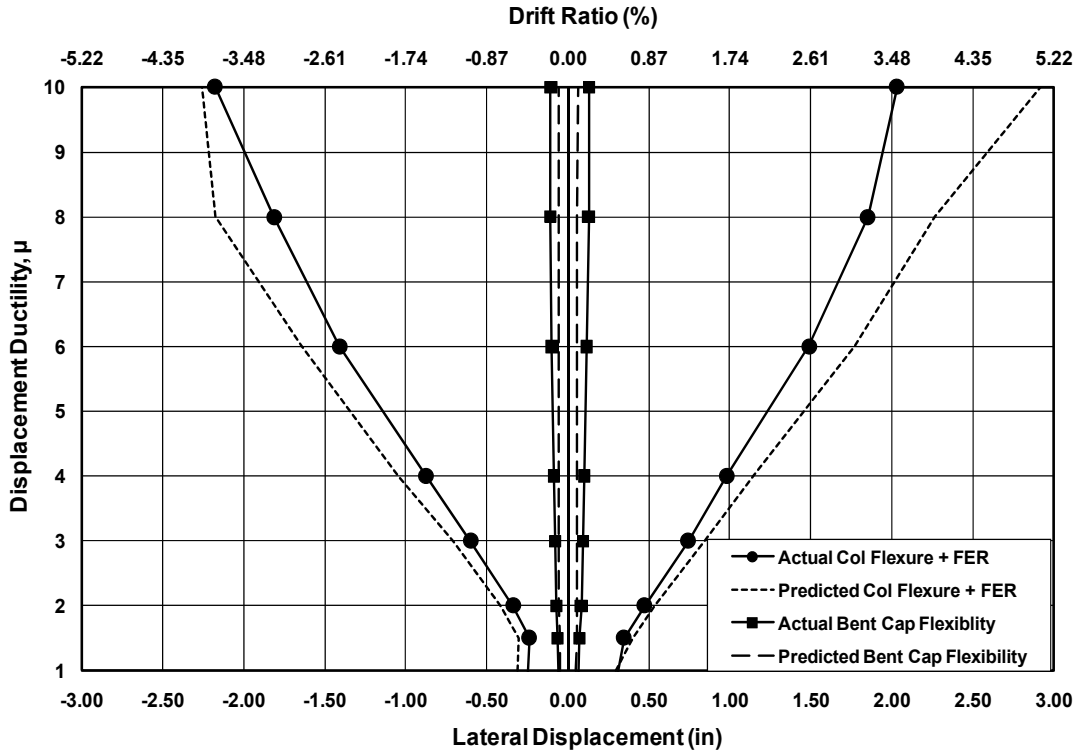

Figure 3-18. Displacement Components—Predicted vs. Actual

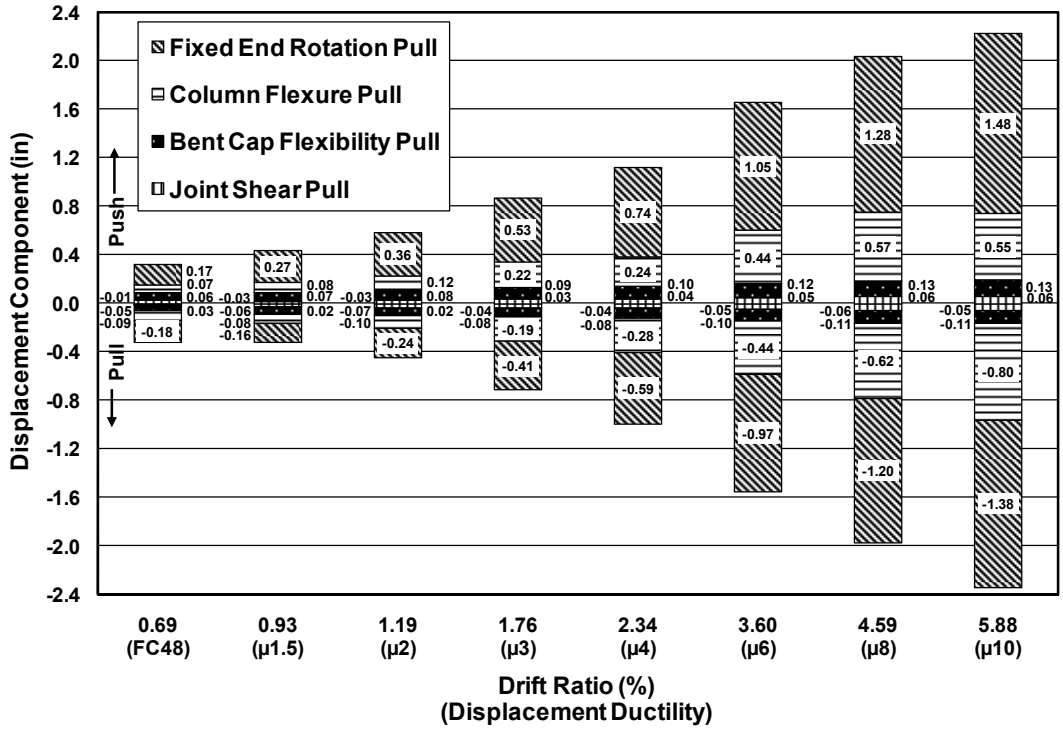

Figure 3-19. Displacement Decomposition Component Values

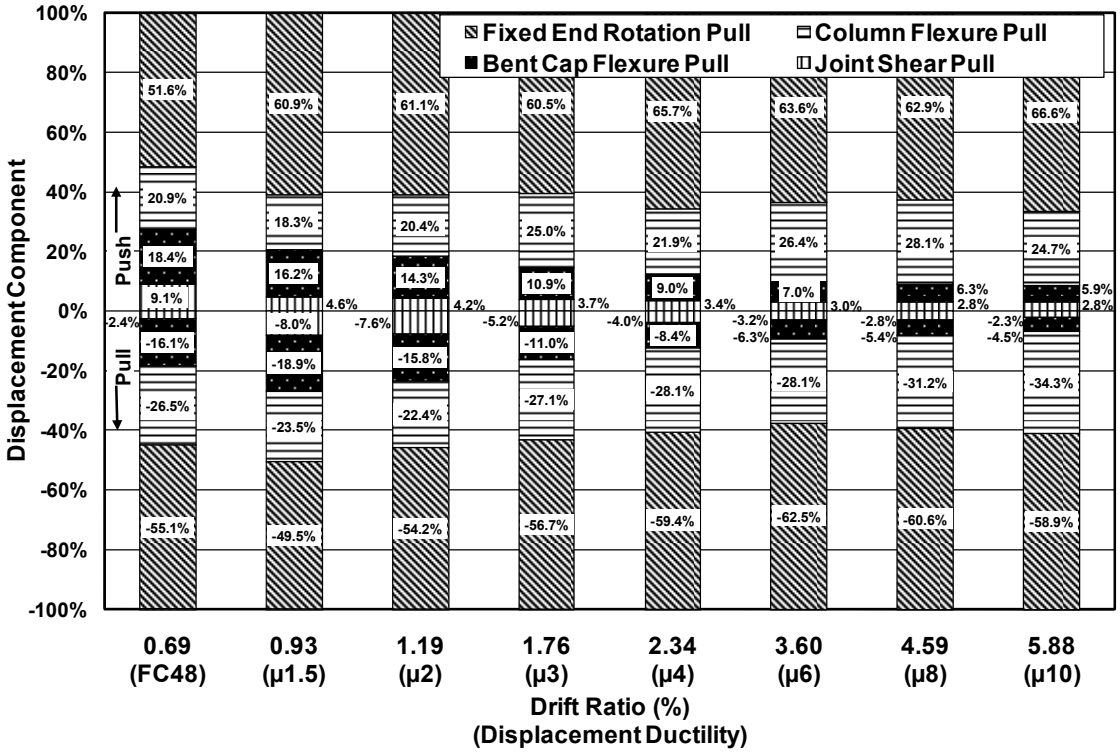

Figure 3-20. Displacement Decomposition Component Percentages

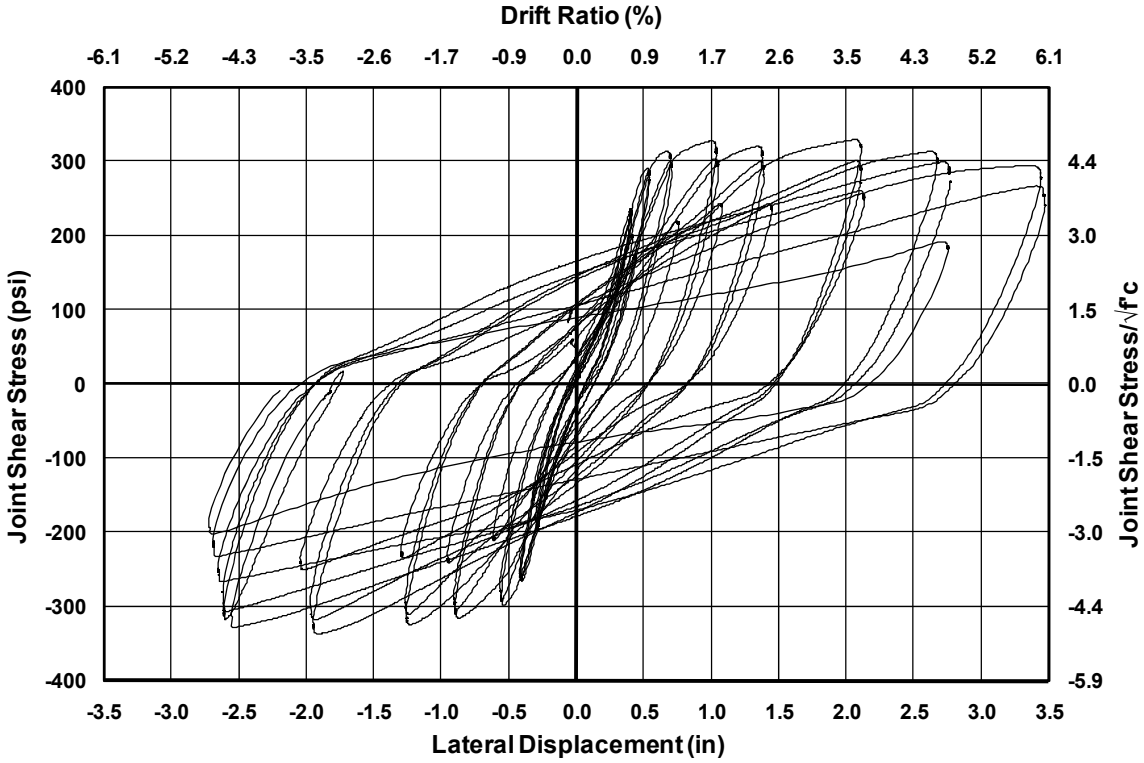

Figure 3-21. Average Joint Shear Stress vs. Lateral Displacement

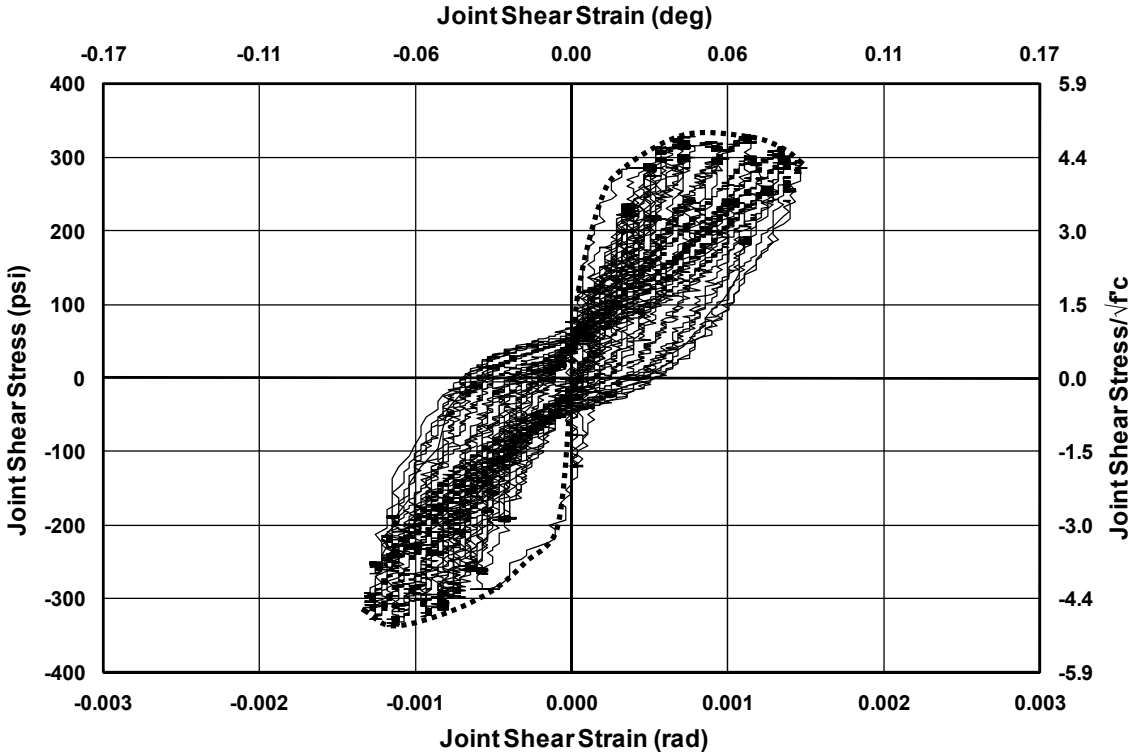

Figure 3-22. Joint Shear Stress vs. Joint Shear Strain

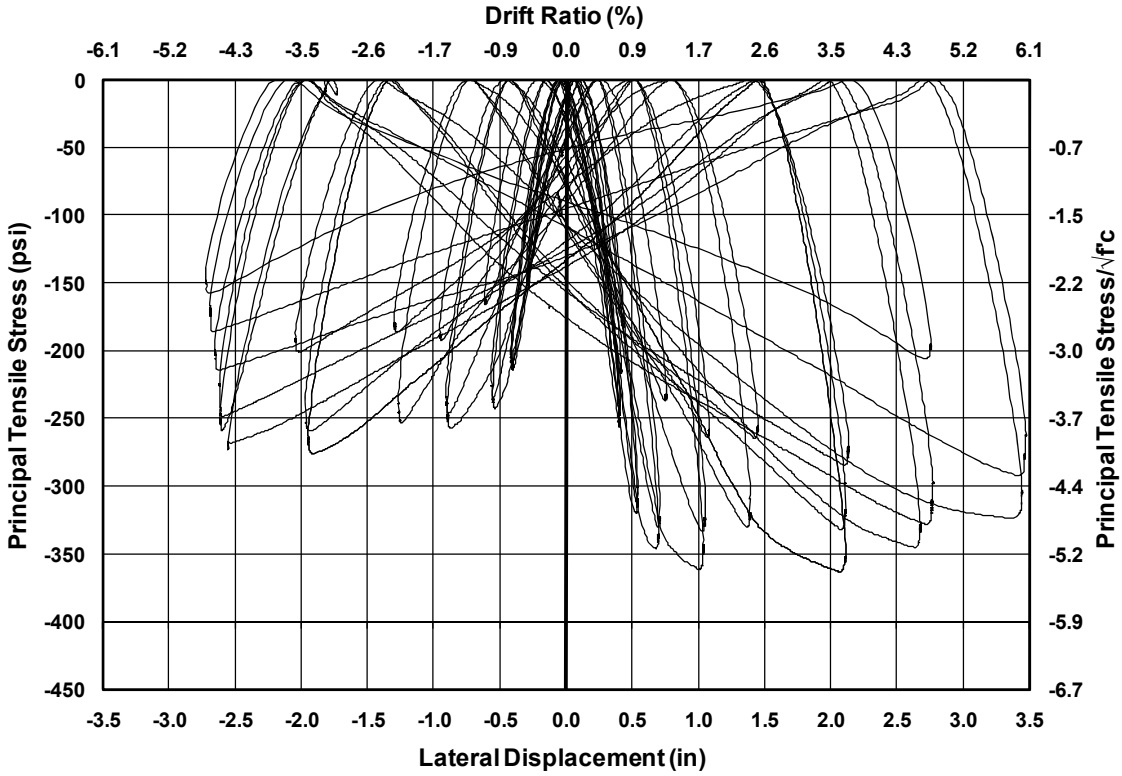

Figure 3-23. Principal Tensile Stress vs. Lateral Displacement

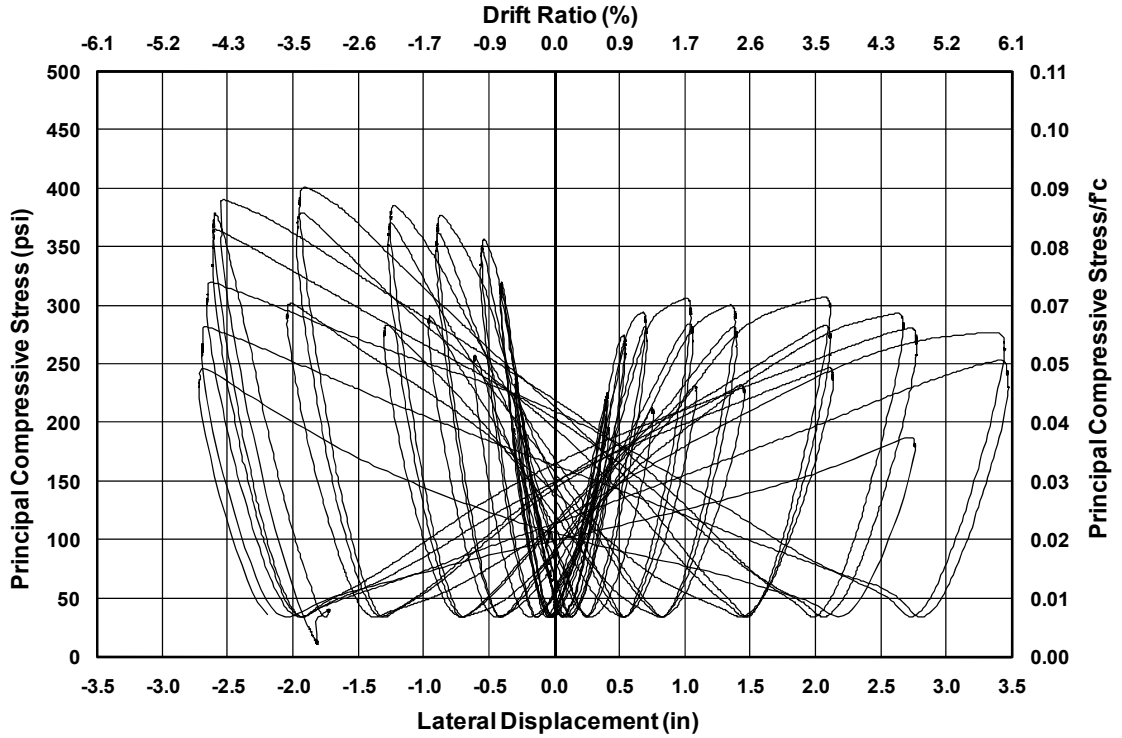

Figure 3-24. Principal Compressive Stress vs. Lateral Displacement

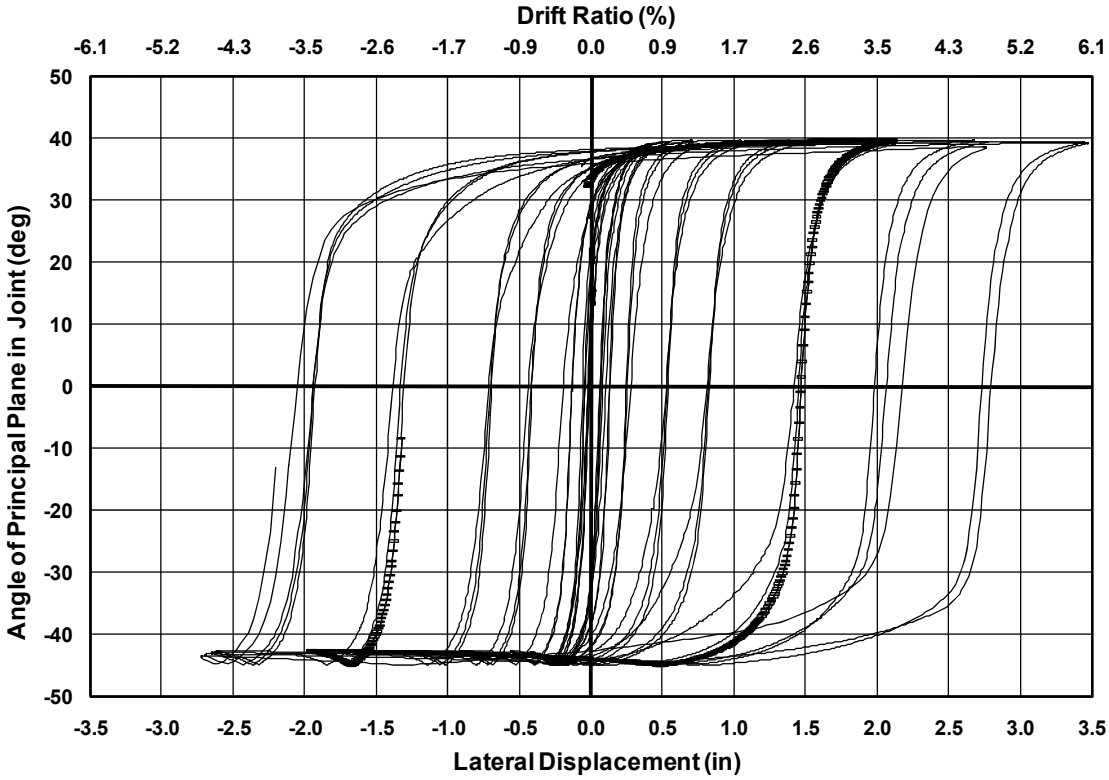

Figure 3-25. Angle of Principal Plane in Joint vs. Lateral Displacement

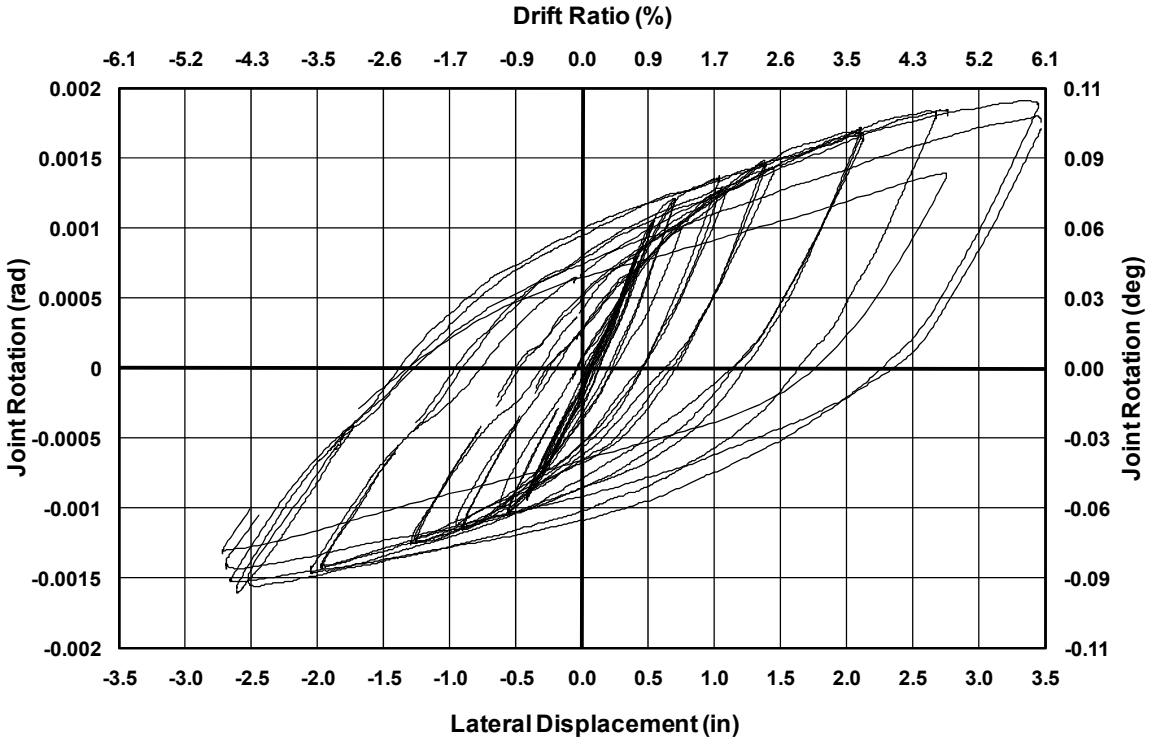

Figure 3-26. Joint Rotation vs. Lateral Displacement

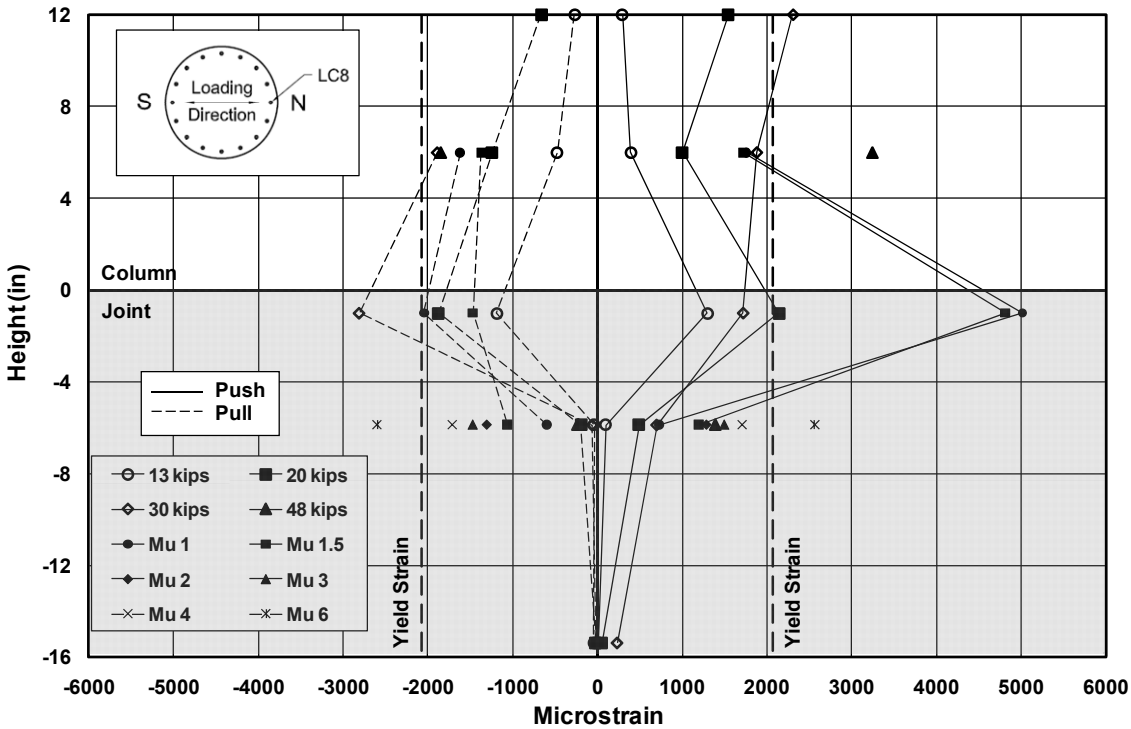

Figure 3-27. Strain Profile—Column Longitudinal Rebar (North)

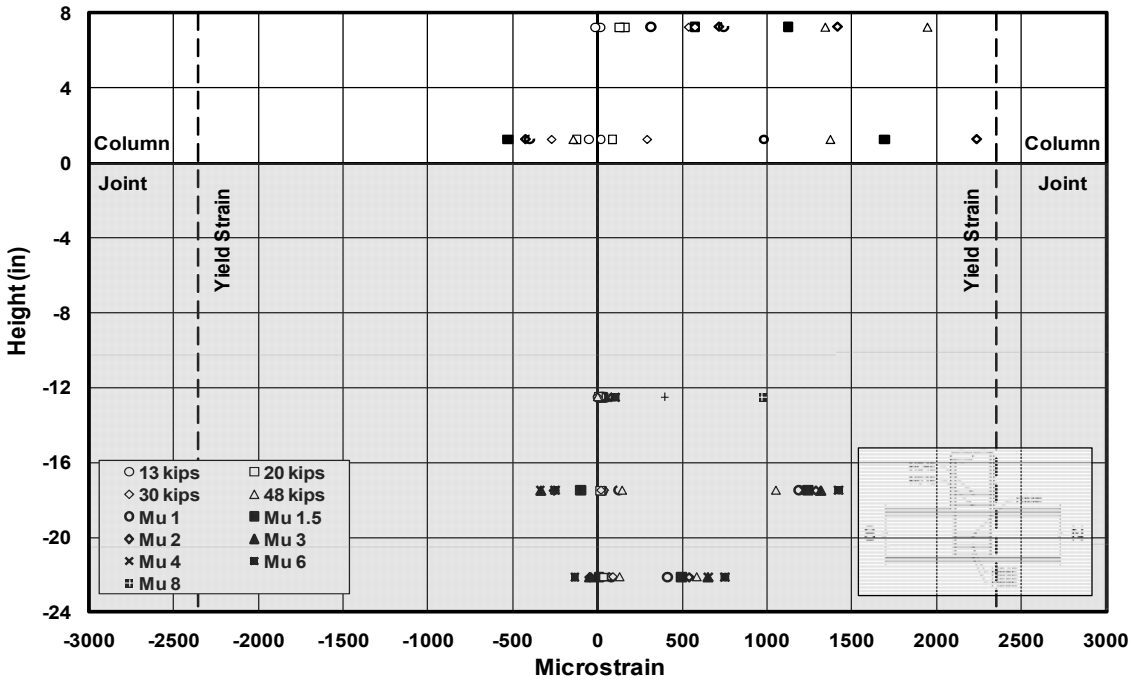

Figure 3-28. Strain Profile—Hoops in Column and Joint (East)

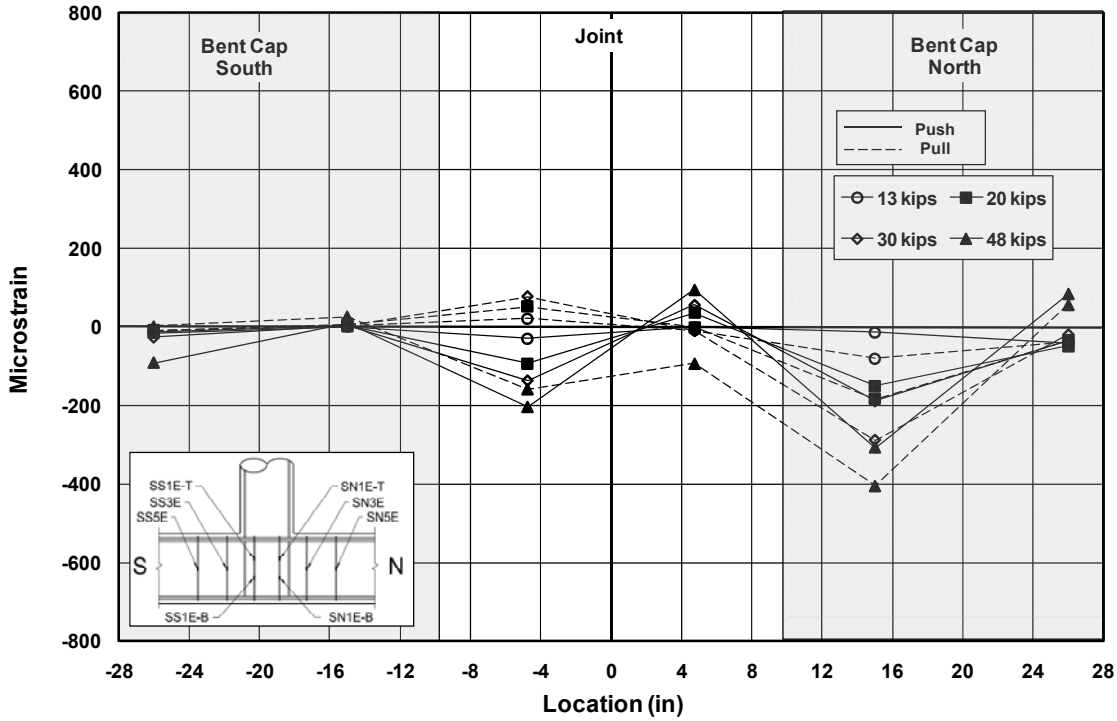

Figure 3-29. Strain Profile—Stirrups in Bent Cap (Midheight) and Joint (Top), Force Control

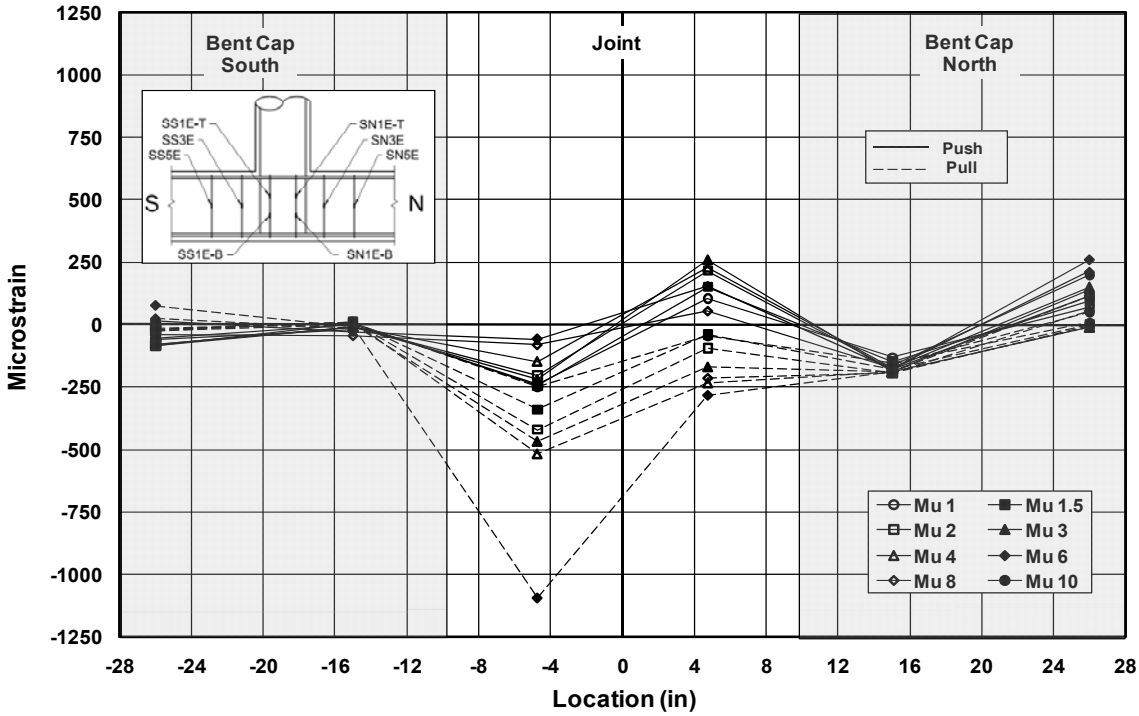

Figure 3-30. Strain Profile—Stirrups in Bent Cap (Midheight) and Joint (Top), Displacement Control

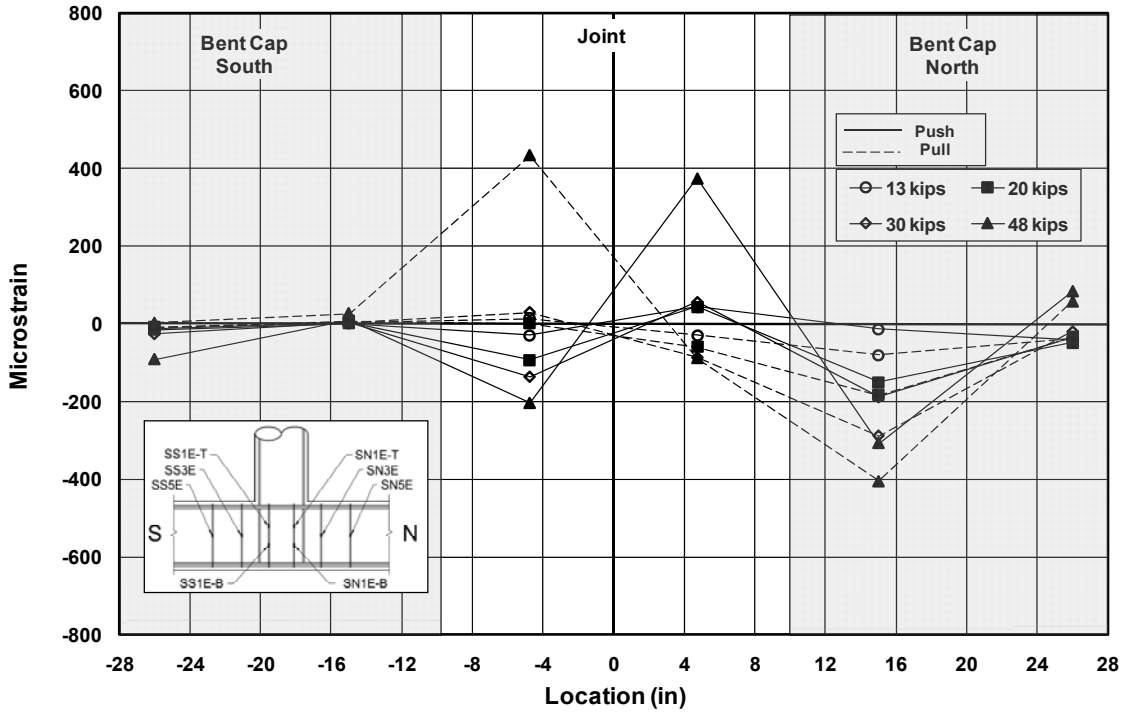

Figure 3-31. Strain Profile—Stirrups in Bent Cap (Midheight) and Joint (Bottom), Force Control

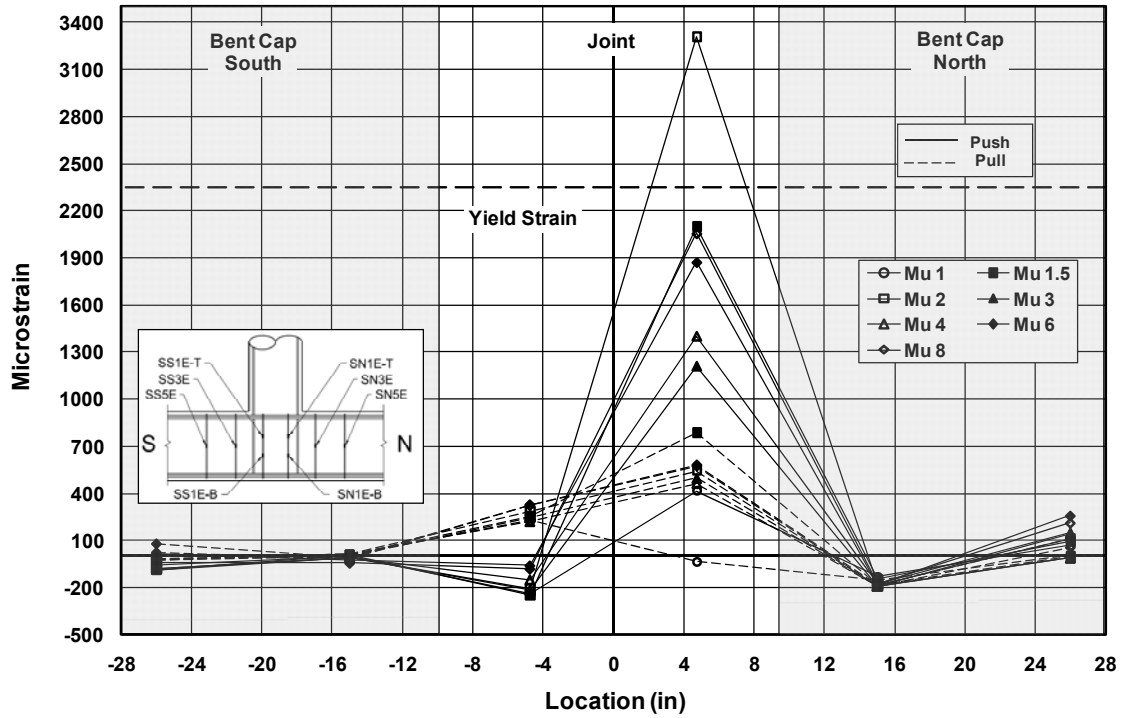

Figure 3-32. Strain Profile—Stirrups in Bent Cap (Midheight) and Joint (Bottom), Displacement Control

4.0 Summary and Conclusions

4.1 Summary

This report, Emulative Precast Bent Cap Connections for Seismic Regions: Component Tests—Cast-in-place Specimen (Unit 1), is the first in the series of four reports summarizing the California State University, Sacramento (CSUS) component tests supporting National Cooperative Highway Research Program (NCHRP) Project 12-74, "Development of Precast Bent Cap Systems for Seismic Regions". CSUS is investigating two emulative connections—cap pocket and grouted duct—for nonintegral precast bent caps.

CSUS designed the Cast-in-place (CIP) prototype bridge (and emulative component specimens) in accordance with the AASHTO LRFD Bridge Design Specifications, Third Edition, 2004, with 2006 Interims (2006 LRFD BDS) and the 2006 Recommended LRFD Guidelines for the Seismic Design of Highway Bridges (2006 LRFD RSGS) prepared as part of NCHRP 20-07 Task 193. The 2006 LRFD RSGS was superseded by the 2007 Proposed AASHTO Guide Specifications for LRFD Seismic Bridge Design and later updated to the current 2009 AASHTO Guide Specifications for LRFD Seismic Bridge Design (2009 LRFD SGS). In addition, the 2006 LRFD RSGS contains different—and in some aspects more liberal (i.e., less conservative)—joint reinforcement requirements than the current 2009 LRFD SGS. For a major seismic event, the CIP prototype bridge was designed and detailed to exhibit ductile plastic hinging in the column adjacent to the capacity-protected bent cap and joint. CSUS designed the NCHRP component specimens using a 42% scale of the central portion of the prototype bridge. The CIP control specimen—loaded in the transverse direction under quasi-static force control and displacement control sequences—was expected to perform similarly to the prototype bridge.

Specimen response was analyzed including experimental observations, hysteretic response, column curvature response, displacement decomposition, joint response, and strain records. Specimen response was dominated by plastic hinging of the column adjacent to the bent cap. In contrast to significant column flexural (and shear) cracks

associated with increasing lateral load, relatively minor joint and bent cap cracks developed. Post-test inspection revealed that the core remained primarily intact with concrete crushing localized over 1-2 in of the extreme compression zone. Several column bars buckled and fractured at the column faces at ultimate. The specimen exhibited excellent ductility to a large drift of 5.9%, which corresponded to a nominal displacement ductility of 10.

The load-displacement response indicated stable hysteretic behavior with loops of increasing area without appreciable strength degradation. A comparison of the load-displacement envelope to the predicted envelope showed a good correlation. The hysteretic response also portrayed appropriate stiffness, strength, ductility and other features such as crack distribution and widths representative of CIP response for a beam-column connection test.

The displacement decomposition confirmed the dominance of plastic hinging and showed that displacement components were reasonably determined and predictions were reasonably made. For example, at 3.6% drift (μ6), the flexural components (fixed end rotation and column flexure) accounted for 90% of the column displacement (vs. prediction of 86%). The contribution of joint shear to overall displacement was minor, not exceeding 10%,and was confirmed by visual observations of minor joint cracking. Splitting cracks formed in the bent cap and column, and the top surface of the bent cap (as tested) exhibited splitting cracks and local spalling; however, bar slip was minor, contributing less than 4% on average to the displacement component attributable to fixed end rotation. Column bars were well anchored within the joint.

Analysis of the joint indicated that the principal tensile stress was limited to, $5.4\sqrt{f_c'}$less than half of the 2006 LRFD RSGS limit of $12\sqrt{f_c'}$, but about 50% larger than $3.5\sqrt{f_c'}$, the level at which more extensive (additional) joint reinforcement is required for development of the force transfer mechanism. Principal compressive stress did not exceed $0.09f_c'$, less than a third of the 2006 LRFD RSGS limit of $0.25f_c'$. These values correspond well with the intentions of the design and the observed joint performance. The

maximum crack width was 0.025 in. The joint deformation was very small, with maximum change in panel area limited to less than 0.2%.

Strain records provided confirmation of plastic hinging and significant strain penetration, including bar yield at 6 in into the joint. Hoop confinement effects were evident for both the plastic hinging region as well the joint. Bent cap bars reached only 46% of yield, even though the specimen design did not include the additional bent cap longitudinal reinforcement ($0.245A_{st}$) required by 2009 LRFD SGS. Stirrup strain outside the joint remained well below yield, but the north construction stirrup within the joint yielded, indicating its contribution to the stable joint performance and the importance of vertical stirrups inside the joint. The test specimen, designed per 2006 LRFD RSGS, did not require stirrups inside the joint; however, two joint stirrups with an area of $0.089A_{st}$ were included for construction. These stirrups provided an area 66% of that required by the 2009 LRFD SGS ($0.135A_{st}$).

4.2 Conclusions

Based on the observed response and data analysis for the CIP specimen, the following conclusions can be drawn:

1. Despite the less conservative design basis of the specimen using the 2006 Recommended LRFD Guidelines for the Seismic Design of Highway Bridges compared to current 2009 AASHTO Guide Specifications for LRFD Seismic Bridge Design—including a smaller area of vertical stirrups within the joint and smaller area of bent cap longitudinal reinforcement—the CIP specimen satisfied the performance goal of the design, achieving an extensive drift without appreciable strength degradation and exhibiting extensive plastic hinging of the column, limited joint distress, and essentially elastic behavior of the bent cap.
2. The CIP specimen provided an appropriate benchmark (control) for comparison with the precast grouted duct and cap pocket specimens.
3. Test results can be reliably used as a supporting basis for developing design and construction specifications for seismic precast bent cap systems.

References

1. Ralls, M.L., Hyzak, M. D., Medlock, R. D., and Wolf, L. M., "Current U.S. Practice and Issues," *Proceedings of the Prefabricated Bridge Elements and Systems Workshop*, New Brunswick, NJ (September 2004).
2. Matsumoto, E.E., Waggoner, M.C., Kreger, M.E., Vogel, J., Wolf, L., "Development of a Precast Concrete Bent-Cap System," *PCI Journal*, Vol. 53, No. 3 (May-June 2008) pp.74-99.
3. Matsumoto, E.E., Waggoner, M.C., Sumen, G., Kreger, M.E., Wood, S.L., and Breen, J.E., *Development of a Precast Bent Cap System*, Research Report 1748-2, Center for Transportation Research, The University of Texas at Austin, TX (January 2001) 372 pp.
4. Mislinski, Steve, "Anchorage of Grouted Connectors For a Precast Bent Cap System in Seismic Regions (Part 2)", M.S. Thesis, California State University Sacramento, Sacramento, CA (2003).
5. Tobolski, M.J., Restrepo, J.I., Matsumoto, E.E., and Ralls, M.L., *Development of Precast Bent Cap Concepts*, SSRP Report No. 06/10. University of California, San Diego, La Jolla, CA (September 2006) 176 pp.
6. Asnaashari, A., Grafton, J., and Johnnie, M., "Precast Concrete Design-Construction of San Mateo-Hayward Bridge Widening Project," *PCI Journal*, Vol. 50 No. 1 (January-February 2005) pp. 26-43.
7. Restrepo, J.I. and Matsumoto, E.E., *National Cooperative Highway Research Program (NCHRP), Project 12-74, Development of Precast Bent Cap Systems for Seismic Regions*, Proposal to Research Board (March 31, 2005).
8. Matsumoto, E.E., Wright J., Johnsen, S., Mislinski, S., "Proposed Bridge Design Calculations and Drawings of the Prototype Bridge and Test Specimen", Submittal by Restrepo, J.I. and Matsumoto, E.E. to National Cooperative Highway Research Program Project 12-74 Panel (August 11, 2006) 232 pp.
9. American Association of State Highway and Transportation Officials. AASHTO LRFD Bridge Design Specifications (Third Edition), Washington, DC (2004, with 2006 Interims).
10. Imbsen, R. A., *Recommended LRFD Guidelines for the Seismic Design of Highway Bridges, 2006,* TRC/Imbsen & Associates, Inc, Rancho Cordova, CA (May 2006).
11. Imbsen, R. A., *Proposed AASHTO Guide Specifications for LRFD Seismic Bridge Design*, AASHTO Subcommittee on Bridges and Structures, Imbsen Consulting, Rancho Cordova, CA (March 2007).
12. American Association of State Highway and Transportation Officials. AASHTO Guide Specifications for LRFD Seismic Design Specifications (First Edition), Washington, DC (2009).
13. SEISAB, User's Manual, TRC/Imbsen Software Systems, Rancho Cordova, CA (2006).

14. Seyed-Mahan, M., User's Manual for XSection, Cross Section Analysis Program, California Department of Transportation, Sacramento, CA (1998).
15. Seyed-Mahan, M., User's Manual for WFprep and WFrame, 2-D Push Analysis of Bridge Bents and Frames, California Department of Transportation, Sacramento, CA (1995).
16. Sritharan, S., Priestley, M.J.N., and Seible, F., *Seismic Response of Column/Cap Beam Tee Connections with Cap Beam Prestressing*, SSRP Report No. 96/09, University of California, San Diego, La Jolla, CA (December 1996) 296 pp.
17. XTRACT, User's Manual, TRC/Imbsen Software Systems, Rancho Cordova, CA (2006).
18. Sritharan, S. "Improved Seismic Design Procedure for Concrete Bridge Joints," *Journal of Structural Engineering*, American Society of Civil Engineers, Reston, VA, Vol. 131, No. 9 (September 2005) pp. 1334-1344.

Notation

A_c	Cross sectional area of column (in^2)
A_L	Area of hysteretic loop for a complete cycle (push and pull) (kip-in)
A_R	Area of rectangle bounded by maximum loads and displacements of a complete hysteretic loop (kip-in)
B_{cap}	Thickness of the bent cap (in)
BS	Bar Slip (in)
CD	Column displacement (in)
CT	Component total for column displacement (in)
d_{bl}	Nominal diameter of longitudinal column reinforcing steel bars (in)
D_c	Diameter or depth of column in direction of loading (ft or in)
D'_c	Diameter or depth of column in direction of bending (ft or in)
E_c	Modulus of elasticity of concrete (ksi)
FC	Force control
f'_c	Nominal compressive concrete strength (ksi)
f'_{cg}	Nominal compressive grout strength (ksi)
FER	Fixed end rotation of column (in)
f_h	Average normal stress in the horizontal direction within a moment resisting joint (ksi)
f_v	Average normal stress in the vertical direction within a moment resisting joint (ksi)
f_y	Specified minimal yield stress (ksi)
G_c	Shear modulus of concrete (ksi)
h	Distance from c.g. of tensile force in column to c.g. of compressive force on the section (in)
H_{cap}	Height of bent cap (in)
h_i	Height of cell i (in)
h_j	Joint panel height (in)
h_1	Height of cell 1 (in)

$I_{e\,col}$ Effective moment of inertia of column (in^4)

$I_{t\,col}$ Transformed moment of inertia of column (in^4)

L_c Distance from critical section of column (bent cap soffit) to point of contraflexure (in)

L_{cap} Length of bent cap (in)

l_{ac} Length of column reinforcement embedded into bent cap (in)

l_i Distance from point of contraflexure of column to the midheight of cell I (in)

l_j Diagonal joint panel length (in)

l_1 Distance from point of contra flexure of column to the midheight of cell 1 (in)

l'_g Strain penetration length of cell 1 (in)

l_{sp} Equivalent strain penetration length taken as $0.022 f_y d_{bl}$ (in)

M_{YE} Theoretical column moment at effective yield based on moment-curvature analysis (kip-in or kip-ft)

M_{Yexp} Experimental first yield moment of column (kip-in or kip-ft)

p_c Principal compressive stress (ksi)

P_H Horizontal actuator force on side of column stub (kips)

p_t Principal tensile stress (ksi)

P_V Vertical actuator force on top of column stub (kips)

T_c Column tensile force (kip)

v_{jv} Nominal vertical shear stress in a moment resisting joint (ksi)

w_c Width of cell (in)

w_j Joint panel width (in)

γ_j Nominal vertical shear strain in a moment resisting joint (ksi)

Δ_{bs} Column displacement due to bar slip (in)

$\Delta_{bs,s}$ Bar slip displacement, south (in)

$\Delta_{bs,n}$ Bar slip displacement, north (in)

$\Delta_{F,i}$ Column Displacement due to flexure at cell i (in)

$\Delta_{F,1}$ Column displacement due to fixed end rotation at cell 1 (in)

$\delta h_{i,n}$ Column displacement of cell i, north (in)

$\delta h_{i,s}$	Column displacement of cell i, south (in)
δ_j	Increase in diagonal joint panel length (in)
δ'_j	Increase in diagonal joint panel length in direction perpendicular to l_j (in)
Δ_{jr}	Column displacement due to joint rotation (in)
$\delta_{jr,n}$	Vertical displacement of bent cap at north end of joint (in)
$\delta_{jr,s}$	Vertical displacement of bent cap at south end of joint (in)
Δ_{js}	Column displacement due to joint shear (in)
δ_n	Joint rotation displacement, north (in)
δ_s	Joint rotation displacement, south (in)
Δ_s	Column displacement due to column shear (in)
Δ_Y	System first yield displacement (in)
Δ_{ye}	Member effective yield displacement (in)
Δ_{YE}	System effective yield displacement (in)
ξ	Equivalent viscous Damping ratio
μ_D	Displacement ductility demand
φ	Column curvature (1/in)

List of Equations

Average joint shear strain	$\gamma_j = \frac{\delta_j - \delta'_j}{2l_j}\left(\frac{h_j}{w_j} + \frac{w_j}{h_j}\right)$
Average joint shear stress	$v_{jv} = \frac{T_c}{l_{ac}B_{cap}}$
Average principal angle in joint	$\theta_p = \frac{A_c}{2} tan^{-1}\left(v_{jv} / \frac{f_h - f_v}{2}\right)$
Average principal compressive stress in joint	$p_c = \frac{(f_h + f_v)}{2} + \sqrt{\left(\frac{f_h - f_v}{2}\right)^2 + {v_{jv}}^2}$
Average principal tensile stress in joint	$p_t = \frac{(f_h + f_v)}{2} - \sqrt{\left(\frac{f_h - f_v}{2}\right)^2 + {v_{jv}}^2}$
Column displacement due to bar slip	$\Delta_{bs} = \left(\frac{\Delta_{bs,s} - \Delta_{bs,n}}{D'_c}\right)\left(L_c + H_{cap}\right)$
Column displacement due to column shear (analytical)	$\Delta_s = \frac{P_H L_c}{0.9 A_c G_c}\left(\frac{E_c I_{tcol}}{E_c I_{ecol}}\right)$
Column displacement due to flexure at cell i	$\Delta_{F,i} = l_i \frac{\left(\delta h_{i,n} - \delta h_{i,s}\right)}{w_c}$
Column displacement due to joint rotation	$\Delta_{jr} = \frac{(\delta_n - \delta_s)}{w_j}\left(L_c + H_{cap}\right)$
Column displacement due to joint shear	$\Delta_{js} = \gamma_j\left(L_c - D_c \frac{\left(H_{cap}/2\right)}{L_{cap}}\right)$
Column curvature, cell i	$\varphi = \frac{\Delta_{F,i}/W_c}{l'_g}$
Column tensile force	$T_c = \frac{M_o^{col}}{h} = \frac{P_h L_c}{h}$

Equivalent viscous damping ratio	$\xi = \left(\frac{2}{\pi}\right)\left(\frac{A_L}{A_R}\right)$
Joint rotation angle	$\theta_{jr} = \frac{\delta_{jr,n} - \delta_{jr,s}}{D_c}$
Modified height of cell 1 accounting for strain penetration	$l'_g = l_{sp} + h_1\left(1 - 1.67\, {h_1}/{L_c}\right)$
System effective yield displacement	$\Delta_{YE} = \frac{M_{YE}}{M_{Yexp}}\Delta_Y$

California State University, Sacramento
College of Engineering and Computer Science
Research Report

EMULATIVE PRECAST BENT CAP CONNECTIONS FOR SEISMIC REGIONS: COMPONENT TESTS— GROUTED DUCT SPECIMEN (UNIT 2)

Eric E. Matsumoto, Ph.D., P.E.

November 19, 2009

Final Report for: NCHRP 12-74, Development of Precast Bent Cap Systems for Seismic Regions

ECS Report Number: ECS-CSUS-2009-02

College of Engineering and Computer Science

California State University, Sacramento

Sacramento, California 95819-6023

California State University, Sacramento
College of Engineering and Computer Science
Research Report

EMULATIVE PRECAST BENT CAP CONNECTIONS FOR SEISMIC REGIONS: COMPONENT TESTS—GROUTED DUCT SPECIMEN (UNIT 2)

Eric E. Matsumoto, Ph.D., P.E.
Associate Professor, Structural Engineering

November 19, 2009

Final Report for: NCHRP 12-74, Development of Precast Bent Cap Systems for Seismic Regions

ECS Report Number: ECS-CSUS-2009-02

College of Engineering and Computer Science
California State University, Sacramento
Sacramento, California 95819-6023

Please cite this report as follows:
Matsumoto, Eric. E., *Emulative Precast Bent Cap Connections for Seismic Regions: Component Tests—Grouted Duct Specimen (Unit 2)*, ECS Report No. ECS-CSUS-2009-02, California State University, Sacramento, CA (November 2009) 102 pp.

DISCLAIMER

The research presented in this report was conducted as part of the National Cooperative Highway Research Program, Project 12-74, Development of Precast Bent Cap Systems for Seismic Regions. The opinions and conclusions expressed or implied in the report are solely those of the author. They are not necessarily those of the Transportation Research Board, the National Research Council, the Federal Highway Administration, the American Association of State Highway and Transportation Officials, or the individual states participating in the National Cooperative Highway Research Program.

ACKNOWLEDGMENT OF SPONSORSHIP

This work was sponsored by the American Association of State Highway and Transportation Officials, in cooperation with the Federal Highway Administration, and was conducted in the National Cooperative Highway Research Program, which is administered by the Transportation Research Board of the National Research Council.

OTHER ACKNOWLEDGEMENTS

The author gratefully acknowledges the significant contributions from many graduate and undergraduate students, as well as laboratory technicians at California State University, Sacramento. Of particular note are David Van Zanen, P.E., Arvind Gopalakrishna, Jeremy Wright, P.E., Andy Wilson, Jim Ster, and Brett Anthony. The author also gratefully acknowledges contributions from the NCHRP 12-74 Team, including Dr. Jose I. Restrepo and Matthew Tobolski, University of California, San Diego; Mary Lou Ralls, P.E., Ralls-Newman LLC; and Steve Mislinski, P.E, AECOM/LAN Engineering. Finally, the author gratefully acknowledges the many contributions of Clark Pacific, West Sacramento, CA (Glen Underwood, Don Clark, and others) for fabrication support, as well as Robert J. Gulyas, BASF Construction Products, LLC, for grouting support.

EXECUTIVE SUMMARY

This report, Emulative Precast Bent Cap Connections for Seismic Regions: Component Tests—Grouted Duct Specimen (Unit 2), is the second in the series of four reports summarizing the California State University, Sacramento (CSUS) component tests supporting National Cooperative Highway Research Program (NCHRP) Project 12-74, "Development of Precast Bent Cap Systems for Seismic Regions". CSUS is investigating two emulative connections—cap pocket and grouted duct—for nonintegral precast bent caps.

CSUS designed a Cast-in-place (CIP) prototype bridge and emulative component specimens including the Grouted Duct (GD) specimen in accordance with the 2006 Recommended LRFD Guidelines for the Seismic Design of Highway Bridges (2006 LRFD RSGS), which contains less conservative joint reinforcement requirements—including a smaller area of vertical stirrups within the joint and smaller area of bent cap longitudinal reinforcement—than the 2009 AASHTO Guide Specifications for LRFD Seismic Bridge Design (2009 LRFD SGS). For a major seismic event, the CIP prototype bridge was designed and detailed to exhibit ductile plastic hinging in the column adjacent to the capacity-protected bent cap and joint. The GD specimen was designed using a 42% scale of the central portion of the prototype bridge.

Specimen response was dominated by plastic hinging of the column adjacent to the bent cap. Post-test inspection revealed that the core and bedding layer remained primarily intact with column bars buckling and two bars fracturing at ultimate. The specimen exhibited excellent ductility to a large average drift of 5.2%, which corresponded to a nominal displacement ductility of 8. Similar to the CIP specimen, the GD load-displacement response indicated stable hysteretic behavior without appreciable strength degradation.

Displacement decomposition confirmed the dominance of plastic hinging. For example, at 2.6% drift (μ4, average), the flexural components (fixed end rotation and column flexure) accounted for 84% of the column displacement. The contribution of joint shear to overall displacement was minor, not exceeding 8%. This was confirmed by

visual observations of joint crack widths limited to 0.040 in. The joint shear stiffness based on the joint shear stress-strain response compared closely to the CIP, with limited joint softening evident at increasing drift ratios. Column bars were well anchored within the joint, with bar slip contributing less than 9% on average to fixed end rotation. Displacement component magnitudes and percentages for the GD and CIP specimens compared very favorably.

Principal tensile stresses exceeded $3.5\sqrt{f_c'}$ and justified the use of additional joint reinforcement required for development of a force transfer mechanism. The test specimen, designed per 2006 LRFD RSGS, did not require stirrups inside the joint; however, two joint stirrups were included for construction, providing an area 65% of that required by the 2009 LRFD SGS ($0.135A_{st}$). Strain records confirmed plastic hinging, effective hoop confinement in the column and joint, and strain penetration into the joint. Bent cap longitiduinal bars reached only 53% of yield, even though the specimen design did not include the additional bent cap longitudinal reinforcement ($0.245A_{st}$) required by 2009 LRFD SGS. Stirrup strain outside the joint reached 68% of yield and, although the construction stirrups within the joint did not yield, the south stirrup reached 75% of yield, indicating its contribution to the stable joint performance and the importance of vertical stirrups inside the joint. The CIP specimen exhibited a similar trend of large stirrup strains (exceeding yield) within the joint.

Despite the less conservative design basis compared to the 2009 LRFD SGS, the GD specimen satisfied the performance goal of the design, achieving an extensive drift without appreciable strength degradation and exhibiting extensive plastic hinging of the column, limited joint distress, and essentially elastic behavior of the bent cap. Emulative performance is concluded for the GD specimen based on closely matching overall behavior between the GD and CIP specimens, including lateral load-displacement response, dominance of plastic hinging, joint shear stiffness, level of joint distress, pattern of joint cracking, strain patterns of bent cap and joint reinforcement, integral behavior between the bedding layer, column, ducts, and bent cap, and minor effects due

to bar slip. The importance of the fabrication and assembly processes, as well as the use of stirrups within the joint region, should be addressed in future recommendations.

TABLE OF CONTENTS

Page

LIST OF TABLES

Chapter 1

Chapter 2

Chapter 3

LIST OF FIGURES

Chapter 2

Chapter 3

1.0 Introduction

1.1 Background

This report, Emulative Precast Bent Cap Connections for Seismic Regions: Component Tests—Grouted Duct Specimen (Unit 2), is the second in the series of four reports summarizing the California State University, Sacramento (CSUS) component tests supporting National Cooperative Highway Research Program (NCHRP) Project 12-74, "Development of Precast Bent Cap Systems for Seismic Regions". CSUS is investigating two emulative connections—cap pocket and grouted duct—for nonintegral precast bent caps. It is recommended that readers review the Unit 1 Test Report [1] for further project background.

1.2 NCHRP 12-74 Research Objective

To address the uncertainties associated with seismic behavior of precast bent cap systems and the lack of specifications, the National Cooperative Highway Research Program (NCHRP) funded Project 12-74, Development of Precast Bent Cap Systems for Seismic Regions, to develop design methodologies, design and construction specifications, design examples, and semi-standard details for seismic precast bent cap systems using emulative and hybrid connections for nonintegral and integral systems. [2, 3]

1.3 CSUS Research Objective and Approach

The California State University, Sacramento (CSUS) research objective is to develop design methodologies, design and construction specifications, design examples, and semi-standard details for nonintegral emulative precast bent caps. As reported in Reference 2, two emulative connections types—grouted duct and cap pocket—were selected for development based on a review of past connection usages and consideration of expected seismic performance, durability, constructability, and cost.

Nine tasks are included in NCHRP 12-74 to reach the overall research objectives. [3] As part of Task 6—Conduct of Analytical and Experimental Work—CSUS conducted tests and associated analysis to investigate grouted duct and cap pocket connections.

Table 1-1 shows the Test Matrix for CSUS component tests, including a brief summary of the four test specimens (units).

1.4 Scope of Report

This report, Emulative Precast Bent Cap Connections for Seismic Regions: Component Tests—Grouted Duct Specimen (Unit 2), is the second in a series of four reports that summarize the experimental and analytical efforts for each CSUS test unit. This report includes the following chapters:

1.0 Introduction: Background, statement of NCHRP research objective, CSUS research objective and approach, and scope of report.

2.0 Specimen Design, Fabrication, and Testing: Summary of the Grouted Duct (GD) specimen design, fabrication and testing, including key aspects of fabrication processes and issues, as well as specimen material properties, test setup, loading sequence, instrumentation and pretest predictions.

3.0 Specimen Response and Analysis: Experimental observations, hysteretic response, column curvature response, displacement decomposition, joint response, and strain records. An important additional aspect is the comparisons between the GD (Unit 2) results and the Cast-in-place (CIP) (Unit 1) results.

4.0 Summary and Conclusions.

1.5 Tables

Table 1-1. CSUS Component Test Matrix for Bent Cap-Column Connections

Test Unit	Brief Description
1. Cast-in-place (CIP)	Control specimen for comparison to precast connections, with bent cap and column detailing intended to achieve full ductility
2. Grouted Duct Connection (GD)	Individual ducts cast in bent cap to connect each column bar, with bent cap and column detailing intended to achieve full ductility
3. Cap Pocket Full Ductility (CPFD)	Single pipe cast in bent cap to connect all column bars, with bent cap and column detailing intended to achieve full ductility
4. Cap Pocket Limited Ductility (CPLD)	Single pipe cast in bent cap to connect all column bars, with bent cap and column detailing intended to achieve limited ductility

2.0 Specimen Design, Fabrication, and Testing

2.1 Design

The GD specimen used the same full-ductility design basis as the CIP specimen reported in Reference 1, for direct comparison. Figure 2-1 shows the portion of the prototype bridge used for the 42% scaled specimen design.

The design of the GD specimen assumed emulative response would be achieved despite the following differences between the GD test specimen when compared to the CIP specimen:

- Separate precast elements, including the bent cap and column
- Use of closely spaced 1.75-in diameter corrugated ducts in the bent cap and high strength non-shrink cementitious grout to anchor the column bars
- Use of a 1.5-in bedding layer between the bent cap soffit and column to accommodate tolerances

Specimen drawings are shown in Figures 2-2 through 2-6. In addition, Table 2-1 provides a detailed comparison of the column, bent cap, and joint reinforcement for the CIP prototype and GD specimen. Ratios of the specimen reinforcement to the similitude (or design) ratio are shown to be reasonably close to 1.0.

It is recommended that readers review the Unit 1 Test Report [1] for further design background.

2.2 Fabrication

2.2.1 Specimen

The GD specimen consisted of a separately cast bent cap and column, as shown in Figures 2-2 through 2-6. As for the CIP control specimen, the bent cap used a 25 in x 25 in cross section, 12-#5's (0.65%) for flexural reinforcement, and #3's at 6 in for transverse (shear) reinforcement. The 20-in diameter column included 16-#5's (1.58%) and #3 hoops at 2 in within the plastic hinge region. Joint reinforcement included three sets of 4-leg #3 stirrups at 5 in (with two sets of #3 cross ties through the depth) adjacent to each side of the joint, #3's at 5 in hoop reinforcement, and an embedment depth of column bars equal to the joint depth less 3 in (i.e., 22 in). Figure 2-6 shows a somewhat

congested but constructible joint region, including two 2-leg stirrups intentionally placed in the joint to represent construction stirrups sometimes used for support of the rebar cage or limit states other than seismic. Due to the use of ducts, the joint region of the bent cap was more congested than that of the CIP specimen, but not excessively. Bent cap flexural bars were threaded between ducts longitudinally, and construction stirrups were threaded through the ducts transversely.

Table 2-2 summarizes select details of the GD specimen, including tolerances, duct clearance, and bedding layer.

2.2.2 Material Properties

Portland cement concrete, non-shrink grout, and reinforcing steel used in the fabrication of the bent cap and column were tested to determine material properties. Sampling, preparing, and testing of specimens were generally performed in accordance with governing ASTM standards.

2.2.2.1 Portland Cement Concrete

The bent cap and column were constructed with normal weight concrete using the concrete mix proportions shown in Table 2-3. The mix design was expected to achieve a 28-day compressive strength of 4000 psi based on a water-cement ratio of approximately 0.49. A 3/8-inch maximum coarse aggregate size was used in the concrete mix in accordance with specimen scaling. Standard 6 x 12-in cylinders were cast from the concrete batch used for the specimen fabrication. Concrete cylinders were cured for the same length of time and in the same conditions as the concrete specimens.

Compression and tensile (split cylinder) tests were conducted in the CSUS Structural Laboratory. Concrete cylinders were produced for each casting and tested over a range of days including test day.

The design and actual properties of the concrete are shown in Table 2-4, and representative concrete compressive strength gain curves are shown in Figure 2-7. The same batch of concrete was used for the bent cap and column.

2.2.2.2 Non-shrink Grout

Masterflow 928 (MF928) was selected as the grout material. It is a prepackaged, hydraulic cement-based, mineral-aggregate high strength, non-shrink grout with an extended working time, meeting the requirements of ASTM C 1107 (Standard Specification for Packaged Dry, Hydraulic-Cement Grout (Nonshrink)), Grades B and C, and the Army Corp of Engineers' CRD C 621 (Specification for Non-Shrink Grout), Grades B and C. [4] MF928 was selected based on its performance in previous CSUS and Texas Department of Transportation (TxDOT) testing that showed MF928 to have exceptional strength and fluidity, extended working time, versatility under a wide range of temperatures, and durability. [5, 6]

For each batch of grout, 2-in cubes were prepared, cured, stored, and tested in accordance with ASTM C109 (Standard Test Method for Compressive Strength of Hydraulic Cement Mortars). The grout strength at time of specimen testing was intended to exceed the concrete compressive strength by at least 1000 psi, to help ensure that the grout was not the weak link in the connection. As shown in Figure 2-8, this was achieved.

2.2.2.3 Steel

The column and bent cap longitudinal reinforcing steel consisted of ASTM A706 Grade 60 deformed #5 rebar, and the column hoops and stirrups consisted of ASTM A615 Grade 60 (weldable) #3's. Uniaxial tensile tests were conducted on samples from the rebar lot; rebar specimens were prepared in accordance with ASTM requirements. Yield and tensile strengths are shown in Table 2-5 for the different bar sizes. Figure 2-9 shows the stress-strain plot for the #3 reinforcing bars, displaying expected strength and ductility. Although limitation in the data collection limited the exact determination of yield strength, it is reasonably bounded within a narrow range. The extensometer was removed prior to bar fracture.

Corrugated duct material was galvanized, cold-rolled steel per ASTM A653. Ducts were spiral, 1.75-in nominal diameter, 22-gage, with a corrugation height of 0.060 in. Ducts used interlocking seams and were semi-rigid.

2.2.3 Fabrication and Issues

2.2.3.1 Fabrication

All CSUS specimens were fabricated with the assistance of Clark Pacific, West Sacramento, CA. The fabrication and assembly of the specimens were intended to replicate as much as possible the expected field process, and thereby examine constructability issues. Therefore, all specimens, including the GD specimen, were built in the upright position. Assembly of the bent cap and column into the T-shaped specimen was performed in the CSUS Structural Laboratory.

Construction Sequence

The construction sequence for the GD specimen included the following (Figures 2-10 through 2-19):

1. Fabricate rebar cages for the bent cap and column, including strain gages, at CSUS.
2. Transport rebar cages to Clark Pacific, prepare bent cap and column forms, and cast bent cap and column concrete.
3. Transport precast cap and column to CSUS.
4. Prepare column and bent cap for assembly, and conduct cap setting operation in upright position.
5. Prepare connection for grouting and pump grout into the bedding layer.
6. Invert specimen and install in test area.

The cap was set and the bars placed within the tolerances shown in Table 2-2.

Grouting Operation

As shown in Figure 2-16, a hand pump system and collar were used for grouting the bedding layer and ducts. Grout was pumped from the bottom of the bedding layer up into the ducts, and an air vent system at the top of the bedding layer helped prevent air entrapment within the connection.

Preparation: The fluidity of grout was determined before grouting using a flow cone test in accordance with the ASTM C 939 (Figure 2-16). The inside surface of the corrugated ducts and column bars were lightly brushed with a wire brush to remove any

residual concrete. Column bars were reasonably centered and did not touch any duct. After the bedding layer form was attached and sealed, the bedding layer was pre-watered for approximately 24 hours to ensure sealing and prevent loss of moisture from the grout. After draining the water, bar slip rods were attached to the column bars. Finally, the grout pump was assembled and primed.

Grout Mixing and Placement: Grout with a flow cone efflux time between 20-30 sec was established on the day of grouting. Several batches were prepared in accordance with manufacturer's recommendations, including using the grout within the recommended temperature range, adding mixing water to the mixer before the packaged grout, and mixing the grout for the recommended time. After mixing using a paddle-type mortar mixer, grout was poured into buckets, which were carried to the specimen. Within the 30 minute working time, grout was placed in the connection. Grout was first placed into the grout hopper, which used a 0.5-in screen to remove any clumps (Figure 2-16). Grout in the hopper was lightly tamped before pumping to remove any air. After the grout hose was attached to the bedding layer form, grout was smoothly pumped at the rate of approximately one stroke per two sec. The hopper was kept filled and a cut-off valve used to prevent entrapping air during pumping. Once grout flowed through the air vents in the bedding layer, the vents were sealed. Grout was pumped within 2 in of the top of the ducts. The pumping valve was then closed, and grout was added manually to top off each duct, with tamping of the grout and bar (Figures 2-17 and 2-18). After hardening, curing compound was applied to the top surface.

Form Removal and Inspection: After several days, the bedding layer form was removed and the bedding layer and top of the ducts were inspected. No air voids were observed.

After grouting, the specimen was inverted, as shown in Figure 2-19, and installed into the test area.

2.2.3.2 Issues

The specimen was fabricated and assembled according to the drawings and procedures, except as noted in Table 2-6, which summarizes significant specimen

as-builts for column bars and hoops. The most significant deviation from the drawing was the placement of the first column hoop below the top of column approximately 1.25 in below its intended location, due to interference with a threaded rod used for curvature.

2.3 Testing

2.3.1 Test Setup

The specimen test setup, shown in Figure 2-20, includes the following:

- Simply supported bent cap, with an equivalent pin support at the north end with vertical and lateral restraint (right side as shown) and an equivalent roller at the south end with vertical support only (left side as shown). This simple setup allowed accurate establishment of specimen forces. Although scaled modeling of the moment gradient along the cap was not required, accurate conditions adjacent to the faces of the joint were required and modeled in appropriate proportion to resist the column moment. [7, 8] The test setup ensured accurate conditions at each end of the joint so that the force transfer mechanism in the joint could be investigated.
- Inverted specimen, with a column stub. This allowed biaxial loading of the specimen, using a vertical hydraulic actuator to apply scaled gravity load and the horizontal hydraulic actuator to induce seismic response.
- Different axial force conditions in the bent cap for the push and pull directions. The push direction was considered more critical, as the axial force causes tension at the joint face, in contrast to the compression for the pull direction. However, the magnitude of axial force remained relatively small during testing.

2.3.2 Loading Sequence

The vertical and horizontal hydraulic actuators were used to apply specified Force Control and Displacement Control sequences to the specimen, as shown in Figures 2-21 and 2-22. The stages of loading are briefly summarized as follows:

1. <u>Vertical Load</u>: A monotonic increasing concentrated vertical load representing gravity load was applied to the top of the column stub to a

maximum load of 38 kips. Force Control was used to maintain the vertical load throughout the horizontal loading sequence. A very slight change in vertical load developed during testing.

2. Horizontal Load: After the vertical load was applied, a horizontal load or displacement, representing seismic-induced load or displacement, was applied in two sequences: Force Control, followed by Displacement Control.

   Force Control: An increasing horizontal load was applied to the side of the column stub using one cycle per load level (Figure 2-21). A cycle consisted of both push and pull for the specified load. Load was held at select cycle peaks for crack marking, photographing and documenting. The Force Control sequence was discontinued after an approximate determination of first yield of column longitudinal bars in the push and pull directions.

   Establishment of Effective Yield: Column strain gages and displacement measurements were intended to be used to calculate the system effective yield displacement, Δ_{YE}, and thus displacement ductility demand, μ_D, for the Displacement Control sequence. Establishment of first yield was approximate due to loss of some gages, leading to the application of a relatively large force during Force Control, and thus a relatively nominal response during the first stages of Displacement Control (through ~μ2). The following equation specifies the relationship between the experimental first yield displacement of the system, Δ_Y, and the system effective yield displacement, Δ_{YE}, used for establishing the Displacement Control sequence:

$$\Delta_{YE} = \frac{M_{YE}}{M_{Y\exp}} \Delta_Y$$

   where M_{YE} is the theoretical moment at effective yield based on moment-curvature analysis, and M_{Yexp} is the experimental first yield moment (experimental force at the first yield times the distance between the actuator and soffit). The ratio of M_{YE}/M_{YEexp} was approximately 1.4.

Displacement Control: Displacements were applied quasi-statically to the column stub in 3 cycles: two cycles at the target displacement ductility, followed by one cycle at the displacement ductility of the prior level (see Figure 2-22). Application of reversed cyclic displacements permitted examination of hysteretic loop stability. Displacement ductility demand, as multiples of system effective yield displacement, was applied at the following levels, or until the residual capacity of the specimen dropped below 30% of the maximum load: $\mu 1$, $\mu 1.5$, $\mu 2$, $\mu 3$, $\mu 4$, $\mu 6$, $\mu 8$. (Note: $\mu 1$ = nominal (target) displacement ductility of 1.0, $\mu 2$ = nominal displacement ductility of 2.0, etc.) Four cycles were used for the final stage of loading at $\mu 8$. Data reduction accounted for the slight additional lateral load applied to the specimen due to the inclination of the vertical actuator under cyclic displacements.

2.3.3 Instrumentation

Extensive instrumentation was used for the test specimen, including internal gages (strain gages mounted on bent cap and column rebar) and external gages (linear potentiometers and LVDTs mounted on the column, joint, and cap). Figures 2-23 through 2-27 show the instrumentation drawings, which define gage locations, and Figures 2-28 through 2-32 show various photos of the instrumentation attached to the specimen.

Strain gages on column longitudinal bars and hoops were intended to help quantify column flexure, including plastic hinging and strain penetration. Strain gages on bent cap longitudinal bars and stirrups, including in the joint region, were expected to provide evidence of joint distress and a force transfer mechanism through and adjacent to the joint. Strain gages on the ducts were expected to show the magnitude, orientation, and distribution of duct strain.

Linear potentiometers and LVDTs provide column displacement, column curvature, panel deformation, joint rotation, bar slip, and specimen rigid body motion. Column curvature required the use of two linear potentiometers, one on each side of the column, to determine curvature. Four sets were used to divide the column into four

curvature cells. Table 2-7 summarizes column curvature cell as-builts. Two sets of panel deformation gages were used to examine joint panel deformation. On the east side of the specimen, five linear potentiometers were used, whereas on the west side a simplified measurement with two linear potentiometers was used. To limit the number of gages, bent cap curvature was not explicitly examined. However, the bent cap was assumed to remain essentially elastic. Strain gages were used to monitor strain levels in the bent cap flexural reinforcement.

In addition to active instrumentation, specimen response was documented using digital photos, crack markings and measurements, video recording, and hand notes.

2.3.4 Pretest Predictions

2.3.4.1 Stages of Cracking

Four stages of initial specimen cracking were examined: 1) initial bent cap cracking in flexure due to gravity loads (specimen self weight plus the vertical actuator force, P_V; 2) initial bent cap cracking in flexure with the additional horizontal actuator force, P_H; 3) initial column flexural cracking; and 4) initial joint cracking.

Table 2-8 summarizes the predicted values of vertical and horizontal actuator loads for the stages of cracking. Bent cap flexural cracking was not expected under specimen self-weight and the maximum applied vertical load, P_V, of 38 kips. However, the addition of a minor horizontal load, P_H, of 8 kips was expected to generate the first flexural crack. Column cracking was anticipated at a slightly larger horizontal load of 13 kips. Finally, joint shear cracking was not expected until P_H reached a large value of 46 kips. It should be noted that prediction of cracking load is considered an estimate, as it depends on the highly variable tensile strength of concrete and possible effects of preexisting cracks.

2.3.4.2 Lateral Load-Lateral Displacement Envelope

An envelope of the lateral load-lateral displacement response of the column was predicted before testing. Figure 2-33 shows a close comparison between this prediction and that for the CIP specimen. Deflection at each stage was taken as the sum of the

column displacements due to column elastic deflection to yield, column plastic deflection, column shear, and bent cap flexibility.

Flexural component contributions were calculated using moment-curvature results from the sectional analysis software, which used stress-strain models for the concrete and steel based on actual material tests of the concrete and steel used in the specimen. An effective yield curvature based on a bilinear moment-curvature response with best fit secondary stiffness was used to define the member effective yield displacement, Δ_{ye}. Various levels of displacement ductility were established as a multiple of the effective yield displacement of the system, Δ_{YE}.

2.3.4.3 Moment-Curvature Envelope

An envelope of the normalized moment-curvature response of the column was also predicted, using XTRACT, as shown in Figure 2-34. [9] Note that the curvature was normalized by multiplying curvature by the column diameter; moment was not modified. This prediction is shown to be close to that for the CIP specimen.

2.4 Tables

Table 2-1. Comparison of Reinforcement for CIP Prototype and GD Specimen

GD		Prototype Design	Similitude [or Design] Requirement	Test Specimen	Specimen to Similitude [or Design] Ratio
Column					
Longitudinal Reinforcement					
Bar Size (diameter, in)		#11 (1.41)	0.59	#5 (0.63)	1.06
No. of bars		16	14	16	1.14
f_y	ksi	66.0	—	64.5	—
ρ		0.0138	0.0138	0.0158	1.14
M_n^*	K·ft	3760	272	215	0.79
M_n/D^3	K·ft/ft^3	58.7	58.7	46.4	0.79
Transverse Reinforcement					
Bar Size (diameter, in)		#6 (0.75)	0.31	#3 (0.38)	1.20
Spacing	in	3.0	[1.8]	2.0	[1.11]
f_y	ksi	66.0	—	64.1	—
ρ		0.0139	0.0139	0.0125	0.90
Bent Cap					
Longitudinal Reinforcement					
Bar Size (diameter, in)		#11 (1.41)	0.59	#5 (0.63)	1.06
No. of bars		12	—	12	—
f_y	ksi	66.0	—	64.5	—
ρ		0.0051	0.0051	0.0065	1.27
M_n^*	K·ft	6680	483	443	0.92
M_n/bh^2	K·ft/ft^3	44.2	44.2	49.0	1.11
Transverse Reinforcement					
Bar Size (diameter, in)		#6 (0.75)	0.31	#3 (0.38)	1.20
Spacing	in	12.0	[8.4]	6.0	[0.71]
f_y	ksi	66.0	—	64.1	—
Joint					
Inside Joint					
Transverse Reinforcement (ρ_s)					
Bar No. (diameter, in)		#6 (0.75)	—	#3 (0.38)	—
Spacing	in	3.0	—	5.0	—
ρ_s/ρ_{min}		5.56†	—	1.22	—
f_y	ksi	66.0	—	64.1	—
Side Face Reinforcement (A_s^{sf})					
No. of bars - Bar Size		8 - #6	—	4 - #3	—
A_s/A_{cap}	in^2/ in^2	0.19	[0.10]	0.12	[1.20]
f_y	ksi	60.0	—	64.1	—
Construction Stirrups					
No. of bars - Bar Size		2 2-leg – #6	—	2 2-leg - #3	—
Area	in^2	1.76	—	0.44	—
f_y	ksi	66.0	—	64.1	—
Adjacent to Joint					
Vertical Stirrups (A_s^{jv})					
No. of bars - Bar Size		5 4-leg - #6	—	3 4-leg - #3	—
Spacing	in	6.0	—	5.0	—
A_s^{jv}/A_{st}	in^2/ in^2	0.35	[0.20]	0.27	[1.33]
f_y	ksi	66.0	—	64.1	—
Horizontal Ties (A_s^{jh})					
No. of bars - Bar Size		4 - #6	—	2 - #3	—
Spacing	in	12.0	—	8.0	—
A_s^{jh}/A_{st}	in^2/ in^2	0.35	[0.10]	0.13	[1.33]
f_y	ksi	60.0	—	64.1	—

Note: Prototype and Specimen Design per 2006 LRFD RSGS [10]

*Nominal moment @ ε_c=0.003

†Represents extension of column hoops into the joint

Table 2-2. Select Design Details

Issue	Detail
Fabrication and Placement Tolerance for Column Bars	+/- 0.56 in
Clearance between Ducts	1.03 in
Bedding Layer	1.5-in thick layer; no shims; no hoop reinforcement

Table 2-3. Concrete Mix Proportions

Material Designation	(Based on Saturated Surface Dry)		
	Quantity	Weight (lbs)	Volume (ft^3)
ASTM C 150 – Type I/II		564	2.87
ASTM C 33 – 3/8"		1,826	10.92
ASTM C 33 – Concrete Sand		1,217	7.39
ASTM C 494 – Super plasticizer	45 oz	3	0.05
Water	W/C=0.49	276	4.43
Total Air Content	5.00%		1.35
TOTAL		3,886	27.0

Table 2-4. Concrete Properties

Parameter	Design	Actual
Slump	5½" +/- 2½"	~ 3 in, cap and column
Unit Weight	143.9 pcf	–
Compressive Strength	4000 psi (28 day)	Cap and Column: 4557 psi (194 day)
Modulus of Elasticity	N/A	Cap and Column: 3400 ksi (194 day)

Table 2-5. Yield and Tensile Strength of Reinforcing Bars

Rebar Size	Type	Yield Strength (ksi)	Tensile Strength (ksi)
#3	Bent cap stirrups; Column hoops	64.1	99.0
#5	Bent cap longitudinal; Column longitudinal	64.5	95.2

*Due to testing limitations, yield strength was taken as value of first data point indicating strain hardening. Actual value of yield strength may be slightly lower than listed value.

Table 2-6. Significant Column As-builts

Description	Drawing	As-built
Length of column reinforcement embedded into bent cap, l_{ac}	22 in	22 in +/- 3/8 in (average)
Column bar location relative to center of duct	0.0 in	≤ 5/16 in
Column hoop spacing within plastic hinge	0.0 in	+/- 1/8 in
First column hoop below top of column	≤1 in	2.25 in (ave); varied due to interference with threaded rod

Table 2-7. Column Curvature Cell As-builts—GD vs. CIP

Cell Number	Drawing		GD		CIP	
	Cell Height (in)	Cell Width (in)	Cell Height (in)	Cell Width (in)	Cell Height (in)	Cell Width (in)
Cell 1	3.5	26	3.74	26.27	3.67	26.79
Cell 2	3.0	26	2.89	26.22	3.00	26.04
Cell 3	4.0	26	4.15	26.11	4.14	26.01
Cell 4	9.5	26	9.46	26.16	9.25	26.07

Table 2-8. Predicted Stages of Specimen Cracking

Item	Load (kips)	
	P_V	P_H
Bent Cap—Flexural	None	-
	38.0	8.0
Column—Flexural	38.0	12.6
Joint Shear	38.0	46.0

2.5 Figures

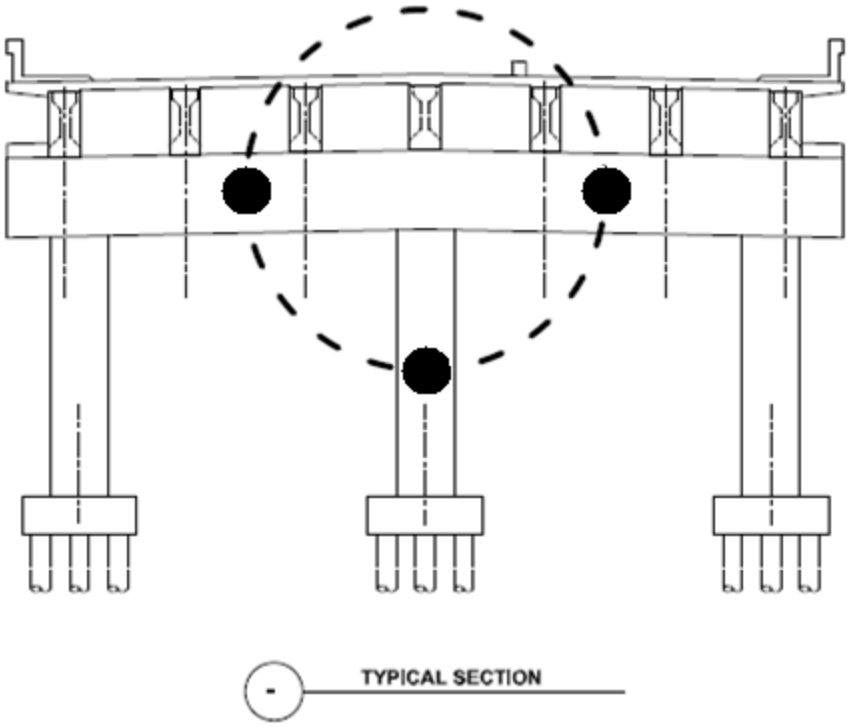

Figure 2-1. Portion of Prototype Used for Specimen Design

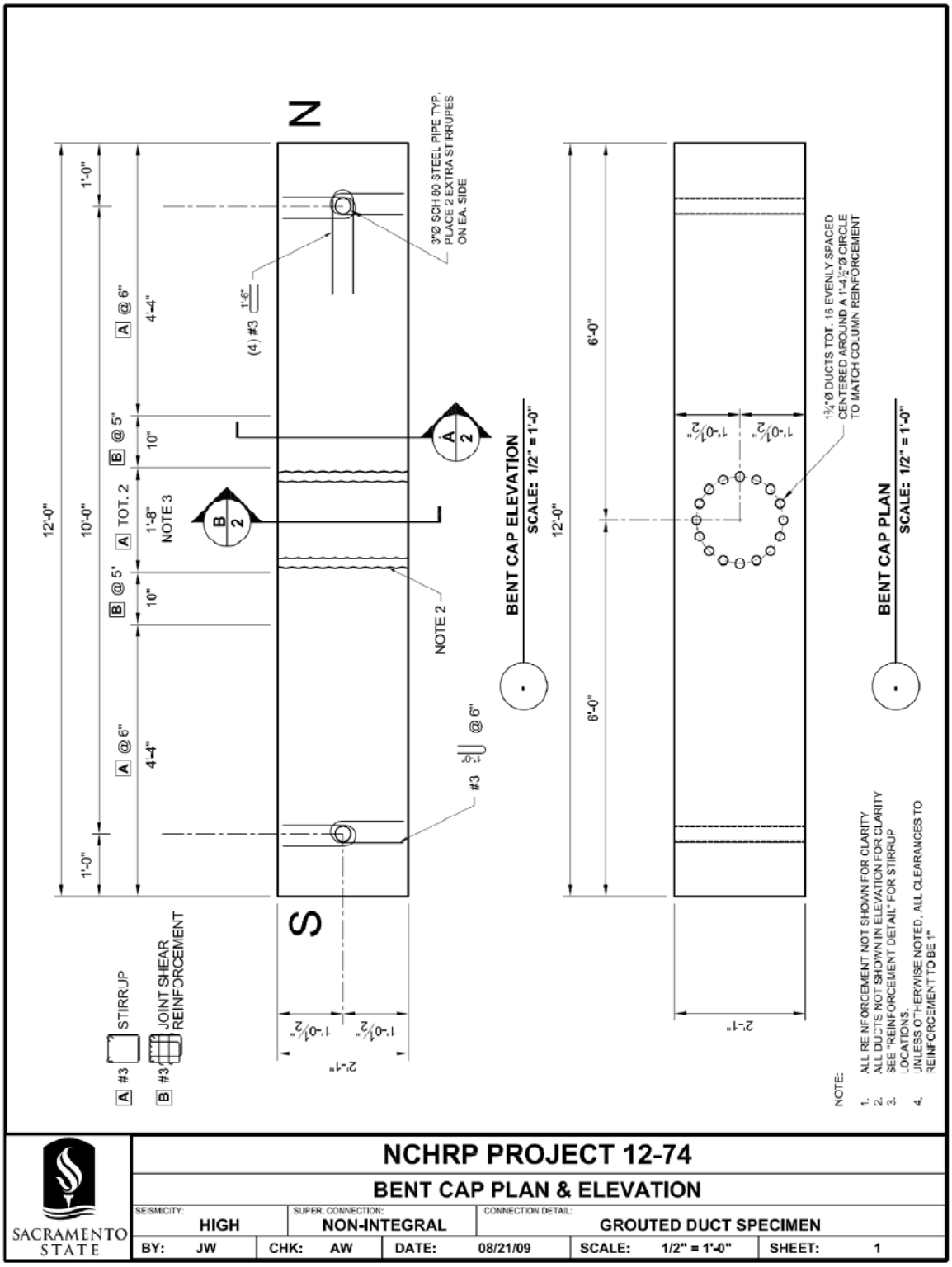

Figure 2-2. Grouted Duct Specimen Design—Bent Cap Plan and Elevation

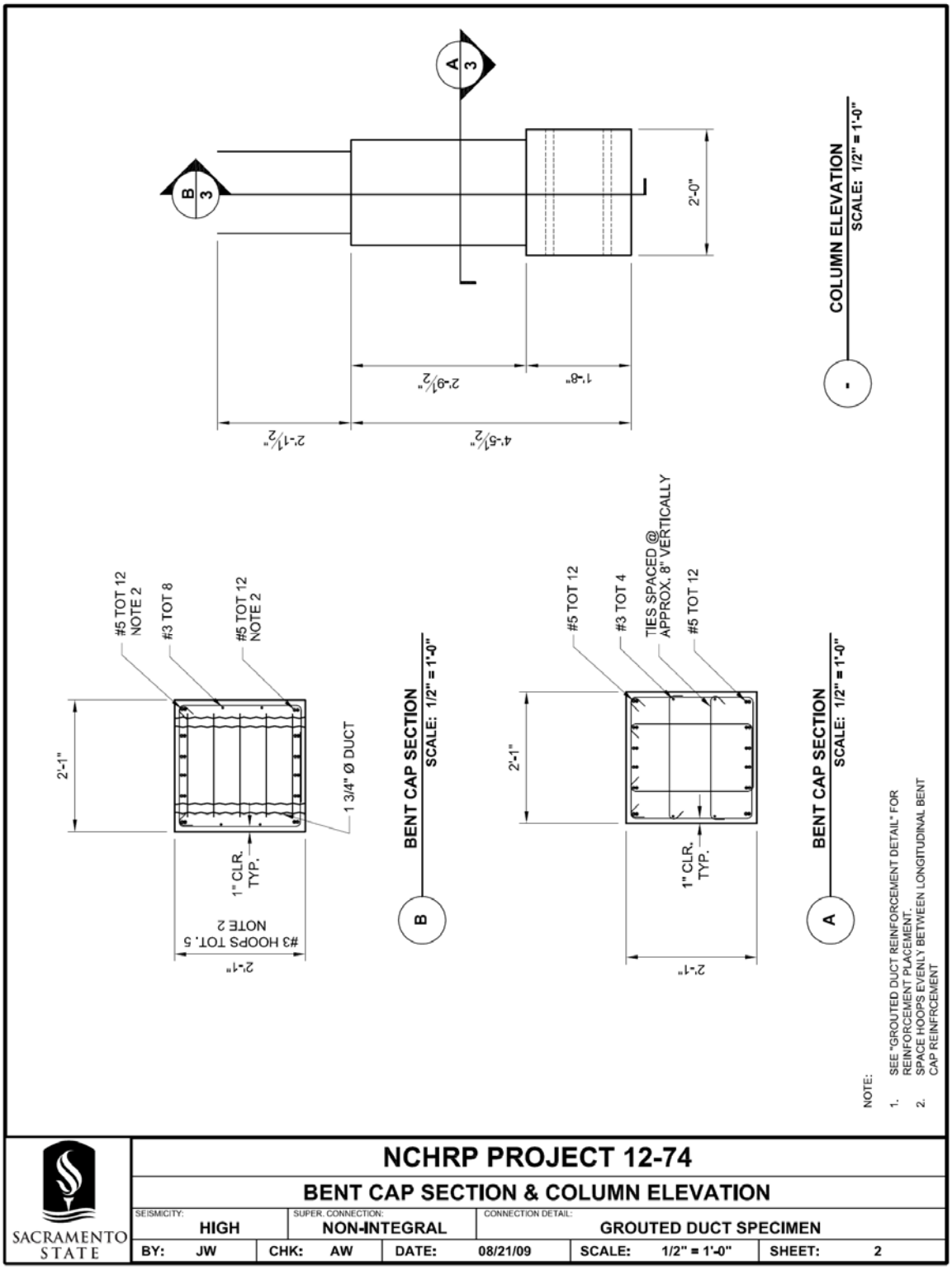

Figure 2-3. Grouted Duct Specimen Design—Bent Cap Section and Column Elevation

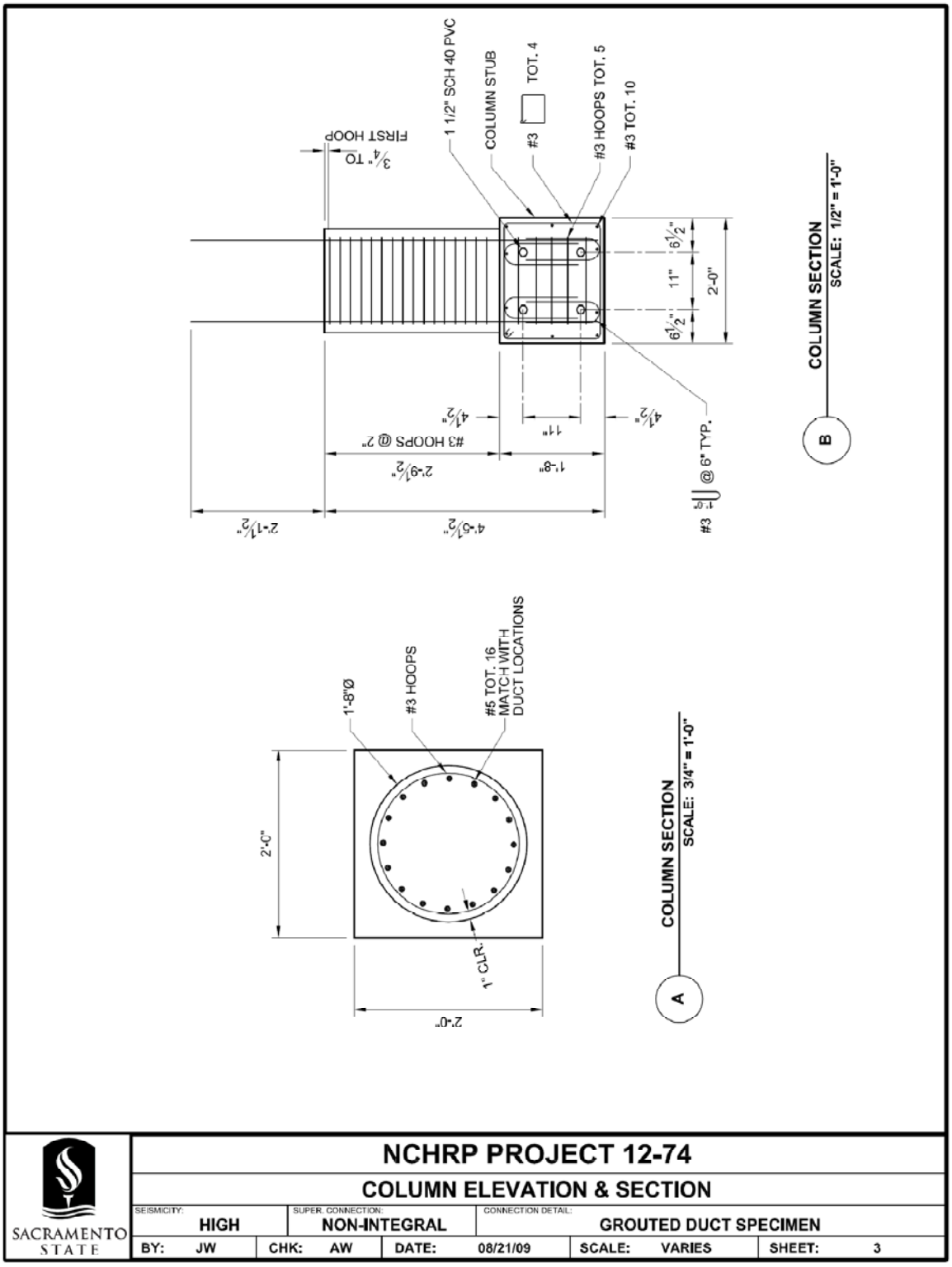

Figure 2-4. Grouted Duct Specimen Design—Column Elevation and Section

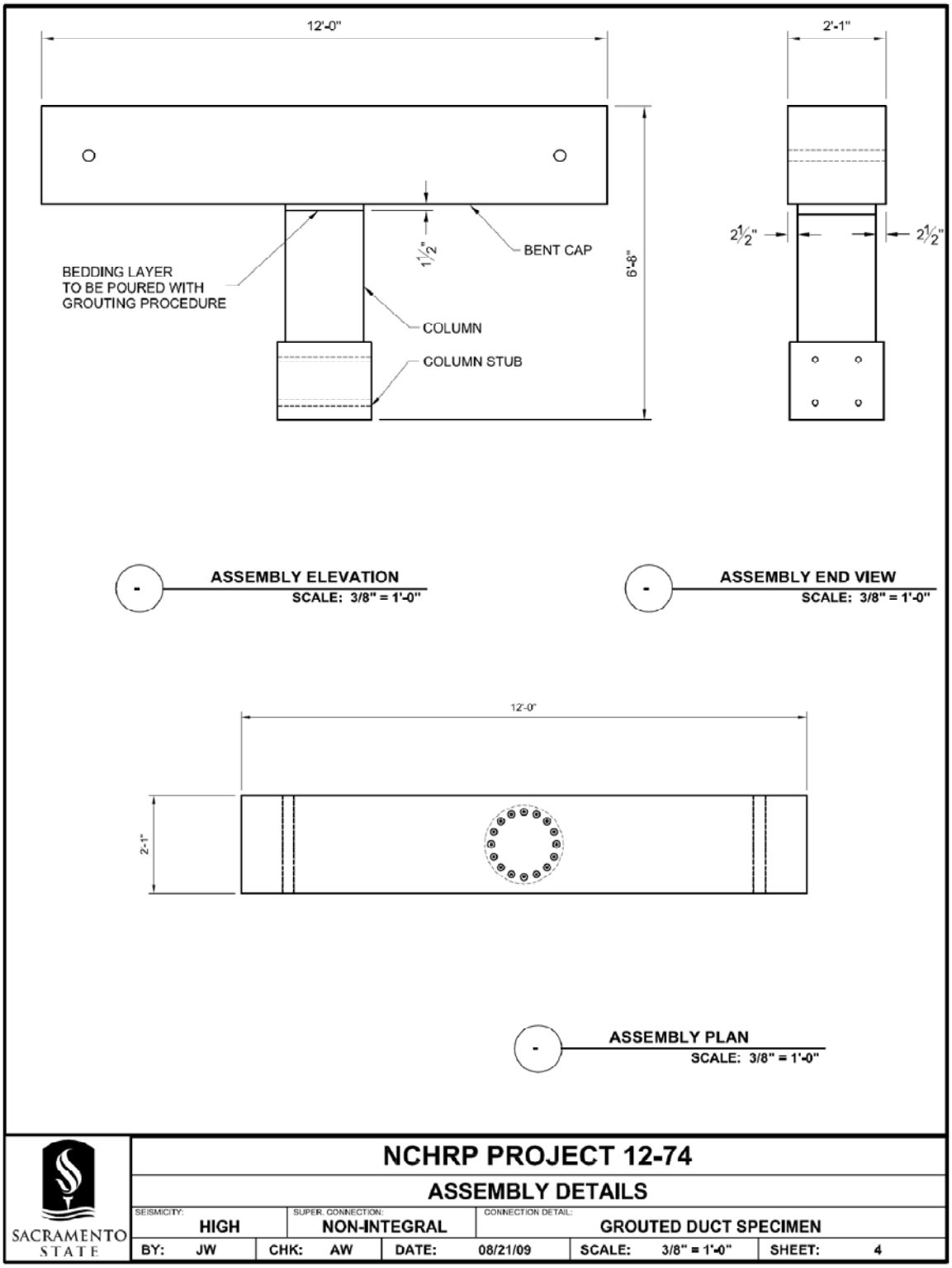

Figure 2-5. Grouted Duct Specimen Design—Assembly Details

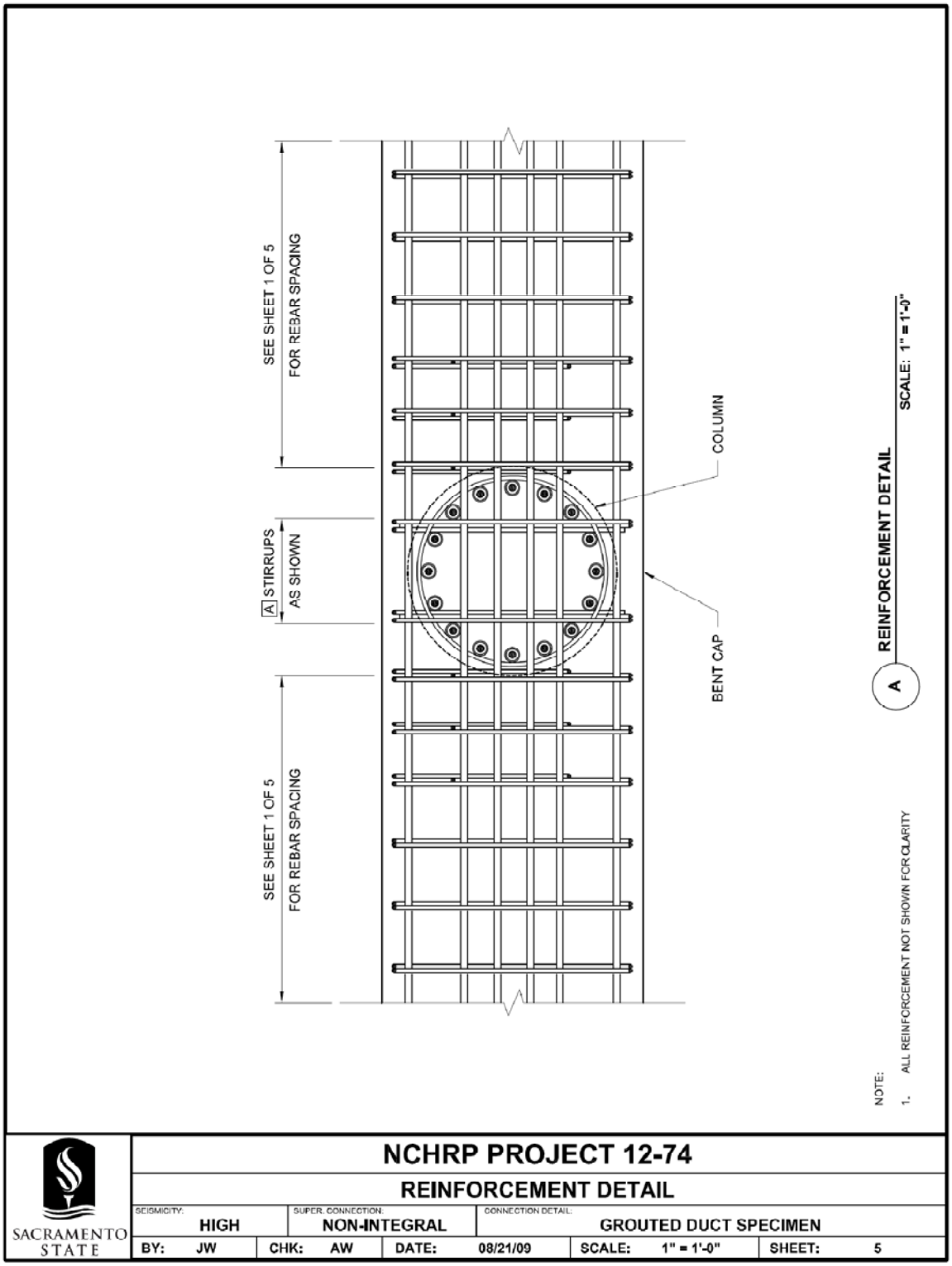

Figure 2-6. Grouted Duct Specimen Design—Bent Cap Reinforcement Detail

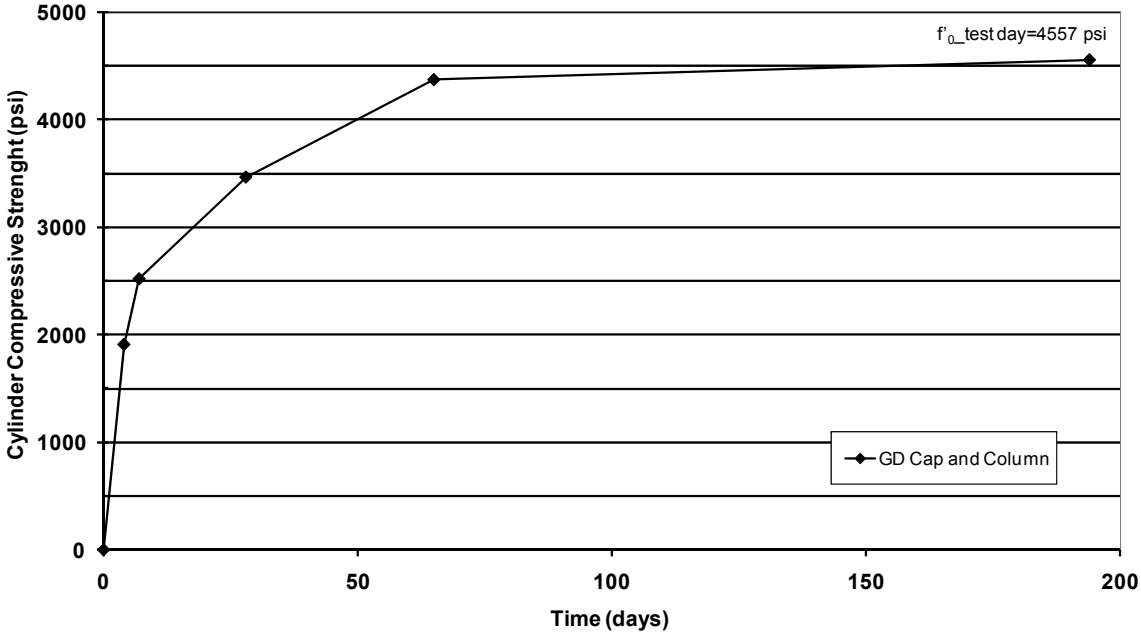

Figure 2-7. Concrete Cylinder Compressive Strength vs. Time

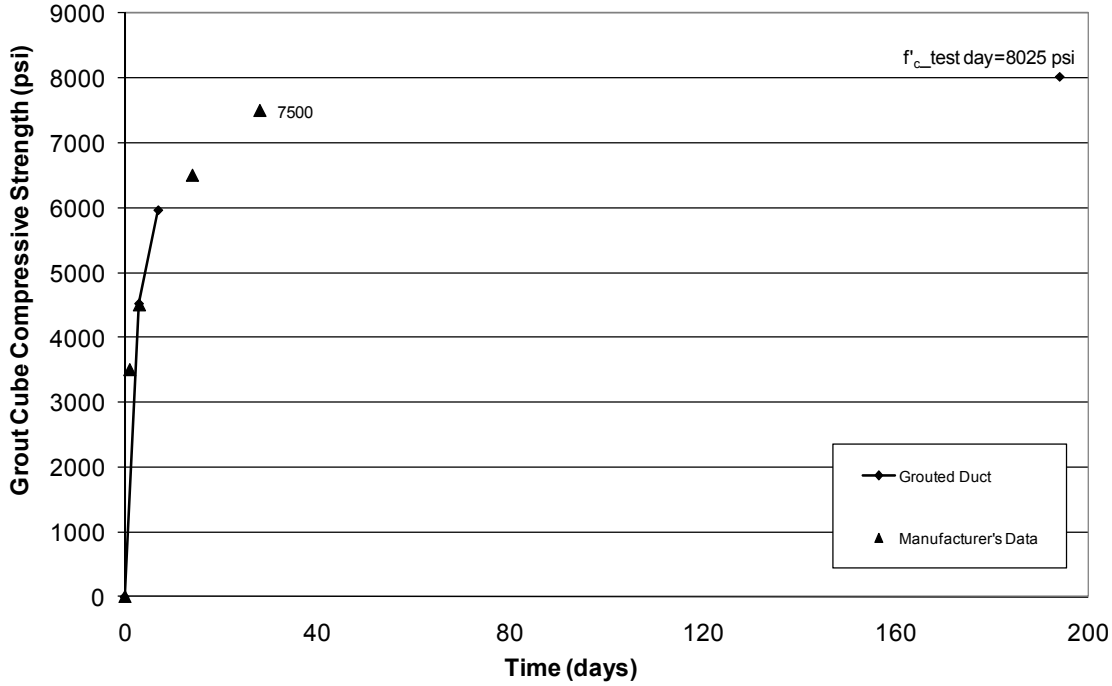

Figure 2-8. Grout Cube Compressive Strength vs. Time

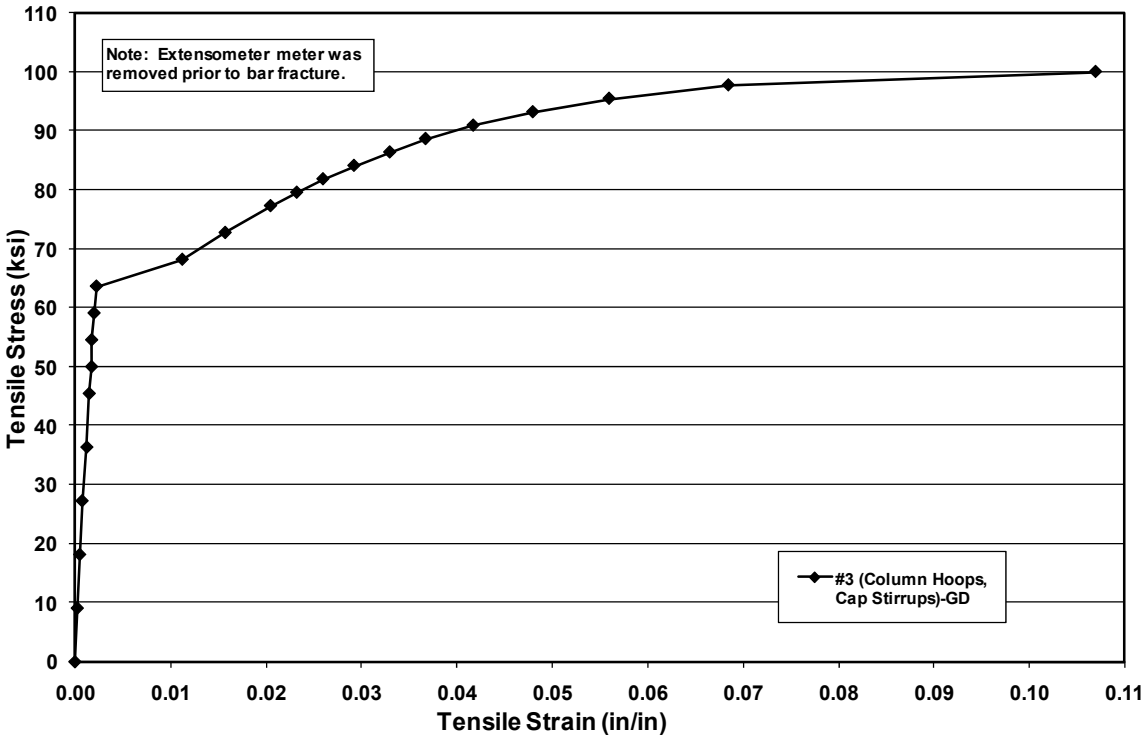

Figure 2-9. Tensile Stress-Strain for Reinforcing Bars

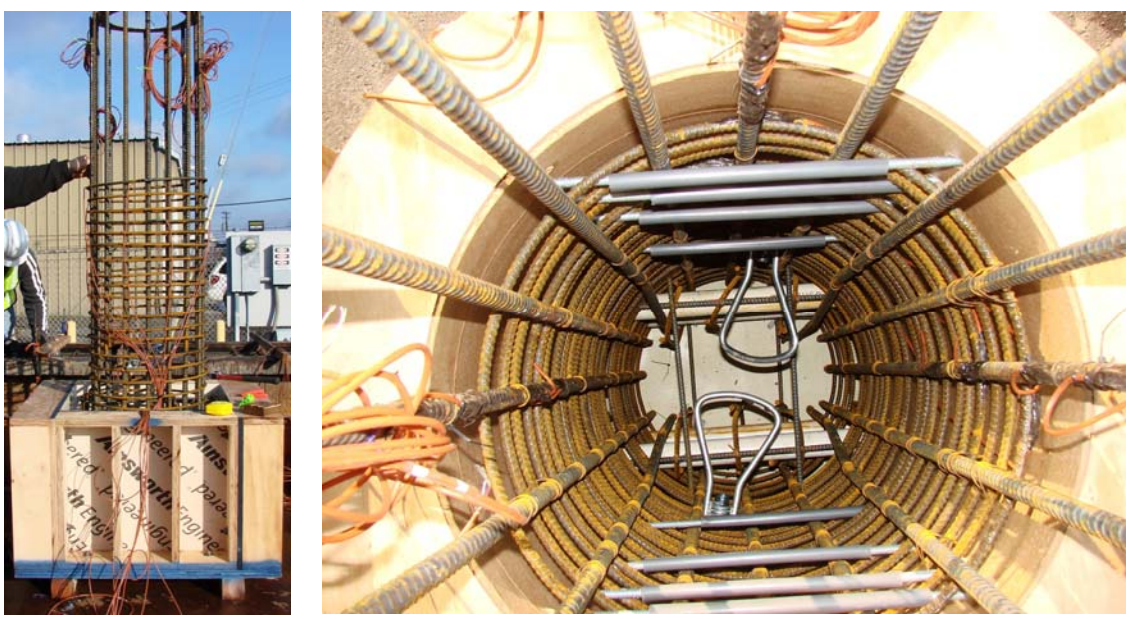

Figure 2-10. Assembly of Column Rebar Cage

Figure 2-11. Bent Cap Rebar Cage in Form during Fabrication

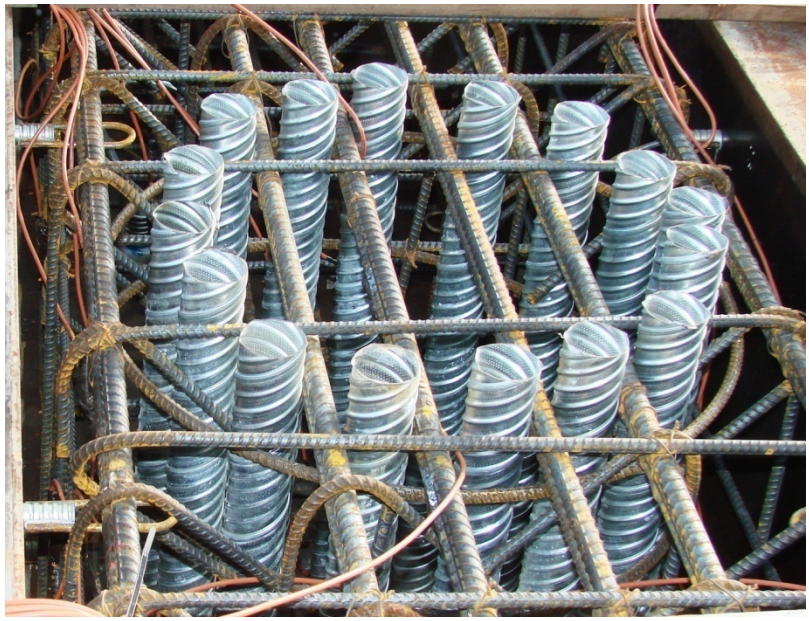

Figure 2-12. Joint Region of Bent Cap during Fabrication

Figure 2-13. Casting of Bent Cap

Figure 2-14. Lowering of Cap during Cap Setting Operation

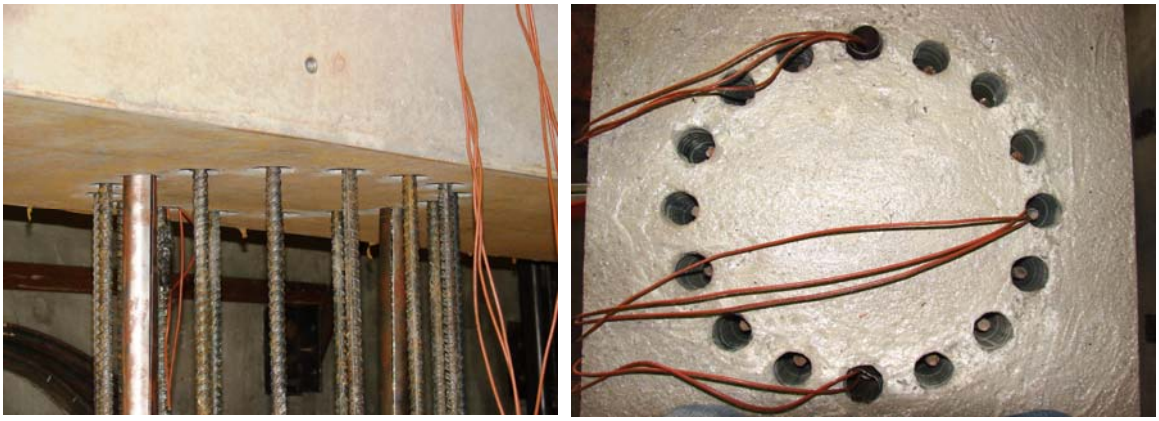

Figure 2-15. Cap Placement During and After Cap Setting Operation

Figure 2-16. Mixing and Pumping of Grout

Figure 2-17. Topping off Ducts with Grout and Cap Top Post-Grouting

Figure 2-18. Cap Top and Bedding Layer after Hardening of Grout

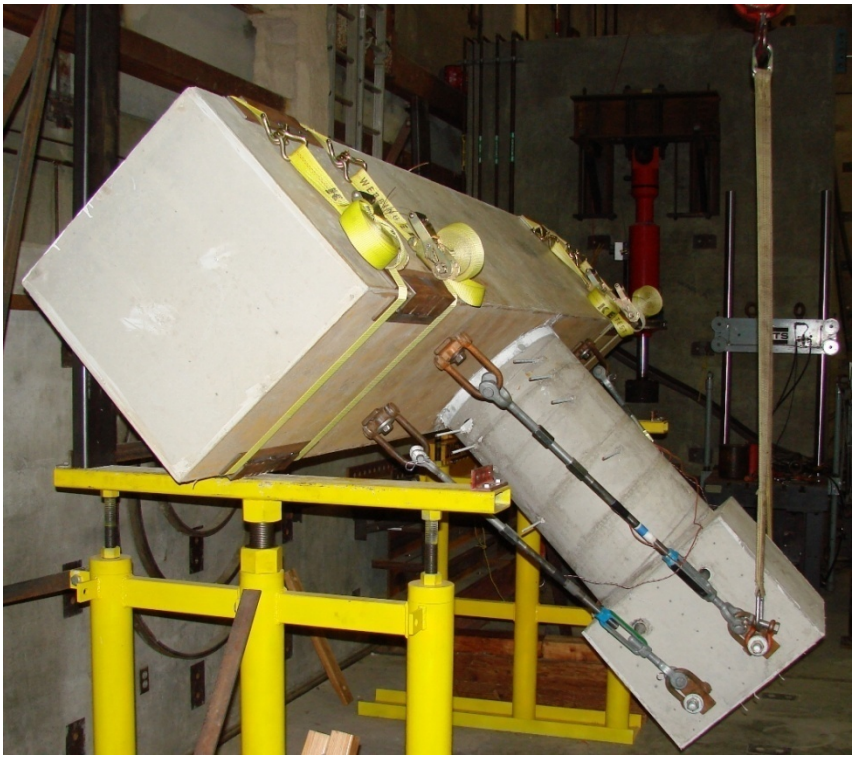

Figure 2-19. Inversion of Specimen Prior to Installation in Test Area

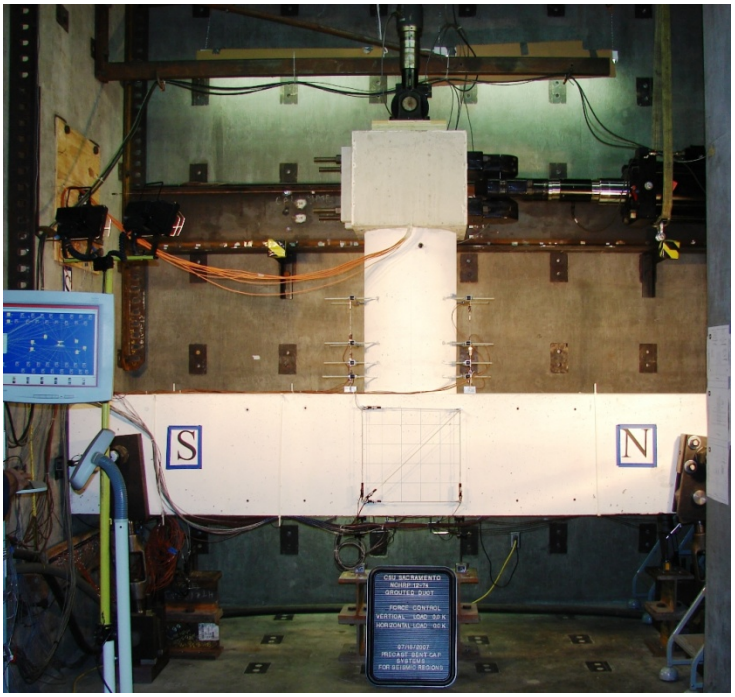

Figure 2-20. Specimen in Preparation for Testing

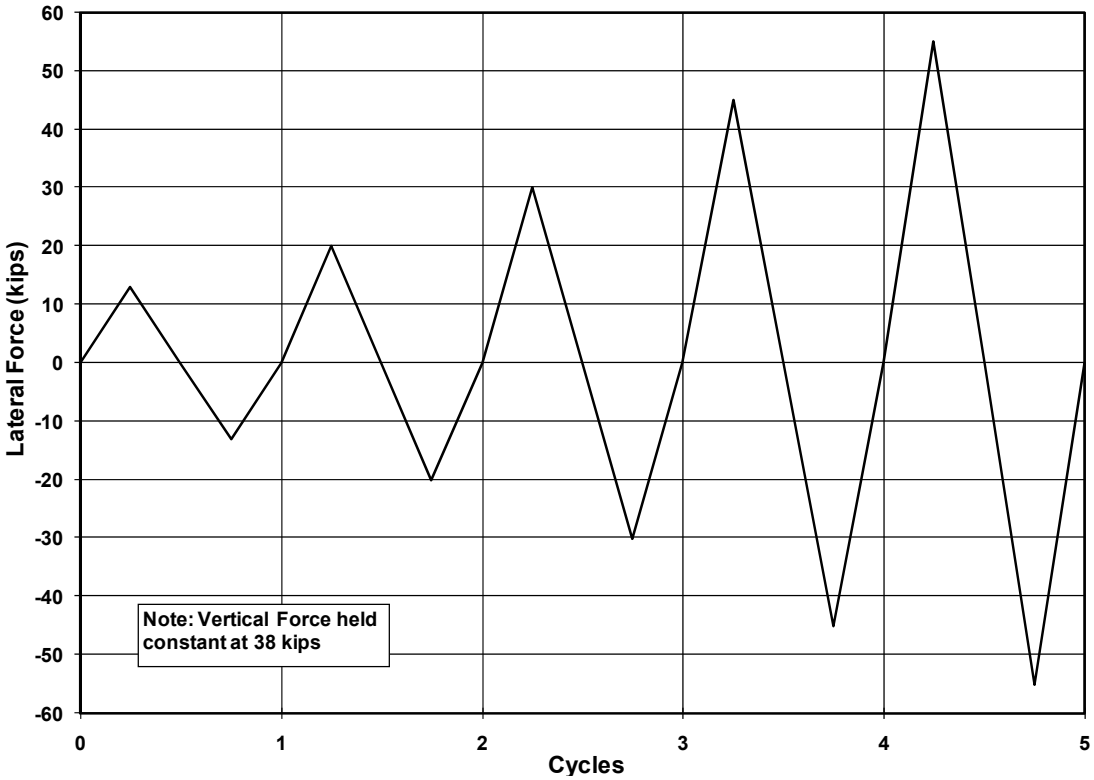

Figure 2-21. Force Control Sequence

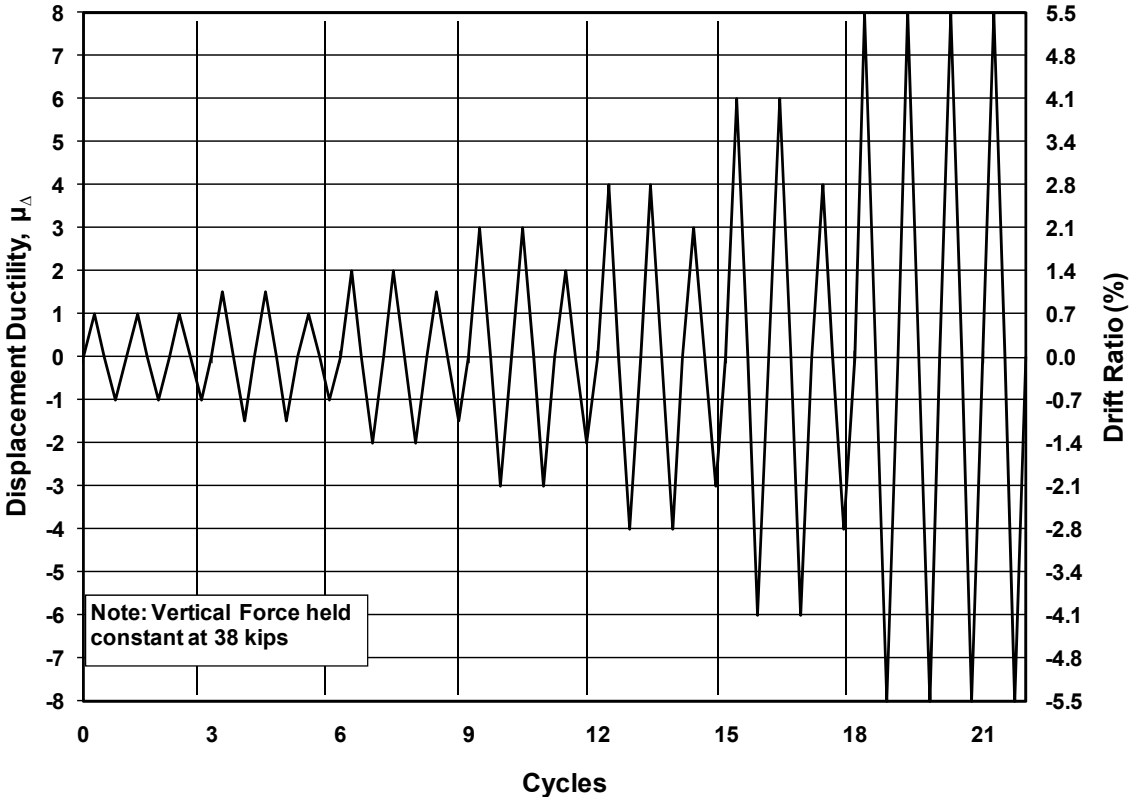

Figure 2-22. Displacement Control Sequence

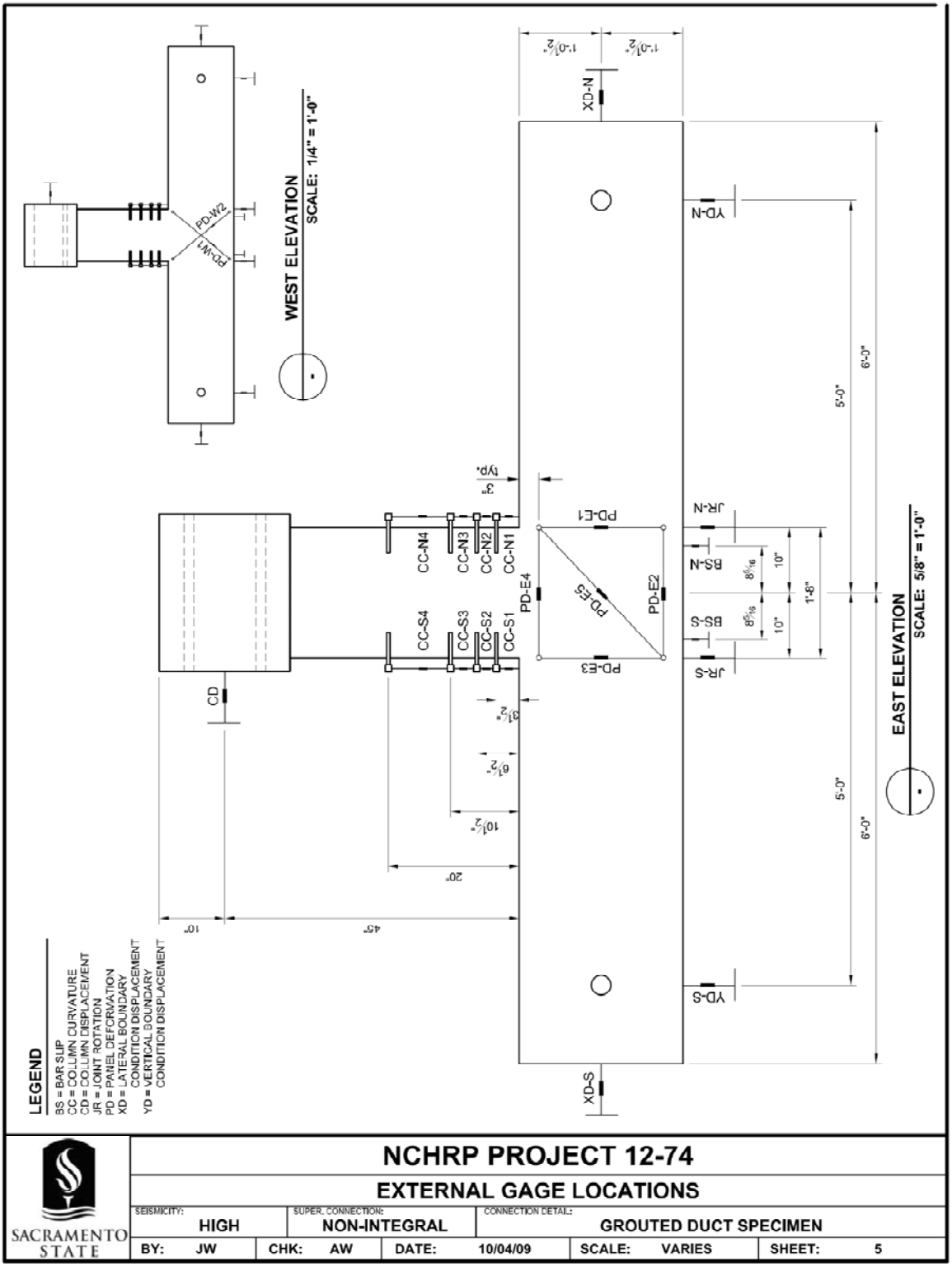

Figure 2-23. Instrumentation Drawings—External Gage ID

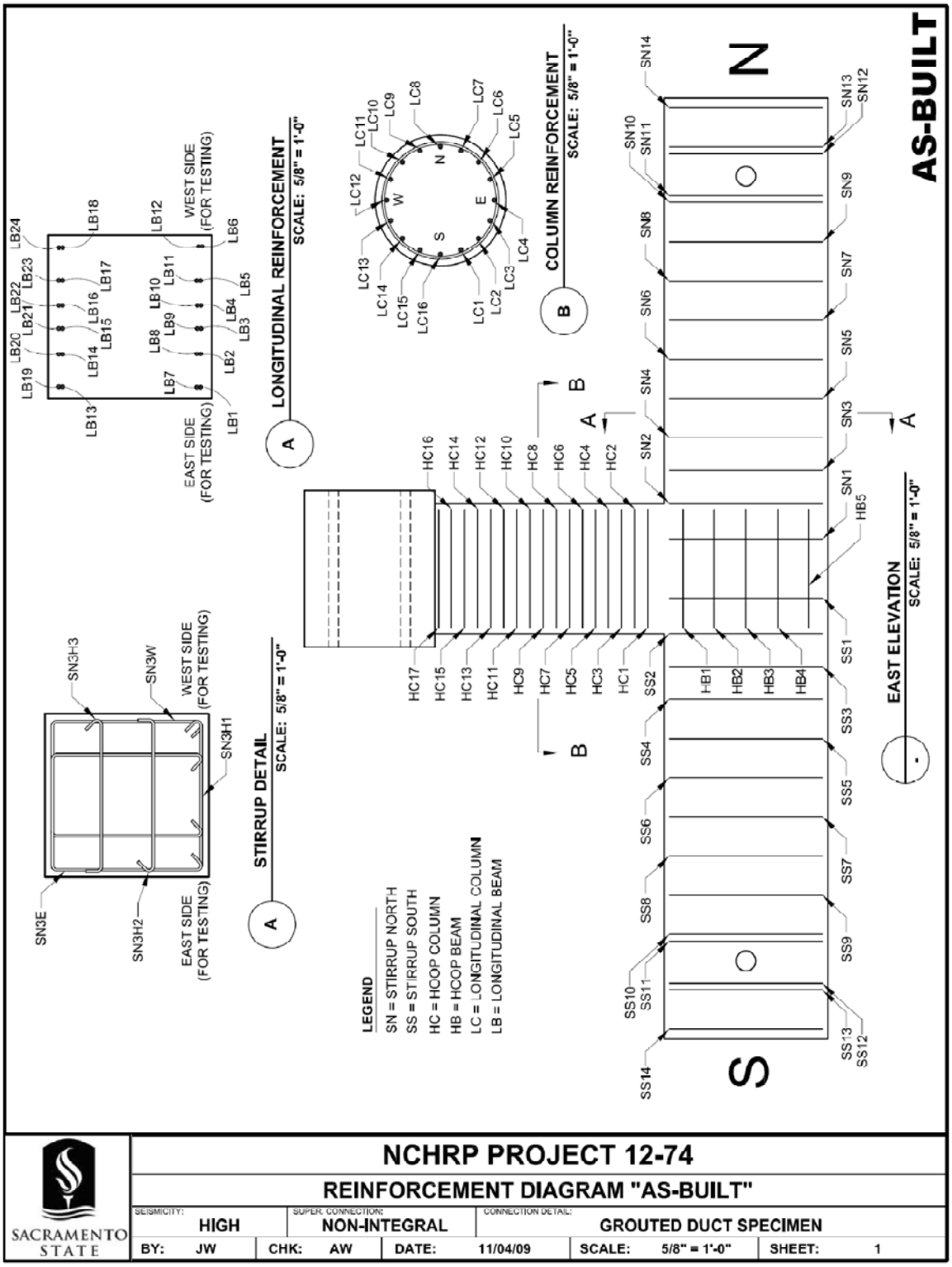

Figure 2-24. Instrumentation Drawings—Reinforcing Bar ID (As-built)

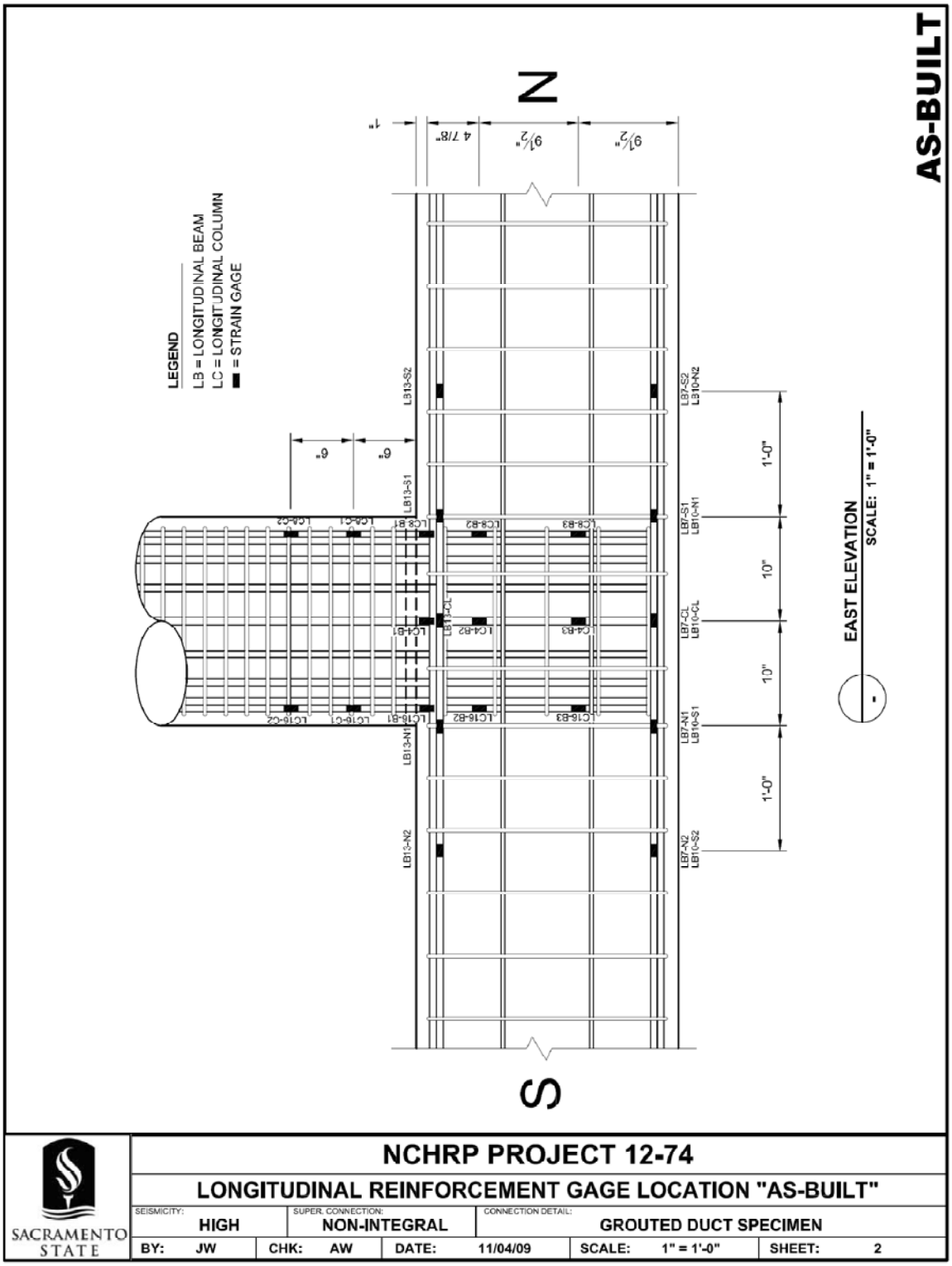

Figure 2-25. Instrumentation Drawings—Longitudinal Reinforcement Strain Gage Locations (As-built)

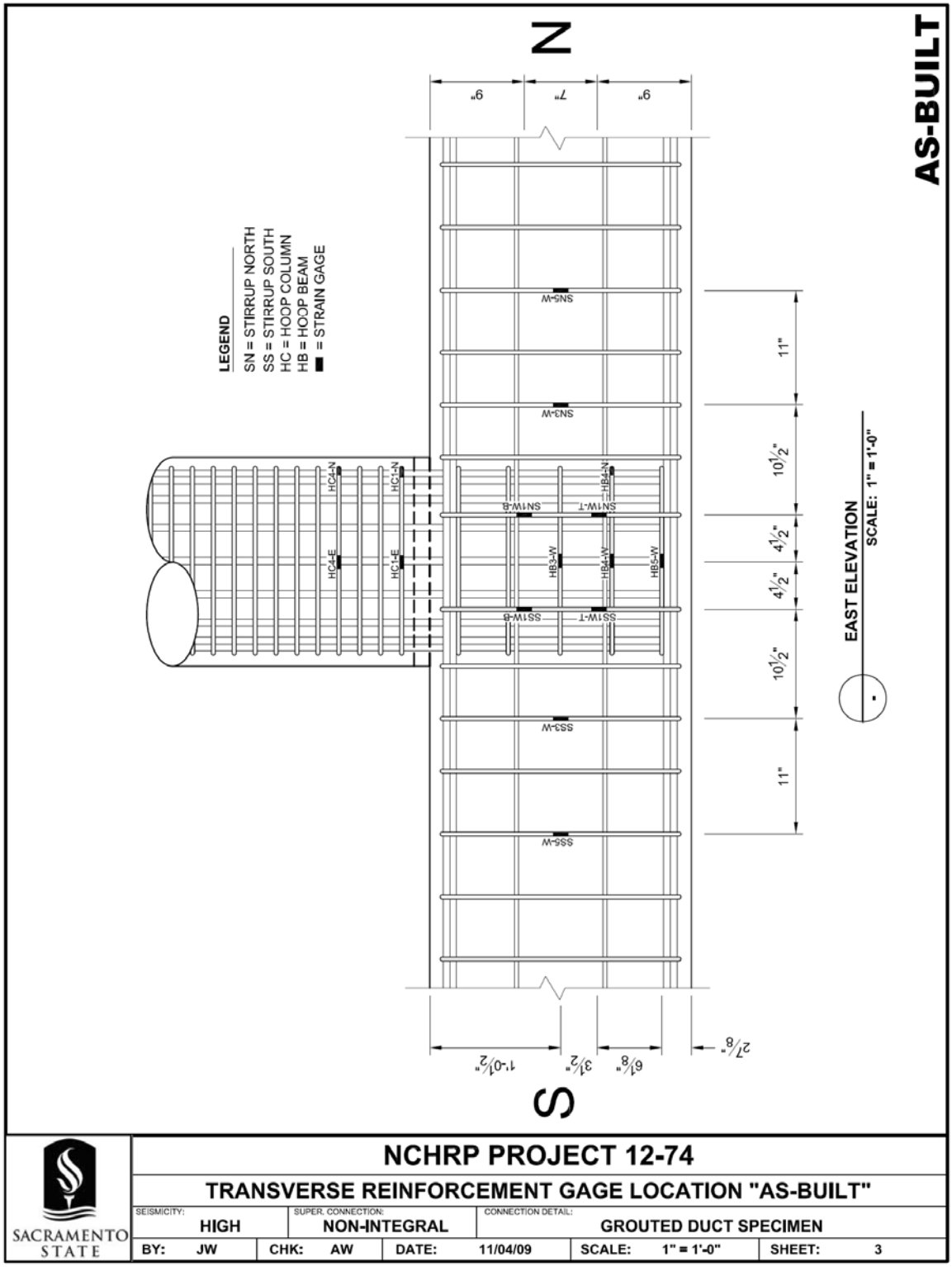

Figure 2-26. Instrumentation Drawings—Transverse Reinforcement Strain Gage Locations (As-built)

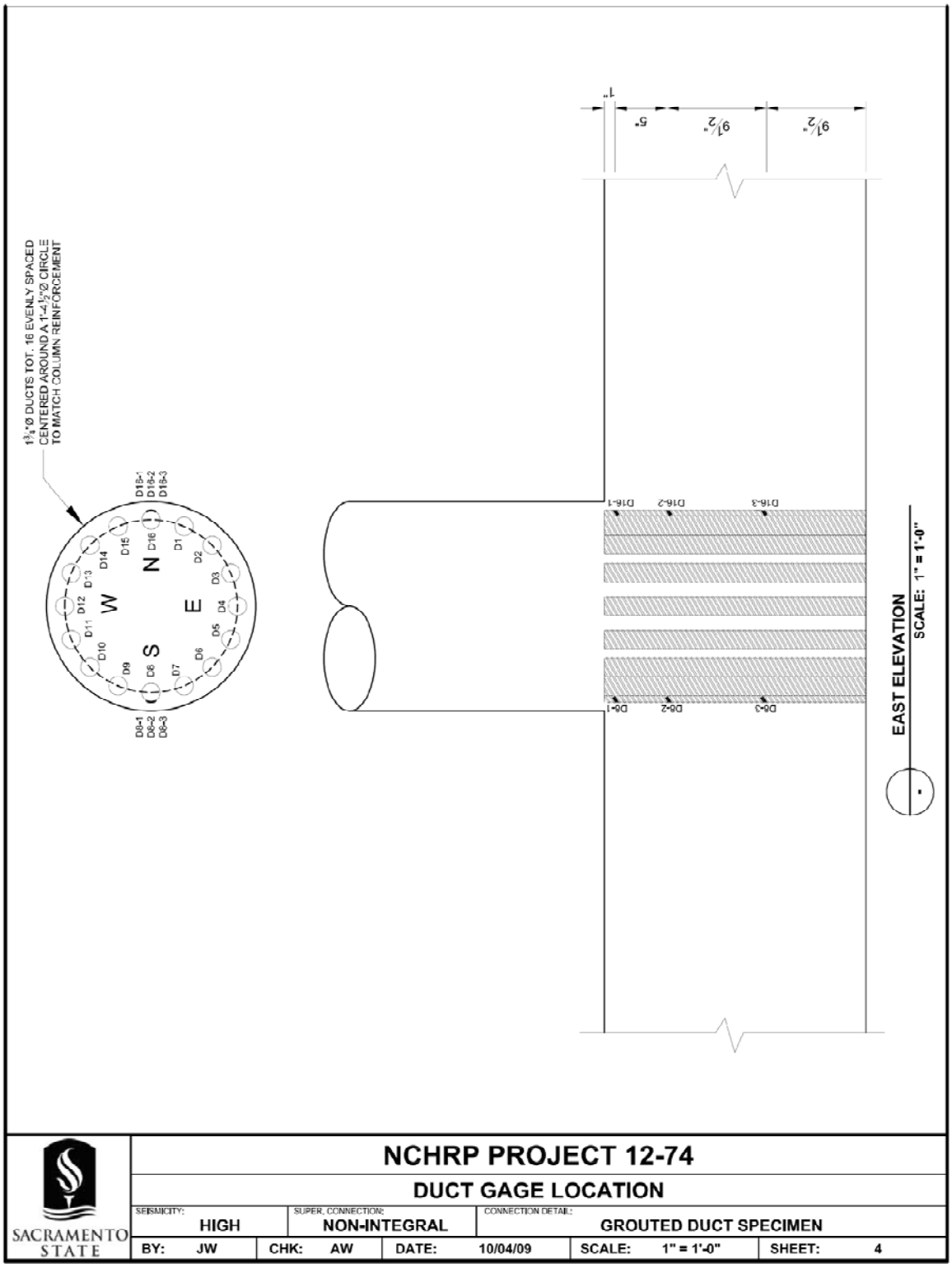

Figure 2-27. Instrumentation Drawings—Duct Strain Gage Locations

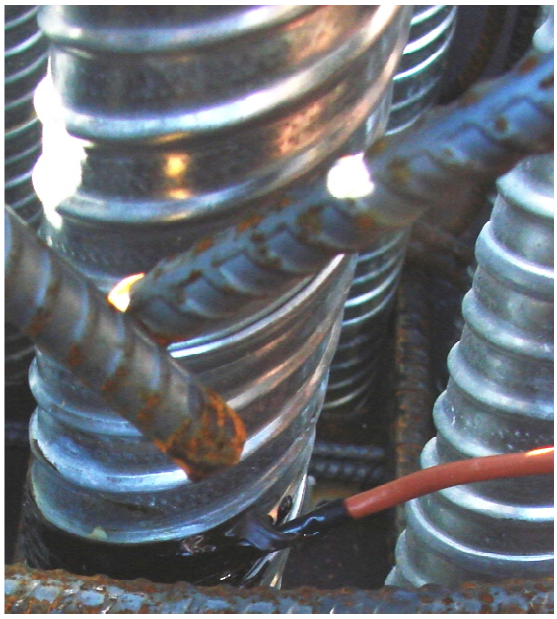

Figure 2-28. Internal Instrumentation Photos—Strain Gage on Duct

Figure 2-29. Internal Instrumentation Photos—Strain Gages on Rebar

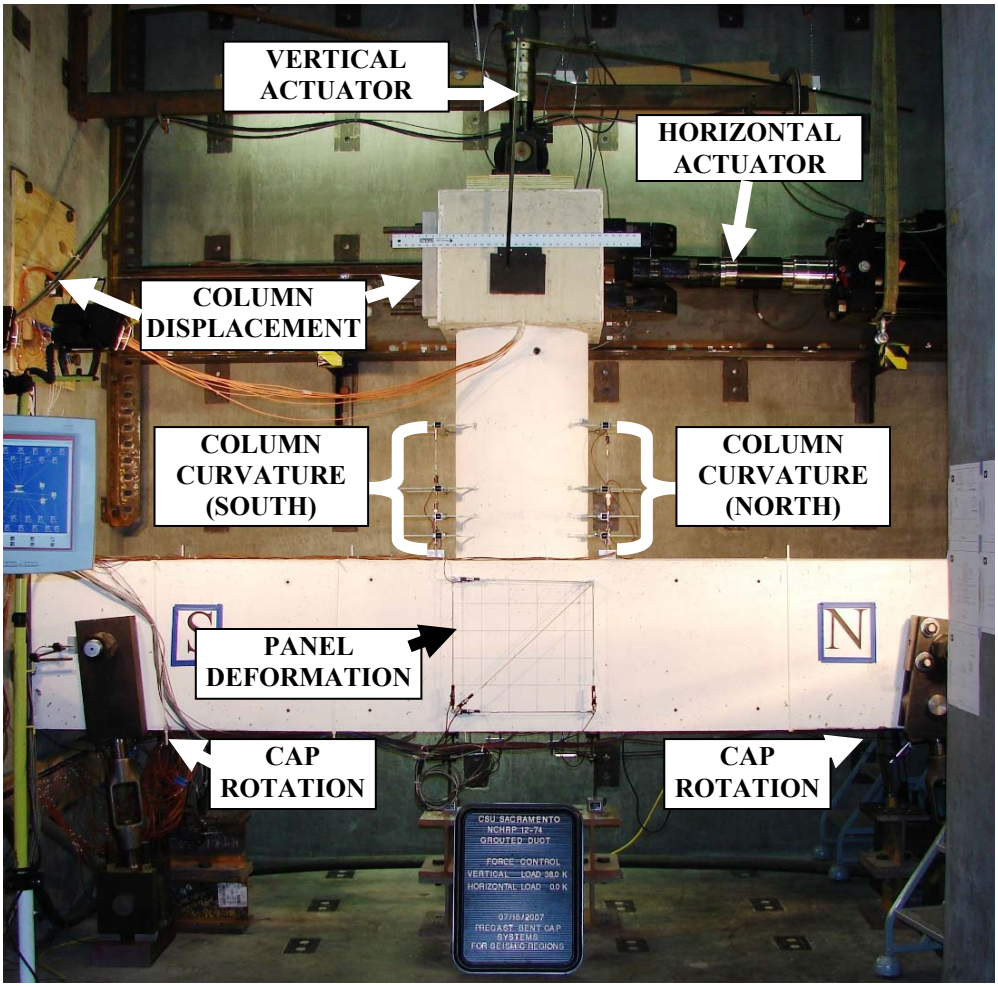

Figure 2-30. External Instrumentation Photos—Overall View

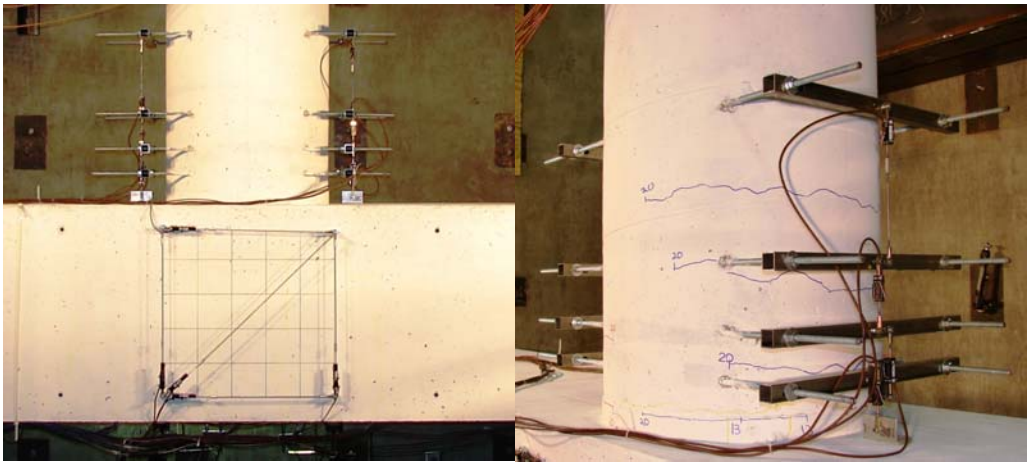

Figure 2-31. External Instrumentation Photos—Panel Deformation and Column Curvature

Figure 2-32. External Instrumentation Photos—Joint Rotation and Bar Slip

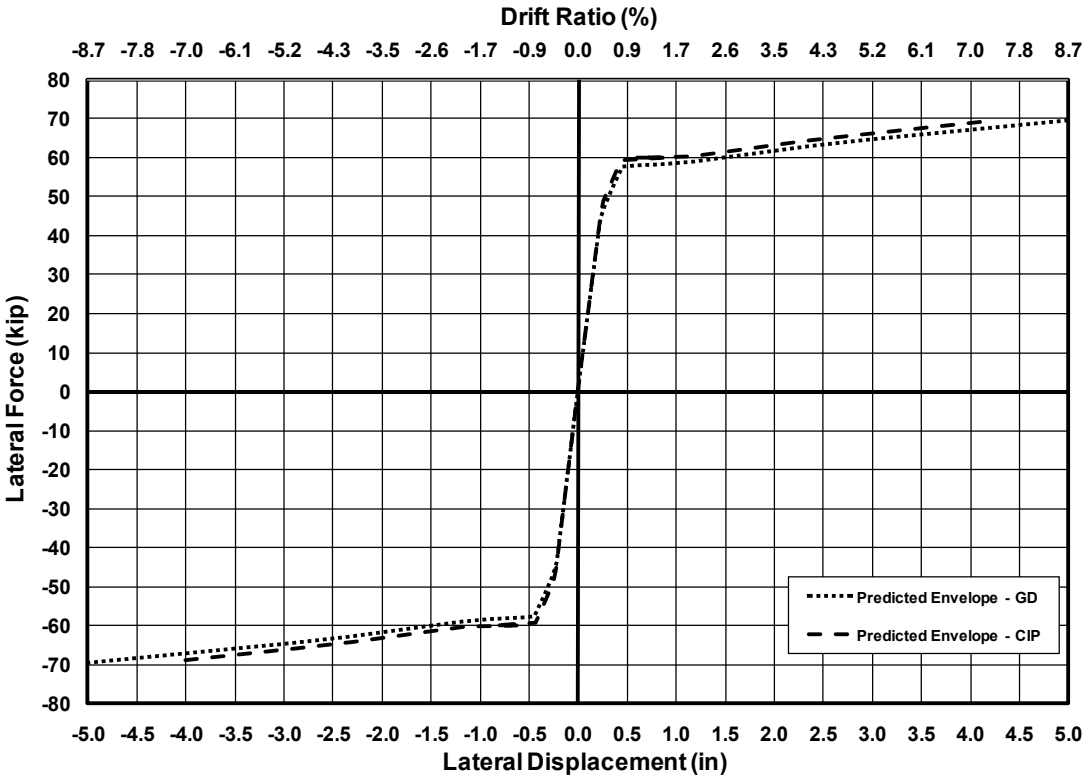

Figure 2-33. Predicted Lateral Force vs. Lateral Displacement Envelope—GD vs. CIP

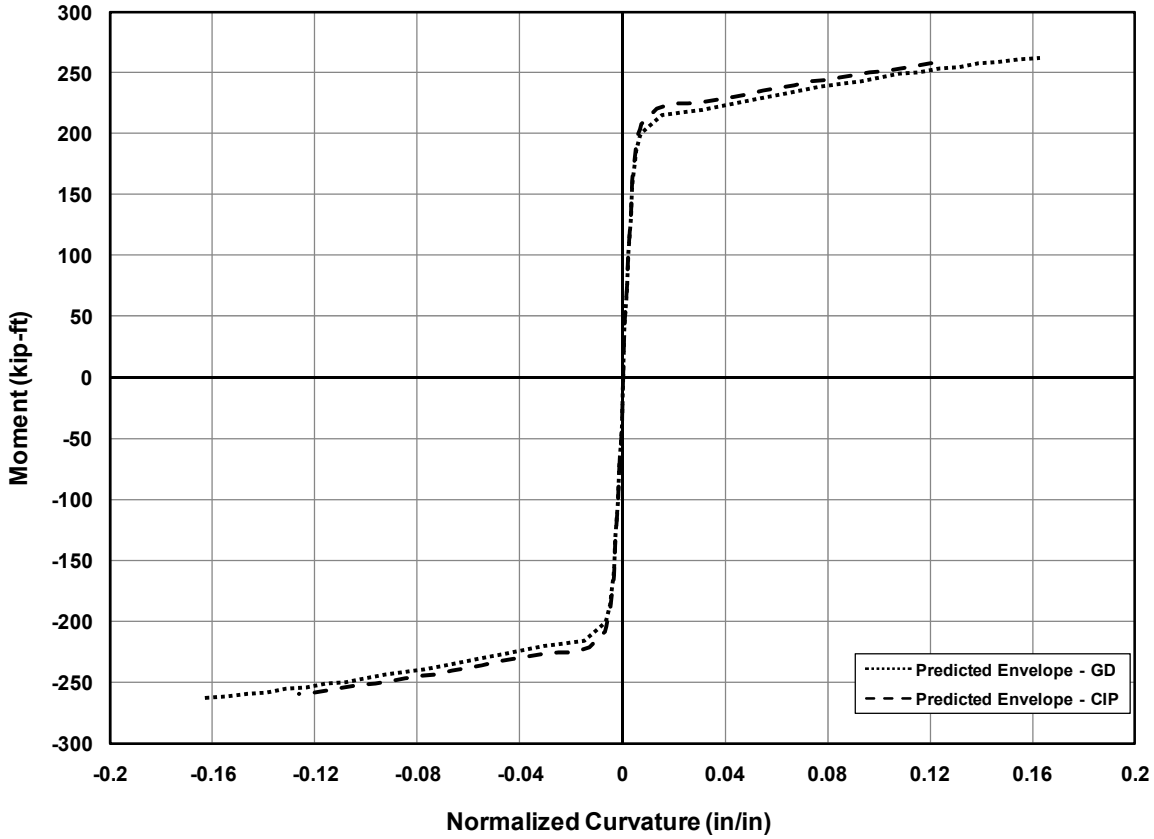

Figure 2-34. Predicted Normalized Moment vs. Curvature Envelope—GD vs. CIP

3.0 Specimen Response and Analysis

3.1 Experimental Observations

This section summarizes experimental observations made during testing, based on visual inspection and digital photos. Photos of the specimen include color-coded markings adjacent to cracks, as follows:

- Yellow: Pre-existing cracks prior to applied loading
- Brown: Cracks that formed or extended under vertical actuator loading
- Blue: Cracks that formed or extended under push direction loading
- Red: Cracks that formed or extended under pull direction loading

Markings also included: 1) load level or displacement ductility level; 2) transverse mark perpendicular to marking to identify end of crack. Crack widths were measured while the specimen load or displacement was held nearly constant.

In reporting specimen response, displacement ductility, μ, and drift ratio are both used. (Note: "drift ratio" and "drift" are used interchangeably.) Drift ratio is defined as the column displacement divided by the column height, as a percent. This is a more consistent basis for comparison of specimen response. System ductility levels are also reported but, though reasonable, these values should be considered nominal (i.e., approximate) due to the approximate determination of first yield. Table 3-1 summarizes the associated values of force, displacement, ductility, and drift ratio for Force Control and Displacement Control stages (push and pull, Cycle 1). Table 3-2 provides a summary for comparing the Table 3-1 values for GD to that for CIP (Push, Cycle 1).

3.1.1 Stages of Cracking

The specimen was observed for crack formation and growth under loading sequences. Some pre-existing hairline vertical cracks were observed along the bent cap, adjacent to the joint and within the joint region, but cracks appeared to have a negligible effect on response. Table 3-3 compares the predicted and actual stages of specimen cracking under Force Control and shows initial bent cap, column and joint cracking very close to the predicted loads. Cracks first formed in the joint region under Force Control

loading at 45 kips and crack widths did not exceed 0.005 in. Figures 3-1 and 3-2 show the specimen crack pattern at the last two Force Control sequences (45 kips and 55 kips).

3.1.2 Select Observations

Specimen response was dominated by plastic hinging of the column adjacent to the bent cap, as intended by the specimen design. This is clearly shown in Figures 3-3 through 3-6, which document response for increasing drift ratios (μ2 to μ8). In contrast to the significant column flexural (and shear) cracks associated with increasing lateral load, relatively minor joint and bent cap cracks developed. This corresponded well with the capacity protection philosophy implemented in design. Hysteretic response is discussed in further detail in subsequent sections.

The following additional observations were made:

- Initial diagonal cracking in the joint occurred at 45 kips (both push and pull directions, under Force Control). Under additional Force Control loading to 55 kips, joint cracking extended and widened from 0.005 in to 0.016 in. Under Displacement Control, cracks widened and at μ4 (cycle 2) an additional joint crack on west face developed. Figures 3-1 through 3-6 show this progressive development.
- Initial spalling of the column at the column-bedding layer interface and vertical cracks in the bedding layer developed at 1.2% drift (μ1.5) as shown in Figure 3-7. Figure 3-8 shows vertical cracks at 1.4% drift (μ2). Progressive spalling occurred at higher drift. Initial crushing of concrete above the bedding layer was observed at 2.7% drift (μ4).
- Initial radial splitting crack in the top surface of the bent cap (as tested) extended from the column bar at 1.4% drift (μ2). Splitting cracks also developed vertically along column longitudinal bars. See Figure 3-8.
- Flexural cracks developed in the bent cap, but remained relatively minor during testing.

- Column bar buckling may have initiated at a drift of 4.1% (μ6, pull), although fracture of two bars eventually occurred at the north end at a drift of 4.9% (μ8, push) (Figure 3-9). This corresponded with load degradation.
- At ultimate, spalling occurred along a length of approximately 10 in along the plastic hinging region (length equal to 50% of the column diameter). See Figure 3-6.
- Some twisting of the column developed near ultimate during pushing to 4.9% drift (μ8), but did not appear to affect joint response or plastic hinging.
- Post-test inspection revealed that the column core remained primarily intact, although concrete above the grout-concrete interface crushed. The bedding layer remained intact. Column growth and distortion of the column hoops due to plastic hinging were evident. Bars were well anchored within the ducts, and although splitting cracks developed between ducts (at the top and bottom of the bent cap per Figure 3-33), there was no evidence of grout splitting within ducts, initiation of pullout failure, significant bar slip or duct slip.
- Overall, the specimen exhibited excellent ductility due to confinement in the plastic hinge region. The joint cracking was relatively minor, and only minor surface spalling on the west face was evident post test. The post-test crack pattern is shown in Figure 3-10.
- It is noted that, although the specimen achieved a high level of drift (over 5% at μ8), the location of the first column hoop below the top of column (as fabricated) was approximately 1.25 in below its intended location due to interference with a threaded rod used for instrumentation. This may have contributed to buckling of the column bars, but load-displacement response suggests that the maximum load was already reached.

3.1.3 Comparison with Cast-in-Place Specimen

As shown in Table 3-4, concrete and rebar strengths for the bent cap compare very closely for the specimens, although the CIP column compressive strength was approximately 1600 psi (or 35%) higher than the GD column.

GD specimen stages of cracking compare very closely to the CIP specimen. Both specimens developed flexural cracking in the bent cap and column, as well as joint shear cracking, at similar loads and at loads close to predictions.

Select observations of response for the specimens also compare closely. Response for both specimens was dominated by extensive plastic hinging of the column adjacent to the bent cap, with relatively minor joint and bent cap cracks. Failure was precipitated by buckling of column bars, followed by fracture.

3.2 Hysteretic Response

3.2.1 Column Load-Displacement Response

The lateral force-lateral displacement (hysteretic) response of the column, used to characterize the fundamental performance of the specimen, is shown in Figure 3-11 together with the response envelope and predictions. The primary aspects of the response were:

- Plastic hinging of the column enabling the specimen to undergo a very large drift ratio of 4.9% (μ8, push) and 5.5% (μ8, pull)
- Stable hysteretic behavior with loops of increasing area and strength degradation of 18% at the maximum drift (push)
- Maximum loading of approximately 56 kips, with 96% of this load sustained up to a drift of 3.8% (μ6, push)
- Strength degradation of 18% (between first cycles) at a drift of 4.9% (μ8, push) associated with column bar buckling; in addition, strength degradation of 20% between first and second cycles at μ8

A comparison of the response envelope to the predicted envelope shows a good correlation. Although the specimen capacity was slightly smaller than predicted, the specimen maintained 95% of its capacity through the first cycle at a drift of 3.8% (μ6) and 82% through the first cycle at a drift of 4.9% (μ8). In the pull direction, load was maintained to a larger drift with smaller degradation.

The hysteretic response also portrayed appropriate stiffness, strength, ductility and other features such as crack distribution and width representative of emulative

response. The dominance of ductile plastic hinging in the column and minimal damage in the capacity-protected joint and bent cap satisfied the performance goal for the Grouted Duct as an emulative specimen.

As mentioned in Section 2.3.2, establishment of first yield was approximate due to loss of some gages, leading to the application of a relatively large force during Force Control, and thus a relatively nominal response during the first stages of Displacement Control (through~μ2). As a consequence, some plots use FC45 (Force Control, 45 kips) and FC55 (Force Control, 55 kips), in the same way that the CIP (Unit 1) Report used FC48 (Force Control, 48 kips) for analysis in the initial stage of Displacement Control.

Column displacement data was corrected to remove rigid body translation and rotation.

3.2.2 Equivalent Viscous Damping

Determination of the equivalent viscous damping ratio provides a quantitative means to establish the energy dissipating characteristic of the specimen for comparison to the CIP control and other precast specimens. The equivalent viscous damping ratio, ξ, represents the energy dissipation per cycle, determined as follows:

$$\xi = \left(\frac{2}{\pi}\right)\left(\frac{A_L}{A_R}\right)$$

where:

A_L =Area of hysteretic loop for a complete cycle (push and pull);

A_R =Area of rectangle bounded by maximum loads and displacements of a complete hysteretic loop.

Figure 3-12 plots the equivalent viscous damping ratio, ξ, versus drift ratio, including the first two cycles for each drift ratio. ξ increased significantly with increasing drift ratio, reaching approximately 22% (first cycle, 5.5% drift). This level is considered suitable for ductile response of an emulative beam-column connection. ξ increased slightly between the first and second cycles.

3.2.3 Comparison with Cast-in-Place Specimen

Figure 3-13 shows the envelopes for the GD and CIP hysteretic response. A very close comparison is evident. The strength, stiffness, and ductility up to approximately 3.7% drift (push) are nearly identical. Overall, the CIP achieved a higher drift (5.9% vs. 5.5%), but a 6% lower load. It should be noted that differences at higher levels of drift correspond to strength degradation associated with column bar buckling rather than precast connection response.

Figure 3-14 compares the equivalent viscous damping ratio, ξ, versus drift ratio for the GD and CIP specimens. Nearly identical values are shown through a drift of 4.1% for both cycles. Some variation is noted at higher drifts, due primarily to the failure of the GD specimen before the CIP specimen. Nevertheless, values for the first cycle differed by only 1.1% at a 5.4% drift.

3.3 Column Curvature Response

3.3.1 Moment-Curvature

Figures 3-15 and 3-16 plot normalized moment-curvature response for the first two curvature cells up the column, together with the predicted envelope. Predicted and measured response envelopes are shown to compare favorably. Although column spalling limited data collection for Cell 1 (through 2.7% drift, μ4) and Cell 2 (through 4.1% drift, μ6), extensive curvature ductility associated with plastic hinging is still evident. Cell 1 maximum curvature was approximately 13 times the effective yield curvature (estimated), and 15 times for Cell 2.

The moment at the midheight of the cell was used for plotting, except that strain penetration was accounted for Cell 1. In addition, data was corrected for joint rotation to provide a matching basis to the predictions. Note that the curvature was normalized by multiplying curvature by the column diameter; moment was not modified.

3.3.2 Curvature over Height

Figures 3-17 and 3-18 show the normalized curvature profile over the column height for the Force Control and Displacement Control sequences, respectively. These profiles demonstrate the concentration of plasticity adjacent to the soffit, as well as the

spread of plastic hinging up the column under increased load and drift. Based on an estimated first yield normalized curvature of approximately 0.0038 in/in, it is evident that under the final two loading cycle of Force Control (45 kips and 55 kips) yielding occurred. Despite the limitation of curvature gages noted previously, Figure 3-18 indicates that much more significant inelastic response developed over an increasing height under Displacement Control.

3.3.3 Comparison with Cast-in-Place Specimen

Figure 3-19 plots the Cell 1 normalized moment-curvature prediction and response envelopes for the GD and CIP specimens. A very close comparison is evident for the response envelopes. Curvature over height can be compared for the GD and CIP specimens by comparing Figures 3-17 and 3-18 to Figures 3-20 and 3-21. These figures demonstrate a similar trend for the GD and CIP specimens under Force Control and Displacement Control.

These similarities provide evidence of emulative behavior of the GD specimen relative to the CIP control specimen.

3.4 Displacement Decomposition

Displacement decomposition refers to the separation of the column displacement into the various components that contribute to the overall lateral displacement of the column. Components include column flexure, fixed end rotation (due to plastic hinging and bar slip), column shear, bent cap flexibility, and joint shear. Decomposition quantifies the magnitude of each component, and is determined for comparison of analytical predictions to experimental measurements. Figure 3-22 shows a schematic representation of the displacement components, including applicable equations.

Some limitations exist when comparing predicted and measured displacements. For example, in the test program the column shear displacement was not measured but was estimated analytically, and the joint shear displacement was not determined analytically but was measured. This leads to some approximation.

Properly designed cast-in-place and emulative bridge bents are expected to display flexural plastic hinging, which results in flexural displacement components

dominating the displacement at increasing drift or displacement ductility levels. The total experimental flexural component is taken as the sum of the fixed end rotation plus column flexure. Fixed end rotation represents displacement due to plastic hinging within the first curvature cell plus displacement due to bar slip. However, because the plastic hinging length extended beyond the first curvature cell, plastic hinging response also contributed to the column flexure component. Thus, the total predicted flexural displacement is compared to the sum of column flexure and fixed end rotation.

To match the assumption of ideal pin and roller support conditions, rigid body translation and rotation of the specimen were removed from the raw data during data reduction.

3.4.1 Overview

Table 3-5 summarizes the displacement decomposition for the first push and pull cycles for drift ratios from 0.6% to 5.5%. For each drift ratio, results are tabulated in two columns. The first column includes two sections: 1) the top section summarizes the column displacement (CD) and the corresponding drift and force; and 2) the bottom section lists the displacement components determined from measurements, as shown in Figure 3-22, and the sum of the components (Component Total, CT). At the bottom of the table is the CT/CD ratio, indicating what portion of actual displacement is represented by the measured components.

The second column shows the analytically predicted displacement components. Although the load-displacement envelope was predicted pretest, the actual displacements imposed on the specimen were not well defined pretest, as these are dependent on the establishment of first yield, which was approximate. Thus, the second column shows predicted displacement components that sum up the imposed displacement in the test (i.e., CT/CD=1.0). In addition, predicted displacements are based on actual material properties. This approach allows actual and predicted displacement components to be appropriately compared, as shown in the third column (Actual/Predicted ratio).

Some approximation is expected in predicted and measured values. Joint shear was not predicted and column shear was predicted but not measured. The difference

between CT and CD represents column displacement due to column shear, joint shear and potential inaccuracies in measurements. Joint shear was not expected to represent a large percentage of the total measured displacement in full ductility specimens. Although prediction of column shear is considered approximate, inclusion of this component in predictions allows a more realistic comparison in Actual/Predicted ratios: omission of column shear in predictions would require its portion to be incorrectly assigned to column flexure and bent cap rotation, biasing ratios. Significant column shear cracking is clearly shown in Figures 3-1 through 3-6. To some extent, these approximations tend to offset one another; however, some error is introduced in the process.

3.4.2 Fixed End Rotation, Column Flexure, and Bent Cap Flexibility

As shown in Table 3-5 for the push direction, the CT/CD ratios ranged from 0.84 to 0.95 (0.92 average) through a drift of 2.6% (μ4, push). This suggests that the displacement components were reasonably determined. (As noted previously and in Table 3-5, spalling limited column curvature gage reliability at higher drift ratios). The Actual/Predicted ratios for flexure ranged between 0.80 and 0.93, which also indicate reasonably accurate predictions for flexure. Bent cap flexibility was less accurately predicted; however, joint rotation was underestimated in predictions. In addition, as shown in Figure 3-23, the bent cap flexibility contribution to overall displacement was much smaller than column flexure. Similar overall trends are evident in Table 3-5 for the pull direction.

Figure 3-24 plots the displacement decomposition component values for the push and pull directions. The height of each bar segment shows the relative contribution of a component. In correlation with experimental observations of the specimen, flexural components (fixed end rotation, FER, and column flexure) dominated the response and increased significantly with increasing drift. Bent cap flexibility provided a smaller contribution with joint shear clearly being the smallest contributor.

Figure 3-25 plots the displacement decomposition components as a percentage of the total component displacement (CT). For example, at a push drift of 1.1% (FC55 stage, as noted in table), the combined flexural components (fixed end rotation and

column flexure) accounted for 76% of CT (column elastic plus plastic deformation was predicted to represent 77%). However, at 2.6% drift (μ4), the flexural components accounted for 84% of CT (vs. prediction of 85%). This corresponded well with the observed dominance of plastic hinging in the column. The push and pull drifts differ for FC55 because the specimen was loaded under force control; however, Figure 3-25 shows a similar percentage for push and pull displacement components even for the FC55 stage. The contribution of column shear to column displacement was not directly measured, and significant shear cracks did develop in the column; thus, predictions are considered approximate, as previously mentioned.

As shown in Figure 3-24, the bent cap flexibility (joint rotation) component increased in magnitude with drift (and bent cap cracking). Figure 3-25 shows its relative contribution to CT decreased with increasing drift, from 27% at 0.6% drift to 12% at 2.6% drift.

It should be noted that the values in Table 3-5 for the first two displacement ductility levels are labeled as FC45 and FC55 rather than μ levels because these stages used data from the last stages of Force Control. This was required since the specimen was loaded under Force Control to a force and displacement larger than that expected for effective yield (determined from analysis).

3.4.3 Joint Shear

Figures 3-24 and 3-25 confirm the minor contribution of joint shear, with the joint shear displacement not exceeding an 8% contribution to CT. Joint shear was the smallest measured contributor to column displacement.

3.4.4 Bar Slip

Table 3-6 summarizes bar slip component of column displacement and compares bar slip to fixed end rotation. By definition, fixed end rotation includes the effect of bar slip on rotation. As shown in the table, bar slip was minor, contributing about 9% on average to the displacement component attributable to fixed end rotation. Due to bar anchorage forces, splitting cracks formed in the bent cap and column, and the top surface of the bent cap (as tested) exhibited splitting cracks and local spalling; however, column

bars were well anchored within the joint. In addition, post-test inspection revealed splitting cracks between ducts (at both the top and bottom of the bent cap), but there was no evidence of grout splitting within ducts, initiation of pullout failure, significant bar slip or duct slip.

The embedment depth of the #5 column bars into the bent cap, l_{ac}, was 22 in, or an l_{ac}/d_b ratio of 35.2. This depth matches that used for the CIP specimen, which conforms to joint requirements of the 2006 Recommended LRFD Guidelines for the Seismic Design of Highway Bridges (2006 LRFD RSGS) and 2009 AASHTO Guide Specifications for LRFD Seismic Bridge Design (2009 LRFD SGS), which require column bars to be extended as close as practically possible to the opposite face of the bent cap for development of the force transfer mechanism. [10, 12] Prior research on column bars anchored in grouted ducts indicate that an l_{ac}/d_b ratio of at least $2f_y/f'_{cg}$ should be used (based on bar anchorage only). [13] For the GD specimen, this corresponds to an l_{ac}/d_b ratio of 18.5 (for a specified grout compressive strength not to exceed 6500 psi, per Reference 13). The large embedment depth, together with a properly grouted connection, helped ensured adequate bar anchorage and minimal slip.

3.4.5 Comparison with Cast-in-Place Specimen

The displacement decomposition percentages for the GD and CIP specimens are shown in Figures 3-25 and 3-26, respectively. A review of values (FER+Column flexure, bent cap flexibility, and joint shear) shows a close comparison between the GD and CIP specimens. The relative contributions were similar, as well as the individual magnitudes. For example, at a push drift of approximately 1.8% (GD, 1.88%; CIP, 1.76%), FER+Column flexure percentages were within 4% of one another (81.5% GD vs. 85.5% CIP). Bent cap flexibility for GD was 13.6% vs. CIP 10.9%, while joint shear for the GD was 4.9% and 3.7% for CIP. The ranges of CT/CD ratios for GD also compared favorably to the CIP.

Table 3-6 summarizes bar slip component of column displacement for both GD and CIP specimens. Although the GD slip is shown to be larger than the CIP slip by a

factor of approximately 2.5 on average, bar slip for both specimens was found to be a minor component of FER: on average, 9% for GD and 3% for CIP.

3.5 Joint Response

This section summarizes joint response in terms of joint shear stress, principal stresses and angle, joint cracking, joint deformation, and bedding layer.

3.5.1 Joint Shear Stress, Principal Stresses, and Principal Angle

The average joint shear stress, plotted in Figure 3-27, exhibits a similar hysteretic trend as the load-displacement plot and relatively small stresses. Figure 3-28 shows the joint shear stress vs. shear strain, including appropriate stiffness and limited softening at increasing drift ratios. Shear stress and shear strain are calculated as shown in the List of Equations and, strictly speaking, refer to average (or nominal) values applicable to the joint region.

Shear stresses, which did not exceed $5.0\sqrt{f_c'}$, were used in determining the principal stresses and principal angle shown in Figures 3-29 through 3-31. Figure 3-29 shows that the principal tensile stress was limited to $5.2\sqrt{f_c'}$, less than half of the 2006 LRFD RSGS limit of $12\sqrt{f_c'}$, but about 50% larger than $3.5\sqrt{f_c'}$, the level at which more extensive (additional) joint reinforcement is required for development of the force transfer mechanism. Figure 3-30 indicates that the principal compressive stress was limited to approximately $0.08f_c'$, or a third of the 2006 LRFD RSGS limit of $0.25f_c'$. These values correspond well with the intentions of the design and the observed joint performance.

Figure 3-31 plots the angle of the principal plane in the joint, which is shown to be approximately 40-45 degrees from horizontal, with the push direction shown to be slightly smaller. These values correlate well with the expected response.

3.5.2 Joint Cracking

Joint crack widths were consistent with the level of joint stresses reported. Figure 3-5 shows the crack pattern in the joint at 3.8% drift (μ6, push) and Figure 3-10 shows the pattern post-test. Some flexural cracks were evident, and diagonal cracks in the middle to upper portion of the joint were consistent with the principal angles reported in

the previous section. Table 3-7 summarizes the maximum measured surface crack widths in the joint region at the various drift and lateral force levels. The maximum crack width was 0.040 in, which first occurred at a drift of 1.9% (μ3, push) and a force slightly lower than the maximum applied force. Only minor surface spalling developed on the east side face of the bent cap.

3.5.3 Joint Rotation and Deformation

Joint rotation and panel deformation were measured during the test. Figure 3-32 shows joint rotation magnitude, which was limited to less than 0.0023 rad (0.13 deg). This was approximately twice that assumed in predictions; however, predictions were based on an estimate of cracked bent cap section properties.

The deformation of the joint was measured using linear potentiometers in the region of the joint. The maximum change in panel area was very small, limited to less than 0.2%. This corresponds with the limited joint cracking and joint stresses.

3.5.4 Bedding Layer

The 1.5-in bedding layer appeared to perform integrally with the column through 5.5% drift and did not produce unusual behavior in the joint or specimen. Vertical cracks in the bedding layer developed at 1.2% drift (μ1.5), as shown in Figure 3-8. Crushing of the column concrete initiated directly above the bedding layer at a 2.7% drift (μ4), indicating the preferable condition that the grout was not a weak link in the system. As shown in Figure 3-33, post-test inspection exhibited crushing of the concrete at the top surface of the grout-concrete interface.

3.5.5 Comparison with Cast-in-Place Specimen

The precast joint region for the GD specimen performed with limited distress during the test and compared closely to the CIP joint. Table 3-8 summarizes the maximum joint response for stresses, principal angle, joint rotation and change in panel area. This table shows that the maximum joint shear stress, principal tensile and compressive stresses compare very closely for the specimens, with the GD stresses differing from the CIP by 8% or less. The maximum applied force for GD was 3% larger than CIP. The maximum principal angle for the specimens was 45.0 deg for both

specimens. The maximum joint rotation and change in panel area for GD were 15% and 19% larger, respectively.

Figure 3-34 compares the crack patterns for the GD and CIP joint regions. In general, diagonal joint crack patterns due to push and pull loading were reasonably consistent on east and west faces of the joint. Flexural crack patterns were similar as well. Maximum joint crack widths for the GD specimen were somewhat larger (0.040 in vs. 0.025 in), though not excessively, and were consistent with the level of joint stresses and the principal angles reported. Although crack widths were generally influenced by the force level, cracks were sometimes observed to widen and grow at larger drifts and additional cycling even when the applied load decreased. Minor surface spalling developed on the east face of the bent cap for GD, whereas no spalling developed for CIP.

3.6 Strain Records

This section uses strain profiles and tables to present select results from specimen strain records, as well as comparisons to the CIP specimen. Profiles show the strain levels for a series of strain gages at specific regions of the specimen and for specific load or ductility (drift) levels. Profiles include strain for: 1) column longitudinal rebar (locations along the column and into the joint); 2) hoops in the column and joint; and 3) stirrups in the bent cap and joint. A table is provided for the bent cap longitudinal rebar (locations along the bent cap, including through the joint). Figures 2-25 through 2-29 show the instrumentation drawings and photos associated with the strain gages.

Some gages reliably recorded large strains well in excess of yield, while others produced unreliable data typically after bar yield. Plots reflect only data considered reliable.

Only select strain gage records are discussed. These strain records and others will be further analyzed and addressed through future efforts.

3.6.1 Column Longitudinal Rebar

3.6.1.1 Grouted Duct Specimen

Figure 3-35 shows the strain profile for the extreme column bar on the north side of the specimen, for both Force Control and Displacement Control. As expected, column strains were largest in the plastic hinging region and dropped off at distances above (column) and below (joint). Strain penetration was evident, including bar yield at 6 in into the joint (for bar LC16 on south end of column, not shown).

3.6.1.2 Comparison with Cast-in-Place Specimen

Figure 3-36 shows the strain profile for the extreme column bar on the north side of the CIP specimen. Although the highest CIP recorded strains were more concentrated just below the interface between the joint and column, an overall pattern similar to the GD response was observed, with largest column strains in the plastic hinging region, dropping off above and below the plastic hinging region. In addition, significant strain penetration was evident, including bar yield at 6 in into the joint.

3.6.2 Duct Strain

Table 3-9 summarizes tensile strains in the column longitudinal bars at two locations within the corrugated duct (1 in and 6 in into the joint), as well as the duct strains at those same locations. Strain values are provided for FC45 and the maximum recorded value. The pattern of strain in the ducts reasonably followed that of the bar strain at the two depths. For example, at 1 in into the joint, the north bar and the duct yielded at FC45. At 6 in into the joint, both strain levels decreased but were significant. A similar trend at a lower strain level was evident for the south bar.

3.6.3 Hoops in Column and Joint

3.6.3.1 Grouted Duct Specimen

Figure 3-37 shows the strain values for the hoops in the column and joint on the east side (as tested). A larger number of gages were used for the east side, where out-of-plane transverse tension can produce larger hoop strains than in plane of loading (North/South). However, due to the significant spacing between gages, profile lines are not shown connecting strain values. Hoop strains in the plastic hinging regions were

large, and yield was reached at FC55 just above the bedding layer, reflecting the confining effect of the hoop. At FC45, the hoop at approximately 12 in into the joint yielded, although strains at approximately 18 in into the joint were well below yield.

3.6.3.2 Comparison with Cast-in-Place Specimen

Similar to the GD specimen, the CIP hoop strains in the plastic hinging region were large, reflecting confinement (Figure 3-38). Hoop strains peaked at different locations within the joint. For example, at 12 in into the joint, the GD hoop strain was larger than the CIP, but at 18 in into the joint, the CIP hoop strain was larger than the GD.

3.6.4 Bent Cap Longitudinal Rebar

3.6.4.1 Grouted Duct Specimen

Table 3-10 lists bent cap longitudinal bar strain (top and bottom bars) for the first cycle of three nominal displacement ductilities of Displacement Control (μ2, μ4, μ6) during which the maximum load was reached. This table shows that strain levels for bottom and top bars were largest within the joint (S1, CL, and N1 positions) and that the strain level did not exceed 53% of yield. Strain patterns reasonably matched expected distribution per an assumed force transfer model similar to that of Reference 14. It should be noted that the test specimens, designed per 2006 LRFD RSGS, did not include the significant additional area of bent cap longitudinal reinforcement ($0.245A_{st}$) required by 2009 LRFD SGS.

3.6.4.2 Comparison with Cast-in-Place Specimen

Table 3-11 compares the longitudinal bent cap strain (top and bottom bars) for the GD and CIP specimens. Strain patterns are shown to be reasonably consistent, indicating similar joint behavior. The maximum strains for GD and CIP were 53% and 46% of yield, respectively, for bottom bars at the south side (S1). Slightly smaller strains developed at the center line for both specimens. Data was limited at some locations.

3.6.5 Stirrups in Bent Cap and Joint

3.6.5.1 Grouted Duct Specimen

Figures 3-39 through 3-42 show the strain profiles for stirrups within the bent cap and joint. Two 2-leg stirrups were placed within the joint for constructability reasons, as

explained in Section 2.2.1. Two strain gages were placed on the leg of each stirrup, at approximately the 1/3 and 2/3 points along the stirrups (Figure 2-26). Since stirrups in the regions adjacent to the joint used gages at the mid-height of the stirrup, two sets of plots are shown: 1) mid-height gages on stirrups outside the joint together with the top gage on the joint stirrups (Figures 3-39 and 3-40); and 2) mid-height gages on stirrups outside the joint together with the bottom gage on the joint stirrups (Figures 3-41 and 3-42).

Figure 3-39 shows a minor strain level in the stirrups both outside the joint and inside the joint (top location) under Force Control. Strains within the joint were larger but limited to only 37% of yield. Under Displacement Control (Figure 3-40), stirrup strains within the joint remained minor, but the south most stirrup outside the joint increased to 68% of yield.

Figures 3-41 and 3-42 show strain demands on the joint stirrups, which reached 75% of yield at the south end of the joint and a lower level at the north end. The high level of strain for this construction stirrup indicates the importance of its contribution to joint performance.

It should be noted that although test specimens designed per 2006 LRFD RSGS did not require stirrups inside the joint, the 2007 Proposed AASHTO Guide Specifications for LRFD Seismic Bridge Design (2007 LRFD PSGS) and 2009 LRFD SGS require an area of $0.135A_{st}$ for vertical stirrups within the joint. The two construction stirrups placed within the joint provided an area approximately 65% of that required by the 2009 LRFD SGS.

3.6.5.2 Comparison with Cast-in-Place Specimen

A comparison of Figures 3-39 to 3-42 (GD top and bottom stirrups) to Figures 3-43 and 3-44 (CIP top and bottom stirrups, Displacement Control) shows that large construction stirrup strains close to or exceeding yield developed in the joint. Although strain magnitudes and gage locations differed somewhat, construction stirrups clearly played a significant role in joint performance. The south most GD stirrup outside the joint exhibited a larger strain than the CIP stirrup at the same location.

3.7 Tables

Table 3-1. Associated Values of Force, Displacement, Ductility, and Drift Ratio—GD

Push (Cycle 1)					
Stage	Force (kips)	Disp. (in)	Displacement Ductility, μ		Drift (%)
			Actual	Nominal	
Force Control	13.1	0.025	-	-	0.04
	20.1	0.058	-	-	0.10
	30.2	0.134	-	-	0.23
	45.4	0.325	-	-	0.56
	55.9	0.644	-	-	1.12
Displacement Control	36.8	0.459	1.16	1.0	0.80
	44.1	0.623	1.58	1.5	1.08
	49.7	0.758	1.92	2.0	1.32
	56.4	1.078	2.73	3.0	1.88
	56.9	1.469	3.73	4.0	2.55
	54.8	2.188	5.55	6.0	3.81
	44.7	2.836	7.19	8.0	4.93
Pull (Cycle 1)					
Stage	Force (kips)	Disp. (in)	Displacement Ductility, μ		Drift (%)
			Actual	Nominal	
Force Control	-13.1	-0.023	-	-	-0.04
	-20.2	-0.065	-	-	-0.11
	-30.4	-0.146	-	-	-0.25
	-45.5	-0.304	-	-	-0.53
	-55.5	-0.816	-	-	-1.42
Displacement Control	-29.9	-0.525	1.33	1.0	-0.91
	-39.5	-0.661	1.68	1.5	-1.15
	-46.5	-0.784	1.99	2.0	-1.36
	-55.3	-1.159	2.94	3.0	-2.02
	-54.8	-1.557	3.95	4.0	-2.71
	-50.8	-2.346	5.95	6.0	-4.08
	-44.8	-3.159	8.01	8.0	-5.49

Table 3-2. Associated Values of Force, Displacement, Ductility, and Drift Ratio (Push, Cycle 1)—GD vs. CIP

Push (Cycle 1)—GD					
Stage	Force (kips)	Disp. (in)	Displacement Ductility, μ		Drift (%)
			Actual	Nominal	
Force Control	13.1	0.025	-	-	0.04
	20.1	0.058	-	-	0.10
	30.2	0.134	-	-	0.23
	45.4	0.325	-	-	0.56
	55.9	0.644	-	-	1.12
Displacement Control	36.8	0.459	1.16	1.0	0.80
	44.1	0.623	1.58	1.5	1.08
	49.7	0.758	1.92	2.0	1.32
	56.4	1.078	2.73	3.0	1.88
	56.9	1.469	3.73	4.0	2.55
	54.8	2.188	5.55	6.0	3.81
	44.7	2.836	7.19	8.0	4.93

Push (Cycle 1)—CIP					
Stage	Force (kips)	Disp. (in)	Displacement Ductility, μ		Drift %
			Actual	Nominal	
Force Control	13.0	0.034	-	-	0.06
	20.0	0.072	-	-	0.13
	30.1	0.154	-	-	0.27
	48.4	0.397	-	-	0.69
Displacement Control	40.0	0.406	1.13	1.0	0.71
	49.4	0.533	1.49	1.5	0.93
	53.3	0.684	1.91	2.0	1.19
	55.6	1.014	2.83	3.0	1.76
	54.6	1.345	3.75	4.0	2.34
	55.9	2.070	5.77	6.0	3.60
	53.2	2.638	7.36	8.0	4.59
	50.0	3.383	9.43	10.0	5.88

Table 3-3. Predicted vs. Actual Stages of Specimen Cracking

Stage	P_V (kips)		P_H (kips)	
	Predicted	Actual	Predicted	Actual
Bent Cap—Flexural	None	None	-	-
	38	38	10.2	13.0
Column—Flexural	38	38	12.9	13.0
Joint Shear	38	38	36.5	45.0

Table 3-4. Select Material Properties—GD vs. CIP

Parameter	GD		CIP	
Concrete Compressive Strength, f'c	Cap and Column: 4557 psi		Cap: 4553 psi Column: 6178 psi	
Steel Rebar Strength	Yield	Tensile	Yield	Tensile
#3 (Bent cap stirrups; Column hoops)	64.1	99.0	68.2	95.5
#5 (Bent cap longitudinal; Column longitudinal)	64.5	95.2	64.5	90.0
Grout Compressive Strength (Bedding layer and ducts)	8026 psi (6421 psi, equivalent cylinder strength)		N/A	

Table 3-5. Displacement Decomposition (1st Push and Pull Cycles)

Displacement Decomposition—Grouted Duct (1st Push Cycle)										
		Actual	Predicted	Act/Pred	Actual	Predicted	Act/Pred	Actual	Predicted	Act/Pred
Displacement Ductility	(μ)	FC45**	-	-	FC55**	-	-	3.0	-	-
Col Displacement [CD]	(in)	0.325	0.325	1.00	0.644	0.644	1.00	1.078	1.078	1.00
Drift	(%)	0.56	-	-	1.12	-	-	1.88	-	-
Force	(Kip)	45.4	51.3	0.89	55.9	58.0	0.96	56.4	58.7	0.96
Column Flexure	(in)	0.075	0.255	0.80	0.148	0.499	0.93	0.252	0.896	0.92
Fixed End Rotation	(in)	0.128			0.314			0.575		
Column Shear	(in)	*	0.024	*	*	0.092	*	*	0.128	*
Bent Cap Flexibility	(in)	0.078	0.047	1.65	0.109	0.053	2.06	0.138	0.054	2.58
Joint Shear	(in)	0.023	*	*	0.040	*	*	0.049	*	*
Component Total [CT]	(in)	0.305	0.326		0.611	0.644		1.014	1.078	
CT/CD		0.94	1.00		0.95	1.00		0.94	1.00	
		Actual	Predicted	Act/Pred	Actual	Predicted	Act/Pred	Actual	Predicted	Act/Pred
Displacement Ductility	(μ)	4.0	-	-	6.0	-	-	8.0	-	-
Col Displacement [CD]	(in)	1.469	1.469	1.00	2.188	2.188	1.00	2.836	2.836	1.00
Drift	(%)	2.55	-	-	3.81	-	-	4.93	-	-
Force	(Kip)	56.9	59.9	0.95	54.8	62.3	0.88	44.7	64.3	0.69
Column Flexure	(in)	0.359	1.242	0.83	0.655	1.869	***	***	2.433	***
Fixed End Rotation	(in)	0.670			***			***		
Column Shear	(in)	*	0.171	*	*	0.263	*	*	0.345	*
Bent Cap Flexibility	(in)	0.148	0.055	2.68	0.157	0.057	2.73	0.141	0.059	2.40
Joint Shear	(in)	0.056	*	*	0.062	*	*	0.054	*	*
Component Total [CT]	(in)	1.232	1.469		***	2.189		***	2.836	
CT/CD		0.84	1.00		***	1.00		***	1.00	
Displacement Decomposition—Grouted Duct (1st Pull Cycle)										
		Actual	Predicted	Act/Pred	Actual	Predicted	Act/Pred	Actual	Predicted	Act/Pred
Displacement Ductility	(μ)	FC45**	-	-	FC55**	-	-	3.0	-	-
Col Displacement [CD]	(in)	-0.304	-0.304	1.00	-0.816	-0.816	1.00	-1.159	-1.159	1.00
Drift	(%)	-0.53	-	-	-1.42	-	-	-2.02	-	-
Force	(Kip)	-45.5	-50.0	0.91	-55.5	-58.3	0.95	-55.3	-58.8	0.94
Column Flexure	(in)	-0.083	-0.236	0.86	-0.213	-0.653	0.98	-0.213	-0.972	0.85
Fixed End Rotation	(in)	-0.120			-0.424			-0.612		
Column Shear	(in)	*	-0.022	*	*	-0.110	*	*	-0.133	*
Bent Cap Flexibility	(in)	-0.043	-0.046	0.92	-0.092	-0.053	1.74	-0.115	-0.054	2.13
Joint Shear	(in)	-0.022	*	*	-0.049	*	*	-0.062	*	*
Component Total [CT]	(in)	-0.267	-0.305		-0.778	-0.816		-1.002	-1.159	
CT/CD		0.88	1.00		0.95	1.00		0.86	1.00	
		Actual	Predicted	Act/Pred	Actual	Predicted	Act/Pred	Actual	Predicted	Act/Pred
Displacement Ductility	(μ)	4.0	-	-	6.0	-	-	8.0	-	-
Col Displacement [CD]	(in)	-1.557	-1.557	1.00	-2.346	-2.346	1.00	-3.159	-3.159	1.00
Drift	(%)	-2.71	-	-	-4.08	-	-	-5.49	-	-
Force	(Kip)	-54.8	-60.2	0.91	-50.8	-62.8	0.81	-44.8	-65.1	0.69
Column Flexure	(in)	-0.302	-1.319	0.73	-0.396	-2.006	***	***	-2.713	***
Fixed End Rotation	(in)	-0.655			***			***		
Column Shear	(in)	*	-0.182	*	*	-0.283	*	*	-0.386	*
Bent Cap Flexibility	(in)	-0.124	-0.055	2.25	-0.128	-0.058	2.21	-0.127	-0.059	2.13
Joint Shear	(in)	-0.068	*	*	-0.073	*	*	-0.070	*	*
Component Total [CT]	(in)	-1.149	-1.557		***	-2.347		***	-3.159	
CT/CD		0.74	1.00		***	1.00		***	1.00	

Note: *Column shear displacement not measured; Joint shear displacement not predicted. **Specimen loaded to ~μ2.0 under Force Control; 45 kip and 55 kip Force Control data reported. ***Column curvature gages removed; data not reliable.

Table 3-6. Bar Slip and Fixed End Rotation Components—GD vs. CIP

Drift (%)	Displace. Ductility	Force (GD) (kips)	Force (CIP) (kips)	BS (GD) (in)	BS (CIP) (in)	BS/FER (GD)	BS/FER (CIP)	BS/FER (GD/CIP)
0.72	*	49.5	48.4	0.019	0.008	0.114	0.049	2.34
0.85	*	54.3	49.4	0.025	0.014	0.100	0.051	1.98
1.13	μ2	—	53.3	—	0.014	—	0.038	—
1.72	μ3	55.4	55.6	0.041	0.016	0.074	0.031	2.40
2.31	μ4	55.5	54.6	0.046	0.016	0.072	0.022	3.24
3.57	μ6	54.3	55.9	0.055	0.022	—	0.021	—
4.55	μ8	44.0	53.2	0.052	0.030	—	0.023	—

*Same drift is used, but from different stages for CIP and GD
—Not available

Table 3-7. Maximum Measured Crack Width on Joint Surface (East Face)

Drift Ratio (%) Push (Pull)	Displacement Ductility	Force (kips) Push (Pull)	Crack Width (0.001 in) Push (Pull)
0.98 (1.29)	FC55	55.3 (55.0)	25 (—)
1.08 (1.15)	μ1.5	44.1 (39.5)	—
1.32 (1.36)	μ2	49.7 (46.5)	—
1.88 (2.02)	μ3	56.4 (55.3)	40 (16)
2.55 (2.71)	μ4	56.9 (54.8)	**
3.81 (4.08)	μ6	54.8 (50.8)	40 (—)
4.93 (5.49)	μ8	44.7 (44.8)	—

—Not available. **Unreliable.
Note: In general, crack widths for east face were slightly smaller than west face.

Table 3-8. Maximum Joint Response for Select Parameters—GD vs. CIP

Parameter (Maximum)		GD		CIP		GD/CIP
Joint Shear Stress	(psi)	312	$(4.62\sqrt{f'c})$	328	$(4.86\sqrt{f'c})$	0.95
Principal Tensile Stress	(psi)	343	$(5.09\sqrt{f'c})$	363	$(5.38\sqrt{f'c})$	0.94
Principal Compressive Stress	(psi)	370	$(0.081f'c)$	401	$(0.088f'c)$	0.92
Angle of Principal Plane	(deg)	45.0		45.0		1.00
Joint Rotation	(rad)	2.25×10^{-3}		1.95×10^{-3}		1.15
Change in Panel Area	(%)	0.19		0.16		1.19

Table 3-9. Tensile Strains in Column Longitudinal Bars and Bent Cap Ducts

Location of Gage in Joint Region	Bar Strain (με)		Duct Strain (με)	
	FC45	Max.	FC45	Max.
North (1 in into joint)	9823	9823*	1283	1283**
North (6 in into joint)	2001	2639	862	862**
South (1 in into joint)	1795	1795*	566	1240
South (6 in into joint)	—	—	413	663

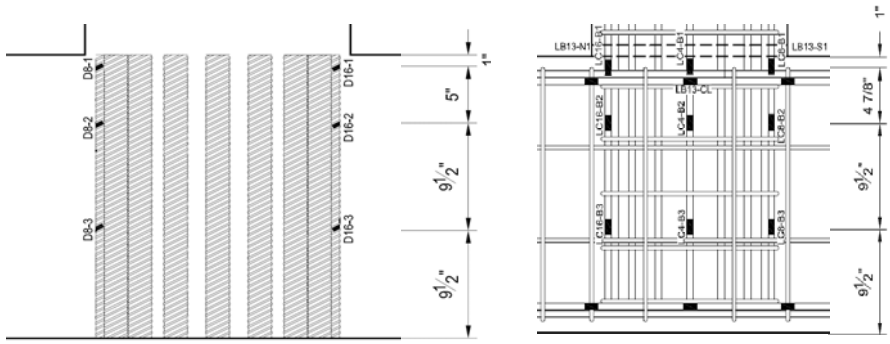

— Not available
*Data unreliable after FC45. Thus, maximum strains reported at FC45.
**Gage saturation limited maximum value.

Table 3-10. Bent Cap Longitudinal Bar Strain—GD

Top Bar		S2		S1		CL		N1		N2	
		Push	Pull	Push	Pull	Push	Pull	Push	Pull	Push	Pull
GD (LB13)	μ2	-221	40	72	380	307	466	538	123	56	-212
	μ4	-228	102	260	386	391	757	497	-73	229	-201
	μ6	-222	100	277	380	398	811	525	-107	306	-179
	$\varepsilon_{max}/\varepsilon_y$	-0.10	0.05	0.12	0.17	0.18	0.36	0.24	0.06	0.14	-0.10
Bottom Bar		**S2**		**S1**		**CL**		**N1**		**N2**	
		Push	Pull	Push	Pull	Push	Pull	Push	Pull	Push	Pull
GD (LB10)	μ2	872	-257	1,065	113	759	436	—	—	26	634
	μ4	934	-303	1,156	129	861	525	—	—	4	670
	μ6	891	-282	1,169	156	898	566	—	—	26	638
	$\varepsilon_{max}/\varepsilon_y$	0.42	-0.14	0.53	0.07	0.40	0.25	—	—	0.01	0.30

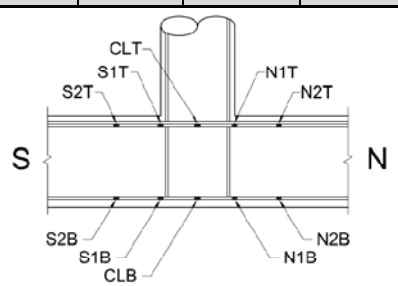

Note: Reference Table 3-1 for associated drift and force levels.
— Not available

Table 3-11. Bent Cap Longitudinal Bar Strain—GD vs. CIP

Top Bars		S2		S1		CL		N1		N2	
		Push	Pull	Push	Pull	Push	Pull	Push	Pull	Push	Pull
CIP (LB13)	μ2	-218	118	146	252	—	—	267	-208	—	—
	μ4	-194	141	80	228	—	—	168	-392	—	—
	μ6	-229	116	30	302	—	—	53	-581	—	—
	$\varepsilon_{max}/\varepsilon_y$	-0.10	0.06	0.07	0.14	—	—	0.12	-0.26	—	—
GD (LB13)	μ2	-221	40	72	380	307	466	538	123	56	-212
	μ4	-228	102	260	386	391	757	497	-73	229	-201
	μ6	-222	100	277	380	398	811	525	-107	306	-179
	$\varepsilon_{max}/\varepsilon_y$	-0.10	0.05	0.12	0.17	0.18	0.36	0.24	0.06	0.14	-0.10

Bottom Bars		S2		S1		CL		N1		N2	
		Push	Pull	Push	Pull	Push	Pull	Push	Pull	Push	Pull
CIP (LB10)	μ2	823	-108	968	68	891	221	259	755	78	535
	μ4	867	-135	875	132	947	334	349	876	59	587
	μ6	890	-164	1,021	157	961	434	449	1,018	35	685
	$\varepsilon_{max}/\varepsilon_y$	0.40	-0.07	0.46	0.07	0.43	0.20	0.20	0.46	0.04	0.31
GD (LB10)	μ2	872	-257	1,065	113	759	436	—	—	26	634
	μ4	934	-303	1,156	129	861	525	—	—	4	670
	μ6	891	-282	1,169	156	898	566	—	—	26	638
	$\varepsilon_{max}/\varepsilon_y$	0.42	-0.14	0.53	0.07	0.40	0.25	—	—	0.01	0.30

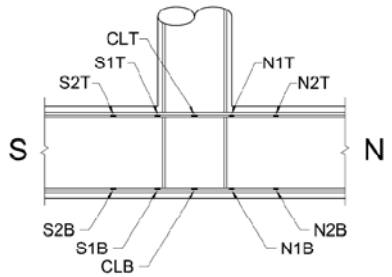

Note: Reference Tables 3-1 and 3-2 for associated drift and force levels.
— Not available

3.8 Figures

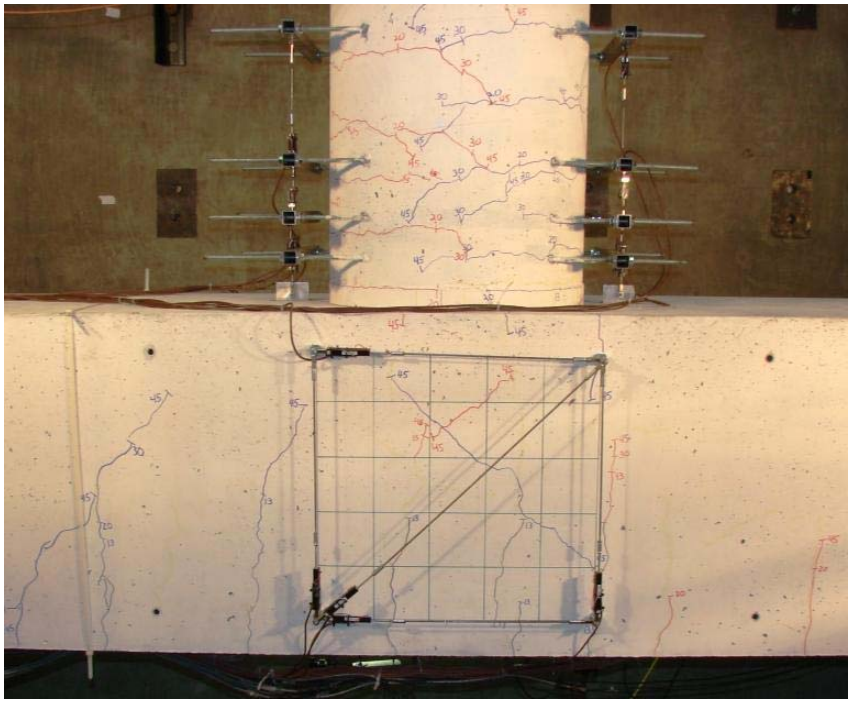

Figure 3-1. Specimen Crack Pattern during Force Control Sequence (45 kips)

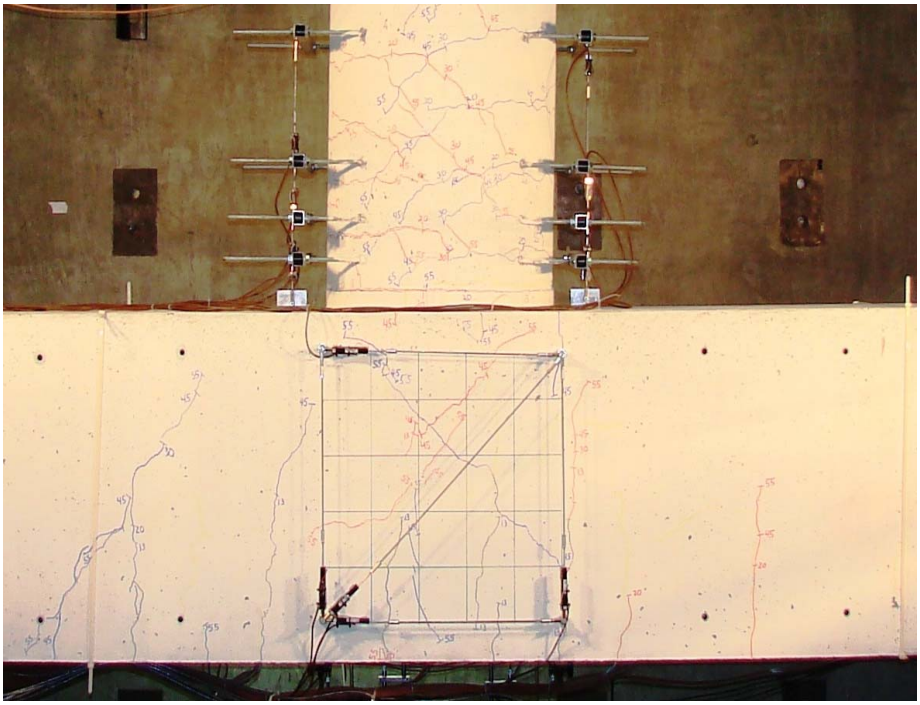

Figure 3-2. Specimen Crack Pattern at End of Force Control Sequence (55 kips)

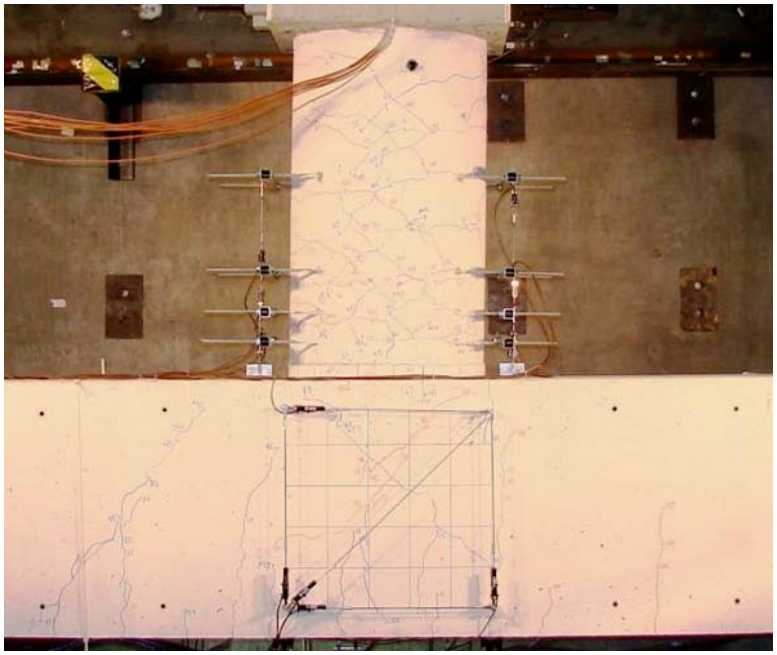

Figure 3-3. Specimen Response at 1.4% Drift Ratio (μ2)

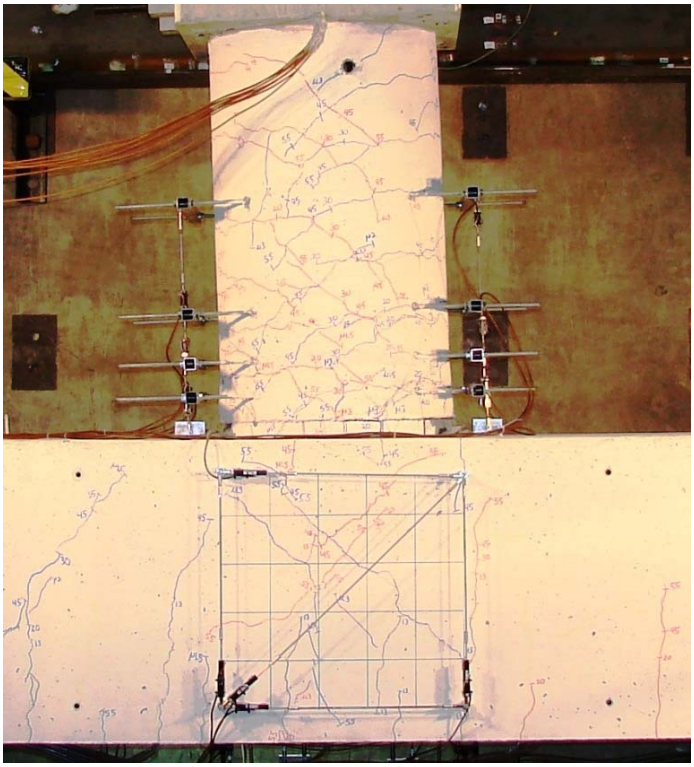

Figure 3-4. Specimen Response at 2.7% Drift Ratio (μ4)

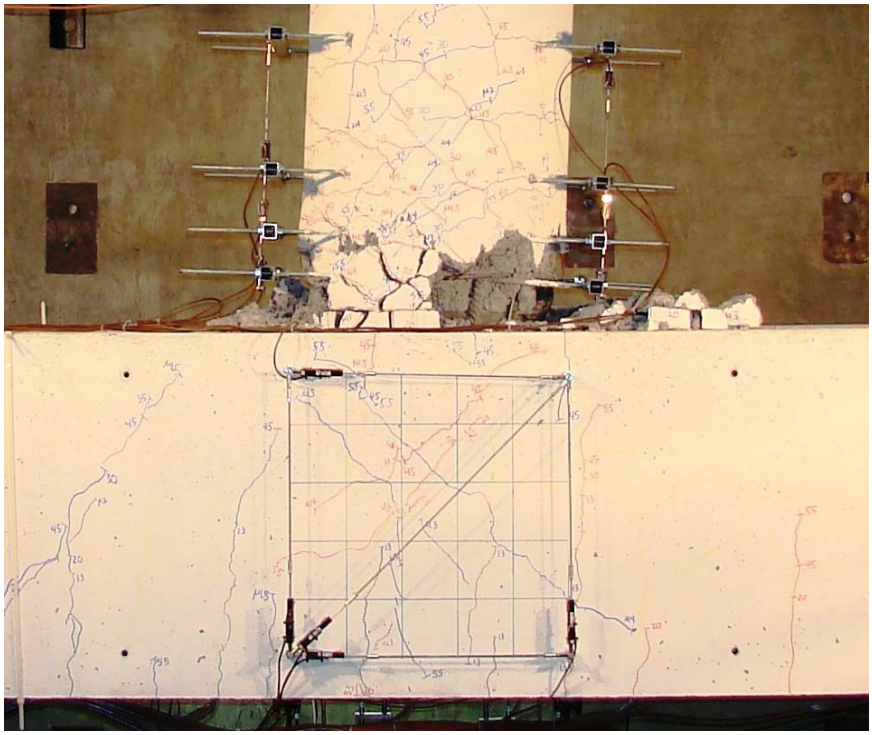

Figure 3-5. Specimen Response at 4.1% Drift Ratio (μ6)

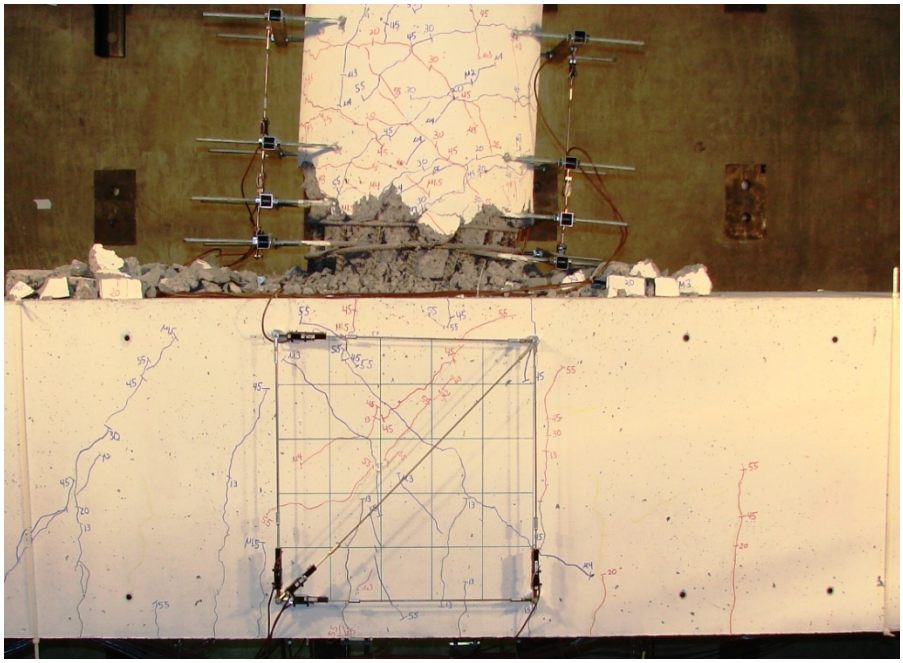

Figure 3-6. Specimen Response at 5.5% Drift Ratio (μ8)

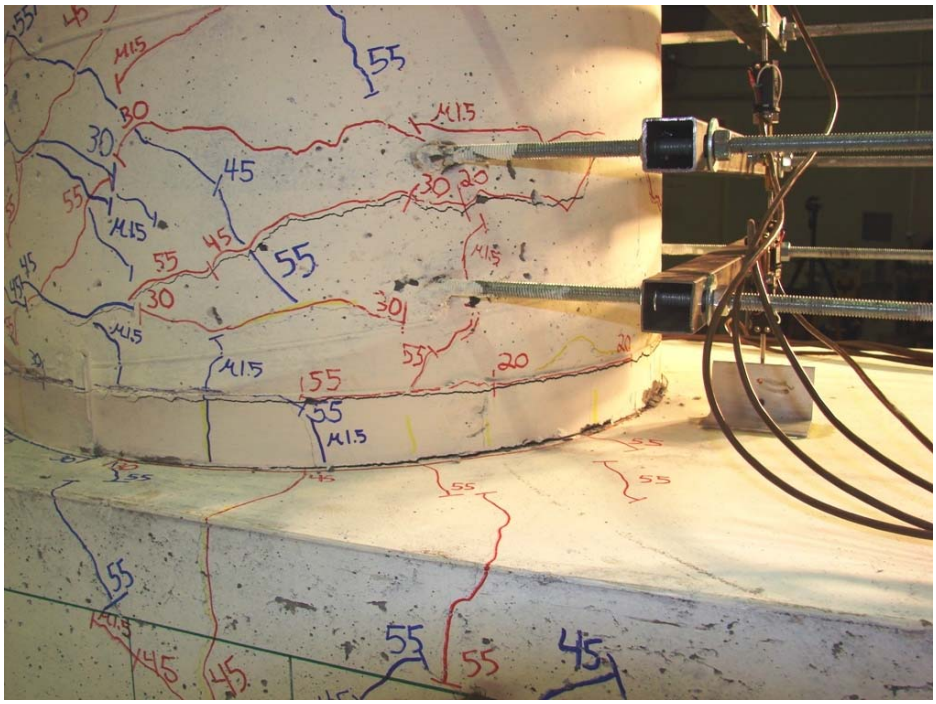

Figure 3-7. Initial Column Spalling at 1.2% Drift Ratio (μ1.5) (South)

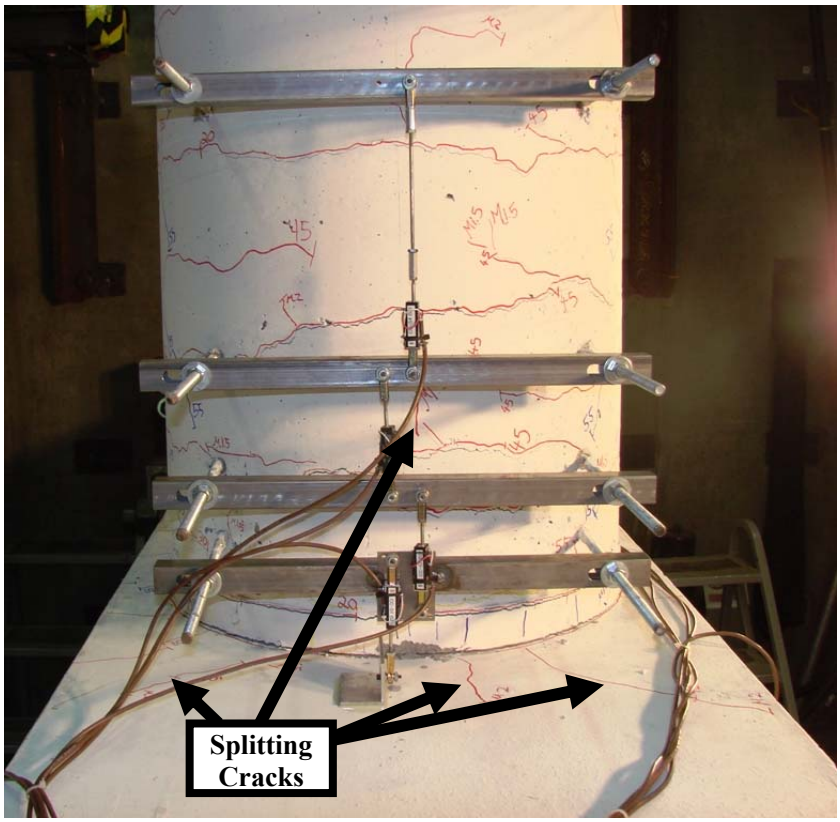

Figure 3-8. Splitting Cracks at Bent Cap and Column at 1.4% Drift Ratio (μ2) (South)

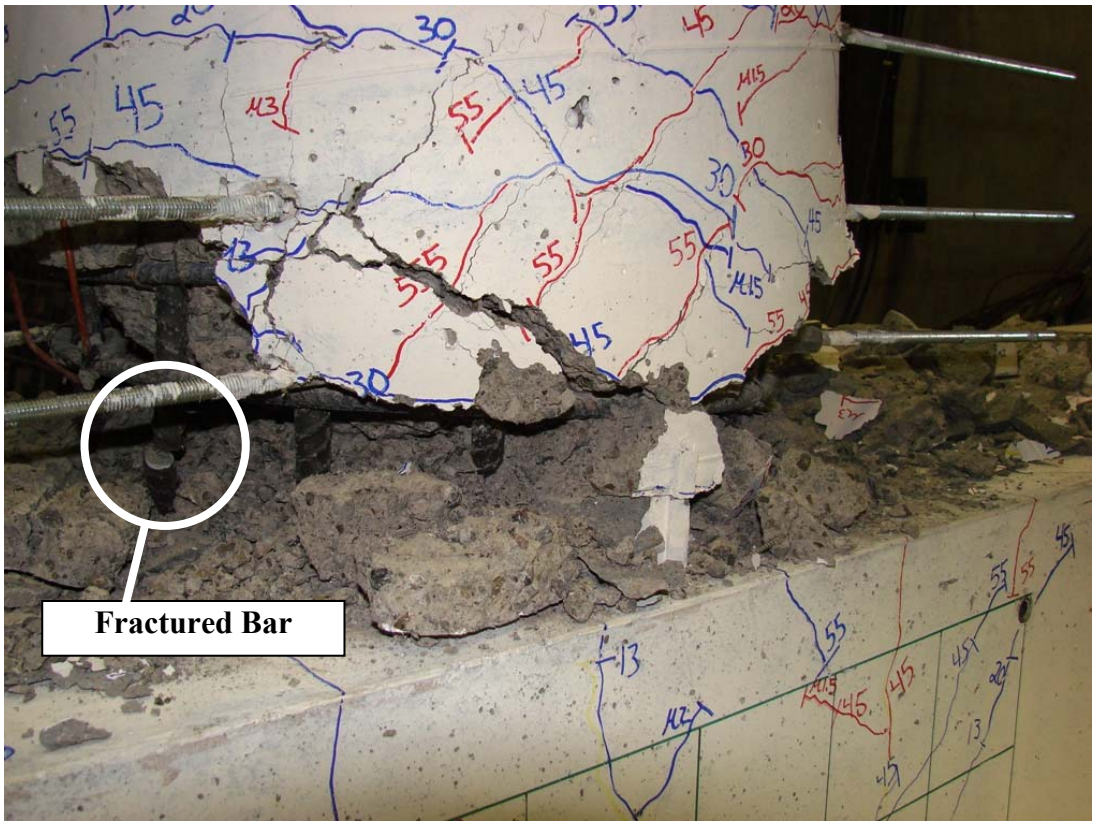

Figure 3-9. Fractured Bars in Plastic Hinge Region (North End, Post Test)

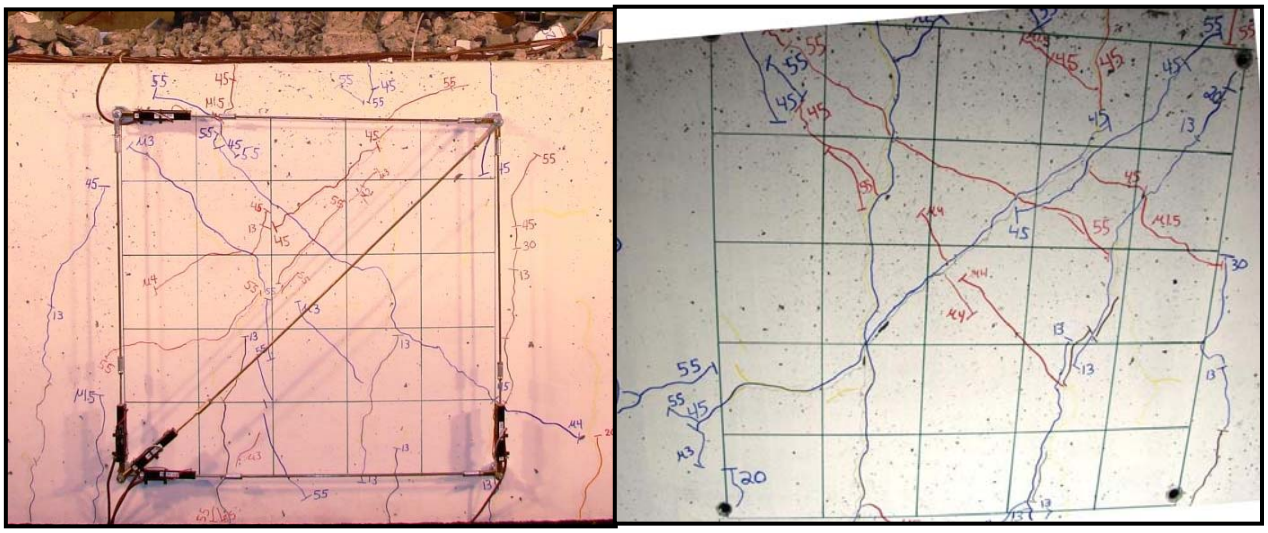

A. East Side B. West Side

Figure 3-10. Joint Region Cracking Post-Test

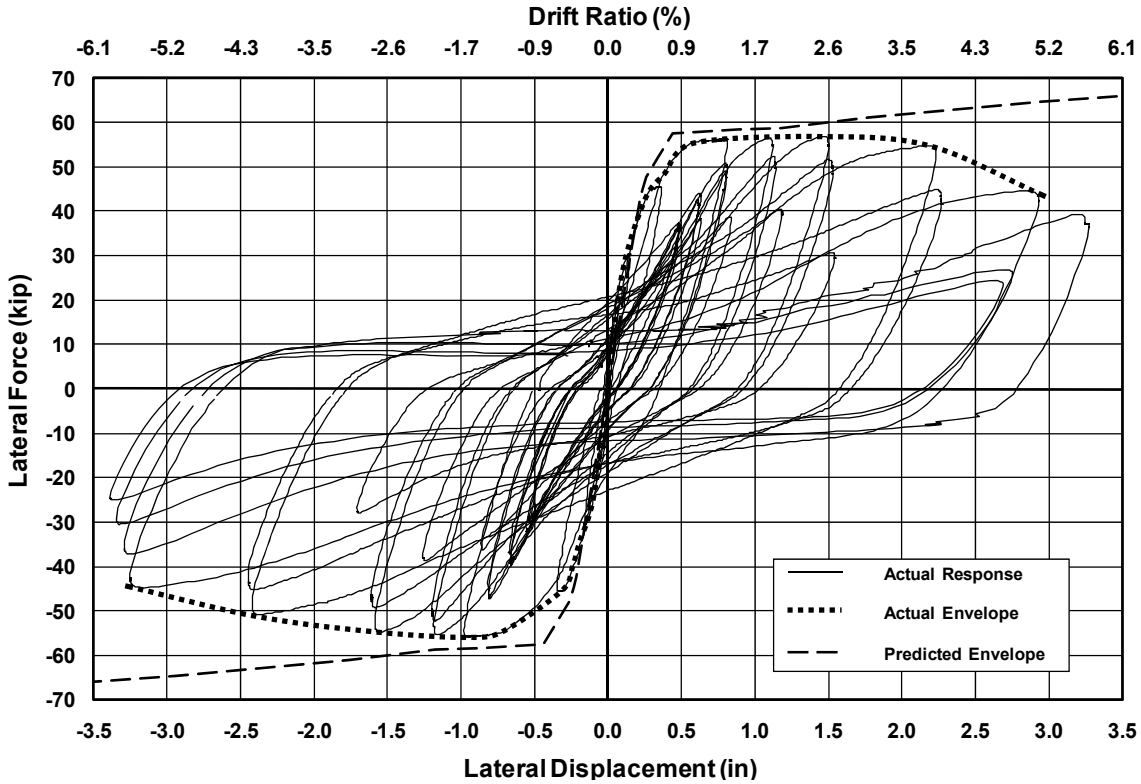

Figure 3-11. Lateral Force vs. Lateral Displacement

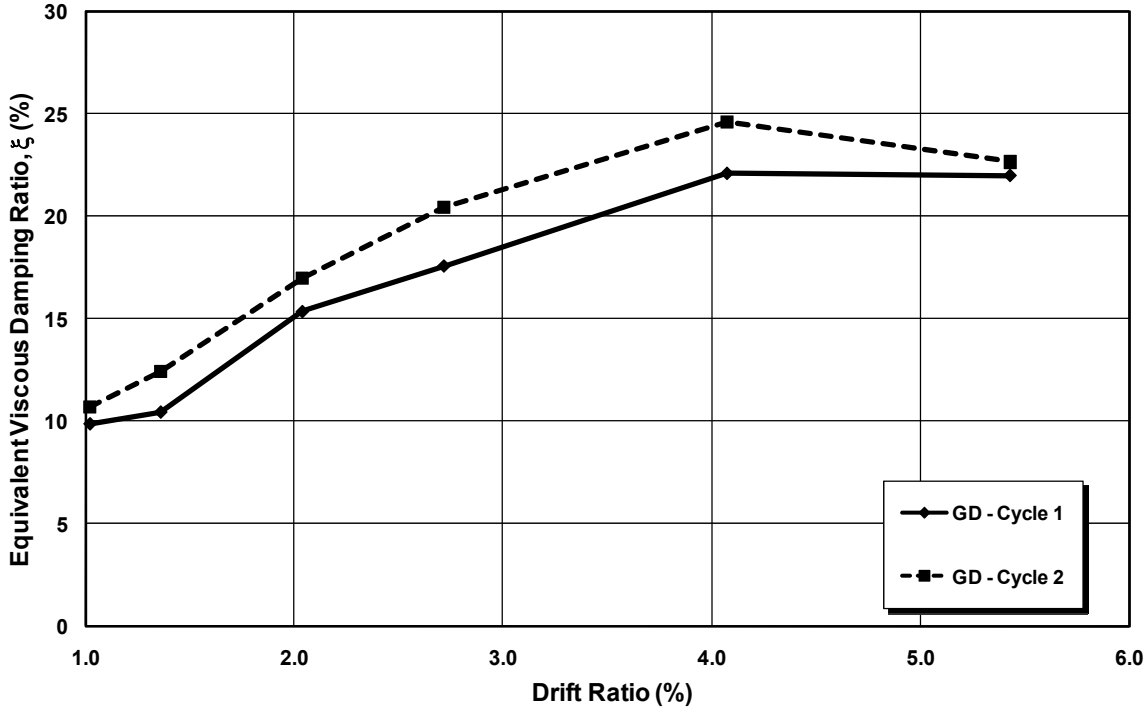

Figure 3-12. Equivalent Viscous Damping Ratio vs. Drift Ratio

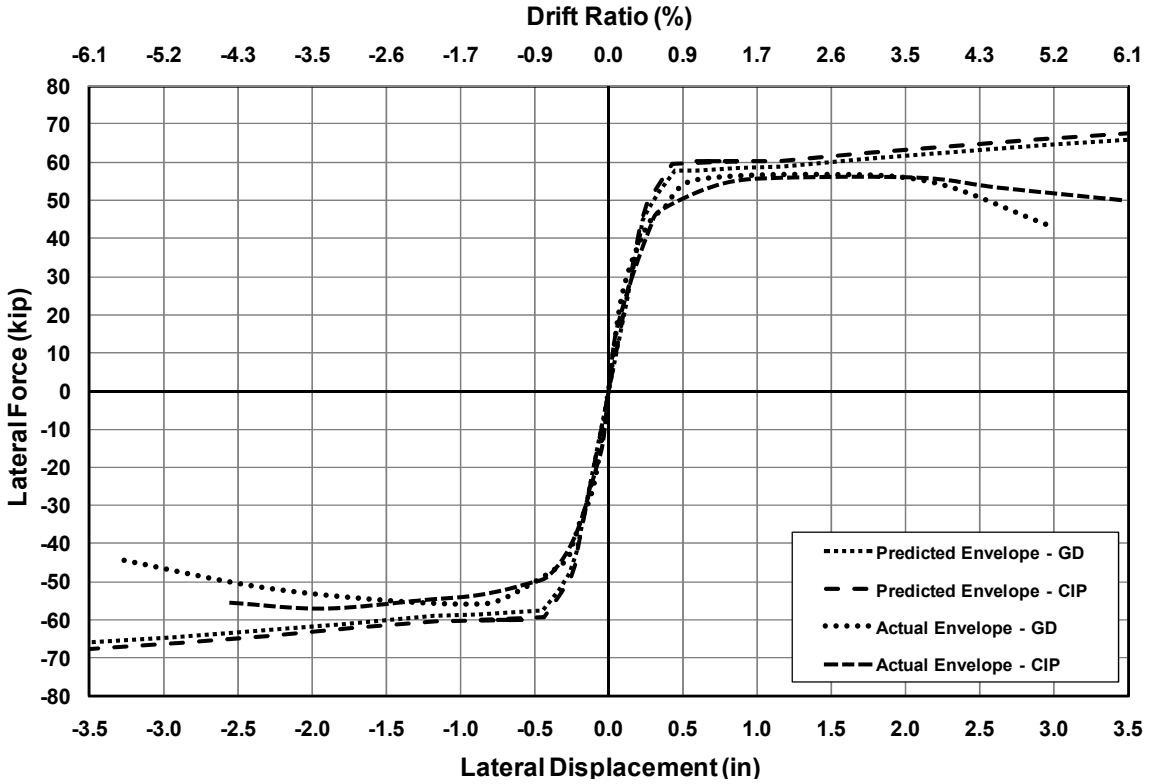

Figure 3-13. Lateral Force vs. Lateral Displacement Envelopes—GD vs. CIP

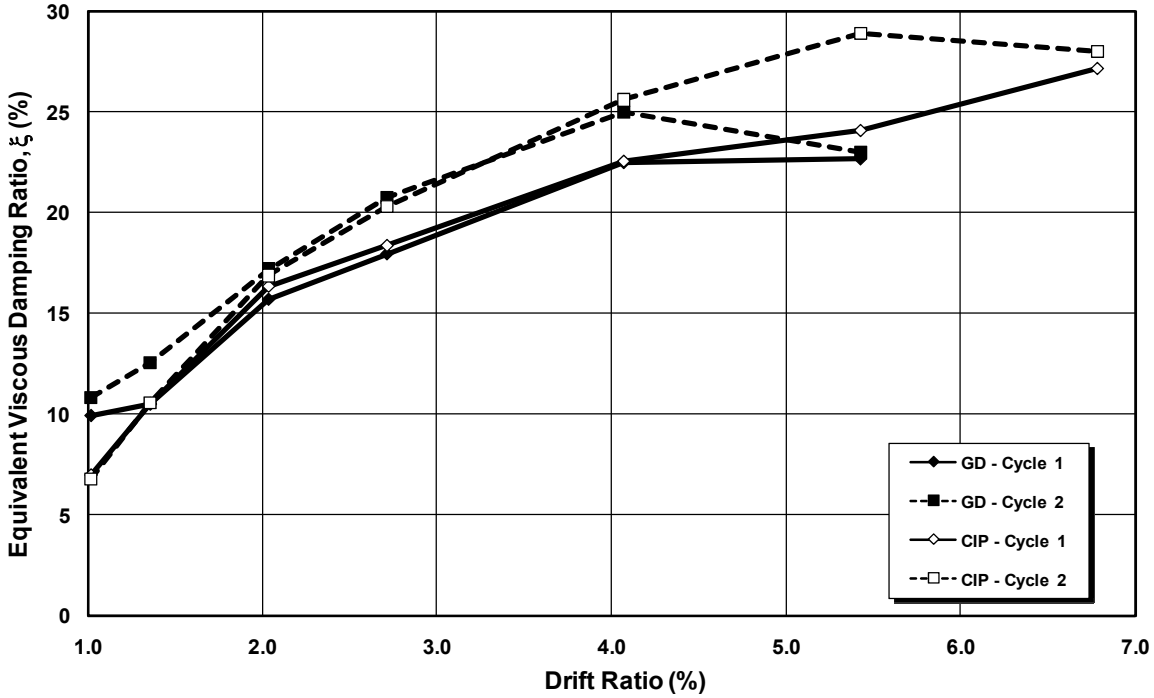

Figure 3-14. Equivalent Viscous Damping Ratio vs. Drift Ratio—GD vs. CIP

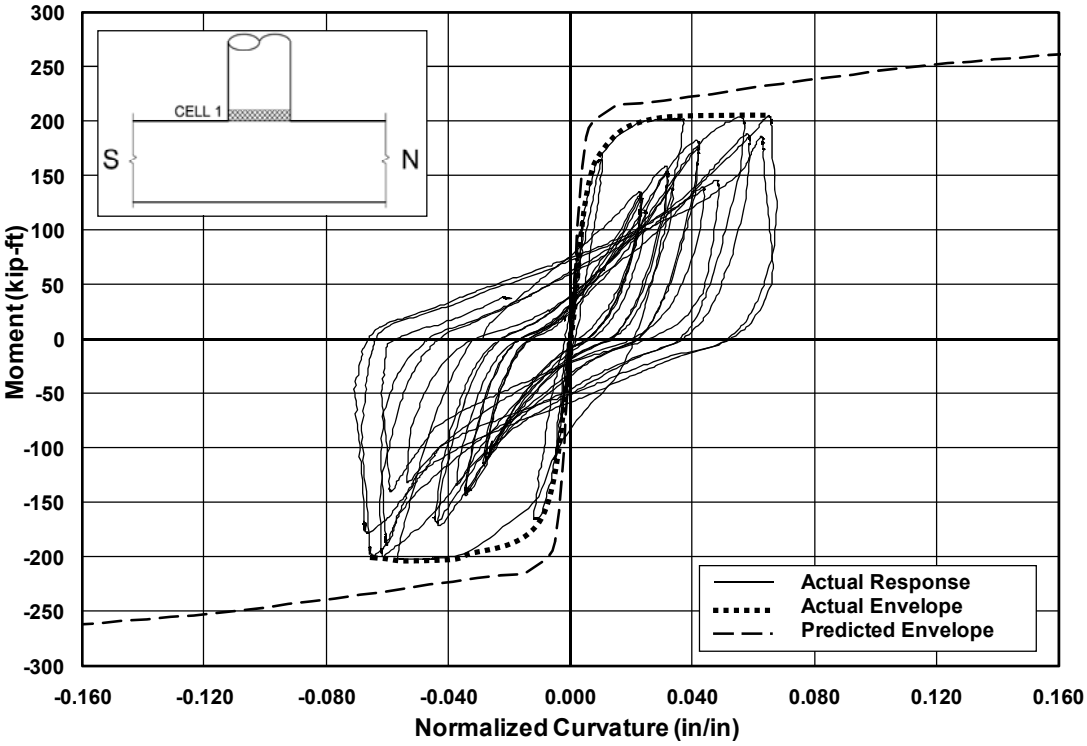

Figure 3-15. Normalized Moment-Curvature Response—Cell 1

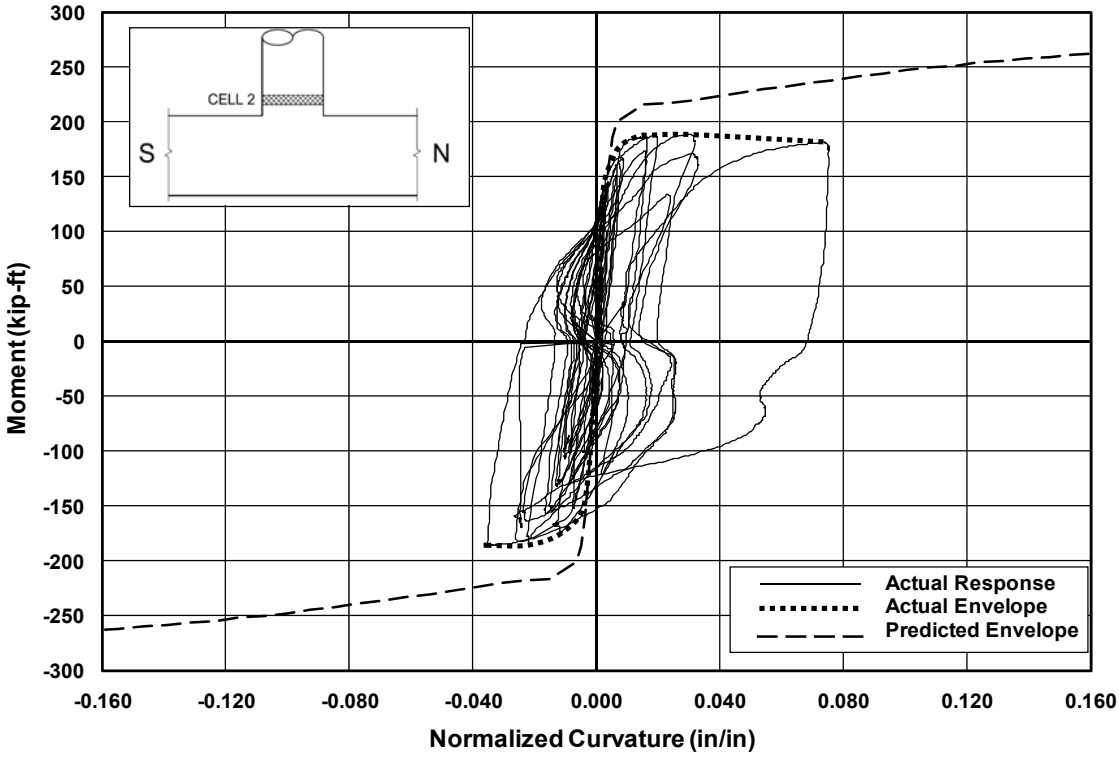

Figure 3-16. Normalized Moment-Curvature Response—Cell 2

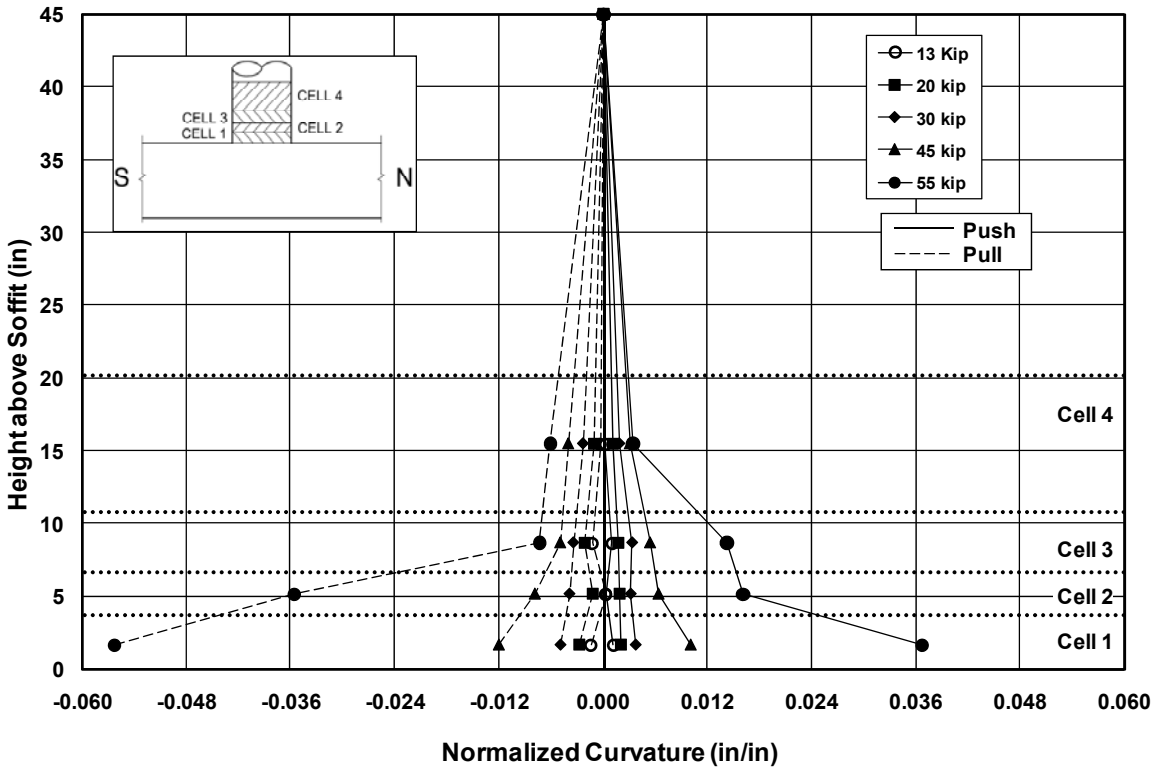

Figure 3-17. Curvature Profile—Force Control

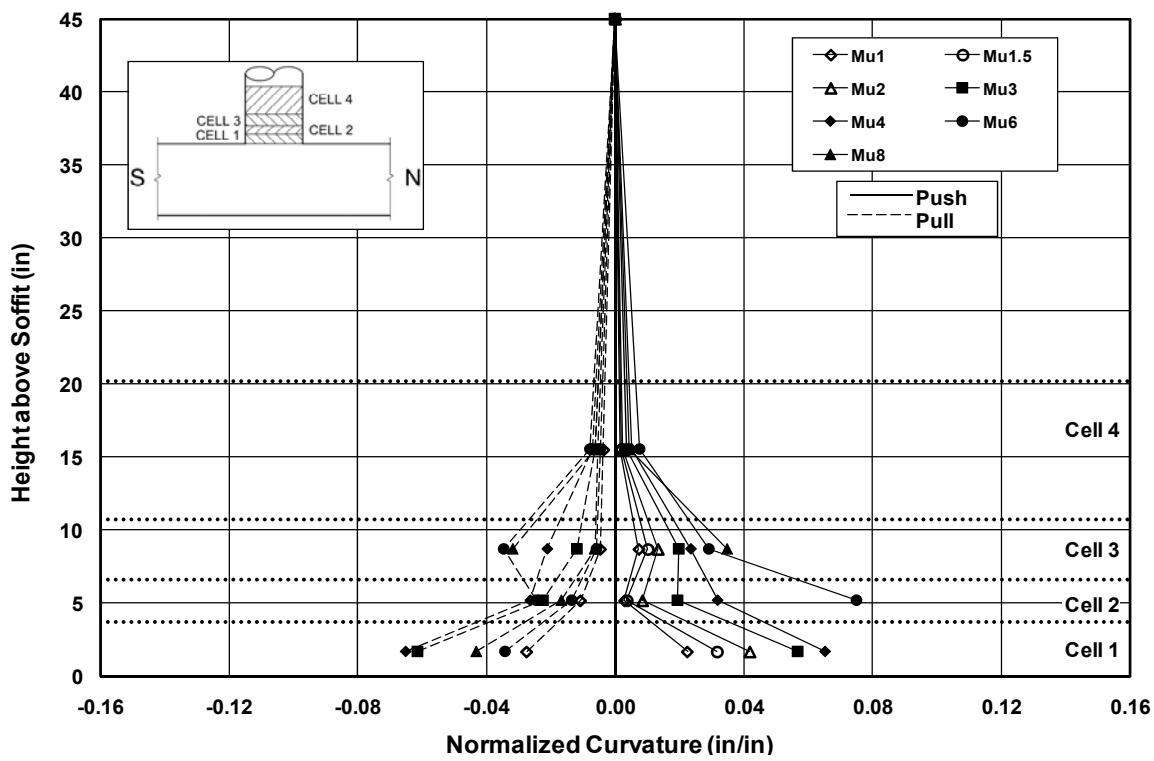

Figure 3-18. Curvature Profile—Displacement Control

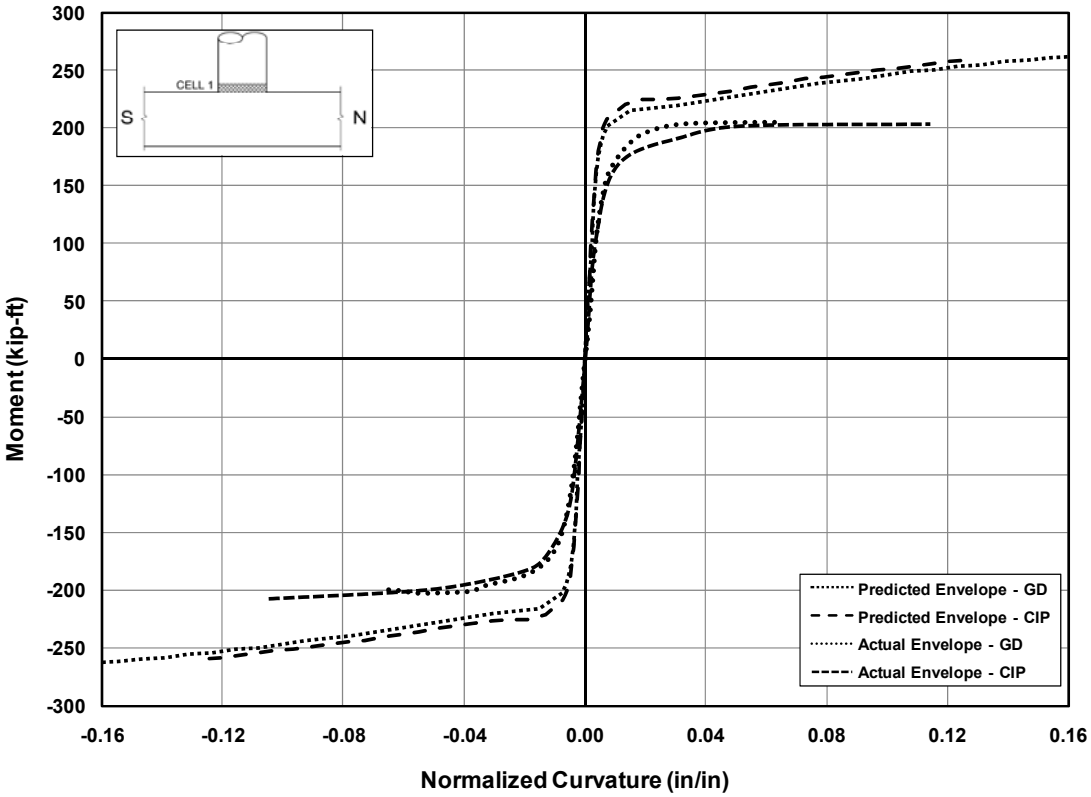

Figure 3-19. Normalized Moment-Curvature Response (Cell 1)—GD vs. CIP

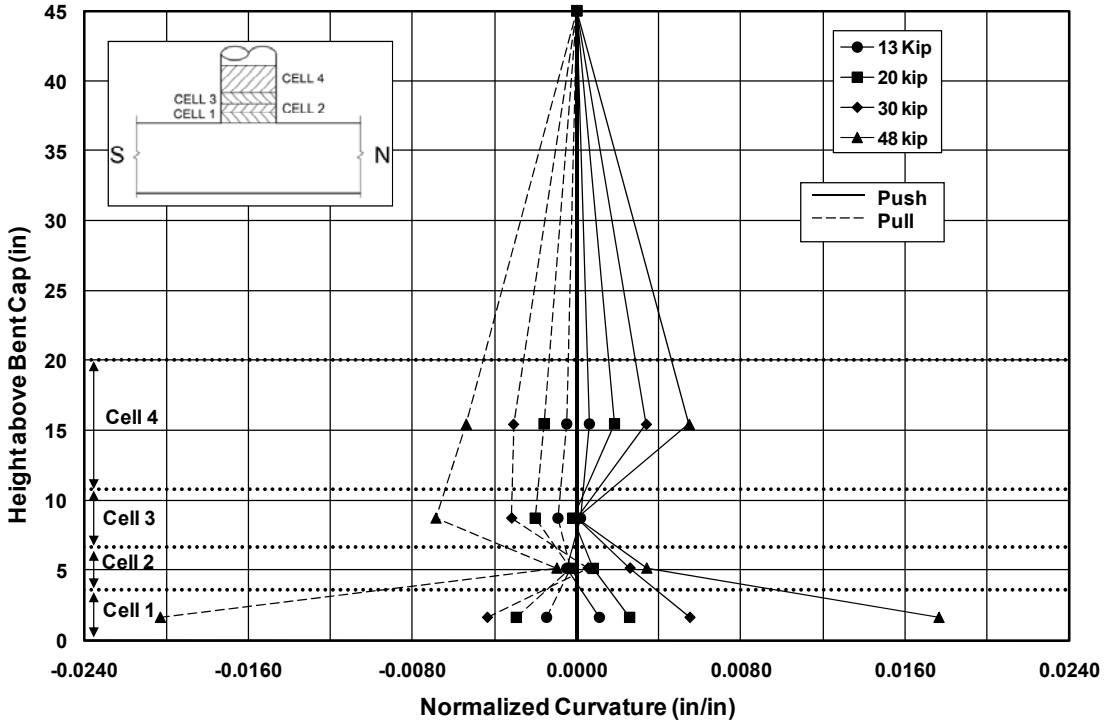

Figure 3-20. Curvature Profile (Force Control)—CIP

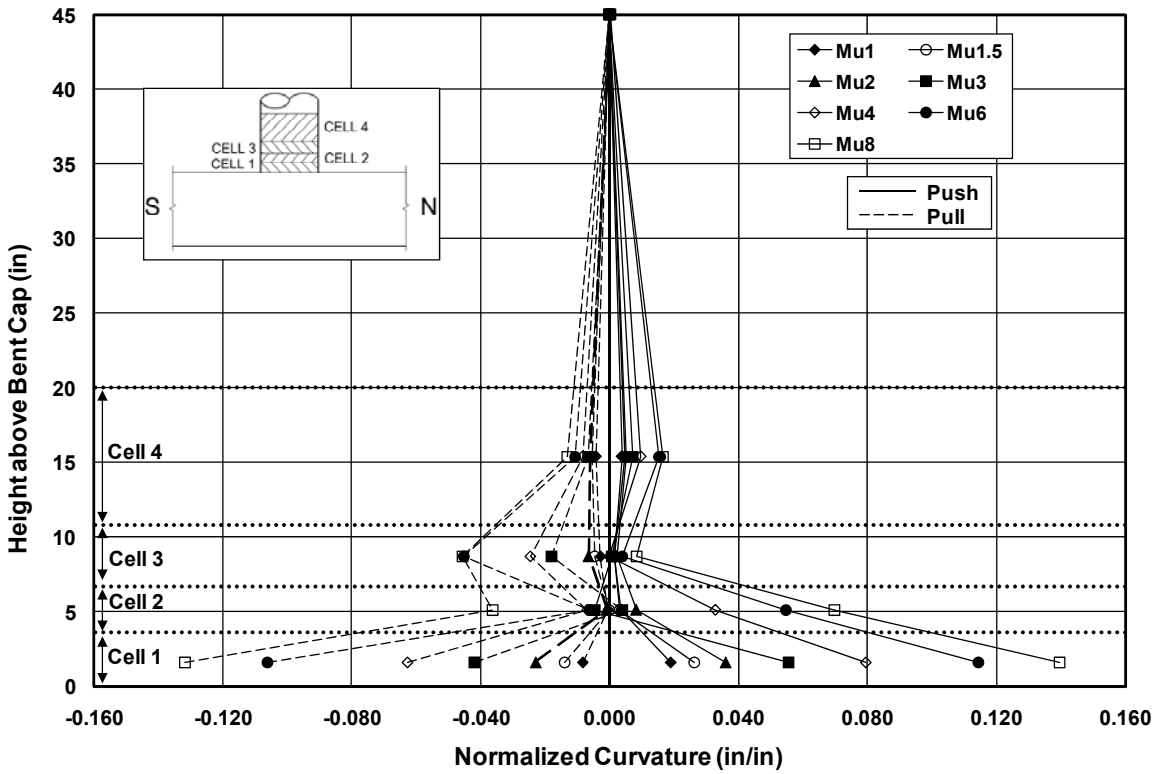

Figure 3-21. Curvature Profile (Displacement Control)—CIP

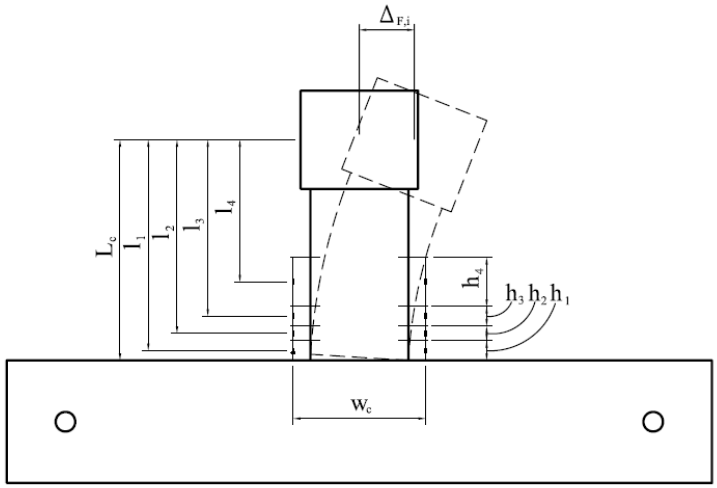

$$\Delta_{F,i} = l_i \frac{(\delta h_{i,n} - \delta h_{i,s})}{w_c}$$

$$\Delta_{F,1} = (l_1 + l'_g) \frac{(\delta h_{i,n} - \delta h_{i,s})}{w_c}$$

$$l'_g = h_1 + (0.022 \ f_y \ d_{bl})$$

A. Column Flexure and Fixed End Rotation (Cell 1)

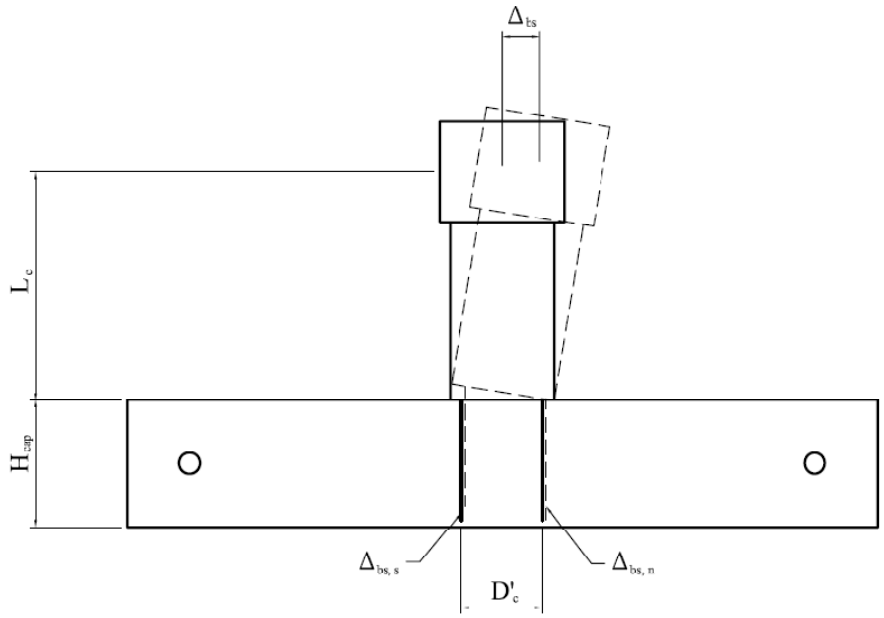

$$\Delta_{bs} = \left(\frac{\Delta_{bs,s} - \Delta_{bs,n}}{D'_c}\right)(L_c + H_{cap})$$

B. Bar Slip

Figure 3-22. Schematic Representation of Column Displacement Components

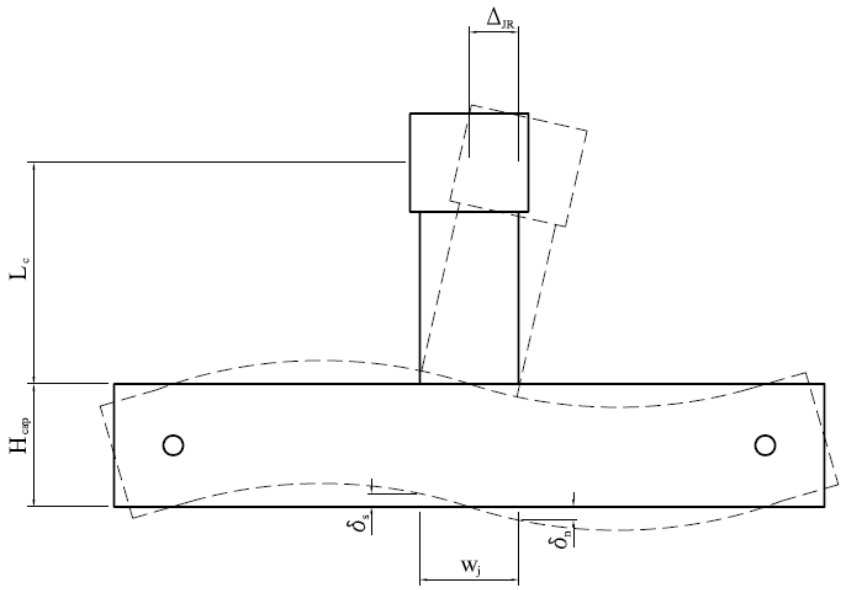

$$\Delta_{JR} = \frac{(\delta_n - \delta_s)}{w_j} (L_c + H_{cap})$$

C. Bent Cap Rotation

Figure 3-22. Schematic Representation of Column Displacement Components (Cont.)

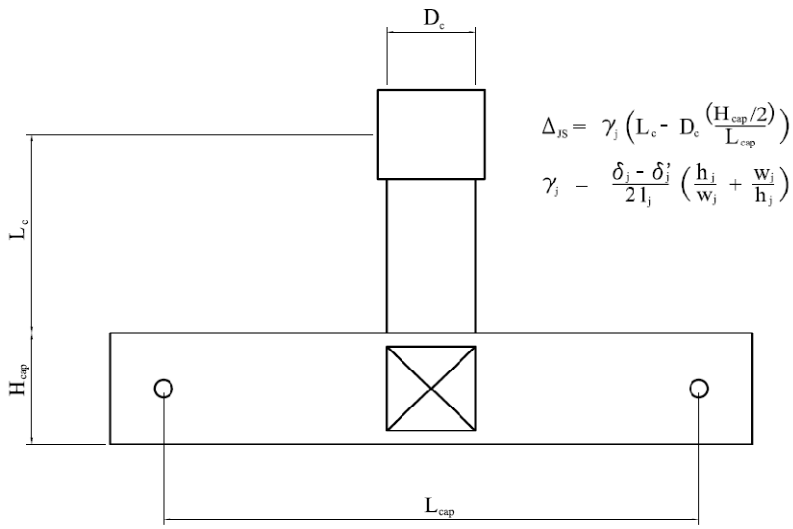

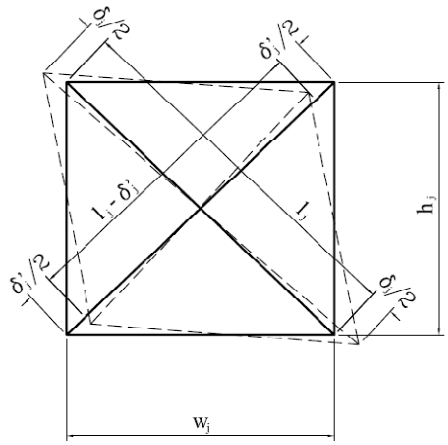

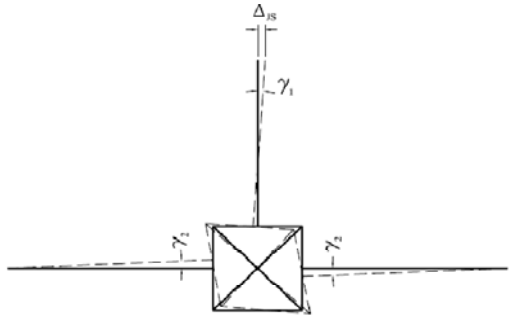

$$\gamma_j = \gamma_1 + \gamma_2$$

D. Joint Shear

Figure 3-22. Schematic Representation of Column Displacement Components (Cont.)

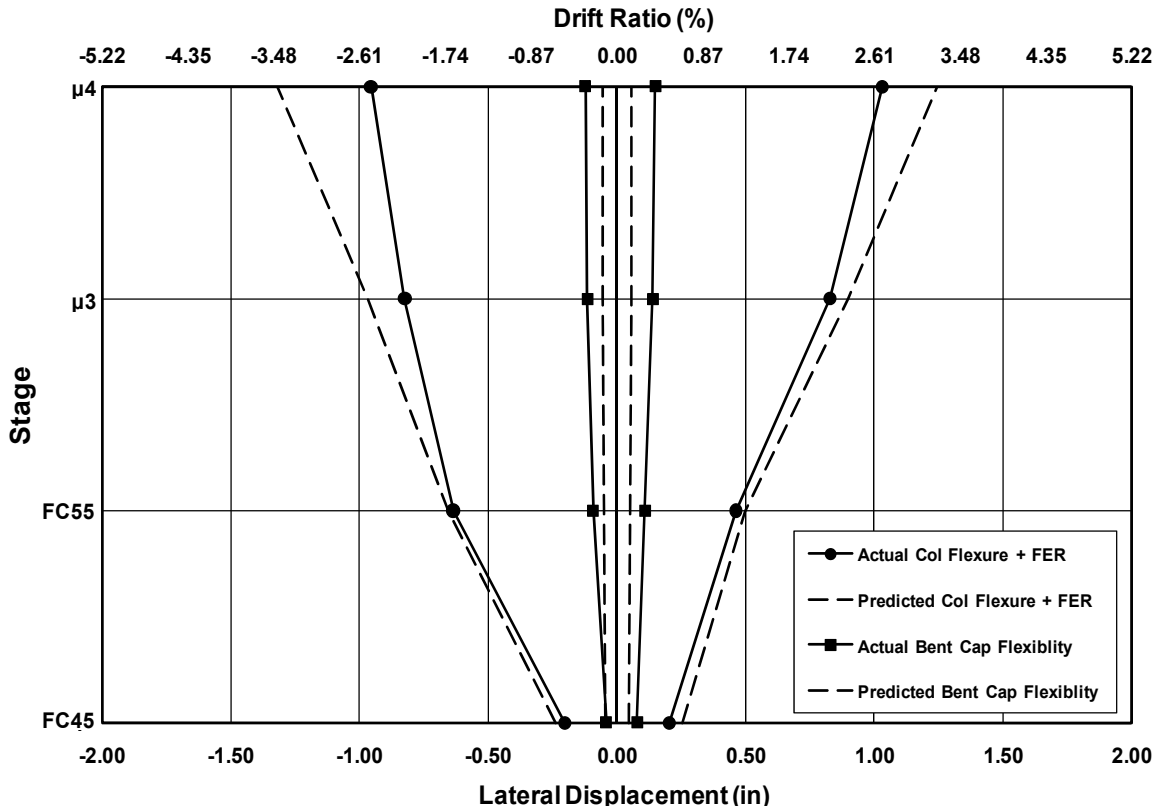

Figure 3-23. Displacement Components—Predicted vs. Actual

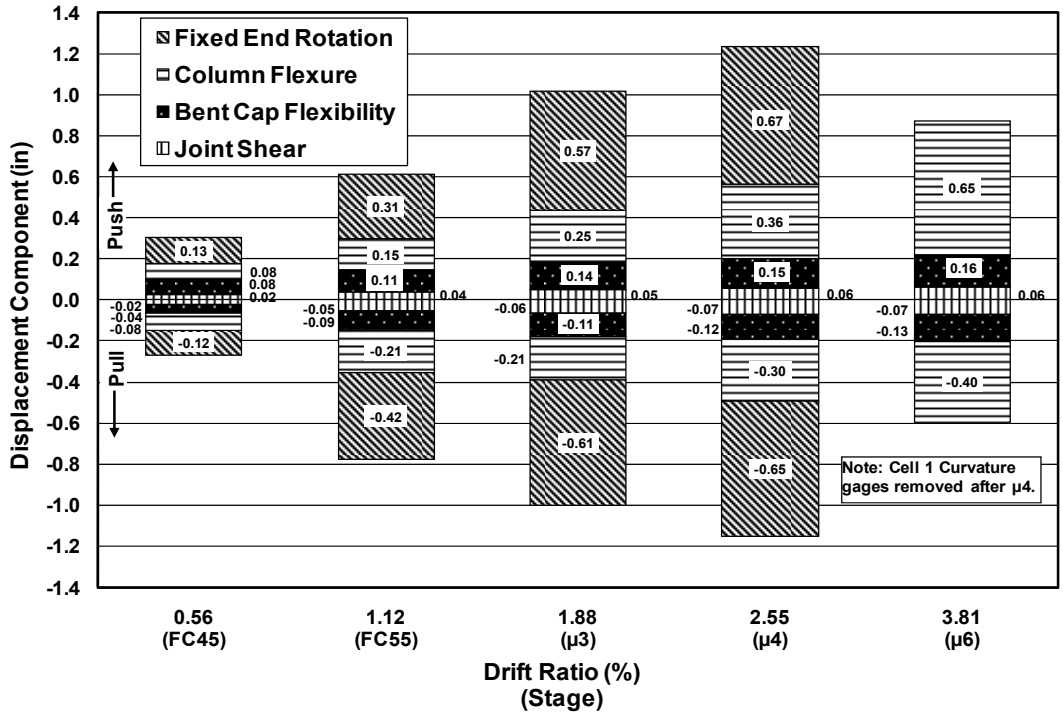

Figure 3-24. Displacement Decomposition Component Values

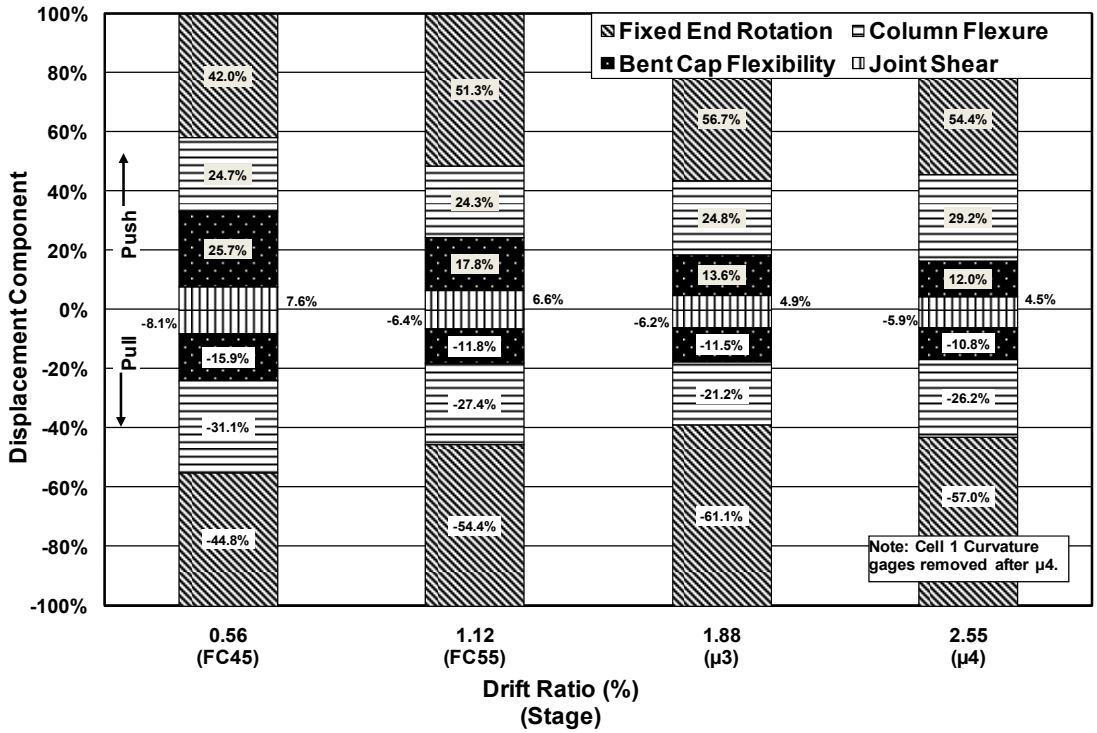

Figure 3-25. Displacement Decomposition Component Percentages

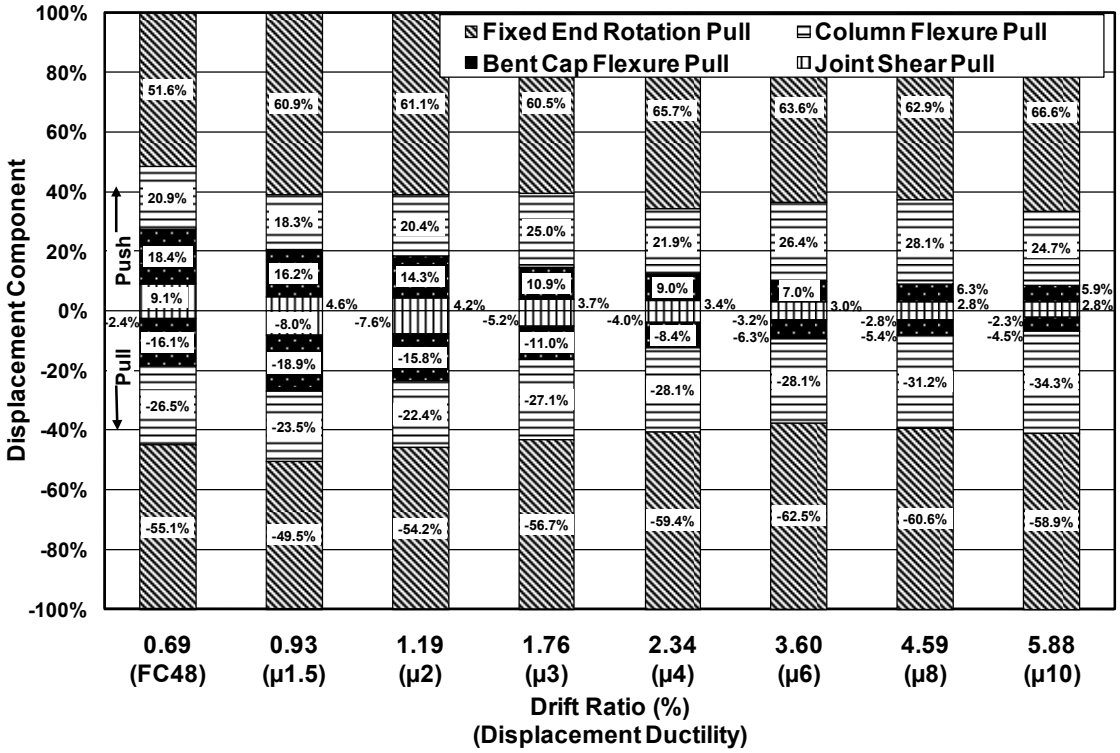

Figure 3-26. Displacement Decomposition Component Percentages—CIP

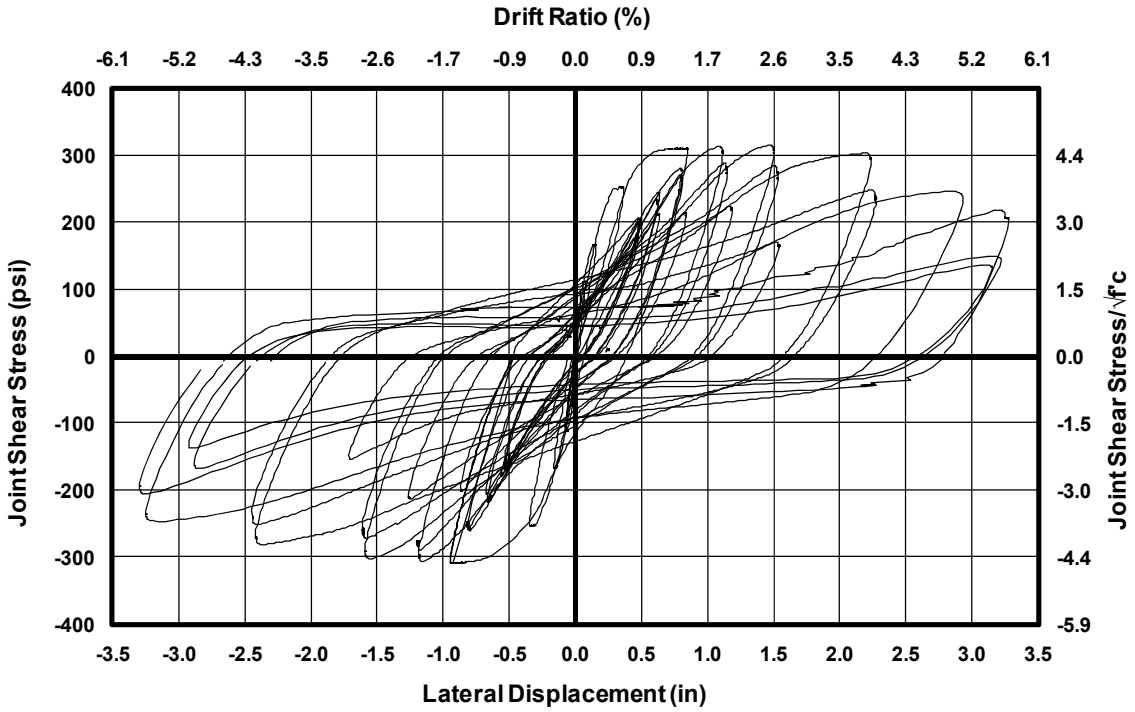

Figure 3-27. Average Joint Shear Stress vs. Lateral Displacement

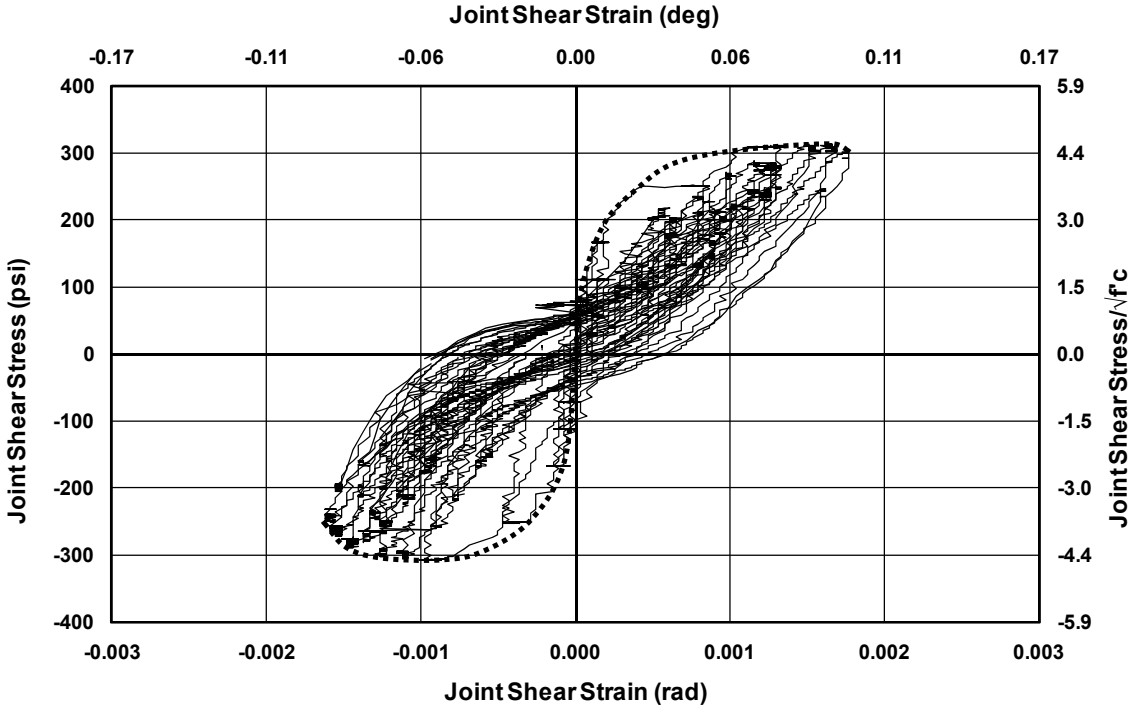

Figure 3-28. Joint Shear Stress vs. Joint Shear Strain

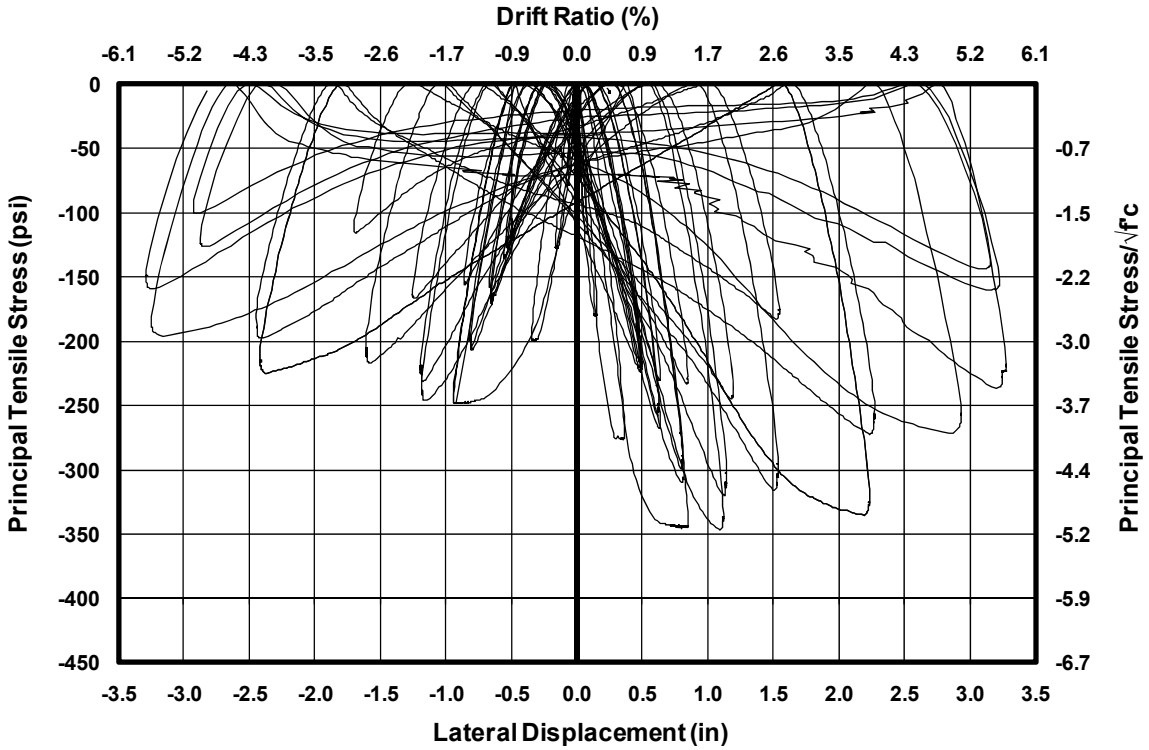

Figure 3-29. Principal Tensile Stress vs. Lateral Displacement

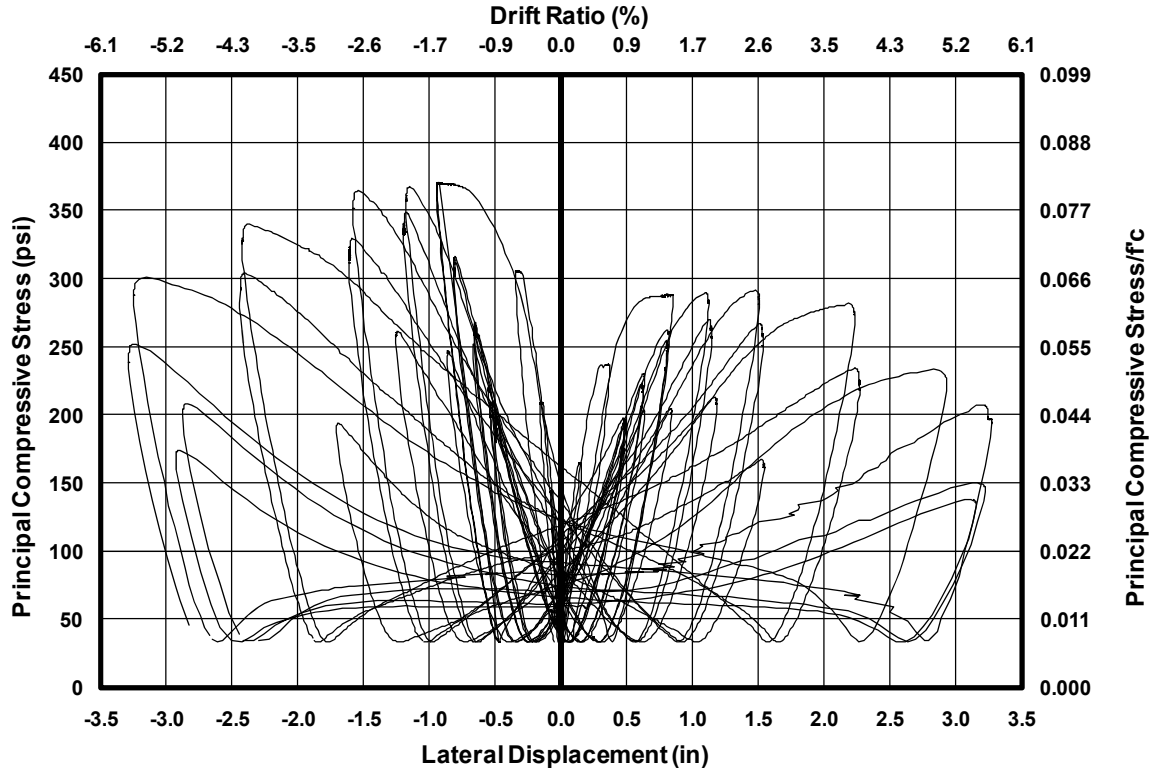

Figure 3-30. Principal Compressive Stress vs. Lateral Displacement

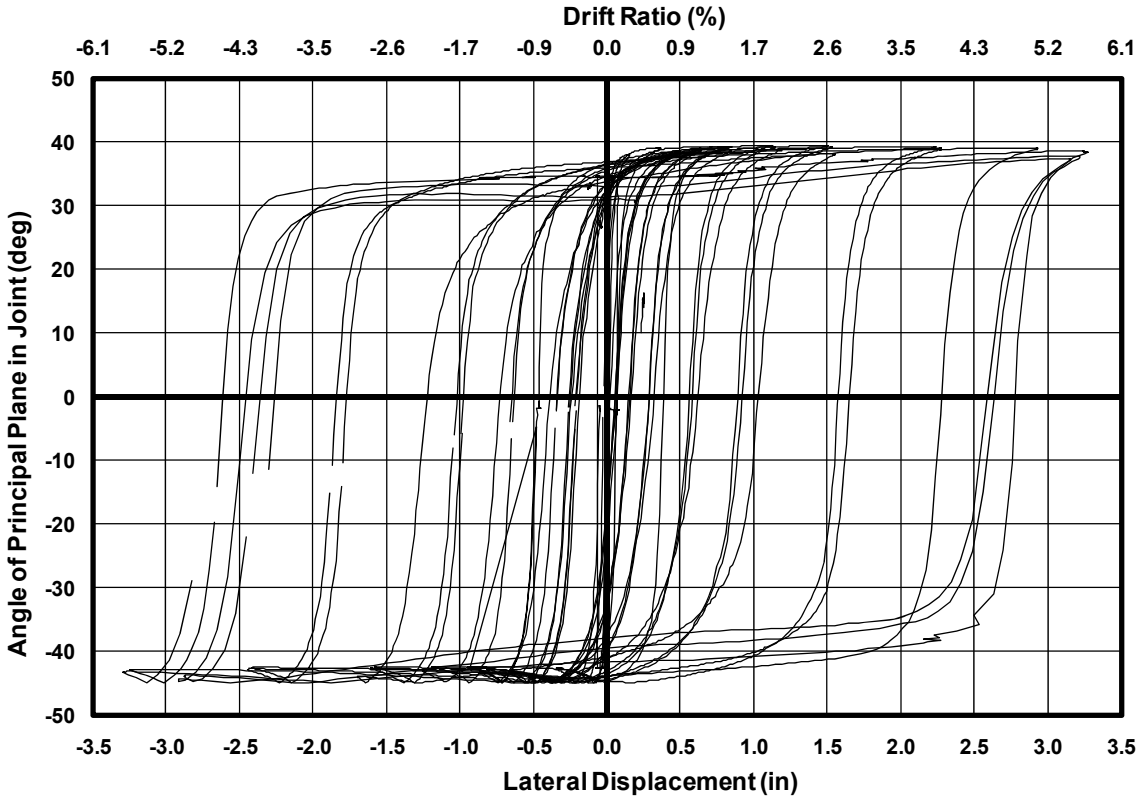

Figure 3-31. Angle of Principal Plane in Joint vs. Lateral Displacement

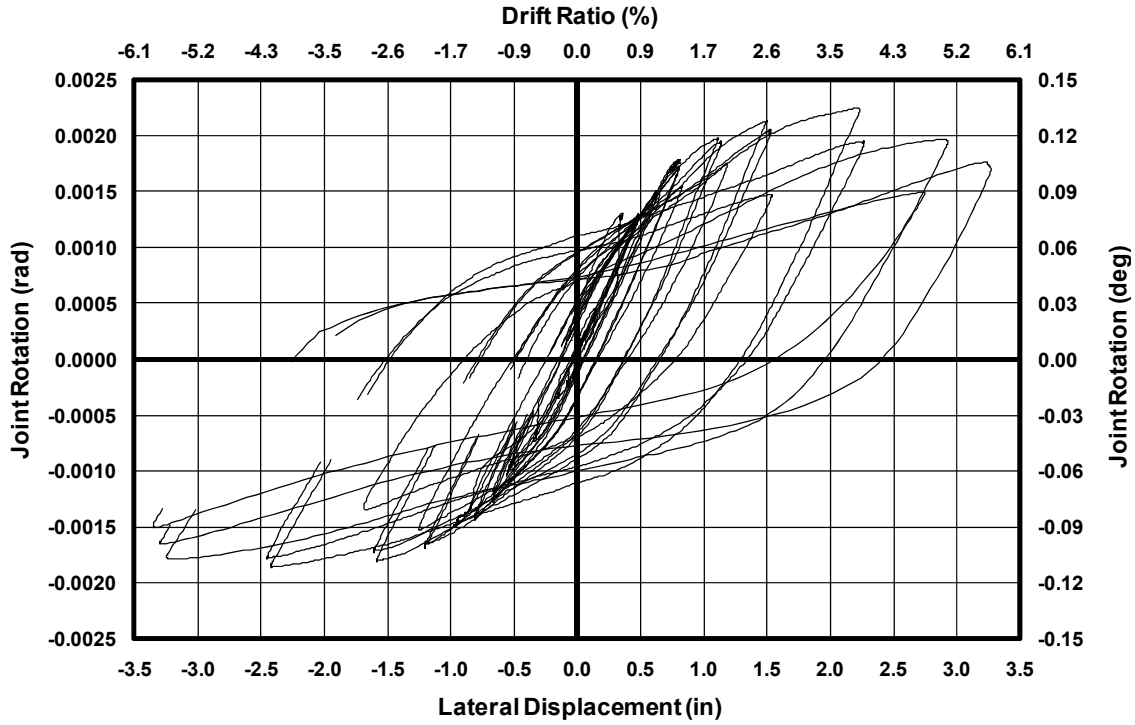

Figure 3-32. Joint Rotation vs. Lateral Displacement

A. Crushed Concrete above Bedding Layer B. Splitting Cracks between Ducts

Figure 3-33. Bedding Layer and Splitting Cracks (Post Test)

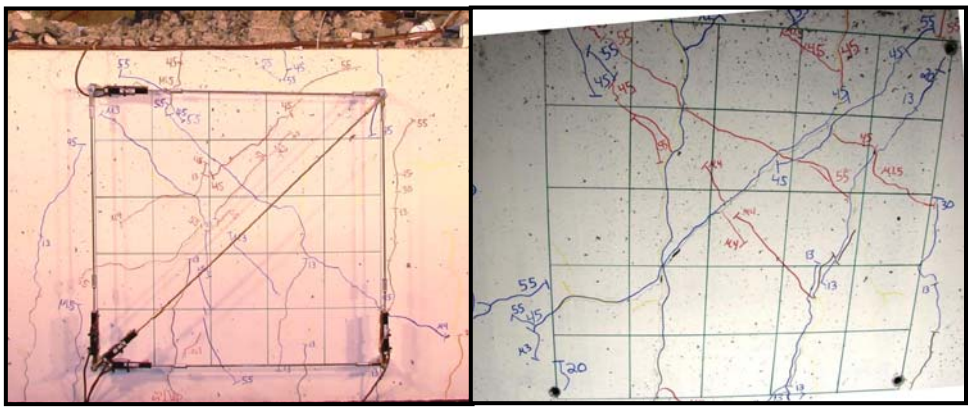

A. East Side—GD B. West Side—GD

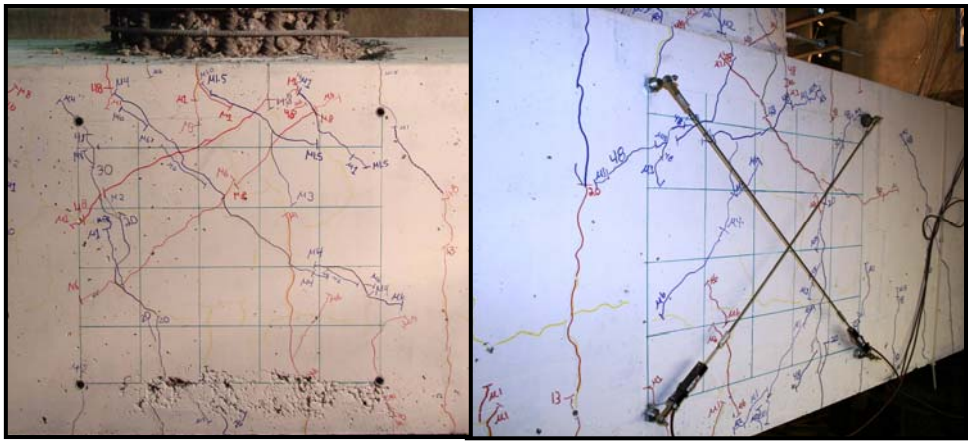

C. East Side—CIP D. West Side—CIP

Figure 3-34. Joint Region Cracking Post Test—GD vs. CIP

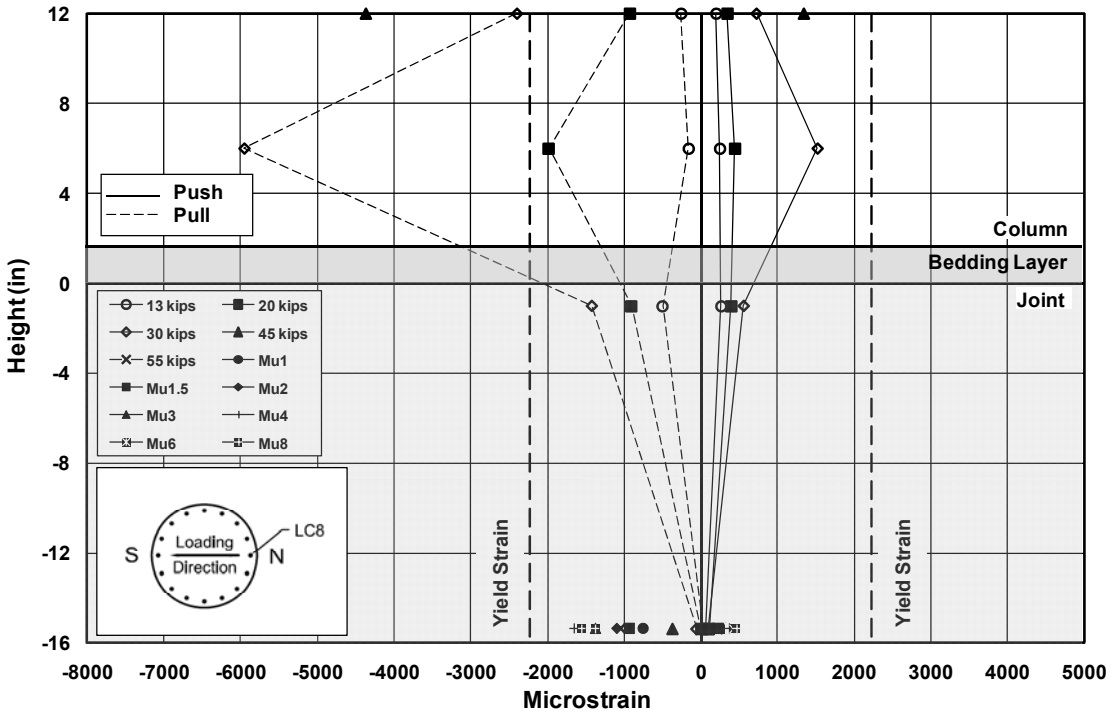

Figure 3-35. Strain Profile—Column Longitudinal Rebar (North)—GD

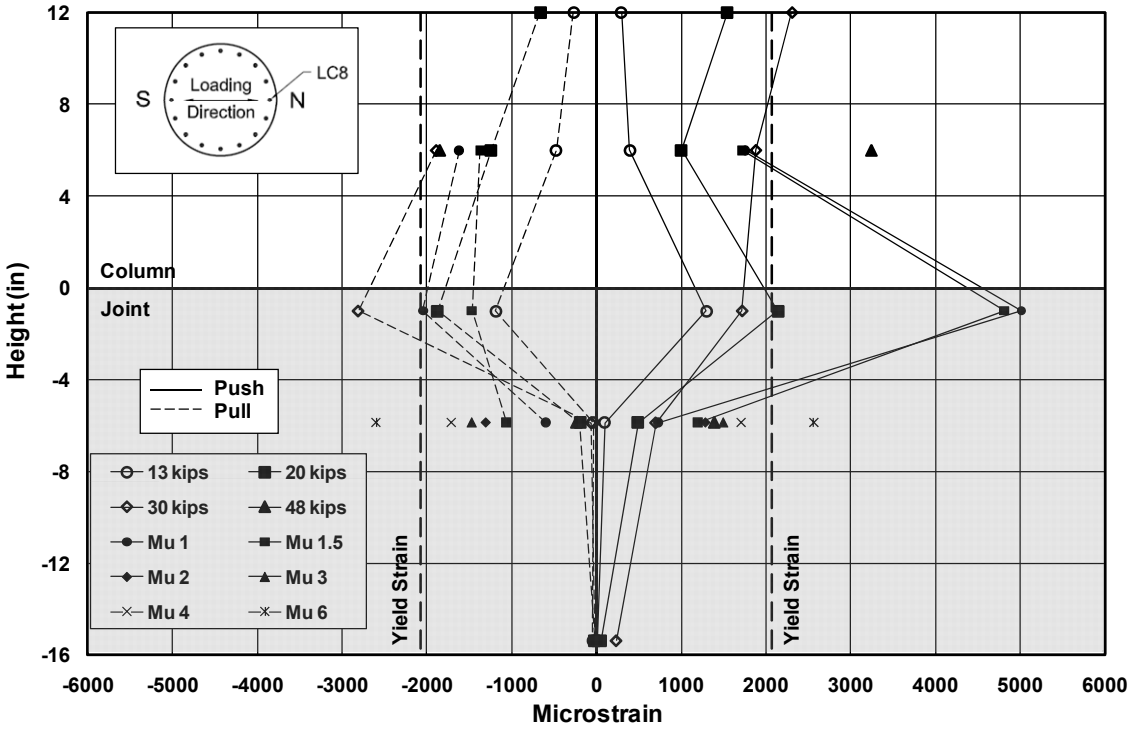

Figure 3-36. Strain Profile—Column Longitudinal Rebar (North)—CIP

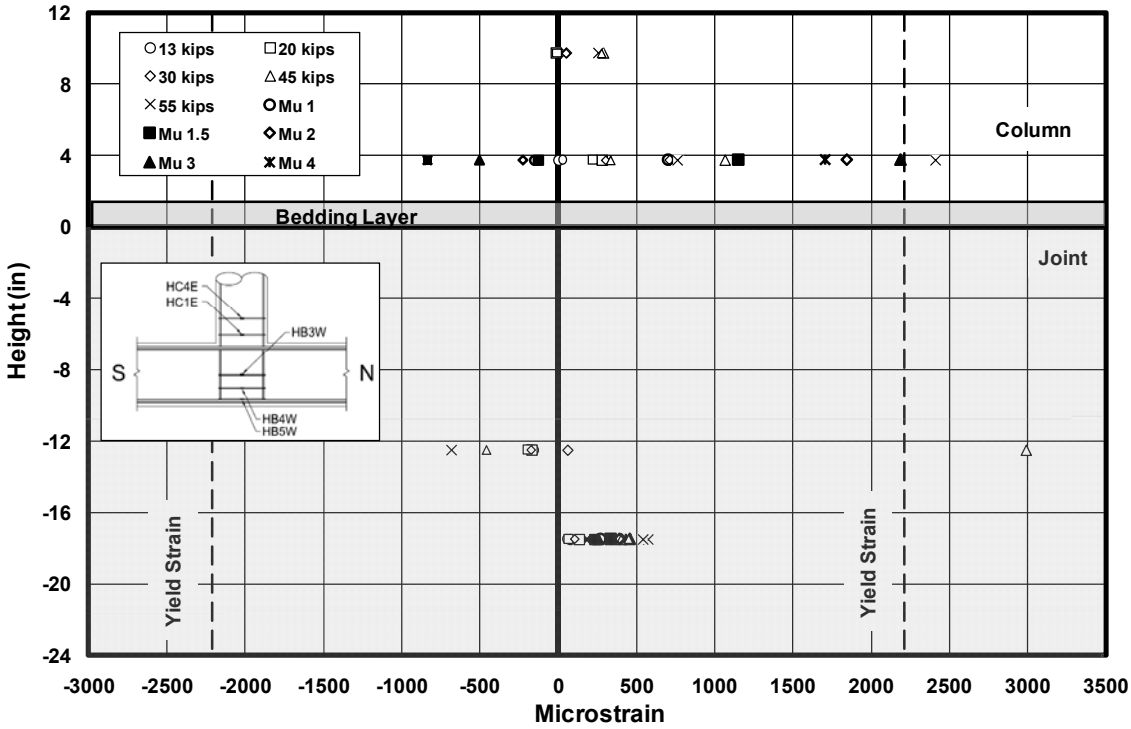

Figure 3-37. Strain Profile—Hoops in Column and Joint (East)—GD

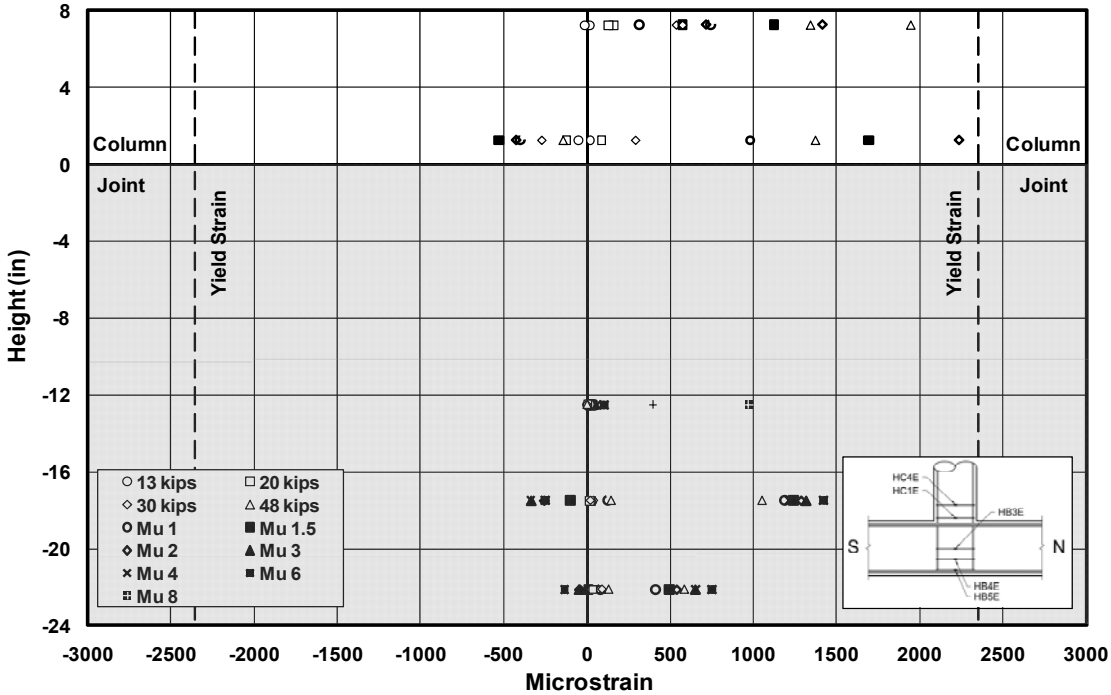

Figure 3-38. Strain Profile—Hoops in Column and Joint (East)—CIP

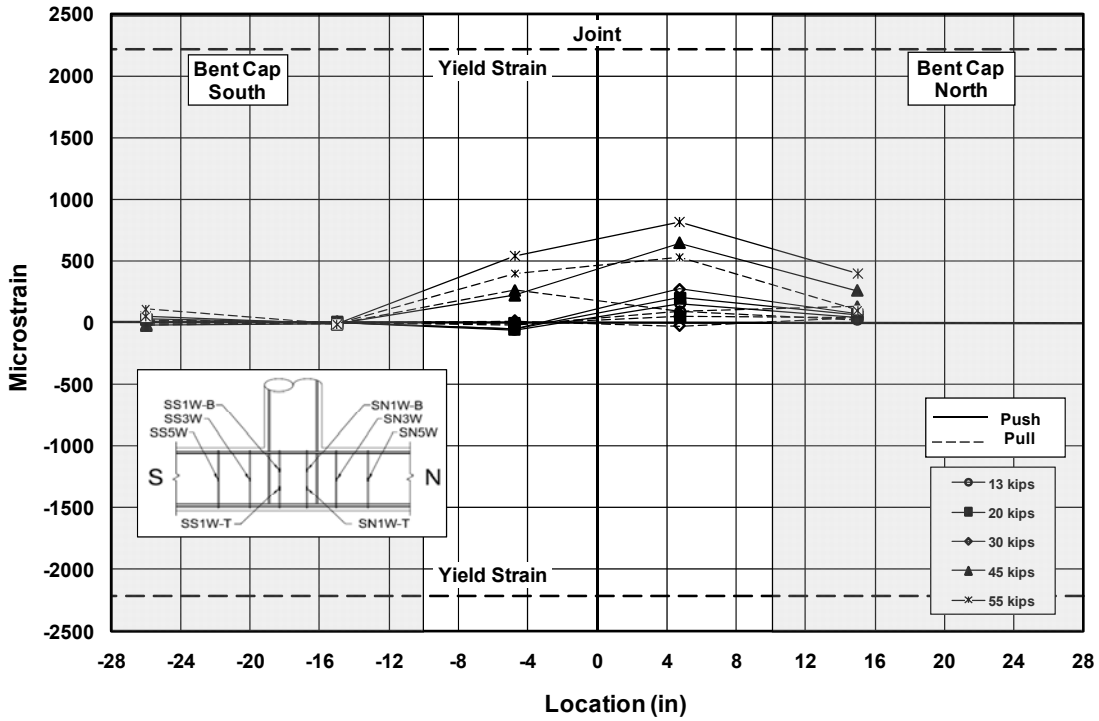

Figure 3-39. Strain Profile—Stirrups in Bent Cap (Midheight) and Joint (Top), Force Control—GD

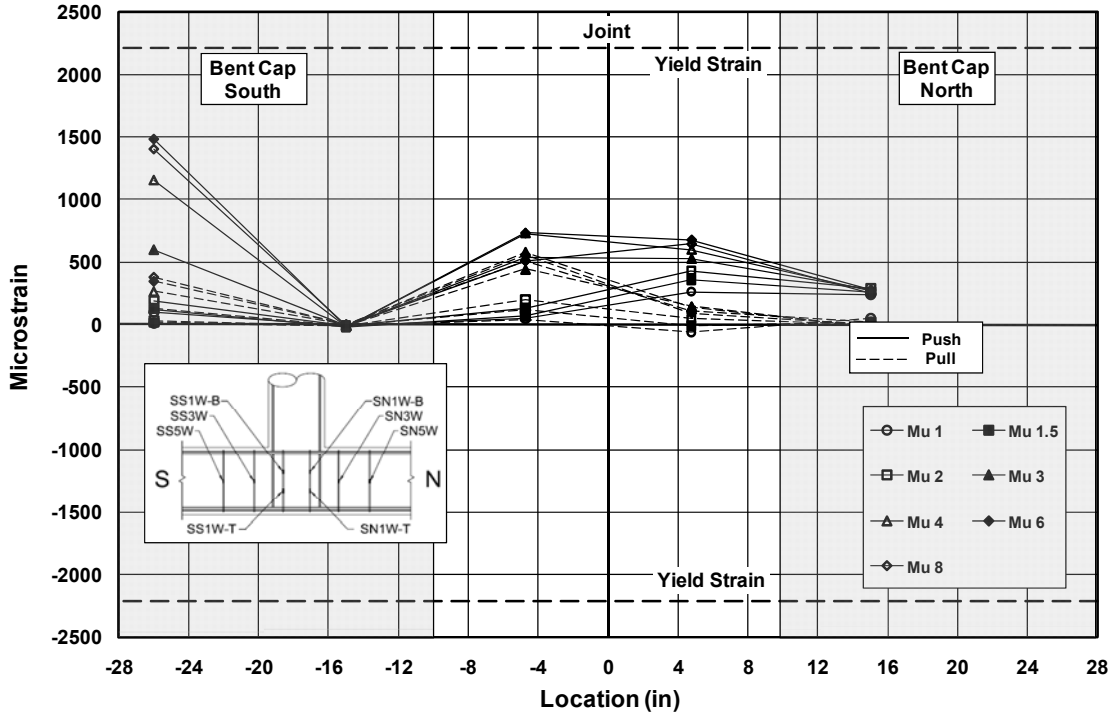

Figure 3-40. Strain Profile—Stirrups in Bent Cap (Midheight) and Joint (Top), Displacement Control—GD

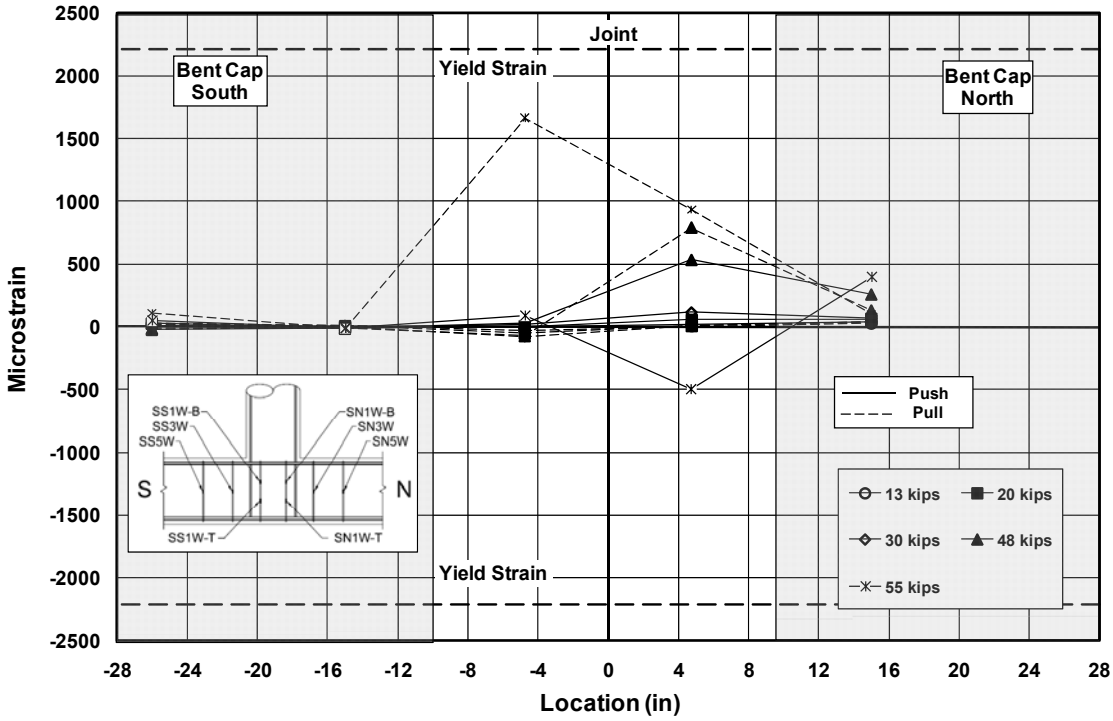

Figure 3-41. Strain Profile—Stirrups in Bent Cap (Midheight) and Joint (Bottom), Force Control—GD

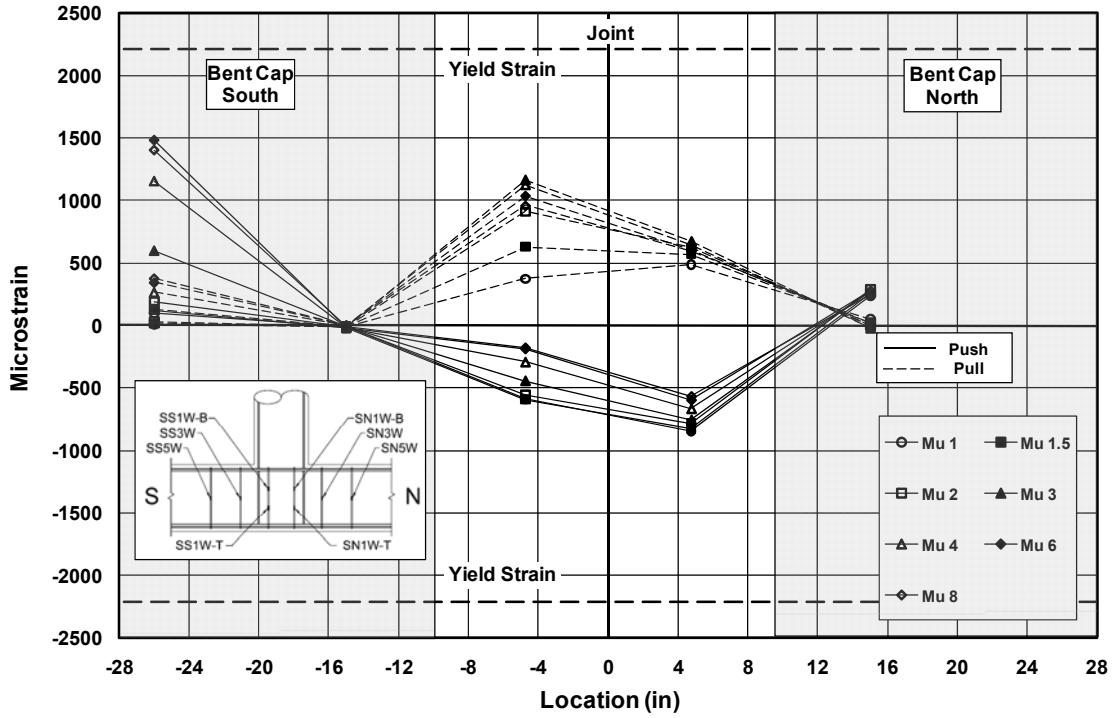

Figure 3-42. Strain Profile—Stirrups in Bent Cap (Midheight) and Joint (Bottom), Displacement Control—GD

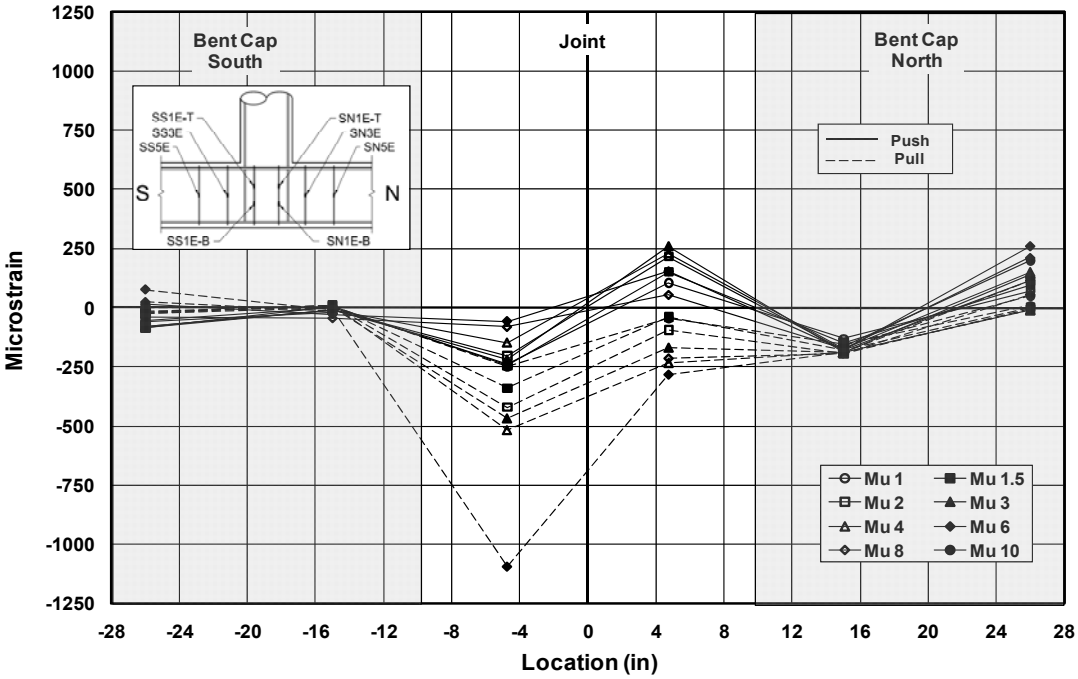

Figure 3-43. Strain Profile—Stirrups in Bent Cap (Midheight) and Joint (Top), Displacement Control—CIP

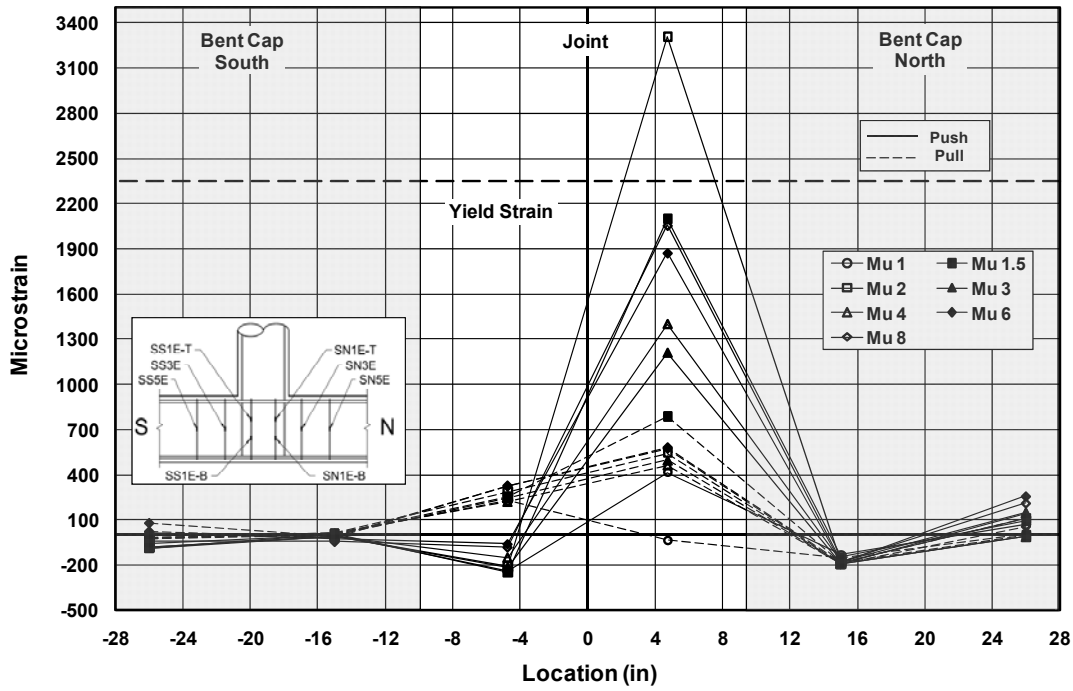

Figure 3-44. Strain Profile—Stirrups in Bent Cap (Midheight) and Joint (Bottom), Displacement Control—CIP

4.0 Summary and Conclusions

4.1 Summary

This report, Emulative Precast Bent Cap Connections for Seismic Regions: Component Tests—Grouted Duct Specimen (Unit 2), is the second in the series of four reports summarizing the California State University, Sacramento (CSUS) component tests supporting National Cooperative Highway Research Program (NCHRP) Project 12-74, "Development of Precast Bent Cap Systems for Seismic Regions". CSUS is investigating two emulative connections—cap pocket and grouted duct—for nonintegral precast bent caps.

For a major seismic event, the Cast-in-Place (CIP) prototype bridge was designed and detailed to exhibit ductile plastic hinging in the column adjacent to the capacity-protected bent cap and joint. CSUS designed the NCHRP component specimens using a 42% scale of the central portion of the prototype bridge. The scaled Grouted Duct (GD) specimen—loaded in the transverse direction under quasi-static Force Control and Displacement Control sequences—was investigated for emulative performance by evaluating its response and comparing it to the CIP (Unit 1) test specimen.

Specimen response was analyzed including experimental observations, hysteretic response, column curvature response, displacement decomposition, joint response, and strain records. Specimen response was dominated by plastic hinging of the column adjacent to the bent cap, as intended by the CIP prototype design basis and the emulative assumption for the GD specimen. In contrast to significant column flexural (and shear) cracks associated with increasing lateral load, relatively minor joint and bent cap cracks developed. Post-test inspection revealed that the column core remained primarily intact, although concrete directly above the grout-concrete interface crushed. The bedding layer remained intact. At ultimate, column bars buckled and two bars eventually fractured at the north face of the column. The specimen exhibited excellent ductility to a large drift of 4.9% (push) and 5.5% (pull), which corresponded to a nominal displacement ductility of 8.0.

The load-displacement response indicated stable hysteretic behavior with loops of increasing area without appreciable strength degradation, as well as stiffness, strength, ductility and other features such as crack distribution anticipated for an emulative beam-column connection test. A comparison of the load-displacement envelope to the predicted envelope showed a good correlation. In addition, very close comparisons were found between the GD and CIP specimens for: 1) load-displacement hysteretic response envelopes; 2) equivalent viscous damping ratio; and 3) moment-curvature envelopes. Although the CIP specimen achieved a higher displacement ductility than the GD specimen (5.9% vs. 5.2% average), the GD specimen attained a slightly higher force and thus imposed a slightly larger force demand on the joint.

The displacement decomposition confirmed the dominance of plastic hinging and showed that displacement components were reasonably determined and that predictions were reasonably made. For example, at 2.6% drift (μ4), the flexural components (fixed end rotation and column flexure) accounted for 84% of the column displacement (vs. prediction of 85%). The contribution of joint shear to overall displacement was minor, not exceeding 8%, and was confirmed by visual observations of minor joint cracking. Column bars were well anchored within the ducts, and although splitting cracks developed between ducts (at the top and bottom of the bent cap), there was no evidence of grout splitting within ducts, initiation of pullout failure, significant bar slip or duct slip. Bar slip contributed less than 9% on average to the displacement component attributable to fixed end rotation. Displacement component magnitudes and percentages for the GD and CIP specimens compared very favorably.

The precast joint region for the GD specimen performed with limited distress during the test and compared closely to the CIP joint. Analysis of the joint indicated that the principal tensile stress was limited to $5.1\sqrt{f_c'}$. This is less than half of the 2006 LRFD RSGS limit of $12\sqrt{f_c'}12\sqrt{f_c^{'}}$, but about 50% larger than $3.5\sqrt{f_c'}3.5\sqrt{f_c^{'}}$, the level at which more extensive (additional) joint reinforcement is required for development of a force transfer mechanism. Principal compressive stresses did not exceed $0.08f_c'$, less than a third of the 2006 LRFD RSGS limit of $0.25f_c'$. These values correspond well

with the intentions of the design and the observed joint performance. The maximum crack width was 0.040 in. The joint deformation was very small, with maximum change in panel area limited to less than 0.2%.

GD and CIP joint stresses compared very closely, and the maximum principal angle was 45.0 deg for both specimens. The joint shear stiffness based on the joint shear stress-strain response compared closely. The maximum joint rotation and change in panel area for GD was slightly larger than CIP. Diagonal joint crack patterns were reasonably consistent for the specimens, as were flexural crack patterns. Maximum joint crack widths for the GD specimen were somewhat larger (0.040 in vs. 0.025 in), though not excessively, and were consistent with the level of joint stresses and the principal angles reported. Minor surface spalling developed on the east face of the bent cap for GD, whereas no spalling developed for CIP.

Only the precast connection used a bedding layer between the column and cap. The bedding layer appeared to perform integrally with the column through 5.5% drift and did not produce unusual behavior in the joint or specimen.

Strain records provided confirmation of plastic hinging and strain penetration into the joint. A similar strain pattern was evident for the GD and CIP specimens. The increase in strain in the ducts reasonably followed bar strain near the bedding layer and at 6 in into the joint. Hoop confinement effects were evident for the plastic hinging region as well the joint for both specimens, although the strains peaked at different locations within the joint.

Bent cap longitudinal bars reached only 53% of yield, even though the specimen design did not include the additional bent cap longitudinal reinforcement ($0.245A_{st}$) required by 2009 LRFD SGS. CIP longitudinal reinforcement also did not yield, reaching 46% of yield. Stirrup strain outside the joint reached 68% of yield and, although the construction stirrups within the joint did not yield, the south construction stirrup reached 75% of yield, indicating its contribution to the stable joint performance and the importance of vertical stirrups inside the joint. The CIP specimen exhibited a similar trend of large stirrup strains (exceeding yield) within the joint. The test specimen,

designed per 2006 LRFD RSGS, did not require stirrups inside the joint; however, two joint stirrups with a total area of $0.089A_{st}$ were included for construction. These stirrups provided an area 66% of that required by the 2009 LRFD SGS ($0.135A_{st}$).

4.2 Conclusions

Based on the observed response and data analysis for the GD (Unit 2) specimen and a detailed comparison with the CIP (Unit 1) specimen, the following conclusions can be drawn:

1. Despite the less conservative design basis of the specimen using the 2006 Recommended LRFD Guidelines for the Seismic Design of Highway Bridges compared to current 2009 AASHTO Guide Specifications for LRFD Seismic Bridge Design—including a smaller area of vertical stirrups within the joint and smaller area of bent cap longitudinal reinforcement—the GD specimen satisfied the performance goal of the design, achieving an extensive drift without appreciable strength degradation and exhibiting extensive plastic hinging of the column, limited joint distress, and essentially elastic behavior of the bent cap.
2. Emulative performance is concluded for the GD specimen based on the closely matching overall behavior between the GD and CIP specimens, including lateral load-displacement response, plastic hinging, joint shear stiffness, level of joint distress, pattern of joint cracking, strain patterns of bent cap and joint reinforcement, integral behavior between the bedding layer, column, ducts, and bent cap, and minor effects due to bar slip.
3. GD response indicates that design specifications for a full ductility grouted duct connection should address: 1) vertical joint stirrups inside and outside the joint; 2) horizontal cross ties inside the joint; 3) transverse joint shear reinforcement; and 4) additional longitudinal bent cap reinforcement.
4. Construction specifications should address fabrication and assembly processes as well as grout used for the connection.

5. Additional analysis is required to develop a new model that fully characterizes joint behavior, including joint forces, crack patterns, and strain distributions.

References

1. Matsumoto, Eric. E., *Emulative Precast Bent Cap Connections for Seismic Regions: Component Tests—Cast-in-place Specimen (Unit 1)*, ECS Report No. ECS-CSUS-2009-01, California State University, Sacramento, CA (November 2009) 89 pp.
2. Tobolski, M.J., Restrepo, J.I., Matsumoto, E.E., and Ralls, M.L., *Development of Precast Bent Cap Concepts*, SSRP Report No. 06/10. University of California, San Diego, La Jolla, CA (September 2006) 176 pp.
3. Restrepo, J.I. and Matsumoto, E.E., *National Cooperative Highway Research Program (NCHRP), Project 12-74, Development of Precast Bent Cap Systems for Seismic Regions*", Proposal to Research Board (March 31, 2005).
4. BASF Building Systems, Masterflow 928 Product Data Sheet, http://www.buildingsystems.basf.com/productdetailpage.asp, (As of February 1, 2009).
5. Matsumoto, E.E., Waggoner, M.C., Sumen, G., Kreger, M.E., Wood, S.L., and Breen, J.E., *Development of a Precast Bent Cap System*, Research Report 1748-2, Center for Transportation Research, The University of Texas at Austin (January 2001) 372 pp.
6. Mislinski, Steve, "Anchorage of Grouted Connectors For a Precast Bent Cap System in Seismic Regions (Part 2)", M.S. Thesis, California State University Sacramento, Sacramento, CA (2003).
7. Matsumoto, E.E., Wright J., Johnsen, S., Mislinski, S., "Proposed Bridge Design Calculations and Drawings of the Prototype Bridge and Test Specimen", Submitted by Restrepo, J.I. and Matsumoto, E.E. to National Cooperative Highway Research Program Project 12-74 Panel (August 11, 2006) 232 pp.
8. Sritharan, S., Priestley, M.J.N., and Seible, F., *Seismic Response of Column/Cap Beam Tee Connections with Cap Beam Prestressing*, SSRP Report No. 96/09. University of California, San Diego, La Jolla, CA (December 1996) 296 pp.
9. XTRACT, User's Manual, TRC/Imbsen Software Systems, Rancho Cordova, CA (2006).
10. Imbsen, R. A., *Recommended LRFD Guidelines for the Seismic Design of Highway Bridges, 2006,* TRC/Imbsen & Associates, Inc, Rancho Cordova, CA (May 2006).
11. Draft Seismic Guide Specification – March 2007, AASHTO Subcommittee on Bridges and Structures, http://bridges.transportation.org/sites/bridges/docs/2007-03-09GuideSpec.pdf (As of March 22, 2007).
12. American Association of State Highway and Transportation Officials. AASHTO Guide Specifications for LRFD Seismic Design Specifications (First Edition), Washington, DC (2009).
13. Matsumoto, E.E., Waggoner, M.C., Kreger, M.E., Vogel, J., Wolf, L., "Development of a Precast Concrete Bent-Cap System," *PCI Journal*, Vol. 53, No. 3 (May-June 2008) pp.74-99.

14. Sritharan, S. “Improved Seismic Design Procedure for Concrete Bridge Joints,” *Journal of Structural Engineering*, American Society of Civil Engineers, Reston, VA, Vol. 131, No. 9 (September 2005) pp. 1334-1344.

Notation

A_c	Cross sectional area of column (in^2)
A_L	Area of hysteretic loop for a complete cycle (push and pull) (kip-in)
A_R	Area of rectangle bounded by maximum loads and displacements of a complete hysteretic loop (kip-in)
B_{cap}	Thickness of the bent cap (in)
BS	Bar Slip (in)
CD	Column displacement (in)
CT	Component total for column displacement (in)
d_{bl}	Nominal diameter of longitudinal column reinforcing steel bars (in)
D_c	Diameter or depth of column in direction of loading (ft or in)
D'_c	Diameter or depth of column in direction of bending (ft or in)
E_c	Modulus of elasticity of concrete (ksi)
FC	Force control
f'_c	Nominal compressive concrete strength (ksi)
f'_{cg}	Nominal compressive grout strength (ksi)
FER	Fixed end rotation of column (in)
f_h	Average normal stress in the horizontal direction within a moment resisting joint (ksi)
f_v	Average normal stress in the vertical direction within a moment resisting joint (ksi)
f_y	Specified minimal yield stress (ksi)
G_c	Shear modulus of concrete (ksi)
h	Distance from c.g. of tensile force in column to c.g. of compressive force on the section (in)
H_{cap}	Height of bent cap (in)
h_i	Height of cell i (in)
h_j	Joint panel height (in)
h_1	Height of cell 1 (in)

$I_{e\,col}$ Effective moment of inertia of column (in^4)

$I_{t\,col}$ Transformed moment of inertia of column (in^4)

L_c Distance from critical section of column (bent cap soffit) to point of contraflexure (in)

L_{cap} Length of bent cap (in)

l_{ac} Length of column reinforcement embedded into bent cap (in)

l_i Distance from point of contraflexure of column to the midheight of cell I (in)

l_j Diagonal joint panel length (in)

l_1 Distance from point of contra flexure of column to the midheight of cell 1 (in)

l'_g Strain penetration length of cell 1 (in)

l_{sp} Equivalent strain penetration length taken as $0.022 f_y d_{bl}$ (in)

M_{YE} Theoretical column moment at effective yield based on moment-curvature analysis (kip-in or kip-ft)

M_{Yexp} Experimental first yield moment of column (kip-in or kip-ft)

p_c Principal compressive stress (ksi)

P_H Horizontal actuator force on side of column stub (kips)

p_t Principal tensile stress (ksi)

P_V Vertical actuator force on top of column stub (kips)

T_c Column tensile force (kip)

v_{jv} Nominal vertical shear stress in a moment resisting joint (ksi)

w_c Width of cell (in)

w_j Joint panel width (in)

γ_j Nominal vertical shear strain in a moment resisting joint (ksi)

Δ_{bs} Column displacement due to bar slip (in)

$\Delta_{bs,s}$ Bar slip displacement, south (in)

$\Delta_{bs,n}$ Bar slip displacement, north (in)

$\Delta_{F,i}$ Column Displacement due to flexure at cell i (in)

$\Delta_{F,1}$ Column displacement due to fixed end rotation at cell 1 (in)

$\delta h_{i,n}$ Column displacement of cell i, north (in)

$\delta h_{i,s}$	Column displacement of cell i, south (in)
δ_j	Increase in diagonal joint panel length (in)
δ'_j	Increase in diagonal joint panel length in direction perpendicular to l_j (in)
Δ_{jr}	Column displacement due to joint rotation (in)
$\delta_{jr,n}$	Vertical displacement of bent cap at north end of joint (in)
$\delta_{jr,s}$	Vertical displacement of bent cap at south end of joint (in)
Δ_{js}	Column displacement due to joint shear (in)
δ_n	Joint rotation displacement, north (in)
δ_s	Joint rotation displacement, south (in)
Δ_s	Column displacement due to column shear (in)
Δ_Y	System first yield displacement (in)
Δ_{ye}	Member effective yield displacement (in)
Δ_{YE}	System effective yield displacement (in)
ξ	Equivalent viscous Damping ratio
μ_D	Displacement ductility demand
φ	Column curvature (1/in)

List of Equations

Average joint shear strain	$\gamma_j = \frac{\delta_j - \delta'_j}{2l_j}\left(\frac{h_j}{w_j} + \frac{w_j}{h_j}\right)$
Average joint shear stress	$v_{jv} = \frac{T_c}{l_{ac}B_{cap}}$
Average principal angle in joint	$\theta_p = \frac{A_c}{2} tan^{-1}\left(v_{jv} / \frac{f_h - f_v}{2}\right)$
Average principal compressive stress in joint	$p_c = \frac{(f_h + f_v)}{2} + \sqrt{\left(\frac{f_h - f_v}{2}\right)^2 + {v_{jv}}^2}$
Average principal tensile stress in joint	$p_t = \frac{(f_h + f_v)}{2} - \sqrt{\left(\frac{f_h - f_v}{2}\right)^2 + {v_{jv}}^2}$
Column displacement due to bar slip	$\Delta_{bs} = \left(\frac{\Delta_{bs,s} - \Delta_{bs,n}}{D'_c}\right)\left(L_c + H_{cap}\right)$
Column displacement due to column shear (analytical)	$\Delta_s = \frac{P_H L_c}{0.9 A_c G_c}\left(\frac{E_c I_{tcol}}{E_c I_{ecol}}\right)$
Column displacement due to flexure at cell i	$\Delta_{F,i} = l_i \frac{\left(\delta h_{i,n} - \delta h_{i,s}\right)}{w_c}$
Column displacement due to joint rotation	$\Delta_{jr} = \frac{(\delta_n - \delta_s)}{w_j}\left(L_c + H_{cap}\right)$
Column displacement due to joint shear	$\Delta_{js} = \gamma_j\left(L_c - D_c \frac{\left(H_{cap}/2\right)}{L_{cap}}\right)$
Column curvature, cell i	$\varphi = \frac{\Delta_{F,i}/W_c}{l'_g}$
Column tensile force	$T_c = \frac{M_o^{col}}{h} = \frac{P_h L_c}{h}$

Equivalent viscous damping ratio	$\xi = \left(\frac{2}{\pi}\right)\left(\frac{A_L}{A_R}\right)$
Joint rotation angle	$\theta_{jr} = \frac{\delta_{jr,n} - \delta_{jr,s}}{D_c}$
Modified height of cell 1 accounting for strain penetration	$l'_g = l_{sp} + h_1\left(1 - 1.67\, {h_1}/{L_c}\right)$
System effective yield displacement	$\Delta_{YE} = \frac{M_{YE}}{M_{Yexp}}\Delta_Y$

California State University, Sacramento
College of Engineering and Computer Science
Research Report

EMULATIVE PRECAST BENT CAP CONNECTIONS FOR SEISMIC REGIONS: COMPONENT TESTS— CAP POCKET FULL DUCTILITY SPECIMEN (UNIT 3)

Eric E. Matsumoto, Ph.D., P.E.

November 19, 2009

Final Report for: NCHRP 12-74, Development of Precast Bent Cap Systems for Seismic Regions

ECS Report Number: ECS-CSUS-2009-03

College of Engineering and Computer Science

California State University, Sacramento

Sacramento, California 95819-6023

California State University, Sacramento
College of Engineering and Computer Science
Research Report

EMULATIVE PRECAST BENT CAP CONNECTIONS FOR SEISMIC REGIONS: COMPONENT TESTS— CAP POCKET FULL DUCTILITY SPECIMEN (UNIT 3)

Eric E. Matsumoto, Ph.D., P.E.
Associate Professor, Structural Engineering

November 19, 2009

Final Report for:	NCHRP 12-74, Development of Precast Bent Cap Systems for Seismic Regions
ECS Report Number:	ECS-CSUS-2009-03

College of Engineering and Computer Science
California State University, Sacramento
Sacramento, California 95819-6023

Please cite this report as follows:

Matsumoto, Eric. E., *Emulative Precast Bent Cap Connections for Seismic Regions: Component Tests—Cap Pocket Full Ductility Specimen (Unit 3)*, ECS Report No. ECS-CSUS-2009-03, California State University, Sacramento, CA (November 2009) 113 pp.

DISCLAIMER

The research presented in this report was conducted as part of the National Cooperative Highway Research Program, Project 12-74, Development of Precast Bent Cap Systems for Seismic Regions. The opinions and conclusions expressed or implied in the report are solely those of the author. They are not necessarily those of the Transportation Research Board, the National Research Council, the Federal Highway Administration, the American Association of State Highway and Transportation Officials, or the individual states participating in the National Cooperative Highway Research Program.

ACKNOWLEDGMENT OF SPONSORSHIP

This work was sponsored by the American Association of State Highway and Transportation Officials, in cooperation with the Federal Highway Administration, and was conducted in the National Cooperative Highway Research Program, which is administered by the Transportation Research Board of the National Research Council.

OTHER ACKNOWLEDGEMENTS

The author gratefully acknowledges the significant contributions from many graduate and undergraduate students, as well as laboratory technicians at California State University, Sacramento. Of particular note are Jeremy Wright, P.E., Arvind Gopalakrishna, David Van Zanen, P.E., Andy Wilson, Jim Ster, and Brett Anthony. The author also gratefully acknowledges contributions from the NCHRP 12-74 Team, including Dr. Jose I. Restrepo and Matthew Tobolski, University of California, San Diego; Mary Lou Ralls, P.E., Ralls-Newman LLC; and Steve Mislinski, P.E, AECOM/LAN Engineering. Finally, the author gratefully acknowledges the many contributions of Clark Pacific, West Sacramento, CA, including those of Glen Underwood and Don Clark, for fabrication support.

EXECUTIVE SUMMARY

This report, Emulative Precast Bent Cap Connections for Seismic Regions: Component Tests—Cap Pocket Full Ductility Specimen (Unit 3), is the third in the series of four reports summarizing the California State University, Sacramento (CSUS) component tests supporting National Cooperative Highway Research Program (NCHRP) Project 12-74, "Development of Precast Bent Cap Systems for Seismic Regions". CSUS is investigating two emulative connections—cap pocket and grouted duct—for nonintegral precast bent caps.

The Cast-in-place (CIP) prototype bridge and emulative component specimens, including the Cap Pocket Full Ductility (CPFD) specimen, were designed in accordance with the 2006 Recommended LRFD Guidelines for the Seismic Design of Highway Bridges (2006 LRFD RSGS), which contains less conservative joint reinforcement requirements—including a smaller area of vertical stirrups within the joint and smaller area of bent cap longitudinal reinforcement—than the 2009 AASHTO Guide Specifications for LRFD Seismic Bridge Design (2009 LRFD SGS). For a major seismic event, the CIP prototype bridge was designed and detailed to exhibit ductile plastic hinging in the column adjacent to the capacity-protected bent cap and joint. The CPFD specimen was designed using a 42% scale of the central portion of the prototype bridge.

Specimen response was dominated by plastic hinging of the column adjacent to the bent cap. Post-test inspection revealed that two column bars fractured after buckling. The specimen exhibited excellent ductility to a large average drift of 4.3%, which corresponded to a nominal displacement ductility of 8. Similar to the CIP specimen, the CPFD load-displacement response indicated stable hysteretic behavior without appreciable strength degradation.

Displacement decomposition confirmed the dominance of plastic hinging. For example, at 2.2% drift ($\mu 4$), the flexural components (fixed end rotation and column flexure) accounted for 87% of the column displacement. The contribution of joint shear to overall displacement was minor, not exceeding 9%. In addition, a distinct crack pattern developed in the joint, different from the CIP specimen. Diagonal cracking

formed above and below the corrugated pipe through a drift of 3.1% (μ6, pull), at which stage diagonal cracks passed through the central portion of the joint. Particularly striking were the narrow diagonal cracks, limited to 0.009 in, in contrast to 0.025 in for the CIP specimen. However, the joint shear stiffness based on the joint shear stress-strain response compared closely, with limited joint softening evident at increasing drift ratios. Column bars were well anchored within the joint, with bar slip contributing 9% or less to fixed end rotation. Displacement component magnitudes and percentages for the CPFD and CIP specimens compared very favorably.

Principal tensile stresses exceeded $3.5\sqrt{f_c'}$ and justified the use of additional joint reinforcement required for development of an assumed force transfer mechanism. The test specimen, designed per 2006 LRFD RSGS, did not require stirrups inside the joint; however, two joint stirrups were included for construction, providing an area 65% of that required by the 2009 LRFD SGS ($0.135A_{st}$). Strain records confirmed plastic hinging, effective confinement in the column and joint, and strain penetration into the joint. Bent cap longitudinal bar strains exhibited a pattern similar to the CIP speicmen especially for the bottom bar, although CPFD longitidinal bars yielded within the joint. However, specimens did not include the significant additional bent cap longitudinal reinforcement ($0.245A_{st}$) required by 2009 LRFD SGS.

Evidence of different joint behavior for the specimens included different patterns of strains in confining reinforcement and in stirrups. The peak strain in the CPFD corrugated pipe was located at mid-depth, whereas the CIP hoop strain was minimum at the same depth and peaked at approximately two-thirds of the depth of the cap. Supplementary hoops that were placed at the ends of the pipe to reinforce the pipe and limit dilation and potential unraveling reached up to 52% of yield, indicating their importance in joint performance. Stirrup strains within the joint only reached 25% of yield, but yielded for the CIP. Test specimens, designed per 2006 LRFD RSGS, did not require stirrups inside the joint; however, two joint stirrups with a total area of $0.089A_{st}$ were included for construction. These stirrups provided an area 66% of that required by the 2009 LRFD SGS ($0.135A_{st}$).

Despite the less conservative design basis compared to the 2009 LRFD SGS, the CPFD specimen satisfied the performance goal of the design, achieving an extensive drift without appreciable strength degradation and exhibiting extensive plastic hinging of the column, limited joint distress, and essentially elastic behavior of the bent cap. Emulative performance is concluded for the CPFD specimen based on closely matching overall behavior between the CPFD and CIP specimens, including lateral load-displacement response, dominance of plastic hinging, joint shear stiffness, strain patterns of bent cap longitudinal reinforcement, integral behavior between the bedding layer, column, pipe, and bent cap, and minor effects due to bar slip. The importance of the fabrication and assembly processes, as well as the use of stirrups within the joint region, pipe design, supplementary hoops, area of longitudinal bent cap bars, and flowable concrete within the cap pocket should be addressed in future recommendations. Additional analysis to develop a new joint model is also recommended to maximize efficiency in design.

TABLE OF CONTENTS

Page

LIST OF TABLES

Chapter 1

Chapter 2

Chapter 3

LIST OF FIGURES

Chapter 2

Chapter 3

1.0 Introduction

1.1 Background

This report, Emulative Precast Bent Cap Connections for Seismic Regions: Component Tests—Cap Pocket Full Ductility Specimen (Unit 3), is the third in the series of four reports summarizing the California State University, Sacramento (CSUS) component tests supporting National Cooperative Highway Research Program (NCHRP) Project 12-74, "Development of Precast Bent Cap Systems for Seismic Regions". It is recommended that readers review the Unit 1 Test Report [1] for further project background.

1.2 NCHRP 12-74 Research Objective

To address the uncertainties associated with seismic behavior of precast bent cap systems and the lack of specifications, the National Cooperative Highway Research Program (NCHRP) funded Project 12-74, Development of Precast Bent Cap Systems for Seismic Regions, to develop design methodologies, design and construction specifications, design examples, and semi-standard details for seismic precast bent cap systems using emulative and hybrid connections for nonintegral and integral systems. [2, 3]

1.3 CSUS Research Objective and Approach

The California State University, Sacramento (CSUS) research objective is to develop design methodologies, design and construction specifications, design examples, and semi-standard details for nonintegral emulative precast bent caps. As reported in Reference 2, two emulative connections types—grouted duct and cap pocket—were selected for development based on a review of past connection usages and consideration of expected seismic performance, durability, constructability, and cost.

Nine tasks are included in NCHRP 12-74 to reach the overall research objectives. [3] As part of Task 6—Conduct of Analytical and Experimental Work—CSUS conducted tests and associated analysis to investigate grouted duct and cap pocket connections. Table 1-1 shows the Test Matrix for CSUS component tests, including a brief summary of the four test specimens (units).

1.4 Scope of Report

This report, Emulative Precast Bent Cap Connections for Seismic Regions: Component Tests—Cap Pocket Full Ductility Specimen (Unit 3), is the third in a series of four reports that summarize the experimental and analytical efforts for each CSUS test unit. This report includes the following chapters:

1.0 Introduction: Background, statement of NCHRP research objective, CSUS research objective and approach, and scope of report.

2.0 Specimen Design, Fabrication, and Testing: Summary of the Cap Pocket Full Ductility (CPFD) specimen design, fabrication and testing, including key aspects of fabrication processes and issues, as well as specimen material properties, test setup, loading sequence, instrumentation and pretest predictions.

3.0 Specimen Response and Analysis: Experimental observations, hysteretic response, column curvature response, displacement decomposition, joint response, and strain records. An important additional aspect of this report is the comparison of CPFD results to those of the Cast-in-place (CIP) (Unit 1).

4.0 Summary and Conclusions.

1.5 Tables

Table 1-1. CSUS Component Test Matrix for Bent Cap-Column Connections

Test Unit	Brief Description
1. Cast-in-place (CIP)	Control specimen for comparison to precast connections, with bent cap and column detailing intended to achieve full ductility
2. Grouted Duct Connection (GD)	Individual ducts cast in bent cap to connect each column bar, with bent cap and column detailing intended to achieve full ductility
3. Cap Pocket Full Ductility (CPFD)	Single pipe cast in bent cap to connect all column bars, with bent cap and column detailing intended to achieve full ductility
4. Cap Pocket Limited Ductility (CPLD)	Single pipe cast in bent cap to connect all column bars, with bent cap and column detailing intended to achieve limited ductility

2.0 Specimen Design, Fabrication, and Testing

2.1 Design

The CPFD specimen used the same full-ductility design basis as the CIP specimen reported in Reference 1, for direct comparison. Figure 2-1 shows the portion of the prototype bridge used for the 42% scaled specimen design.

The design of the CPFD specimen assumed emulative response would be achieved despite the following differences for the CPFD specimen compared to the CIP specimen:

- Separate precast elements, including the bent cap and column
- Use of a single 18-in diameter pipe in the bent cap to house the column longitudinal reinforcement and serve as both a stay-in-place form and joint hoop reinforcement
- Use of normal weight concrete within the pipe to anchor the column bars
- Use of a 1.5-in bedding layer between the bent cap soffit and column to accommodate tolerances

Specimen drawings are shown in Figures 2-2 through 2-6. In addition, Table 2-1 provides a detailed comparison of the column, bent cap, and joint reinforcement for the CIP prototype and CPFD specimen. Ratios of the specimen reinforcement to the similitude (or design) ratio are shown to be reasonably close to 1.0. The hoop ratio (specimen/design) is significantly larger than 1.0 because the test specimen hoop force is based on the actual yield stress (57.9 ksi not nominal 30 ksi used in design) and also includes 2 end hoops. In addition, the design assumes a reinforcement ratio close to the minimum required, not the common practice of extending column hoops into the joint. It is recommended that readers review the Unit 1 Test Report [1] for further design background.

Helical corrugated pipe was selected for use in the CPFD specimen. Although annular pipe has potentially advantageous performance characteristics such as seams with resistance spot welding or riveting, its production process is more labor intensive and availability is much more restrictive. [4] Helical corrugated pipe corrugation is used in

nearly 95% of the applications throughout the United States and is produced nationwide. It is normally seamed together using a lock seam per ASTM A 760, Standard Specification for Corrugated Steel Pipe, Metallic-Coated for Sewers and Drains and AASHTO T 249, Standard Method of Test for Helical Lock Seam Corrugated Pipe. [7, 17] Figure 2-7 shows a schematic of the detail. Continuous butt welds are very rarely used. Standard corrugations are established for given pipe sizes. The specifications of the helical corrugated pipe for the CPFD specimen are shown in Table 2-2. Figure 2-8 shows the corrugation and lock seam details for the pipe that was used.

The pipe thickness was a specific design parameter. Pipe thickness was calculated to provide the same circumferential hoop force in the joint as that required for the CIP specimen per 2006 Recommended LRFD Guidelines for the Seismic Design of Highway Bridges (2006 LRFD RSGS) [5], based on a yield strength of 30 ksi for the pipe material (per references in the literature) and the horizontal component of the helical pipe. Subsequent coupon tests conducted on the pipe material indicated a larger yield strength than assumed, as mentioned in Section 2.2.2.2. However, calculations using the assumed 30 ksi yield strength resulted in a pipe thickness that matched the thinnest readily available pipe material. No change in required hoop area was incorporated between the 2006 LRFD RSGS and 2007 Proposed AASHTO Guide Specifications for LRFD Seismic Bridge Design (2007 LRFD PSGS) [6].

In addition, a #3 hoop was placed approximately 1 in from each end of the pipe to reinforce the pipe and limit dilation and potential unraveling, as shown in Figure 2-9. This was considered a reasonably simple yet conservative measure, given the limited number of specimen tests and unknown performance of this innovative detail. Table 2-2 shows a hoop force ratio (pipe/hoop) of 1.03 when supplementary hoops are neglected, and 1.38 when accounting for the hoops.

2.2 Fabrication

2.2.1 Specimen

The CPFD specimen consisted of a separately cast bent cap and column, as shown in Figures 2-2 through 2-6. As for the CIP control specimen, the bent cap used a 25 in x

25 in cross section, 12-#5's (0.65%) for flexural reinforcement, and #3's at 6 in for transverse (shear) reinforcement. The 20-in diameter column included 16-#5's (1.58%) and #3 hoops at 2 in within the plastic hinge region. Joint reinforcement included three sets of 4-leg #3 stirrups at 5 in (with two sets of #3 cross ties through the depth) adjacent to each side of the joint, #3's at 5 in hoop reinforcement, and an embedment depth of column bars equal to the joint depth less 3 in (i.e., 22 in). Figure 2-6 shows a constructible joint region, including two 2-leg stirrups intentionally placed in the joint to represent construction stirrups sometimes used for support of the rebar cage or limit states other than seismic. As shown in later fabrication photos, with the use of a single pipe, the joint region was not particularly congested. In addition, the pipe was designed to be placed between top and bottom bent cap bars, eliminating conflict between the ducts and longitudinal rebar. However, construction stirrups still had to be placed around the pipe transversely. Table 2-2 summarizes select design details of the CPFD specimen, including the corrugated pipe, supplementary hoops, tolerances, and bedding layer.

2.2.2 Material Properties

Portland cement concrete and steel used in the fabrication and assembly of the bent cap, column, and pipe were tested to determine material properties. Sampling, preparing, and testing of specimens were generally performed in accordance with governing ASTM standards.

2.2.2.1 Portland Cement Concrete

The bent cap, column, and pocket were constructed with normal weight concrete using the concrete mix proportions shown in Table 2-3. The mix design was expected to achieve a 28-day compressive strength of at least 4000 psi based on a water-cement ratio of approximately 0.49. A 3/8-inch maximum coarse aggregate size was used in the concrete mix in accordance with specimen scaling. Standard 6x12 in cylinders were cast from the concrete batch used for the specimen fabrication and assembly. Concrete cylinders were cured for the same length of time and in the same conditions as the concrete specimens.

Compression and tensile (split cylinder) tests were conducted in the CSUS Structural Laboratory. Concrete cylinders were produced for each casting and tested over a range of days including test day. The design and actual properties of the concrete are shown in Table 2-4, and representative concrete compressive strength gain curves are shown in Figure 2-10. It is noted that the bent cap and column used the same batch of concrete. The pocket concrete, cast at a time later than that of the bent cap (i.e., during assembly operations), was intended to achieve a strength and stiffness approximately equal to that of the bent cap. Reasonable pocket-to-bent cap ratios were achieved: compressive strength, 0.90; tensile strength, 1.19; modulus of elasticity, 1.05.

2.2.2.2 Steel

The column and bent cap longitudinal reinforcing steel consisted of ASTM A706 Grade 60 deformed #5 rebar, and the column hoops and stirrups consisted of ASTM A615 Grade 60 (weldable) #3's. Uniaxial tensile tests were conducted on samples from the rebar lot; rebar specimens were prepared in accordance with ASTM requirements. Yield and tensile strengths are shown in Table 2-5 for the different bar sizes. Figure 2-11 shows a stress-strain plot for a representative reinforcing bar, displaying expected strength and ductility.

The corrugated pipe was fabricated from steel with properties and dimensions as shown in Tables 2-2 and 2-5. The nominal steel yield strength was 30 ksi, but test coupons exhibited a yield strength of 57.9 ksi. The coupon tensile strength was only slightly higher, 61.0 ksi.

2.2.3 Fabrication and Issues

2.2.3.1 Fabrication

All CSUS specimens were fabricated with the assistance of Clark Pacific, West Sacramento, CA. The fabrication and assembly of the specimens were intended to replicate as much as possible the expected field process, and thereby examine constructability issues. Therefore, all specimens, including the CPFD specimen, were built in the upright position. Assembly of the bent cap and column into the T-shaped specimen was performed in the CSUS Structural Laboratory.

Construction Sequence

The construction sequence for the CPFD specimen included the following (Figures 2-12 through 2-24):

1. Fabricate the rebar cages for the bent cap and column, including strain gages, at CSUS.
2. Transport rebar cages to Clark Pacific, prepare bent cap and column forms including special damming of the corrugated pipe, and cast bent cap and column concrete.
3. Transport precast cap and column to CSUS.
4. Prepare column and bent cap for assembly, and conduct cap setting operation in upright position.
5. Prepare connection for concreting and fill pocket with concrete from top.
6. Invert specimen and install in test area.

The cap was set and the bars located within the tolerances shown in Table 2-2.

Concreting Operation

As shown in Figure 2-21, concrete was placed in the pocket and bedding layer using a bucket at the top of the pocket. Concrete was cast into the pocket through the cap reinforcement from above, and a collar with an air vent system was used to help remove entrapped air at the bedding layer.

Preparation: The concrete mix was selected to be the same as that used for the bent cap and column, with the intention of achieving a strength and stiffness approximately equal to that of the bent cap. The inside surface of the corrugated pipe was cleaned out using light sand blasting to remove debris and residue. This cleaned out the pipe and slightly roughened the inside surface. Column bars were placed within the tolerances of Table 2-6 and did not touch the pipe. After the bedding layer form was attached and sealed, the bedding layer was prewatered for approximately 24 hours to ensure sealing and prevent loss of moisture from the pocket concrete (Figure 2-20). Water was drained from the pipe approximately two hours before casting of concrete.

Concrete Mixing and Placement: Concrete was batched at the Clark Pacific plant at West Sacramento and hauled in a trailer to the CSUS Structural Laboratory. After mixing and discharging the concrete, buckets were used to fill the pocket, as shown in Figure 2-21, in several layers with vibration. The pocket was filled within approximately 30 minutes. Once concrete flowed through the air vents in the bedding layer, the vents were sealed. Figure 2-22 shows the top view after concreting. After hardening, curing compound was applied to the top surface.

Form Removal and Inspection: After several days, the bedding layer form was removed and the bedding layer and top of the ducts were inspected. Several air voids were observed at the top of the bedding layer and were grouted as shown in Figure 2-23. This is discussed in the next section.

After concreting, the specimen was inverted, as shown in Figure 2-24, and installed into the test area (Figure 2-25).

2.2.3.2 Issues

The specimen was fabricated and assembled according to the drawings and procedures, except as noted in Table 2-6, which summarizes significant specimen as-builts for column bars and hoops as well as key construction aids.

Fabrication and Assembly

The most significant deviation from the drawings was the placement of the first column hoop below the top of column, approximately 2 in below its intended location during fabrication. This left the column bars at the bedding layer with an unsupported length of nearly twice that intended by design. As discussed in Section 3, this reduced the overall drift to some extent, but did not affect the maximum load induced in the joint or behavior associated with the precast connection.

An error in Figure 2-4 (Column Elevation and Section Drawing) resulted in the column being fabricated 1.5 in longer than the intended design. This caused CPFD drift values to differ from the CIP (and GD) specimen by less than 1%.

In addition, during the assembly process, the concrete mix for the cap pocket was considerably stiffer than designed due to accidental omission of the plasticizer (which

was not included in the batch because of the travel time from the precaster to the laboratory). A slump of approximately 2 in was achieved without the plasticizer. However, water was not added to the batch at the laboratory in an attempt to achieve cap pocket concrete properties comparable to the bent cap (given the shorter time frame for pocket concrete to gain strength and stiffness before specimen testing). As mentioned in Section 2.2.2.1, comparable properties were achieved. Pocket concrete was well vibrated; however, a number of small air voids (1/16 to 1/8 in high) still developed at the top of the bedding layer. Although voids in practice may be a durability concern, for specimen testing, voids were minor, comprising less than 2% of the bearing area, being located for the most part away from the extreme fibers of the section, and extending no more than 1 in into the bedding layer. Nonetheless, voids were cleaned out, prewatered, and filled with a high strength (8000 psi) non-shrink grout (Figure 2.23B). As discussed in Section 3, there was no indication that results were affected by this condition. Post-test inspection confirmed that grout filled the majority of voids.

Construction Aids

Two construction aids were particularly useful in specimen fabrication: 1) a Sonotube dam at the top and bottom of the corrugated pipe, and 2) a column bar template. Figures 2-13 and 2-14 show the use of a carefully cut Sonotube placed on top (and bottom) of the corrugated pipe to serve as a dam for concreting the bent cap. To accommodate the longitudinal bent cap bars and stirrups in the joint region, the Sonotube was cut and bent within the pipe. Duct tape and Styrofoam were used to seal all voids. In addition, the entire void was filled with sand to prevent leaks and collapse during casting of concrete. As shown in Figures 2-18 and 2-19, this approach was very effective, although a precaster could use other approaches for casting.

Another construction aid was a column bar template (Figure 2-17). A steel template was fabricated for use during and after fabrication. During fabrication the template maintained accurate positioning of all column bars, thus satisfying the tight tolerance in fabrication. After fabrication, the template maintained bar positions to help ensure a successful cap setting operation (Figures 2-18 and 2-19). While tolerances were

somewhat exacerbated by the fabrication of a scaled specimen, the same type of template can readily be used in the field. The limited range of readily available corrugated pipe sizes also contributed to the tight tolerance that had to be satisfied.

2.3 Testing

2.3.1 Test Setup

The specimen test setup, shown in Figure 2-25, includes the following:

- Simply supported bent cap, with an equivalent pin support at the north end with vertical and lateral restraint (right side as shown) and an equivalent roller at the south end with vertical support only (left side as shown). This simple setup allowed accurate establishment of specimen forces. Although scaled modeling of the moment gradient along the cap was not required, accurate conditions adjacent to the faces of the joint were required and modeled in appropriate proportion to resist the column moment. [9, 10] The test setup ensured accurate conditions at each end of the joint so that the force transfer mechanism in the joint could be investigated.
- Inverted specimen, with a column stub. This allowed biaxial loading of the specimen, using a vertical hydraulic actuator to apply scaled gravity load and the horizontal hydraulic actuator to induce seismic response.
- Different axial force conditions in the bent cap for the push and pull directions. The push direction was considered more critical, as the axial force causes tension at the joint face, in contrast to the compression for the pull direction. However, the magnitude of axial force remained relatively small during testing.

2.3.2 Loading Sequence

The vertical and horizontal hydraulic actuators were used to apply specified Force Control and Displacement Control sequences to the specimen, as shown in Figures 2-26 and 2-27. The stages of loading are briefly summarized as follows:

1. <u>Vertical Load</u>: A monotonic increasing concentrated vertical load representing gravity load was applied to the top of the column stub to a

maximum load of 38 kips. Force Control was used to maintain the vertical load throughout the horizontal loading sequence. A very slight change in vertical load developed during testing.

2. Horizontal Load: After the vertical load was applied, a horizontal load or displacement, representing seismic-induced load or displacement, was applied in two sequences: Force Control, followed by Displacement Control.

   Force Control: An increasing horizontal load was applied to the side of the column stub using one cycle per load level (Figure 2-26). A cycle consisted of both push and pull for the specified load. Load was held at select cycle peaks for crack marking, photographing and documenting. The Force Control sequence was discontinued after an approximate determination of first yield of column longitudinal bars in the push and pull directions.

   Establishment of Effective Yield: Column strain gages and displacement measurements were intended to be used to calculate the system effective yield displacement, Δ_{YE}, and thus displacement ductility demand, μ_D, for the Displacement Control sequence. Establishment of first yield was approximate. The following equation specifies the relationship between the experimental first yield displacement of the system, Δ_Y, and the system effective yield displacement, Δ_{YE}, used for establishing the Displacement Control sequence:

$$\Delta_{YE} = \frac{M_{YE}}{M_{Y\exp}} \Delta_Y$$

   Where M_{YE} is the theoretical moment at effective yield based on moment-curvature analysis, and M_{Yexp} is the experimental first yield moment (experimental force at the first yield times the distance between the actuator and soffit). The ratio of M_{YE}/M_{YEexp} was approximately 1.4.

   Displacement Control: Displacements were applied quasi-statically to the column stub in 3 cycles: two cycles at the target displacement ductility, followed by one cycle at the displacement ductility of the prior level (see

Figure 2-27). Application of reversed cyclic displacements permitted examination of hysteretic loop stability. Nominal displacement ductility demand, as multiples of system effective yield displacement, was applied at the following levels, or until the residual capacity of the specimen dropped below 30% of the maximum load: μ1, μ1.5, μ2, μ3, μ4, μ6, μ8. (Note: μ1 = nominal (target) displacement ductility of 1.0, μ2 = nominal displacement ductility of 2.0, etc.) Data reduction accounted for the slight additional lateral load applied to the specimen due to the inclination of the vertical actuator under cyclic displacements.

2.3.3 Instrumentation

Extensive instrumentation was used for the test specimen, including internal gages (strain gages mounted on bent cap and column rebar) and external gages (linear potentiometers and LVDTs mounted on the column, joint, and cap). Figures 2-28 to 2-32 show the instrumentation drawings, which define gage locations, and Figures 2-33 through 2-37 show various photos of the instrumentation attached to the specimen.

Strain gages on column longitudinal bars and hoops were intended to help quantify column flexure, including plastic hinging and strain penetration. Strain gages on bent cap longitudinal bars and stirrups, including in the joint region, were expected to provide evidence of joint distress and a force transfer mechanism through and adjacent to the joint. Strain gages on the pipe were expected to show the magnitude, orientation, and distribution of pipe strain.

Linear potentiometers and LVDTs provide column displacement, column curvature, panel deformation, joint rotation, bar slip, and specimen rigid body motion. Column curvature required the use of two linear potentiometers, one on each side of the column, to determine curvature. Four sets were used to divide the column into four curvature cells. Table 2-7 summarizes column curvature cell as-builts. Two sets of panel deformation gages were used to examine joint panel deformation. On the east side of the specimen, five linear potentiometers were used, whereas on the west side a simplified measurement with two linear potentiometers was used. To limit the number of

gages, bent cap curvature was not explicitly examined. However, the bent cap was assumed to remain essentially elastic. Strain gages were used to monitor strain levels in the bent cap flexural reinforcement.

In addition to active instrumentation, specimen response was documented using digital photos, crack markings and measurements, video recording, and hand notes.

2.3.4 Pretest Predictions

2.3.4.1 Stages of Cracking

Four stages of initial specimen cracking were examined: 1) initial bent cap cracking in flexure due to gravity loads (specimen self weight plus the vertical actuator force, P_V; 2) initial bent cap cracking in flexure with the additional horizontal actuator force, P_H; 3) initial column flexural cracking; and 4) initial joint cracking.

Table 2-8 summarizes the predicted values of vertical and horizontal actuator loads for the stages of cracking. Bent cap flexural cracking was not expected under specimen self-weight and the maximum applied vertical load, P_V, of 38 kips. However, the addition of a horizontal load, P_H, of 13 kips was expected to generate the first flexural crack. Column cracking was also anticipated at a horizontal load of approximately 13 kips. Finally, joint shear cracking was not expected until P_H reached a large value of 39 kips. It should be noted that prediction of cracking load is considered an estimate, as it depends on the highly variable tensile strength of concrete and possible effects of preexisting cracks.

2.3.4.2 Lateral Load-Lateral Displacement Envelope

An envelope of the lateral load-displacement response of the column was predicted before testing. Figure 2-38 shows a close comparison between this prediction and that for the CIP specimen. Deflection at each stage was taken as the sum of the column displacements due to column elastic deflection to yield, column plastic deflection, column shear, and bent cap flexibility.

Flexural component contributions were calculated using moment-curvature results from the sectional analysis software, which used stress-strain models for the concrete and steel based on actual material tests of the concrete and steel used in the specimen. An

effective yield curvature based on a bilinear moment-curvature response with best fit secondary stiffness was used to define the member effective yield displacement, Δ_{ye}. Various levels of displacement ductility were established as a multiple of the effective yield displacement of the system, Δ_{YE}.

2.3.4.3 Moment-Curvature Envelope

An envelope of the normalized moment-curvature response of the column was also predicted, using XTRACT, as shown in Figure 2-39. [11] Note that the curvature was normalized by multiplying curvature by the column diameter; moment was not modified. This prediction is shown to be close to that for the CIP specimen.

2.4 Tables

Table 2-1. Comparison of Reinforcement for CIP Prototype and CPFD Specimen

CPFD		Prototype Design	Similitude [or Design] Requirement	Test Specimen	Specimen to Similitude [or Design] Ratio
Column					
Longitudinal Reinforcement					
Bar Size (diameter, in)		#11 (1.41)	0.59	#5 (0.63)	1.06
No. of bars		16	14	16	1.14
f_y	ksi	66.0	—	63.6	—
ρ		0.0138	0.0138	0.0158	1.14
M_n^*	K·ft	3760	272	216	0.79
M_n/D^3	K·ft/ft^3	58.7	58.7	46.6	0.79
Transverse Reinforcement					
Bar Size (diameter, in)		#6 (0.75)	0.31	#3 (0.38)	1.20
Spacing	in	3.0	[1.8]	2.0	[1.11]
f_y	ksi	66.0	—	63.5	—
ρ		0.0139	0.0139	0.0125	0.90
Bent Cap					
Longitudinal Reinforcement					
Bar Size (diameter, in)		#11 (1.41)	0.59	#5 (0.63)	1.06
No. of bars		12	—	12	—
f_y	ksi	66.0	—	63.6	—
ρ		0.0051	0.0051	0.0065	1.27
M_n^*	K·ft	6680	483	448	0.93
M_n/bh^2	K·ft/ft^3	44.2	44.2	49.5	1.12
Transverse Reinforcement					
Bar Size (diameter, in)		#6 (0.75)	0.31	#3 (0.38)	1.20
Spacing	in	12.0	[8.4]	6.0	[0.71]
f_y	ksi	66.0	—	63.5	—
Joint					
Inside Joint					
Transverse Reinforcement (ρ_s or Equivalent Pipe)					
Hoops or Pipe		#6 (0.75 in) @ 3 in O.C.	—	16 gage (0.065 in) pipe	—
Hoop Force†	kips	552	95.8; [36.3]‡	82.9	0.87; [2.28]
f_y	ksi	61.0	—	57.9	—
Side Face Reinforcement (A_s^{sf})					
No. of bars - Bar Size		8 - #6	—	4 - #3	—
A_s/A_{cap}	in^2/ in^2	0.19	[0.10]	0.12	[1.20]
f_y	ksi	60.0	—	63.5	—
Construction Stirrups					
No. of bars - Bar Size		Two 2-leg – #6	—	Two 2-leg - #3	—
Area	in^2	1.76	—	0.44	—
f_y	ksi	66.0	—	63.5	—
Adjacent to Joint					
Vertical Stirrups (A_s^{jv})					
No. of bars - Bar Size		Five 4-leg - #6	—	Three 4-leg - #3	—
Spacing	in	6.0	—	5.0	—
A_s^{jv}/A_{st}	in^2/ in^2	0.35	[0.20]	0.27	[1.33]
f_y	ksi	66.0	—	63.5	—
Horizontal Ties (A_s^{jh})					
No. of bars - Bar Size		4 - #6	—	2- #3	—
Spacing	in	12.0	—	8.0	—
A_s^{jh}/A_{st}	in^2/ in^2	0.35	[0.10]	0.13	[1.33]
f_y	ksi	66.0	—	63.5	—

Note: Prototype and Specimen Design per 2006 LRFD RSGS [5]

* Nominal moment @ ε_c=0.003

† Prototype hoop force is based on extension of column hoops into the joint; Test specimen hoop force is based on actual yield stress (not nominal 30 ksi used in design). It also includes 2 end hoops.

‡ Represents close to the minimum required amount (ρ/ρ_s=1.22), not the extension of column hoops.

Table 2-2. Select Joint Design Details

Issue	Detail
Helical Corrugated Pipe [7, 17] Diameter Corrugation Angle Corrugation Dimensions Pipe Thickness Seam Connection Type; Strength Steel yield strength (nominal)	 18 in (nominal) 20 deg 2-2/3 in (pitch) x ½ in (deep) 16 gage (0.064 in) lock seam; 240 lb/in [7] 30 ksi
Hoop Force Ratio (Pipe/Hoop)	1.03 (neglecting supplementary hoops) 1.38 (assuming contribution of supplementary hoops at ends)
Fabrication and Placement Tolerance for Column Bars in Pipe	+ 0.38 in
Bedding Layer	1.5-in thick, no shims, no hoop reinforcement

Table 2-3. Concrete Mix Proportions

Material Designation	(Based on Saturated Surface Dry)		
	Quantity	Weight (lbs)	Volume (ft^3)
ASTM C 150 – Type I/II	–	564	2.87
ASTM C 33 – 3/8"	–	1,826	10.92
ASTM C 33 – Concrete Sand	–	1,217	7.39
ASTM C 494 – Super plasticizer	45 oz	3	0.05
Water	W/C=0.49	276	4.43
Total Air Content	5.00%	–	1.35
TOTAL	–	3,886	27.0

Table 2-4. Concrete Properties—Bent Cap, Column, and Pocket

Parameter	Design	Actual
Slump	5½" +/- 2½"	~ 3 in, cap and column
Unit Weight	143.9 pcf	–
Compressive Strength	4,000 psi (28 day)	Cap and Column: 5,620 psi (41 day) Pocket: 5,040 psi (26 day)
Tensile Strength (Split Cylinder)	N/A	Cap and Column: 400 psi (41 day) Pocket: 475 psi (26 day)
Modulus of Elasticity	N/A	Cap and Column: 3,440 ksi (41 day) Pocket: 3,605 (26 day)

Table 2-5. Yield and Tensile Strengths—Reinforcing Bars and Pipe

Size	Type	Yield Strength (ksi)	Tensile Strength (ksi)
#3	Bent cap stirrups; Column hoops	63.5	99.6
#5	Bent cap longitudinal; Column longitudinal	63.6	91.0
16 gage (0.065 in)	Pipe	57.9	61.0

Table 2-6. Significant As-builts and Construction Aids

Description	Drawing	As-built
Length of column reinforcement embedded into bent cap, l_{ac}	22 in	22 in +/- 1/8 in (average)
Column bar location in pipe	0.0 in	≤ 3/8 in
Column hoop spacing within plastic hinge	0.0 in	+/- 1/16 in
First column hoop below top of column	≤1 in	2.94 in (average)
Column length (stub to column top)	2 ft 11 in	2 ft 11 in (Note: drawing should have shown 2 ft 9½ in)
Helical Corrugated Pipe [7] Corrugation Angle Average Pitch Average Depth Average Thickness	 20 deg 2.667 in 0.500 in 0.064 in	 20 deg 2.656 in 0.508 in 0.065 in
Construction Aids	1. Column bar template to ensure match between column bars and pipe during cap setting 2. Sonotube dam at top and bottom of pipe, as well as sand fill, to prevent concrete intrusion and maintain integrity of forms during casting	

Table 2-7 Column Curvature Cell As-builts—CPFD vs. CIP

Cell Number	Drawing		CPFD		CIP	
	Cell Height (in)	Cell Width (in)	Cell Height (in)	Cell Width (in)	Cell Height (in)	Cell Width (in)
Cell 1	3.5	26	4.78	26.05	3.67	26.79
Cell 2	3.0	26	2.87	26.13	3.00	26.04
Cell 3	4.0	26	3.99	25.99	4.14	26.01
Cell 4	9.5	26	9.59	26.01	9.25	26.07

Table 2-8. Predicted Stages of Specimen Cracking

Item	Load (kips)	
	P_V	P_H
Bent Cap—Flexural	None	-
	38.0	15.1
Column—Flexural	38.0	13.5
Joint Shear	38.0	39.6

2.5 Figures

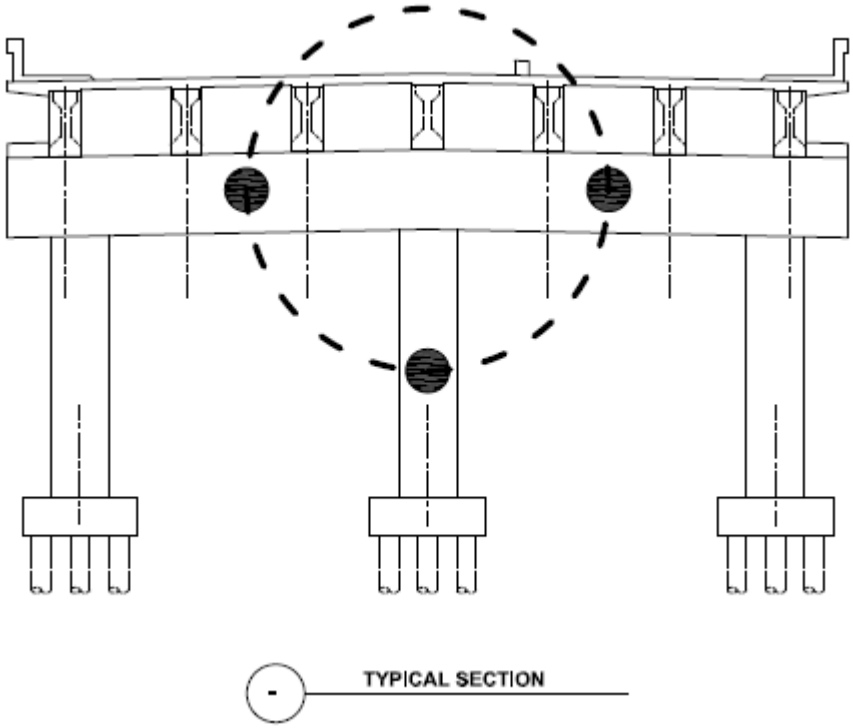

Figure 2-1. Portion of Prototype Used for Specimen Design

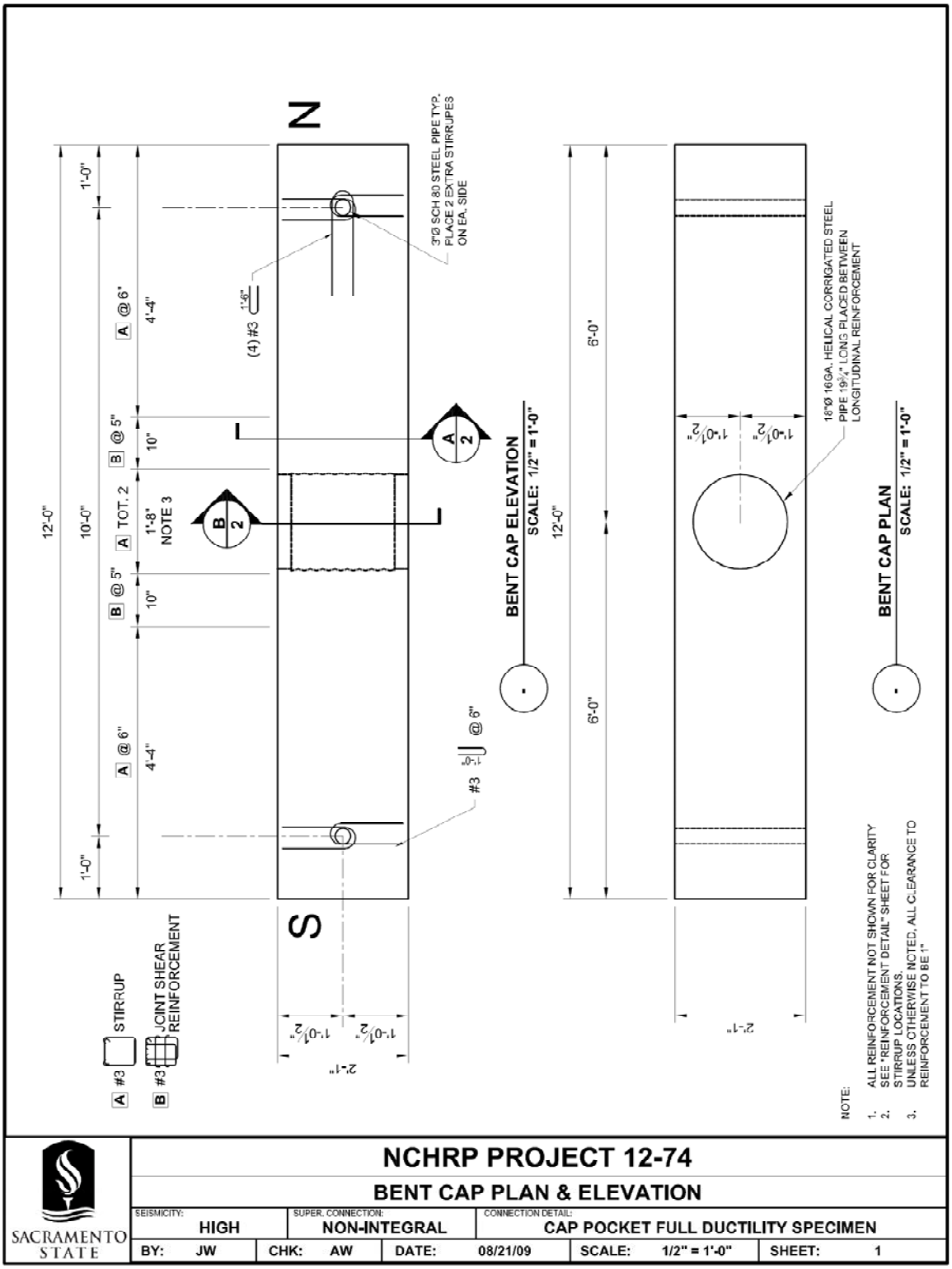

Figure 2-2. Cap Pocket Full Ductility Specimen Design—Bent Cap Plan and Elevation

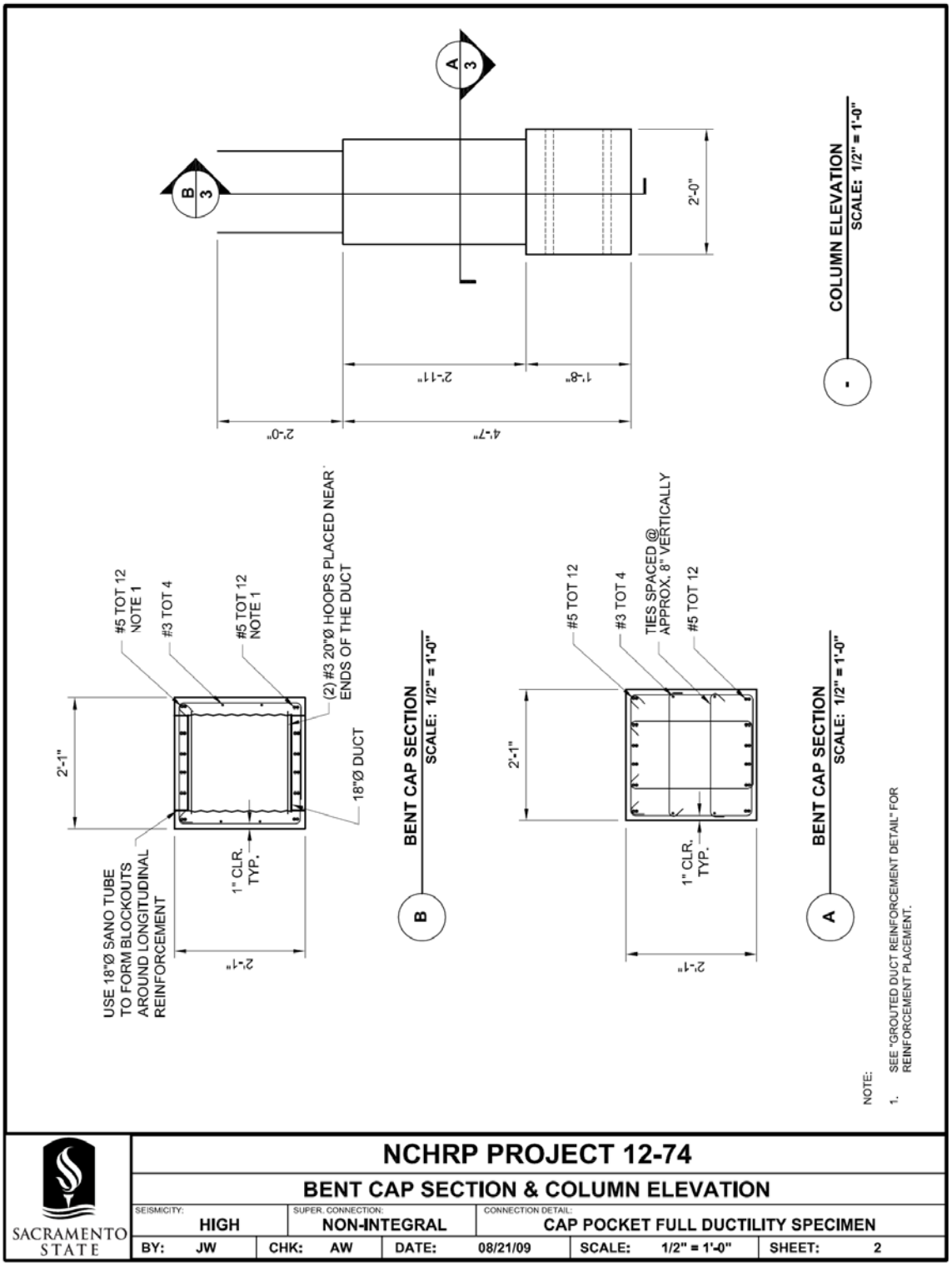

Figure 2-3. Cap Pocket Full Ductility Specimen Design—Bent Cap Section and Column Elevation

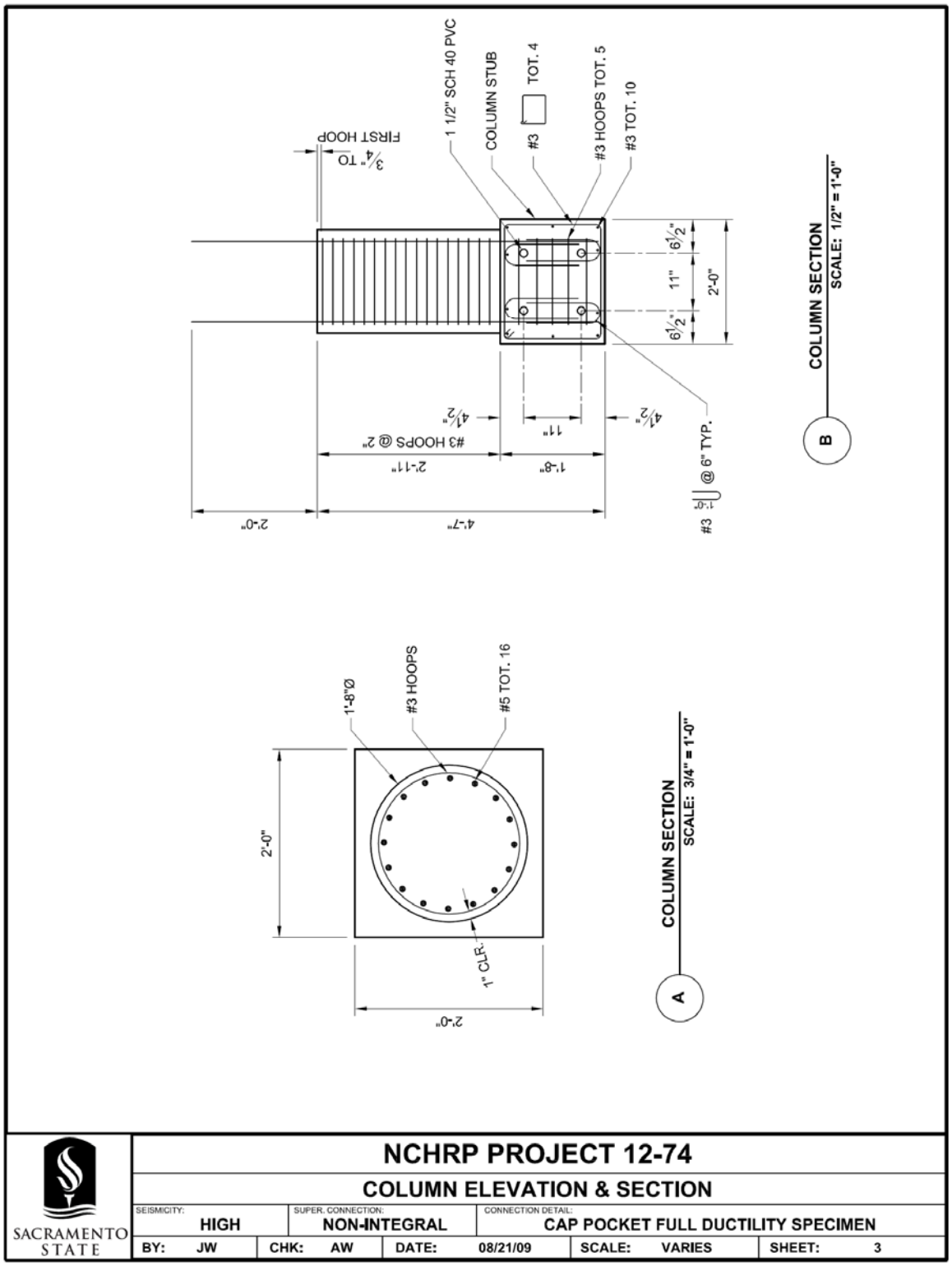

Figure 2-4. Cap Pocket Full Ductility Specimen Design—Column Elevation and Section

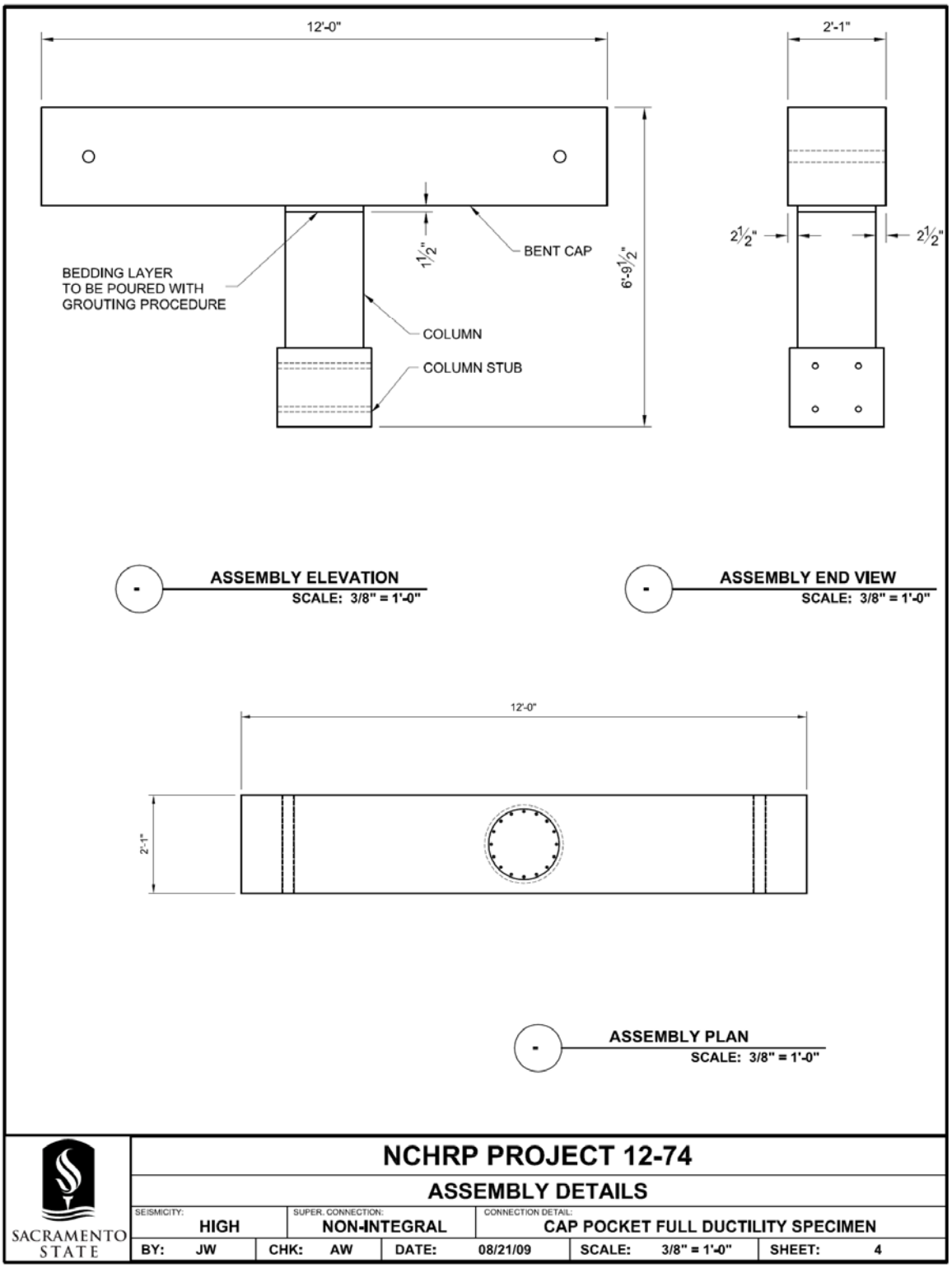

Figure 2-5. Cap Pocket Full Ductility Specimen Design—Assembly Details

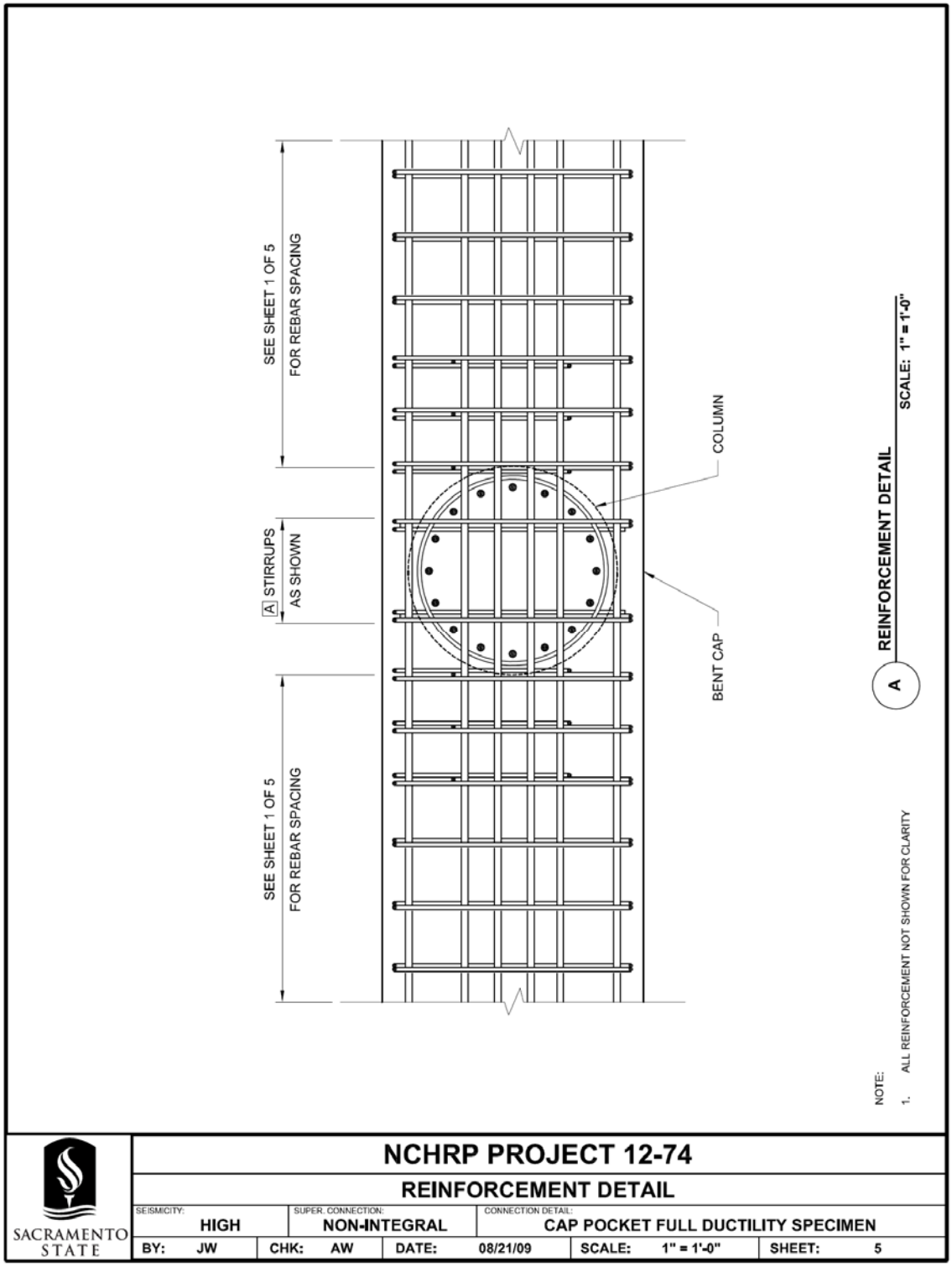

Figure 2-6. Cap Pocket Full Ductility Specimen Design—Bent Cap Reinforcement Detail

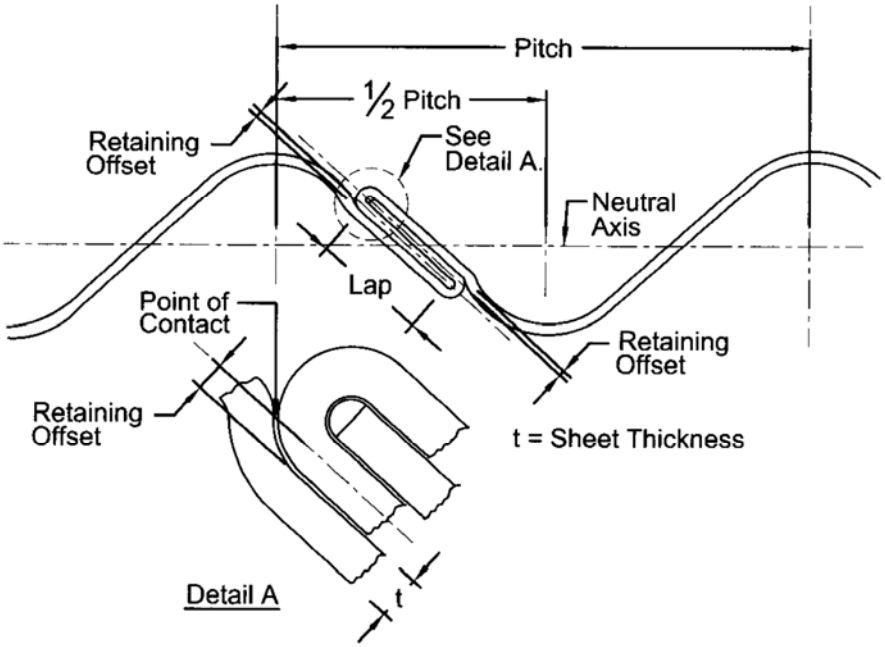

Figure 2-7. Type I Lock Seam Cross Section [8]

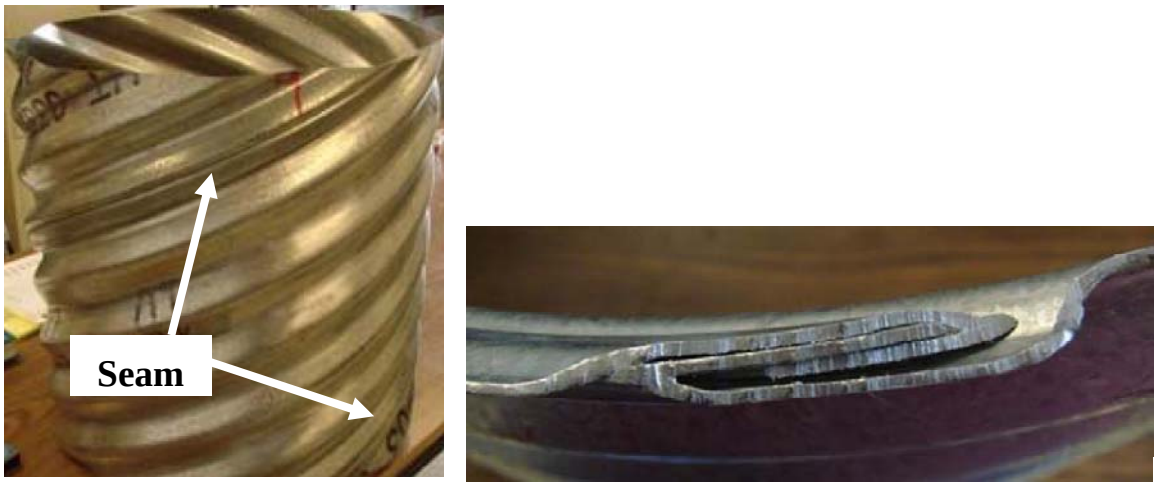

A. Corrugation and Lock Seam B. Close–up of Lock Seam

Figure 2-8. Corrugation and Lock Seam Details for CPFD Specimen

Figure 2-9. Cap Pocket Rebar Cage with Corrugated Pipe and Supplementary Hoop at Each End of Pipe

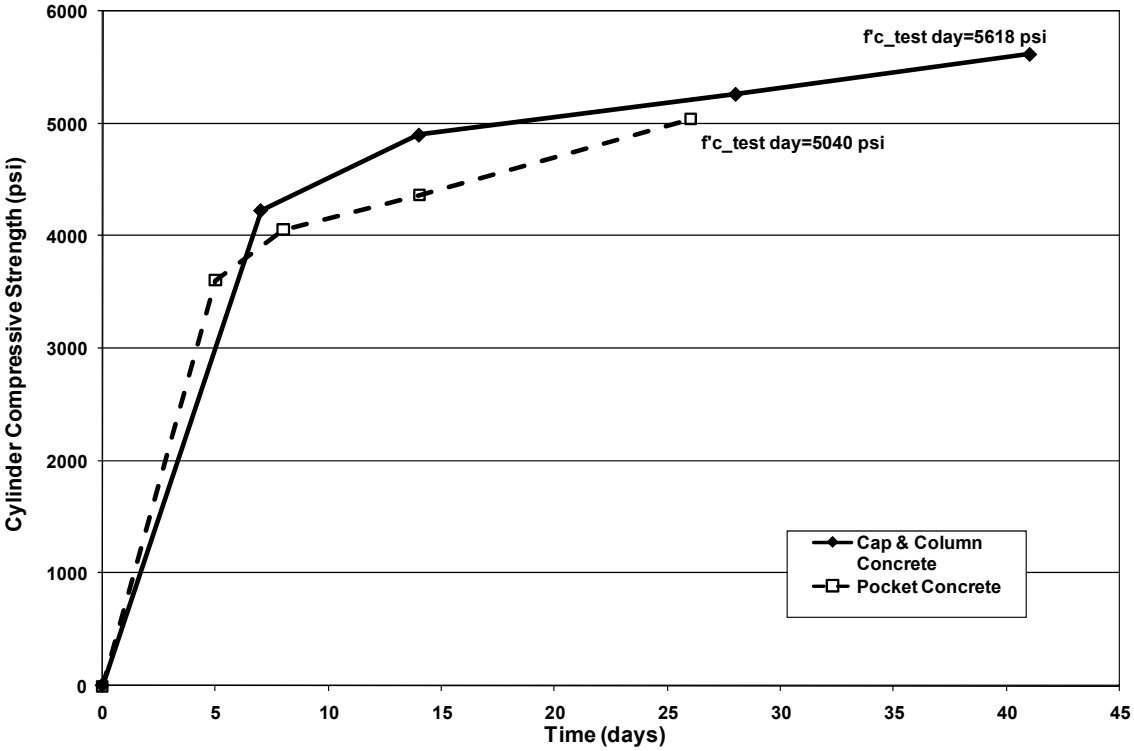

Figure 2-10. Concrete Cylinder Compressive Strength vs. Time

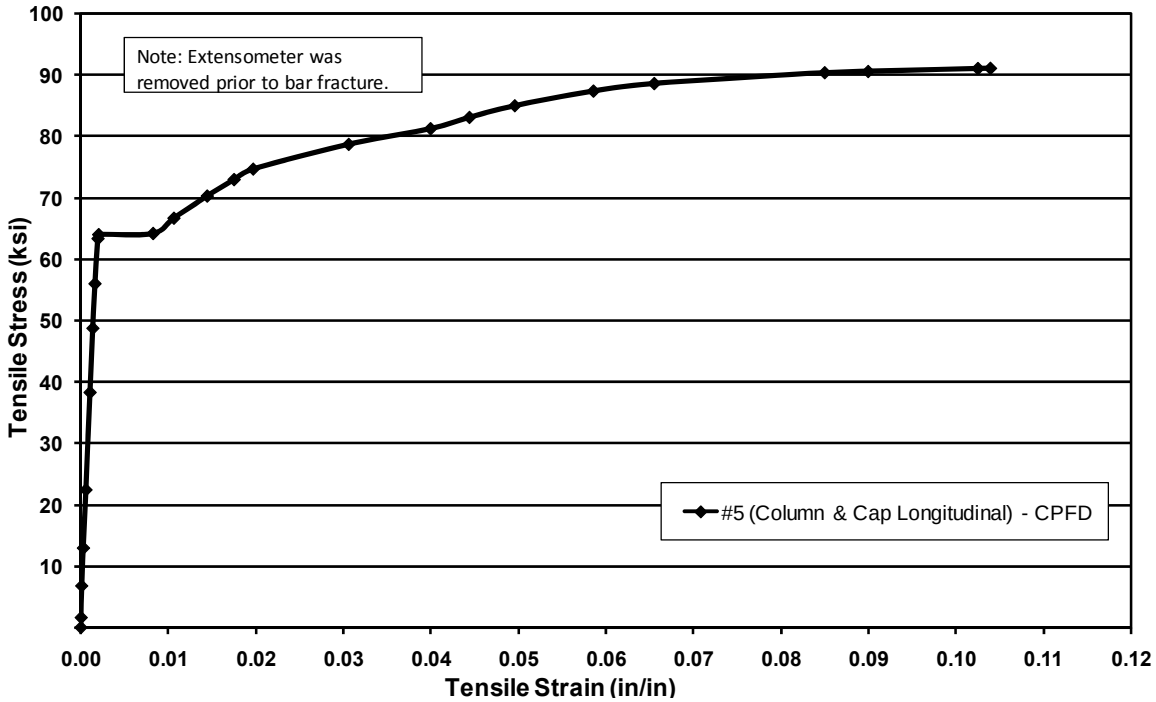

Figure 2-11. Tensile Stress-Strain Plot for Reinforcing Bars

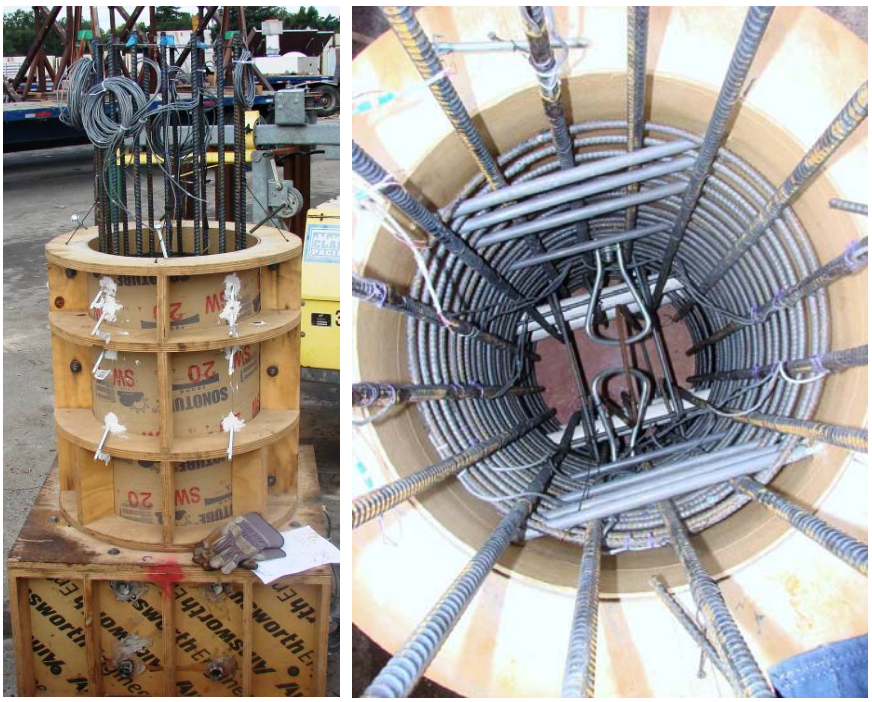

Figure 2-12. Assembly of Column Rebar Cage

Figure 2-13. Bent Cap Rebar Cage in Form during Fabrication

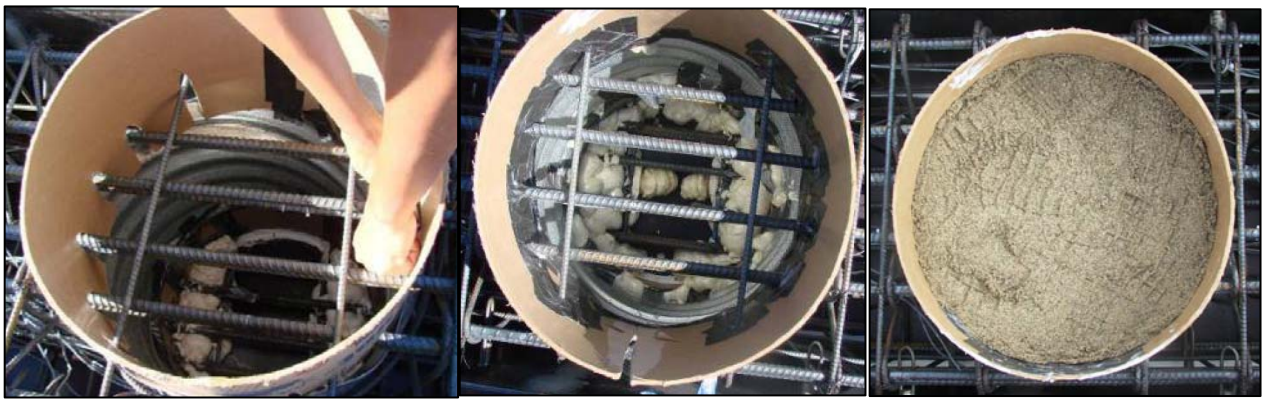

A. Sonotube Dam around Rebar at Top of Duct

B. Dam Sealed with Foam and Duct Tape (Prior to Placement of Sand)

C. Duct filled with Sand

Figure 2-14. Joint Region of Bent Cap during Fabrication

Figure 2-15. Casting Bent Cap

Figure 2-16. Cap Prepared for Cap Setting Operation

Figure 2-17. Steel Template at Top of Column Bars

Figure 2-18. Lowering of Cap during Cap Setting Operation

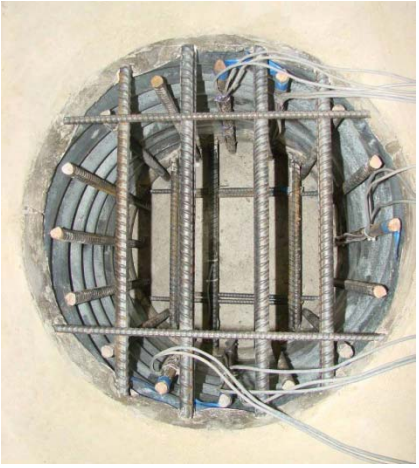

Figure 2-19. Plan View of Pocket after Cap Setting

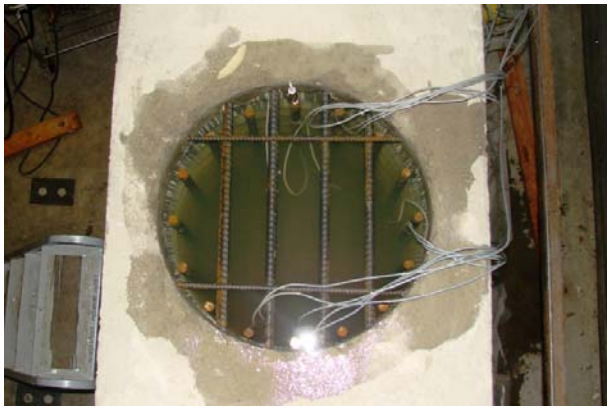

A. Prewatering Pocket

B. Bedding Layer

Figure 2-20. Preparation of Pocket and Bedding Layer

A. Concrete Discharged from Mixer

B. Filling Buckets with Concrete

C. Bucketing Concrete into Pocket

D. Vibrating Concrete in Pocket

Figure 2-21. Concreting of Cap Pocket Connection

Figure 2-22. Top View of Cap Pocket Connection after Concreting

A. Bedding Layer Post-Concreting

B. Grouting Air Voids

Figure 2-23. Bedding Layer Post-Concreting

Figure 2-24. Inversion of Specimen Prior to Installation in Test Area

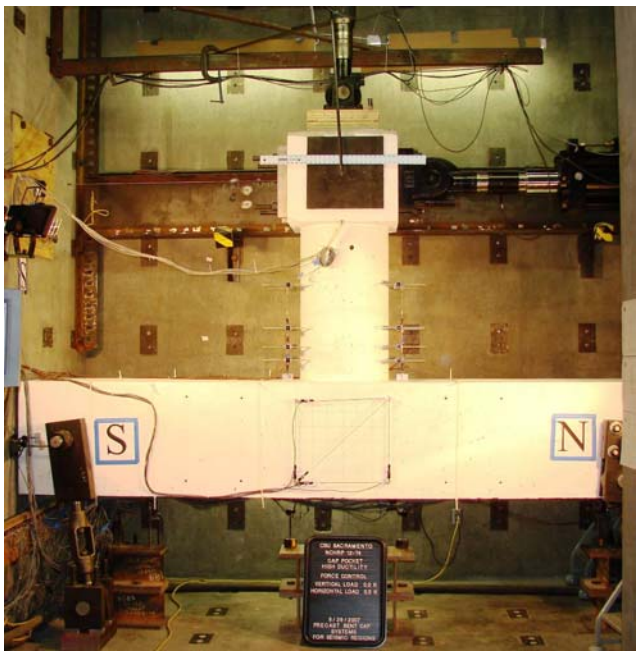

Figure 2-25. Specimen in Preparation for Testing

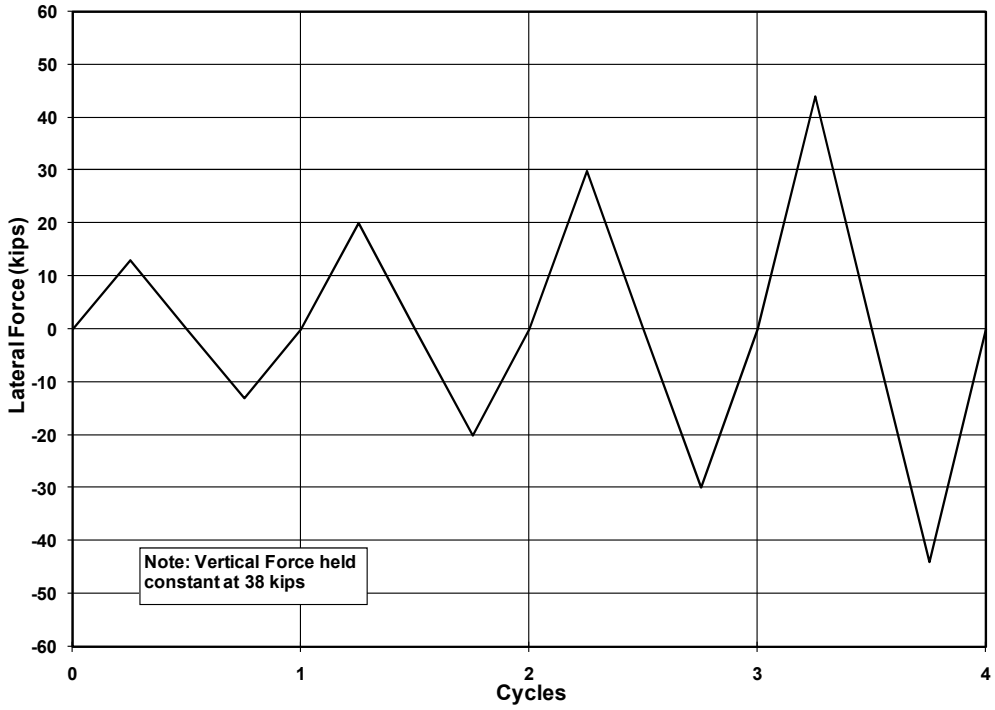

Figure 2-26. Force Control Sequence

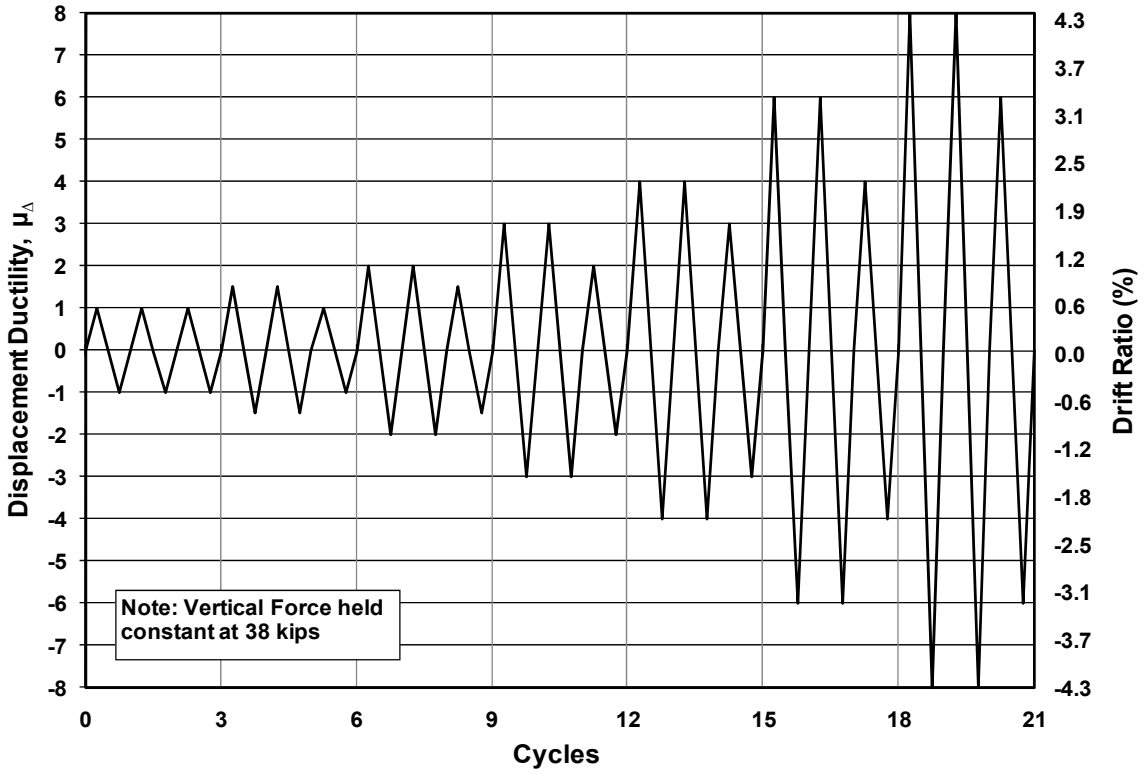

Figure 2-27. Displacement Control Sequence

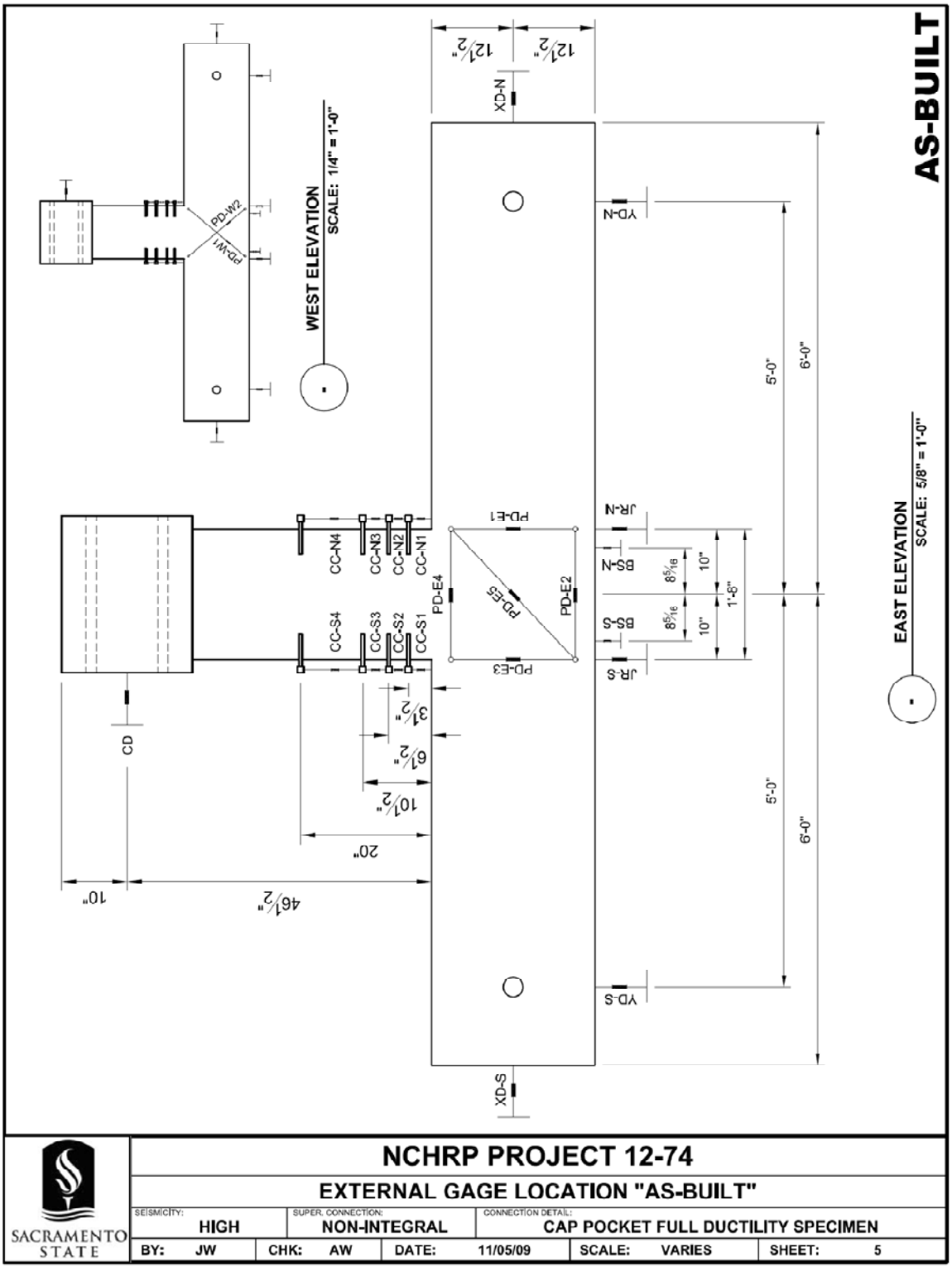

Figure 2-28. Instrumentation Drawings—External Gage ID (As-built)

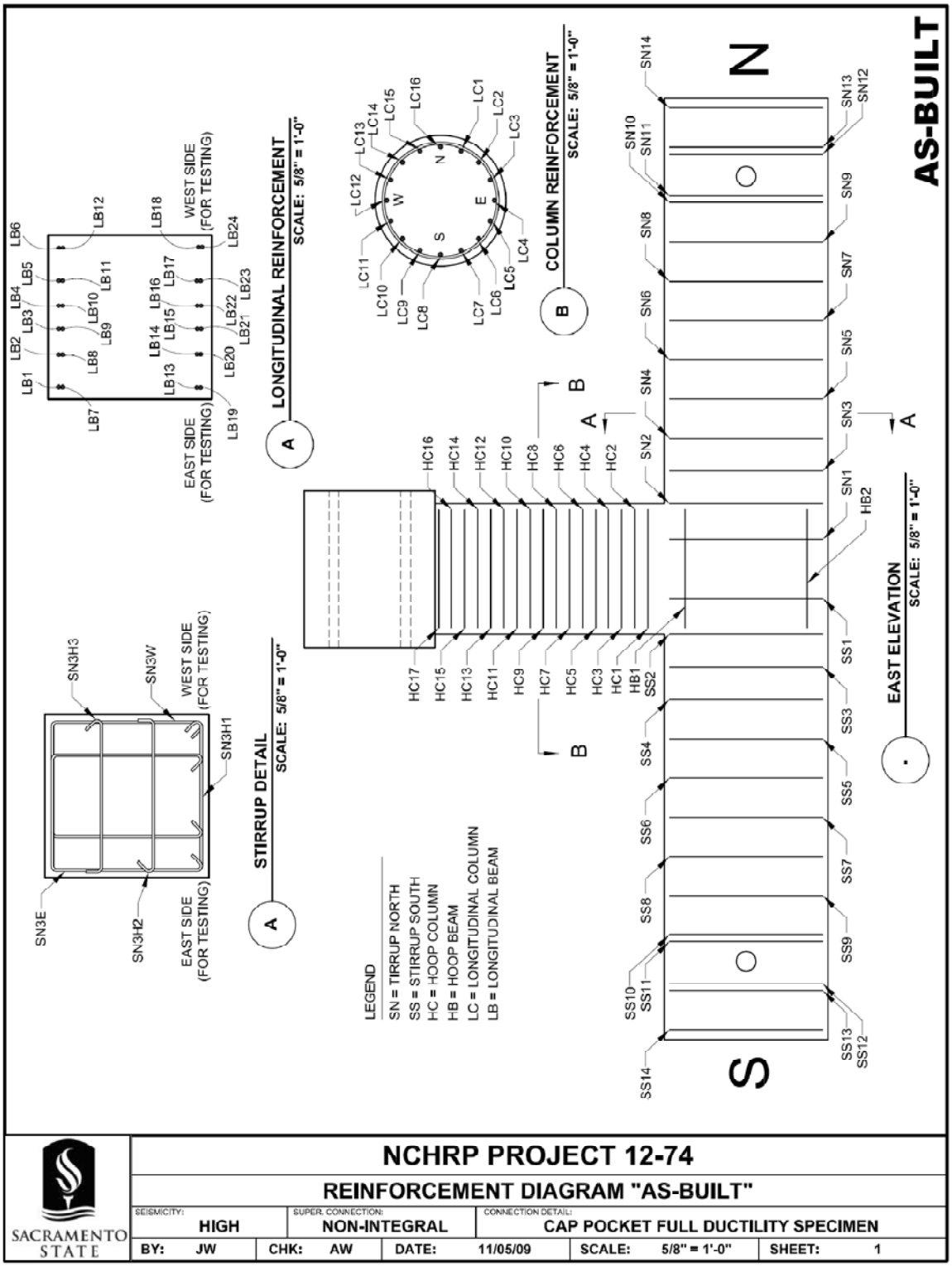

Figure 2-29. Instrumentation Drawings—Reinforcing Bar ID (As-built)

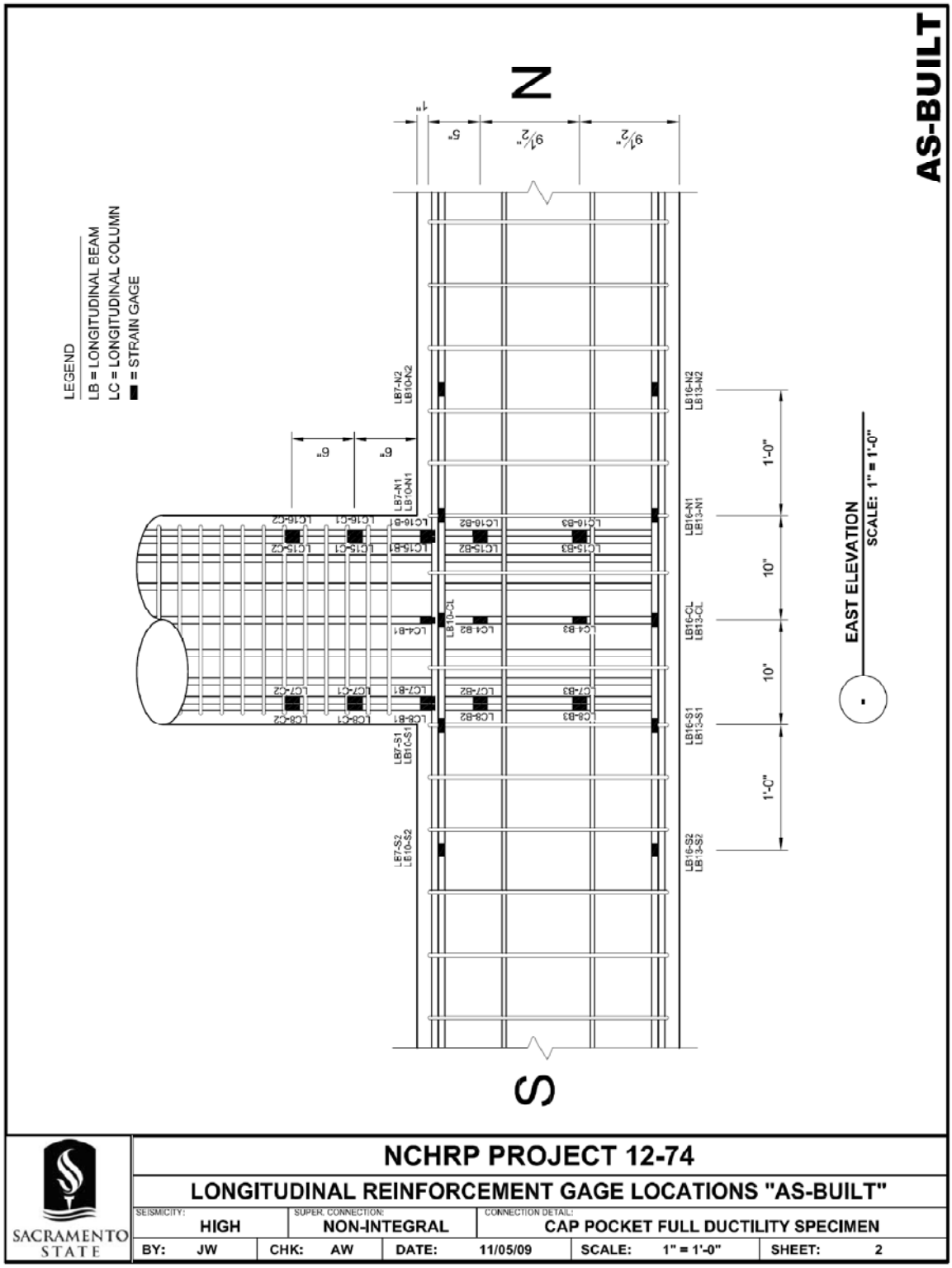

Figure 2-30. Instrumentation Drawings—Longitudinal Reinforcement Strain Gage Locations (As-built)

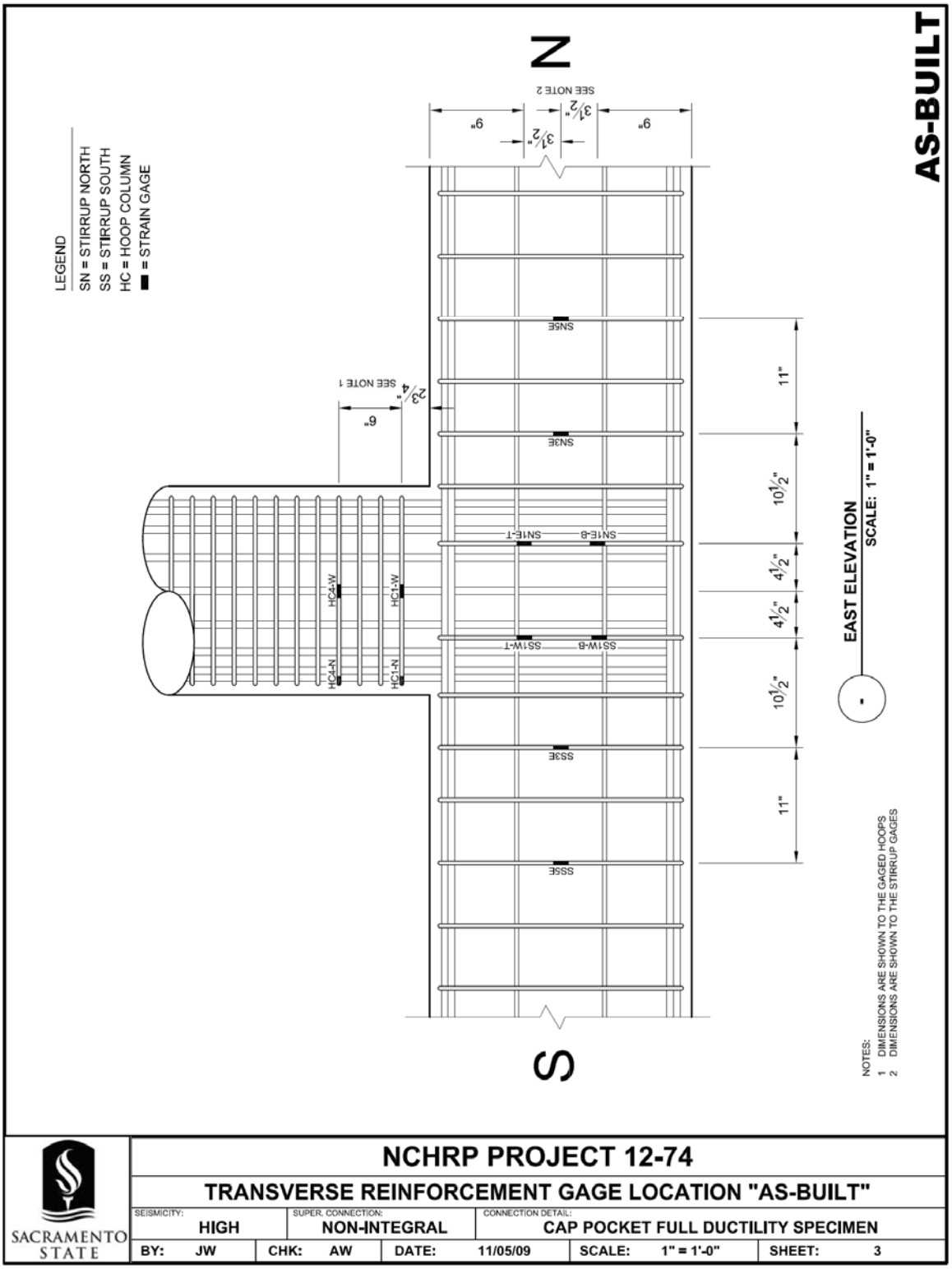

Figure 2-31. Instrumentation Drawings—Transverse Reinforcement Strain Gage Locations (As-built)

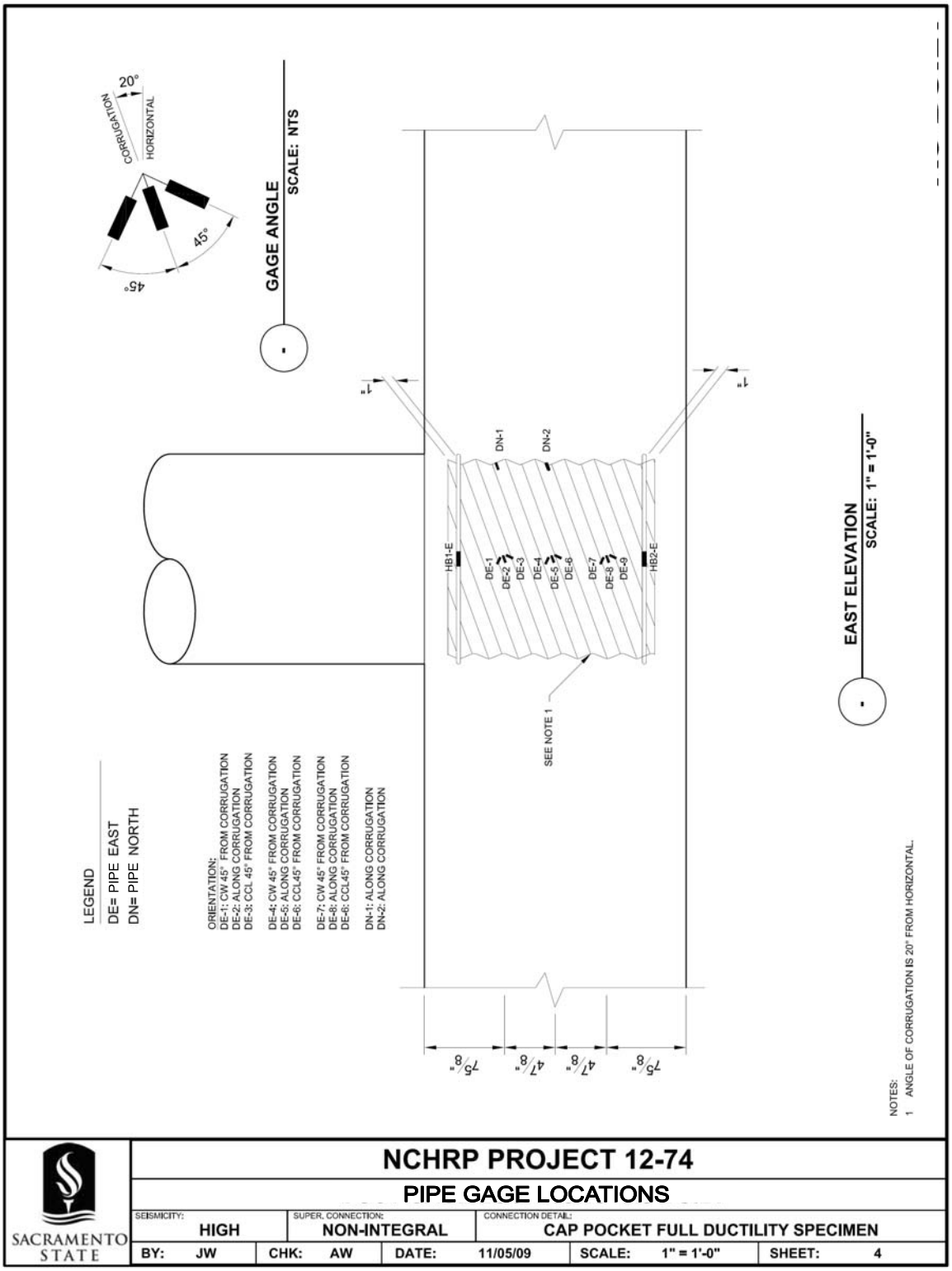

Figure 2-32. Instrumentation Drawings—Pipe Strain Gage Locations

Figure 2-33. Internal Instrumentation Photos—Strain Gage on Pipe

Figure 2-34. Internal Instrumentation Photos—Strain Gages on Rebar

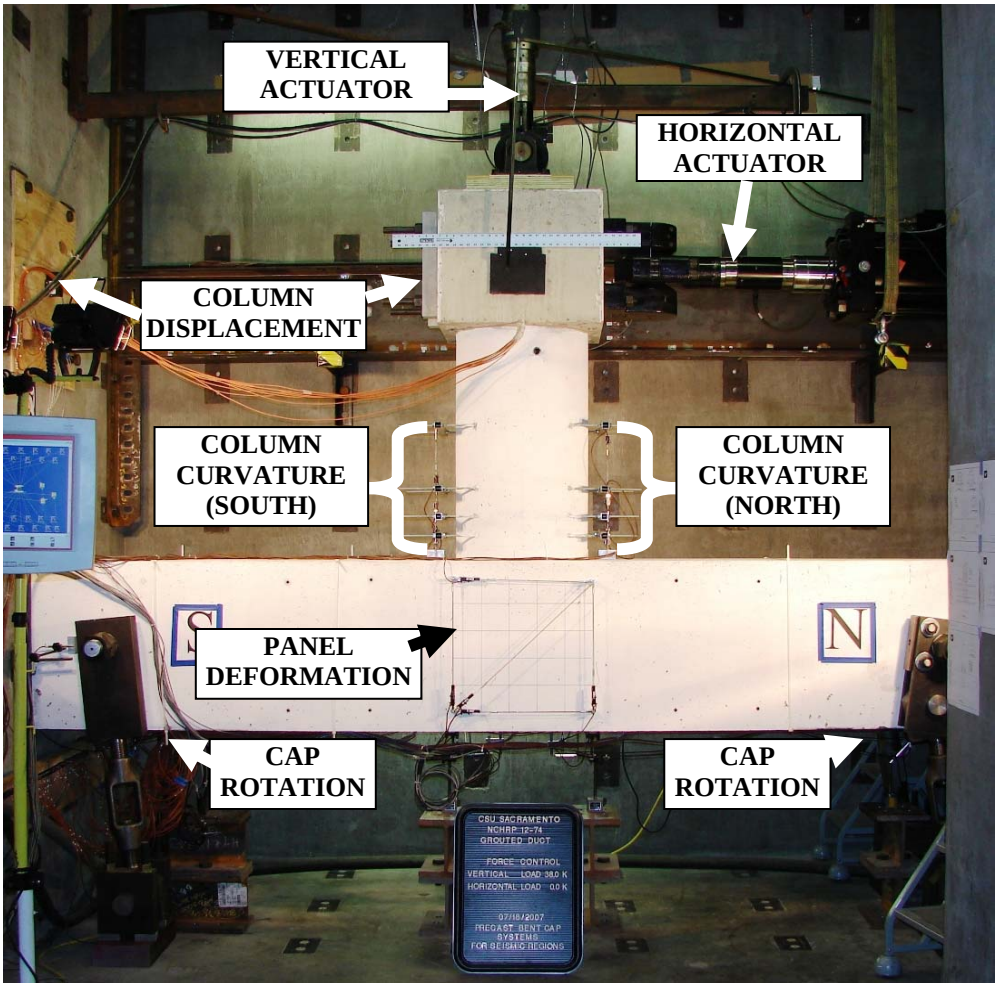

Figure 2-35. External Instrumentation Photos—Overall View

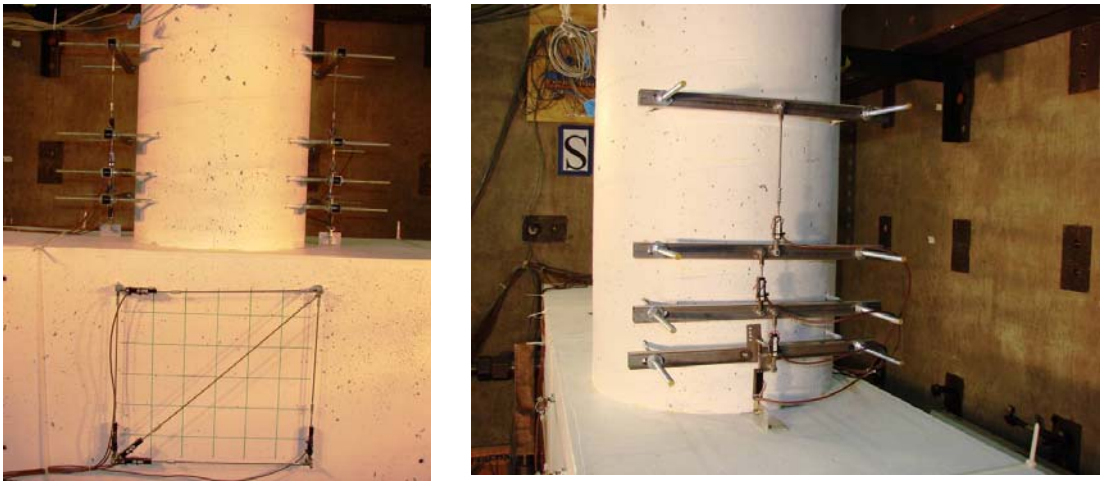

Figure 2-36. External Instrumentation Photos—Panel Deformation and Column Curvature

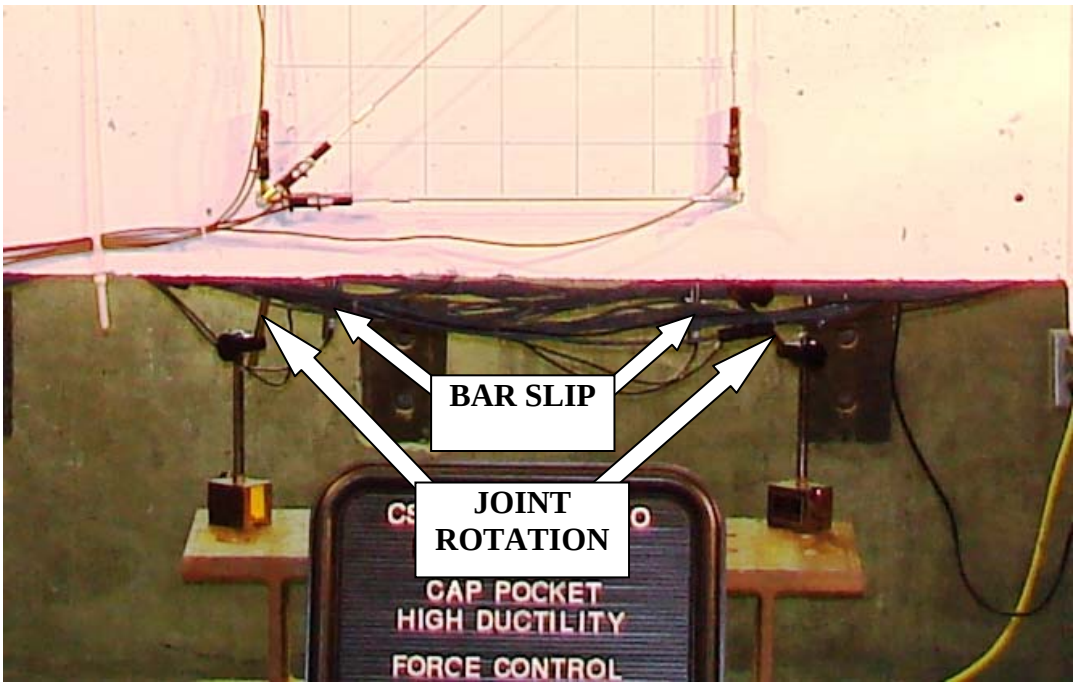

Figure 2-37. External Instrumentation Photos—Joint Rotation and Bar Slip

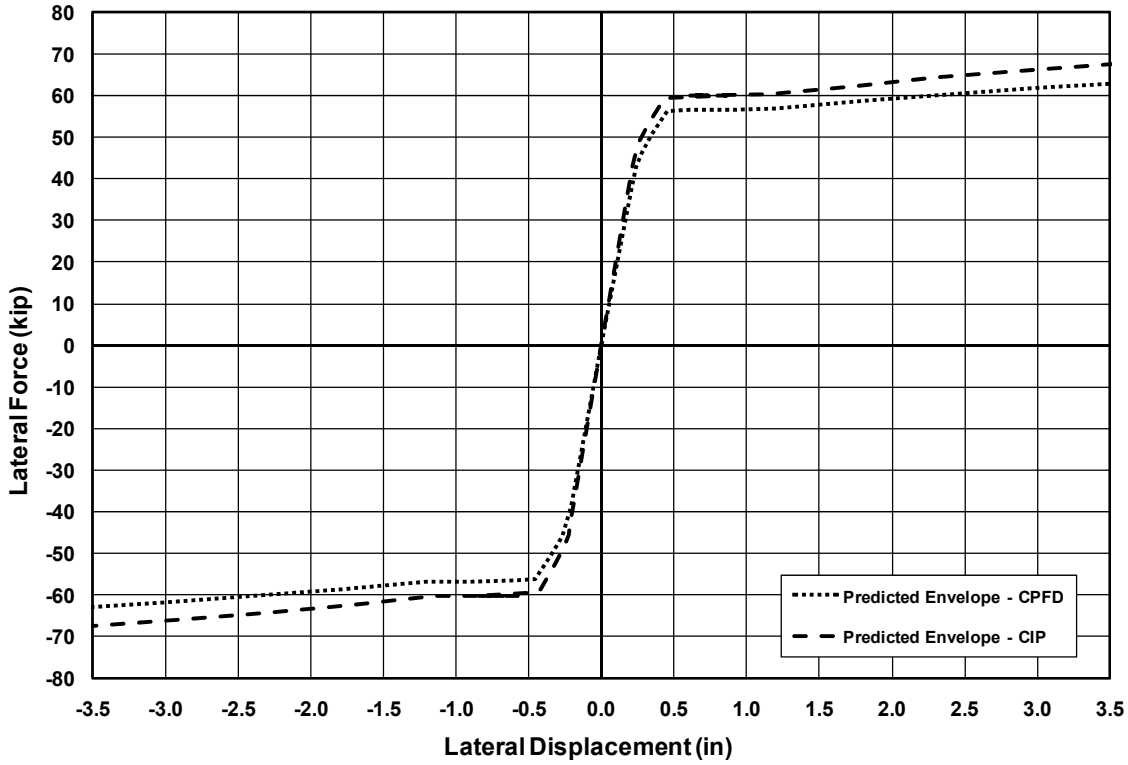

Figure 2-38. Predicted Lateral Force vs. Lateral Displacement Envelope—CPFD vs. CIP

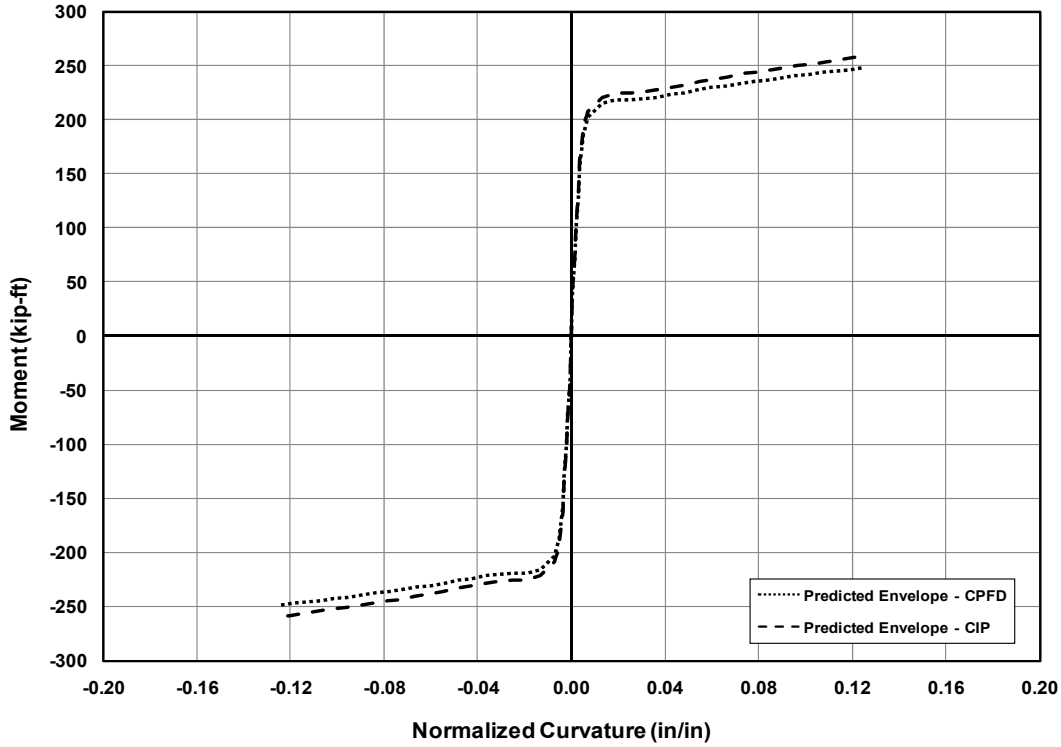

Figure 2-39. Predicted Normalized Moment vs. Curvature Envelope—CPFD vs. CIP

3.0 Specimen Response and Analysis

3.1 Experimental Observations

This section summarizes experimental observations made during testing, based on visual inspection and digital photos. Photos of the specimen include color-coded markings adjacent to cracks, as follows:

- Yellow: Pre-existing cracks prior to applied loading
- Brown: Cracks that formed or extended under vertical actuator loading
- Blue: Cracks that formed or extended under push direction loading
- Red: Cracks that formed or extended under pull direction loading

Markings also included: 1) load level or displacement ductility level; and 2) transverse mark perpendicular to marking to identify end of crack. Crack widths were measured while the specimen load or displacement was held nearly constant.

In reporting specimen response, displacement ductility, μ, and drift ratio are both used. (Note: "drift ratio" and "drift" are used interchangeably.) Drift ratio is defined as the column displacement divided by the column height, as a percent. This is a more consistent basis for comparison of specimen response. System ductility levels are also reported but, though reasonable, these values should be considered nominal (i.e., approximate) due to the approximate determination of first yield. Table 3-1 summarizes the associated values of force, displacement, ductility, and drift ratio for Force Control and Displacement Control stages (push and pull, Cycle 1). Table 3-2 provides a summary for comparing the Table 3-1 values for CPFD to that for CIP (Push, Cycle 1).

3.1.1 Stages of Cracking

The specimen was observed for crack formation and growth under loading sequences. Some pre-existing hairline horizontal cracks were observed along the column, but cracks appeared to have a negligible effect on response. Table 3-3 compares the predicted and actual stages of specimen cracking under Force Control and shows that observed bent cap, column and joint cracking occurred reasonably close to predicted loads. It should be noted that observation of initial (visible) hairline cracks is approximate and also depends on load increments selected because the specimen was not

inspected until after the peak load associated with a load increment was reached. Diagonal cracks were first observed in the joint region under Force Control loading at 44 kips, and crack widths did not exceed 0.003 in. Cracks did not extend through the joint region as in earlier specimens, but were limited to locations above and below the pipe location. Figures 3-1 and 3-2 show the specimen crack pattern at the last two Force Control sequences (30 kips and 44 kips).

3.1.2 Select Observations

Specimen response was dominated by plastic hinging of the column adjacent to the bent cap, as intended by the specimen design. This is clearly shown in Figures 3-3 through 3-6, which document response for drift ratios of 1.1% to 4.3% (μ2 to μ8). In contrast to the significant column flexural (and shear) cracks associated with increasing lateral load, relatively minor joint and bent cap cracks developed. This corresponded well with the capacity design philosophy. Hysteretic response is discussed in further detail in subsequent sections.

The following additional observations were made:

- Initial diagonal cracking in the joint occurred at 44 kips (both push and pull directions, under Force Control). However, joint shear cracking was limited to locations above and below the corrugated pipe. Additional diagonal cracks formed above and below the pipe location on the east and west faces at increasing loads corresponding with drifts from 0.6% (μ1, 46.8 kips) to 3.2% (μ6, 54.4 kips). Only at a 3.2% drift (μ6, pull) did diagonal cracks pass through the central portion of the joint itself. Particularly striking was the relatively small crack widths that developed for all diagonal cracks (≤0.009 in). No spalling occurred in the joint region during testing. In addition, a 9-in long horizontal crack near mid-depth formed south of the joint on the west side, opening to 0.03 in. A similar crack developed more progressively north of the joint. Figure 3-10 shows the joint crack patterns for east and west sides of the cap.

- Two symmetrical vertical flexural cracks developed in the joint, near the locations of the vertical construction stirrups. These cracks extended nearly through the entire depth of the bent cap and widened to a maximum of 0.02 in. Other flexural cracks developed in the bent cap, but widths were relatively minor. As shown in Figure 3-34, flexural cracks at the bottom of the cap (as tested) extended through the width of the bent cap, including the cap pocket.
- Initial spalling of the column above bedding layer at a drift of 0.9% (μ1.5) with spalling much more evident at a drift of 3.2% (μ6). See Figures 3-5 and 3-7.
- Minor radial splitting cracks formed at 1.1% drift (μ2) on the top surface of the bent cap (as tested) and extended down the side face of cap at larger drifts. Splitting cracks also developed vertically along column longitudinal bars. See Figures 3-8 and 3-9.
- Column longitudinal bar buckling initiated at a drift of 4.3% (μ8, push), followed by fracture of two longitudinal bars (μ8, pull), as shown in Figure 3-9. Buckling corresponded with load degradation.
- At ultimate, spalling had developed along a length of approximately 6.5 in along the plastic hinging region (length equal to 33% of the column diameter). See Figures 3-6 and 3-9.
- Post-test inspection revealed that the cap pocket concrete and bedding layer performed integrally with the surrounding concrete (Figure 3-33). Column longitudinal bars were well anchored within the pipe, and although splitting cracks developed in the bent cap, there was no evidence of splitting between bars within the pipe, initiation of pullout failure, significant bar slip or pipe slip.
- Overall, the specimen exhibited excellent ductility, achieving a high level of drift (over 4.3% at μ8). Although the first column hoop below the top of column (as fabricated) was placed 1.94 in below its intended location, contributing to buckling of the column longitudinal bars after spalling, system response indicates that the maximum lateral load had already been reached.

3.1.3 Comparison with Cast-in-Place Specimen

As shown in Table 3-4, concrete and rebar strengths for the bent cap compare reasonably closely for the specimens. Table 3-5 compares the CPFD and CIP stages of specimen cracking. CPFD specimen stages of cracking compare reasonably well with the CIP specimen. Specimens developed flexural cracking in the column and joint at very similar loads, although flexural cracking of the CPFD specimen occurred during initial vertical loading.

Select observations of response for the specimens also compare closely. Response for both specimens was dominated by extensive plastic hinging of the column adjacent to the bent cap, with relatively minor cracking in the joint and bent cap. Failure was precipitated by buckling of column bars, followed by bar fracture.

3.2 Hysteretic Response

3.2.1 Column Load-Displacement Response

The lateral force-lateral displacement (hysteretic) response of the column, used to characterize the fundamental performance of the specimen, is shown in Figure 3-11 together with the response envelope and predictions. The primary aspects of the response were:

- Plastic hinging of the column enabling the specimen to undergo a large drift ratio of 4.3% (μ8, push and pull)
- Stable hysteretic behavior with loops of increasing area and a strength degradation of 17% at the maximum drift (push)
- Maximum loading of approximately 55 kips (push) with 99% of this load sustained up to a drift of 3.2% (μ6, push); 100% of 57 kips sustained to 3.1% (pull)
- Strength degradation of 18% (between first cycles) at a drift of 4.3% (μ8, push) associated with column bar buckling; in addition, strength degradation of 18% between first and second cycles at μ8

A comparison of the response envelope to the predicted envelope shows a good correlation. Although the specimen capacity was slightly smaller than predicted, the

specimen maintained 99% of its capacity through the first cycle at a drift of 3.2% (μ6) and 82% through the first cycle at a drift of 4.3% (μ8). In the pull direction, a slightly larger load was maintained to a similar drift with a smaller degradation (14%).

The hysteretic response also portrayed appropriate stiffness, strength, ductility and other features such as crack distribution and width representative of emulative response. The dominance of ductile plastic hinging in the column and minimal damage in the capacity-protected joint and bent cap satisfied the performance goal for the CPFD as an emulative specimen.

3.2.2 Equivalent Viscous Damping

Determination of the equivalent viscous damping ratio provides a quantitative means to establish the energy dissipating characteristics and loop stability of the specimen for comparison to the CIP control and other precast specimens. The equivalent viscous damping ratio, ξ, represents the energy dissipation per cycle, determined as follows: [12]

$$\xi = \left(\frac{2}{\pi}\right)\left(\frac{A_L}{A_R}\right)$$

where:

A_L =area of hysteretic loop for a complete cycle (push and pull)

A_R =area of rectangle bounded by maximum loads and displacements of a complete hysteretic loop

Figure 3-12 plots the equivalent viscous damping ratio, ξ, versus drift ratio, including the first two cycles for each drift ratio. ξ increased significantly with increasing drift ratio, reaching approximately 26% (first cycle, 4.3% drift). This level is considered suitable for ductile response of a precast beam-column connection emulating a conventional cast-in-place connection. ξ increased slightly between the first and second cycles at larger drifts.

3.2.3 Comparison with Cast-in-Place Specimen

Figure 3-13 shows the envelopes for the CPFD and CIP hysteretic response. A very close comparison is evident. The strength, stiffness, and ductility up to

approximately 1.9 in (3.2% drift, push) are nearly identical. Overall, the CIP achieved a higher drift (5.9% vs. 4.3%), but a 3% lower load. It should be noted that differences at higher levels of drift correspond to strength degradation associated with column bar buckling rather than precast connection response.

Figure 3-14 compares the equivalent viscous damping ratio, ξ, versus drift ratio for the CPFD and CIP specimens. CPFD values are shown to be slightly larger, although a similar trend is evident. For example, at a drift of 4%, the first cycle ξ was 25% for CPFD and 23% for CIP, a minor difference.

3.3 Column Curvature Response

3.3.1 Moment-Curvature

Figure 3-15 plots normalized moment-curvature response for the first curvature cell up the column, together with the predicted envelope. Predicted and measured response envelopes are shown to compare favorably. Extensive curvature ductility associated with plastic hinging is evident. Cell 1 maximum curvature was approximately 21 times the effective yield curvature (estimated). The performance of the Cell 2 linear potentiometers in the push direction was questionable.

The moment at the midheight of the cell was used for plotting, except that strain penetration was accounted for Cell 1. In addition, data was corrected for joint rotation to provide a matching basis for predictions. Note that the curvature was normalized by multiplying curvature by the column diameter; moment was not modified.

3.3.2 Curvature over Height

Figures 3-16 and 3-17 show the normalized curvature profile over the column height for the Force Control and Displacement Control sequences, respectively. Curvature for the first cycle is used for Displacement Control values. These profiles demonstrate the concentration of plasticity adjacent to the soffit, as well as the spread of plastic hinging up the column under increasing displacement. Based on an estimated first yield normalized curvature of approximately 0.0036 in/in, it is evident that under the final loading cycle of Force Control (44 kips) column bars yielded. Figure 3-17 indicates that

much more significant inelastic response developed over an increasing height under Displacement Control.

3.3.3 Comparison with Cast-in-Place Specimen

Figure 3-18 plots the Cell 1 normalized moment-curvature prediction and response envelopes for the CPFD and CIP specimens. A very close comparison is evident for the response envelopes. Curvature over height can be compared for the CPFD and CIP specimens by comparing Figures 3-16 and 3-17 to Figures 3-19 and 3-20. These figures demonstrate a similar trend for the CPFD and CIP specimens.

These similarities provide evidence of emulative behavior of the CPFD specimen relative to the CIP control specimen.

3.4 Displacement Decomposition

Displacement decomposition refers to the separation of the column displacement into the various components that contribute to the overall lateral displacement of the column. Components include column flexure, fixed end rotation (due to plastic hinging plus bar slip), column shear, bent cap flexibility, and joint shear. Decomposition quantifies the magnitude of each component, and is determined for comparison of analytical predictions to experimental measurements. Figure 3-21 shows a schematic representation of the experimental column displacement components, including applicable equations based on measured quantities.

Some limitations exist when comparing predicted and measured displacements. For example, in the test program the column shear displacement was not measured but was estimated analytically. In addition, the joint shear displacement was not determined analytically but was measured. This leads to some approximation.

Properly designed cast-in-place and emulative bridge bents are expected to display flexural plastic hinging, which result in flexural displacement components dominating the displacement at increasing drift or displacement ductility levels. The total experimental flexural component is taken as the sum of the fixed end rotation plus column flexure. Fixed end rotation represents displacement due to plastic hinging within the first curvature cell plus displacement due to bar slip. However, because the plastic

hinging length extended beyond the first curvature cell, plastic hinging response also contributed to the column flexure component. Thus, the total predicted flexural displacement is compared to the sum of column flexure and fixed end rotation.

To match the assumption of ideal pin and roller support conditions, rigid body translation and rotation of the specimen were removed from the raw data during data reduction.

3.4.1 Overview

Table 3-6 summarizes the displacement decomposition for the first push and pull cycles for drift ratios from 0.6% to 4.3%. For each drift ratio, results are tabulated in two columns. The first column includes two sections: 1) the top section summarizes the column displacement (CD) and the corresponding drift and force; and 2) the bottom section lists the displacement components determined from measurements, as shown in Figure 3-21, and the sum of the components (Component Total, CT). At the bottom of the table is the CT/CD ratio, indicating what portion of actual displacement is represented by the measured components.

The second column shows the analytically predicted displacement components. Although the load-displacement envelope was predicted pretest, the actual displacements imposed on the specimen were not well defined pretest, as these are dependent on the establishment of first yield, which was approximate. Thus, the second column shows predicted displacement components that sum up the imposed displacement in the test (i.e., CT/CD=1.0). In addition, predicted displacements are based on actual material properties. This approach allows actual and predicted displacement components to be appropriately compared, as shown in the third column (Actual/Predicted ratio).

Some approximation is expected in predicted and measured values. Joint shear was not predicted and column shear was predicted but not measured. The difference between CT and CD represents column displacement due to column shear, joint shear and potential inaccuracies in measurements. Joint shear was not expected to represent a large percentage of the total measured displacement in full ductility specimens. Although prediction of column shear is considered approximate, inclusion of this component in

predictions allows a more realistic comparison in Actual/Predicted ratios: omission of column shear in predictions would require its portion to be incorrectly assigned to column flexure and bent cap rotation, biasing ratios. Significant column shear cracking is clearly shown in Figures 3-1 through 3-6. To some extent, these approximations tend to offset one another; however, some error is introduced in the process.

3.4.2 Fixed End Rotation, Column Flexure, and Bent Cap Flexibility

As shown in Table 3-6 for the push direction, the CT/CD ratios ranged from 0.90 to 0.96 (0.92 average) through a drift of 2.2% (μ4, push), and a lower value of 0.74 at μ6. This suggests that the displacement components were reasonably determined overall. (Some column curvature gage readings were not reliable at 4.3% drift (μ8)). The Actual/Predicted ratios for flexure ranged between 0.76 and 1.00 (0.91 average), which also indicate reasonably accurate predictions for flexure. Bent cap flexibility was less accurately predicted; however, joint rotation was underestimated in predictions. In addition, as shown in Figure 3-22, the bent cap flexibility contribution to overall displacement was much smaller than column flexure. Similar overall trends are evident in Table 3-6 for the pull direction.

Figure 3-23 plots the displacement decomposition component values for the push and pull directions. The height of each bar segment shows the relative contribution of a component. In correlation with experimental observations of the specimen, the flexural component (fixed end rotation, FER, and column flexure) dominated the response and increased significantly with increasing drift. Bent cap flexibility provided a smaller contribution with joint shear clearly being the smallest contributor.

Figure 3-24 plots the displacement decomposition components as a percentage of the total component displacement (CT). For example, at a push drift of 0.9% (μ1.5), the flexural component (fixed end rotation and column flexure) accounted for 76% of CT (column elastic plus plastic deformation was predicted to represent 75%). However, at a push drift of 2.2% (μ4), the flexural component accounted for 87% of CT (vs. prediction of 84%). This corresponded well with the observed dominance of plastic hinging in the column. Similar ratios developed for the pull direction.

Although the flexural component for push and pull directions match predictions well, it is noted that the fixed end rotation for the push direction was clearly larger than for the pull direction. This can be explained in part by Figure 3-25, which shows that the large flexural crack that developed at the bottom of the column for push direction loading remained within Cell 1, whereas for the pull direction the flexural crack extended into Cell 2.

As shown in Figures 3-23 and 3-24, the bent cap flexibility (joint rotation) component increased in magnitude but decreased in percentage of CT with drift. This component averaged 14%, and its relative contribution decreased from 20% at μ1 to 9% at μ6.

3.4.3 Joint Shear

Figures 3-23 and 3-24 confirm the minor contribution of joint shear, with the joint shear displacement averaging a 5% contribution to CT in the push direction. Joint shear was the smallest measured contributor to column displacement.

3.4.4 Bar Slip

Table 3-7 summarizes the bar slip component of column displacement and compares bar slip to fixed end rotation. By definition, fixed end rotation includes the effect of bar slip on rotation. Because of limited data, comparisons are made using data from Cycle 2 at a 3.2% drift.

As shown in the table, bar slip was minor, contributing less than 7% on average to the displacement component attributable to fixed end rotation. Due to bar anchorage forces, splitting cracks formed in the bent cap and column, and the top surface of the bent cap (as tested) exhibited splitting cracks; however, column bars were well anchored within the joint. In addition, there was no evidence of splitting within the pipe, initiation of pullout failure, significant bar slip or pipe slip.

The embedment depth of the #5 column bars into the bent cap, l_{ac}, was 22 in, or an l_{ac}/d_b ratio of 35.2. This depth matches that used for the CIP specimen, which conforms to joint requirements of the 2006 LRFD RSGS and 2009 AASHTO Guide Specifications for LRFD Seismic Bridge Design (2009 LRFD SGS), which require

column bars to be extended as close as practically possible to the opposite face of the bent cap for development of the force transfer mechanism. [5, 13] Prior research on column bars anchored in grout pockets indicate that an l_{ac}/d_b ratio of $2.3f_y/f'_c$ should be used (based on bar anchorage only). [14, 15] For the CPFD specimen, this corresponds to an l_{ac}/d_b ratio of 29.0. The large embedment depth, together with a properly concreted pocket, helped ensured adequate bar anchorage and minimal slip.

3.4.5 Comparison with Cast-in-Place Specimen

The displacement decomposition percentages for the CPFD and CIP specimens are shown in Figures 3-24 and 3-26, respectively. A review of values (FER+Column flexure, bent cap flexibility, and joint shear) shows a close comparison between the CPFD and CIP specimens. The relative contributions were similar, as well as the individual magnitudes. For example, at a push drift of approximately 1.1% (CPFD, 1.10%; CIP, 1.19%), FER+Column flexure percentages were within 3% of one another (78.5% CPFD vs. 81.5% CIP). Bent cap flexibility for CPFD was 16% vs. CIP 14%, while joint shear for the CPFD was 5.8% and 4.2% for CIP. The ranges of CT/CD ratios for CPFD also compared favorably to the CIP.

Table 3-7 summarizes the bar slip component of column displacement for both the CPFD and CIP specimens, at a drift of 3.2%. The CPFD slip is shown to be very close to the CIP slip, exceeding it by only 15% on average. For both specimens bar slip was found to be a very minor component of FER: approximately 7% for CPFD and 6% for the CIP, on average.

3.5 Joint Response

This section summarizes joint response in terms of joint shear stress, principal stresses and angle, joint cracking, joint deformation, and bedding layer.

3.5.1 Joint Shear Stress, Principal Stresses, and Principal Angle

The average joint shear stress, plotted in Figure 3-27, exhibits a similar hysteretic trend as the load-displacement plot and relatively small stresses. Figure 3-28 shows the joint shear stresses vs. shear strain, including appropriate stiffness and limited softening at increasing drift ratios. Shear stress and shear strain are calculated as shown in the List

of Equations and, strictly speaking, refer to average (or nominal) values applicable to the joint region.

Shear stresses, which did not exceed $4.4\sqrt{f_c^{'}}$, were used in determining the principal stresses and principal angle shown in Figures 3-29 though 3-31. Figure 3-29 shows that the principal tensile stress was limited to $4.8\sqrt{f_c^{'}}$, less than half of the 2006 LRFD RSGS limit of $12\sqrt{f_c^{'}}$, but 37% larger than $3.5\sqrt{f_c^{'}}$, the level at which more extensive (additional) joint reinforcement is required by 2006 LRFD RSGS. Figure 3-30 indicates that the principal compressive stress did not exceed $0.07 f_c^{'}$, less than a third of the 2006 LRFD RSGS limit of $0.25 f_c^{'}$. These values correspond well with the intentions of the design and the observed joint performance.

Figure 3-31 plots the angle of the principal plane angle in the joint, which is shown to be approximately 40-45 degrees from horizontal, with the push direction shown to be slightly smaller. These values correlate well with the expected response.

3.5.2 Joint Cracking

Diagonal cracking was limited within the joint region. Figure 3-10 shows the joint crack patterns for east and west sides of the cap post test. Only at a 3.1% drift (μ6, pull) did diagonal cracks pass through the central portion of the joint itself. These east face cracks were consistent with the principal angles reported in the previous section. Diagonal cracks also developed above and below the corrugated pipe at earlier stages of loading. In addition, two symmetrical vertical flexural cracks developed through the joint, near the locations of the vertical construction stirrups in the joint. These cracks extended nearly the entire depth of the bent cap and widened to 0.02 in. In addition, a 9-in long horizontal crack formed south of the joint on the west side, opening to 0.03 in.

Table 3-8 summarizes the maximum measured surface crack widths for diagonal cracks in the joint region at the various drift and lateral force levels. Particularly striking was the relatively small crack widths that developed for all joint cracks. The maximum

crack width was only 0.009 in, which occurred at the maximum applied force (1.4% drift, μ3 pull). No spalling occurred in the joint region during testing.

3.5.3 Joint Rotation and Deformation

Joint rotation and panel deformation were measured during the test. Figure 3-32 shows joint rotation magnitude, which was limited to less than 0.0017 rad (0.10 deg). This was approximately twice that assumed in predictions; however, predictions were based on an estimate of cracked bent cap section properties.

The deformation of the joint was measured using linear potentiometers in the region of the joint. The maximum change in panel area was very small, limited to less than 0.2%. This corresponds with the limited joint cracking.

3.5.4 Bedding Layer

The 1.5-in bedding layer appeared to perform integrally with the column through 4.3% drift and did not produce unusual behavior in the joint or specimen. As shown in Table 2-4, strength and stiffness properties for the column and pocket concrete matched well. There was no discernable boundary between the bedding layer and column. The bedding layer concrete was not a weak link in the system. In addition, closely spaced vertical cracks did not develop at the bedding layer. Figure 3-33 shows the interface between the bedding layer and column concrete post test. The boundary between the two surfaces was difficult to distinguish, although after removal of core concrete, it was more evident.

Post-test inspection indicated that grouting of air voids at the bedding layer provided a suitable bearing and did not appear to affect response.

3.5.5 Cap Pocket

Figure 3-34 shows the exposed surface of the cap pocket (bottom of cap as tested). Two flexural cracks developed through most or all of the bent cap width, including across the pipe. No slip was visible between the pocket concrete and bent cap. This suggests integral behavior between the pocket concrete, pipe, and surrounding concrete.

3.5.6 Comparison with Cast-in-Place Specimen

The precast joint region for the CPFD specimen performed with limited distress during the test and compared reasonably closely to the CIP joint in terms of the parameters listed in Table 3-9: maximum stresses, principal angle, joint rotation and change in panel area. Accounting for the different concrete strengths (Table 3-4), the CPFD maximum stresses (nominal joint shear, principal tensile, and principal compressive) were 11%-19% smaller. The principal angle differed by 2%. The maximum applied force was nearly the same for both specimens.

Although joint distress was limited for both specimens, there were significant differences in panel deformation and joint crack patterns. Table 3-9 shows that the maximum change in the CPFD panel area was approximately 20% less than that for the CIP specimen. This smaller deformation corresponds with the fewer diagonal cracks in the CPFD joint region and significantly smaller maximum diagonal crack width (0.009 in) compared to the CIP joint (0.025 in). However, joint shear stress-strain response, including stiffness and maximum strain, was similar for the two specimens.

Joint crack patterns differed significantly between the specimens, as shown in Figure 3-35. CPFD diagonal cracking was limited to regions above and below the corrugated pipe through a drift of 3.1% (μ6, pull) at 57.0 kips, which was approximately 2% less than the maximum lateral load. Diagonal cracking did not extend into the central joint region for the push direction, which reached a 3% lower load than for the pull direction. In addition, two symmetrical vertical flexural cracks developed through the joint, near the locations of the vertical construction stirrups in the joint. The CIP joint exhibited a more extensive pattern of diagonal cracks through the joint region for both push and pull loading. CIP vertical flexural cracks in the joint region were not as extensive as the CPFD flexural cracks. The different CPFD crack pattern and widths suggest a somewhat different load path in the joint region due to the corrugated pipe. No spalling occurred for either specimen within the joint.

3.6 Strain Records

This section uses strain profiles and tables to present select results from specimen strain records, as well as comparisons to the CIP specimen. Profiles show the strain levels for a series of strain gages at specific regions of the specimen and for specific load or ductility (drift) levels. Profiles include strain for: 1) column longitudinal rebar (locations along the column and into the joint); 2) hoops in the column and joint; and 3) stirrups in the bent cap and joint. A table is provided for the bent cap longitudinal rebar (locations along the bent cap, including through the joint).

Some gages reliably recorded large strains well in excess of yield, while others produced unreliable data typically after bar yield. Plots reflect only data considered reliable.

Only select strain gage records are discussed. These strain records and others will be further analyzed and addressed through future efforts.

3.6.1 Column Longitudinal Rebar

3.6.1.1 Cap Pocket Specimen

Figure 3-36 shows the strain profile for the extreme column bar on the north side of the specimen. As expected, column strains were largest in the plastic hinging region, with strain penetration including bar yield confirmed 6 in above and 6 in below the bedding layer. Records demonstrate that the strain dropped off at further distances away from the plastic hinging region.

3.6.1.2 Comparison with Cast-in-Place Specimen

Figure 3-37 shows the strain profile for the extreme column bar on the north side of the CIP specimen. An overall pattern similar to the CPFD response is evident, with the largest column strains in the plastic hinging region and reduced strains above and below. In addition, significant strain penetration was evident, including bar yield at 6 in into the joint. Somewhat larger strains developed for the CPFD specimen at 16 in below the bedding layer.

3.6.2 Column Hoops

3.6.2.1 Cap Pocket Specimen

Table 3-10 shows the strains in the hoops for three column gages above the bedding layer (as tested). Two of the gages were placed on the west side, where out-of-plane transverse tension caused by concrete dilation can produce larger hoop strains. Tabulated values show that hoop strains in the plastic hinging regions exceeded yield for all gages, reflecting the confining effect of the hoops. Strain levels decreased at distances away from the bedding layer, and yield of the hoops extended up the column as plastic hinging progressed.

3.6.2.2 Comparison with Cast-in-Place Specimen

Similar to the CIP specimen (Figure 3-38), CPFD hoop strains shown in Table 3-10 in the plastic hinging region were largest, reflecting confinement. In addition, strains at 6 in above the joint remained near or above yield for both specimens.

3.6.3 Pipe Strain

3.6.3.1 Cap Pocket Specimen

Table 3-11 summarizes tensile strains in the corrugated pipe at several locations, as well as strains for several column longitudinal bars at similar depths as the pipe gages. As shown in the table, strain gage rosettes were used on the east side of the pipe, but only linear strain gages (along the corrugation) on the north side. Thus, Table 3-11 shows the principal strain and principal angle strain for the rosettes as well as the linear strain and its angle along the corrugation for the other gages. Values are provided for a drift of 1.6% (μ3), which corresponded to the maximum applied lateral load. In addition, strains for hoops placed 1.2 in from each end of the pipe are reported. An examination of these strains shows that strain levels in the pipe were minor, in contrast to the large strains in the column bars within the pipe. Column bars reached yield at various depths, but pipe principal strains did not exceed 37% of yield.

However, the hoops, which were placed at the ends of the pipe to reinforce the pipe and limit dilation and potential unraveling, achieved strains up to 52% yield, indicating the importance of their participation in the joint performance. It should be

noted that hoops first developed large strains at a load of 44 kips. This corresponded to the initial formation of diagonal cracks in the joint region, particularly at the ends of the pipe, as well as development and extension of other cracks.

Behavior of the pipe was not symmetrical in the push and pull directions. However, in the push direction, the strain along the corrugation dominated the response (e.g., compare DE-2 to DE-123). In addition, maximum strains occurred near mid-depth of the pipe.

3.6.3.2 Comparison with Cast-in-Place Specimen

The distribution of strains in the CPFD pipe differed considerably from the CIP hoops. The peak strain in the pipe was located at mid-depth (12.5 in), whereas the hoop strain was minimum at the same depth at most drift ratios. In addition, the hoop strain exhibited a peak at approximately two-thirds of the depth of the cap (18 in), per Figure 3-38. This suggests different joint behavior for the two specimens.

The magnitude of strains for the pipe and hoops also differed. In contrast to the minor levels of principal strain in the pipe (37% of pipe yield), the CIP hoops exhibited a peak strain of nearly twice as large (64% of bar yield). However, the hoop force associated with the pipe was approximately twice that required for equivalence to the CIP hoops because the pipe yield strength turned out to be approximately twice the nominal value used in pipe design.

3.6.4 Bent Cap Longitudinal Rebar

3.6.4.1 Cap Pocket Specimen

Table 3-12 lists bent cap longitudinal bar strain (top and bottom bars) for the first cycle of three nominal displacement ductilities of Displacement Control (μ2, μ4, μ6) during which the maximum load was reached. This table shows that strain levels for bottom and top bars were largest within the joint (S1, CL, and N1 positions) and that yield was nearly reached and/or exceeded at the centerline (CL) of the joint for both top and bottom bars. In addition, strain levels of approximately 70% of yield were reached on the bottom bar at the faces of the joint. Strain patterns reasonably matched expected distribution per an assumed force transfer model similar to that of Reference 16. It

should be noted that the test specimens, designed per 2006 LRFD RSGS, did not include the significant additional area of bent cap longitudinal reinforcement ($0.245A_{st}$) required by 2009 LRFD SGS.

3.6.4.2 Comparison with Cast-in-Place Specimen

Table 3-13 compares the longitudinal bent cap strain (top and bottom bars) for the CPFD and CIP specimens. Strain patterns are shown to be reasonably consistent. The maximum strains for the bottom bar occurred in the joint region, with the CIP reaching 43%-46% of yield and the CPFD reaching 70% of yield or yielding (centerline). Strains at the south most (S2) and north most (N2) bars were similar. More limited comparisons are available for the top bar; however, the CPFD bar reached 99% of yield at the centerline.

3.6.5 Stirrups in Bent Cap and Joint

3.6.5.1 Cap Pocket Specimen

Figures 3-39 through 3-42 show the strain profiles for stirrups within the bent cap and joint. Two 2-leg stirrups were placed within the joint for constructability and other reasons, as explained in Section 2.2.1. Two strain gages were placed on the leg of each construction stirrup, at approximately the 1/3 and 2/3 points along the stirrups (Figure 2-31). Since stirrups in the regions adjacent to the joint used gages at the mid-height of the stirrup, two sets of plots are shown: 1) mid-height gages on stirrups outside the joint together with the top gage on the joint stirrups (Figures 3-39 and 3-40); and 2) mid-height gages on stirrups outside the joint together with the bottom gage on the joint stirrups (Figures 3-41 and 3-42).

Figures 3-39 and 3-40 show that strain in stirrups adjacent to the joint remained at very low levels under both Force Control and Displacement Control. In addition, stirrup strains were limited to 24% of yield within the joint under Displacement Control. Stirrups at the bottom location reached a similar minor level of 25% of yield (Figures 3-41 and 3-42). The low level of strain for these construction stirrups indicates its lack of contribution to joint performance.

3.6.5.2 Comparison with Cast-in-Place Specimen

The CPFD stirrup strain profiles reveal a significant departure from the CIP profiles shown in Figures 3-43 and 3-44. Although both CIP and CPFD stirrups show minor strains at regions adjacent to the joint region, CIP construction stirrups display a pronounced peak strain within the joint, reaching yield in tension at the north stirrup and 47% of yield in compression at the south stirrup. This is in contrast to the relatively minor strains (25% of yield or less) displayed for the CPFD construction stirrups. This indicates different joint behavior for the two specimens and minor contribution of the CPFD stirrups to joint performance.

3.7 Tables

Table 3-1. Associated Values of Force, Displacement, Ductility, and Drift Ratio—CPFD

Push (Cycle 1)					
Stage	Force (kips)	Disp (in)	Displacement Ductility, μ		Drift (%)
			Actual	Nominal	
Force Control	13.2	0.028	-	-	0.05
	20.4	0.048	-	-	0.08
	30.5	0.113	-	-	0.19
	44.6	0.265	-	-	0.45
Displacement Control	46.8	0.375	1.15	1.0	0.63
	51.5	0.504	1.54	1.5	0.85
	53.7	0.648	1.99	2.0	1.10
	55.1	0.955	2.93	3.0	1.62
	54.5	1.280	3.92	4.0	2.17
	54.4	1.887	5.78	6.0	3.20
	45.2	2.534	7.76	8.0	4.30
Pull (Cycle 1)					
Stage	Force (kips)	Disp (in)	Displacement Ductility, μ		Drift (%)
			Actual	Nominal	
Force Control	-12.9	-0.037	-	-	-0.06
	-20.1	-0.070	-	-	-0.12
	-30.2	-0.154	-	-	-0.26
	-44.4	-0.296	-	-	-0.50
Displacement Control	-42.8	-0.271	0.83	1.0	-0.46
	-48.8	-0.402	1.23	1.5	-0.68
	-50.6	-0.550	1.69	2.0	-0.93
	-53.0	-0.848	2.60	3.0	-1.44
	-54.3	-1.192	3.65	4.0	-2.02
	-57.0	-1.851	5.67	6.0	-3.14
	-49.0	-2.546	7.80	8.0	-4.32

Table 3-2. Associated Values of Force, Displacement, Ductility, and Drift Ratio (Push, Cycle 1)—CPFD vs. CIP

Push (Cycle 1)—CPFD					
Stage	Force (kips)	Disp (in)	Displacement Ductility, μ		Drift %
			Actual	Nominal	
Force Control	13.2	0.028	-	-	0.05
	20.4	0.048	-	-	0.08
	30.5	0.113	-	-	0.19
	44.6	0.265	-	-	0.45
Displacement Control	46.8	0.375	1.15	1.0	0.63
	51.5	0.504	1.54	1.5	0.85
	53.7	0.648	1.99	2.0	1.10
	55.1	0.955	2.93	3.0	1.62
	54.5	1.280	3.92	4.0	2.17
	54.4	1.887	5.78	6.0	3.20
	45.2	2.534	7.76	8.0	4.30

Push (Cycle 1)—CIP					
Stage	Force (kips)	Disp (in)	Displacement Ductility, μ		Drift %
			Actual	Nominal	
Force Control	13.0	0.034	-	-	0.06
	20.0	0.072	-	-	0.13
	30.1	0.154	-	-	0.27
	48.4	0.397	-	-	0.69
Displacement Control	40.0	0.406	1.13	1.0	0.71
	49.4	0.533	1.49	1.5	0.93
	53.3	0.684	1.91	2.0	1.19
	55.6	1.014	2.83	3.0	1.76
	54.6	1.345	3.75	4.0	2.34
	55.9	2.070	5.77	6.0	3.60
	53.2	2.638	7.36	8.0	4.59
	50.0	3.383	9.43	10.0	5.88

Table 3-3. Predicted vs. Actual Stages of Specimen Cracking

Stage	P_V (kips)		P_H (kips)	
	Predicted	Actual	Predicted	Actual
Bent Cap—Flexural	None	38	-	-
	38	-	3.6	-
Column—Flexural	38	38	11.3	13.0
Joint Shear	38	38	39.6	44.0

Table 3-4. Select Material Properties—CPFD vs. CIP

Parameter	CPFD		CIP	
Concrete Compressive Strength, f'_c	Cap and Column: 5,620 psi		Cap: 4,553 psi Column: 6,178 psi	
Steel Rebar Strength	Yield	Tensile	Yield	Tensile
#3 (Bent cap stirrups; Column hoops)	63.5	99.6	68.2	95.5
#5 (Bent cap longitudinal; Column longitudinal)	63.6	91.0	64.5	90.0
Cap Pocket Compressive Strength, f'_c	5,040 psi		N/A	

Table 3-5. Actual Stages of Specimen Cracking—CPFD vs. CIP

Stage	P_V (kips)		P_H (kips)	
	CIP	CPFD	CIP	CPFD
Bent Cap—Flexural	None	38	-	-
	38	-	13.0	-
Column—Flexural	38	38	20.0	13.0
Joint Shear	38	38	48.0	44.0

Table 3-6. Displacement Decomposition (1st Push and Pull Cycles)

Displacement Decomposition—Cap Pocket Full Ductility (1st Push Cycle)

	Actual	Predicted	Act/Pred	Actual	Predicted	Act/Pred	Actual	Predicted	Act/Pred	Actual	Predicted	Act/Pred
Displacement Ductility (μ)	**1.0**	-	-	**1.5**	-	-	**2.0**	-	-	**3.0**	-	-
Col Displacement [CD] (in)	0.375	0.375	1.00	0.504	0.504	1.00	0.648	0.648	1.00	0.955	0.955	1.00
Drift (%)	0.63	-	-	0.85	-	-	1.10	-	-	1.62	-	-
Force (kip)	46.8	51.9	0.90	51.5	56.3	0.91	53.7	56.5	0.95	55.1	56.7	0.97
Column Flexure (in)	0.045	0.290	0.85	0.051	0.376	0.92	0.054	0.501	0.95	0.123	0.779	1.00
Fixed End Rotation (in)	0.202			0.296			0.422			0.655		
Column Shear (in)	*	0.034	*	*	0.073	*	*	0.093	*	*	0.123	*
Bent Cap Flexibility (in)	0.068	0.050	1.35	0.083	0.054	1.54	0.095	0.054	1.77	0.102	0.054	1.88
Joint Shear (in)	0.022	*	*	0.028	*	*	0.035	*	*	0.040	*	*
Component Total [CT] (in)	0.336	0.375		0.459	0.504		0.606	0.648		0.920	0.955	
CT/CD	0.90	1.00		0.91	1.00		0.93	1.00		0.96	1.00	

	Actual	Predicted	Act/Pred	Actual	Predicted	Act/Pred	Actual	Predicted	Act/Pred
Displacement Ductility (μ)	**4.0**	-	-	**6.0**	-	-	**8.0**	-	-
Col Displacement [CD] (in)	1.280	1.280	1.00	1.887	1.887	1.00	2.534	2.534	1.00
Drift (%)	2.17	-	-	3.20	-	-	4.30	-	-
Force (kip)	54.5	57.1	0.95	54.4	58.9	0.92	45.2	60.6	0.75
Column Flexure (in)	0.176	1.081	0.95	0.116	1.610	0.76	**	2.175	**
Fixed End Rotation (in)	0.847			1.104			**		
Column Shear (in)	*	0.144	*	*	0.220	*	*	0.301	*
Bent Cap Flexibility (in)	0.112	0.055	2.03	0.119	0.056	2.12	0.119	0.058	2.04
Joint Shear (in)	0.045	*	*	0.049	*	*	0.047	*	*
Component Total [CT] (in)	1.180	1.280		1.388	1.887		**	2.534	
CT/CD	0.92	1.00		0.74	1.00		**	1.00	

Displacement Decomposition—Cap Pocket Full Ductility (1st Pull Cycle)

	Actual	Predicted	Act/Pred	Actual	Predicted	Act/Pred	Actual	Predicted	Act/Pred	Actual	Predicted	Act/Pred
Displacement Ductility (μ)	**1.0**	-	-	**1.5**	-	-	**2.0**	-	-	**3.0**	-	-
Col Displacement [CD] (in)	-0.271	-0.271	1.00	-0.402	-0.402	1.00	-0.550	-0.550	1.00	-0.848	-0.848	1.00
Drift (%)	-0.46	-	-	-0.68	-	-	-0.93	-	-	-1.44	-	-
Force (kip)	-42.8	-46.1	0.93	-48.8	-53.4	0.91	-50.6	-56.4	0.90	-53.0	-56.6	0.94
Column Flexure (in)	-0.077	-0.208	0.86	-0.113	-0.306	0.94	-0.172	-0.416	1.02	-0.223	-0.679	0.95
Fixed End Rotation (in)	-0.102			-0.174			-0.252			-0.420		
Column Shear (in)	*	-0.018	*	*	-0.045	*	*	-0.080	*	*	-0.114	*
Bent Cap Flexibility (in)	-0.035	-0.044	0.79	-0.047	-0.051	0.91	-0.057	-0.054	1.06	-0.069	-0.054	1.27
Joint Shear (in)	-0.017	*	*	-0.022	*	*	-0.027	*	*	-0.032	*	*
Component Total [CT] (in)	-0.230	-0.270		-0.357	-0.402		-0.509	-0.550		-0.743	-0.848	
CT/CD	0.85	1.00		0.89	1.00		0.92	1.00		0.88	1.00	

	Actual	Predicted	Act/Pred	Actual	Predicted	Act/Pred	Actual	Predicted	Act/Pred
Displacement Ductility (μ)	**4.0**	-	-	**6.0**	-	-	**8.0**	-	-
Col Displacement [CD] (in)	-1.192	-1.192	1.00	-1.851	-1.851	1.00	-2.546	-2.546	1.00
Drift (%)	-2.02	-	-	-3.14	-	-	-4.32	-	-
Force (kip)	-54.3	-56.8	0.96	-57.0	-58.8	0.97	-49.0	-60.6	0.81
Column Flexure (in)	-0.232	-1.004	0.84	-0.242	-1.579	0.78	**	-2.185	**
Fixed End Rotation (in)	-0.611			-0.986			**		
Column Shear (in)	*	-0.134	*	*	-0.216	*	*	-0.303	*
Bent Cap Flexibility (in)	-0.076	-0.055	1.38	-0.089	-0.056	1.59	-0.089	-0.058	1.53
Joint Shear (in)	-0.032	*	*	-0.042	*	*	-0.044	*	*
Component Total [CT] (in)	-0.951	-1.192		-1.359	-1.851		**	-2.546	
CT/CD	0.80	1.00		0.73	1.00		**	1.00	

Note: *Column shear displacement not measured; Joint shear displacement not predicted. ** Column curvature gages not reliable.

Table 3-7. Bar Slip and Fixed End Rotation Components (μ6, Cycle 2)—CPFD vs. CIP

Drift Ratio (%)	Force (CPFD) (kips)	Force (CIP) (kips)	BS (CPFD) (in)	BS (CIP) (in)	BS/FER (CPFD)	BS/FER (CIP)	BS/FER (CPFD/CIP)
0.33	20.0	27.4	0.014	0.022	0.126	0.097	1.30
0.63	25.0	29.8	0.016	0.022	0.081	0.069	1.18
0.99	30.0	32.2	0.019	0.022	0.061	0.053	1.16
1.30	35.0	34.4	0.020	0.022	0.049	0.044	1.12
1.60	40.0	36.4	0.021	0.022	0.042	0.038	1.09
1.98	45.0	39.2	0.021	0.022	0.035	0.033	1.05
				Average:	0.066	0.056	1.15

Table 3-8. Maximum Measured Diagonal Crack Width on Joint Surface (East Face)

Note: In general, crack widths for east face were slightly larger than for west face.

Drift Ratio (%) Push (Pull)	Displacement Ductility	Force (kips) Push (Pull)	Crack Width (0.001 in) Push (Pull)
0.63 (0.46)	μ1	46.8 (42.8)	3 (3)
0.85 (0.68)	μ1.5	51.5 (48.8)	5 (3)
1.10 (0.93)	μ2	53.7 (50.6)	5 (3)
1.62 (1.44)	μ3	55.1 (53.0)	5 (9)
2.17 (2.02)	μ4	54.5 (54.3)	5 (9)
3.20 (3.14)	μ6	54.4 (57.0)	5 (9)
4.30 (4.32)	μ8	45.2 (49.0)	5 (9)

Table 3-9. Maximum Joint Response for Select Parameters—CPFD vs. CIP

Parameter (Maximum)	CPFD	CIP	CPFD/CIP
Joint Shear Stress (psi)	323 ($4.31\sqrt{f_c'}$)	328 ($4.86\sqrt{f_c'}$)	0.89
Principal Tensile Stress (psi)	356 ($4.75\sqrt{f_c'}$)	363 ($5.38\sqrt{f_c'}$)	0.88
Principal Compressive Stress (psi)	398 ($0.071f_c'$)	401 ($0.088f_c'$)	0.81
Angle of Principal Plane in Joint (deg)	44.2	45.0	0.98
Joint Rotation (rad)	1.73×10^{-3}	1.95×10^{-3}	0.89
Change in Panel Area (%)	0.13	0.16	0.81

Table 3-10. Column Hoop Strain

Drift Ratio (%)	μ	HC1-W			HC1-N			HC4-W		
		Push	Pull	Max/Yield	Push	Pull	Max/Yield	Push	Pull	Max/Yield
0.63	1.0	1514	-390	0.69	789	-707	0.36	211	7	0.10
0.85	1.5	3898	-343	1.78	966	-828	0.44	233	22	0.11
1.10	2.0	4908	-707	2.24	2486	-935	1.14	252	34	0.12
1.62	3.0	7700	-895	3.52	3539	-742	1.62	3266	74	1.49

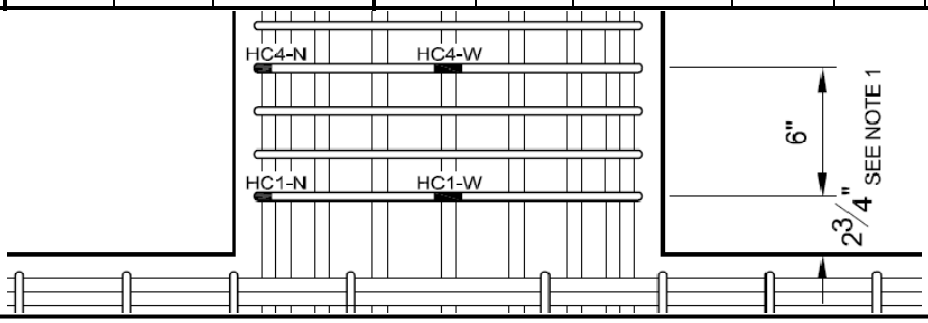

Table 3-11. Strains in Corrugated Duct and Column Longitudinal Bars

Push to 1.62% Drift (μ3, 55.2 kips)									
Pipe							Column		
Location (from top) (in)	Gage ID	Angle	Strain	Gage ID	Principal Strain	Principal Angle	Location (from top) (in)	Gage ID	Max Strain
3.63	HB1-E	-	420	-	-	-	1.00	LC4-B1	1443
7.63	DE-2	20	585	DE-123	684	-37.9	1.00	LC7-B1	*
9.00	DN-1	20	962	-	-	-	1.00	LC16-B1	1352
12.50	DE-5	20	676	DE-456	707	19.1	6.00	LC4-B2	3447
16.00	DN-2	20	*	-	-	-	6.00	LC7-B2	-937
20.13	DE-8	20	394	DE-789	461	11.7	6.00	LC16-B2	*
21.38	HB2-E	-	533	-	-	-	15.50	LC4-B3	1454
							15.50	LC7-B3	204
							15.50	LC16-B3	*

Pull to 1.49% Drift (μ3, 53.3 kips)									
Pipe							Column		
Location (from top) (in)	Gage ID	Angle	Strain	Gage ID	Principal Strain	Principal Angle	Location (from top) (in)	Gage ID	Max Strain
3.63	HB1-E	-	236	-	-	-	1.00	LC4-B1	916
7.63	DE-2	20	-62	DE-123	131	-14.1	1.00	LC7-B1	*
9.00	DN-1	20	668	-	-	-	1.00	LC16-B1	-8054
12.50	DE-5	20	45	DE-456	170	-14.8	6.00	LC4-B2	-6
16.00	DN-2	20	232	-	-	-	6.00	LC7-B2	4764
20.13	DE-8	20	16	DE-789	101	-13.2	6.00	LC16-B2	*
21.38	HB2-E	-	533	-	-	-	15.50	LC4-B3	-1453
							15.50	LC7-B3	1909
							15.50	LC16-B3	*

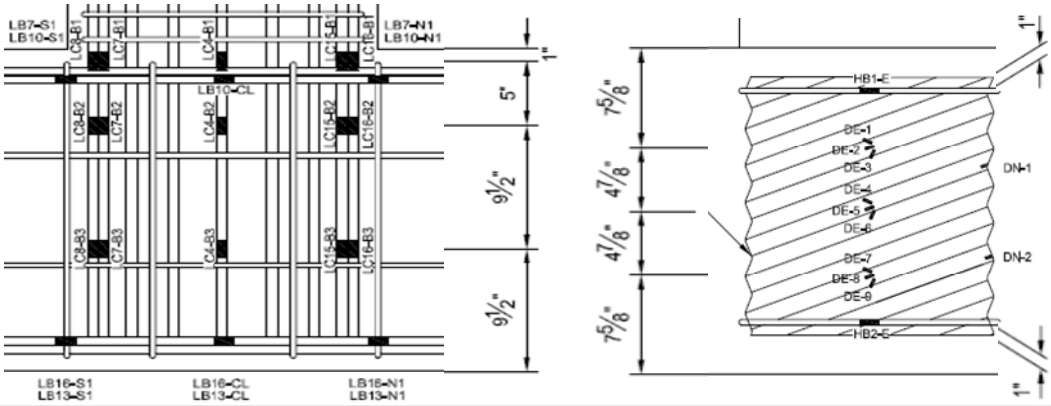

Table 3-12. Bent Cap Longitudinal Bar Strain—CPFD

Top Bars		S2		S1		CL		N1		N2	
		Push	Pull	Push	Pull	Push	Pull	Push	Pull	Push	Pull
CPFD (LB7)	$\mu 2$	–	–	–	–	774	1,233	160	-461	72	-166
	$\mu 4$	–	–	20	-31	833	1,725	144	-472	87	-180
	$\mu 6$	–	–	-134	-189	1,050	2,169	189	-494	75	-167
	$\varepsilon_{max}/\varepsilon_y$	–	–	-0.06	-0.09	0.48	0.99	0.09	-0.23	0.04	-0.08
Bottom Bars		**S2**		**S1**		**CL**		**N1**		**N2**	
		Push	Pull	Push	Pull	Push	Pull	Push	Pull	Push	Pull
CPFD (LB13)	$\mu 2$	674	-107	585	-20	1,792	525	188	1,138	21	418
	$\mu 4$	737	-121	1,315	279	2,357	800	270	1,372	15	448
	$\mu 6$	757	-135	1,540	446	3,094	890	343	1,549	–	–
	$\varepsilon_{max}/\varepsilon_y$	0.35	-0.06	0.70	0.20	1.41	0.41	0.16	0.71	0.01	0.20

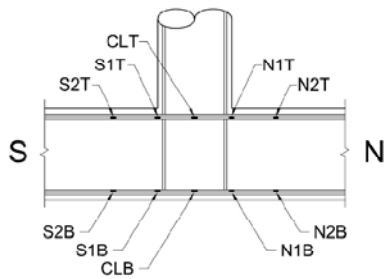

Note: Reference Table 3-1 for associated drift and force levels.

– Not available

Table 3-13. Bent Cap Longitudinal Bar Strain—CPFD vs. CIP

Top Bars		S2		S1		CL		N1		N2	
		Push	Pull	Push	Pull	Push	Pull	Push	Pull	Push	Pull
CIP (LB13)	$\mu 2$	-218	118	146	252	–	–	267	-208	–	–
	$\mu 4$	-194	141	80	228	–	–	168	-392	–	–
	$\mu 6$	-229	116	30	302	–	–	53	-581	–	–
	$\varepsilon_{max}/\varepsilon_y$	-0.10	0.06	0.07	0.14	–	–	0.12	-0.26	–	–
CPFD (LB7)	$\mu 2$	–	–	–	–	774	1,233	160	-461	72	-166
	$\mu 4$	–	–	20	-31	833	1,725	144	-472	87	-180
	$\mu 6$	–	–	-134	-189	1,050	2,169	189	-494	75	-167
	$\varepsilon_{max}/\varepsilon_y$	–	–	-0.06	-0.09	0.48	0.99	0.09	-0.23	0.04	-0.08

Bottom Bars		S2		S1		CL		N1		N2	
		Push	Pull	Push	Pull	Push	Pull	Push	Pull	Push	Pull
CIP (LB10)	$\mu 2$	823	-108	968	68	891	221	259	755	78	535
	$\mu 4$	867	-135	875	132	947	334	349	876	59	587
	$\mu 6$	890	-164	1,021	157	961	434	449	1,018	35	685
	$\varepsilon_{max}/\varepsilon_y$	0.40	-0.07	0.46	0.07	0.43	0.20	0.20	0.46	0.04	0.31
CPFD (LB13)	$\mu 2$	674	-107	585	-20	1,792	525	188	1,138	21	418
	$\mu 4$	737	-121	1,315	279	2,357	800	270	1,372	15	448
	$\mu 6$	757	-135	1,540	446	3,094	890	343	1,549	–	–
	$\varepsilon_{max}/\varepsilon_y$	0.35	-0.06	0.70	0.20	1.41	0.41	0.16	0.71	0.01	0.20

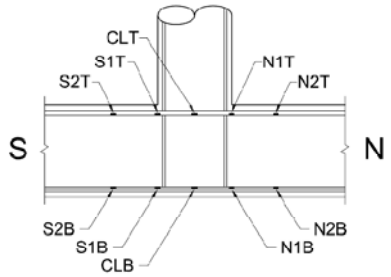

Note: Reference Tables 3-1 and 3-2 for associated drift and force levels.

– Not available

3.8 Figures

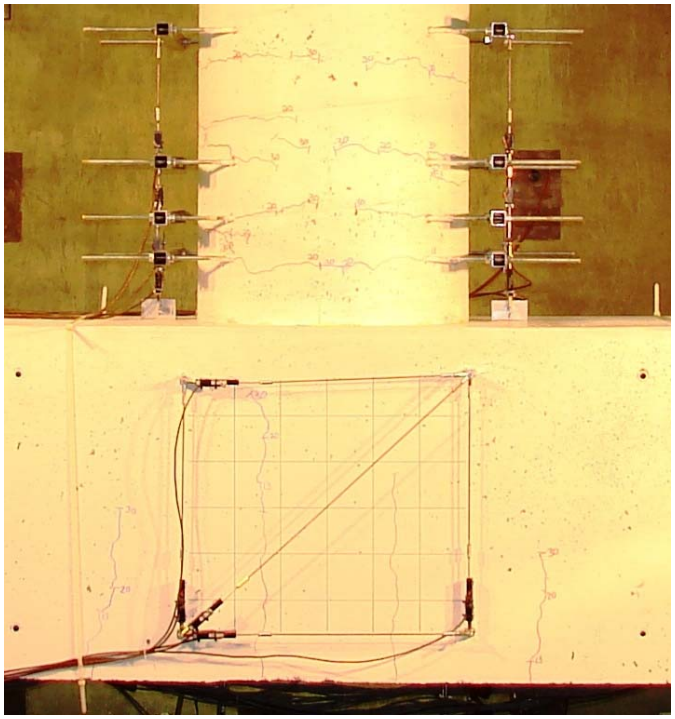

Figure 3-1. Specimen Crack Pattern during Force Control Sequence (30 kips)

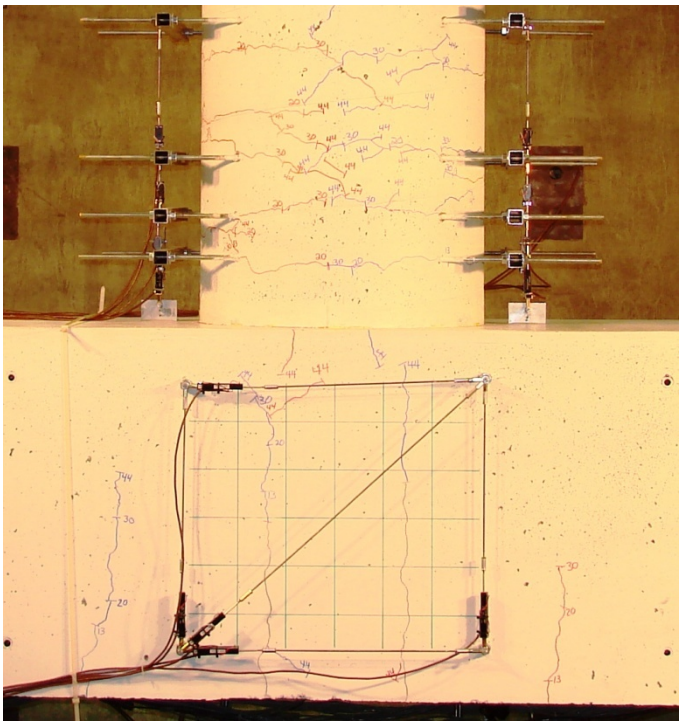

Figure 3-2. Specimen Crack Pattern at End of Force Control Sequence (44 kips)

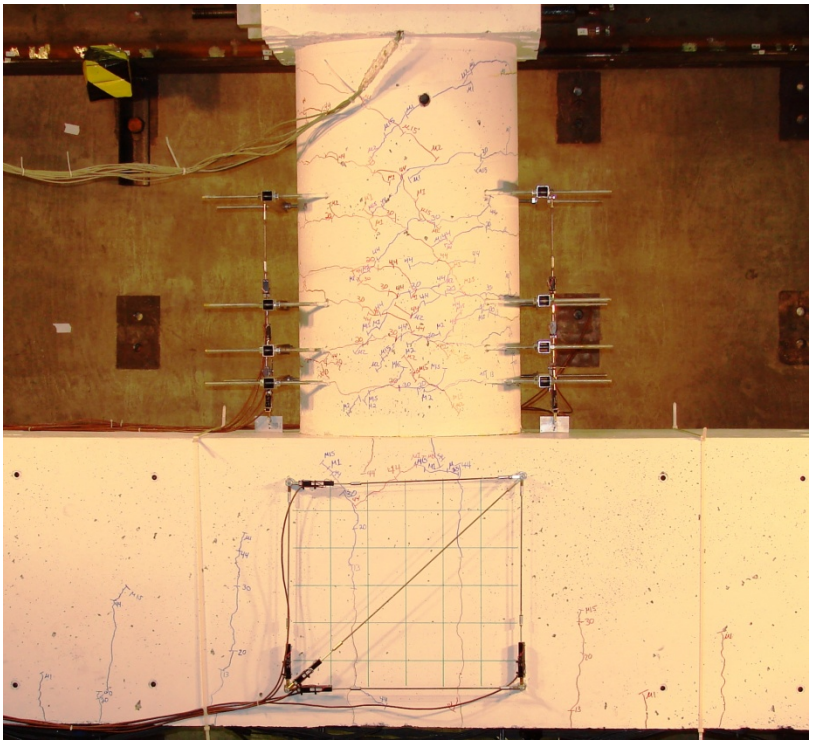

Figure 3-3. Specimen Response at 1.1% Drift Ratio (μ2)

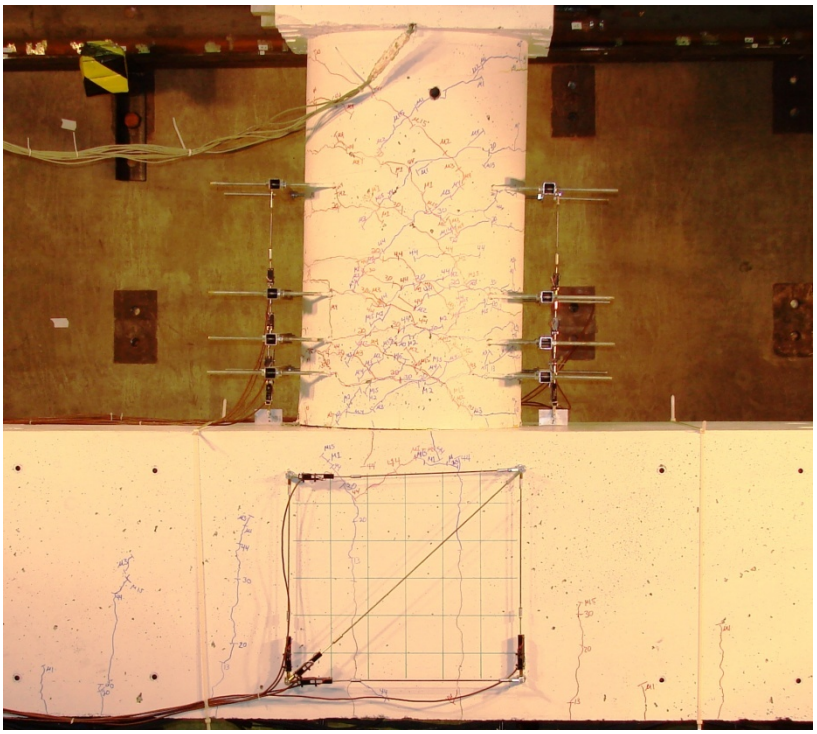

Figure 3-4. Specimen Response at 2.2% Drift Ratio (μ4)

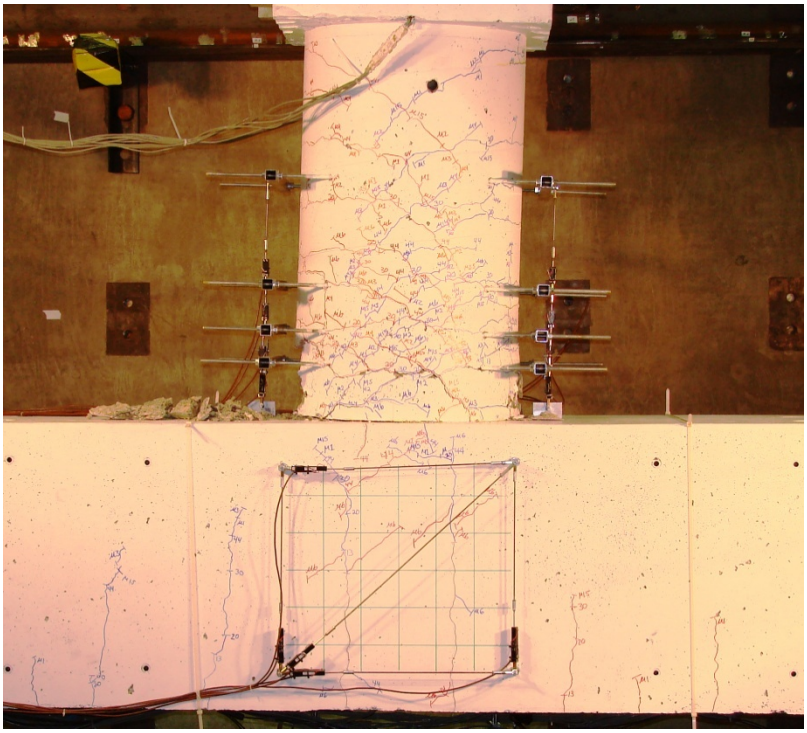

Figure 3-5. Specimen Response at 3.2% Drift Ratio (μ6)

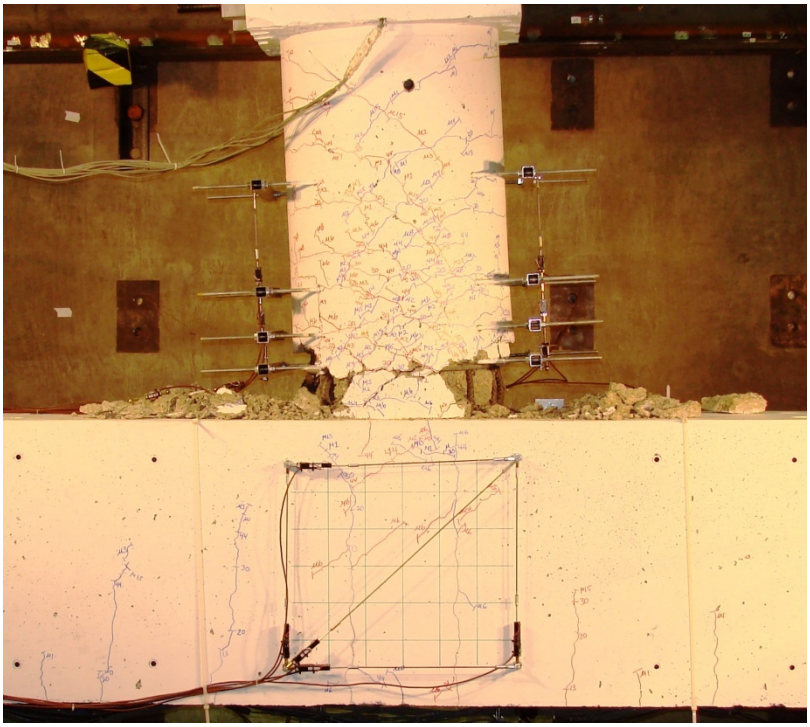

Figure 3-6. Specimen Response at 4.3% Drift Ratio (μ8)

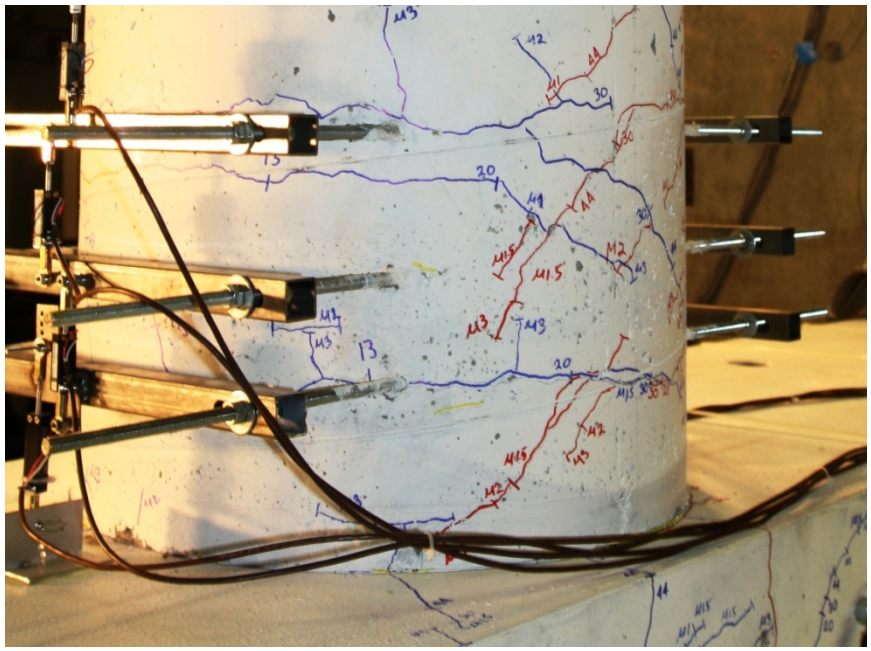

Figure 3-7. Column Spalling at 1.6% Drift Ratio (μ3) (North)

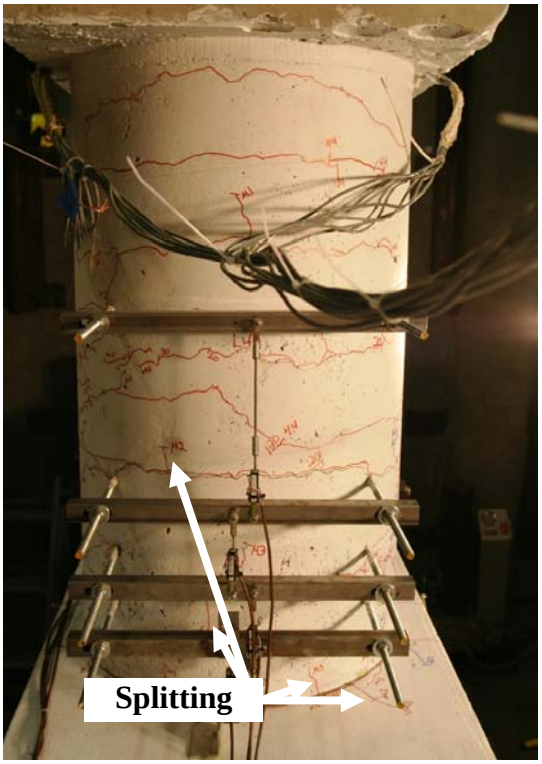

Figure 3-8. Splitting Cracks in Bent Cap and Column at 1.4% Drift Ratio (μ3, South Face)

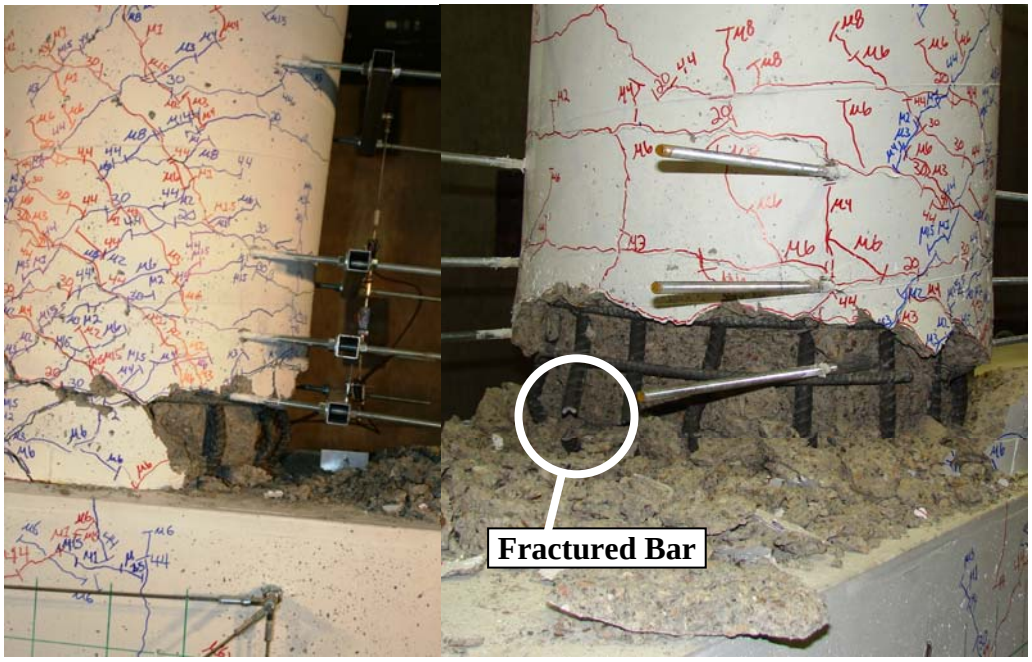

A. Buckled Bars (μ 8) B. Fractured Bars (Post-test)

Figure 3-9. Fractured Bars in Plastic Hinge Region (North End, Post Test)

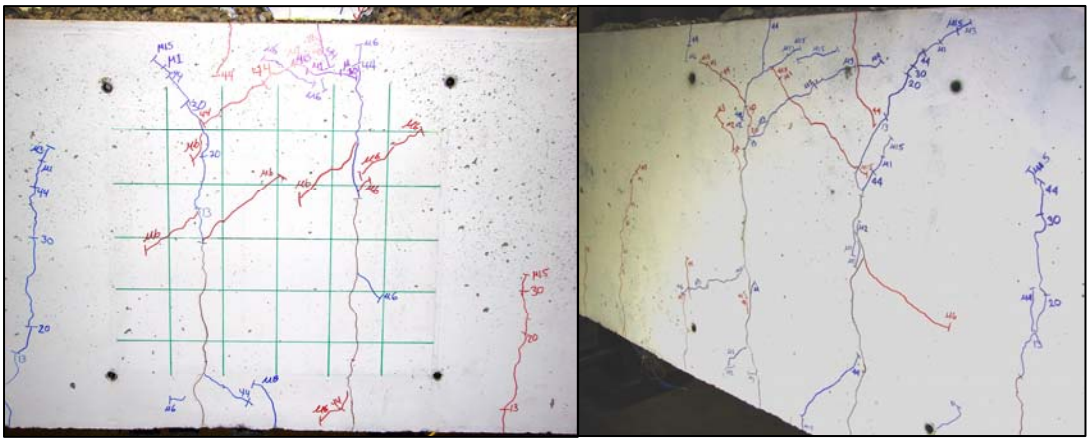

A. East Side B. West Side

Figure 3-10. Joint Region Cracking Post-Test

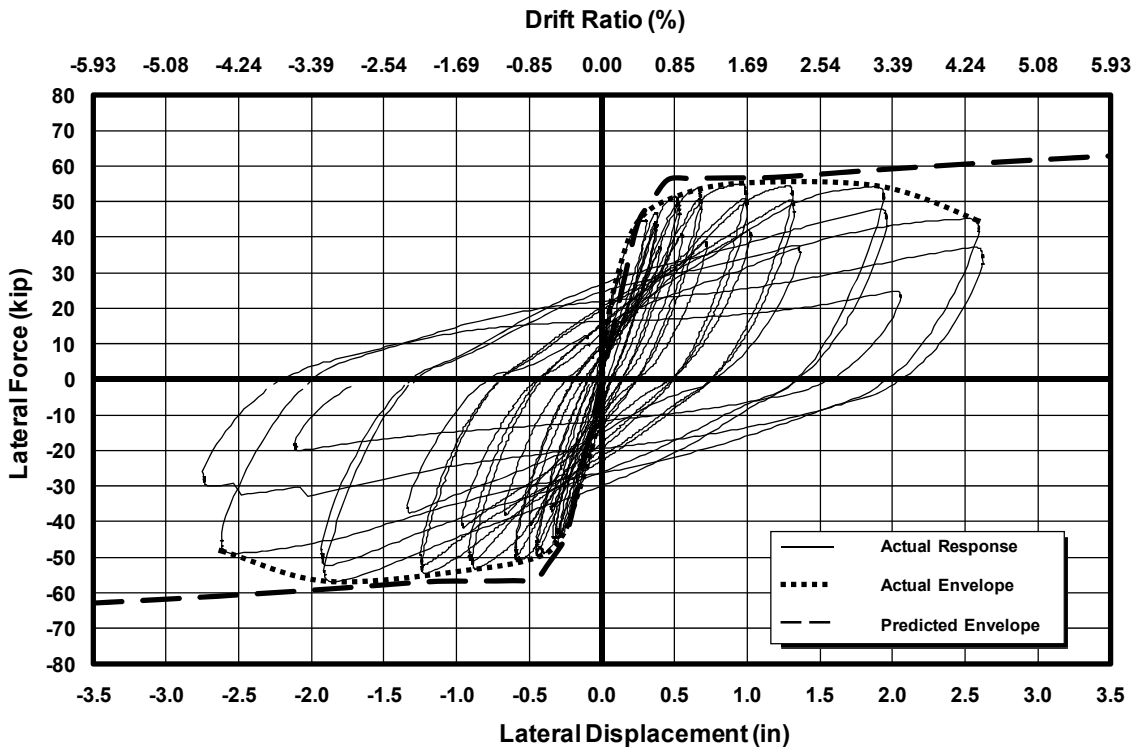

Figure 3-11. Lateral Force vs. Lateral Displacement

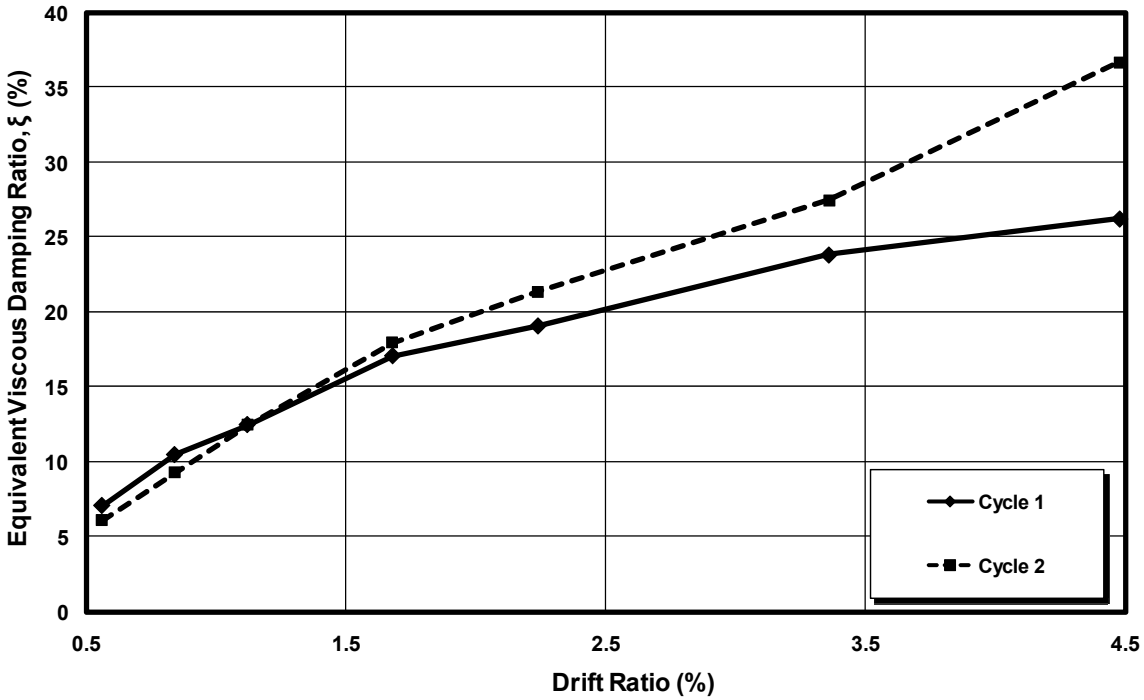

Figure 3-12. Equivalent Viscous Damping Ratio vs. Drift Ratio

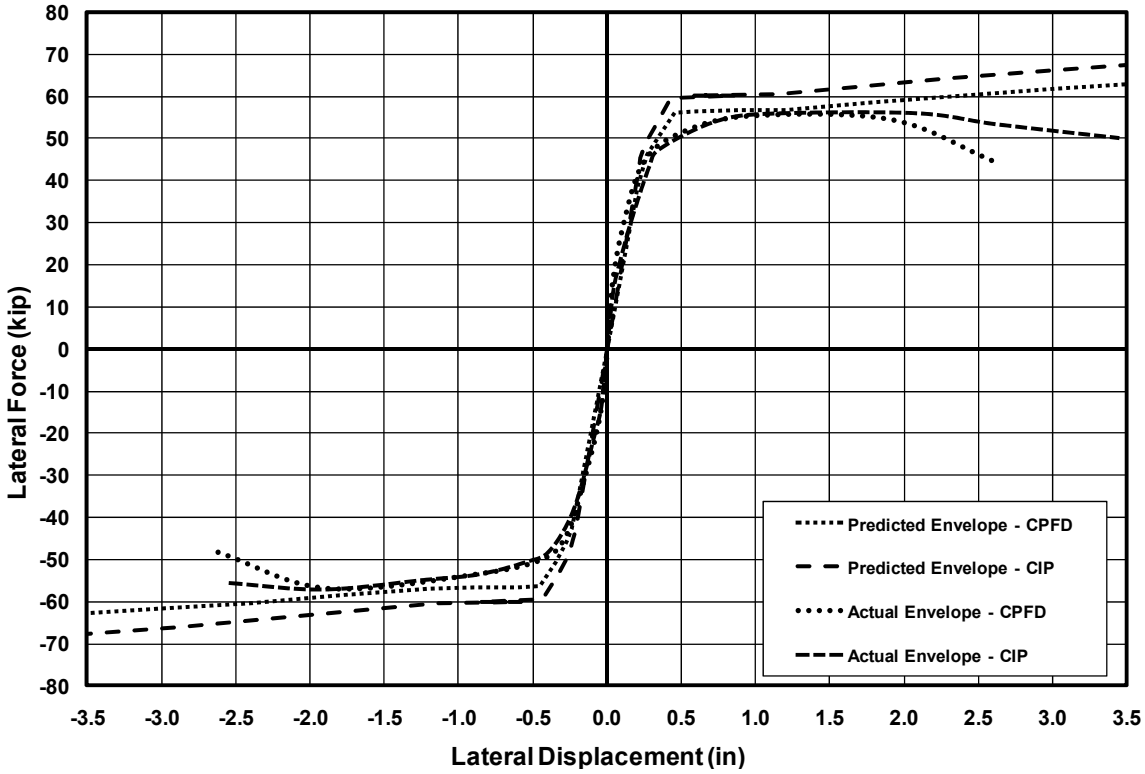

Figure 3-13. Lateral Force vs. Lateral Displacement Envelopes—CPFD vs. CIP

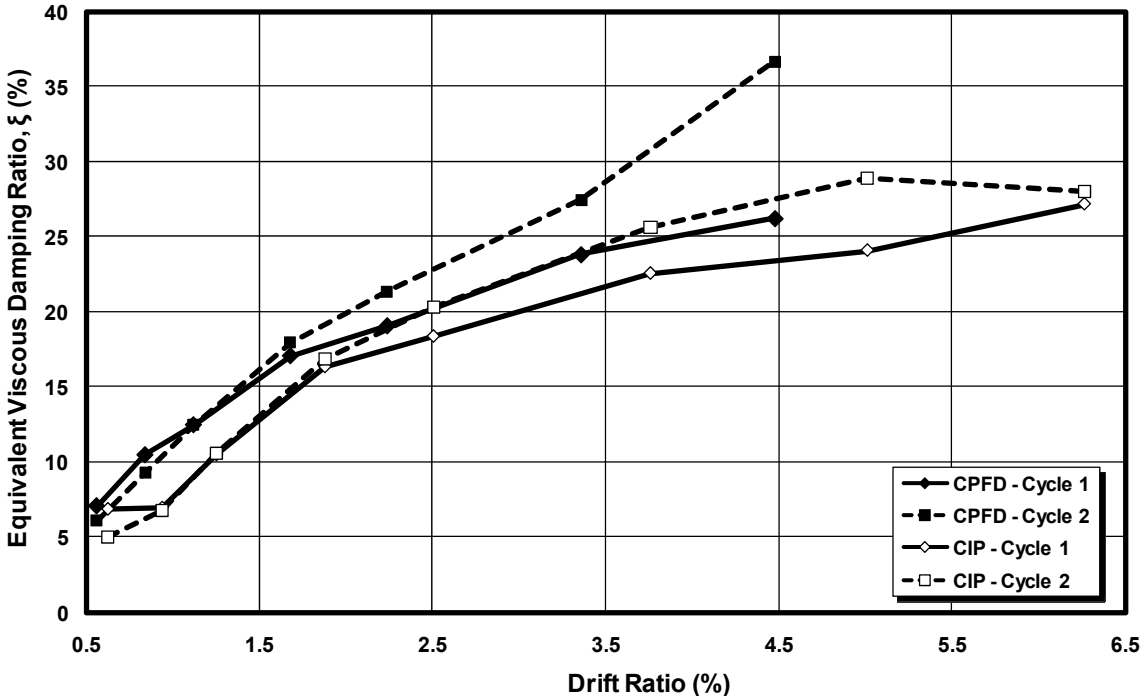

Figure 3-14. Equivalent Viscous Damping Ratio vs. Drift Ratio—CPFD vs. CIP

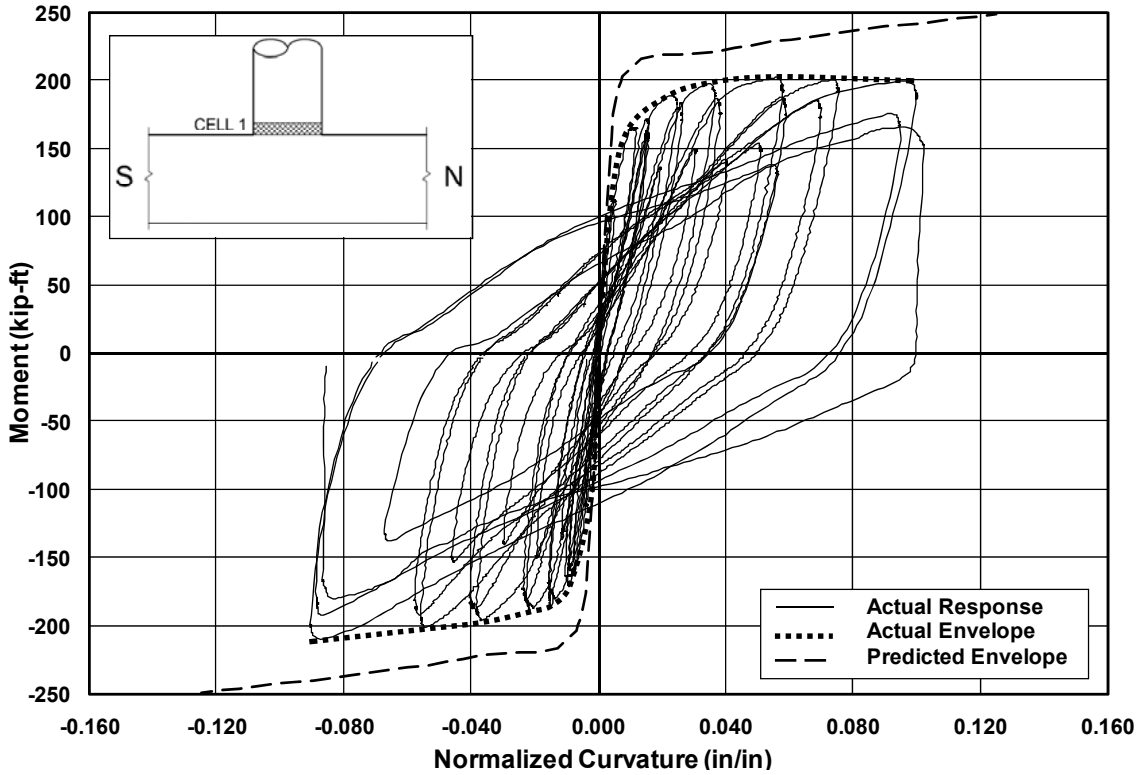

Figure 3-15. Normalized Moment-Curvature Response—Cell 1

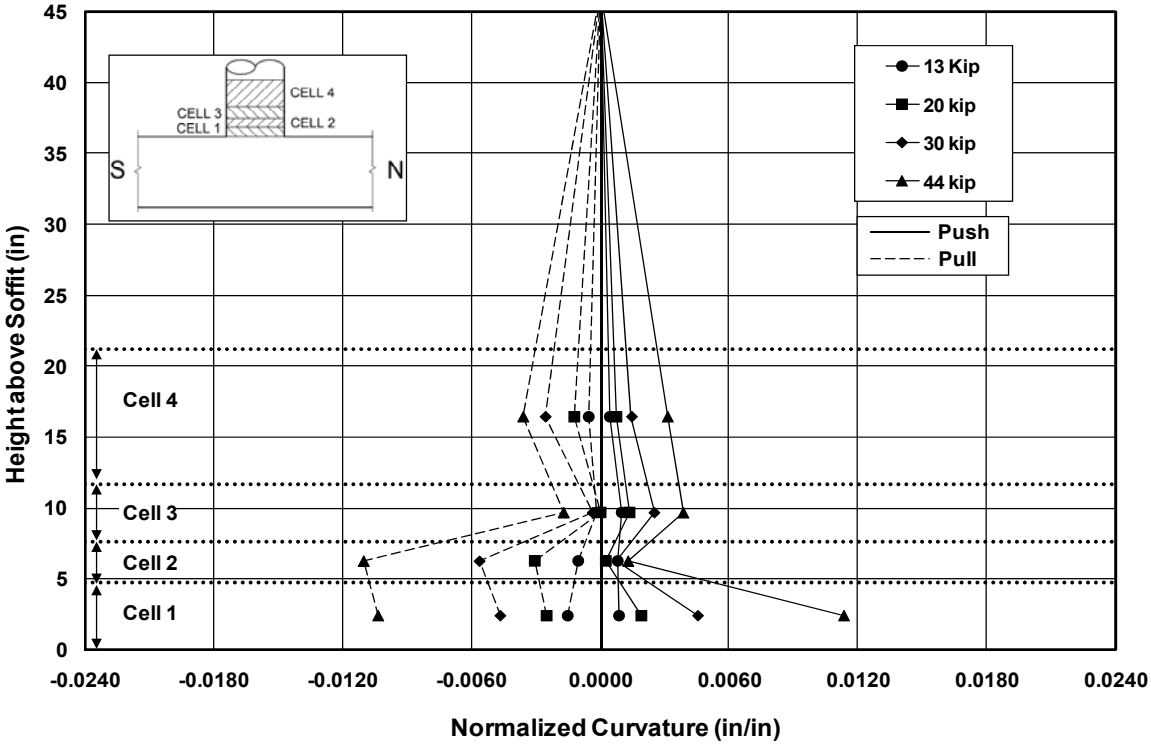

Figure 3-16. Curvature Profile—Force Control

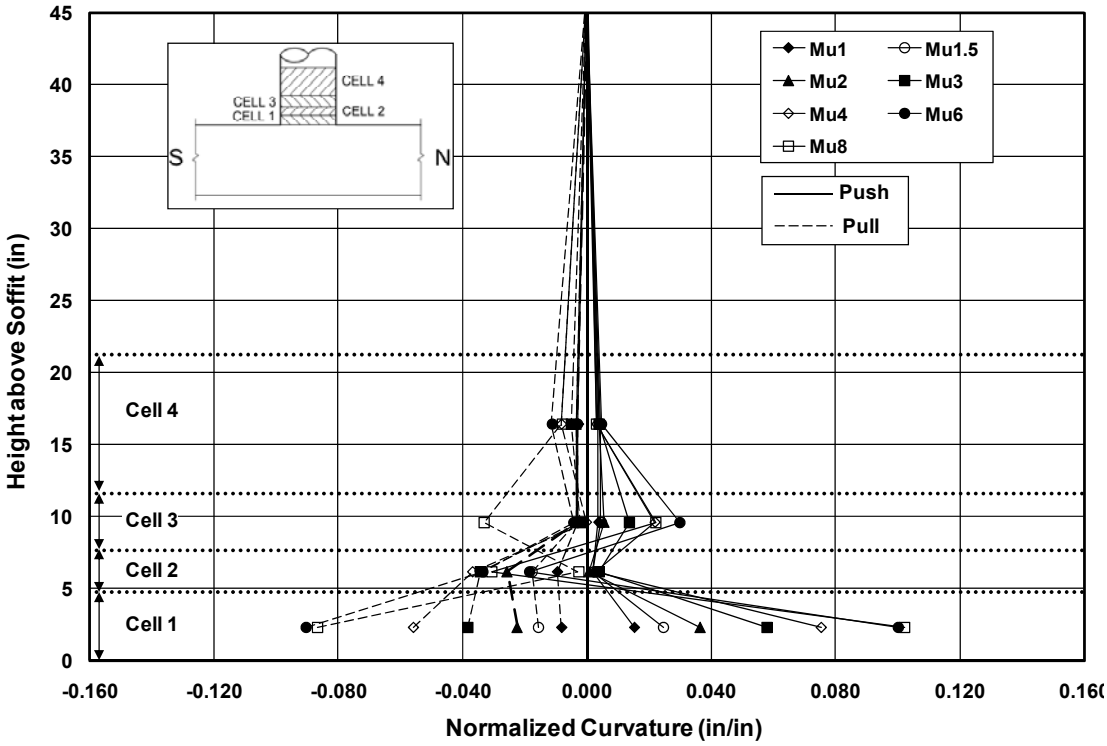

Figure 3-17. Curvature Profile—Displacement Control

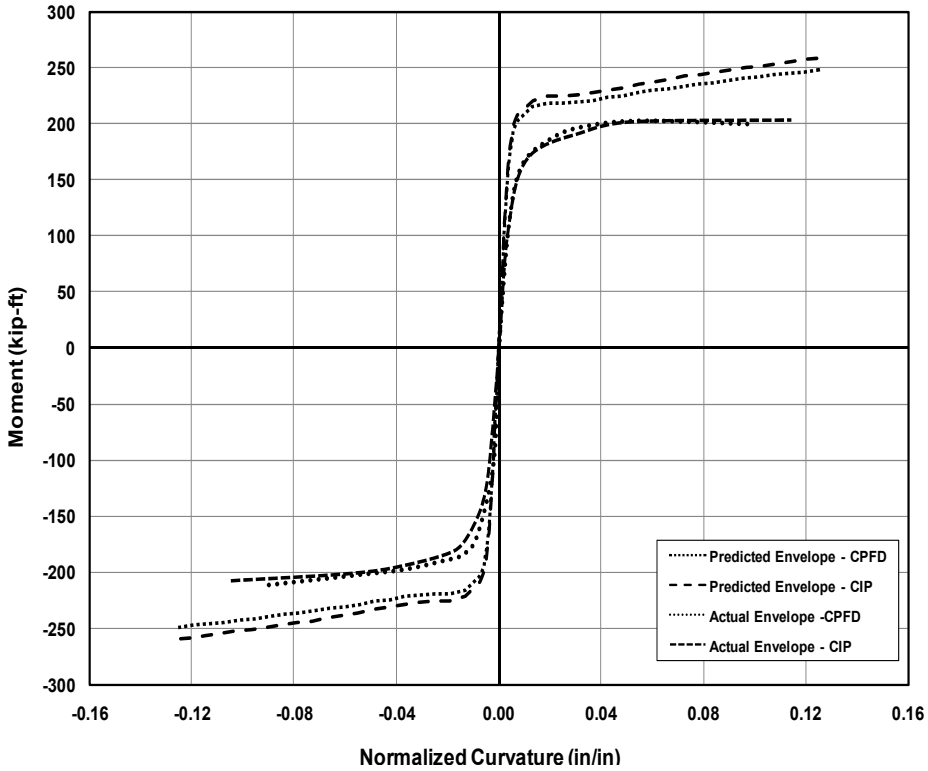

Figure 3-18. Normalized Moment-Curvature Response (Cell 1)—CPFD vs. CIP

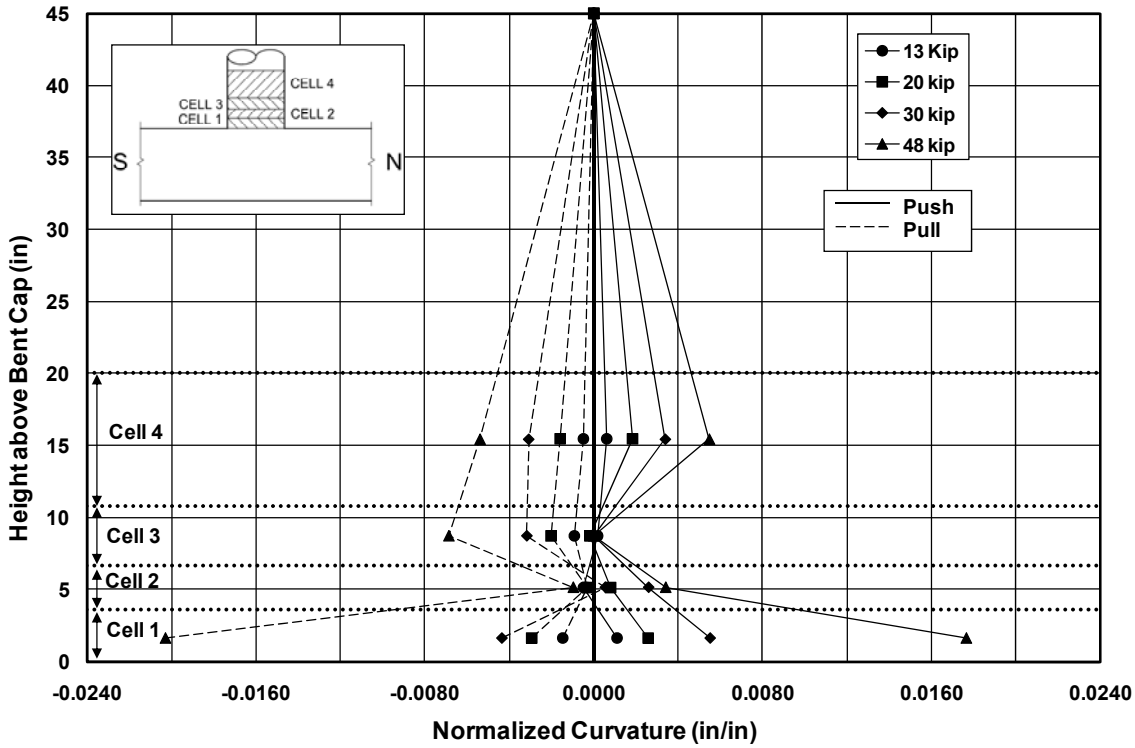

Figure 3-19. Curvature Profile (Force Control)—CIP

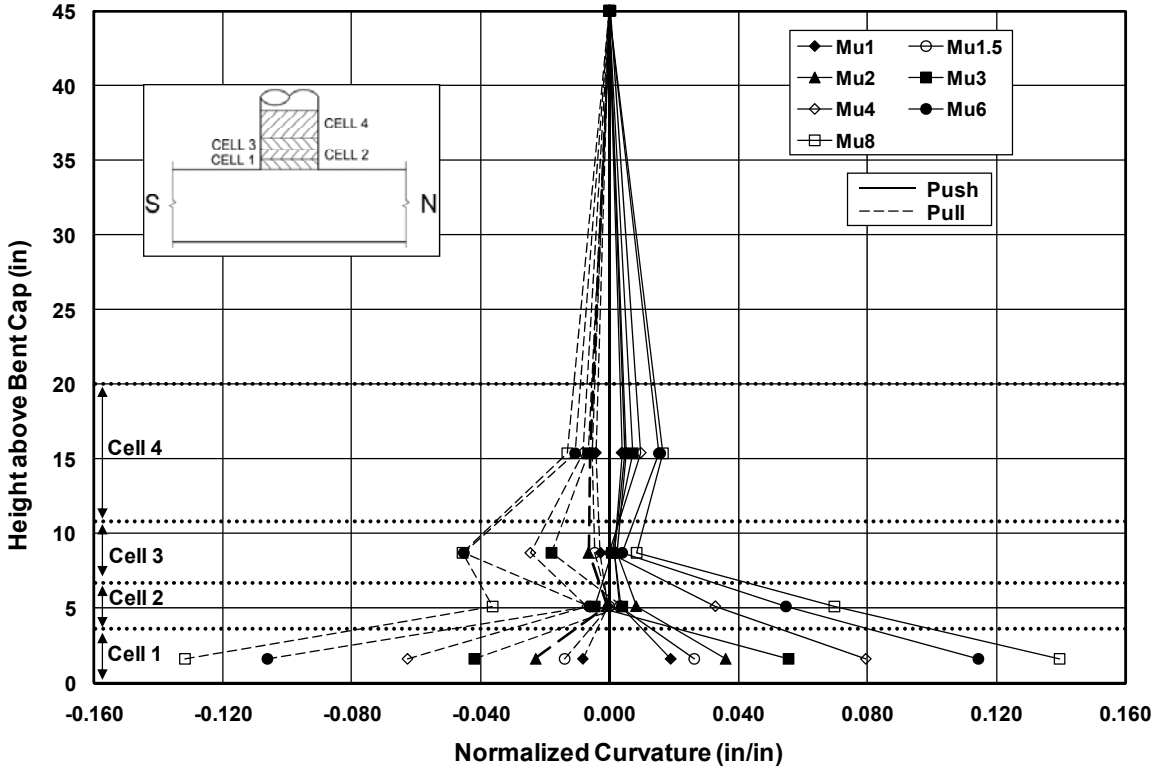

Figure 3-20. Curvature Profile (Displacement Control)—CIP

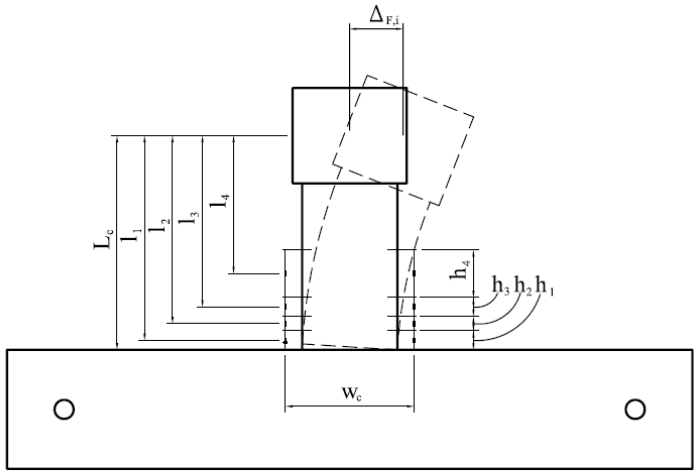

$$\Delta_{F,i} = l_i \frac{(\delta h_{i,n} - \delta h_{i,s})}{w_c}$$

$$\Delta_{F,1} = (l_1 + l'_g) \frac{(\delta h_{i,n} - \delta h_{i,s})}{w_c}$$

$$l'_g = h_1 + (0.022 \ f_y \ d_{bl})$$

A. Column Flexure and Fixed End Rotation (Cell 1)

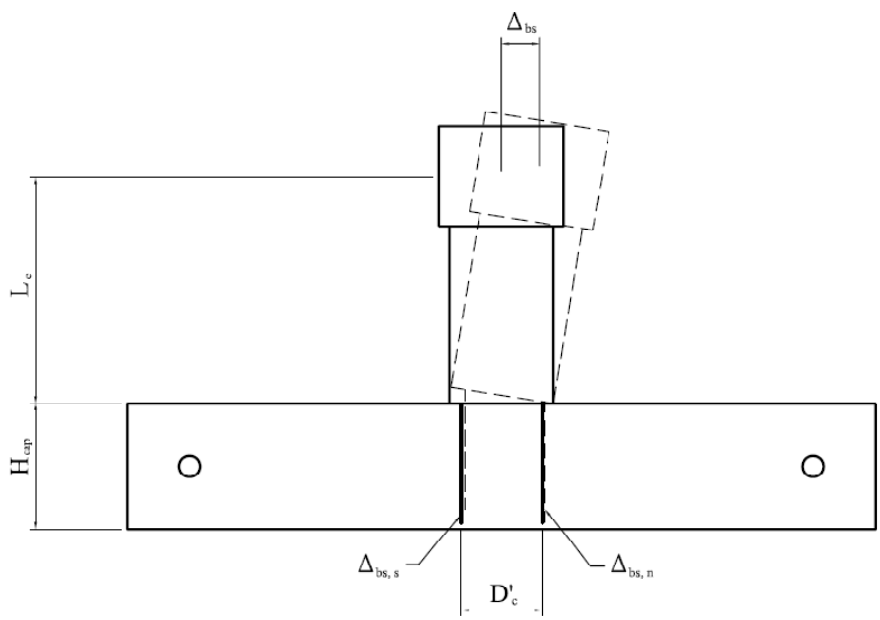

$$\Delta_{bs} = \left(\frac{\Delta_{bs,s} - \Delta_{bs,n}}{D'_c}\right)(L_c + H_{cap})$$

B. Bar Slip

Figure 3-21. Schematic Representation of Column Displacement Components, Experimental

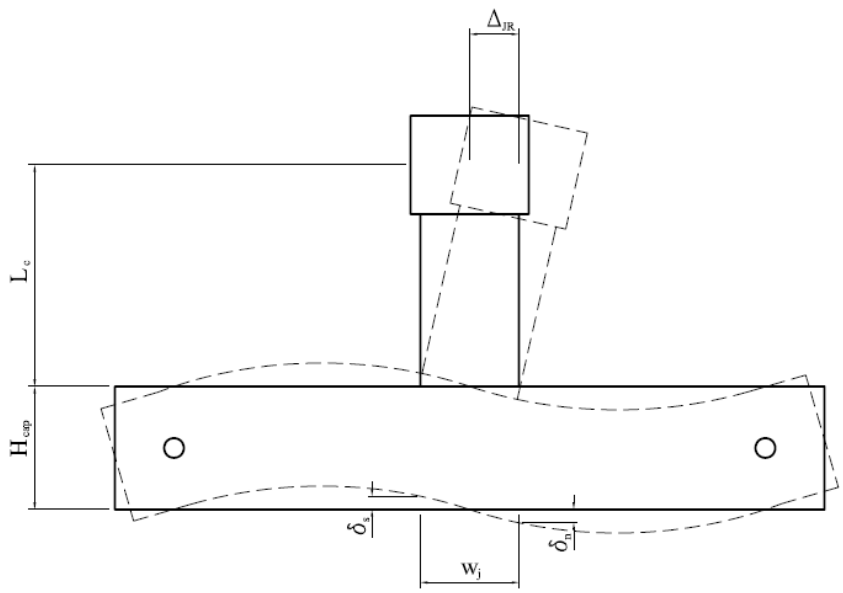

$$\Delta_{JR} = \frac{(\delta_n - \delta_s)}{w_j} (L_c + H_{cap})$$

C. Bent Cap Rotation

Figure 3-21. Schematic Representation of Column Displacement Components, Experimental (Cont.)

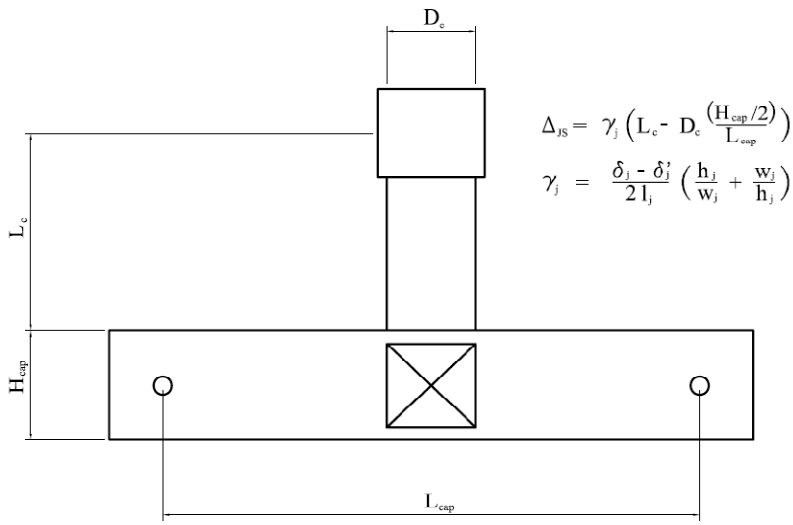

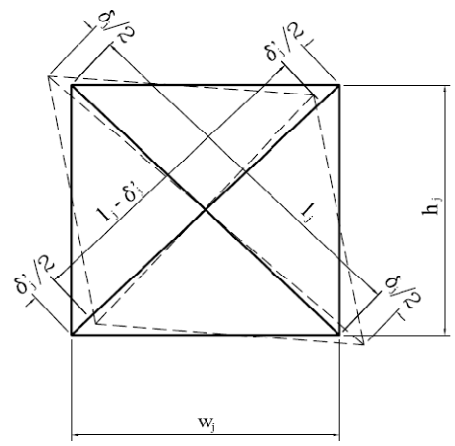

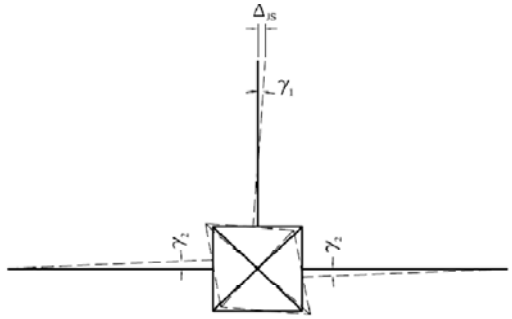

$$\gamma_j = \gamma_1 + \gamma_2$$

D. Joint Shear

Figure 3-21. Schematic Representation of Column Displacement Components, Experimental (Cont.)

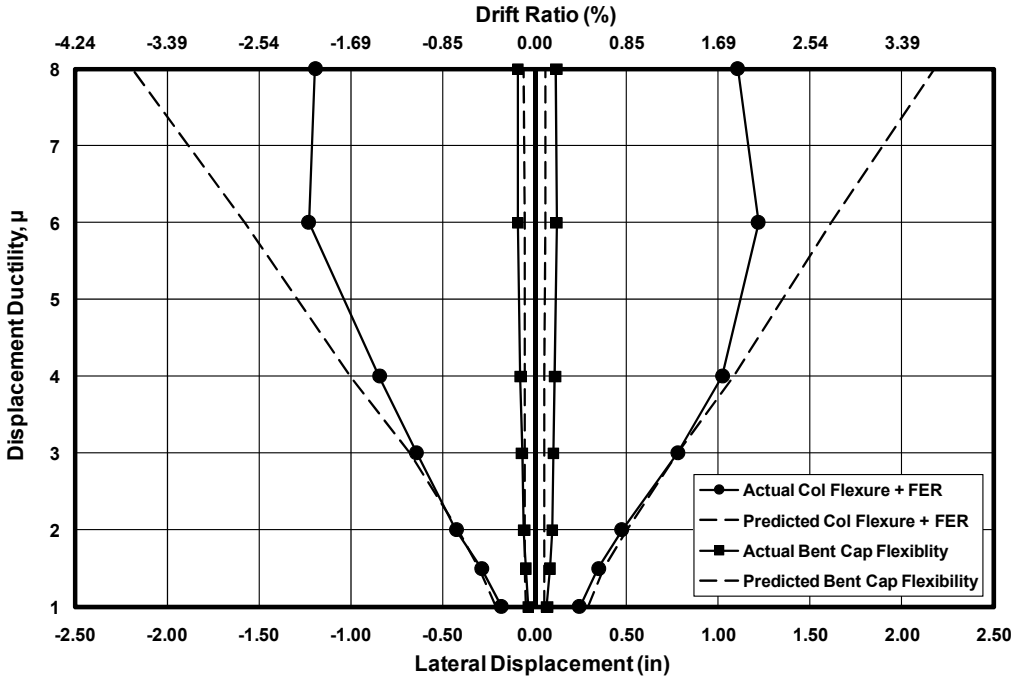

Figure 3-22. Displacement Components—Predicted vs. Actual

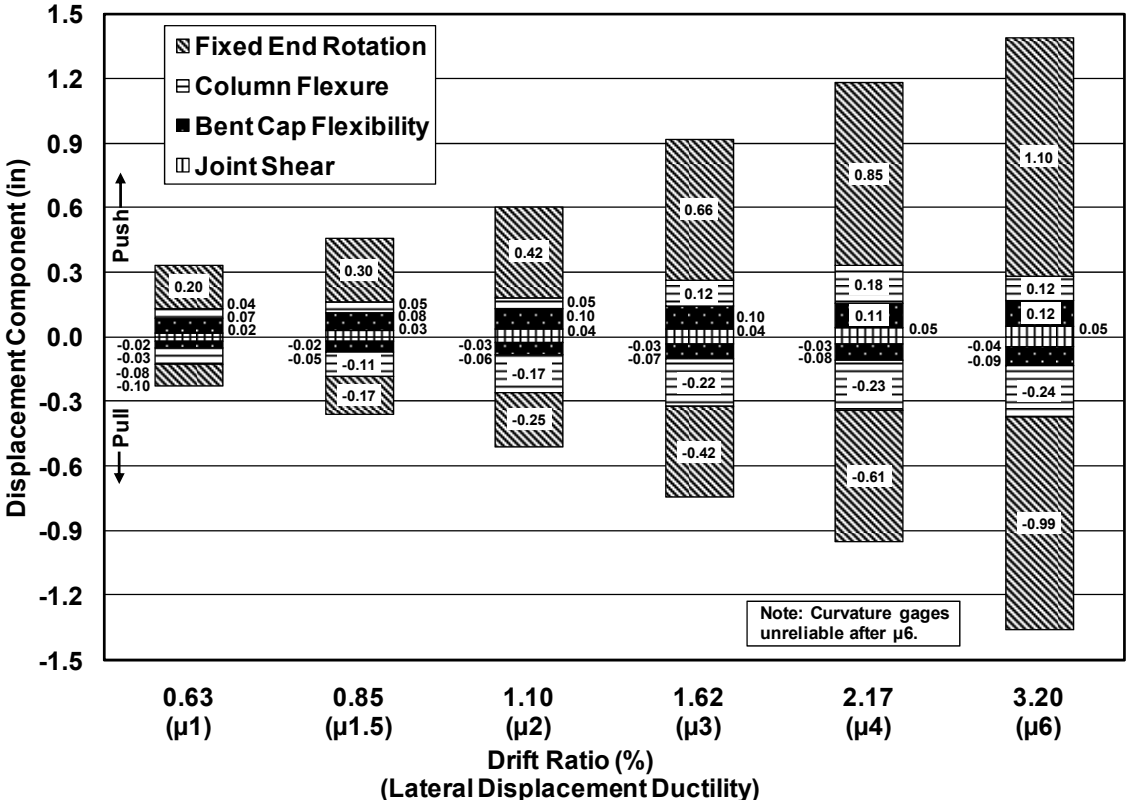

Figure 3-23. Displacement Decomposition Component Values

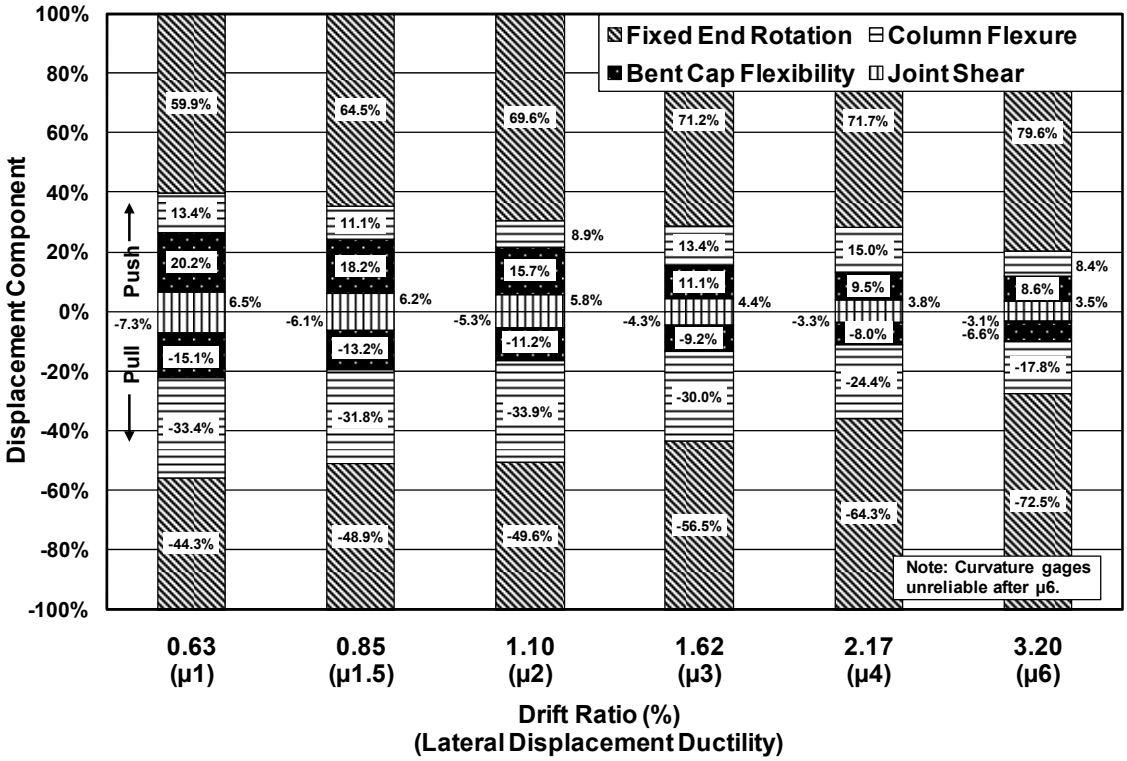

Figure 3-24. Displacement Decomposition Component Percentages

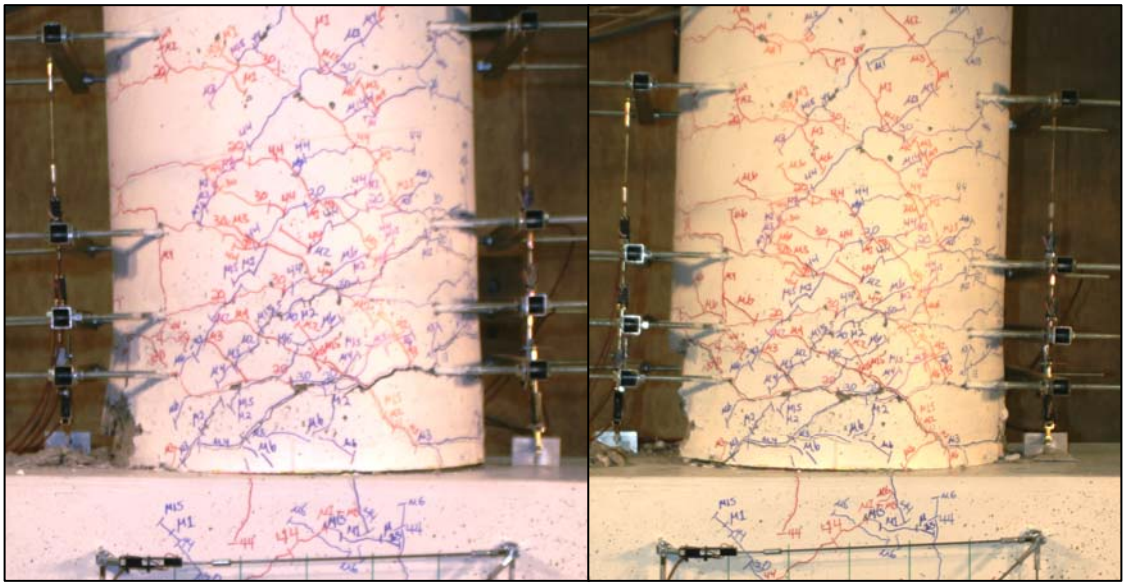

A. Push B. Pull

Figure 3-25. Large Flexural Crack at Bottom of Column

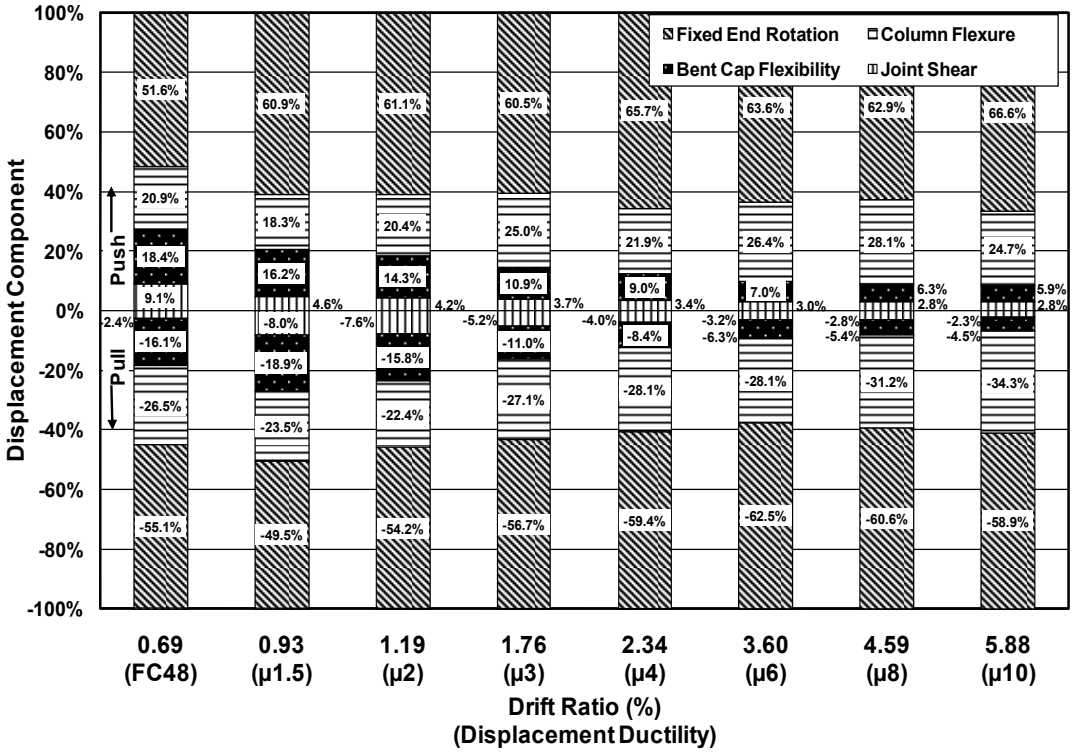

Figure 3-26. Displacement Decomposition Component Percentages—CIP

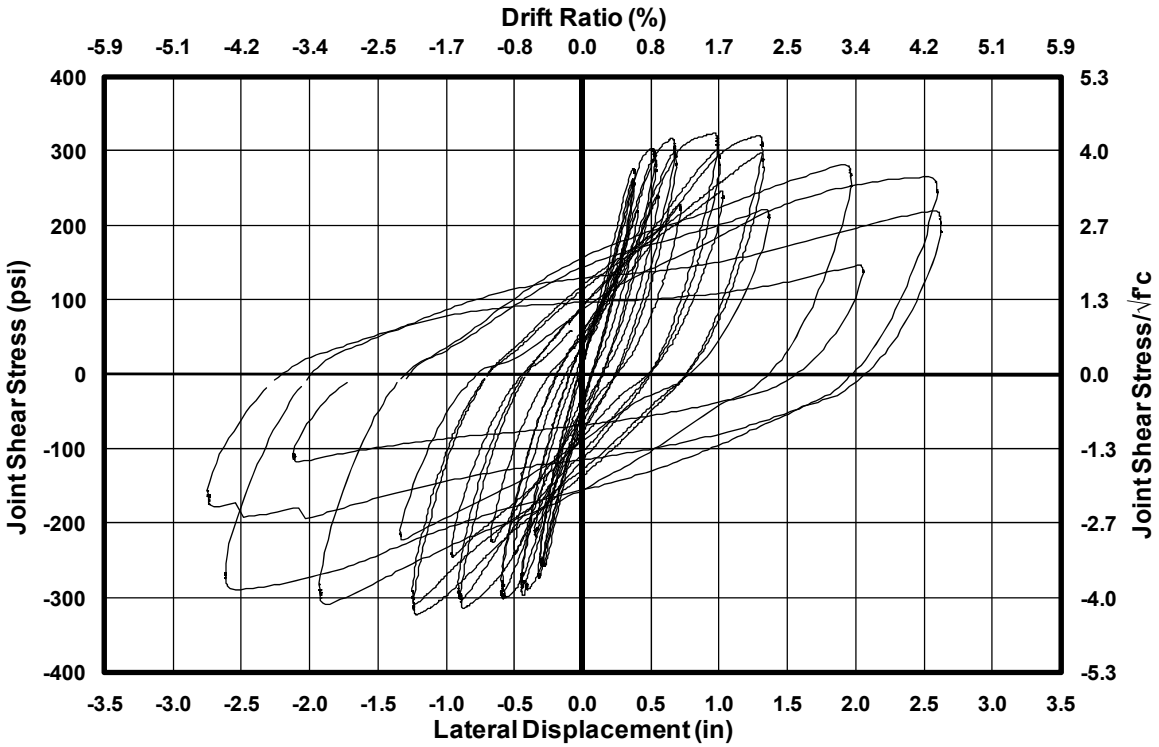

Figure 3-27. Nominal Joint Shear Stress vs. Lateral Displacement

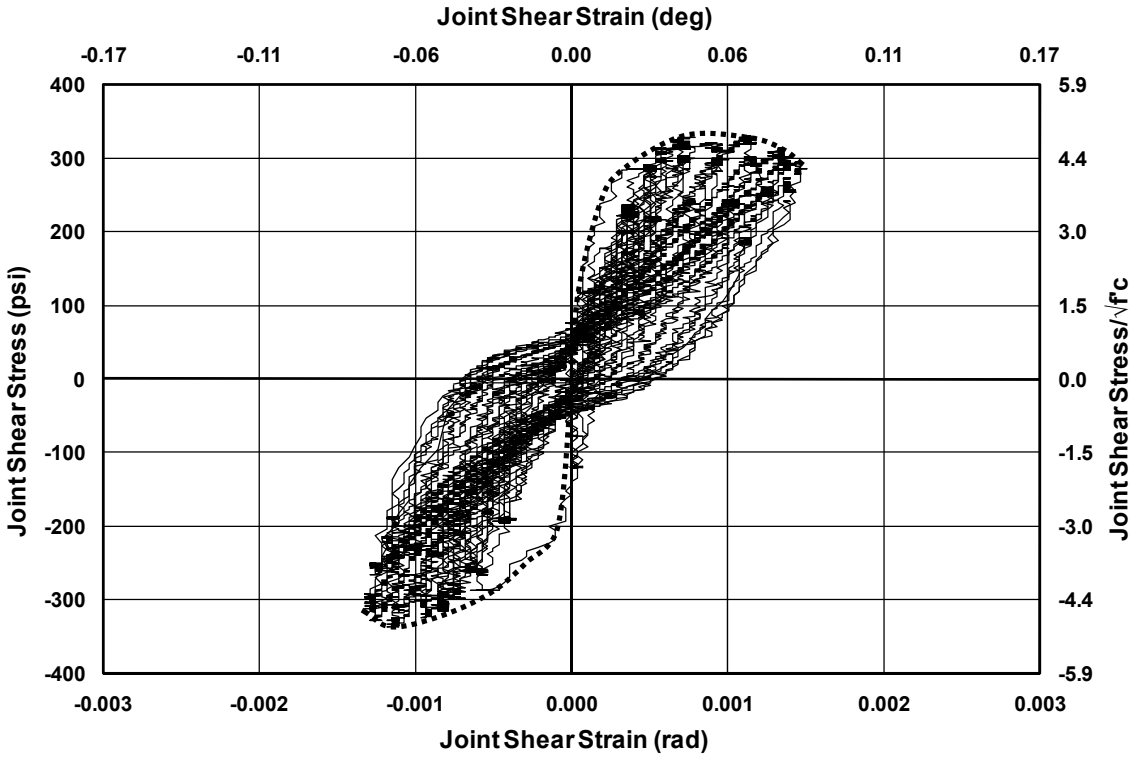

Figure 3-28. Joint Shear Stress vs. Joint Shear Strain

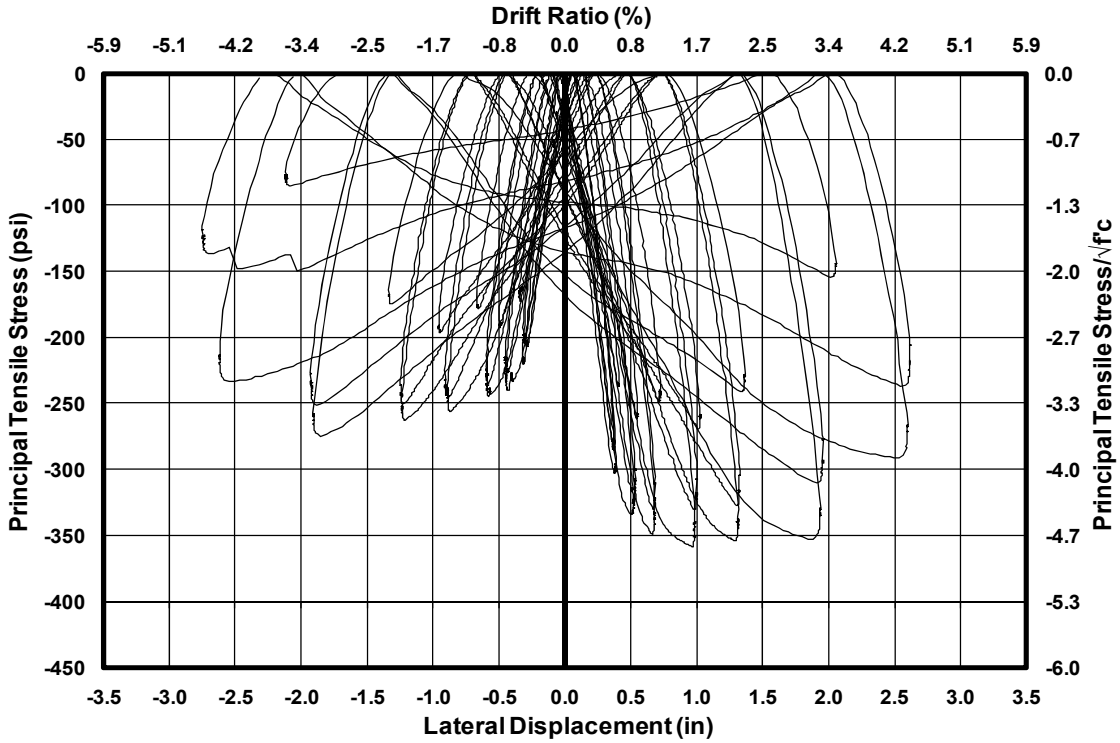

Figure 3-29. Nominal Principal Tensile Stress vs. Lateral Displacement

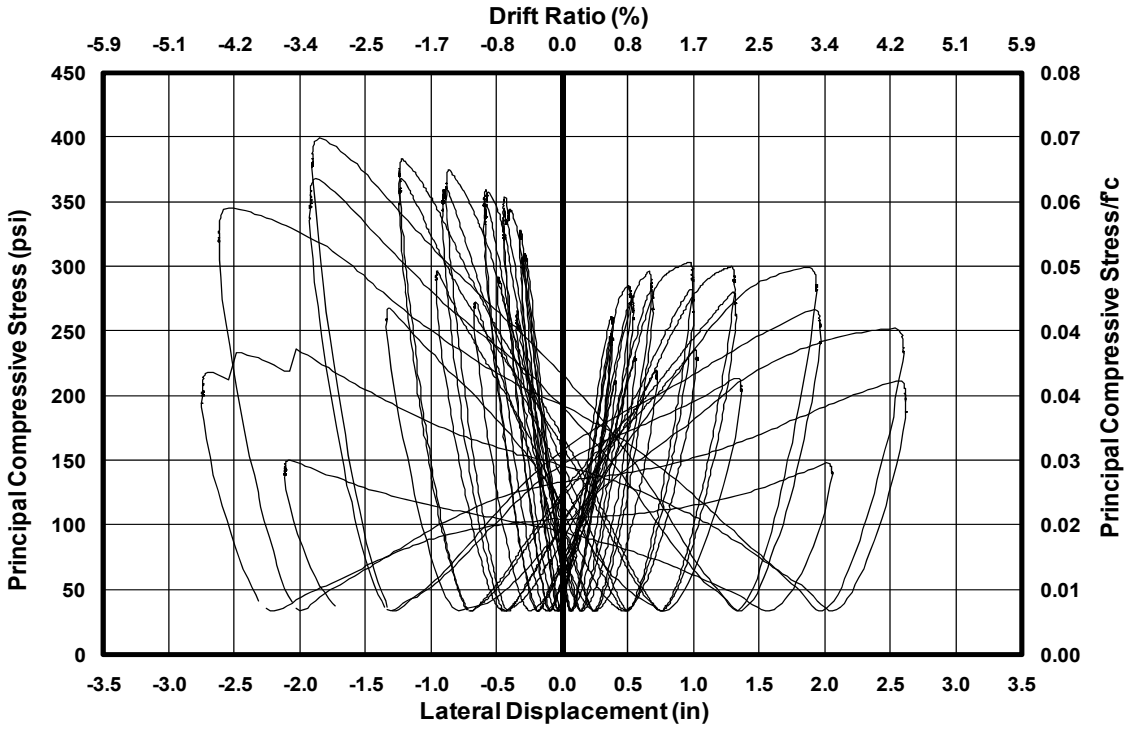

Figure 3-30. Nominal Principal Compressive Stress vs. Lateral Displacement

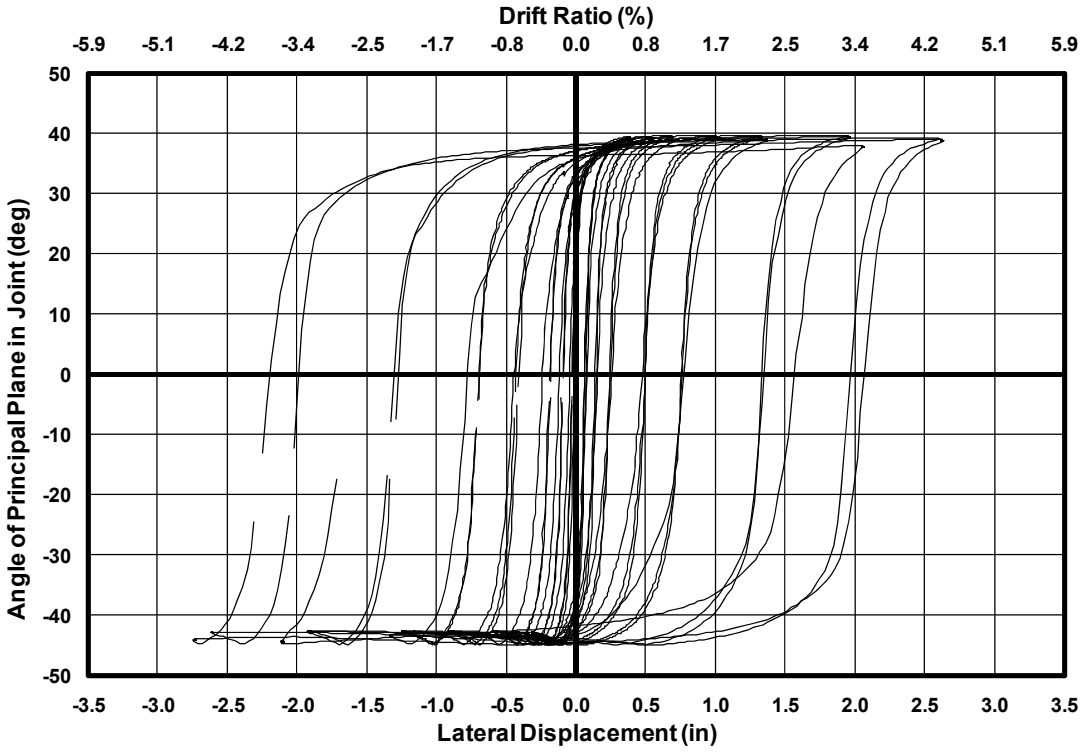

Figure 3-31. Nominal Angle of Principal Plane in Joint vs. Lateral Displacement

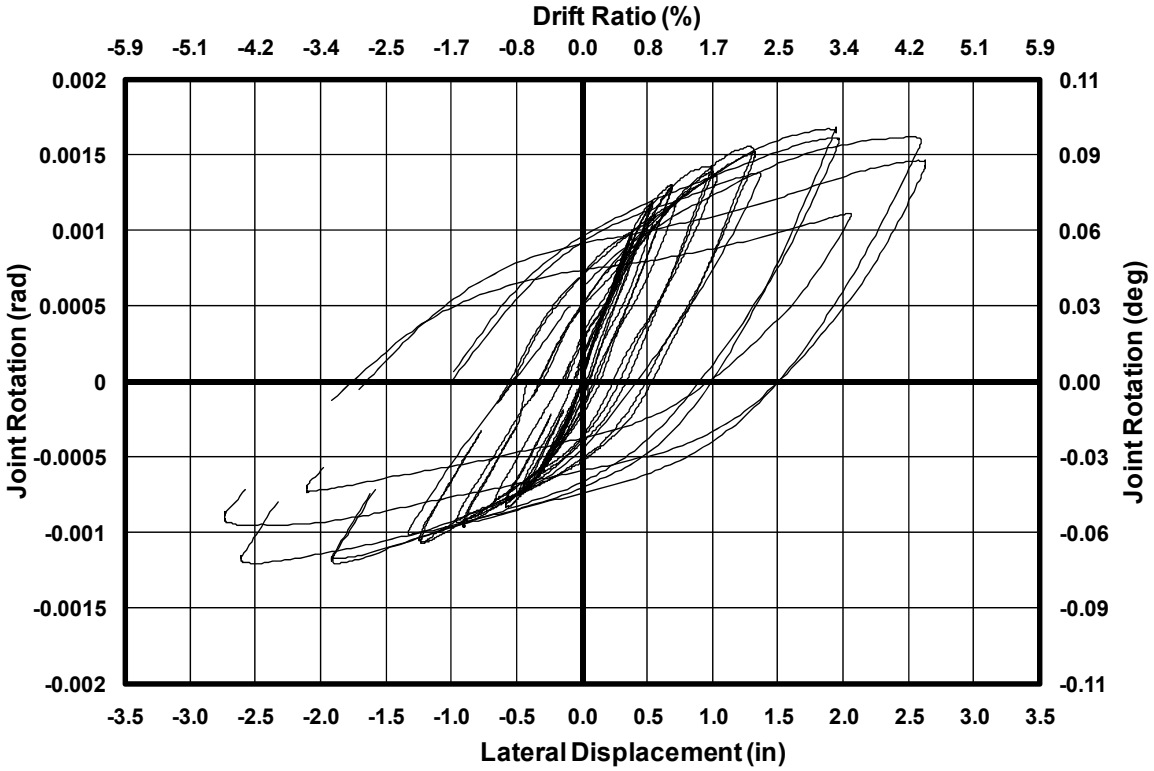

Figure 3-32. Joint Rotation vs. Lateral Displacement

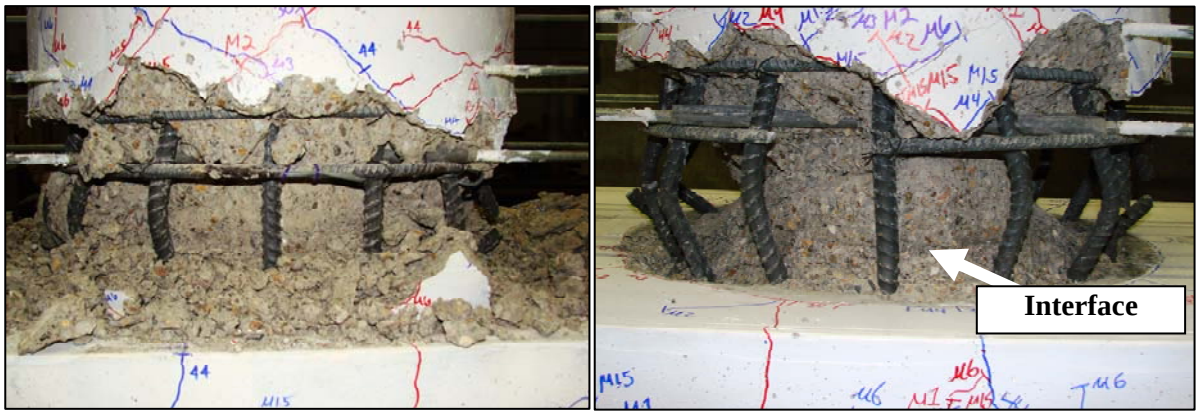

A. Before Removal of Core Concrete B. After Removal of Core Concrete

Figure 3-33. Bedding Layer (Post Test)

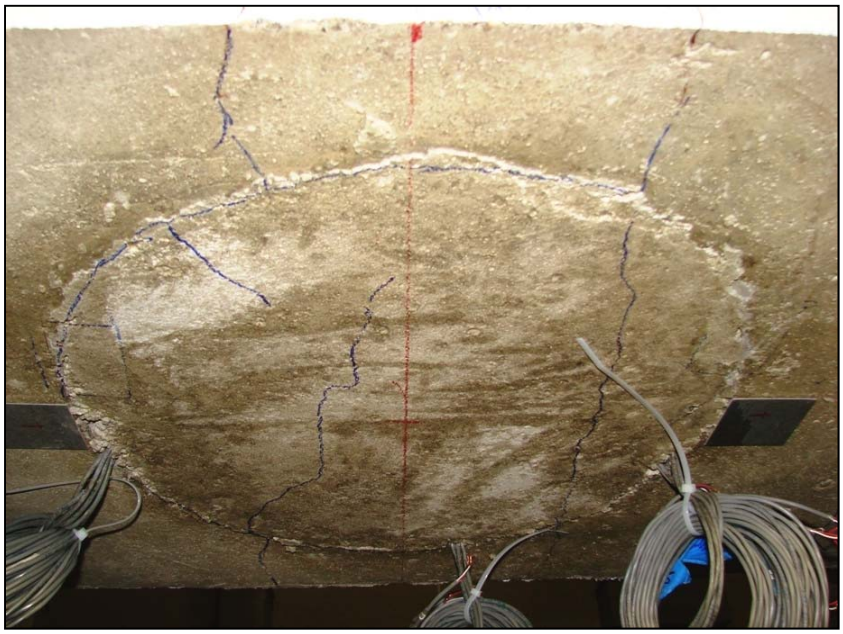

Figure 3-34. Flexural Cracks at Exposed Cap Pocket Surface (Post Test)

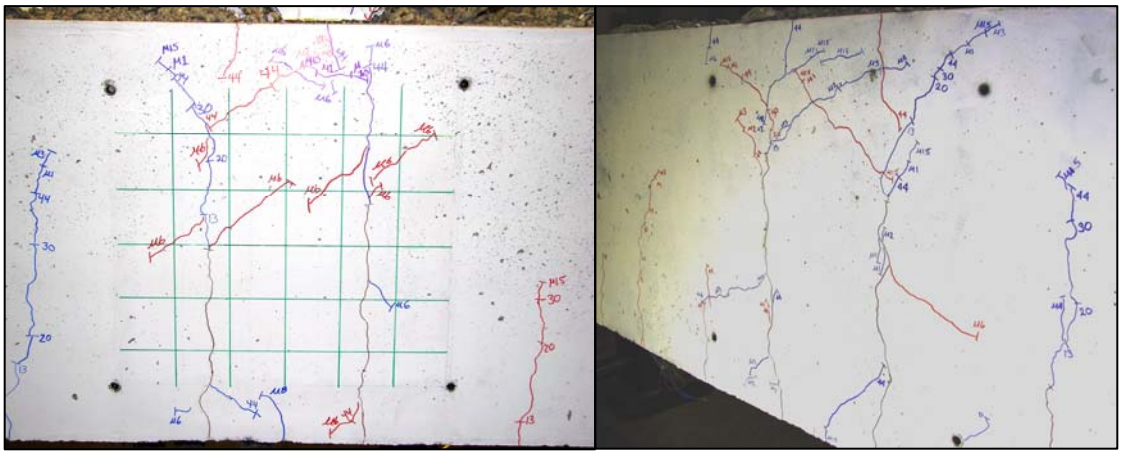

A. East Side—CPFD B. West Side—CPFD

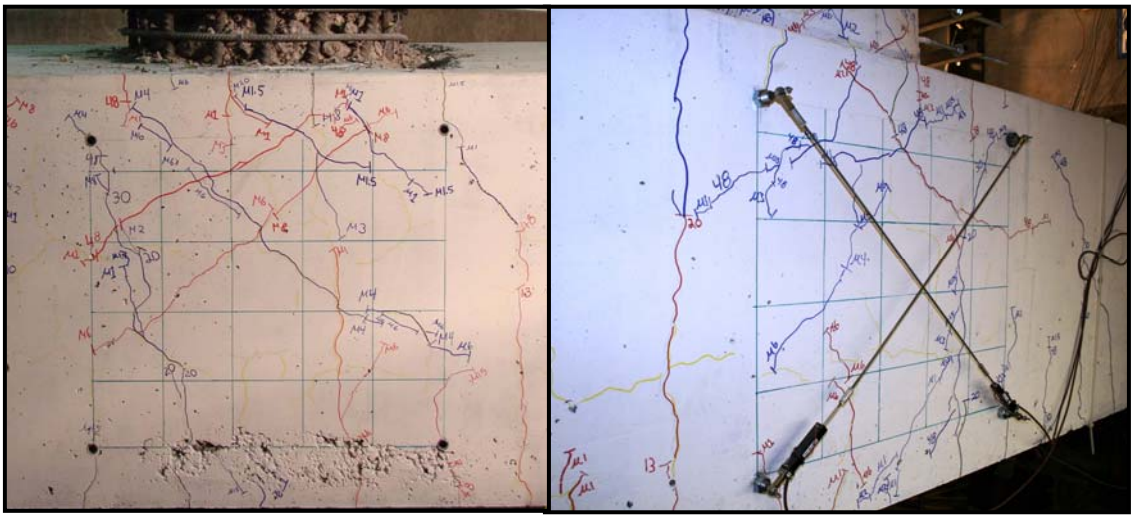

C. East Side—CIP D. West Side—CIP

Figure 3-35. Joint Region Cracking Post Test—CPFD vs. CIP

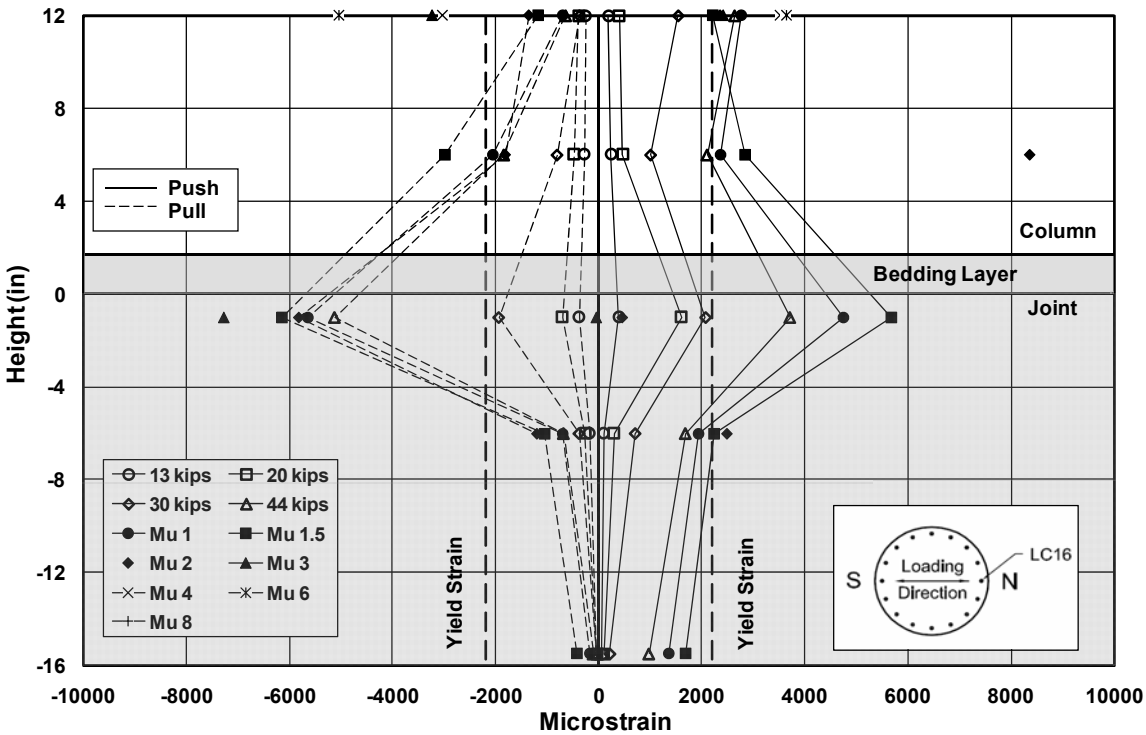

Figure 3-36. Strain Profile—Column Longitudinal Rebar (North)—CPFD

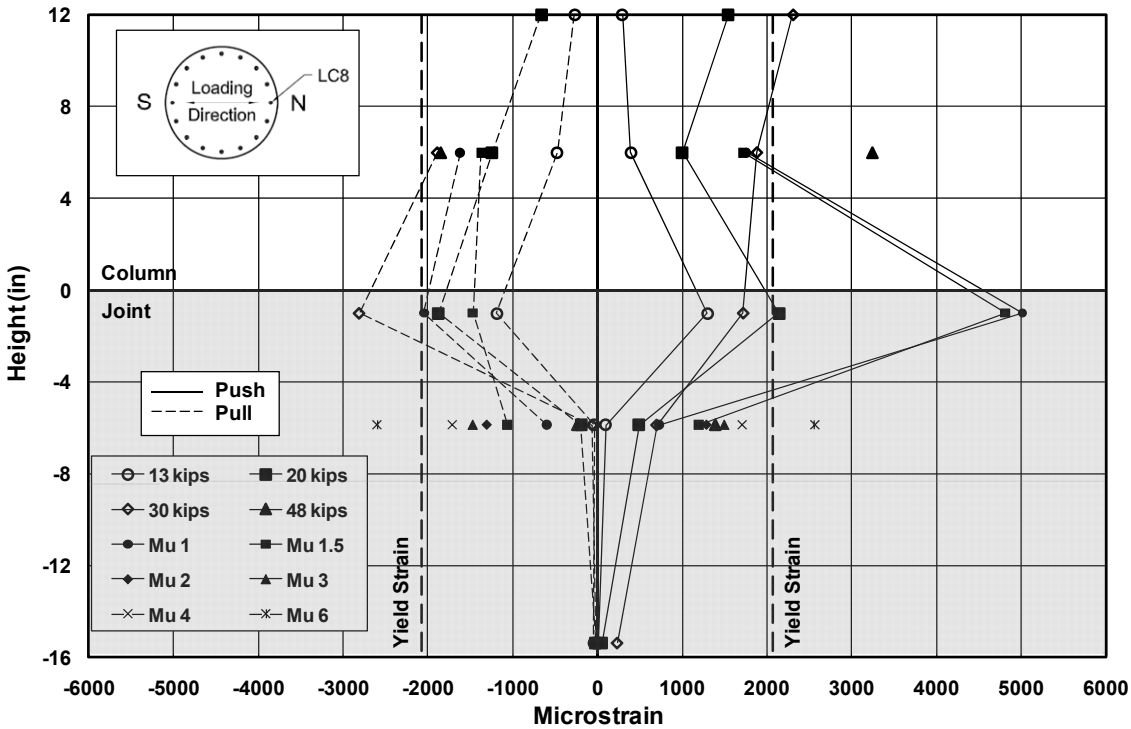

Figure 3-37. Strain Profile—Column Longitudinal Rebar (North)—CIP

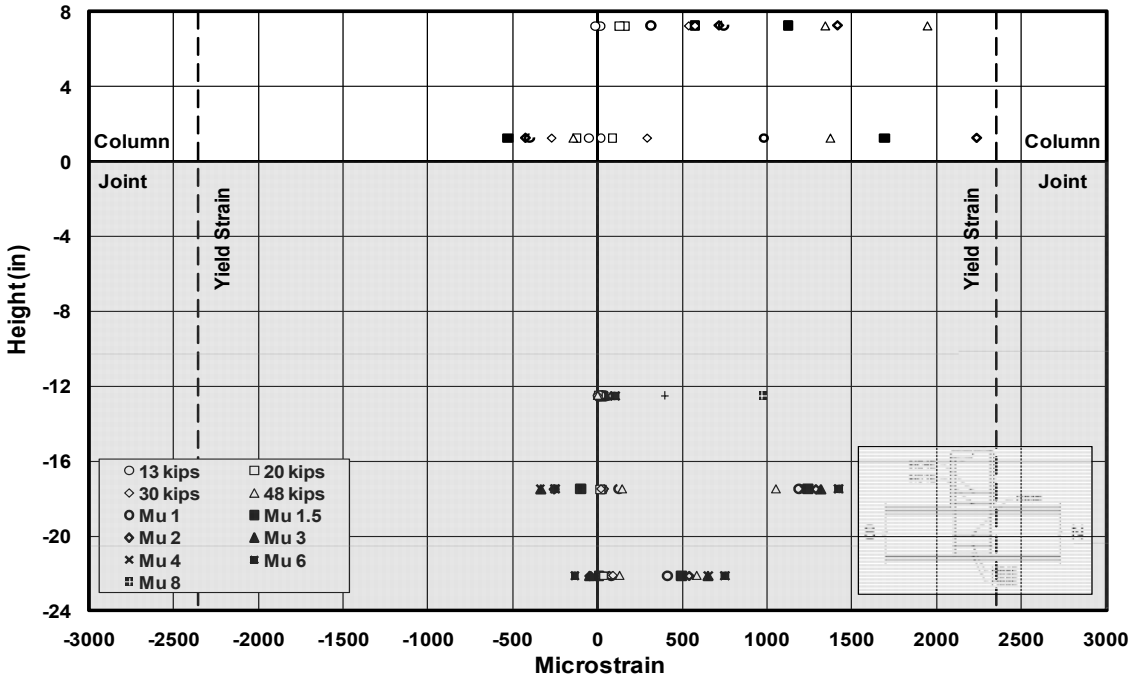

Figure 3-38. Strain Profile—Hoops in Column and Joint (East)—CIP

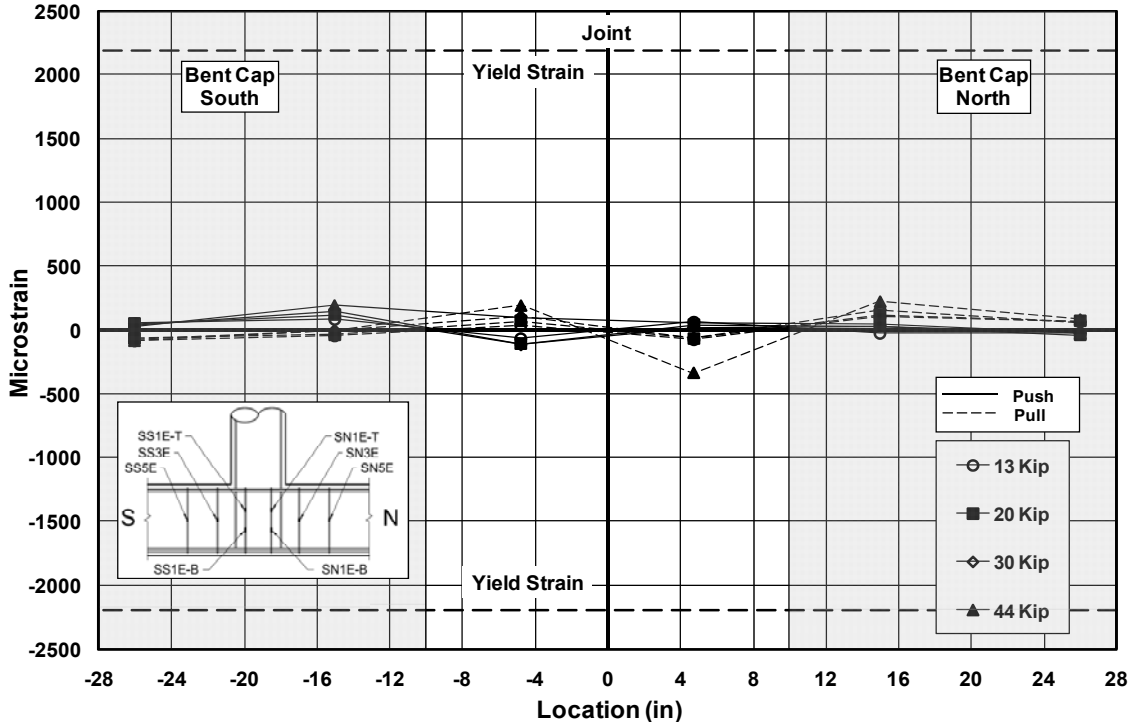

Figure 3-39. Strain Profile—Stirrups in Bent Cap (Midheight) and Joint (Top), Force Control—CPFD

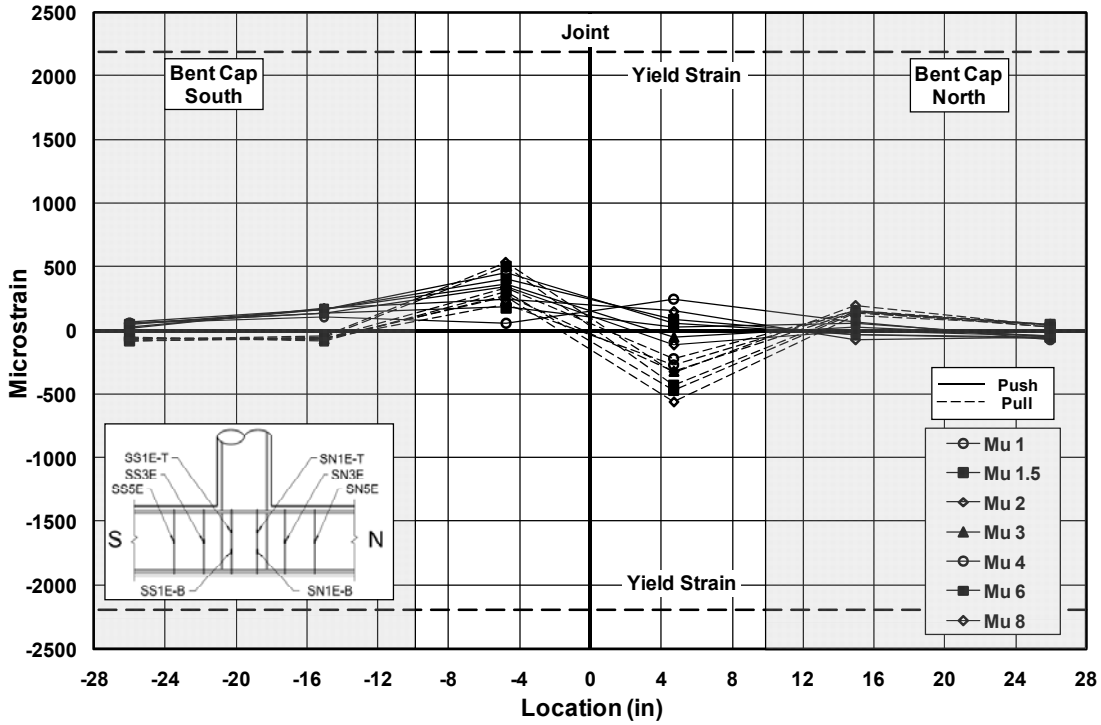

Figure 3-40. Strain Profile—Stirrups in Bent Cap (Midheight) and Joint (Top), Displacement Control—CPFD

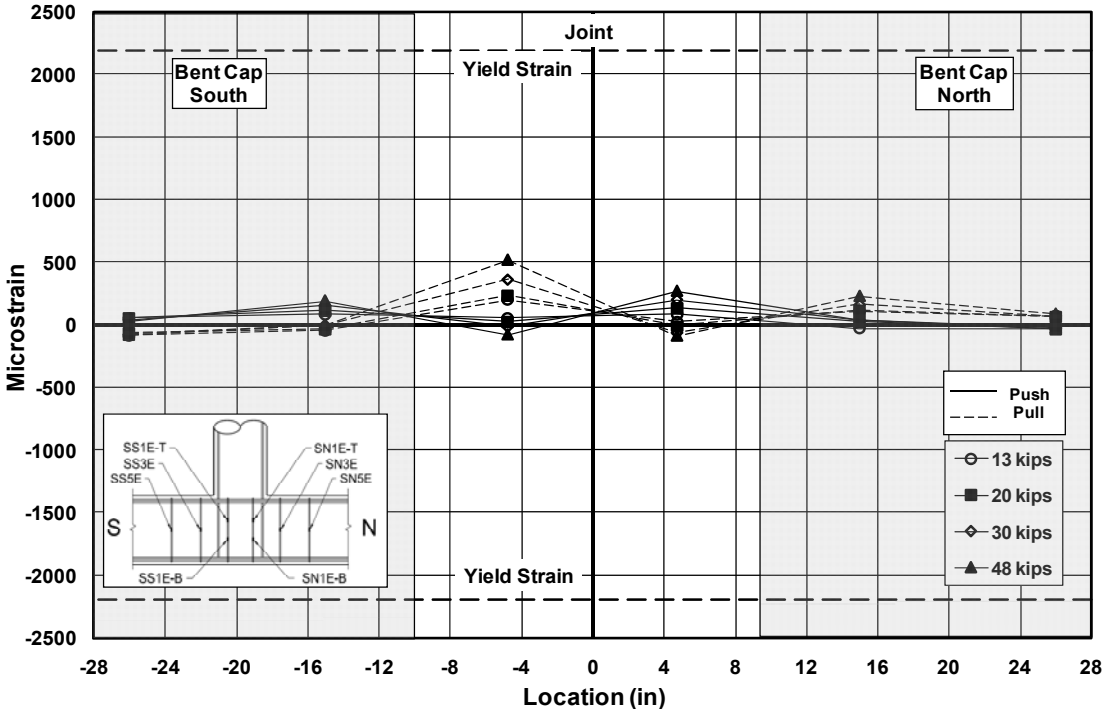

Figure 3-41. Strain Profile—Stirrups in Bent Cap (Midheight) and Joint (Bottom), Force Control—CPFD

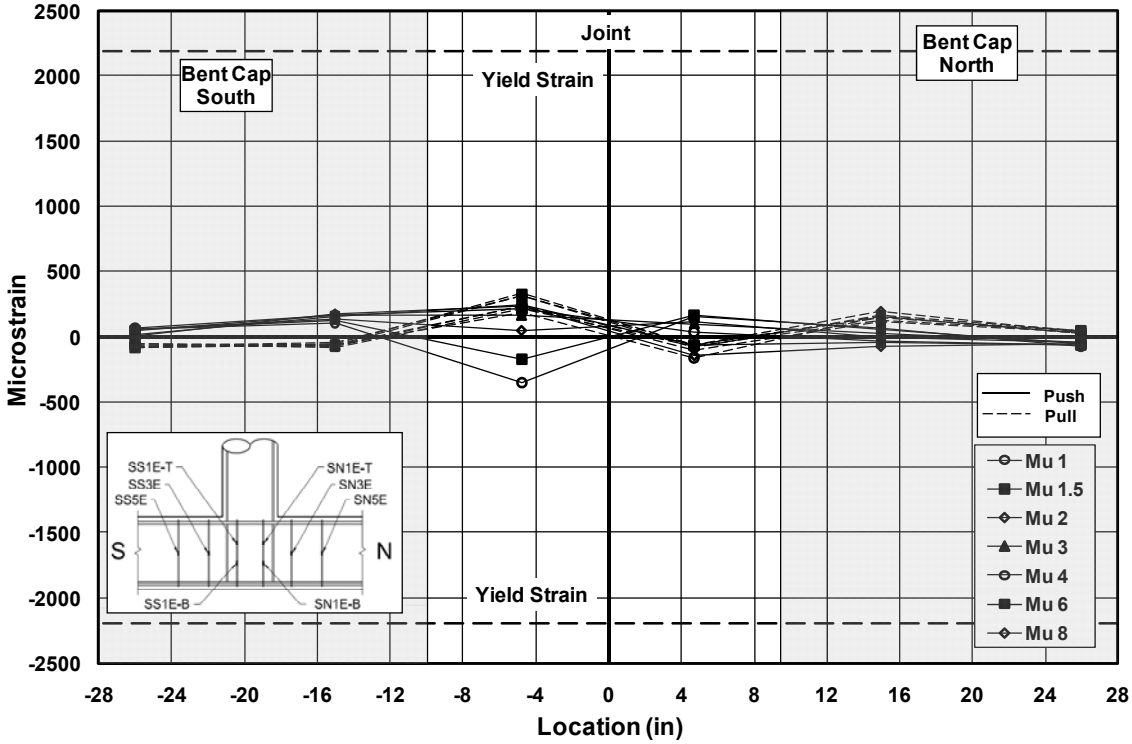

Figure 3-42. Strain Profile—Stirrups in Bent Cap (Midheight) and Joint (Bottom), Displacement Control—CPFD

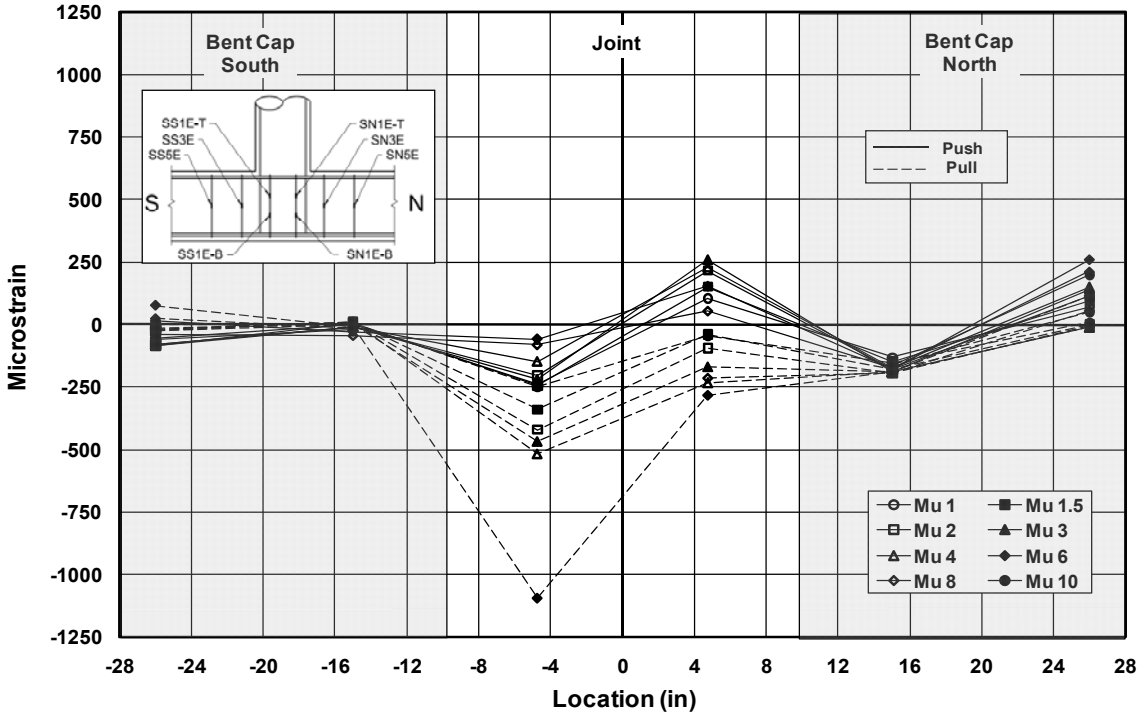

Figure 3-43. Strain Profile—Stirrups in Bent Cap (Midheight) and Joint (Top), Displacement Control—CIP

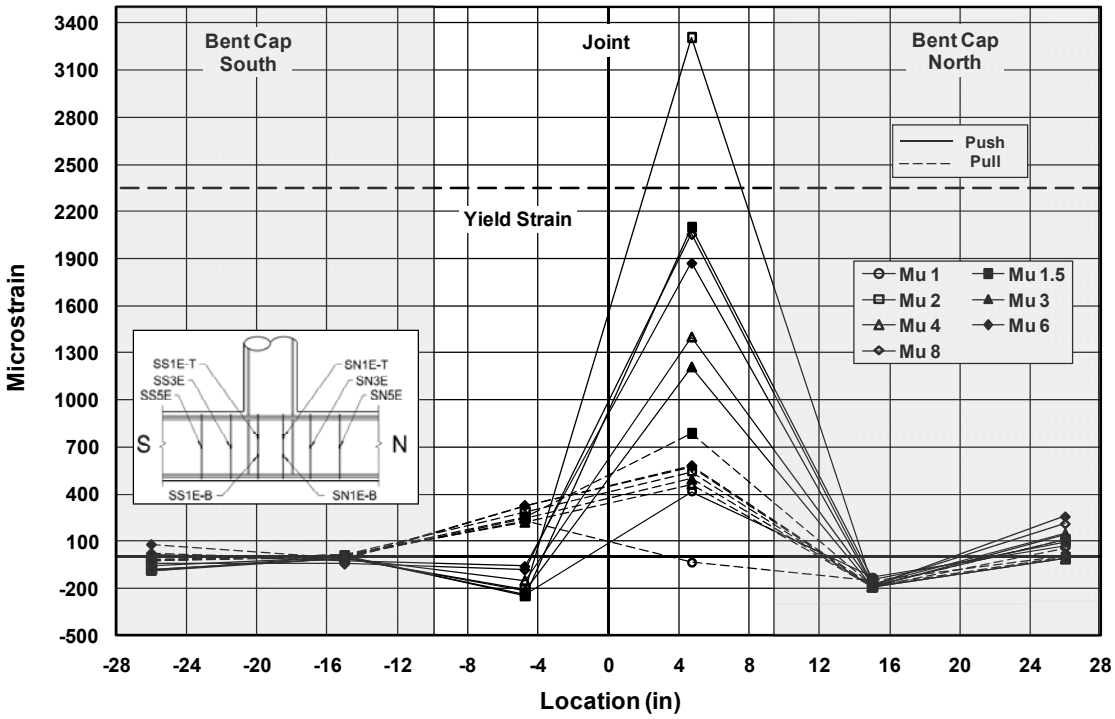

Figure 3-44. Strain Profile—Stirrups in Bent Cap (Midheight) and Joint (Bottom), Displacement Control—CIP

4.0 Summary and Conclusions

4.1 Summary

This report, Emulative Precast Bent Cap Connections for Seismic Regions: Component Tests—Cap Pocket Full Ductility Specimen (Unit 3), is the third in the series of four reports summarizing the California State University, Sacramento (CSUS) component tests supporting National Cooperative Highway Research Program (NCHRP) Project 12-74, "Development of Precast Bent Cap Systems for Seismic Regions". CSUS is investigating two emulative connections—cap pocket and grouted duct—for nonintegral precast bent caps. CSUS is investigating two emulative connections—cap pocket and grouted duct—for nonintegral precast bent caps.

The Cast-in-place (CIP) prototype bridge and emulative component specimens including the Cap Pocket Full Ductility (CPFD) specimen were designed in accordance with the 2006 Recommended LRFD Guidelines for the Seismic Design of Highway Bridges (2006 LRFD RSGS), which contains less conservative joint reinforcement requirements—including a smaller area of vertical stirrups within the joint and smaller area of bent cap longitudinal reinforcement—than the 2009 AASHTO Guide Specifications for LRFD Seismic Bridge Design (2009 LRFD SGS). For a major seismic event, the CIP prototype bridge was designed and detailed to exhibit ductile plastic hinging in the column adjacent to the capacity-protected bent cap and joint. The CPFD specimen was designed using a 42% scale of the central portion of the prototype bridge and loaded in the transverse direction under quasi-static Force Control and Displacement Control sequences.

Specimen response was analyzed including experimental observations, hysteretic response, column curvature response, displacement decomposition, joint response, and strain records. Specimen response was dominated by plastic hinging of the column adjacent to the bent cap, as intended by the CIP prototype design basis and the emulative assumption for the CPFD specimen. In addition, joint distress was minor. However, a distinct crack pattern in the joint developed, different from that observed for the CIP specimen. Diagonal cracking formed above and below the corrugated pipe through a

drift of 3.1% (μ6, pull), at which stage diagonal cracks passed through the central portion of the joint. Particularly striking were the relatively small crack widths that developed for all diagonal cracks (≤0.009 in). In addition, two symmetrical vertical flexural cracks developed in the joint, near the locations of the vertical construction stirrups, and extended nearly through the entire depth of the bent cap. A horizontal crack also formed at the north and south sides of the joint. No spalling occurred in the joint region.

Post-test inspection revealed that the cap pocket concrete and bedding layer performed integrally with the surrounding column and bent cap concrete. Column longitudinal bars were well anchored within the pipe, and there was no evidence of initiation of pullout failure, significant bar slip or pipe slip. At ultimate, two column bars fractured after buckling at the south face of the column. The specimen exhibited excellent ductility to a large drift of 4.3%, which corresponded to a nominal displacement ductility of 8.

The load-displacement response indicated stable hysteretic behavior with loops of increasing area without appreciable strength degradation, as well as stiffness, strength, ductility and other features such as flexural crack distribution anticipated for an emulative beam-column connection test. A comparison of the load-displacement envelope to the predicted envelope showed a good correlation. In addition, close comparisons were found between the CPFD and CIP specimens for: 1) load-displacement hysteretic response envelopes; 2) equivalent viscous damping ratio; and 3) moment-curvature envelopes. The CIP specimen achieved a higher drift than the CPFD specimen (5.9% vs. 4.3%); however, misplacement of the first CPFD column hoop contributed to buckling of the column longitudinal bars. Differences are not attributable to precast connection performance, and system response indicates that the maximum lateral load had been attained at the 4.3% drift.

The displacement decomposition confirmed the dominance of plastic hinging and showed that displacement components were reasonably determined and that predictions were reasonably made. For example, at 2.2% drift (μ4), the flexural components (fixed end rotation and column flexure) accounted for 87% of the column displacement (vs.

prediction of 84%). The contribution of joint shear to overall displacement was minor, not exceeding 9%, and was confirmed by visual observations of minor joint cracking. Column bars were well anchored within the pipe, and although splitting cracks developed in the bent cap related to anchorage of column bars, bar slip was shown to contribute less than 7% to fixed end rotation, similar to 5% for the CIP specimen. Displacement component magnitudes and percentages for the CPFD and CIP specimens compared very favorably.

The precast joint region for the CPFD specimen performed with limited distress during the test. Analysis of the joint indicated that the principal tensile stress was limited to $4.8\sqrt{f_c^{'}}$. This is less than half of the 2006 LRFD RSGS limit of $12\sqrt{f_c^{'}}$, but approximately 40% larger than $3.5\sqrt{f_c^{'}}$, the level at which more extensive (additional) joint reinforcement is required for development of an assumed force transfer mechanism. Principal compressive stresses did not exceed $0.08 f_c^{'}$, less than a third of the 2006 LRFD RSGS limit of $0.25 f_c^{'}$. These values correspond well with the intention of the design and the observed joint performance. As previously mentioned, the maximum joint diagonal crack width was exceptionally small, limited to 0.009 in, although other cracks adjacent to the joint region and flexural cracks reached larger widths. Joint deformation was also very small, with a maximum change in panel area of only 0.13%.

CPFD and CIP joint stresses compared closely, with CPFD normalized nominal joint stresses 11%-19% less than those for the CIP specimen, and the same maximum principal angle (45 deg). The joint shear stiffness based on the joint shear stress-strain response also compared closely, with limited joint softening evident. The maximum change in panel area for the CPFD was considerably smaller than that of the CIP. In addition, the maximum diagonal joint crack width for the CPFD specimen (0.009 in) was considerably smaller than that for the CIP specimen (0.025 in) and the crack pattern differed significantly.

Unlike the CIP specimen, the precast connection used cap pocket concrete which filled the bedding layer between the column and cap. Strength and stiffness properties

for the column and pocket concrete matched within 20%. The bedding layer appeared to perform integrally with the column, did not produce unusual behavior in the joint or specimen, and was not a weak link in the system. Post-test inspection demonstrated integral behavior between components of the specimen based on the following: 1) there was no easily discernable boundary between the bedding layer and column; 2) two flexural cracks developed through the bent cap width, including across the corrugated pipe; 3) no slip was evident between the pocket concrete, pipe, and bent cap; and 4) grout filled the minor air voids at the bedding layer and provided a suitable bearing.

Strain records for column longitudinal bars and hoops provided confirmation of progressive development of plastic hinging and significant strain penetration, including bar yield at 6 in above and below the bedding layer. A similar strain pattern was evident for the CIP specimen. Longitudinal bars yielded (bottom) or nearly yielded (99% of yield, top) within the joint. Patterns and magnitudes, especially for the bottom bar, reasonably followed those of the CIP specimen, although CIP strains reached only yield 46% of yield. Patterns and magnitudes also reasonably matched an assumed force transfer model similar to that of Reference 14. Test specimens, designed per 2006 LRFD RSGS, did not include the significant additional area of bent cap longitudinal reinforcement ($0.245A_{st}$) required by 2009 LRFD SGS.

Evidence of different joint behavior for the specimens included different patterns of strains in confining reinforcement and in stirrups. The peak strain in the CPFD pipe was located at mid-depth, whereas the CIP hoop strain was minimum at the same depth and peaked at approximately two-thirds of the depth of the cap. Principal strains in the pipe were relatively minor, not exceeding 37% of yield, whereas column longitudinal bars yielded at various depths. In addition, supplementary hoops that were placed at the ends of the pipe to reinforce the pipe and limit dilation and potential unraveling reached up to 52% of yield, indicating their importance in joint performance. Stirrup strains within the joint only reached 25% of yield, but yielded for the CIP. Test specimens, designed per 2006 LRFD RSGS, did not require stirrups inside the joint; however, two

joint stirrups with a total area of $0.089A_{st}$ were included for construction. These stirrups provided an area 66% of that required by the 2009 LRFD SGS ($0.135A_{st}$).

4.2 Conclusions

Based on the observed response and data analysis for the CPFD (Unit 3) specimen and a detailed comparison with the CIP (Unit 1) specimen, the following conclusions can be drawn:

1. Despite the less conservative design basis of the specimen using the 2006 Recommended LRFD Guidelines for the Seismic Design of Highway Bridges compared to current 2009 AASHTO Guide Specifications for LRFD Seismic Bridge Design—including a smaller area of vertical stirrups within the joint and smaller area of bent cap longitudinal reinforcement—the CPFD specimen satisfied the performance goal of the design, achieving an extensive drift without appreciable strength degradation and exhibiting extensive plastic hinging of the column, limited joint distress, and essentially elastic behavior of the bent cap.
2. Emulative performance is concluded for the CPFD specimen based on the closely matching overall behavior between the CPFD and CIP specimens, including lateral load-displacement response, plastic hinging, joint shear stiffness, strain patterns of bent cap longitudinal reinforcement, integral behavior between the bedding layer, column, pipe, and bent cap, and minor effects due to bar slip.
3. CPFD response indicates that design specifications for a full ductility cap pocket connection should address: 1) vertical joint stirrups inside and outside the joint; 2) pipe thickness based on providing the same circumferential hoop force in the joint as that required by transverse reinforcement provisions of Article 8.13.3 of the 2009 AASHTO Guide Specifications for LRFD Seismic Bridge Design; 3) supplementary hoop at ends of the pipe; and 4) additional longitudinal bent cap reinforcement.

4. Construction specifications should address fabrication and assembly processes as well as concrete within the cap pocket.
5. Additional analysis is required to develop a new model that fully characterizes cap pocket joint behavior, including joint forces, pipe effects, crack patterns, and strain distributions.

References

1. Matsumoto, Eric. E., *Emulative Precast Bent Cap Connections for Seismic Regions: Component Tests—Cast-in-place Specimen (Unit 1)*, ECS Report No. ECS-CSUS-2009-01, California State University, Sacramento, CA (November 2009) 89 pp.
2. Tobolski, M.J., Restrepo, J.I., Matsumoto, E.E., and Ralls, M.L., *Development of Precast Bent Cap Concepts*, SSRP Report No. 06/10. University of California, San Diego, La Jolla, CA (September 2006) 176 pp.
3. Restrepo, J.I. and Matsumoto, E.E., *National Cooperative Highway Research Program (NCHRP), Project 12-74, Development of Precast Bent Cap Systems for Seismic Regions*, Proposal to Research Board (March 31, 2005).
4. National Corrugated Steel Pipe Association, http://www.ncspa.org, (As of May 1, 2007).
5. Imbsen, R. A., *Recommended LRFD Guidelines for the Seismic Design of Highway Bridges, 2006,* TRC/Imbsen & Associates, Inc, Rancho Cordova, CA (May 2006).
6. Draft Seismic Guide Specification – March 2007, AASHTO Subcommittee on Bridges and Structures, http://bridges.transportation.org/sites/bridges/docs/2007-03-09GuideSpec.pdf (As of March 22, 2007).
7. "Standard Specification for Corrugated Steel Pipe, Metallic-Coated for Sewers and Drains, AASHTO Standard Specifications for Transportation Materials and Methods of Sampling and Testing," ASTM Designation A760/A760M-09, American Society for Testing and Materials ASTM Standards Vol. 01.06, Philadelphia, PA (2009).
8. "Standard Method of Test for Helical Lock Seam Corrugated Pipe," AASHTO T 249-03, American Association of State and Highway Officials, Washington, DC (2007).
9. Matsumoto, E.E., Wright J., Johnsen, S., Mislinski, S., "Proposed Bridge Design Calculations and Drawings of the Prototype Bridge and Test Specimen", Submitted by Restrepo, J.I. and Matsumoto, E.E. to National Cooperative Highway Research Program Project (NCHRP) 12-74 Panel (August 11, 2006) 232 pp.
10. Sritharan, S., Priestley, M.J.N., and Seible, F., *Seismic Response of Column/Cap Beam Tee Connections with Cap Beam Prestressing*, SSRP Report No. 96/09. University of California, San Diego, La Jolla, CA (December 1996) 296 pp.
11. XTRACT, User's Manual, TRC/Imbsen Software Systems, Rancho Cordova, CA (2006).
12. Chopra, A. K., *Dynamics of Structures: Theory and Applications to Earthquake Engineering*, Prentice Hall (2000).
13. American Association of State Highway and Transportation Officials. AASHTO Guide Specifications for LRFD Seismic Design Specifications (First Edition), Washington, DC (2009).

14. Matsumoto, E.E., Waggoner, M.C., Sumen, G., Kreger, M.E., Wood, S.L., and Breen, J.E., *Development of a Precast Bent Cap System*, Research Report 1748-2, Center for Transportation Research, The University of Texas at Austin, TX (January 2001) 372 pp.
15. Matsumoto, E.E., Waggoner, M.C., Kreger, M.E., Vogel, J., Wolf, L., "Development of a Precast Concrete Bent-Cap System," *PCI Journal*, Vol. 53, No. 3 (May-June 2008) pp.74-99.
16. Sritharan, S. "Improved Seismic Design Procedure for Concrete Bridge Joints," *Journal of Structural Engineering*, American Society of Civil Engineers, Reston, VA, Vol. 131, No. 9 (September 2005) pp. 1334-1344.
17. "Standard Specification for Steel Sheet, Metallic-Coated by the Hot-Dip Process for Corrugated Steel pipe," ASTM Designation A929/A929M-01, American Society for Testing and Materials ASTM Standards Vol. 01.01, Philadelphia, PA (2007).

Notation

A_c	Cross sectional area of column (in^2)
A_L	Area of hysteretic loop for a complete cycle (push and pull) (kip-in)
A_R	Area of rectangle bounded by maximum loads and displacements of a complete hysteretic loop (kip-in)
B_{cap}	Thickness of the bent cap (in)
BS	Bar Slip (in)
CD	Column displacement (in)
CT	Component total for column displacement (in)
d_{bl}	Nominal diameter of longitudinal column reinforcing steel bars (in)
D_c	Diameter or depth of column in direction of loading (ft or in)
D'_c	Diameter or depth of column in direction of bending (ft or in)
E_c	Modulus of elasticity of concrete (ksi)
FC	Force control
f'_c	Nominal compressive concrete strength (ksi)
f'_{cg}	Nominal compressive grout strength (ksi)
FER	Fixed end rotation of column (in)
f_h	Average normal stress in the horizontal direction within a moment resisting joint (ksi)
f_v	Average normal stress in the vertical direction within a moment resisting joint (ksi)
f_y	Specified minimal yield stress (ksi)
G_c	Shear modulus of concrete (ksi)
h	Distance from c.g. of tensile force in column to c.g. of compressive force on the section (in)
H_{cap}	Height of bent cap (in)
h_i	Height of cell i (in)
h_j	Joint panel height (in)
h_1	Height of cell 1 (in)

$I_{e\,col}$ Effective moment of inertia of column (in^4)

$I_{t\,col}$ Transformed moment of inertia of column (in^4)

L_c Distance from critical section of column (bent cap soffit) to point of contraflexure (in)

L_{cap} Length of bent cap (in)

l_{ac} Length of column reinforcement embedded into bent cap (in)

l_i Distance from point of contraflexure of column to the midheight of cell I (in)

l_j Diagonal joint panel length (in)

l_1 Distance from point of contra flexure of column to the midheight of cell 1 (in)

l'_g Strain penetration length of cell 1 (in)

l_{sp} Equivalent strain penetration length taken as $0.022 f_y d_{bl}$ (in)

M_{YE} Theoretical column moment at effective yield based on moment-curvature analysis (kip-in or kip-ft)

M_{Yexp} Experimental first yield moment of column (kip-in or kip-ft)

p_c Principal compressive stress (ksi)

P_H Horizontal actuator force on side of column stub (kips)

p_t Principal tensile stress (ksi)

P_V Vertical actuator force on top of column stub (kips)

T_c Column tensile force (kip)

v_{jv} Nominal vertical shear stress in a moment resisting joint (ksi)

w_c Width of cell (in)

w_j Joint panel width (in)

γ_j Nominal vertical shear strain in a moment resisting joint (ksi)

Δ_{bs} Column displacement due to bar slip (in)

$\Delta_{bs,s}$ Bar slip displacement, south (in)

$\Delta_{bs,n}$ Bar slip displacement, north (in)

$\Delta_{F,i}$ Column Displacement due to flexure at cell i (in)

$\Delta_{F,1}$ Column displacement due to fixed end rotation at cell 1 (in)

$\delta h_{i,n}$ Column displacement of cell i, north (in)

$\delta h_{i,s}$	Column displacement of cell i, south (in)
δ_j	Increase in diagonal joint panel length (in)
δ'_j	Increase in diagonal joint panel length in direction perpendicular to l_j (in)
Δ_{jr}	Column displacement due to joint rotation (in)
$\delta_{jr,n}$	Vertical displacement of bent cap at north end of joint (in)
$\delta_{jr,s}$	Vertical displacement of bent cap at south end of joint (in)
Δ_{js}	Column displacement due to joint shear (in)
δ_n	Joint rotation displacement, north (in)
δ_s	Joint rotation displacement, south (in)
Δ_s	Column displacement due to column shear (in)
Δ_Y	System first yield displacement (in)
Δ_{ye}	Member effective yield displacement (in)
Δ_{YE}	System effective yield displacement (in)
ξ	Equivalent viscous Damping ratio
μ_D	Displacement ductility demand
φ	Column curvature (1/in)

List of Equations

Average joint shear strain	$\gamma_j = \frac{\delta_j - \delta'_j}{2l_j}\left(\frac{h_j}{w_j} + \frac{w_j}{h_j}\right)$
Average joint shear stress	$v_{jv} = \frac{T_c}{l_{ac}B_{cap}}$
Average principal angle in joint	$\theta_p = \frac{A_c}{2} tan^{-1}\left(v_{jv} / \frac{f_h - f_v}{2}\right)$
Average principal compressive stress in joint	$p_c = \frac{(f_h + f_v)}{2} + \sqrt{\left(\frac{f_h - f_v}{2}\right)^2 + {v_{jv}}^2}$
Average principal tensile stress in joint	$p_t = \frac{(f_h + f_v)}{2} - \sqrt{\left(\frac{f_h - f_v}{2}\right)^2 + {v_{jv}}^2}$
Column displacement due to bar slip	$\Delta_{bs} = \left(\frac{\Delta_{bs,s} - \Delta_{bs,n}}{D'_c}\right)\left(L_c + H_{cap}\right)$
Column displacement due to column shear (analytical)	$\Delta_s = \frac{P_H L_c}{0.9 A_c G_c}\left(\frac{E_c I_{tcol}}{E_c I_{ecol}}\right)$
Column displacement due to flexure at cell i	$\Delta_{F,i} = l_i \frac{\left(\delta h_{i,n} - \delta h_{i,s}\right)}{w_c}$
Column displacement due to joint rotation	$\Delta_{jr} = \frac{(\delta_n - \delta_s)}{w_j}\left(L_c + H_{cap}\right)$
Column displacement due to joint shear	$\Delta_{js} = \gamma_j\left(L_c - D_c \frac{\left(H_{cap}/2\right)}{L_{cap}}\right)$
Column curvature, cell i	$\varphi = \frac{\Delta_{F,i}/W_c}{l'_g}$
Column tensile force	$T_c = \frac{M_o^{col}}{h} = \frac{P_h L_c}{h}$

Equivalent viscous damping ratio	$\xi = \left(\frac{2}{\pi}\right)\left(\frac{A_L}{A_R}\right)$
Joint rotation angle	$\theta_{jr} = \frac{\delta_{jr,n} - \delta_{jr,s}}{D_c}$
Modified height of cell 1 accounting for strain penetration	$l'_g = l_{sp} + h_1\left(1 - 1.67\, {h_1}/{L_c}\right)$
System effective yield displacement	$\Delta_{YE} = \frac{M_{YE}}{M_{Yexp}}\Delta_Y$

California State University, Sacramento
College of Engineering and Computer Science
Research Report

EMULATIVE PRECAST BENT CAP CONNECTIONS FOR SEISMIC REGIONS: COMPONENT TESTS— CAP POCKET LIMITED DUCTILITY SPECIMEN (UNIT 4)

Eric E. Matsumoto, Ph.D., P.E.

November 20, 2009

Final Report for: NCHRP 12-74, Development of Precast Bent Cap Systems for Seismic Regions

ECS Report Number: ECS-CSUS-2009-04

College of Engineering and Computer Science

California State University, Sacramento

Sacramento, California 95819-6023

California State University, Sacramento
College of Engineering and Computer Science
Research Report

EMULATIVE PRECAST BENT CAP CONNECTIONS FOR SEISMIC REGIONS: COMPONENT TESTS— CAP POCKET LIMITED DUCTILITY SPECIMEN (UNIT 4)

Eric E. Matsumoto, Ph.D., P.E.
Associate Professor, Structural Engineering

November 20, 2009

Final Report for: NCHRP 12-74, Development of Precast Bent Cap Systems for Seismic Regions

ECS Report Number: ECS-CSUS-2009-04

College of Engineering and Computer Science
California State University, Sacramento
Sacramento, California 95819-6023

Please cite this report as follows:

Matsumoto, Eric. E., *Emulative Precast Bent Cap Connections for Seismic Regions: Component Tests—Cap Pocket Limited Ductility Specimen (Unit 4)*, ECS Report No. ECS-CSUS-2009-04, California State University, Sacramento, CA (November 2009) 135 pp.

DISCLAIMER

The research presented in this report was conducted as part of the National Cooperative Highway Research Program, Project 12-74, Development of Precast Bent Cap Systems for Seismic Regions. The opinions and conclusions expressed or implied in the report are solely those of the author. They are not necessarily those of the Transportation Research Board, the National Research Council, the Federal Highway Administration, the American Association of State Highway and Transportation Officials, or the individual states participating in the National Cooperative Highway Research Program.

ACKNOWLEDGMENT OF SPONSORSHIP

This work was sponsored by the American Association of State Highway and Transportation Officials, in cooperation with the Federal Highway Administration, and was conducted in the National Cooperative Highway Research Program, which is administered by the Transportation Research Board of the National Research Council.

OTHER ACKNOWLEDGEMENTS

The author gratefully acknowledges the significant contributions from many graduate and undergraduate students, as well as laboratory technicians at California State University, Sacramento. Of particular note are Arvind Gopalakrishna, Andy Wilson, Jeremy Wright, P.E., Jim Ster, and Brett Anthony. The author also gratefully acknowledges contributions from the NCHRP 12-74 Team, including Dr. Jose I. Restrepo and Matthew Tobolski, University of California, San Diego; Mary Lou Ralls, P.E., Ralls-Newman LLC; and Steve Mislinski, P.E, AECOM/LAN Engineering. Finally, the author gratefully acknowledges the many contributions of Clark Pacific, West Sacramento, CA, including those of Glen Underwood and Don Clark, for fabrication support.

EXECUTIVE SUMMARY

This report, Emulative Precast Bent Cap Connections for Seismic Regions: Component Tests—Cap Pocket Limited Ductility Specimen (Unit 4), is the fourth in the series of four reports summarizing the California State University, Sacramento (CSUS) component tests supporting National Cooperative Highway Research Program (NCHRP) Project 12-74, "Development of Precast Bent Cap Systems for Seismic Regions". CSUS is investigating two emulative connections—cap pocket and grouted duct—for nonintegral precast bent caps.

The Cast-in-place (CIP) prototype bridge and emulative full ductility component specimens (Grouted Duct and Cap Pocket Full Ductility (CPFD)) were designed in accordance with the 2006 Recommended LRFD Guidelines for the Seismic Design of Highway Bridges (2006 LRFD RSGS), which contains less conservative joint reinforcement requirements than the 2009 AASHTO Guide Specifications for LRFD Seismic Bridge Design (2009 LRFD SGS). For a major seismic event, the CIP prototype bridge and full ductility specimens were designed and detailed to exhibit ductile plastic hinging in the column adjacent to the capacity-protected bent cap and joint.

Similar to the CPFD specimen, the Cap Pocket Limited Ductility (CPLD) specimen used a 42% scale of the central portion of the prototype bridge that was loaded in the transverse direction under quasi-static Force Control and Displacement Control sequences. However, the CPLD joint detailing was modified from CPFD to examine the limited ductility SDC B design: 1) elimination of the construction stirrups within the joint; 2) elimination of all joint-related stirrups and horizontal ties placed external to the joint; and 3) elimination of the extra hoops at the ends of the pipe. In addition, bent cap flexural reinforcement was reduced to eliminate potential strengthening of the joint, and bent cap transverse reinforcement, including adjacent to the joint, was reduced to the minimum required based on bent cap shear associated with plastic hinging of the column. It was anticipated that more extensive joint damage than for the CPFD would be exhibited as the specimen displacement ductility approached $\mu 2$, and possibly result in joint failure at larger ductility levels.

Response was characterized by a combination of plastic hinging of the column and joint shear cracking. As diagonal cracks developed in the joint region with increasing lateral load, significant column flexural (and shear) cracks also developed, and flexure eventually dominated the response. The system achieved an unexpectedly large drift ratio of 5.1%, which corresponded to a nominal displacement ductility of 8. Failure was due to buckling of column longitudinal reinforcement followed by fracture of two bars in the plastic hinging region, rather than joint failure. At ultimate, significant joint shear cracks with minor spalling had developed as well as a moderate amount of bar slip.

Similar to the CIP and CPFD specimens, the CPLD load-displacement response indicated stable hysteretic behavior without appreciable strength degradation. However, the CPLD achieved a curvature approximately 30% less than the CPFD and CIP specimens at the same drift, due to softening of the joint due to shear cracking. Displacement decomposition demonstrated that the CPLD column displacement due to joint shear was nearly an order of magnitude larger, and the flexural component was approximately 25% less than that of the full ductility specimens. The CPLD flexure/shear displacement component ratio averaged 2.2, nearly an order of magnitude smaller than that of the CPFD and CIP specimens (16.5 and 20.0, respectively). Also, the bar slip component of column displacement was approximately 11 times that of the CIP and CPFD specimens. However, a bar anchorage equation from prior research on grout pockets indicated a larger development length for the CPLD column bars (beyond that required by 2006 LRFD RSGS) may have helped reduce slip.

The precast joint region for the CPLD specimen exhibited a significant level of distress that increased throughout the test. Analysis of the joint indicated that the principal tensile stress reached $7.0\sqrt{f_c'}$, twice the $3.5\sqrt{f_c'}$ limit at which extensive (additional) joint reinforcement is required because of the likelihood of joint shear cracking. However, per SDC B design, the CPLD specimen intentionally did not include joint reinforcement to limit growth of joint shear cracks. The CPLD maximum stresses (nominal joint shear, principal tensile, and principal compressive) were 47%-86% larger

than the CPFD and 30%-48% larger than the CIP. In addition, the change in the CPLD panel area was approximately three times that of the full ductility specimens.

Diagonal cracks were as wide as 0.050 at μ2 and increased to 0.080 in at ultimate, with minor associated spalling. In contrast, CPFD joint diagonal crack widths were limited to 0.009 in, and CIP crack widths were 0.025 in maximum. Joint shear stress-strain response revealed significant joint softening at increasing drift ratios. This was in contrast to the stiff joint response and limited joint shear strains that developed for the full ductility specimens. In addition, the CPLD diagonal cracks resembled the CIP pattern much more than those of the CPFD. Joint stirrups were not used for the CPLD; however, CIP analysis demonstrated that construction stirrups with an area 65% of that required by the 2009 LRFD SGS were highly effective, reaching yield, and limiting crack development and opening. CPFD stirrups reached smaller levels of strain.

Strain records confirmed plastic hinging, effective confinement in the column and joint, and strain penetration into the joint. However, due to joint shear cracking, significant column spalling and associated hoop strains developed at a much larger drift than for the full ductility specimens. In addition, much larger pipe strains developed for the CPLD, up to 70% of yield, compared to the CPFD. Strain distributions also differed.

Strain patterns for the longitudinal bent cap bars were reasonably consistent between specimens, especially for the bottom bars. At the centerline, the CPLD and CPFD bars yielded, and the CIP reached 46% of yield. Patterns reasonably matched expected distribution per an assumed force transfer model. Specimens did not include the signfiicant additional bent cap longitudinal reinforcement ($0.245A_{st}$) required by the 2009 LRFD SGS. CPLD stirrups reached 61% of yield outside the joint, compared to 10% of yield for the other specimens. Construction stirrups within the CIP joint yielded and reached approximately 25% of yield for the CPFD. The lack of vertical joint stirrups in the CPLD specimen allowed joint shear cracks to develop and grow unrestrained.

Despite elimination of joint reinforcement used in the full ductility specimens—including construction stirrups within the joint, joint-related stirrups and horizontal ties external to the joint, and hoops at the ends of the pipe—as well as reduction of bent cap

flexural reinforcement and bent cap transverse reinforcement, the CPLD specimen satisfied the main performance goal of the SDC B design, exhibiting ductile plastic hinging and reaching an extensive drift without appreciable strength degradation, which is attributed to the effectiveness of the corrugated steel pipe within the joint. However, due to the absences of vertical joint stirrups per the SDC B design, extensive joint shear cracking developed, softening the joint, contributing significantly to column drift, and delaying (but not preventing) flexural plastic hinging. It can be reasonably deduced that similar, or more severe, joint behavior would likely develop for a similarly detailed SDC B CIP connection. Thus, emulative behavior can be concluded for the CPLD specimen, although the joint shear damage does not match the expressed intent of the 2009 LRFD SGS for limited ductility structures, limiting inelastic action to the flexural plastic hinges. Hence, design specifications for a limited ductility cap pocket connection should address minimum area of vertical joint stirrups and minimum transverse reinforcement (i.e., pipe thickness). Similar provisions are recommended for SDC B CIP joints. Construction specifications should address fabrication and assembly processes and flowable concrete within the cap pocket. Additional analysis is recommended to develop a new joint model that fully characterizes cap pocket joint behavior.

TABLE OF CONTENTS

Page

LIST OF TABLES

Chapter 1

Chapter 2

Chapter 3

LIST OF FIGURES

Chapter 2

Chapter 3

1.0 Introduction

1.1 Background

This report, Emulative Precast Bent Cap Connections for Seismic Regions: Component Tests—Cap Pocket Limited Ductility Specimen (Unit 4), is the fourth in the series of four reports summarizing the California State University, Sacramento (CSUS) component tests supporting National Cooperative Highway Research Program (NCHRP) Project 12-74, "Development of Precast Bent Cap Systems for Seismic Regions". It is recommended that the reader review the Cast-in-place Specimen (Unit 1) Test Report as well as the Cap Pocket Full Ductility (Unit 3) Test Report for details on the project background and related results. [1, 2]

1.2 NCHRP 12-74 Research Objective

To address the uncertainties associated with seismic behavior of precast bent cap systems and the lack of specifications, the National Cooperative Highway Research Program (NCHRP) funded Project 12-74, Development of Precast Bent Cap Systems for Seismic Regions, to develop design methodologies, design and construction specifications, design examples, and semi-standard details for seismic precast bent cap systems using emulative and hybrid connections for nonintegral and integral systems. [3, 4]

1.3 CSUS Research Objective and Approach

The California State University, Sacramento (CSUS) research objective is to develop design methodologies, design and construction specifications, design examples, and semi-standard details for nonintegral emulative precast bent caps. As reported in Reference 3, two emulative connections types—grouted duct and cap pocket—were selected for development based on a review of past connection usages and consideration of expected seismic performance, durability, constructability, and cost.

Nine tasks are included in NCHRP 12-74 to reach the overall research objectives. [4] As part of Task 6—Conduct of Analytical and Experimental Work—CSUS conducted tests and associated analysis to investigate grouted duct and cap pocket connections.

Table 1-1 shows the Test Matrix for CSUS component tests, including a brief summary of the four test specimens (units).

1.4 Scope of Report

This report, Emulative Precast Bent Cap Connections for Seismic Regions: Component Tests—Cap Pocket Limited Ductility Specimen (Unit 4), is the fourth in a series of four reports that summarize the experimental and analytical efforts for each CSUS test unit. This report includes the following chapters:

1.0 Introduction: Background, statement of NCHRP 12-74 research objective, CSUS research objective and approach, and scope of report.

2.0 Specimen Design, Fabrication, and Testing: Summary of the Cap Pocket Limited Ductility (CPLD) specimen design, fabrication and testing, including key aspects of fabrication processes and issues, as well as specimen material properties, test setup, loading sequence, instrumentation and pretest predictions.

3.0 Specimen Response and Analysis: Experimental observations, hysteretic response, column curvature response, displacement decomposition, joint response, and strain records. An important additional aspect of this report is the comparison of CPLD results to those of the CPFD (Unit 3) and the Cast-in-place (CIP) (Unit 1).

4.0 Summary and Conclusions.

1.5 Tables

Table 1-1. CSUS Component Test Matrix for Bent Cap-Column Connections

Test Unit	Brief Description
1. Cast-in-place (CIP)	Control specimen for comparison to precast connections, with bent cap and column detailing intended to achieve full ductility
2. Grouted Duct Connection (GD)	Individual ducts cast in bent cap to connect each column bar, with bent cap and column detailing intended to achieve full ductility
3. Cap Pocket Full Ductility (CPFD)	Single pipe cast in bent cap to connect all column bars, with bent cap and column detailing intended to achieve full ductility
4. Cap Pocket Limited Ductility (CPLD)	Single pipe cast in bent cap to connect all column bars, with bent cap and column detailing intended to achieve limited ductility

2.0 Specimen Design, Fabrication, and Testing

2.1 Design

The Grouted Duct (GD) and CPFD specimens used the same full-ductility design basis as the CIP specimen reported in Reference 1. The GD and CPFD specimens were intended to be a direct comparison to the CIP control specimen. In contrast, the CPLD specimen was intended to investigate the response of a precast cap pocket connection designed according to the principles of limited ductility rather than the full ductility basis used for the other specimens, as given in the 2006 Recommended LRFD Guidelines for the Seismic Design of Highway Bridges (2006 LRFD RSGS) for SDC B. [5] A list of equations used for design, testing, and analysis can be found at the end of this report.

As mentioned in Reference 1, the CIP prototype bridge and emulative full ductility component specimens were designed in accordance with the 2006 LRFD RSGS prepared as part of NCHRP 20-07 Task 193. The 2006 LRFD RSGS was superseded by the 2007 Proposed AASHTO Guide Specifications for LRFD Seismic Bridge Design (2007 LRFD PSGS) and later updated to the current 2009 AASHTO Guide Specifications for LRFD Seismic Bridge Design (2009 LRFD SGS). [6, 7] The 2006 LRFD RSGS contains different—and in some aspects more liberal (i.e., less conservative)—joint reinforcement requirements than the current 2009 LRFD SGS. For example, in contrast the 2006 LRFD RSGS, the 2009 LRFD SGS specifies vertical joint stirrups both inside and outside the joint region, a larger total area of joint stirrups, as well as a significant increase in bent cap longitudinal reinforcement for full ductility structures. Other provisions such as partitions for Seismic Design Categories are the same.

2.1.1 Comparison of SDC D and SDC B Provisions

To illustrate the differences in design and detailing requirements for a full ductility vs. limited ductility structure, this section summarizes major seismic provisions in 2006 LRFD RSGS (and later revisions). Full ductility provisions for structures correspond to Seismic Design Category (SDC) D, whereas limited ductility provisions correspond to SDC B. (SDC C can be considered limited ductility, but 2006 LRFD RSGS and 2009 LRFD SGS provisions for SDC C are more closely related to SDC D.) Use of

these provisions for the specimens is based on the assumption that precast connections would achieve emulative performance and thus that 2006 LRFD RSGS provisions developed for CIP structures also apply to the cap pocket connections.

As shown in Table 2-1, the partitions for SDC A through D are based on S_{D1}, the design earthquake response spectral acceleration coefficient at a 1.0 sec period. S_{D1} for SDC D is 0.50 or larger, while SDC B is ranges from 0.15 and 0.30.

The significantly lower design earthquake response spectral acceleration for SDC B compared to SDC D produces a much lower seismic demand and thus permits in a more liberal design and detailing approach. The SDC Core Flowchart of Figure 2-1 shows that, in contrast to SDC D (full ductility), SDC B (limited ductility) design [5, 6]:

1. Does not require identification of an Earthquake Resisting System
2. Allows for an implicit determination of displacement ductility using an approximate equation rather than a pushover analysis
3. Does not require capacity protection
4. Uses a less stringent level of detailing

This corresponds to the expectation that SDC B structures will be subjected to lower displacement ductility demands than for SDC D structures, and SDC B substructure elements are expected to achieve a displacement ductility, μ_D, of (at least) 2.0. [7, Articles C8.3.2, C4.11.1, 4.7.1] SDC D multi-column bents are designed and detailed to achieve a μ_D of 6.0 or more.

Figure 2-2 shows the Detailing Procedure Flow Chart. [6, 5] The repeated listing of special provisions for SDC D (and SDC C), but not for SDC B, emphasizes the significant differences in level of detailing. Table 2-5 summarizes the significant differences in design and detailing levels for SDC D and SDC B. Of the 18 provisions listed, only 6 apply to SDC B structures, whereas all 18 apply to the SDC D structures.

It is especially important to note that joint design of SDC B structures per 2006 LRFD RSGS (and 2009 LRFD AASHTO SGS) is not based on determination of the joint principal tensile stress and does not even include minimum joint (transverse) reinforcement or vertical stirrups. In contrast, SDC D structures require minimum joint

reinforcement and additional joint reinforcement based on the magnitude of the joint principal tensile stress (i.e., relative to likely joint shear cracking). In addition, for full ductility structures, 2006 LRFD RSGS does not distinguish joint reinforcement inside and outside (adjacent to) the joint, whereas 2009 LRFD SGS clearly distinguishes between inside and outside joint reinforcement (both A_s^{jv} and A_s^{jh}).

2.1.2 Design Basis

For direct comparison, the CPLD specimen used as its initial basis the CPFD design, which is summarized in the prototype bridge and specimen design calculations and in the CPFD specimen report. [2, 8] Figure 2-3 shows the portion of the prototype bridge used for the 42% scaled design used for all specimens including the CPLD. CPLD specimen drawings are shown in Figures 2-4 through 2-8.

Table 2-2 provides a detailed comparison of the column, bent cap, and joint reinforcement for the CIP prototype and CPLD specimen. Ratios of the specimen reinforcement to the similitude (or design) ratio vary in important aspects from the other specimens, as explained subsequently. Elimination of joint reinforcement (other than the corrugated steel pipe) according to the SDC B provisions was an intentional design goal.

Emulative performance of the CPLD specimen was to be examined, especially through a displacement ductility of 2, even though a limited ductility CIP specimen was not tested for direct comparison. Thus, although a direct comparison to CPFD and CIP specimens—which were designed and detailed with joint reinforcement for full ductility performance—is not appropriate for making conclusions relative to emulative behavior, comparisons do provide important insight for conclusions.

Differences for the CPLD specimen compared to the CIP specimen included the following:

- Separate precast elements, including the bent cap and column
- Use of a single 18-in diameter pipe in the bent cap to house the column longitudinal reinforcement and serve as both a stay-in-place form and joint hoop reinforcement
- Use of normal weight concrete within the pipe to anchor the column bars

- Use of a 1.5-in bedding layer between the bent cap soffit and column to accommodate tolerances

Table 2-3 summarizes select joint details for the CPLD specimen, including the specifications for the helical corrugated pipe with lock seams. Background and advantages to this pipe are provided in References 2, 9, 10, and 17. The corrugation and lock seam details used for the cap pocket specimens are shown in Figures 2-9 to 2-11.

A comparison of overall specimen details for the CPLD and CPFD is presented in Table 2-4. As mentioned in Reference 2, the CPFD pipe thickness was designed to provide the same nominal circumferential hoop force in the joint as that required for the CIP specimen per 2006 LRFD RSGS, based on a yield strength of 30 ksi for the pipe material and the horizontal component of the helical pipe. In addition, the pipe served as a stay-in-place form for the column bars. The same pipe size and thickness were used for the CPLD and CPFD specimens to allow a direct comparison of specimens. The pipe thickness was not considered excessive and was the minimum size readily available for construction. Table 2-5 indicates that transverse (hoop) joint reinforcement is required for SDC D but not for SDC B.

Table 2-4 reveals important differences that were intentionally incorporated into the CPLD joint detailing to examine the limited ductility specimen, in accordance with the intent and provisions of the 2006 LRFD RSGS for SDC B: 1) elimination of the construction stirrups within the joint region; 2) elimination of all joint-related stirrups and horizontal ties (A_s^{jv}, A_s^{jh}) placed external to the CPFD joint; and 3) elimination of the extra hoop at each end of the pipe. Construction stirrups were added in full ductility specimens to reflect a potential—but not required—field addition to assist in fabrication. Other nonseismic reasons for possibly including vertical stirrups within the joint (e.g., temperature and shrinkage per AASHTO LRFD Bridge Design Specifications [18]) were not addressed. Table 2-4 also reveals that bent cap flexural reinforcement was reduced to eliminate potential strengthening of the joint due to higher bent cap flexural strength (and thus allow potential yielding of flexural reinforcement adjacent to and within the joint) and to provide more accurate prototype scaling. Bent cap transverse reinforcement,

including that adjacent to the joint, was reduced to the minimum required based on bent cap shear associated with plastic hinging of the column, not a joint force transfer mechanism. These modifications were implemented despite the possibility that principal tensile stresses in the joint could exceed the 2006 LRFD RSGS limit of $3.5\sqrt{f_c'}$, at which the additional joint reinforcement is required (but not checked for SDC B).

In addition, CPLD column reinforcement (including confining reinforcement) was not reduced but designed to match the SDC D-based requirements of the CPFD design. This was intended to help ensure that the column would not prematurely become a weak link in the system, but impose as large of a demand and as many cycles as possible through on the joint.

These measures were deemed reasonably conservative for testing to examine limited ductility performance and potential failure modes. The impact of these measures was unknown. However, it was anticipated that more extensive joint damage than for the CPFD would be exhibited as the specimen displacement ductility approached μ2, and possibly result in joint failure at larger ductility levels. It was understood that more stringent detailing could be adopted for SDC B design as required.

2.2 Fabrication

2.2.1 Specimen

The CPLD specimen consisted of a separately cast bent cap and column, as shown in Figures 2-4 through 2-8. Table 2-3 summarizes select design details of the CPLD specimen. The CPLD bent cap used a 25 in x 25 in cross section; however, as summarized in Table 2-4, 8-#5's and 2-#4's (0.50%) were used for flexural reinforcement rather than 12-#5's, and #3's were spaced at 8 in rather than 6 in for transverse (shear) reinforcement. The 20-in diameter column used 16-#5 (1.58%) longitudinal bars and #3 hoops at 2 in, matching the CPFD specimen. No joint reinforcement was used. Column bar embedment depth within the joint was equal the cap depth less 3 in (i.e., 22 in). Figure 2-8 shows a very constructible joint region, without 2-leg construction stirrups in the joint region, in contrast to the CPFD specimen. As shown in later fabrication photos, the joint region was not congested. In addition, the pipe was designed

to be placed between top and bottom bent cap bars, eliminating conflict between the ducts and longitudinal rebar.

2.2.2 Material Properties

Portland cement concrete and steel used in the fabrication and assembly of the bent cap, column, and pipe were tested to determine material properties. Sampling, preparing, and testing of specimens were generally performed in accordance with governing ASTM standards.

2.2.2.1 Portland Cement Concrete

The bent cap, column, and pocket were constructed with normal weight concrete using the concrete mix proportions shown in Table 2-6. The mix design was expected to achieve a 28-day compressive strength of at least 4000 psi based on a water-cement ratio of approximately 0.49. A 3/8-inch maximum coarse aggregate size was used in the concrete mix in accordance with specimen scaling. Standard 6x12 in cylinders were cast from the concrete batch used for the specimen fabrication and assembly. Concrete cylinders were cured for the same length of time and in the same conditions as the concrete specimens. Compression and tensile (split cylinder) tests were conducted in the CSUS Structural Laboratory. Concrete cylinders were produced for each casting and tested over a range of days including test day.

The design and actual properties of the concrete are shown in Table 2-7, and representative concrete compressive strength gain curves are shown in Figure 2-12. Because an additional batch of concrete was required for the last part of specimen casting (top of column, i.e., plastic hinge area), Table 2-7 lists plastic hinge concrete properties as well as the cap/column and pocket. The pocket concrete, cast at a time later than that of the bent cap (i.e., during assembly operations), was intended to achieve a strength and stiffness approximately equal to that of the bent cap. Reasonable pocket-to-bent cap ratios were achieved: compressive strength, 1.00; tensile strength, 1.02; and modulus of elasticity, 0.96. Plastic hinge-column/cap concrete ratios were slightly higher: compressive strength, 1.13, and modulus of elasticity, 1.10.

2.2.2.2 Steel

The column and bent cap longitudinal reinforcing steel consisted of ASTM A706 Grade 60 deformed #5 and #4 rebar, and the column hoops and bent cap stirrups consisted of ASTM A615 Grade 60 (weldable) #3's. Uniaxial tensile tests were conducted on samples from the rebar lot; rebar specimens were prepared in accordance with ASTM requirements. Yield and tensile strengths are shown in Table 2-8 for the different bar sizes. Figure 2-13 shows a stress-strain plot for two representative reinforcing bars. The #3 rebar exhibits the more typical tensile stress-strain response, including a distinct yield point. However, the #5 rebar exhibited a more gradual stress-strain response without a clear yield point. This behavior was accounted for in column moment-curvature calculations.

The pipe was fabricated of steel with properties and dimensions as shown in Tables 2-3 and 2-8. The nominal steel yield strength was 30 ksi, but test coupons exhibited a yield strength of 57.5 ksi. The coupon tensile strength was only slightly higher, 61.0 ksi.

2.2.3 Fabrication and Issues

2.2.3.1 Fabrication

All CSUS specimens were fabricated with the assistance of Clark Pacific, West Sacramento, CA. The fabrication and assembly of the specimens were intended to replicate as much as possible the expected field process, and thereby examine constructability issues. Therefore, all specimens, including the CPLD specimen, were built in the upright position. Assembly of the bent cap and column into the T-shaped specimen was performed in the CSUS Structural Laboratory.

<u>Construction Sequence</u>

The construction sequence for the CPLD specimen included the following (Figures 2-14 through 2-24):

1. Fabricate the rebar cages for the bent cap and column, including strain gages, at CSUS.

2. Transport rebar cages to Clark Pacific, prepare bent cap and column forms including special damming of the corrugated pipe, and cast bent cap and column concrete.
3. Transport precast cap and column to CSUS.
4. Prepare column and bent cap for assembly, and conduct cap setting operation in upright position.
5. Prepare connection for concreting and fill pocket with concrete from top.
6. Invert specimen and install in test area.

The cap was set and the bars located within the tolerance shown in Table 2-9, which summarizes significant as-builts and construction aids. Figure 2-20 shows the location of column bars after cap setting.

Concreting Operation

As shown in Figures 2-20 and 2-21, concrete was placed in the pocket and bedding layer using a bucket at the top of the pocket. Concrete was cast into the pocket through the cap reinforcement from above, and a collar with an air vent system was used to help remove entrapped air at the bedding layer.

Preparation: The concrete mix was selected to be the same as that used for the bent cap and column, with the intention of achieving a strength and stiffness approximately equal to that of the bent cap. The inside surface of the corrugated pipe was cleaned out using light sand blasting to remove debris and residue. This cleaned out the pipe and slightly roughened the inside surface. Column bars were placed within the tolerances of Table 2-9 and did not touch the pipe. After the bedding layer form was attached and sealed, the bedding layer was prewatered for approximately 24 hours to ensure sealing and prevent loss of moisture from the pocket concrete. Water was drained from the pipe approximately two hours before casting of concrete.

Concrete Mixing and Placement: Concrete was batched at the Clark Pacific plant at West Sacramento and hauled in a trailer to the CSUS Structural Laboratory. After mixing and discharging the concrete, buckets were used to fill the pocket, as shown in Figure 2-21, in several layers with vibration. The pocket was filled within approximately

30 minutes. Once concrete flowed through the air vents in the bedding layer, the vents were sealed. Figure 2-22 shows the top view after concreting. After hardening, curing compound was applied to the top surface.

Form Removal and Inspection: After several days, the bedding layer form was removed and the bedding layer and top of the ducts were inspected. No air voids were observed at the top of the bedding layer.

After concreting, the specimen was inverted, as shown in Figure 2-24, and installed into the test area.

2.2.3.2 Issues

Although the specimen was fabricated and assembled within the tolerances noted in Table 2-9, several issues are worthy of note.

Fabrication and Assembly

During the final stages of fabrication, the column cage was evidently rotated due to a conflict with a lifting insert. This resulted in a conflict between column longitudinal bars and bent cap bottom longitudinal bars when placing the cap over the column as originally designed. To account for this conflict, the following measures were taken:

1. The bent cap was rotated 7.1 deg counterclockwise to allow column bars to thread through the bent cap longitudinal bars as intended in design. As shown in Table 2-9, column bars were positioned within 1/8 in of the design location. After inversion and installation of the specimen in the test area, the column stub reflected the 7.1 deg rotation relative to the bent cap, as shown in Figure 2-25.
2. To ensure in-plane loading of the column (parallel to longitudinal axis of the cap), the test setup was modified as follows (Figure 2-26): 1) A steel adaptor was fabricated and installed between column stub and actuator, including gussets for stiffness, a spacer block to maintain relative positions and prevent racking, and spacers on each side of the actuator pin to establish and maintain vertical alignment of the pin; and 2) To maintain in-plane displacement of the

actuator and column, a hinged strut was attached, allowing the actuator to hinge during displacement but prevent lateral movement.

3. Column rotation was monitored during testing to verify that the modifications were effective. (Note: As mentioned in Chapter 3, these modifications were effective, with column rotation limited to 0.33 deg through μ6 and 0.96 deg through μ8.)
4. Measured curvature was modified (less than 1%) to account for 7.1 deg rotation of curvature rods.

Based on these measures, the impact of this fabrication error was considered negligible.

To match the CPFD column length, which was fabricated 1.5 in longer than intended in design, the CPLD column was also fabricated to the same length. This longer length caused drift values for cap pocket specimens to differ from the CIP and GD specimens by less than 1%.

Handling

During the lowering of the specimen onto supports in the testing area, the specimen inadvertently bumped a vertical support and the south wall of the test bay. Vertical and inclined hairline cracks developed in and near the east and west faces of the joint (Figure 3-1). These cracks were accounted for as pre-existing cracks during testing and are discussed further in Section 3.1.1.2.

Construction Aids

Two construction aids were particularly useful in specimen fabrication for the CPLD, as for the CPFD: 1) a Sonotube dam at the top and bottom of the corrugated pipe; and 2) a column bar template. Figure 2-16 compares the two approaches used for the Sonotube dam for the CPLD and CPFD specimens. Like the CPFD, the CPLD used a carefully cut Sonotube for forming above and below the pipe. However, the CPLD used a wood insert attached to the bottom form below the pipe and used a wood ring above the pipe, instead of the sand used for the CPFD.

Another construction aid was a column bar template (Figure 2-19). A steel template was fabricated for use during and after fabrication. During fabrication the

template maintained accurate positioning of all column bars, thus satisfying the tight tolerance in fabrication. After fabrication, the template maintained bar positions to help ensure a successful cap setting operation. While tolerances were somewhat exacerbated by the fabrication of a scaled specimen, the same type of template can readily be used in the field. The limited range of readily available corrugated pipe sizes also contributed to the tight tolerance that had to be satisfied.

2.3 Testing

2.3.1 Test Setup

The specimen test setup, shown in Figure 2-27, includes the following:

- Simply supported bent cap, with an equivalent pin support at the north end with vertical and lateral restraint (right side as shown) and an equivalent roller at the south end with vertical support only (left side as shown). This simple setup allowed accurate establishment of specimen forces. Although scaled modeling of the moment gradient along the cap was not required, accurate conditions adjacent to the faces of the joint were required and modeled in appropriate proportion to resist the column moment. [8, 11] The test setup ensured accurate conditions at each end of the joint so that the force transfer mechanism in the joint could be investigated.
- Inverted specimen, with a column stub. This allowed biaxial loading of the specimen, using a vertical hydraulic actuator to apply scaled gravity load and the horizontal hydraulic actuator to induce seismic response.
- Different axial force conditions in the bent cap for the push and pull directions. The push direction was considered more critical, as the axial force causes tension at the joint face, in contrast to the compression for the pull direction. However, the magnitude of axial force remained relatively small during testing.

2.3.2 Loading Sequence

The vertical and horizontal hydraulic actuators were used to apply specified Force Control and Displacement Control sequences to the specimen, as shown in Figures 2-28 and 2-29. The stages of loading are briefly summarized as follows:

1. Vertical Load: A monotonic increasing concentrated vertical load representing gravity load was applied to the top of the column stub to a maximum load of 38 kips. Force Control was used to maintain the vertical load throughout the horizontal loading sequence. A very slight change in vertical load developed during testing.
2. Horizontal Load: After the vertical load was applied, a horizontal load or displacement, representing seismic-induced load or displacement, was applied in two sequences: Force Control, followed by Displacement Control.

   Force Control: An increasing horizontal load was applied to the side of the column stub using one cycle per load level (Figure 2-28). A cycle consisted of both push and pull for the specified load. Load was held at select cycle peaks for crack marking, photographing, and documenting. The Force Control sequence was discontinued after an approximate determination of first yield of column longitudinal bars in the push and pull directions.

   Establishment of Effective Yield: Column strain gages and displacement measurements were intended to be used to calculate the system effective yield displacement, Δ_{YE}, and thus displacement ductility demand, μ_D, for the Displacement Control sequence. Establishment of first yield was approximate. The following equation specifies the relationship between the experimental first yield displacement of the system, Δ_Y, and the system effective yield displacement, Δ_{YE}, used for establishing the Displacement Control sequence:

$$\Delta_{YE} = \frac{M_{YE}}{M_{Y\exp}} \Delta_Y$$

where M_{YE} is the theoretical moment at effective yield based on moment-curvature analysis, and M_{Yexp} is the experimental first yield moment (experimental force at the first yield times the distance between the actuator and soffit). The ratio of M_{YE}/M_{YEexp} was approximately 1.4.

Displacement Control: Displacements were applied quasi-statically to the column stub in 3 cycles: two cycles at the target displacement ductility, followed by one cycle at the displacement ductility of the prior level (see Figure 2-29). Application of reversed cyclic displacements permitted examination of hysteretic loop stability. Nominal displacement ductility demand, as multiples of system effective yield displacement, was applied at the following levels, or until the residual capacity of the specimen dropped below 30% of the maximum load: μ1, μ1.5, μ2, μ3, μ4, μ6, μ8. (Note: μ1= nominal (target) displacement ductility of 1.0, μ2 = nominal displacement ductility of 2.0, etc.) Data reduction accounted for the slight additional lateral load applied to the specimen due to the inclination of the vertical actuator under cyclic displacements.

2.3.3 Instrumentation

Extensive instrumentation was used for the test specimen, including internal gages (strain gages mounted on bent cap and column rebar) and external gages (linear potentiometers and LVDTs mounted on the column, joint, and cap). Figures 2-30 through 2-34 show the instrumentation drawings, which define gage locations, and Figures 2-35 through 2-39 show various photos of the instrumentation attached to the specimen.

Strain gages on column longitudinal bars and hoops were intended to help quantify column flexure, including plastic hinging and strain penetration. Strain gages on bent cap longitudinal bars and stirrups were expected to provide evidence of joint distress and a force transfer mechanism through and adjacent to the joint. Strain gages on the pipe were expected to show the magnitude, orientation, and distribution of pipe strain.

Linear potentiometers and LVDTs provide column displacement, column curvature, panel deformation, joint rotation, bar slip, and specimen rigid body motion. Column curvature required the use of two linear potentiometers, one on each side of the column, to determine curvature. Four sets were used to divide the column into four curvature cells. Table 2-10 summarizes column curvature cell as-builts. Two sets of panel deformation gages were used to examine joint panel deformation. On the east side of the specimen, five linear potentiometers were used, whereas on the west side a simplified measurement with two linear potentiometers was used. To limit the number of gages, bent cap curvature was not explicitly examined. However, the bent cap was assumed to remain essentially elastic. Strain gages were used to monitor strain levels in the bent cap flexural reinforcement.

In addition to active instrumentation, specimen response was documented using digital photos, crack markings and measurements, video recording, and hand notes.

2.3.4 Pretest Predictions

2.3.4.1 Stages of Cracking

Four stages of initial specimen cracking were examined: 1) initial bent cap cracking in flexure due to gravity loads (specimen self weight plus the vertical actuator force, P_V; 2) initial bent cap cracking in flexure with the additional horizontal actuator force, P_H; 3) initial column flexural cracking; and 4) initial joint cracking.

Table 2-11 summarizes the predicted values of vertical and horizontal actuator loads for the stages of cracking. Bent cap flexural cracking was not expected under specimen self-weight and the maximum applied vertical load, P_V, of 38 kips. However, the addition of a horizontal load, P_H, of 13 kips was expected to generate the first flexural crack. Column cracking was also anticipated at a horizontal load of approximately 12 kips. Finally, joint shear cracking was not expected until P_H reached a large value of approximately 33 kips. It should be noted that prediction of cracking load is considered an estimate, as it depends on the highly variable tensile strength of concrete and possible effects of preexisting cracks.

2.3.4.2 Load-Displacement Envelope

An envelope of the horizontal load-displacement response of the column was predicted before testing. Figure 2-40 shows a close comparison between this prediction and that for the CIP specimen. Deflection at each stage was taken as the sum of the column displacements due to column elastic deflection to yield, column plastic deflection, column shear, and bent cap flexibility.

Flexural component contributions were calculated using moment-curvature results from the sectional analysis software, which used stress-strain models for the concrete and steel based on actual material tests of the concrete and steel used in the specimen. An effective yield curvature based on a bilinear moment-curvature response with best fit secondary stiffness was used to define the member effective yield displacement, Δ_{ye}. Various levels of displacement ductility were established as a multiple of the effective yield displacement of the system, Δ_{YE}.

2.3.4.3 Moment-Curvature Envelope

An envelope of the normalized moment-curvature response of the column was also predicted, using XTRACT, as shown in Figure 2-41. [12] This prediction is shown to be close to that for the CPFD and CIP specimens. Note that the curvature was normalized by multiplying curvature by the column diameter; moment was not modified. There was some difference in as-built cell heights (summarized in Table 2-10) which contributed to the difference between specimens.

2.4 Tables

Table 2-1. Partitions for Seismic Design Categories [6]

Value of $S_{D1}=F_vS_1$	SDC
$S_{D1} < 0.15$	A
$0.15 \leq S_{D1} < 0.30$	B
$0.30 \leq S_{D1} < 0.50$	C
$0.50 \leq S_{D1}$	D

Table 2-2. Comparison of Reinforcement for CIP Prototype and CPLD Specimen

CPLD		Prototype Design	Similitude [or Design] Requirement	Test Specimen	Specimen to Similitude [or Design] Ratio
Column					
Longitudinal Reinforcement					
Bar Size (diameter, in)		#11 (1.41)	0.59	#5 (0.63)	1.06
No. of bars		16	14	16	1.14
f_y	ksi	66.0	—	63.6	—
ρ		0.0138	0.0138	0.0158	1.14
M_n^*	K·ft	3760	272	206	0.75
M_n/D^3	K·ft/ft^3	58.7	58.7	44.5	0.76
Transverse Reinforcement					
Bar Size (diameter, in)		#6 (0.75)	0.31	#3 (0.38)	1.20
Spacing	in	3.0	[1.8]	2.0	[1.11]
f_y	ksi	66.0	—	63.5	—
ρ		0.0139	0.0139	0.0125	0.90
Bent Cap					
Longitudinal Reinforcement					
Bar Size (diameter, in)		#11 (1.41)	0.59	#5 (0.63) and #4 (0.5)	1.06 (#5)
No. of bars		12	—	8- #5; 2- #4	—
f_y (Bar no.)	ksi	66.0	—	59.6 (#4); 63.6 (#5)	—
ρ		0.0051	0.0051	0.005	0.98
M_n^*	K·ft	6680	483	333	0.69
M_n/bh^2	K·ft/ft^3	44.2	44.2	36.9	0.83
Transverse Reinforcement					
Bar Size (diameter, in)		#6 (0.75)	0.31	#3 (0.375)	1.20
Spacing	in	12.0	[8.4]	6.0	[0.71]
f_y	ksi	66.0	—	63.5	—
Joint					
Inside Joint					
Transverse Reinforcement (ρ_s or Equivalent Pipe)					
Hoops or Pipe		#6 (0.75 in) @ 3 in O.C.	—	16 gage (0.065 in) pipe	—
Hoop Force†	kips	552	95.8; [36.3] †‡	68.5	0.72; [1.89]
f_y	ksi	66.0	—	57.5‡	—
Side Face Reinforcement (A_s^{sf})					
No. of bars - Bar Size		8 - #6	—	4 - #3	—
A_s/A_{cap}	in^2/ in^2	0.19	[0.10]	0.12	[1.20]
f_y	ksi	60.0	—	63.5	—
Construction Stirrups					
No. of bars - Bar Size		Two 2-leg #6	—	0.0	—
Area	in^2	1.76	—	NA	—
f_y	ksi	66.0	—	NA	—
Adjacent to Joint					
Vertical Stirrups (A_s^{jv})					
No. of bars - Bar Size		Five 4-leg #6	—	0.0	—
Spacing	in	6.0	—	NA	—
A_s^{jv}/A_{st}	in^2/ in^2	0.35	[0.20]	0.0	[0.0]
f_y	ksi	66.0	—	NA	—
Horizontal Ties (A_s^{jh})					
No. of bars - Bar Size		4 - #6	—	0.0	—
Spacing	in	12.0	—	NA	—
A_s^{jh}/A_{st}	in^2/ in^2	0.35	[0.10]	0.0	[0.0]
f_y	ksi	66.0	—	NA	—

Note: Prototype and Specimen Design per 2006 LRFD RSGS

* Nominal moment @ ε_c=0.003

† Prototype hoop force is based on extension of column hoops into the joint

‡ Test specimen hoop force is based on actual yield stress (not nominal 30 ksi used in design).

†‡ Represents close to the minimum required amount (ρ/ρ_s=1.22), not the extension of column hoops

Table 2-3. Select Joint Design Details

Issue	Detail
Helical Corrugated Pipe [9, 17] Diameter Corrugation Angle Corrugation Dimensions Pipe Thickness Seam Connection Type; Strength Steel yield strength (nominal)	 18 in (nominal) 20 deg 2-2/3 in (pitch) x ½ in (deep) 16 gage (0.064 in) lock seam; 240 lb/in [9] 30 ksi
Hoop Force Ratio (Pipe/Hoop)	1.03
Fabrication and Placement Tolerance for Column Bars in Pipe	+ 0.38 in
Bedding Layer	1.5-in thick, no shims, no hoop reinforcement

Table 2-4. Comparison of Specimen Details—CPLD vs. CPFD

Item	CPLD	CPFD	Notes
Joint			
Helical Pipe: Pipe Diameter (nom) Pipe Thickness (gage)	18 in 0.065 in (16)	18 in 0.065 in (16)	Same basis allows direct comparison of specimens
Hoop Force Ratio: CPFD Pipe / Design (#3 hoops)	1.03 (without end hoops)	1.38 (with end hoops) 1.03 (without end hoops)	Potential benefit of end hoops eliminated for CPLD
Vertical Stirrups; Horizontal Ties	None	External to Joint Only (2006 LRFD RSGS)	No joint reinforcement used for CPLD
Other Reinforcement	None	Two 2-leg vertical construction stirrups placed within joint	Potential benefit of vertical stirrups eliminated for CPLD
Column			
Longitudinal Reinforcement	16#5 (1.58%, Specimen/Prototype ratio=1.14)	16#5 (1.58%, Specimen/Prototype ratio=1.14)	
Transverse Reinforcement	#3 hoops @ 2 in	#3 hoops @ 2 in	Same basis allowed CPLD joint to potentially be challenged to greater extent
Bent Cap			
Longitudinal Reinforcement	8#5 and 2#4 top and bottom (0.50%, Specimen/Prototype ratio=0.99)	12#5 top and bottom (0.65%, Specimen/Prototype ratio=1.27)	Potential benefit of flexural reinforcement reduced for CPLD
Transverse Reinforcement	2-leg #3 stirrups @ 8 in	2-leg #3 stirrups @ 6 in	CPLD stirrups reduced to minimum requirement

Table 2-5. Major Differences in Design and Detailing Provisions for Reinforced Concrete Components, SDC D vs. SDC B [6]

Criteria	SDC D (Full Ductility)	SDC B (Limited Ductility)
Force Demands (8.3.2; 8.3.3)	Based on forces resulting from the overstrength plastic hinging moment capacity or the maximum connection capacity following the capacity design principles specified in Article 4.11.	The lesser of the forces resulting from the overstrength plastic hinging moment capacity or unreduced elastic seismic forces in columns or pier walls.
Ductility Demands (8.3.4)	The local displacement ductility demands, μ_D, of members shall be determined based on the analysis method adopted in Section 5. The local displacement ductility demand shall not exceed the maximum allowable displacement ductilities established in Article 4.9.	N/A
Column Shear Demand, *Vu* (8.6.1)	Based on the force, V_{po}, associated with the overstrength moment, M_{po}, defined in Article 8.5 and outlined in Article 4.11.	Based on the lesser of: 1) Force obtained from an elastic linear analysis; 2) Force, V_{po}, for to plastic hinging of the column including an overstrength factor
Concrete Shear Capacity (8.6.2)	Using concrete shear stress for circular columns with hoops, modified by: $\alpha' = \frac{0.03}{\mu_D}\rho_s f_{yh}$ where μ_D is 6 (multi-column bent), or lower inside PH region, per Eq. 4.9-5	Using concrete shear stress for circular columns with hoops, modified by: $\alpha' = \frac{0.03}{\mu_D}\rho_s f_{yh}$ where μ_D is 2
Minimum Column Shear Reinforcement (Spiral) (8.6.5)	$\rho_s \geq 0.005$	$\rho_s \geq 0.003$
Minimum Longitudinal Reinforcement (8.8.2)	$A_l \geq 0.010\, A_g$, columns	$A_l \geq 0.007\, A_g$, columns
Splicing of Longitudinal Reinforcement in Columns (8.8.2)	$A_l \geq 0.010\, A_g$, columns	$A_l \geq 0.007\, A_g$, columns
Minimum Longitudinal Reinforcement (8.8.3)	Outside plastic hinging region	N/A
Minimum Development Length into Cap Beams (8.8.4)	$l_{ac} = \frac{0.79 d_b f_{ye}}{\sqrt{f_c'}}$, not to be reduced; extended as close as practically possible to opposite face	N/A*
Anchorage of Bundled Bars into Cap Beams (8.8.5)	Increased by 20% for a two-bar bundle and 50% for a three-bar bundle. Four-bar bundles are not permitted in ductile elements.	N/A
Maximum Bar Diameter (8.8.6)	$d_{bl} = \frac{0.79\sqrt{f_c'}(L - 0.5D_c)}{f_{ye}}$	N/A

*AASHTO LRFD provisions (i.e., 5.10.11.4.3), in contrast to 2006 LRFD RSGS and 2007 LRFD PSGS provisions, require even longer lengths for column bar extension into joint.

Table 2-5. Major Differences in Design and Detailing Provisions for Reinforced Concrete Components, SDC D vs. SDC B [6], Continued

Criteria	**SDC D (Full Ductility)**	**SDC B (Limited Ductility)**
Lateral Reinforcement Inside Plastic Hinge Region (8.8.7)	Butt-welded hoops or spirals	N/A
Lateral Reinforcement Outside Plastic Hinge Region (8.8.8)	Volumetric ratio shall not be less than 50% of that determined in 8.8.7 and 8.6. Reinforcement shall be of the same type. Lateral reinforcement shall extend into bent caps a distance which is as far as is practical and adequate to develop the reinforcement for development of plastic hinge mechanisms.	N/A
Requirements for Lateral Reinforcement (8.8.9)	Various detailing requirements.	N/A
Capacity Protection Requirements (8.9)	Capacity-protected members such as bent caps shall be designed to remain essentially elastic when the plastic hinge reaches its overstrength moment capacity, *Mpo*. The expected nominal capacity is used in establishing the capacity of essentially elastic members.	N/A
Superstructure Capacity Design (8.10; 8.11)	For longitudinal direction, the superstructure shall be designed as a capacity protected member. For transverse direction, integral bent caps shall be designed as an essentially elastic member. Longitudinal flexural bent cap beam reinforcement shall be continuous. Splicing of reinforcement shall, at a minimum, be accomplished using mechanical couplers capable of developing 125% of the expected yield strength, f_{ye}, of the reinforcing bars.	N/A
Superstructure Design for Nonintegral Bent Cap (8.12)	For superstructure to substructure connections not intended to fuse, provide a lateral force transfer mechanism at the interface. For connections intended to fuse, minimum lateral force at interface shall be 0.40 times the dead load reaction plus the overstrength shear key(s) capacity. Nonintegral cap beams supporting superstructures with expansion joints at the cap shall have sufficient support length to prevent unseating.	N/A
Joint Design (8.13)	Major joint design and detailing provisions, such as bent cap width, joint shear reinforcement (vertical stirrups inside and outside the joint, and horizontal ties/J-bars), transverse joint reinforcement, additional bent cap longitudinal reinforcement, and side face reinforcement.	N/A

Table 2-6. Concrete Mix Proportions

Material Designation	(Based on Saturated Surface Dry)		
	Quantity	Weight (lbs)	Volume (ft^3)
ASTM C 150 – Type I/II		564	2.87
ASTM C 33 – 3/8"		1,826	10.92
ASTM C 33 – Concrete Sand		1,217	7.39
ASTM C 494 – Super plasticizer	45 oz	3	0.05
Water	W/C=0.49	276	4.43
Total Air Content	5.00%		1.35
TOTAL		3,886	27.0

Table 2-7. Concrete Properties—Bent Cap, Column, and Pocket

Parameter	Design	Actual
Slump	5½" +/- 2½"	~ 3.5 in, cap and column
Unit Weight	143.9 pcf	145.1 lbs
Compressive Strength	4000 psi (28 day)	Cap and Column: 3451 psi (35 day) Plastic Hinge: 3892 psi (35 day) Pocket: 3454 psi (29 day)
Tensile Strength (Split Cylinder)	N/A	Cap and Column: 365 psi (35 day) Pocket: 374 psi (40 day)
Modulus of Elasticity	N/A	Cap and Column: 2646 ksi (35 day) Plastic Hinge: 2904 ksi (29 day) Pocket: 2548 (35 day)

Table 2-8. Yield and Tensile Strengths—Reinforcing Bars and Pipe

Size	Type	Yield Strength (ksi)	Tensile Strength (ksi)
#3	Bent cap stirrups; Column hoops	63.5	99.6
#4	Bent cap longitudinal	59.6	101.1
#5	Bent cap longitudinal; Column longitudinal	63.6	95.0
16 gage (0.065 in)	Pipe	57.5	59.9

Table 2-9. Significant As-builts and Construction Aids

Description	Drawing	As-built
Length of column reinforcement embedded into bent cap, l_{ac}	22 in	21.0 in (average)
Column bar location relative to cap pocket	0.0 in	< 1/8 in; See Figure 2-20 for bar locations
Column hoop spacing within plastic hinge	0.0 in	+/- 1/8 in
First column hoop below top of column	≤1 in	0.95 in
Column length (stub to column top)	2 ft 11 in	2 ft 11 in
<u>Helical Corrugated Pipe [9]</u> Corrugation Angle Average Pitch Average Depth Average Thickness	 20 deg 2.667 in 0.500 in 0.064 in	 20 deg 2.656 in 0.508 in 0.065 in
Construction Aids	1. Column bar template to ensure match between column bars and pipe during cap setting 2. Sonotube dam at top and bottom of pipe, as well as sand fill, to prevent concrete intrusion and maintain integrity of forms during casting	

Table 2-10. Column Curvature Cell As-builts—CPLD, CPFD, CIP

Cell Number	Drawing		CPLD		CPFD		CIP	
	Cell Height (in)	Cell Width (in)	Cell Height (in)	Cell Width (in)	Cell Height (in)	Cell Width (in)	Cell Height (in)	Cell Width (in)
Cell 1	3.5	26	2.84	26.13	4.78	26.05	3.67	26.79
Cell 2	3.0	26	3.59	26.06	2.87	26.13	3.00	26.04
Cell 3	4.0	26	4.19	25.69	3.99	25.99	4.14	26.01
Cell 4	9.5	26	9.02	25.75	9.59	26.01	9.25	26.07

Table 2-11. Predicted Stages of Specimen Cracking

Item	Load (kips)	
	P_V	P_H
Bent Cap—Flexural	None	-
	38.0	4.8
Column—Flexural	38.0	12.0
Joint Shear	38.0	32.6

2.5 Figures

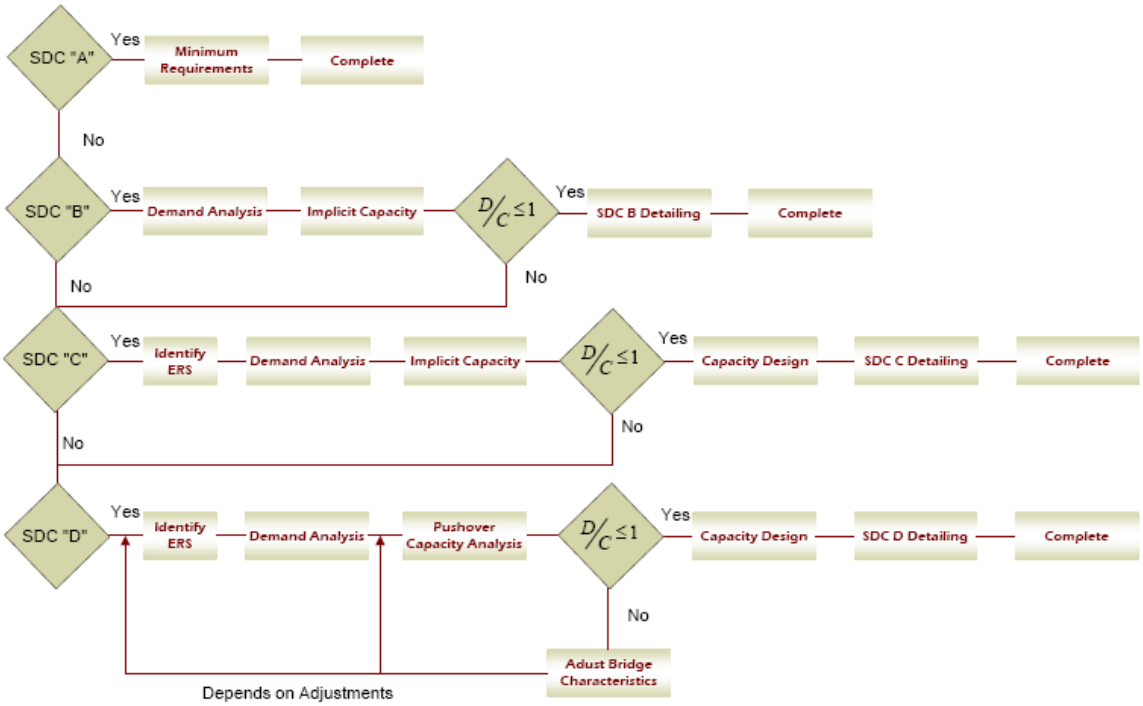

Figure 2-1. Seismic Design Category (SDC) Core Flowchart [6]

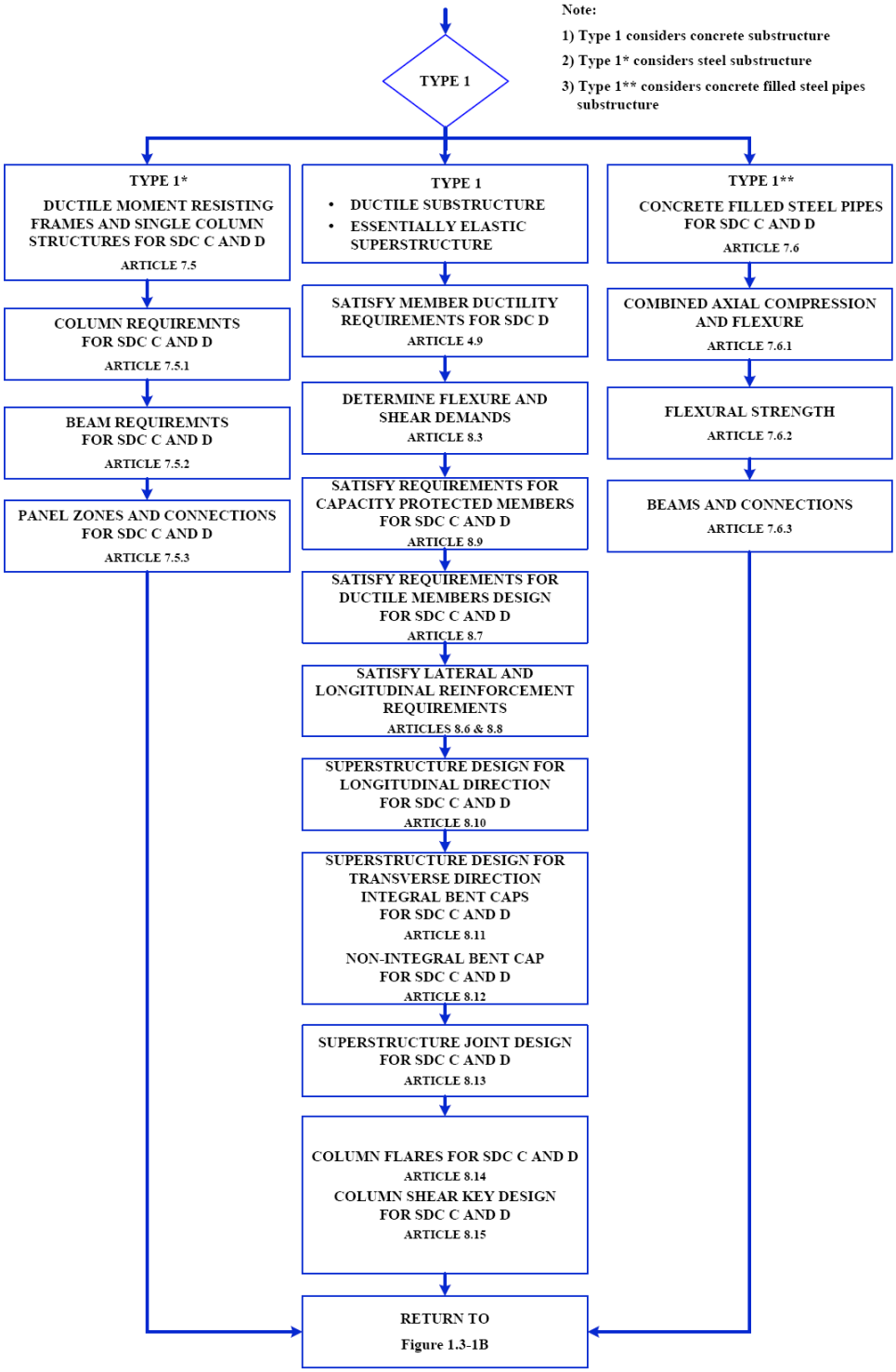

Figure 2-2. Detailing Procedure Flow Chart [6]

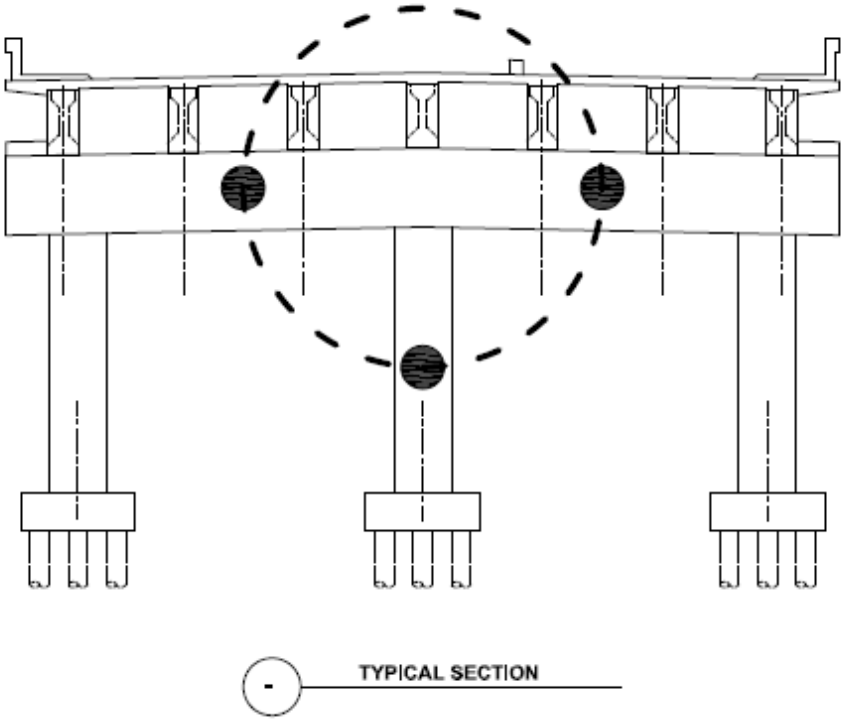

Figure 2-3. Portion of Prototype Used for Specimen Design

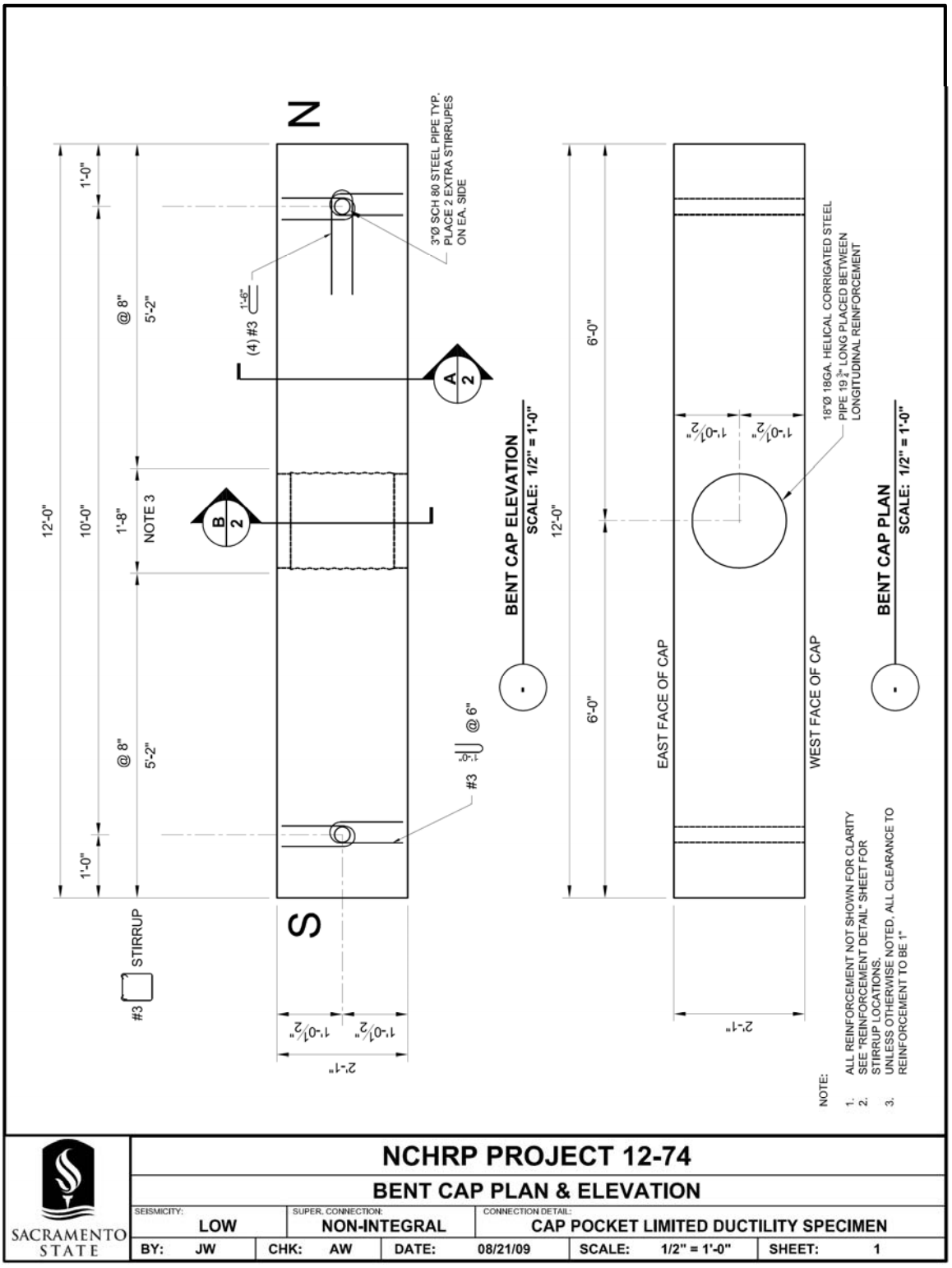

Figure 2-4. Cap Pocket Limited Ductility Specimen Design—Bent Cap Plan and Elevation

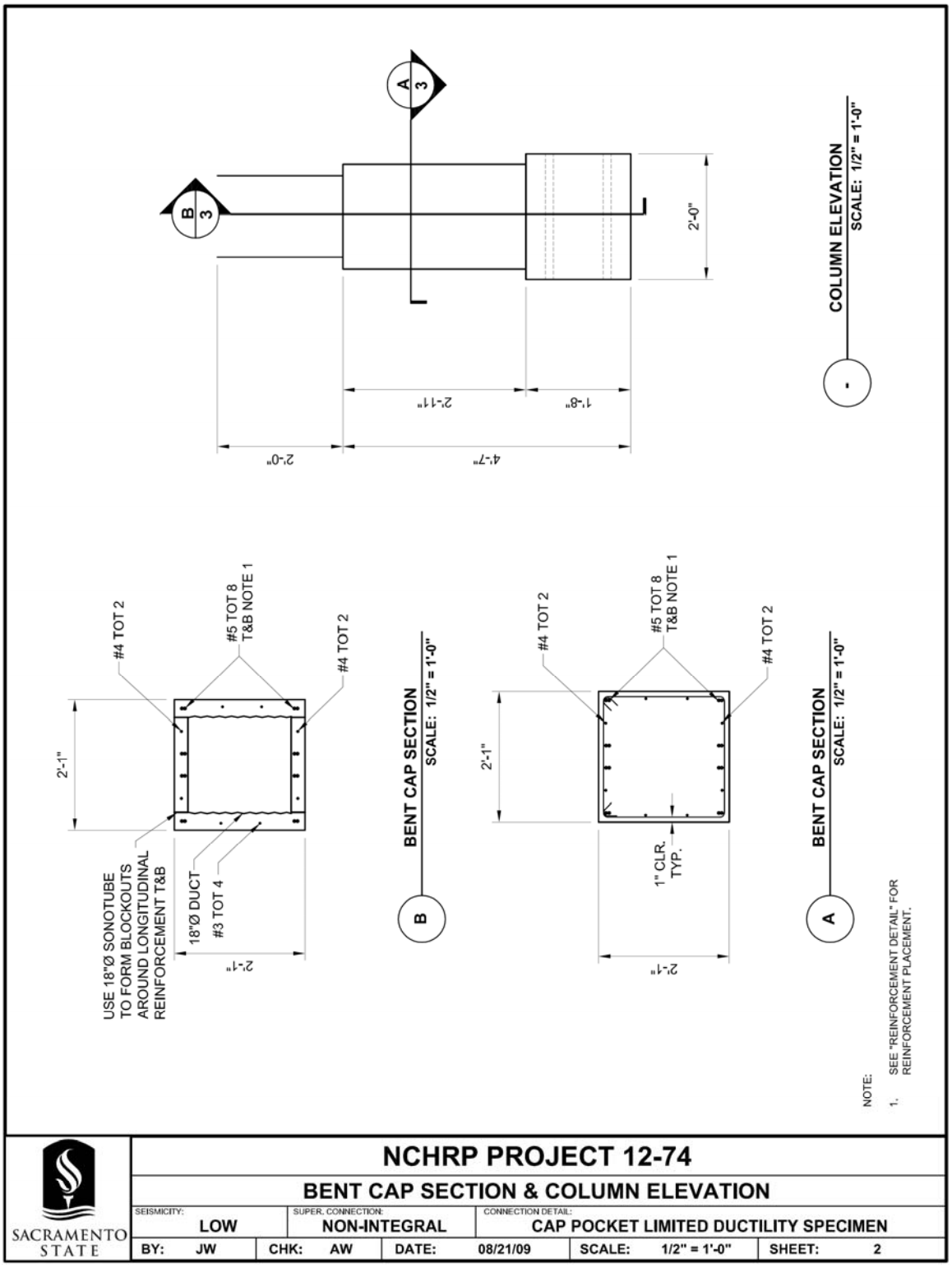

Figure 2-5. Cap Pocket Limited Ductility Specimen Design—Bent Cap Section and Column Elevation

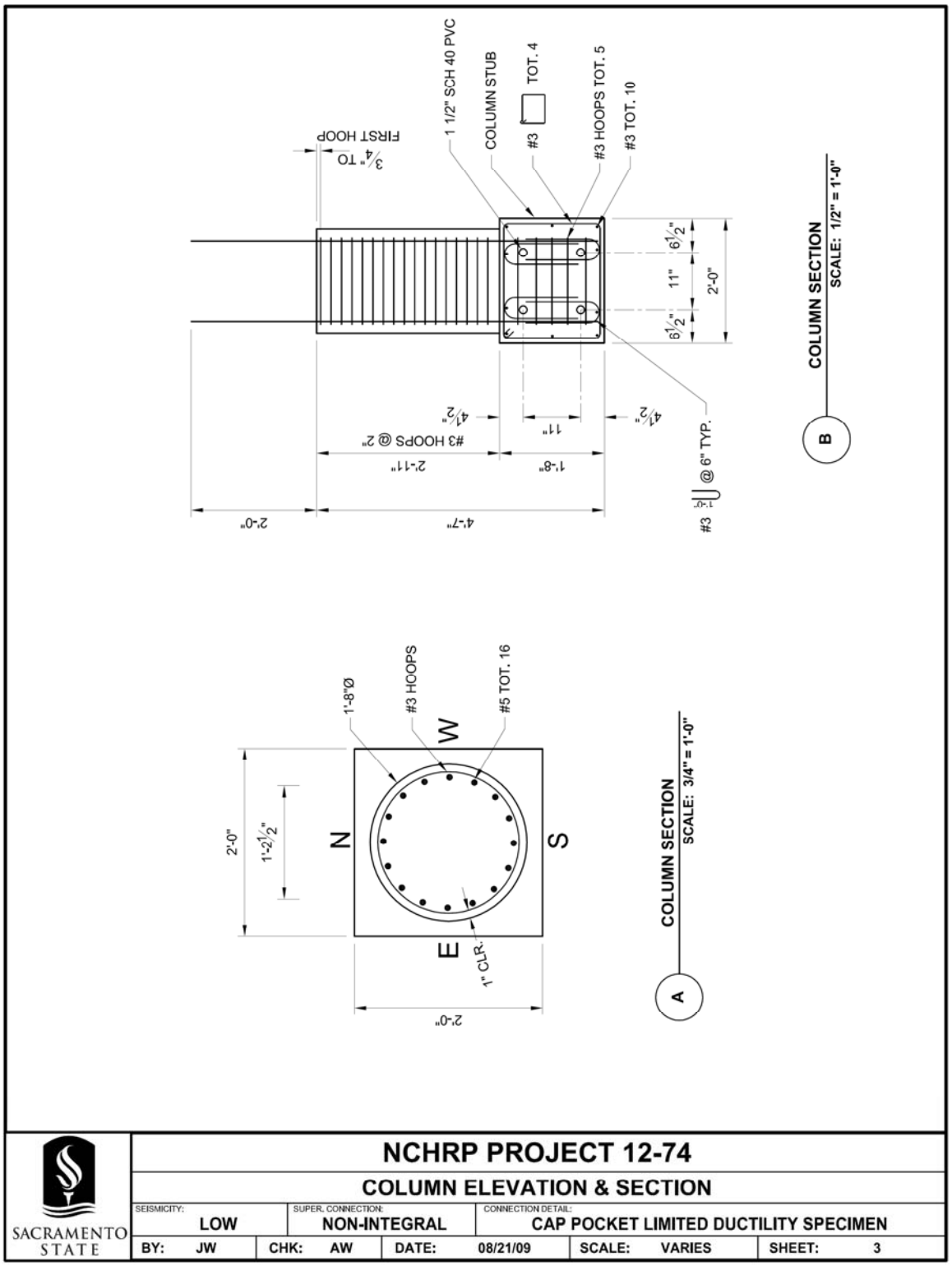

Figure 2-6. Cap Pocket Limited Ductility Specimen Design—Column Elevation and Section

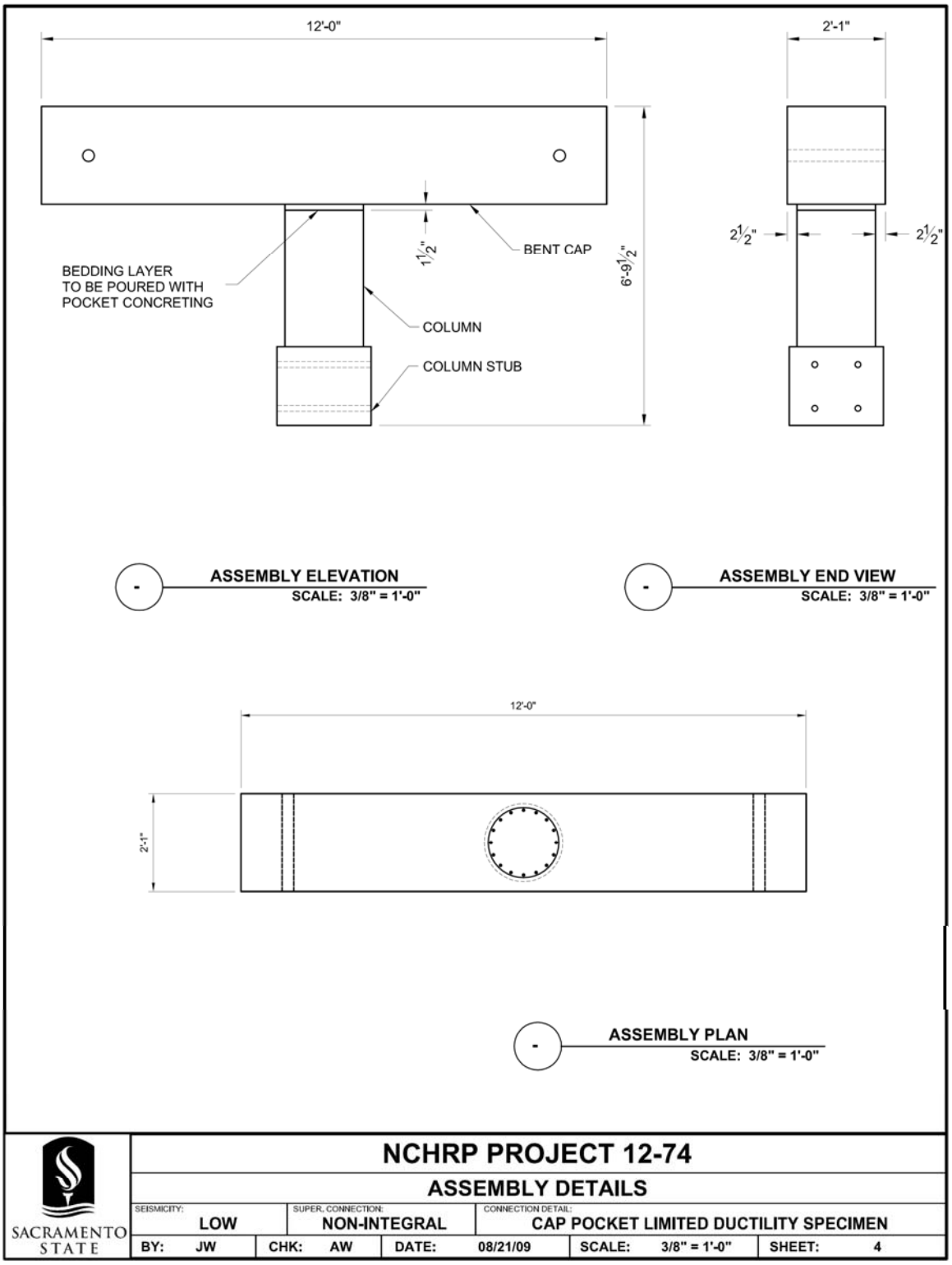

Figure 2-7. Cap Pocket Limited Ductility Specimen Design—Assembly Details

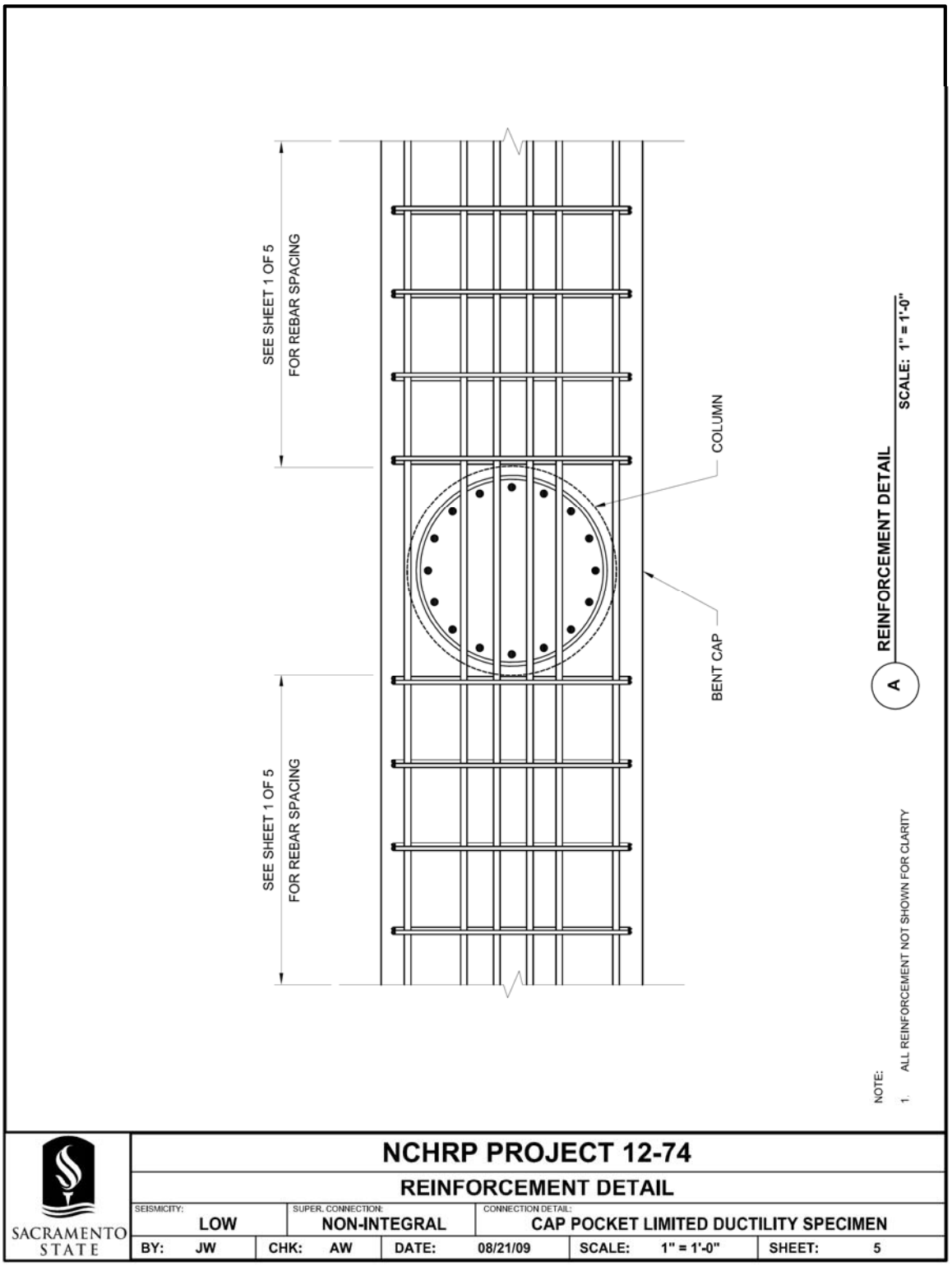

Figure 2-8. Cap Pocket Limited Ductility Specimen Design—Bent Cap Reinforcement Detail

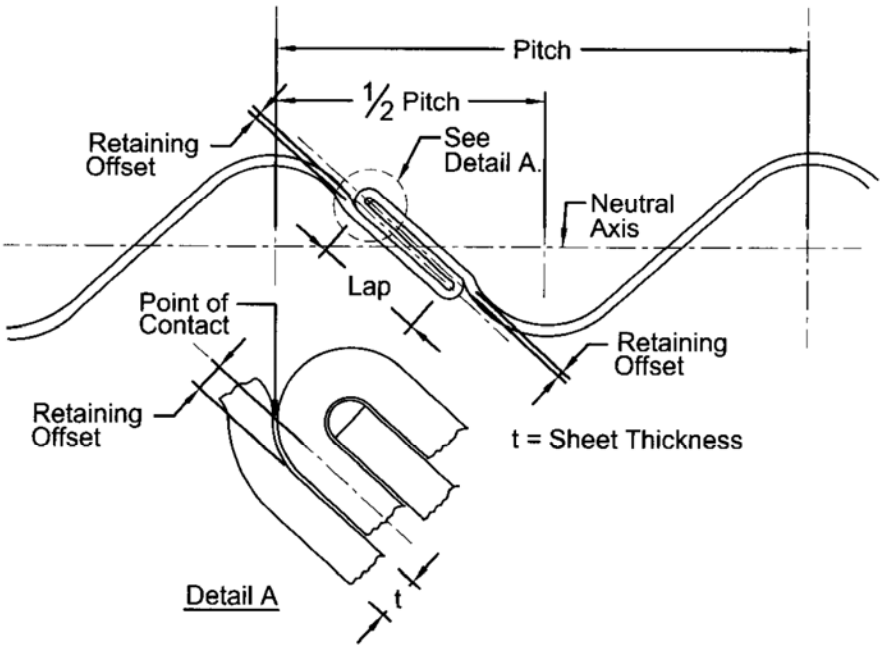

Figure 2-9. Lock Seam Detail [10]

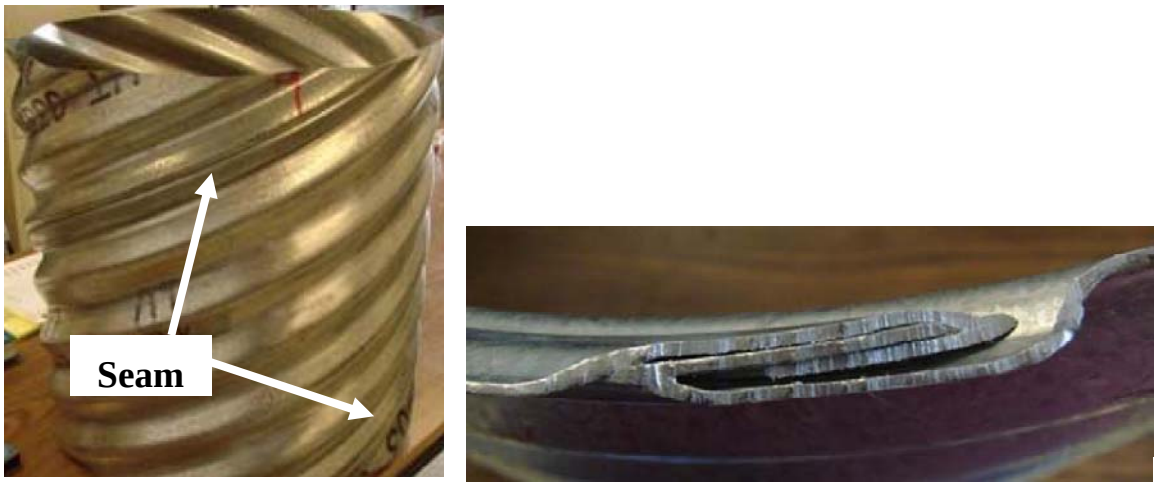

A. Corrugation and Lock Seam B. Close–up of Lock Seam

Figure 2-10. Corrugation and Lock Seam Details for Cap Pocket Specimens (from CPFD)

Figure 2-11. Rebar Cage with Corrugated Pipe—CPLD Specimen

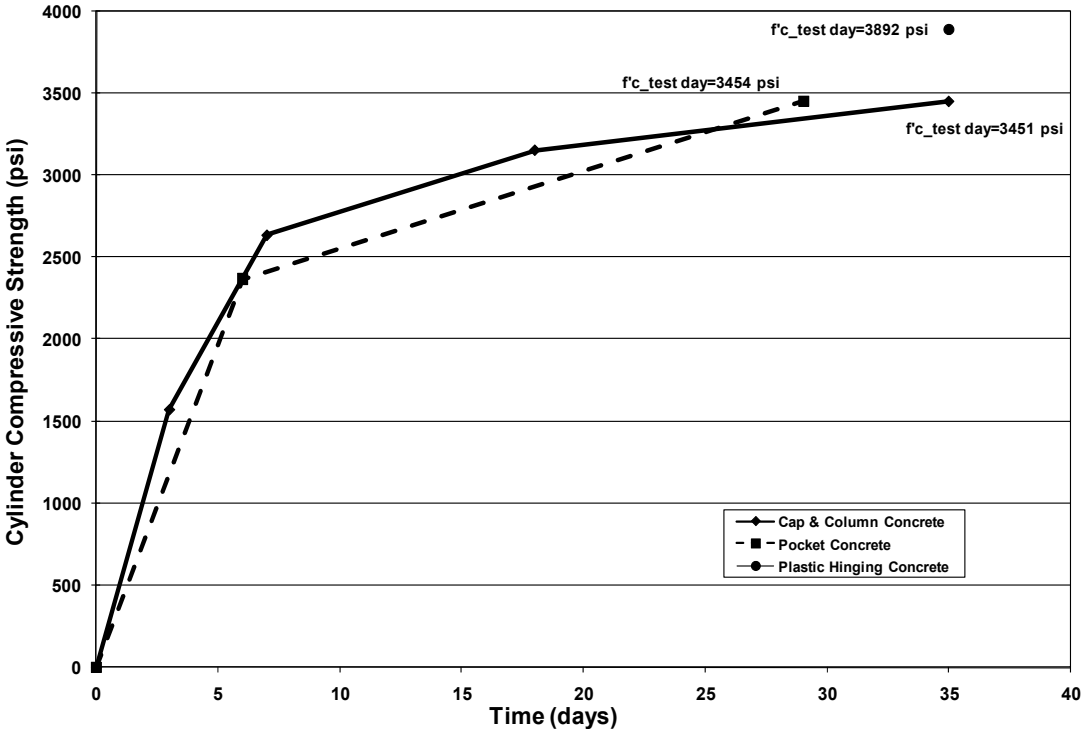

Figure 2-12. Concrete Cylinder Compressive Strength vs. Time

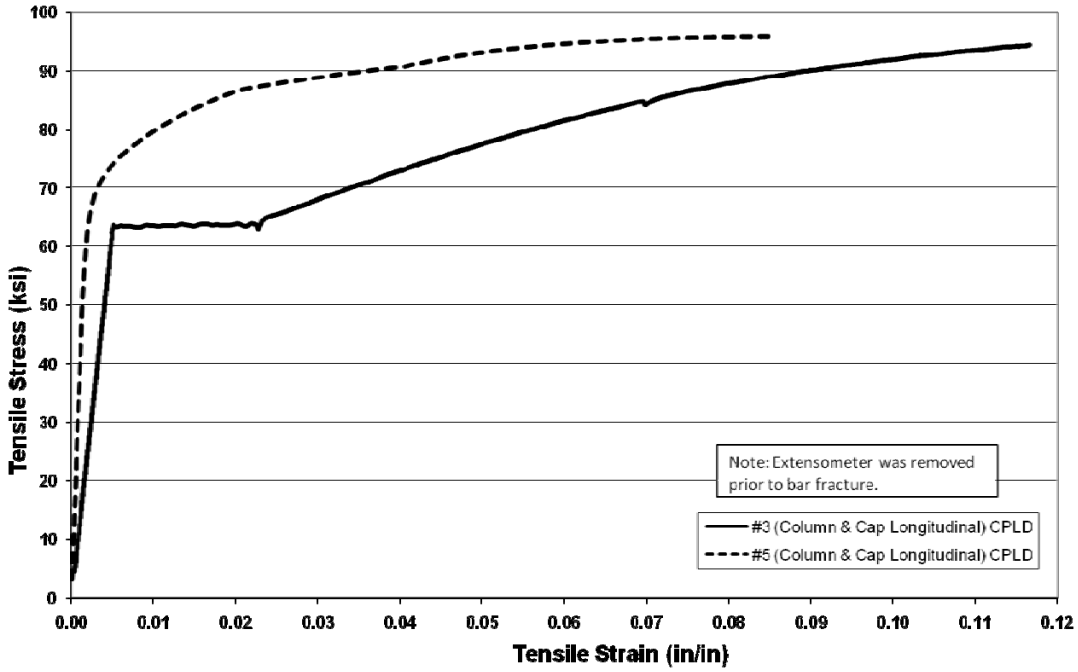

Figure 2-13. Tensile Stress-Strain Response for Reinforcing Bars

Figure 2-14. Assembly of Column Rebar Cage

A. CPLD

B. CPFD

C. CPLD (West Face)

D. CPFD (West Face)

Figure 2-15. Comparison of Cap Pocket Bent Cap Rebar Cages during Fabrication

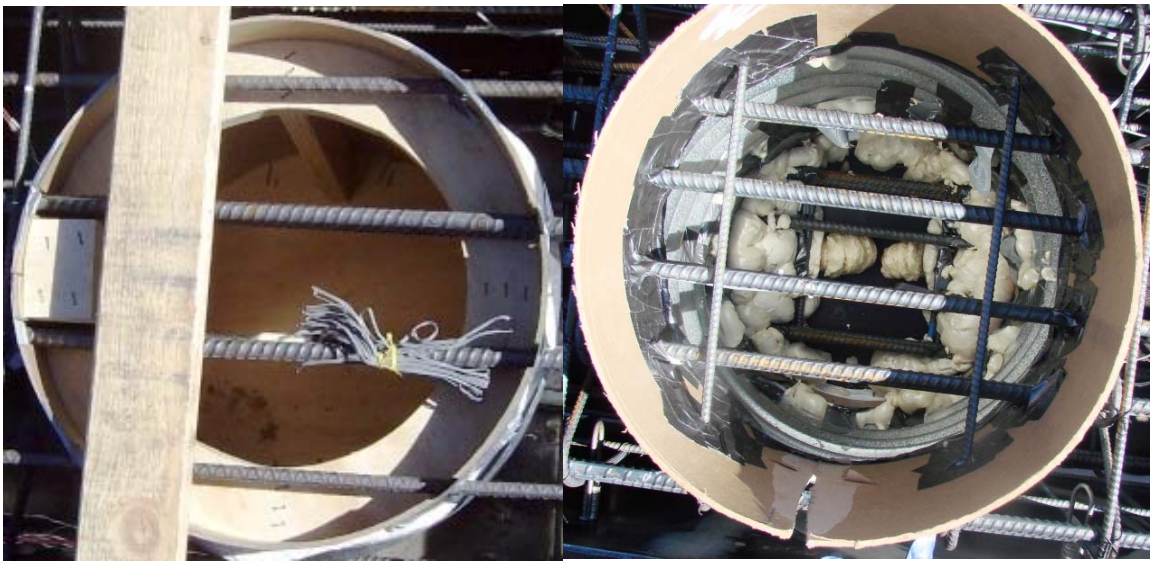

A. CPLD B. CPFD

Figure 2-16. Joint Region of Bent Cap during Fabrication

Figure 2-17. Casting of Bent Cap

Figure 2-18. Lowering of Cap during Cap Setting Operation

Figure 2-19. Steel Template at Top of Column Bars

A. Plan View of Pocket

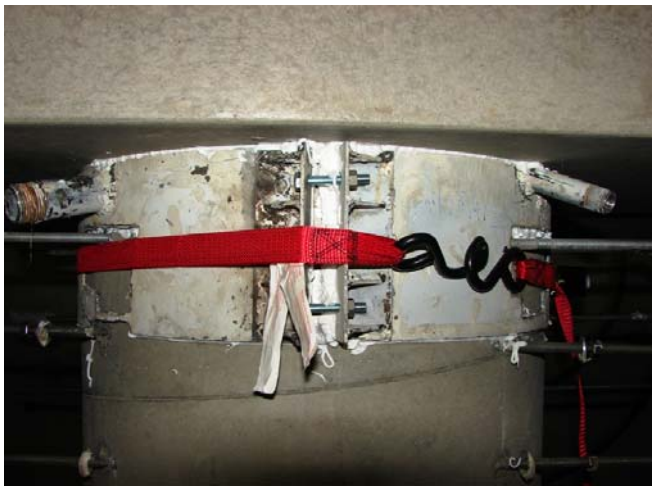

B. Bedding Layer

Figure 2-20. Pocket and Bedding Layer Before Concreting

A. Pocket Vibration – 1st Layer

B. Pocket Vibration – 3rd Layer

C. Topping Off Connection

Figure 2-21. Concreting of Cap Pocket Connection

Figure 2-22. Top View of Cap Pocket Connection after Concreting

Figure 2-23. Bedding Layer Post-Concreting

Figure 2-24. Inversion of Specimen Prior to Installation in Test Area

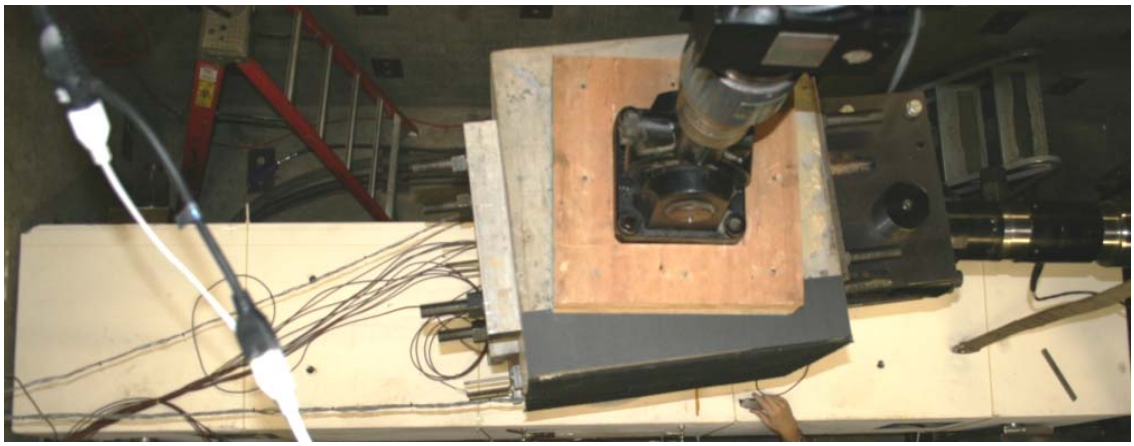

Figure 2-25. Plan View of Specimen Showing Column Stub Rotation (7.1 deg)

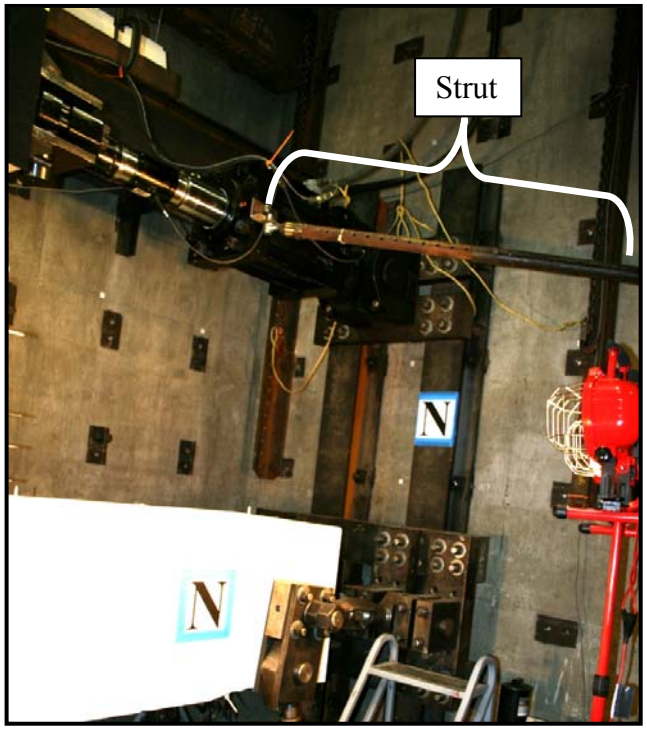

A. Hinged Strut

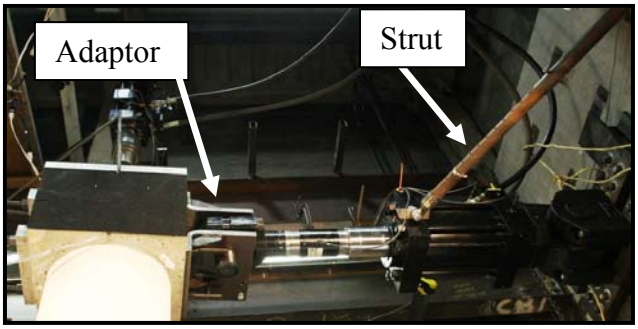

B. Steel Adaptor (left) and Strut (right)

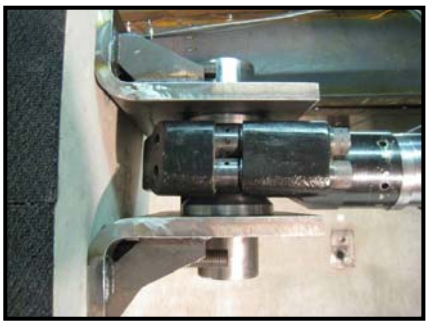

C. Steel Adaptor

Figure 2-26. Test Setup Modifications

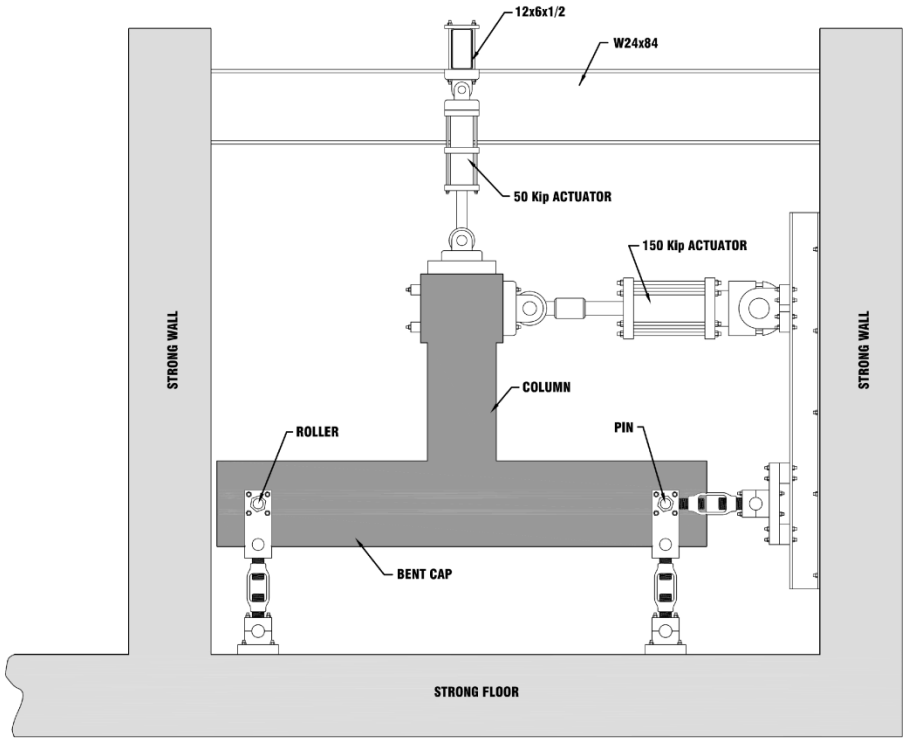

A. Schematic

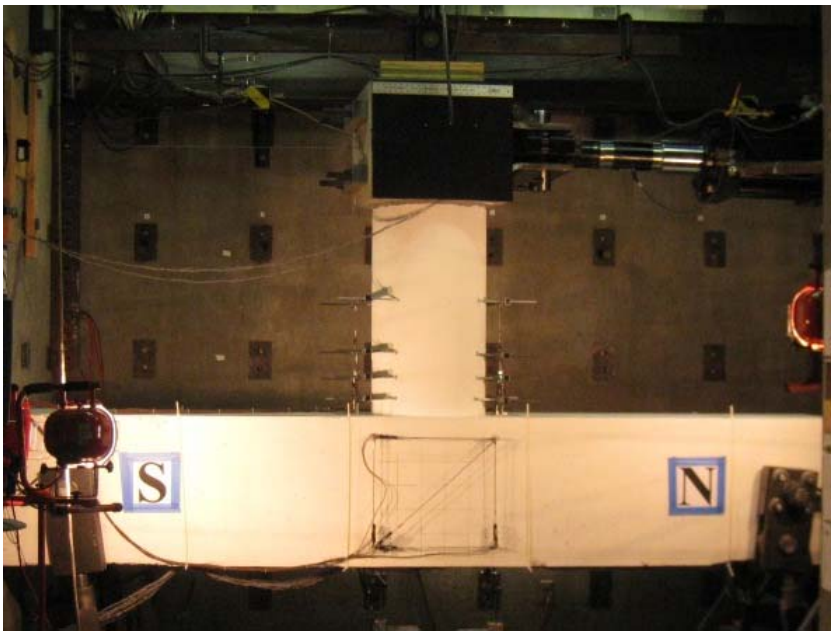

B. Actual

Figure 2-27. Specimen in Preparation for Testing

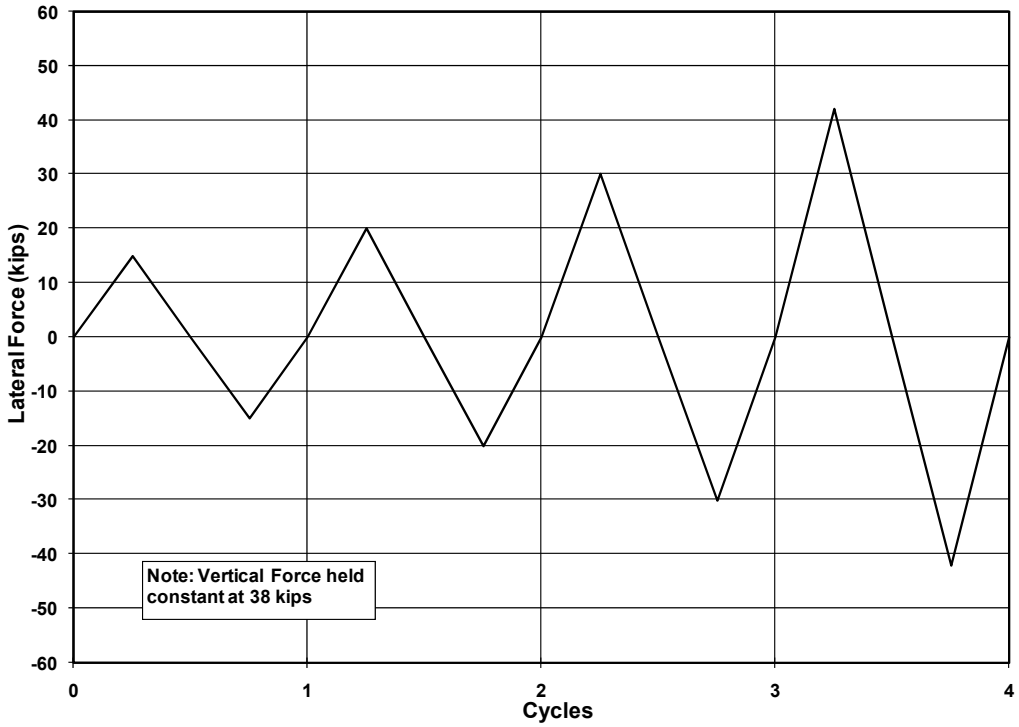

Figure 2-28. Force Control Sequence

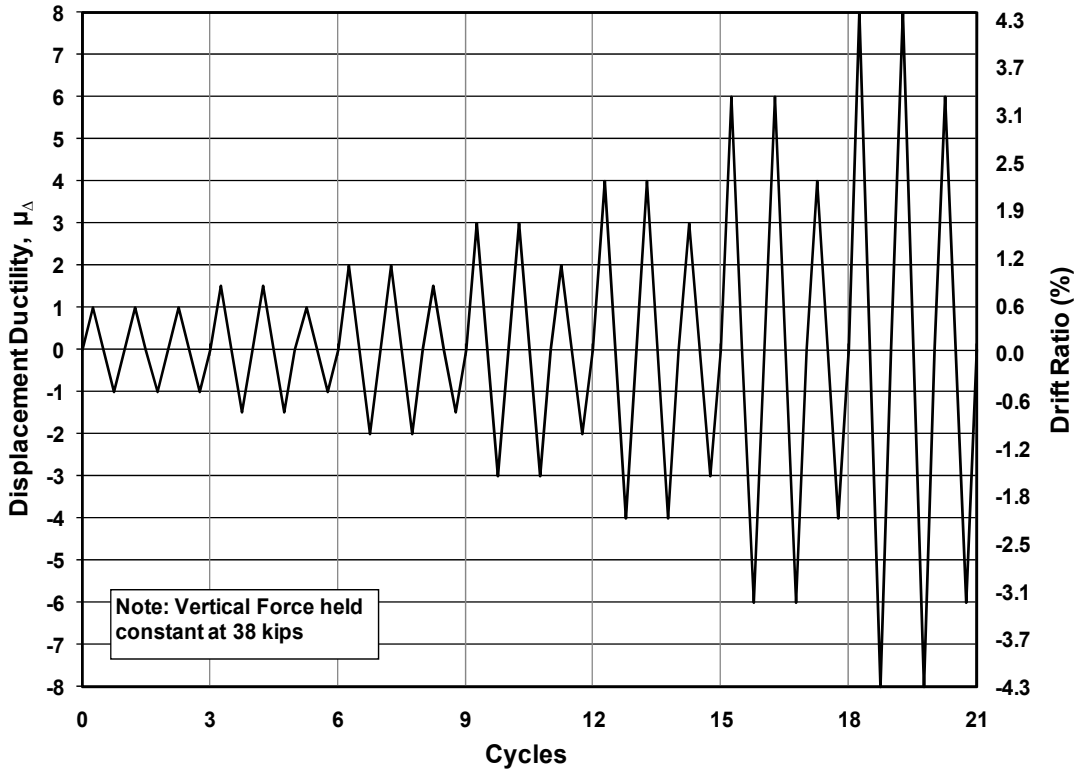

Figure 2-29. Displacement Control Sequence

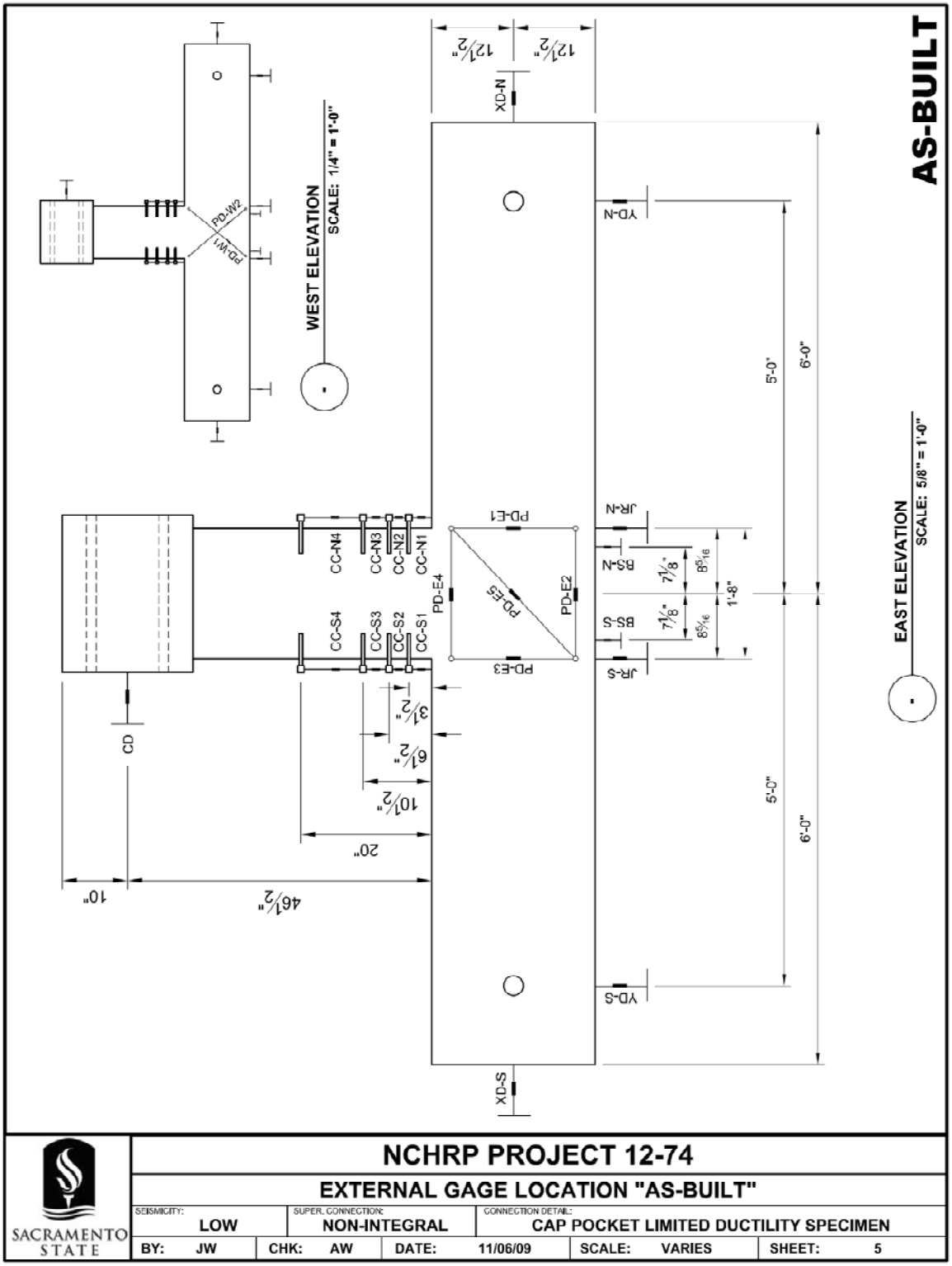

Figure 2-30. Instrumentation Drawings—External Gage ID (As-built)

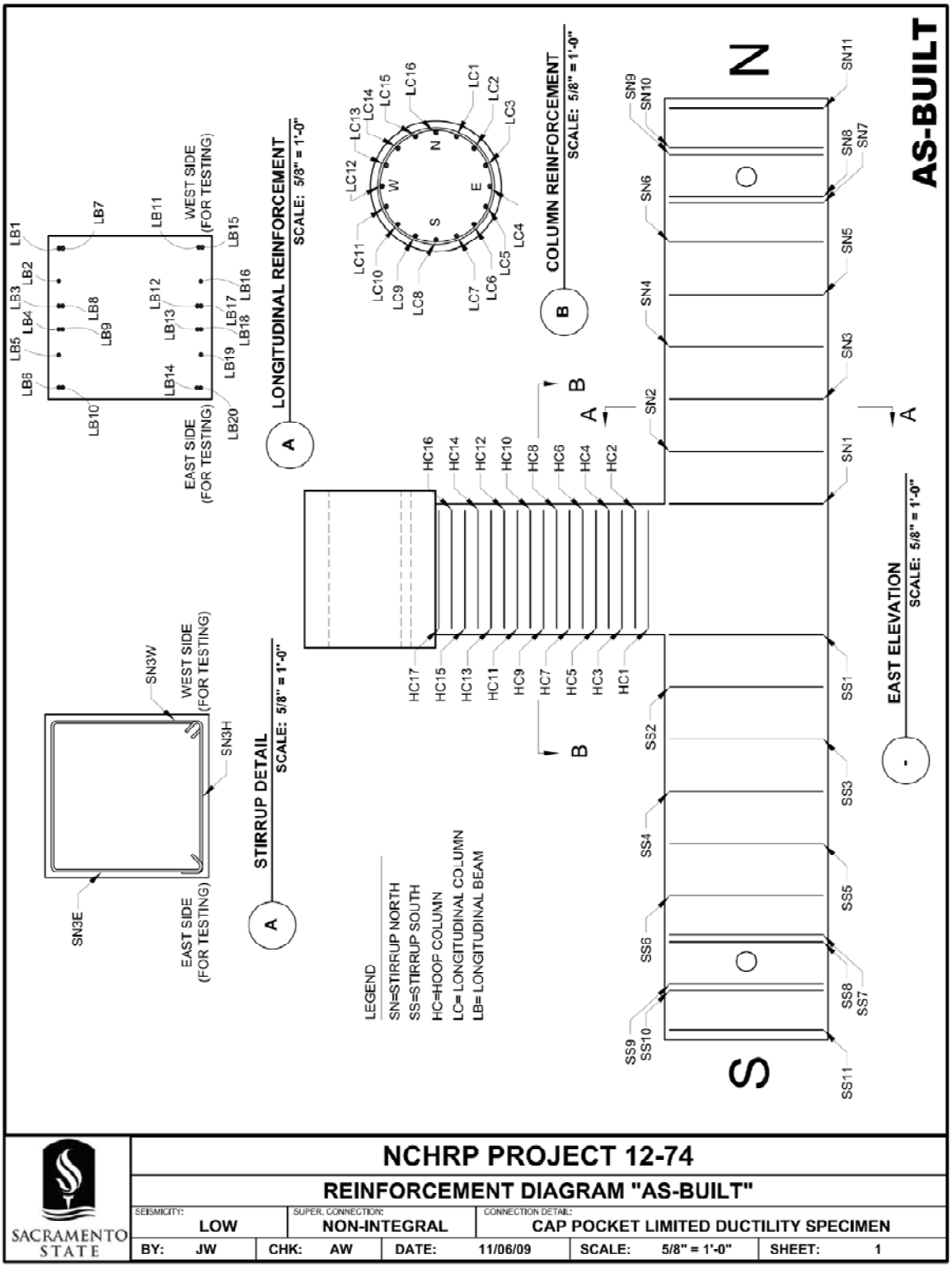

Figure 2-31. Instrumentation Drawings—Reinforcing Bar ID (As-built)

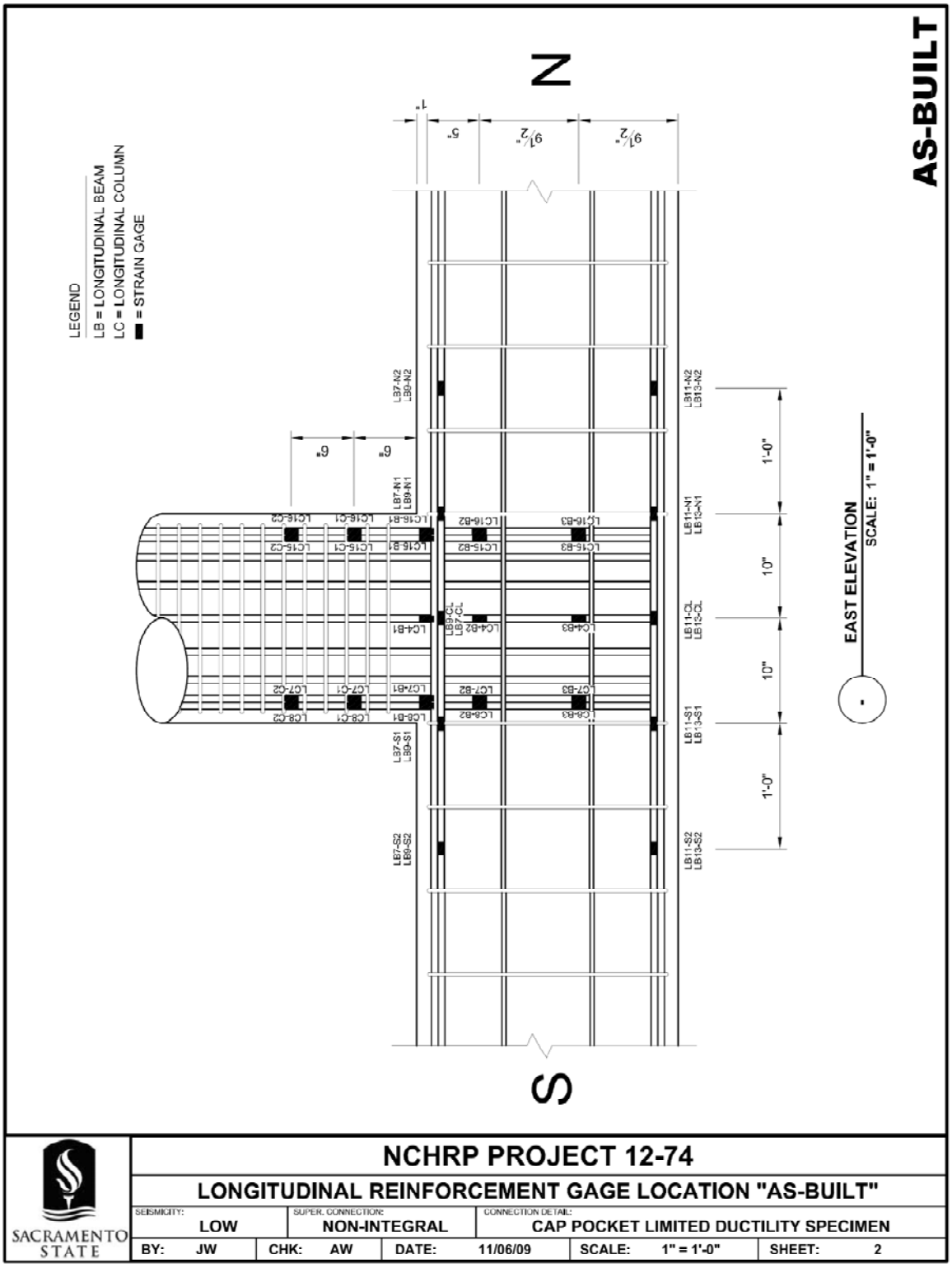

Figure 2-32. Instrumentation Drawings—Longitudinal Reinforcement Strain Gage Locations (As-built)

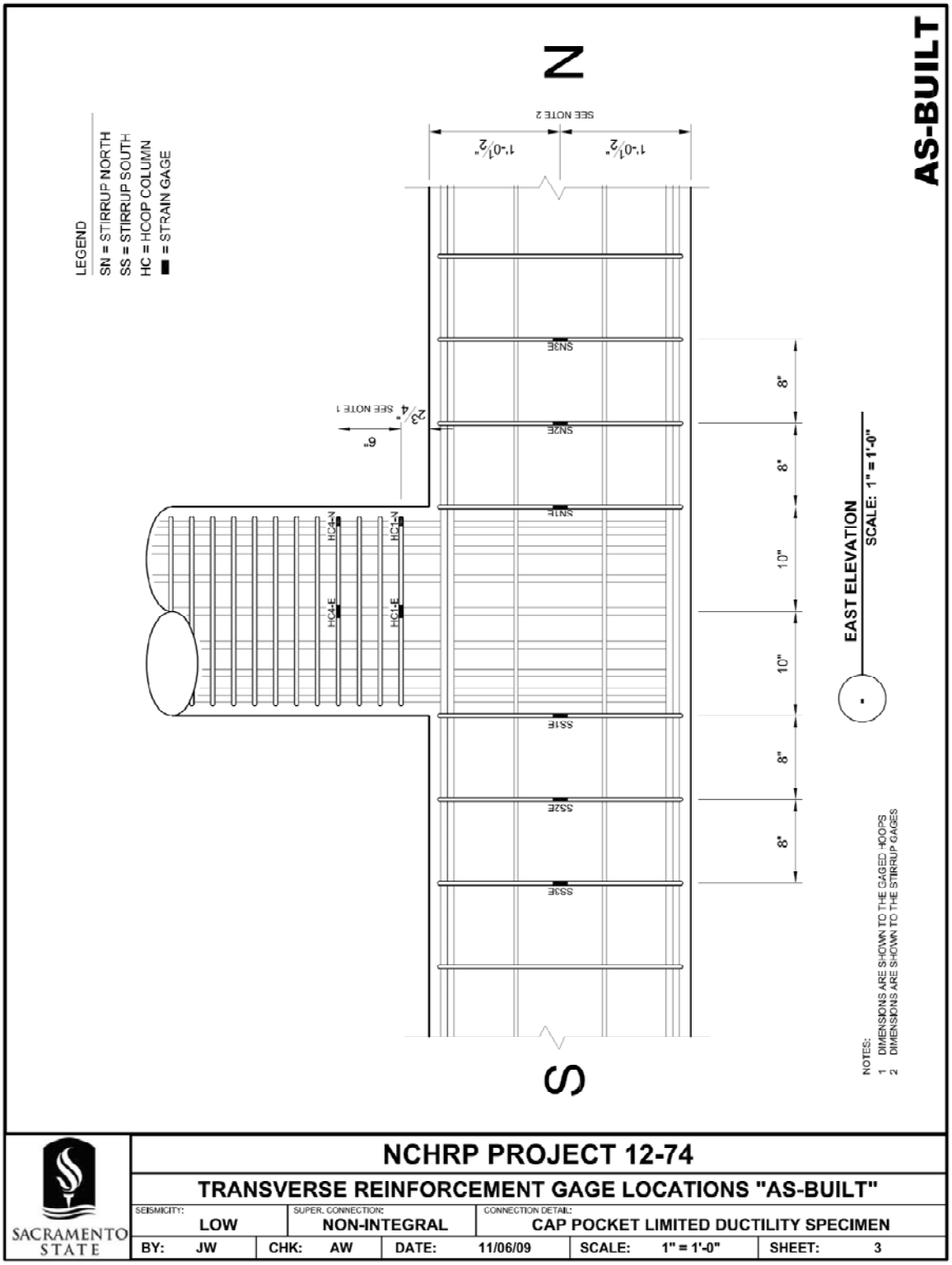

Figure 2-33. Instrumentation Drawings—Transverse Reinforcement Strain Gage Locations

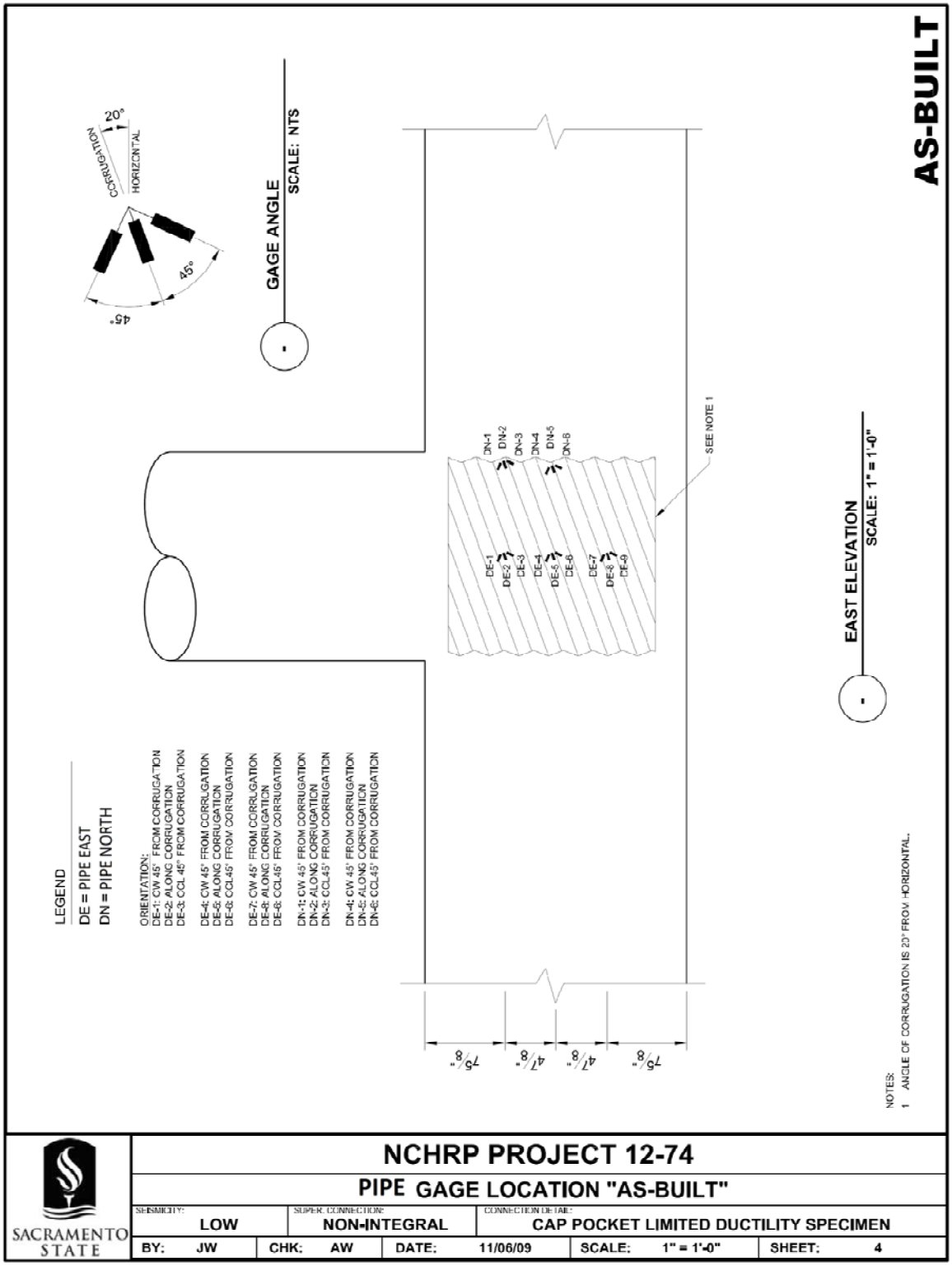

Figure 2-34. Instrumentation Drawings—Pipe Strain Gage Locations

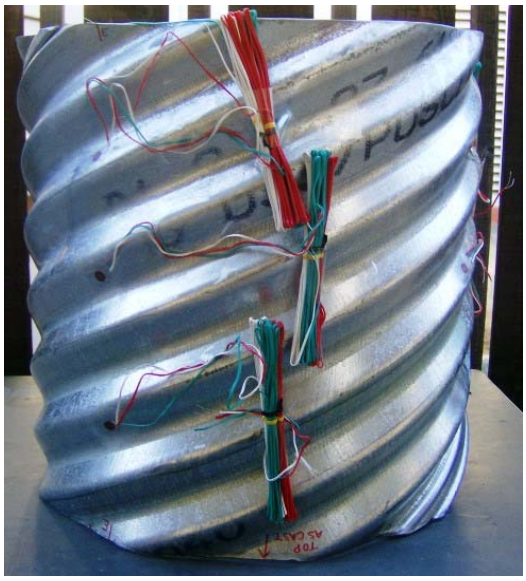

Figure 2-35. Internal Instrumentation Photos—Strain Gage on Pipe

Figure 2-36. Internal Instrumentation Photos—Strain Gage on Rebar

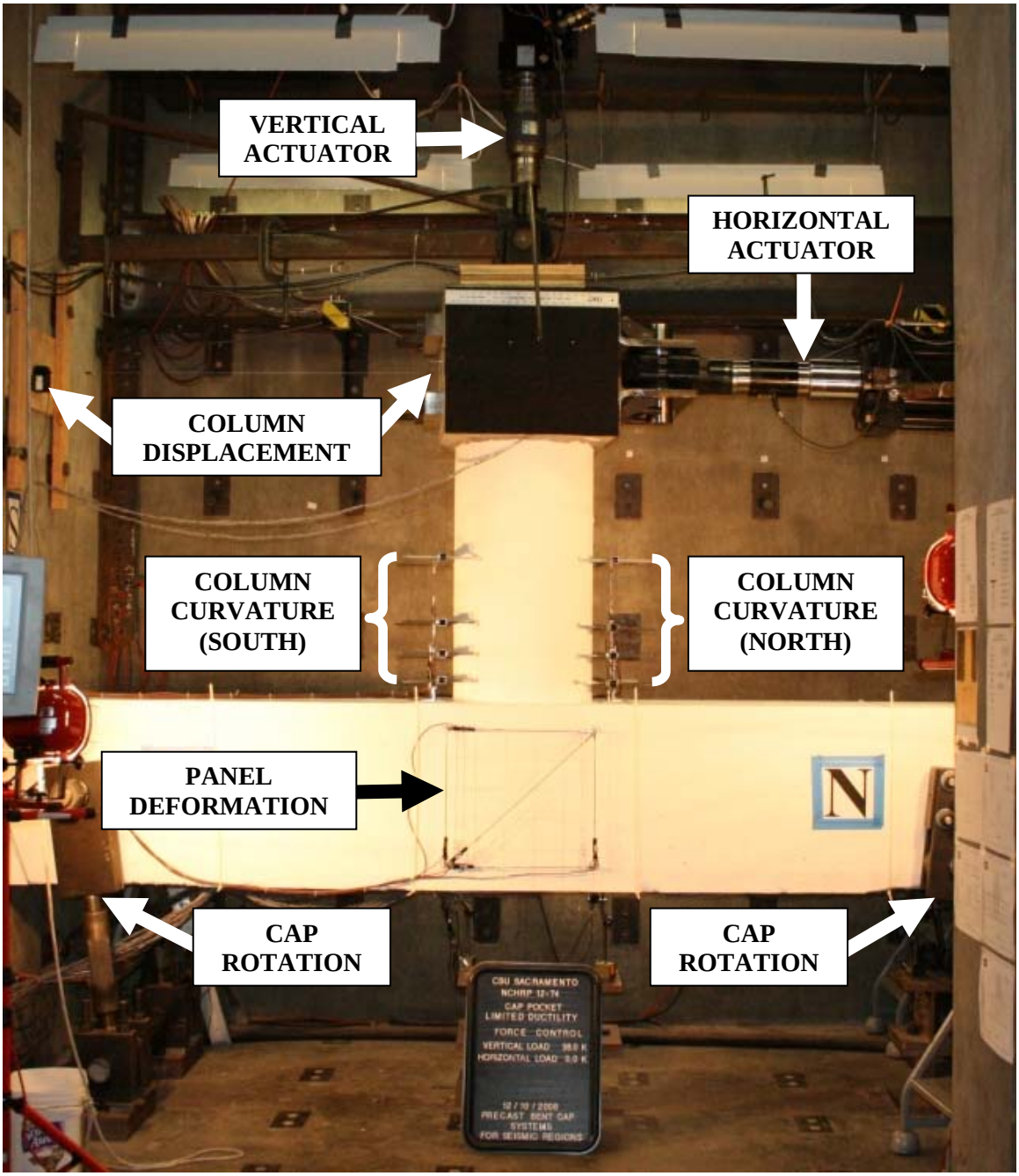

Figure 2-37. External Instrumentation Photos—Overall View

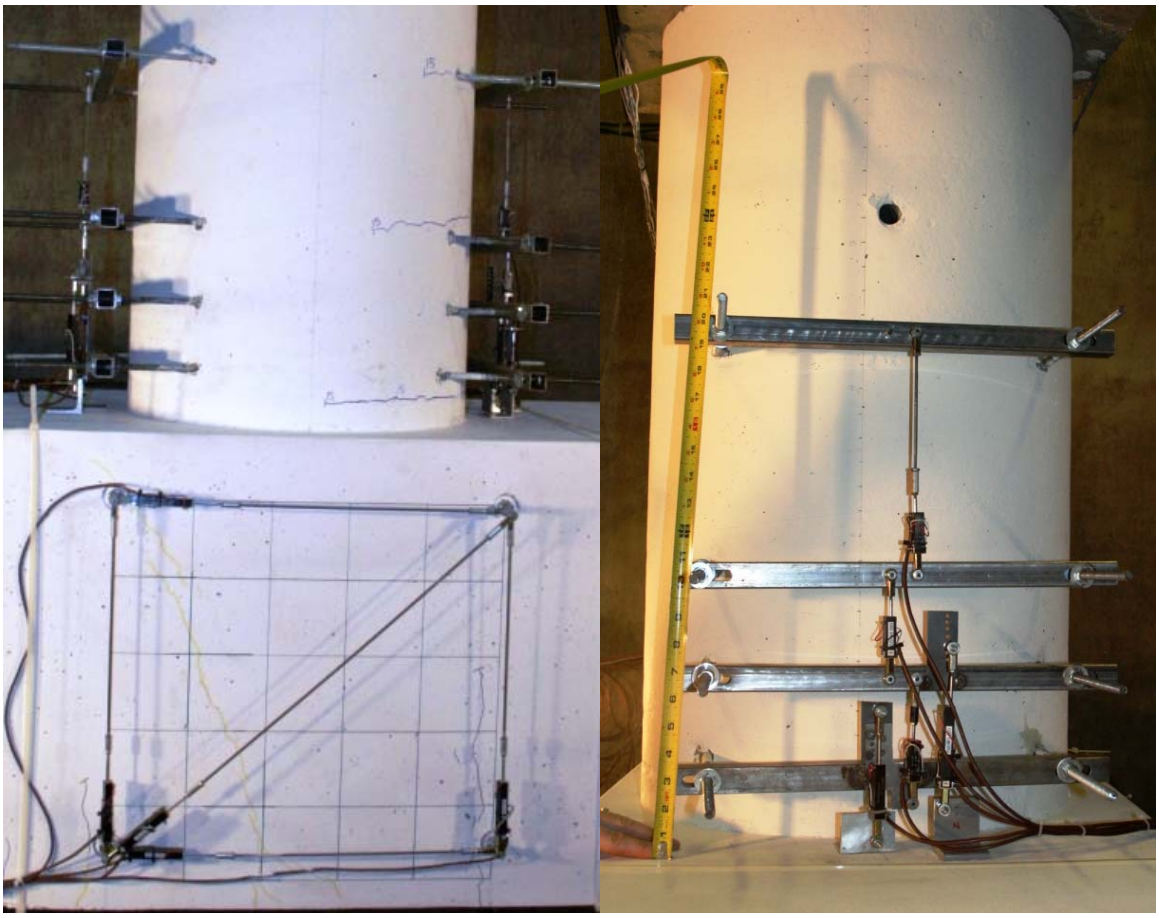

Figure 2-38. External Instrumentation Photos—Panel Deformation and Column Curvature

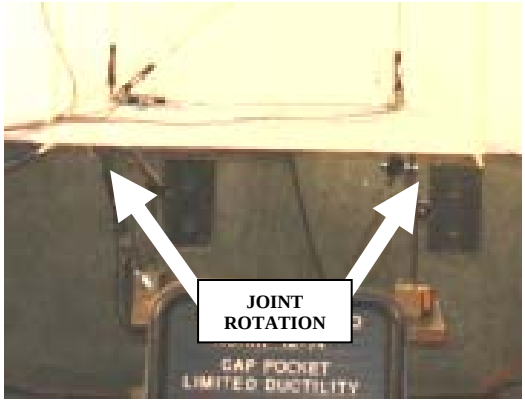

Figure 2-39. External Instrumentation Photos—Joint Rotation

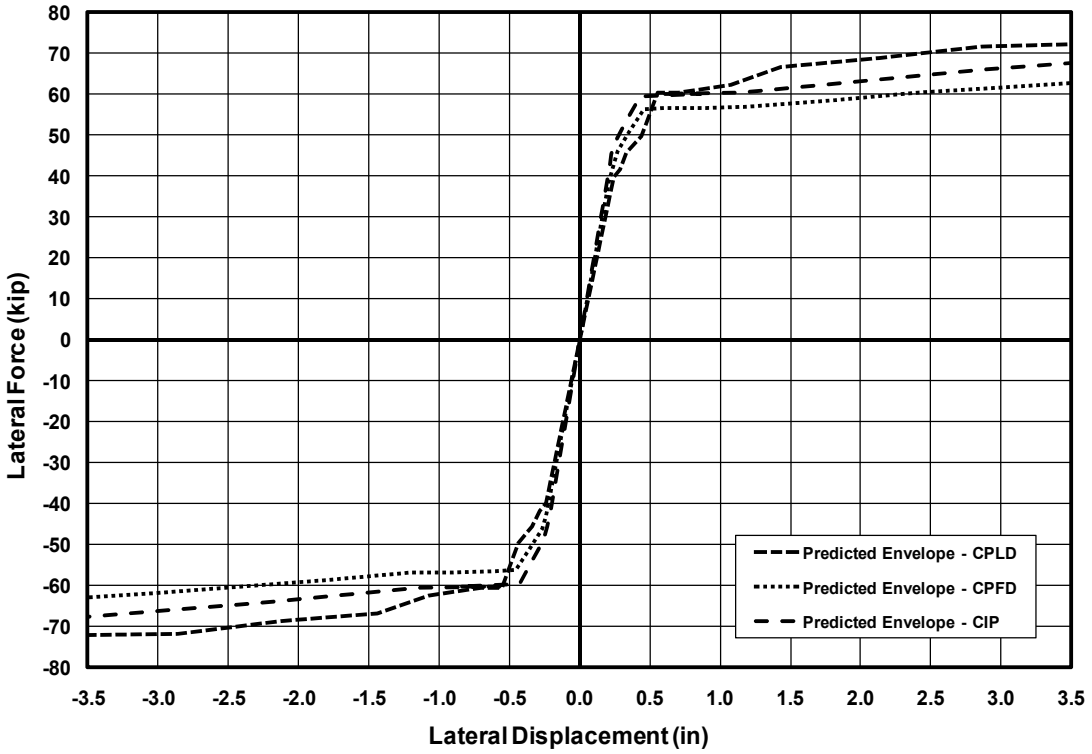

Figure 2-40. Predicted Lateral Force vs. Lateral Displacement Envelope—CPLD, CPFD, CIP

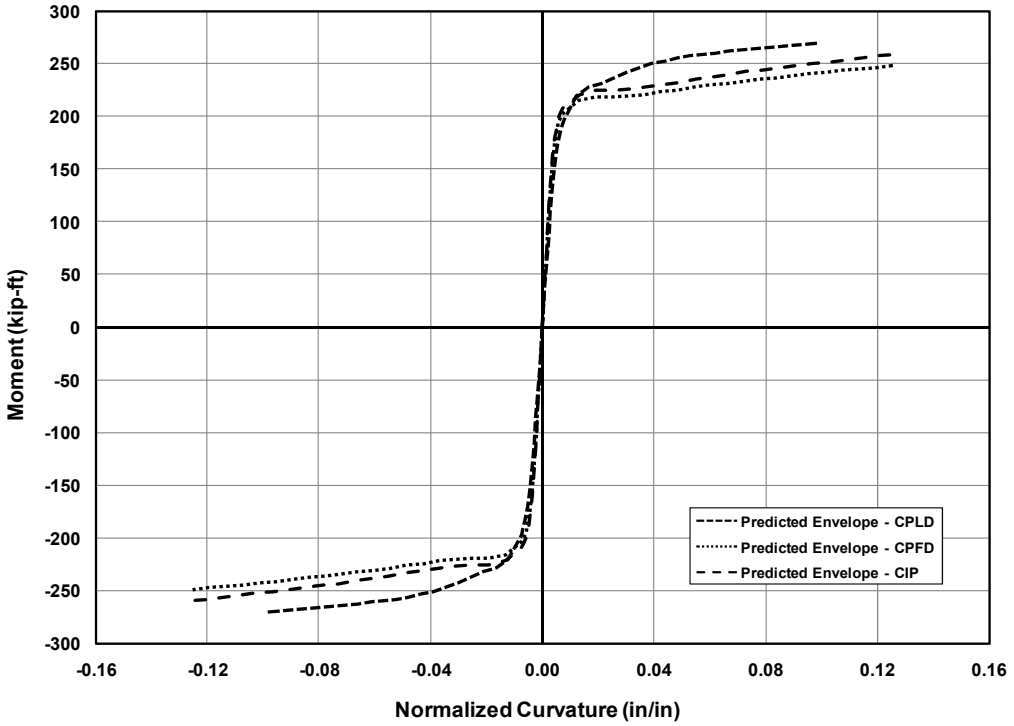

Figure 2-41. Predicted Normalized Moment vs. Curvature Envelope—CPLD, CPFD, CIP

3.0 Specimen Response and Analysis

3.1 Experimental Observations

This section summarizes experimental observations made during testing, based on visual inspection and digital photos. Photos of the specimen include color-coded markings adjacent to cracks, as follows:

- Yellow: Pre-existing cracks prior to applied loading
- Brown: Cracks that formed or extended under vertical actuator loading
- Blue: Cracks that formed or extended under push direction loading
- Red: Cracks that formed or extended under pull direction loading

Markings also included: 1) load level or displacement ductility level; and 2) transverse mark perpendicular to marking to identify end of crack. Crack widths were measured while the specimen load or displacement was held nearly constant.

In reporting specimen response, displacement ductility, μ, and drift ratio are both used. (Note: "drift ratio" and "drift" are used interchangeably.) Drift ratio is defined as the column displacement divided by the column height, as a percent. This is a more consistent basis for comparison of specimen response. System ductility levels are also reported but, though reasonable, these values should be considered nominal (i.e., approximate) due to the approximate determination of first yield. Table 3-1 summarizes the associated values of force, displacement, ductility, and drift ratio for Force Control and Displacement Control stages (push and pull, Cycle 1). Table 3-2 provides a summary for comparing the Table 3-1 values for CPLD to that for CPFD and CIP (Push, Cycle 1).

Comparisons between the CPLD, CPFD, and CIP are presented in subsequent sections of the report; however, differences in specimen properties, detailing, and condition should be recognized.

3.1.1 Stages of Cracking

3.1.1.1 Predicted vs. Actual Specimen Cracking

The specimen was observed for crack formation and growth under loading sequences. Table 3-3 compares the predicted and actual stages of specimen cracking

under Force Control, and shows that observed bent cap, column and joint cracking occurred reasonably close to predicted loads. It should be noted that observation of initial (visible) hairline cracks is approximate and also depends on load increments selected because the specimen was not inspected until after the peak load associated with a load increment was reached.

3.1.1.2 Pre-existing Cracks and Joint Shear Cracks

Some cracks existed in the joint prior to testing. During the lowering of the specimen onto supports in the testing area, the specimen inadvertently bumped a vertical support and the south wall of the test bay. Figure 3-1 shows vertical and inclined hairline cracks that developed in and near the east and west faces of the joint due to handling. This included one joint crack on each side.

Figure 3-2 shows that the inclined pre-existing crack on the east face eventually opened under push direction loading and the pre-existing crack on the west face eventually opened under pull direction loading, as the crack inclinations reasonably matched the orientation that diagonal cracks would tend to develop. However, as for other specimens, significant additional joint cracking occurred close to the predicted load for joint cracking. For example, various cracks independent of the pre-existing cracks appeared on the east and west face of the joint under push direction loading (Figure 3-2). On the east face diagonal cracks appeared primarily above and below the pipe region, and at the next stage of loading ($\mu 1$, 45.7 kips), a major diagonal crack developed through the joint north of the pre-existing crack (Figure 3-3). At 41.9 kips and subsequent (push) loading, the west face developed two major diagonal cracks (0.013 in at 45.7 kips for south crack), independent of pre-existing crack locations and orientations for both east and west faces. A major east face pull direction joint crack developed at 41.9 kips (0.010 in) with some differences in location and orientation from the pre-existing crack. Also, under pull direction loading, additional diagonal cracks formed on the west face parallel to the pre-existing joint crack.

Thus, although pre-existing cracks contributed to crack patterns, new joint cracks formed in both the push and pull directions. This suggests that joint performance was not

unduly influenced by pre-existing cracks. In addition, joint cracking was predicted to form during Force Control loading due to the relatively low concrete strength. More liberal SDC B detailing than the CPFD specimen (e.g., removal of construction stirrups and end hoops around pipe, as well as removal of joint shear reinforcement) provided less restraint to crack opening and growth.

3.1.2 Select Observations

Visual observations suggest that the limited ductility specimen response was characterized by a combination of plastic hinging of the column adjacent to the bent cap and joint shear cracking. As diagonal cracks developed in the joint region with increasing lateral load (Section 3.1.1.2), significant column flexural (and shear) cracks also developed. The relative contributions of each mode are discussed in subsequent sections. Failure was due to buckling of column longitudinal reinforcement followed by bar fracture. Joint failure did not occur.

Figures 3-2 and 3-3 show the development of joint shear cracking during Force Control and Displacement Control sequences. Figures 3-4 and 3-5 show the overall specimen crack pattern at the last two Force Control stages (30 kips and 42 kips), and Figures 3-6 through 3-9 show the crack patterns for drift ratios of 1.2% to 5.1% ($\mu 2$ to $\mu 8$); cracks grew to a large width of 0.080 in at $\mu 8$. Hysteretic response is discussed in further detail in subsequent sections.

The following additional observations were made:

- In addition to the joint shear cracks, flexural cracks developed in the bent cap, with widths up to 0.025 in. As shown in Figure 3-37, flexural cracks at the bottom of the cap (as tested) extended through the width of the bent cap, including the cap pocket.
- Initial joint spalling occurred at a drift of 0.7% ($\mu 1$) but remained relatively minor throughout testing (Figure 3-3). Initial spalling of the column occurred at the bedding layer at a drift of 1.2% ($\mu 2$) with significant spalling in the plastic hinge region developing at $\mu 6$ (3.7% drift); see Figures 3-9 and 3-11.

- Radial splitting cracks formed at 0.5% drift (μ1, pull) on the top surface of the bent cap (as tested) and extended down the side face of cap at larger drifts. Splitting cracks also developed vertically along column longitudinal bars. (Figure 3-10)
- Column longitudinal bar buckling initiated at a drift of 5.0% (μ8, pull), followed by fracture of two longitudinal bars (μ8, pull), as shown in Figure 3-11. Buckling corresponded with load degradation.
- At ultimate, spalling of column cover had developed along a length of approximately 7.5 in along the plastic hinge region (i.e., a length equal to 38% of the column diameter) as shown in Figures 3-9 and 3-11. Although joint cracks grew to a width of 0.080 in at ultimate, loss of load was not attributed to joint response, but buckling of column longitudinal bars.
- Post-test inspection revealed: 1) a crack pattern consisting of a series of diagonal cracks through the center of the joint and minor associated joint spalling; 2) column longitudinal bars that appeared well anchored within the pipe, with a clear pattern of splitting cracks extending from the column into the cap top (Figure 3-12) as well as between bars within the pipe; and 3) intact concrete within the cap pocket and at the bedding layer, suggesting integral performance with the surrounding concrete. Some crushing was evident at the top of the bedding layer (Figure 3-12). Although there was no visual evidence of column bar pullout from the pipe or bar slip between the pipe and concrete, a more detailed discussion of bar slip based on data is presented in subsequent sections.
- Overall, the specimen exhibited exceptional ductility, achieving a high level of drift (over 5.0% at μ8), well beyond μ2, despite the development of significant joint shear cracks.
- The modified test setup ensured in-plane loading of the column during testing. Column rotation was limited to 0.33 deg through μ6 and 0.96 deg through μ8.

3.1.3 Comparison with CPFD and CIP Specimens

As shown in Table 3-4, CPLD concrete compressive strengths were considerably lower than for the CPFD and CIP specimens, due primarily to the earlier age at which the specimen was tested. Steel rebar strengths compared closely for the specimens. Table 3-5 compares the stages of specimen cracking, and shows reasonably close comparisons.

Select observations of specimen response show similarities in flexure, but clear differences in joint behavior. For example, as shown in Table 3-2, the maximum push drift ratios were as follows: CPLD (5.0%), CPFD (4.3%), CIP (5.9%), indicating an exceptionally high level of drift for CPLD even beyond CPFD, without joint failure. However, diagonal cracking in the CPLD joint was much more extensive, reaching a surface crack width of 0.050 in at μ2 and 0.080 in maximum, with minor spalling. In contrast, the maximum diagonal joint crack width was only 0.009 in for CPFD and 0.025 in for CIP, both without spalling. In addition, the pattern of joint cracking differed, as explained in Section 3.5.2.

Compared to full ductility specimen response, CPLD joint cracking significantly softened the joint, allowing the column to displace to higher drift levels before spalling of the concrete cover over the column reinforcement could occur and plastic hinging could clearly dominate. See Section 3.4 for further details.

Similar bent cap flexural cracking developed for all specimens, and failure of all specimens was precipitated by buckling of column bars, followed by bar fracture.

3.2 Hysteretic Response

3.2.1 Column Load-Displacement Response

The lateral force-lateral displacement (hysteretic) response of the column, used to characterize the fundamental performance of the specimen, is shown in Figure 3-13 together with the response envelope and predictions. The primary aspects of the response were:

- Plastic hinging of the column enabling the specimen to undergo a large drift ratio of 5.0% (μ8, push) and 5.1% (μ8, pull)

- Stable hysteretic behavior with loops of increasing area and a strength degradation of 12% at the maximum drift (push)
- Maximum loading of approximately 60 kips (push) and 63 kips (pull) with 100% of this load sustained up to a drift ration of approximately 3.7% (μ6) in both the push and pull directions
- Strength degradation of 13% (between first cycles) at a drift ratio of 5.0% (μ8, push) associated with column bar buckling; in addition, strength degradation of 17% between first and second cycles at μ8

A comparison of the response envelope to the predicted envelope—which assumed full flexural capacity without any limitation based on potential joint failure—shows a reasonable correlation. The specimen achieved a capacity slightly higher than predicted through several stages for both push and pull directions.

The hysteretic response also portrayed appropriate stiffness, strength, ductility and other features such as flexural crack distribution and width representative of emulative response. However, it should be noted that ductile plastic hinging in the column was accompanied by significant joint shear cracking, although joint failure did not occur.

3.2.2 Equivalent Viscous Damping

Determination of the equivalent viscous damping ratio provides a quantitative means to establish the energy dissipating characteristics and loop stability of the specimen for comparison to the CIP control and other precast specimens. The equivalent viscous damping ratio, ξ, represents the energy dissipation per cycle, determined as follows [13]:

$$\xi = \left(\frac{2}{\pi}\right)\left(\frac{A_L}{A_R}\right)$$

where:

A_L =area of hysteretic loop for a complete cycle (push and pull)

A_R =aea of rectangle bounded by maximum loads and displacements of a complete hysteretic loop

Figure 3-14 plots the equivalent viscous damping ratio, ξ, versus drift ratio, including the first two cycles for each drift ratio. ξ increased significantly with increasing drift ratio, reaching approximately 28% (first cycle, μ8). This level is considered suitable for ductile response of a precast beam-column connection emulating a conventional cast-in-place connection. ξ varied slightly between the first and second cycles.

3.2.3 Comparison with CPFD and CIP Specimens

Figure 3-15 shows the envelopes for the CPLD, CPFD and CIP hysteretic response. A close comparison is evident in stiffness, strength and ductility. The CPLD specimen achieved a noticeably higher capacity (9%-12%) than the other specimens and a ductility of the same order. Differences between the CPLD and CPFD at higher drift ratios correspond to strength degradation associated with column longitudinal bar buckling rather than precast connection response.

Figure 3-16 compares the equivalent viscous damping ratio, ξ, versus drift ratio for the three specimens. CPLD values are very similar to that for CPFD and slightly larger than CIP, although a similar trend is evident.

3.3 Column Curvature Response

3.3.1 Moment-Curvature

Figure 3-17 plots normalized moment-curvature response for the first curvature cell up the column, together with the predicted envelope. Predicted and measured response envelopes are shown to compare favorably. As for the load-displacement response, the actual moment exceeds the predicted curve at lower curvatures. Extensive curvature ductility associated with plastic hinging is evident. Cell 1 maximum curvature was approximately 20 times the effective yield curvature (estimated).

Cell 1 data is plotted through μ6, as μ8 data was unreliable. As for the CPFD, the performance of the CPLD Cell 2 linear potentiometers in the push direction was questionable.

The moment at the mid-height of the cell was used for plotting, except that strain penetration was accounted for Cell 1. In addition, data was corrected for joint rotation to

provide a matching basis for predictions. Note that the curvature was normalized by multiplying curvature by the column diameter; moment was not modified.

3.3.2 Curvature over Height

Figures 3-18 and 3-19 show the normalized curvature profile over the column height for the Force Control and Displacement Control sequences, respectively. Curvature for the first cycle is used for Displacement Control values. These profiles demonstrate the concentration of plasticity adjacent to the soffit, as well as the spread of plastic hinging up the column under increasing displacement. First yield normalized curvature was estimated analytically as 0.0036 in/in, though limited data indicated a first yield value of approximately 0.0060 in/in. Both indicate that during the final loading cycle of Force Control (42 kips) column bars yielded. Figure 3-19 indicates that much more significant inelastic response developed over an increasing height under Displacement Control.

3.3.3 Comparison with CPFD and CIP Specimens

Figure 3-20 plots the Cell 1 normalized moment-curvature prediction and response envelopes for the CPLD, CPFD and CIP specimens. A reasonably close comparison is evident for the response envelopes, although the CPLD is shown to achieve a slightly higher capacity. Curvature over height can be compared for the specimens by comparing Figure 3-19 to Figures 3-21 and 3-22. These figures show a reasonably similar trend of spread of plasticity and level of curvature for the specimens.

However, Table 3-6 shows that at the same drift ratio (and stage of displacement ductility), the CPLD achieved a curvature approximately 30% less than the CPFD and CIP full ductility specimens. This can be attributed to the softening of the joint due to shear cracking, which increased the joint shear contribution to column displacement. Thus, for a given drift, the CPLD flexural contribution (i.e., curvature) was less than for the full ductility specimens that exhibited more limited joint shear cracking. See Section 3.4.2 for further discussion.

3.4 Displacement Decomposition

Displacement decomposition refers to the separation of the column displacement into the various components that contribute to the overall lateral displacement of the column. Components include column flexure, fixed end rotation (FER; due to plastic hinging plus bar slip), bent cap flexibility, and joint shear. Decomposition quantifies the magnitude of each component and is determined for comparison of analytical predictions to experimental measurements. Figure 3-23 shows a schematic representation of the experimental column displacement components, including applicable equations based on measured quantities.

Some limitations exist when comparing predicted and measured displacements. For example, in the test program the joint shear displacement was not determined analytically but was measured. This leads to some approximation.

Properly designed, full ductility cast-in-place and emulative bridge bents are expected to display extensive flexural plastic hinging, which results in flexural displacement components dominating the displacement at increasing drift or displacement ductility levels. This trend should be reflected in full ductility precast specimens when emulative performance is achieved. Similarly, limited ductility emulative bridge bents are expected to exhibit flexural plastic hinging, but, as discussed in Section 2.1, they are expected to achieve a significantly lower displacement ductility capacity (in the range of $\mu 2$) due to less stringent joint and column detailing requirements. CPLD column detailing matched that of the CPFD, allowing the CPLD to develop plastic hinging and exhibit large flexural displacement components at increasing drift or displacement ductility levels.

However, 2006 LRFD RSGS and 2009 LRFD SGS do not require joint reinforcement, including vertical stirrups. The less stringent CPLD joint detailing permits more extensive joint damage to occur at increasing drift; thus, joint shear components would be expected to contribute significantly.

The total experimental flexural component is taken as the sum of the fixed end rotation plus column flexure. Fixed end rotation represents displacement due to plastic

hinging within the first curvature cell plus displacement due to bar slip. However, because the plastic hinge length extended beyond the first curvature cell, plastic hinging response also contributed to the column flexure component. Thus, the total predicted flexural displacement is compared to the sum of column flexure and fixed end rotation.

To match the assumption of ideal pin and roller support conditions, rigid body translation and rotation of the specimen were removed from the raw data during data reduction.

3.4.1 Overview

Table 3-7 summarizes the displacement decomposition for the first push and pull cycles for drift ratios from 0.5% to 5.1%. For each drift ratio, results are tabulated in two columns. The first column includes two sections: 1) the top section summarizes the column displacement (CD) and the corresponding drift and force; and 2) the bottom section lists the displacement components determined from measurements, as shown in Figure 3-23, and the sum of the components (Component Total, CT). At the bottom of the table is the CT/CD ratio, indicating what portion of actual displacement is represented by the measured components.

The second column shows the analytically predicted displacement components. Although the load-displacement envelope was predicted pretest, the actual displacements imposed on the specimen were not well defined pretest, as these are dependent on the establishment of first yield, which was approximate. Thus, the second column shows predicted displacement components that sum up the imposed displacement in the test (i.e., CT/CD=1.0). In addition, predicted displacements are based on actual material properties. This approach allows actual and predicted displacement components to be appropriately compared, as shown in the third column (Actual/Predicted ratio).

Some approximation is expected in predicted and measured values. Joint shear was not predicted and column shear was predicted but not measured. The difference between CT and CD represents column displacement due to column shear, joint shear and potential inaccuracies in measurements. Joint shear was expected to represent a significant percentage of the total measured displacement in CPLD, a limited ductility

specimen. Although prediction of column shear is considered approximate, inclusion of this component in predictions allows a more realistic comparison in Actual/Predicted ratios. Significant column shear cracking is clearly shown in Figures 3-4 through 3-9.

3.4.2 Flexural and Joint Shear Components

As shown in Table 3-7 for the push direction, the CT/CD ratios ranged from 0.79 to 1.39 (1.08 average) through a drift of 5.0% (μ8, push). Some variation in determining displacement components is evident, although components were reasonably determined on average. The Actual/Predicted ratios for flexure (FER plus column flexure) ranged between 0.73 and 0.88 (0.80 average), which indicates flexure was under-predicted by approximately 20% on average. Bent cap flexibility and applied force corresponding to CD were also shown to be approximately predicted. These differences are shown in Figure 3-24. Many of these differences can be attributed to the fact that the joint shear displacement component was not predicted. However, for the CPLD specimen, in particular, joint shear displacements contributed a significant 28% to CT on average. Similar overall trends are evident in Table 3-7 for the pull direction.

Figure 3-25 plots the displacement decomposition component values for the push and pull directions. The height of each bar segment shows the relative contribution of a component. In correlation with experimental observations of flexural plastic hinging as well as joint shear cracking, the flexural component (FER plus column flexure) and the joint shear component were both significant. However, the flexural component increased at a greater rate than the joint shear component with increasing drift, as column flexure was more dominant at higher drifts. Column flexure and fixed end rotation both contributed to the increase in the flexural component. Bent cap flexibility provided the smallest contribution to system displacement.

Figure 3-26 plots the displacement decomposition components as a percentage of the total component displacement (CT) and provides further insight into system behavior. For example, at a push drift ratio of 0.8% (μ1.5), the flexural component (FER plus column flexure) accounted for 48% of CT, while joint shear accounted for a smaller but significant 31%; this corresponds to a flexure/shear ratio of 1.58. However, at a push

drift ratio of 2.5% (μ4), the flexural component increased to 63% of CT, and joint shear reduced to 26%, for a flexure/shear ratio of 2.42. Overall, the flexure/shear ratio increased at increasing drift, averaging 2.2. In addition, the flexural component averaged 60%, compared to 25% for joint shear. This corresponded well with visual observations that flexural plastic hinging dominated, but joint shear was an important factor in response. Similar response developed for the pull direction.

As shown in Figures 3-25 and 3-26, the bent cap flexibility (joint rotation) component remained relatively constant in magnitude but decreased in percentage of CT with drift. Bent cap flexibility averaged 15% and reduced from 19% at μ1 to 8% at μ8.

3.4.3 Bar Slip

Table 3-8 summarizes the CPLD bar slip component of column displacement and compares bar slip to fixed end rotation displacements. By definition, fixed end rotation includes the effect of bar slip on rotation. As shown in the table, the CPLD bar slip component was significant, contributing 33% on average to the fixed end displacement component. As the drift ratio increased to 2.3% (μ4), the bar slip component reduced slightly, as the fixed end rotation increased.

The significant bar slip contribution to column displacement is mainly attributed to the extensive cracking in the joint, which reduced the confinement effect of the bent cap concrete on the corrugated pipe, allowing pipe dilation. However, an appropriate load path still developed to anchor the column bars within the pipe through a significant number of cycles during Displacement Control at or near the maximum load. Thus, although significant joint cracking and splitting developed, neither joint failure nor bar pullout failure occurred. Nevertheless, as shown in Figure 3-27, the bar slip component did increase appreciably between μ6 and μ8 (3.6% to 4.6% drift), as the load decreased 12% (due to column bar buckling in the plastic hinging region). This corresponded with the largest joint crack widths.

It should be noted that the actual slip of the bar within the pipe (in contrast to the bar slip contribution to column lateral displacement) was 0.08 in at μ2, 0.11 in at μ6, and a noticeably larger value of 0.18 in at ultimate (μ8).

The embedment depth of the #5 column bars into the bent cap, l_{ac}, was 21 in, or a l_{ac}/d_b ratio of 33.6, conforming to the 2006 LRFD RSGS and 2009 LRFD SGS joint requirement that column bars to be extended as close as practically possible to the opposite face of the bent cap for development of a force transfer mechanism. [5, 7] Prior research on column bars anchored in grout pockets indicate that an l_{ac}/d_b ratio of $2.3f_y/f'_c$ should be used (based on bar anchorage only). [14, 15] For the CPLD specimen, this corresponds to a fairly large l_{ac}/d_b ratio of 42.4, due to the low cap pocket compressive strength. Although the ratio of 42.4/33.6=1.26 is within the factor of safety incorporated into bar anchorage equation, the relatively short embedment depth, combined with the significant joint shear cracking, contributed to conditions for increased bar slip.

3.4.4 Comparison with CPFD and CIP Specimens

The displacement decomposition percentages for the CPLD, CPFD and CIP specimens are shown in Figures 3-26, 3-28 and 3-29, respectively. Although all specimens, including the CPLD, reached a high level of drift, the percentages quantified important differences in response for limited vs. full ductility specimens that were observed visually, namely, that the CPLD specimen achieved significant plastic hinging but was accompanied by significant joint shear cracking without joint failure, whereas the full ductility specimens achieved significant plastic hinging with minor joint shear cracking.

Figure 3-30 compares the joint shear and flexural (push) response for the specimens. System displacement due to joint shear is shown to be nearly an order of magnitude larger for the limited ductility specimen compared to the full ductility specimens. Specifically, the joint shear component averaged 28% for CPLD, but only approximately 4% for CPFD and 3% for CIP. On the other hand, differences in flexure were much less: the flexural component (push) for CPLD averaged 63%, compared to 68% for both CPFD and CIP, i.e., flexure was approximately 5% less for CPLD than for full ductility specimens. In addition, the CPLD flexure/shear ratio averaged 2.2, but nearly an order of magnitude larger for the full ductility specimens (average of 16.5 for CPFD; 20.0 for CIP).

Tables 3-8 and 3-9 compare the CPLD bar slip component to that for the CIP and CPFD specimens, respectively. Table 3-8 shows that the CPLD bar slip component was at least an order of magnitude larger than the CIP (factor of 16 on average) for all stages of response. Table 3-9 shows that, on average, the CPLD bar slip component was an order of magnitude larger than the CPFD bar slip during Cycle 2 of μ6. Both trends correspond well with observations of specimen joint cracking (and l_{ac}/d_b). In addition, Figure 3-27 compares the CPLD and CIP lateral force vs. bar slip for several cycles of μ6 and μ8. The much larger CPLD slip is again evident, as well as the significant increase towards ultimate, as the load decreased. This may indicate that bar pullout was impending, but did not mobilize before column bar fracture occurred. Thus, as previously noted, although significant CPLD joint cracking and splitting developed, neither joint failure nor column bar pullout failure occurred.

The bent cap flexibility component was similar for all specimens, averaging 15% for CPLD, 13% for CPFD, and 11% for CIP.

3.5 Joint Response—Additional Aspects

This section summarizes additional aspects of joint response not previously addressed, including joint shear stress, principal stresses and angle, joint cracking, joint deformation, and bedding layer.

3.5.1 Joint Shear Stress, Principal Stresses, and Principal Angle

The average joint shear stress, plotted in Figure 3-31, exhibits a similar hysteretic trend as the load-displacement plot. Figure 3-32 shows the joint shear stresses vs. shear strain, including stiffness and extensive straining at increasing drift ratios in accordance with joint shear crack history summarized previously. Significant joint softening is evident. Joint Shear stress and shear strain are calculated as shown in the List of Equations and, strictly speaking, refer to average (or nominal) values applicable to the joint region. Shear stresses were as large as $6.3\sqrt{f_c'}$ and were used in determining the principal stresses and principal angle shown in Figures 3-33 through 3-35.

As intended by design, the CPLD specimen did not include 2006 LRFD RSGS SDC D additional joint shear reinforcement (for full ductility specimens) or supplemental

construction stirrups placed in the joint as for other specimens (CIP, GD, CPFD). Figure 3-34 shows that the principal tensile stress reached $7.0\sqrt{f_c'}$, i.e., twice the $3.5\sqrt{f_c'}$ limit at which extensive (additional) joint reinforcement is required by 2006 LRFD RSGS requirements because of the likelihood of joint shear cracking, but less than the upper limit of $12\sqrt{f_c'}$. This level of tensile stress indicates that significant joint cracking could develop, which was in fact observed. Figure 3-34 indicates that the principal compressive stress reached $0.13 f_c'$, approximately half the 2006 LRFD RSGS limit of $0.25 f_c'$.

Figure 3-35 plots the angle of the principal plane angle in the joint, which is shown to be approximately 40-45 degrees from horizontal, with the push direction shown to be slightly smaller. These values correlate well with the expected response.

3.5.2 Joint Cracking

Diagonal cracking was extensive within the joint region. Shear cracks developed during Force Control as mentioned in Section 3.1.1.2 and then further developed and widened during Displacement Control as shown in Figure 3-3 and discussed in Section 3.1.2. The post-test crack pattern consisted of a series of diagonal cracks through the center of the joint (Figure 3-3).

Table 3-10 summarizes the maximum measured diagonal crack widths on the surface of the joint (east and west faces) at the various drift and lateral force levels (push and pull). Cracks were as wide as 0.050 in at μ2 (push, both faces), and although cracks increased to large widths at ultimate (0.070 in, east face; 0.080 in west face), joint failure did not occur. Minor spalling in the joint occurred (Figure 3-3).

3.5.3 Joint Rotation and Deformation

Joint rotation and panel deformation were measured during the test. Joint rotation was limited to less than 0.0029 rad (0.16 deg). Although this was larger than that assumed in predictions, predictions were based on an estimate of cracked bent cap section properties, which did not accurately account for the extent of joint shear and flexural cracking and the influence on section properties.

The deformation of the joint was measured using linear potentiometers in the region of the joint. With joint cracking, the maximum change in panel area was 0.46%.

3.5.4 Bedding Layer

The 1.5-in bedding layer appeared to perform integrally with the column through 5.1% drift and did not produce unusual behavior in the joint or specimen. As shown in Table 2-7, strength and stiffness properties for the concrete in the column (plastic hinge region) and cap pocket matched well. Figure 3-36 shows the interface between the bedding layer and column concrete post test. The boundary between the two surfaces was somewhat difficult to distinguish, although after removal of cover concrete, it was more evident. The bedding layer concrete was not a weak link in the system, though some crushed concrete was evident at the interface with the column post-test (Figure 3-12). In addition, several minor hairline vertical cracks spaced at approximately 4 in to 8 in developed at the bedding layer.

3.5.5 Cap Pocket

Figure 3-37 shows the exposed surface of the cap pocket (bottom of cap as tested). Several flexural cracks developed through most or all of the bent cap width, including across the pipe. No slip was visible between the pocket concrete, pipe, and bent cap, suggesting integral behavior between the pocket concrete, pipe, and surrounding concrete.

3.5.6 Comparison with CPFD and CIP Specimens

The precast joint region for the CPLD specimen exhibited a significant level of distress that increased throughout the test. This was in contrast to the relatively minor joint distress evident for the CPFD and CIP joints. Table 3-11 compares maximum stresses, principal angle, joint rotation and change in panel area. Accounting for the lower CPLD concrete strengths (Table 3-4), the CPLD maximum stresses (nominal joint shear, principal tensile, and principal compressive) were significantly larger than the full ductility specimens: 47%-86% larger than the CPFD and 30%-48% larger than the CIP. Also the maximum applied force for CPLD was 9%-12% larger than the full ductility specimens. The maximum principal angle (45 deg) differed by 1%. These larger stresses

corresponded with the more significant CPLD joint distress. Figure 3-38 compares the joint shear stress-strain envelopes for the specimens, showing a significantly larger CPLD strain and slightly smaller initial stiffness in accordance with the joint cracking history.

The CPLD joint distress was also reflected in larger panel deformation and joint cracks. Table 3-11 shows that the CPLD change in the panel area was approximately three times that of the full ductility specimens.

Diagonal cracking in the CPLD joint was significant, reaching a surface crack width of 0.050 in at μ2 and 0.070 in maximum, with minor joint spalling evident. In contrast, CPFD joint diagonal cracking was minor, reaching only 0.005 in at μ2 and 0.009 in maximum, without spalling. CIP specimen cracking was intermediate, with a crack width of 0.009 at μ2 and 0.025 in maximum, without spalling.

In addition, the pattern of joint diagonal cracks differed significantly, as shown in Figure 3-39. The CPLD series of diagonal cracks on both faces resembled the CIP pattern much more than that of the CPFD, although the CPLD cracks were much wider. The CPFD diagonal cracking was limited to regions above and below the corrugated pipe until a drift ratio of 3.7% (μ6, pull), and diagonal cracking did not extend into the central joint region for the push direction. In addition, two symmetrical vertical flexural cracks developed through the CPFD joint (maximum width of 0.020 in), near the locations of the vertical construction stirrups.

It should be noted that CIP analysis demonstrated the construction stirrups in the joint region were highly effective (reaching yield) in resisting joint stresses and limiting crack opening. These stirrups played a lesser role for the CPFD specimen, which exhibited more limited cracking, although the stirrups influenced the joint vertical crack pattern. In addition, the CPFD hoops at the ends of the pipe reached up to 52% of yield, indicating their contribution to joint performance.

The CPLD and CIP vertical (flexural) cracks in the joint region were not as extensive as the CPFD vertical cracks. The CPFD also exhibited a horizontal crack (0.030 in) south of the joint on the west face.

3.6 Strain Records

This section uses strain profiles and tables to present select results from specimen strain records, as well as comparisons to the CPFD and CIP specimens. Profiles show the strain levels for a series of strain gages at specific regions of the specimen and for specific load or ductility (drift) levels. Profiles include strain for: 1) column longitudinal rebar (locations along the column and into the joint); 2) hoops in the column and joint; and 3) stirrups in the bent cap and joint. A table is provided for the bent cap longitudinal rebar (locations along the bent cap, including through the joint).

Some gages reliably recorded large strains well in excess of yield, while a few produced unreliable data typically after bar yield. Plots reflect only data considered reliable.

Only select strain gage records are discussed. These strain records and others will be further analyzed and addressed through future efforts.

3.6.1 Column Longitudinal Rebar

3.6.1.1 CPLD Specimen

Figure 3-40 shows the strain profile for the extreme column bar on the north side of the specimen. As expected, column strains were largest in the plastic hinge region, with strain penetration including bar yield confirmed 12 in above and 6 in below the bedding layer. Records demonstrate that the strain dropped off at further depths from the bedding layer.

3.6.1.2 Comparison with CPFD and CIP Specimens

Figures 3-41 and 3-42 show the strain profile for an extreme column bar (north) for the CPFD and the CIP specimens, respectively. An overall pattern similar to the CPLD response is evident, with the largest column strains in the plastic hinge region and reduced strains above and below. In addition, significant strain penetration was evident, including bar yield at least 6 in into the joint.

3.6.2 Column Hoops

3.6.2.1 CPLD Specimen

Table 3-12 shows the strains in the hoops for two column gages above the bedding layer (as tested). These gages were placed on the east side, where out-of-plane transverse tension caused by concrete dilation can produce larger hoop strains. Tabulated values show that hoop strains developed gradually in the plastic hinge region, with yield eventually being reached. This corresponds with visual observations. As mentioned previously, significant column spalling did not occur in the plastic hinge region until μ6 (3.7% drift ratio). The large drift required to cause column spalling may be attributed to the significant joint shear cracking that developed at earlier stages. Due to a significant joint shear component to column drift, column flexural behavior tended to dominate at larger drifts. The large hoop strains reflected the effective confining effect of the hoops after spalling.

3.6.2.2 Comparison with CPFD and CIP Specimens

Similar to the CPFD (Table 3-13) and CIP (Figure 3-42), CPLD hoop strains in the plastic hinge region achieved yield, reflecting the confining effect (Table 3-12). In addition, strains in the region several inches above the joint remained near or above yield for all specimens.

However, significant column spalling developed at a much larger drift for the CPLD than for the CPFD. Thus, a comparison of Tables 3-12 to 3-13 shows that the CPLD hoop strains developed much more gradually (i.e., at much larger drifts) than for CPFD. This is attributed to the more extensive joint shear cracking for the CPLD.

3.6.3 Pipe Strain

3.6.3.1 CPLD

Table 3-14 summarizes tensile strains in the corrugated pipe at several locations, as well as strains for several column longitudinal bars at similar depths as the pipe gages. As shown in the table, strain gage rosettes were used on the east and north sides of the pipe. Table 3-14 also shows the principal strain and principal angle strain for the rosettes as well as the linear strain and its angle along the corrugation for each rosette for

comparison. Values are provided for a drift of approximately 1.8% (μ3), which corresponded to an applied lateral load within 1%-2% of the maximum.

An examination of push direction principal strains shows that the maximum pipe strain was quite large, reaching up to 66% of yield on the east face at a depth of 8 in from the cap top (as tested) and on the east face. Considerably larger strains beyond yield developed in the column bars at similar depths in the joint (B2 location in Table 3-16).

For the push direction, pipe strains decreased with depth. North face pipe strains were considerably smaller than corresponding east face strains. Strain along the corrugation dominated the response at the top and bottom locations (123 and 789 gages) and were within 10% of principal strains. Principal angles for those gages were close to the 20 deg corrugation angle. In contrast, mid-depth corrugation gages (456 gages) exhibited a considerably different pattern of strain and principal angle. This was the location of maximum damage in the joint.

Pull direction behavior led to a similarly large strain of 70% of yield at the east face top gage, and a similar pattern of reduced strain with depth. However, principal angles were significantly different than push direction, and strains along the corrugation were not close to the principal strain at any location.

3.6.3.2 Comparison with CPFD and CIP Specimens

Tables 3-14 and 3-15 summarize the pipe strain for CPLD and CPFD, respectively. A review of the tables shows much larger pipe strains for the CPLD, corresponding to the more significant joint distress observed. The ratio of CPLD/CPFD principal strain through the depth (east face) for the push direction was: 1.85 (123 gage), 1.40 (456 gage), 1.91 (789 gage). Ratios for the pull direction were much larger (10.3, 5.3, 8.6, respectively), as the strain levels were much smaller for the CPFD, which exhibited only minor cracking in the joint region. Distribution of strains also differed for both push and pull directions.

CPLD pipe strain also differed considerably from the CIP hoop strain shown in Figure 3-43. Although only a limited comparison is possible, CIP hoop strain peaked at approximately two-thirds of the depth of the cap (18 in), while pipe strain was maximum

near the top of the pipe (7.6 in). In addition, hoop strain was minimum near mid-depth where pipe strain was still significant. This suggests some difference in joint behavior between the specimens. Strains for the pipe and hoops were of a similar magnitude, although the hoop force associated with the pipe was approximately twice that required for equivalence to the CIP hoops (because pipe yield strength was approximately twice the nominal value used for pipe design).

3.6.4 Bent Cap Longitudinal Rebar

3.6.4.1 CPLD

Table 3-17 lists bent cap longitudinal bar strain (top and bottom bars) for the first cycle of three nominal displacement ductilities of Displacement Control (μ2, μ4, μ6) during which the maximum load was reached. This table shows that strain levels for bottom and top bars were largest within the joint (S1, CL, and N1 positions) and that yield was reached at the centerline (CL) of the joint for the bottom bar and 62% of yield was reached at the south face of the joint (S1) for the top bar. Strain patterns reasonably matched expected distribution per an assumed force transfer model similar to that of Reference 16. It should be noted that the test specimens, designed per 2006 LRFD RSGS, did not include the significant additional area of bent cap longitudinal reinforcement ($0.245A_{st}$) required by 2009 LRFD SGS.

3.6.4.2 Comparison with CPFD and CIP Specimens

Table 3-18 compares the longitudinal bent cap strain (top and bottom bars) for the CPLD, CPFD, and CIP specimens. Strain patterns are shown to be reasonably consistent, especially for the bottom bars. The maximum strain for the bottom bars occurred in the joint region. At the centerline (CL), the CIP reached 46% of yield, whereas the CPFD and the CPLD yielded. Strains at the south most (S2) and north most (N2) bars were similar. More limited comparisons are available for the top bar; however, the CPLD strains were not as large or consistent with the CPFD within the joint.

3.6.5 Stirrups in Bent Cap

3.6.5.1 CPLD

The CPLD specimen used 2-leg stirrups in the bent cap for conventional design, but seismic joint shear reinforcement or construction stirrups were not used within the joint. Figures 3-44 and 3-45 show the strain profiles for instrumented stirrups within the bent cap adjacent to the joint. Stirrup strains are shown to be very small for Force Control, but increase significantly under Displacement Control (push) to 61% of yield at the north face of the joint and 33% of yield at the south most stirrup.

3.6.5.2 Comparison with CPFD and CIP Specimens

The CPLD did not include vertical stirrups within the joint, in contrast to the CPFD and CIP joints, as explained in Section 2.1.2. For the CPFD and CIP joints, two strain gages were placed on each of the two construction stirrups, at approximately the 1/3 and 2/3 points along the stirrup height. Since stirrups in the regions adjacent to the joint used gages at the mid-height of the stirrup, two sets of plots were developed. Figures 3-46 (CPFD) and 3-47 (CIP) show the mid-height gages on stirrups outside the joint together with the top gage on the joint stirrups, and Figures 3-48 (CPFD) and 3-49 (CIP) show the mid-height gages on stirrups outside the joint together with the bottom gage on the joint stirrups. CPLD included strain gages on stirrups placed at the face of the joint, unlike the other specimens. Thus, stirrup strain gage locations did not match for all specimens.

In contrast to CPLD stirrups at the north face of the joint reaching 61% of yield and south most stirrups reaching 33% of yield, maximum CPFD and CIP strains outside the joint were limited to approximately 10% of yield. In addition, as shown in Figures 3-47 and 3-49, construction stirrups within the joint for the CIP yielded and reached approximately 25% of yield for the CPFD (Figures 3-46 and 3-48). The lack of vertical joint stirrups in the CPLD specimen allowed joint shear cracks to develop and grow unrestrained.

3.7 Tables

Table 3-1. Associated Values of Force, Displacement, Ductility, and Drift Ratio—CPLD

Push (Cycle 1)					
Stage	Force (kips)	Disp (in)	Displacement Ductility, μ		Drift Ratio (%)
			Actual	Nominal	
Force Control	15.2	0.052	-	-	0.09
	20.2	0.144	-	-	0.24
	30.3	0.173	-	-	0.29
	42.4	0.360	-	-	0.61
Displacement Control	41.9	0.309	1.03	1.0	0.52
	48.5	0.466	1.55	1.5	0.79
	54.3	0.643	2.14	2.0	1.09
	59.2	0.959	3.19	3.0	1.62
	59.8	1.455	4.84	4.0	2.47
	60.0	2.164	7.20	6.0	3.67
	52.7	2.928	9.74	8.0	4.96
Pull (Cycle 1)					
Stage	Force (kips)	Disp (in)	Displacement Ductility, μ		Drift Ratio (%)
			Actual	Nominal	
Force Control	-15.0	-0.035	-	-	-0.06
	-20.2	-0.058	-	-	-0.10
	-30.2	-0.136	-	-	-0.23
	-42.2	-0.269	-	-	-0.46
Displacement Control	-45.7	-0.416	1.38	1.0	-0.71
	-50.7	-0.545	1.81	1.5	-0.92
	-56.9	-0.731	2.43	2.0	-1.24
	-61.9	-1.074	3.57	3.0	-1.82
	-63.0	-1.337	4.45	4.0	-2.27
	-62.8	-2.156	7.17	6.0	-3.65
	-56.2	-2.981	9.91	8.0	-5.05

Table 3-2. Associated Values of Force, Displacement, Ductility, and Drift Ratio (Push, Cycle 1)—CPLD, CPFD, and CIP

Push (Cycle 1)—CPLD					
Stage	Force (kips)	Disp (in)	Displacement Ductility, μ		Drift Ratio (%)
			Actual	Nominal	
Force Control	15.2	0.052	-	-	0.09
	20.2	0.144	-	-	0.24
	30.3	0.173	-	-	0.29
	42.4	0.360	-	-	0.61
Displacement Control	41.9	0.309	1.03	1.0	0.52
	48.5	0.466	1.55	1.5	0.79
	54.3	0.643	2.14	2.0	1.09
	59.2	0.959	3.19	3.0	1.62
	59.8	1.455	4.84	4.0	2.47
	60.0	2.164	7.20	6.0	3.67
	52.7	2.928	9.74	8.0	4.96

Push (Cycle 1)—CPFD					
Stage	Force (kips)	Disp (in)	Displacement Ductility, μ		Drift Ratio (%)
			Actual	Nominal	
Force Control	13.2	0.028	-	-	0.05
	20.4	0.048	-	-	0.08
	30.5	0.113	-	-	0.19
	44.6	0.265	-	-	0.45
Displacement Control	46.8	0.375	1.15	1.0	0.63
	51.5	0.504	1.54	1.5	0.85
	53.7	0.648	1.99	2.0	1.10
	55.1	0.955	2.93	3.0	1.62
	54.5	1.280	3.92	4.0	2.17
	54.4	1.887	5.78	6.0	3.20
	45.2	2.534	7.76	8.0	4.30

Table 3-2. Associated Values of Force, Displacement, Ductility, and Drift Ratio (Push, Cycle 1)—CPLD, CPFD, and CIP, Continued

Push (Cycle 1)—CIP					
Stage	Force (kips)	Disp (in)	Displacement Ductility, μ		Drift Ratio (%)
			Actual	Nominal	
Force Control	13.0	0.034	-	-	0.06
	20.0	0.072	-	-	0.13
	30.1	0.154	-	-	0.27
	48.4	0.397	-	-	0.69
Displacement Control	40.0	0.406	1.13	1.0	0.71
	49.4	0.533	1.49	1.5	0.93
	53.3	0.684	1.91	2.0	1.19
	55.6	1.014	2.83	3.0	1.76
	54.6	1.345	3.75	4.0	2.34
	55.9	2.070	5.77	6.0	3.60
	53.2	2.638	7.36	8.0	4.59
	50.0	3.383	9.43	10.0	5.88

Table 3-3. Predicted vs. Actual Stages of Specimen Cracking

Stage	P_V (kips)		P_H (kips)	
	Predicted	Actual	Predicted	Actual
Bent Cap—Flexural	None	38	-	-
	38	-	0	-
Column—Flexural	38	38	11.0	15.0
Joint Shear	38	38	32.0	42.0

Table 3-4. Select Material Properties—CPLD, CPFD, and CIP

Parameter	CPLD		CPFD		CIP	
Concrete Compressive Strength, f'_c						
Bent Cap and Column	3451 psi		5620 psi		Cap: 4553 psi Column: 6178 psi	
Plastic Hinge Region (13 in)	3892 psi		N/A		N/A	
Cap Pocket	3454 psi		5040 psi		N/A	
Steel Rebar Strength	Yield	Tensile	Yield	Tensile	Yield	Tensile
#3 (Bent cap stirrups; Column hoops)	63.5	99.6	63.5	99.6	68.2	95.5
#4 (Bent cap longitudinal)	59.6	101.1	N/A	N/A	N/A	N/A
#5 (Bent cap longitudinal; Column longitudinal)	63.6	95.0	63.6	91.0	64.5	90.0

Table 3-5. Actual Stages of Specimen Cracking—CPLD, CPFD, and CIP

Stage	CPLD		CPFD		CIP	
	P_V (kips)	P_H (kips)	P_V (kips)	P_H (kips)	P_V (kips)	P_H (kips)
Bent Cap—Flexural	38	-	38	-	38	13
Column—Flexural	38	15	38	13	38	20
Joint Shear	38	42	38	44	38	48

Table 3-6. Comparison Curvature at Select Drift Ratios—CPLD, CPFD, and CIP

Drift (%)	**CPLD (in^{-1} 10^{-4})**	**CPFD (in^{-1} 10^{-4})**	**CIP (in^{-1} 10^{-4})**	**CPLD/ CPFD**	**CPLD/ CIP**
0.61	5.49	6.80	7.49	0.81	0.73
0.83	7.65	11.42	11.01	0.67	0.70
1.09	11.40	17.41	15.90	0.65	0.72
1.62	16.52	28.14	24.52	0.59	0.67
2.14	24.47	36.68	35.93	0.67	0.68
3.17	38.91	49.09	50.79	0.79	0.77
			Average:	0.70	0.71

Table 3-7. Displacement Decomposition (1st Push and Pull Cycles)

Displacement Decomposition—CPLD (1st Push Cycle)

		Actual	Predicted	Act/Pred	Actual	Predicted	Act/Pred	Actual	Predicted	Act/Pred	Actual	Predicted	Act/Pred
Displacement Ductility	(μ)	1.0	-	-	1.5	-	-	2.0	-	-	3.0	-	-
Col Displacement [CD]	(in)	0.309	0.309	1.00	0.466	0.466	1.00	0.643	0.643	1.00	0.959	0.959	1.00
Drift	(%)	0.52	-	-	0.79	-	-	1.09	-	-	1.62	-	-
Force	(kip)	41.9	43.5	0.96	48.5	52.2	0.93	54.3	60.5	0.90	59.2	61.7	0.96
Column Flexure	(in)	0.031	0.233	0.88	0.043	0.357	0.76	0.059	0.472	0.81	0.131	0.751	0.81
Fixed End Rotation	(in)	0.174			0.228			0.324			0.476		
Column Shear	(in)	*	0.021	*	*	0.043	*	*	0.093	*	*	0.129	*
Bent Cap Flexibility	(in)	0.083	0.056	1.47	0.117	0.067	1.73	0.146	0.078	1.88	0.162	0.079	2.04
Joint Shear	(in)	0.142	*	*	0.171	*	*	0.202	*	*	0.240	*	*
Component Total [CT]	(in)	0.430	0.310		0.559	0.467		0.732	0.643		1.009	0.959	
CT/CD		1.39	1.00		1.20	1.00		1.14	1.00		1.05	1.00	

		Actual	Predicted	Act/Pred	Actual	Predicted	Act/Pred	Actual	Predicted	Act/Pred
Displacement Ductility	(μ)	4.0	-	-	6.0	-	-	8.0	-	-
Col Displacement [CD]	(in)	1.455	1.455	1.00	2.164	2.164	1.00	2.928	2.928	1.00
Drift	(%)	2.47	-	-	3.67	-	-	4.96	-	-
Force	(kip)	59.8	66.7	0.90	60.0	68.8	0.87	52.7	71.6	0.74
Column Flexure	(in)	0.256	1.186	0.83	0.442	1.785	0.80	0.923	2.432	0.73
Fixed End Rotation	(in)	0.726			0.982			0.844		
Column Shear	(in)	*	0.184	*	*	0.291	*	*	0.405	*
Bent Cap Flexibility	(in)	0.161	0.086	1.87	0.148	0.088	1.68	0.175	0.092	1.89
Joint Shear	(in)	0.406	*	*	0.411	*	*	0.362	*	*
Component Total [CT]	(in)	1.550	1.456		1.983	2.164		2.303	2.928	
CT/CD		1.07	1.00		0.92	1.00		0.79	1.00	

Displacement Decomposition—CPLD (1st Pull Cycle)

		Actual	Predicted	Act/Pred	Actual	Predicted	Act/Pred	Actual	Predicted	Act/Pred	Actual	Predicted	Act/Pred
Displacement Ductility	(μ)	1.0	-	-	1.5	-	-	2.0	-	-	3.0	-	-
Col Displacement [CD]	(in)	-0.416	-0.416	1.00	-0.545	-0.545	1.00	-0.731	-0.731	1.00	-1.074	-1.074	1.00
Drift	(%)	-0.71	-	-	-0.92	-	-	-1.24	-	-	-1.82	-	-
Force	(kip)	-45.7	-48.7	0.94	-50.7	-59.7	0.85	-56.9	-60.6	0.94	-61.9	-62.2	0.99
Column Flexure	(in)	-0.071	-0.325	0.84	-0.083	-0.391	0.85	-0.116	-0.549	0.85	-0.176	-0.853	0.88
Fixed End Rotation	(in)	-0.202			-0.250			-0.350			-0.576		
Column Shear	(in)	*	-0.029	*	*	-0.078	*	*	-0.105	*	*	-0.141	*
Bent Cap Flexibility	(in)	-0.090	-0.063	1.43	-0.106	-0.077	1.38	-0.121	-0.078	1.55	-0.148	-0.080	1.85
Joint Shear	(in)	-0.189	*	*	-0.243	*	*	-0.311	*	*	-0.413	*	*
Component Total [CT]	(in)	-0.552	-0.417		-0.683	-0.545		-0.899	-0.731		-1.313	-1.074	
CT/CD		1.33	1.00		1.25	1.00		1.23	1.00		1.22	1.00	

		Actual	Predicted	Act/Pred	Actual	Predicted	Act/Pred	Actual	Predicted	Act/Pred
Displacement Ductility	(μ)	4.0	-	-	6.0	-	-	8.0	-	-
Col Displacement [CD]	(in)	-1.337	-1.337	1.00	-2.156	-2.156	1.00	-2.981	-2.981	1.00
Drift	(%)	-2.27	-	-	-3.65	-	-	-5.05	-	-
Force	(kip)	-63.0	-65.4	0.96	-62.8	-68.8	0.91	-56.2	-71.7	0.78
Column Flexure	(in)	-0.197	-1.083	0.90	-0.413	-1.779	0.84	-0.852	-2.476	0.85
Fixed End Rotation	(in)	-0.773			-1.087			-1.256		
Column Shear	(in)	*	-0.170	*	*	-0.289	*	*	-0.413	*
Bent Cap Flexibility	(in)	-0.149	-0.084	1.77	-0.135	-0.088	1.53	-0.031	-0.092	0.34
Joint Shear	(in)	-0.338	*	*	-0.470	*	*	-0.545	*	*
Component Total [CT]	(in)	-1.457	-1.338		-2.105	-2.156		-2.683	-2.981	
CT/CD		1.09	1.00		0.98	1.00		0.90	1.00	

Table 3-8. Bar Slip and Fixed End Rotation Components—CPLD vs. CIP

Drift Ratio (%)	Force (CPLD) (kips)	Force (CIP) (kips)	BS (CPLD) (in)	BS (CIP) (in)	BS/FER (CPLD)	BS/FER (CIP)	BS/FER (CPLD /CIP)
0.93	47.0	49.4	0.081	0.014	0.317	0.051	6.3
1.19	54.1	53.3	0.108	0.014	0.312	0.038	8.2
1.76	57.5	55.6	0.161	0.016	0.323	0.031	10.5
2.34	59.4	54.6	0.183	0.016	0.263	0.022	11.9
3.60	59.9	55.9	0.286	0.022	0.293	0.021	14.2
4.59	52.1	53.2	0.403	0.030	0.476	0.023	20.5
				Average:	0.331	0.031	11.9

Table 3-9. Bar Slip and Fixed End Rotation Components (μ6, Cycle 2)—CPLD vs. CPFD

Drift Ratio (%)	Force CPLD (kips)	Force CPFD (kips)	BS CPLD (in)	BS CPFD (in)	BS/FER (CPLD)	BS/FER (CPFD)	BS/FER (CPLD/CPFD)
0.63	28.4	25.0	0.247	0.016	0.936	0.081	11.6
0.99	31.6	30.0	0.267	0.019	0.680	0.061	11.2
1.30	34.1	35.0	0.278	0.020	0.561	0.049	11.4
1.60	36.5	40.0	0.286	0.021	0.478	0.042	11.4
1.98	39.2	45.0	0.300	0.021	0.418	0.035	11.9
0.63	28.4	25.0	0.247	0.016	0.936	0.081	11.6
				Average:	0.614	0.054	11.5

Table 3-10. Maximum Measured Diagonal Crack Width on Joint Surfaces

Drift Ratio (%) Push (Pull)	Displacement Ductility	Force (kips) Push (Pull)	Crack Width East Face (0.001 in) Push (Pull)	Crack Width West Face (0.001 in) Push (Pull)
0.52 (0.71)	μ1	41.9(45.7)	25 (25)	25 (30)
0.79 (0.92)	μ1.5	48.5 (50.7)	40 (25)	25 (40)
1.09 (1.24)	μ2	54.3 (56.9)	50 (25)	50 (40)
1.62 (1.82)	μ3	59.2 (61.9)	60 (25)	40 (50)
2.47 (2.27)	μ4	59.8 (63.0)	60 (40)	50 (60)
3.67 (3.65)	μ6	60.0 (62.8)	70 (50)	50 (70)
4.96 (5.05)	μ8	52.7 (56.2)	70 (70)	40 (80)

Table 3-11. Maximum Joint Response for Select Parameters—CPLD, CPFD, CIP

Parameter		CPLD	CPFD	CIP	CPLD/ CPFD	CPLD/ CIP
Joint Shear Stress	(psi)	371 ($6.32\sqrt{f_c'}$)	323 ($4.31\sqrt{f_c'}$)	328 ($4.86\sqrt{f_c'}$	1.47	1.30
Principal Tensile Stress	(psi)	411 ($6.99\sqrt{f_c'}$	356 ($4.75\sqrt{f_c'}$	363 ($5.38\sqrt{f_c'}$)	1.47	1.30
Principal Compressive Stress	(psi)	460 ($0.13f_c'$)	398 ($0.071f_c'$)	401 ($0.088f_c'$)	1.86	1.48
Angle of Principal Plane	(deg)	44.8	44.2	45.0	1.01	1.00
Joint Rotation	(rad)	2.87×10^{-3}	1.73×10^{-3}	1.95×10^{-3}	1.66	1.47
Change in Panel Area	(%)	0.46	0.13	0.16	3.26	2.82

Table 3-12. Column Hoop Strain—CPLD

Drift Ratio (%)	μ	HC1-E			HC4-E		
		Push	Pull	Max/Yield	Push	Pull	Max/Yield
0.71	1.0	14	-19	0.01	430	42	0.20
0.92	1.5	39	31	0.02	696	134	0.32
1.24	2.0	92	87	0.04	1054	285	0.48
1.82	3.0	222	265	0.12	1406	565	0.64
2.47	4.0	317	405	0.18	1570	828	0.72
3.67	6.0	687	1012	0.46	1911	1608	0.87
5.05	8.0	*	*	*	4024	3665	1.83

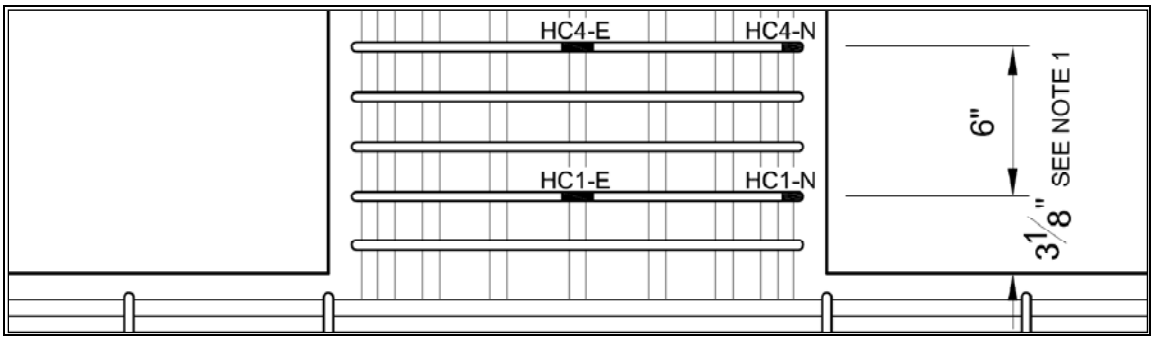

* Data not available

Table 3-13. Column Hoop Strain—CPFD

Drift Ratio (%)	μ	HC1-W			HC1-N			HC4-W		
		Push	Pull	Max/Yield	Push	Pull	Max/Yield	Push	Pull	Max/Yield
0.63	1.0	1514	-390	0.69	789	-707	0.36	211	7	0.10
0.85	1.5	3898	-343	1.78	966	-828	0.44	233	22	0.11
1.10	2.0	4908	-707	2.24	2486	-935	1.14	252	34	0.12
1.62	3.0	7700	-895	3.52	3539	-742	1.62	3266	74	1.49

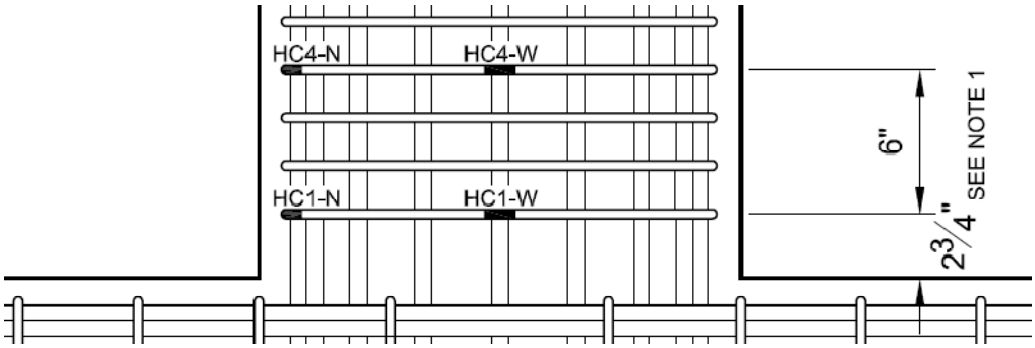

Table 3-14. Strains in Corrugated Pipe and Column Longitudinal Bars—CPLD

Push to 1.77% Drift (μ3, 59.4 kips)									
Pipe							Column		
Location (from top) (in)	Gage ID	Angle	Strain	Gage ID	Principal Strain	Principal Angle	Location (from top) (in)	Gage ID	Max Strain
7.63	DE-2	20	1170	DE-123	1268	14	1.00	LC4-B1	*
7.63	DN-2	20	523	DN-123	504	23.1	1.00	LC7-B1	-1053
12.50	DE-5	20	752	DE-456	993	5.9	1.00	LC16-B1	5850
12.50	DN-5	20	370	DN-456	597	7.8	6.00	LC4-B2	2396
17.38	DE-8	20	799	DE-789	879	18.8	6.00	LC7-B2	-1133
							6.00	LC16-B2	4977
							15.50	LC4-B3	1193
							15.50	LC7-B3	-117
							15.50	LC16-B3	1878

Pull to 1.70% Drift (μ3, 61.8 kips)									
Pipe							Column		
Location (from top) (in)	Gage ID	Angle	Strain	Gage ID	Principal Strain	Principal Angle	Location (from top) (in)	Gage ID	Max Strain
7.63	DE-2	20	374	DE-123	1348	-2.6	1.00	LC4-B1	*
7.63	DN-2	20	427	DN-123	630	-24.1	1.00	LC7-B1	4199
12.50	DE-5	20	-189	DE-456	896	-7.2	1.00	LC16-B1	-7342
12.50	DN-5	20	-118	DN-456	247	42.8	6.00	LC4-B2	2816
17.38	DE-8	20	-325	DE-789	864	-2	6.00	LC7-B2	6116
							6.00	LC16-B2	-4995
							15.50	LC4-B3	1343
							15.50	LC7-B3	1878
							15.50	LC16-B3	-156

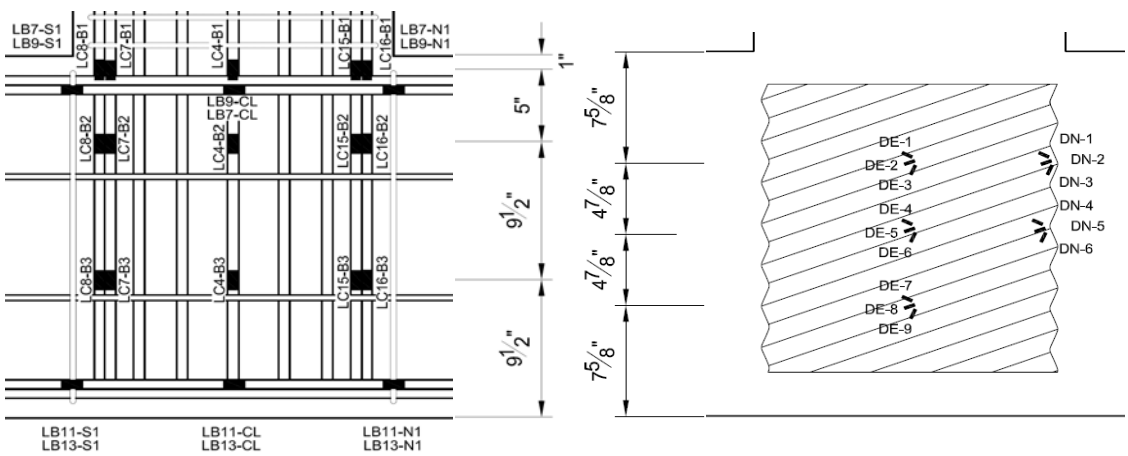

Table 3-15. Strains in Corrugated Pipe and Column Longitudinal Bars—CPFD

Push to 1.62% Drift (μ3, 55.2 kips)									
Pipe							Column		
Location (from top) (in)	Gage ID	Angle	Strain	Gage ID	Principal Strain	Principal Angle	Location (from top) (in)	Gage ID	Max Strain
3.63	HB1-E	-	420	-	-	-	1.00	LC4-B1	1443
7.63	DE-2	20	585	DE-123	684	-37.9	1.00	LC7-B1	*
9.00	DN-1	20	962	-	-	-	1.00	LC16-B1	1352
12.50	DE-5	20	676	DE-456	707	19.1	6.00	LC4-B2	3447
16.00	DN-2	20	*	-	-	-	6.00	LC7-B2	-937
20.13	DE-8	20	394	DE-789	461	11.7	6.00	LC16-B2	*
21.38	HB2-E	-	533	-	-	-	15.50	LC4-B3	1454
							15.50	LC7-B3	204
							15.50	LC16-B3	*
Pull to 1.49% Drift (μ3, 53.3 kips)									
Pipe							Column		
Location (from top) (in)	Gage ID	Angle	Strain	Gage ID	Principal Strain	Principal Angle	Location (from top) (in)	Gage ID	Max Strain
3.63	HB1-E	-	236	-	-	-	1.00	LC4-B1	916
7.63	DE-2	20	-62	DE-123	131	-14.1	1.00	LC7-B1	*
9.00	DN-1	20	668	-	-	-	1.00	LC16-B1	-8054
12.50	DE-5	20	45	DE-456	170	-14.8	6.00	LC4-B2	-6
16.00	DN-2	20	232	-	-	-	6.00	LC7-B2	4764
20.13	DE-8	20	16	DE-789	101	-13.2	6.00	LC16-B2	*
21.38	HB2-E	-	533	-	-	-	15.50	LC4-B3	-1453
							15.50	LC7-B3	1909
							15.50	LC16-B3	*

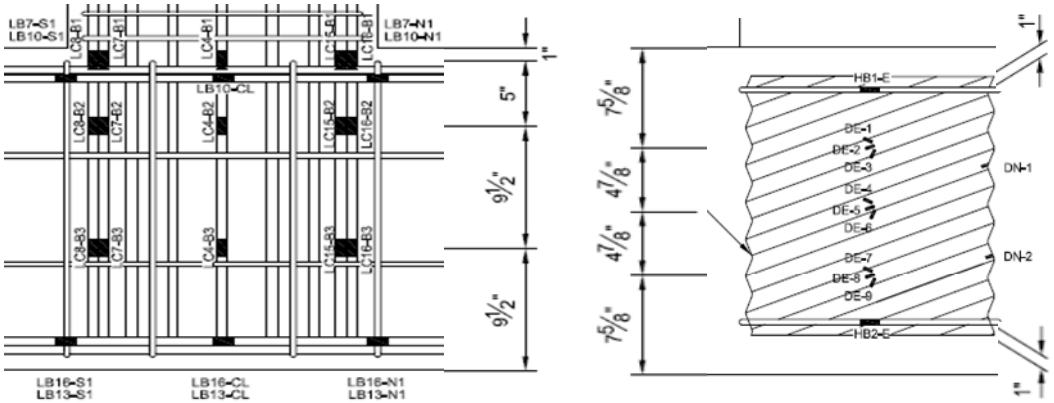

Table 3-16. Bent Cap Longitudinal Bar Strain—CPLD

Top Bar		S2		S1		CL		N1		N2	
		Push	Pull	Push	Pull	Push	Pull	Push	Pull	Push	Pull
CPLD (LB7)	μ2	-70	106	682	326	605	235	409	217	—	—
	μ4	-107	82	1,207	519	642	344	516	412	—	—
	μ6	-64	163	1,365	691	667	292	712	855	—	—
	$\varepsilon_{max}/\varepsilon_y$	-0.05	0.07	0.62	0.32	0.30	0.16	0.32	0.39	—	—

Bottom Bar		S2		S1		CL		N1		N2	
		Push	Pull	Push	Pull	Push	Pull	Push	Pull	Push	Pull
CPLD (LB13)	μ2	1,131	180	1,069	799	1,145	854	574	580	288	617
	μ4	1,112	113	1,096	790	1,161	866	383	699	312	638
	μ6	1,200	239	1,133	847	1,265	6,000	176	868	472	768
	$\varepsilon_{max}/\varepsilon_y$	0.55	0.11	0.52	0.39	0.58	2.74	0.26	0.40	0.22	0.35

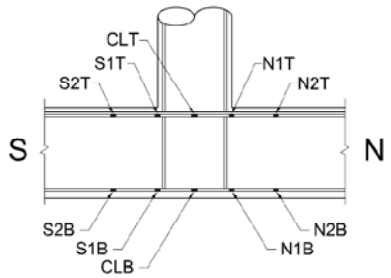

Note: Reference Table 3-1 for associated drift and force levels.
— Not available

Table 3-17. Bent Cap Longitudinal Bar Strain—CIP, CPFD, CPLD

Top Bars		S2		S1		CL		N1		N2	
		Push	Pull	Push	Pull	Push	Pull	Push	Pull	Push	Pull
CIP (LB13)	μ2	-218	118	146	252	—	—	267	-208	—	—
	μ4	-194	141	80	228	—	—	168	-392	—	—
	μ6	-229	116	30	302	—	—	53	-581	—	—
	$\varepsilon_{max}/\varepsilon_y$	-0.10	0.06	0.07	0.14	—	—	0.12	-0.26	—	—
CPFD (LB7)	μ2	—	—	—	—	774	1233	160	-461	72	-166
	μ4	—	—	20	-31	833	1725	144	-472	87	-180
	μ6	—	—	-134	-189	1050	2169	189	-494	75	-167
	$\varepsilon_{max}/\varepsilon_y$	—	—	-0.06	-0.09	0.48	0.99	0.09	-0.23	0.04	-0.08
CPLD (LB7)	μ2	-70	106	682	326	605	235	409	217	—	—
	μ4	-107	82	1207	519	642	344	516	412	—	—
	μ6	-64	163	1365	691	667	292	712	855	—	—
	$\varepsilon_{max}/\varepsilon_y$	-0.05	0.07	0.62	0.32	0.30	0.16	0.32	0.39	—	—
Bottom Bars		**S2**		**S1**		**CL**		**N1**		**N2**	
		Push	Pull	Push	Pull	Push	Pull	Push	Pull	Push	Pull
CIP (LB10)	μ2	823	-108	968	68	891	221	259	755	78	535
	μ4	867	-135	875	132	947	334	349	876	59	587
	μ6	890	-164	1,021	157	961	434	449	1,018	35	685
	$\varepsilon_{max}/\varepsilon_y$	0.40	-0.07	0.46	0.07	0.43	0.20	0.20	0.46	0.04	0.31
CPFD (LB13)	μ2	674	-107	585	-20	1,792	525	188	1,138	21	418
	μ4	737	-121	1,315	279	2,357	800	270	1,372	15	448
	μ6	757	-135	1,540	446	3,094	890	343	1,549	—	—
	$\varepsilon_{max}/\varepsilon_y$	0.35	-0.06	0.70	0.20	1.41	0.41	0.16	0.71	0.01	0.20
CPLD (LB13)	μ2	1131	180	1069	799	1145	854	574	580	288	617
	μ4	1112	113	1096	790	1161	866	383	699	312	638
	μ6	1200	239	1133	847	1265	6000	176	868	472	768
	$\varepsilon_{max}/\varepsilon_y$	0.55	0.11	0.52	0.39	0.58	2.74	0.26	0.40	0.22	0.35

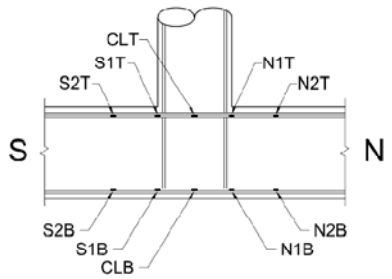

Note: Reference Tables 3-1 and 3-2 for associated drift and force levels.
— Not available

3.8 Figures

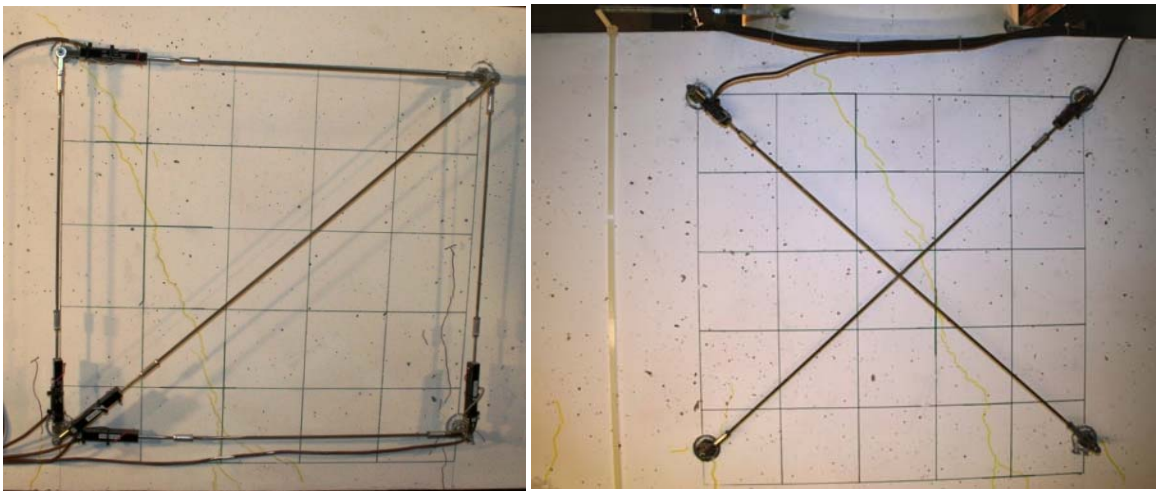

A. East Face B. West Face

Figure 3-1. Pre-Existing Hairline Cracks in Joint Region

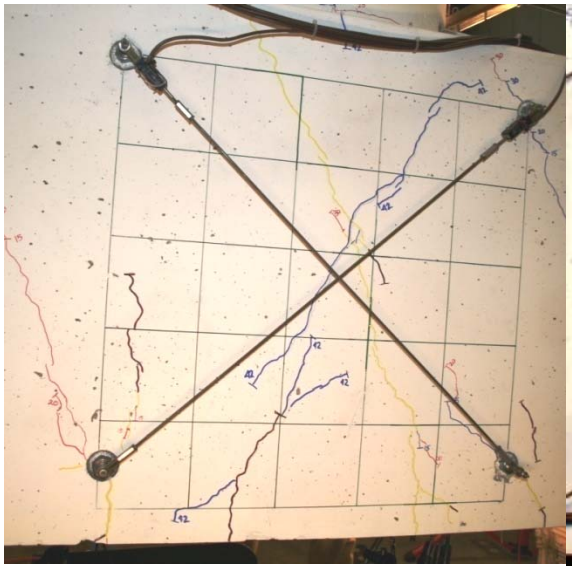

A. West Face (42 kips push)

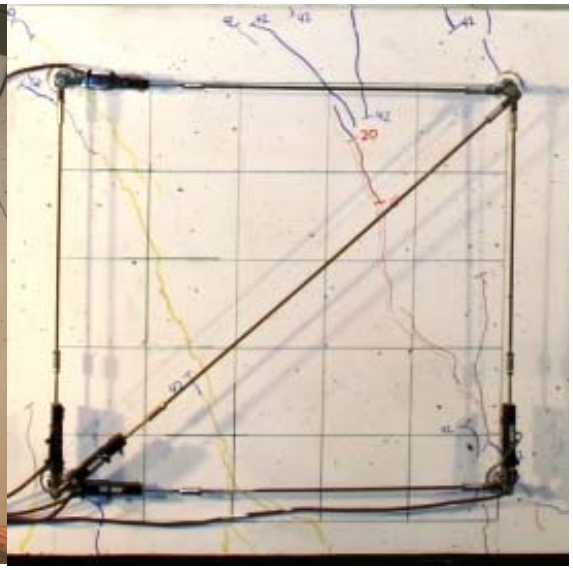

B. East Face (42 kips push)

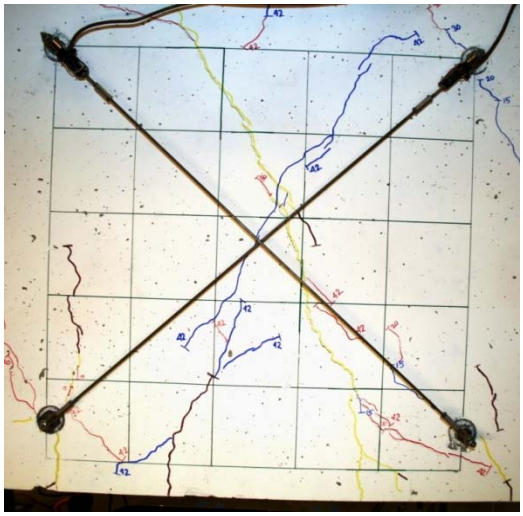

C. West Face (42 kips pull)

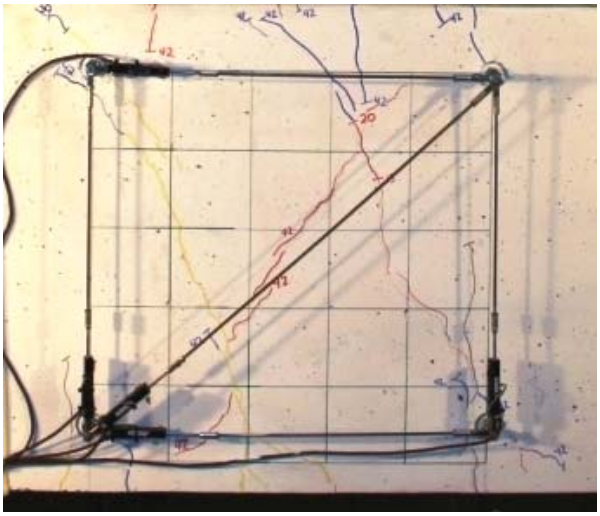

D. East Face (42 kips pull)

Figure 3-2. Crack Pattern in Joint Region at End of Force Control Sequence (42 kips)

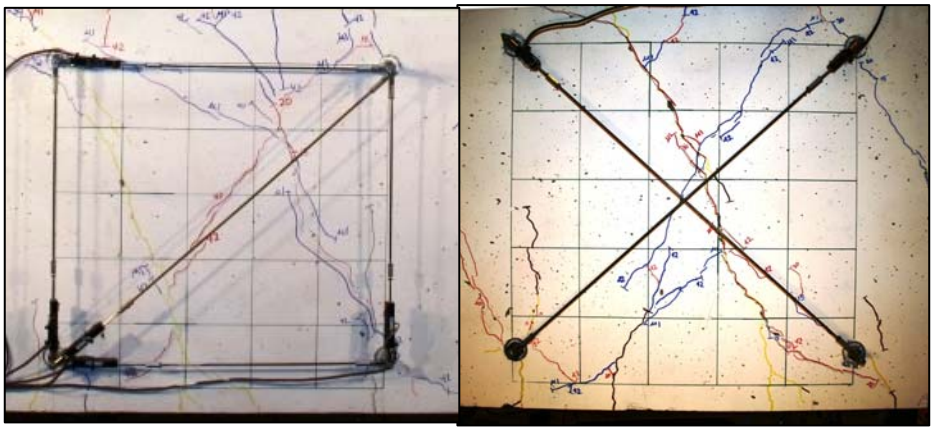

A. East Face (μ1 Pull) B. West Face (μ1 Pull)

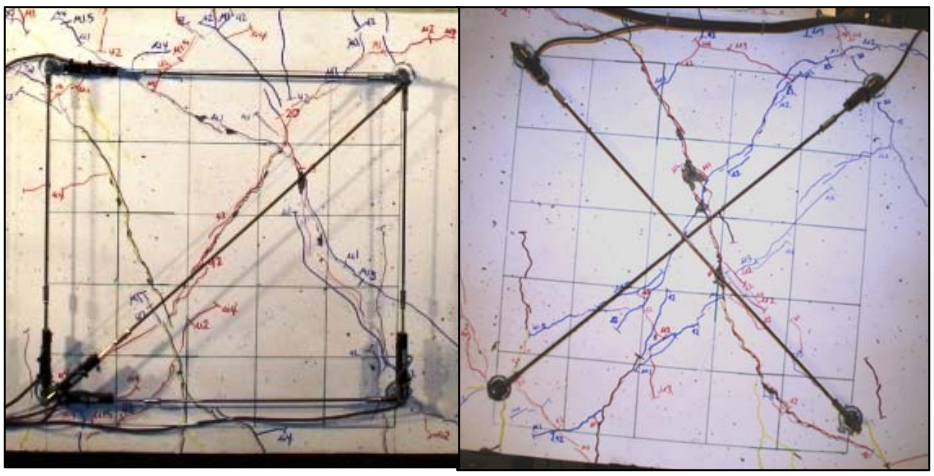

C. East Face (μ4 Pull) D. West Face (μ4 Pull)

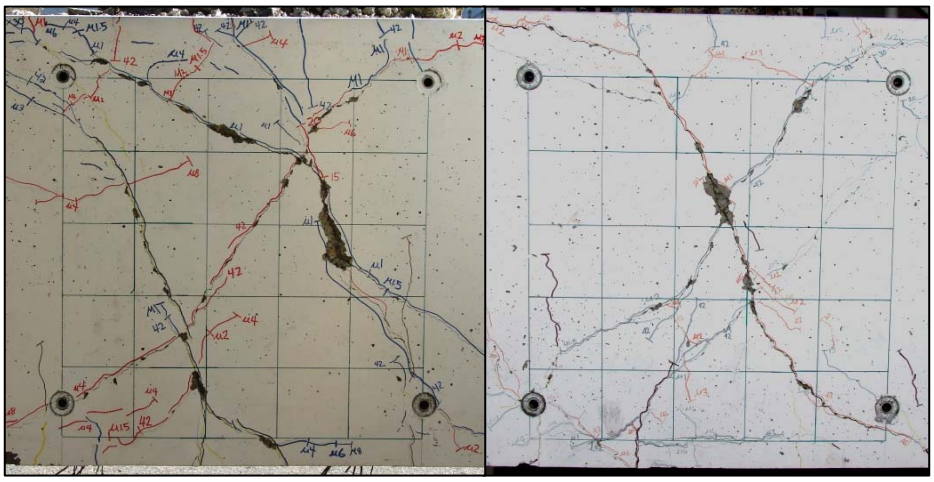

E. East Face (Post-Test) F. West Face (Post-Test)

Figure 3-3. Crack Pattern in Joint Region (Displacement Control and Post-Test)

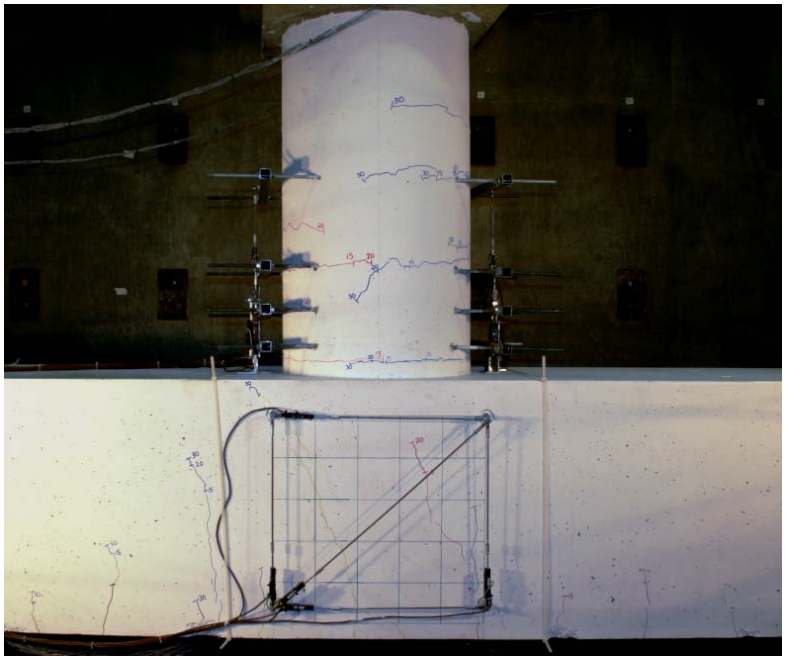

Figure 3-4. Specimen Crack Pattern during Force Control Sequence (30 kips)

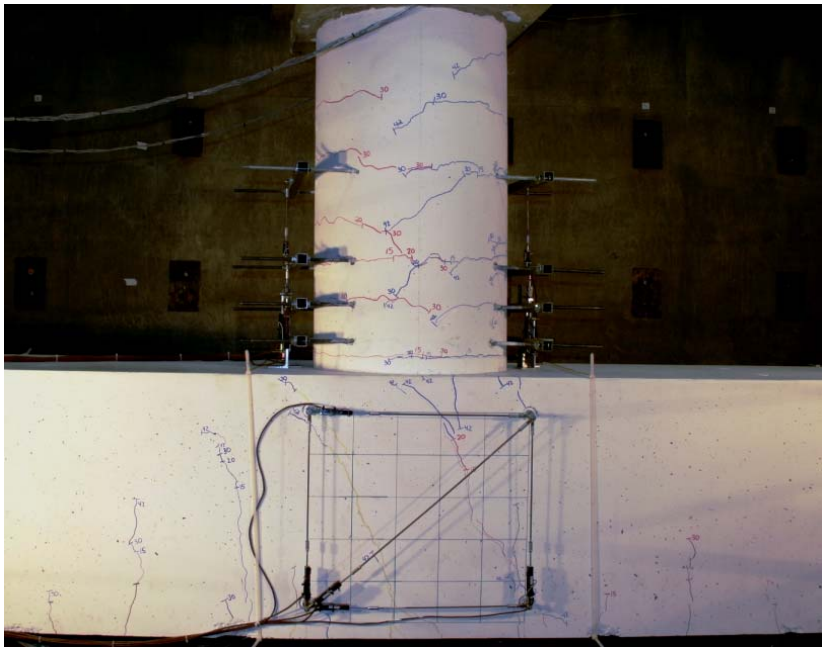

Figure 3-5. Specimen Crack Pattern at End of Force Control Sequence (42 kips)

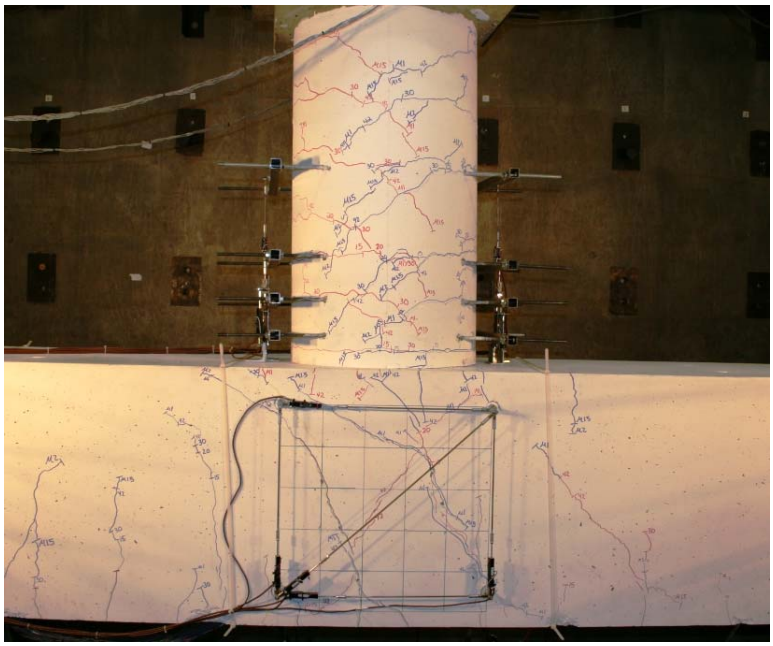

Figure 3-6. Specimen Response at 1.2% Drift Ratio (μ2)

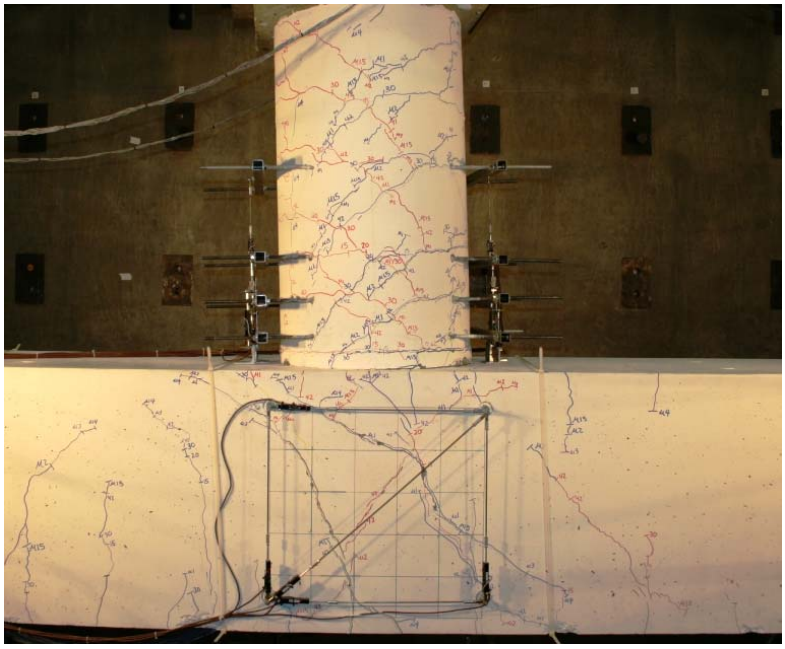

Figure 3-7. Specimen Response at 2.5% Drift Ratio (μ4)

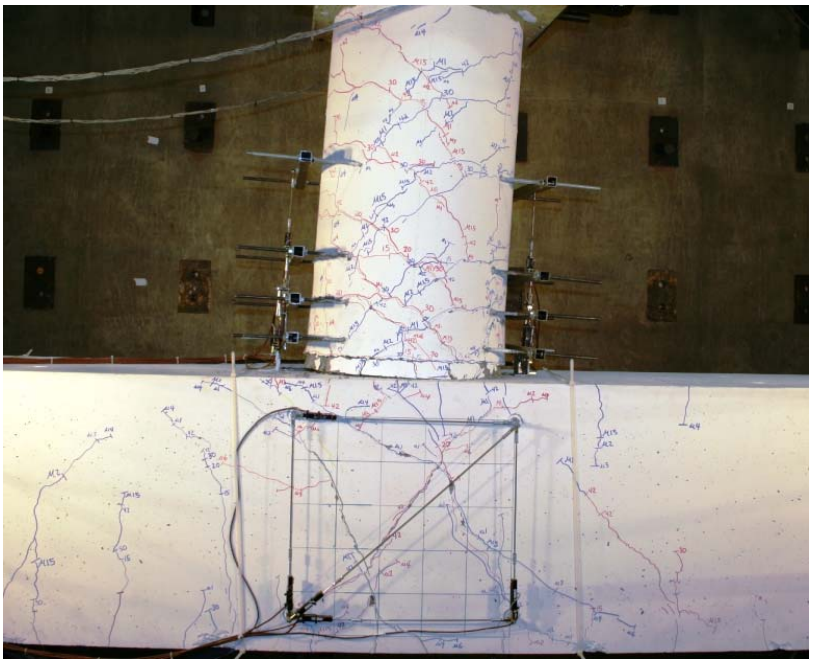

Figure 3-8. Specimen Response at 3.7% Drift Ratio (μ6)

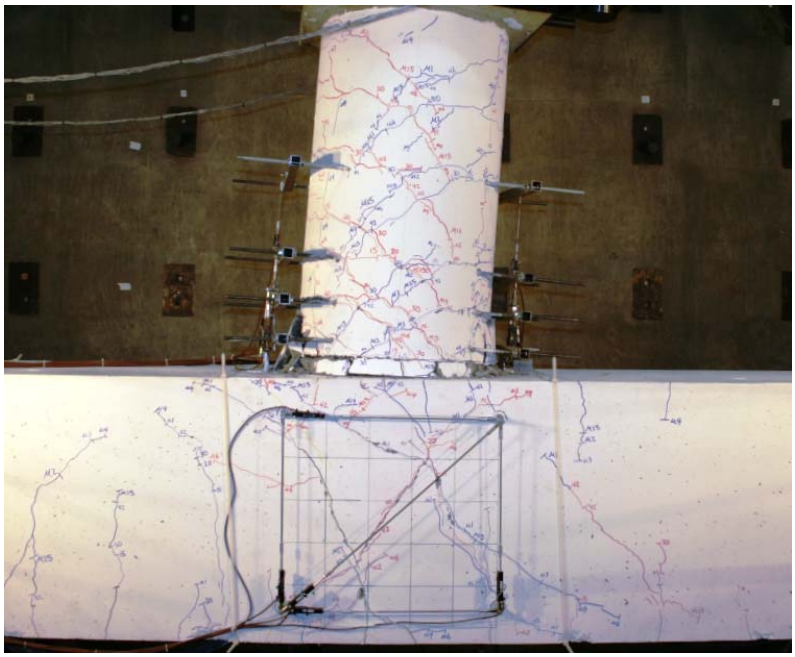

Figure 3-9. Specimen Response at 5.1% Drift Ratio (μ8)

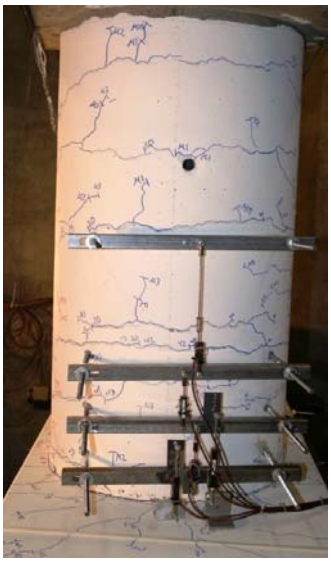

Figure 3-10. Splitting Cracks in Bent Cap and Column at 1.62% Drift Ratio (μ3, North Face)

Figure 3-11. Fractured Bars in Plastic Hinge Region (South End, Post Test)

A. Crushed Concrete above Bedding Layer B. Splitting Cracks

Figure 3-12. Bedding Layer and Splitting Cracks (Post Test)

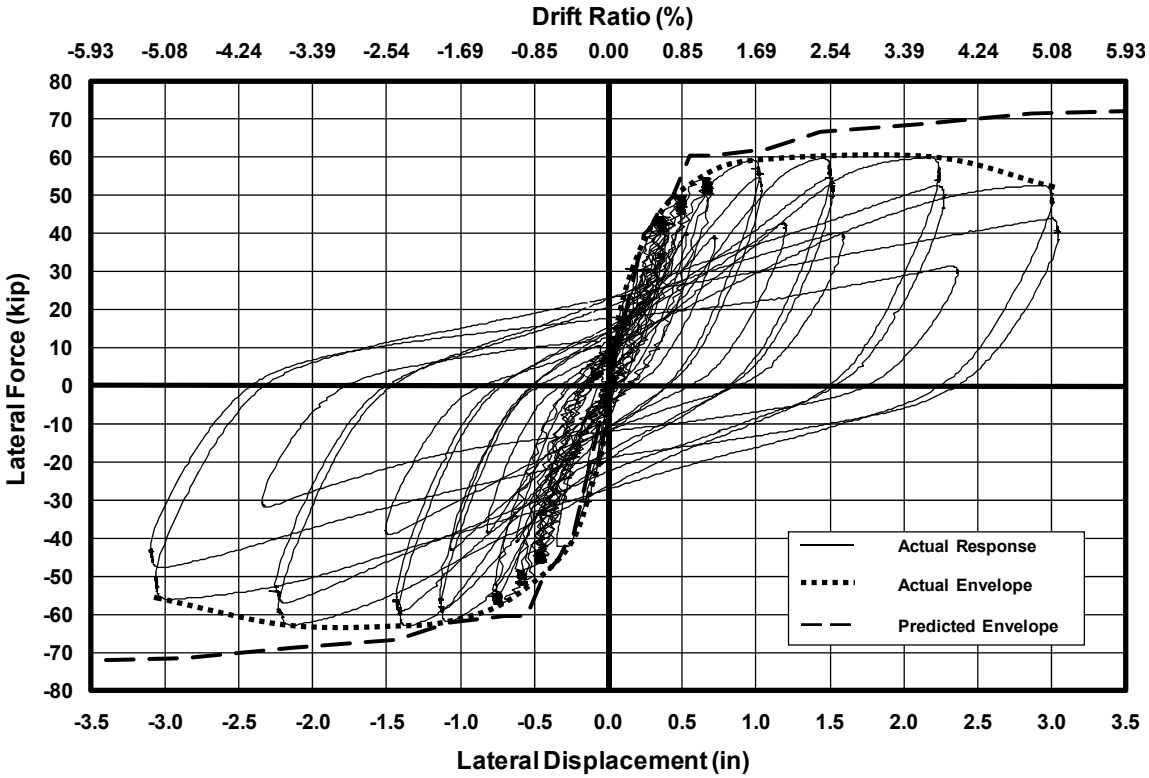

Figure 3-13. Lateral Force vs. Lateral Displacement

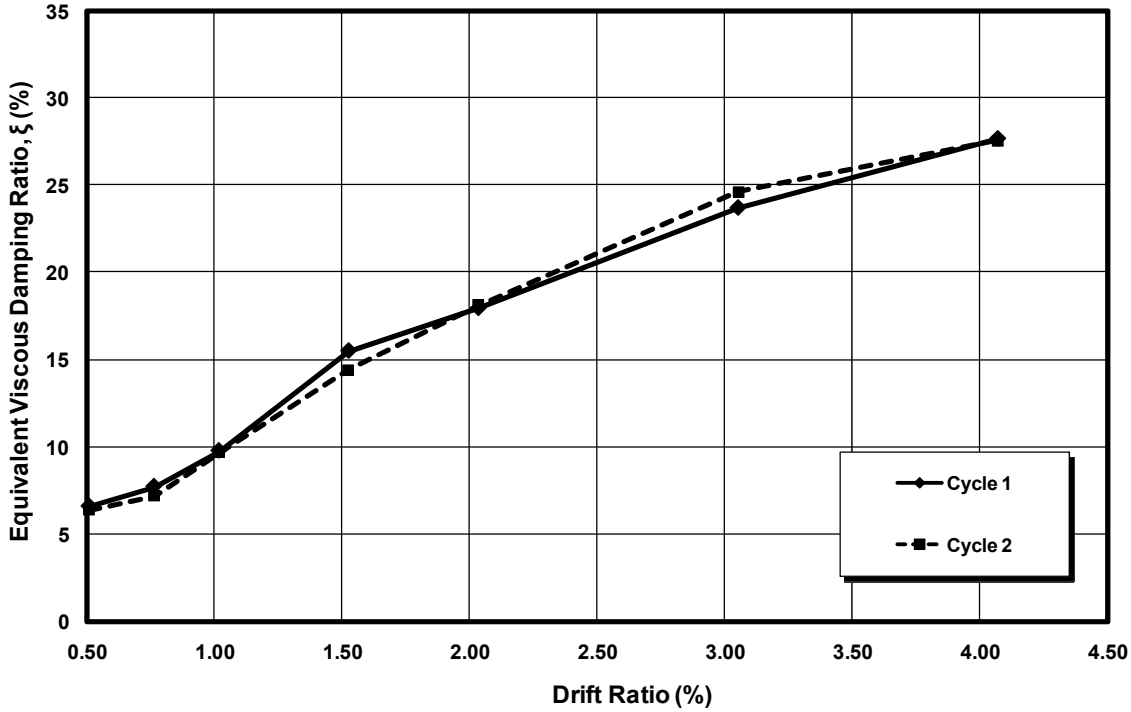

Figure 3-14. Equivalent Viscous Damping Ratio vs. Drift Ratio

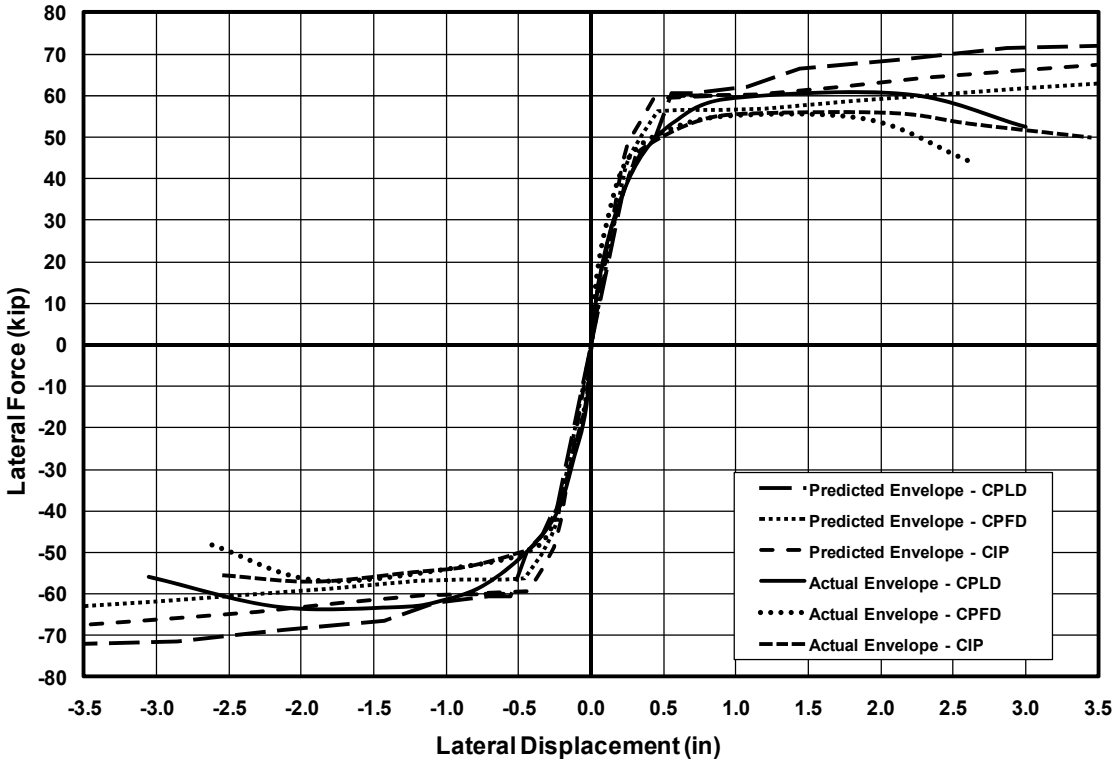

Figure 3-15. Lateral Force vs. Lateral Displacement Envelopes—CPLD, CPFD, CIP

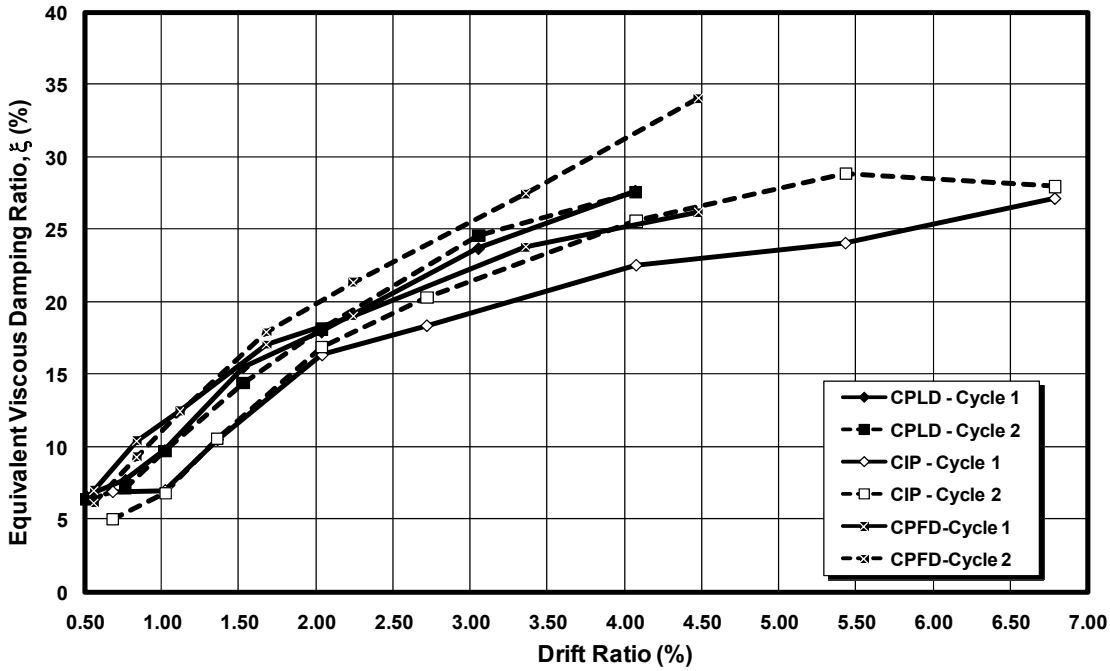

Figure 3-16. Equivalent Viscous Damping Ratio vs. Drift Ratio—CPLD, CPFD, CIP

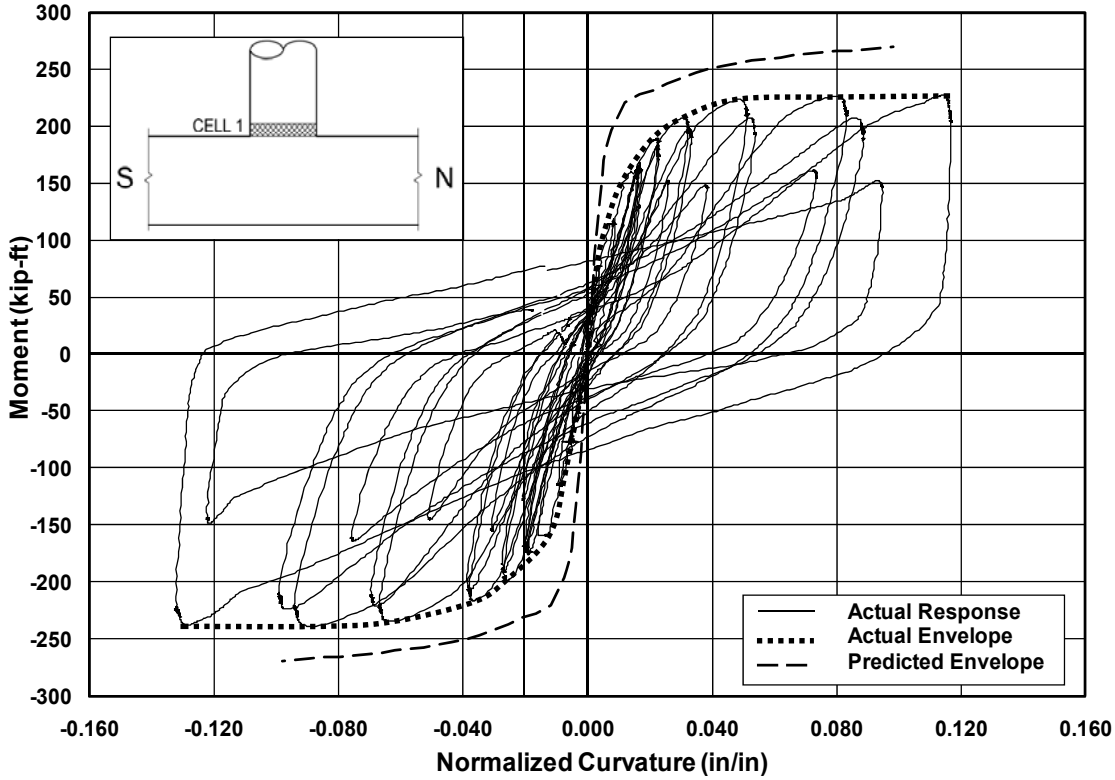

Figure 3-17. Normalized Moment-Curvature Response—Cell 1

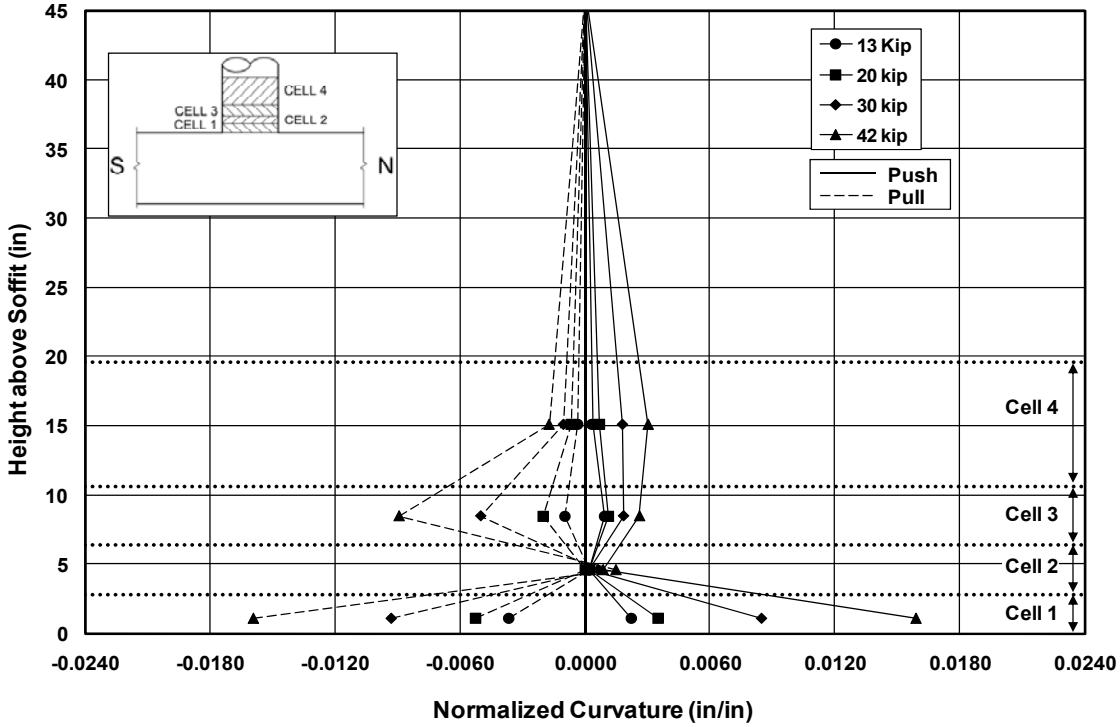

Figure 3-18. Curvature Profile—Force Control

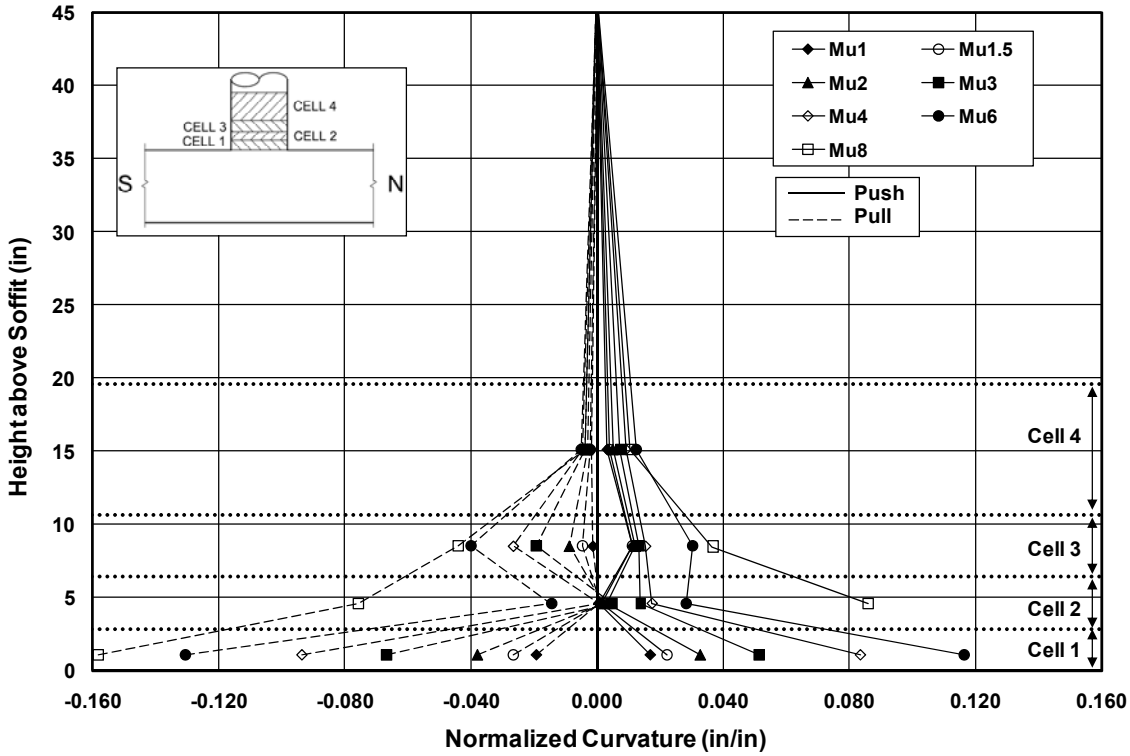

Figure 3-19. Curvature Profile—Displacement Control

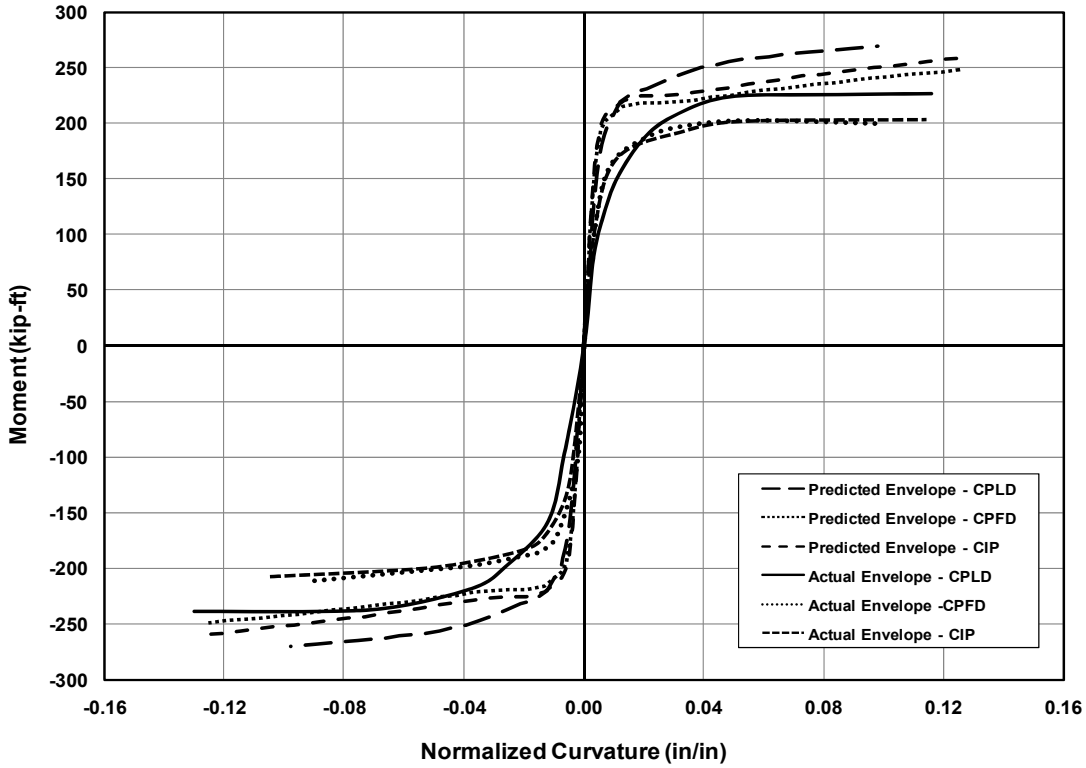

Figure 3-20. Normalized Moment-Curvature Response (Cell 1)—CPLD, CPFD, CIP

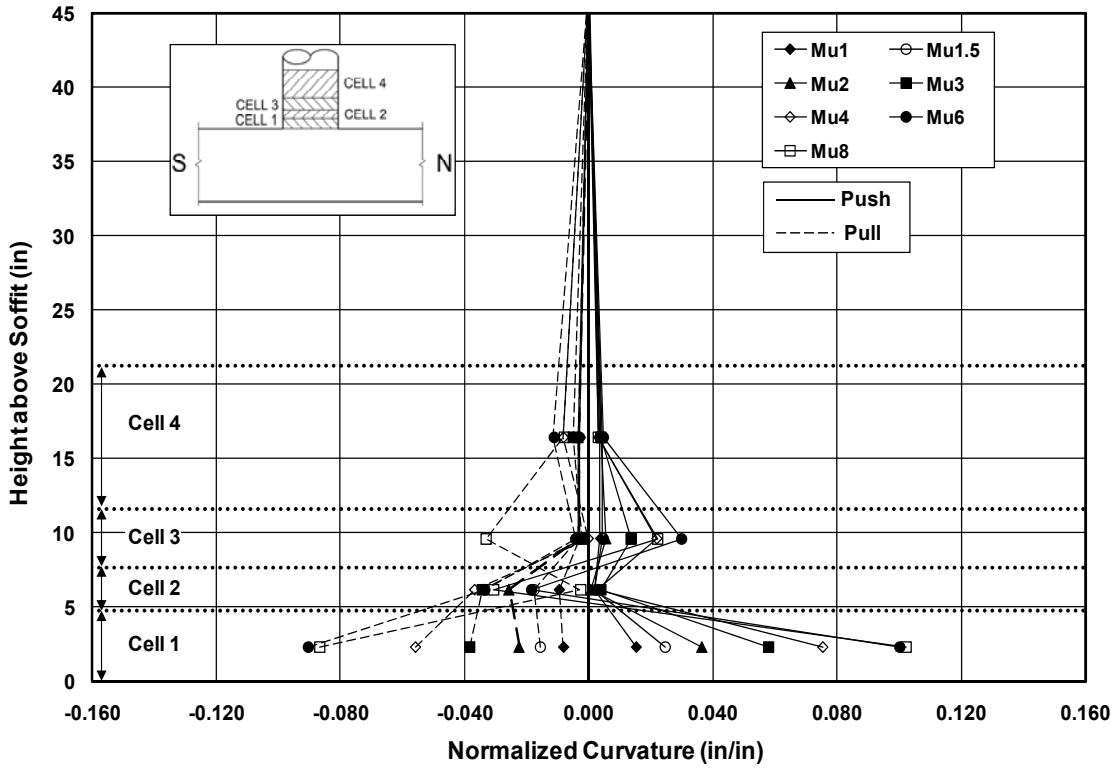

Figure 3-21. Curvature Profile (Displacement Control)—CPFD

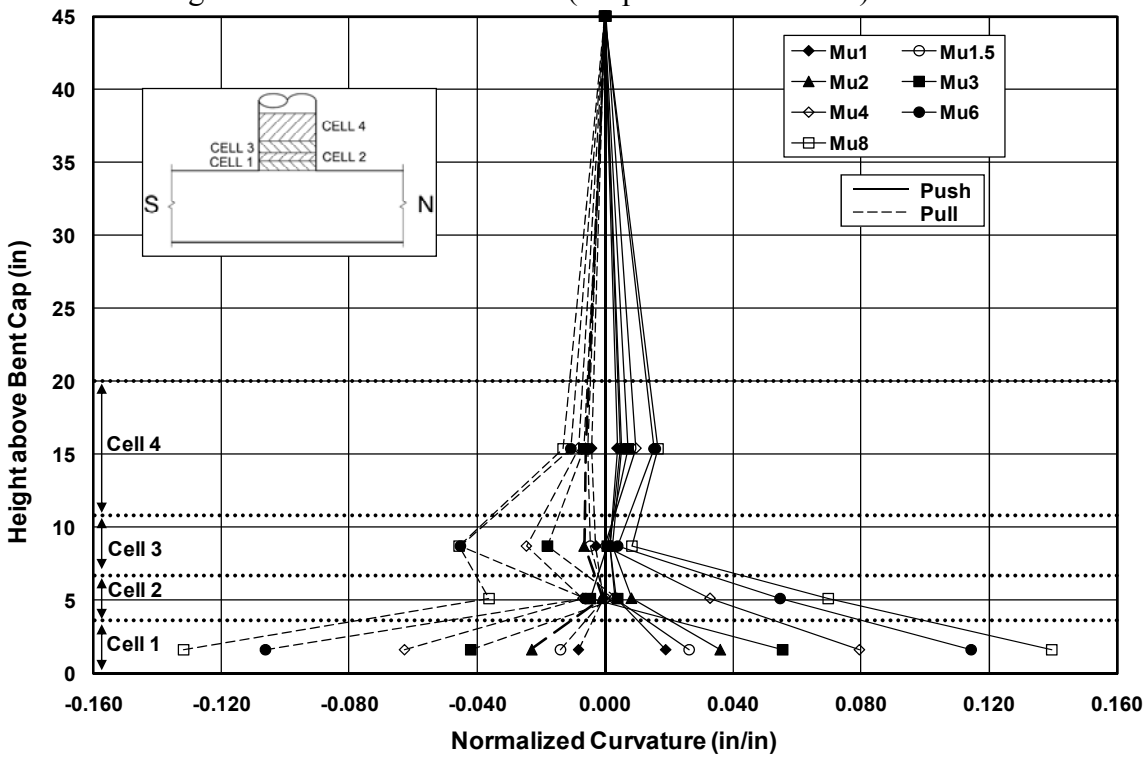

Figure 3-22. Curvature Profile (Displacement Control)—CIP

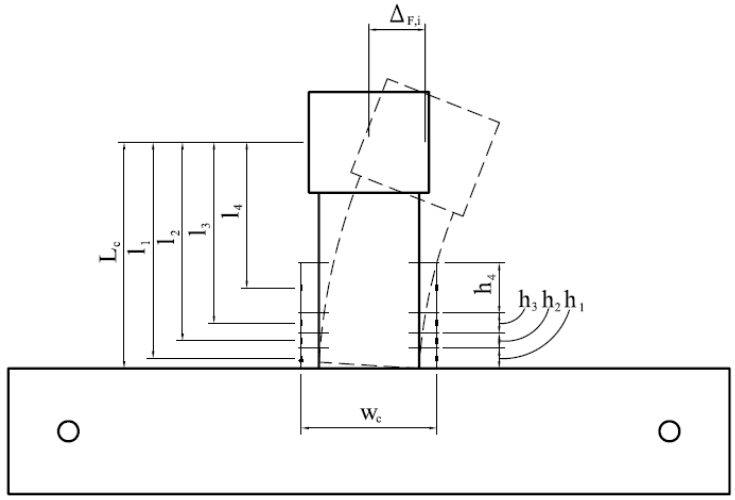

$$\Delta_{F,i} = l_i \frac{(\delta h_{i,n} - \delta h_{i,s})}{w_c}$$

$$\Delta_{F,1} = (l_1 + l'_g) \frac{(\delta h_{i,n} - \delta h_{i,s})}{w_c}$$

$$l'_g = h_1 + (0.022 \ f_y \ d_{bl})$$

A. Column Flexure and Fixed End Rotation (Cell 1)

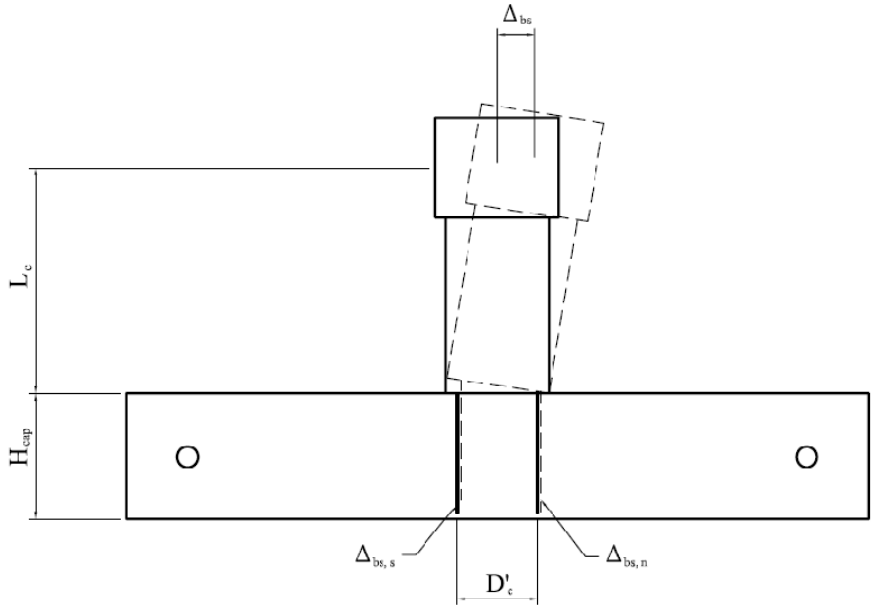

$$\Delta_{bs} = \left(\frac{\Delta_{bs,s} - \Delta_{bs,n}}{D'_c}\right)(L_c + H_{cap})$$

B. Bar Slip

Figure 3-23. Schematic Representation of Column Displacement Components

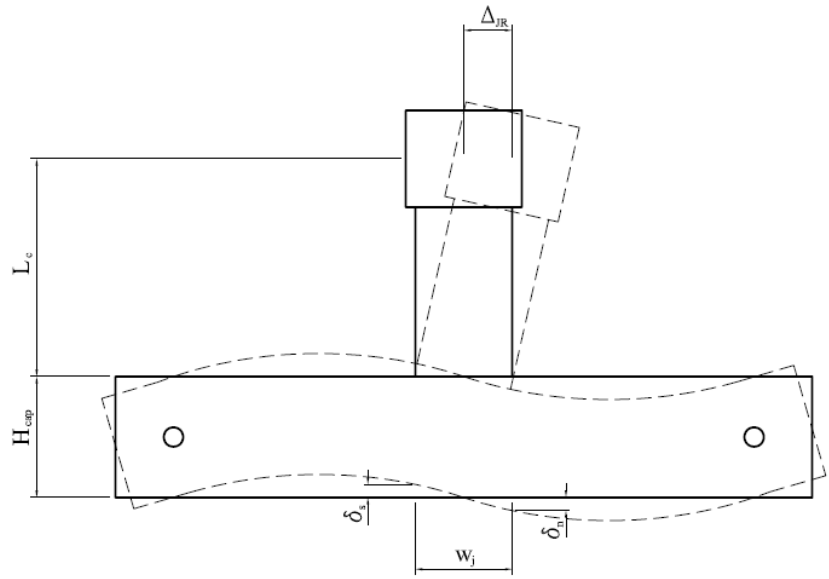

$$\Delta_{JR} = \frac{(\delta_n - \delta_s)}{w_j} (L_c + H_{cap})$$

C. Bent Cap Rotation

Figure 3-23. Schematic Representation of Column Displacement Components, Continued

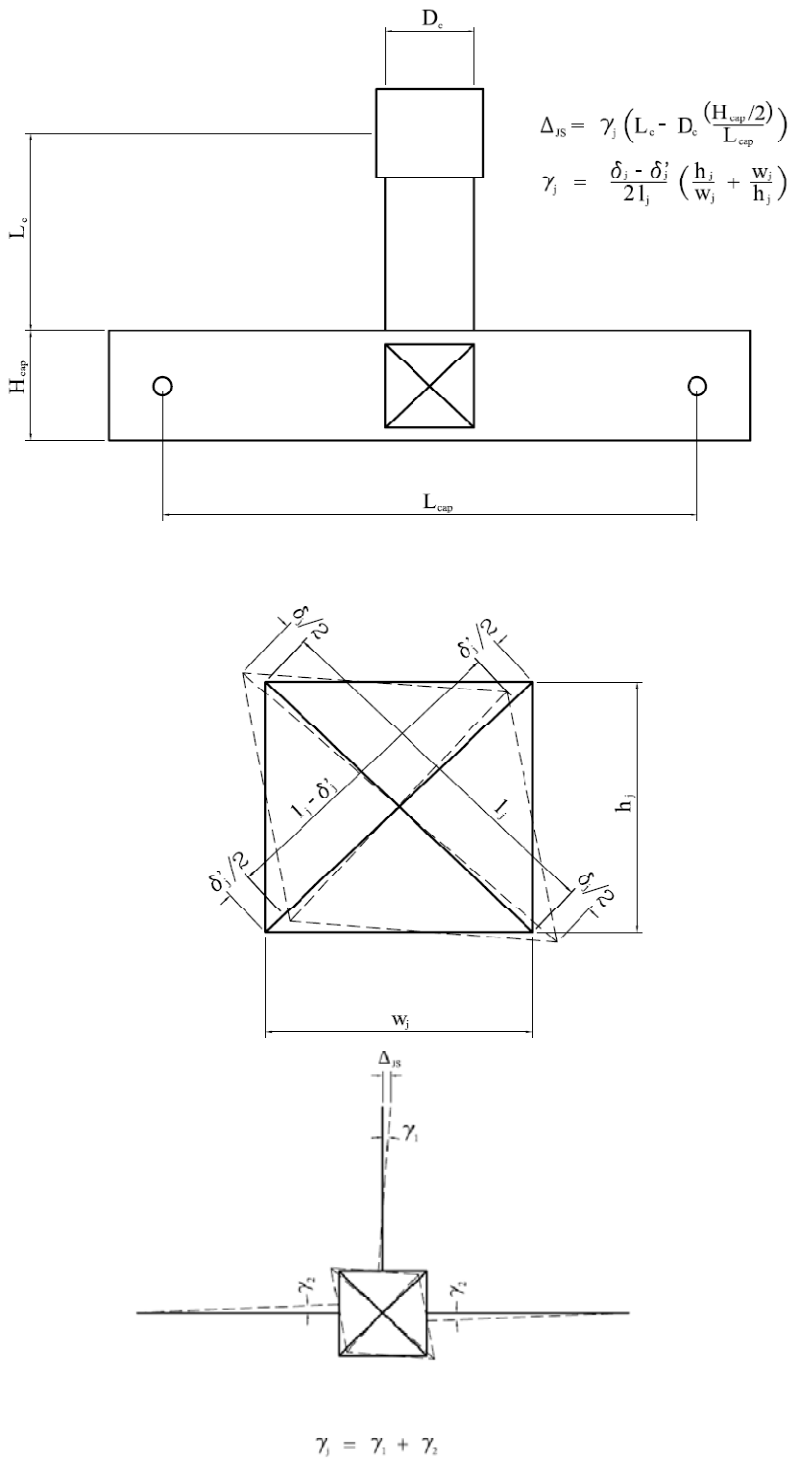

D. Joint Shear

Figure 3-23. Schematic Representation of Column Displacement Components, Continued

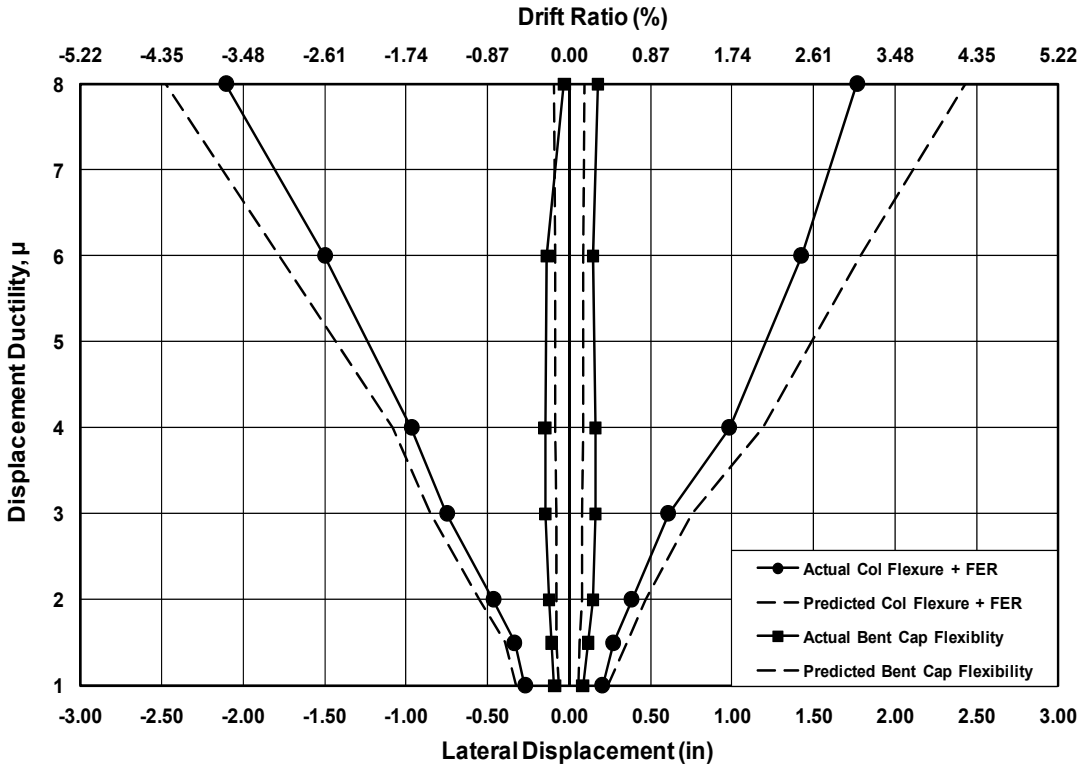

Figure 3-24. Displacement Components—Predicted vs. Actual

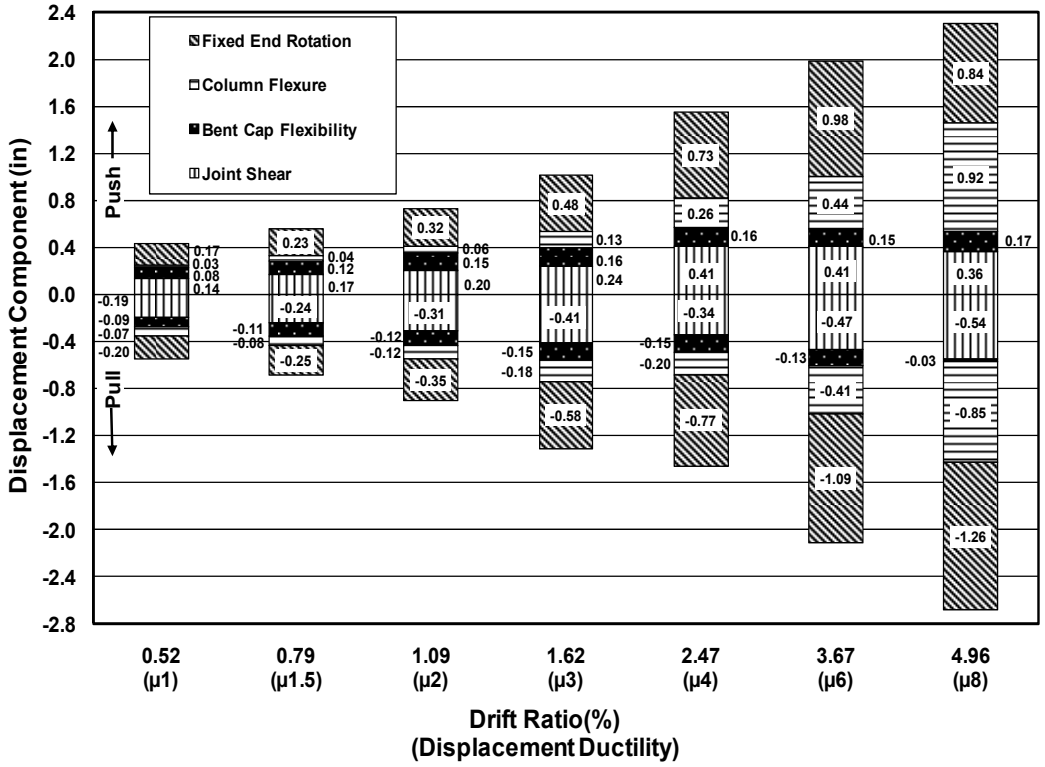

Figure 3-25. Displacement Decomposition Component Values

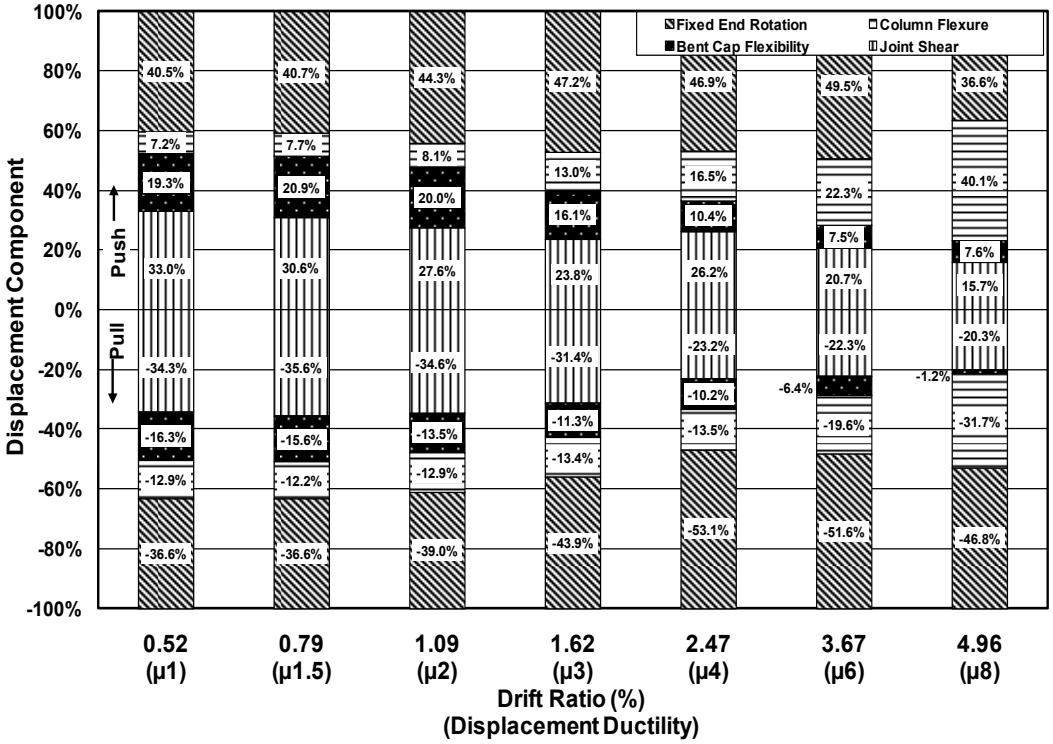

Figure 3-26. Displacement Decomposition Component Percentages

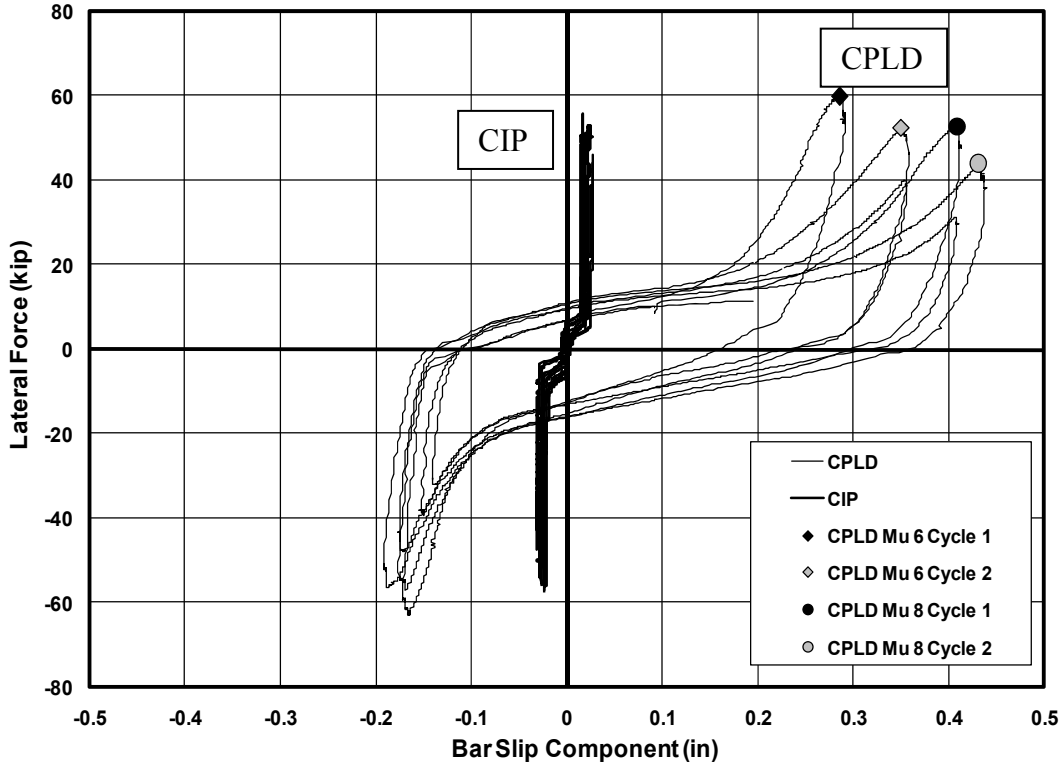

Figure 3-27. Lateral Force vs. Bar Slip Displacement Component—CPLD vs. CIP

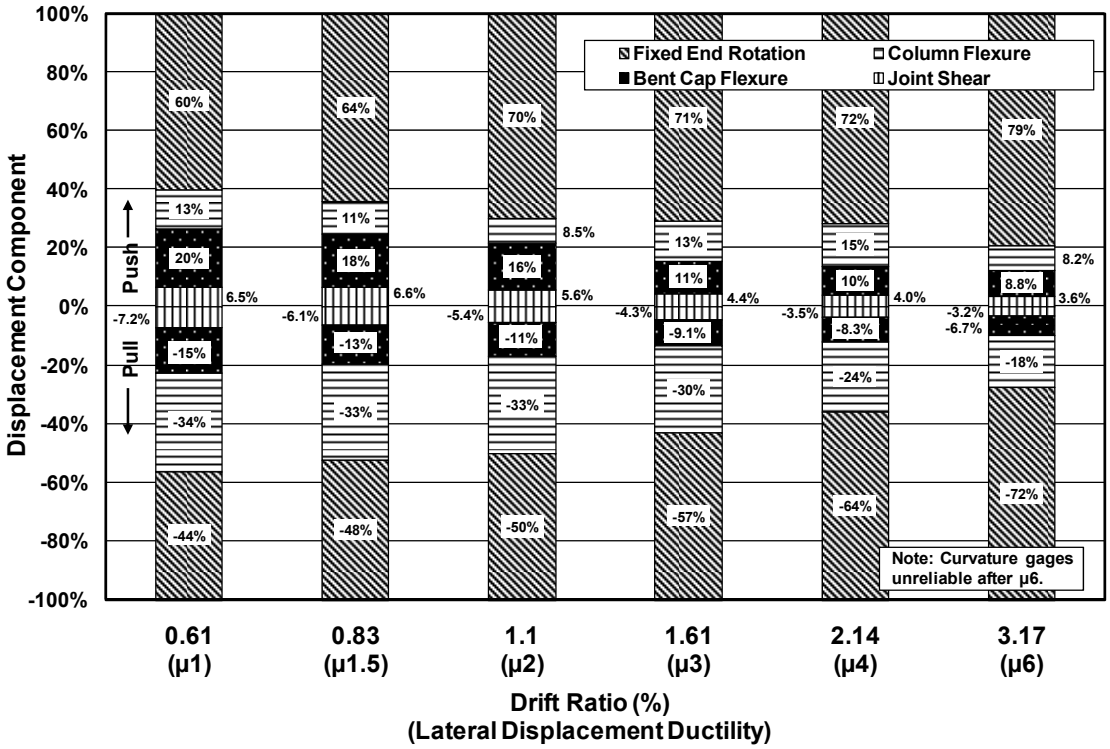

Figure 3-28. Displacement Decomposition Component Percentages—CPFD

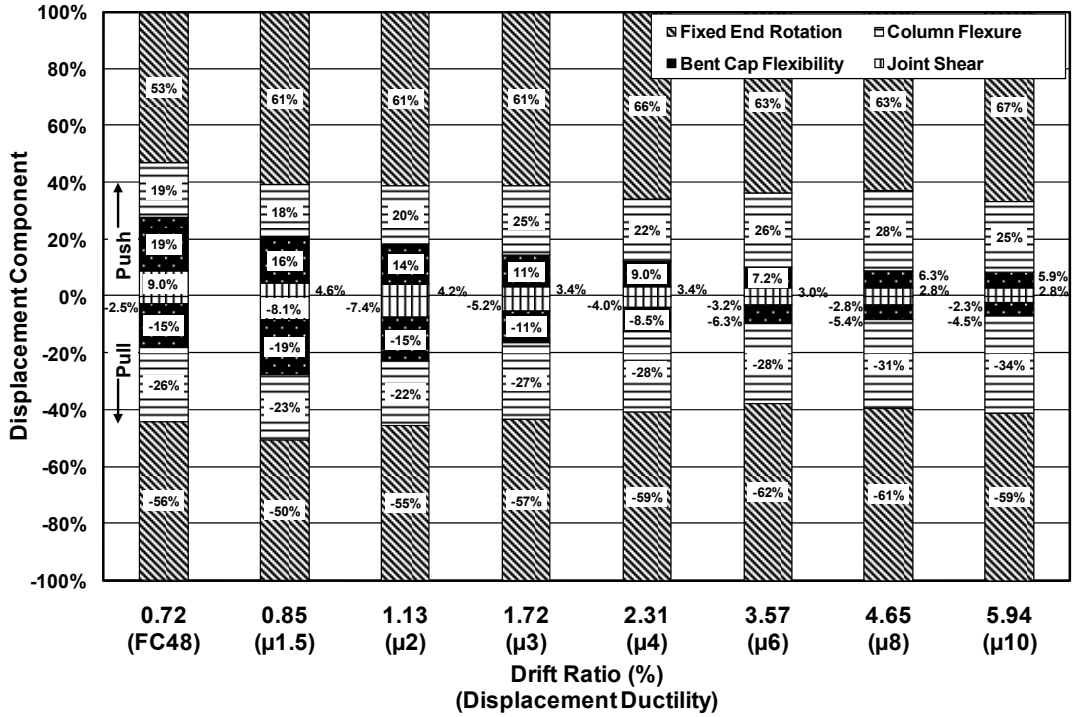

Figure 3-29. Displacement Decomposition Component Percentages—CIP

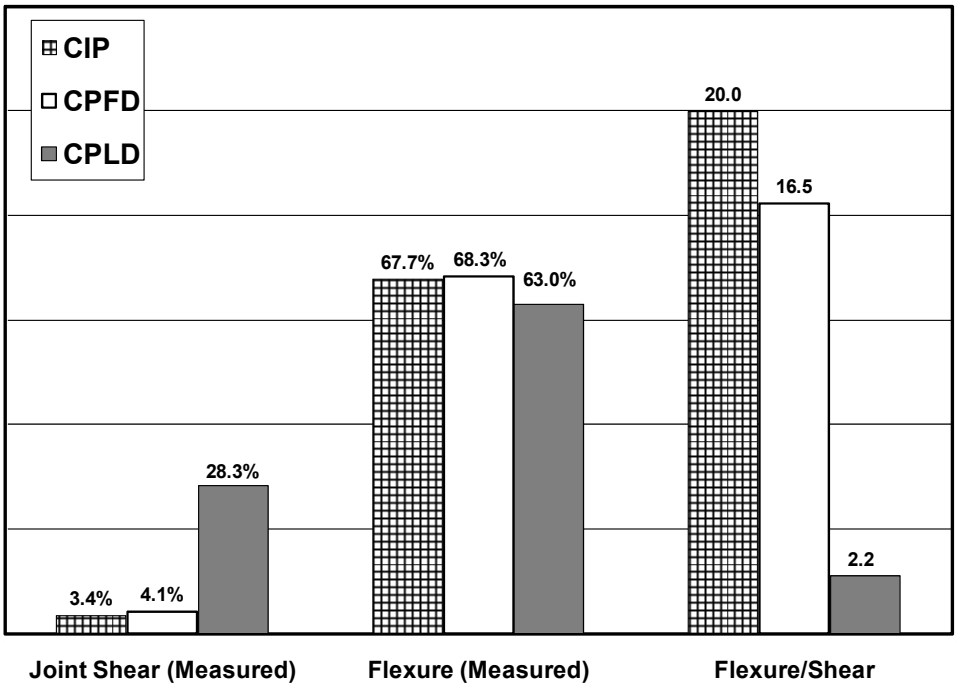

Figure 3-30. Comparison of Flexural and Joint Shear Displacement Components—CPLD, CPFD, CIP

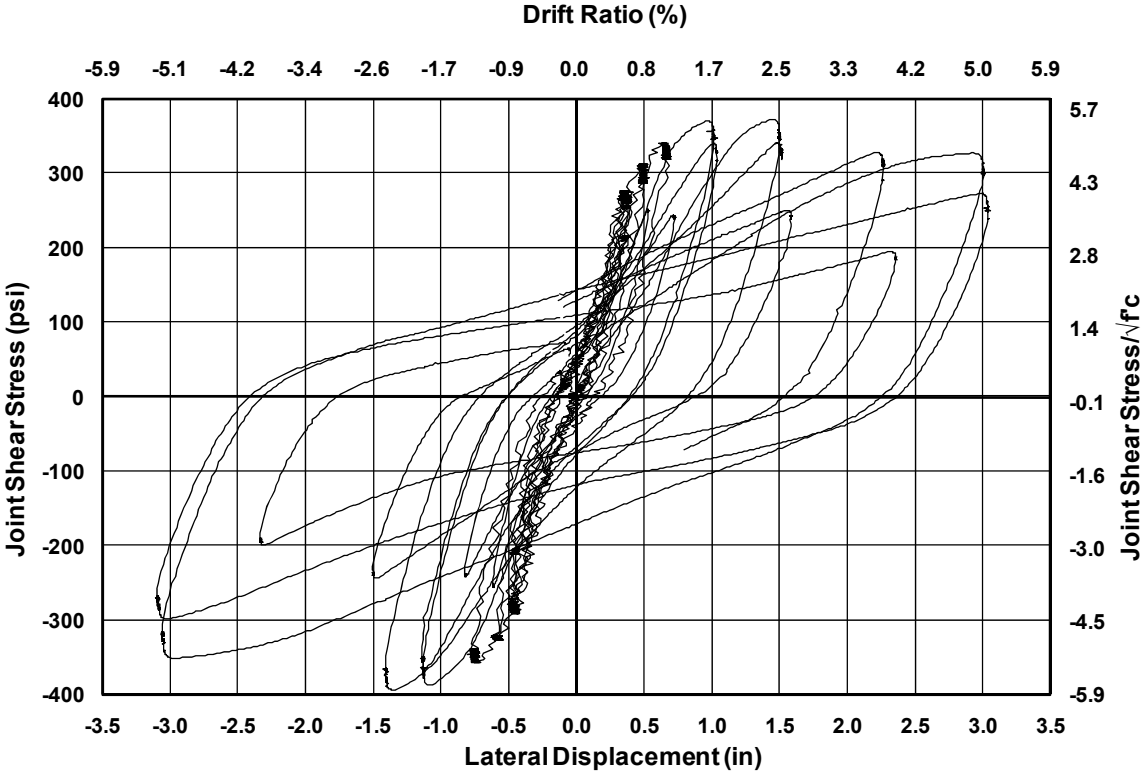

Figure 3-31. Joint Shear Stress vs. Lateral Displacement

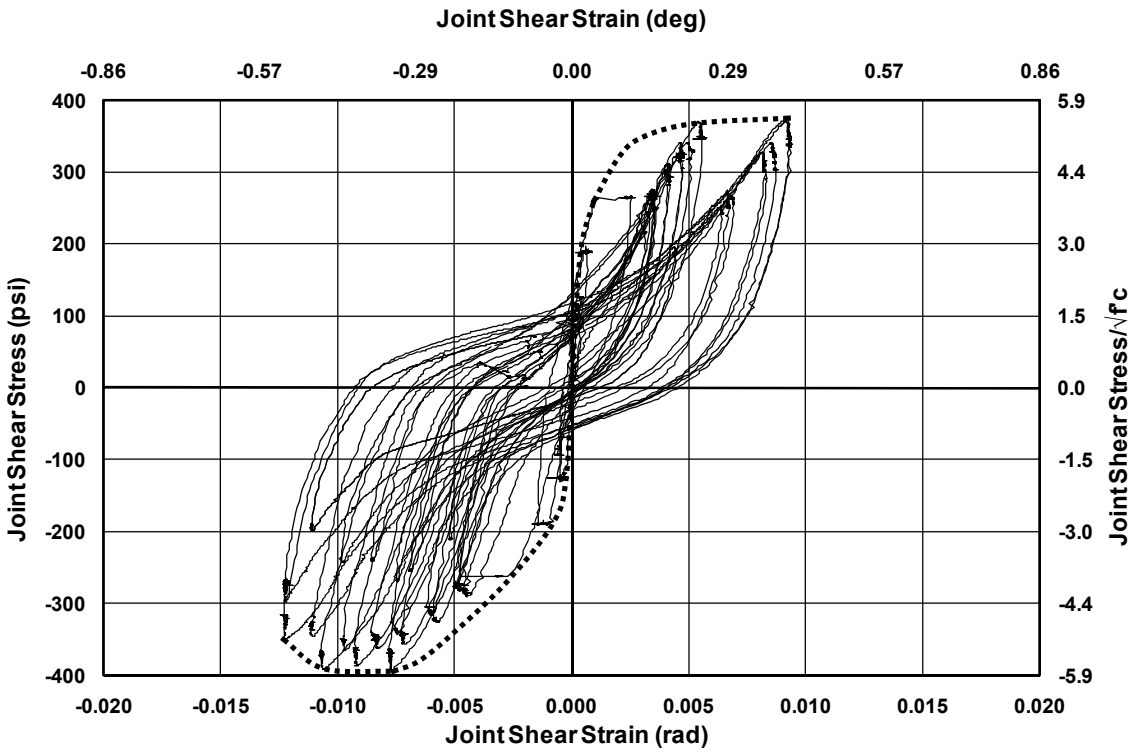

Figure 3-32. Joint Shear Stress vs. Joint Shear Strain

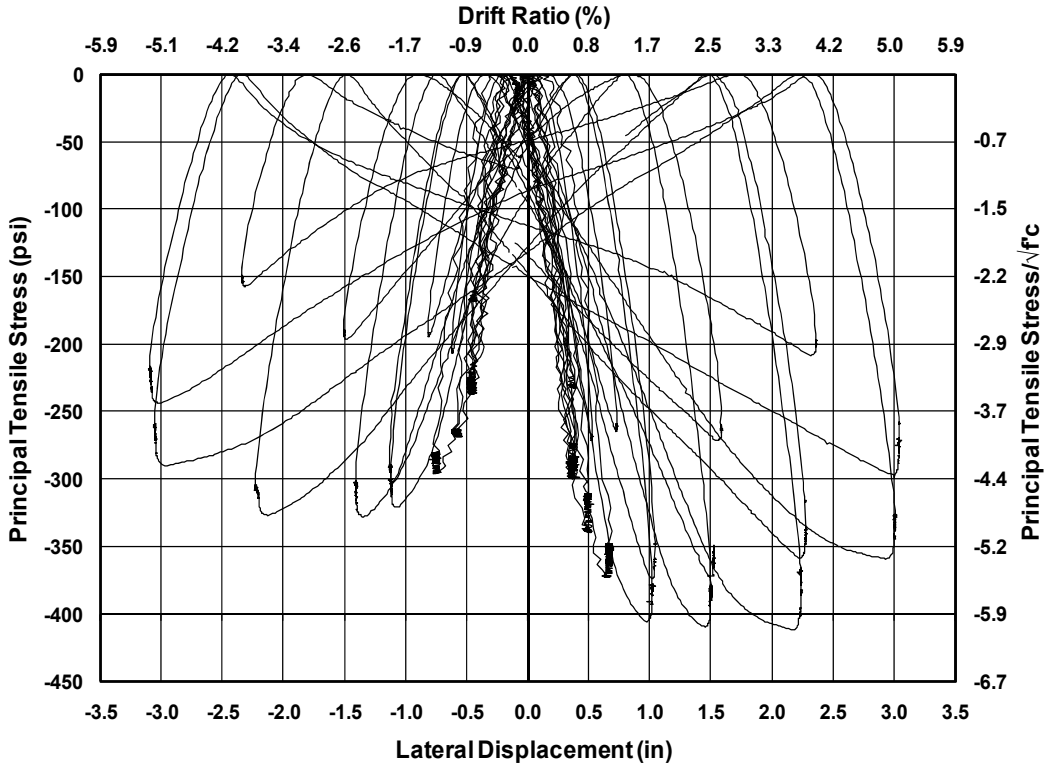

Figure 3-33. Principal Tensile Stress vs. Lateral Displacement

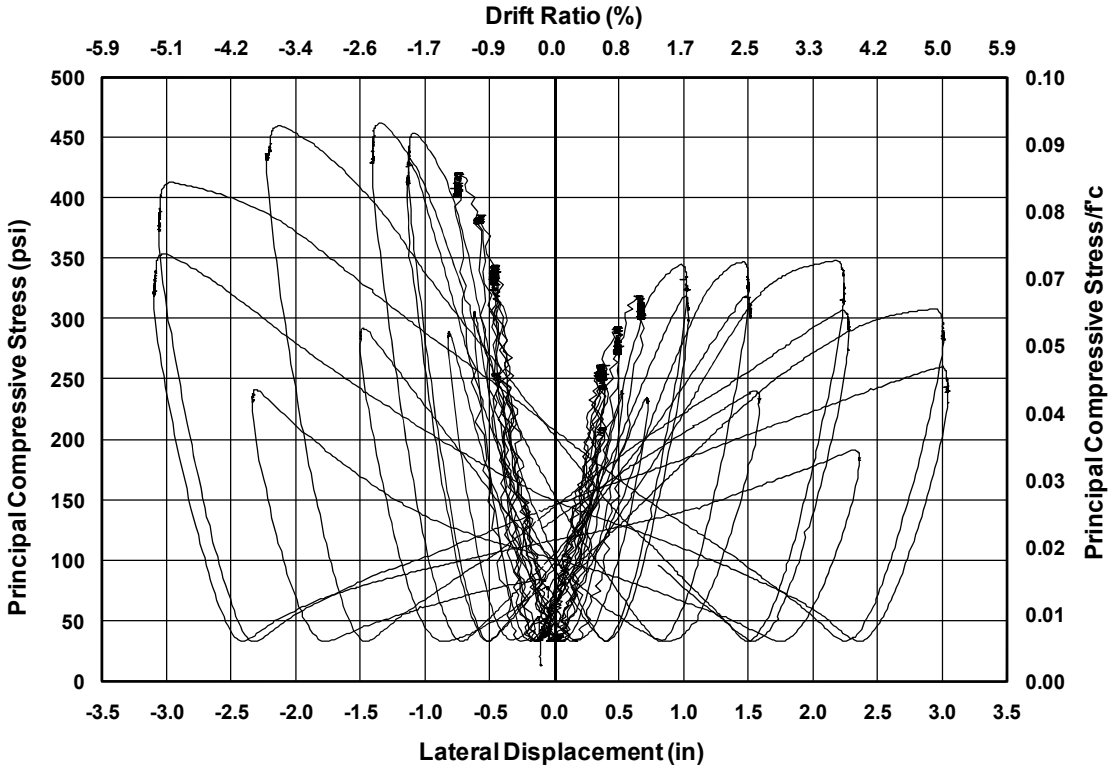

Figure 3-34. Principal Compressive Stress vs. Lateral Displacement

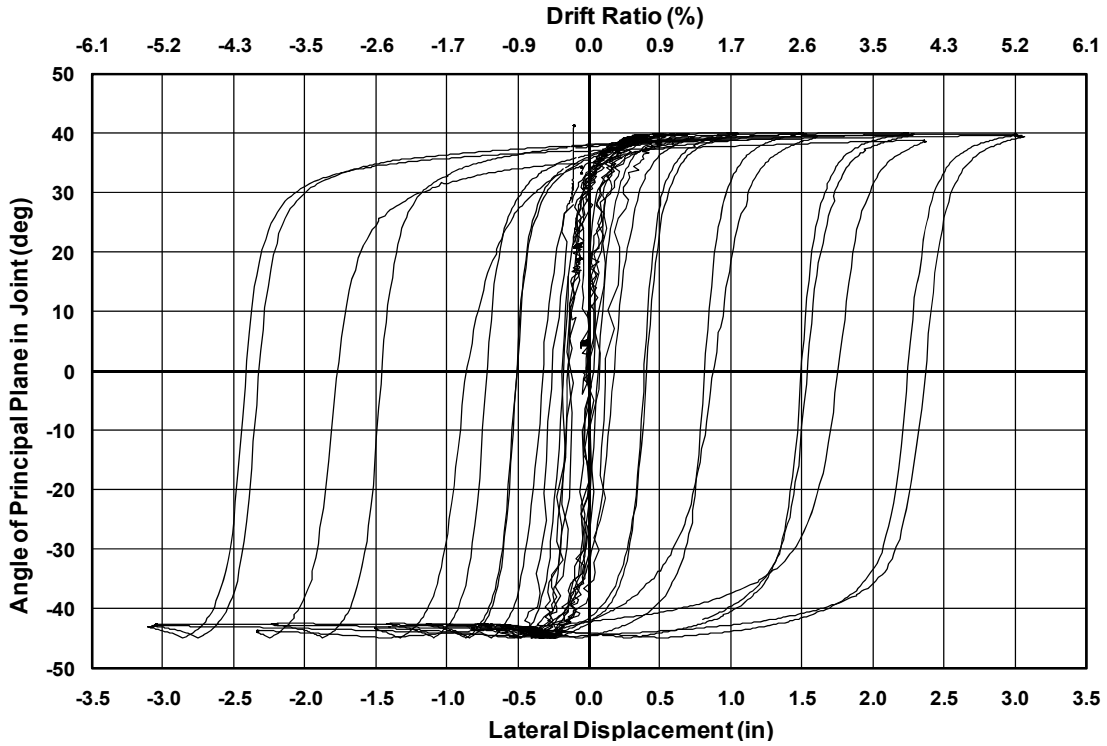

Figure 3-35. Angle of Principal Plane in Joint vs. Lateral Displacement

A. Before Removal of Loose Concrete B. After Removal of Loose Concrete

Figure 3-36. Bedding Layer (Post Test)

Figure 3-37. Flexural Cracks at Exposed Cap Pocket Surface (Post Test)

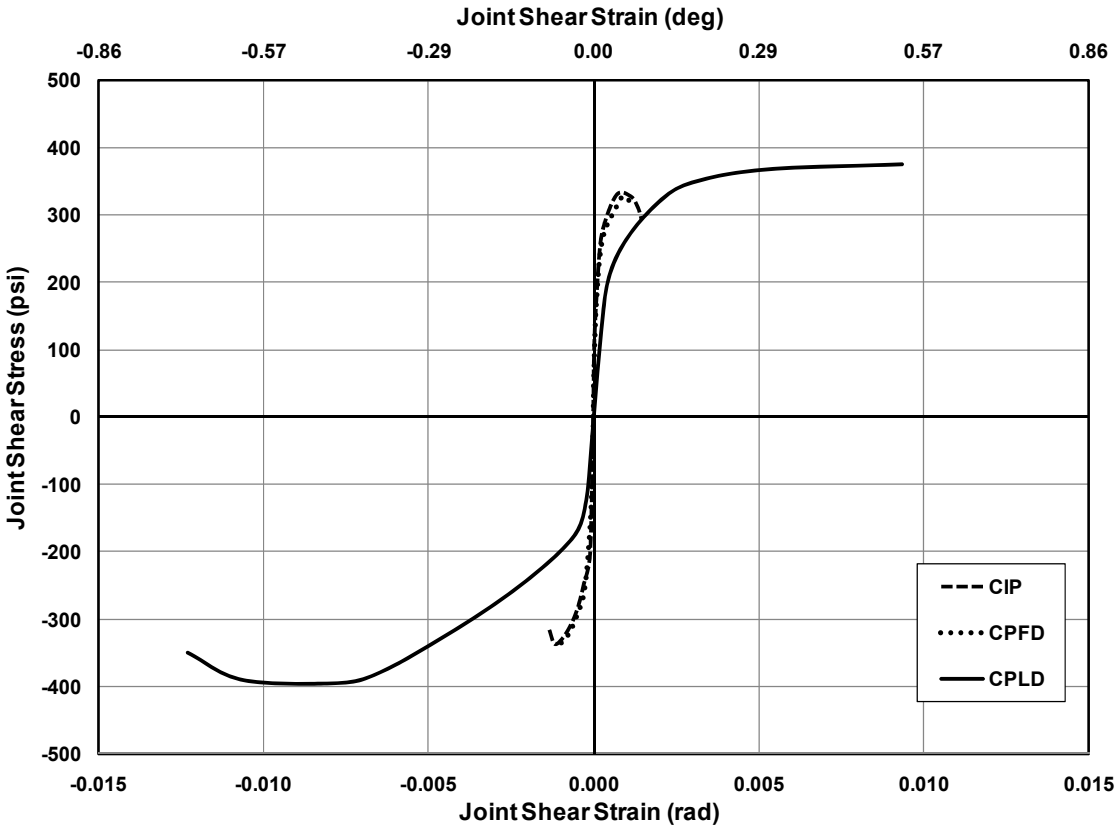

Figure 3-38. Joint Shear Stress vs. Joint Shear Strain Envelope—CIP, CPFD, CPLD

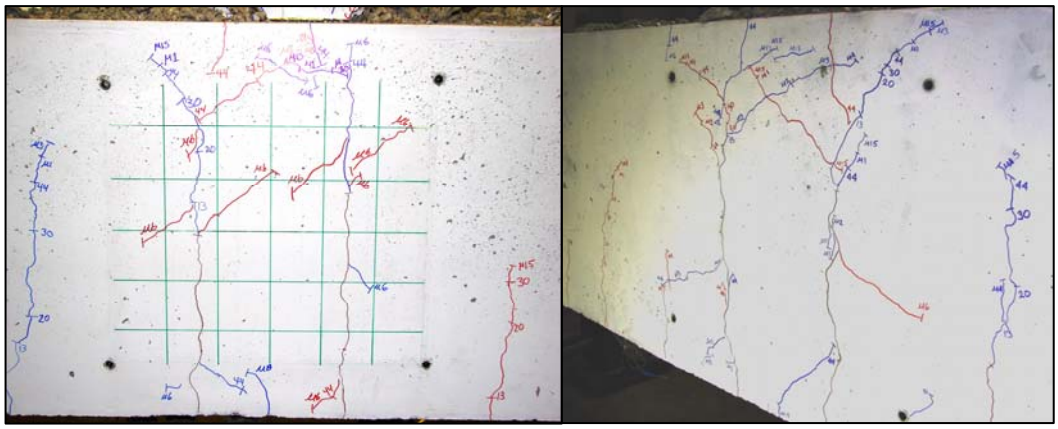

A. East Side—CPFD B. West Side—CPFD

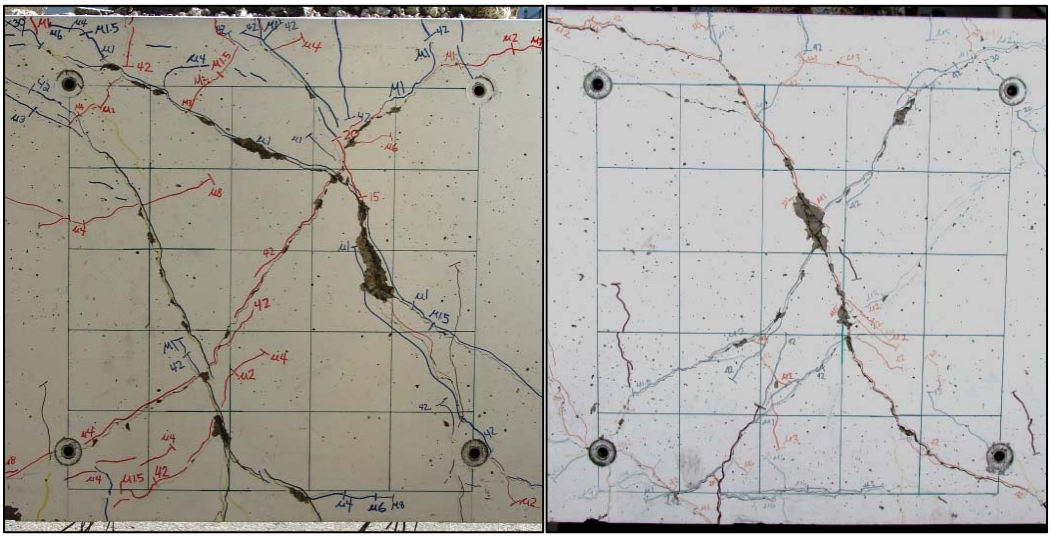

C. East Side—CPLD D. West Side—CPLD

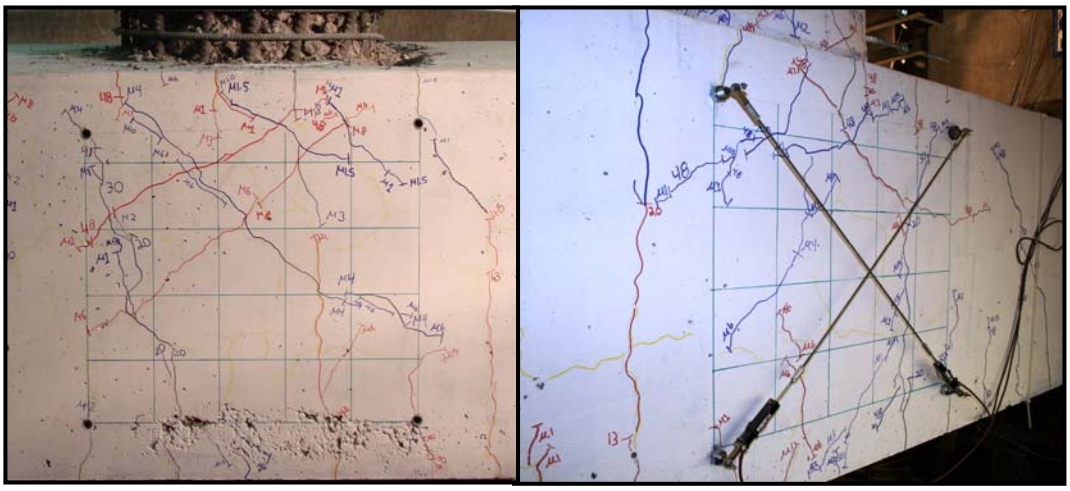

E. East Side—CIP F. West Side—CIP

Figure 3-39. Joint Region Cracking Post Test—CPLD, CPFD, CIP

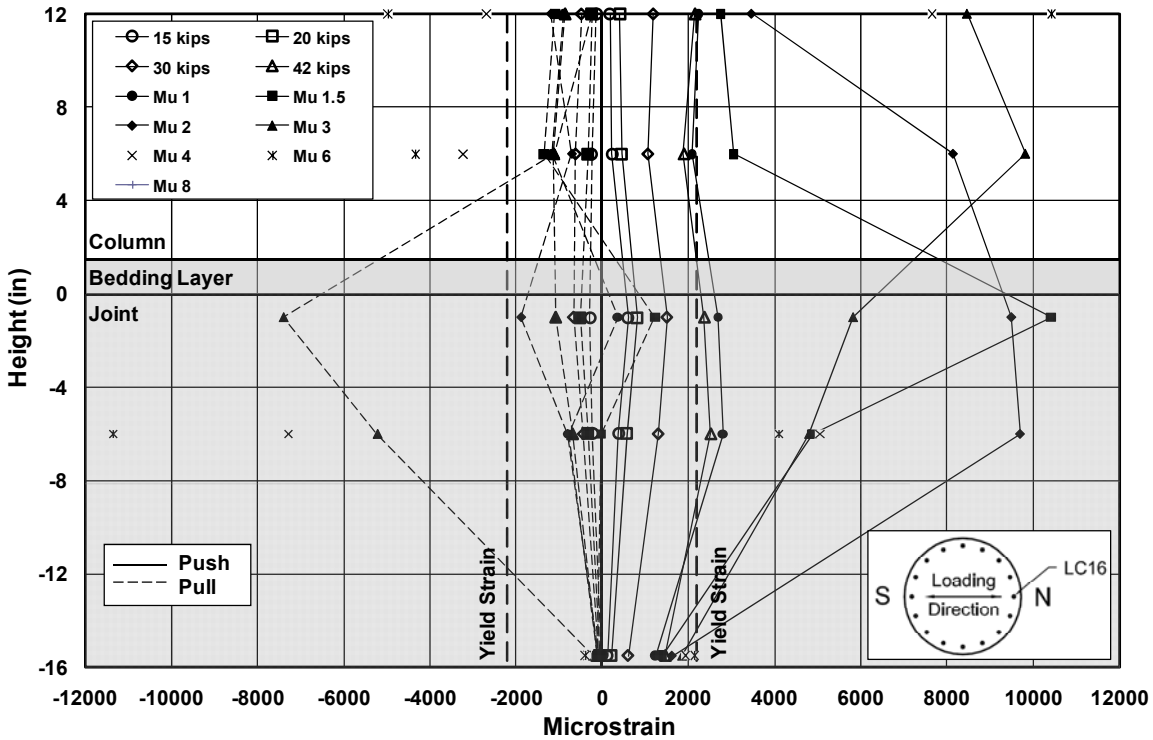

Figure 3-40. Strain Profile—Column Longitudinal Rebar (North)—CPLD

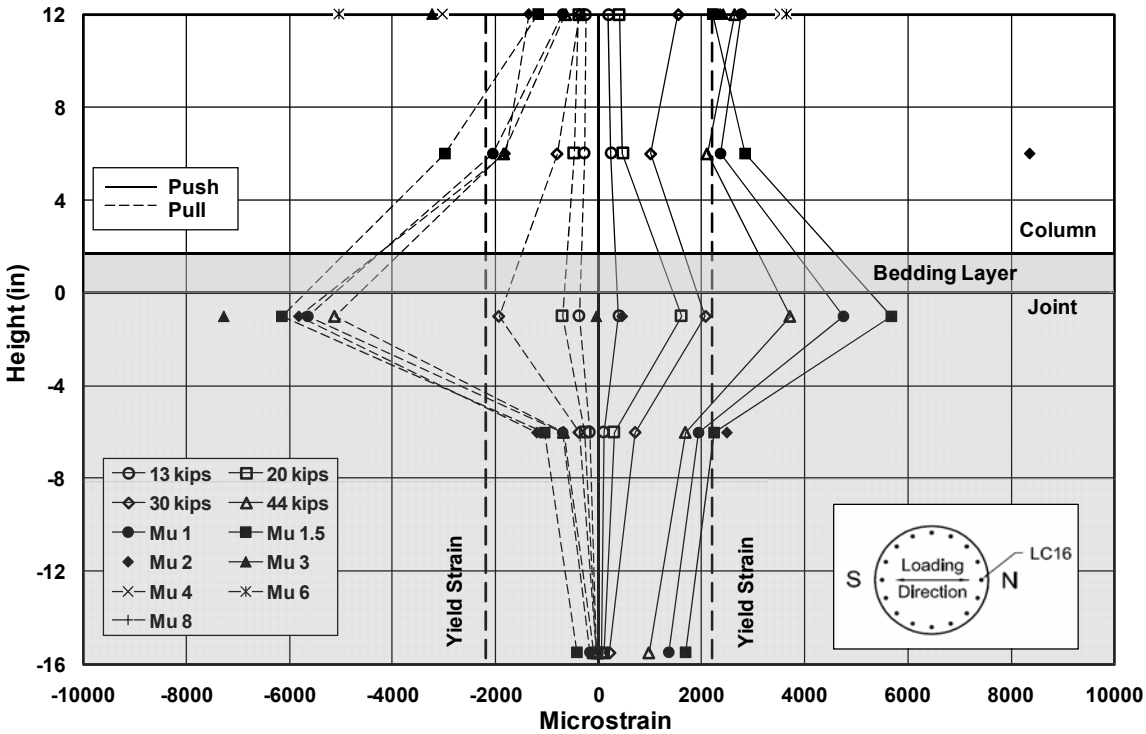

Figure 3-41. Strain Profile—Column Longitudinal Rebar (North)—CPFD

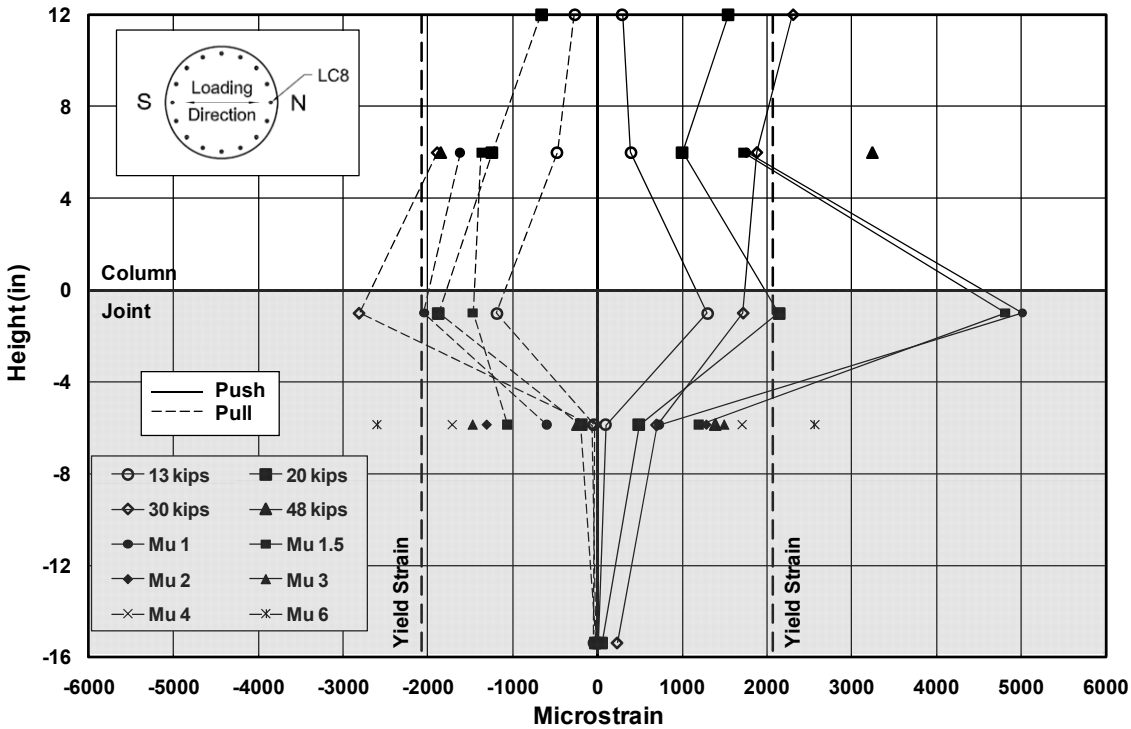

Figure 3-42. Strain Profile—Column Longitudinal Rebar (North)—CIP

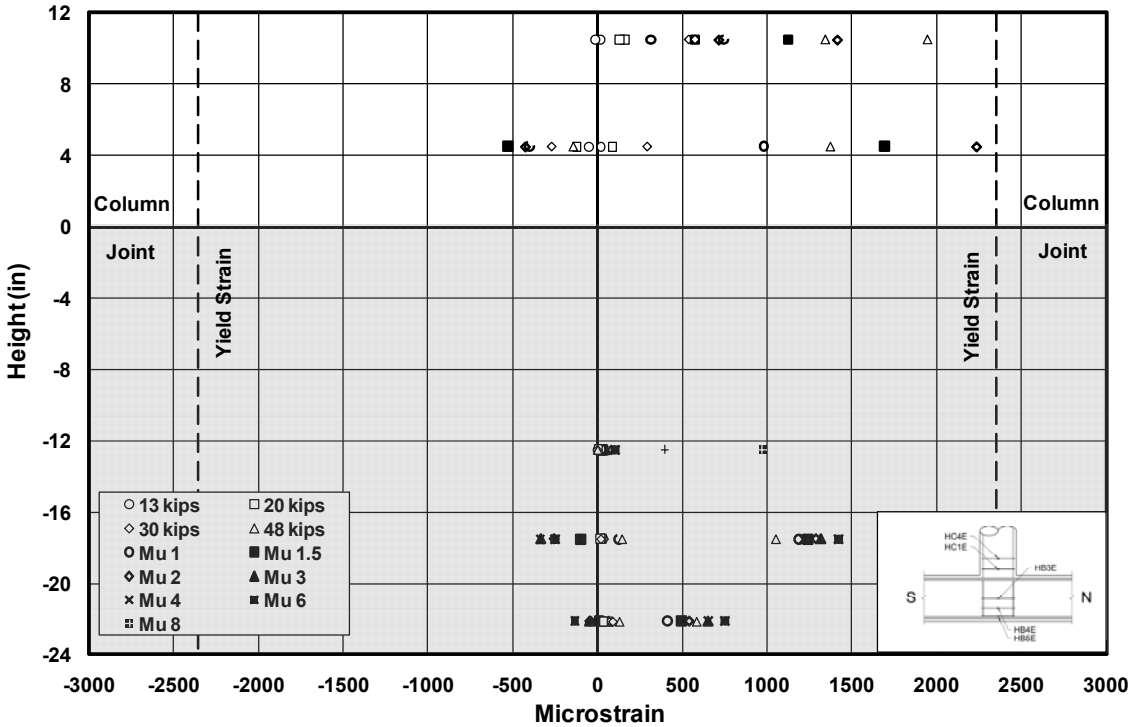

Figure 3-43. Strain Profile—Hoops in Column and Joint (East)—CIP

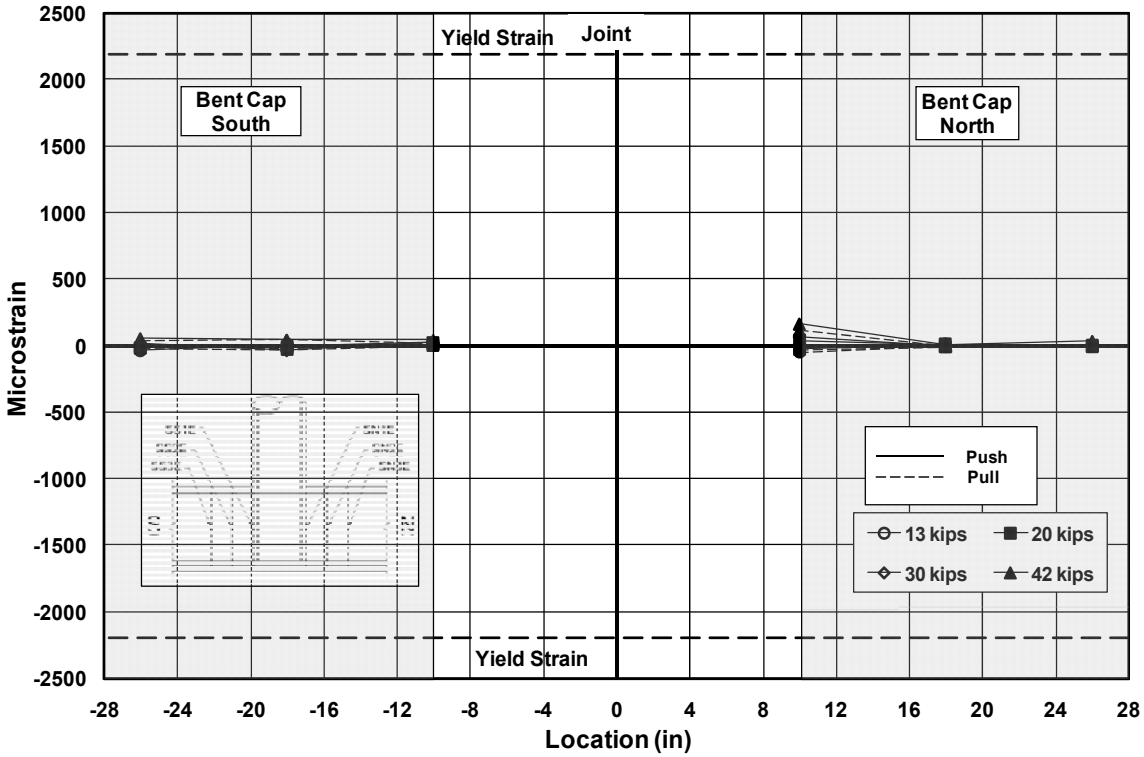

Figure 3-44. Strain Profile—Stirrups in Bent Cap, Force Control—CPLD

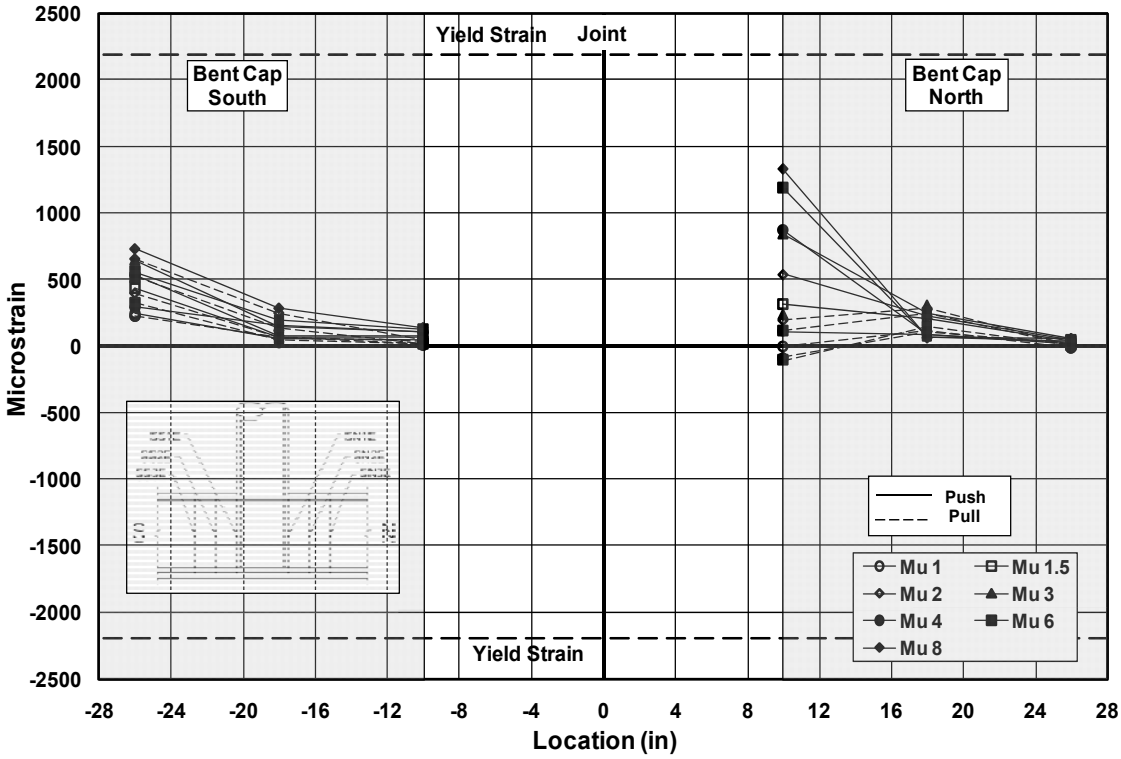

Figure 3-45. Strain Profile—Stirrups in Bent Cap, Displacement Control—CPLD

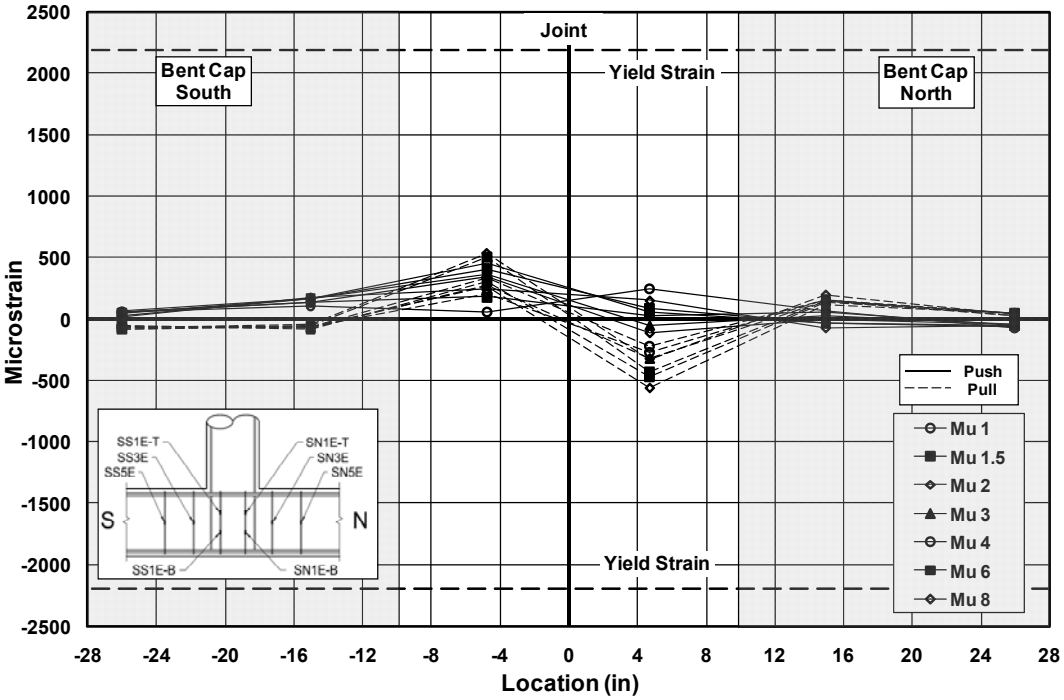

Figure 3-46. Strain Profile—Stirrups in Bent Cap (Mid-height) and Joint (Top), Displacement Control—CPFD

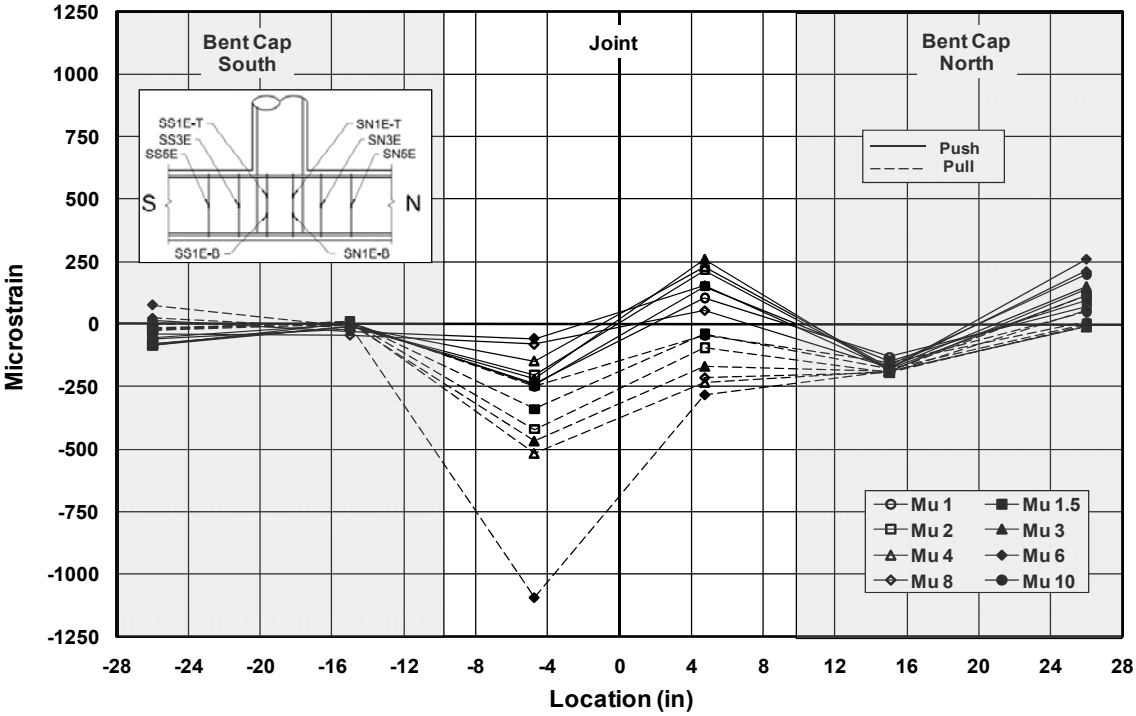

Figure 3-47. Strain Profile—Stirrups in Bent Cap (Mid-height) and Joint (Top), Displacement Control—CIP

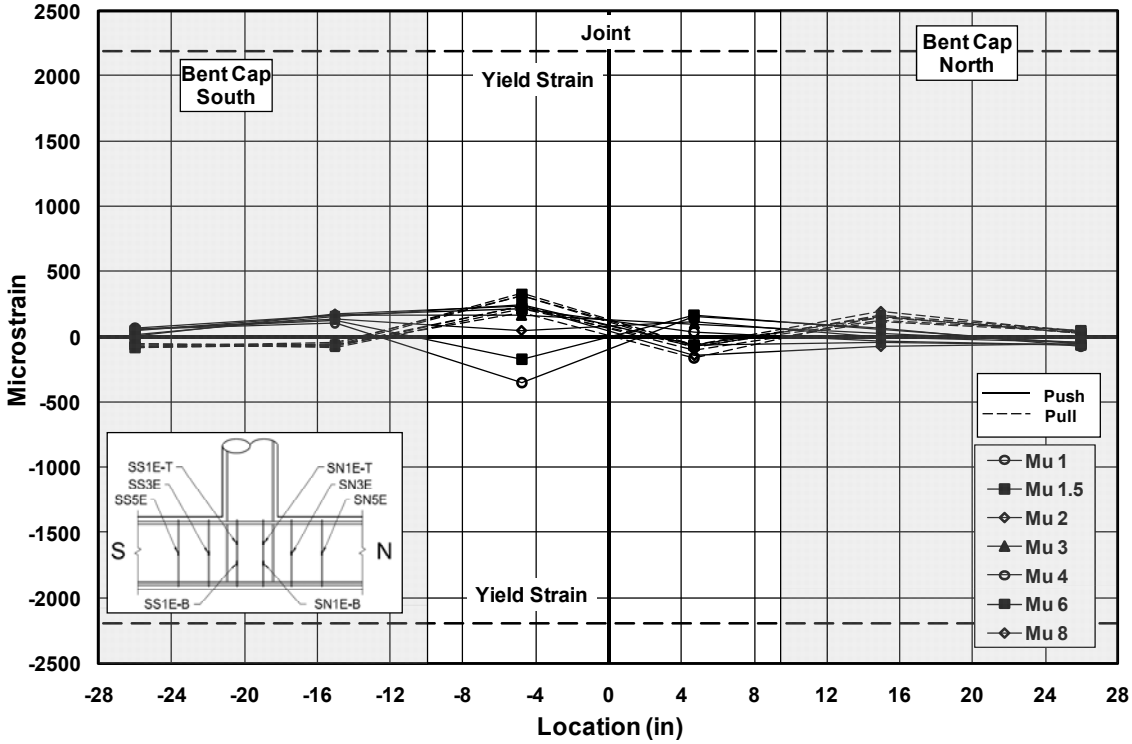

Figure 3-48. Strain Profile—Stirrups in Bent Cap (Midheight) and Joint (Bottom), Displacement Control—CPFD

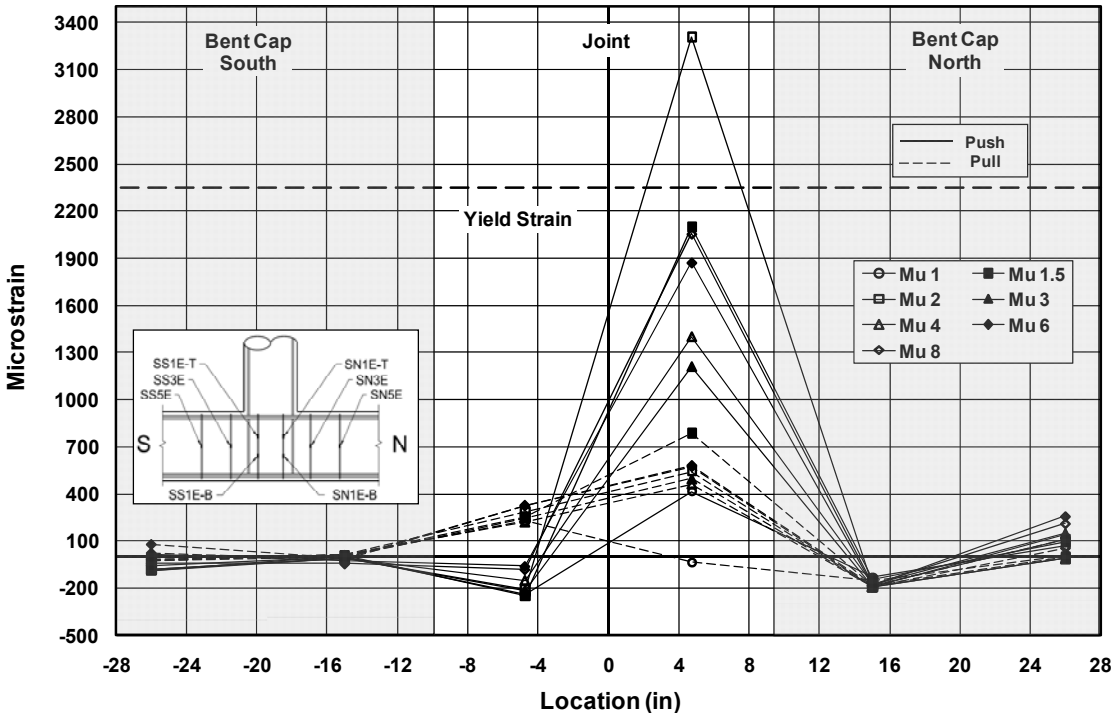

Figure 3-49. Strain Profile—Stirrups in Bent Cap (Midheight) and Joint (Bottom), Displacement Control—CIP

4.0 Summary and Conclusions

4.1 Summary

This report, Emulative Precast Bent Cap Connections for Seismic Regions: Component Tests—Cap Pocket Limited Ductility Specimen (Unit 4), is the fourth in the series of four reports summarizing the California State University, Sacramento (CSUS) component tests supporting National Cooperative Highway Research Program (NCHRP) Project 12-74, "Development of Precast Bent Cap Systems for Seismic Regions". CSUS is investigating two emulative connections—cap pocket and grouted duct—for nonintegral precast bent caps. CSUS is investigating two emulative connections—cap pocket and grouted duct—for nonintegral precast bent caps.

4.1.1 CPLD Design Basis

For a major seismic event, the full ductility Cast-in-Place (CIP) prototype bridge was designed and detailed to exhibit ductile plastic hinging in the column adjacent to the capacity-protected bent cap and joint. The full ductility component specimens were designed using a 42% scale of the central portion of the prototype bridge in accordance with the 2006 Recommended LRFD Guidelines for the Seismic Design of Highway Bridges (2006 LRFD RSGS), which contains less conservative joint reinforcement requirements—including a smaller area of vertical stirrups within the joint and smaller area of bent cap longitudinal reinforcement—than the 2009 AASHTO Guide Specifications for LRFD Seismic Bridge Design (2009 LRFD SGS).

The Cap Pocket Limited Ductility (CPLD) specimen also used a 42% scale of the central portion of the prototype bridge but was designed according to the principles of limited ductility rather than the full ductility basis used for the other specimens, as given in the 2006 LRFD RSGS. The specimen was similarly loaded in the transverse direction under quasi-static Force Control and Displacement Control sequences to investigate limited ductility performance. Emulative performance of the CPLD specimen was to be examined, especially through a displacement ductility of 2.0, even though a limited ductility CIP specimen was not tested for direct comparison. Thus, although a direct comparison to CPFD and CIP specimens—which were designed and detailed with joint

reinforcement for full ductility performance—is not appropriate for making conclusions relative to emulative behavior, comparisons do provide important insight for rational conclusions.

Important differences were intentionally incorporated into the CPLD joint detailing to examine the limited ductility design, in accordance with the intent and provisions of the 2006 LRFD RSGS for SDC B: 1) elimination of the construction stirrups within the joint region; 2) elimination of all joint-related stirrups and horizontal ties (A_s^{jv}, A_s^{jh}) placed external to the CPFD joint; and 3) elimination of the extra hoop at each end of the pipe. In addition, bent cap flexural reinforcement was reduced to eliminate potential strengthening of the joint, and bent cap transverse reinforcement, including adjacent to the joint, was reduced to the minimum required based on bent cap shear associated with plastic hinging of the column. The joint force demand was also maximized by use close column hoop spacing and a relatively small column axial stress. Thus, these measures were deemed reasonably conservative for testing to examine limited ductility performance and potential failure modes. It was understood that more stringent detailing could be adopted for SDC B design as required.

CPLD column reinforcement was not reduced but designed to match the SDC D-based requirements of the CPFD design. This was intended to help ensure that the column would not prematurely become a weak link in the system, but impose as large of a demand and as many cycles as possible through on the joint.

It was anticipated that these measures would likely result in more extensive joint damage as the specimen displacement ductility approached μ2 and possibly joint failure at larger ductility levels.

4.1.2 Test Results

Specimen response was analyzed including experimental observations, hysteretic response, column curvature response, displacement decomposition, joint response, and strain records. As anticipated by the limited ductility design, response was characterized by a combination of plastic hinging of the column and joint shear cracking. As diagonal cracks developed in the joint region with increasing lateral load, significant column

flexural (and shear) cracks also developed and flexure eventually dominated response. The system achieved an unexpectedly large drift ratio of 5.1% (corresponding to a nominal displacement ductility of 8) with eventual failure due to buckling of column longitudinal reinforcement followed by fracture of two bars in the plastic hinging region, rather than joint failure. At ultimate, significant joint shear cracks with minor spalling had developed as well as a moderate amount of bar slip. The load-displacement response indicated stable hysteretic behavior with loops of increasing area without appreciable strength degradation (12% at maximum drift), as well as stiffness, strength, ductility and other features, such as flexural crack distribution, anticipated for an emulative beam-column connection test. However, it should be noted that ductile plastic hinging in the column was accompanied by significant joint shear cracking, although joint failure did not occur. A comparison of the load-displacement envelope to the predicted envelope showed a good correlation, although the specimen achieved a higher strength at early drift ratios than predicted.

Reasonably close comparisons were found between CPLD, CPFD, and CIP specimens for load-displacement hysteretic response envelopes and equivalent viscous damping ratio. Although the CPLD specimen achieved a higher capacity (9%-12%) than the CIP and CPFD specimens, drift ratios and nominal displacement ductilities were of the same order. However, the CPLD achieved a curvature approximately 30% less than the CPFD and CIP specimens at the same drift. This is attributed to softening of the joint due to shear cracking, which increased the joint shear component of column displacement.

In agreement with visual observations, the displacement decomposition demonstrated that the CPLD column displacement due to joint shear was nearly an order of magnitude larger, and the flexural component was approximately 25% less than that of the full ductility specimens. For example, at a push drift ratio of 2.5% ($\mu 4$), the flexural component was 63% of the column displacement, and joint shear was 26%, corresponding to a flexure/shear ratio of only 2.4. But for the CPFD, at 2.2% drift ($\mu 4$), the flexural component accounted for 87% of the column displacement, and joint shear was 6% for a

flexure/shear ratio of 15. Overall, the CPLD flexure/shear ratio averaged 2.2, nearly an order of magnitude smaller than that for the CPFD and CIP specimens (16.5 and 20.0, respectively).

The precast joint region for the CPLD specimen exhibited a significant level of distress that increased throughout the test. Analysis of the joint indicated that the principal tensile stress reached $7.0\sqrt{f_c^{'}}$, twice the $3.5\sqrt{f_c^{'}}$ limit at which extensive (additional) joint reinforcement is required because of the likelihood of joint shear cracking. Per SDC B design, the CPLD specimen intentionally did not include joint reinforcement to limit growth of joint shear cracks. Principal compressive stresses reached $0.13\,f_c^{'}$, approximately half the 2006 LRFD RSGS limit of $0.25\,f_c^{'}$.

The CPLD normalized nominal joint stresses and associated distress were larger than for the CPFD and CIP joints. The CPLD maximum stresses (nominal joint shear, principal tensile, and principal compressive) were significantly larger than the full ductility specimens: 47%-86% larger than the CPFD and 30%-48% larger than the CIP. In addition, the change in the CPLD panel area was approximately three times that of the full ductility specimens.

Diagonal cracking was extensive within the CPLD joint region. Shear cracks developed during Force Control and further developed and widened during Displacement Control. Diagonal cracks were as wide as 0.050 at μ2 and increased to large widths at ultimate (0.080 in), with minor associated spalling. The post-test crack pattern consisted of a series of diagonal cracks through the center of the joint. In contrast, CPFD joint diagonal cracking was minor, reaching only 0.005 in at μ2 and 0.009 in maximum, without spalling. CIP specimen cracking was intermediate, with a crack width of 0.009 at μ2 and 0.025 in maximum, without spalling. Joint shear stress-strain response revealed significant joint softening at increasing drift ratios. This was in contrast to the stiff joint response and limited joint shear strains that developed for the full ductility specimens.

The pattern of joint diagonal cracks between specimens differed significantly. The CPLD diagonal cracks on both faces resembled the CIP pattern much more than

those of the CPFD, although CPLD cracks were much wider. The CPFD diagonal cracking was limited to regions above and below the corrugated pipe until diagonal cracking at 3.2% drift (μ6, pull). In addition, two symmetrical vertical flexural cracks developed through the CPFD joint, near the locations of the vertical construction stirrups. Joint stirrups were not used for the CPLD; however, CIP analysis demonstrated that construction stirrups were highly effective, reaching yield, and contributed to resisting joint stresses and limiting crack opening. These stirrups played a lesser role for the CPFD specimen. The CPFD also exhibited a significant horizontal crack south of the joint and used hoops at the ends of the pipe, which were found to be highly effective. Although different joint crack patterns correspond to different load paths, the most important effect of the joint cracking on overall specimen response was the significant increase in joint shear displacements due to softening of the CPLD joint.

The CPLD bar slip component of column displacement was approximately 11 times that of the CIP and CPFD specimens. In addition, a significant increase in CPLD slip towards ultimate was observed, even as the load decreased. Splitting cracks also formed in the bent cap and column due to column bar anchorage. Although bar pullout may have been impending, pullout did not mobilize before column bar buckling failure occurred. However, a bar anchorage equation from prior research on grout pockets indicated a larger development length for the CPLD column bars (beyond that required by 2006 LRFD RSGS) may have helped reduce slip.

The CPLD specimen, however, used concrete which exhibited closely matching strength and stiffness properties between the column and pocket concrete, within 4%. The bedding layer appeared to perform integrally with the column, did not produce unusual behavior in the joint or specimen, and was not a weak link in the system. In addition, integral behavior between the pocket concrete, pipe, and surrounding concrete was evident.

Strain records for column longitudinal bars and hoops provided confirmation of progressive development of plastic hinging and significant strain penetration, including bar yield at 6 in above and below the bedding layer. A similar strain pattern was evident

for the CIP and CPFD specimens. However, significant column spalling developed at a much larger drift for the CPLD specimen. Thus, CPLD hoop strains developed much more gradually (i.e., at much larger drifts) than for the other specimens. This is attributed to the more extensive joint shear cracking for the CPLD.

Much larger pipe strains developed for the CPLD, up to 70% of yield, corresponding to the more significant joint distress observed. The ratio of CPLD/CPFD principal strain through the depth (east face) ranged from 1.40 to 1.91 for the push direction and much larger ratios for the pull direction, as CPFD strains were much smaller. Distribution of strains also differed.

Strain patterns for the longitudinal bent cap bars were reasonably consistent between specimens, especially for the bottom bars. For bottom bars at centerline, the CIP reached 46% of yield, whereas the CPFD and the CPLD yielded. Limited and less consistent comparisons resulted for the top bar. Strain patterns reasonably matched expected distribution per an assumed force transfer model.

In contrast to CPLD stirrups at the face of the joint reaching 61% of yield, maximum CPFD and CIP strains outside the joint were limited to approximately 10% of yield. However, construction stirrups within the joint for the CIP yielded and reached approximately 25% of yield for the CPFD. The lack of vertical joint stirrups in the CPLD specimen allowed joint shear cracks to develop and grow unrestrained.

4.2 Conclusions

Based on the observed response and data analysis for the CPLD (Unit 4) specimen and a detailed comparison with the full ductility CIP (Unit 1) control specimen and CPFD (Unit 3) specimen, the following conclusions can be drawn:

1. Despite elimination of joint reinforcement used in the full ductility specimens—including vertical stirrups within the joint, joint-related stirrups and horizontal cross ties external to the joint, and hoops at the ends of the pipe—as well as reduction of bent cap flexural reinforcement and bent cap transverse reinforcement, the CPLD specimen satisfied the main performance goal of the SDC B design: exhibiting ductile plastic hinging and reaching an

extensive drift of 5.1% (μ8 nominal), well beyond a displacement ductility of 2.0 ($\mu 2$), with only minor (12%) load degradation at maximum drift. This is attributed to the effectiveness of the corrugated steel pipe within the joint.

2. Extensive joint shear cracking softened the CPLD joint, contributed significantly to column drift, and delayed (but did not prevent) flexural plastic hinging. This response is attributed to the absence of vertical joint stirrups, which permitted unrestrained development, growth, and widening of joint shear cracks. Although this response was in contrast to the full ductility CIP and CPFD specimens, it can be reasonably deduced that similar, or more severe, joint behavior would likely develop for a similarly detailed CIP limited ductility connection because an SDC B CIP joint would incorporate less extensive and less effective transverse reinforcement (based on the inadequate provisions of AASHTO LRFD Bridge Design Specifications) than that provided by the steel pipe.
3. Based on the foregoing conclusions, emulative behavior can be concluded for the CPLD specimen. Similarities in performance between the limited ductility and full ductility specimens, including plastic hinging, lateral load-displacement response, equivalent viscous damping, and integral behavior between the bedding layer, column, pipe, and bent cap, support this conclusion.
4. Despite the extensive plastic hinging, the development of significant joint shear damage (but not failure) observed for the CPLD specimen does not match the expressed intent of Article 4.7.1 of the 2009 AASHTO Guide Specifications for LRFD Seismic Bridge Design for limited ductility structures, including the requirement that: "Inelastic action is intended to be restricted to flexural plastic hinges in the column…".
5. CPLD response indicates that design specifications for a limited ductility cap pocket connection should incorporate minimum reinforcement requirements to help produce emulative behavior characterized by flexural plastic hinging

with limited effects of joint shear cracking: 1) minimum area of vertical joint stirrups; and 2) pipe thickness based on providing the same circumferential hoop force in the joint as that required by minimum transverse reinforcement provisions of Article 8.13.3 of the 2009 AASHTO Guide Specifications for LRFD Seismic Bridge Design.

6. CPLD response also has important implications for CIP design. The following provisions are recommended for inclusion in the AASHTO Guide Specifications for LRFD Seismic Bridge Design for CIP structures in SDC B (limited ductility) to help produce emulative behavior characterized by flexural plastic hinging with limited effects of joint shear cracking: 1) minimum area of vertical joint stirrups; and 2) minimum joint transverse reinforcement based on Article 8.13.3 of the 2009 AASHTO Guide Specifications for LRFD Seismic Bridge Design. This reinforcement can be determined prescriptively, avoiding extensive seismic analysis, and constructible details result. Similar provisions can also be adopted for SDC A.
7. Construction specifications should address fabrication and assembly processes and flowable concrete within the cap pocket.
8. Additional analysis is required to develop a new model that fully characterizes cap pocket joint behavior, including joint forces, pipe effects, crack patterns, and differences in strain distributions between the limited and full ductility specimens.

References

1. Matsumoto, Eric. E., *Emulative Precast Bent Cap Connections for Seismic Regions: Component Tests—Cast-in-place Specimen (Unit 1)*, ECS Report No. ECS-CSUS-2009-01, California State University, Sacramento, CA (November 2009) 89 pp.
2. Matsumoto, Eric. E., *Emulative Precast Bent Cap Connections for Seismic Regions: Component Tests—Cap Pocket Full Ductility Specimen (Unit 3)*, ECS Report No. ECS-CSUS-2009-03, California State University, Sacramento, CA (November 2009) 111 pp.
3. Tobolski, M.J., Restrepo, J.I., Matsumoto, E.E., and Ralls, M.L., *Development of Precast Bent Cap Concepts*, SSRP Report No. 06/10. University of California, San Diego, La Jolla, CA (September 2006) 176 pp.
4. Restrepo, J.I. and Matsumoto, E.E., *National Cooperative Highway Research Program (NCHRP), Project 12-74, Development of Precast Bent Cap Systems for Seismic Regions*, Proposal to Research Board (March 31, 2005).
5. Imbsen, R. A., *Recommended LRFD Guidelines for the Seismic Design of Highway Bridges, 2006, Task 193 (2006 LRFD RSGS)*, TRC/Imbsen & Associates, Inc, Rancho Cordova, CA (May 2006).
6. Draft Seismic Guide Specification – March 2007, AASHTO Subcommittee on Bridges and Structures, http://bridges.transportation.org/sites/bridges/docs/2007-03-09GuideSpec.pdf (As of March 22, 2007).
7. American Association of State Highway and Transportation Officials. AASHTO Guide Specifications for LRFD Seismic Design Specifications (First Edition), Washington, DC (2009).
8. Matsumoto, E.E., Wright J., Johnsen, S., Mislinski, S., "Proposed Bridge Design Calculations and Drawings of the Prototype Bridge and Test Specimen," Submitted by Restrepo, J.I. and Matsumoto, E.E. to National Cooperative Highway Research Program Project (NCHRP) 12-74 Panel (August 11, 2006) 232 pp.
9. "Standard Specification for Corrugated Steel Pipe, Metallic-Coated for Sewers and Drains, AASHTO Standard Specifications for Transportation Materials and Methods of Sampling and Testing," ASTM Designation A760/A760M-09, American Society for Testing and Materials ASTM Standards Vol. 01.06, Philadelphia, PA (2009).
10. "Standard Method of Test for Helical Lock Seam Corrugated Pipe," AASHTO T 249, American Association of State and Highway Officials, Washington, DC (2003).
11. Sritharan, S., Priestley, M.J.N., and Seible, F., *Seismic Response of Column/Cap Beam Tee Connections with Cap Beam Prestressing*, SSRP Report No. 96/09. University of California, San Diego, La Jolla, CA (December 1996) 296 pp.
12. XTRACT, User's Manual, TRC/Imbsen Software Systems, Rancho Cordova, CA (2006).
13. Chopra, A. K., *Dynamics of Structures: Theory and Applications to Earthquake Engineering*, Prentice Hall (2000).

14. Matsumoto, E.E., Waggoner, M.C., Sumen, G., Kreger, M.E., Wood, S.L., and Breen, J.E., *Development of a Precast Bent Cap System*, Research Report 1748-2, Center for Transportation Research, The University of Texas at Austin, TX (January 2001) 372 pp.
15. Matsumoto, E.E., Waggoner, M.C., Kreger, M.E., Vogel, J., Wolf, L., "Development of a Precast Concrete Bent-Cap System," *PCI Journal*, Vol. 53, No. 3 (May-June 2008) pp.74-99.
16. Sritharan, S. "Improved Seismic Design Procedure for Concrete Bridge Joints," *Journal of Structural Engineering*, American Society of Civil Engineers, Reston, VA, Vol. 131, No. 9 (September 2005) pp. 1334-1344.
17. "Standard Specification for Steel Sheet, Metallic-Coated by the Hot-Dip Process for Corrugated Steel pipe," ASTM Designation A929/A929M-01, American Society for Testing and Materials ASTM Standards Vol. 01.01, Philadelphia, PA (2007).
18. American Association of State Highway and Transportation Officials. AASHTO LRFD Bridge Design Specifications (Third Edition), Washington, DC (2004, with 2006 Interims).

Notation

A_c	Cross sectional area of column (in^2)
A_L	Area of hysteretic loop for a complete cycle (push and pull) (kip-in)
A_R	Area of rectangle bounded by maximum loads and displacements of a complete hysteretic loop (kip-in)
B_{cap}	Thickness of the bent cap (in)
BS	Bar Slip (in)
CD	Column displacement (in)
CT	Component total for column displacement (in)
d_{bl}	Nominal diameter of longitudinal column reinforcing steel bars (in)
D_c	Diameter or depth of column in direction of loading (ft or in)
D'_c	Diameter or depth of column in direction of bending (ft or in)
E_c	Modulus of elasticity of concrete (ksi)
FC	Force control
f'_c	Nominal compressive concrete strength (ksi)
f'_{cg}	Nominal compressive grout strength (ksi)
FER	Fixed end rotation of column (in)
f_h	Average normal stress in the horizontal direction within a moment resisting joint (ksi)
f_v	Average normal stress in the vertical direction within a moment resisting joint (ksi)
f_y	Specified minimal yield stress (ksi)
G_c	Shear modulus of concrete (ksi)
h	Distance from c.g. of tensile force in column to c.g. of compressive force on the section (in)
H_{cap}	Height of bent cap (in)
h_i	Height of cell i (in)
h_j	Joint panel height (in)
h_1	Height of cell 1 (in)

$I_{e\,col}$ Effective moment of inertia of column (in^4)

$I_{t\,col}$ Transformed moment of inertia of column (in^4)

L_c Distance from critical section of column (bent cap soffit) to point of contraflexure (in)

L_{cap} Length of bent cap (in)

l_{ac} Length of column reinforcement embedded into bent cap (in)

l_i Distance from point of contraflexure of column to the midheight of cell I (in)

l_j Diagonal joint panel length (in)

l_1 Distance from point of contra flexure of column to the midheight of cell 1 (in)

l'_g Strain penetration length of cell 1 (in)

l_{sp} Equivalent strain penetration length taken as $0.022 f_y d_{bl}$ (in)

M_{YE} Theoretical column moment at effective yield based on moment-curvature analysis (kip-in or kip-ft)

M_{Yexp} Experimental first yield moment of column (kip-in or kip-ft)

p_c Principal compressive stress (ksi)

P_H Horizontal actuator force on side of column stub (kips)

p_t Principal tensile stress (ksi)

P_V Vertical actuator force on top of column stub (kips)

T_c Column tensile force (kip)

v_{jv} Nominal vertical shear stress in a moment resisting joint (ksi)

w_c Width of cell (in)

w_j Joint panel width (in)

γ_j Nominal vertical shear strain in a moment resisting joint (ksi)

Δ_{bs} Column displacement due to bar slip (in)

$\Delta_{bs,s}$ Bar slip displacement, south (in)

$\Delta_{bs,n}$ Bar slip displacement, north (in)

$\Delta_{F,i}$ Column Displacement due to flexure at cell i (in)

$\Delta_{F,1}$ Column displacement due to fixed end rotation at cell 1 (in)

$\delta h_{i,n}$ Column displacement of cell i, north (in)

$\delta h_{i,s}$	Column displacement of cell i, south (in)
δ_j	Increase in diagonal joint panel length (in)
δ'_j	Increase in diagonal joint panel length in direction perpendicular to l_j (in)
Δ_{jr}	Column displacement due to joint rotation (in)
$\delta_{jr,n}$	Vertical displacement of bent cap at north end of joint (in)
$\delta_{jr,s}$	Vertical displacement of bent cap at south end of joint (in)
Δ_{js}	Column displacement due to joint shear (in)
δ_n	Joint rotation displacement, north (in)
δ_s	Joint rotation displacement, south (in)
Δ_s	Column displacement due to column shear (in)
Δ_Y	System first yield displacement (in)
Δ_{ye}	Member effective yield displacement (in)
Δ_{YE}	System effective yield displacement (in)
ξ	Equivalent viscous Damping ratio
μ_D	Displacement ductility demand
φ	Column curvature (1/in)

List of Equations

Average joint shear strain	$\gamma_j = \frac{\delta_j - \delta'_j}{2l_j}\left(\frac{h_j}{w_j} + \frac{w_j}{h_j}\right)$
Average joint shear stress	$v_{jv} = \frac{T_c}{l_{ac}B_{cap}}$
Average principal angle in joint	$\theta_p = \frac{A_c}{2} tan^{-1}\left(v_{jv} / \frac{f_h - f_v}{2}\right)$
Average principal compressive stress in joint	$p_c = \frac{(f_h + f_v)}{2} + \sqrt{\left(\frac{f_h - f_v}{2}\right)^2 + {v_{jv}}^2}$
Average principal tensile stress in joint	$p_t = \frac{(f_h + f_v)}{2} - \sqrt{\left(\frac{f_h - f_v}{2}\right)^2 + {v_{jv}}^2}$
Column displacement due to bar slip	$\Delta_{bs} = \left(\frac{\Delta_{bs,s} - \Delta_{bs,n}}{D'_c}\right)\left(L_c + H_{cap}\right)$
Column displacement due to column shear (analytical)	$\Delta_s = \frac{P_H L_c}{0.9 A_c G_c}\left(\frac{E_c I_{tcol}}{E_c I_{ecol}}\right)$
Column displacement due to flexure at cell i	$\Delta_{F,i} = l_i \frac{\left(\delta h_{i,n} - \delta h_{i,s}\right)}{w_c}$
Column displacement due to joint rotation	$\Delta_{jr} = \frac{(\delta_n - \delta_s)}{w_j}\left(L_c + H_{cap}\right)$
Column displacement due to joint shear	$\Delta_{js} = \gamma_j\left(L_c - D_c \frac{\left(H_{cap}/2\right)}{L_{cap}}\right)$
Column curvature, cell i	$\varphi = \frac{\Delta_{F,i}/W_c}{l'_g}$
Column tensile force	$T_c = \frac{M_o^{col}}{h} = \frac{P_h L_c}{h}$

Equivalent viscous damping ratio	$\xi = \left(\frac{2}{\pi}\right)\left(\frac{A_L}{A_R}\right)$
Joint rotation angle	$\theta_{jr} = \frac{\delta_{jr,n} - \delta_{jr,s}}{D_c}$
Modified height of cell 1 accounting for strain penetration	$l'_g = l_{sp} + h_1\left(1 - 1.67\, {h_1}/{L_c}\right)$
System effective yield displacement	$\Delta_{YE} = \frac{M_{YE}}{M_{Yexp}}\Delta_Y$

University of California, San Diego

Department of Structural Engineering

Structural Systems Research Project

NCHRP 12-74 Hybrid Systems Final Report

By

Matthew J. Tobolski, Ph.D., P.E.

Graduate Student Researcher

José I. Restrepo, Ph.D.

Professor of Structural Engineering

Report Submitted to the National Cooperative Highway Research Program Under Contract No.
NCHRP Project 12-74

Department of Structural Engineering

University of California, San Diego

La Jolla, California 92093-0085

November 2009

DISCLAIMER

The opinions and conclusions expressed or implied in this report are those of the research agency. They are not necessarily those of the Transportation Research Board, the National Research Council, the Federal Highway Administration, the American Association of State Highway and Transportation Officials, or the individual states participating in the National Cooperative Highway Research Program.

EXECUTIVE SUMMARY

Throughout the United States and abroad, there are numerous bridge structures in need of structural repair or replacement to rectify deficiencies or enhance the operational performance of transportation networks. With ever increasing congestion and a public desire to minimize the impact of highway construction, accelerated bridge construction practices are becoming more prevalent. Precast concrete bridge system off many advantages over traditional cast-in-place methods and can help to meet the public desire to minimize the impacts of bridge construction. Precast concrete systems can accelerate construction, reduce environmental impacts, improve construction safety and provide structures that are more durable. Due to limited knowledge of the performance of precast systems in seismic events, their usage in regions susceptible to earthquake shaking has been limited.

In using precast concrete systems for bridge bent cap and column systems, additional improvements to seismic performance can be realized through innovative design practices. Traditional methods of precast construction aim at providing response similar to cast-in-place systems in which significant damage is allowed in specially detailed regions, which can sustain large inelastic deformations. However, an alternative method of seismic response can be achieved in precast systems using controlled rocking of the column and bent system. The use of controlled rocking response provides large deformation capacity while significantly reducing the damage to the column as well as reducing the residual deformation of the system. To achieve stable seismic response, a combination of unbonded post-tensioning and mild reinforcement are used to produce a system that can dissipate an appreciable amount of seismic energy, provide large displacement capacity, minimize structural damage and provide a system with reduced residual deformations. These systems of combined post-tensioning and mild reinforcement are classified as hybrid systems.

This report presents the findings of an extensive research program conducted under the National Cooperative Highway Research Program (NCHRP) Project 12-74, “Development of Precast Bent Cap Systems for Seismic Regions.” This includes an introduction of hybrid systems and literature review, development of prototype system, development of analytical approaches, design of test specimens, experimental efforts and results, and general design recommendations. Three hybrid details were investigated in this study and include: 1) conventional hybrid detail, 2) concrete filled pipe hybrid detail and 3) dual shell hybrid detail. Each detail was developed and designed to provide an enhancement to the constructability or seismic performance. These details are discussed extensively in the report.

This report is divided into seven chapters. Chapter 1 provides an introduction to the use of precast bent cap systems and detailed background about hybrid systems. Additionally, this chapter presents the basic components of the three hybrid details investigated. Chapter 2 presented the analytical approaches developed for this project relating to the prediction of lateral response for each hybrid detail. Chapter 3 provides background of the basis of the experimental efforts including the prototype bridge structure and associated cast-in-place control specimen. Chapter 4 provides complete details of the design, fabrication, erection, testing and experimental results for the conventional hybrid specimen. Chapter 5 provides complete details of the design, fabrication, erection, testing and experimental results for the concrete filled pipe hybrid specimen. Chapter 6 provides complete details of the design, fabrication, erection, testing and experimental results for the dual shell hybrid specimen. Chapter 7 presents a summary of the results from analytical and experimental efforts. Additionally, a summary of design recommendations developed through this research program are presented.

ACKNOWLEDGEMENTS

This research project was sponsored by the American Association of State Highway and Transportation Officials, in cooperation with the Federal Highway Administration, and was conducted in the National Cooperative Highway Research Program (NCHRP) under Project 12-74 “Development of Precast Bent Cap Systems for Seismic Regions”, which is administered by the Transportation Research Board of the National Research Council. This financial support is greatly acknowledged.

The authors would like to acknowledge the dedicated efforts and valuable comments of the NCHRP 12-74 Research Team, including: Dr. Eric Matsumoto (Co-PI), Mary Lou Ralls, Steve Mislinski, Jon Grafton and Dr. Nigel Priestley. In addition, the efforts of the NCHRP 12-74 Technical Advisory Group are greatly appreciated, including: Dr. Reid Castrodale, Bill Spence, Scott Harrigan, Lucian Bodgan, Daniel Tassin and Robert Gulyas. The insightful comments and guidance of the NCHRP 12-74 Project Panel are also greatly appreciated.

The experimental efforts described herein could not have been performed if not for the dedicated and skillful efforts of the staff at the Charles Lee Powell Structural Research Laboratories at the University of California, San Diego. The following individuals are acknowledged: Andrew Gunthardt, Dr. Chris Latham, Bob Parks, John Ward, Paul Greco, Mieko McCue, Tim Chow and Michelle Chen.

Industry support has greatly contributed to the success of this research program. Material donations were provided by the following companies: CMC Rebar Fabricators and CMC Fontana Steel (conventional reinforcement), Dywidag Systems International (post-tensioning hardware and strand) and Pacific Corrugated Pipe (corrugated pipe). Significant discounts were provided by the following companies: Pomeroy Corporation (precast member fabrication) and Tell Steel (stainless steel reinforcement).

TABLE OF CONTENTS

LIST OF FIGURES

LIST OF TABLES

NOTATIONS

A_{cs}	Shear area of concrete section, in^2
A_s	Area of energy dissipating reinforcement crossing joint, in^2
A_{ps}	Area of post-tensioning tendons crossing joint, in^2
A_t	Area of transverse reinforcement (spirals and hoops), in^2
c	Distance from extreme compression fiber to neutral axis at joint, in
C_c	Resultant compression force in concrete, kip
c_c	Distance from extreme unconfined fiber to extreme confined fiber, in
C_s	Resultant compression force in energy dissipating reinforcement, kip
d	Total diameter of concrete section, in
d_b	Diameter of energy dissipating reinforcement bar, in
d_c	Diameter of confined concrete core, in
d_s	Diameter of circle encompassing energy dissipaters, in
d_{ps}	Distance from extreme unconfined compression fiber to centroid of post-tensioning force, in
E_c	Modulus of elasticity of concrete, ksi
E_{ps}	Modulus of elasticity of post-tensioning steel, ksi
E_s	Modulus of elasticity of energy dissipating reinforcement, ksi
$E_{\sec}$	Secant modulus of elasticity of confined concrete at peak stress, ksi
f_c	Compressive stress in concrete, ksi
$f_c^{'}$	Unconfined concrete compressive strength, ksi
$f_{cc}^{'}$	Confined concrete compressive strength, ksi

f_l	Lateral confining stress provided by transverse reinforcement , ksi
$f_l^{'}$	Effective lateral confining stress provided by transverse reinforcement, ksi
f_{ps}	Stress in post-tensioning tendon, ksi
f_{psi}	Initial stress in post-tensioning tendon, ksi
f_s	Stress in energy dissipating reinforcement, ksi
f_u	Tensile strength of energy dissipating reinforcement, ksi
f_y	Tensile yield stress in energy dissipating reinforcement, ksi
f_{yt}	Tensile yield stress in transverse reinforcement, ksi
G_c	Concrete shear modulus, ksi
h	Total height of column, in
I_g	Gross moment of inertia of concrete section, in^4
K_e	Correction factor to determine effective lateral confining stress
L_{ups}	Length over which post-tensioning tendon is unbonded, in
L_{sp}	Length of strain penetration of energy dissipating reinforcement, in
L_u	Length over which energy dissipating reinforcement is deliberately debonded, in
M	Moment in section at joint, kip-in
M_s	Contribution of energy dissipating reinforcement to M, kip-in
M_y	Yield moment at joint (nominal flexural strength), kip-in
n_j	Number of fixed end connections in column (1 if fixed-pinned, 2 if fixed-fixed)
P	Effective dead load acting on column, kip
s	Spacing of transverse reinforcement, in
t_p	Thickness of steel shell, in

T_{ps}	Post-tensioning force, kip
T_{pse}	Post-tensioning force after short and long-term losses (end of service), kip
T_{pslp}	Post-tensioning force at limit of proportionality, kip
T_{psi}	Post-tensioning force at beginning of service life (end of construction), kip
T_s	Resultant tension force in energy dissipating reinforcement, kip
V	Shear in section at joint, kip
y_c	Location of resultant compression force in concrete, in
y_{sc}	Location of resultant compression force in energy dissipating reinforcement, in
y_{st}	Location of resultant tension force in energy dissipating reinforcement, in
α_c	Shape factor for resultant compression force in energy dissipating reinforcement
α_{cc}	Shape factor for equivalent stress block in confined concrete core
α_t	Shape factor for resultant tension force in energy dissipating reinforcement
β	Shape factor for depth of equivalent stress block in unconfined concrete core
β_{cc}	Shape factor for depth of equivalent stress block in confined concrete core
ε_c	Compressive strain at extreme concrete fiber
ε_{cc}	Strain in confined concrete at peak stress
ε_{cu}	Ultimate confined concrete compressive strain
ε_s	Strain in energy dissipater
ε_{su}	Uniform tensile strain in energy dissipater from monotonic testing
$\varepsilon^R{}_{su}$	Reduced ultimate tensile strain in energy dissipater
ε_{sut}	Ultimate tensile strain in transverse reinforcement

ε_y	Yield tensile strain in energy dissipater from monotonic testing
Δ	Total system displacement, in
Δ_f	System displacement due to elastic flexure, in
Δ_j	System displacement due to fixed end rotation at joint, in
Δ_{ps}	Elongation of post-tensioning tendon, in
Δ_s	Elongation of energy dissipaters, in
Δ_v	System displacement due to shear, in
θ_c	Angle in cross-section to location of equivalent stress block in concrete, radians
θ_j	Fixed end rotation at joint, radians
θ_{jy}	Yield fixed end rotation at joint, radians
θ_{ju}	Ultimate fixed end rotation at joint, radians
θ_s	Angle in cross-section to neutral axis, radians
ψ_t	Shape factor for location of resultant tension force in energy dissipaters
ψ_c	Shape factor for location of resultant compression force in energy dissipaters
ρ_s	Transverse reinforcement ratio

Chapter 1 Introduction

Throughout the United States, there is a great number of bridges that are in need of repair or replacement to rectify structural deficiencies and/or to meet the operational needs of a region (ASCE 2009). According to the U.S. Department of Transportation (2007), approximately 25% of the United States bridges are classified as either structurally deficient or functionally obsolete. Many of these bridges serve as key links in local and national transportation networks with severe impacts associated with bridge closures. In addition, a large portion of these bridges is located in regions where seismic loading needs consideration. To mitigate the impact of bridge construction and replacement in seismically active regions, innovative bridge systems must be developed that are robust, cost effective and constructible. For seismic response, a key element of a bridge system is the substructure, which must be capable of resisting force or displacement demands that are imposed during strong ground shaking.

A common mentality for developing new seismic bridge substructure systems is to create a system that mimics a traditional reinforced concrete substructure. The downfall to this mentality is the acceptance of significant structural damage due to seismic actions leading to potential long-term repairs or the need for complete structural replacement. An attractive alternative is the development of systems that can resist imposed seismic demands while experiencing limited structural damage. This goal can be achieved using hybrid structural systems using a combination of unbonded post-tensioning and steel reinforcement. These systems can resist seismic actions through controlled rocking of the structural system while dissipating energy through specially detailed reinforcing elements.

This report presents the results of a portion of the analytical and experimental program focused on three hybrid column details conducted under the National Cooperative Highway Research Program (NCHRP) Project 12-74, Development of Precast Bent Cap Systems for Seismic Regions. Three 42% scale specimens were constructed and subjected to quasi-static, hysteretic lateral loads to investigate the seismic resistance.

1.1 Overview

Conventional practice for the design of seismically resistant concrete substructure bridges is to allow non-linear response to occur in the form of flexural plastic hinging of properly detailed reinforced concrete columns (Caltrans 2006)(Priestley, Seible and Calvi 1996)(AASHTO 2009). Both experimental and post-earthquake assessments have shown this method of seismic response

to be satisfactory in preventing the collapse of structures when subjected to seismically induced displacement demands (Priestley, Seible and Calvi 1996). The fundamental basis of this form of non-linear response is allowing damage to occur in the supporting bridge columns as a means to facilitate large deformations, dissipate energy and limit force demands to other structural components. The underlying basis for typical designs is that the primary system resisting seismic loading should exhibit a “fat” hysteresis behavior such that significant energy can be dissipated through cycled response. However, the notion of hysteretic energy dissipation means that one expects significant damage to occur during the design level earthquake and alludes to the need for significant post-event repairs or, in the extreme case, complete replacement of the structure. A promising approach to resist seismically induced displacement demands with significantly less damage is using controlled rocking of bridge columns (Priestley and Tao 1993). Key features of properly designed rocking systems include: i) significantly less structural damage and ii) negligible residual deformations (i.e. self-centering system).

Conventionally, the non-linear behavior of a reinforced concrete column is facilitated through the distribution of inelastic actions into the column some distance, termed the spread of plasticity (Hines, Restrepo and Seible 2004). Conversely, in a rocking system the non-linear response is developed through the opening of discrete joints at the column ends. The restoring force of a rocking system is attributed to the combination of gravity loads acting on the column and post-tensioning. Post-tensioning is deliberately left unbonded to reduce the increase in stress in the tendon during joint opening as a means to ensure the tendon remains elastic for as long as possible. The concept of rocking systems can be further divided into two primary categories: jointed and hybrid.

Jointed systems rely solely on post-tensioning and gravity loads to resist seismic demands as the joint opens. During idealized response, this type of system would rock back and forth with little to no energy dissipation. The non-linear response in this case can be characterized as non-linear, elastic with the system unloading along the same path as during loading (see Figure 1.1). The non-linear behavior of a joint system is provided by the joint opening, though it is difficult to predict this hysteretic response accurately due to the extreme sensitivity of the effective yield point, especially in a dynamic context.

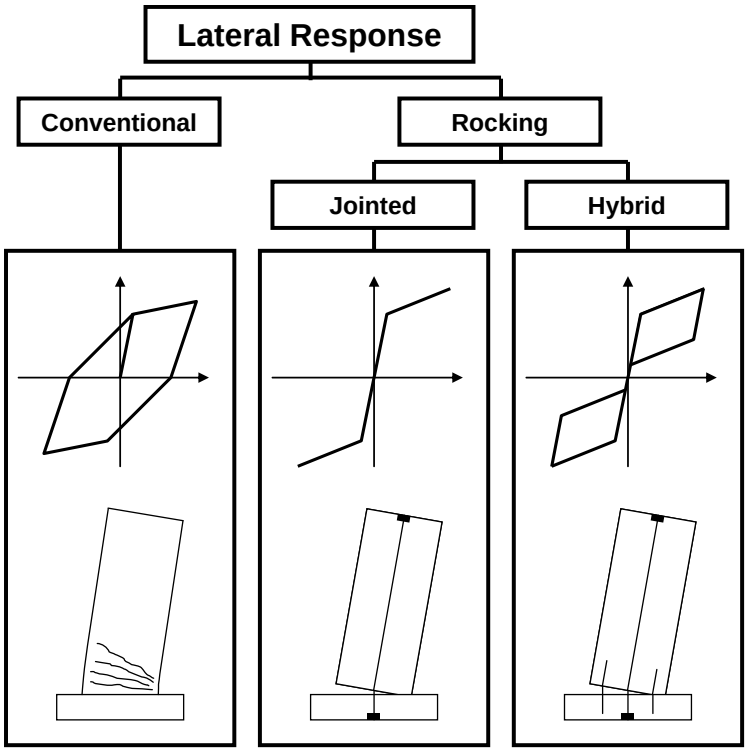

Figure 1.1 An overview of idealized lateral response for various concrete columns

Hybrid systems are an extension of the jointed concept with the main difference being that hybrid systems employ a combination of both unbonded post-tensioning and specially detailed energy dissipaters. The characteristic response of a purely jointed system lacks any appreciable amount of energy dissipation, thus it is desirable to include addition elements aimed at increasing the ability of a rocking system to absorb seismic energy. The idealized hysteretic response of a hybrid system, as shown in Figure 1.1, is commonly referred to as flag-shaped where some level of hysteretic energy dissipation capacity is observed depending on the amount of energy dissipation reinforcement included. The energy dissipaters must be designed and detailed to ensure the bars do not fracture prior to achieving the design displacement to ensure the system can still self-center.

1.2 Background

The first formal development of the rocking concept was formulated by Priestley and Tao (1993) where they investigated the behavior of building moment frames incorporating partially unbonded post-tensioning tendons. That research program was spurred by a structure that was constructed in 1981 over the South Rangitikei River in New Zealand, which was specifically designed to rock during an earthquake (Priestley, Seible and Calvi 1996). The focus of the work

by Priestley and Tao was to analytically investigate the seismic response and potential use of concrete systems incorporating unbonded post-tensioning. Building on this initial work, MacRae and Priestley (1994) conducted experimental work on beam-column subassemblages incorporating these unbonded post-tensioning details. The initial system considered was a purely jointed rocking system incorporating no energy dissipaters across the joints. Based on the promising results from these initial studies, another project was soon conducted on a rocking system incorporating mild reinforcement across the joint to act as energy dissipation (Stone, Cheok and Stanton 1995). The promising results from the aforementioned studies resulted in the funding of the PREcast Seismic Structural Systems (PRESSS) program in which an array of precast rocking systems was investigated (Priestley, Sritharan, et al. 1999). All of this work related to the use of rocking systems eventually led to the construction of a 39-story hybrid structure in the high seismic region of San Francisco, CA (Englekirk 2002). The early development of rocking systems was focused on implementation in building frame systems; however, there has been a fair deal of interest in the use of rocking systems in bridges in the past decade.

One of the first major projects considering the use of rocking systems for bridge piers was carried out by Mander and Cheng (Mander and Cheng 1997) where the experimental response of bridges incorporating unbonded post-tensioning was studied. This project was followed by an experimental program conducted by Hewes and Priestley (2002) in which they investigated the response of segmental bridge piers incorporating unbonded post-tensioning. Following this work, a variety of analytical studies were carried out aimed at considering the potential extension of rocking systems for use in bridge piers (Kwan and Billington, Unbonded Posttensioned Concrete Bridge Piers. I: Monotonic and Cyclic Analyses 2003) (Kwan and Billington 2003) (Sakai and Mahin, Analytical Investigations of New Methods for Reducing Residual Displacements of Reinforced Concrete Bridge Columns 2004) (Palermo, Pampanin and Calvi 2004) (Heiber, et al. 2005). Shake table testing of cast-in-place hybrid concrete bridge substructure systems was performed to consider the dynamic response characteristics of these systems (Sakai, Hyungil and Mahin 2006). This work confirmed the potential benefits of using unbonded post-tensioning including reduced damage and significant reduction of residual drifts following even strong intensity ground shaking.

More recently, the American Concrete Institute published design requirements for the use of hybrid precast shear wall systems for seismic resistance (ACI 2009). This report provides recommendations for the design and detailing of all components of a precast shear wall system.

Many of the design requirements presented in this report are similar to those developed under this project.

1.3 Hybrid Details Investigated

As a part of NCHRP Project 12-74, three hybrid details were developed for investigation. Each unit is designed and detailed such that it will exhibit the beneficial characteristics of a hybrid specimen with distinct details aimed at improving response. All of these specimens were designed to be precast such that the column and bent cap are fabricated independently and connected on-site. These three specimens are referred to in this report as:

- Conventional Hybrid Specimen (or “HYB-1”)
- Concrete Filled Pipe Hybrid Specimen (or “HYB-2”)
- Dual Shell Hybrid Specimen (or “HYB-3”)

The conventional hybrid specimen is intended to have the least differences as compared to an emulative precast assembly using a grouted duct connection. Spiral reinforcement is used to confined the column ends along with provide shear reinforcement over the length of the specimen. Unbonded post-tensioning is used in combination with a lesser amount of mild reinforcement as compared to emulative systems. The mild reinforcement runs full height of the column section and acts as primary reinforcement in the mid-height of the section in addition to the post-tensioning. This reinforcement is locally debonded at the column ends to reduce strain levels imparted on the reinforcement due to localized joint opening.

Concentrated end rotations due to joint openings result in significant compressive strains in the concrete. To facilitate these large strain levels, significant spiral or hoop reinforcement is required locally at column ends. Outside of the highly strained end regions, the volumetric fraction of spirals or hoops can be reduced as needed to provide adequate shear resistance.

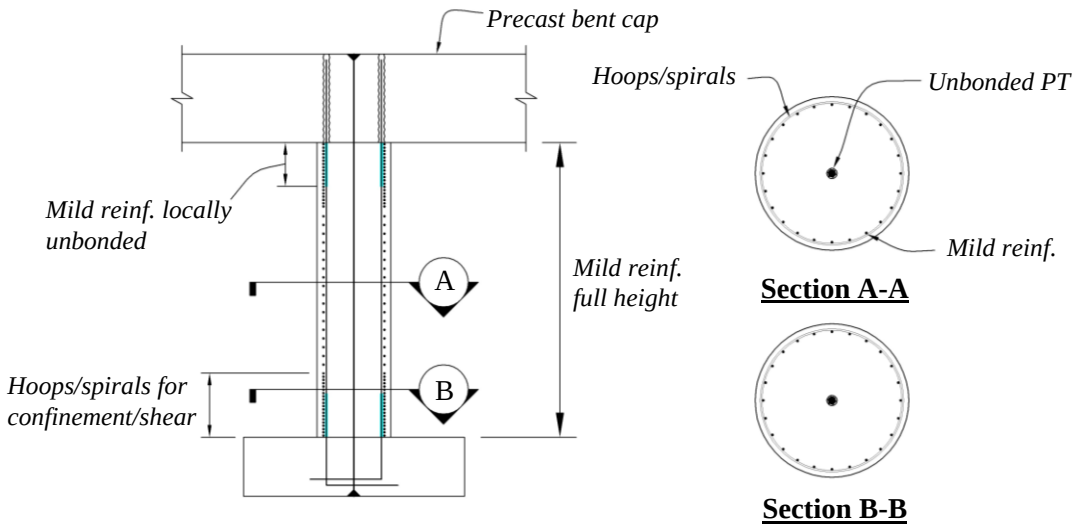

Figure 1.2 HYB-1 System overview

The concrete filled pipe hybrid specimen was developed to facilitate easier fabrication of the column by using a full height steel jacket. In addition, the steel jacket will provide enhanced confinement effects and reduce the damage under lower level seismic events. The steel jacket is designed to act as the confinement reinforcement at the column ends in addition to the shear reinforcement over the entire height of the column. Additionally, the jacket is specially detailed to act as longitudinal reinforcement over the height of the column. Mild reinforcing bars are only used at the column ends to facilitate the dissipation of seismic energy through cyclic yielding and are discontinued in the column once adequate development is achieved.

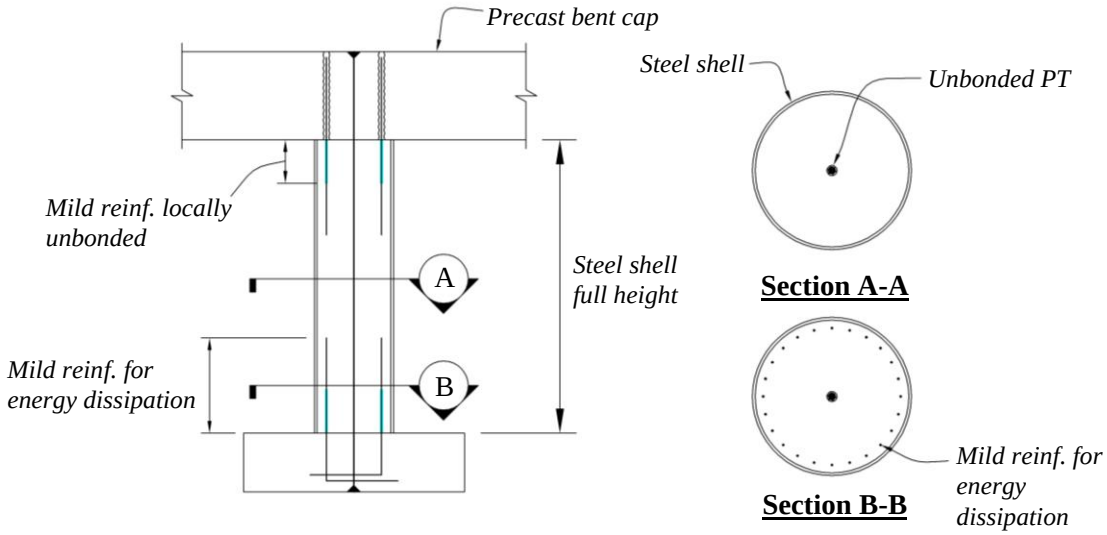

Figure 1.3 HYB-2 System overview

The dual shell hybrid specimen is an extension of the concrete filled pipe hybrid specimen. Review of the concrete filled pipe specimen indicated excellent promise for enhanced seismic behavior; however, the specimen is still relatively heavy for precast construction. To mitigate this problem, the dual shell specimen was developed which is essentially a hollow core column. A steel jacket is used on the outside of the column in the same manner as the concrete filled pipe specimen. However, on the inside of the column a corrugate metal pipe was used to form the interior void and prevent implosion of the column under large compressive stresses.

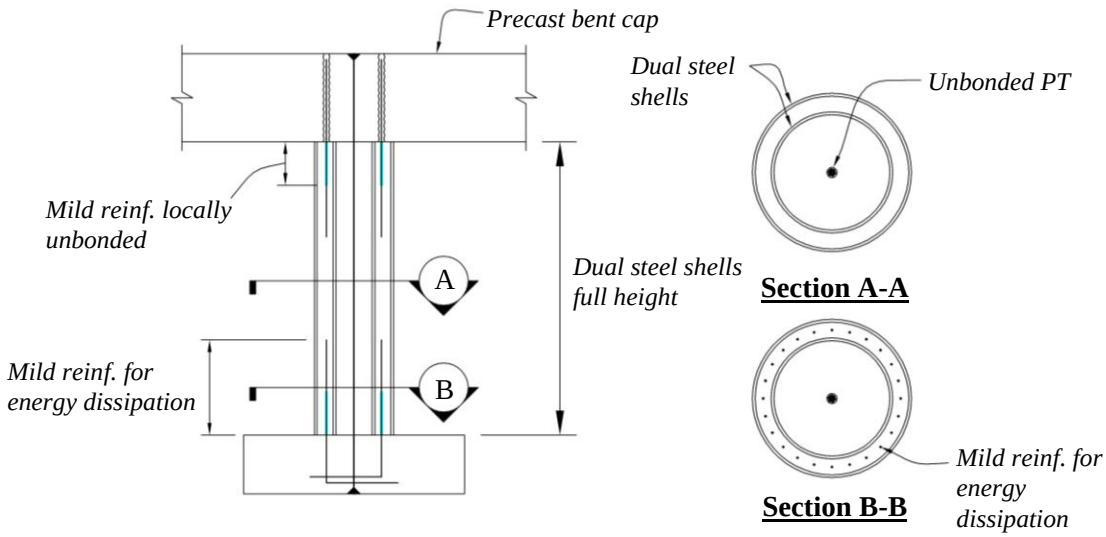

Figure 1.4 HYB-3 System overview

More in depth details of each test unit are provided in the following chapters included detailed description of seismic performance.

1.4 Scope of Report

This report is focuses on the analytical and experimental work conducted on the hybrid precast bent cap units developed under NCHRP Project 12-74. The report is divided into the following sections:

- Section 1: Introduction
    - Provides a discussion of relevant background to the project and hybrid systems in general
    - Outlines the general characteristics of the test units under consideration
- Section 2: Design Approach

    - Provides an overview of the analytical techniques used in the design and analysis of the hybrid units
- Section 3: Experimental Basis
    - Provides a summary of the development of test specimens according to a prototype structural design
- Section 4: Conventional Specimen
    - Provides a summary of the specimen design, fabrication and testing including system response
- Section 5: Concrete Filled Pipe Specimen
    - Provides a summary of the specimen design, fabrication and testing including system response
- Section 6: Dual Steel Shell Specimen
    - Provides a summary of the specimen design, fabrication and testing including system response
- Section 7: Discussion and Design Recommendations
    - Provides a discussion of the observed structural performance and associated design recommendations

Chapter 2 Design Approach

An essential element for the use of hybrid bridge systems in practice is a simplified approach for the seismic design of these innovative systems. This section presents two analytical methods for characterizing the response of hybrid bridge columns that could be used in practice.

2.1 Mechanics Considerations

When characterizing the response of a hybrid bridge column, a variety of fundamental principles must be considered. At specified demand levels there are certain basic behavioral characteristics of hybrid systems that can be achieved through proper design and detailing, including the prevention of: (i) tendon yielding, (ii) fracture of reinforcing steel and (iii) crushing of the confined concrete core. The lack of bonding of reinforcement across the joint regions results in a lack of strain compatibility resulting in difficulties when considering concrete strain levels. The following section provides appropriate background information regarding key components affecting the response of a hybrid system, as well as the proper consideration of system deformations.

2.1.1 Control of Concrete Strains

For the hybrid systems discussed herein, rebar is locally debonded at the beam-to-column interface in order to limit the tensile strains and prevent premature fracture of the rebar. With the tendons also be unbounded over the entire length, strain compatibility at the joint cannot be considered. Without strain compatibility, there are complications in considering the strain state in the compressed concrete toe during rocking response. As the column rocks, the concrete must deform over the compressed region as a means to facilitate base rotations. To accommodate this deformation, the concrete must have distributed localized straining in the column. Based on previous experimental work by Restrepo and Rahman (Restrepo and Rahman 2007) and confirmation through experimental efforts of this study, it is conservatively assumed that there is approximately uniform strain vertically into the column a distance equal to the neutral axis depth, see Figure 2.1. Results from this study indicate the distribution of compressive strain is over a smaller region; however, this will increase the actual lateral capacity.

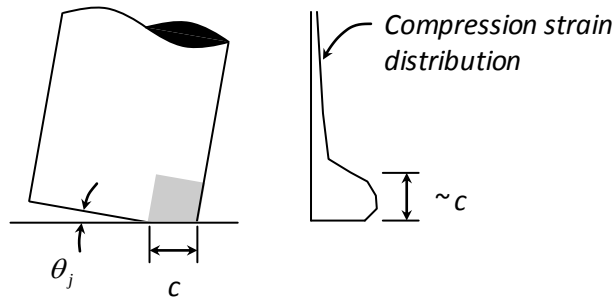

Figure 2.1 Assumed compression strain distribution

Based on the approximated region of uniform compression strain, the joint rotation and average strain can be related by the following relationship:

$$\tan\theta_j \cong \theta_j = \frac{\varepsilon_c\, c}{c} = \varepsilon_c \qquad 2\text{-}1$$

See the Notation section for a description of all variables used in this report. This requirement is bars on the previous research conducted by Restrepo and Rahman on precast hybrid shear wall systems (2007). For the remainder of this report, all tangent terms modifying small angles such as base rotation will be represented directly by the angle (in radians) as these angles are adequately small.

As the majority of the deformation of a hybrid system is attributed to base rotation, the need for greater confinement to facilitate adequate displacement capacity at the collapse prevention performance objective is apparent from Equation 2-1. In other words, the ultimate rotation is related directly to the ultimate concrete compressive strain from the design standpoint. As the facilitation of large drifts is thereby related to the level of confinement detailing used, alternate methods to confine concrete aside from hoop reinforcement should be considered. An appropriate level of confinement can be easily achieved using an external steel shell, as investigated by researchers in the past (Hewes and Priestley 2002).

In addition to providing greater levels of confinement, care must be taken to control the neutral axis depth during lateral shaking. To minimize the magnitude of strains in the confined concrete core, the neutral axis depth should be limited to approximately 25% of the confined concrete core dimension. If one assumes that the plane sections analogy can be considered for this type of system, it is evident that for the same lateral displacement demand a system with a deeper neutral axis will undergo significantly greater concrete strains. Larger strains in the concrete core will

lead to greater residual straining of the confined core and an overall reduction in the self-centering capacity.

2.1.2 Control of Post-Tensioning Stress

A characteristic of a hybrid system is the opening of discrete joints at the column ends during lateral response. The opening of these joints results in the elongation of the post-tensioning tendons and consequently an increase in the stress during increasing lateral displacements. For a hybrid system to preserve its self-centering ability, the post-tensioning tendons should preferably remain elastic up to the design level displacement, thus there must be explicit control over the stresses induced in the tendon during rocking response.

When considering the placement location of the post-tensioning tendons, the nature of earthquake actions must be considered. As seismically induced demands can cause the bridge column to displace in any direction, the tendons are best placed in the middle of the column to produce a system that has the lowest chance of overstressing the tendons during lateral shaking.

A typical cross-section of a conventionally confined hybrid bridge column is shown in Figure 2.2. As the column rocks during lateral motion, following the spalling of cover concrete, the corresponding elongation of the post-tensioning tendon is:

$$\Delta_{ps} = n_j \theta_j (d_{ps} - c_c - c) \qquad 2\text{-}2$$

The formulation presented in Equation 2-2 is based on the assumption that the top and bottom joint rotations are roughly equal which is a valid assumption for most bridge substructures. If there was a significant variation in axial load between the top and bottom joints of a bridge column, the assumption may not be valid.

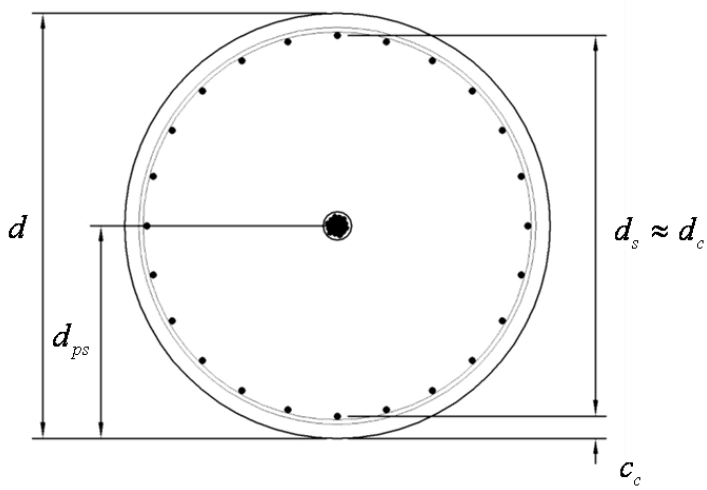

Figure 2.2 Cross-section of hybrid column

The tendon elongation is converted to stress as:

$$f_{ps} = f_{psi} + n_j \theta_j E_{ps} \frac{d_{ps} - c_c - c}{L_{ups}} \qquad 2\text{-}3$$

A limit on the initial post-tensioning force is imposed too ensure the post-tensioning tendon does not yield prior to achieving the desired ultimate lateral displacement capacity. The maximum post-tensioning force in a given tendon is determined by assuming the tendon reaches the limit of proportionality as the concrete reaches its ultimate strain. The maximum force is calculated by combining Equations 2-1 and 2-3 and is calculated as:

$$T_{psi} \leq T_{pslp} - n_j \varepsilon_{cu} E_{ps} A_{ps} \frac{d_{ps} - c_c - c}{L_{ups}} \qquad 2\text{-}4$$

From this equation it is apparent that the maximum initial post-tensioning level is dependent on the loading and geometric configuration (i.e. it is dependent on the neutral axis depth at ultimate). If the initial post-tensioning force is greater than this level, then the post-tensioning tendons will yield prior to reaching the ultimate confined concrete strain. Thus, a reduction in self-centering ability will be observed as the system approaches the ultimate state. If the initial post-tensioning force for a tendon is less than this value, the post-tensioning force is expected to remain elastic up to the displacement level associated with the ultimate concrete compressive strain.

2.1.3 Design of Mild Reinforcement for Dissipation

Prior research has shown that the response of rocking systems that do not employ any form of energy dissipation devices (such as mild reinforcement) typically result in larger displacement demands and difficult to predict response characteristics (Toranzo 2002). The use of specifically detailed energy dissipation devices in a rocking system provides a means to increase the ability of a hybrid system to dissipate seismic energy and can result in more reliable response predictions. These elements must be properly designed and detailed to preclude premature fracture and to ensure these elements can be forced back to a zero displacement state following large displacement excursions.

A variety of details can be employed to act as energy dissipation devices. The simplest method, and that which is used in this experimental program, is to use reinforcing steel that is locally debonded at the joint. In this study, reinforcing stainless steel is used to cross the joint region with the steel wrapped with bond breaker to allow for distributed straining along the reinforcing bar. As the stress state in these reinforcing bars will approach ultimate at large lateral displacements, significant bond stresses will develop in the bonded portion of the bar. This will result in yield penetration and the formation of tensile cracks in the column as bond develops. Additionally, there will be yield penetration into the bent cap. These facts will result in an increase in the effective debond length under large deformations.

A possible means to prevent bond cracks and significant yield penetration is the milling of the reinforcing bar over the debonded regions. By milling the bars, the bond stresses that must develop are reduced due to the relative increase in the cross-sectional perimeter along the bonded portion of the bar. This method provides less damage to the column by minimizing cracking associated with the development of reinforcement. However, the costs associated with milling are likely to cause minimal use in practice.

During cyclic response of a hybrid system, the energy dissipaters should remain intact to facilitate the dissipation of seismic energy and ensure minimal post-event repairs are required. Similar to post-tensioning, these elements undergo elongation during seismic loading. For the purposes of this report, it is assumed that the energy dissipaters will be distributed about the column similar to conventionally reinforced concrete columns. The elongation of the extreme energy dissipation element in tension at the ultimate state is:

$$\Delta_s = \left(\frac{d_c + d_s}{2} - c \right) \theta_{ju} \cong \left(d_s - c \right) \varepsilon_{cu} \qquad \text{2-5}$$

Note that the diameter of the confined concrete core can be considered roughly equal to the diameter over which the energy dissipaters are placed. This simplification will be made for the remainder of this report. The associated strain in the extreme dissipater is:

$$\varepsilon_s = \frac{\Delta_s}{L_u + L_{sp}} = \frac{\left(d_s - c\right)\varepsilon_{cu}}{L_u + L_{sp}} \qquad 2\text{-}6$$

Prior research indicates that the length of strain penetration can be taken as (Priestley, Seible and Benzoni, Seismic Performance of Circular Columns with Low Longitudinal Steel Ratios 1994):

$$L_{sp} = 0.15 f_y d_b \qquad 2\text{-}7$$

Considering a specified maximum permitted strain in the energy dissipater, the minimum unbounded length of the energy dissipaters is:

$$L_u \geq \frac{\varepsilon_{cu}}{\varepsilon^R_{su}}\left(d_s - c\right) - L_{sp} \qquad 2\text{-}8$$

To consider an appropriate value for the specified maximum permitted strain in the energy dissipater, the use of mild reinforcing bars is considered. When loaded cyclically with plastic straining in both the tension and compression regime, conventional mild reinforcing bars cannot achieve the same ultimate uniform tensile strains that they can if loaded monotonically to failure. This behavior was investigated in depth by previous researchers who conducted a series of cyclic tests on mild reinforcing bars (Dodd and Restrepo-Posada 1995). Results from this study indicated that the maximum uniform strain obtained from a monotonic test is essentially a strain range, which shifts when the bar is cycled into compression.

Additionally, the uniform tensile strain considered must also be reduced to account for the fact that the reinforcing bars also undergo flexural deformations during joint opening (Holden, Restrepo and Mander 2001). For simplification, the influence of bar flexure is accounted for through the reduction of the usable strain by one-third.

The reduction in the ultimate tensile strain due to load reversals is calculated by considering the strain range a bar is subjected to during a single reversal. Figure 2.3 shows the strains of the extreme energy dissipaters at the ultimate state assuming a linear strain distribution across the section in the dissipaters at the base. Based on the linear distribution of strains, the shift in the ultimate tensile strain is shown in Figure 2.4 (Paulay and Priestley 1992).

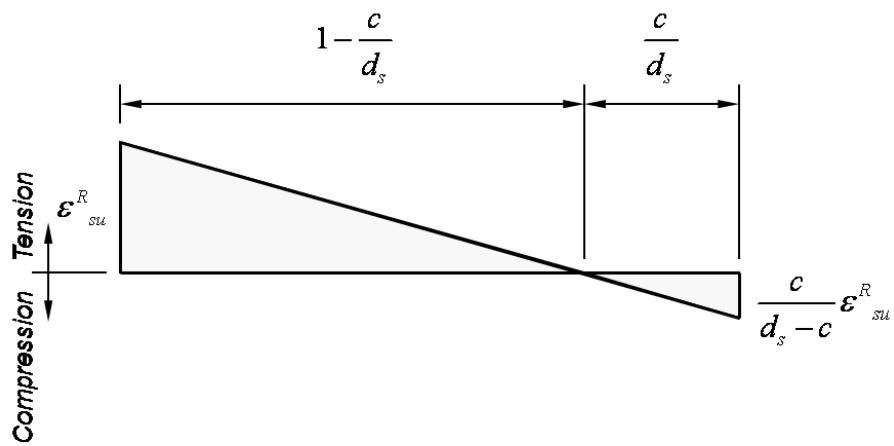

Figure 2.3 Strain in mild reinforcement

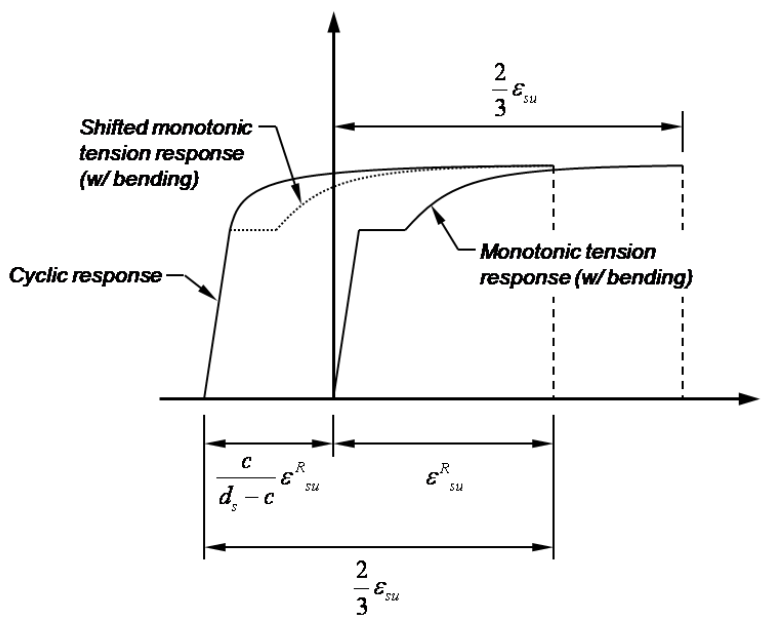

Figure 2.4 Kato's strain shift of ultimate tensile strain in mild reinforcement

The following relationship can be derived for the maximum usable tensile strain in the mild reinforcing bars:

$$\varepsilon^R_{su} = \frac{2}{3}\varepsilon_{su}\left(1-\frac{c}{d_s}\right) \qquad 2\text{-}9$$

As previously discussed, it is desirable to have a hybrid system in which the neutral axis depth is limited to 25% of the confined concrete core dimension. From Equation 2-9 it is calculated that the resulting usable tensile strain in the mild reinforcing bars is approximately one half that

determined from monotonic testing. This value is less than recommendations of the AASHTO Guide Specifications for LRFD Seismic Bridge Design, which state that the usable tensile strain is 75% of the ultimate tensile strain from monotonic testing (AASHTO 2009).

To ensure the hybrid system is able to self-center following the maximum displacement excursion, the reinforcing bar must be yielded back to a nominally zero strain state. Considering the cyclic nature of a conventional reinforcing bar, this means that a compressive force of the order of the ultimate tensile force in the bars must be applied to bring the bars back to a zero strain state. The gravity load in the column, in combination with the effective post-tensioning force, is responsible for providing the required restoring force. To ensure the reinforcing bars can be forced to a near zero strain state, the following relationship must be satisfied:

$$0.9P + T_{pse} \geq \alpha_t A_s f_u \qquad \text{2-10}$$

This equation is a function of the total tensile force in the energy dissipation devices at the ultimate state, which is only a portion of the total tensile capacity of the energy dissipaters (i.e. not all bars are at the ultimate state in tension). The requirements of ACI ITG-5.2-09 provide a similar requirement to ensure the mild reinforcement returns to a zero strain state (ACI 2009):

$$0.9P + T_{pse} \geq A_s f_u \qquad \text{2-11}$$

However, in the ACI requirements, it is expected that the majority of mild reinforcement is placed at the center of the column and will subsequently all experience tensile strains. In the circular column systems considered in this project, the reinforcement is distributed around the diameter of the column and thus a smaller portion of the total reinforcement at ultimate is considered.

A reasonable and conservative estimate of this force is used to simplify the previous equation:

$$0.9P + T_{pse} \geq 0.75 A_s f_u \qquad \text{2-12}$$

Using this relationship, the maximum area of mild reinforcing bars to ensure the system can self center is:

$$A_s \leq \frac{4}{3}\left(\frac{0.9P + T_{pse}}{f_u}\right) \qquad \text{2-13}$$

Additionally, to achieve reliable hybrid response there must be adequate contribution from the energy dissipaters. To consider this requirement, a minimum response contribution is required, specified in terms of flexural moment contribution at effective yield:

$$\frac{M_s}{M_y} = \frac{T_s y_{st} + C_s y_{sc}}{M_y} \geq 0.25 \qquad \text{2-14}$$

The flexural moment contribution from the energy dissipaters includes the dissipaters in both tension and compression. The design requirements of ACI ITG-5.2-09 provide a similar requirement that the energy dissipation reinforcement accounts for at least 25% of the nominal flexural strength (ACI 2009).

2.2 Simplified Analysis Method

The lateral force-deflection response of a hybrid system can be represented with reasonable accuracy by considering a bi-linear function. From a behavioral standpoint, the key points used to define the force-deflection response are the effective yield and the ultimate state. For both conditions, the basic premise used to determine the response characteristics is the same and is simply imposing equilibrium conditions across the section at the joint. This method lends itself to the use of a conventional computer program such as MathCAD or Microsoft Excel. The following section describes the method for determining the force-displacement response.

2.2.1 Ultimate Limit State

The main criteria for defining the ultimate limit state are to ensure that the bridge does not collapse or pose significant risk to the public. For the purposes of the hybrid systems considered herein, this limit state not only focuses of the protection of life, but also on the ability to self-center up to this displacement level.

Based on previous discussions, an initial post-tensioning force can be specified in a tendon that will result in an ultimate state where the post-tensioning reaches the limit of proportionality as the confined concrete core begins crushing. The initial post-tensioning force can be calculated using Equation 2-4. To calculate this force, the neutral axis depth must first be determined through consideration of equilibrium of forces at the joint.

To determine the neutral axis depth at the ultimate state, it is assumed that the post-tensioning tendon is at the limit of proportionality. Additionally, at the ultimate state the assumption is made that the extreme energy dissipater is at its ultimate tensile strain. Figure 2.5 depicts the assumed distribution of stresses at the ultimate limit state. As the mild reinforcing bars are distributed around the section, the total tension and compression forces in these elements are a function of the neutral axis depth.

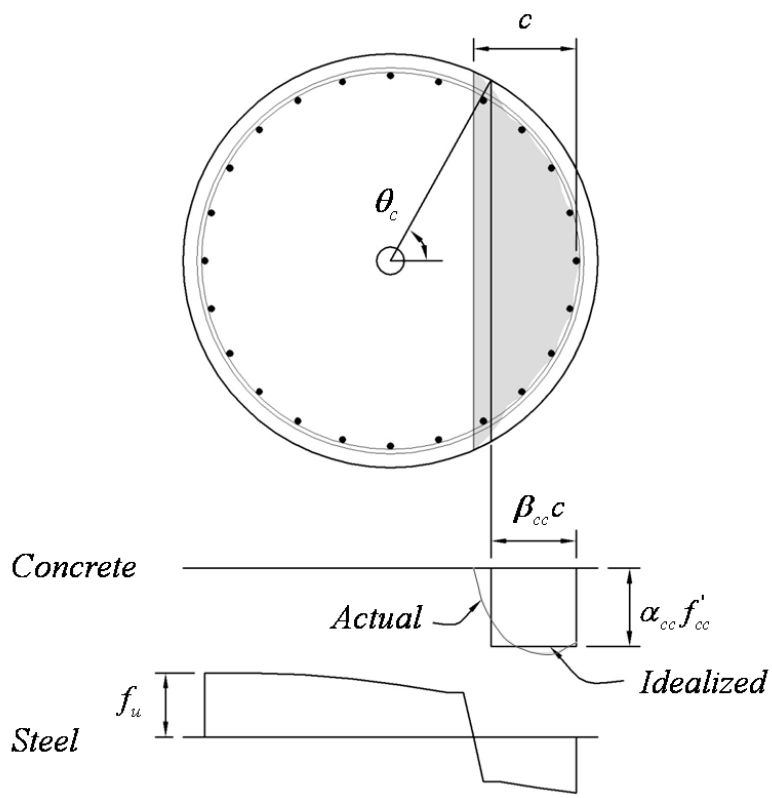

Figure 2.5 Assumed material stress distributions at ultimate limit state

The resulting force in the energy dissipaters is calculated as:

$$T_s = \alpha_t A_s f_u \qquad \text{2-15}$$

and,

$$C_s = \alpha_c A_s f_u \qquad \text{2-16}$$

The shape factors in the preceding equations account for the distribution of stresses in the reinforcing bars that are distributed around the section. For conventional reinforcing steel, the following approximate equations can be used:

$$\alpha_t = 0.8 - 0.35\frac{c}{d_s} \qquad \text{2-17}$$

and,

$$\alpha_c = 0.05 + 0.4\frac{c}{d_s} \qquad \text{2-18}$$

The net compressive force in the concrete is determined using an assumed rectangular stress block, similar to what is done for conventional concrete design, except confinement effects are also considered. At the ultimate limit state, it is assumed that the unconfined concrete cover will have spalled and is neglected in determining the net resultant force. To consider the behavior of confined concrete, the Mander model is considered (Mander, Priestley and Park, Theoretical Stress-Strain Model for Confined Concrete 1988). The uniform stress used when considering an equivalent uniform stress block differs for confined concrete when compared to the typical unconfined concrete model used in practice. Figure 2.6 shows the influence of confinement properties on the uniform stress and depth of the rectangular stress block, based on the text of Pauley and Priestley (Paulay and Priestley 1992).

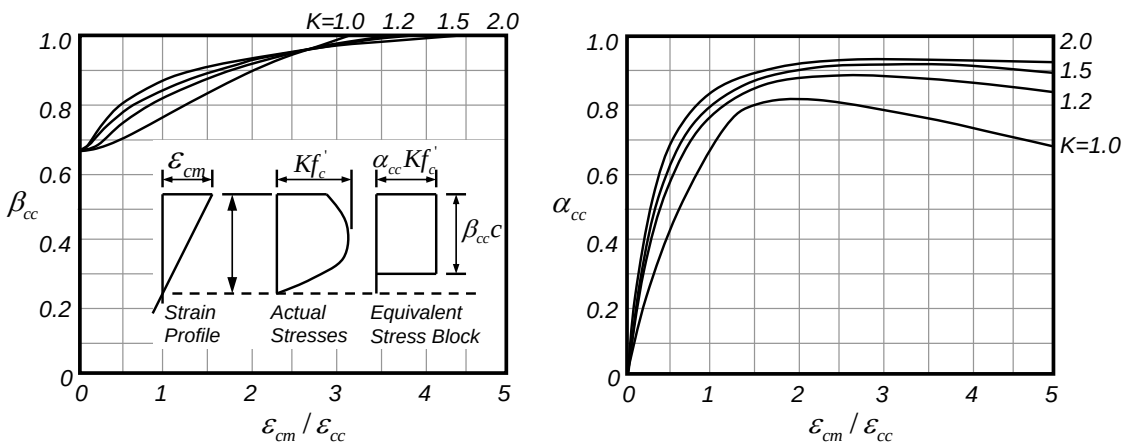

Figure 2.6 Equivalent stress block factors (Paulay and Priestley 1992)

Considering a uniform stress block acting over a portion of the confined concrete core in a circular cross-section, the resultant compressive force in the confined concrete is:

$$C_c = \alpha_{cc} f_{cc}^{'} d_s^{\,2} \frac{\theta_c - \sin\theta_c \cos\theta_c}{4} \qquad \text{2-19}$$

where,

$$\theta_c = \cos^{-1}\left(\frac{d_s - 2\beta_{cc}c}{d_s}\right) \qquad \text{2-20}$$

The neutral axis depth is determined considering equilibrium across the joint:

$$T_s + T_s + P = C_c + C_s \qquad \text{2-21}$$

Based on Equation 2-4, the maximum post-tensioning force can be calculated to determine the maximum initial post-tensioning force that should be applied. With an initial post-tensioning force less than or equal to the maximum value, the failure mode at the ultimate state is assumed to be crushing of the confined concrete core. With a selected initial post-tensioning force, the force in the post-tensioning can be determined again considering equilibrium across the joint:

$$T_{ps} = T_{psi} + \varepsilon_{cu} E_{ps} A_{ps} \frac{d_{ps} - c_c - c}{L_{ups}} \qquad 2\text{-}22$$

The flexural moment at the ultimate limit state is determined considering moment equilibrium across the joint. To achieve this, the location of the resultant forces must be determined. For this procedure, the moments will be summed about the centerline of the column through which gravity and post-tensioning forces are assumed to act. The location of the resultant forces in the energy dissipation elements are:

$$y_{st} = \psi_t d_s \qquad 2\text{-}23$$

and,

$$y_{sc} = \psi_c d_s \qquad 2\text{-}24$$

The shape factors for the location of the resultant forces can be approximated as:

$$\psi_t = 0.10 + 0.24 \frac{c}{d_s} \qquad 2\text{-}25$$

and,

$$\psi_c = 0.50 - 0.16 \frac{c}{d_s} \qquad 2\text{-}26$$

For the confined concrete core, the location of the resultant compressive force for a rectangular stress block is:

$$y_c = \frac{d_s \sin^3 \theta_c}{3\left(\theta_c - \sin\theta_c \cos\theta_c\right)} \qquad 2\text{-}27$$

From moment equilibrium at the joint, the flexural moment at the ultimate limit state is:

$$M = C_c y_c + C_s y_{sc} + T_s y_{st} \qquad 2\text{-}28$$

with the associated base shear of:

$$V = \frac{M}{h/n_j} = \frac{C_c y_c + C_s y_{sc} + T_s y_{st}}{h/n_j} \qquad 2\text{-}29$$

The flexural and shear demands can then be used to determine the associated deflection at the ultimate limit state. Additionally, the minimum required debond length is also calculated at this time using Equation 2-8. It is important to note that any debond length significantly greater than the required length calculated may influence the lateral force capacity through reduction in the force resisted by the energy dissipaters.

2.2.2 Effective Yield Limit State

The effective yield point is considered as the location at which significant non-linearity is observed in the lateral response. At this point, the concrete has surpassed its linear limit (i.e. strains in excess of 0.002 in/in) and the reinforcement has begun yielding. The unconfined concrete cover is assumed to be intact and thus the full column diameter is considered effective when considering the compressive resistant of concrete. Base rotations do occur at this level, but the associated increase in stress in the post-tensioning is neglected. Thus, the post-tensioning force considered is the effective post-tensioning force.

To simplify the calculation of the force in mild reinforcement, the total area of the reinforcing steel is considered smeared evenly over the circumference of the diameter containing the reinforcement. The assumed distribution of stresses is shown in Figure 2.7.

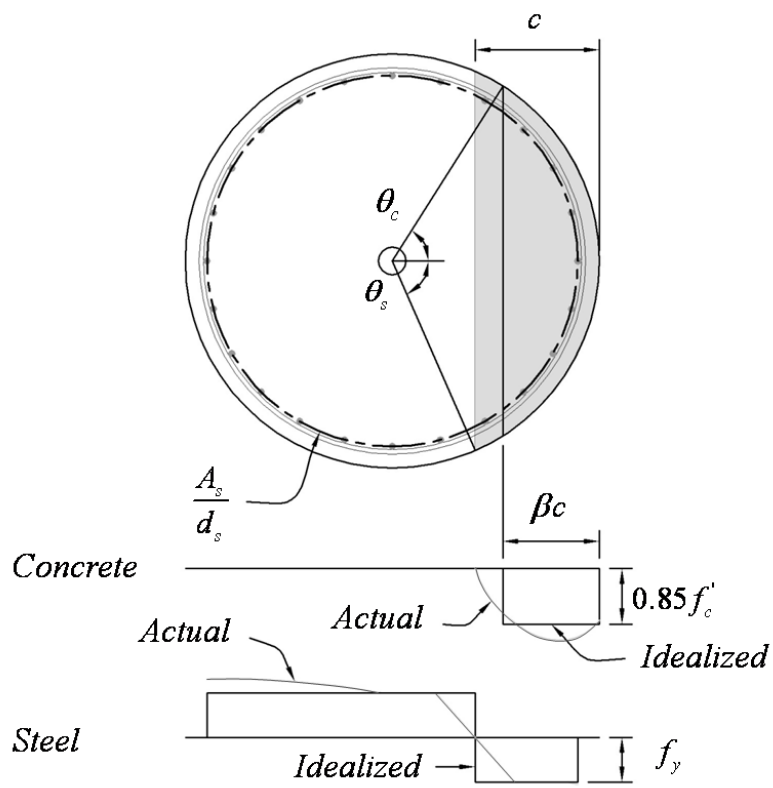

Figure 2.7 Assumed material stress distributions at effective yield

The total tension and compression forces can thereby be calculated as:

$$T_s = A_s f_y \frac{\pi - \theta_s}{\pi} \qquad 2\text{-}30$$

and,

$$C_s = A_s f_y \frac{\theta_s}{\pi} \qquad 2\text{-}31$$

where,

$$\theta_s = \cos^{-1}\left(\frac{d - 2c}{d_s}\right) \qquad 2\text{-}32$$

The resultant compressive force in concrete, using a rectangular stress distribution, is:

$$C_c = 0.85 f_c^{'} d^2 \frac{\theta_c - \sin\theta_c \cos\theta_c}{4} \qquad 2\text{-}33$$

where,

$$\theta_c = \cos^{-1}\left(\frac{d - 2\beta c}{d}\right) \qquad 2\text{-}34$$

The neutral axis depth can be iteratively determined considering equilibrium across the joint. The location of the resultant tension and compression forces in the mild reinforcement about the centerline of the column are:

$$y_{st} = \frac{d_s}{2}\frac{\sin(\pi - \theta_s)}{\pi - \theta_s} \qquad 2\text{-}35$$

and,

$$y_{sc} = \frac{d_s}{2}\frac{\sin\theta_s}{\theta_s} \qquad 2\text{-}36$$

The location of the resultant compression force in the concrete is:

$$y_c = \frac{d\sin^3\theta_c}{3(\theta_c - \sin\theta_c\cos\theta_c)} \qquad 2\text{-}37$$

The flexural moment and base shear at the effective yield state are determined according to Equations 2-28 and 2-29. The base rotation at the effective yield state is determined by considering the base rotation at two times the first yield of the extreme energy dissipater:

$$\theta_{jy} = \frac{2\varepsilon_y L_u}{d + d_s - 2c} \qquad 2\text{-}38$$

This value, based on twice the actual yield, was determined based on inspection of numerous complete moment-rotation analyses, which indicated effective yield occurs well after first yield of reinforcing steel. The requirement for minimum area of energy dissipaters is determined in accordance with Equation 2-14.

2.3 System Deformations

Calculations to determine predicted system deformations are presented in this section. The procedures presented focus on estimation of deformations associated with the column, and therefore do not consider flexibility of the connected members. These additional modes of deformation can be easily included using traditional engineering mechanics methods.

2.3.1 Concrete Section

The deflection of a hybrid system can be determined as a combination of elastic flexural displacement, shear displacement and displacements arising out of joint rotation:

$$\Delta = \Delta_f + \Delta_v + \Delta_j \qquad 2\text{-}39$$

This calculation assumes that the connecting elements are sufficiently rigid to have negligible effect on the overall deformation of the system. However, any associated displacement from deformability of connecting elements can easily be incorporated into this calculation. The elastic flexural displacement of the system can be defined as:

$$\Delta_f = \frac{Vh^3}{3n_j^{\,2} E_c I_g} \qquad 2\text{-}40$$

This equation is formed to allow for the determination of flexural displacement for a cantilever system or a framed system through the incorporation of the n_j term that determines the number of connections. The height term, *H*, is the clear height of the column. The concrete modulus of elasticity, E_c, can be calculated using common code provisions. The gross moment of inertia, I_g, is used as opposed to a cracked moment of inertia as the section is post-tensioned and is expected to exhibit minimal damage outside the joint region.

Displacements due to shear deformability are determined as:

$$\Delta_v = \frac{Vh}{G_c A_{cs}} \qquad 2\text{-}41$$

The concrete shear modulus can be taken approximately equal to 40% of the concrete modulus of elasticity. The shear area can be reasonably assumed to equal approximately 90% of the gross section area.

Displacements due to joint rotations can be calculated as:

$$\Delta_j = \theta_j h \qquad 2\text{-}42$$

2.3.2 Concrete Filled Steel Tube and Hollow Dual Shell

The calculation of deformations for concrete filled steel tube and hollow dual shell members follow the same logic as that for the concrete section. The general mechanics derivation is the same, although the section properties must be determined considering the composite action of the concrete and steel section. The moment of inertia and shear area must be developed to be

consistent with the concrete modulus of elasticity and shear modulus. For the same dimension system, the concrete filled steel tube deformations from flexure and shear are expected to be less than the conventional concrete deformations due to the increase in elastic stiffness. For the hollow dual shell systems, the deformations would be greater as compared to the concrete filled tube section.

2.4 Complete Analysis Method

To better characterize the moment-rotation behavior of a jointed system, a sectional analysis program was developed. The coding and interface for this program was written in the computer software program, MATLAB (MATLAB 2009). This sectional analysis program is intended to be an analysis program (as opposed to design) as all properties, dimensions, etc. must be input to the program. A graphical interface was developed for this program to allow for the quick input and iterative design of the component specimens designed for this project (see Figure 2.8). This program considered the stress-strain relationships for unconfined and confined concrete, mild reinforcement and post-tensioning.

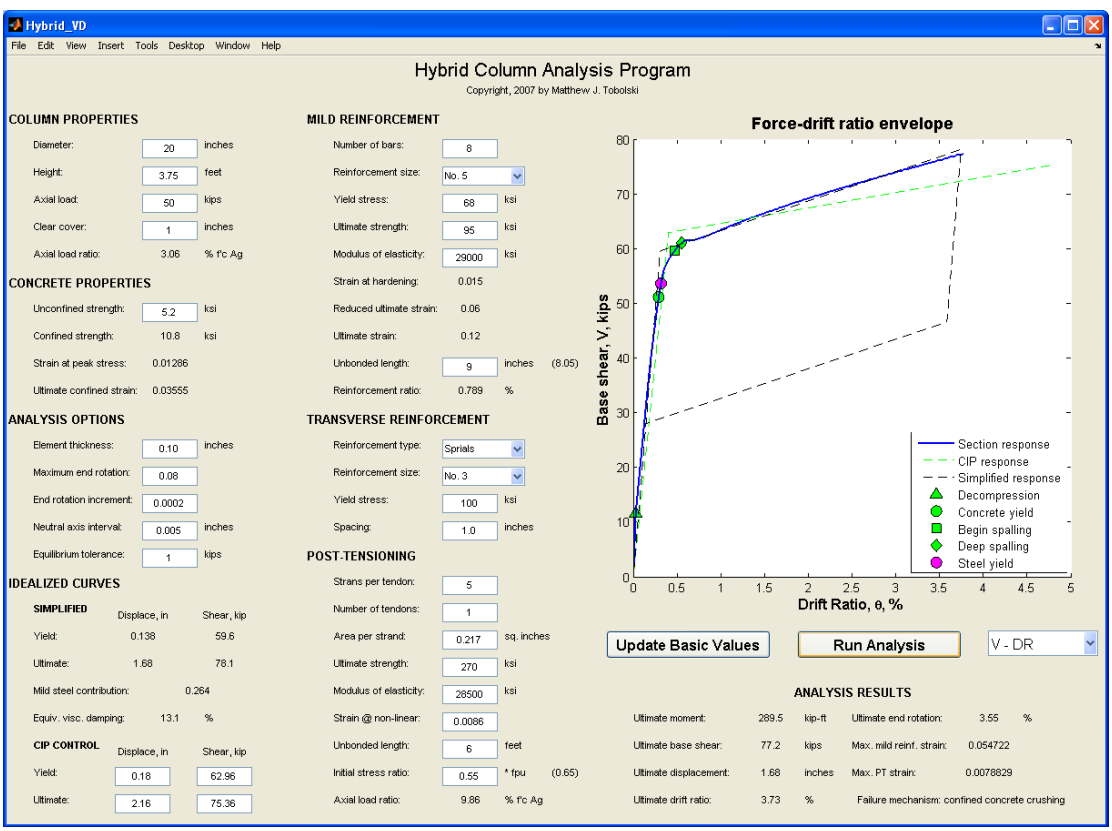

Figure 2.8 Hybrid sectional analysis program graphical interface

The basic premise of the program is that a series of incremental fixed end rotations are applied to the section and the neutral axis is iteratively determined until a force equilibrium tolerance is satisfied. The following section describes the method used to derive the analytical moment-rotation relationship.

2.4.1 Material Relationships

The following section describes the assumed stress-strain relationships for each material used in the analysis program.

Concrete

This program determines the stress across a circular concrete section by discretizing the circular section into a series of small rectangular slices. Slices are separated based on the geometric definition of the unconfined concrete cover and the confined concrete core. The width is taken as the width of the circular section at mid-height of the slice. The stress is assumed constant over the entire slice, with the stress determined as based on the strain at the center of the slice. When a small slice thickness is used, this method provides very accurate results.

For each applied rotation at the column end, the strain in the extreme concrete fiber can be determined using the relationship presented in Equation 2-1. The strain at the center of each rectangular slice is then calculated based on a plane sections, linear strain distribution. The strain for each slice is converted to a stress using Mander's relationship for both unconfined and confined concrete elements (Mander, Priestley and Park 1988). Prior to running the program, the user must input the longitudinal and transverse reinforcement, which is used to determine the confined concrete properties. The confined concrete strength is determined as:

$$f_{cc}^{'} = f_c^{'}\left(2.254\sqrt{1+\frac{7.94 f_l^{'}}{f_c^{'}}} - \frac{2 f_l^{'}}{f_c^{'}} - 1.254\right) \qquad \text{2-43}$$

where,

$$f_l^{'} = K_e f_l \qquad \text{2-44}$$

$$f_l = \frac{\rho_s f_{yh}}{2} \qquad \text{2-45}$$

The transverse reinforcement ratio is determined as:

$$\rho_s = \frac{4A_t}{s \cdot d_c} \text{ for spirals, hoops} \qquad 2\text{-}46$$

$$\rho_s = \frac{4t_p}{d_c} \text{ for steel tubes} \qquad 2\text{-}47$$

The strain in confined concrete at the peak stress is calculated as:

$$\varepsilon_{cc} = 0.002\left[1 + 5\left(\frac{f_{cc}^{'}}{f_c^{'}} - 1\right)\right] \qquad 2\text{-}48$$

The resulting ultimate confined concrete compressive strain is:

$$\varepsilon_{cu} = 0.004 + \frac{1.4\rho_s f_{yt}\varepsilon_{sut}}{f_{cc}^{'}} \qquad 2\text{-}49$$

To determine the stress in concrete at any strain level, the following relationship is used:

$$f_c = \frac{f_{cc}^{'} xr}{r - 1 + x^r} \qquad 2\text{-}50$$

where,

$$x = \frac{\varepsilon_c}{\varepsilon_{cc}} \qquad 2\text{-}51$$

$$r = \frac{E_c}{E_c - E_{\sec}} \qquad 2\text{-}52$$

$$E_{\sec} = \frac{f_{cc}^{'}}{\varepsilon_{cc}} \qquad 2\text{-}53$$

This stress-strain relationship also holds true for unconfined concrete when the confinement is taken as zero. Once the stress for each slice is determined, it is multiplied by the area of the slice to determine the total compression force. Tensile capacity of concrete is neglected as there is a discrete joint between precast members with the strength of the grout considered negligible. In actuality, the grout will provide some level of tensile resistance across the joint. Finally, the moment contribution provided by the concrete is determined by multiplying the force in the slice and the distance to the center of the section.

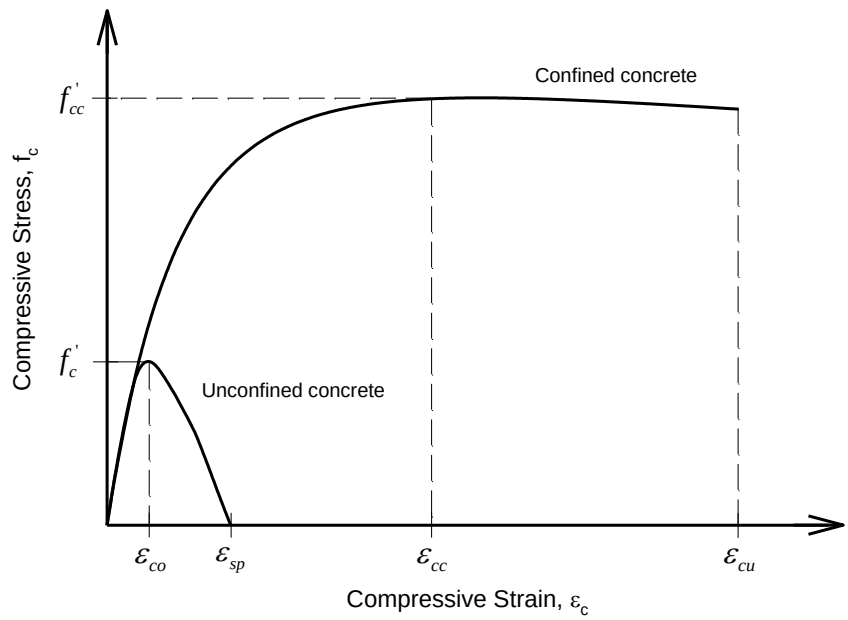

Figure 2.9 Concrete stress-strain relationship

Energy Dissipaters - Rebar

Based on the column end rotation and neutral axis depth, the strain in the mild reinforcement can be determined for each discrete bar assuming a linear strain distribution. The strain in each bar is converted to stress using the following bilinear stress-strain relationship for steel reinforcement:

$$f_s = \begin{cases} E_s \varepsilon_s & ; \text{if } \varepsilon_s \le \varepsilon_y \\ f_y + \left(\varepsilon_s - \varepsilon_{ye}\right) \dfrac{f_u - f_y}{\varepsilon^R{}_{su} - \varepsilon_y} & ; \text{if } \varepsilon_y < \varepsilon_s \le \varepsilon^R{}_{su} \end{cases} \qquad \text{2-54}$$

This equation is not the same as that presented in AASHTO Seismic Guide Specifications as the relationship presented in that document is based on monotonic testing (AASHTO 2009). The stress-strain relationship used in this program is intended to better capture the cyclic behavior of steel reinforcement. In this program, the analysis terminates if any rebar strain exceeds the specified maximum strain. The force in each bar is determined by multiplying the its respective stress and area and the moment contribution is determined by multiplying the force in each bar by its distance to the center of the cross section.

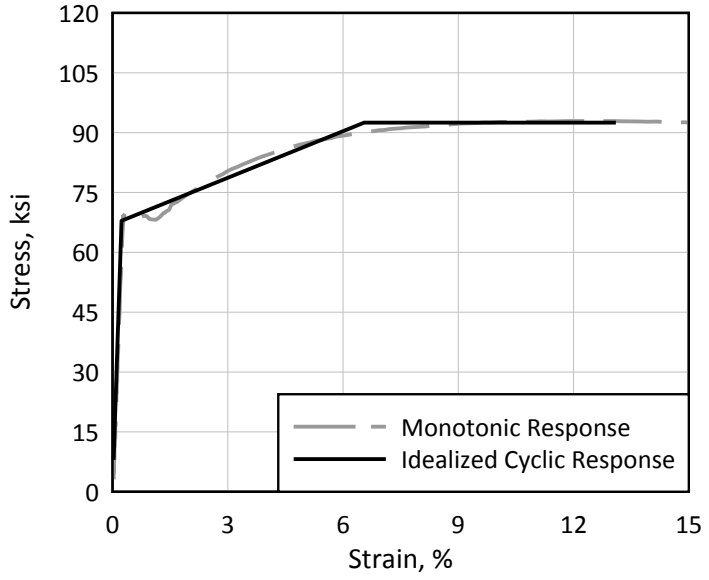

Figure 2.10 Steel idealized stress-strain relationship

Post-Tensioning

The strain in the post-tensioning tendon is determined in the same manner as for the energy dissipaters. The stress is then calculated by multiplying the strain by the modulus of elasticity of the post-tensioning as specified by AASHTO (2009). The non-linear relationship is not considered in this analysis program as the analysis is set to terminate if the tendon reaches it limit of proportionality. This is because of the design goal to maintain an elastic post-tensioning restoring force.

2.4.2 Overview of Program Procedure

The moment-rotation program operates by imposing a series of column end rotations until a failure mode is reached. The circular section is divided into a series of small rectangular sections with assumed constant stress on that section. The reinforcing bars are taken at their assumed location based on the diameter of the circle containing the bars and the number of bars. For analysis, it is judged a reasonable analytical assumption to consider that plane sections remain plane across the joint. Thus, the strain in an individual rectangular section can be determined and the resulting stress calculated. For concrete sections, the rectangular sections are broken down into confined and unconfined concrete sections to properly account for the material stress-strain relationships.

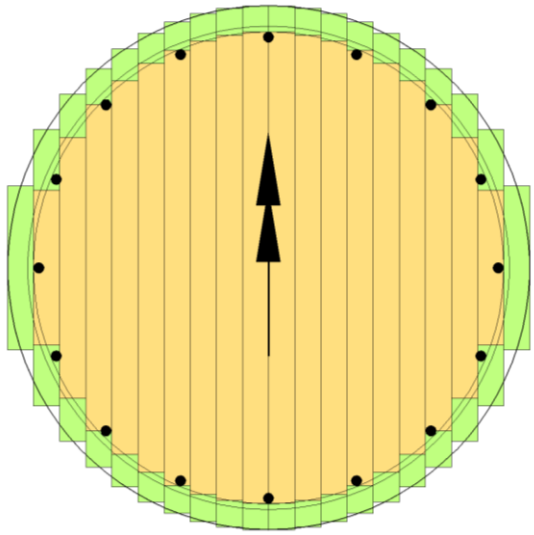

Figure 2.11 Example sectional analysis discretization

At each step, an assumed end rotation is applied to the section. The neutral axis depth for a given end rotation is determined through iteration for sectional force equilibrium. The program imposes the end rotation and then systematically assumes a neutral axis depth. With the end rotation and neutral axis depth, the force in all materials can be determined. The summation of these forces across the section is compared against an input force equilibrium tolerance to determine if section equilibrium is considered satisfied. If equilibrium is not satisfied, the neutral axis depth is updated and the process is repeated until convergence is achieved. The flexural moment is then determined based on the summation of moments about the column center, which is then converted to a related base shear based on the distance to the assumed inflection point in the column.

For this program, failure is defined as reaching one of these four criteria: 1) exceeding the ultimate confined concrete compressive strain, 2) reaching the limit of proportionality of the post-tensioning tendon, 3) reaching the ultimate reduced tensile strain in the mild reinforcement or 4) lateral resistance drops below 80% of the maximum observed lateral resistance.

Chapter 3 Experimental Basis

The experimental program conducted for the hybrid bridge columns was aimed at providing a solid comparison between conventional and hybrid bridge columns. Additionally, the testing conducted was intended to validate the analytical tools presented previously. The specimens designed and tested were based on a scaled prototype bridge and a cast-in-place control specimen tested at California State University, Sacramento. This section describes the basis for development of the experimental program.

3.1 Prototype Structure

An initial step in this research program was the development of an appropriate prototype structure for the design of a cast-in-place control specimen. This prototype structure was selected and designed in coordination with the NCHRP 12-74 Panel to represent a typical bridge structure seen throughout the United States. This specimen served as the basis of the design of all non-integral specimens constructed and tested under the NCHRP 12-74 program.

3.1.1 Bridge Description

The prototype structure is a two-span continuous, post-tensioned concrete bridge with symmetric 100’ spans, see Figure 3.1. This bridge is intended to represent a typical highway overcrossing in an urban region. The total structure width was 58’ with seven girders and three columns in the single bent configuration. Figure 3.2 shows a typical cross-section of the bridge at the bent location.

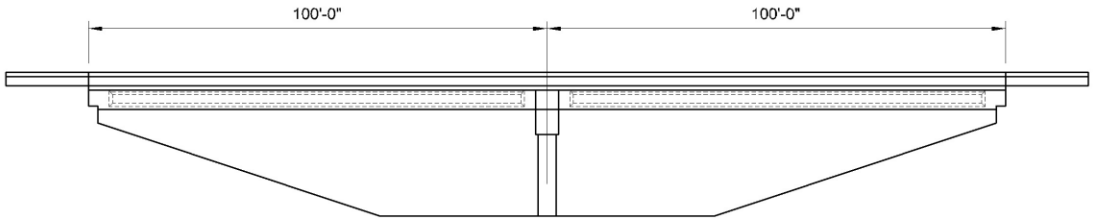

Figure 3.1 Prototype bridge elevation

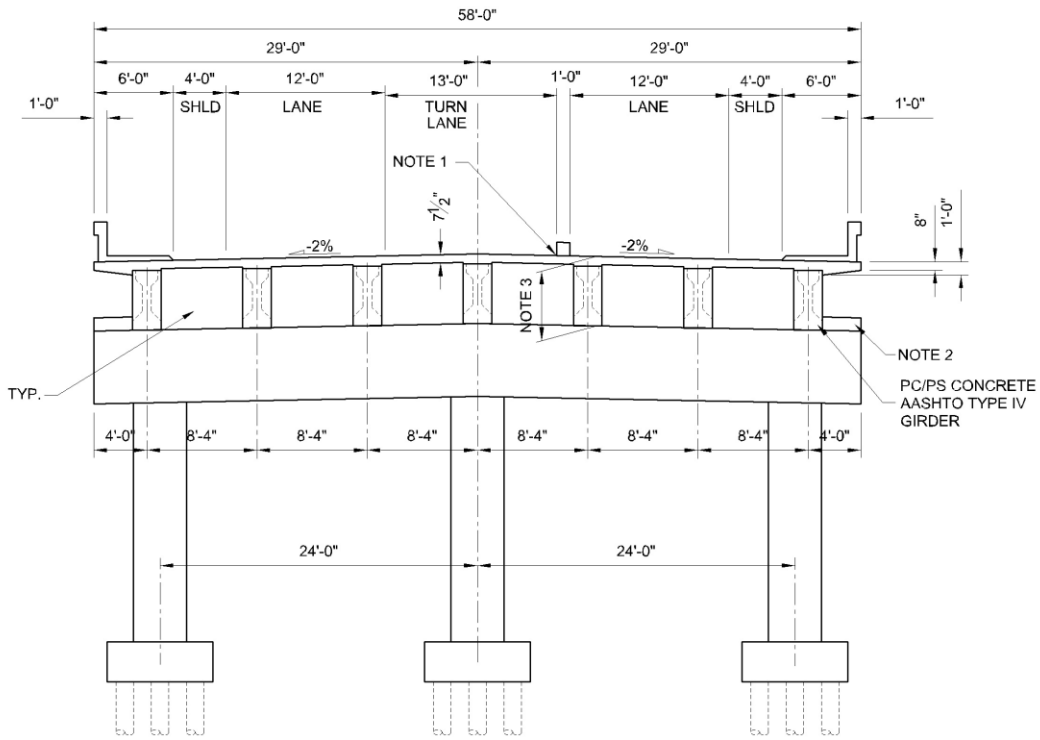

Figure 3.2 Prototype bridge section at bent

The service level design of the prototype bridge was conducted in accordance with the AASHTO LRFD Bridge Design Specifications, 3rd Edition with 2006 Interim Revisions (AASHTO 2007). Seismic design and detailing was performed using the NCHRP 20-07 Task 193 Proposed AASHTO Guide Specifications for LRFD Seismic Bridge Design as provided by the NCHRP 12-74 Panel. The seismic design criteria has since been superseded by the AASHTO Seismic Guide Specifications (AASHTO 2009). Although the prototype structure and cast-in-place control specimens were designed based on the proposed AASHTO Guide Specification, all hybrid specimens were designed and detailed in accordance with the actual Draft AASHTO Guide Specification as approved by AASHTO T-3.

The prototype bridge design was based on an assumed site with a one-second rock acceleration of 0.8 g and a 0.2-second rock acceleration of 1.5 g. For this design, the structure was assumed located on Site Class D soil with a peak rock acceleration of 0.6 g. This site was intended to represent high seismic demand in the region of Southern California; however, it was assumed that the structure was not located within 6 miles of any known faults. Therefore, near source effects were neglected in this prototype design. The specified seismic input demand results in seismic

classification of Seismic Design Category (SDC) D. This category requires demand analysis, displacement capacity analysis, pushover analysis, explicit capacity design and SDC D detailing.

To determine the seismic displacement demands, an elastic dynamic analysis was performed. Columns were assumed to be fixed at the base and all sources of column foundation flexibility were neglected. Results from the seismic analysis indicated the first mode (longitudinal) period is 1.27 seconds and the second mode (transverse) period is 0.58 seconds. As this testing program is intended to test the bent cap to column connection, and the superstructure is only connected with bearings and shear keys, the transverse demands are simulated during testing. The elastic seismic demand analysis indicated the transverse displacement demand was 5.3", which considers short period displacement amplification. This relates to a design level drift demand of approximately 2.5%.

3.1.2 Scaling of Prototype

Geometry and demands were used from this prototype structure to define the geometry and reinforcing requirements for the cast-in-place control specimen. Based on laws of similitude, scale factors shown in Table 3.1 were used.

Table 3.1 Specimen scale factors

Length/Displacement	0.417
Force	0.174
Moment	0.073

Demands were scaled based on the aforementioned scaling principles. Reinforcing sizes were also scaled using the same principles to best represent the reinforcing arrangement in the full-scale prototype. Detailing of the bent cap, per the seismic design criteria, was performed based on the actual specimen size, reinforcing and demands as opposed to just scaling the detailing from the prototype structure.

3.2 Hybrid Specimen versus Conventional Specimen

Lateral behavior of hybrid specimens differs from that of the cast-in-place control specimen due to the presence of unbounded post-tensioning and locally unbounded reinforcing steel. The prototype structure was designed as a cast-in-place (or emulative) structure and not a hybrid structure. Therefore, the lateral response of hybrid specimens cannot match that of the control specimen in terms of hysteretic response nor backbone response.

To achieve a somewhat comparable lateral behavior, the hybrid specimens were designed with the intent of having the same lateral force as the control specimen at approximately 1.0% drift ratio. However, due to variation in post-tensioning anchor set losses, this target was not achieved and the hybrid specimens generally had larger lateral strength.

3.3 Testing Setup

The testing setup consists of two supports and two actuators, as shown in Figure 3.3. A pin connection is used at the north end of the specimen at mid-depth of the bent cap. This connection allows rotation but restricts both vertical and horizontal displacements. On the south end, a roller connection is used to restrict only vertical displacements and still allow for rotation of the member. A vertical actuator is connected to the top of the beam and applies a constant force during the test to simulate axial load that is present on the column during a seismic event. A horizontal actuator is connected to the top of the column to simulate lateral earthquake demands. This actuator is actively controlled through force and displacement depending on the level of imposed demand.

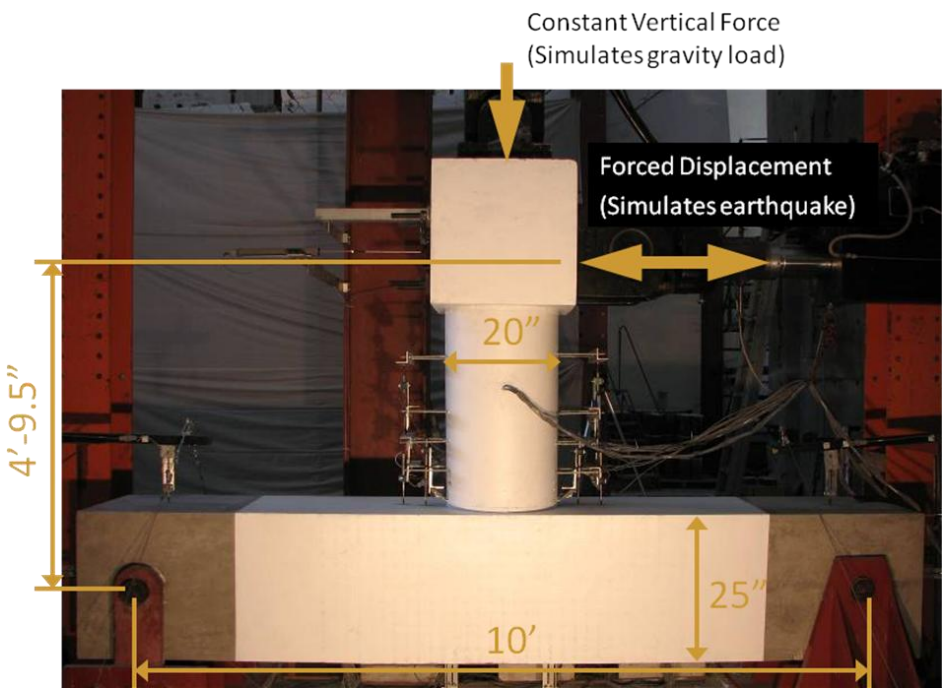

Figure 3.3 General testing configuration

The goal of the test specimen design is to provide loading on the bent cap and system similar to the scaled prototype system. The design level applied moment demand on the precast bent cap, as compared to the scaled prototype demands is shown in Figure 3.4.

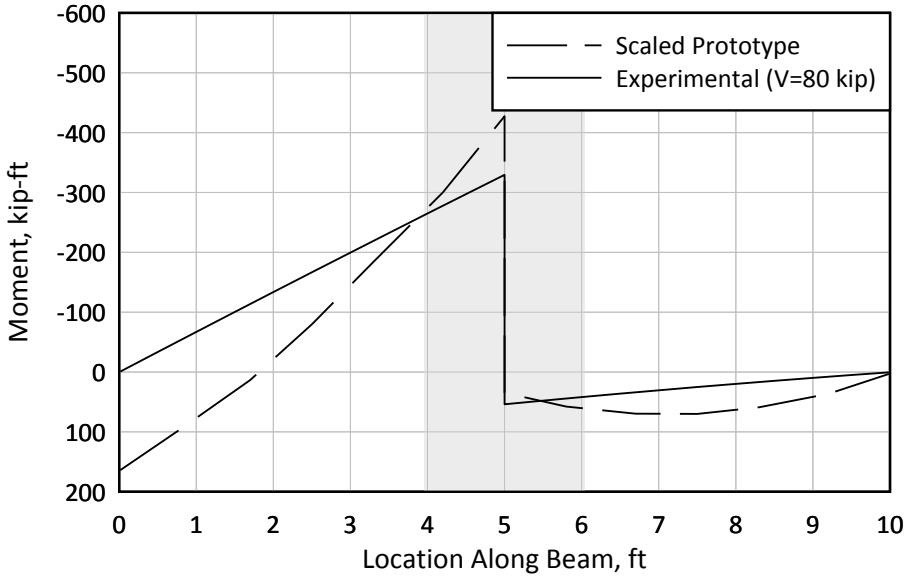

Figure 3.4 Scaled prototype bent cap moment demands compared to test

3.4 Steel Material Properties

Steel reinforcing and post-tensioning materials were tested to characterize their strength and deformability.

3.4.1 Conventional Mild Reinforcement

All conventional reinforcement used in these specimens conforms to the specifications of ASTM A706. Stress-strain test results from uniaxial tension tests for representative samples are provided in Figure 3.5. The yield and ultimate strengths for each bar type, as well as average uniform strain, are provided in Table 3.2.

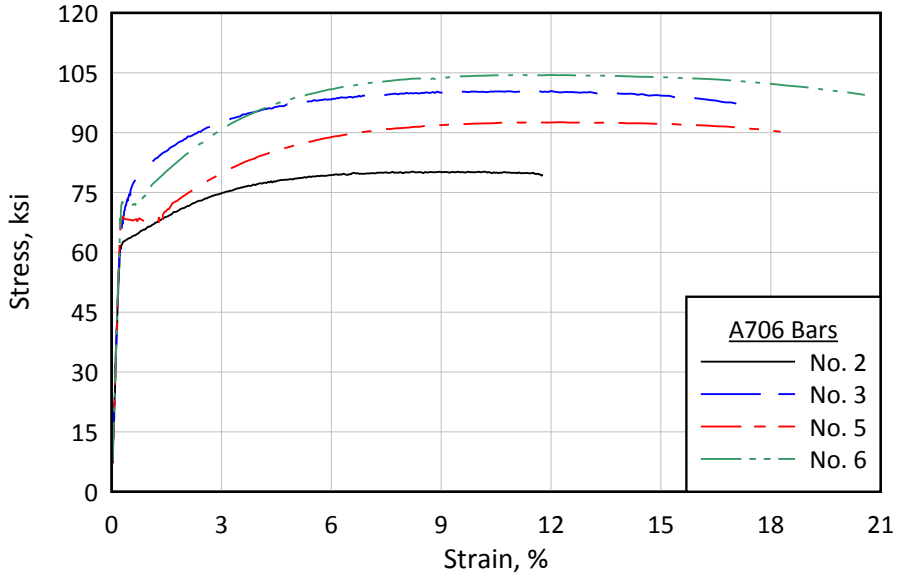

Figure 3.5 A706 Rebar stress-strain curves

Table 3.2 A706 Rebar Strength and Deformability

Bar Description	*Size*	*Yield, ksi*	*Ultimate, ksi*	*Uniform Strain*
Concrete strain	#2	61.0	79.1	7.3%
Column spiral	#3	75.9	100.8	12.7%
Bent cap longitudinal	#5	67.9	92.5	13.1%
Bent cap longitudinal	#6	72.3	104.4	12.4%
Bent cap spiral	#3	75.9	100.8	12.7%
Bent cap joint	#3	75.9	100.8	12.7%

3.4.2 Stainless Steel Reinforcement

Hybrid systems should be designed to ensure there is little to no joint opening during service load situations. However, during seismic shaking or extreme live load events it is expected that the joints at the ends of the columns will open. This provides a potential moisture path to the reinforcing steel that crosses the joint. Traditionally in the United States, anti-corrosion measures related to reinforcing bars include epoxy coating or galvanizing. However, both epoxy coating and galvanizing are surface treatments and are expected to be damaged if a reinforcing bar undergoes post-yield strains. Under frequently occurring seismic events it is possible for yielding of reinforcement, which has the potential to damage and render ineffective these surface

treatments. Stainless steel, however, has a chemical composition, which is resistant to corrosion, thus yielding will not affect a stainless steel rebar's corrosion resistance.

Results from uniaxial tension tests are shown in Figure 3.6 for a group of four samples tested of 316LN reinforcing steel rebar. These tests indicate the 316LN steel has similar yield and ultimate strength as compared to A706 steel, with significantly more deformability. Figure 3.7 focuses on the yield region of the uniaxial tension tests. It can be observed that these test specimens do not exhibit a typical yield plateau present in A706 rebar but transition into a strain hardening behavior directly after yield. Average material properties are provided in Table 3.3

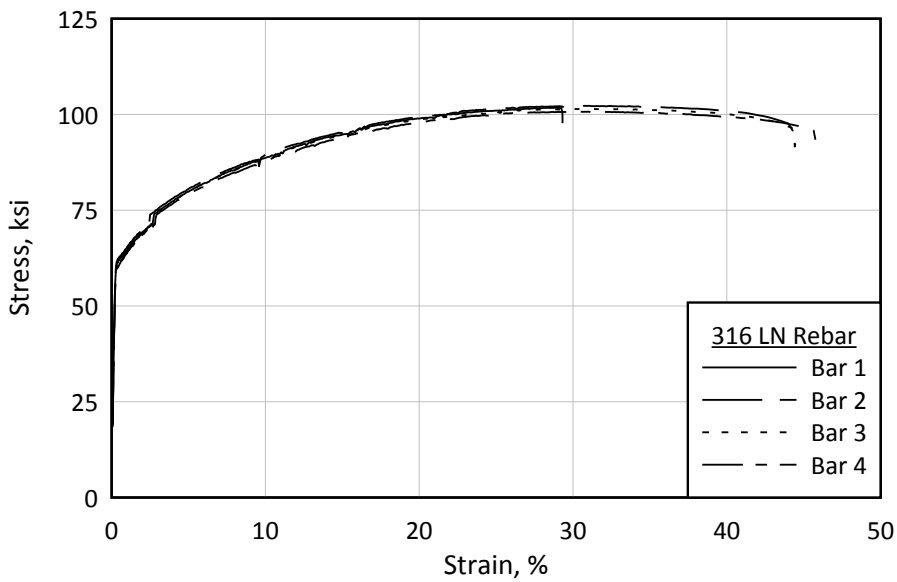

Figure 3.6 316LN Rebar stress-strain curves

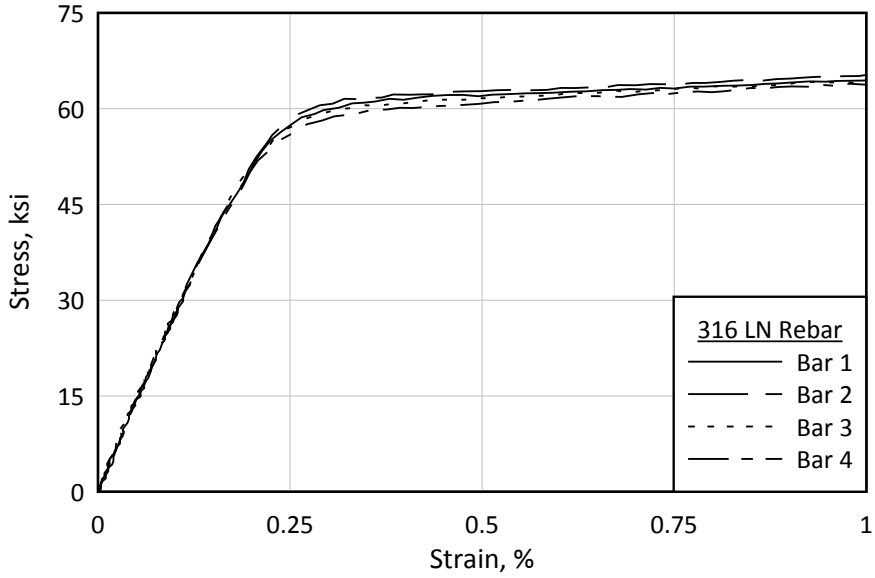

Figure 3.7 316LN Rebar stress-strain curves at yield

Table 3.3 316LN Rebar Strength and Deformability

Bar Description	*Size*	*Yield, ksi*	*Ultimate, ksi*	*Uniform Strain*
Column longitudinal	#5	61.7	102.2	33.2%

A comparison between representative No. 5 uniaxial tension specimens is shown in Figure 3.8. Results indicate the A706 specimen has slightly higher yield strength as compared to the 316LN specimen; however, the 316LN specimen has a higher ultimate strength. In terms of deformation capacity, it is observed that the 316LN specimen has approximately three times greater ultimate strain capacity when compared to the A706 specimen. For hybrid specimens, where large joint opening is expected, this means a shorter debond length can be used for 316LN rebar as the steel can accommodate larger displacements prior to fracture. Short debond lengths will result in generally stiffer structures at the pre-yield state which is important for controlling deformations under service loading.

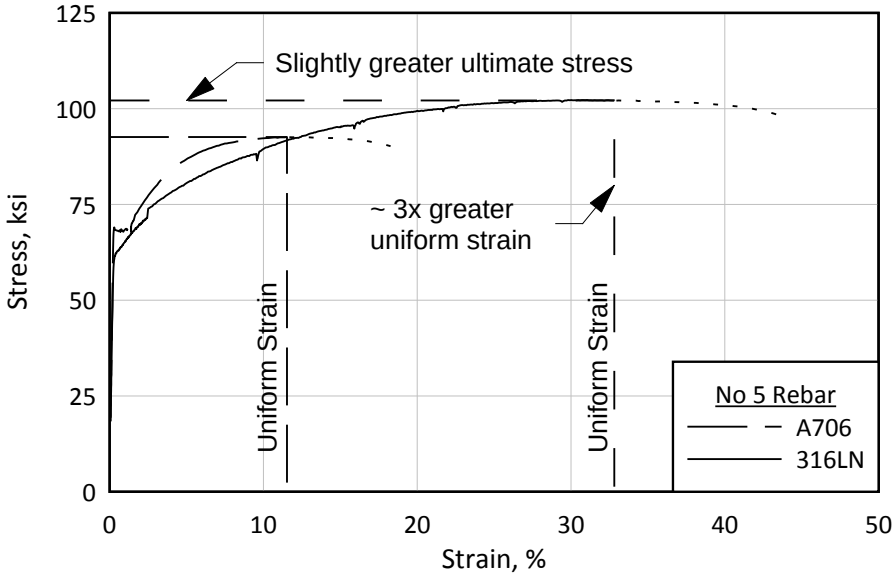

Figure 3.8 Comparison of A706 and 316LN stress-strain

In addition to monotonic tension testing, cyclic rebar tests were also conducted to obtain insight into cyclic hardening properties of the stainless steel reinforcement. Figure 3.9a provides the cyclic response up to approximately 2.6% tensile strain. The target compression strain was approximately one-third the previous tension strain. From this plot it is apparent that the cyclic stress-strain relationship for the 316LN stainless steel bar is approximately equal to that of the A706 bar. The initial tension cycle did show a more defined yield plateau for the A706 bar, as was also observed for the monotonic tension testing. However, after this first cycle, the cyclic response for the two bars was rather similar indicating that the traditional cyclic stress-strain relationships for mild steel reinforcement may be appropriate for use with 316LN stainless steel. Figure 3.9b provides the entire recorded stress-strain relationship. Following cyclic loading past 5%, the bars were pulled monotonically in tension. This plot indicates that for the loading protocol used, the bars have similar uniform tensile strain capacities as compared to the monotonic tension tests.

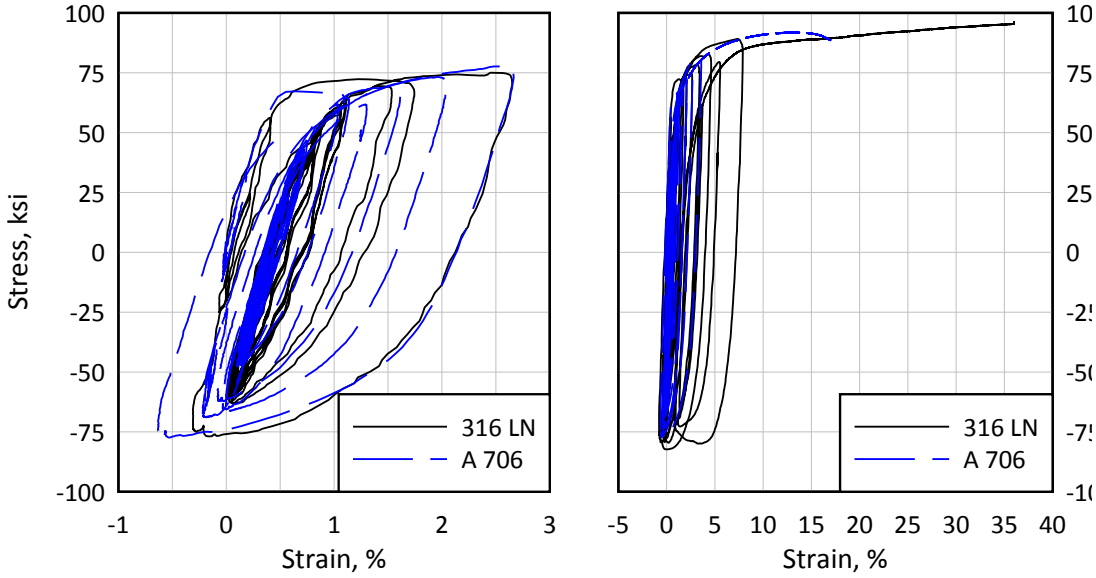

Figure 3.9 Comparison of cyclic stress-strain a) up to 3% and b) complete

3.4.3 Post-Tensioning

Uniaxial tension tests were conducted on three samples of low-relaxation post-tensioning strands. These specimens were instrumented with high-yield strain gages to capture deformations. Results from these tests are shown in Figure 3.10. The results of these tests show a slightly lower strength as compared to the assumed stress-strain behavior presented in AASHTO Guide Specifications. In addition, the ultimate strain is significantly lower than that specified by AASHTO. It is postulated that the reduction in both strength and deformability is a result of the loading grips used for these material tests. The laboratory facility does not own a proper post-tensioning test setup, which uses anchor wedges. Instead, these tests relied on actual grips that locally pinch the specimens thus locally reducing the area of the specimen and inducing stress concentrations. All specimens tested failed at the grip location reaffirming the belief that these reductions are a byproduct of the test configuration.

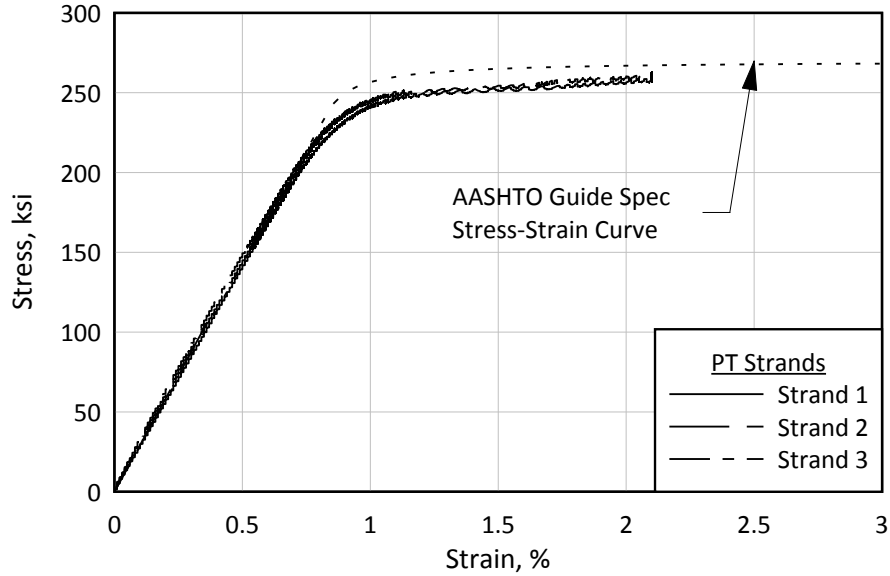

Figure 3.10 Post-tensioning stress-strain curves

Based on the observations of the post-tensioning stress-strain curves developed at UCSD, it was decided to also consider coupon testing provided by the manufacturer of the strands. Testing data was provided by the post-tensioning strand supplier from the same lot of material. A summary of data collected from these tests is provided in Table 3.4. The results of the coupon testing show strength and elongation properties that are as expected.

Table 3.4 Post-tensioning strength and deformability

Specimen	*Yield, ksi*	*Ultimate, ksi*	*Elongation*
Specimen 1	249.8	272.0	7.0%
Specimen 2	248.5	269.4	6.2%
AVERAGE	**249.1**	**270.7**	**6.6%**

3.4.4 External Steel Shells

The external steel shells specified for use on this project were specified as ASTM A 572 GR 50. Coupon testing was not conducted by the university laboratory for these materials. Instead, certified material testing reports provided for this stock of material were provided by the steel supplier. Results from these tests are shown in Table 3.5.

Table 3.5 External steel shell material properties

Test Number	*Yield, ksi*	*Ultimate, ksi*	*Elongation*
Coupon 1	69.5	79.0	21%
Coupon 2	65.0	75.5	21%

Chapter 4 Conventional Specimen

The conventional hybrid specimen (also referred to as HYB-1) uses traditional confinement and longitudinal rebar details with rebar extending full height and a tightly spaced spiral. Details of this specimen and experimental results are provided in this section.

4.1 Design Details

Based on the prototype structure and cast-in-place unit design, the test specimen details were developed (Matsumoto 2008). The general specimen dimensions were held constant as compared to the cast-in-place control specimen resulting in a 42% scale specimen. Details of the specimen are provided in this section.

4.1.1 Column

The outside diameter of the column section is 20 inches with a 1-inch clear cover to the spiral reinforcement (Figure 4.1). The column has a variable pitch spiral with a tight 1.5-inch pitch at the column base for a distance equal to one-half the column diameter. Outside this highly confined region, the spiral pitch was increased to 2.5 inches based on shear design (see Figure 4.2). The confinement ratio at the base of the column is equal to 1.63%.

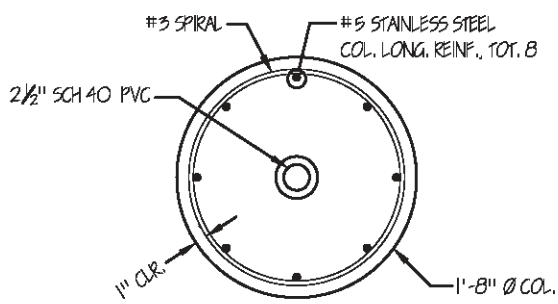

Figure 4.1 HYB-1 typical column cross-section

The primary longitudinal reinforcement in the column consists of a combination of unbonded post-tensioning and bonded rebar. There are 7-0.6 inch diameter post-tensioning strands making up the single tendon that runs down the center of the column. There are 8-No. 5 316LN stainless steel rebars spaced equally around the column section, providing a reinforcement ratio of 0.79%. The void for the post-tensioning tendon was form with a PVC pipe, however in practice the void should be formed with corrugate plastic post-tensioning ducts or high-density polyethylene (HDPE) pipe based on corrosion protection. The recommended practice for this system is to use a

smooth HDPE pipe and grout the void following stressing. This will provide a corrosions barrier around the tendon but will debond during a seismic event due to lack of development properties.

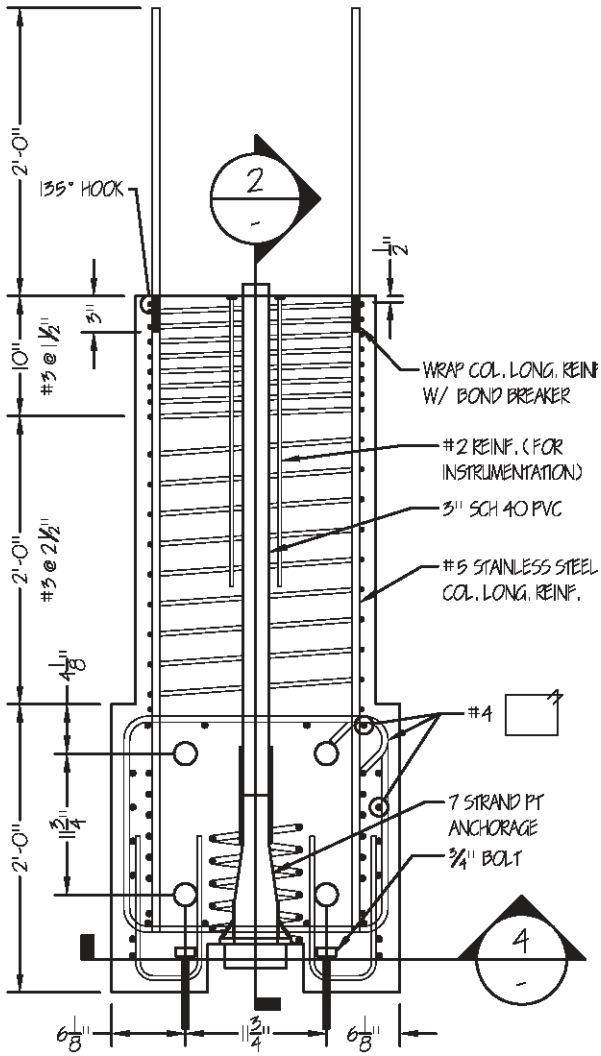

Figure 4.2 HYB-1 column vertical section

4.1.2 Bent Cap

Figure 4.3 and Figure 4.4 provide details of the bent cap member. The bent cap cross-section is a square with a dimension of 25 inches. Primary longitudinal reinforcement was designed based on capacity protection measures and force-transfer mechanism requirements as presented in the AASHTO Seismic Guide Specification (AASHTO 2009). Shear reinforcement near the joint region and joint shear reinforcement were designed in accordance with the assumed force transfer mechanism of AASTHO as modified for the presence of post-tensioning.

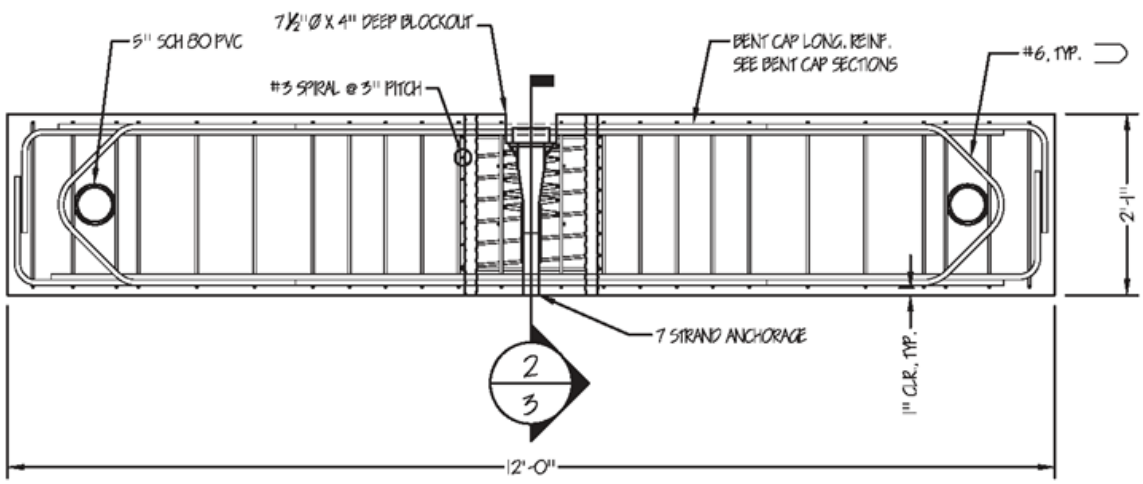

Figure 4.3 HYB-1 bent cap longitudinal section

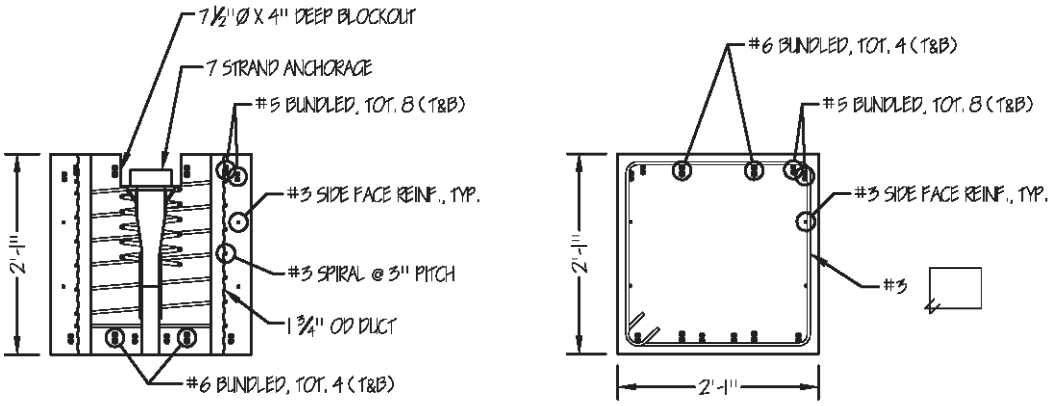

Figure 4.4 HYB-1 bent cap section a) at anchorage b) outside anchorage

4.1.3 Instrumentation

This test specimen was instrumented to capture the major response characteristics of the specimen when subjected to simulated lateral loading. This instrumentation includes strain gages mounted on rebar components and external gages mounted on the exterior of the specimen.

Strain gages were placed on column and bent cap reinforcement to capture the distribution of forces and deformations inside the specimen and the spread of plastic actions. The locations of these gages are shown in Figure 4.5. A summary of the strain gage categories based on callouts is provided:

- CL series Column longitudinal reinforcement strains
- CS series Column spiral reinforcement strains
- CC series Confined concrete strains (longitudinal strains in #2 embedded bars)
- BL series Bent cap longitudinal reinforcement strains
- BS series Bent cap shear reinforcement strains
- BJ series Bent cap joint shear reinforcement strains

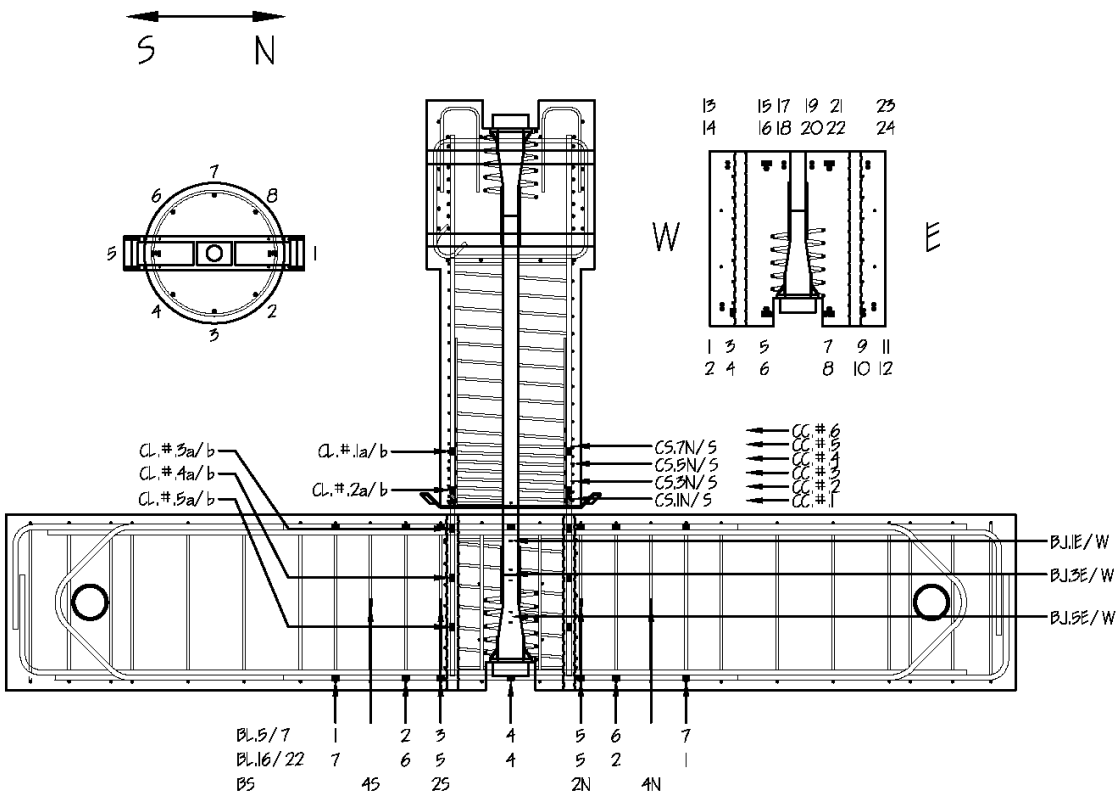

Figure 4.5 HYB-1 strain gage layout

External instrumentation consists of linear potentiometers and inclinometers mounted on the exterior of the specimen. A summary of external instrumentation is shown in Figure 4.6. Linear potentiometers are placed to capture column displacement, column curvature, base rotation, bent cap joint deformations, column bar slip, bent cap rotation and rigid body movement. An inclinometer was placed on the load stub to record the rotation of the load stub at the actuator location.

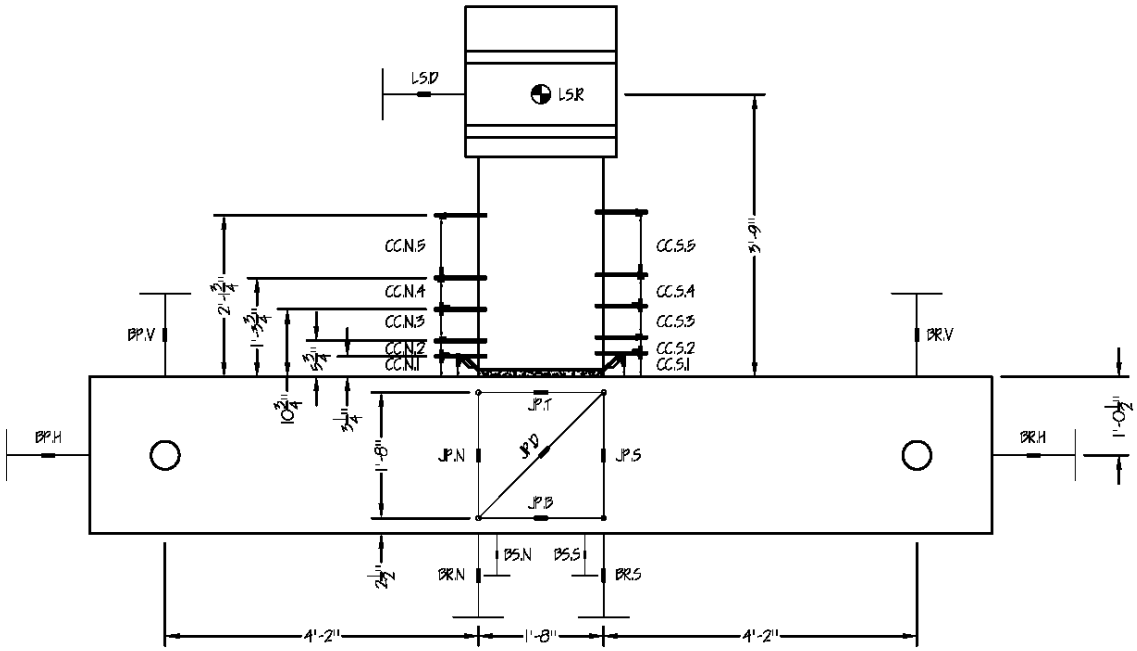

Figure 4.6 HYB-1 external instrumentation layout

In addition to active measurement provided by strain gages and external instrumentation, specimen response was documented through digital photos, crack markings, video recording and notations.

4.2 Fabrication and Assembly

This section describes the process of section fabrication and assembly.

4.2.1 Precast Component Fabrication

This specimen was fabricated at Pomeroy Corporation located in Perris, CA. The reinforcing bars that were instrumented were shipped to UCSD for installation of the strain gages and then transported to Perris for fabrication. All fabrication activities at the precast yard were closely monitored by a representative from UCSD to ensure all tolerances were achieved and to acquire feedback from the precast concrete fabricator relating to the ease of fabrication. The column and load stub cage were constructed horizontally and then lifted to a vertical orientation for casting. The completed column and load stub cage prior to installation in the form is shown in Figure 4.7a. As seen in this figure, the variable pitch of the spiral caused twisting of the column reinforcement. This was corrected by using a template that was secured to the column form after

installation (see Figure 4.7b). As can be seen in this figure, the column strain gage leads were run out of the column at approximately mid-height through holes drilled in the sonotube forms.

The precast concrete fabricator indicated that fabrication of the column cage as not difficult and can be replicated on a larger scale. However, a significant concern that was voiced relates to the casting of the column. As this specimen was scaled and only half height was built, the column was fabricated in a vertical position with relative ease. For a full-scale bridge column, this could require the fabrication of a vertical column in excess of 15 feet tall. Typical precast concrete fabricators are geared up for fabrication of long, short members and are not readily equipped to fabricate very tall, slender sections. The fabricator indicated that if fabrication of columns became common practice they would consider methods to fabricate and cast these members in a horizontal position. Another option that will facilitate the horizontal fabrication of column elements is the use of octagonal sections as opposed to circular sections. In this case, one face of the column could remain open to allow for the pouring and vibration of concrete.

Figure 4.7 HYB-1 column a) cage and b) cage installed in form

The bent cap cage, prior to installation in the form, is shown in Figure 4.8. The flexural and shear reinforcement were tied prior to installation in the form without the inclusion of the post-

tensioning anchorage and corrugated ducts. For these items, wood “donuts” were installed on the form to ensure the accuracy of placement, and maintain the location of the column bars to ensure the required tolerances were achieved.

Figure 4.8 HYB-1 bent cap reinforcing cage

The bent cap cage installed in the form is shown in Figure 4.9. Once the cage was installed, the post-tensioning anchorage and corrugated ducts we installed using a template that was attached to the form. During the installation of these items, the bent cap longitudinal and shear reinforcement were partially untied near the joint to facilitate their shifting to install the anchorage and ducts. Feedback from the fabricator indicated that this installation process involved additional effort and quality control due to tolerance considerations but was easily manageable for the given reinforcement configuration. Following the installation of the anchorage, ducts and support pipes, the other side of the form was installed and braced.

Figure 4.9 HYB-1 bent cap reinforcing cage installed in form

The casting of the bent cap is shown in Figure 4.10. Due to the relative congestion and lack of vibrator access in the joint, a concrete mix with a 7” slump was specified to ensure adequate consolidation of joint concrete. This higher slump mix was also desirable for casting of the column, which provided very limited vibrator access. The casting of the column was performed by pouring concrete through the top access hole in the form.

Figure 4.10 HYB-1 casting of bent cap

Unlike traditional bridge beams, these specimens were not steam cured thus additional cure time was required to achieve appropriate strength prior to removing from the forms. The forms were removed once the concrete achieved a compressive strength of 3 ksi. Following the removal of the forms, the specimen surfaces were finished following traditional acceptance procedures. These two components were then loaded onto a tractor-trailer unit and shipped the 75 miles to the UCSD campus (see Figure 4.11).

Figure 4.11 HYB-1 specimen loaded on truck for shipment

4.2.2 Fabricator Feedback

The precast concrete fabricator indicated that fabrication of the column cage was not difficult and can be replicated on a larger scale. However, a significant concern that was voiced relates to the casting of the column. As this specimen was scaled and only half height was built, the column was fabricated in a vertical position with relative ease. For a full scale bridge column, this could require the fabrication of a vertical column in excess of 15 feet tall. Typical precast concrete fabricators are geared up for fabrication of long, short members and are not readily equipped to fabricate very tall, slender sections. The fabricator indicated that if fabrication of columns became common practice they would consider methods to fabricate and cast these members in a horizontal position. Another option that will facilitate the horizontal fabrication of column elements is the use of octagonal sections as opposed to circular sections. In this case, one face of the column could remain open to allow for the pouring and vibration of concrete.

The fabricator did not indicate any significant issues with the construction of the reinforcement cage for the bent cap. However, minor difficulties were encountered when placing all of the required reinforcement, hoops and ties within the joint region. Additionally, the placement of the corrugated ducts and post-tensioning anchorage in the joint added an additional complication but the use of templates made this process relatively simple. One issue that was noted is that the top template blocked access from the top of the member causing difficulties for vibration during casting. On a larger scale member, the precast fabricators indicated they would likely need to add access ports from the template to facilitate adequate confinement within the joint.

4.2.3 Specimen Assembly

Once on campus, the column was set on two concrete blocks to allow for access to the load stub ("dead end") post-tensioning anchorage and then leveled. The bent cap temporary support structure was then constructed around the column using traditional scaffolding and dunnage. The bedding layer form was installed in preparation for the cap setting operation. The bent cap was set on the column in the upright position using the overhead crane in the lab. A steel pipe was placed through one of the corrugated ducts to help guide the cap beam over the column reinforcement, Figure 4.12. The strain gage leads were also pulled through the ducts and carefully watched during the setting operation.

Figure 4.12 HYB-1 bent cap setting operation

The cap setting operation went smoothly without any significant problems. At the bent cap-to-column interface, the column reinforcement lined up well. However, many of the reinforcing bars were slightly inclined or bent resulting in the bars being offset at the top of the bent cap. Figure 4.13 shows the best (optimum) rebar location at the top of the bent cap and the worst observed location at the top of the bent cap.

Figure 4.13 HYB-1 a) optimum reinforcement location and b) worst observed location

The bedding layer and corrugated ducts were then grouted by pumping Masterflow 928 grout through one of the ducts (BASF 2006). The tube was push through the duct until it reached the top of column and then pulled up approximately 2 inches. As the grout was observed in the adjacent ducts, the grout tube was slowly retracted (see Figure 4.14). The grouting operation went smoothly with the exception of the slight malfunctioning of the grout pump at certain times. There was slight bleeding of water from the top of the bedding layer form during grouting which was expected. This will not result in adverse performance of the grout material.

Figure 4.14 HYB-1 grouting of bedding layer and ducts

4.2.4 Post-Tensioning

After allowing the grout to cure for 10 days, the system was post-tensioned by Dywidag Systems International. The strands were individually threaded through the column and set in the wedge plate to ensure their alignment is maintained inside the column. Due to the short length of this column, the misalignment of a strand would result in variable stressing in the individual strands. Six strands were strain gaged during the stressing operation; however only three gages survived the installation of the strands. Stressing during the post-tensioning operation is shown in Figure 4.15.

Figure 4.15 HYB-1 post-tensioning of specimen

After 20% of the specified jacking force was applied to the specimen, the elongation of the strand was measured. The strands were then jacked to the specified force relating to 75% GUTS. Based on the strain gage readings the actual jacking stress was 78.8% GUTS. The elongation of the strands was then measured at the jacking stress. Next, the stress was released to 20% of the jacking stress and the elongation was again measured. Based on the recorded measurements the

wedge pull-in was 0.188 inches. Back calculating the pull-in based on the strain gage readings indicated the pull-in was 0.156 inches. Both of these values are significantly less than the anticipated 0.250" pull-in based on the manufacturer's recommendations. The strain gage readings are assumed more accurate and will be used from this point when discussing the immediate losses in the tendon. The strain gage history during stressing is shown in Figure 4.16.

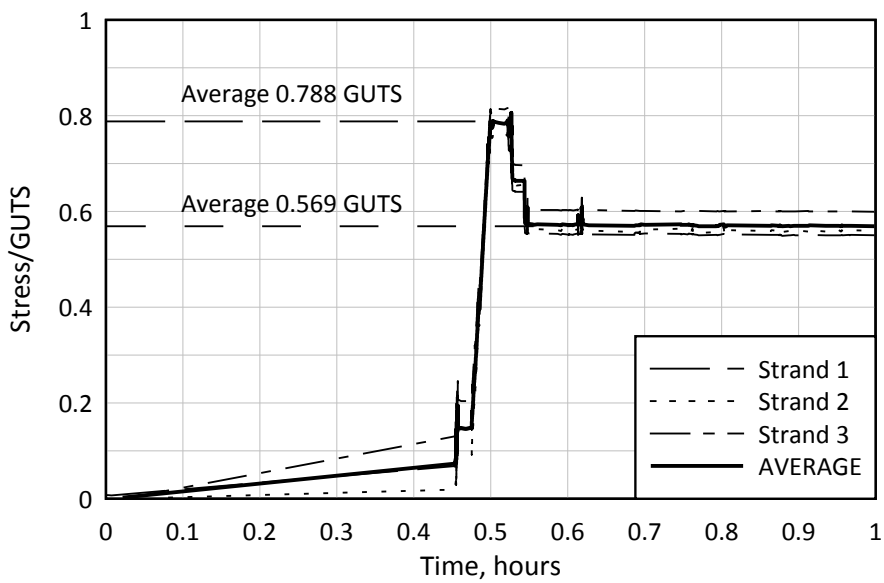

Figure 4.16. HYB-1 post-tensioning strain gage history during stressing

The reduction in the wedge pull-in results in a significant increase in the effective post-tensioning force due to the relatively short length of the post-tensioning strand. The resulting force was 32% greater than the design effective post-tensioning force. This resulted in a significant migration of the neutral axis depth resulting in depths approximately equal to 40% of the diameter of the confined core. The implication of this is discussed in more detail in the discussion of experimental results.

4.3 Cementitious Material Properties

The bent cap and column were fabricated with normal weight concrete developed to achieve a target compressive strength of 4 ksi at 28 days. The mix design was developed using a nominal 3/8 inch maximum aggregate size based on scaling of from the prototype specimen.

The cementitious grout selected for use on this project was Masterflow 928 grout. This material is a prepackaged hydraulic cement-based mineral-aggregate high strength, non-shrink grout with an extended working time. The grout material is developed to meet the requirements of ASTM C

1107, Standard Specification for Packaged Dry, Hydraulic-Cement Grout (Non-shrink)), Grades B and C, and the Army Corps of Engineers' CRD C 621, Specification for Non-Shrink Grout, Grades B and C.

Compression strengths for cementitious materials were established through cylinder testing at multiple times following casting and at day of test (D.O.T.). Results from compression testing for both concrete and grout are listed in Table 4.1 and Table 4.2. The values presented are based on the average of three specimens tested. Variation of cementitious material compressive strength versus material age is presented in Figure 4.17.

Table 4.1 HYB-1 concrete strength

Material Age	*Strength, ksi*
7 days	3.10
14 days	3.68
28 days	4.07
42 days (D.O.T)	4.11

Table 4.2 HYB-1 grout strength

Material Age	*Strength, ksi*
7 days	7.16
25 days (D.O.T)	7.79
28 days	8.04

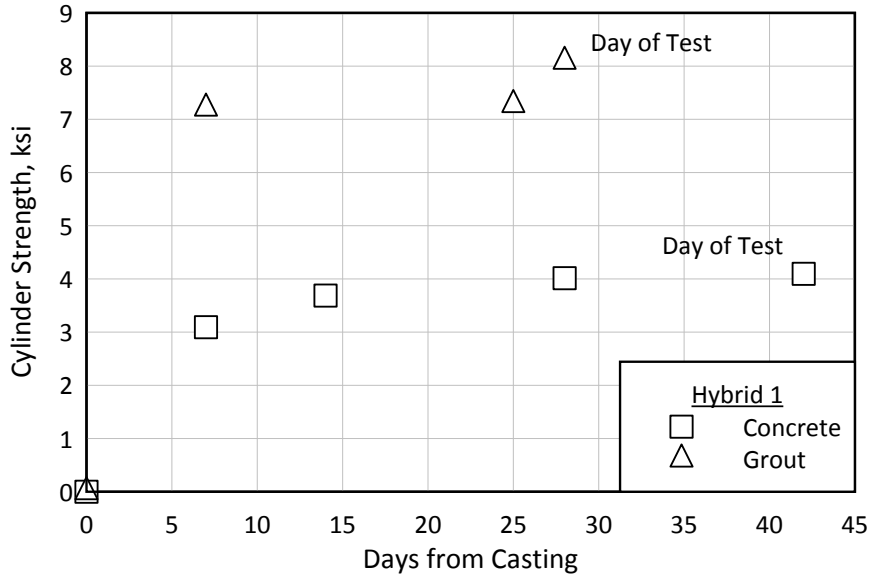

Figure 4.17 HYB-1 cementitious material strengths

4.4 Experimental Procedure and Observations

The loading procedure and observations noted during testing are presented in this section.

4.4.1 Load Protocol

The preliminary stage of loading consists of application of vertical load on the specimen simulating the gravity load during a seismic event. The vertical load was applied as a ramp load over approximately one minute. Following the application of vertical load, lateral loading began. The first stage of loading consisted of ramping of lateral load to a specified target, i.e. force controlled control. Each loading stage consisted of three cycles of push and pull excursions. The first lateral load cycle was based on the expected lateral load required to achieve zero stress at the extreme tension fiber. The next stage had a target lateral load of twice the first stage. Finally, the third stage in force control consisted of a push cycle to expected first yield or 0.50% drift ratio, whichever occurred first. In this test, the drift limit was reached at approximately the same time as first yield of reinforcement. The loading protocol for the force-controlled stages is graphically shown in Figure 4.18.

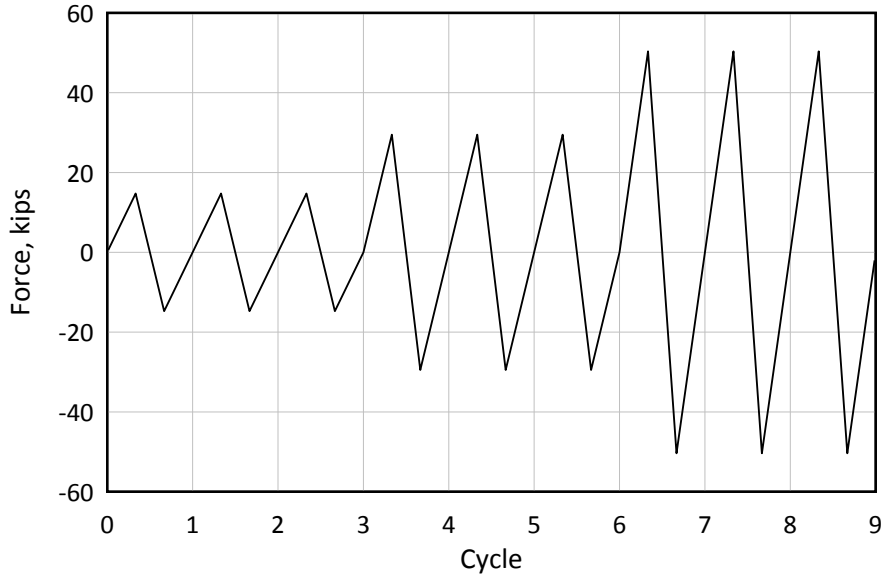

Figure 4.18 HYB-1 force-controlled loading protocol

Upon completion of the force controlled loading cycles, the actuator control was switched to displacement control. Displacement controlled stages were loaded to target drifts. For the first two cycles, three displacement excursions occurred in both the push and pull directions (target drift levels of 0.50% and 0.75%). For the remaining loading stages, the specimen underwent two displacement cycles to the specified drift, followed by one cycle to the previous drift level. For example, during the 1.00% drift ratio cycle the specimen underwent two cycles at 1.00% drift ratio followed by one cycle to 0.75% drift ratio. The displacement control loading protocol is graphically shown in Figure 4.19.

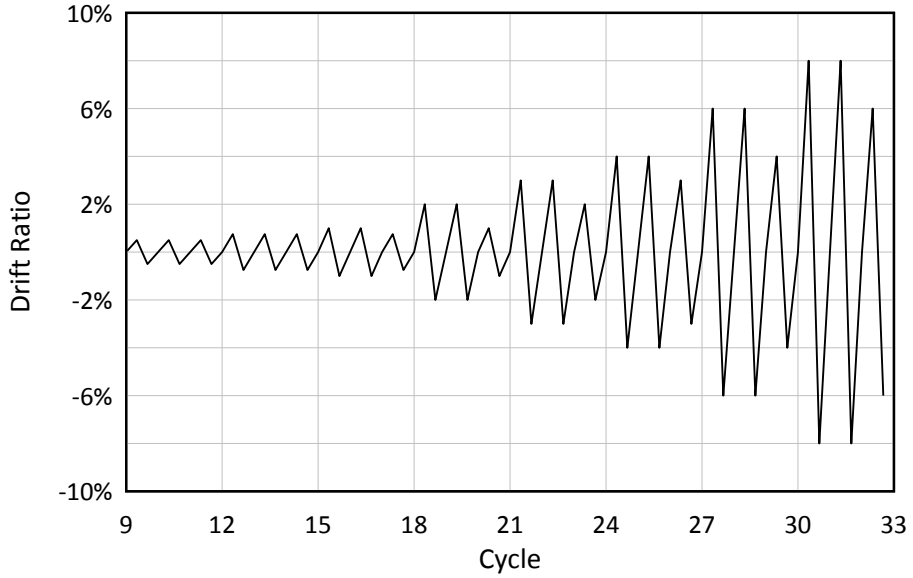

Figure 4.19 HYB-1 displacement controlled loading protocol

4.4.2 Observations During the Test

The following section summarizes the observations made during testing. Observations and photographs were taken at the final cycle at a given force or displacement. For the cases where the specimen underwent two cycles to a given displacement followed by one cycle at a previous displacement, the observations and photographic documentation only occurred at the end of the second cycle in both push and pull directions. Cracks were marked using markers corresponding to a given displacement direction. Red markers were used to indicate cracking due to pushing while blue markers were used to indicate cracking due to pulling.

The test unit prior to testing is shown in Figure 4.20 with vertical and horizontal actuators attached. For the purposes of damage descriptions, the direction of pushing will be referred to as “south” and the direction of pulling will be referred to as “north”. “East” and “west” can thereby be inferred by standard convention.

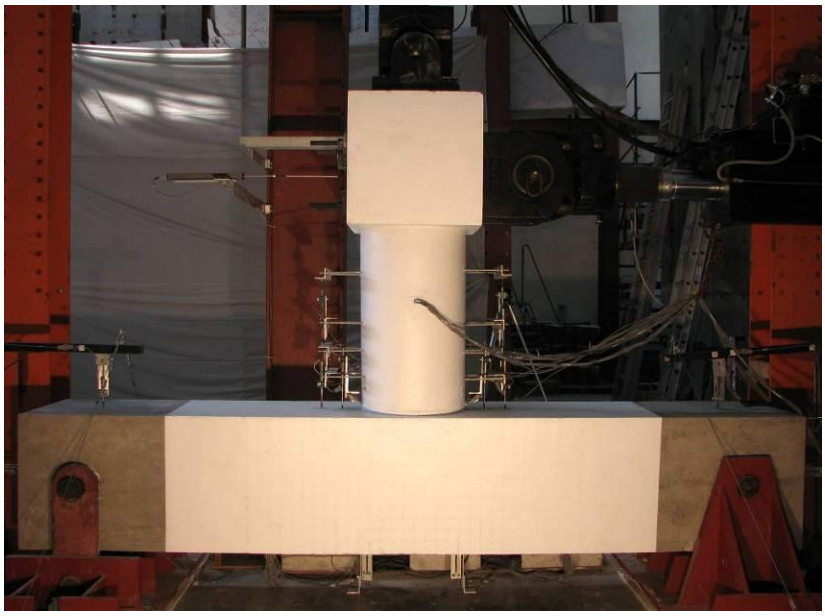

Figure 4.20 HYB-1 prior to testing

Application of 50 kip Vertical Load

Following the application of the vertical load, there was no observed damage on either the bent cap or column.

3 Cycles at ± 15 Kips

During the both the push and pull cycles, a very small hairline crack was observed at the base of the bedding layer at the extreme tension fiber.

3 Cycles at ± 30 Kips

The initial crack observed during the previous push cycle exhibited a slight extension. In the pull direction, one additional hairline crack was observed in addition to a slight extension of the previous crack.

3 Cycles at ± 0.5% Drift Ratio

Originally, this cycle was to be proceeded by a cycle to first bar yield, however first yield of reinforcement was observed at nearly the same time as the displacement associated with 0.50% drift ratio.

Two flexural cracks were observed on the southern side of both faces of the bent cap. These cracks were within approximately 15 inches of the joint interface. A small crack also initiated on

the west face of the bent cap near the northern joint interface. Similar cracking was observed in the pull direction with the exception that a third crack occurred on the east face of the bent cap. The cracking observed on the west face of the bent cap was significantly smaller in length and went to about 25 inches from the joint interface.

The crack at the base of the bedding layer extended and began opening more noticeably during the push cycle. After the pull cycle, the crack at the base of the bedding layer extended, however less than the extension observed in the pull direction. In the pull direction, a long crack was formed at the top of the bedding layer running from roughly the centerline of the column on both sides.

3 Cycles at ± 0.75% Drift Ratio

The flexural cracks on both faces of the bent cap extended during the push cycles. A new flexural crack was observed on the east face of the cap at roughly the centerline of the column. Two additional flexural cracks were observed on the west face: one small crack inside the joint region and another approximately 25 inches from the joint interface. Similar extensions were observed on the east face following the pull cycles. Diagonal cracking was observed in the joint region following the pull cycle on both faces of the bent cap (see Figure 4.21).

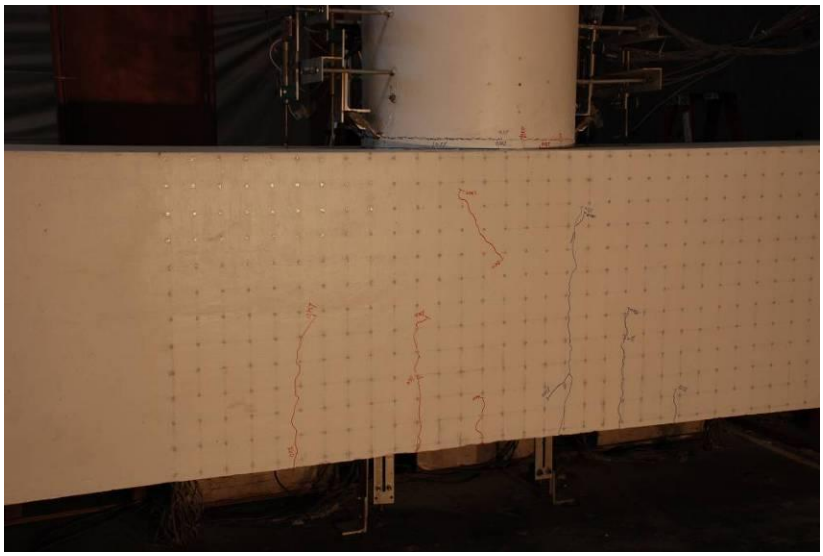

Figure 4.21 HYB-1 east face of bent cap at 0.75% drift ratio

Cracking and gap opening was observed following the push cycle at the top of the bedding layer. All cracks extended to roughly mid-depth of the column from both push and pull cycles. A single

flexural crack was observed after both push and pull cycles on the respective tension side of the column at a height of approximately 14”.

2 Cycles at ± 1.0% Drift Ratio

In the push direction, significant extension of the previous joint diagonal crack was observed on the east face of the bent cap. Minor extensions of the flexural cracks were observed on both faces of the cap with one flexural crack extending with inclination. A new diagonal joint crack was observed on the west face of the bent cap. Minor extensions of the previous diagonal joint crack were observed on the east face.

Both top and bottom bedding layer cracks extended past mid-depth of the column on both push and pull cycles. There is the appearance of incipient spalling from the push cycle; however, the integrity of the concrete appears to be aided by to the presence of the white paint (see Figure 4.22). The flexural crack during the pull cycle extended with a minor inclination.

Figure 4.22 HYB-1 south end of column at 1.0% drift ratio

2 Cycles at ± 1.5% Drift Ratio

A new diagonal joint crack was observed on the east face of the cap due to the push cycles. Minor extensions in the diagonal joint cracks were observed on the west face following the push cycle. No crack extensions were observed in the bent cap due to the pull cycles.

Incipient spalling was noticeable following the push cycle with signs of spalling extending up a height 4.25” and inward from the extreme compression fiber 3.38”. Incipient spalling was similar in the pull direction. There was continual noticeable opening of the cracks in the bedding layer.

Figure 4.23 shows the extent of spalling from the previous push cycle (red hatch marks) and shows the noticeable opening of cracks at both top and bottom of the bedding layer. A new flexural crack was observed at a height of approximately 22” in the push direction.

Figure 4.23 HYB-1 south end of column at 1.5% drift ratio

2 Cycles at ± 2.0% Drift Ratio

Two new joint diagonal cracks were observed on both faces of the bent cap in the pull direction (see Figure 4.24). No other changes were observed in the bent cap.

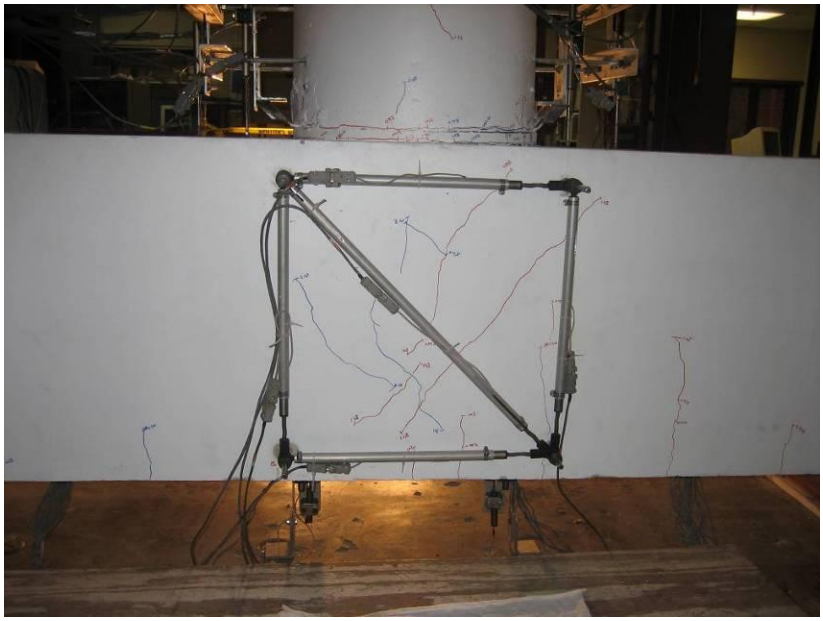

Figure 4.24 HYB-1 west face of bent cap at 2.0% drift ratio

A new flexure-shear crack was observed in the push direction at a height of approximately 18”. There was no noticeable increase in the neutral axis location based on visual observation. The bedding layer cracks continued to opening in both directions. From both push and pull cycles, there were vertical cracks noticed in the column near the location of the mild reinforcement. These cracks are due to the development of the mild reinforcing bars.

2 Cycles at ± 3.0% Drift Ratio

No additional damage was noted on both the east and west side of the cap. Tension cracks were noted on the top of the bent cap at the locations of the corrugated ducts following both push and pull cycles. One of these cracks joined one of the previously noted diagonal joint cracks on the west side of the bent cap.

Under both push and pull loading, the spalling of cover concrete was more severe (see Figure 4.25). Note that the integrity of the concrete was partially maintained by the presence of the paint that was applied prior to testing. This paint had a thicker consistency than usual and helped to mitigate cracking and spalling.

Figure 4.25 HYB-1 south end of column at 3.0% drift ratio

The joint rotation and gap opening at top and bottom of the bedding layer continued to increase. Figure 4.26 shows the bedding layer at a drift ratio of 3.0%. There is very noticeable gap opening and the deterioration of the extreme bedding layer grout as significant spalling occurred. Bond

cracks in the column also extended approximately 8” vertically in the column under the push cycles. The diagonal cracks in the column also continued to extend.

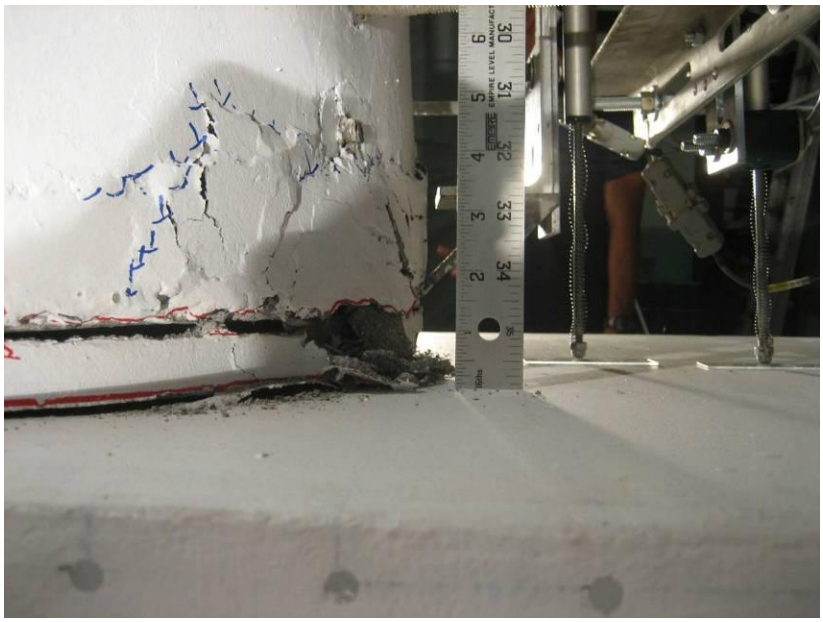

Figure 4.26 HYB-1 north end of column at 3.0% drift ratio

2 Cycles at ± 4.0% Drift Ratio

On the top of the bent cap, one additional tension crack was observed following the push cycles. Following the pull cycles, one new diagonal joint crack was observed on both faces of the bent cap (see Figure 4.27). No other additional bent cap damage was observed.

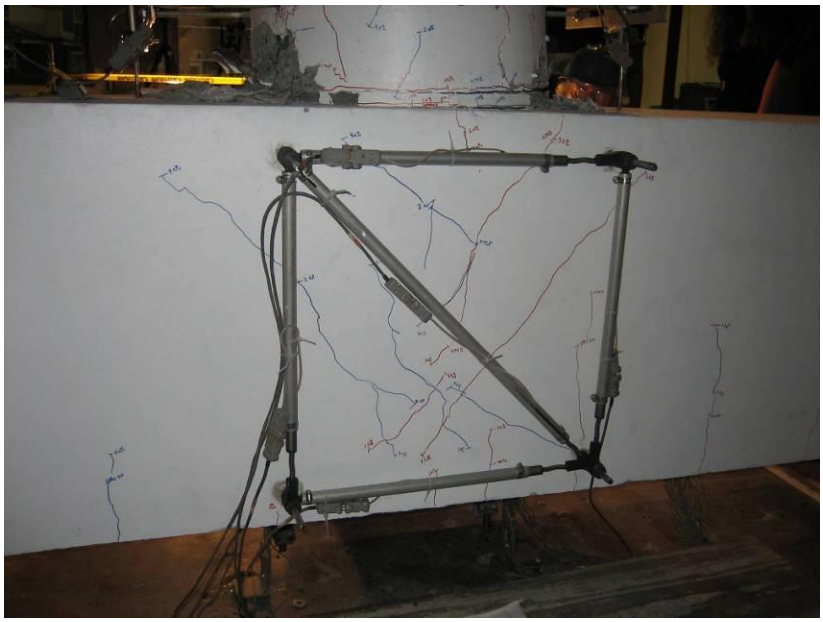

Figure 4.27 HYB-1 west face of bent cap at 4.0% drift ratio

The spalling of column concrete continued and resulted in the exposure of the column spiral on both sides of the column, Figure 4.28. The diagonal cracks in the column continued to grow under both push and pull displacement cycles. Vertical bond cracks in the column also continued to grow. Figure 4.29 shows the condition of the column base following the push cycle. Significant localized damage is observed at the compression toe of the column due to the large compressive strains to which the system was exposed.

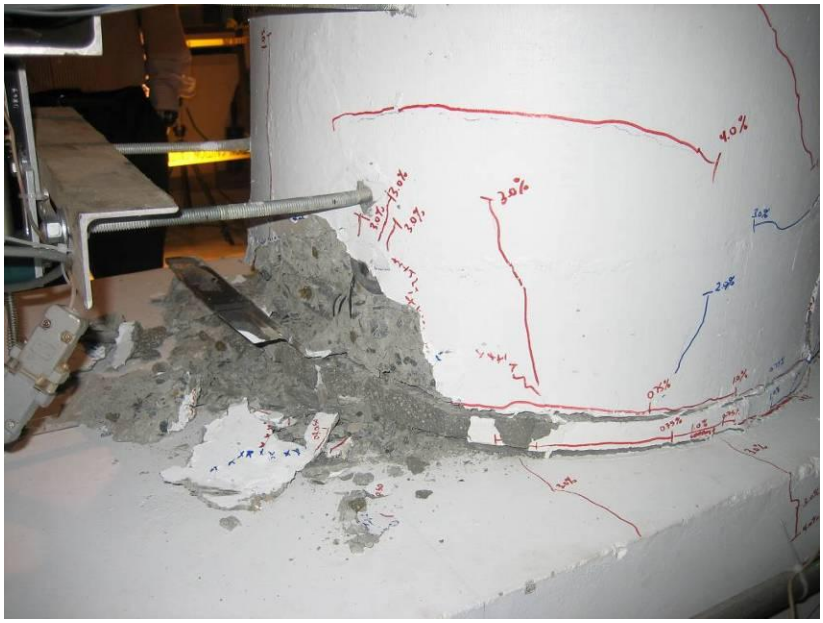

Figure 4.28 HYB-1 north end of column at 4.0% drift ratio

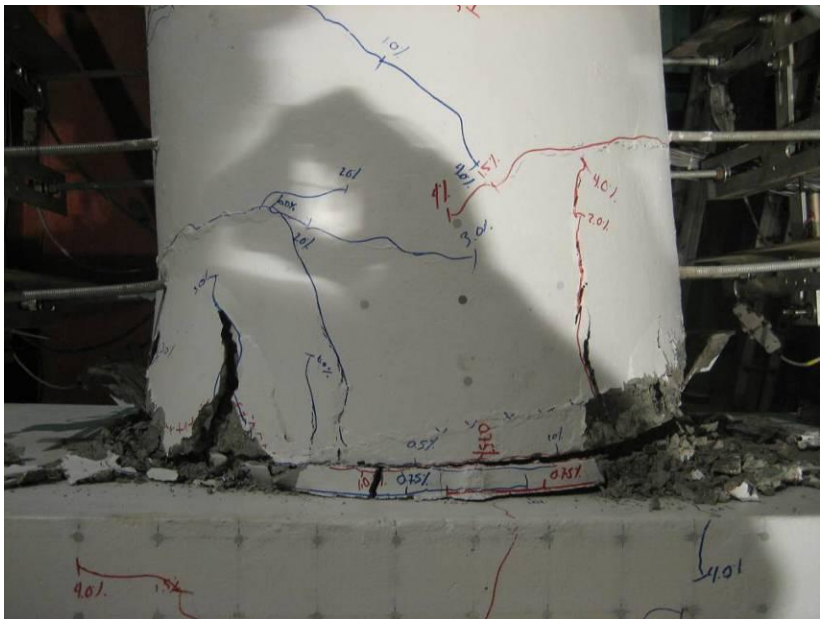

Figure 4.29 HYB-1 east view of column damage at 4.0% drift ratio

2 Cycles at ± 6.0% Drift Ratio

No additional damage was observed on the bent cap after the 6.0% drift ratio cycles.

Significant damage was observed in the column following both directions of loading. A total of three bars on each side of the column were noticeably buckled following both push and pull loading. Figure 4.30 shows the buckling of the extreme bar on the south side of the column. It can also be noticed from this figure that the buckling of the bar has forced the column spiral apart providing a greater distance over which to buckle.

Figure 4.30 HYB-1 buckled bar on south end of column at 6.0% drift ratio

The horizontal force dropped during this displacement cycle due to the reduction in force maintained in the mild reinforcement due to buckling. Following the two cycles to 6.0% drift ratio, the system was cycled to 4.0% drift ratio. During the push cycle to 4.0%, the extreme bar on the north face fractured as shown in Figure 4.31.

Figure 4.31 HYB-1 fracture of extreme bar following bucking on north end of column at 6.0% drift ratio

1 Cycle at ± 8.0% Drift Ratio

With the fracture of one of the mild reinforcing bars, the specimen was officially said to have failed. However, the additional displacement capacity was investigated by pushing the system to one cycle at 8.0% drift ratio. During the push cycle the next two bars in tension fractured. There was also significant spalling of concrete and severe buckling of the three extreme bars on the south side. When approaching 8.0% drift ratio in the pull direction, the three buckled bars on the south side of the column began fracturing in succession. Figure 4.32 shows these fractured bars.

Figure 4.32 HYB-1 fractured bars on south end of column at 8.0% drift ratio

The specimen at the final pull cycle to 8.0% drift ratio is shown in Figure 4.33. Significant damage is observed at the base of the column. It should be noted that although significant damage exists, this is at a significant drift level and all damage is highly localized to the base of the column. Furthermore, as compared to a cast-in-place system the damage is significantly less in both the column and bent cap. This system achieved larger ultimate drifts than a comparable cast-in-place system.

Figure 4.33 HYB-1 specimen at 8.0% drift ratio

End of Test

The state of the specimen is shown in Figure 4.34 through Figure 4.39. It is observed that the damage at the base of the column is not symmetric between the east and west sides. The extent of spalling extends almost twice as far up the column on the east side whereas the damage is localized to the first 6 inches on the west side.

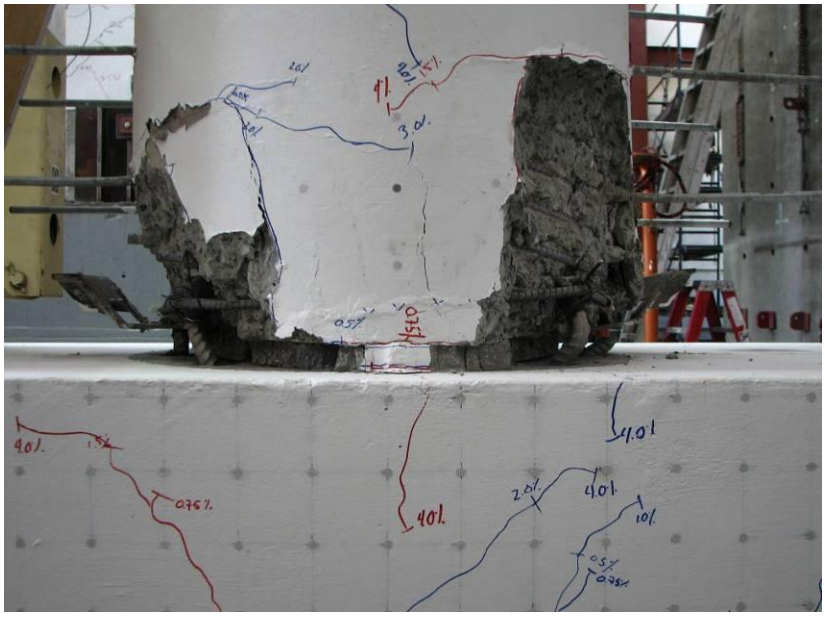

Figure 4.34 HYB-1 east view of damage to column post-test

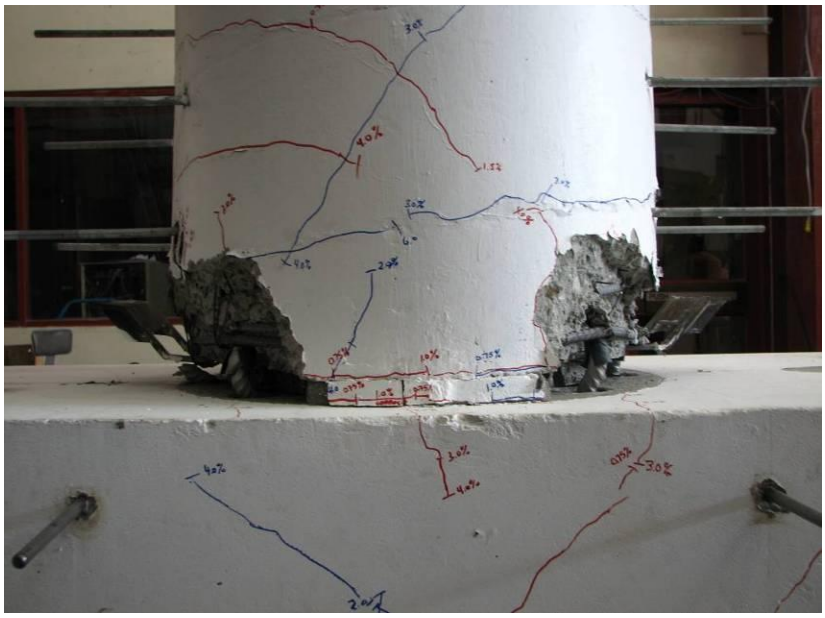

Figure 4.35 HYB-1 west view of damage to column post-test

Residual gaps in the bedding layer were observed on both the north and south side of the column (see Figure 4.36). This signifies there was residual straining in the concrete and bedding layer resulting from large compressive strains. The larger effective post-tensioning force causes an increase in the neutral axis depth and a subsequent significant increase in the compressive strains in concrete. This also means that the compressive force in the column is flowing through the center of the column at the base, not uniformly across the section. This residual straining is suspected to be the reason the system was unable to self-center as intended. As the majority of the compressive force flows through the center of the column, it is postulated that insufficient compressive forces were acting on the mild reinforcement to force them back to a zero strain state at the end of each cycle. This means the system would not be origin oriented as a lateral force would be required to maintain the zero displacement state.

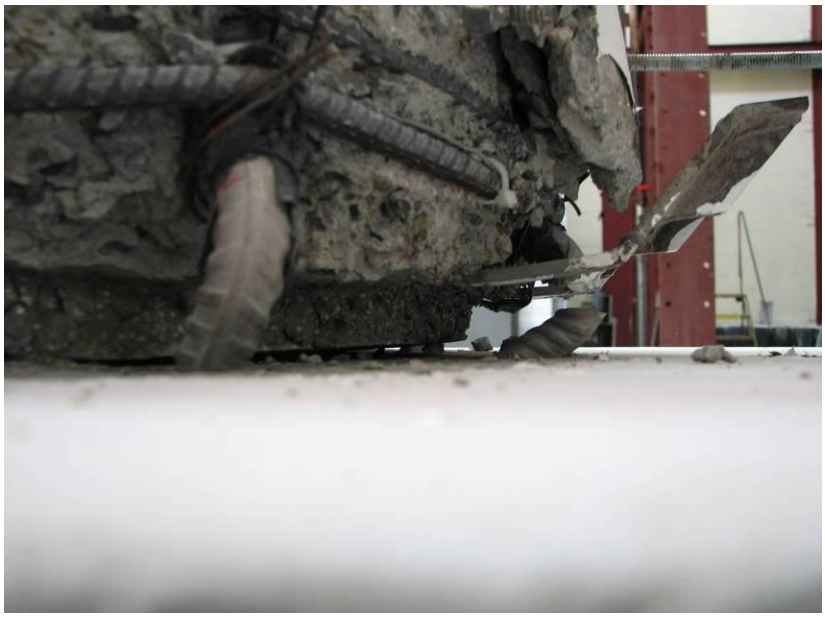

Figure 4.36 HYB-1 residual gap at north end of bedding layer post-test

The damage to the bent cap joint region can be seen in Figure 4.37 and Figure 4.38. The damage observed on both faces of the bent cap was minor and consisted of small diagonal tension cracks in combination with flexural tension cracks at the bottom of the specimen. The damage on both sides of the specimen is comparable with slightly more observed distress on the west face of the bent cap.

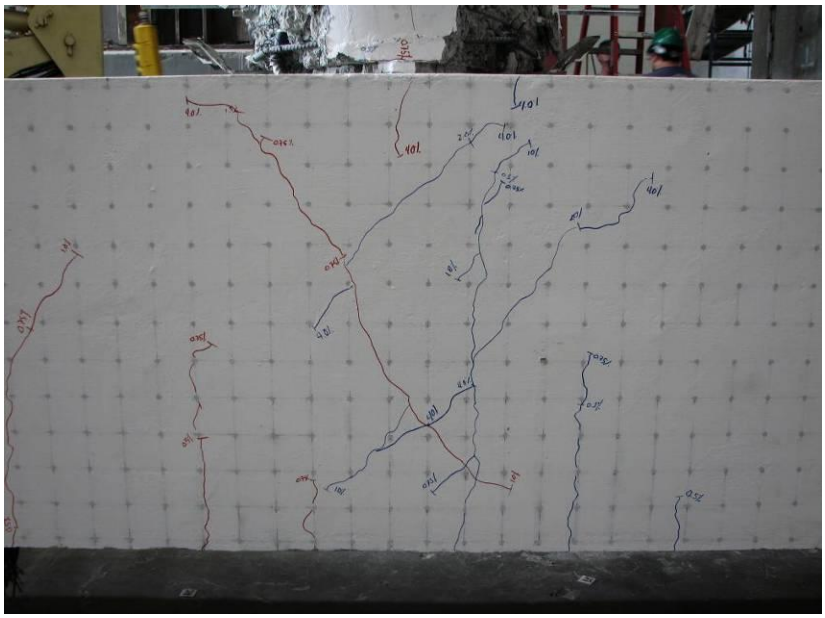

Figure 4.37 HYB-1 east face of bent cap post-test

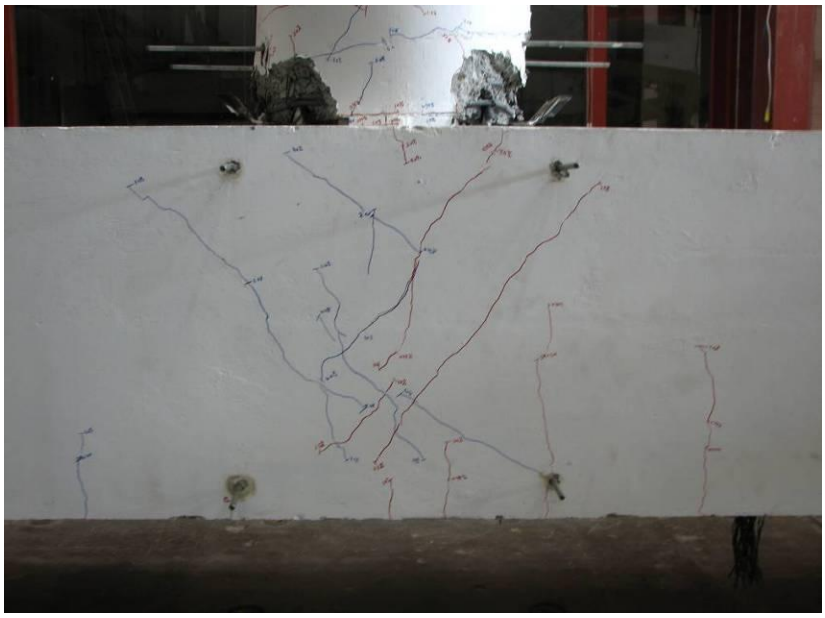

Figure 4.38 HYB-1 west face of bent cap post-test

Figure 4.39 shows the post-test condition of the extreme bar on the south side of the column. The severity of the bar buckling can be observed from this photo. Not only did the bar buckle far outward, but also circumferentially along the column spiral. The debonding material used on the mild reinforcement can be seen in this photo (black plastic). This material was cut away from the front of the bar following the test to show more clearly the buckling mode.

Figure 4.39 HYB-1 evidence of severe bar buckling and fracture

4.5 Experimental Results

Data collected during testing from instrumentation is presented and discussed in the following section.

4.5.1 Global Response

Vertical Load History

The vertical load history recorded during testing is presented in Figure 4.40. It is noted that the load is rather constant at 50 kips during the entirety of the test. However, measurements indicated that during the pull cycles there tends to be more variation in the vertical load as compared to the push cycles. This variation is approximately two kips and will not significantly affect the behavior of this specimen.

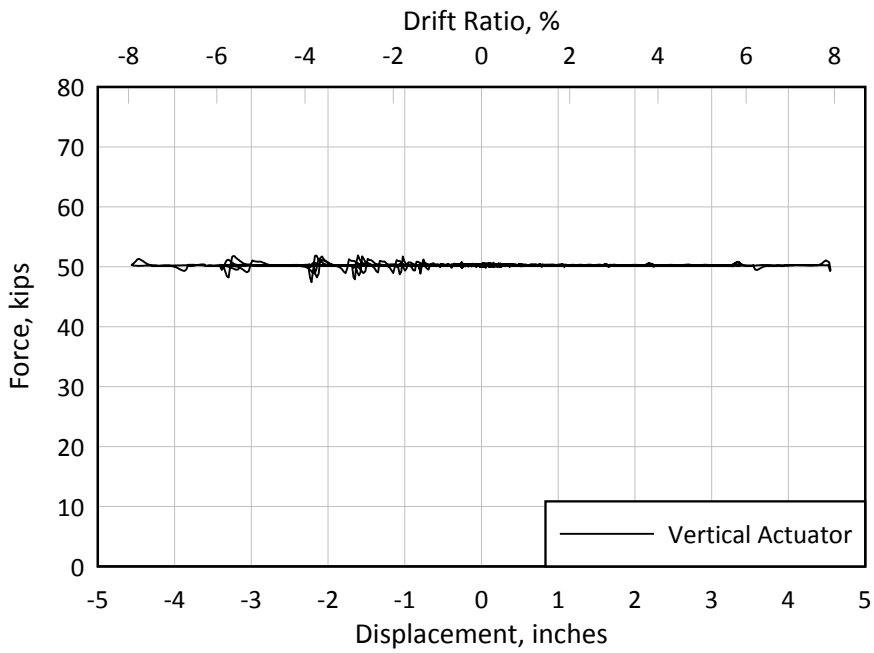

Figure 4.40 HYB-1 vertical load history

Force-Displacement Response

The complete force-displacement curve obtained for this specimen is shown in Figure 4.41. The lateral force presented is the actual lateral force considering the effects of system deformation during testing. Stable lateral response is observed up to and including drift levels of 6.0%. During the cycles to 8.0%, a considerable drop in the lateral load resistance is observed. During testing, it was noted by auditory observation that the first reinforcing bar actually fractured during the push cycle to 4.0% drift ratio following the two cycles to 6.0% drift ratio. This can be observed in the experimental data with the sudden short drop in lateral load just prior to reaching 4.0% drift ratio in the push direction. The nominal capacity calculated using the simplified analysis technique is also provided in the force-displacement figure.

The force-displacement curve up to 3.0% drift ratio is shown in Figure 4.42. The hysteretic response in this region is stable and indicates appreciable energy is dissipated through cyclic actions. Additionally, it is observed that the response of the system is more origin oriented as compared with traditional cast-in-place systems. However, it is apparent that the system does exhibit residual displacements at increasing amplitudes.

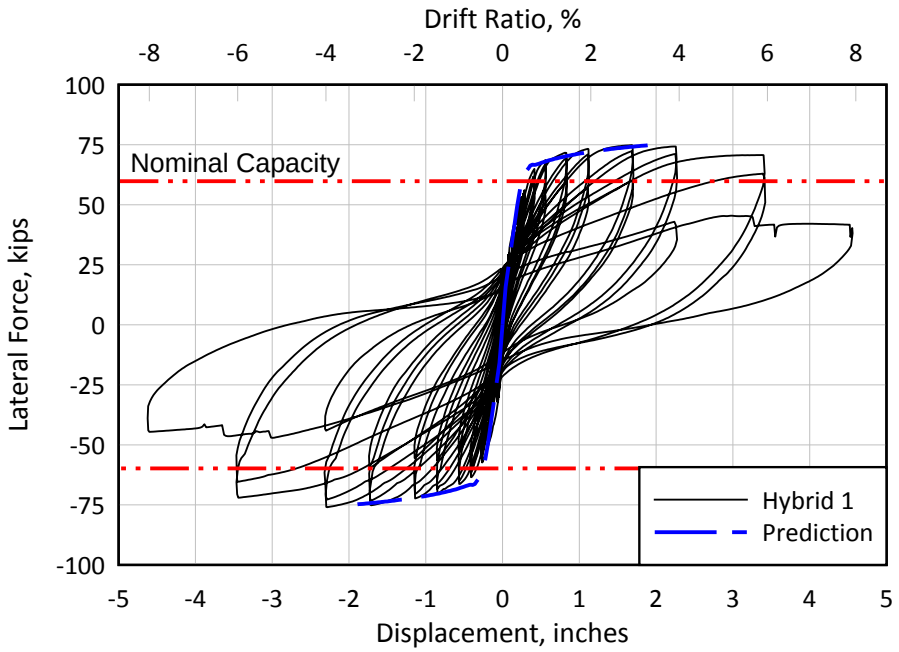

Figure 4.41 HYB-1 force-displacement response

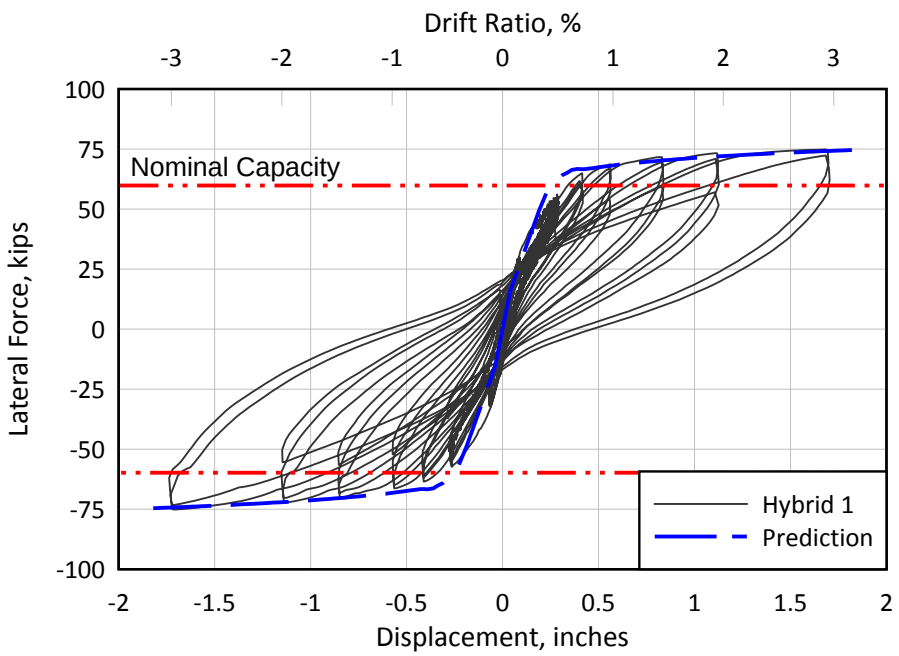

Figure 4.42 HYB-1 force-displacement response to 3.0% drift ratio

The force-displacement response for both cycles at approximately 2% drift ratio is shown in Figure 4.43. It can be observed from this plot that there are only minor reductions in stiffness and strength due to cyclic loading at a drift level approximately equal to the design level drift. This response characteristic is consistent with the desired stable lateral response in the design level displacement range.

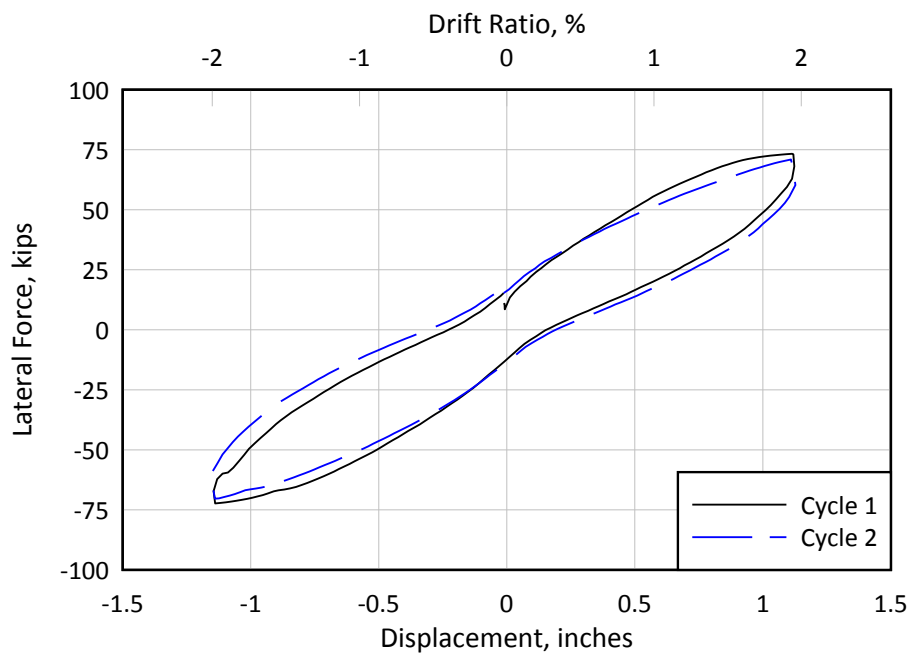

Figure 4.43 HYB-1 force-displacement response at 2% drift ratio

The predicted force-displacement envelope matches well with the observed experimental results. The actual envelope versus the predicted envelope is provided in Figure 4.44. The ultimate lateral displacement capacity was greatly underestimated by predictions as is apparent in the force-displacement envelope plot. The ultimate lateral displacement prediction was related to the ultimate confined concrete strain as predicted by the Mander et. al (1988). This model typically underestimates the ultimate strain, especially for a highly disturbed region such at the compression toe of a rocking column. The predicted failure mode of crushing of the confined concrete core was not observed, but instead fracture of the extreme reinforcing bar in tension.

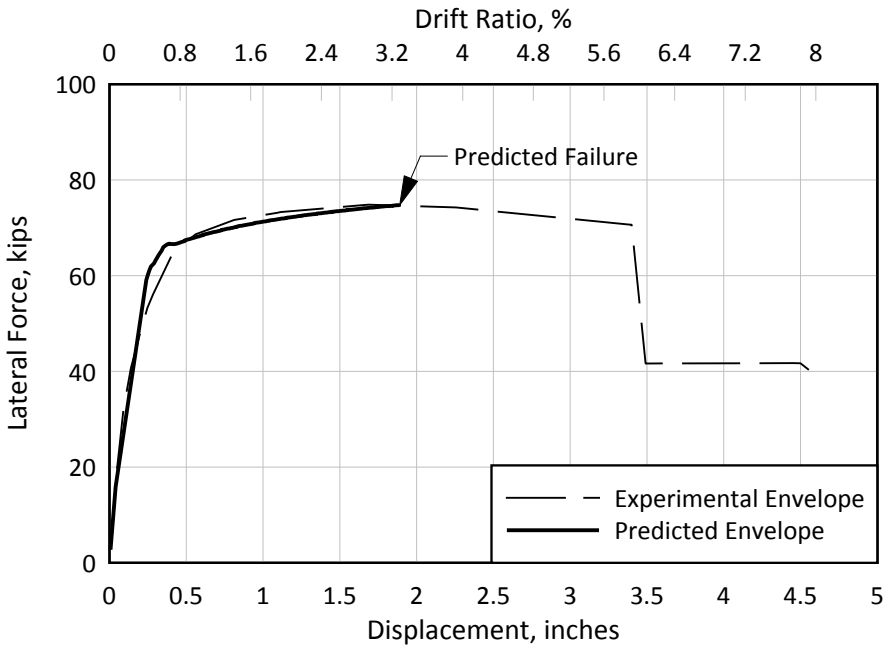

Figure 4.44 HYB-1 force-displacement envelope

Displacement Decomposition

Figure 4.45 provides a graphical breakdown of the key components of the lateral deformation captured with instrumentation during testing. This plot provides a summary of the relative contribution of a given mode of deformation as compared to the total displacement recorded at the same instant of time. From this plot, it is observed that with increasing lateral deformation, the relative contribution of end rotations becomes more dominant as the relative contribution of column flexure and beam rotation reduce. This trend is expected as the system facilitates larger deformations through concentrated end rotations. The reduction in total displacement modes recorded at larger drift ratios indicates the presence of additional modes of response occurring at large drift ratios.

The difference between the sum of the relative contributions and 100% are due to additional system deformations not explicitly isolated with instrumentation during testing.

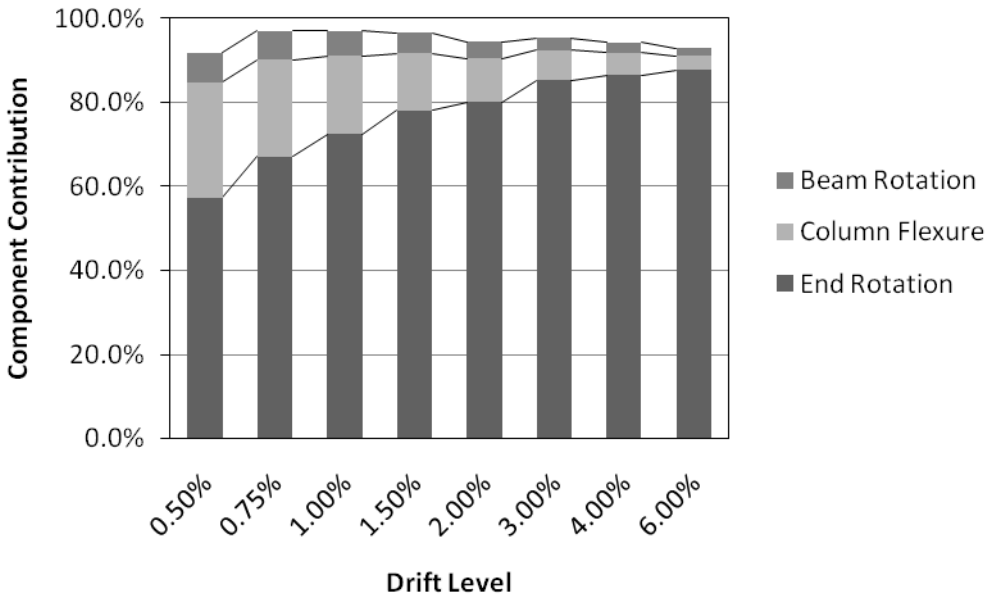

Figure 4.45 HYB-1 displacement decomposition

Out-of-Plane Displacement

During testing, the out-of-place displacement at the actuator was monitored as a safety precaution to ensure the vertical actuator control remains stable while under force control. Figure 4.46 shows the displacement orbit for the test specimen. As is apparent, the out-of-place movement was significantly more pronounced during the push cycle reaching a maximum out-of-plane drift ratio of 1.45% to the west. During the pull cycle, the maximum out-of-plane drift ratio observed was 0.35% to the east.

At the final push cycle, the lateral displacement increases appreciably indicating the presence of localized damage likely on the west side resulting in a global lateral sway of the column tip. This response may likely also create a twisting action in the column that can induce additional stresses on the column longitudinal reinforcement.

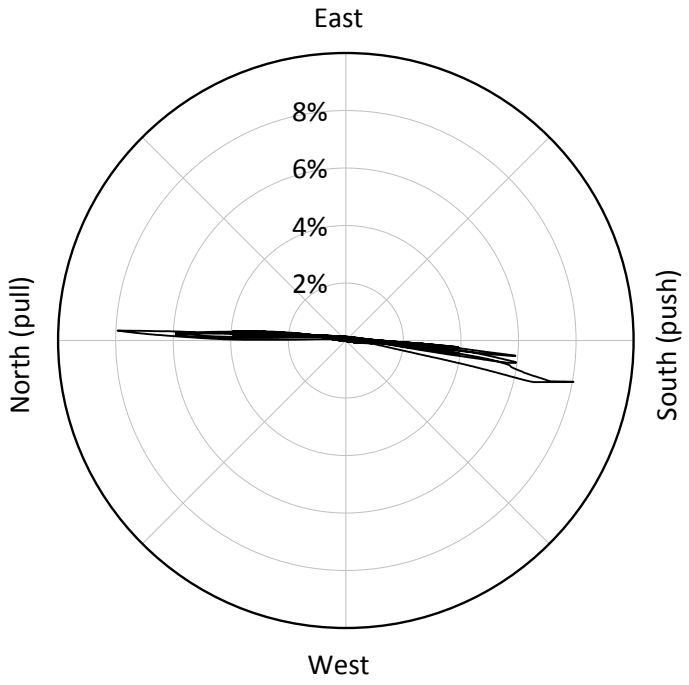

Figure 4.46 HYB-1 drift ratio orbit

Equivalent Viscous Damping

Based on the recorded force-displacement response of the specimen, the equivalent viscous damping was calculated. Figure 4.47 shows the variation of equivalent viscous damping over different lateral drift levels. As lateral drift increases, there is a subsequent increase in the level of equivalent viscous damping. Additionally, the second cycle to a given drift level exhibits slightly greater levels of equivalent viscous damping due to the observed accumulation of damage.

The relatively minor increase in damping from cycle 1 to cycle 2 indicates that the system does not have significant deterioration upon subsequent cycles. The main objective of considering equivalent viscous damping is to show relative stability between hysteresis loops at the same drift level. As the first and second cycles have similar equivalent viscous damping, the loops are relatively stable during cycles at the same drift level.

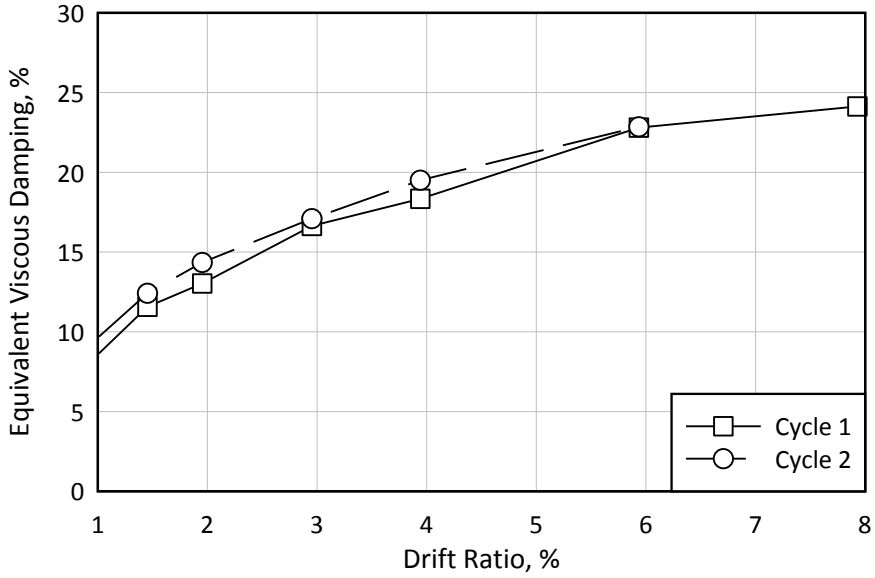

Figure 4.47 HYB-1 equivalent viscous damping

Residual Displacement

One of the major aims of a hybrid bridge column system is to reduce the residual displacements during cyclic lateral loading. Figure 4.48 provides a plot of the recorded residual drift following the first and second displacement cycles as compared to the maximum drift recorded during the respective cycles. Note that the maximum ratio for push and pull directions is recorded in this plot. This plot indicates that the residual drifts increase from first to second cycles. Additionally it is observed that the residual displacements increase in magnitude and relative ratio as the drift levels.

During previous earthquakes such as Kobe, a common trend was that bridge columns with drift levels in excess of one degree would require replacement. This rotation angle corresponds to a drift in the range of 1.75 percent. From inspection of the plots, it can be concluded that this specimen can undergo drift levels in excess of 4% while still meeting this residual drift requirement.

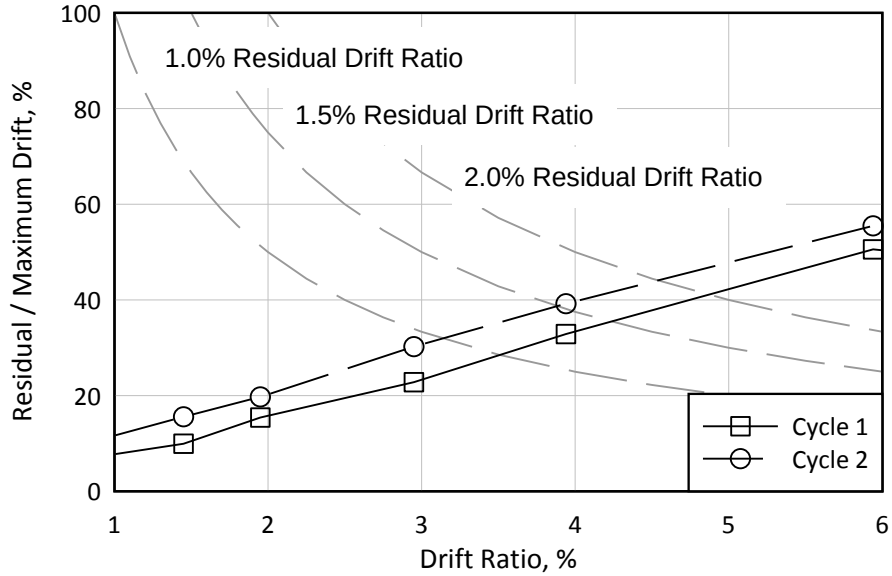

Figure 4.48 HYB-1 residual drift ratios

Recorded residual drift ratios for this specimen are compared against results of the cast-in-place specimen, as shown in Figure 4.49. This plot clearly shows a reduction in residual deformation when comparing the hybrid unit versus the cast-in-place unit. The hybrid specimen can undergo over 4% drift ratios and still have residual drift angle less than one degree. However, the cast-in-place unit can only undergo approximately 2.75% drift ratio while meeting this same requirement.

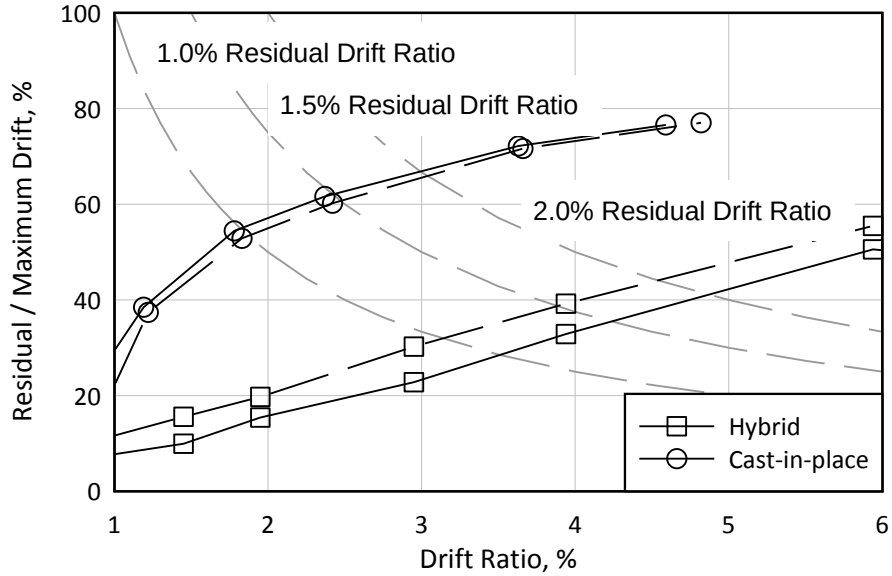

Figure 4.49 HYB-1 comparison of residual drift ratios with CIP

Bedding Layer

The axial deformation at the centerline of the grout bedding layer was determined for the entirety of the test using the curvature gages at the base of the column. These results are presented in Figure 4.50. The actual observed extension of the bedding layer increased under increasing lateral displacements, as expected. Following lateral displacement cycles to approximately 2% drift ratio, the bedding layer was observed to reduce in dimension when at the zero displacement state. This indicates the accumulation of damage at the grout bedding layer resulted in permanent reduction in the thickness of the bedding layer by up to 7% following displacement cycles to 6% drift ratio.

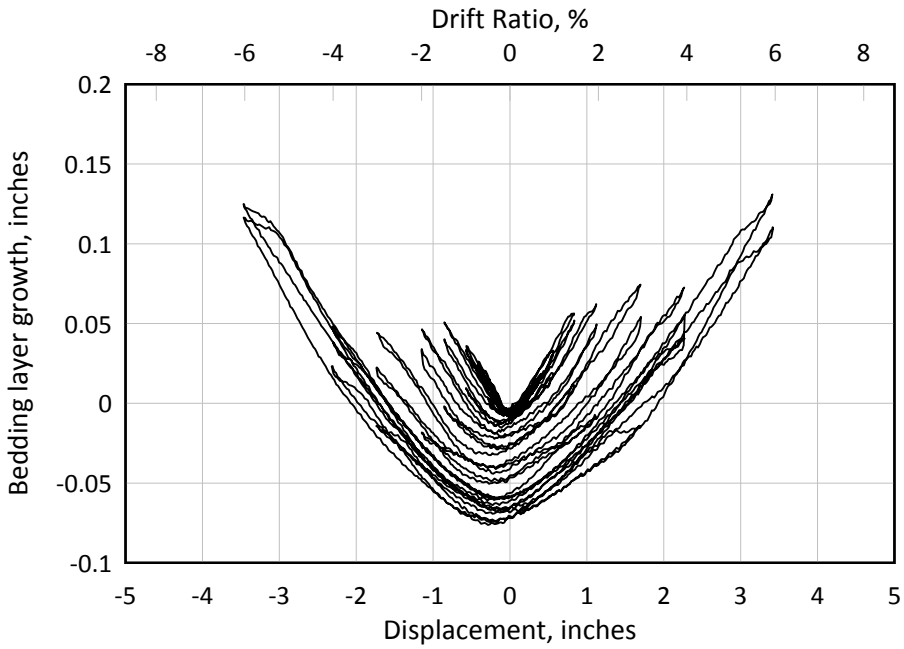

Figure 4.50 HYB-1 centerline of bedding layer deformation

Neutral Axis Depth

The depth of the neutral axis was determined for each drift cycle using the curvature gages at the base of the column. This depth was calculated considering the assumption that plane sections will remain plane in a concrete section that is a reasonable approximation for the purpose of this calculation. Figure 4.51 shows the neutral axis depth for the first displacement cycle at a given drift level for both push and pull directions. This plot clearly shows the specimen has a deep neutral axis depth in excess of 40% of the column diameter. This deep neutral axis depth means the extreme concrete fibers will undergo significant compressive strains. Photographic recordings show the adverse impact of these large strain levels in the form of residual compressive strains in the grout layer and a consequential reduction in the self-centering capacity.

The target neutral axis depth was approximately equal to 25% of the column diameter. However, due to smaller than expected post-tensioning losses the effective post-tensioning force resulted in larger compressive forces across the section.

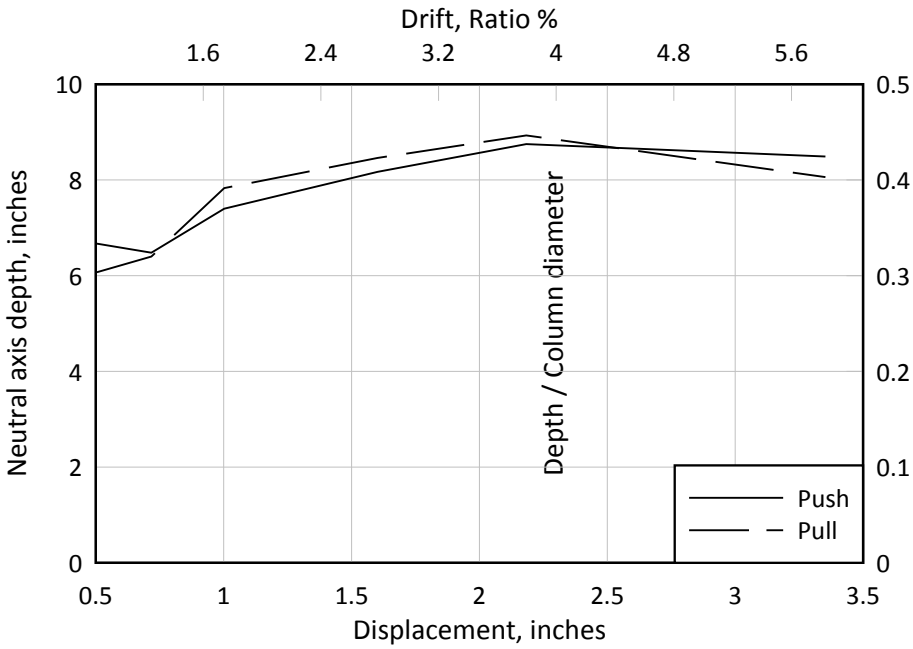

Figure 4.51 HYB-1 neutral axis depth

4.5.2 Rotation Profile

The column rotation profile, as derived from column curvature gages, is provided in Figure 4.52. A rotation profile, as opposed to a traditional curvature profile, was provided for this specimen due to the dominance of response on the column fixed end rotation, which cannot be accurate represented by a curvature approximation. This is due to the lack of an effective gage length for consideration due to intentional debonding at the column end. These results indicate that the majority of column displacement is provided by the column fixed end rotation, with little influence from elastic flexural displacements at higher drift levels.

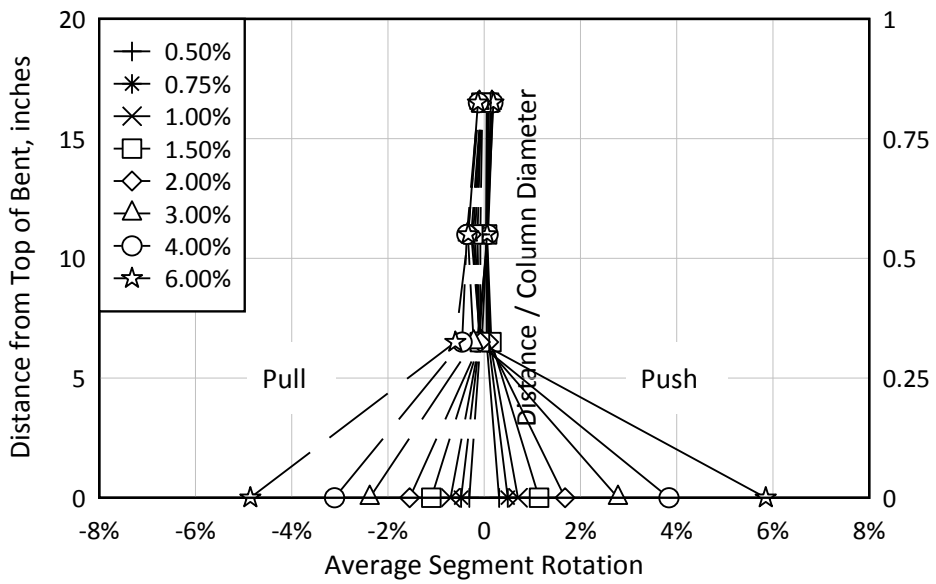

Figure 4.52 HYB-1 column rotation profile

4.5.3 Column Longitudinal Bar Slip

Bar slip readings for the two extreme column bars are presented in Figure 4.53 and Figure 4.54. These recordings indicate that the bond of the column longitudinal reinforcement is adequate with negligible bar slip at the end of the bar. Maximum bar slip recordings were less than one-hundredth of an inch during the entirety of the test. The extreme reinforcing bar in both directions achieved ultimate strength at the joint region without appreciable slip at the bar end. These results indicate that the bond characteristics of the grouted duct connection are sufficient to develop the ultimate strength of the stainless steel reinforcing bar with negligible slip.

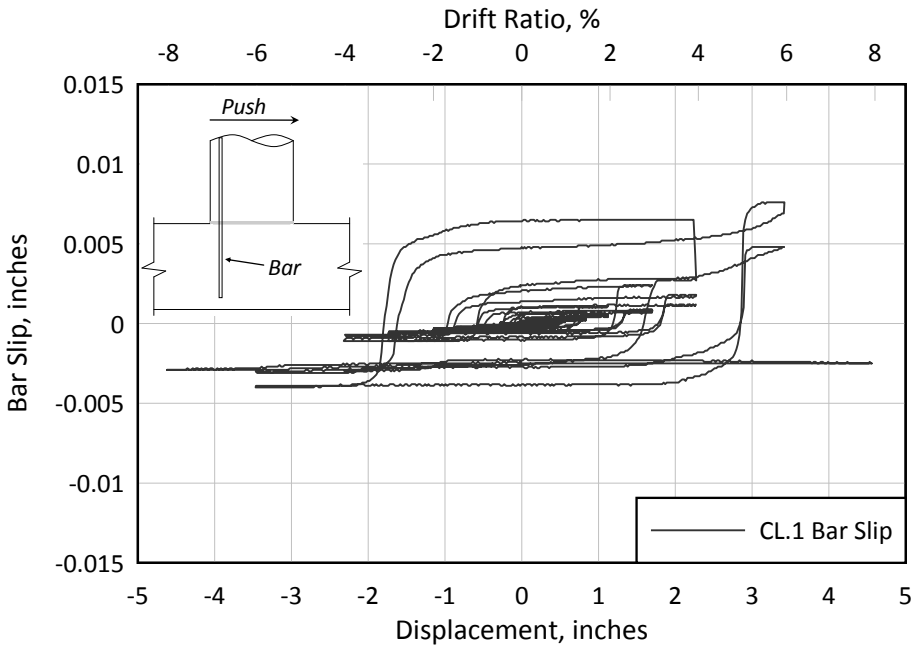

Figure 4.53 HYB-1 column longitudinal bar slip at end of bar (CL.1)

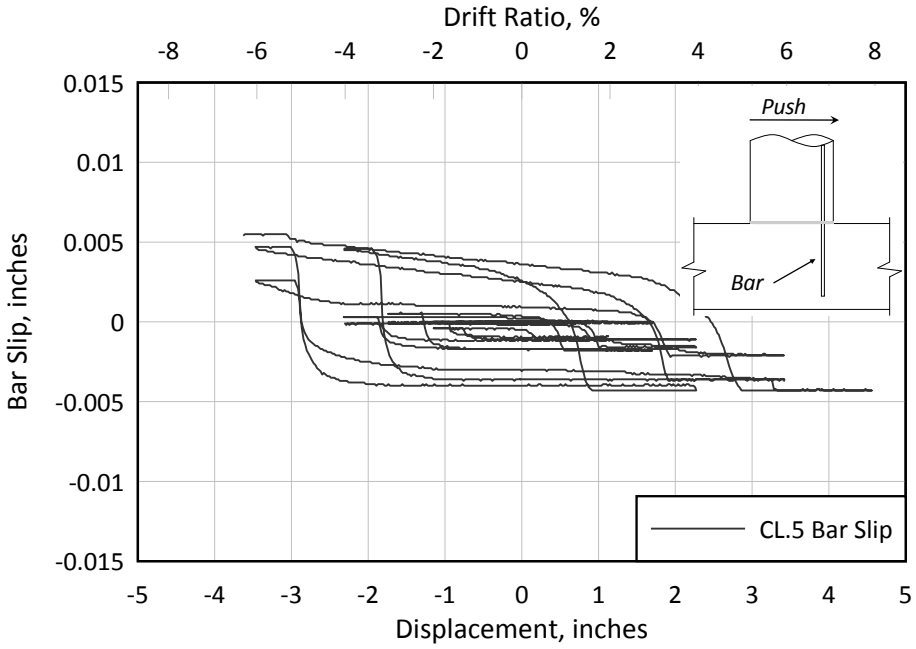

Figure 4.54 HYB-1 column longitudinal bar slip at end of bar (CL.5)

4.5.4 Strain Gage Histories

A number of strain gages are mounted on various pieces of reinforcing steel throughout the specimen. Many of these gages were damaged during fabrication, erection and testing thus many readings are not show herein. Additionally, many plots have incomplete data due to damage or malfunctioning gages. This section provides information on the strain histories recorded by various gages.

Column Longitudinal

Strain histories for gages mounted on the extreme column longitudinal bars on the north and south ends of the column are shown in Figure 4.55 thru Figure 4.62. It can be observed from these photos that yield in the extreme tension bar occurred at a drift level of approximately 0.50% for both push and pull directions. It can also be noted that extensive yielding of the reinforcing bar is evident at three locations during both push and pull loading. The distribution of strain in the column bars can be seen in more detail when looking at the strain profiles in the following section. Based on reading from bar CL.1.5, it is noted that yielding of the extreme flexural reinforcing bar occurred up to 9 inches into the bent cap. This corresponds to 14 times the reinforcing bar diameter.

Another key trend that was observed is the compressive straining of the column bars equal to approximately two-thirds the tension strain. This indicates the neutral axis depth is approximately equal to one-third of the column depth at these loading levels, which is larger than intended during the design phase. Yielding of the column reinforcement was noted well into the bent cap indicating significant yield penetration occurred.

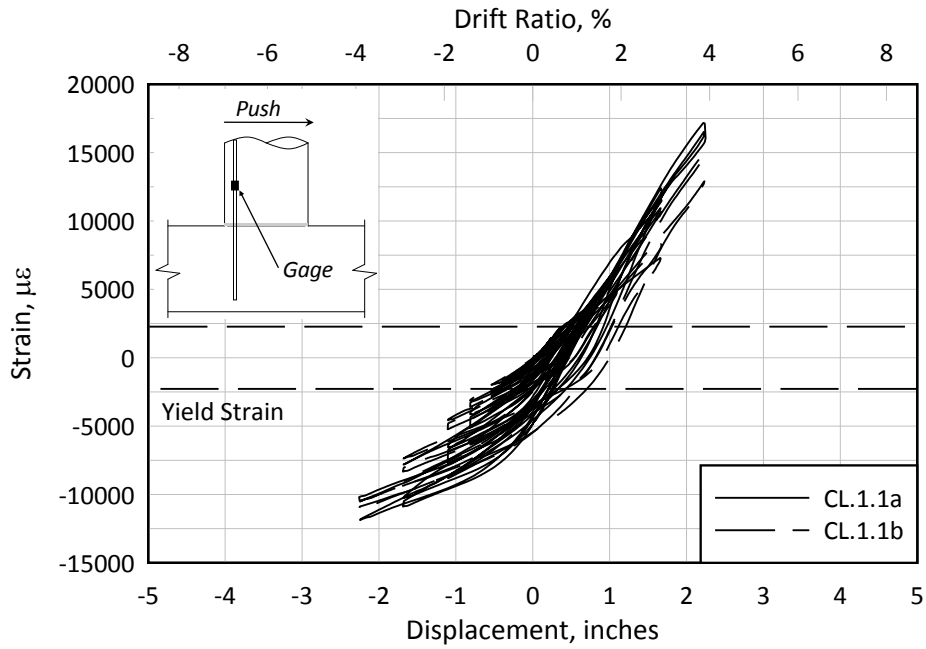

Figure 4.55 HYB-1 column longitudinal rebar strain (CL.1.1)

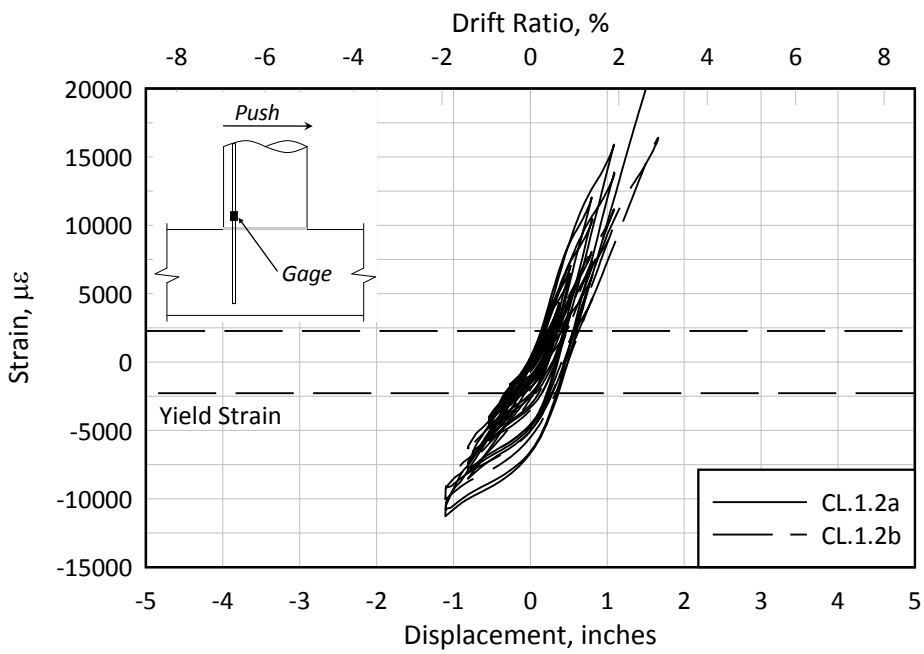

Figure 4.56 HYB-1 column longitudinal rebar strain (CL.1.2)

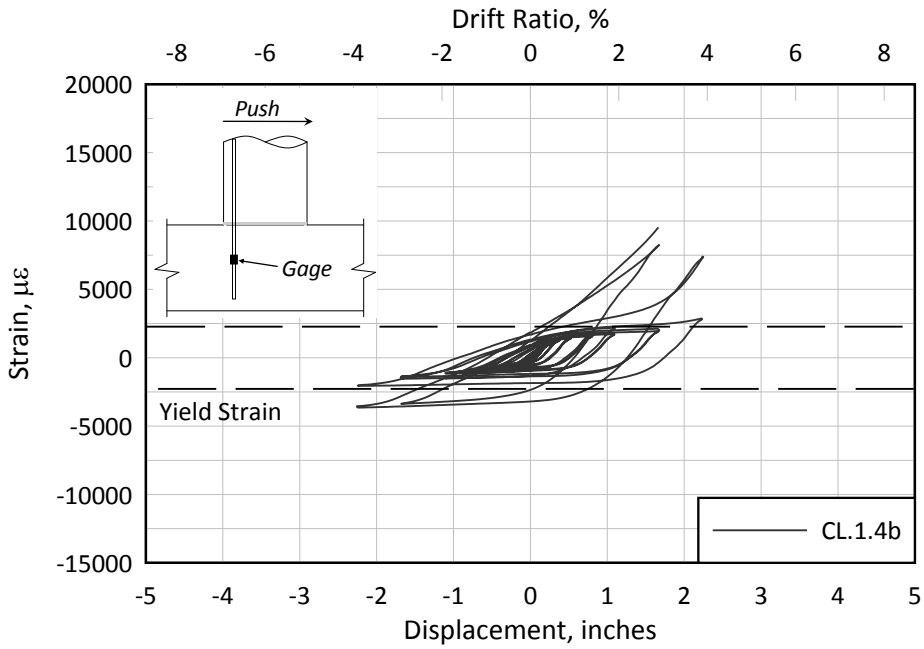

Figure 4.57 HYB-1 column longitudinal rebar strain (CL.1.4)

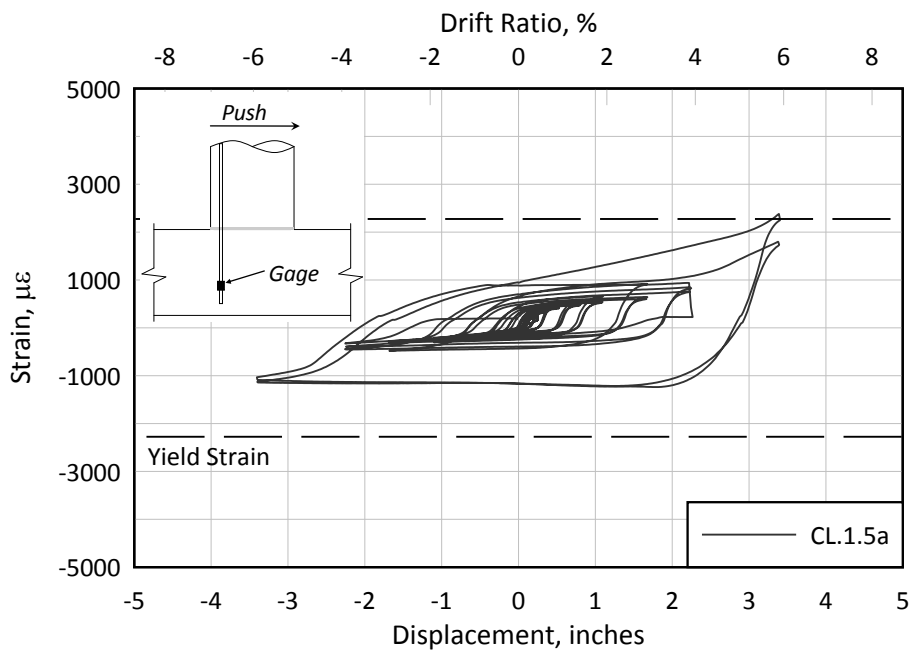

Figure 4.58 HYB-1 column longitudinal rebar strain (CL.1.5)

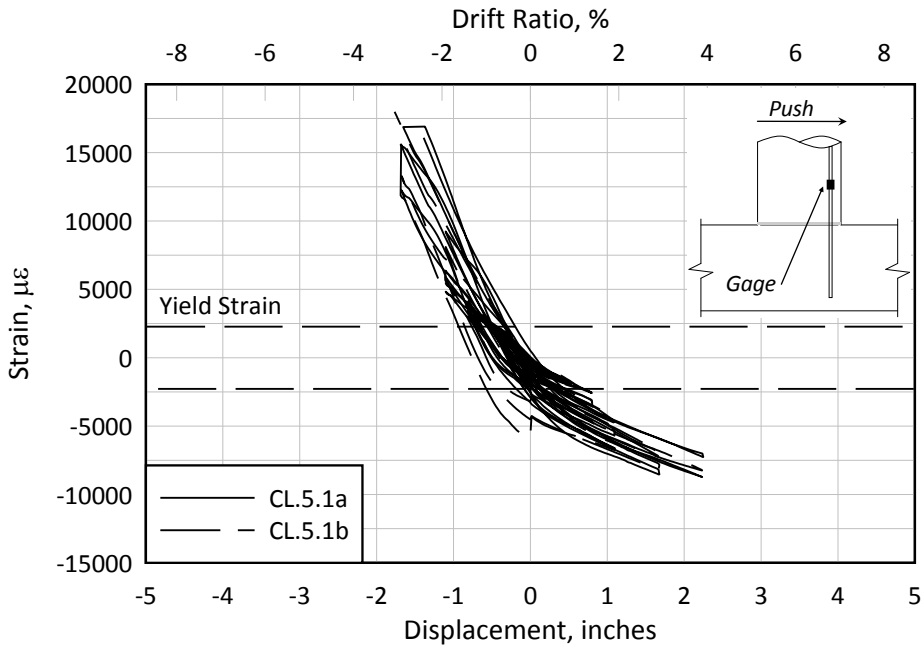

Figure 4.59 HYB-1 column longitudinal rebar strain (CL.5.1)

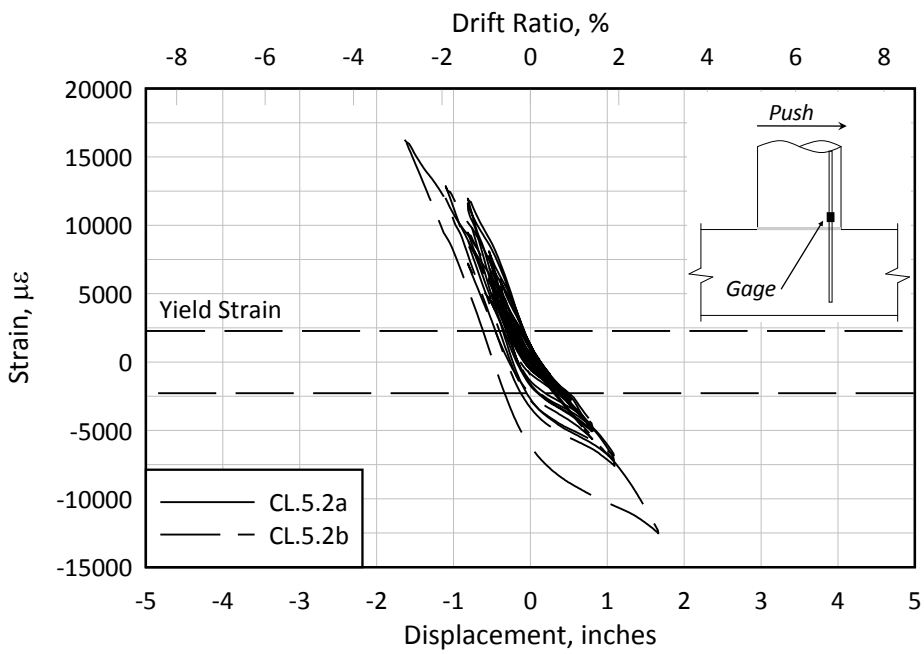

Figure 4.60 HYB-1 column longitudinal rebar strain (CL.5.2)

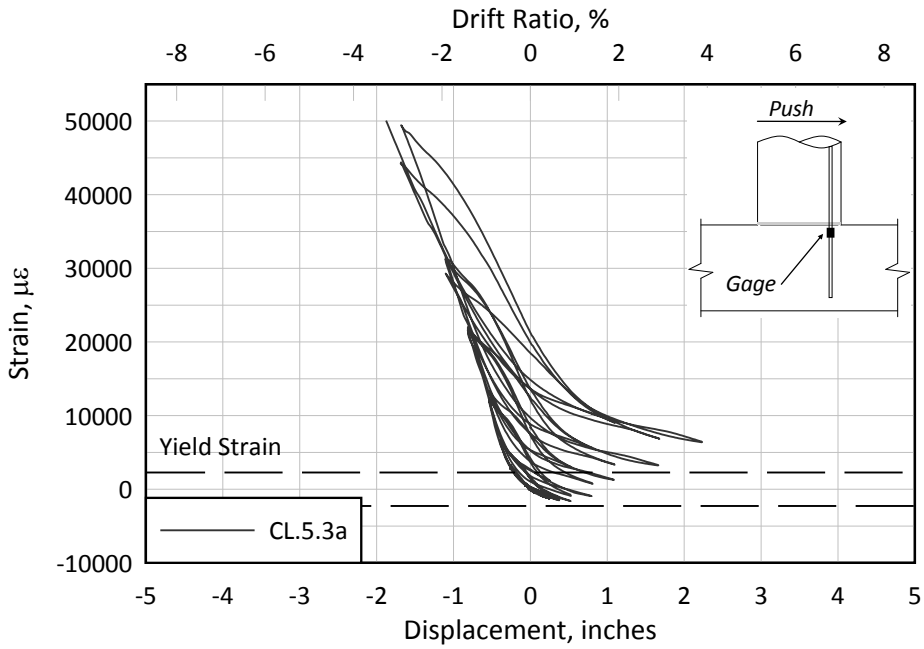

Figure 4.61 HYB-1 column longitudinal rebar strain (CL.5.3)

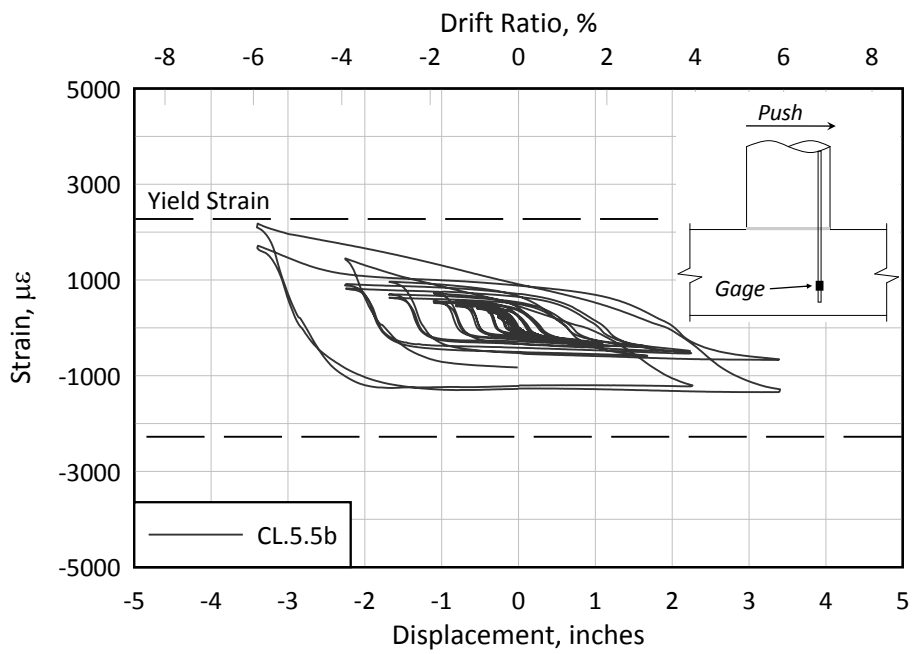

Figure 4.62 HYB-1 column longitudinal rebar strain (CL.5.5)

Post-Tensioning

The strain history for the post-tensioning tendons is shown in Figure 4.63. Strains recorded during both push and pull loading cycles are rather consistent. A negative shift in the strain at zero displacement was noted during large displacement cycles indicating a loss of post-tensioning force. However, based on review of the strain levels in the tendon it is considered more likely that the loss in post-tensioning is due to column shortening caused by degradation of the grout bedding layer.

Additionally, the slope of the post-tensioning strain decreased under larger drift cycles. This reduction in slope is indicative of a reduction in the global stiffness, which was observed in the force-displacement plots for the system.

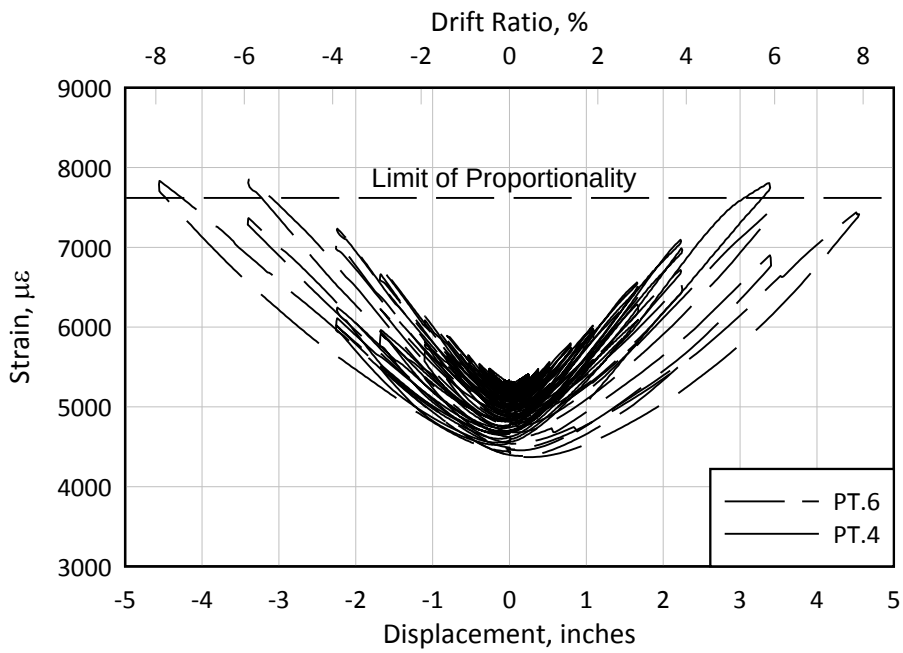

Figure 4.63 HYB-1 post-tensioning strain

Column Confinement

Strain gage histories for gages mounted on the column spiral reinforcement are shown in Figure 4.64 thru Figure 4.71. Results from the first two sets of gages on both the north and south end of the column indicate significant tensile strains were present during pull and push cycles, respectively. These large strains are the result of dilatational behavior of the confined concrete core and the subsequent activation of passive confinement provided by the spiral reinforcement.

The significant yielding observed for these bottom two sets of gages resulted in significant drift in strain readings due to residual straining. However, the fracture of column spiral reinforcement was not observed during testing. The spiral reinforcement was noted to slip vertically as the column longitudinal reinforcement buckled relieving the ultimate stress experienced by the spiral reinforcement.

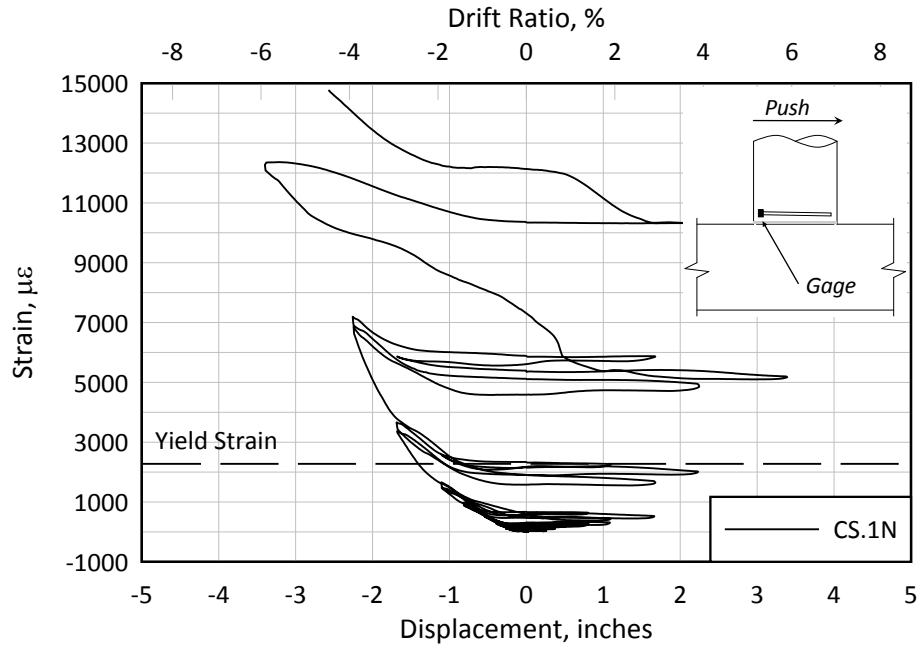

Figure 4.64 HYB-1column spiral rebar strain (CS.1N)

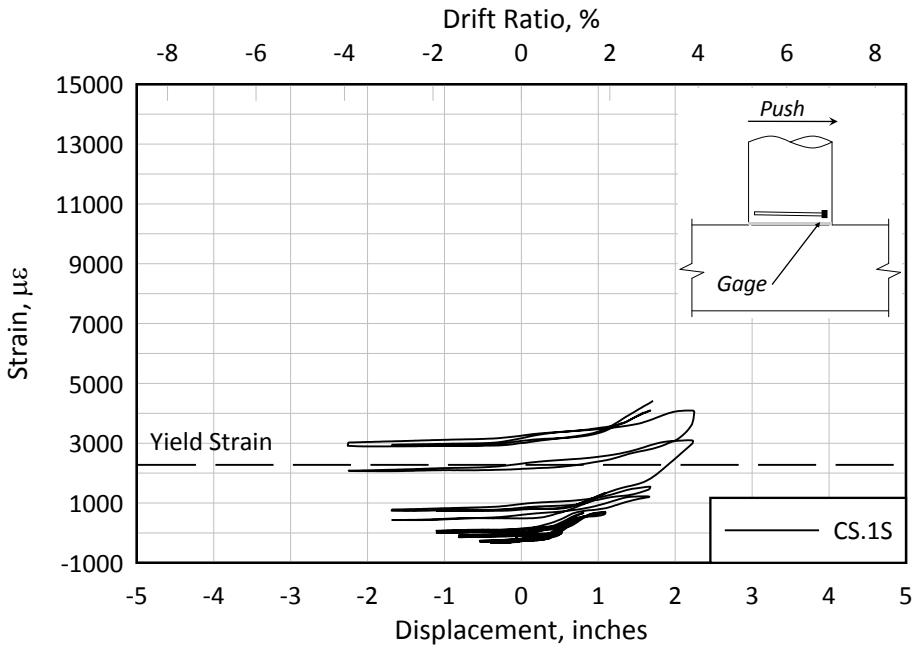

Figure 4.65 HYB-1column spiral rebar strain (CS.1S)

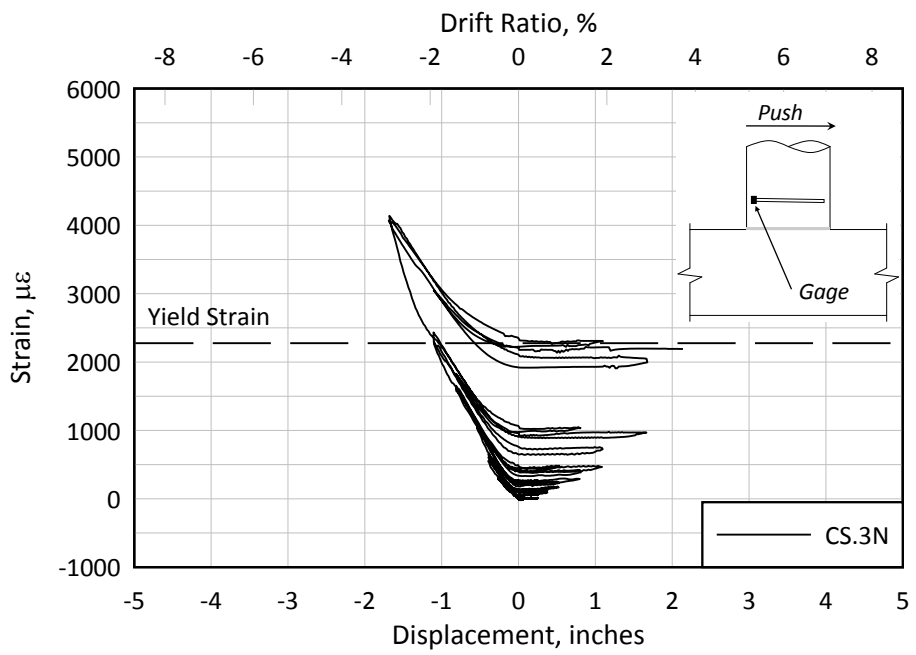

Figure 4.66 HYB-1column spiral rebar strain (CS.3N)

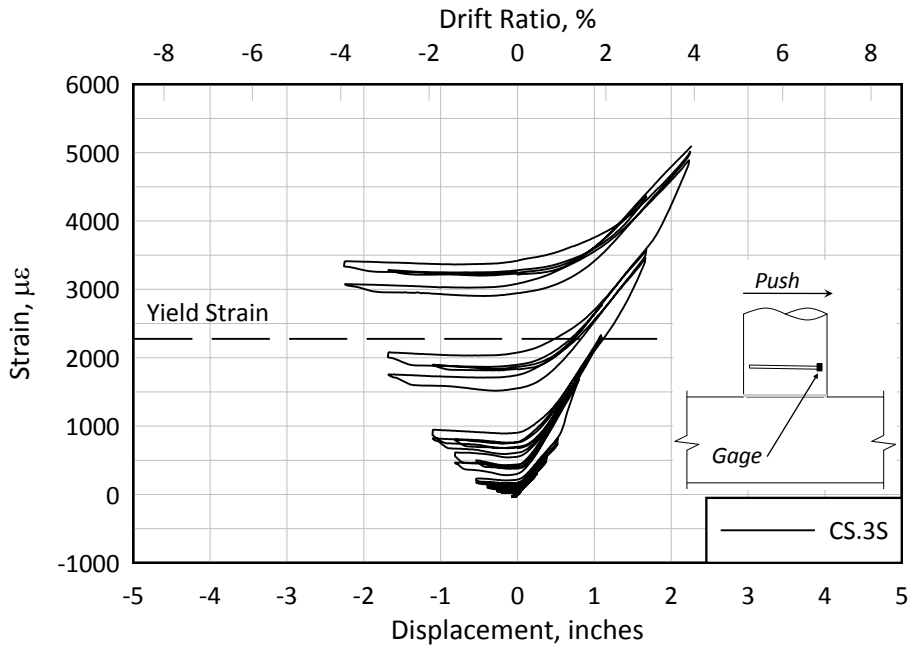

Figure 4.67 HYB-1column spiral rebar strain (CS.3S)

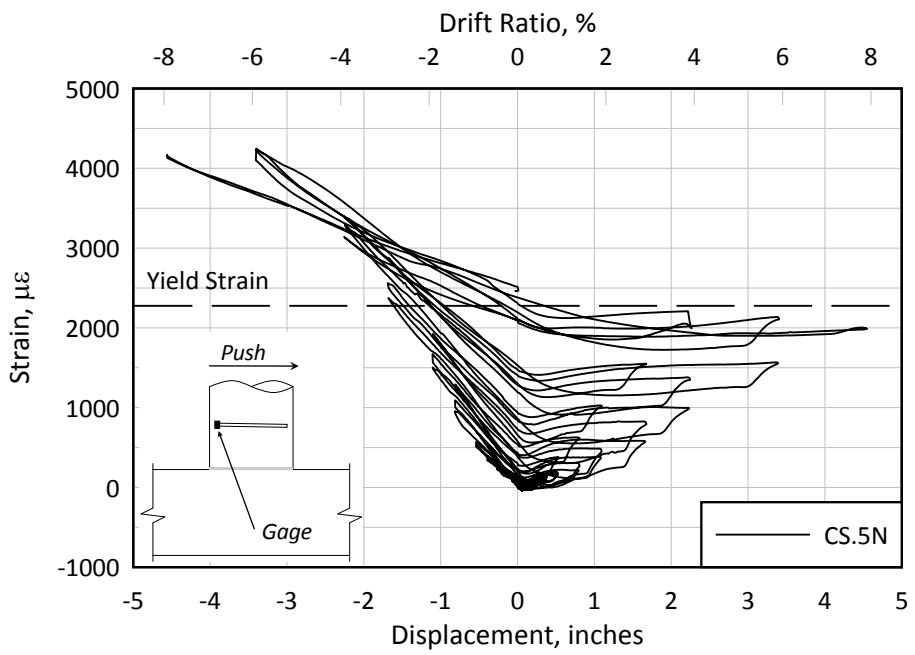

Figure 4.68 HYB-1column spiral rebar strain (CS.5N)

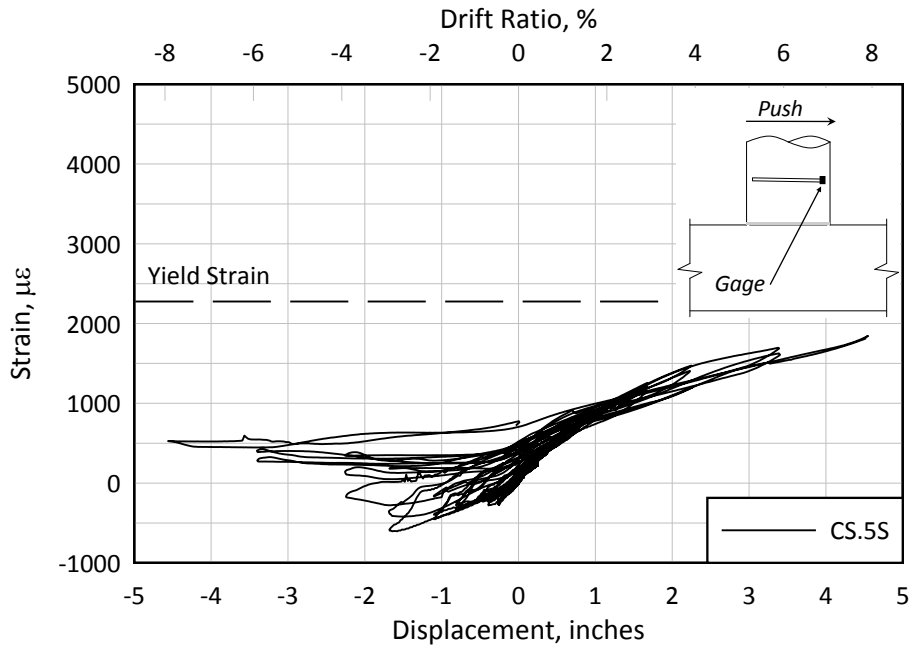

Figure 4.69 HYB-1column spiral rebar strain (CS.5S)

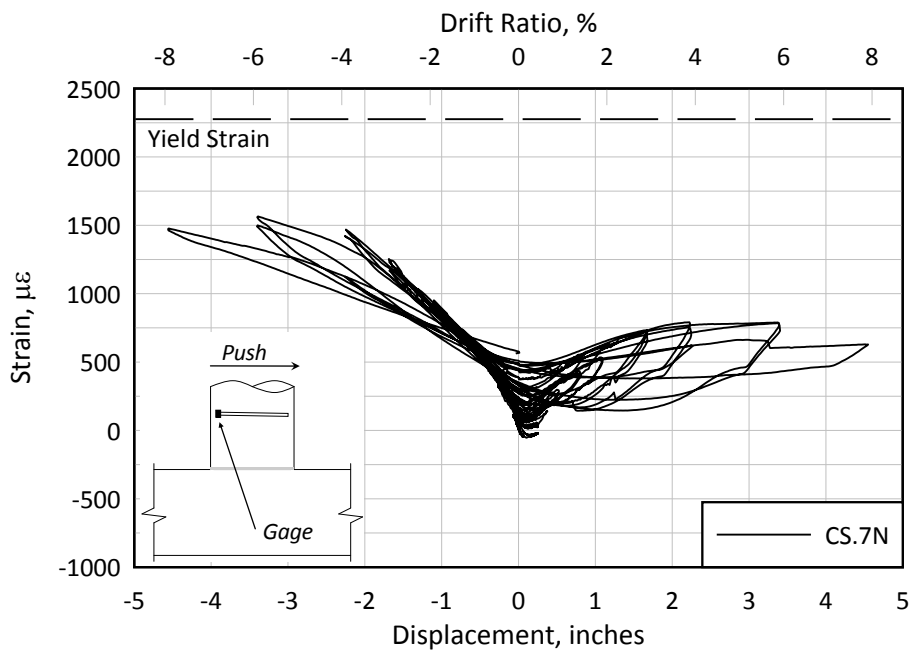

Figure 4.70 HYB-1column spiral rebar strain (CS.7N)

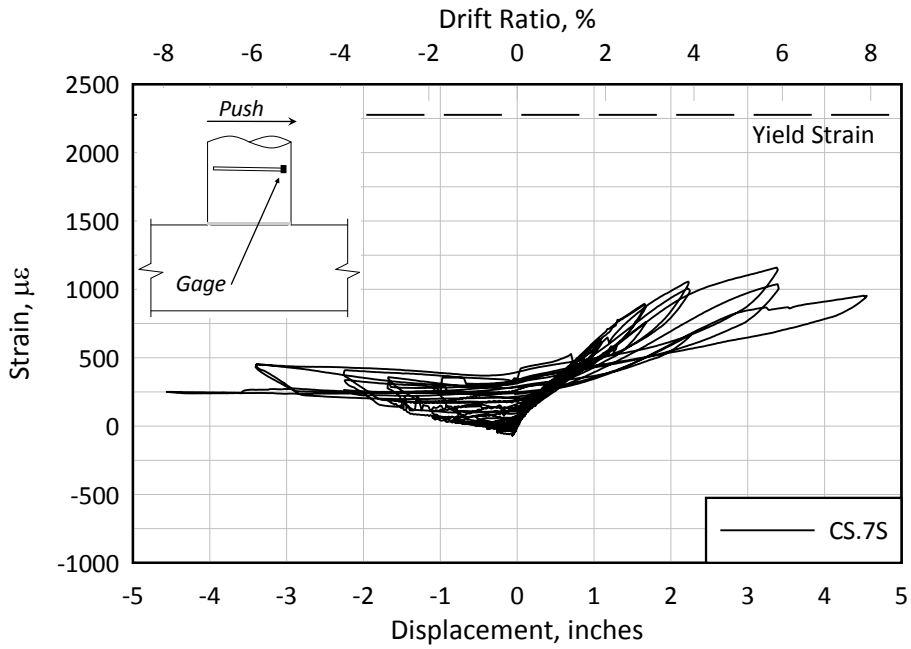

Figure 4.71 HYB-1column spiral rebar strain (CS.7S)

Bent Cap Joint

Strain gage histories for the bent cap joint shear reinforcement are provided in Figure 4.72 thru Figure 4.75. All strain readings are well below the yield strain of the spiral with the largest strains observed in the third turn of the spiral on both east and west sides. The low values of recorded strain in the joint reinforcement indicate the acceptable performance of the joint and observed minimal joint distress.

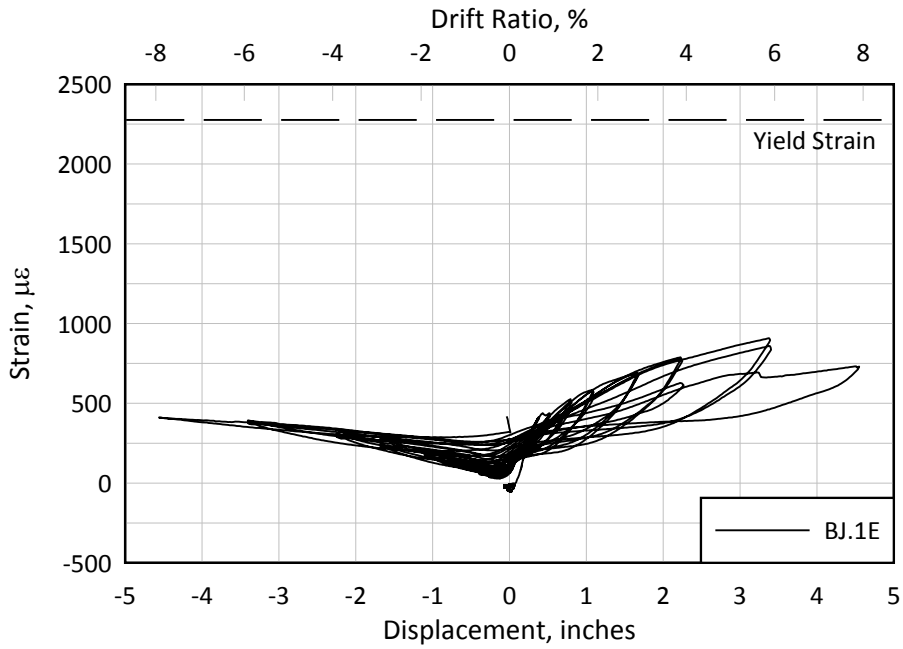

Figure 4.72 HYB-1 bent cap joint shear rebar strain (BJ.1E)

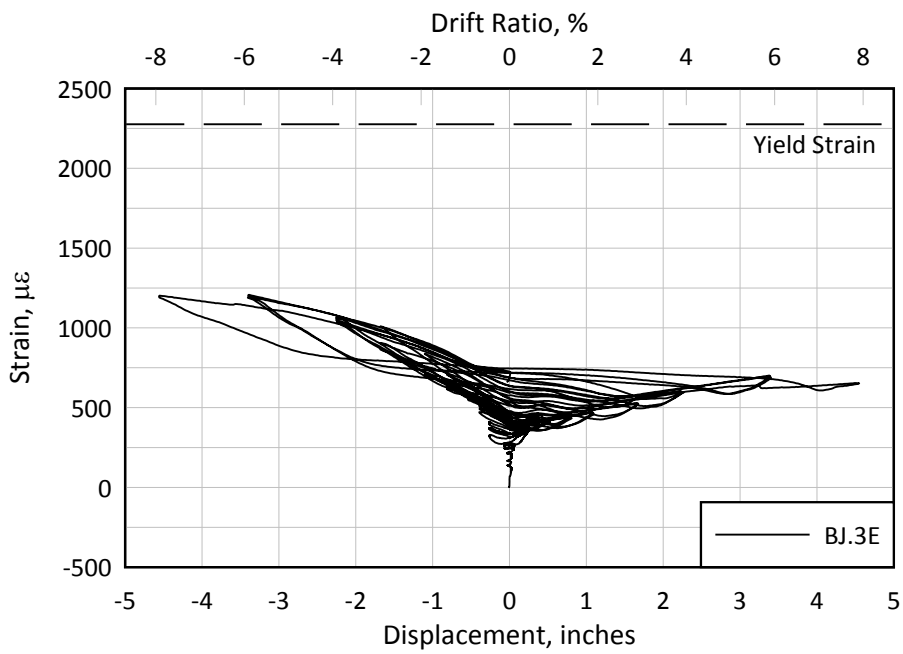

Figure 4.73 HYB-1 bent cap joint shear rebar strain (BJ.3E)

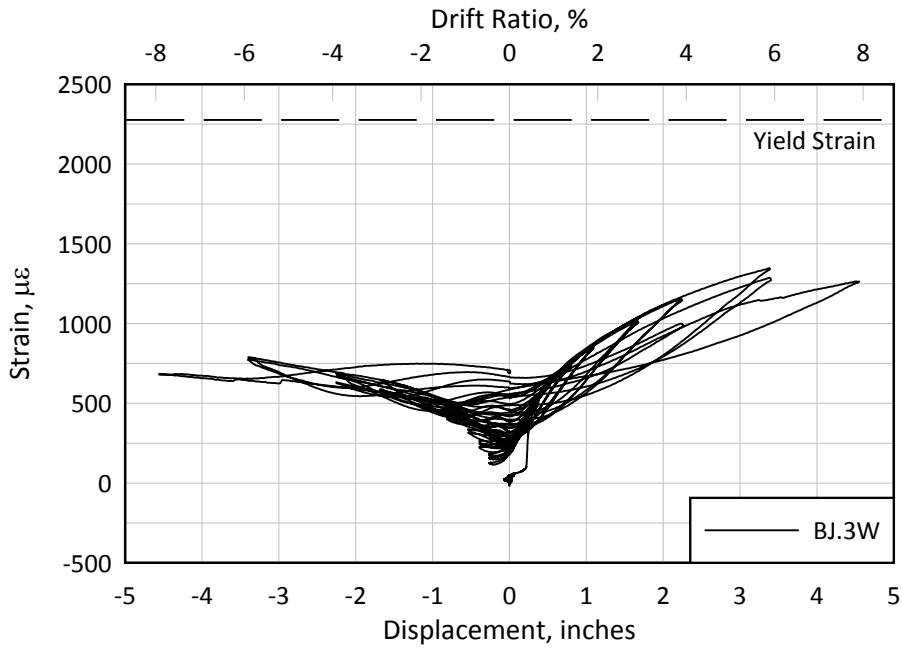

Figure 4.74 HYB-1 bent cap joint shear rebar strain (BJ.3W)

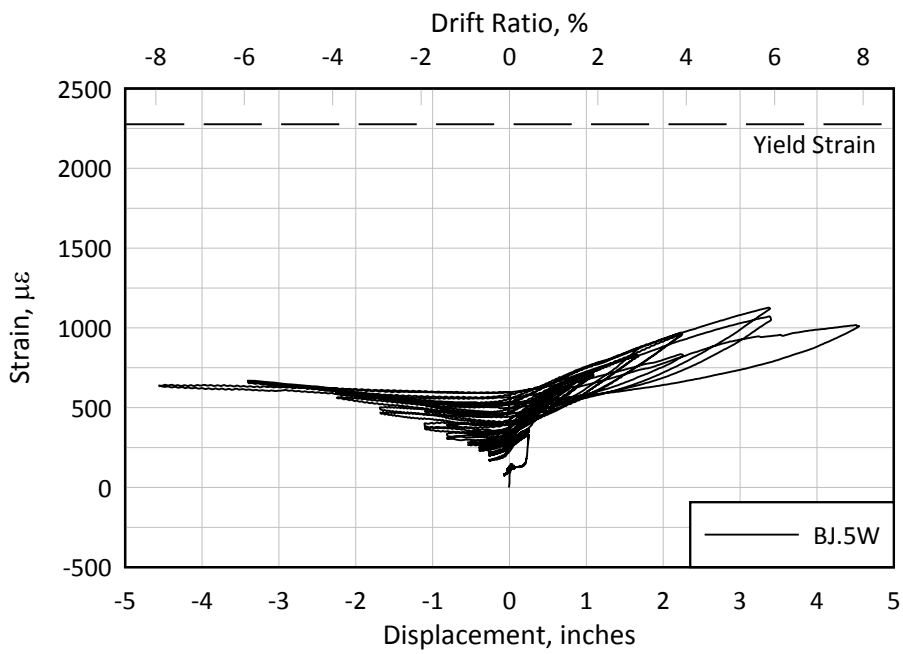

Figure 4.75 HYB-1 bent cap joint shear rebar strain (BJ.5W)

4.5.5 Strain Profiles

Strain gage readings at peak responses in both push and pull directions were used to generate strain profiles for various elements. These profiles were generated for peak points in the loading cycles for the first cycles in both push and pull directions.

Column Concrete Gages

Small diameter, No. 2 reinforcing bars were embedded into the concrete core to capture the compressive strains in the concrete core. These bars were mounted to a plate at the base guaranteeing the transfer of compressive force into the bars. These gages were spaced every two inches from the face of the bent cap up into the column. The profile for both push and pull loading cycles is shown in Figure 4.76. These strain readings are not at the extreme compression fiber but some distance in and therefore not the actual maximum strain in the section. Strain levels at the maximum displacement level are approximately 1.5 to 2.0%, which are far less than expected based on predictions. However, the reliability in these reading at large drift levels is questionable due to the accumulation of damage in the concrete due to large compressive strains and subsequent reduction in expected bond properties.

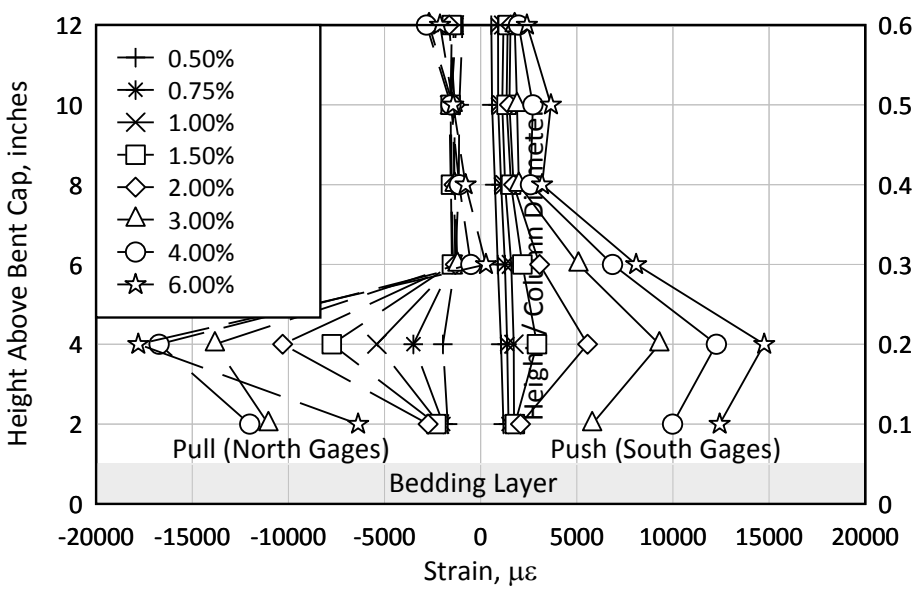

Figure 4.76 HYB-1 No. 2 confined concrete gage strain profile

It is important to note that the largest recorded strains in the confined concrete core occur slightly away from the base of the column. This is also consistent with the recorded strain profiles for the column spiral reinforcement.

Column Longitudinal

Strain gage profiles for column longitudinal bars are provided in Figure 4.77 and Figure 4.78. For column bar CL.1 both strain gages at location 3 were lost prior to testing limiting the information obtained on column rebar strain levels. Readings from bar CL.5 indicate that bar level 3 is subjected to the greatest tensile strains. Readings were only obtained to a drift level of 4.00% prior to losing almost all strain gage readings except for the extreme, minimally stresses locations. Readings from bar CL.5 at location 3 show tensile strains in the extreme bar of approximately 4.9% at a drift level of 3.0%. Assuming the neutral axis depth remains constant with increased lateral displacement, the expected strain at 6.0% drift ratio levels is about 10% which is where fracture of the first reinforcing bar was observed.

The strain profile indicates that the bars are fully developed within the corrugate duct. For all readings, except for bar 5 during 4% drift ratio, the reinforcing bar is fully developed within approximately 16 bar diameters. The requirements specified in ACI ITG-5.2-09 of a development length of 25 times the bar diameter is reasonable based on these results (ACI 2009).

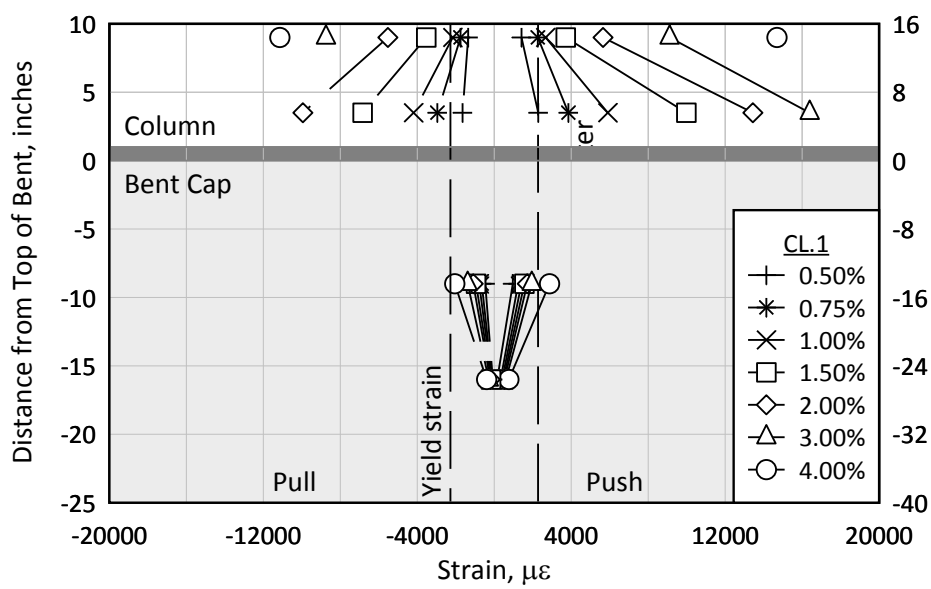

Figure 4.77 HYB-1 column longitudinal rebar strain profile (CL.1-north bar)

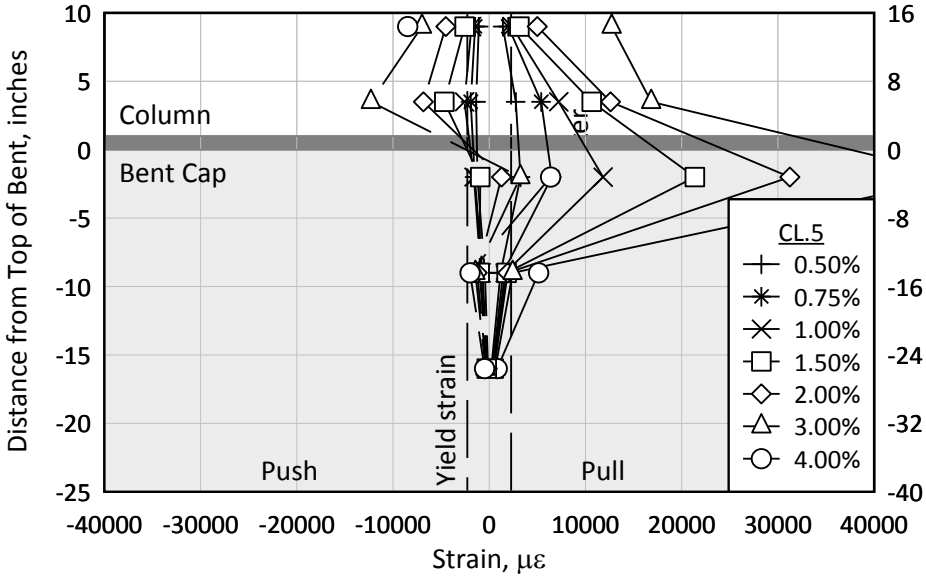

Figure 4.78 HYB-1 column longitudinal rebar strain profile (CL.5-south bar)

Column Spiral

Strain gage profiles for the column spiral reinforcement are shown in Figure 4.79. Reliable measurements were obtained for column drift levels up to and including 4%. These observations show the largest dilation strains occurred approximately five inches from the face of the bent cap. These readings exceeded the yield strain of the reinforcement above 2% drift ratio in both the push and pull directions indicating large strains due to dilation of the confined core at these deformation levels. The reliability of the readings two inches above the face of the bent cap are in question due to observed vertical movement of the spiral due to lateral movement of the longitudinal reinforcement.

These readings are consistent with the column confined concrete gages that indicate the largest strains occurring slightly higher than the column base. These readings should be correlated as the confined concrete core strains will produce dilation in the core resulting in an increase in spiral strains.

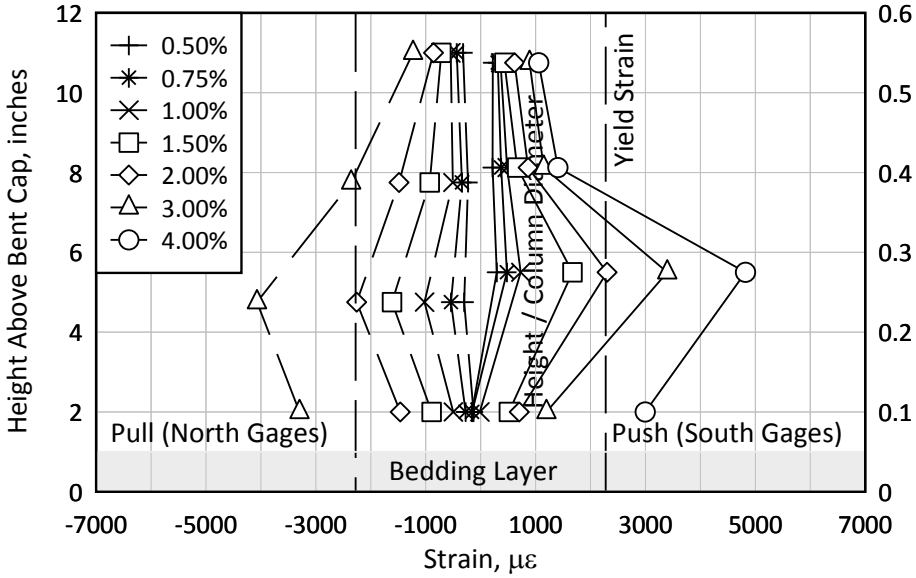

Figure 4.79 HYB-1 column spiral rebar strain profile

Bent Cap Longitudinal

Strain profiles for the bent cap longitudinal reinforcement are provided in Figure 4.80 through Figure 4.83. Readings from these gages indicated that under drifts up to and including 6% column drift, the bent cap longitudinal reinforcement remained well below yield strains. This indicates that the assumed force transfer mechanism is sufficient and conservative for the system tested. Additionally, this verifies the assumption that the bent cap remained essentially elastic under the imposed simulated seismic demands.

Additionally, these results show a relatively flat strain profile across the joint during push and pull cycles. These results indicate that the bent cap longitudinal reinforcement does not develop in the joint but maintains constant force across the majority of the joint. This is consistent with the assumed force-transfer mechanism. The strut-and-tie assumption requires the development of the bent cap tensile force to have occurred in order to develop the assumed nodal response.

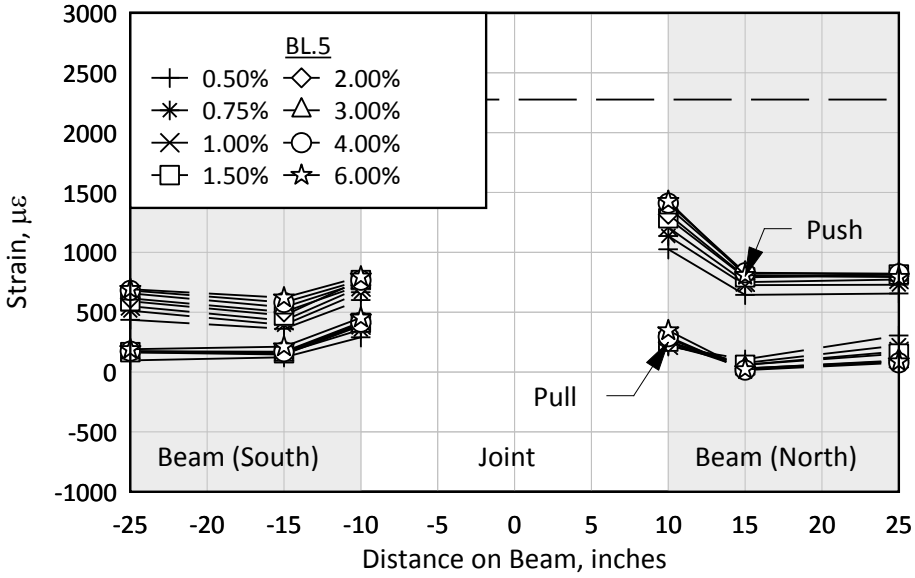

Figure 4.80 HYB-1 bent cap longitudinal rebar strain profile (BL.5)

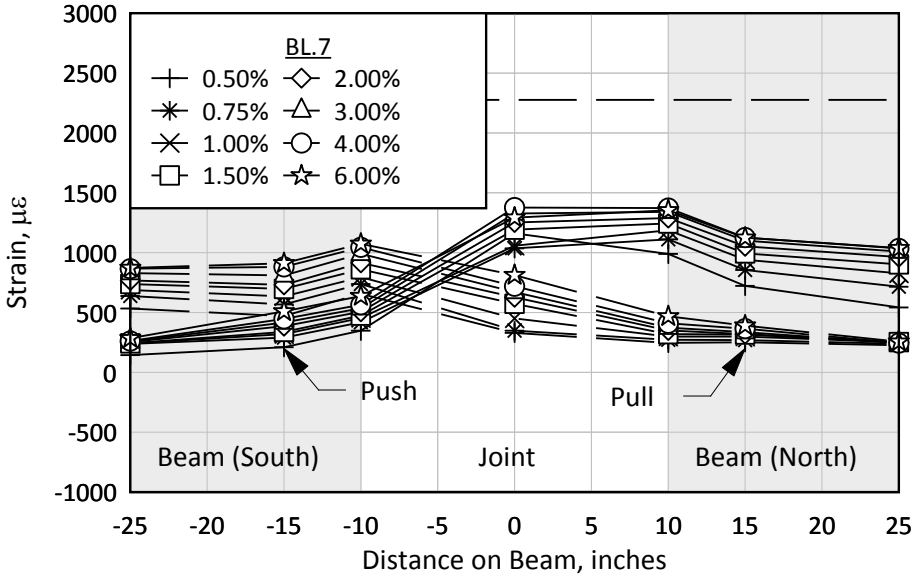

Figure 4.81 HYB-1 bent cap longitudinal rebar strain profile (BL.7)

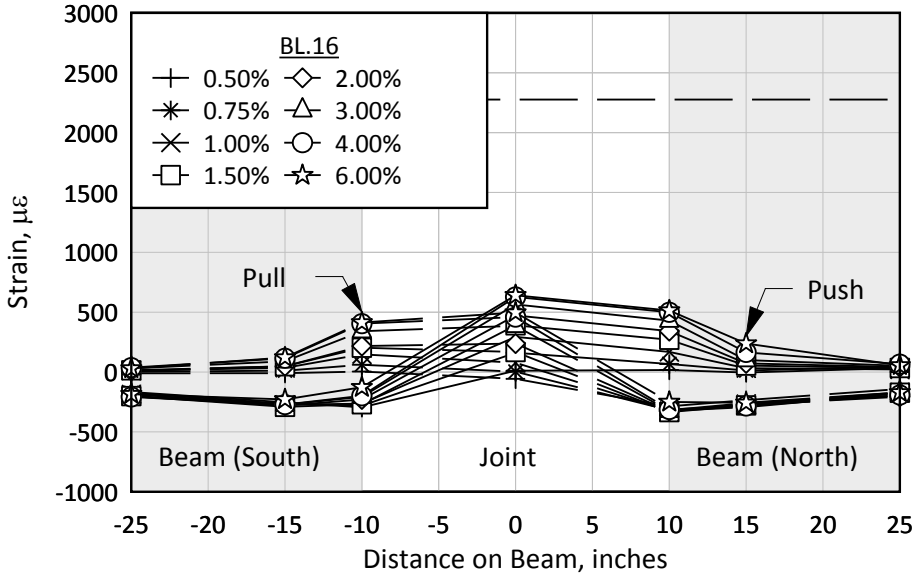

Figure 4.82 HYB-1 bent cap longitudinal rebar strain profile (BL.16)

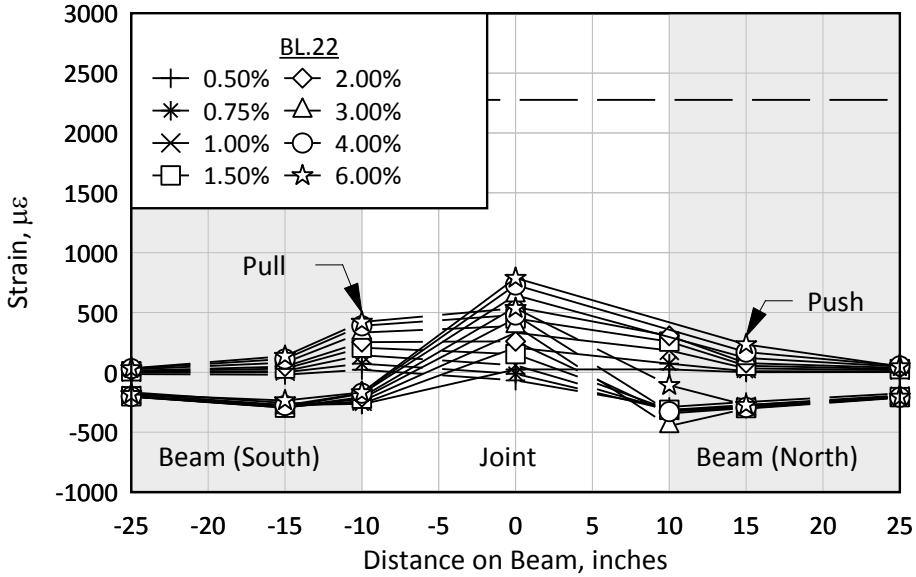

Figure 4.83 HYB-1 bent cap longitudinal rebar strain profile (BL.22)

Bent Cap Shear

Strain profiles from bent cap shear reinforcement are provided in Figure 4.84 and Figure 4.85. These recordings indicate the bent cap shear reinforcement do not yield during simulated seismic loading as intended per the assumed force transfer mechanism. The observed profiles are not

symmetric as would be expected and recorded strains during pull cycles have larger amplitude than during push cycles.

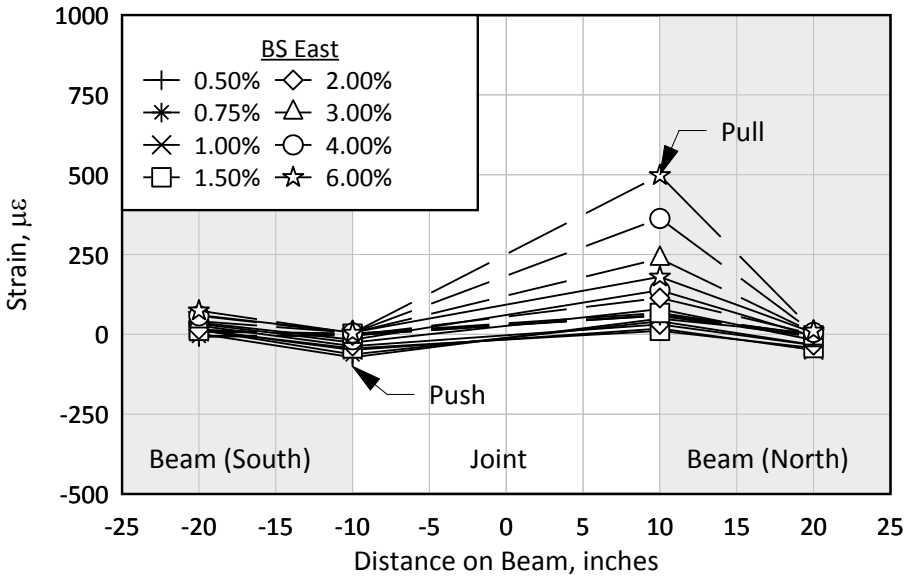

Figure 4.84 HYB-1 bent cap shear rebar strain profile (BS-east gages)

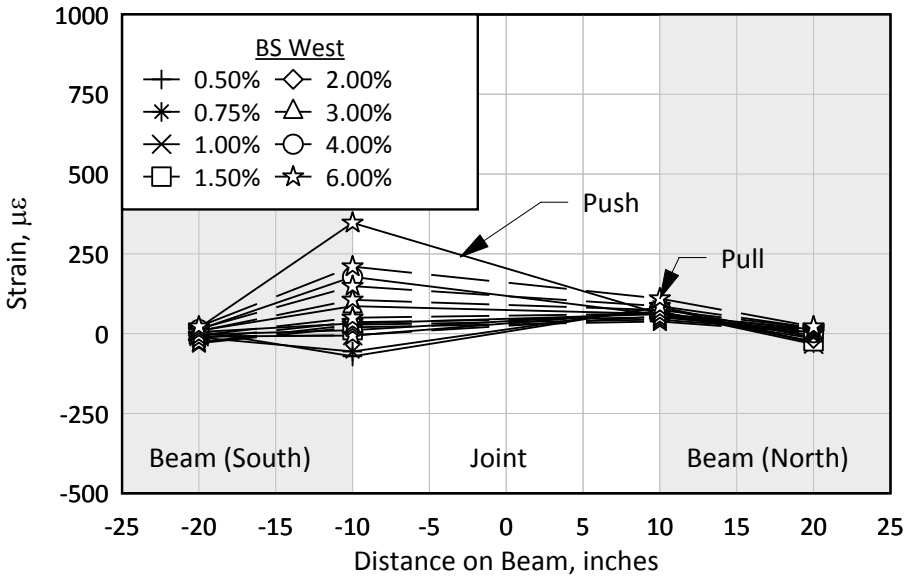

Figure 4.85 HYB-1 bent cap shear rebar strain profile (BS-west gages)

Joint Shear

Strain profiles for the joint shear reinforcement are shown in Figure 4.86 and Figure 4.87. One strain gage on both sides of the bent cap was damaged resulting in limited strain readings during testing. However, the results indicate that the strains in the joint shear reinforcement were well below yield, which agrees with the observed joint performance with limited distress.

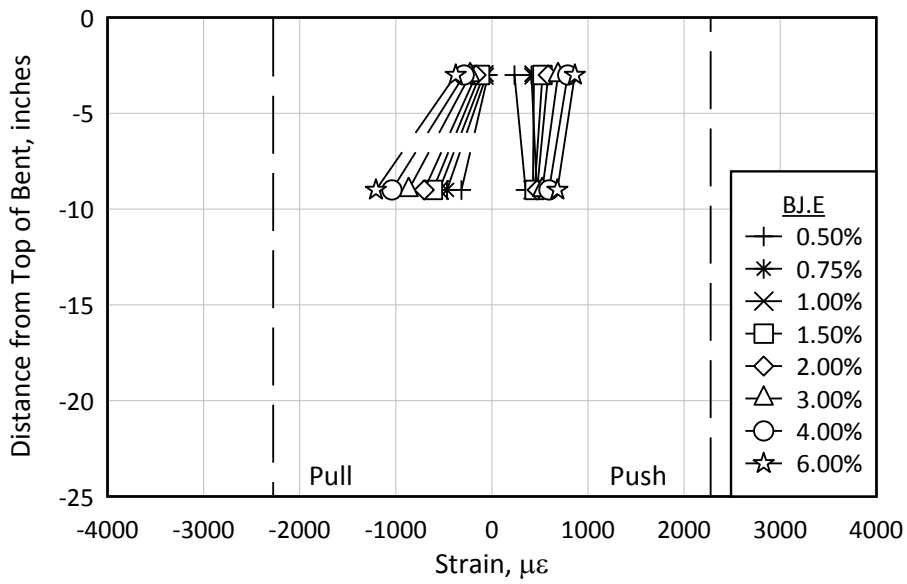

Figure 4.86 HYB-1 bent cap joint shear strain profile (BJ-east gages)

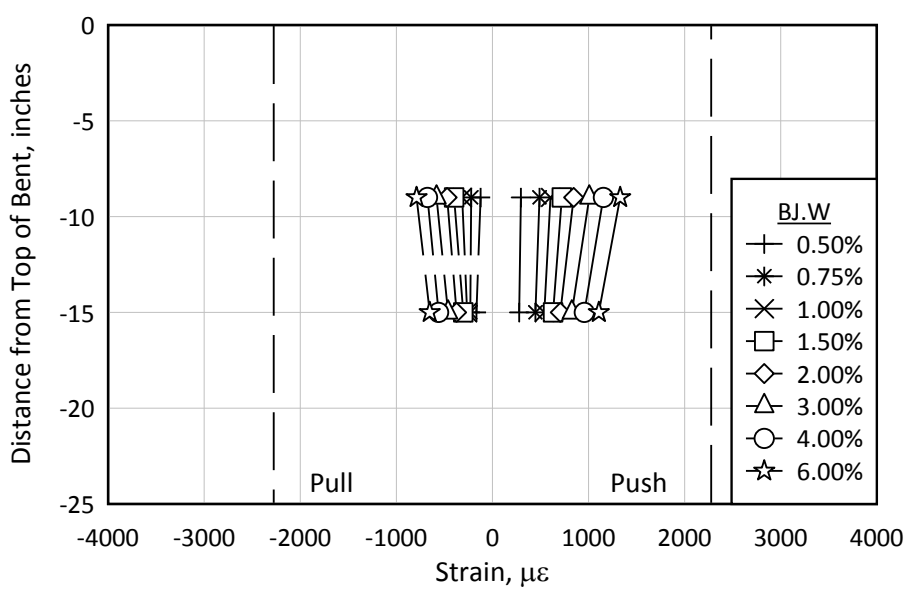

Figure 4.87 HYB-1 bent cap joint shear strain profile (BJ-west gages)

4.6 Summary of Specimen Response

The conventional hybrid specimen was designed to provide similar force-displacement response as compared to the cast-in-place prototype specimen at approximately 1% drift ratio. However, this specimen was designed and detailed to provide significantly different response when considering the cast-in-place counterpart. This unit is intended to provide increased lateral deformation capacity through the controlled rocking of the system at the base. The goal of the hybrid system is to provide a carefully detailed system that can achieve large deformations with a significant reduction in damage and residual offsets. The hybrid specimen was designed, analyzed, constructed and tested to validate the assumptions and response of this system.

Fabrication took place at an industry facility by their personnel without any major complications. A major concern that was voiced during fabrication related to the precasting of circular columns for a full-scale bridge system in the vertical position. A recommended variation discussed with the fabricator is the use of rectangular or octagonal sections to allow for horizontal casting and finishing. The specimen was erected in the university laboratory without any major complications observed.

Observations during testing indicate that the system is capable of resisting large displacement demands with limited, localized damage. The majority of the observed damage was to the sacrificial cover concrete localized to a very confined region of the column compression toe. Other observed damage in the column included very minor flexural and flexural tension cracking, however significantly less than the cast-in-place unit. Performance of the bent cap was observed to have a reduction in damage as compared to the cast-in-place counterpart in terms of cracking in the joint region. The reduction in observed cracking and damage in the joint region is attributable to the inclusion of column post-tensioning and a reduction in anchored column reinforcement. The failure of the system is attributable to the fracture of a column reinforcing bar at approximately 6% drift ratio. This fracture occurred after noticeable buckling of the bar was observed.

Data collected during testing was post-processed and reviewed to provide additional insight into the response of the unit. The force-displacement hysteretic response indicated there is stable response up to approximately 6% drift ratio with appreciable energy dissipation through hysteretic damping. A reduction in residual displacements was observed as compared to the cast-in-place unit indicating an improvement in post-earthquake condition of this structure. Considering past experience from the Kobe Earthquake, concrete systems will likely require

replacement if the residual drift angle is in excess of one degree. For the hybrid unit this signifies that the system can undergo displacements to approximately 4% drift ratio prior to requiring replacement due to excess residual drift. A properly detailed cast-in-place system is expected to achieve only 2.75% drift ratio while still meeting the same requirements.

The predicted force-displacement response of the system provided a reasonable estimate of the system response. However, this prediction greatly underestimated the ultimate system response that was predicted to fail due to confined concrete failure. The actual observed failure mode was fracture of a primary longitudinal reinforcing bar indicating a deficiency in the assumed confined concrete capacity. This is judged to be a deficiency in the assumed confined concrete model when considering highly disturbed regions such as the compression toe of a rocking system.

Both experimental observations and data indicate that the majority of the system deformation response is provided by the concentrated rocking about the base of the column. Minimal damage was observed through visual and instrument readings for the bent cap and joint region. This experimental effort indicates that the assumed force transfer mechanism is conservative for this hybrid system.

4.6.1 Conclusions

Based on experimental observations and readings related to the response of the conventional hybrid specimen, the following conclusions can be made:

- The conventional hybrid specimen met the performance objectives up to the design level drift
- The system provides significant lateral displacement capacity with an ultimate displacement of 6% drift ratio
- Design assumptions and predictions match well the measured response
- System ultimate deformation capacity was underestimated using the Mander model for confined concrete as the failure was attributable to column reinforcing fracture, not failure of the confined core
- Deep neutral axis depth resulted in a reduction in self-centering capacity although substantial enhancement to the self-centering ability was noted as compared to the cast-in-place control specimen
- Neutral axis depth should be limited to 25% of the column dimension at a maximum and the amount of mild reinforcement may be reduced to enhance the self-centering ability.

Chapter 5 Concrete Filled Pipe Specimen

The concrete filled pipe specimen (also referred to as HYB-2) utilizes a steel pipe for confinement and lateral reinforcement outside of the joint region. Using a steel pipe provides greater levels of confinement. Additionally, mild rebar is only used at the joint region and terminates once in the column to facilitate easier construction with minimal need for tying steel rebar cages. Details of this specimen and experimental results are provided in this section.

5.1 Design Details

This specimen was design to have similar lateral response characteristics when compared to the conventional hybrid specimen. The general sectional dimensions are identical to the conventional hybrid specimen that represents a 42% scale factor.

5.1.1 Column

The outside diameter of the steel pipe is 20 inches and the pipe is a 1/4 inch thick pipe. The resulting confinement ratio is 5.19%. The mild reinforcement is placed at the same location as the rebar for the conventional hybrid specimen due to geometric constraints within the bent cap and for uniformity of results. In practice, it is expected that the diameter of the circle encompassing the rebar can be increased to maximize the lateral force resisting capacity of the section. The column cross section is provided in Figure 5.1 and the vertical section is provided in Figure 5.2. The column rebar extends a distance equal to 15 inches into the steel pipe. The length of the bonded region of the rebar and the design and spacing of the weld beads were selected based on a simple force transfer mechanism.

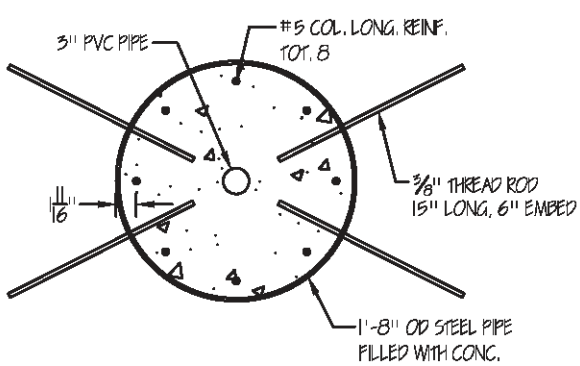

Figure 5.1 HYB-2 typical column cross-section

The primary longitudinal reinforcement at the joint region consists of a combination of unbonded post-tensioning and bonded rebar. There are 5-0.6 inch diameter post-tensioning strands making up the single tendon that runs down the center of the column. There are 8-No. 5 316LN stainless steel rebars located at the column end spaced equally around the column section, providing a reinforcement ratio of 0.79%. At a distance equal to approximately 15 inches from the face of the bent cap, the rebars were terminated. Three weld beads were detailed on the steel shell within this region to transfer the tensile force in the rebar into the surrounding steel shell. For the remainder of the column the primary longitudinal reinforcement consists of a combination of unbounded post-tensioning and the confining steel shell.

The void for the post-tensioning is formed by PVC pipe. In practice, it is recommended that the void be formed by corrugated plastic post-tensioning ducts or high-density polyethylene (HDPE) pipe which are grouted for corrosion resistance. The preferred practice for this system is to use a smooth HDPE pipe and grout the void after stressing. This will provide a corrosion barrier around the tendon but also debond during a seismic event due to the lack of adequate development properties.

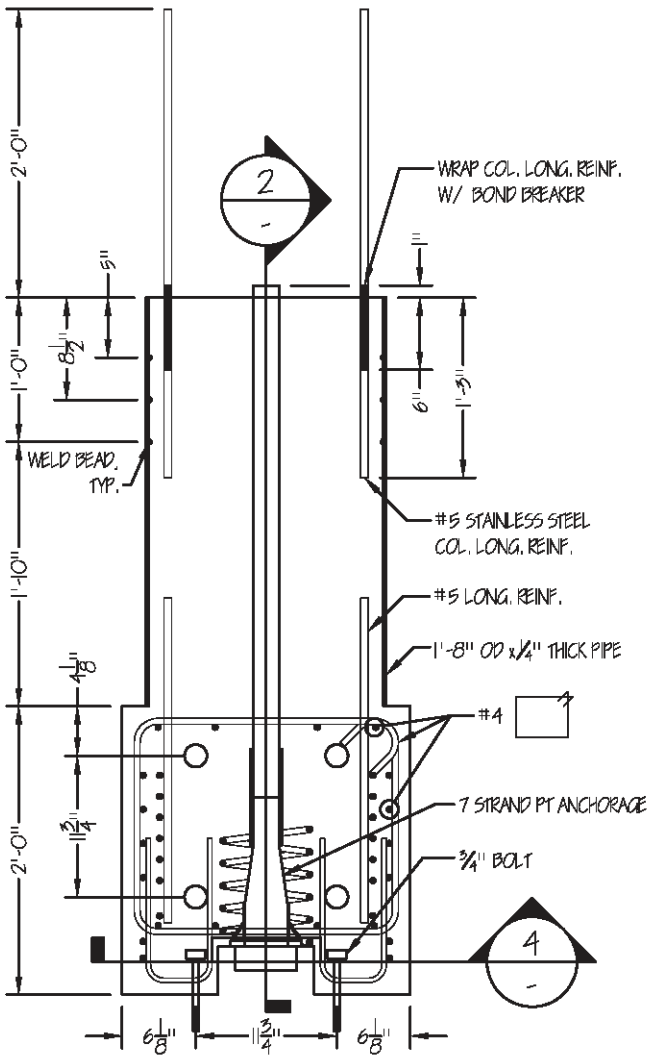

Figure 5.2 HYB-2 column vertical section

5.1.2 Bent Cap

Figure 5.3 and Figure 5.4 provide details of the bent cap member. The bent cap cross-section is a square with a dimension of 25 inches. The detailing and design of this section was identical to that specified in the conventional hybrid specimen.

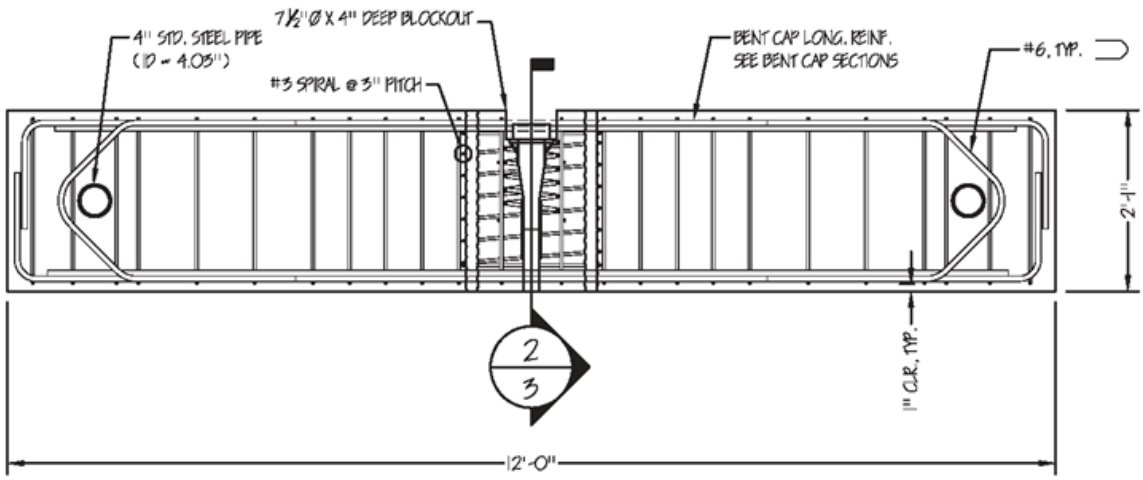

Figure 5.3 HYB-2 bent cap longitudinal section

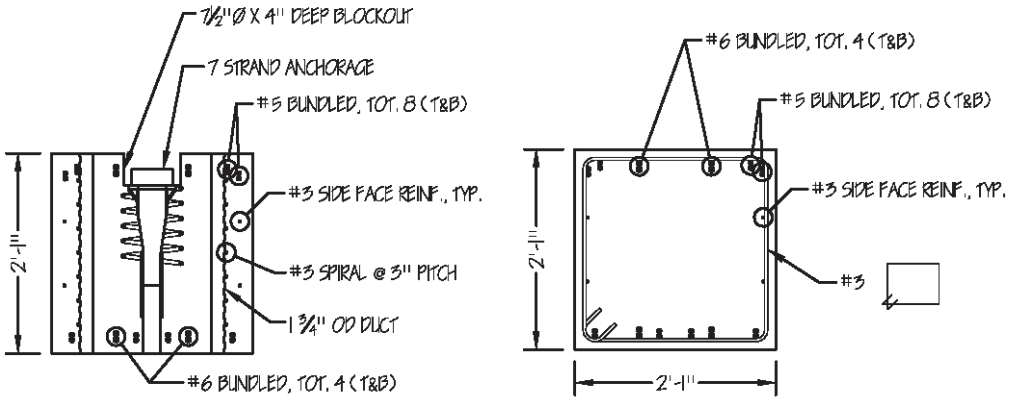

Figure 5.4 HYB-2 bent cap section a) at anchorage b) outside anchorage

5.1.3 Instrumentation

This test specimen was instrumented to capture the major response characteristics of the specimen when subjected to lateral loading. This instrumentation includes strain gages mounted on rebars and external gages mounted on the specimen.

Strain gages were placed on column and bent cap reinforcement to capture the distribution of forces and deformations inside the specimen and the spread of plastic actions. The locations of these gages are shown in Figure 5.5. A summary of the strain gage categories based on callouts is provided below:

- CL series Column longitudinal reinforcement strains
- CS series Steel shell strains (strain gage rosettes)
- BL series Bent cap longitudinal reinforcement strains
- BJ series Bent cap joint shear reinforcement strains

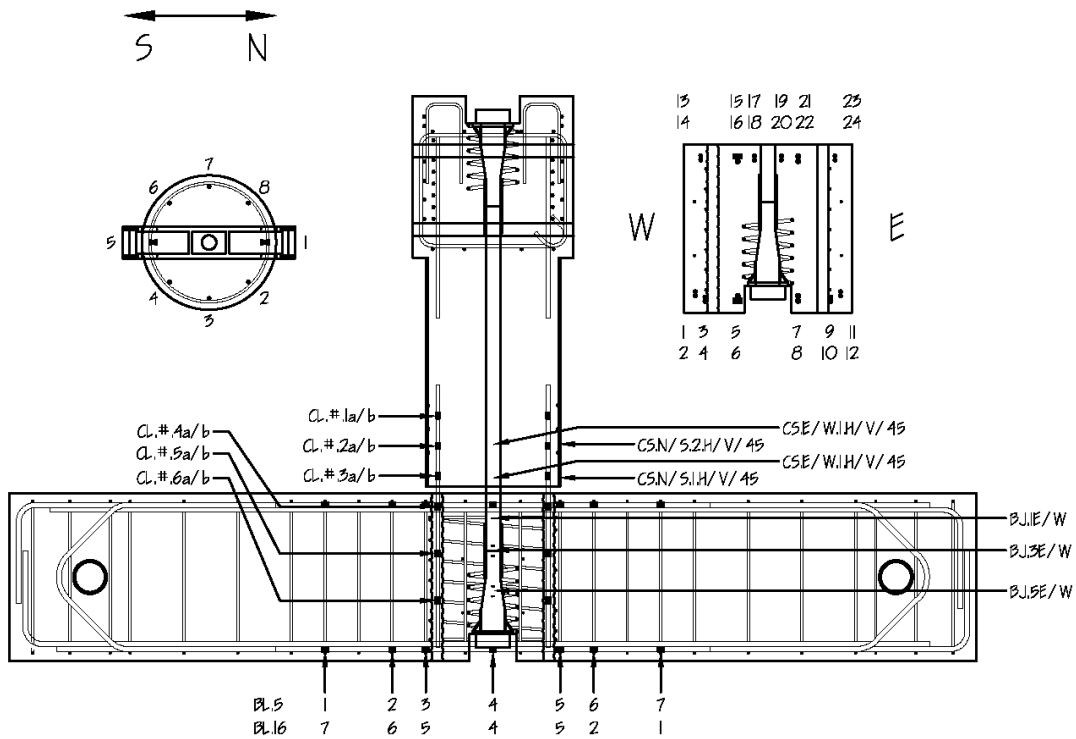

Figure 5.5 HYB-2 strain gage layout

External instrumentation consists of linear potentiometers and inclinometers mounted on the exterior of the specimen. A summary of external instrumentation is shown in Figure 5.6. Linear potentiometers are placed to capture column displacements, column curvature, base rotation, bent cap joint deformations, column bar slip, bent cap rotation and rigid body movements. An inclinometer was placed on the load stub to record the rotation of the load stub at the actuator location.

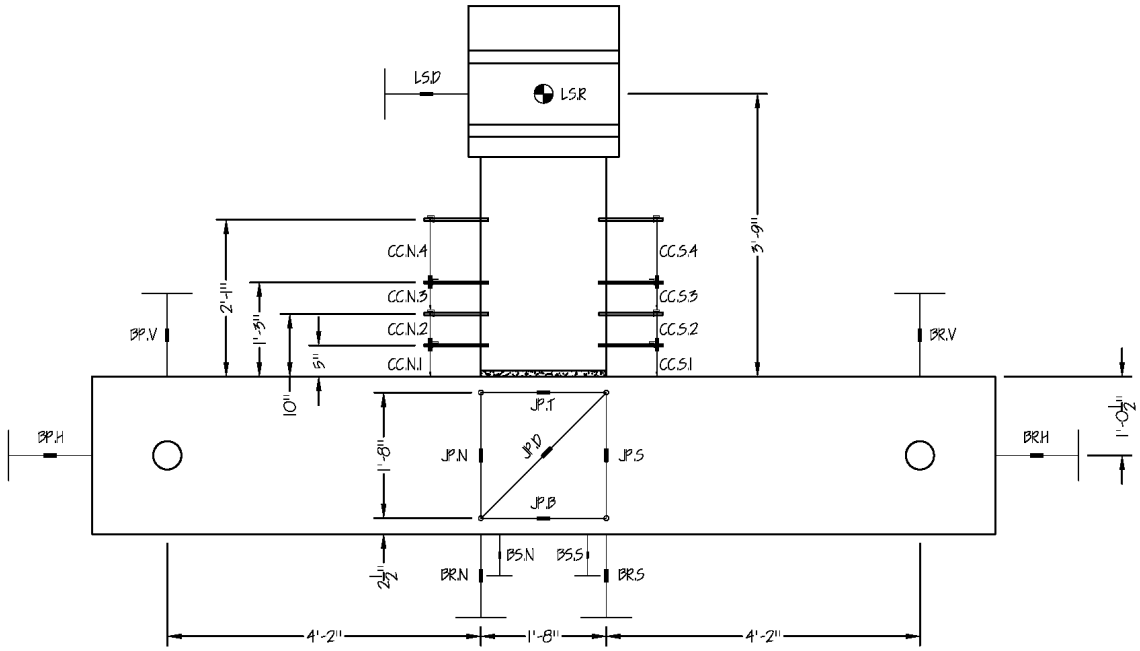

Figure 5.6 HYB-2 external instrumentation layout

In addition to active measurements provided by strain gages and external instrumentation, specimen response was documented through digital photos, crack markings, video recording and notations.

5.2 Fabrication and Assembly

This section describes the process of section fabrication and assembly.

5.2.1 Precast Component Fabrication

This specimen was fabricated at Pomeroy Corporation located in Perris, CA. The reinforcing bars that were instrumented were shipped to UCSD for installation of the strain gages and then transported to Perris for fabrication. All fabrication activities at the precast yard were closely monitored by a representative from UCSD to ensure all tolerances were achieved and to acquire feedback from the precaster relating to the east of fabrication. The column rebars were tied and set inside the steel shell using support from a vertical form. The load stub cage was tied and placed at the base of the form, see Figure 5.7. The load stub form was constructed around this reinforcing cage and the steel shell was then placed atop this form.

Figure 5.7 HYB-2 load stub reinforcement

A view down the steel shell as placed is shown in Figure 5.8. This figure also shows the PVC pipe that runs down the center of the column and the three weld beads that are placed on the steel shell. A close up view of the weld beads is provided in Figure 5.9. These weld beads were placed after the shell was shipped to UCSD. The campus machine shop placed these weld beads with a single pass of a weld rod along the inside of the column and reported no difficulties.

Figure 5.8 HYB-2 view down column showing PVC duct and weld beads

Figure 5.9 HYB-2 close up view of weld beads

After the steel shell was placed on the load stub form, a support structure was constructed to stabilize the system and allow for vertical alignment of the system. This structure was also constructed to provide a platform at the top of the section from which to work. With the structure constructed, the column longitudinal cage was set inside of the steel shell. The support structure was used to hang this cage inside of the shell as shown in Figure 5.10. The cage was tied to two large diameter bars that were then secured to the frame. The vertical alignment of this system was check prior to and after casting to ensure the cage was properly aligned.

Casting of the bent cap and column assembly occurred at the same time. Figure 5.11 shows the casting of the bent cap, which occurred next to the column assembly. Following the bent cap, the column was cast from the top down as shown in Figure 5.12. The concrete mix used was a 3/8 inch maximum aggregate mix with approximately a 9-inch slump.

Figure 5.10 HYB-2 column ready for casting

Figure 5.11 HYB-2 casting of bent cap

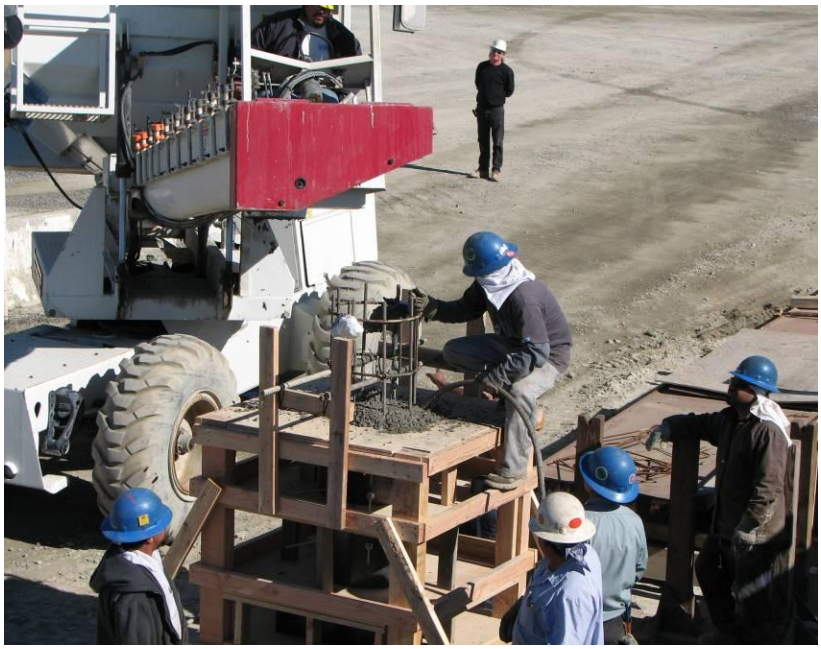

Figure 5.12 HYB-2 casting of column

Unlike traditional bridge members, this specimen was not steam cured thus additional cure time was required to achieve appropriate strength prior to removing the forms. Once the concrete achieved a minimum break strength of 3 ksi, the forms were removed and the members were finished. The members were then shipped to the UCSD campus.

5.2.2 Fabricator Feedback

For the fabrication of a member of this size, the precast fabricator did not note any significant difficulties. However, the fabricator voiced a significant concern about fabricating a circular column for a typical bridge column that may range in upwards of 15 feet. The required construction effort to effectively brace a tall slender column of this height would require significant cost and complexity. Furthermore, construction in the horizontal position is also difficult due to the need for many ports that would be required along the column for pouring concrete and allowing bleeding of air voids from the section. While the fabricator noted that this method would be possible, it is not preferable. Unlike for the first hybrid unit, the use of an octagonal column fabricated on the flat is not a cost effective solution. From discussions with the fabricator, it was noted that the most likely method of construction for a tall column would be to cast horizontally and leave sufficient access ports to be closed following casting.

5.2.3 Specimen Assembly

The column unit as delivered is shown in Figure 5.13. The column top had a rather smooth finish that was removed and roughened through pressure washing. The column was set on two concrete blocks to allow for access to the load stub ("dead end") post-tensioning anchorage and then leveled. A temporary support structure was constructed for the bent cap using traditional scaffolding and dunnage. Figure 5.14 shows the setting of the bent cap onto the support frame while also threading the post-tensioning and rebar into the appropriate ducts. The bent cap was set upright using the overhead gantry crane in the lab. There were no problems observed during the cap setting operation.

Figure 5.13 HYB-2 column as delivered to UCSD

Figure 5.14 HYB-2 bent cap setting operation

The steel bedding form was then placed around the column to facilitate the grouting operation. The bedding layer and ducts were grouted by pumping Masterflow 928 grout through one of the ducts (BASF 2006). Pumping was used to place the grout, however this process was essentially a gravity flow casting of the bedding layer and ducts. There were no significant issues encountered during the grouting operations. Minor bleeding was noted at the top of the bedding layer form due to an inadequate seal that was used, see Figure 5.16.

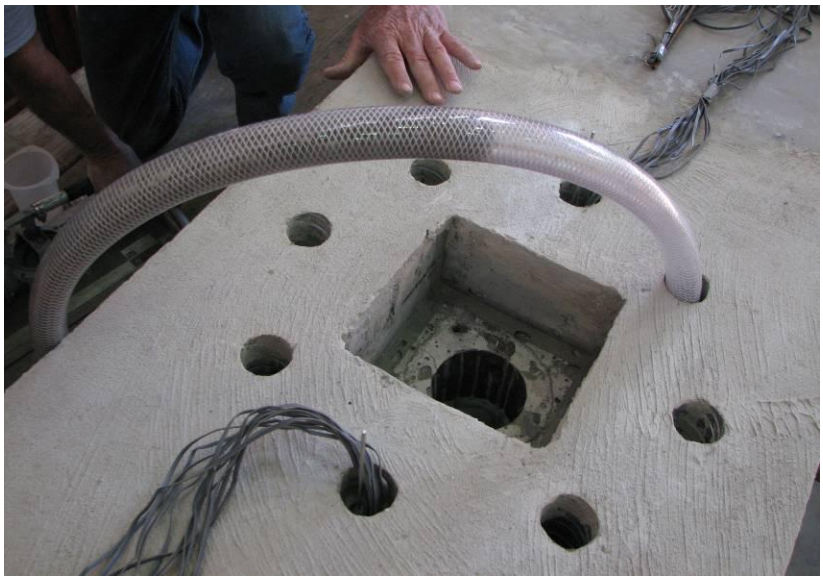

Figure 5.15 HYB-2 grouting of bedding layer and ducts

Figure 5.16 HYB-2 grout leaking from bedding layer

Both HYB-2 and HYB-3 were case and assembled at the same time. Following grouting, these units are shown in Figure 5.17 with HYB-2 in the background and HYB-3 in the foreground. The

units were post-tensioned to provide the design lateral strength. Following post-tensioning, the unit HYB-2 was inverted as shown in Figure 5.18. The specimen was then picked by the overhead crane and set in the test setup, Figure 5.19. There were difficulties in setting the unit in the test setup due to a misaligned PVC pipe in the bent cap. The pipe appears to have floated during casting resulting in the misalignment. The floating of the PVC pipe resulted in a slight rotation of the bent cap during testing which resulted in noticeable lateral drifts during testing. The out-of-plane displacement is discussed in more detail in the experimental results section.

Figure 5.17 HYB-2 specimen after grouting

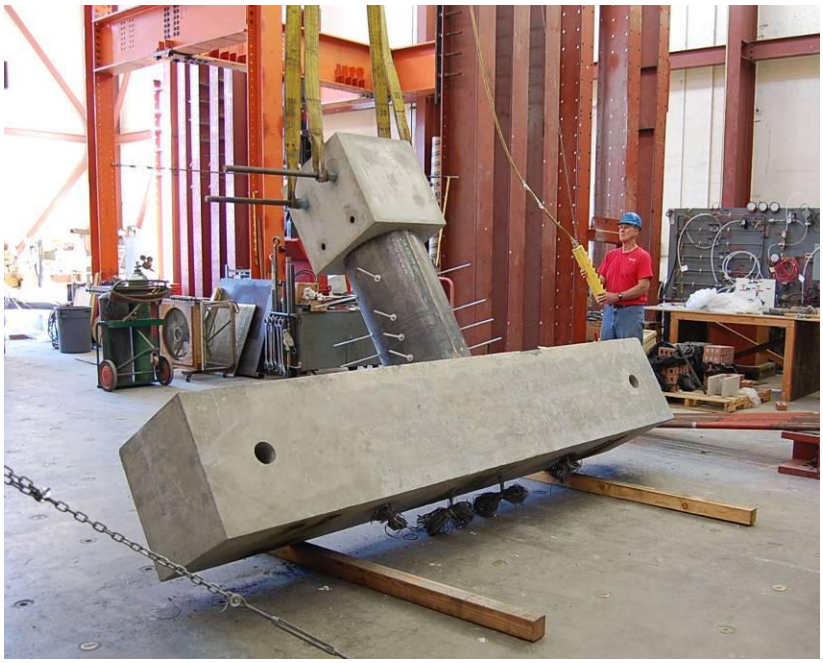

Figure 5.18 HYB-2 specimen during inversion

Figure 5.19 HYB-2 setting of specimen in test setup

5.2.4 Post-Tensioning

After allowing the grout to cure for 7 days, the system was post-tensioned by Dywidag Systems International. The strands were individually threaded through the column and set in the wedge plate to ensure their alignment is maintained inside the column. Due to the short length of this column, the misalignment of a strand would result in variable stressing in the individual strands. All five strands were strain gaged during for stressing operation; however, only four gages survived the entire operation. The stressing operation is shown in Figure 5.20.

Figure 5.20 HYB-2 post-tensioning operation

After 20% of the specified jacking force was applied to the specimen, the elongation of the strand was measured. The strands were then jacked to the specified forced relating to 75% GUTS. Based on the strain gage readings the actual jacking stress was 68.1% GUTS. This stress was 7% less than the target stress level desired for this specimen. The elongation of the strands was then measured at the jacking stress. Next, the stress was released to 20% of the jacking stress and the elongation was again measured. Based on the strain gage readings, the wedge pull-in was 0.210 inches, which is approximately the same as physical elongation measurements. This value is less than the manufacturer's recommended 0.250" pull-in. The recorded strain gage history during stressing is shown in Figure 5.21. The design of this specimen was based on reduced wedge pull-

in based on the results of HYB-1 stressing. However, this specimen did exhibit greater pull-in as compared to HYB-1 that had approximately 0.156-inch pull-in.

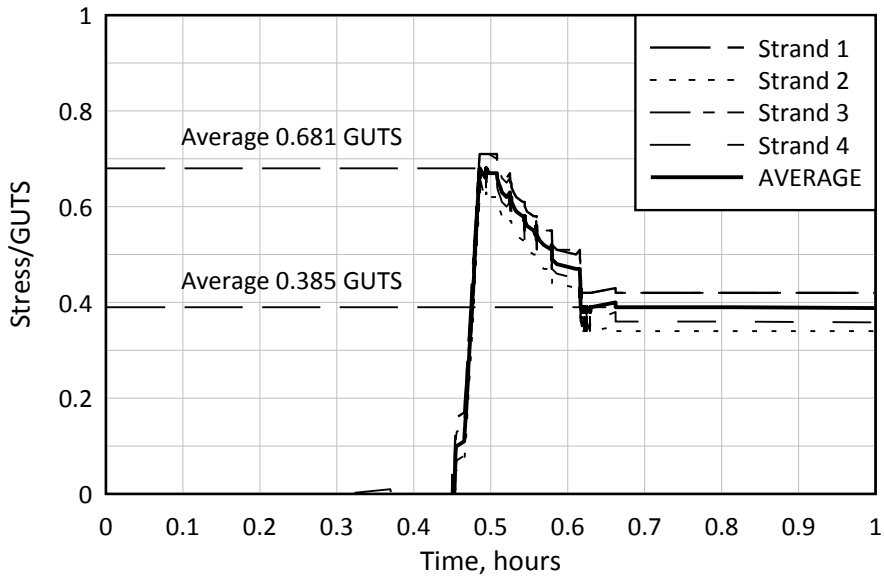

Figure 5.21 HYB-2 post-tensioning strain gage history during stressing

5.3 Cementitious Material Properties

The bent cap and column were fabricated with normal weight concrete developed to achieve a target compressive strength of 7 ksi at 28 days. The mix design was developed using a nominal 3/8 inch maximum aggregate size based on scaling from the prototype specimen.

The cementitious grout selected for use on this specimen was Masterflow 928 grout. This material is a prepackaged hydraulic cement-based mineral-aggregate high strength, non-shrink grout with an extended working time. The grout material is developed to meet the requirements of ASTM C 1107, Standard Specifications for Packaged Dry, Hydraulic-Cement Grout (Non-Shrink), Grades B and C, and the Army Corps of Engineers' CRD C 621, Specification for Non-Shrink Grout, Grades B and C.

Compression strengths for cementitious materials were established through cylinder testing at multiple times following casting and at day of test (D.O.T.). Results from compression testing for both concrete and grout are listed in Table 4.1 and Table 4.2. The values presented are based on the average of three specimens tested. Variation of cementitious material compressive strength versus age is presented in Figure 5.22.

Table 5.1 HYB-2 concrete strength

Material Age	*Strength, ksi*
4 days	4.75
14 days	7.55
28 days	8.01
35 days (D.O.T)	8.49

Table 5.2 HYB-2 grout strength

Material Age	*Strength, ksi*
7 days	6.10
22 days (D.O.T.)	6.35

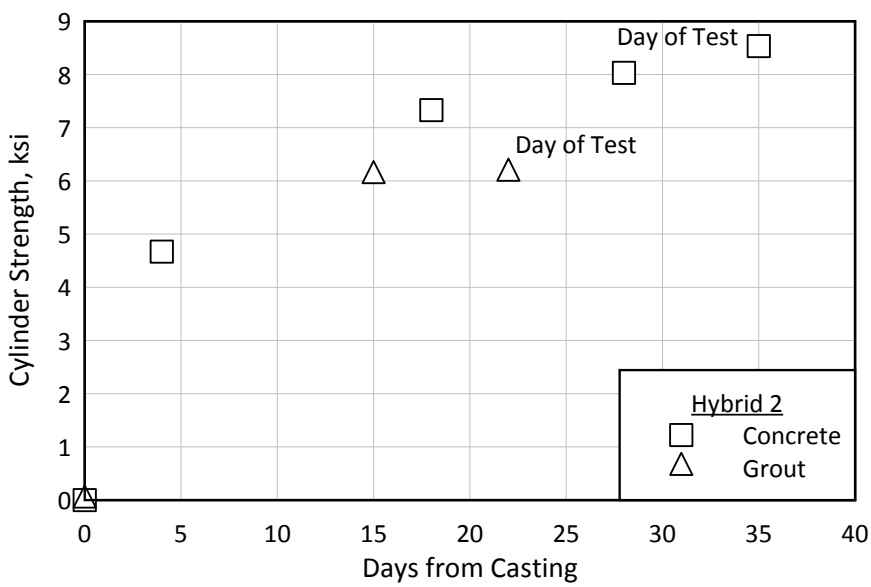

Figure 5.22 HYB-2 cementitious material strengths

5.4 Experimental Procedure and Observations

The loading procedure and observations noted during testing are presented in this section.

5.4.1 Load Protocol

The preliminary stage of loading consists of application of vertical load on the specimen simulating the gravity load during a seismic event. The vertical load was applied as a ramp load

over approximately one minute. Following the application of vertical load, lateral loading began. The first stage of loading consisted of ramping of lateral load to a specified target, i.e. force controlled control. Each loading stage consisted of three cycles of push and pull excursions. The first lateral load cycle was based on the expected lateral load required to achieve zero stress at the extreme tension fiber. The next stage had a target lateral load of twice the first stage. Finally, the third stage in force control consisted of a push cycle to expected first yield or 0.50% drift ratio, whichever occurred first. In this test, the drift limit was reached at approximately the same time as first yield of reinforcement. The loading protocol for the force-controlled stages is graphically shown in Figure 5.23.

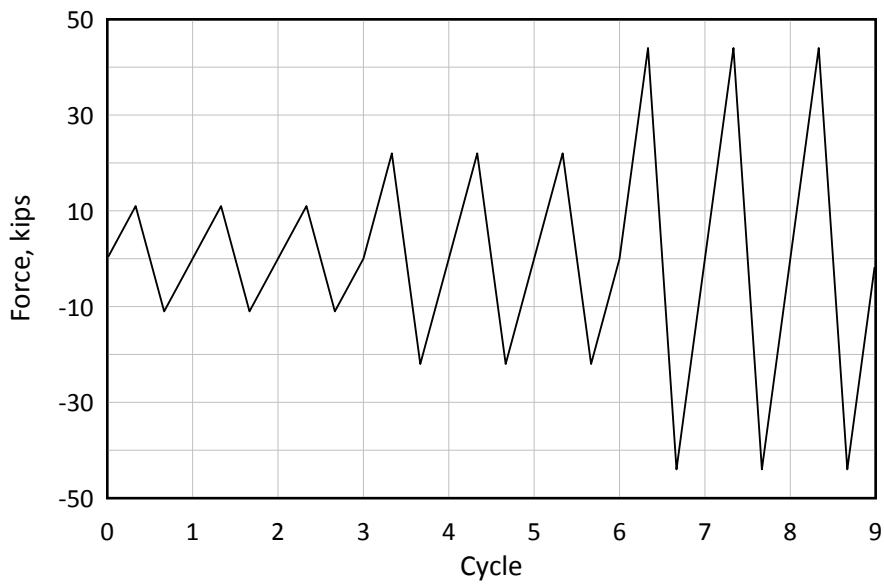

Figure 5.23 HYB-2 force controlled loading protocol

Upon completion of the force controlled loading cycles, the actuator control was switched to displacement control. Displacement controlled stages were loaded to target drifts. For the first two cycles, three displacement excursions occurred in both the push and pull directions (target drift levels of 0.50% and 0.75%). For the remaining loading stages, the specimen underwent two displacement cycles to the specified drift, followed by one cycle to the previous drift level. For example, during the 1.00% drift ratio cycle the specimen underwent two cycles at 1.00% drift ratio followed by one cycle to 0.75% drift ratio. The displacement control loading protocol is graphically shown in Figure 5.24.

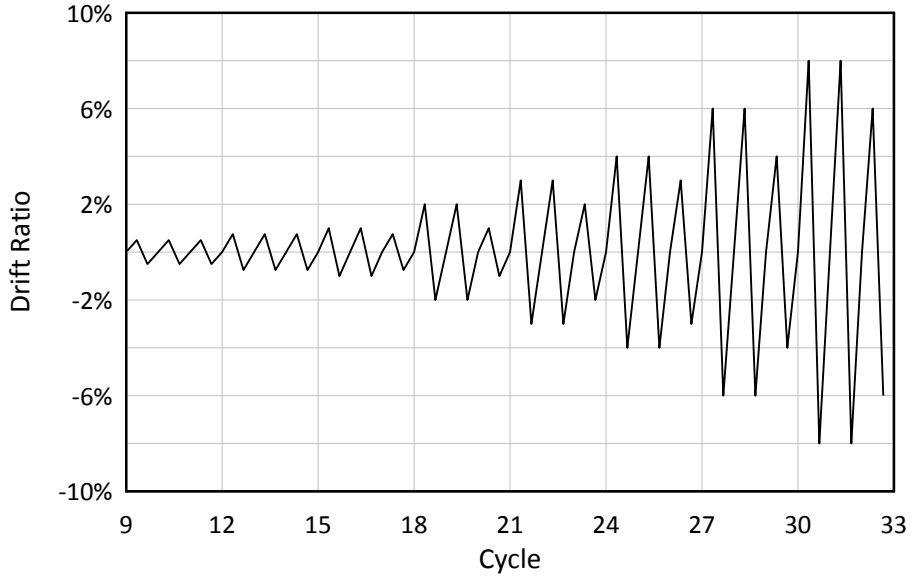

Figure 5.24 HYB-2 displacement controlled loading protocol

5.4.2 Observations During the Test

The following section summarizes the observations made during testing. Observations and photographs were taken at the final cycle at a given force or displacement. For the cases where the specimen underwent two cycles to a given displacement followed by one cycle at a previous displacement, the observations and photographic documentation only occurred at the end of the second cycle in both push and pull directions. Cracks were marked using markers corresponding to a given displacement direction. Red markers were used to indicate cracking due to pushing while blue markers were used to indicate cracking due to pulling.

The test unit prior to testing is shown in Figure 5.25 with vertical and horizontal actuators attached. For the purposes of damage descriptions, the direction of pushing will be referred to as “south” and the direction of pulling will be referred to as “north”. “East” and “west” can thereby be inferred by standard convention.

Figure 5.25 HYB-2 prior to testing

Application of 88 kip Vertical Load

On the west side of the specimen one crack was observed to mid-depth of the cap beam at the south end of the joint and three very small cracks were observed at the bottom of the cap beam in the joint. On the east side of the specimen one crack was observed to mid-depth of the cap beam at the south end of the joint and one small crack was observed at the bottom of the cap beam at the north end of the joint.

3 Cycles at ± 11 Kips

During both the push and pull cycles, no cracking was observed in the specimen.

3 Cycles at ± 22 Kips

During both the push and pull cycles, no cracking was observed in the specimen.

3 Cycles at ± 44 Kips

During the push cycle, one of the existing cracks at the base of the joint extended a couple of inches and the existing flexural crack on the east side extended to approximately two-thirds the depth of the cap. One new crack was observed on the west side extending from the base of the cap beam approximately 6 inches south of the joint up to approximately four inches from the top of the cap beam.

3 Cycles at ± 0.5% Drift Ratio

Two new minor cracks were observed on both the southeast and southwest sides of the specimen during the push cycle. Additionally, minor extensions of two existing cracks were observed in the joint region on the east face of the cap during the push cycle. No new cracks or extensions were observed following the pull cycles.

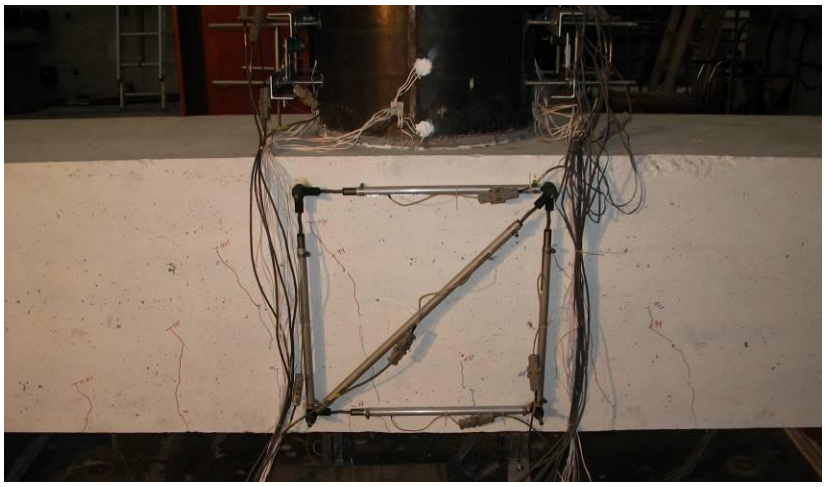

Figure 5.26 HYB-2 east face of bent cap at 0.5% drift ratio

Figure 5.27 HYB-2 west face of bent cap at 0.5% drift ratio

The base gap opened during both the push and pull cycles to approximately mid-depth of the column. There was noticeable joint opening as is shown in Figure 5.28 including the onset of crushing of extreme grout material.

Figure 5.28 HYB-2 south end of column at 0.5% drift ratio

3 Cycles at ± 0.75% Drift Ratio

During the push cycle, minor extensions were observed on four cracks on the west face of the bent cap and minor extensions on the east face. One new crack was observed on the east face of the bent cap in the center of the joint extending approximately 7" from the base of the cap. During the pull cycle, a couple of small crack extensions were observed on the west face of the bent cap and a 5" extension on the east face of the cap inside the joint. See Figure 5.29 and Figure 5.30 for damage to the cap at this drift level.

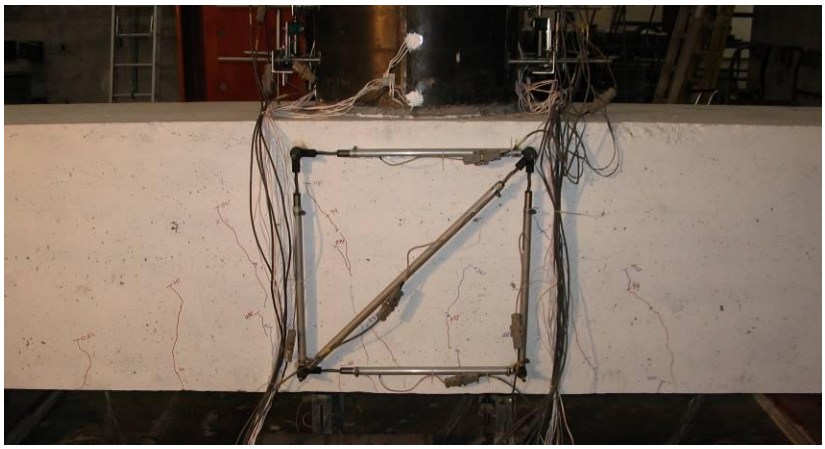

Figure 5.29 HYB-2 east face of bent cap at 0.75% drift ratio

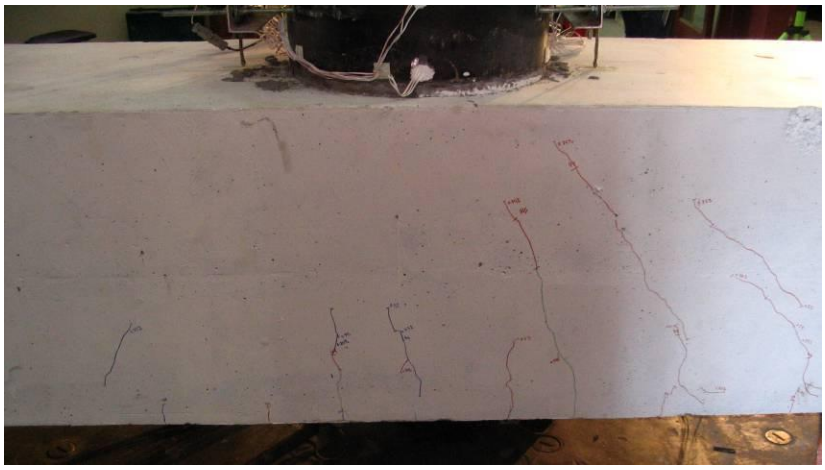

Figure 5.30 HYB-2 west face of bent cap at 0.75% drift ratio

Pronounced damage to the grout bedding layer was observed under both push and pull displacement cycles (Figure 5.31 and Figure 5.32). Gap opening at the base of the column was observed over approximately 2/3 the column diameter.

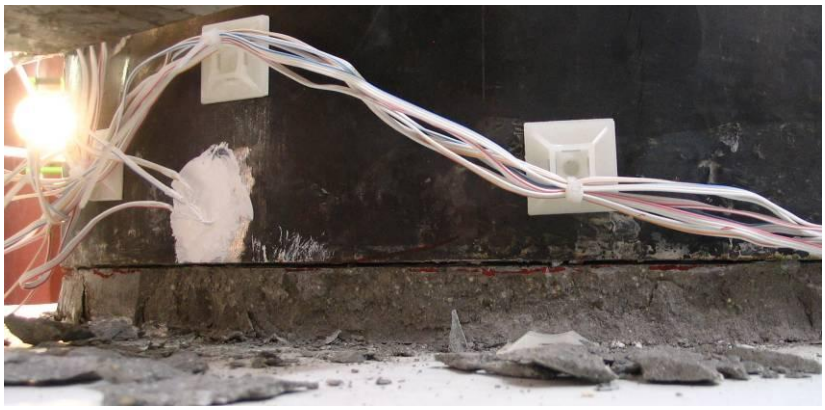

Figure 5.31 HYB-2 grout damage on north end of column at 0.75% drift ratio

Figure 5.32 HYB-2 grout damage on south end of column at 0.75% drift ratio

2 Cycles at ± 1.0% Drift Ratio

During the push cycle, a diagonal tension crack was observed extending from the west face of the bent cap at the pin support location (see Figure 5.33). The crack width was significantly small and did not increase noticeably during the duration of testing.

Additionally during the push cycle, two minor extensions were noted on the west face of the cap south of the joint as well as one minor extension of a crack inside the joint. On the east side, two small crack extensions were observed south of the joint and two small crack extensions were observed inside the joint near the bottom of the cap. Damage to the bent cap can be seen in Figure 5.34 and Figure 5.37.

During the pull cycle, no additional damage was noted on the east face of the bent cap. On the west face, a 3” crack extension was noted near the middle of the joint and a 12” extension just north of the joint. Bedding layer response is shown in Figure 5.35 and Figure 5.36. Additional deterioration of the joint was noted with pronounced gap opening at the top of the bedding layer.

Figure 5.33 HYB-2 minor crack at roller support at 1.0% drift ratio

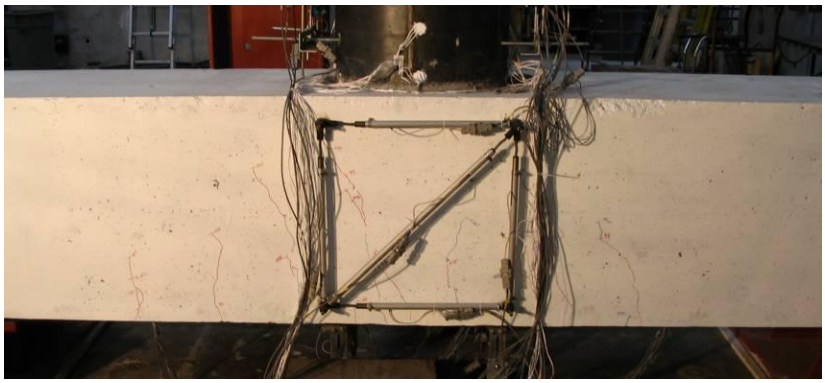

Figure 5.34 HYB-2 east face of bent cap at 1.0% drift ratio

Figure 5.35 HYB-2 joint opening at north end of column at 1.0% drift ratio

Figure 5.36 HYB-2 grout damage at north end of column at 1.0% drift ratio

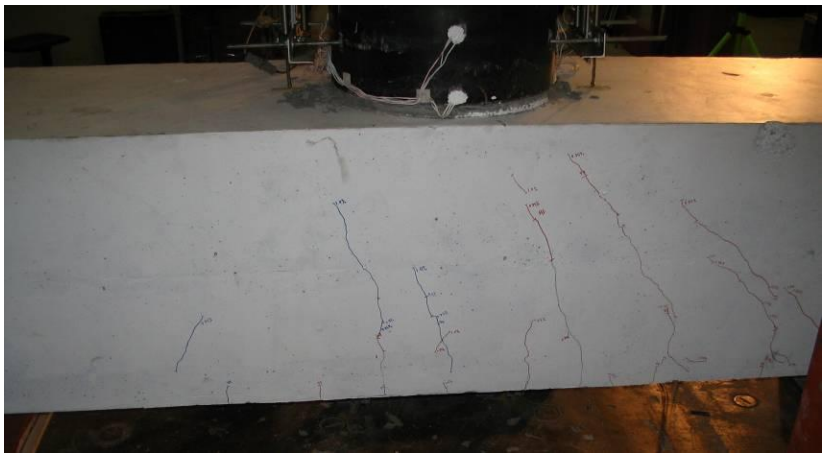

Figure 5.37 HYB-2 west face of bent cap at 1.0% drift ratio

2 Cycles at ± 1.5% Drift Ratio

During the push cycle, a 12” diagonal tension crack was observed extending through the joint on the west face of the bent cap. Additionally, one small crack extension was noted on the west face south of the joint. On the east face, a 10” diagonal tension crack was observed in the joint in addition to an 8” diagonal extension of an existing flexural crack. One 2” crack extension was also noted on the east face of the cap just south of the joint. Figure 5.38 and Figure 5.39 show the damage to the bent cap following this displacement cycle.

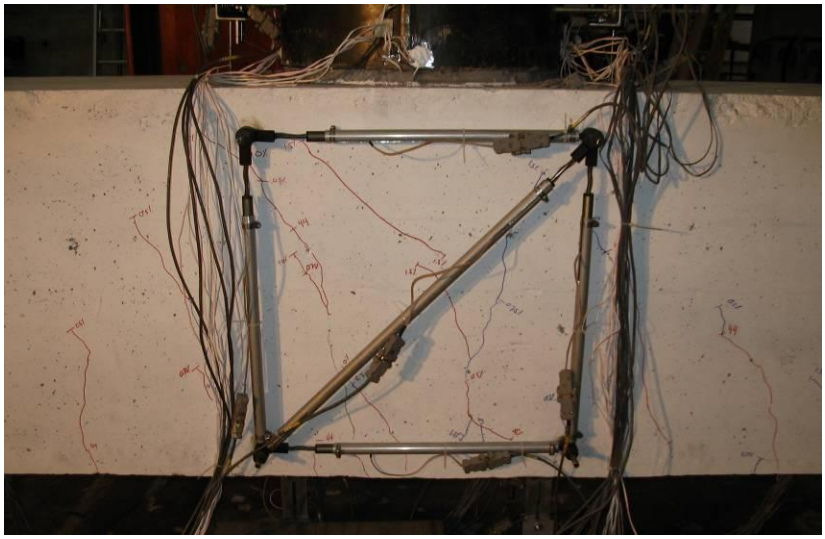

Figure 5.38 HYB-2 east face of bent cap at 1.5% drift ratio

Following the pull cycle a 10” diagonal extension of a previous flexural crack was noted on the east face of the bent cap. Additionally, a 6” crack was observed about 18” north of the joint on

the east face of the cap. A small crack extension was also observed at the base of the cap. On the west face of the cap, a 5” extension was noticed on the north side of the joint.

Bedding layer damage continued with an increase in the observed gap opening during both push and pull cycles. Gap opening only occurred at the top of the bedding layer (see Figure 5.40).

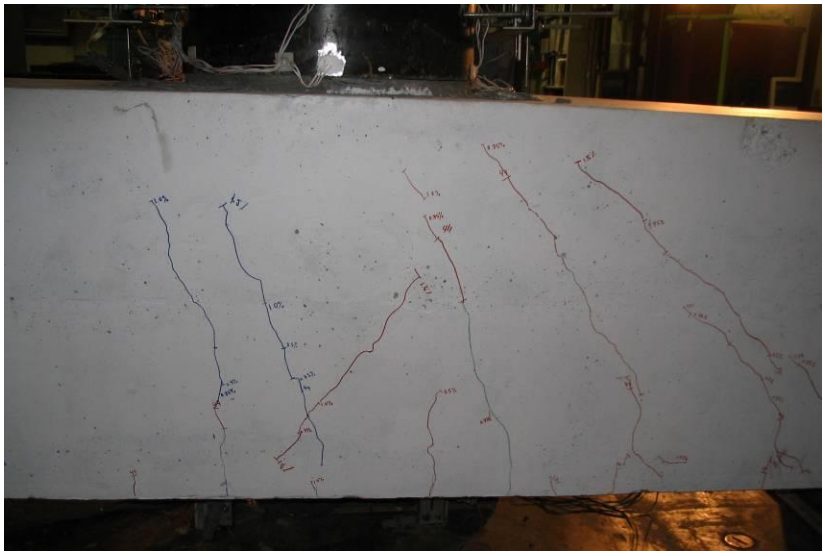

Figure 5.39 HYB-2 west face of bent cap at 1.5% drift ratio

Figure 5.40 HYB-2 joint opening at north end of column at 1.5% drift ratio

2 Cycles at ± 2.0% Drift Ratio

During the push cycle, a small extension of one crack was noted just south of the joint. During the pull cycle, a 4” extension was noted on west face of the cap north of the joint as well as a small crack just north of the joint (see Figure 5.43).

During the push cycle, three bond cracks were noted on top of the bent cap (see Figure 5.41). During the pull cycle, the bond crack on the center bar on the east face extended slightly down the east face of the cap. Gap opening continue to increase with opening at both top and bottom of the bedding layer (see Figure 5.42).

Figure 5.41 HYB-2 bond cracks at top of bent cap at 2.0% drift ratio

Figure 5.42 HYB-2 joint opening at north end of column at 2.0% drift ratio

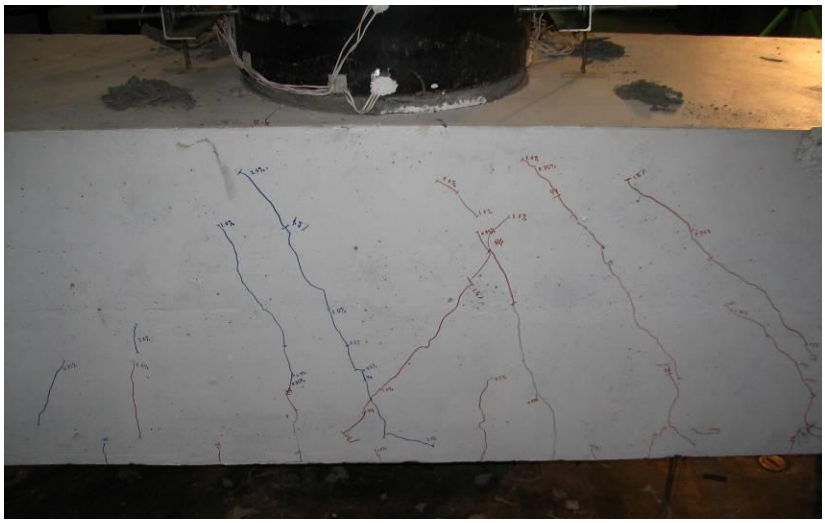

Figure 5.43 HYB-2 west face of bent cap at 2.0% drift ratio

2 Cycles at ± 3.0% Drift Ratio

No additional cracking was observed on both the east and west faces of the bent cap. Significant joint deterioration was observed due to large compressive strains during both push and pull cycles (see Figure 5.44 through Figure 5.46). Appreciable pieces of grout became separated from the bedding layer during joint opening following the compression cycle. This caused a continual decrease in the effective dimension of the column and bedding layer and a resulting decrease in lateral load. Note, a portion of grout from the grouted duct moved with the bedding layer during joint opening (see Figure 5.46).

Figure 5.44 HYB-2 east view of column joint opening at 3.0% drift ratio

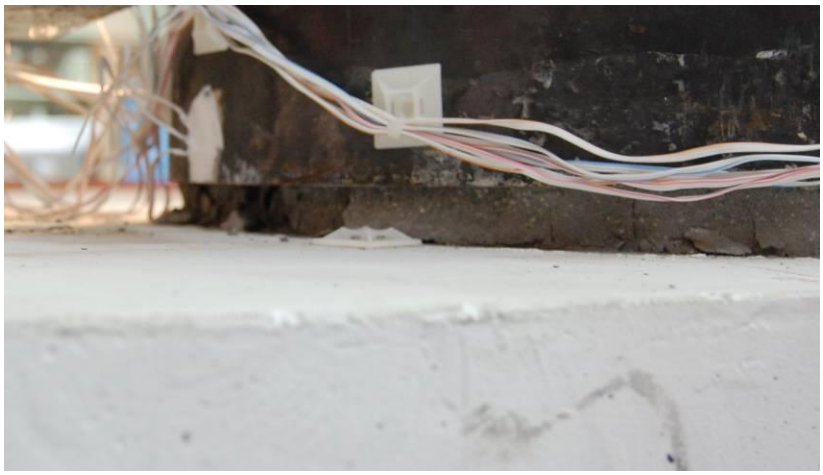

Figure 5.45 HYB-2 loss of grout at north end of column at 3.0% drift ratio

Figure 5.46 HYB-2 joint opening at south end of column at 3.0% drift ratio

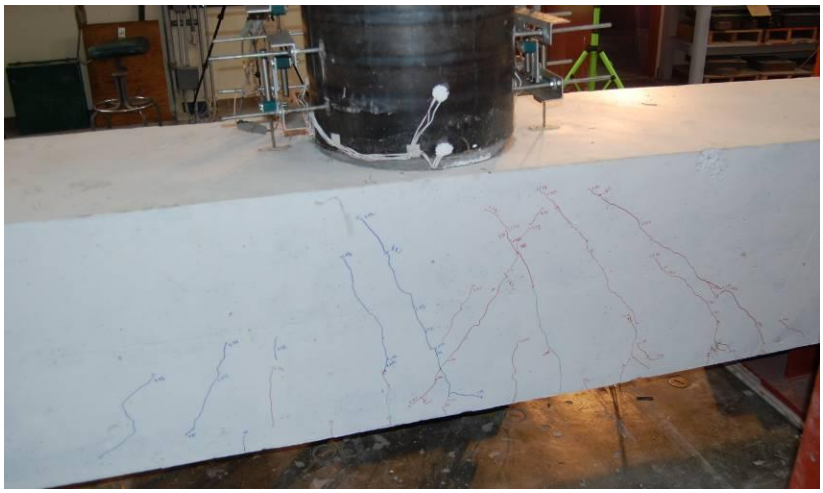

Figure 5.47 HYB-2 west face of bent cap at 3.0% drift ratio

2 Cycles at ± 4.0% Drift Ratio

Bedding layer gap opening continued to increase with significant opening at the top of the bedding layer and smaller opening at the bottom (see Figure 5.48). This gap opening provided a clear view of the extreme reinforcing bars during both push and pull cycles as shown in Figure 5.49. Bedding layer deterioration continued to occur resulting in a continued loss of lateral force capacity. Additionally, large portions of the bedding layer began separating on both sides of the column. No additional cracking was observed in the bent cap.

Figure 5.48 HYB-2 east view of column joint opening at 4.0% drift ratio

Figure 5.49 HYB-2 close up of joint opening at reinforcing bar at 4.0% drift ratio

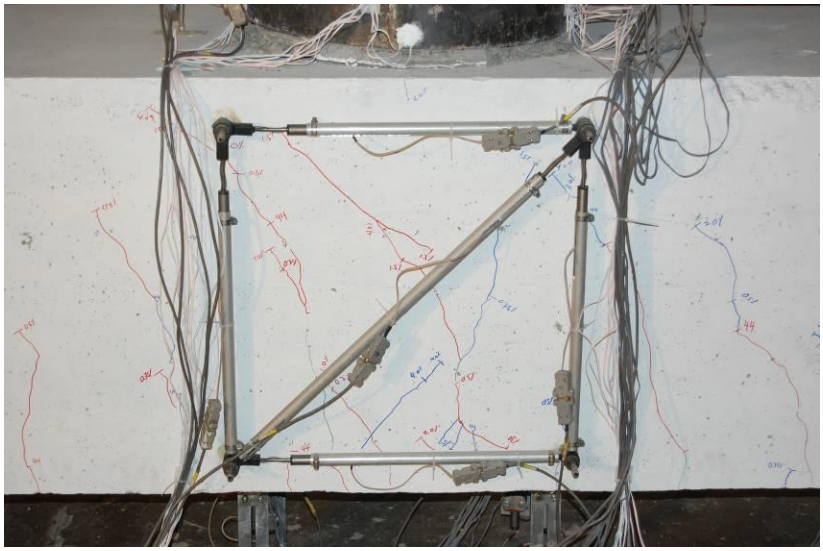

Figure 5.50 HYB-2 east face of bent cap at 4.0% drift ratio

2 Cycles at ± 6.0% Drift Ratio

During the second push cycle to 6.0% drift ratio, a reinforcing bar fractured as the specimen approached the target displacement (see Figure 5.51). Interestingly, the fractured reinforcing bar was not the extreme bar in tension but the next bar to the east. From inspection of the bar, it appears the bar fractured due to a combination of tension, flexure and torsion. Figure 5.52 shows

the out of plan movement of the specimen during this displacement level which results in eccentric loading of the column and effective twisting action in the specimen.

Figure 5.51 HYB-2 close up of reinforcing bar fracture at 6.0% drift ratio

Figure 5.52 HYB-2 out of plane movement at 6.0% drift ratio

No additional damage was noted on the bent cap. Significant bedding layer deterioration continued to occur due to large compressive strains induced on the element. Observed joint opening was significant and was mainly concentrated at the top of the bedding layer as is shown in Figure 5.53 and Figure 5.54. Bedding layer damage following this displacement level can be seen in Figure 5.56.

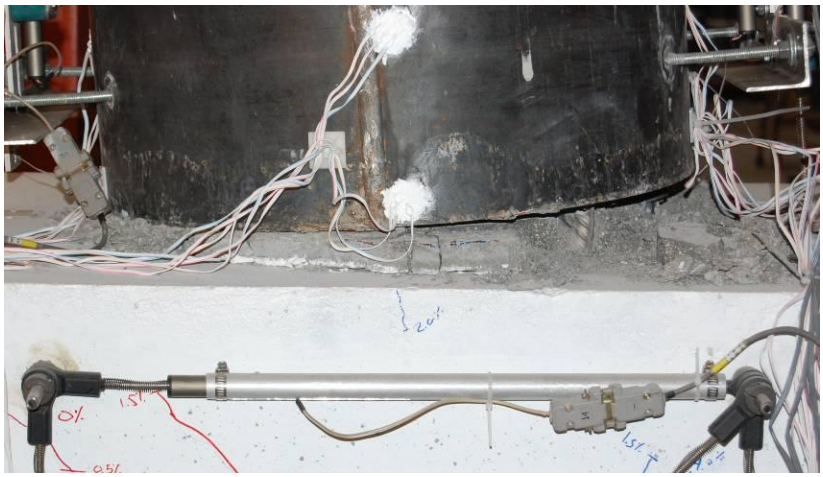

Figure 5.53 HYB-2 east view of joint opening at 6.0% drift ratio

Figure 5.54 HYB-2 close up of column north end joint opening at 6.0% drift ratio

Figure 5.55 HYB-2 grout damage after 6.0% drift ratio

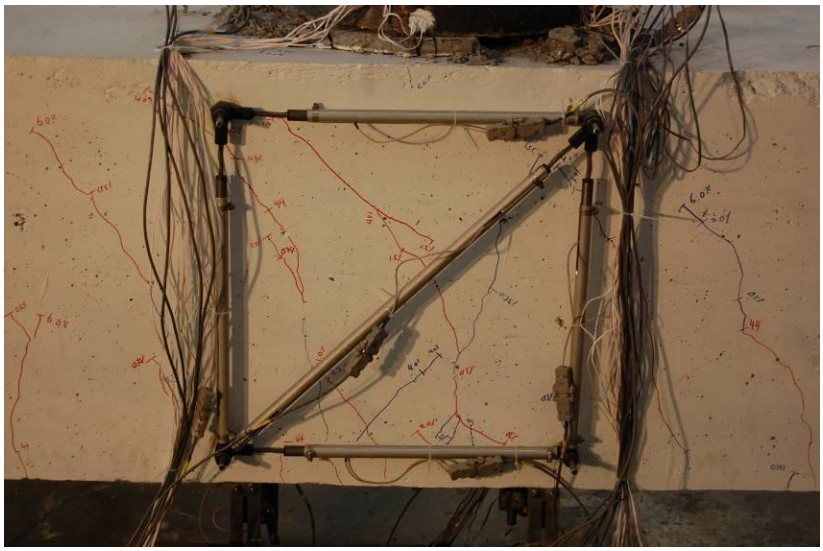

Figure 5.56 HYB-2 east face of bent cap at 6.0% drift ratio

2 Cycles at ± 8.0% Drift Ratio

During the first push cycle to this displacement level, fracture of the extreme rebar in tension and the adjacent bar to the west was observed at relatively small displacements. Significant bedding layer gap opening was observed during this displacement level concentrated solely at the top of the bedding layer.

No rebar fracture was observed as the specimen underwent the first pull displacement cycle. However, on the second displacement cycle three rebar fractures were noted with subsequent drop in lateral force capacity. At this displacement level the steel shell was almost in contact with the top of the bent cap (see Figure 5.58).

Figure 5.57 HYB-2 column joint opening at north end at 8.0% drift ratio

Figure 5.58 HYB-2 column compression toe at 8.0% drift ratio

End of Test

Following the completion of the test, the extent damage and loss of grout was noted as shown in Figure 5.59 and Figure 5.60. Large portions of grout were missing or severely damage all around the bedding layer. Portions of the grout were the consistency of fine sand following the test indicating a complete break down of the material matrix. Furthermore, a residual gap was noted at the base of the column as the specimen was at zero lateral load (see Figure 5.61).

Figure 5.59 HYB-2 east view of column joint damage

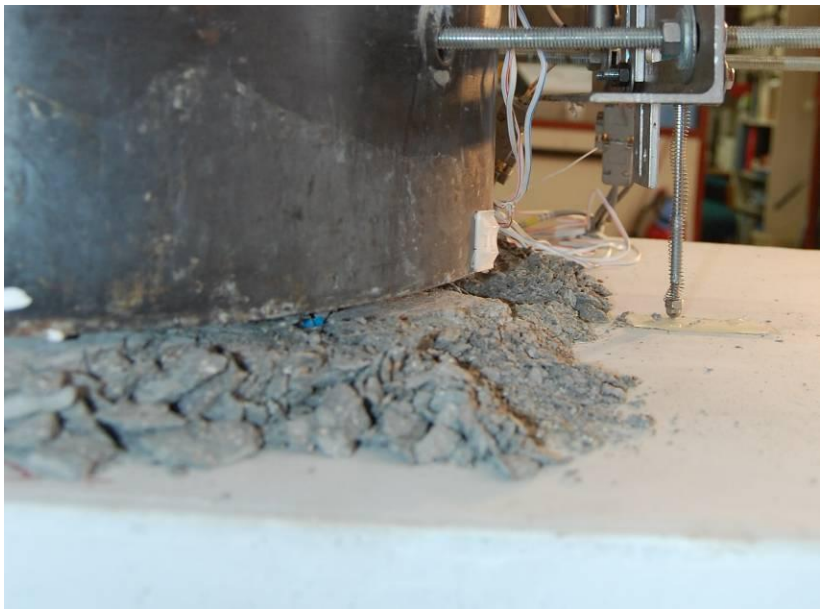

Figure 5.60 HYB-2 damage to grout at south end of column

Figure 5.61 HYB-2 residual opening following test

5.5 Experimental Results

Data collected during testing from instrumentation is presented and discussed in the following section.

5.5.1 Global Response

Vertical Load History

The vertical load history recorded during testing is presented in Figure 5.62. It is noted that the load is rather constant at 88 kips during the entirety of the test. At one point during a large displacement push cycle the vertical force briefly dropped approximately 8 kips but returned to the stable load. This will not affect the member response appreciably.

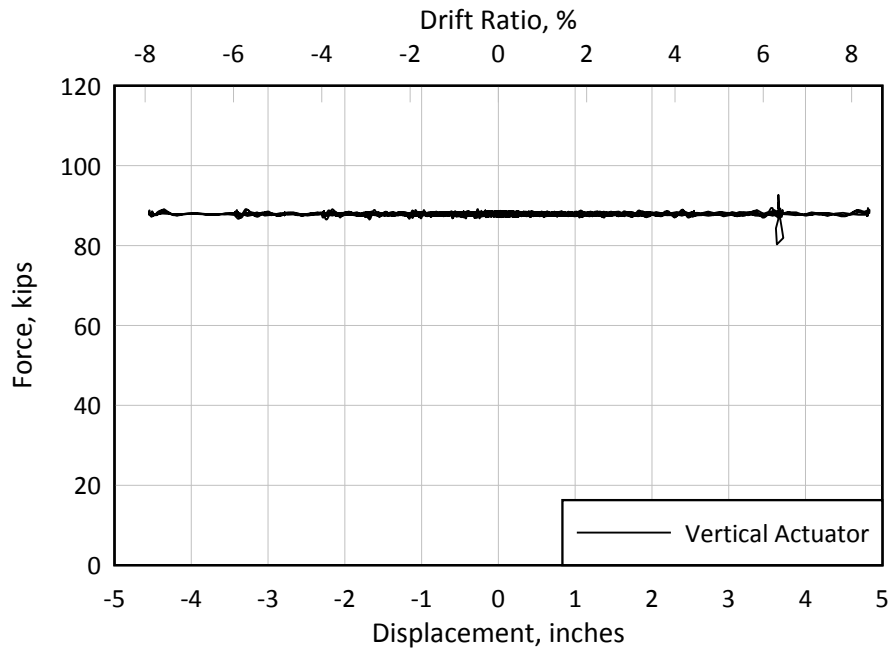

Figure 5.62 HYB-2 vertical load history

Force-Displacement Response

The complete force-displacement curve obtained for this specimen is shown in Figure 5.63. The lateral force presented is the actual lateral force considering the effects of system deformation during testing. Following load cycles to 2% drift ratio a noticeable loss in lateral capacity was observed. The first cycle to 3% drift ratio was approximately 90% of the maximum force recorded during the 2% drift ratio cycles. Every cycle following the 2% drift ratio level resulted in an additional loss in lateral capacity. Based on observations during testing, the accumulation of damage to the grout bedding layer resulted in a reduction in the effective column diameter and a subsequent reduction in the lateral capacity of the specimen. Additionally, the reduction in effective post-tensioning force due to column shortening also resulted in loss of lateral capacity.

At the 4% drift ratio level, the maximum lateral capacity is approximately 84% of the maximum observed lateral capacity. At the 6% drift ratio level, the maximum lateral capacity is approximately 76% of the maximum observed lateral capacity. Considering the common definition of failure which is based on a reduction in lateral strength equal to 80% of the maximum, this specimen could be said to have failed at a drift level around 5%. The nominal capacity calculated using the simplified analysis technique is also provided in the force-displacement figure.

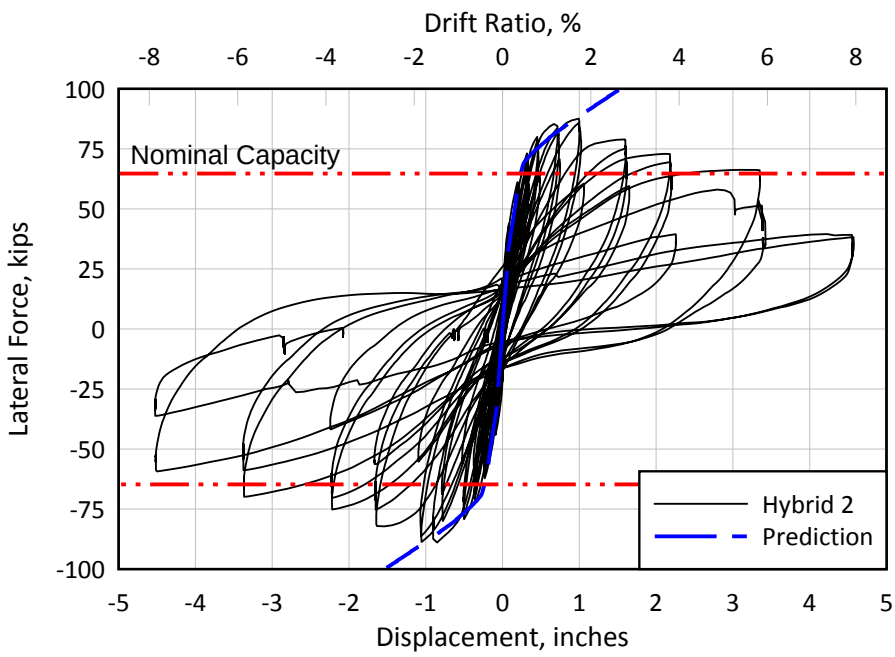

Figure 5.63 HYB-2 force-displacement response

Failure of the first longitudinal reinforcing bar was noted through auditory observations and a noticeable drop in the lateral resistance during the second push cycle to 6% drift ratio. A second bar fracture was also observed as the section reached the 6% drift ratio target.

The force-displacement response up to 3% drift ratio is shown in Figure 5.64. This response shows an origin oriented response with significant improvements in the self-centering ability up to 2% drift ratio when compared to the cast-in-place specimen. At the 2% drift ratio level, the residual deformation for HYB-2 is approximately 26% of the maximum displacement whereas for the cast-in-place specimen the residual drift is approximately 59% of the maximum displacement.

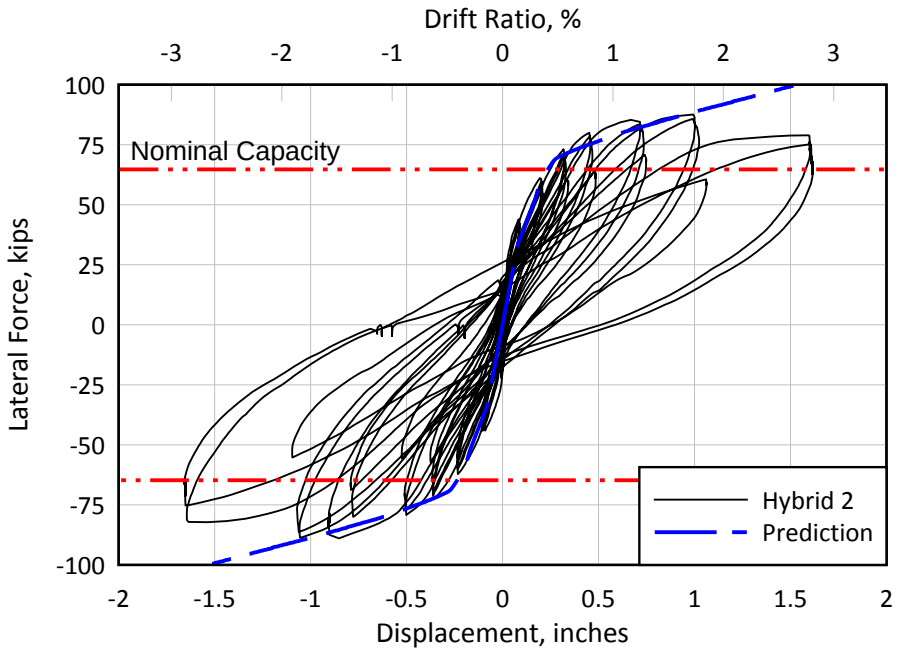

Figure 5.64 HYB-2 force-displacement response to 3.0% drift ratio

The force-displacement response for both cycles at approximately 2% drift ratio is shown in Figure 5.65. It can be observed from this plot that there are only minor reductions in stiffness and strength due to cyclic loading at a drift level approximately equal to the design level drift. This response characteristic is consistent with the desired stable lateral response in the design level displacement range.

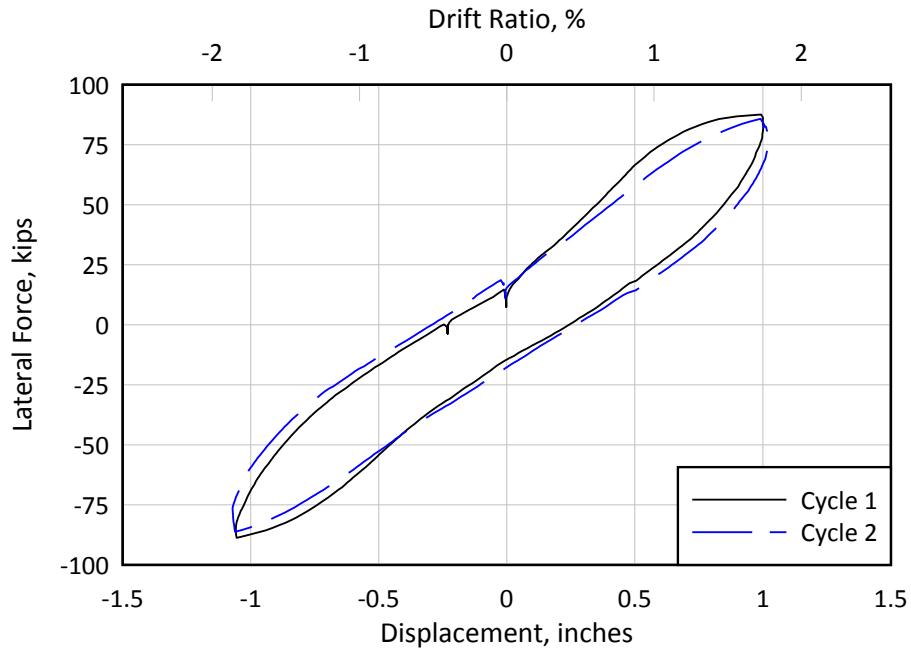

Figure 5.65 HYB-2 force-displacement response at 2% drift ratio

The force-displacement envelope prediction as compared to the actual recorded envelop is shown in Figure 5.66. The prediction is reasonable accurate up to approximately 1.75% drift ratio at which point the prediction continues to increase in lateral capacity whereas the recorded response begins to decay. The reduction in lateral capacity is due to the accumulation of damage in the grout material used in the bedding layer that began to fall apart under increasing drifts. This damage to the bedding layer resulted in a loss of grout material in the bedding layer and an essential reduction in the column effective diameter. Additionally, the bedding layer began to reduce in thickness that resulted in a reduction in the effective post-tensioning force. The lateral resistance of the specimen continued to diminish until the ultimate failure due to fracture of column reinforcing bars.

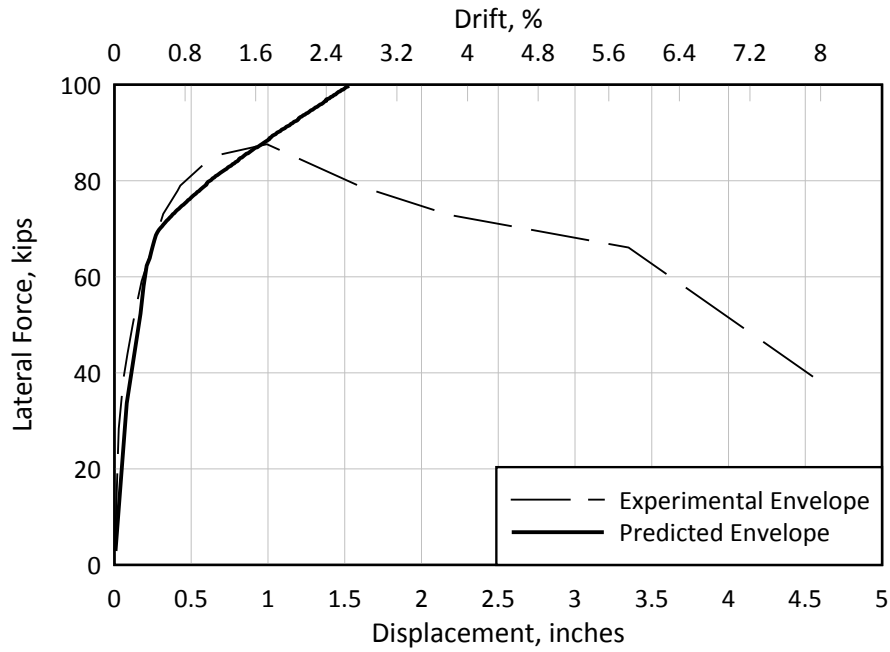

Figure 5.66 HYB-2 force-displacement envelope

Displacement Decomposition

A graphical breakdown of displacement components captured by instrumentation readings during testing is provided in Figure 5.67. This plot provides a summary of the relative contribution of a given mode of deformation as compared to the total displacement recorded at the same instant of time. During lower level lateral displacement cycles it is apparent that there is a relatively large amount of lateral displacement that is not captured using instrumentation. However, as the system undergoes larger lateral deformations the summation of individual contributions becomes closer to the total displacement.

As the magnitude of lateral displacement increases, there is a noticeable increase in the relative contribution of the column end rotation. This is an expected trend as the majority of large magnitude displacement is facilitated through the opening of the joint and associated fixed end rotation. The contribution of column flexure was less significant as compared to the first hybrid specimen due to the increase in flexural stiffness with the composite shell system.

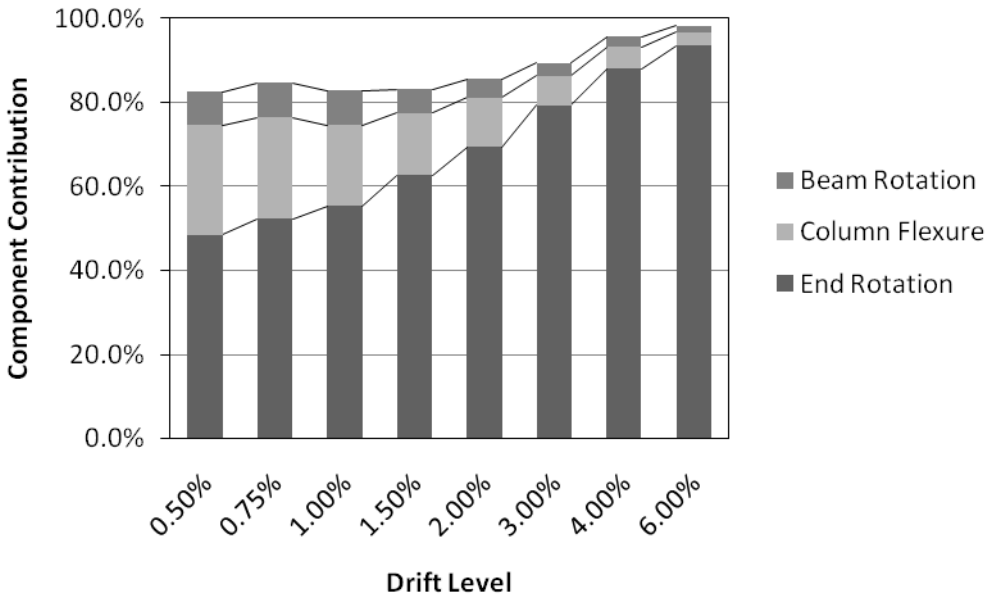

Figure 5.67 HYB-2 displacement decomposition

Out-of-Plane Displacement

During testing, the out-of-plane displacement at the actuator location was monitored as a safety precaution to ensure the vertical actuator control remains stable while under force control. Figure 5.68 shows the displacement orbit of the test specimen. Due to the floating of one PVC pipe during casting, there was noticeable lateral drift towards the west during testing for both push and pull cycles. At the maximum drift level, the out-of-plane drift was in excess of 2%. This will result in a slight reduction in the north-south lateral displacement capacity however as this is a completely symmetric column, the reduction is not overly significant.

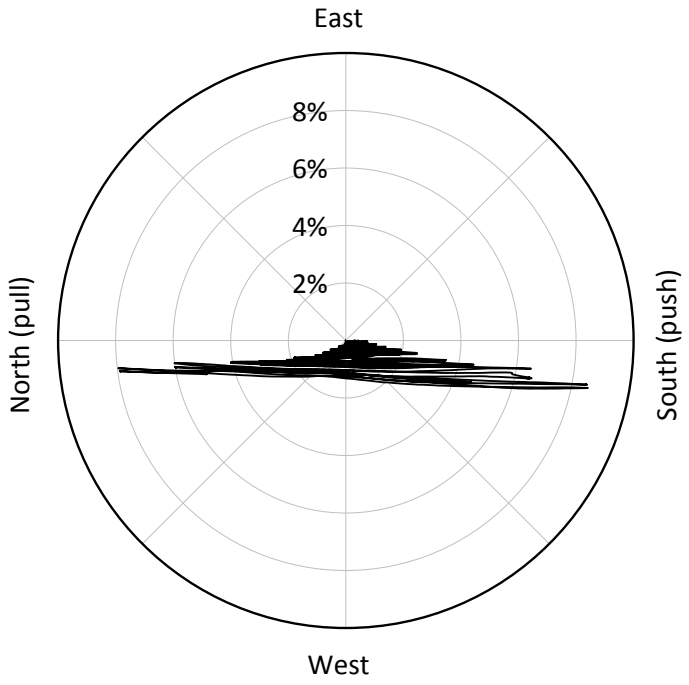

Figure 5.68 HYB-2 drift ratio orbit

Equivalent Viscous Damping

The recorded force-displacement response of the specimen was used to determine the equivalent viscous damping present in the system. Figure 5.69 provides a graphical representation of the equivalent viscous damping over varying lateral drift levels. It is apparent that the equivalent viscous damping inherent in the system increases with increasing lateral drift levels. For the majority of the drift levels, the observed equivalent viscous damping is nearly identical for the first and second loading cycles indicating there is no significant deterioration and increase in damage in the system from the first to second cycle. The main objective of considering equivalent viscous damping is to show relative stability between hysteresis loops at the same drift level. As the first and second cycles have similar equivalent viscous damping, the loops are relatively stable during cycles at the same drift level.

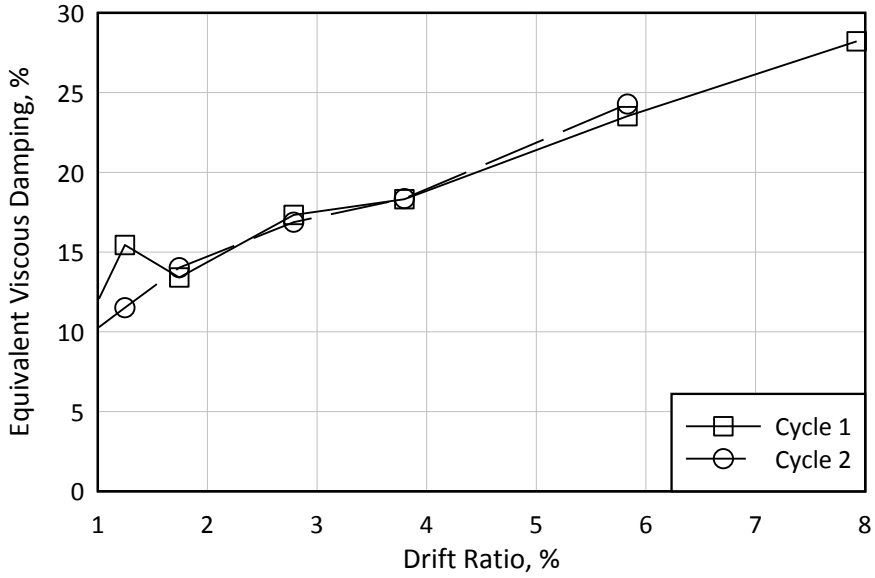

Figure 5.69 HYB-2 equivalent viscous damping

Residual Displacement

Figure 5.70 provides a plot of the recorded residual drift following both the first and second displacement cycles as a ratio of residual drift to maximum drift at a given cycle. Note that the maximum value for both push and pull cycles is presented. This plot indicates that there is a slight increase in the residual drift ratio from the first to second displacement cycle and there is an overall increase in residual drift ratio with increasing drift.

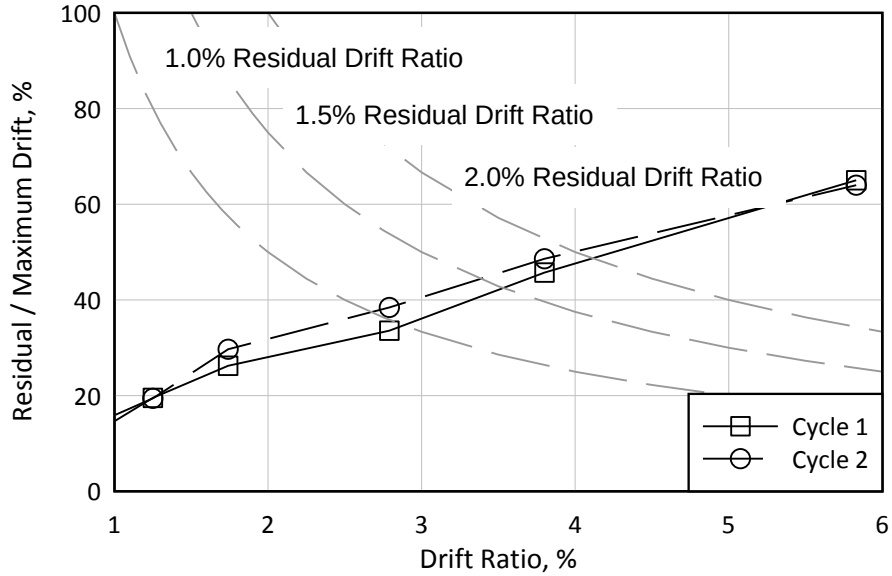

Figure 5.70 HYB-2 residual drift ratios

Figure 5.71 provides a comparison of the residual drift ratios for Hybrid 2 and the cast-in-place control specimen. It is apparent that the hybrid detail has noticeably less residual drift as compared to the control specimen indicating the beneficial performance when considering post-earthquake functionality of the system. Furthermore, if considering the aforementioned residual drift limit of one degree, the hybrid detail would be able to undergo displacement cycles of slightly less than 4% without need for replacement whereas the cast-in-place unit can only experience drift levels of approximately 2.75% to satisfy the same performance requirements.

The residual drift ratios for the hybrid specimen are expected to decrease substantially when using fiber reinforced grout due to the enhanced integrity of the joint.

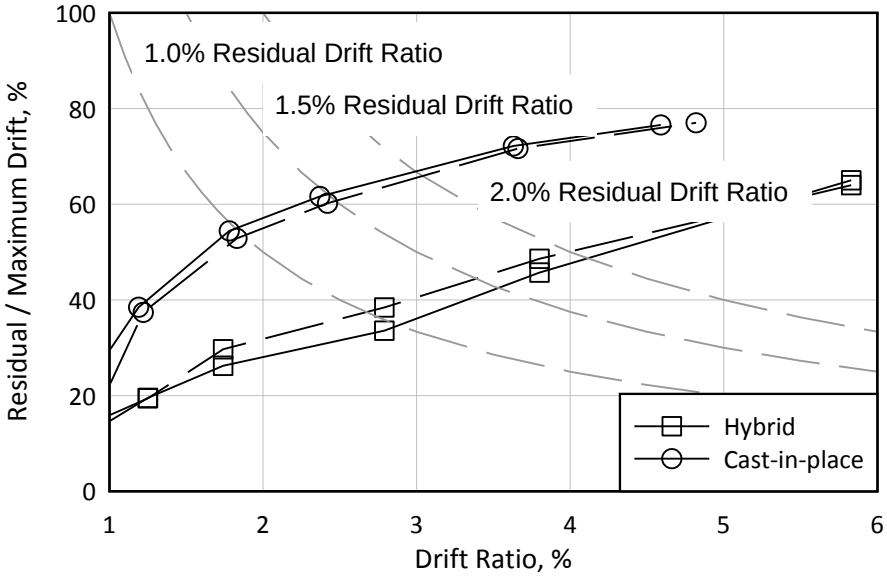

Figure 5.71 HYB-2 comparison of residual drift ratios with CIP

Bedding Layer

The axial deformation at the centerline of the grout bedding layer was determined for the entirety of the test using the curvature gages at the base of the column. These results are presented in Figure 5.72. The bedding layer had an approximately linear increase in centerline axial deformation with increasing lateral drift. Slight variation in the bedding layer axial deformation is observed at the zero drift state indicating minor accumulation of damage resulting in a slight permanent reduction in bedding layer dimension.

Additionally, the recorded bedding layer deformation indicates an unsymmetrical response as the push cycle exhibits significantly larger growth as compared to the pull cycle. The magnitude of bedding layer growth is also appreciably greater than the first hybrid unit, which is due to the shallower neutral axis depth for this specimen.

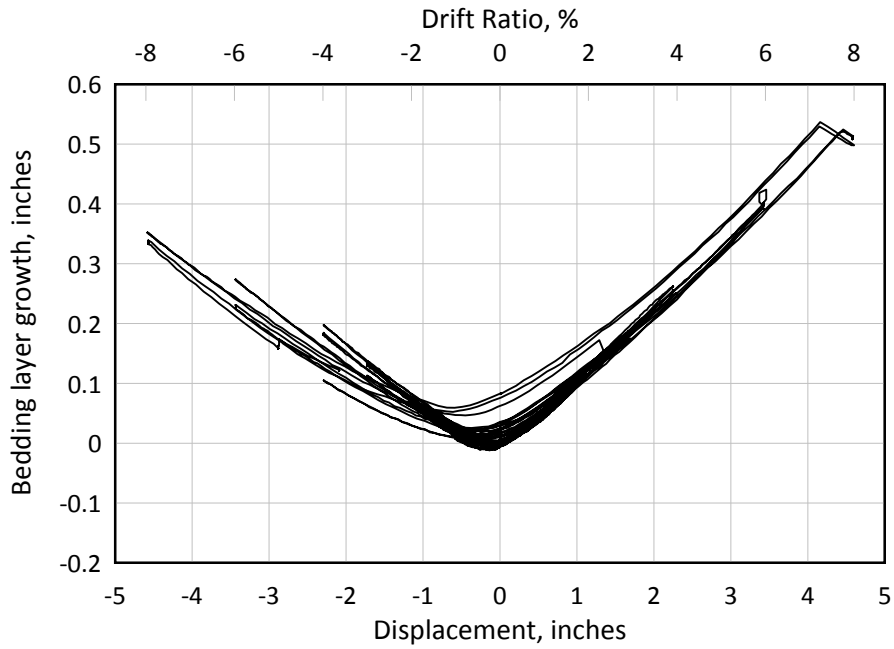

Figure 5.72 HYB-2 centerline of bedding layer deformation

Neutral Axis Depth

Curvature gages at the base of the column were used to determine the depth of the neutral axis for each drift cycle. This depth was calculated considering the assumption that plane sections remain plane in a concrete section, which is a reasonable approximation for the purpose of this calculation. Figure 5.73 shows the neutral axis depth for the first displacement cycle at a given drift level for both push and pull directions. This plot shows a varying neutral axis depth in the push and pull directions with a greater depth during the pull cycles. The neutral axis depth stabilizes at approximately 25% for the push cycle and approximately 30% for the pull cycles. This neutral axis depth for the push cycle is approximately equal to the design depth of 20% of the column diameter. These observed neutral axis depth values are within the range that should minimize localized compressive strains that may reduce the self-centering ability.

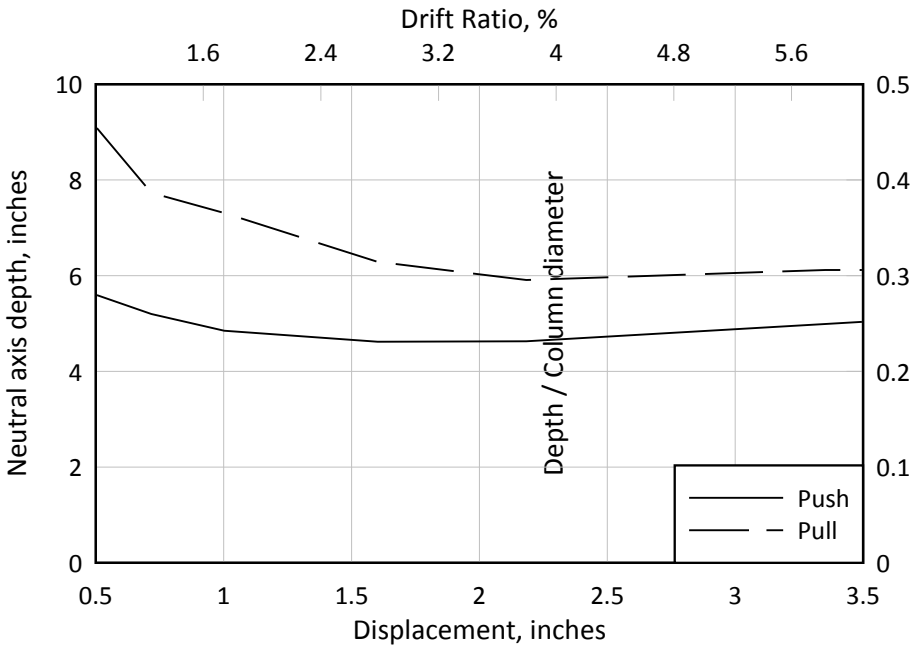

Figure 5.73 HYB-2 neutral axis depth

5.5.2 Rotation Profile

The column rotation profile, as derived from column curvature gages, is provided in Figure 5.74. A rotation profile, as opposed to a traditional curvature profile, was provided for this specimen due to the dominance of response on the column fixed end rotation, which cannot be accurately represented by a curvature approximation. This is due to the lack of an effective gage length for consideration due to intentional debonding of reinforcing and post-tensioning at the column end.

These results indicate that the majority of the column drift is provided by the column fixed end rotation, with little influence from elastic flexural displacements at higher drifts. In comparison to the end rotation, the other rotation components have significantly less influence on the overall system response.

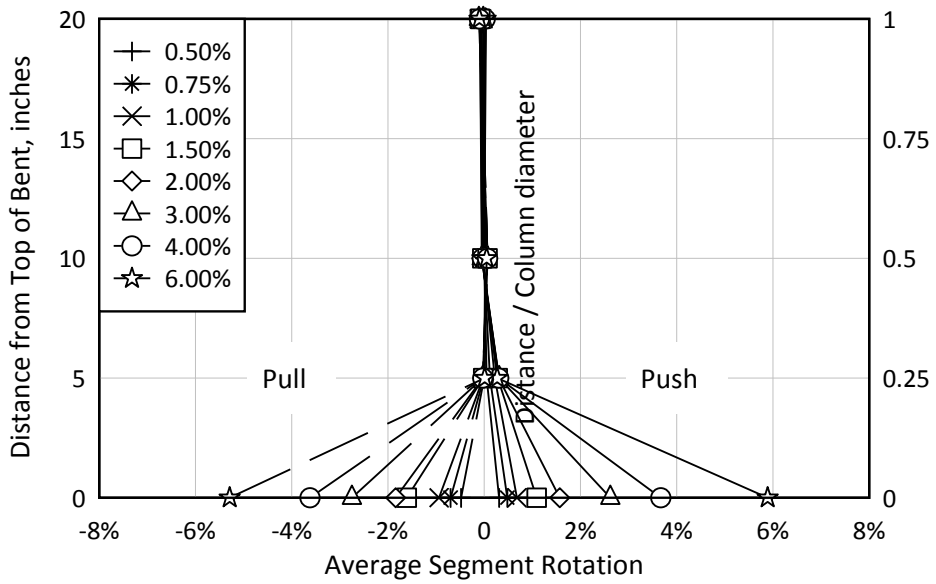

Figure 5.74 HYB-2 column rotation profile

5.5.3 Colum Longitudinal Bar Slip

Bar slip readings for the extreme northern bar are presented in Figure 5.75. These readings indicate that the column longitudinal reinforcing bars have adequate development length in the corrugated ducts with negligible bar end slip. Maximum bar slip readings are less than one-hundredth of an inch during the entirety of the test.

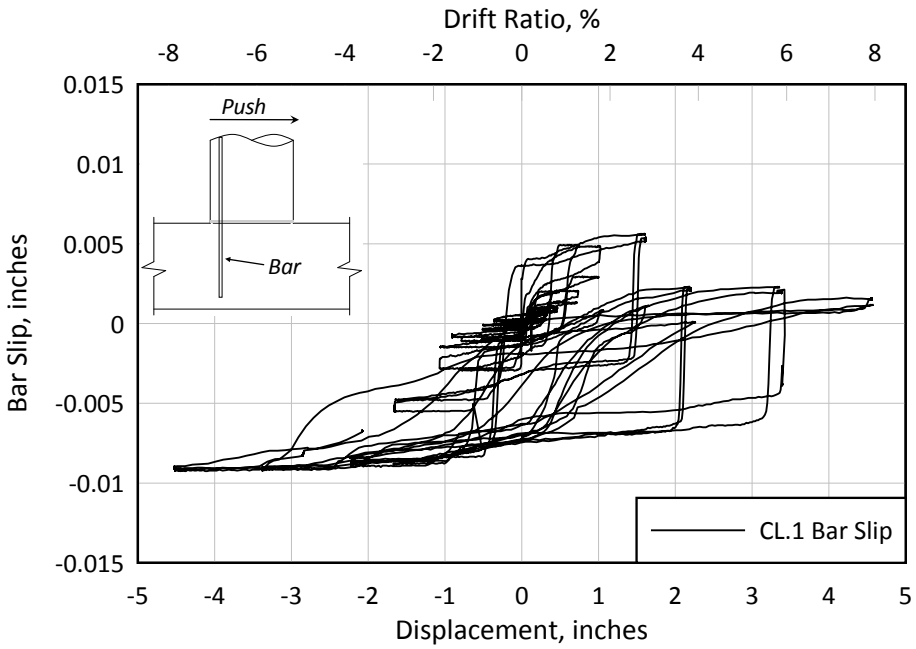

Figure 5.75 HYB-2 column longitudinal bar slip at end of bar (CL.1)

5.5.4 Strain Gage Histories

During construction, a number of strain gages were mounted on various pieces of reinforcing steel throughout the specimen, as well as on the external steel shell. Some gages were damaged during fabrication, erection and testing, thus many readings are not shown herein. Additionally, many plots have incomplete data due to damage or malfunctioning gages. This section provides information on the strain histories recorded by various gages.

Column Longitudinal

Strain histories for gages mounted on the extreme column longitudinal bars on the north and south ends of the column are shown in Figure 5.76 thru Figure 5.81. Results from these plots shows first bar yield occurred at a drift level of approximately 0.50% for both push and pull loading cycles. Gages located in the column assembly all experienced failure after approximately 1.50% drift ratio cycles. Additionally, gages inside of the ducts experienced a number of failures during testing. It is believed that strain gage leads may have been unknowingly damaged during the bent cap setting process. These numerous failures significantly limit the available knowledge of reinforcement strains during large deformation cycles. Loss in strain in the column rebar is noted for those bars in the corrugated duct. This loss is believed to be attributable to the reduction

in bar force due to the reduction in lateral load carrying capacity. This loss in capacity is due to the accumulated grout damage that caused the neutral axis to shift.

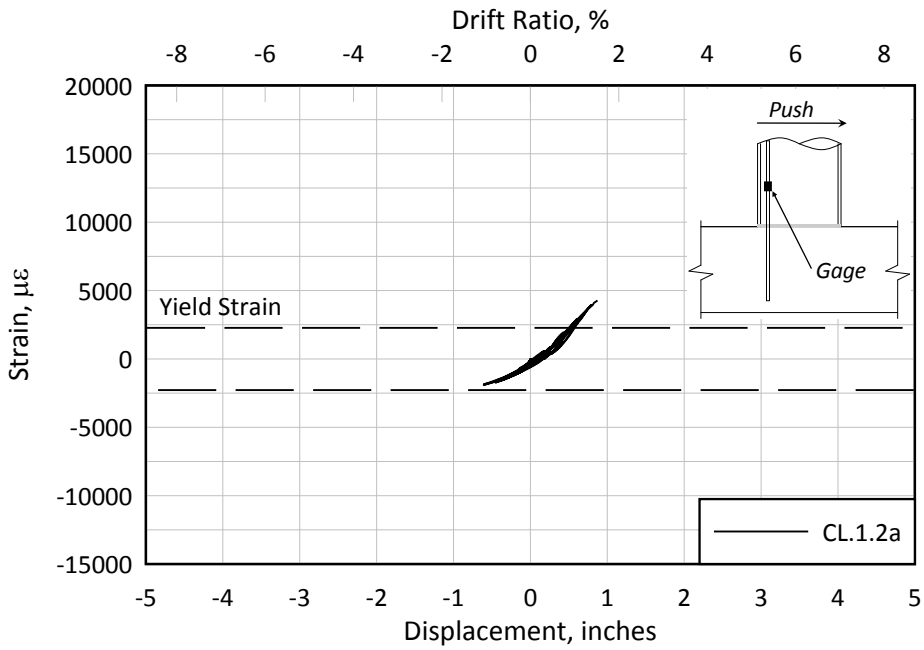

Figure 5.76 HYB-2 column longitudinal rebar strain (CL.1.2)

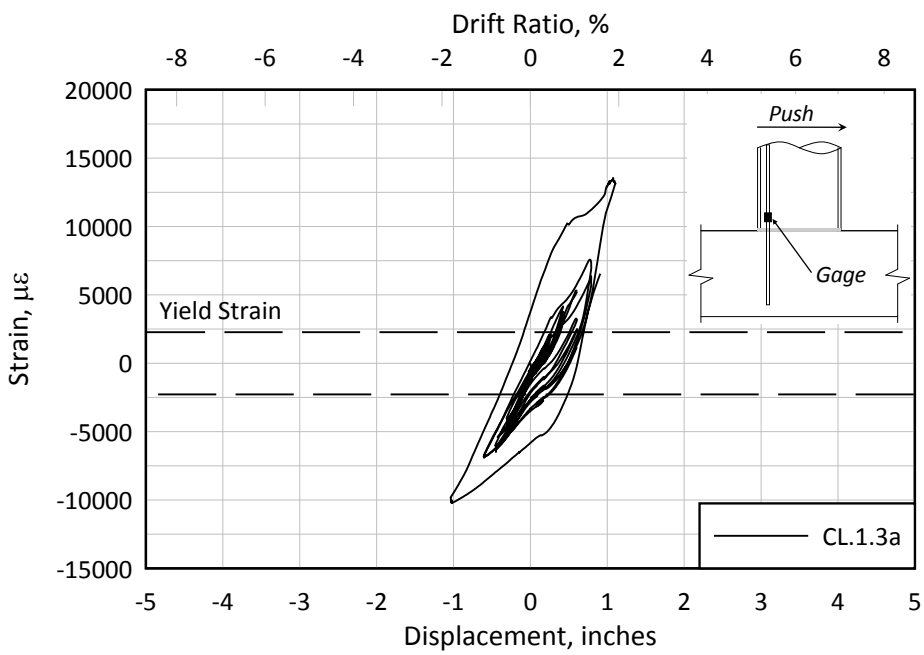

Figure 5.77 HYB-2 column longitudinal rebar strain (CL.1.3)

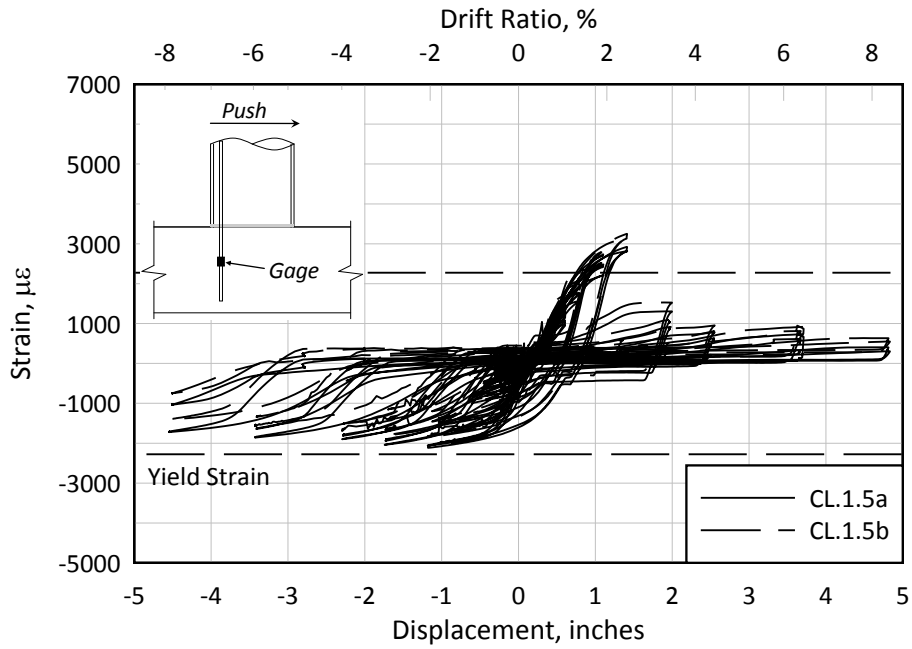

Figure 5.78 HYB-2 column longitudinal rebar strain (CL.1.5)

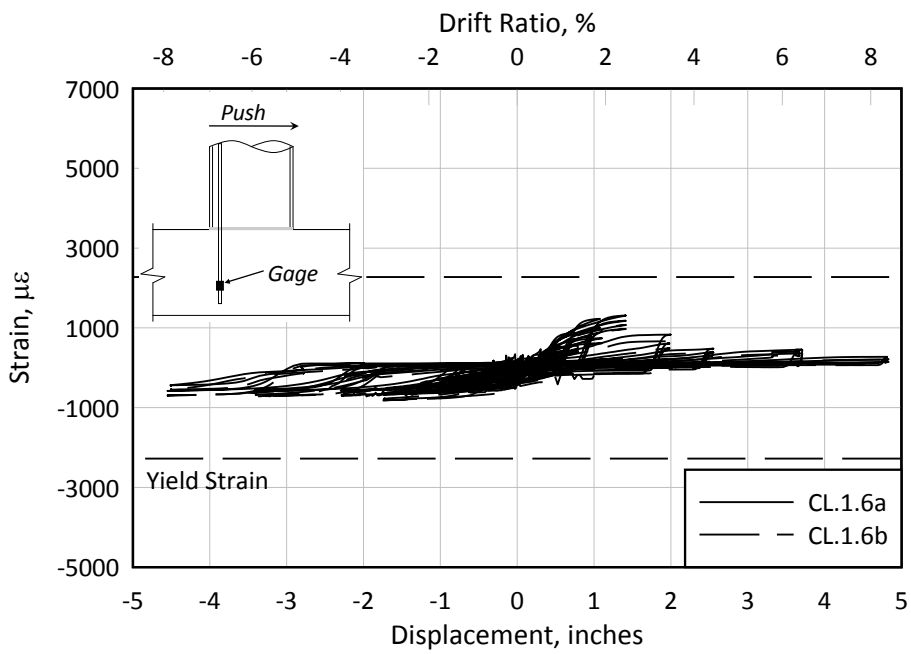

Figure 5.79 HYB-2 column longitudinal rebar strain (CL.1.6)

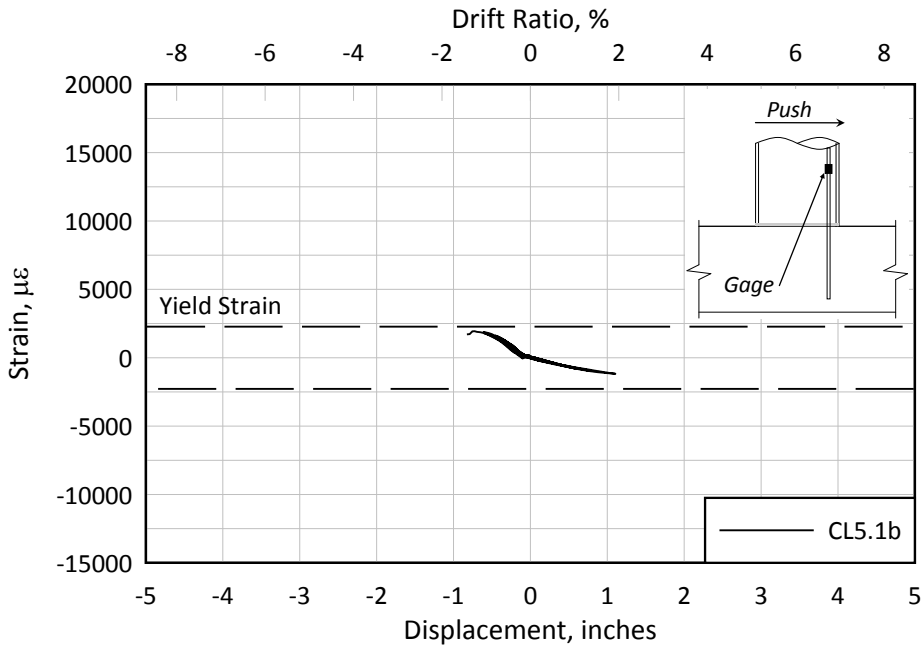

Figure 5.80 HYB-2 column longitudinal rebar strain (CL.5.1)

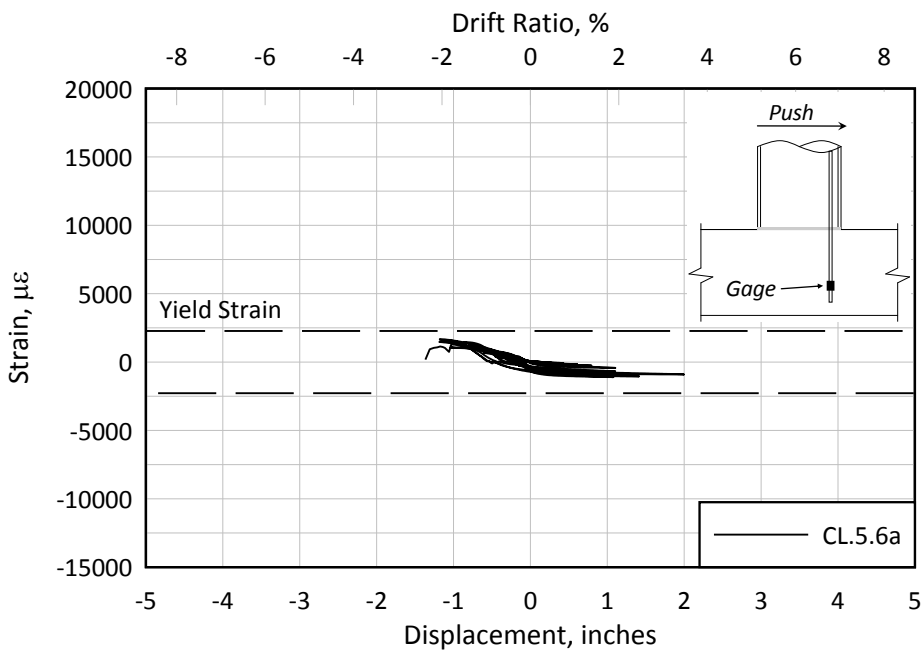

Figure 5.81 HYB-2 column longitudinal rebar strain (CL.5.6)

Post-Tensioning

Strain gage histories for individual post-tensioning strands are provided in Figure 5.82. Strain readings show an approximately linear increase with increasing drifts. The push cycle strain readings are slightly larger than those for the pull cycles. At a push drift level of approximately 7%, one of the strands appears to have surpassed the yield strain while another reaches this strain at approximately 8%. These strain readings have a continual reduction in value at the zero drift state indicating a loss of post-tensioning during the progression of the test. However, this reduction in post-tension is not attributable to yielding of the strands based on observed readings. The reduction in post-tensioning strains over the entirety of the test is expected to result in a reduction in effective post-tensioning force of about 10% GUTS.

Additionally, the effective zero drift point appears to shift under drift levels greater than 6%. This is observed in the post-tensioning strain histories through a shift in the low point of the strain history towards the pull direction. The maximum shift is approximately 0.5 inches following two cycles to 8% drift ratio levels. Under typical drift levels associated with design level seismic actions, not noticeable shift was observed.

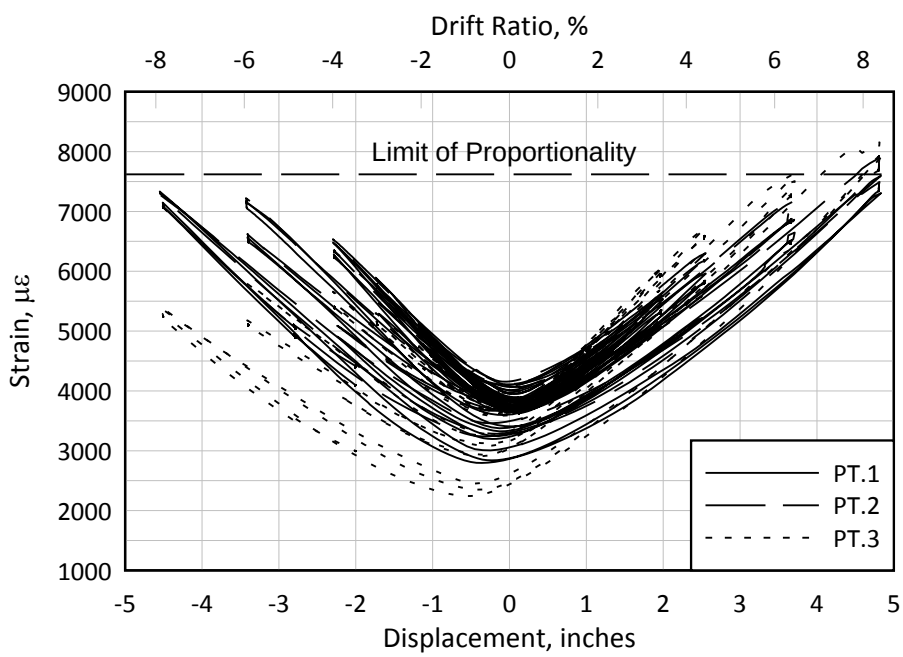

Figure 5.82 HYB-2 post-tensioning strain

Column Confinement (horizontal rosettes on north and south)

Strain gage histories from the horizontal rosette strain gages were used to determine the confinement strains in the shell. These strains will develop due to the dilatational response of the confined core as it attempts to expand under axial strains. The recorded strains are well below the yield strain of the steel shell and indicate an increasing lateral strain with increasing drift up to a drift ratio of 2%. After this displacement level, there is a noticeable reduction in the imposed lateral strain. Tensile strains are recorded for both the push and pull directions. The tensile strain when the corresponding side of the column is in compression relates to the dilation of the column. However, when the corresponding side of the column is in tension, the strains recorded in the column are due to the column reinforcing bar development mechanism that also causes tensile strains in the column shell.

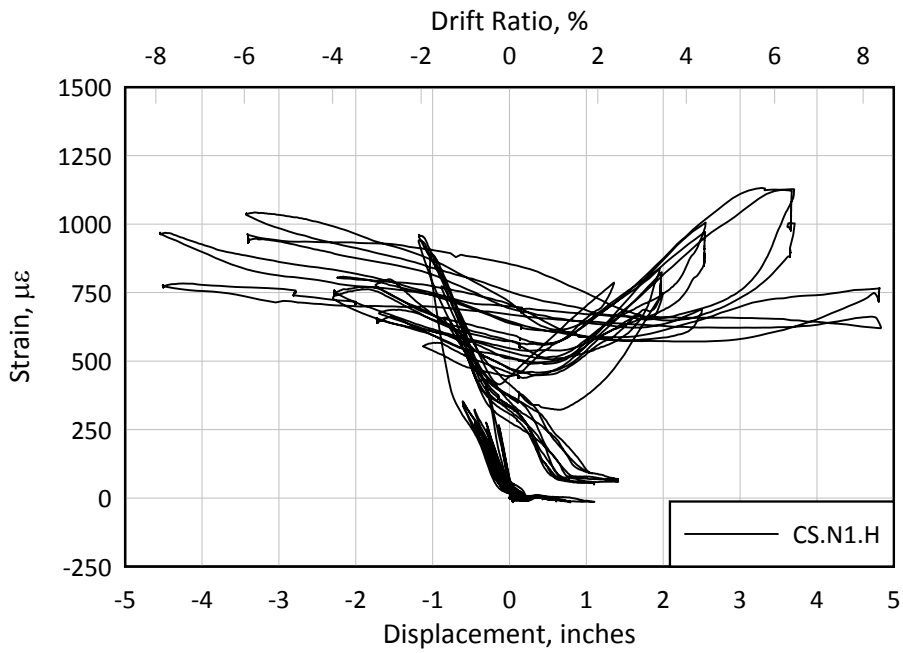

Figure 5.83 HYB-2 column confinement strain (CS.N1.H)

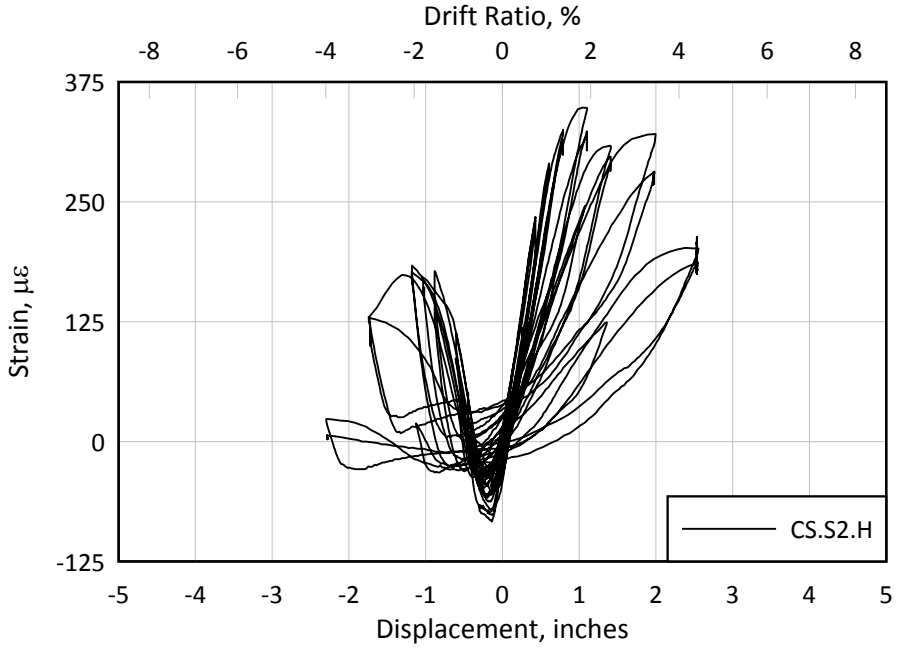

Figure 5.84 HYB-2 column confinement strain (CS.S2.H)

Column Shear (horizontal rosettes on east and west)

Strain gage readings from column shear reinforcement are provided in Figure 5.85 through Figure 5.88. These results indicate a general increase in the shear strain readings with increasing lateral displacement. However, there is a general trend of a reduction in the slope of the strain measurements with increasing displacements. This is expected due to the observed reduction in lateral capacity and therefore an associated reduction in the lateral shear demand. These strain levels are well below yield strain for the shell material.

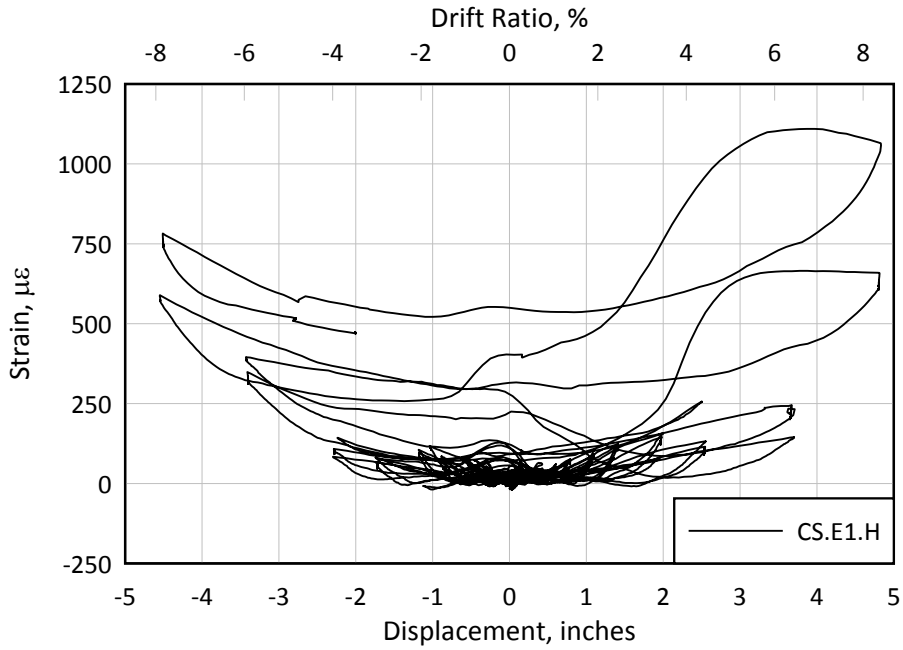

Figure 5.85 HYB-2 column shear (CS.E1.H)

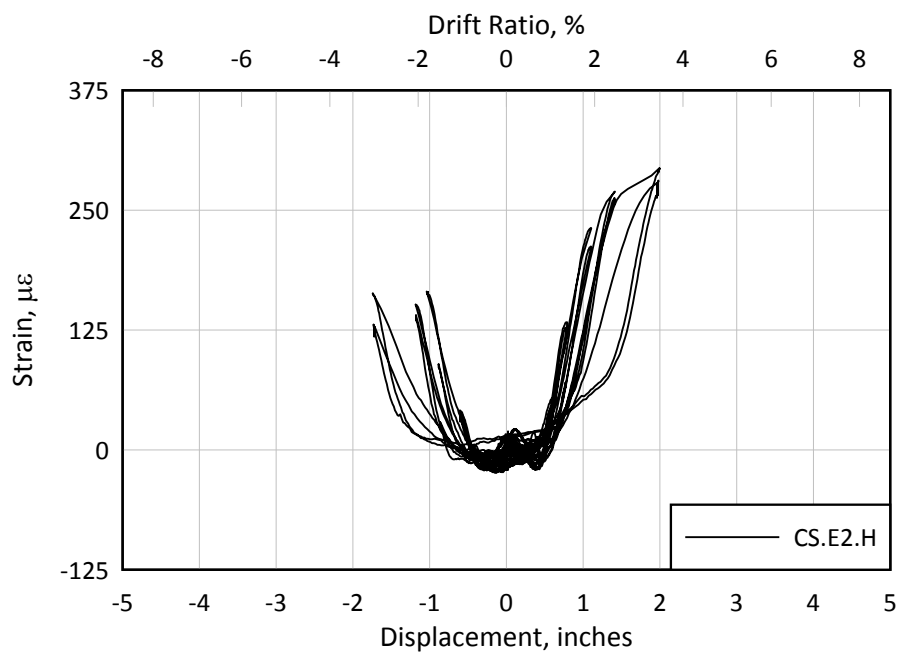

Figure 5.86 HYB-2 column shear (CS.E2.H)

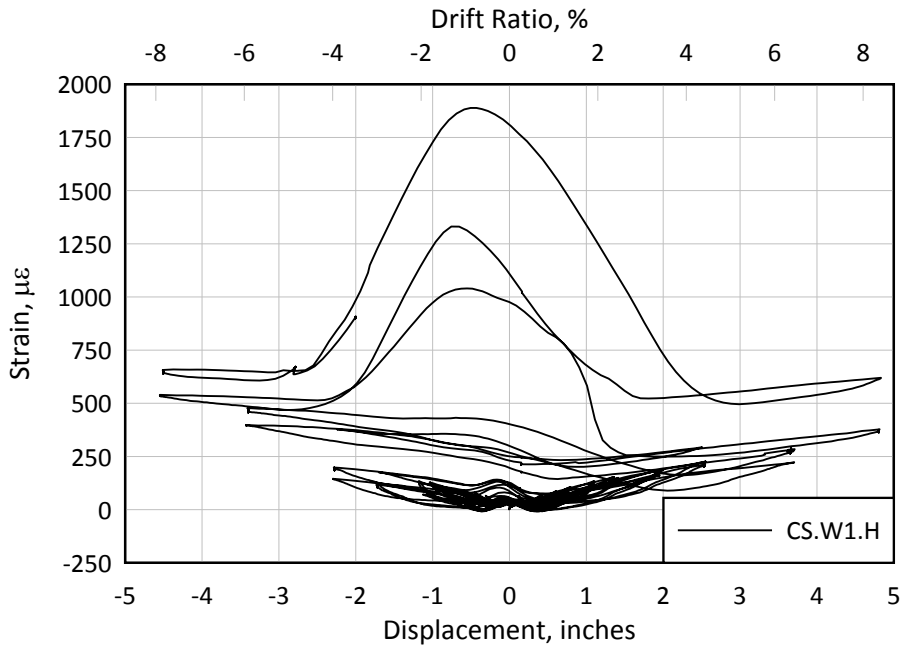

Figure 5.87 HYB-2 column shear (CS.W1.H)

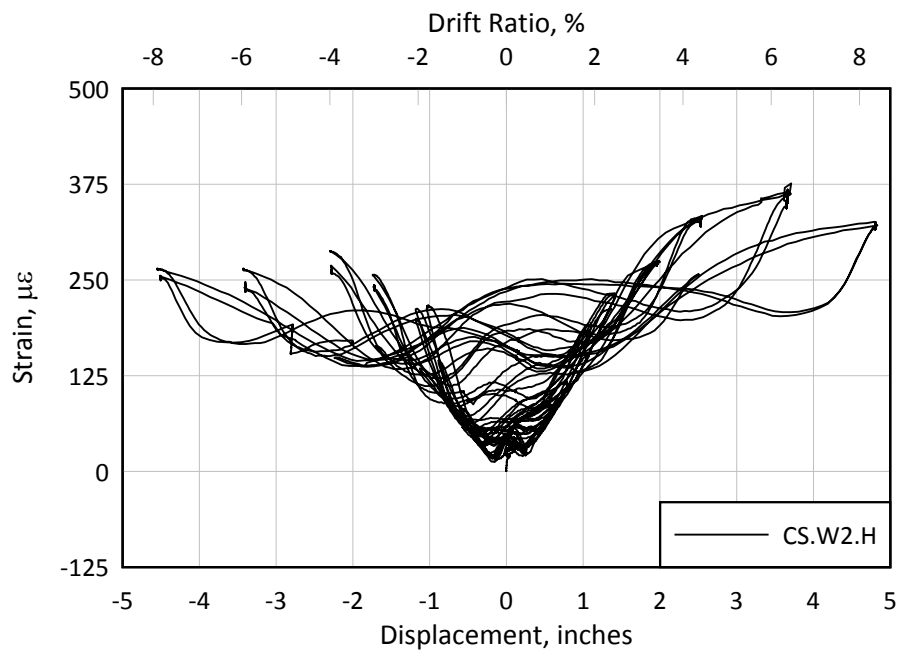

Figure 5.88 HYB-2 column shear (CS.W2.H)

Column Shell Axial (vertical rosettes)

Axial strain readings from vertical rosette gages are provided in Figure 5.89 through Figure 5.91 for the north and south gages. Results from the first gage on the south side of the column are shown in Figure 5.90. These results show a linear increasing contribution of the steel shell up to approximately 1% drift ratio. After this drift level, the results are rather sporadic and do not follow any obvious trends for this strain gage. The results at lower level displacements indicate that the steel shell is taking compression and increasing with lateral drift. However, the change in observed trending at approximately 1% drift does not allow for solid conclusions regarding the contribution of the steel shell in compression at the base.

At a lateral drift of 1% drift ratio, the steel shell appears to have approximately 350 microstrain of compression. This correlates to a stress in the shell of approximately 12 ksi, which is an appreciable load and is approximately 20% of the yield stress of the shell. Extrapolating this to 3% drift ratio levels, assuming the degradation and loss in lateral capacity did not occur, this would correspond to a stress in the shell of approximately 36 ksi. These results indicate that when the grout material below the shell is intact, the shell takes a significant amount of compression loading.

The second level of axial gages on the shell indicate that the shell resists both tensile and compression loadings. This is expected, as the shell should begin to act composite with the concrete core as the distance from the joint increases. Tensile loading is expected as the column reinforcing bars are expected to develop inside of the column due to the provided weld beads on the inside face of the column.

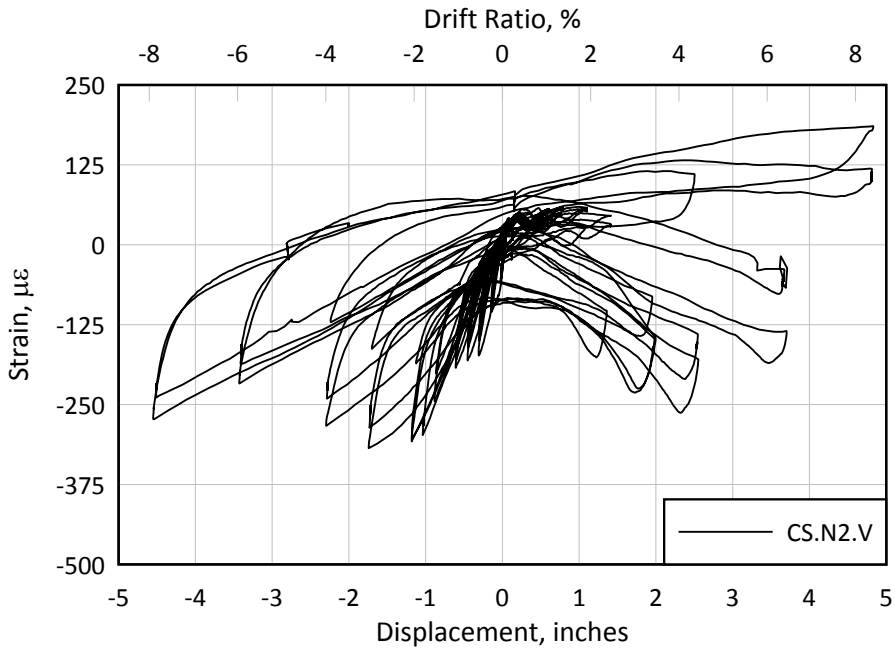

Figure 5.89 HYB-2 column shell axial (CS.N2.V)

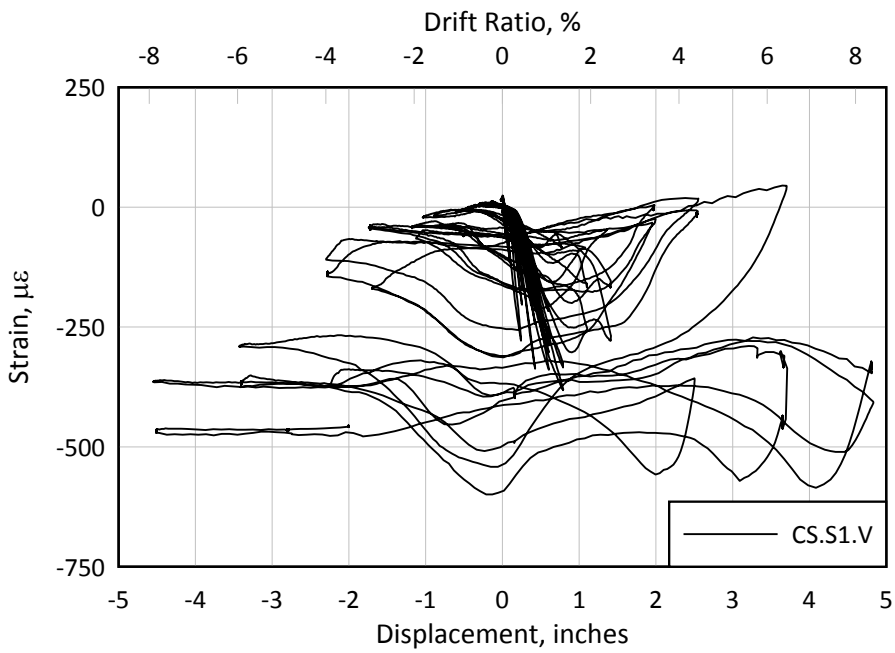

Figure 5.90 HYB-2 column shell axial (CS.S1.V)

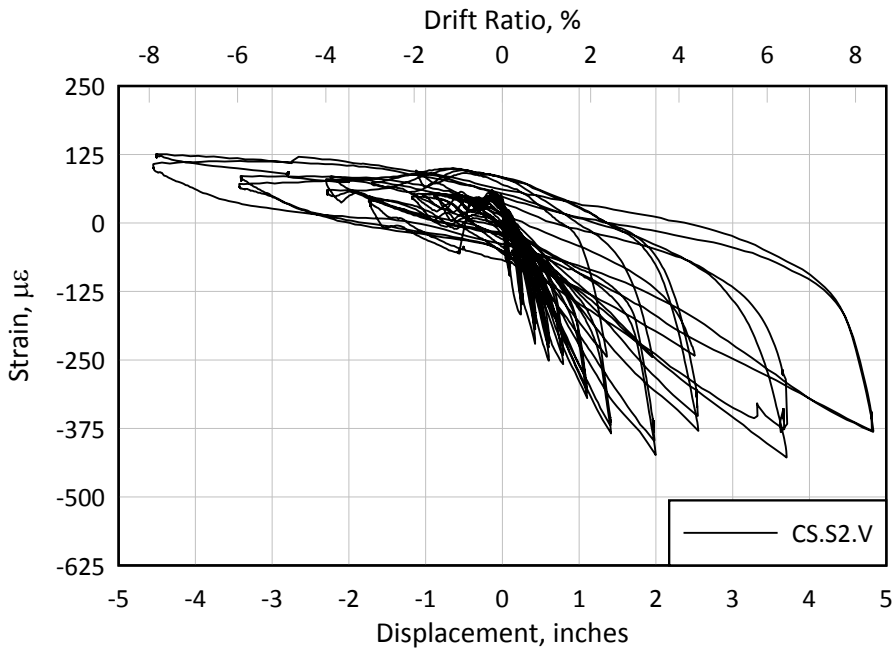

Figure 5.91 HYB-2 column shell axial (CS.S2.V)

Bent Cap Joint

Strain gage histories for the bent cap joint shear reinforcement are provided in Figure 5.92 thru Figure 5.95. All strain readings are well below the yield strain of the spiral with the largest strains observed in the fifth turn of the spiral on both east and west sides. The low-level strains observed are in agreement with the minimal noted joint distress during seismic testing.

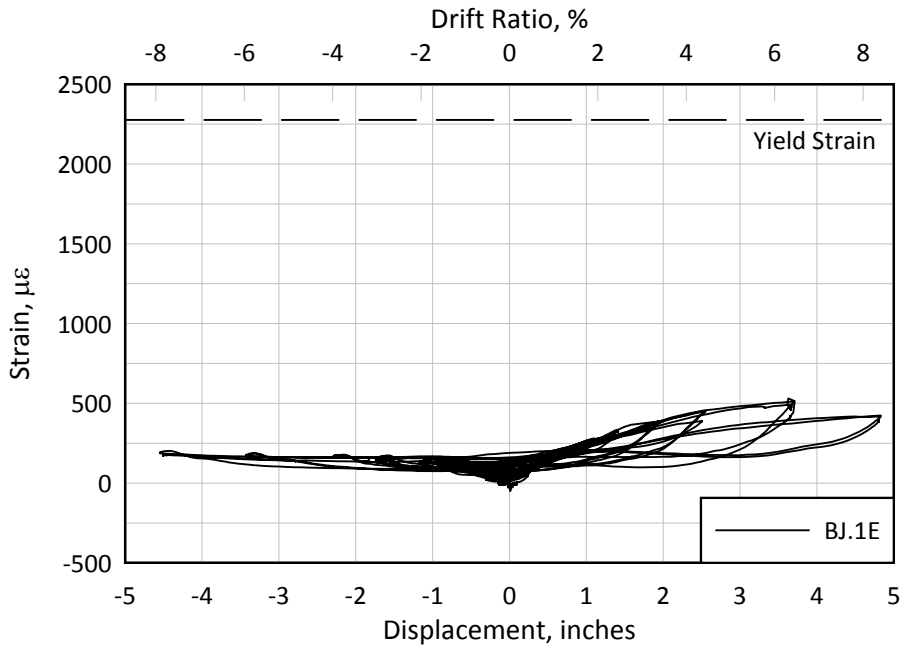

Figure 5.92 HYB-2 bent cap joint shear rebar strain (BJ.1E)

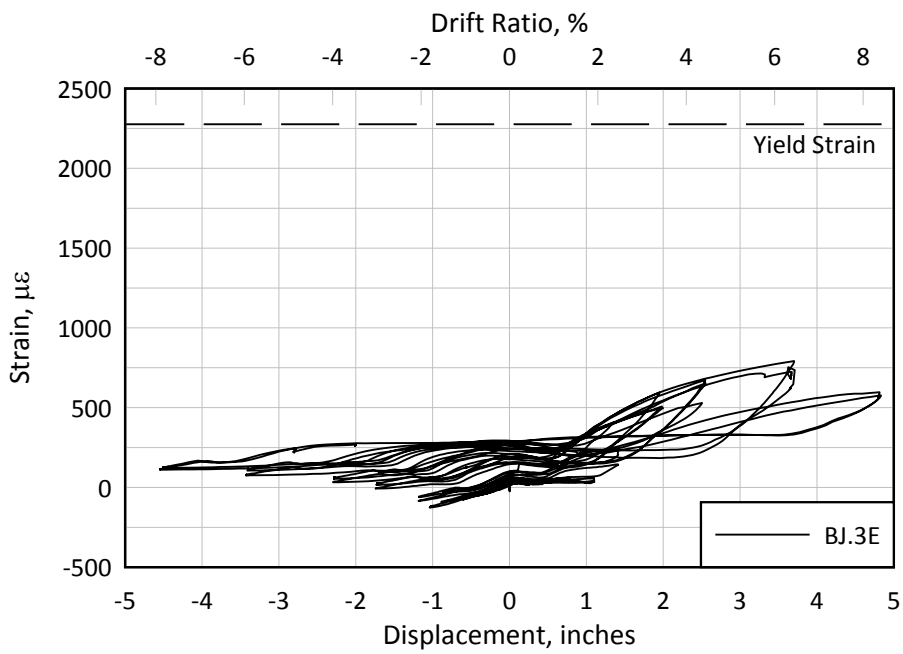

Figure 5.93 HYB-2 bent cap joint shear rebar strain (BJ.3E)

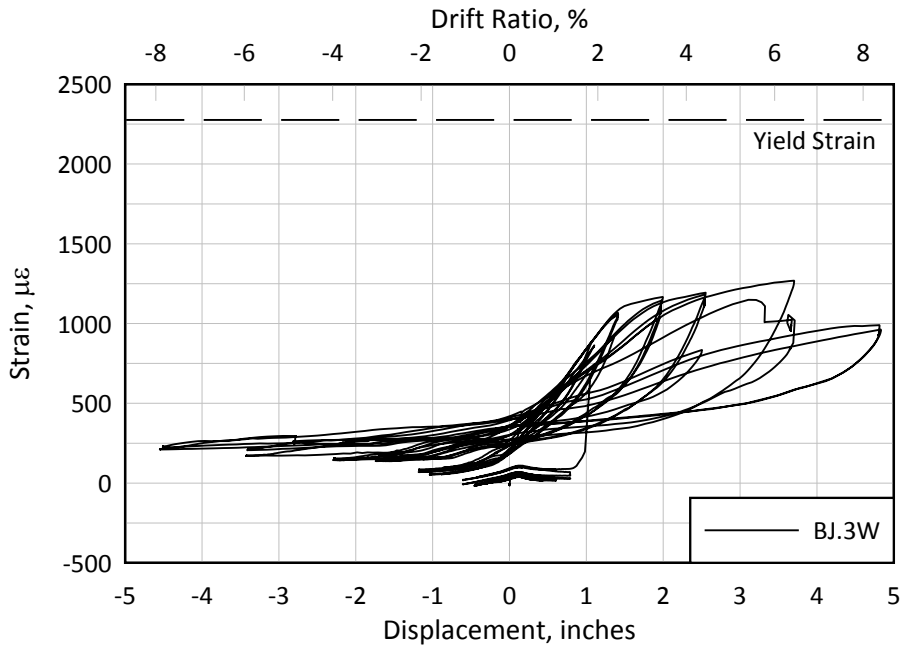

Figure 5.94 HYB-2 bent cap joint shear rebar strain (BJ.3W)

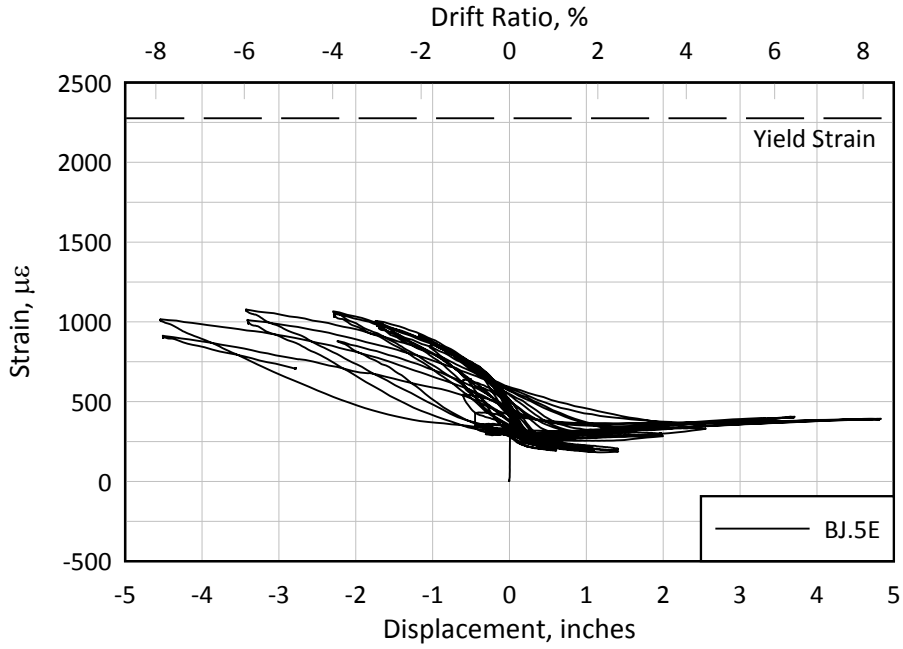

Figure 5.95 HYB-2 bent cap joint shear rebar strain (BJ.5E)

5.5.5 Strain Profiles

Strain gage readings at peak responses in both push and pull directions were used to generate strain profiles for various elements. These profiles were generated for peak points in the loading cycles for the first cycles in both push and pull directions.

Column Longitudinal

Strain gage profiles for the extreme northern column longitudinal bars are provided in Figure 5.96. Gages located in the column and the first gage in the duct were damaged and therefore meaningful data is provided only up to a 1.5% drift ratio level. Based on observed readings, the largest strain at any point occurs at the column to bent cap joint as expected. These strain readings are far in excess of the yield strain for the reinforcing bar. Additionally, it is noted that observed strain levels in the bar are less than or approximately equal to yield strain up to 6% drift ratio at 9 inches into the bent cap. This indicates the bar is fully developed in the duct within the worst case 16 bar diameters. The requirements specified in ACI ITG-5.2-09 of a development length of 25 times the bar diameter is reasonable based on these results (ACI 2009).

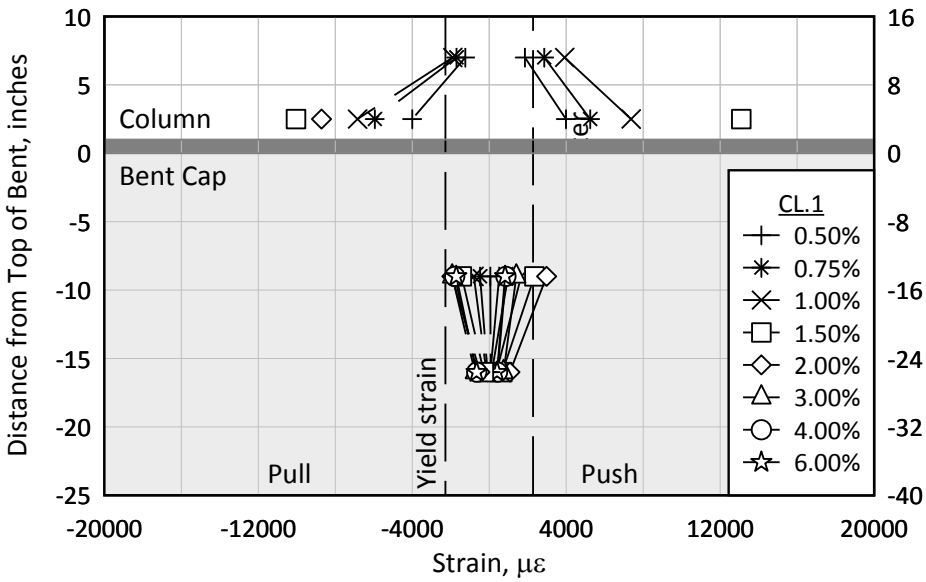

Figure 5.96 HYB-2 column longitudinal rebar strain profile (CL.1-north bar)

Bent Cap Longitudinal

Strain profiles for the bent cap longitudinal reinforcement are provided in Figure 5.97 and Figure 5.98. Readings from these gages indicate that the bent cap longitudinal bar strains are well below

yield for all drift cycles. This indicates that the assumed force transfer mechanism is sufficient and conservative for the system tested. Additionally, this verifies the assumption that the bent cap remains essentially elastic under the imposed simulated seismic demands.

Similar to the first hybrid specimen, the results show a relatively flat strain profile across the joint region during both push and pull cycles (refer to BL.16 profile). These results indicate that the bent cap longitudinal reinforcement does not develop in the joint but maintains constant force across the majority of the joint and is consistent with the assumed force-transfer mechanism.

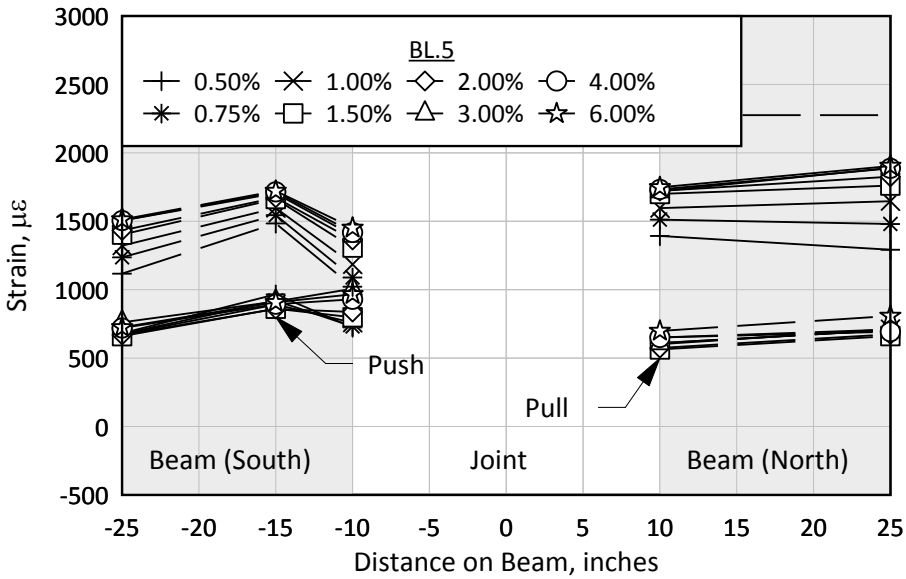

Figure 5.97 HYB-2 bent cap longitudinal rebar strain profile (BL.5)

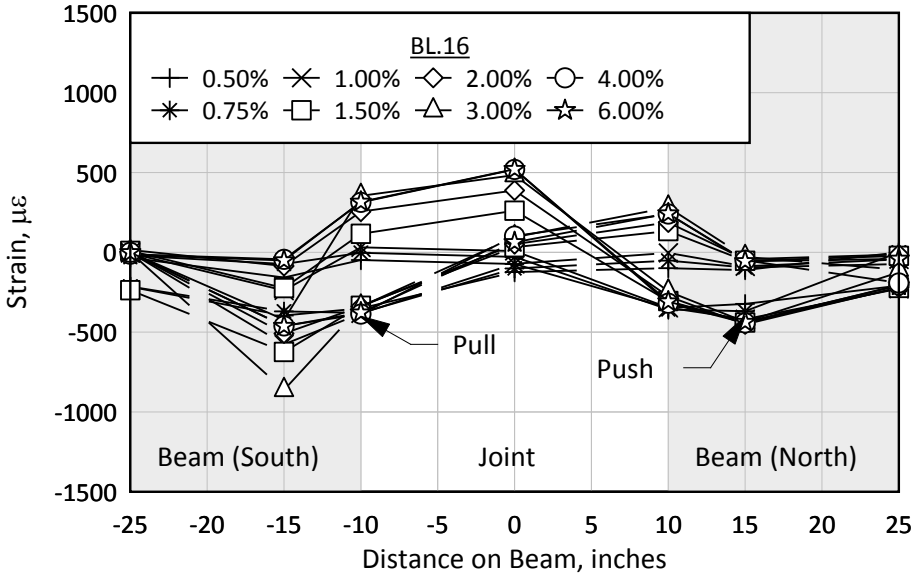

Figure 5.98 HYB-2 bent cap longitudinal rebar strain profile (BL.16)

Joint Shear

Strain profiles for east joint shear reinforcement are shown in Figure 5.99. The western strain gages did not survive to develop appropriate strain profile plots. Results from these readings indicate that the strains in the joint shear reinforcement are far below yield with the largest strains occurring in the lowest strain gage.

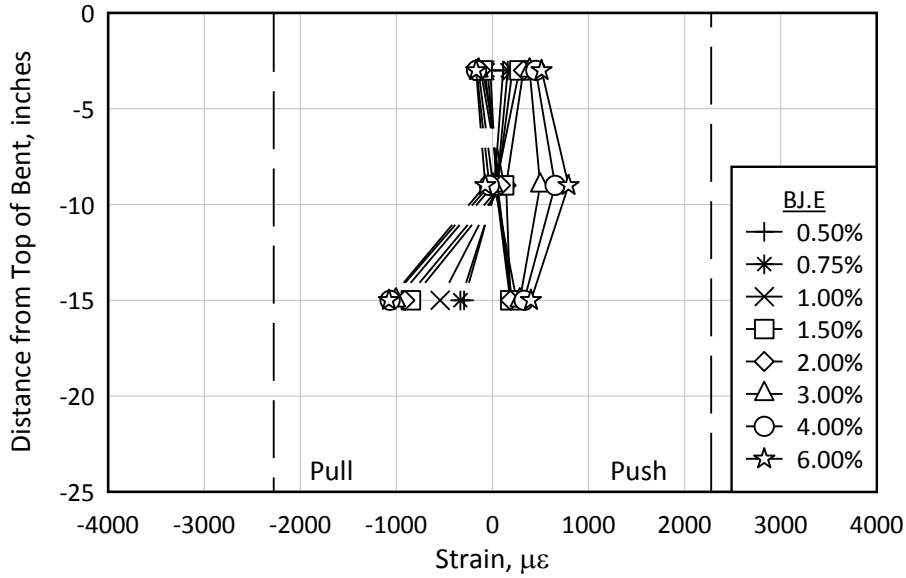

Figure 5.99 HYB-2 bent cap joint shear strain profile (BJ-east gages)

5.6 Summary of Specimen Response

The concrete filled pipe hybrid specimen was designed to have similar force-displacement response as compared to the conventional hybrid specimen. The intent of this system design was to have similar response in terms of lateral capacity and cyclic behavior. Unlike the conventional hybrid unit, this specimen was detailed using a full height steel shell which is intended to provide confinement, shear reinforcement and, within the main portion of the column, flexural reinforcement. The use of a steel shell is intended to enhance the confinement properties of the unit and provide for more simple fabrication. The hybrid specimen was designed, analyzed, constructed and tested to validate the assumptions and response of this system.

Fabrication of this unit took place at an industry facility by experienced precast concrete personnel without any noted complications. The precaster did mention a concern regarding the full-scale fabrication of the concrete filled steel shell column assembly. Fabrication of the unit in the vertical position is expected to result in appreciable complications due to the need to provide adequate lateral support during fabrication. Fabrication and casting of the unit in a horizontal position is expected to be a more manageable solution; however, the is a need to provide numerous access ports to allow for pouring of concrete and to expel air voids from the unit. Erection of the unit took place at the university laboratory without any major complications.

Setting of the unit into the test setup was slightly cumbersome due to a minor misalignment of one of the PVC support pipes that resulted in a slight angle to the pipe when setting in place.

During testing, no noticeable damage was observed in the column except for localized to the grout bedding layer. At the bedding layer, the localized compression strains resulted in the accumulation of damage to the grout and in turn, a loss of grout material under continued cycling. This resulted in a reduction in the effective column diameter, which in turn resulted in a loss of lateral capacity of the system. Damage to the precast bent cap was not overly significant and was of the same order of magnitude as the conventional hybrid specimen. The majority of bent cap observed damaged consisted of minor joint shear distress and flexural cracking of the member. Similar to the conventional hybrid specimen, the damage observed in the bent cap was less than that noted in the cast-in-place control specimen, which is attributable to the inclusion of post-tensioning which reduces the primary tensile stresses in the joint.

Force-displacement results for the specimen indicate a loss in lateral force capacity following drift cycles to approximately 2.0% drift ratio. This reduction in capacity is caused by the accumulation of damage in the grout bedding layer which resulted in a reduction in the effective column diameter. Additionally, the reduction in grout area resulted in a reduction in the grout bedding layer thickness and an associated loss of post-tensioning force. Ultimate failure of the system is attributable to the fracture of a column reinforcing bar at the second cycle to approximately 6.0% drift ratio. The fracture of this first reinforcing bar occurred after apparent buckling of the bar based on photographic evidence. However, in accordance with conventional practice, the failure of the system is typically defined as the point where the lateral capacity falls below 80% of the maximum lateral force resisted by the system. In this case, the system would be said to fail at approximately a 5% drift ratio.

Instrumentation readings from the test were post-processed and reviewed to provide additional insight into the response of the unit. As mentioned before, there was a noticeable reduction in the recorded force-displacement response of the system following drift cycles to approximately 2.0% drift ratio. Appreciable energy dissipation was noted and of increasing magnitude with increasing drift. Residuals drift ratios were significantly less than the cast-in-place control specimen for all displacement levels. Based on recorded displacement measurements, the concrete filled pipe specimen can undergo drifts up to slightly less than 4.0% drift ratio while maintaining a residual drift less than one degree. In comparison, the cast-in-place control specimen could undergo only displacements to approximately 2.75% drift ratio while meeting the same criteria.

The predicted force displacement response of the system provided a reasonable estimate of system response up to approximately 1.75% drift ratio. After this drift level, the predicted response was expected to continue to increase in lateral capacity whereas the recorded test results indicated a steady reduction in capacity past this drift level. The reduction in capacity and subsequent inadequate prediction are related to the deterioration of the grout bedding layer. The use of a tougher bedding material, such as fiber reinforced grout, will serve to provide enhanced resistance of the bedding layer and subsequently an enhancement in the lateral response of the system. Recently published design requirements per ACI ITG-5.2-09 require a minimum 0.1% volume fraction of fibers in the bedding layer (ACI 2009).

Experimental results indicate acceptable lateral response up to drift levels of approximately 2% drift ratio. Following this drift level, the force-displacement prediction and overall response deteriorated due to the accumulation of damage to the bedding layer. This deficiency is expected to be rectified with the use of a high quality, fiber reinforced grout, which is capable of sustaining large compressive strains while maintaining the overall joint integrity. Even with the deterioration in grout, the overall system response shows enhancements as compared to the cast-in-place control specimen in terms of self-centering capacity. Additionally, the excellent response up to approximately 2% drift ratio is a crucial result as the design level response is typically on the order of 2-3% drift ratio. This system provided adequate seismic response even with damage to the grout bedding layer and the overall response is expected to be enhanced through the use of a high quality fiber reinforced grout bedding layer.

5.6.1 Conclusions

Based on experimental observations and readings related to the response of the concrete filled pipe hybrid specimen, the following conclusions can be made:

- The concrete filled pipe hybrid specimen met the performance objectives up to the design level drift
- The system provides significant lateral displacement capacity with an ultimate displacement of 6% drift ratio
- Design assumptions and predictions match well the measured response up to 2% drift ratio
- Grout bedding layer degradation resulted in significant reduction in the system's lateral capacity

- Degradation of the grout bedding layer should be prevented through the use of fiber reinforced grout material with a minimum 0.1% fiber volume fraction
- Neutral axis depth should be limited to 25% of the column dimension at a maximum
- Amount of mild reinforcement can be reduced to enhance the self-centering ability

Chapter 6 Dual Shell Specimen

The dual shell specimen (also referred to as HYB-3) utilities a steel pipe for confinement and lateral reinforcement and an inner corrugated steel pipe to form an inner void and prevent implosion of the concrete section. The use of the outer steel pipe provides enhanced confinement while the inner pipe allows for the creation of a hollow section which can reduce the section weight. Mild rebar is used only at the joint region as in HYB-2 and terminates once in the column to facilitate easier fabrication and construction with minimal need for tying steel rebar cages. Details of this specimen and experimental results are provided in this section.

6.1 Design Details

This specimen was designed to have similar lateral response characteristics when compared to the conventional hybrid specimen and concrete filled pipe specimen. The general sectional dimensions are identical to the conventional hybrid specimen, which represents a 42% scale factor.

6.1.1 Column

The outside diameter of the steel pipe is 20 inches and the pipe is a ¼ thick pipe. The resulting confinement ratio is 5.19%. The mild reinforcement is placed at the same location as the rebar for the conventional hybrid specimen due to geometric constraints within the bent cap and for uniformity of results. In practice, it is expected that the diameter of the circle encompassing the rebar can be increased to maximize the lateral force resisting capacity of the section. The column cross-section is shown in Figure 6.1 and the vertical section is shown in Figure 6.2. The column rebar extends a distance equal to 15 inches into the steel pipe. The length of the bonded region of the rebar and the design spacing of the weld beads were selected based on a simple force transfer mechanism.

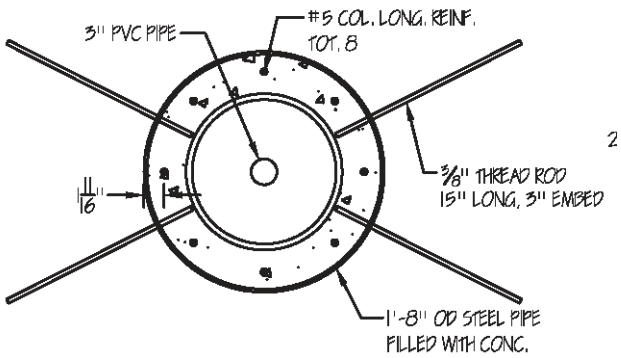

Figure 6.1 HYB-3 typical column cross-section

The primary longitudinal reinforcement at the joint region consists of a combination of unbonded post-tensioning and bonded rebar. There are 5-0.6 inch diameter post-tensioning strands making up the single tendon that runs down the center of the column. There are 8-No. 5 316LN stainless steel rebars located at the column end spaced equally around the column section, providing a reinforcement ratio of 0.79%. At a distance equal to approximately 15 inches from the face of the bent cap, the column rebar is terminated. Three weld beads were detailed on the steel shell within this region to transfer the tensile force in the rebar into the surrounding steel shell. For the remainder of the column, the column primary longitudinal reinforcement consists of a combination of unbonded post-tensioning and the confining steel shell.

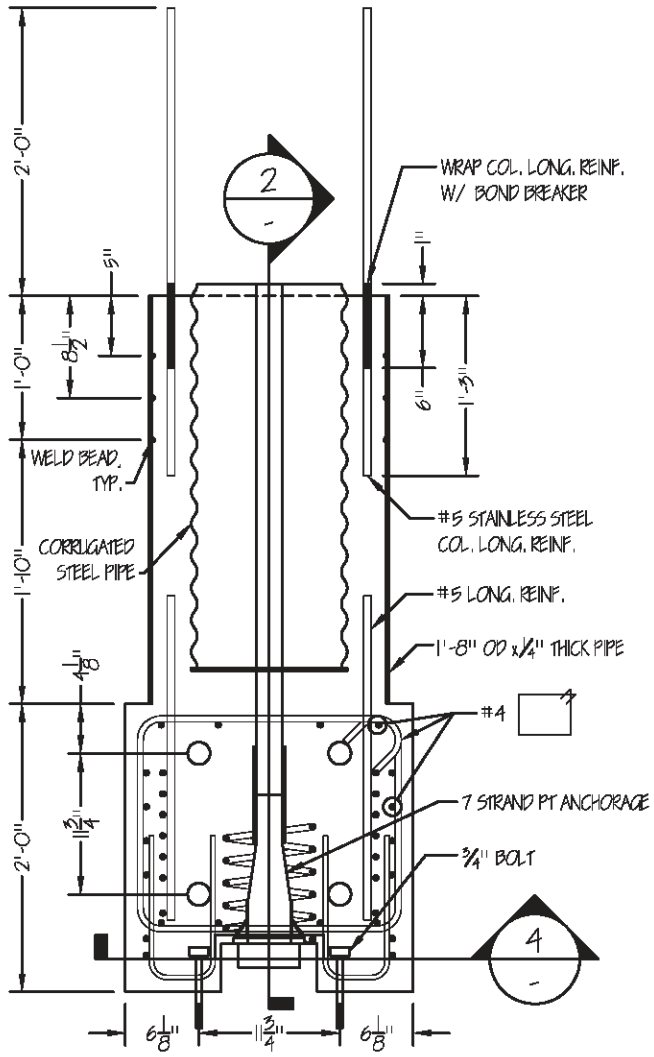

Figure 6.2 HYB-3 column vertical section

The post-tensioning tendon is set inside of a PVC pipe. Although there is a void made by the corrugated pipe, the PVC is still used to provide a guide for placement of the post-tensioning tendon and to provide a means for corrosion protection. In practice, it is recommended that a high-density polyethylene (HDPE) pipe be used to provide a means to set the tendon. Following placement and stressing of the tendon, the duct should be grouted to provide corrosion protection. The smooth HDPE pipe will not provide significant bond and is expected to debond during seismic actions such that the tendon acts as if completed debonded over the length.

6.1.2 Bent Cap

Details for the bent cap member are provided in Figure 6.3 and Figure 6.4. The bent cap cross-section is a square with a dimension of 25 inches. The detailing and design of this section is

identical to that specified for both the conventional hybrid specimen and the concrete filled pipe specimen.

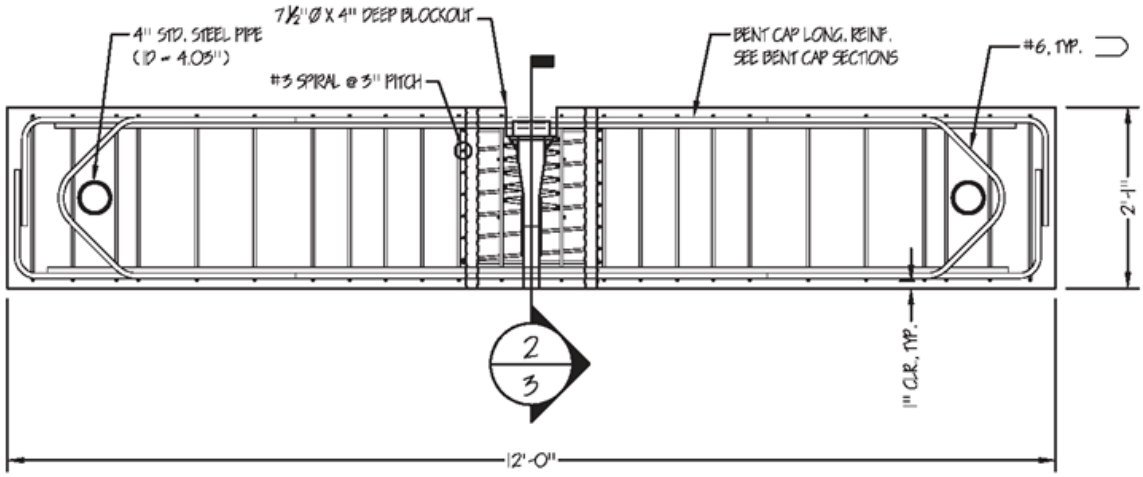

Figure 6.3 HYB-3 bent cap longitudinal section

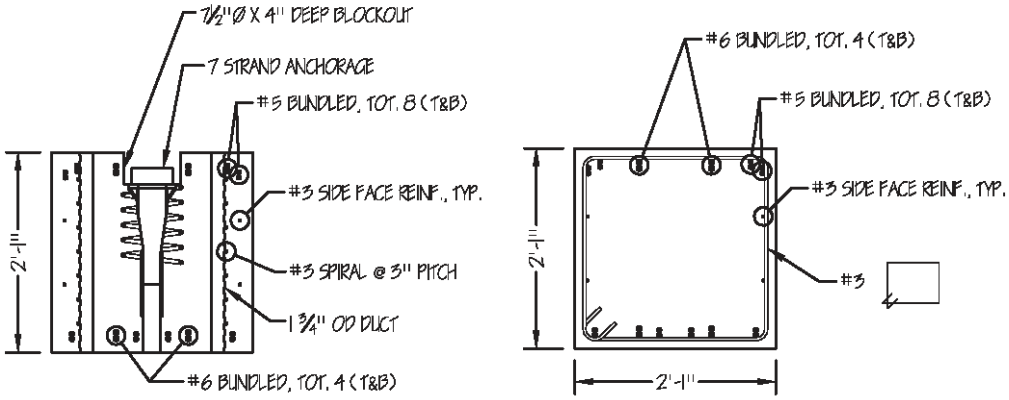

Figure 6.4 HYB-3 bent cap section a) at anchorage b) outside anchorage

6.1.3 Instrumentation

This test specimen was instrumented to capture the major response characteristics of the specimen when subjected to lateral loading. This instrumentation includes strain gages mounted on rebars and external gages mounted on the specimen.

Strain gages were placed on column and bent cap reinforcement to capture the distribution of forces and deformations inside the specimen and the spread of plastic actions. The locations of these gages are shown in Figure 6.5. A summary of the strain gage categories based on callouts is provided below:

- CL series Column longitudinal reinforcement strains
- CS series Steel shell strains (strain gage rosettes)
- IP series Inner corrugated steel shell strains (strain gage rosettes)
- BL series Bent cap longitudinal reinforcement strains
- BJ series Bent cap joint shear reinforcement strains

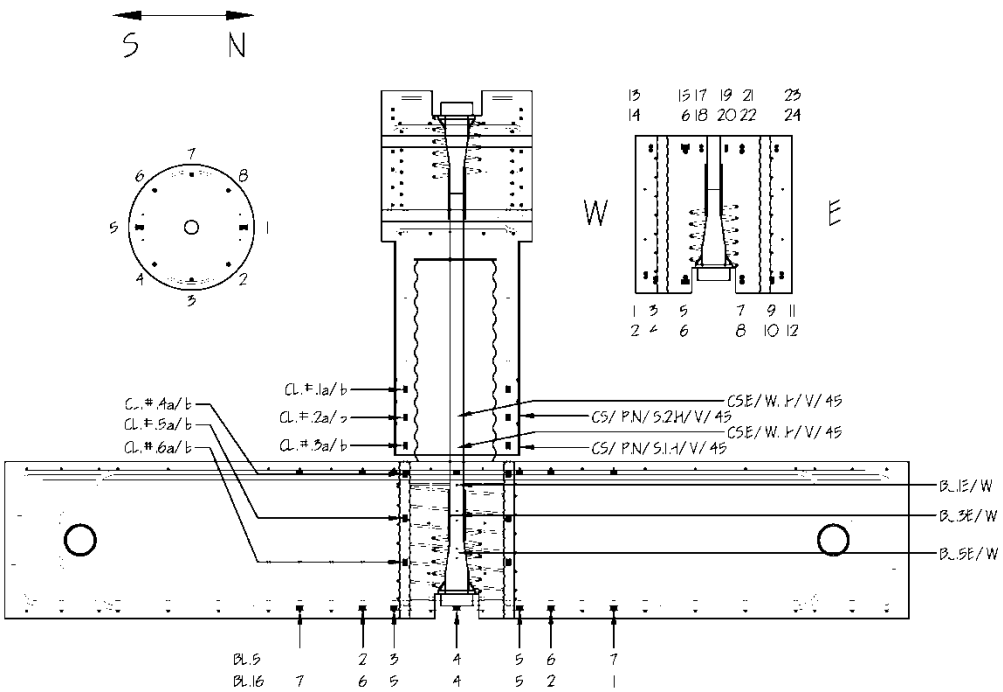

Figure 6.5 HYB-3 strain gage layout

External instrumentation consists of linear potentiometers and inclinometers mounted on the exterior of the specimen. A summary of external instrumentation is shown in Figure 6.6. Linear potentiometers are placed to capture column displacements, column curvature, base rotation, bent cap joint deformations, column bar slip, bent cap rotation and rigid body movements. An inclinometer was placed on the load stub to record the rotation of the load stub at the actuator location.

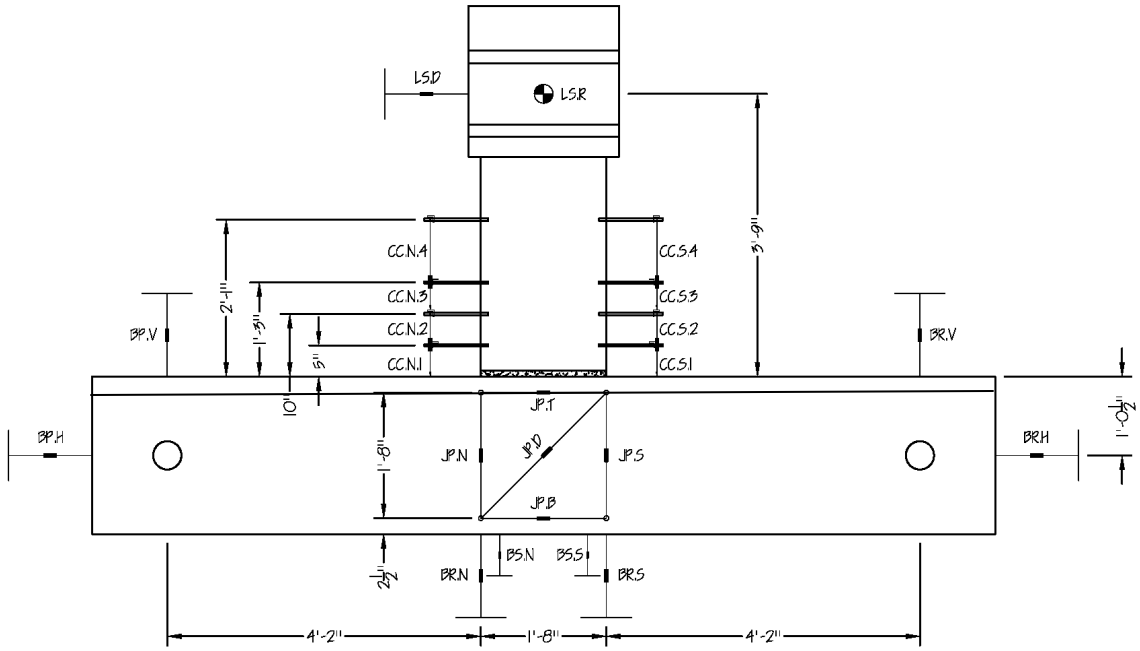

Figure 6.6 HYB-3 external instrumentation layout

In addition to active measurements provided by strain gage and external instrumentation, specimen response was documented through digital photos, crack markings, video recordings and notations.

6.2 Fabrication and Assembly

This section describes the process of section fabrication and assembly.

6.2.1 Precast Component Fabrication

This specimen was fabricated at Pomeroy Corporation located in Perris, CA at the same time as HYB-2. The reinforcing bars that were instrumented were shipped to UCSD for installation of the strain gages and then transported to Perris for fabrication. All fabrication activities at the precast yard were closely monitored by a representative from UCSD to ensure all tolerances were achieved and to acquire feedback from the precaster relating to the ease of fabrication. The column rebars were tied and set inside the dual shell assembly using support from a vertical frame.

A top down view of the inner shell and outer shell prior to placement of column reinforcing is shown in Figure 6.7. The inner shell was kept in alignment using the column curvature gages, which were set to contact the inner shell when tightened. The external shell was maintained at the

correct elevation using the two reinforcing bars that were tack welded along the shear side (to not impose excess stresses on the region subjected to large compressive strains).

Figure 6.7 HYB-3 view of dual steel shell prior to installation of rebar and casting

The column reinforcing cage was set in place using a temporary support system as shown in Figure 6.8. The embedment of the column rebars was maintained using a support assembly, which was attached to the column form bracing system. A view of the reinforcing bar placed in the column is shown in Figure 6.9. In this figure, the steel beads that are used to aide in the development of the reinforcing bar are also noticeable. The debond wrap can be observed in this photo which was used to allow for the distributed straining of the bar to reduce any localized tensile strains in the reinforcing bars under lateral displacements.

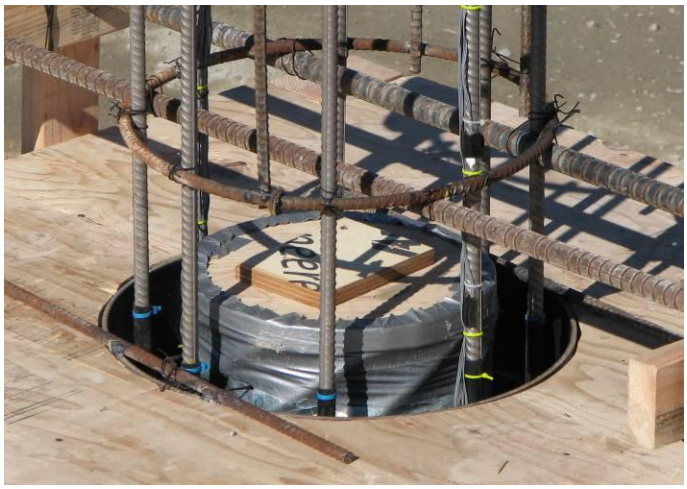

Figure 6.8 HYB-3 column with reinforcing installed prior to casting

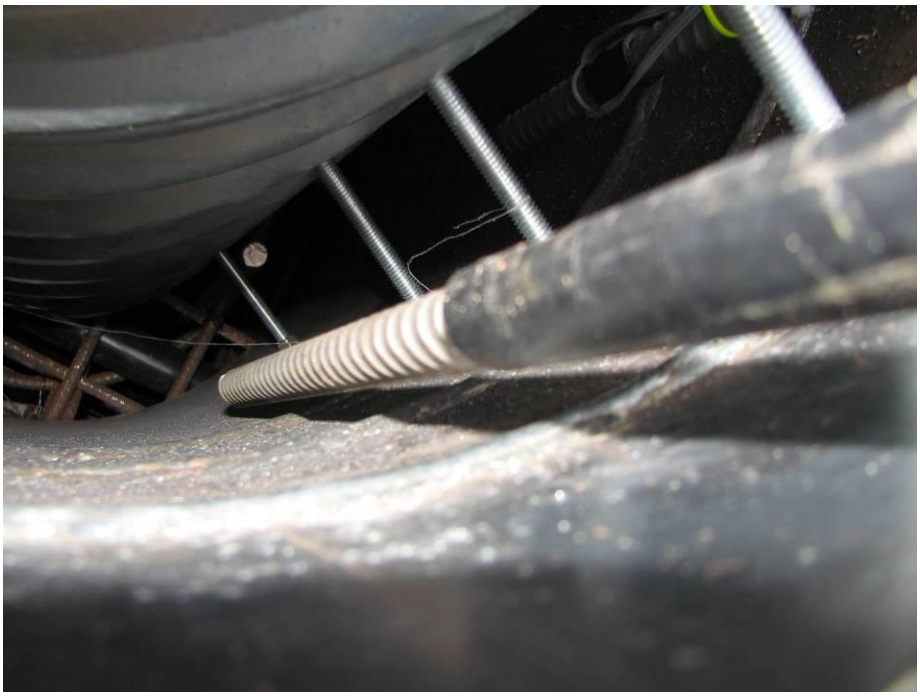

Figure 6.9 HYB-3 close up view of column reinforcing and weld beads

The casting of the column is depicted in Figure 6.10. As is apparent from this photo, a complexity in casting this unit is the small opening at the top of the column and the subsequent interference of the column longitudinal reinforcement.

Figure 6.10 HYB-3 casting of column

The precast bent cap following pouring and finishing of the concrete is shown in Figure 6.11. The column and bent cap were cast at the same time with the same batch of concrete. The concrete design consisted of a nominal 3/8” maximum aggregate size mix with a design slump of 9 inches. Unlike traditional bridge members, this specimen was not steam cured thus additional cure time was required to achieve appropriate strength prior to removing the forms. Once the concrete achieved a minimum break strength of 3 ksi, the forms were removed and the members were finished. The members were then shipped to the UCSD campus.

Figure 6.11 HYB-3 bent cap following casting

6.2.2 Fabricator Feedback

Like the previous two specimens, the precast fabricator found the fabrication of the precast concrete bent cap to be manageable and practical. However, the dual shell column system with the scaling of this size was noted to cause complexities in casting. The main reason the fabricator noted this was the relatively limited opening in the top of the column for casting of the concrete. For a full-scale concrete column, this problem is expected to be less noticeable due to the increase in overall column dimension. However, like the previous two units the precaster noted that the fabrication of a realistic size precast column in the horizontal direction would be complicated due to the need to substantial lateral bracing.

Fabrication of the dual shell column in a horizontal condition is expected to be more complex as compared to the concrete filled pipe hybrid detail. The main reason for this added complexity is the need to properly secure the inner corrugated steel pipe to prevent floating during casting. This

can be accomplished using bracing legs welded to the inner pipe around the diameter and along the length to provide proper setoff from the exterior column. Similar to the concrete filled pipe specimen, access ports will also be required for this unit to allow for pouring of concrete and purging of entrapped air.

6.2.3 Specimen Assembly

The precast bent cap and column were shipped to UCSD for erection. The bent caps for HYB-2 and HYB-3 are shown in Figure 6.12 and the column for HYB-3 is shown in Figure 6.13. The surface of the column top was smooth when delivered to UCSD and was roughened to provide proper bond to the grout bedding layer. The column was set on two concrete blocks to allow for access to the load stub ("dead end") post-tensioning anchorage and then leveled. A temporary support structure was constructed for the bent cap using traditional scaffolding and dunnage.

Figure 6.12 HYB-3 bent cap as delivered to UCSD

Figure 6.13 HYB-3 view of top of column as delivered to UCSD

The bent cap segment was lifted using the overhead gantry crane and placed on the temporary support structure. Figure 6.14 shows the bent cap as it is lowered down onto the temporary support structure. The column reinforcing steel can be seen as it has been aligned with the corrugated ducts in the bent cap as the segment is lowered. There were no problems observed during the cap setting operation and the column longitudinal reinforcing bars were easily threaded into the corrugated ducts.

Figure 6.14 HYB-3 specimen during cap setting

The steel bedding layer form was then placed around the column to facilitate the grouting operation. The bedding layer and ducts were grouted by pumping Masterflow 928 grout through one of the ducts in the bent cap(BASF 2006). Pumping was used to place the grout; however, this process was essentially gravity flow grouting of the bedding layer and ducts. There were no significant issues encountered during the grouting operation.

The grout bedding layer was allowed to cure and the unit was subsequently post-tensioned. Following post-tensioning, the unit was picked and inverted as shown in Figure 6.16. Once inverted the specimen was picked and placed in the test setup. No complications were noted during specimen inversion and placement in the test setup.

Figure 6.15 HYB-3 ducts following grouting operation

Figure 6.16 HYB-3 specimen inversion

6.2.4 Post-Tensioning

After allowing the grout to cure for 6 days, the system was post-tensioned by Dywidag Systems International. The strands were individually threaded through the column and set in the wedge

plate to ensure their alignment was maintained inside the column. Due to the short length of this specimen, the misalignment of a strand would result in variable stressing in the individual strands. All five strands were strain gaged during the stressing operation with all five gages surviving through stressing. The stressing operation is shown in Figure 6.17.

Figure 6.17 HYB-3 post-tensioning operation

The stressing operation was identical to that of HYB-2 as the stressing of both specimens occurred at the same time. The target stressing was 75% GUTS; however, based on strain gage readings the actual jacking stress was approximately 69.1%. This is about 6% less than the target stress level desired for this specimen. Based on the strain gage readings, the wedge pull-in was 0.151 inches. This value is less than the manufacturer's recommended 0.250" pull-in. The recorded strain gage history during stressing is shown in Figure 6.18. The wedge pull-in recorded during stressing of HYB-3 was on the same order as that recorded for HYB-1.

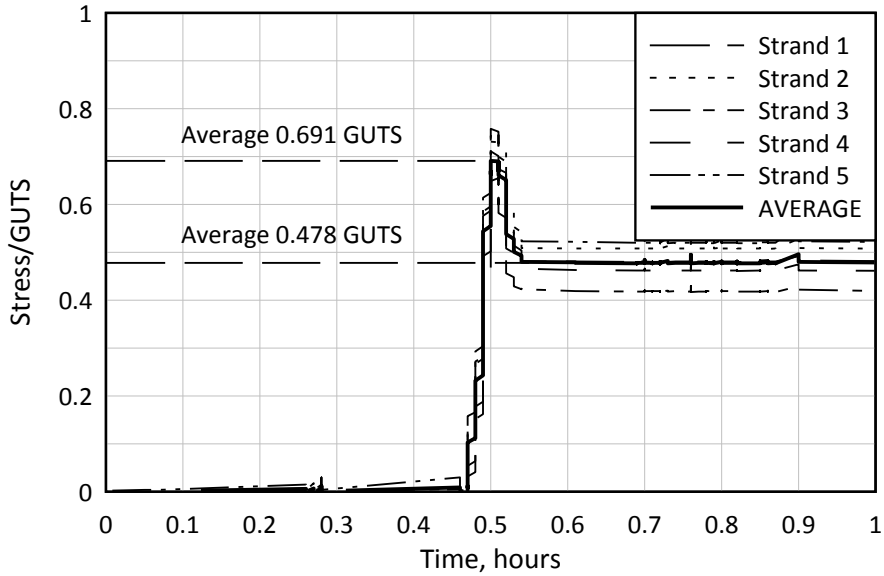

Figure 6.18 HYB-3 post-tensioning strain gage history during stressing

6.3 Cementitious Material Properties

The bent cap and column were fabricated with normal weight concrete developed to achieve a target compressive strength of 7 ksi at 28 days. The mix design was developed using a nominal 3/8 inch maximum aggregate size based on scaling from the prototype specimen.

The cementitious grout selected for use on this specimen was Masterflow 928 grout. This material is a prepackaged hydraulic cement-based mineral-aggregate high strength, non-shrink grout with an extended working time. The grout material is developed to meet the requirements of ASTM C 1107, Standard Specifications for Packaged Dry, Hydraulic-Cement Grout (Non-Shrink), Grades B and C, and the Army Corps of Engineers' CRD C 621, Specification for Non-Shrink Grout, Grades B and C.

Compressive strengths for cementitious materials were established through cylinder testing at multiple times following casting and at day of test (D.O.T.). Results from compression testing for both concrete and grout are listed in Table 6.1 and Table 6.2. These values are based on the average of three compression specimens tested. Variation of cementitious material compressive strength versus age is presented in Figure 6.19.

Table 6.1 HYB-3 concrete strength

Material Age	*Strength, ksi*
4 days	4.75
18 days	7.55
28 days	8.01
35 days	8.49
81 days (D.O.T)	10.27

Table 6.2 HYB-3 grout strength

Material Age	*Strength, ksi*
14 days	6.66
67 days (D.O.T.)	9.49

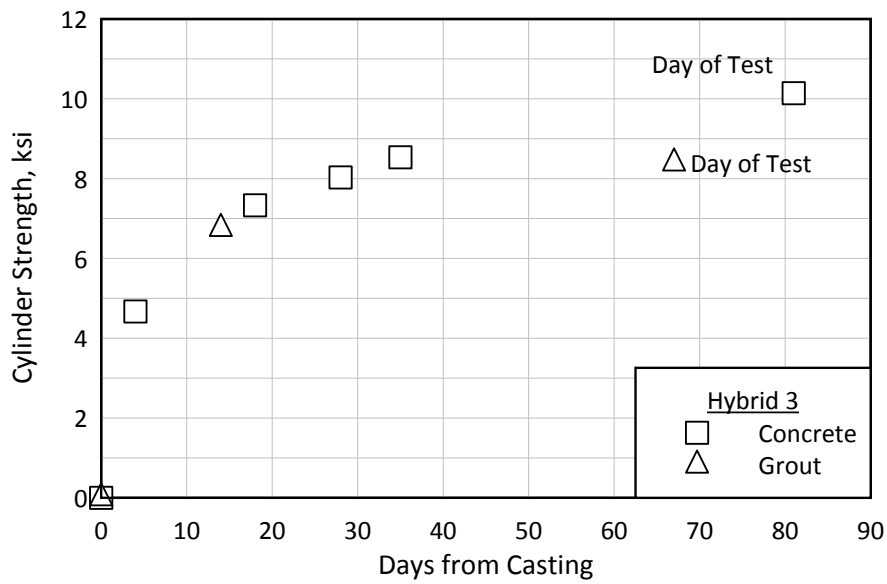

Figure 6.19 HYB-3 cementitious material strengths

6.4 Experimental Procedure and Observations

The loading procedure and observations noted during tested are presented in this section.

6.4.1 Load Protocol

The preliminary stage of loading consists of application of vertical load on the specimen simulating the gravity load during a seismic event. The vertical load was applied as a ramp load over approximately one minute. Following the application of vertical load, lateral loading began. The first stage of loading consisted of ramping of lateral load to a specified target, i.e. force controlled control. Each loading stage consisted of three cycles of push and pull excursions. The first lateral load cycle was based on the expected lateral load required to achieve zero stress at the extreme tension fiber. The next stage had a target lateral load of twice the first stage. Finally, the third stage in force control consisted of a push cycle to expected first yield or 0.50% drift ratio, whichever occurred first. In this test, the drift limit was reached at approximately the same time as first yield of reinforcement. The loading protocol for the force-controlled stages is graphically shown in Figure 6.20

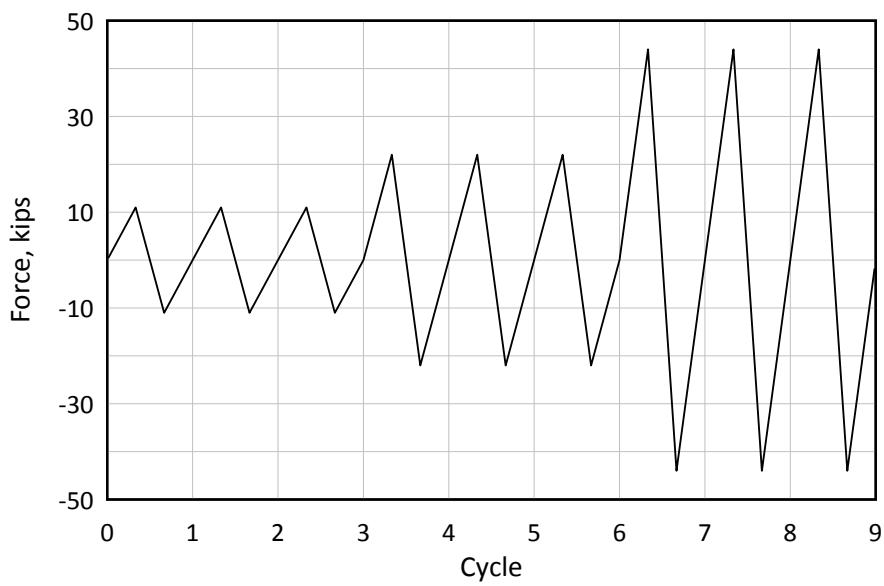

Figure 6.20 HYB-3 force controlled loading protocol

Upon completion of the force controlled loading cycles, the actuator control was switched to displacement control. Displacement controlled stages were loaded to target drifts. For the first two cycles, three displacement excursions occurred in both the push and pull directions (target drift levels of 0.50% and 0.75%). For the remaining loading stages, the specimen underwent two displacement cycles to the specified drift, followed by one cycle to the previous drift level. For example, during the 1.00% drift ratio cycle the specimen underwent two cycles at 1.00% drift

ratio followed by one cycle to 0.75% drift ratio. The displacement control loading protocol is graphically shown in Figure 6.21.

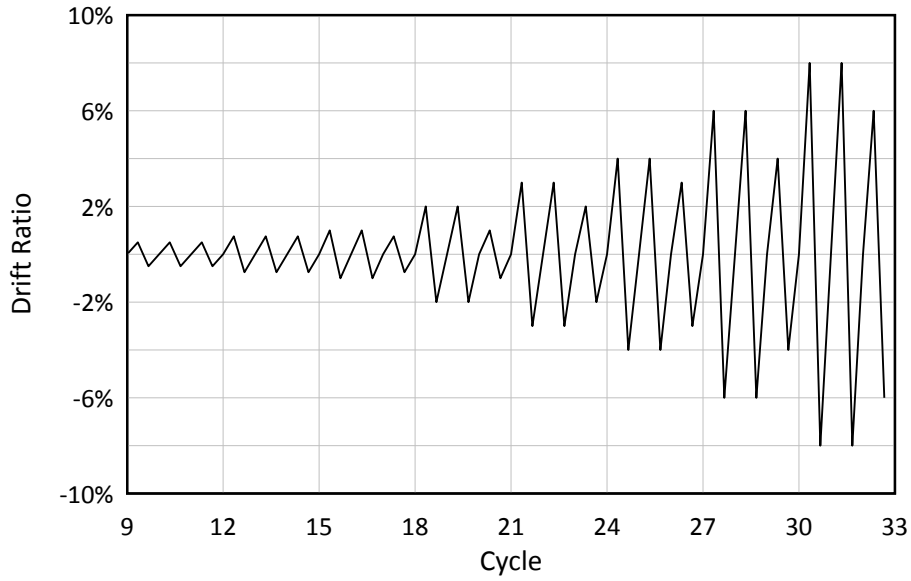

Figure 6.21 HYB-3 displacement controlled loading protocol

6.4.2 Observations During the Test

The following section summarizes the observations made during testing. Observations and photographs were taken at the final cycle at a given force or displacement. For the cases where the specimen underwent two cycles to a given displacement followed by one cycle at a previous displacement, the observations and photographic documentation only occurred at the end of the second cycle in both push and pull directions. Cracks were marked using markers corresponding to a given displacement direction. Red markers were used to indicate cracking due to pushing while blue markers were used to indicate cracking due to pulling.

The test unit prior to testing is shown in Figure 6.22 with vertical and horizontal actuators attached. For the purposes of damage descriptions, the direction of pushing will be referred to as “south” and the direction of pulling will be referred to as “north”. “East” and “west” can thereby be inferred by standard convention.

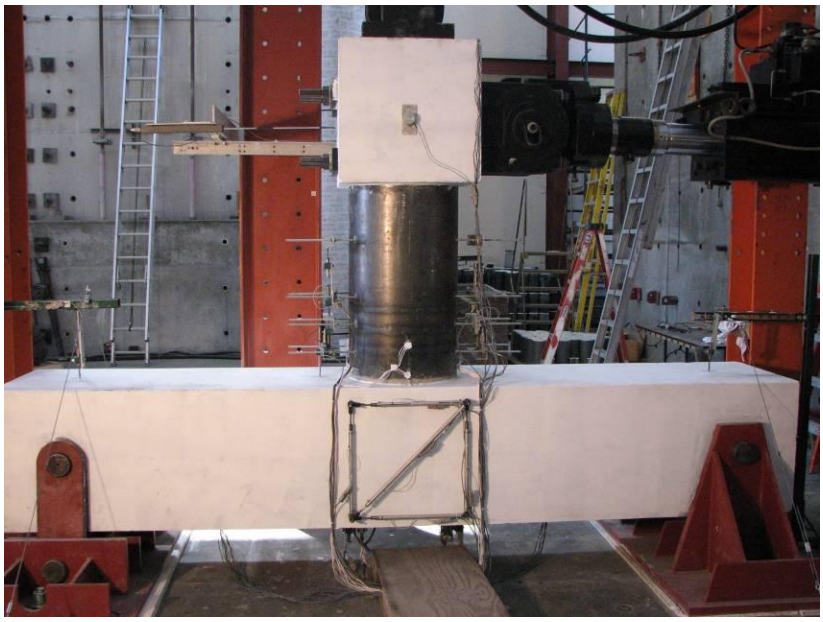

Figure 6.22 HYB-3 specimen prior to testing

Application of 60 kip Vertical Load

Following the application of vertical load, two cracks were noted on the east face of the bent cap. One crack was located just north of the joint approximately 6” in length and the other was in the joint and approximately 2” long (see Figure 6.23). On the west face, one 3” crack was observed in the joint region.

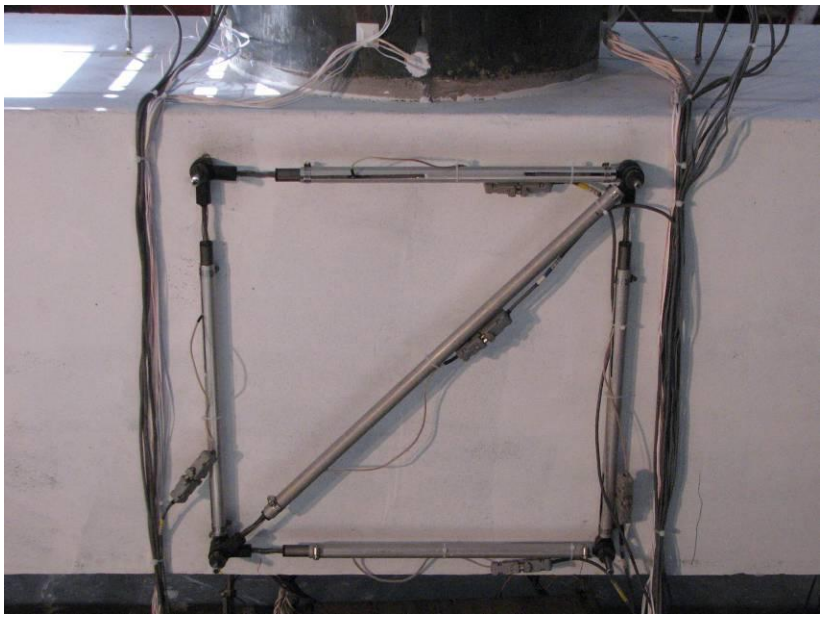

Figure 6.23 HYB-3 minor flexural crack after application of vertical load

3 Cycles at ± 11 Kips

During the push cycle, one 2” crack was observed on the east face of the bent cap at the south end of the joint. On the west face of the bent cap the original crack extended approximately 4” in the joint (see Figure 6.24). During the pull cycle, a 7” vertical crack was observed on the east face of the bent cap in the joint region (see Figure 6.25).

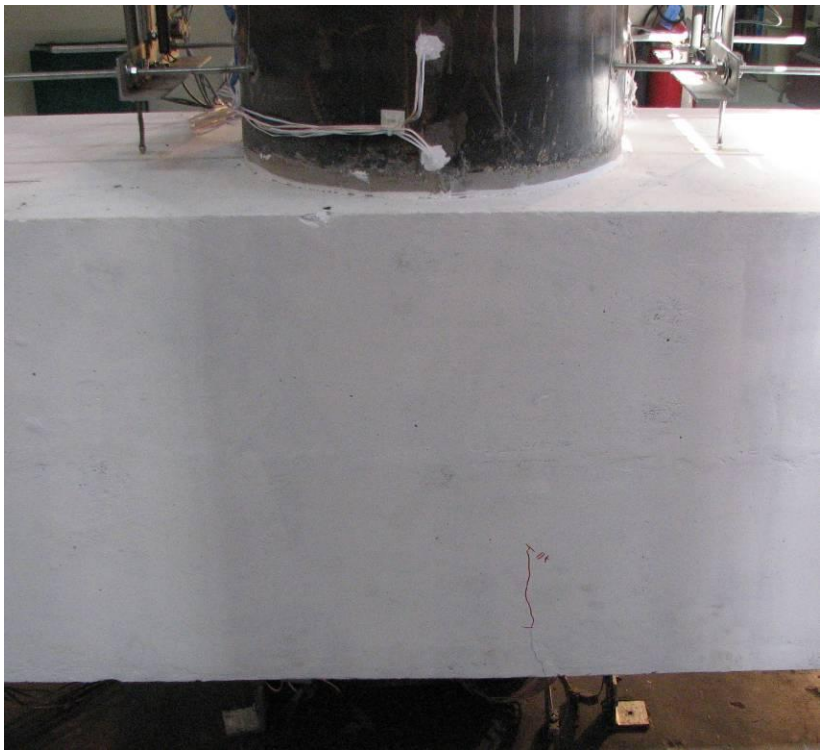

Figure 6.24 HYB-3 west face of bent cap at 11 kips

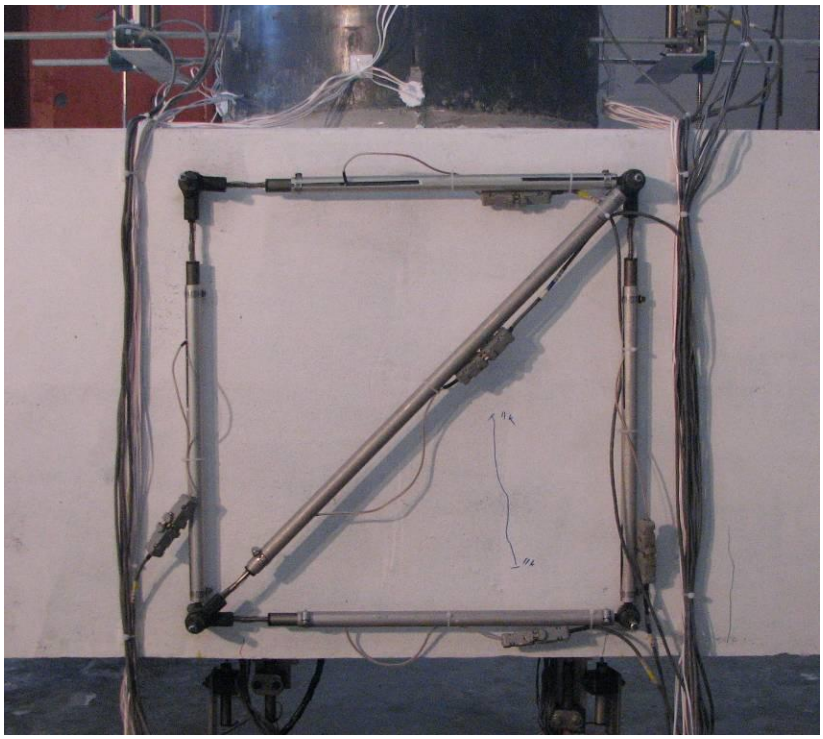

Figure 6.25 HYB-3 east face of bent cap at 11 kips

3 Cycles at ± 22 Kips

Following the push cycles, two cracks to mid-depth of the bent cap were noticed on the east face, one inside the joint and the other just south of the joint. An additional 2” crack was noticed about 8” south of the joint. On the west face, one new 6” crack was noted approximately 3” south of the joint and a 2” crack was observed at the south end of the joint. See Figure 6.26 and Figure 6.27 for crack patterns noted on the bent cap at this load level.

No additional cracks were observed on the east face of the bent cap following the pull cycles. Two new cracks were noted on the west face of the bent cap, an 8” crack in the joint an a 6” crack at the north end of the joint.

No changes were observed at the bedding layer.

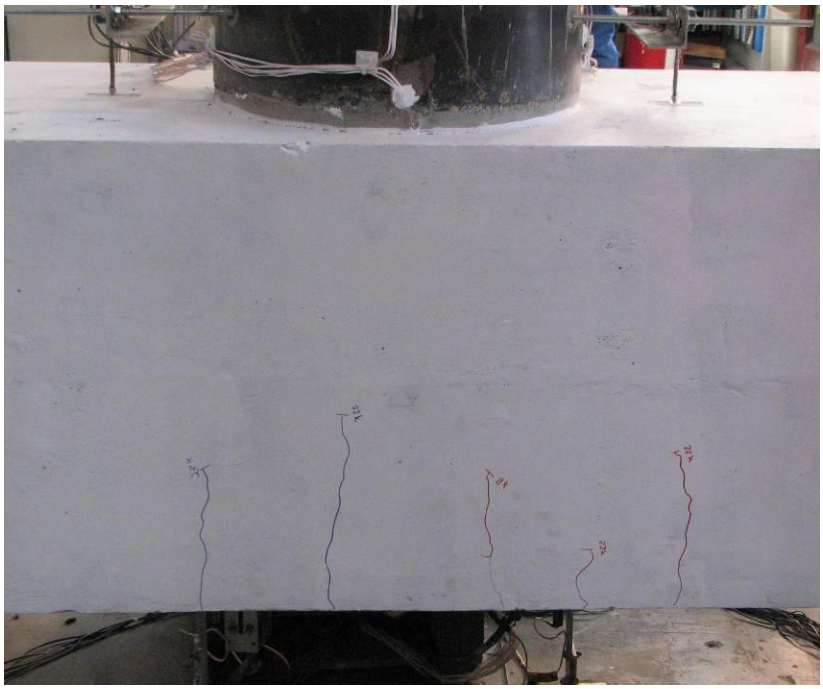

Figure 6.26 HYB-3 west face of bent cap at 22 kips

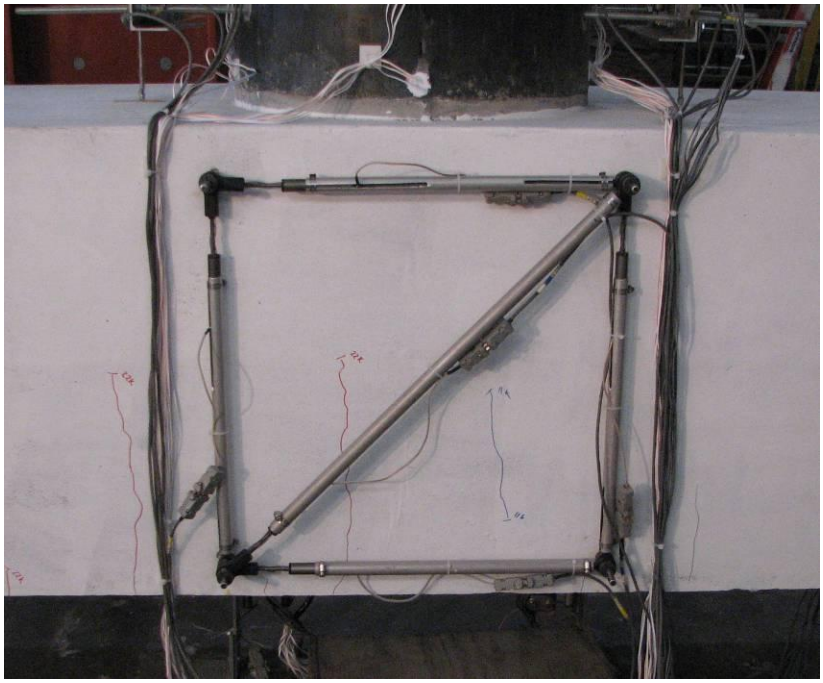

Figure 6.27 HYB-3 east face of bent cap at 22 kips

3 Cycles at ± 44 Kips

At this load level, minor cracking of the grout bedding layer was observed for both the push and pull cycles to approximately mid-depth of the column (see Figure 6.28 and Figure 6.29).

Figure 6.28 HYB-3 column north end at 44 kips

Figure 6.29 HYB-3 column south end at 44 kips

On the west face, on new 6” crack was observed following the push cycle on the west face. The existing crack in the joint extended approximately 2” and the crack 3” south of the joint extended approximately 6”. On the east face one new minor crack, approximately 3” in length was observed at the south end of the joint. The existing crack in the joint extended an additional 7” towards the top of the bent cap with a partially diagonal direction. The existing crack just south of the joint extended approximately 3” and the crack approximately 8” from the joint extended another 4”.

During the pull cycle the existing crack in the joint region extended approximately 6” and a new 8” crack was noted approximately 12” north of the joint on the east face of the bent cap. On the

west face, a new 13” crack was observed on the north end of the joint and an existing crack at the north end of the joint extended approximately 4”. See Figure 6.30 and Figure 6.31 for the condition of the bent cap at this load level.

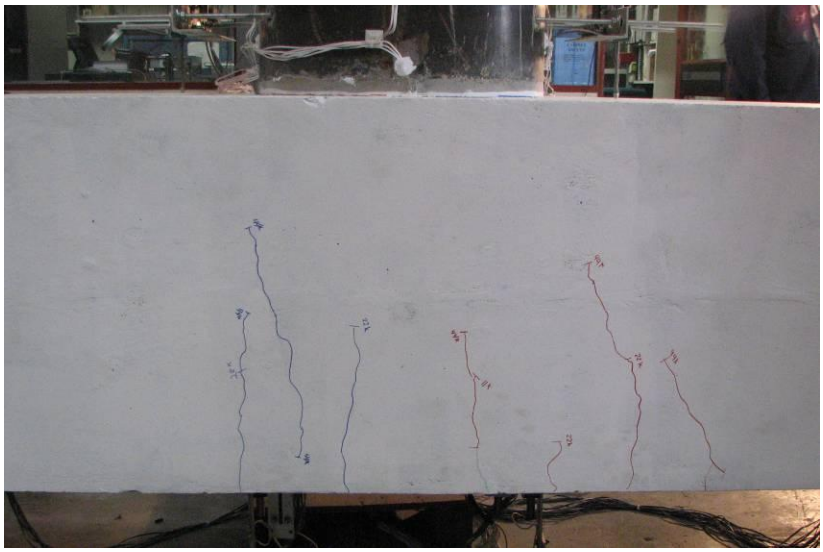

Figure 6.30 HYB-3 west face of bent cap at 44 kips

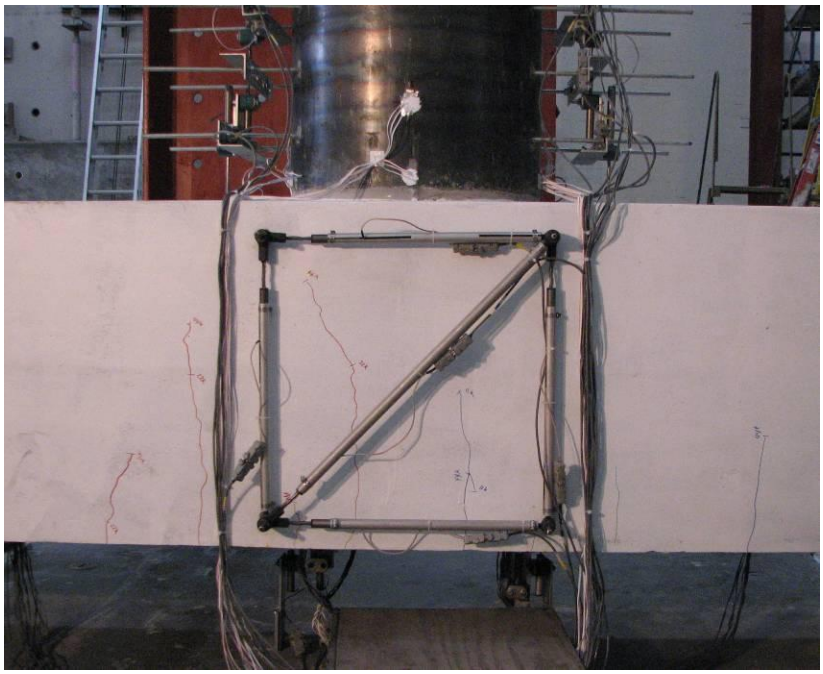

Figure 6.31 HYB-3 east face of bent cap at 44 kips

3 Cycles at ± 0.5% Drift Ratio

During the push cycle, cracking of the bedding layer was observed on both top and bottom of the grout layer. The top crack extended to approximately half the column diameter while the bottom crack extended slightly past half the diameter. At the pull cycle, top and bottom cracks extended slightly past half the column diameter in the bedding layer (see Figure 6.32). Minor spalling of grout material was also noted during both push and pull cycles.

Figure 6.32 HYB-3 south end of column at 0.5% drift ratio

On the east face of the bent cap, the existing long crack in the joint region extended diagonally approximately 4” at the top and split off diagonally approximately 6” from the base and extended to the bottom of the cap following the push cycle. Three existing cracks on the southern half of the bent cap extended between 3” and 5” (see Figure 6.33).

During the pull cycle, one new crack was observed on the east face of the bent cap near the southern joint deformation instrumentation. Additionally, the long crack in the joint extended diagonally another approximately 3” to the dowel for the joint deformation instrumentation (see Figure 6.34). One 1” crack was observed on the west face of the bent cap just north of the joint and another 5” crack was noted approximately 7” north of the joint.

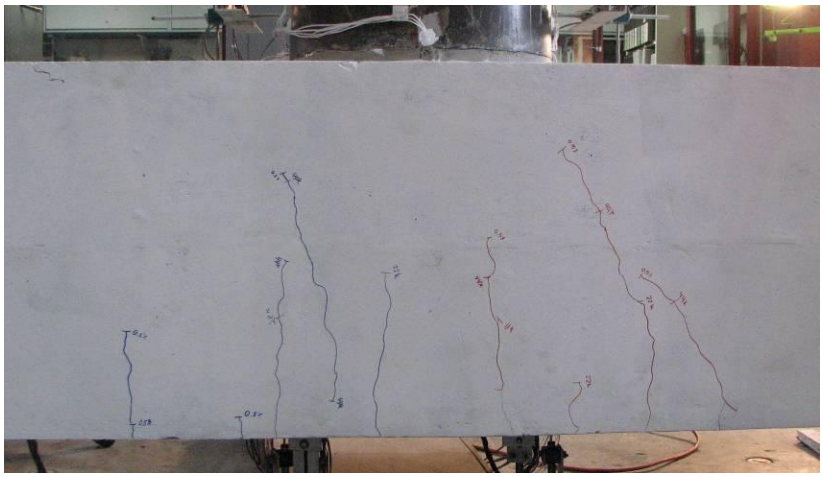

Figure 6.33 HYB-3 west face of bent cap at 0.5% drift ratio

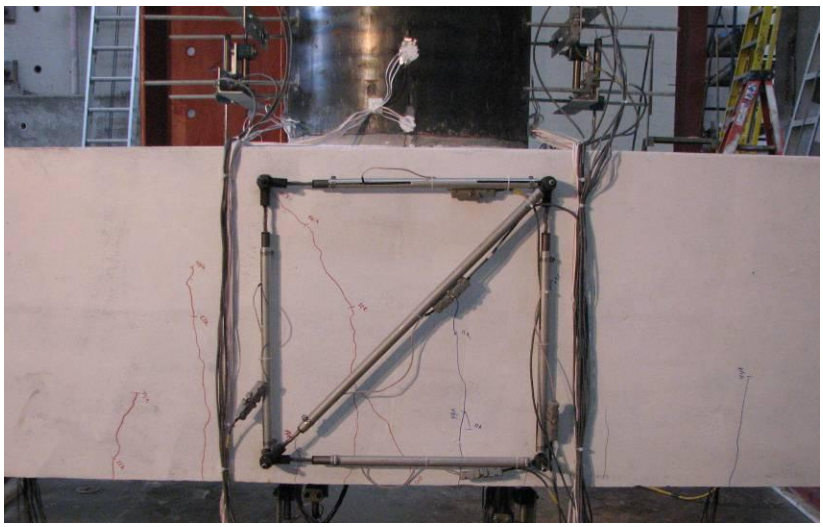

Figure 6.34 HYB-3 east face of bent cap at 0.5% drift ratio

3 Cycles at ± 0.75% Drift Ratio

Cracking and gap opening of the grout bedding layer was observed over approximately 75% of the column diameter. Incipient crushing of grout material was noted along with noticeable opening of the bedding layer gap at the top of the bedding layer (see Figure 6.35 and Figure 6.36). A bond crack was noted at the location of the northeast column rebar as shown in Figure 6.37. This crack extended northeasterly to the edge of the bent cap.

Figure 6.35 HYB-3 column north end at 0.75% drift ratio

Figure 6.36 HYB-3 column south end at 0.75% drift ratio

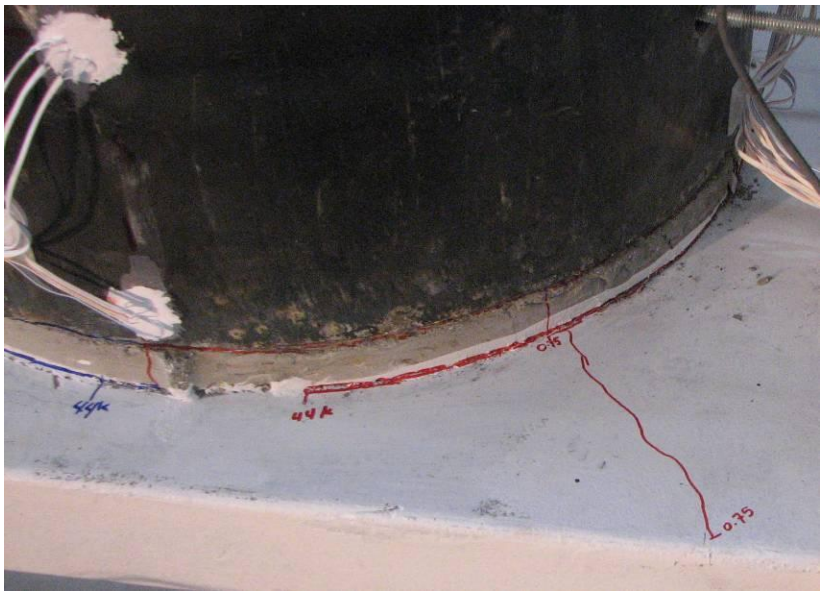

Figure 6.37 HYB-3 bond crack at top of bent cap at 0.75% drift ratio

One new crack approximately 20” south of the bent cap was noted approximately 6” in length on the east face of the bent cap during the push cycle. Additionally, one existing cracks just south of the joint was observed to extend approximately 3” while another further south extended diagonally approximately 6”. On the west face, slight extensions were observed on three cracks. During the pull cycle vertical extensions of two existing cracks were noted on both the east and west face of the bent cap.

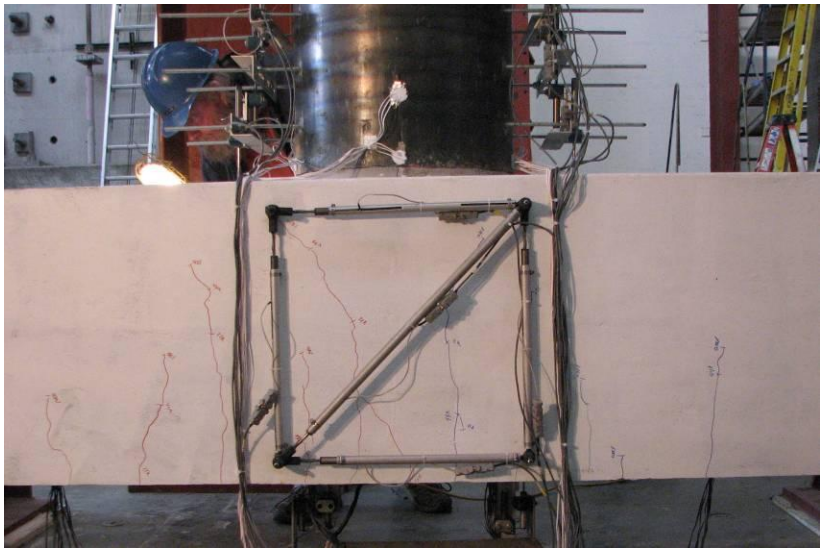

Figure 6.38 HYB-3 east face of bent cap at 0.75% drift ratio

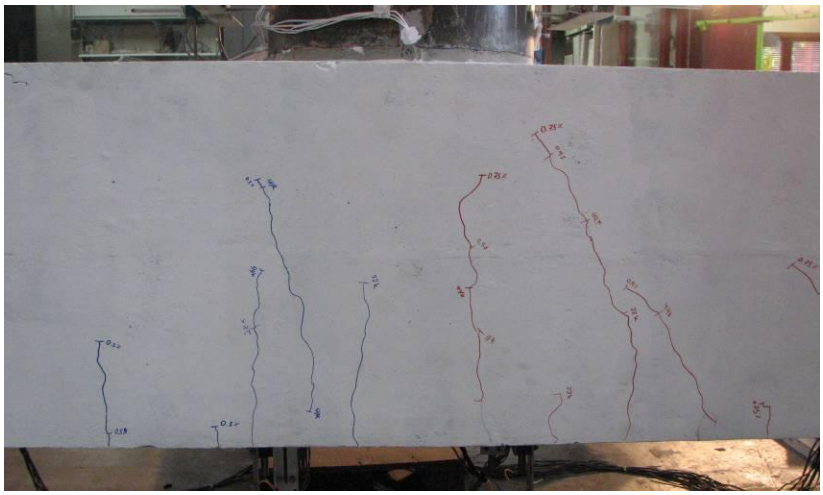

Figure 6.39 HYB-3 west face of bent cap at 0.75% drift ratio

2 Cycles at ± 1.0% Drift Ratio

Continued grout degradation was observed in the bedding layer with minor spalling of grout material onto the top of the bedding layer (see Figure 6.40 and Figure 6.41). Noticeable gap opening was observed on both top and bottom of the bedding layer. During the push cycle, the exiting bond crack on the northeast portion of the column extended approximately 2” down the face of the bent cap (see Figure 6.42). A new crack was also observed on the top of the bent cap appearing to originate at the same rebar and extending eastward and down the face of the bent cap approximately 2”. A new bond crack was also observed on the northeast rebar during the push cycle extending westward and down the face of the cap approximately 2” (see Figure 6.44).

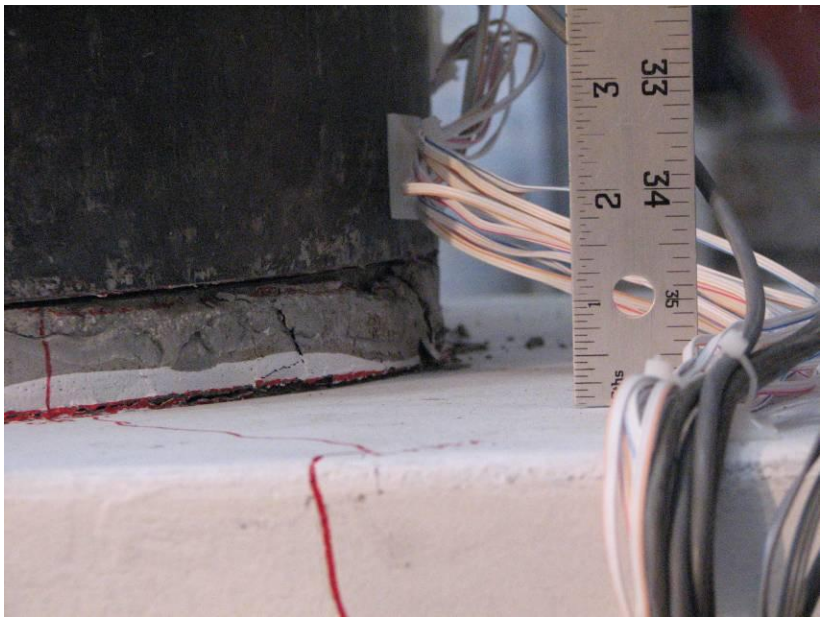

Figure 6.40 HYB-3 column north end at 1.0% drift ratio

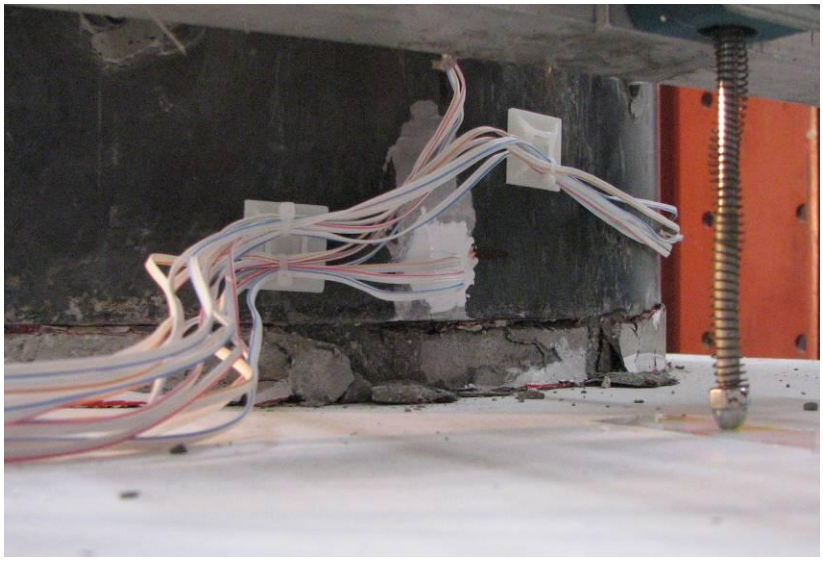

Figure 6.41 Column north end at 1.0% drift ratio

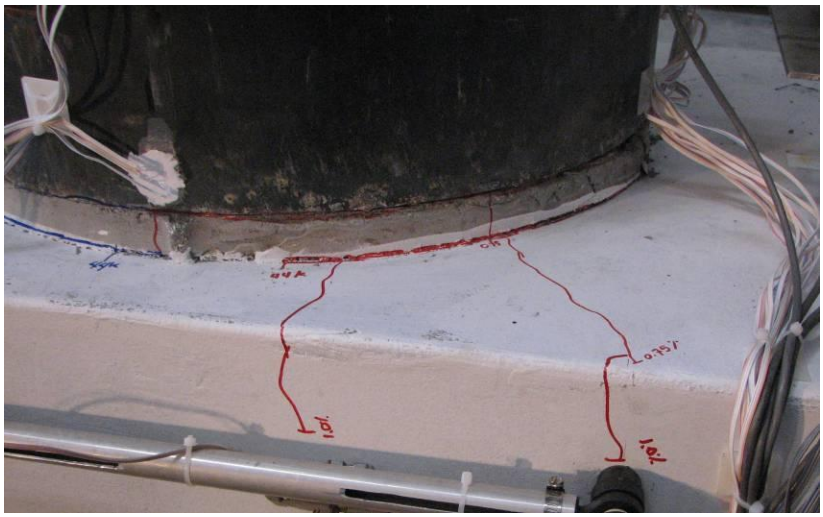

Figure 6.42 HYB-3 bond cracks at top of bent cap at 1.0% drift ratio

During the push cycle, three cracks extended off an original crack extending through the joint on the east face of the bent cap. On the west face, one new diagonal tension crack was observed in the bottom half of the joint extending off an existing vertical crack (see Figure 6.44). During the pull cycle, two extensions of existing cracks were noted on the east face of the cap.

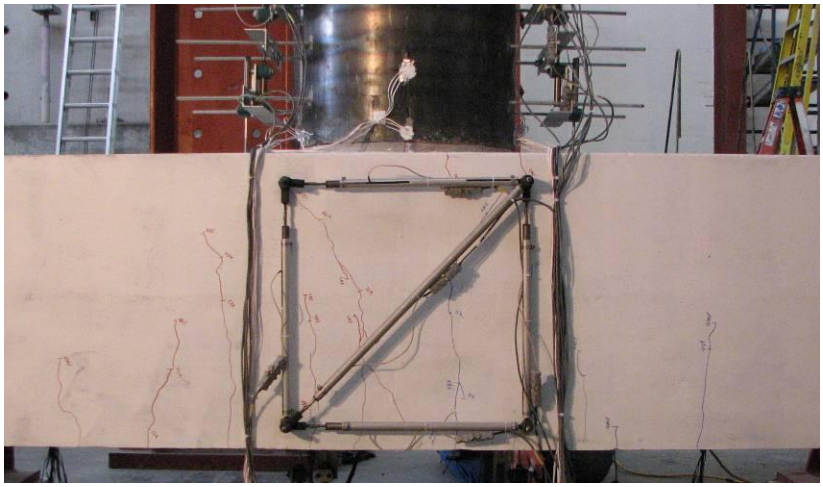

Figure 6.43 HYB-3 east face of bent cap at 1.0% drift ratio

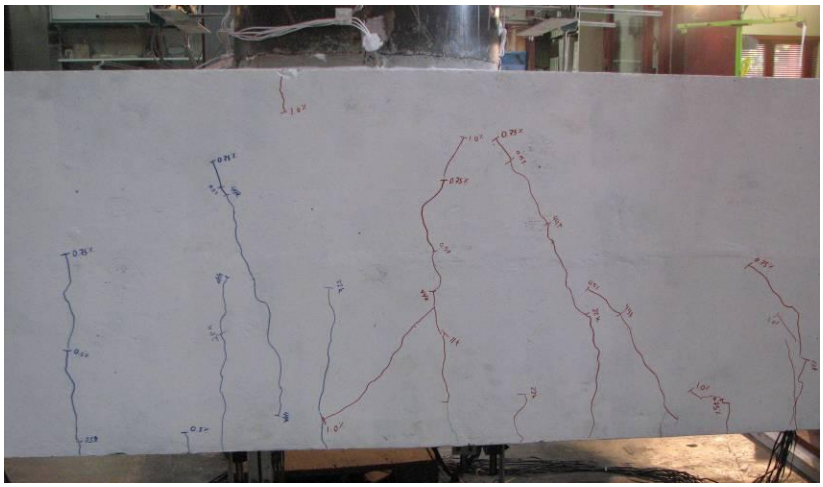

Figure 6.44 HYB-3 west face of bent cap at 1.0% drift ratio

2 Cycles at ± 1.5% Drift Ratio

On both the north and south ends of the column, grout degradation under the steel shell was noticeable subsequent to both push and pull cycles (see Figure 6.45). The damage is likely caused by the significant different in stiffness that exists between the steel shell and the grout material during compression loading.

Figure 6.45 HYB-3 south end of column at 1.5% drift ratio

During the push cycles, on the east face of the bent cap two existing cracks exhibited minor extensions and a new diagonal tension crack formed extending through the joint (see Figure 6.46). Additionally, a new bond crack formed on the top of the bent cap at the eastern bar location and extended east and down the face of the bent cap approximately 2”. On the west face of the bent cap, the previous bond crack extended and split. Six other existing cracks extended during the push cycles (see Figure 6.47).

During the pull cycle, one new diagonal tension crack formed on the upper portion of the bent cap (see Figure 6.46). On the west face, a new diagonal tension crack was observed on the lower portion of the bent cap as seen in Figure 6.47. Two existing cracks on the west face extended slightly. A new bond crack was noted on the southwest rebar, extended in a southwesterly direction and down the face of the bent cap approximately 2” (see Figure 6.48). Additionally, a bond crack was also observed extending from the southeast rebar extending on the top of the cap approximately 5” from the column.

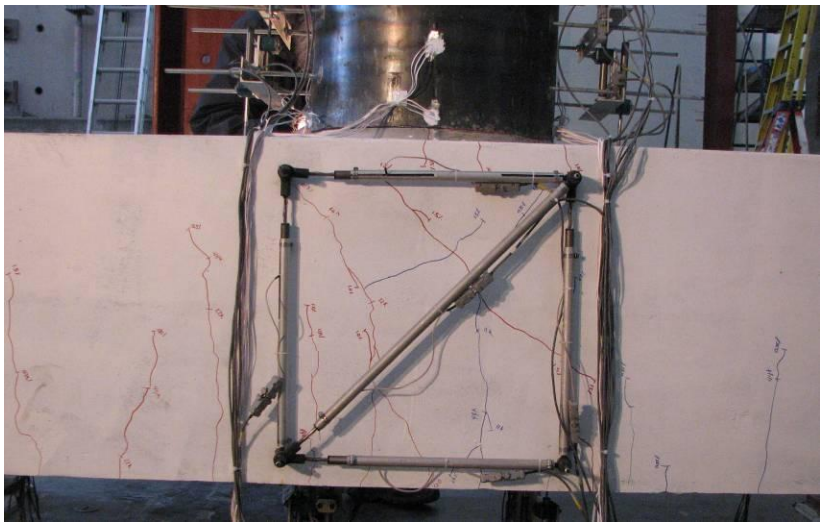

Figure 6.46 HYB-3 east face of bent cap at 1.5% drift ratio

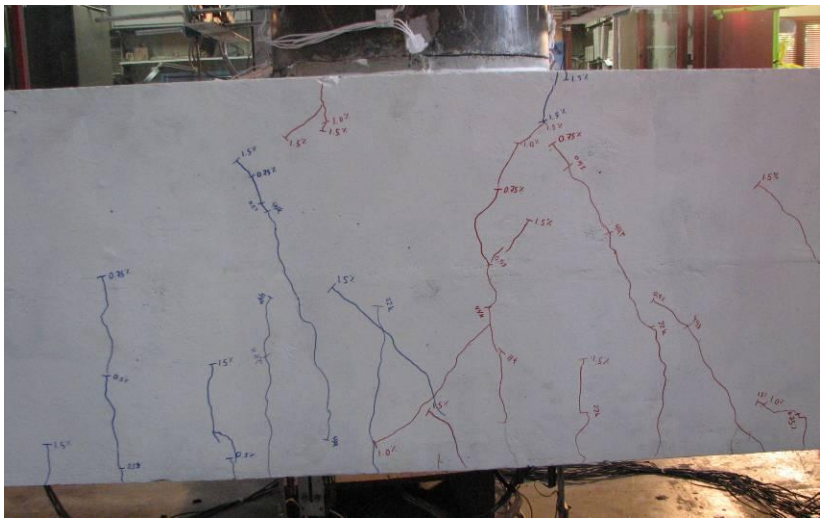

Figure 6.47 HYB-3 west face of bent cap at 1.5% drift ratio

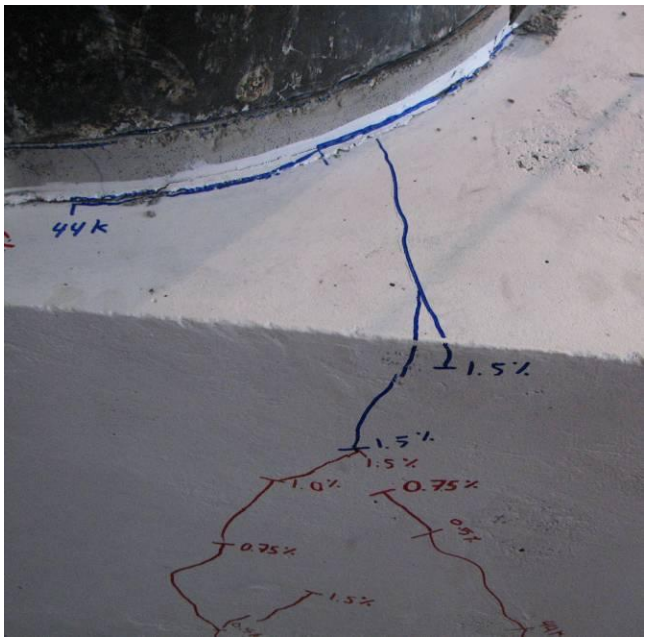

Figure 6.48 HYB-3 bond crack at top of bent cap at 1.5% drift ratio

2 Cycles at ± 2.0% Drift Ratio

Appreciable damage to the bedding layer was observed during both push and pull cycles as shown in Figure 6.49 and Figure 6.50. During testing, it was observed that as grout spalled it displaced previously spalled material in a radial direction outward from the column. This becomes more apparent during larger displacement cycles.

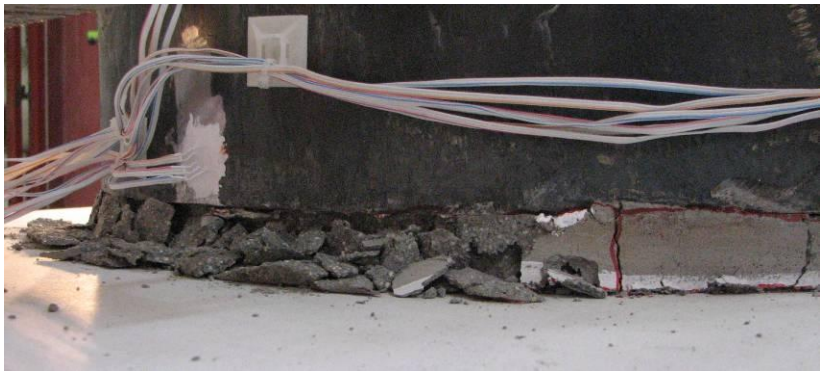

Figure 6.49 HYB-3 north end of column at 2.0% drift ratio

Figure 6.50 HYB-3 south end of column at 2.0% drift ratio

Only two minor extensions of existing cracks were observed on the east face of the bent cap during the push displacement cycle. No additional damage was noted during both push and pull cycles.

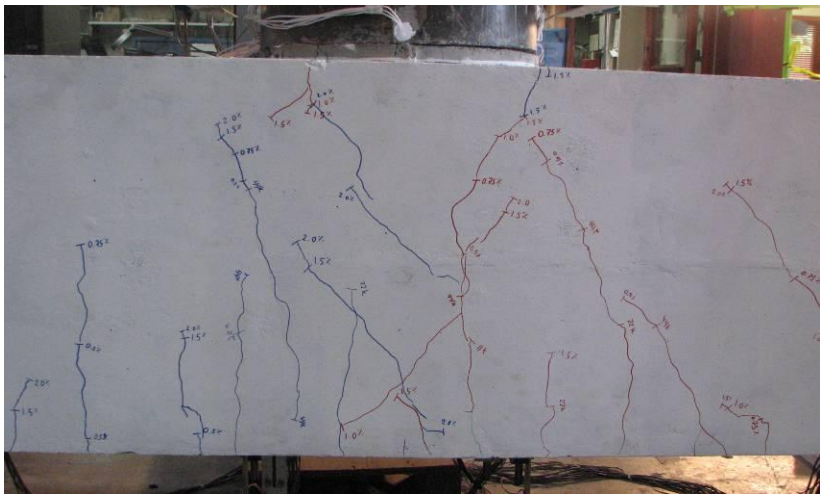

Figure 6.51 HYB-3 west face of bent cap at 2.0% drift ratio

2 Cycles at ± 3.0% Drift Ratio

Significant joint opening and grout damage was observed during push and pull cycles with continued loss of grout material. Figure 6.52 and Figure 6.53 show the bedding layer damage and joint opening, respectively. No additional damage was noted on the bent cap.

Figure 6.52 HYB-3 grout damage at north end of column at 3.0% drift ratio

Figure 6.53 HYB-3 joint opening at south end of column at 3.0% drift ratio

2 Cycles at ± 4.0% Drift Ratio

No new damage was observed on the bent cap during both push and pull displacement cycles. Continued degradation and spreading of damaged grout material was observed as shown in Figure 6.54 and Figure 6.55. Damage was noted around the entire grout bedding layer at this point even near the centerline of the column. Significant gap opening was noted as shown in Figure 6.56.

Figure 6.54 HYB-3 grout damage and spread at north end of column at 4.0% drift ratio

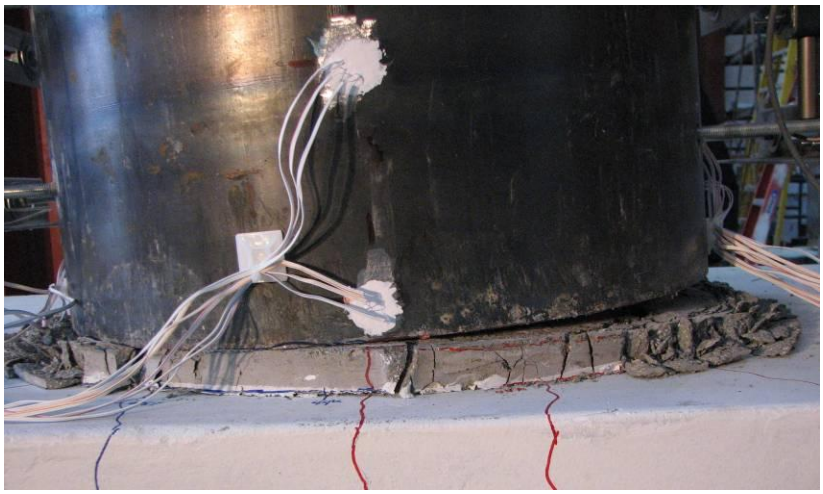

Figure 6.55 HYB-3 east view of column joint opening at 4.0% drift ratio

Figure 6.56 HYB-3 joint opening at south end of column at 4.0% drift ratio

2 Cycles at ± 6.0% Drift Ratio

No new damage was observed on the bent cap during both push and pull displacement cycles. Gap opening increased as shown in Figure 6.58. Grout damage continued with increased loss of competent material, see Figure 6.60.

During the second displacement cycle in the pull direction, the southwest rebar in tension fractured at approximately 1.0” drift. This was confirmed through auditory observation and a noticeable drop in the applied shear. During the push cycle to 4.0% drift ratio following the two cycles to 6.0%, the extreme rebar in tension was noted to fracture at approximately 3.0% drift ratio.

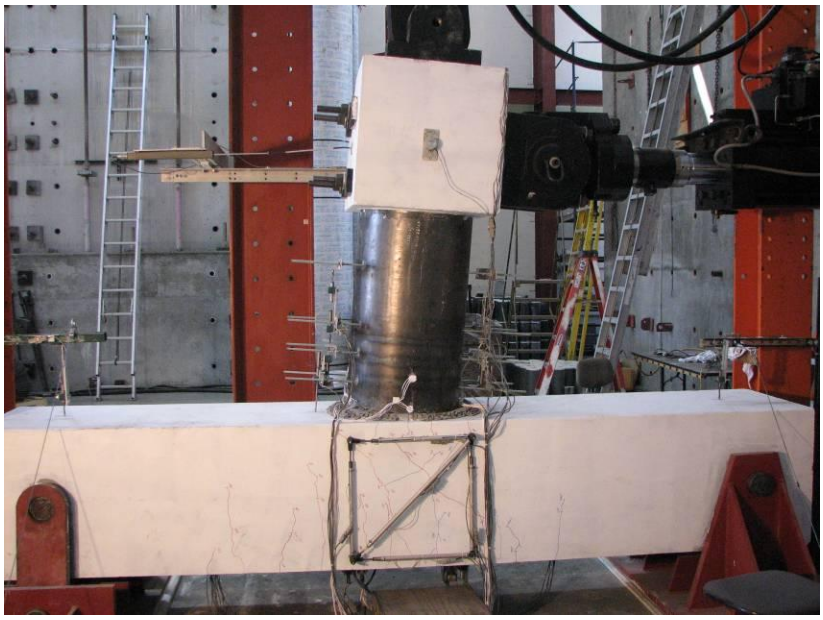

Figure 6.57 HYB-3 east view of specimen at 6.0% drift ratio

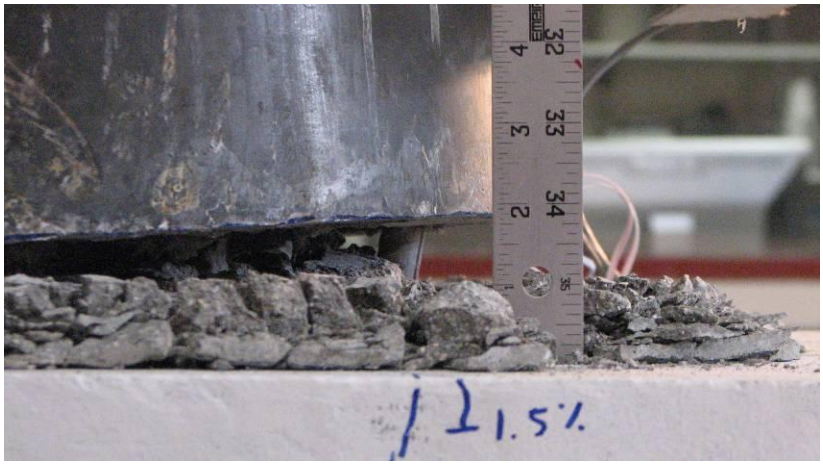

Figure 6.58 HYB-3 joint opening at south end of column at 6.0% drift ratio

Figure 6.59 HYB-3 south end of column at 6.0% drift ratio

Figure 6.60 HYB-3 grout damage after 6.0% drift ratio cycles

2 Cycles at ± 8.0% Drift Ratio

No new damage was observed on the bent cap during both push and pull displacement cycles. The large joint opening at this displacement level provided a clear line of sight into much of the bedding layer. As seen in Figure 6.62, the grout material is significantly damaged past the location where the inner pipe is located.

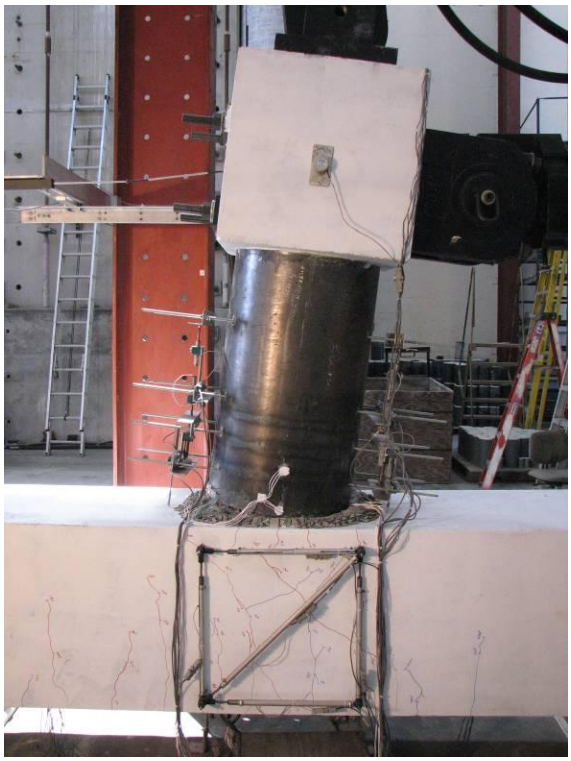

Figure 6.61 HYB-3 east view of column displacement at 8.0% drift ratio

Figure 6.62 HYB-3 south end of column at 8.0% drift ratio

End of Test

Following the end of the test, the extent of radial spreading of the grout material was apparent. Figure 6.63 provides a general overview of the extend of grout loss while Figure 6.64 and Figure 6.65 show the spread of grout material on both north and south ends of the column. The material

degradation is clear in these photos with some locations showing the appearance of a dust-like composition due to crushing. This loss of core material will result in the physical shortening of the column.

Figure 6.63 HYB-3 grout damage at end of test

Figure 6.64 HYB-3 south end spread of grout

Figure 6.65 HYB-3 north end spread of grout

An observation that was made after some grout material was removed is the sliding of the column during testing (see Figure 6.66). The red line drawing on the top of the bent cap represents the location of the initial flexural crack in the bedding layer. Reversed cyclic loading caused the column to shift location approximately 1.125" (see Figure 6.67). The sliding is in the push direction although the final displacement cycle was in the pull direction.

Figure 6.66 HYB-3 evidence of sliding of column toward south (view from north)

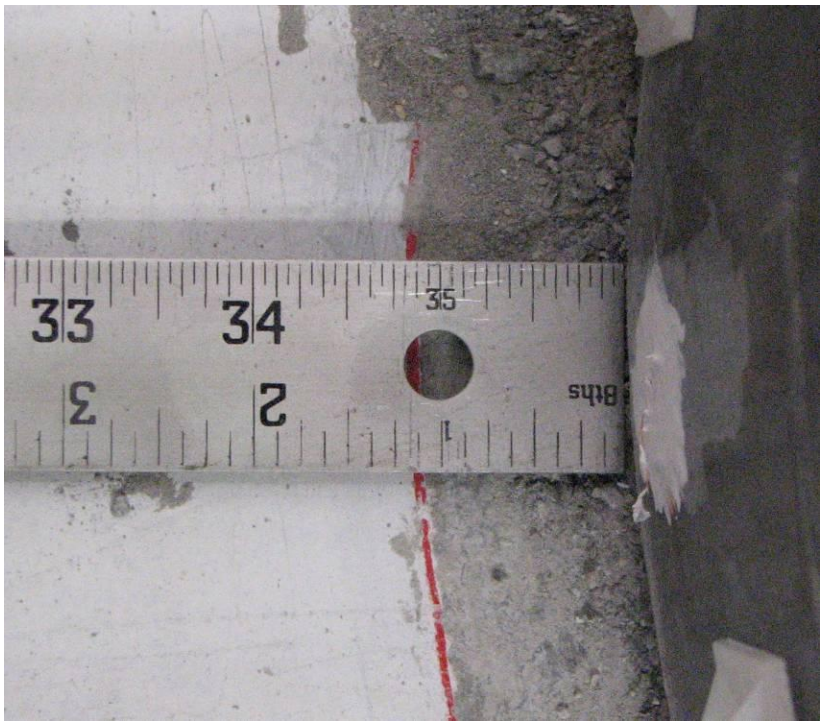

Figure 6.67 HYB-3 close up of column movement

6.5 Experimental Results

Data collected during testing from instrumentation is presented and discussed in the following section.

6.5.1 Global Response

Vertical Load History

The vertical load history recorded during testing is presented in Figure 6.68. From the plot it is evident that the vertical load was maintained at a constant force equal to approximately 60 kips during the entirety of the test. Note, this vertical force was less than that for HYB-2 to compensate for the difference in effective post-tensioning force between the units.

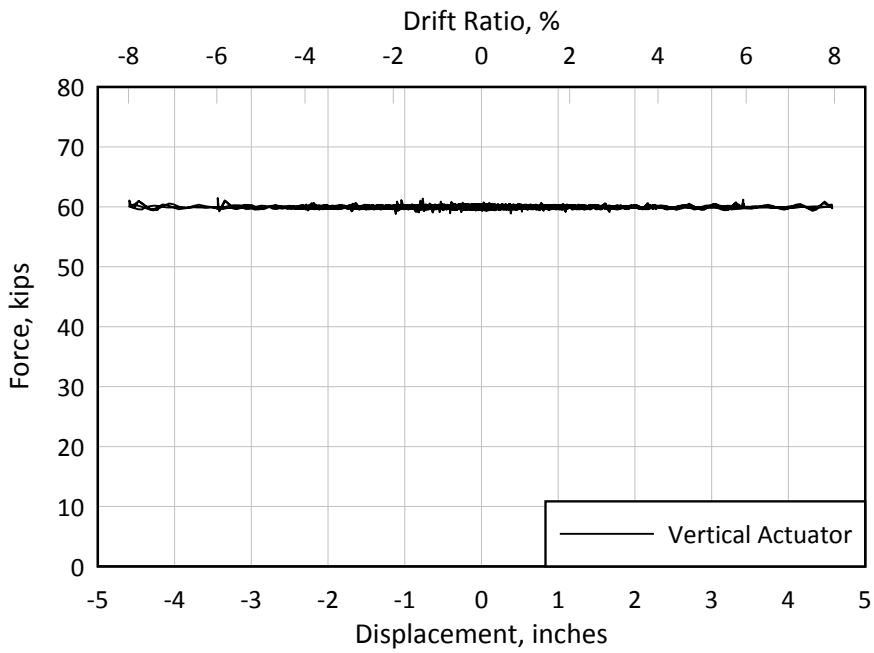

Figure 6.68 HYB-3 vertical load history

Force-Displacement Response

The complete force-displacement curve obtained for this specimen is shown in Figure 6.69. The lateral force presented is the actual lateral force considering the effects of system deformation during testing. Subsequent to the load cycle to 2.0% drift ratio, a noticeable reduction in the lateral capacity was noted. The first cycle to 3% drift ratio was approximately 93% of the maximum force recorded. Every cycle following the 2% drift ratio level resulted in an additional loss in lateral capacity. Observations during testing indicated deterioration in the grout bedding layer at the lateral drifts exceeding 2% drift ratio. This grout performance resulted in a reduction in the effective column diameter consequently reducing the lateral capacity of the system. Furthermore, the reduction in grout area resulted in a net reduction in the thickness of the bedding layer and a consequential reduction in the effective post-tensioning force. The reduction in post-tensioning force was more noticeable as compared to HYB-2. This increased loss is attributable to the smaller section area at the joint due to the hollow column that provides higher bearing stresses and resulting increased shortening of the bedding layer. The nominal capacity calculated using the simplified analysis technique is also provided in the force-displacement figure.

At the 4% drift level, the lateral capacity is approximately equal to 80% of the maximum observed lateral capacity. Considering the common definition of system failure, which is based

on a reduction in lateral strength equal to 80% of the maximum, the specimen could be said to have failed at a drift level of 4% drift ratio.

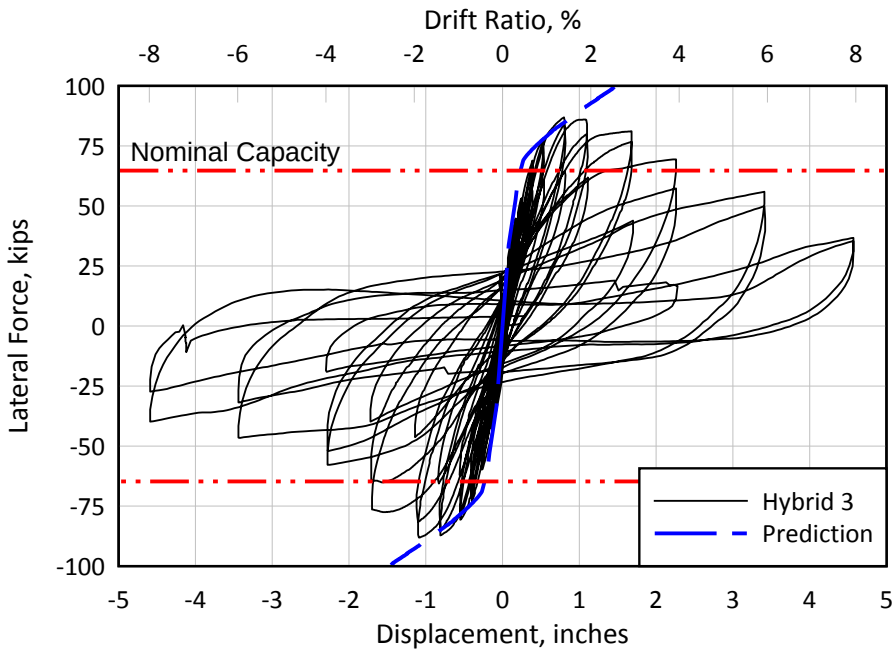

Figure 6.69 HYB-3 force-displacement response

Failure of the first longitudinal reinforcing bar was noted through auditory observations and a noticeable drop in the lateral resistance during the push cycle following two cycles to 6.0% drift ratio with a target drift ratio of 4.0%.

The force-displacement response up to 3% drift ratio is shown in Figure 6.70. This response shows an origin oriented response with significant improvements in the self-centering ability as compared to the cast-in-place specimen.

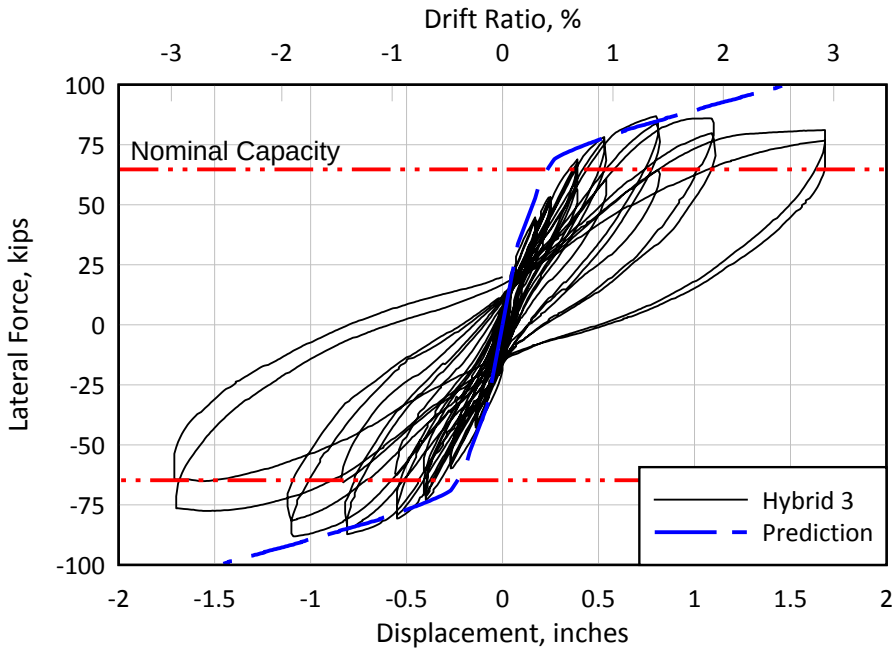

Figure 6.70 HYB-3 force-displacement response to 3.0% drift ratio

The force-displacement response for both cycles at approximately 2% drift ratio is shown in Figure 6.71. It can be observed from this plot that there are more apparent reductions in stiffness and strength due to cyclic loading at a drift level approximately equal to the design level drift as compared to the other hybrid specimens. Although this response is not as desirable as the previous two hybrid specimens, the response characteristic is fairly consistent with the desired stable lateral response in the design level displacement range.

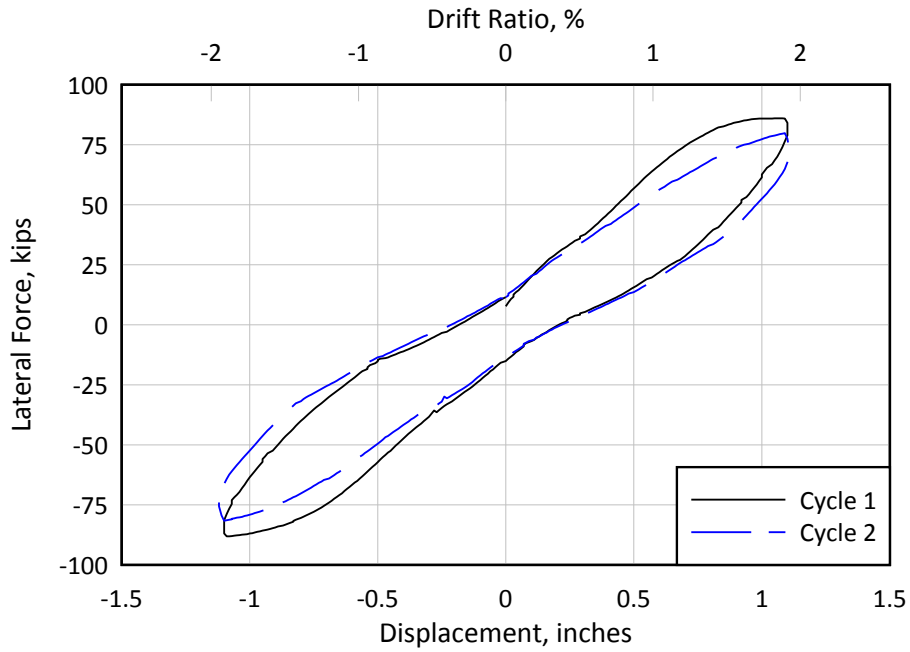

Figure 6.71 HYB-3 force-displacement response at 2% drift ratio

The force-displacement envelope prediction as compared to the actual recorded envelop is shown in Figure 6.72. The prediction is reasonable accurate up to approximately 1.7% drift ratio at which point the prediction continues to increase in lateral capacity whereas the recorded response begins to decay. The reduction in lateral capacity is due to the accumulation of damage in the grout material used in the bedding layer that began to fall apart under increasing drifts. Through the use of fiber reinforced grout, this response characteristic is no expected. This damage to the bedding layer resulted in a loss of grout material in the bedding layer and an essential reduction in the column effective diameter. Additionally, the bedding layer began to reduce in thickness that resulted in a reduction in the effective post-tensioning force. The lateral resistance of the specimen continued to diminish until the ultimate failure due to fracture of column reinforcing bars.

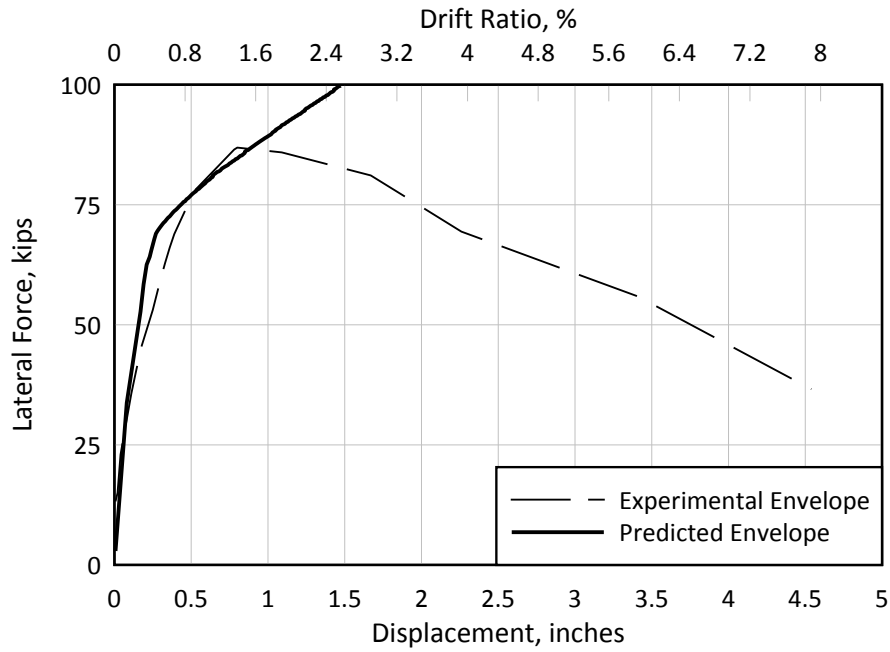

Figure 6.72 HYB-3 force-displacement envelope

Displacement Decomposition

A graphical breakdown of the displacement components captured by instrumentation readings during testing is provided in Figure 6.73. This plot provides a summary of the relative contribution of a given mode of deformation as compared to the total displacement recorded at the same instant of time. During lower level lateral displacement cycles, it is apparent that the individual displacement components considered and monitored capture the majority of the overall system displacement. However, as the displacement levels increase, a greater amount of system deformation is not captured by the recorded measurements. Even at the larger drift levels, the decomposition of displacement components provides a good representation of the overall response.

From the decomposition plot, it is apparent that the contribution of end rotations increases significantly as lateral drift increases. As large deformations are accommodated through concentrated joint rotations, this is an expected trend.

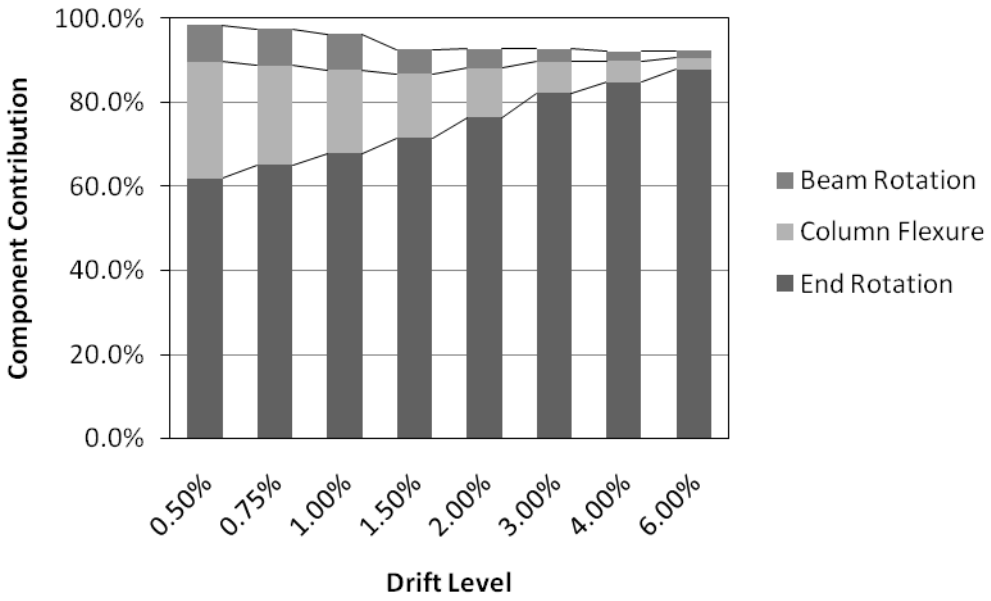

Figure 6.73 HYB-3 displacement decomposition

Out-of-Plane Displacement

During testing, the out-of-plane displacement at the actuator location was monitored. Figure 6.74 shows the displacement orbit of the test specimen. A noticeable eastward drift is observed during the push cycles. The maximum out-of-plane drift ratio recorded was slightly greater than 1%. This out-of-plane drift level will result in a negligible reduction in the lateral displacement capacity.

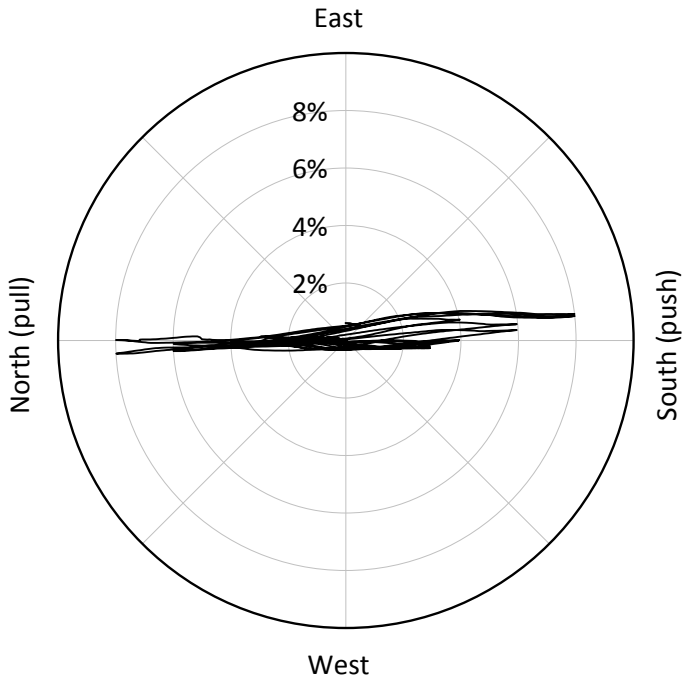

Figure 6.74 HYB-3 drift ratio orbit

Equivalent Viscous Damping

The recorded force-displacement response of the specimen was used to determine the equivalent viscous damping provided through hysteretic system response. Figure 6.75 provides a graphical representation of the equivalent viscous damping over varying drift levels. From the plotted response, it is observed that the equivalent viscous damping increases with increasing lateral drift. For the majority of the cycles, the equivalent viscous damping from the first to second cycle is rather constant. The significant structural non-linearity at larger drifts causes the variations in equivalent viscous damping past 4% drift ratio. The main objective of considering equivalent viscous damping is to show relative stability between hysteresis loops at the same drift level. As the first and second cycles have similar equivalent viscous damping, the loops are relatively stable during cycles at the same drift level.

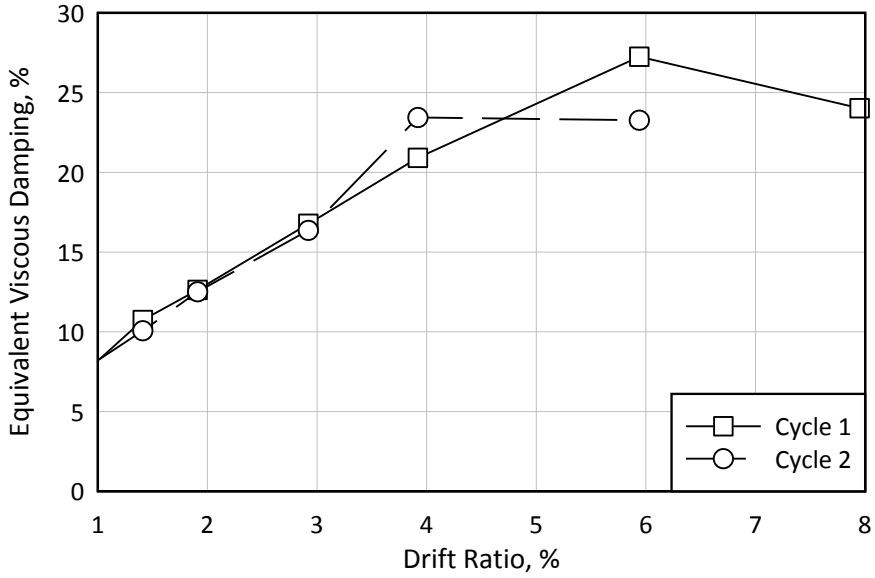

Figure 6.75 HYB-3 equivalent viscous damping

Residual Displacement

A plot of the recorded residual drift following both the first and second cycle to a target drift level is provided in Figure 6.76. This plot presents the residual drift as a ratio of the residual drift to the maximum drift associated with that cycle. Note that the maximum value for both push and pull cycles is presented. This plot indicates that there is a minor increase in residual drift from the first to second cycle. Additionally, there is an overall increase in the residual drift ratio with increasing lateral drift. Following the loading to the 3% drift ratio, a significant increase in the residual drift ratio is observed. This response is the result of the degradation of the grout bedding layer. This response after 3% drift ratio is worse than HYB-2 due to the reduction in available grout area in the bedding layer due to the hollow column shape.

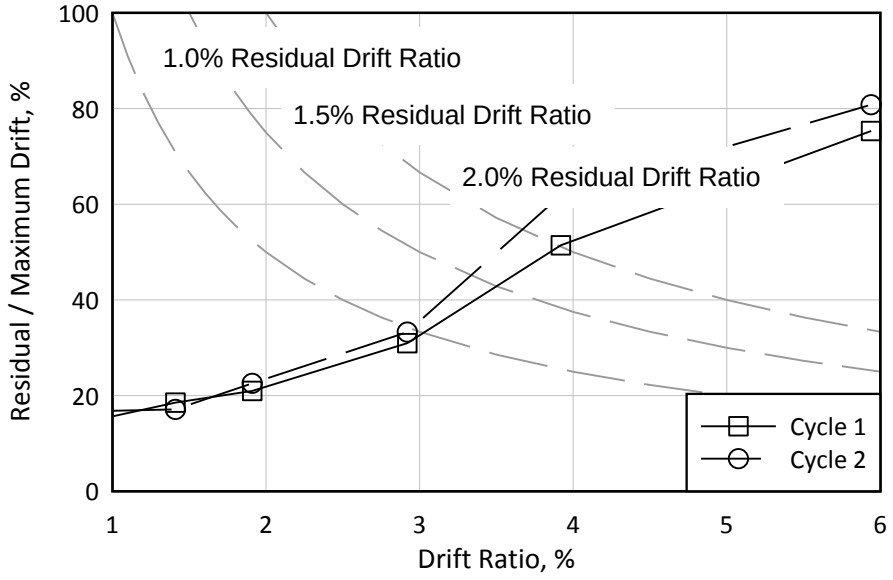

Figure 6.76 HYB-3 residual drift

Figure 6.77 provides a comparison of the residual drift ratios for HYB-3 and the cast-in-place control specimen. It is apparent that the hybrid detail has superior performance as compared to the cast-in-place specimen when considering residual drift ratio. However, subsequent to the 3% drift ratio cycles, the reduction in residual drift ratio become significantly less. Considering the previously discussed limiting 1-degree residual drift angle, this unit could sustain lateral drift ratios of approximately 3.5% while still meeting this criteria. In comparison to the cast-in-place unity, which can only undergo drift levels of approximately 2.75%.

The use of a tougher grout matrix using fiber reinforcement is expected to significantly decrease the residual drift ratio for this hybrid unit and provide enhanced seismic response.

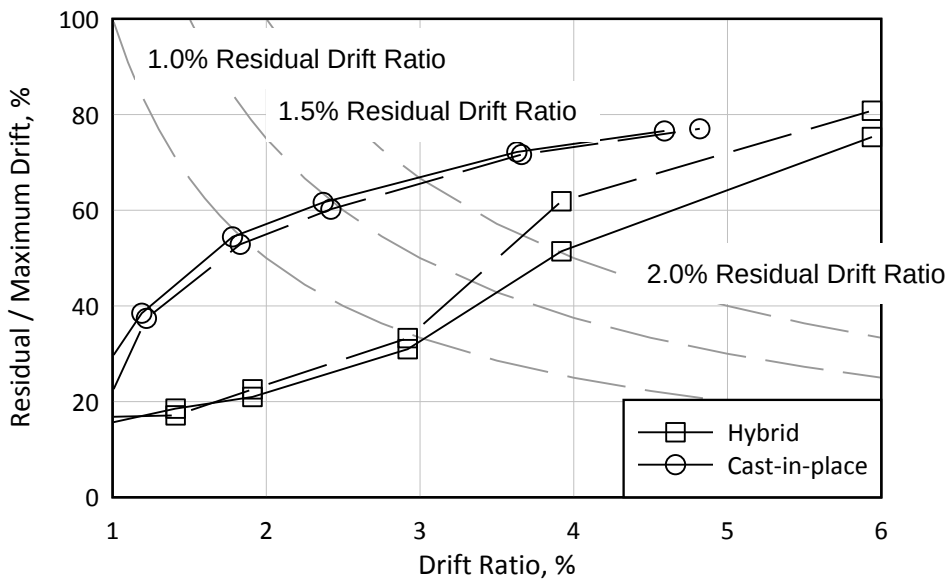

Figure 6.77 HYB-3 comparison of residual drift ratios with CIP

Bedding Layer

Figure 6.78 provides a plot of the axial deformation at the centerline of the grout bedding layer as determined using the curvature gages at the base of the column. The bedding layer had an approximately linear increase in centerline axial deformation with increasing lateral drift up to 3% drift ratio. Following the 3% drift ratio cycles, a continued reduction in the slope of the drift versus bedding layer deformation is observed. In addition, the zero drift deformation showed an increasing reduction in dimension following increasing lateral drifts. Following the lateral seismic testing, the bedding layer reduced in dimension by approximately 30%. This reduction in vertical dimension resulted in the observed significant reduction in column effective post-tensioning. The observed trends also correlate with the visually observed damage during testing as well as the shifting neutral axis due to reduction in competent bedding layer material.

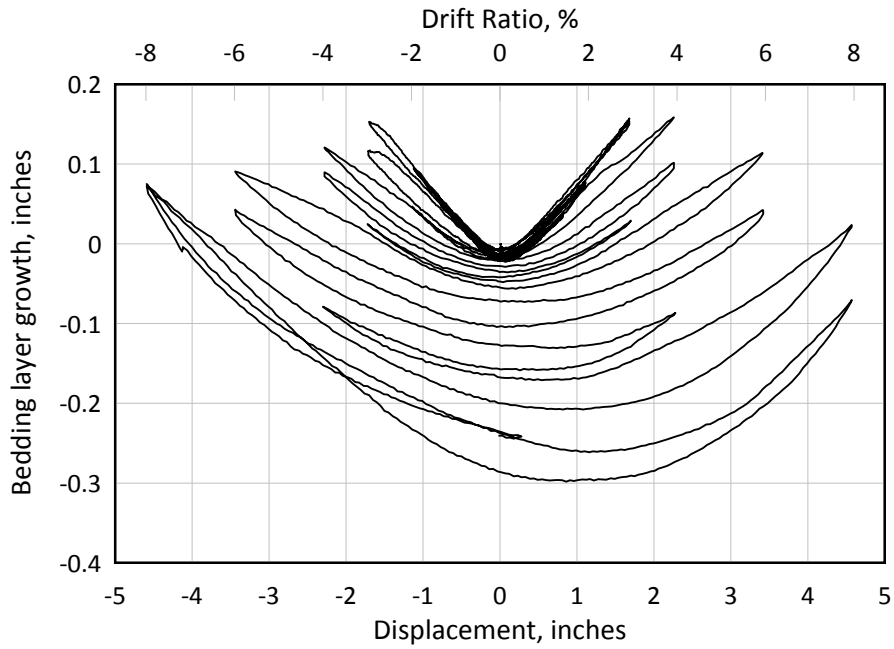

Figure 6.78 HYB-3 centerline of bedding layer deformation

Neutral Axis Depth

Curvature gages at the base of the column were used to determine the depth of the neutral axis for each drift cycle. This depth was calculated considering the assumption that plane sections remain plane in a concrete section, which is a reasonable approximation for the purpose of this calculation. Figure 6.79 shows the neutral axis depth for the first displacement cycle at a given drift level for both push and pull directions. In the initial loading cycles, the neutral axis depth approached 30% of the column diameter at approximately 3% lateral drift ratio. Following these cycles, the neutral axis depth began migrating due to the accumulation of bedding layer grout damage. This results in an observed data trend showing an increase in the recorded neutral axis depth. The neutral axis depth is shown to increase in dimension whereas in reality it is shifting to accommodate the loss of competent grout material. The depth to the neutral axis at the initial stages is slightly greater than desired where the recommended design depth should be no greater than 25% of the column diameter.

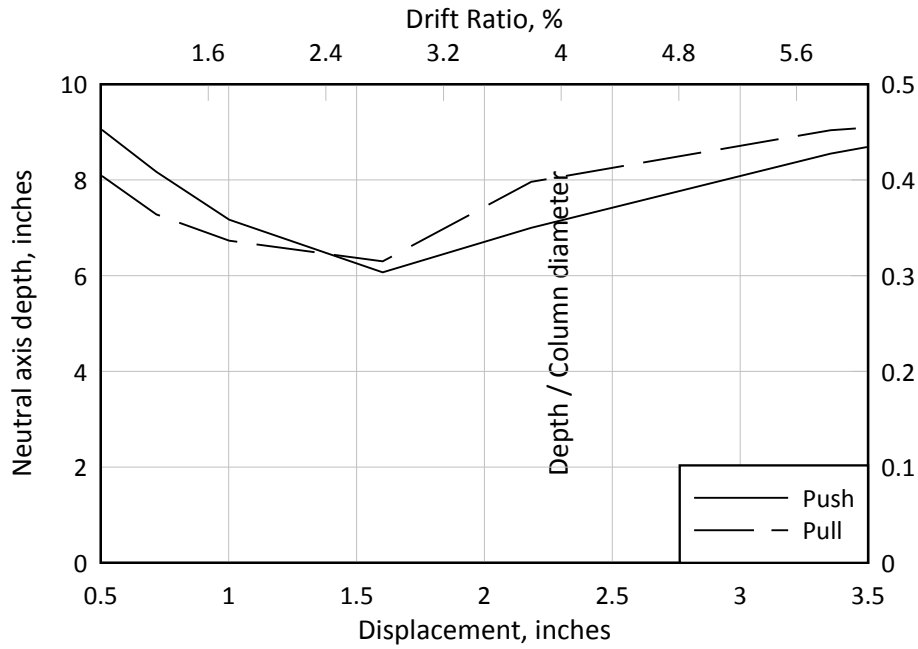

Figure 6.79 HYB-3 neutral axis depth

6.5.2 Rotation Profile

Figure 6.80 provides the column rotation profile, as derived from the column curvature gages. A rotation profile, as opposed to a traditional curvature profile, was provided for this specimen due to the dominance of response on the column fixed end rotation, which cannot be accurately represented by a curvature approximation. This is due to the lack of an effective gage length for consideration due to intentional debonding of reinforcing and post-tensioning at the column end.

These results show that the majority of column drift is provided by the column fixed end rotation, with significantly less influence from the elastic flexural displacements at higher drifts. This observation is consistent with the decomposition of column displacements as previously presented.

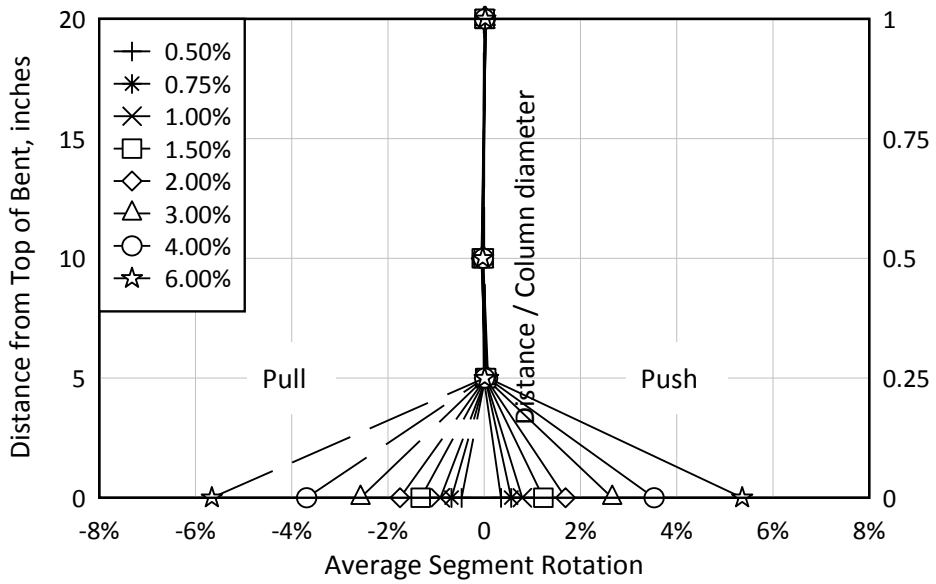

Figure 6.80 HYB-3 column rotation profile

6.5.3 Column Longitudinal Bar Slip

Bar slip readings for the extreme reinforcing bars are presented in Figure 6.81 and Figure 6.82. These readings indicate that the column longitudinal reinforcing bars have adequate development length in the corrugated ducts to properly anchor the bars. The magnitude of longitudinal bar slip is negligible with the maximum recorded value less than three thousandths of an inch during the entirety of the test.

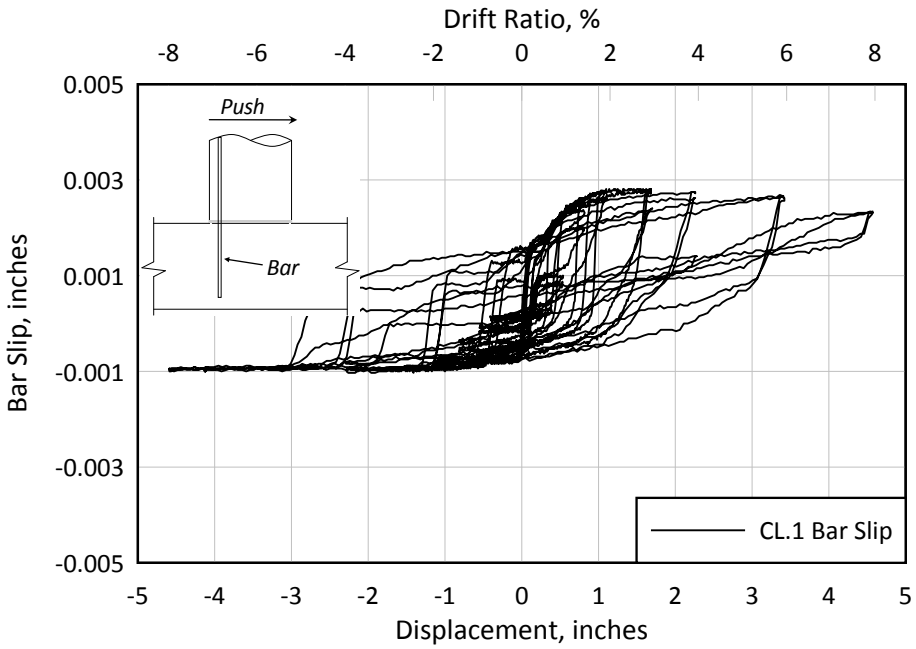

Figure 6.81 HYB-3 column longitudinal bar slip at end of bar (CL.1)

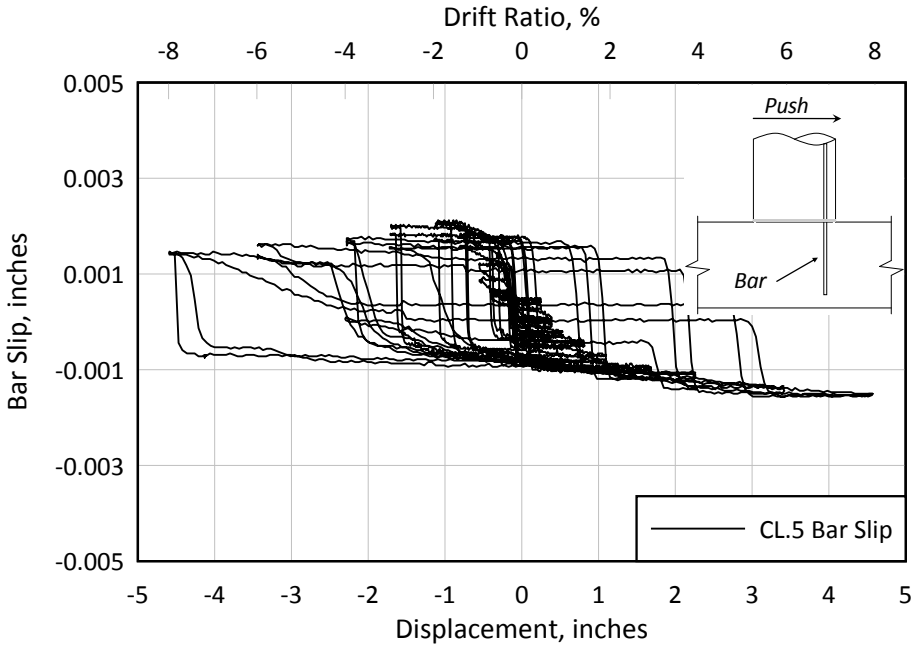

Figure 6.82 HYB-3 column longitudinal bar slip at end of bar (CL.5)

6.5.4 Strain Gage Histories

During construction, a number of strain gages were mounted on various pieces of reinforcing steel throughout the specimen, as well as on the internal and external steel shell. Some gages were damaged during fabrication, erection and testing, thus many readings are not shown herein. Additionally, many plots have incomplete data due to damage or malfunctioning gages. This section provides information on the strain histories recorded by various gages.

Column Longitudinal

Recorded strain gage histories for gages mounted on the extreme column longitudinal bars on the north and south ends of the column are shown in Figure 6.83 thru Figure 6.90. Results from these plots show the first bar yield occurred at a drift level of approximately 0.5% drift ratio for both push and pull directions similar to the other hybrid specimens. Gages mounted in the column all experienced failure subsequent to the 1.5% drift ratio loading cycles. Strain gage readings indicate bars located near the joint were subjected to yielding strains in both the tensile and compressive direction. For bars located in the corrugated duct in the bent cap, only the first strain gage readings indicate strains greater than yield. The other gages further in the bent cap have recorded strains significantly less than yield indicating good development of the reinforcing bar in the duct. Strain readings in the gages that survived past 1.5% drift ratio all show a decrease in tensile strains following the drift cycles to 2% drift ratio. This observation is consistent with the drop in lateral resistance of the system and the associated shift in the neutral axis due to grout degradation.

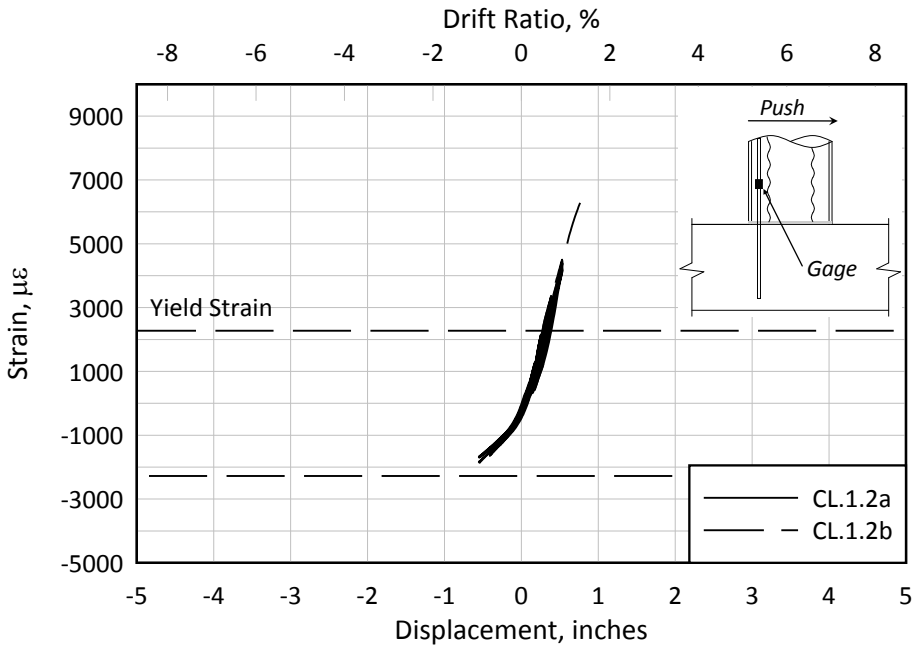

Figure 6.83 HYB-3 column longitudinal rebar strain (CL.1.2)

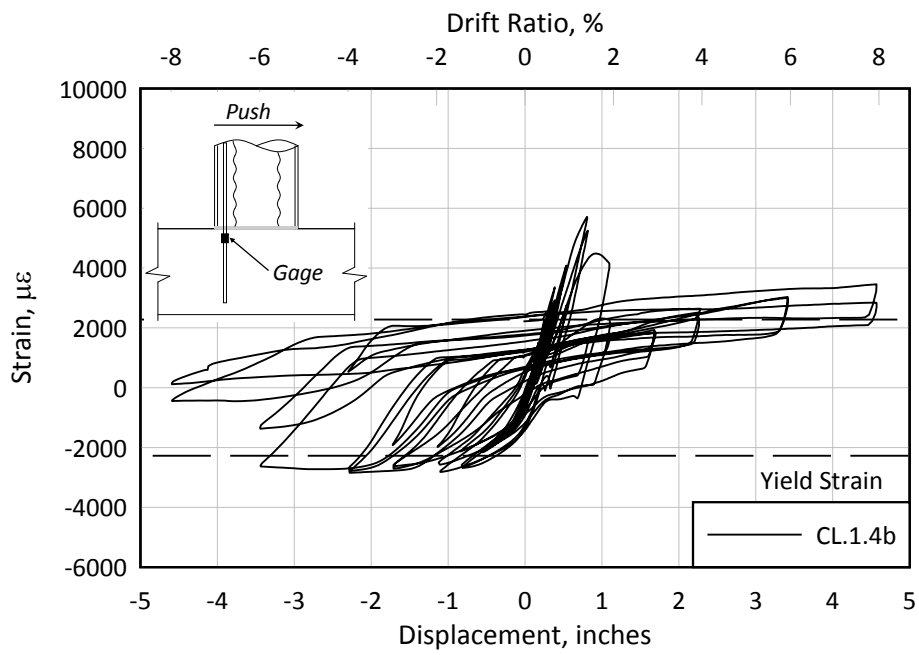

Figure 6.84 HYB-3 column longitudinal rebar strain (CL.1.4)

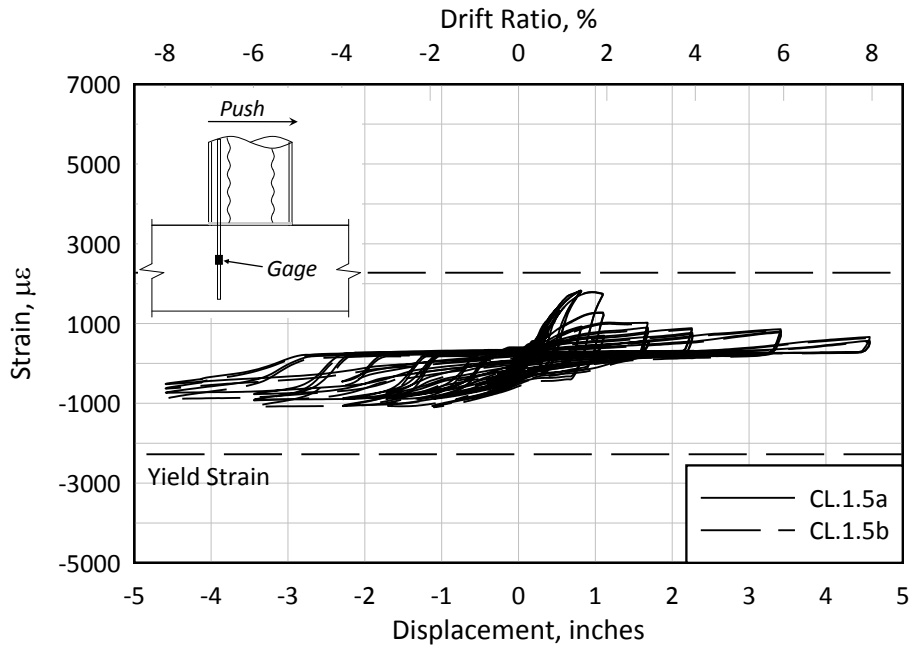

Figure 6.85 HYB-3 column longitudinal rebar strain (CL.1.5)

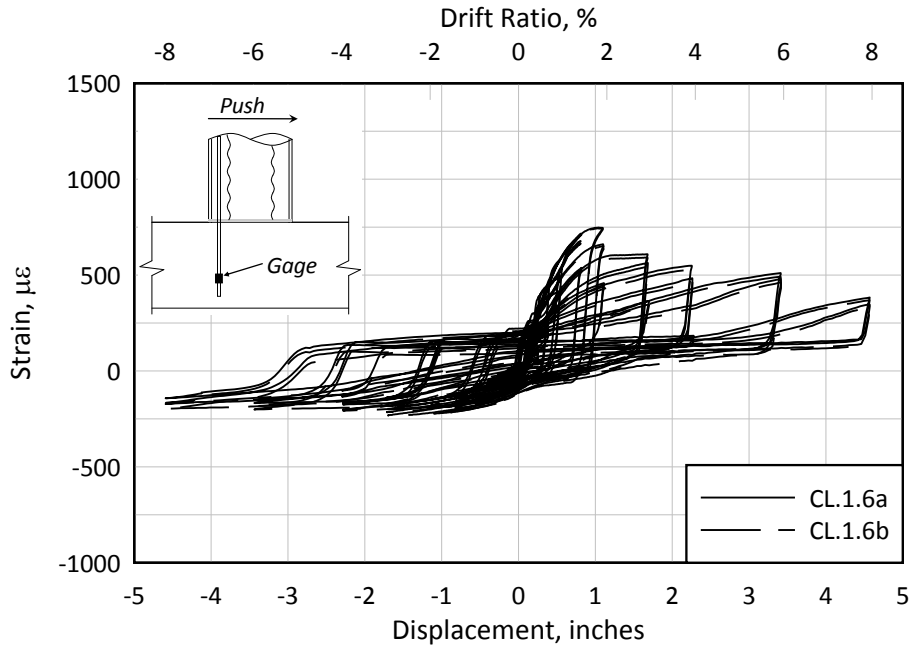

Figure 6.86 HYB-3 column longitudinal rebar strain (CL.1.6)

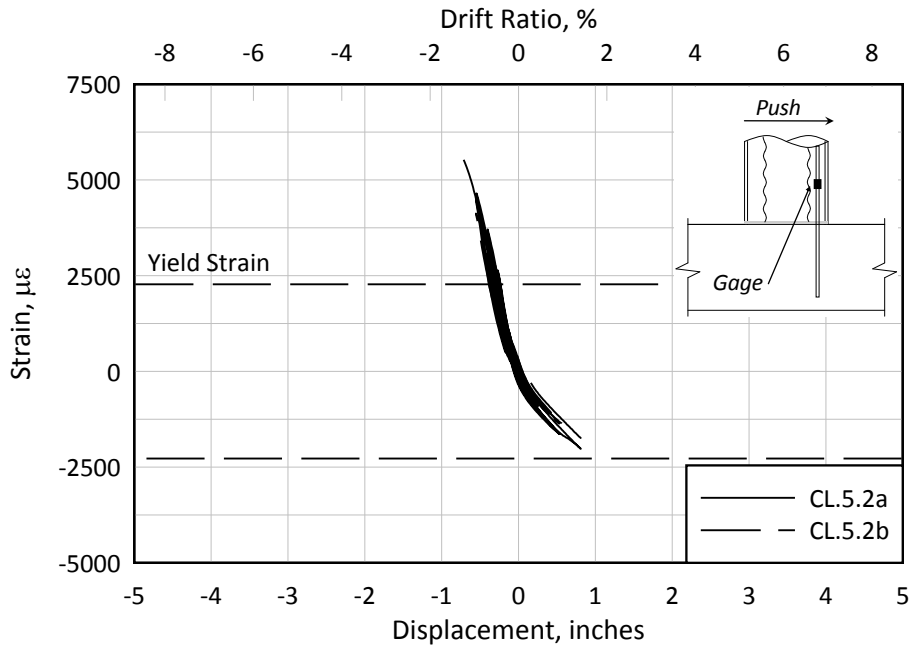

Figure 6.87 HYB-3 column longitudinal rebar strain (CL.5.2)

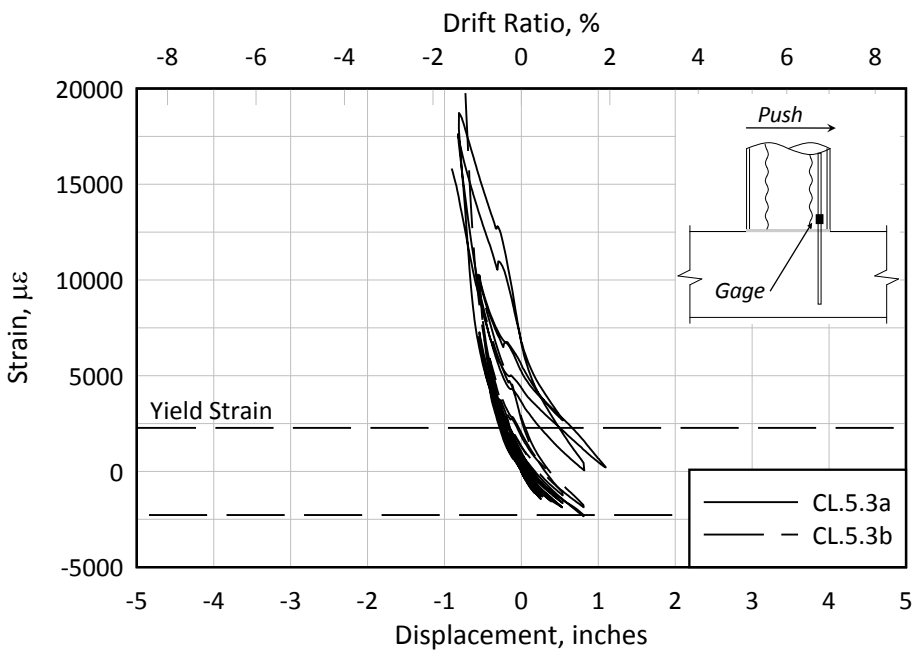

Figure 6.88 HYB-3 column longitudinal rebar strain (CL.5.3)

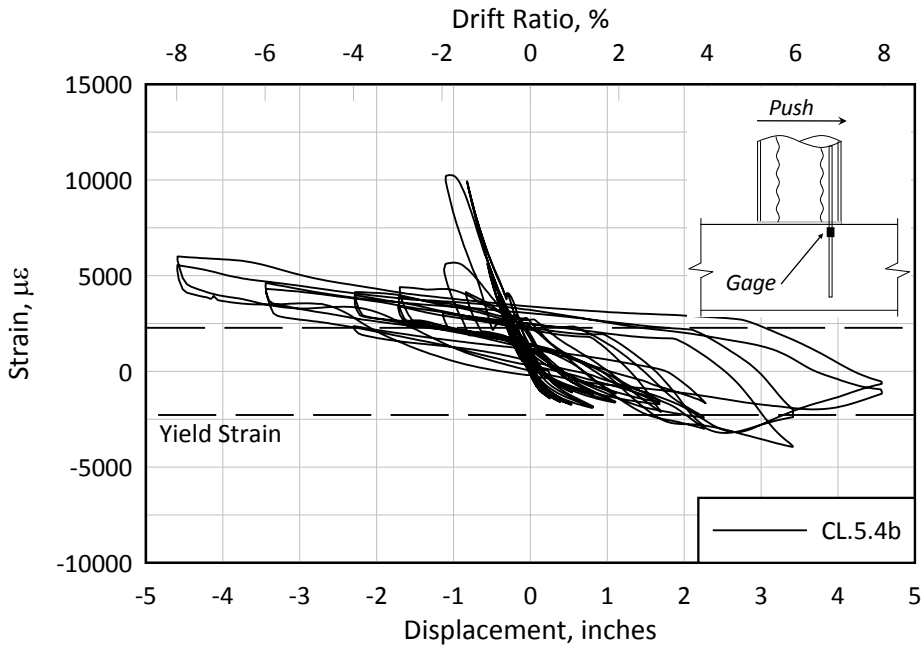

Figure 6.89 HYB-3 column longitudinal rebar strain (CL.5.4)

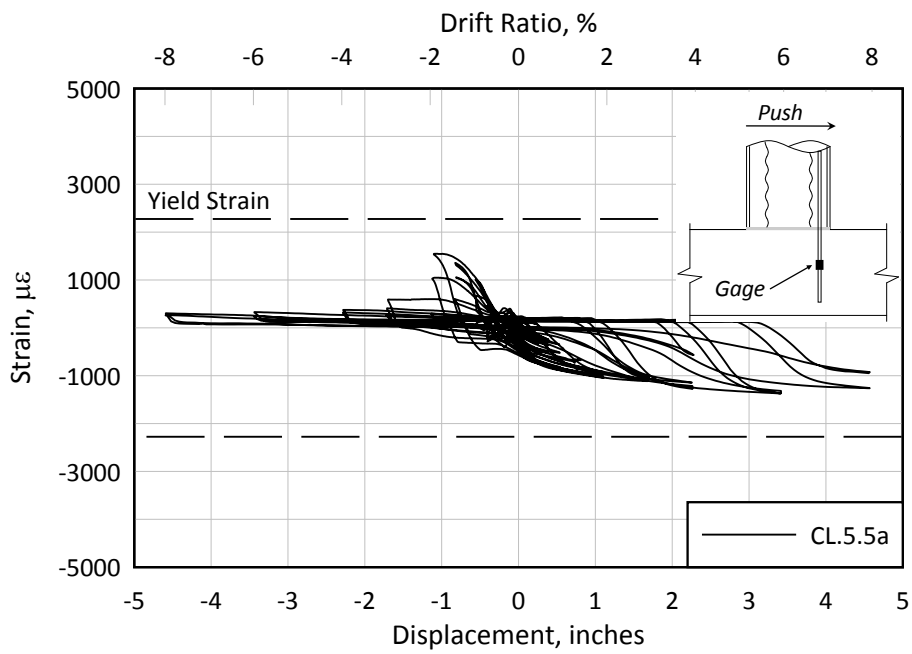

Figure 6.90 HYB-3 column longitudinal rebar strain (CL.5.5)

Post-Tensioning

Strain gage histories for individual post-tensioning strands are provided in Figure 6.91. Strain gage readings show an approximately linear increase in post-tensioning strain with lateral displacement up to approximately 3% drift ratio under both push and pull cycles. Following this drift level, a continuous reduction in stiffness is noted between the lateral displacement and post-tensioning strain. Furthermore, following the lateral drift to 3% drift ratio a continuous reduction in the effective post-tensioning at zero displacement is observed. This signified a reduction in the effective post-tensioning force and an expected reduction in the lateral capacity of the unit, as is observed in the force-displacement response of this specimen. Following the last displacement cycle, the effective post-tensioning stress based on recorded strain is approximately 10% GUTS. The effective post-tensioning at the beginning of testing was approximately 48% GUTS. This loss of effective post-tensioning, coupled with the reduction in effective column diameter, resulted in the continued reduction in lateral capacity observed in the force-displacement response.

Additionally, the effective zero drift point appears to shift under drift levels greater than approximately 6% drift ratio. Based on the post-tensioning histories the total movement at the end of testing appears to be approximately 1 inch to the south, which is consistent with photographic evidence. This sliding response is not noticeable prior to the 6% drift ratio cycles and therefore is not considered a concern for tradition design level drifts.

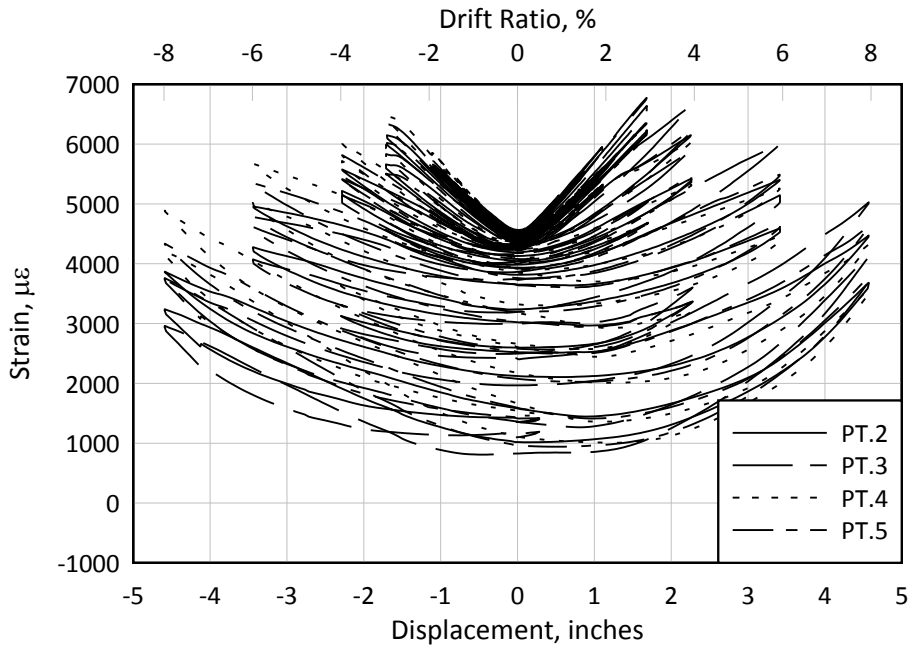

Figure 6.91 HYB-3 post-tensioning strain

Column Confinement (horizontal rosettes on north and south)

Figure 6.92 through Figure 6.95 provide strain gage histories from the horizontal rosette strain gages on the north and south faces of the column shell. These readings relate to the dilatational response of the confined core as it attempts to expand under axial compressive strains. For all measured readings, the strains in the shell are well below the yield strain. However, all strain gage histories show an apparent tensile drift in the zero drift strain under increasing lateral displacements similar to that noted due to yielding. The cause of this drift is unclear due to the significant different between the observed strains and the yield strain of the shell. Under increasing lateral displacement for all readings, a consistent trend is observed with increasing tensile strains for both push and pull directions. The tensile strain in the shell recorded when the shell is on the tensile side of the column are caused by the reinforcing steel development mechanism inside of the shell which also causes dilation of the shell.

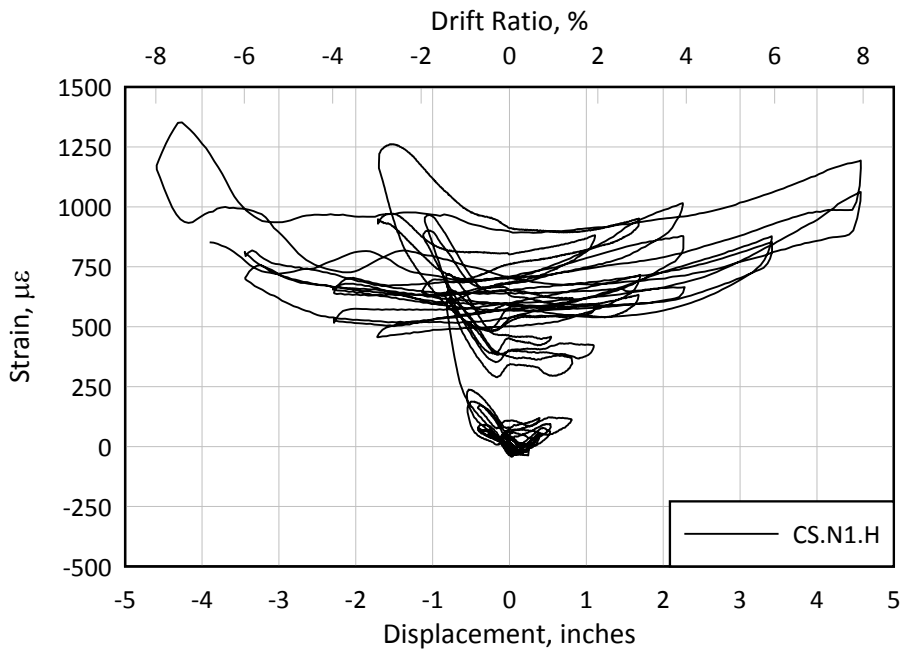

Figure 6.92 HYB-3 column confinement strain (CS.N1.H)

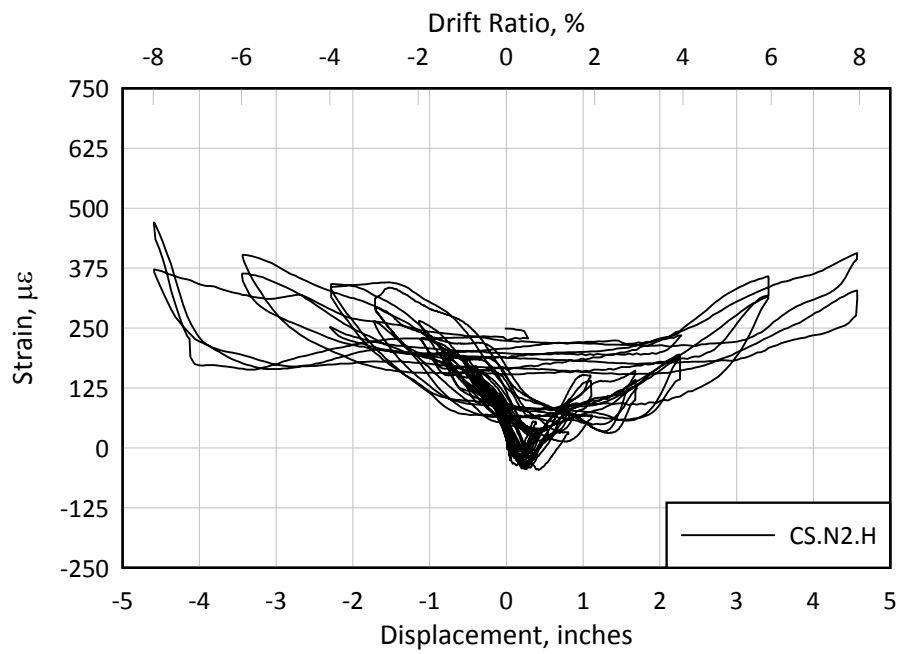

Figure 6.93 HYB-3 column confinement strain (CS.N2.H)

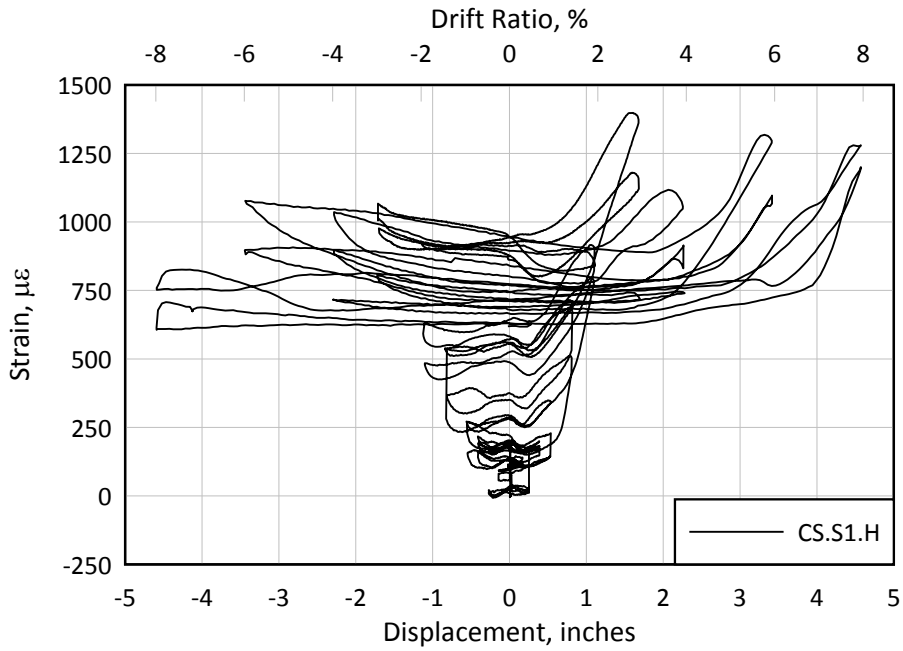

Figure 6.94 HYB-3 column confinement strain (CS.S1.H)

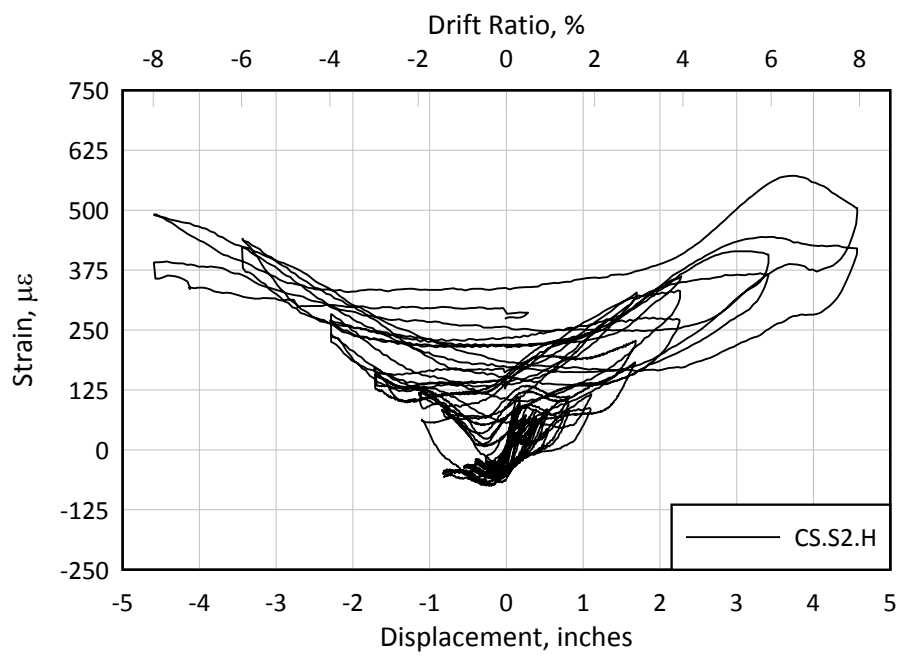

Figure 6.95 HYB-3 column confinement strain (CS.S2.H)

Column Inner Shell Confinement (horizontal rosettes)

Strain gage readings from the horizontal strain gages mounted on the inner corrugated steel pipe are provided in Figure 6.96 and Figure 6.97. The plots provided are only for the northern strain gage readings, as the southern gages did not provide reliable readings during testing. These results indicate that the inner pipe was subjected to significant compressive strains resulting in the yielding of pipe. The large compressive strains were only observed during the cycle in which the section nearest the pipe was in compression. Therefore, this yielding of the pipe is related to the internal pressure induced by the confined concrete onto the pipe. During tensile loading of the section nearest the strain gage, the strain in the pipe is rather constant indicating the reinforcing bar development mechanism does not utilize the inner pipe as expected.

The reduction of the neutral axis depth is expected to reduce the level of inner pipe straining by significantly reducing any internal pressures caused by dilation of the concrete core.

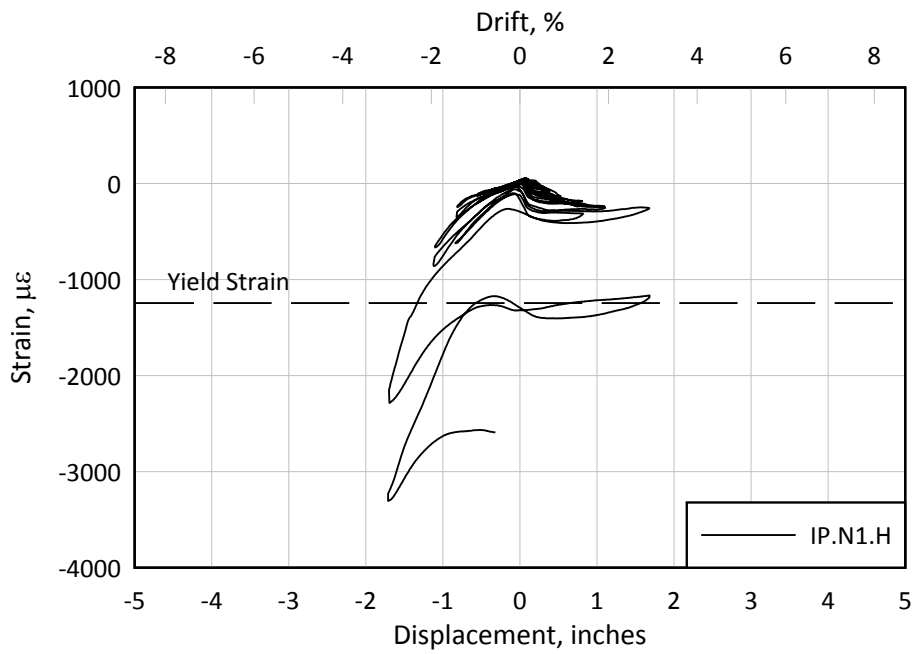

Figure 6.96 HYB-3 inner pipe confinement strain (IP.N1.H)

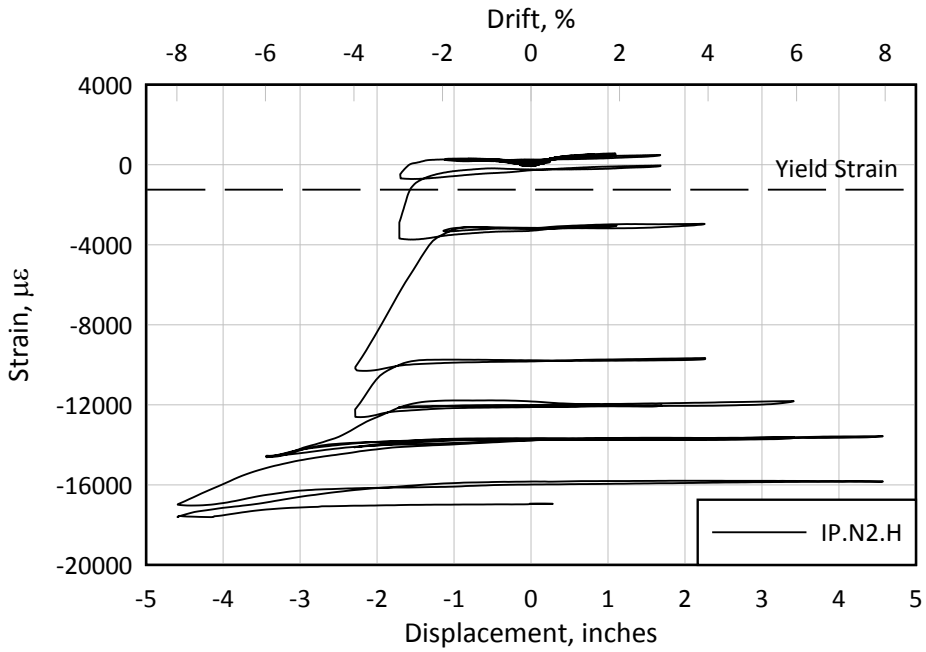

Figure 6.97 HYB-3 inner pipe confinement strain (IP.N2.H)

Column Shear (horizontal rosettes on east and west)

Strain gage readings from the column shear reinforcement are provided in Figure 6.98 through Figure 6.101. These readings indicate a general linear increase in shear with increasing lateral drift up to approximately 3% drift ratio. Following the 3% drift ratio cycles, the magnitude of the shear strain readings decreases due to the reduction in lateral resistance of the system. The recorded strains are well below yield for the shell material.

Figure 6.98 HYB-3 column shear (CS.E1.H)

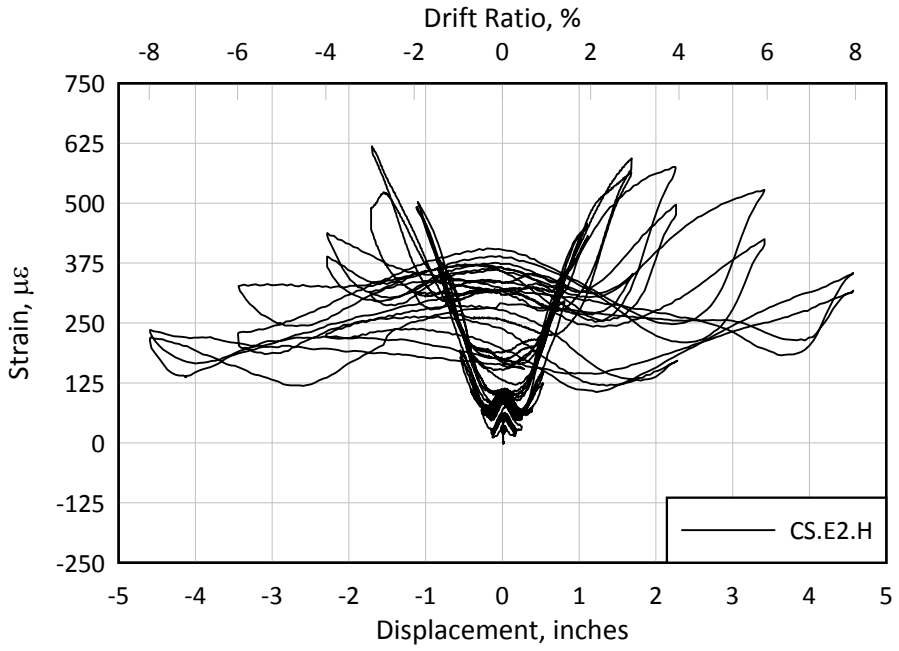

Figure 6.99 HYB-3 column shear (CS.E2.H)

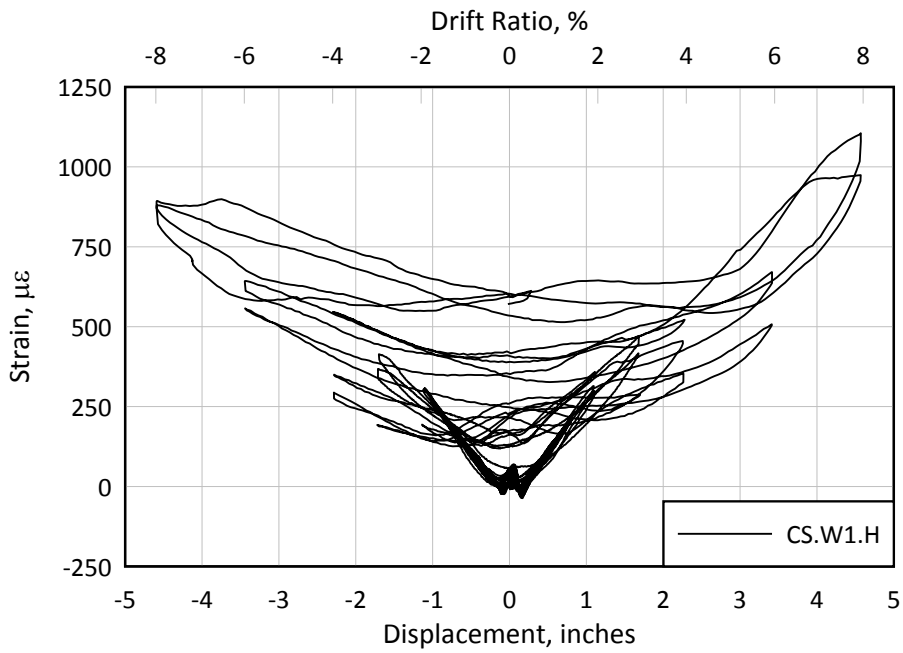

Figure 6.100 HYB-3 column shear (CS.W1.H)

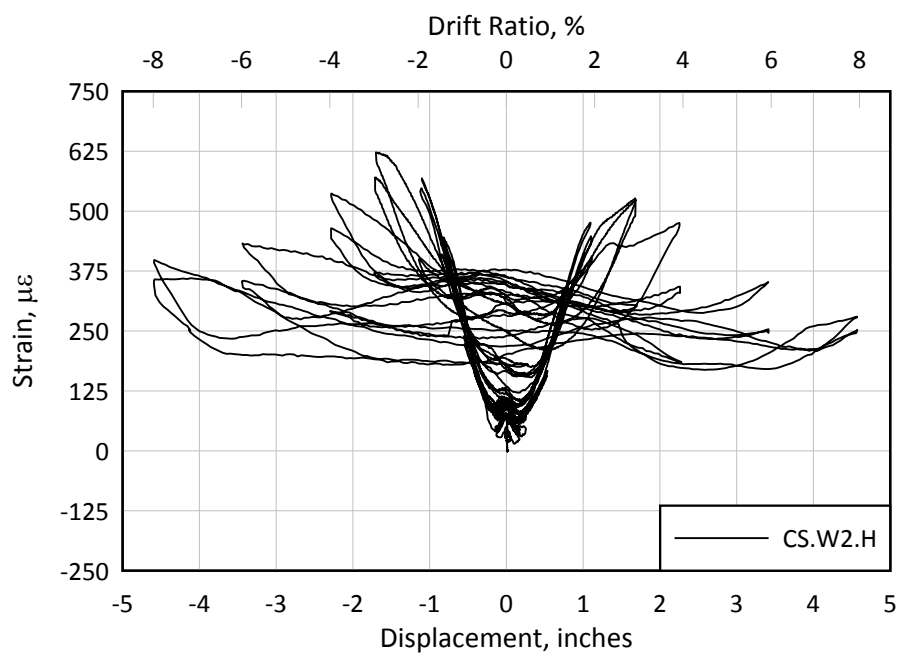

Figure 6.101 HYB-3 column shear (CS.W2.H)

Column Shell Axial (vertical rosettes)

Axial strain readings from the vertical rosette gages are provided in Figure 6.102 through Figure 6.105 for the north and south gages. The recorded strain gage readings from the bottom gages (1" from the end of column) do not have very consistent trends likely caused by the highly disturbed region. However, results do indicate that the axial strain levels in the shell are not significant and are well below yield. The second set of gages into the column show more defined trends with the shell taking both tension and compression during cycled loading. These results confirm the design intention for the shell to begin to act composite as the distance from the joint increases. The shell is expected to take tensile strains as the distance from the end of the shell increases as the design intention is for the tensile force in the column reinforcing bars to transfer into the shell.

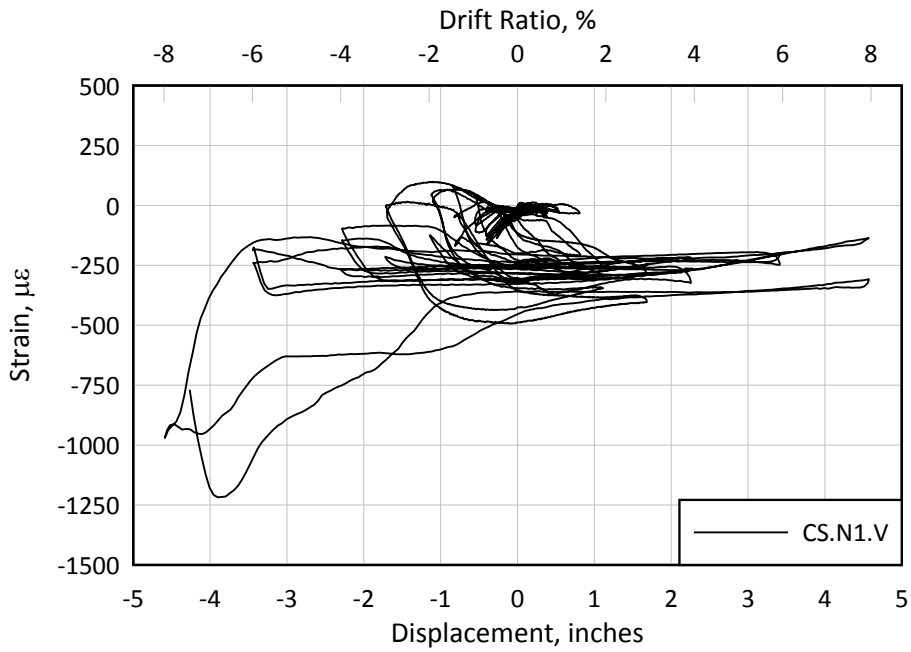

Figure 6.102 HYB-3 column shell axial (CS.N1.V)

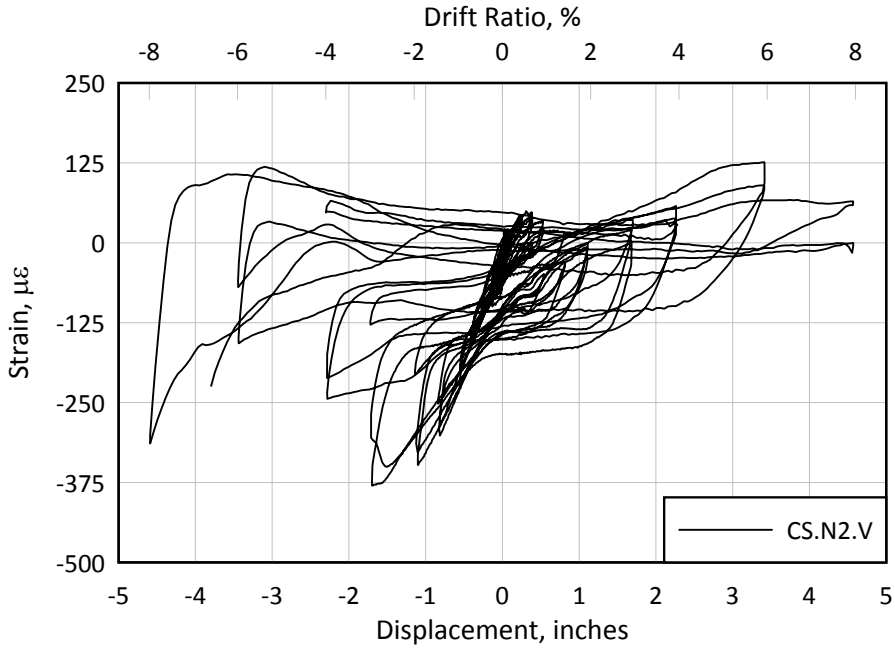

Figure 6.103 HYB-3 column shell axial (CS.N2.V)

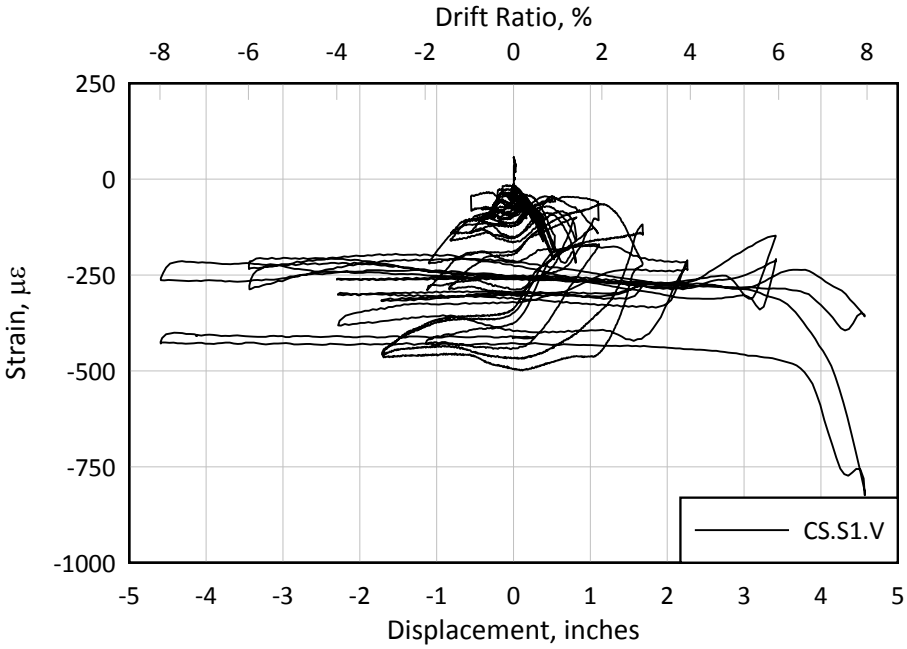

Figure 6.104 HYB-3 column shell axial (CS.S1.V)

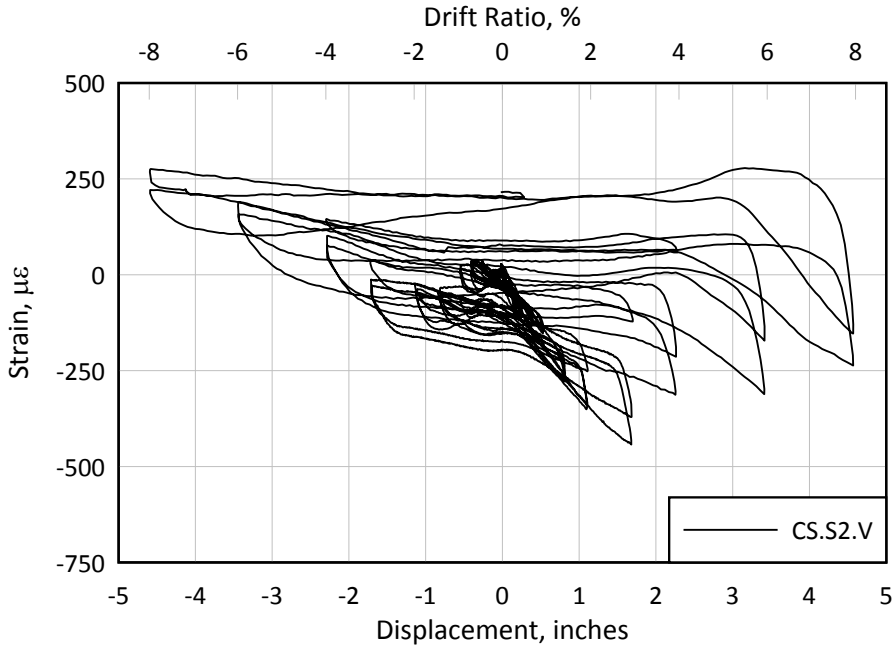

Figure 6.105 HYB-3 column shell axial (CS.S2.V)

Bent Cap Joint

Strain gage histories for the bent cap joint shear reinforcement are provided in Figure 6.106 through Figure 6.111. All recorded strain readings are well below the yield strain of the reinforcing bar except for the east gage on the fifth turn of the spiral. Visual observations during testing, in combination with the recorded strain gage readings, indicate that the level of joint distress was minimal during testing. This is in agreement with the assumed force-transfer mechanism and confirms the joint design assumptions.

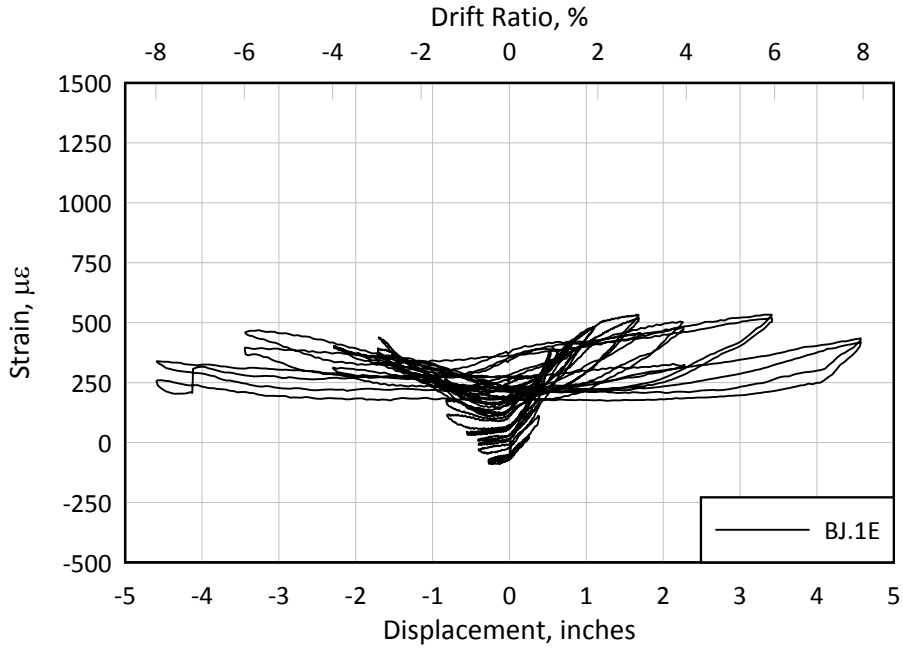

Figure 6.106 HYB-3 bent cap joint shear rebar strain (BJ.1E)

Figure 6.107 HYB-3 bent cap joint shear rebar strain (BJ.1W)

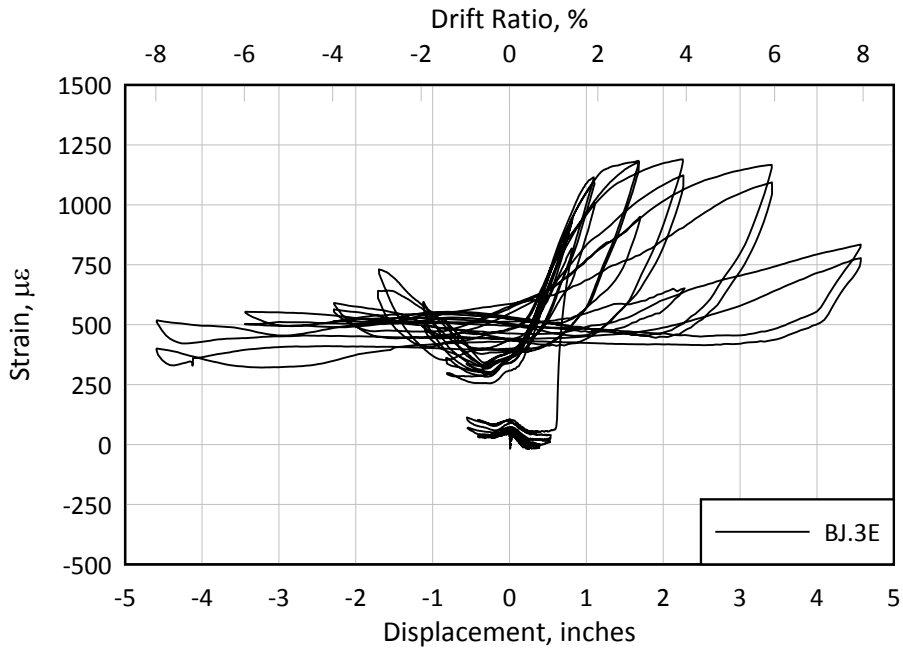

Figure 6.108 HYB-3 bent cap joint shear rebar strain (BJ.3E)

Figure 6.109 HYB-3 bent cap joint shear rebar strain (BJ.3W)

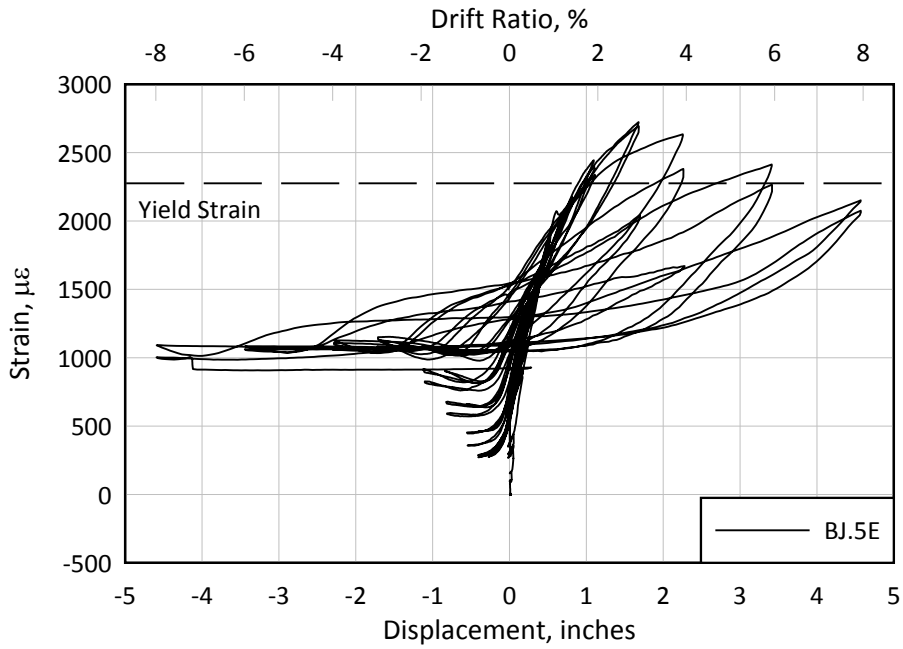

Figure 6.110 HYB-3 bent cap joint shear rebar strain (BJ.5E)

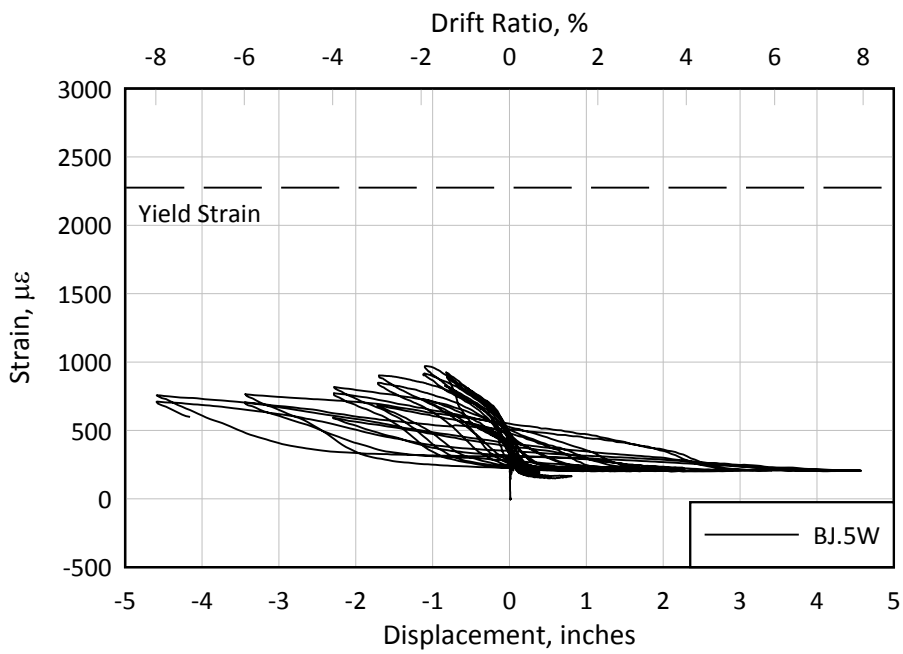

Figure 6.111 HYB-3 bent cap joint shear rebar strain (BJ.5W)

6.5.5 Strain Profiles

Strain gage readings at peak responses in both push and pull directions were used to generate strain profiles for various elements. These profiles were generated for peak points in the loading cycles for the first cycles in both push and pull directions.

Column Longitudinal

Strain gage profiles for the extreme northern and south column longitudinal bars are provided in Figure 6.112 and Figure 6.113, respectively. Column gages were damaged at lower drift levels inside the column and therefore meaningful conclusions can only be provided up to 1% drift ratios. Based on observed readings, the largest strain at any point occurs at the column to bent cap joint as expected, as this is the location of joint opening. Strain penetration into the corrugated ducts is limited and indicates that the bar is fully developed within 12 bar diameters. The requirements specified in ACI ITG-5.2-09 of a development length of 25 times the bar diameter is reasonable based on these results (ACI 2009).

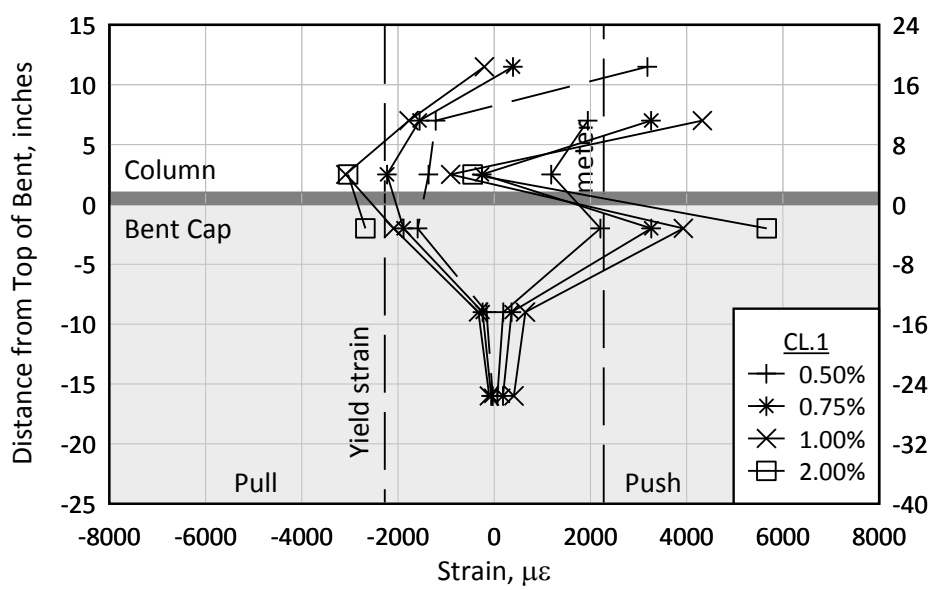

Figure 6.112 HYB-3 column longitudinal rebar strain profile (CL.1-north bar)

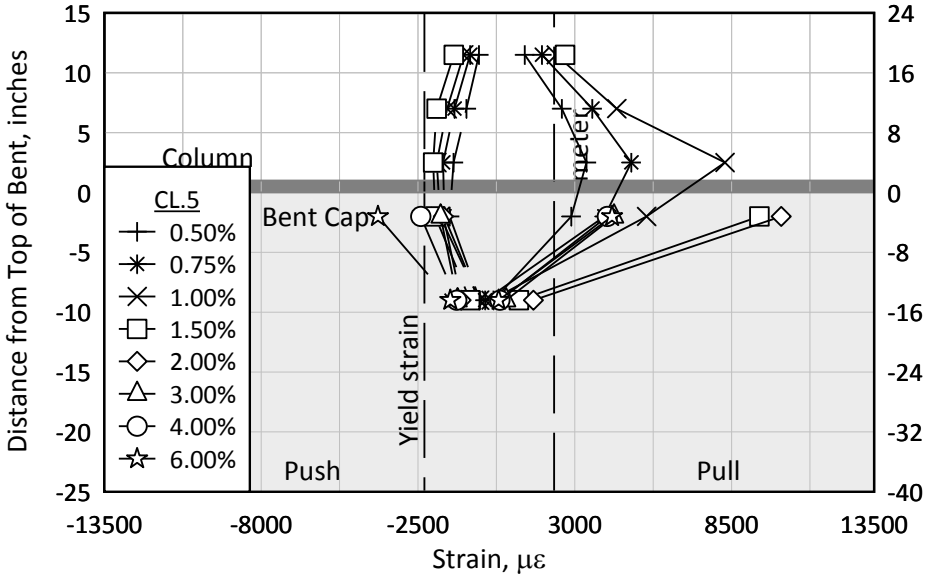

Figure 6.113 HYB-3 column longitudinal rebar strain profile (CL.5-south bar)

Bent Cap Longitudinal

Strain profiles for the bent cap longitudinal reinforcement are provided in Figure 6.114 and Figure 6.115. Readings from these gages indicate that the bent cap longitudinal bar strains are well below yield for all drift cycles. This indicates that the assumed force transfer mechanism is sufficient and conservative for the system tested. Additionally, this verifies the assumption that the bent cap remains essentially elastic under the imposed simulated seismic demands.

Similar to the previous two hybrid specimens, the results show a relative flat strain profile across the majority of the joint during push and pull cycles. These results indicate that the bent cap longitudinal reinforcement does not develop in the joint but maintains constant force across the majority of the joint. This is consistent with the assumed force transfer mechanism.

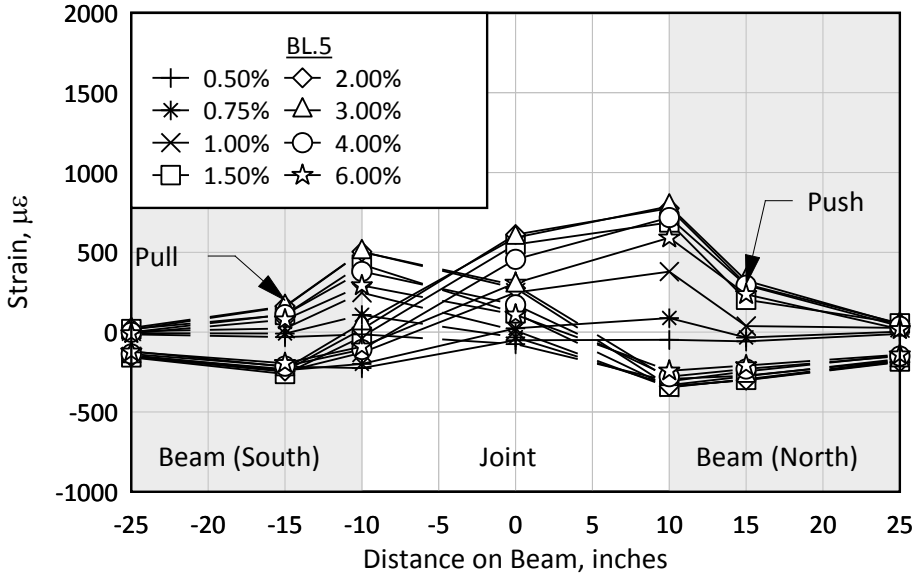

Figure 6.114 HYB-3 bent cap longitudinal rebar strain profile (BL.5)

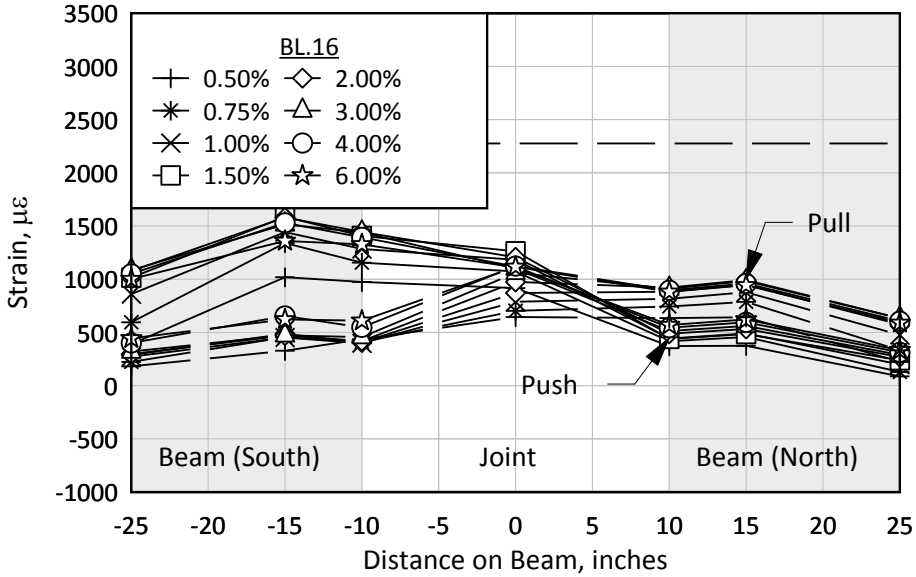

Figure 6.115 HYB-3 bent cap longitudinal rebar strain profile (BL.16)

Joint Shear

Strain profiles for the joint shear reinforcement are shown in Figure 6.116 and Figure 6.117. Results from these readings indicate that the strain in the joint shear reinforcement is all below yield except for the east side at the fifth turn of the spiral, which slightly exceeds yield. The

recorded strain measurements, in combination with visual observations, indicate minimal joint distress occurred during testing.

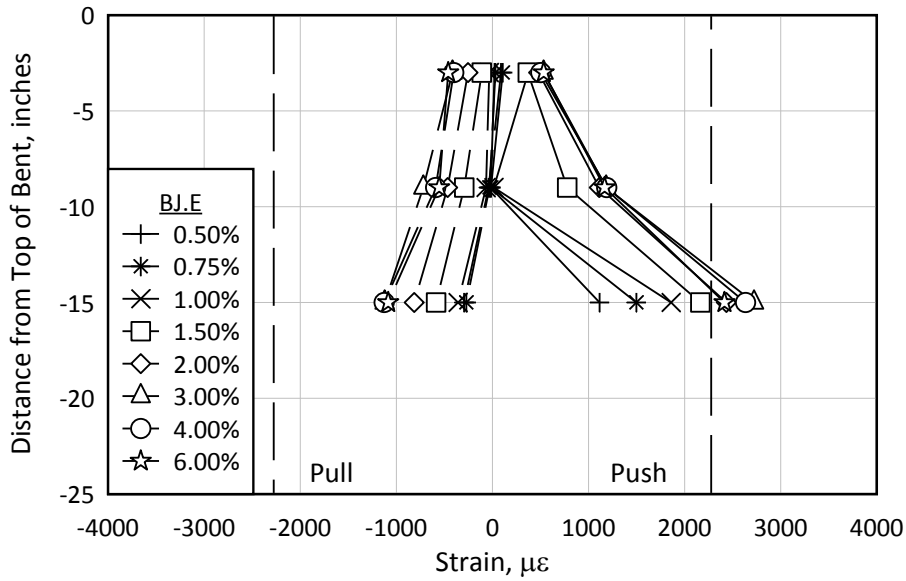

Figure 6.116 HYB-3 bent cap joint shear strain profile (BJ-east gages)

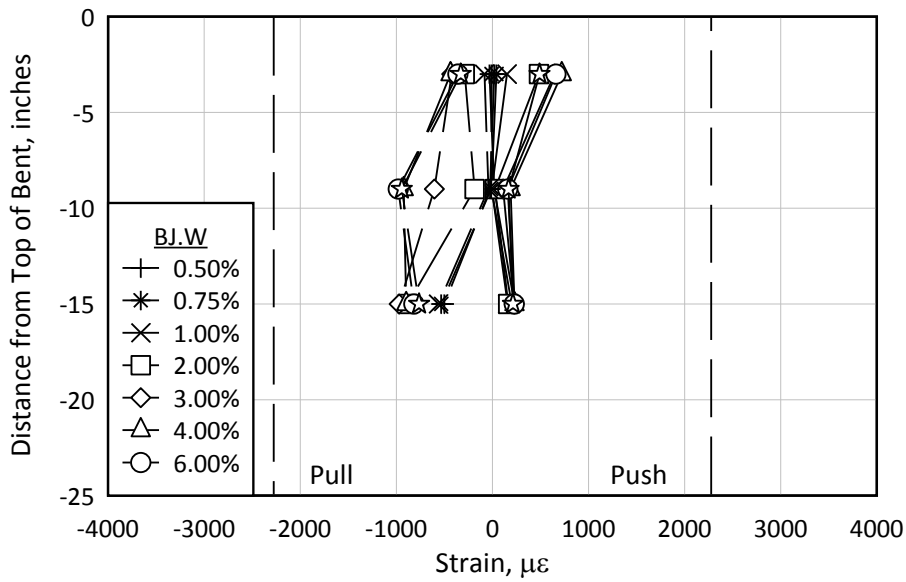

Figure 6.117 HYB-3 bent cap joint shear strain profile (BJ-west gages)

6.6 Summary of Specimen Response and Conclusions

The dual shell hybrid specimen was designed to have similar force-displacement response as compared to the previous two hybrid specimens. The intent of this system design was to have similar response in terms of lateral capacity and cyclic behavior. Similar to the concrete filled pipe hybrid specimen, this unit also utilized a full height steel shell which is intended to provide confinement, shear reinforcement and, within the main portion of the column, flexural reinforcement. However, in addition to the exterior steel shell, this unit also used an interior corrugate metal shell to produce a voided column system. The goal of the voided column is to reduce the column weight and provide a system that is easier to transport and erect in a precast manner. This hybrid specimen was designed, analyzed, constructed and tested to validate the assumptions and response of this system.

Fabrication of this unit took place at an industry facility alongside the concrete filled pipe hybrid specimen by experienced precast concrete personnel without any noted complications. The precaster did voice a concern about casting a full-scale hollow column member. The major concerns relate to the need to provide sufficient support of the internal pipe to prevent floating during the casting operation. Also, similar to the concrete filled pipe detail, the fabricator expects the need to cast the circular column section in a horizontal position with the use of access ports in the exterior shell for pouring concrete and to expel air voids from the unity. Similar to the concrete filled pipe section, the use of non-circular column sections to facilitate easier fabrication does not seem cost-effective. Erection of the unit took place at the university laboratory without any major complications.

During testing, no noticeable damage was observed in the column (specifically in the visible exterior shell). However, localized damage was noted at the bedding layer grout throughout testing. Compressive strains in the bedding layer associated with system lateral response resulted in the accumulation of significant damage to the grout. This damage began to become appreciable following the loading to 2% drift ratio. The degradation of the grout resulted in a reduction in the amount of competent grout material, which in turn resulted in a loss of lateral capacity of the system. Due to the hollow nature of the column, the grout bedding layer area is significantly less than that of the concrete filled pipe hybrid unit. This reduction in area resulted in an increase in bedding layer thickness due to grout degradation as compared to the concrete filled pipe unit.

The majority of the bent cap observed damage consisted of minor joint shear distress and flexural cracking of the member. Similar to the other hybrid specimens, the damage observed in the bent

cap was less than that noted in the cast-in-place control specimen. This reduction in damage is attributable to the inclusion of column post-tensioning which reduced the primary tensile stresses in the joint.

Recorded results for the system force-displacement response shows a loss in lateral capacity subsequent to the 2% drift ratio cycles. This reduction in lateral capacity is attributable to the accumulation of bedding layer damage that resulted in a reduction in the effective column diameter. Furthermore, this damage also resulted in a reduction in the thickness of the bedding layer and in turn a loss of effective post-tensioning force. The ultimate failure of the system was a result of the fracture of a column longitudinal reinforcing bar at the reduced drift cycle following two cycles to 6% drift ratio. Although the ultimate failure was caused by fracture of a column reinforcing bar, conventional practice is to define failure as that point in which the lateral resistance falls below 80% of the maximum lateral resistance. Therefore, for this system failure would be said to occur at 4% drift ratio.

Instrumentation readings from the test were post-processed and reviewed to provide additional insight into the response of the unit. The recorded measurements correlated with the observed reduction in lateral capacity following the drift cycles to approximately 2% drift ratio. Analysis of the hysteretic response indicated appreciable energy dissipation was provided by the system and increased with increasing lateral drift. Up to 3% drift, significant reduction in the residual drift was noted. However, following the 3% drift cycles the residual drifts began to rise rapidly with increasing lateral drift. However, the recorded residual drifts indicate a significant decrease in residual drift as compared to the cast-in-place system.

The predicted force-displacement response of the system provided a reasonable estimate of system response up to approximately 1.7% drift ratio. After this drift level, the predicted response diverged from the recorded response due to the loss of strength of the system during testing. This reduction in capacity and subsequent inadequate prediction of system response are related to the deterioration of the grout bedding layer. The use of fiber reinforced grout will provide enhanced resistance of the bedding layer and subsequently an enhancement in the lateral response of the system. The recently published requirements of ACI ITG-5.2-09 specify a minimum fiber content of 0.1% by volume to provide enhanced toughness of the bedding layer (ACI 2009).

Experimental results indicate acceptable response up to lateral drift levels of approximately 2% drift ratio. Following this lateral displacement level, the overall system response deteriorated due to the accumulation of damage to the bedding layer. This deficiency is expected to be rectified with the use of a high quality, fiber reinforced grout. The goal of using fiber reinforced grout is to

produce a system that is capable of sustaining large compressive strains while maintaining the overall joint integrity. Although the system did not perform entirely as intended, significant enhancements were noted when compared with the cast-in-place control specimen. Improved response was observed in the design level displacement range with significant reductions to the residual drift. Appreciable levels of energy dissipation were observed with only localized system damage as compared to extensive damage noted during the testing of the cast-in-place system. This system provided adequate seismic response even with damage to the grout bedding layer and the overall response is expected to be enhanced through the use of a high quality fiber reinforced grout bedding layer.

6.6.1 Conclusions

Based on experimental observations and readings related to the response of the dual shell hybrid specimen, the following conclusions can be made:

- The dual shell hybrid specimen met the performance objectives up to the design level drift
- The system provides significant lateral displacement capacity with an ultimate displacement of 6% drift ratio
- Design assumptions and predictions match well the measured response up to 2% drift ratio
- Grout bedding layer degradation resulted in significant reduction in the system's lateral capacity
- Degradation of the grout bedding layer should be prevented through the use of fiber reinforced grout material with a minimum 0.1% fiber volume fraction
- Neutral axis depth should be limited to 25% of the column dimension or the 80% of the concrete ring thickness at a maximum
- Amount of mild reinforcement can be reduced to enhance the self-centering ability

Chapter 7 Discussion and Design Recommendations

A comparison of the test specimen performance is provided in this section along with appropriate recommendations for design.

7.1 Discussion of Test Results

All three hybrid specimens were designed, analyzed, constructed and tested to validate the associated design assumptions and procedures. The purpose of the experimental program is to determine if the assumptions used in design provide a reasonable estimate of system response. This section provides an overview of experimental results and a comparison between each specimen detail. Further, a comparison of the design procedures will be presented.

7.1.1 Force-displacement

A comparison of the force-displacement hysteresis response up to a 3% drift ratio is shown in Figure 7.1. It can be observed that the concrete filled pipe and dual shell specimens have generally greater lateral resistance as compared with the conventional hybrid specimen. However, at the 3% drift cycles, the capacities are similar due to the loss of lateral resistance in the second two hybrid specimens due to grout degradation. These hysteretic responses indicate that each system detail has stable lateral response up to 3% drift, which is the extent of the traditional design level displacement.

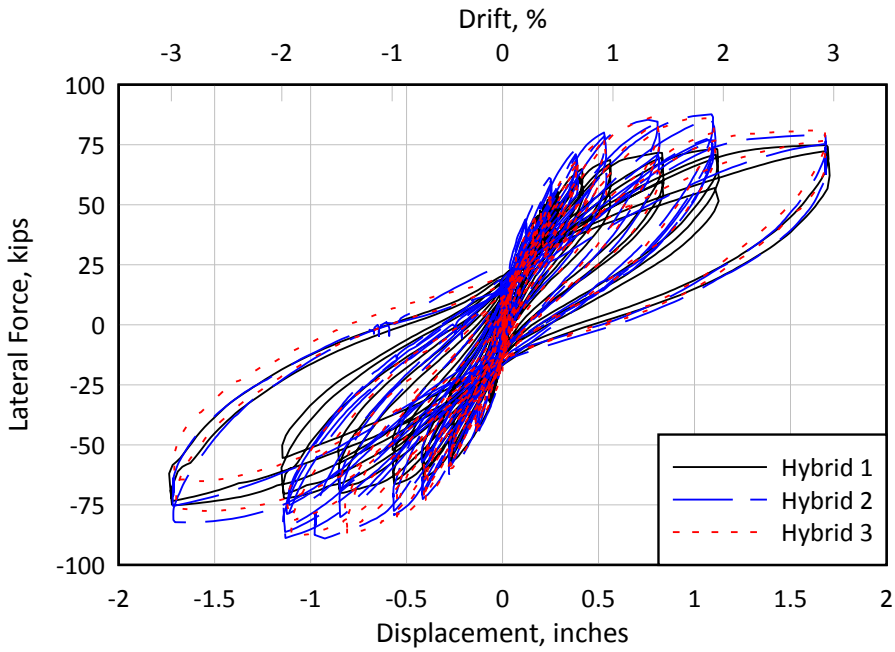

Figure 7.1 Comparison of hybrid specimen response to 3% drift ratio

The first cycle to 2% drift ratio for all three specimens is provided in Figure 7.2. The difference in lateral capacity is again apparent from this plot. Although the lateral resistance of the second and third hybrid specimens is greater than the first, in general the area enclosed by the hysteresis loop is similar implying that each system has a similar energy dissipation capacity. These plots also indicate that each system has an origin-oriented response within the design level drift region. This response characteristic provides an overall self-centering behavior that serves to limit the residual deformations of the system within the design range.

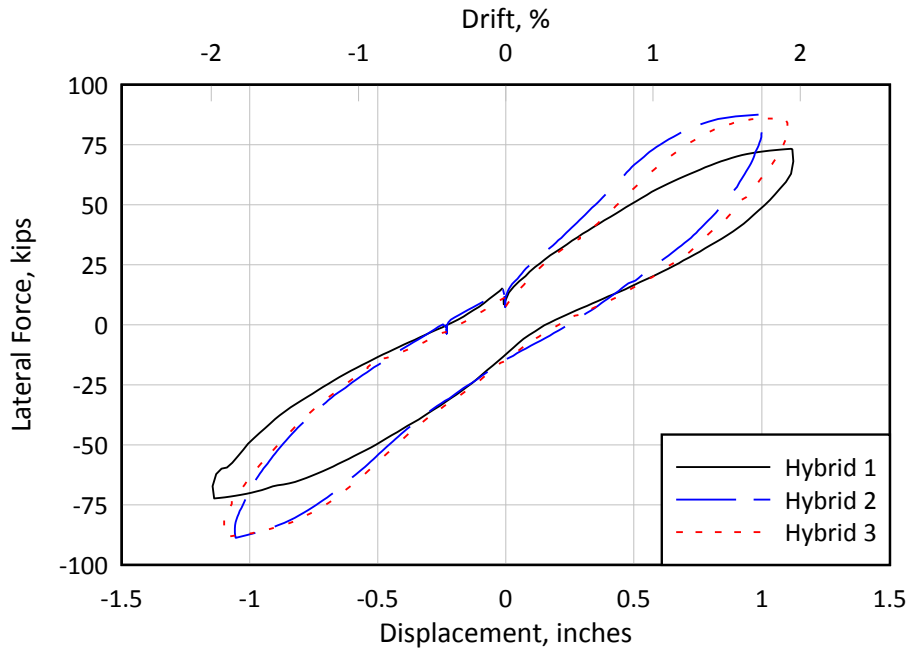

Figure 7.2 Comparison of hybrid specimen response at 2% drift ratio

The overall force-displacement envelopes recorded during testing are provided in Figure 7.3. As mentioned previously, the second and third hybrid specimens have greater lateral resistance as compared to the first specimen up to approximately 3% drift. The degradation of the grout bedding layer in the second two specimens results in a continual reduction in the lateral capacity for specimens two and three. The loss in lateral resistance is greatest for hybrid specimen three, which experienced significant loss in effective post-tensioning due to the reduction in bedding layer thickness caused by grout damage. Each specimen experienced fracture of a longitudinal column bar during a cycle at the 6% drift level.

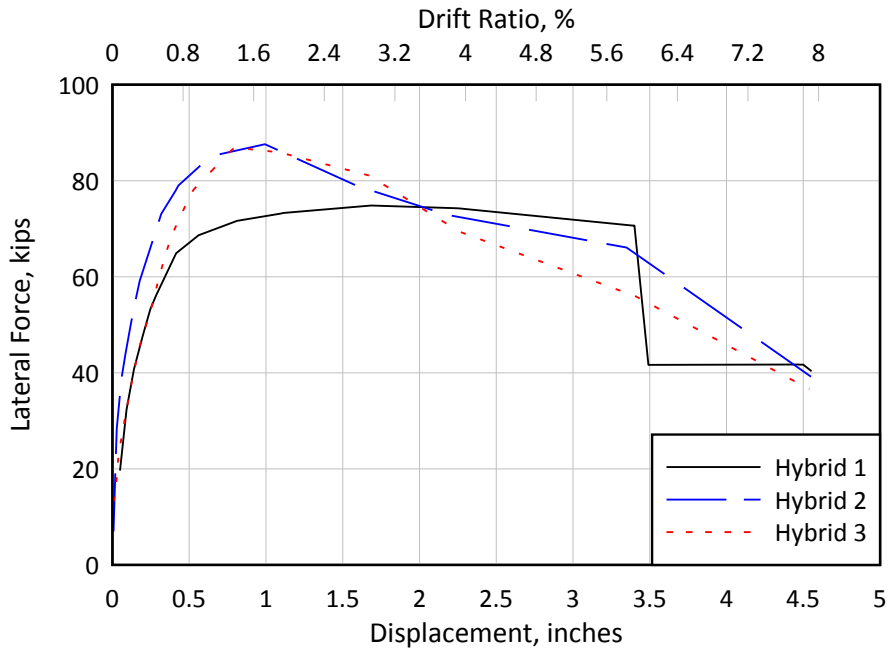

Figure 7.3 Comparison of hybrid specimen force-displacement envelopes

7.1.2 Force-displacement Predictions

The force-displacement predictions using both the complete sectional analysis and the simplified procedure for all three hybrid specimens are shown in Figure 7.4 through Figure 7.6. For the conventional hybrid specimen, both prediction procedures match very well with the observed response from testing. As discussed previously, the complete sectional analysis provides a good representation of the force-displacement envelope up to the predicted failure. However, the prediction underestimates the ultimate displacement capacity, which was predicted to fail due to confined concrete failure. The simplified prediction procedure similarly provides a reasonable representation of the system response in terms of lateral resistance envelope and energy dissipation. The simplified procedure provided an estimate 16.5% equivalent viscous damping at 3% drift ratio with the calculated damping equal to about 17% from the experimental results showing excellent agreement. Both predication methods are therefore deemed reasonable for use with the conventional hybrid details.

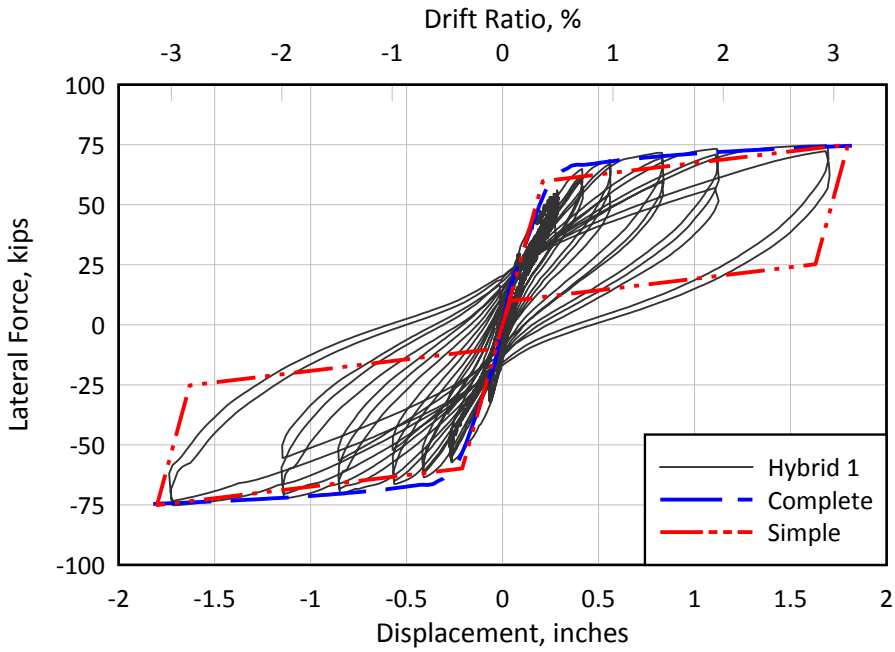

Figure 7.4 Comparison of HYB-1 force-displacement predictions

For the concrete filled pipe hybrid specimen, both predictions provided reasonable estimates of the lateral capacity up to a drift ratio of approximately 2%. Following these drift levels, the experimental performance indicated a reduction in lateral capacity due to degradation of grout, as previously discussed. However, the predictions did not consider this performance and therefore predicted a continuing increase in the lateral capacity following the 2% drift ratio. The simplified prediction method underestimated the energy dissipation present in the system. This method determined the expected equivalent viscous damping to be on the order of 13% whereas the actual calculated damping from experimental results at 3% drift ratio indicated damping on the order of 17.5%. This additional damping observed in testing is partially attributable to the accumulation of damage to the grout bedding layer which will increase the observed damping.

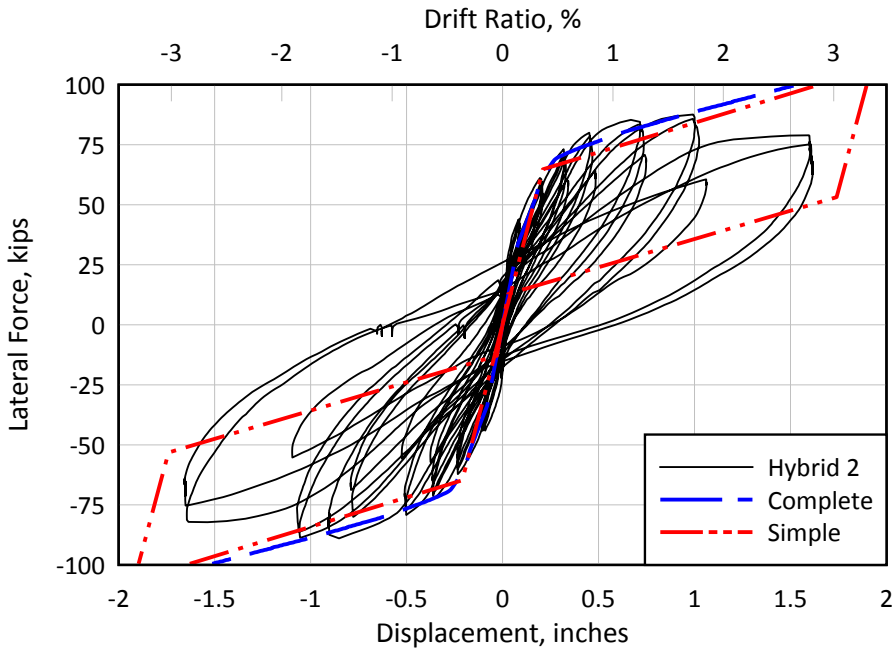

Figure 7.5 Comparison of HYB-2 force-displacement predictions

Similar to the concrete filled pipe specimen, for the dual shell hybrid specimen, both predictions provided reasonable estimates of the lateral capacity up to a drift ratio of approximately 2%. Following these drift levels, the experimental performance indicated a reduction in lateral capacity due to degradation of grout similar to the concrete filled pipe unit. However, the predictions did not consider this performance and therefore predicted a continuing increase in the lateral capacity following the 2% drift ratio. The simplified prediction method underestimated the energy dissipation present in the system. This method determined the expected equivalent viscous damping to be on the order of 13% whereas the actual calculated damping from experimental results at 3% drift ratio indicated damping on the order of 17%. This additional damping observed in testing is partially attributable to the accumulation of damage to the grout bedding layer which will increase the observed damping.

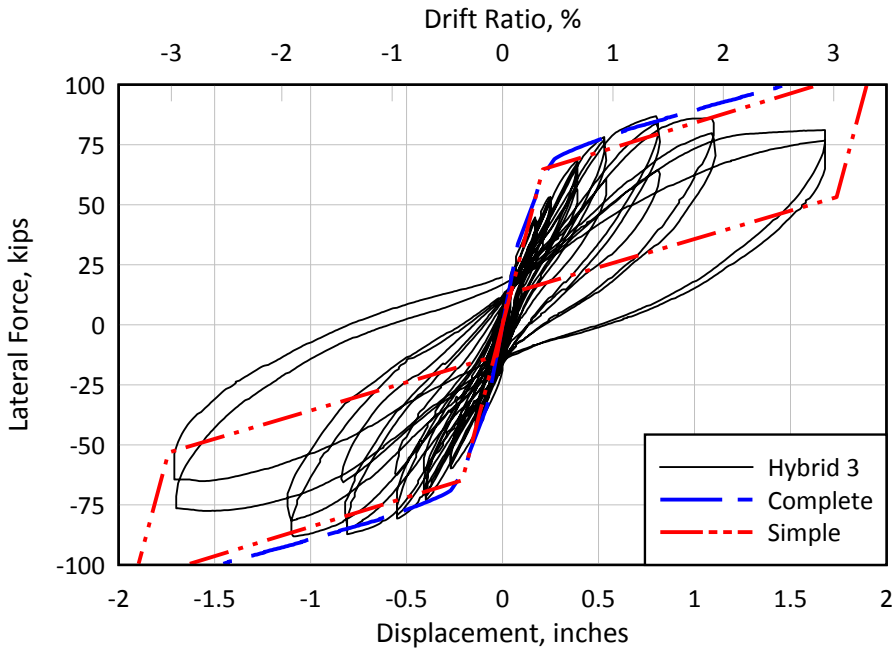

Figure 7.6 Comparison of HYB-3 force-displacement predictions

7.1.3 Residual Drift

The residual drift ratios for each specimen are shown in Figure 7.7. From this plot it is apparent that the second and third hybrid specimens have greater residual drifts as compared to the first hybrid unit. This response is due in part to the more appreciable accumulation of grout damage observed in the last two hybrid units. For the first hybrid unit, the concrete column compressive strength was appreciably less than that of the grout material. Thus, the localized damage to the grout was not as apparent. However, for the second and third hybrid units the column concrete compressive strengths were nearly the same as the grout. Additionally the second two units had enhanced confinement due to the steel shell. The strength and confinement properties of the second two units produced a system with a mismatch in material stiffness where the grout material had a noticeably lower stiffness as compared to the column. This resulted in a concentration of strains that resulted in increases in the bedding layer damage.

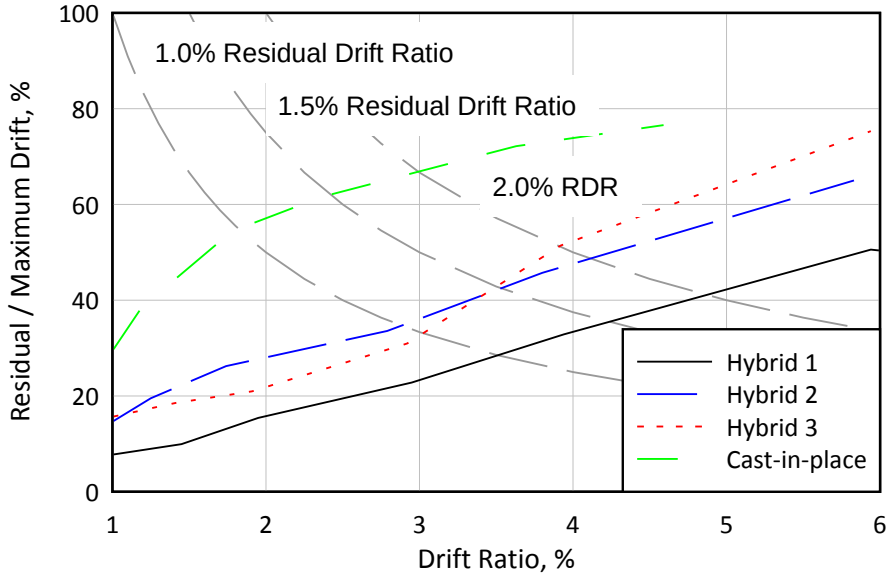

Figure 7.7 Comparison of hybrid specimen residual drift ratio

7.1.4 Conclusions

Based on experimental observations and readings related to the response of the three hybrid specimens, the following conclusions can be made:

- All specimens met the performance objectives up to the design level drift
- All specimens provided significant lateral displacement capacity with an ultimate displacement of approximately 6% drift ratio
- Design assumptions and predictions match well the measured response up to the design level drift
- For the concrete filled pipe and dual shell specimens the predictions diverged from observed response after approximately 2% drift ratio due to grout degradation
- Degradation of the grout bedding layer should be prevented through the use of fiber reinforced grout material with a minimum 0.1% fiber volume fraction
- Ultimate deformation capacity was underestimated using the Mander model for confined concrete as the failure was attributable to column reinforcing fracture, not failure of the confined core
- Neutral axis depth should be limited to 25% of the column dimension at a maximum and the amount of mild reinforcement may be reduced to enhance the self-centering ability.
- Reinforcing bars were shown to fully develop within 16 bar diameters for all specimens

7.2 Design Recommendations

Based on the results obtained from experimental and analytical efforts, the following recommendations are provided for the design of hybrid specimens:

- Both the simplified and complete sectional analysis methods provide reasonable estimates of the lateral response of any of the hybrid details
- The bent cap should be capacity designed considering a maximum seismic moment equal to 1.1 times the moment demand calculated using the ultimate base shear capacity from either the simplified or complete sectional analysis
- For the joint shear design, the provisions from the AASHTO Seismic Design Specification are reasonable and conservative for the design in a hybrid system when considering the influence of the post-tensioning
- Joint shear hoop/spiral reinforcement may be controlled by post-tensioning general zone design and should be considered in addition to joint shear design
- The lateral capacity provided by the mild reinforcement at yield should be minimized and maintained as close to 25% of the overall capacity if practical
- Neutral axis depth at yield and beyond should be kept as low as possible to promote self-centering response and minimize compressive strains in the grout bedding layer
- The maximum neutral axis depth should be limited to a maximum of 25% of column diameter or 80% of thickness of concrete band for hollow columns
- Bedding layer should be constructed of a high quality, non-bleed cementitious grout material using a nominal volumetric fiber fraction of 0.1%
- The recommendations of ACI ITG-5.2-09 should be used for development length of reinforcement in corrugated ducts, which specifies embedment of 25 times the bar diameter (ACI 2009)

REFERENCES

AASHTO. "Guide Specifications for LRFD Seismic Bridge Design, 1st Edition." Washington, DC, 2009.

AASHTO. "LRFD Bridge Design Specifications, 4th Edition." Washington, DC, 2007.

AASHTO. "Recommended Guide Specifications for LRFD Seismic Bridge Design." Washington, D.C., 2007.

ACI. *ACI ITG-5.2-09 Requirements for Design of a Special Unbonded Post-Tensioned Precast Shear Wall Satisfying ACI ITG-5.1 and Commentary.* American Concrete Institute, 2009.

ASCE. *Report Card for America's Infrastructure.* 2009. http://www.infrastructurereportcard.org/ (accessed May 10, 2009).

BASF. *Masterflow 928 Product Data.* 2006.

Caltrans. "Seismic Design Criteria, Version 1.4." Sacramento, CA, 2006.

Dodd, L L, and J I Restrepo-Posada. "Model for Predicting Cyclic Behavior of Reinforcing Steel." *ASCE Journal of Structural Engineering* 121, no. 3 (1995): 433-445.

Englekirk, R E. "Design-Construction of the Paramount - A 39-Story Precast Prestressed Concrete Apartment Building." *PCI Journal* 47, no. 4 (2002): 56-71.

Heiber, D G, J M Wacker, M O Eberhard, and J F Stanton. *Precast Concrete Pier Systems for Rapid Construction of Bridges in Seismic Regions.* Rep. No. WA-RD 611.1, Olympia, WA: Washington Department of Transportation, 2005.

Hewes, J T, and M J N Priestley. "Seismic Design and Perfomance of Precast Concrete Segmental Bridge Columns." Report No. SSRO-2001/25, Department of Structural Engineering, University of California San Diego, La Jolla, CA, 2002.

Hines, E M, J I Restrepo, and F Seible. "Force-Displacement Characterization of Well-Confined Bridge Columns." *ACI Structural Journal* 101, no. 4 (2004): 537-548.

Holden, T J, J I Restrepo, and J B Mander. "A Comparison of the Seismic Performance of Precast Wall Construction: Emulative and Hybrid Approaches." Research Rpt. 2001-4, Depertment of Civil Engineering, University of Canterbury, 2001.

Kwan, W P, and S Billington. "Unbonded Posttensioned Concrete Bridge Piers. I: Monotonic and Cyclic Analyses." *ASCE Journal of Bridge Engineering* 8, no. 2 (2003): 92-101.

Kwan, W P, and S Billington. "Unbonded Posttensioned Concrete Bridge Piers. II: Seismic Analyses." *ASCE Journal of Bridge Engineering* 8, no. 2 (2003): 102-111.

MacRae, G A, and M J N Priestley. "Precast Post-Tensioned Ungrouted Concrete Beam-Column Subassemblage Tests." Report No. SSRP-94/10, Department of Structural Engineering, University of California San Diego, 1994.

Mander, J B, and C-T Cheng. "Seismic Resistance of Bridge Piers Based on Damage Avoidance Design." Technical Report NCEER-97-0014, NCEER, Department of Civil and Environmental Engineering, State University of New York at Buffalo, 1997.

Mander, J B, M J N Priestley, and R Park. "Theoretical Stress-Strain Model for Confined Concrete." *ASCE Journal of Structural Engineering* 114, no. 8 (1988): 1804-1826.

MATLAB. "MATLAB 2009a (V7.8) User's Manuel." 2009.

Matsumoto, E E. "CSUS Component Test Report - Cast-in-place Specimen (Unit 1), Draft." Department of Civil Engineering, California State University Sacramento, 2008, 93.

Palermo, A, S Pampanin, and G M Calvi. "Use of 'Controlled Rocking' in the Seismic Design of Bridges." *Proceedings of the 13th World Conference on Earthquake Engineering.* Vancouver, BC, 2004. Paper No. 4006.

Paulay, T, and M J N Priestley. *Seismic Design of Reinforced Concrete and Masonry Buildings.* New York: John Wiley and Sons, 1992.

Priestley, M J N, and J R T Tao. "Seismic Response of Precast Prestressed Concrete Frames with Partially Debonded Tendons." *PCI Journal* 38, no. 1 (1993): 58-69.

Priestley, M J N, F Seible, and G Benzoni. "Seismic Performance of Circular Columns with Low Longitudinal Steel Ratios." Report No. SSRP 94/08, Department of Structural Engineering, University of California San Diego, La Jolla, CA, 1994.

Priestley, M J N, F Seible, and G M Calvi. *Seismic Design and Retrofit of Bridges.* New York, NY: John Wiley and Sons, 1996.

Priestley, M J N, S Sritharan, J R Conley, and S Pampanin. "Preliiminary Results and Conclusions from the PRESSS Five-Story Precast Concrete Test Building." *PCI Journal* 44, no. 6 (1999): 42-67.

Restrepo, J I, and A M Rahman. "Precast/Prestressed Concrete Sturctures under Natural and Human-made Hazards." *ASCE Journal of Structural Engineering*, 2007.

Sakai, J, and S A Mahin. *Analytical Investigations of New Methods for Reducing Residual Displacements of Reinforced Concrete Bridge Columns.* Rep. No. PEER 2004/02, Berkeley, CA: Pacific Earthquake Enigneering Research Center, 2004.

Sakai, J, J Hyungil, and S A Mahin. "Reinforced Concrete Bridge Columns that Recenter Following Earthquakes." *Proceedings of the 8th U.S. National Conference on Earthquake Engineering.* San Francisco, CA, 2006. Paper No. 1421.

Stone, W C, G S Cheok, and J F Stanton. "Performance of Hybrid Moment-Resisting Precast Beam-Column Concrete Connections Subjected to Cyclic Loading." *ACI Structural Journal* 91, no. 2 (1995): 223-249.

Toranzo, L. "The Use of Rocking Walls in Confined Masonry Structures: A Performance-based Approach." PhD Thesis, Department of Civil Engineering, University of Canterbury, New Zealand, 2002.

U.S. DOT, Research and Innovative Technology Administration, Bureau of Transportation Statistics. "Transportation Statistics Annual Report 2007." Washington, D.C., 2007.

Appendix A Conventional Specimen Drawings

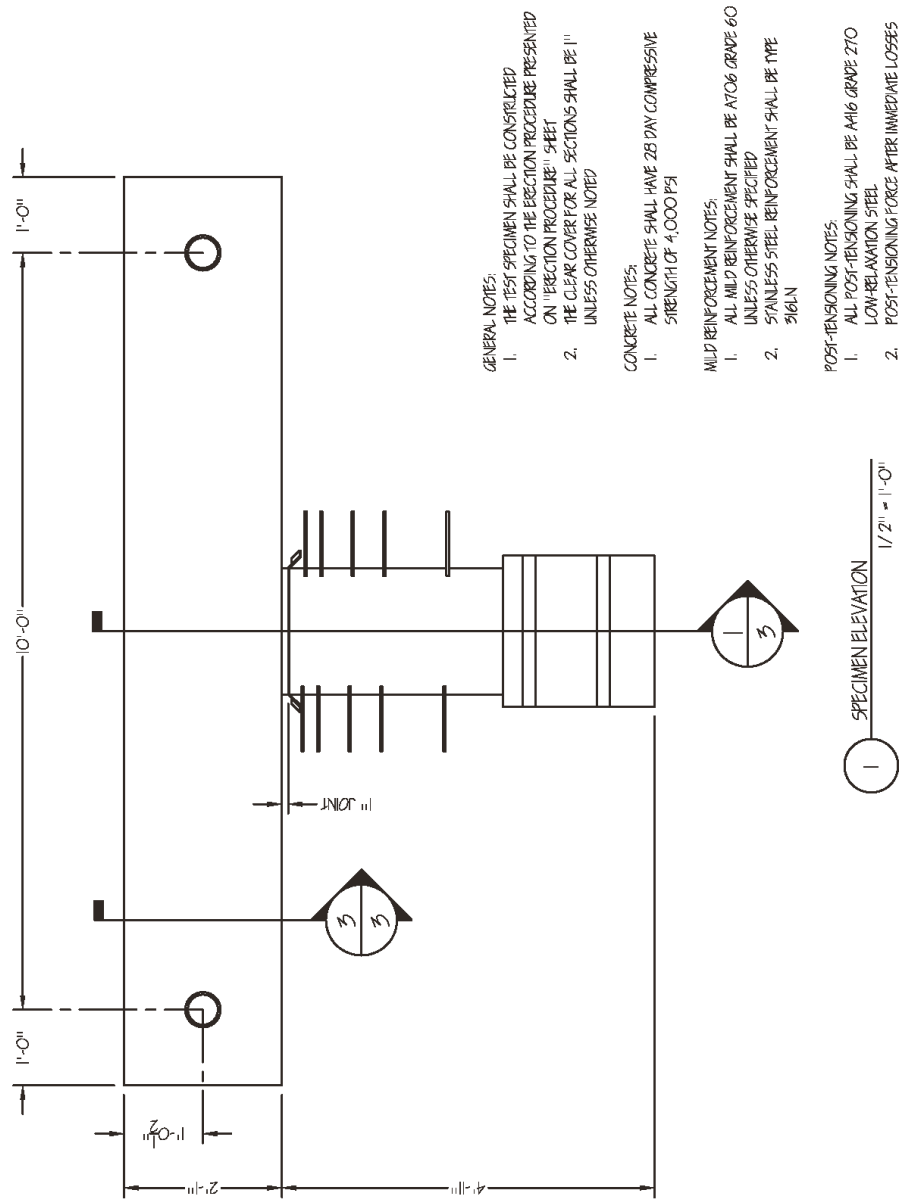

GENERAL NOTES:
1. THE TEST SPECIMEN SHALL BE CONSTRUCTED ACCORDING TO THE ERECTION PROCEDURE PRESENTED ON "ERECTION PROCEDURE" SHEET
2. THE CLEAR COVER FOR ALL SECTIONS SHALL BE 1" UNLESS OTHERWISE NOTED

CONCRETE NOTES:
1. ALL CONCRETE SHALL HAVE 28 DAY COMPRESSIVE STRENGTH OF 4,000 PSI

MILD REINFORCEMENT NOTES:
1. ALL MILD REINFORCEMENT SHALL BE A706 GRADE 60 UNLESS OTHERWISE SPECIFIED
2. STAINLESS STEEL REINFORCEMENT SHALL BE TYPE 316LN

POST-TENSIONING NOTES:
1. ALL POST-TENSIONING SHALL BE A416 GRADE 270 LOW-RELAXATION STEEL
2. POST-TENSIONING FORCE AFTER IMMEDIATE LOSSES SHALL BE 165 KIPS

N.T.S.

UCSD

NCHRP PROJECT 12-74

SPECIMEN ELEVATION

DUCTILITY:	SUPER. CONNECTION:	CONNECTION DETAIL:
FULL	NON-INTEGRAL	CONVENTIONAL HYBRID DETAIL

BY:	CHK:	DATE:	SCALE:	SHEET:
MJT		07/29/07	1/2" = 1'-0"	01

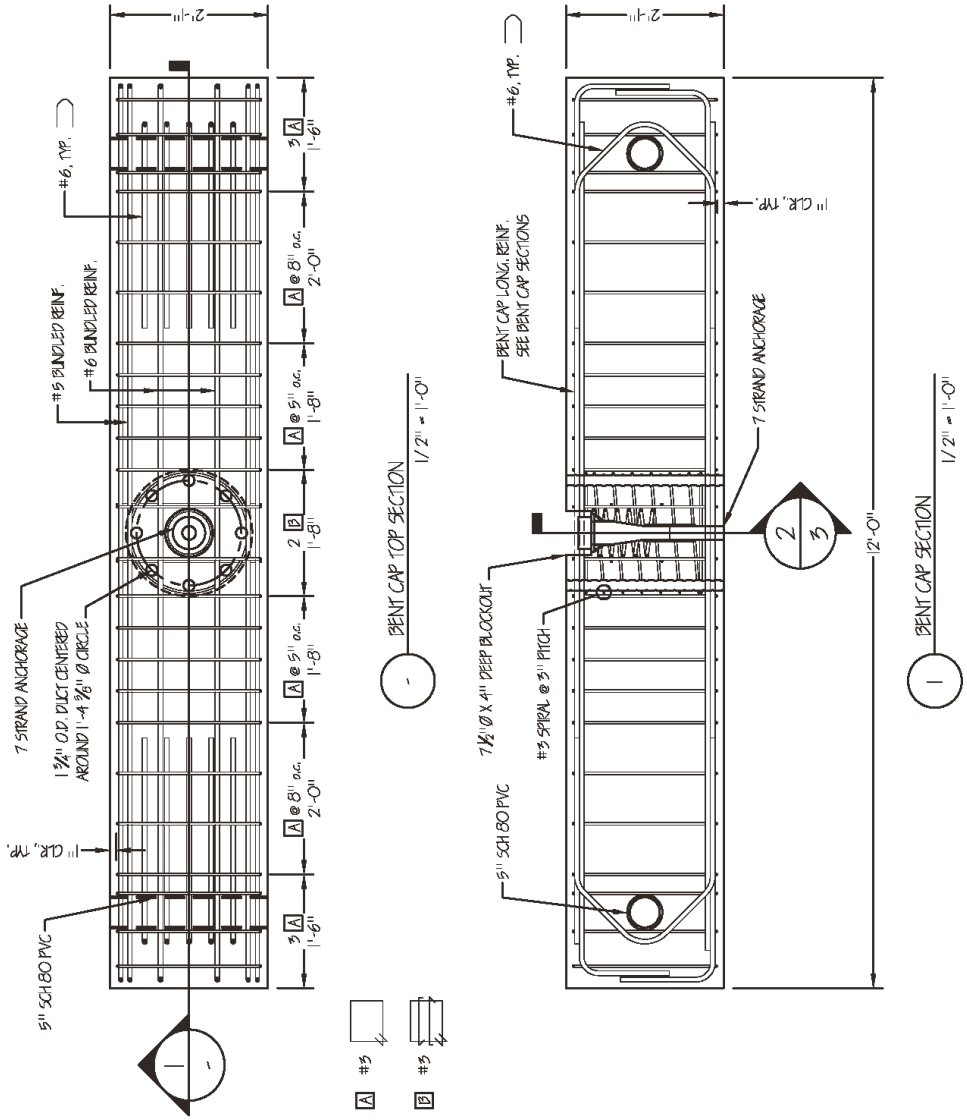

N.T.S.

UCSD

NCHRP PROJECT 12-74

BENT CAP DETAILS

DUCTILITY:	SUPER. CONNECTION:	CONNECTION DETAIL:
FULL	NON-INTEGRAL	CONVENTIONAL HYBRID DETAIL

BY:	CHK:	DATE:	SCALE:	SHEET:
MJT		07/29/07	1/2" = 1'-0"	02

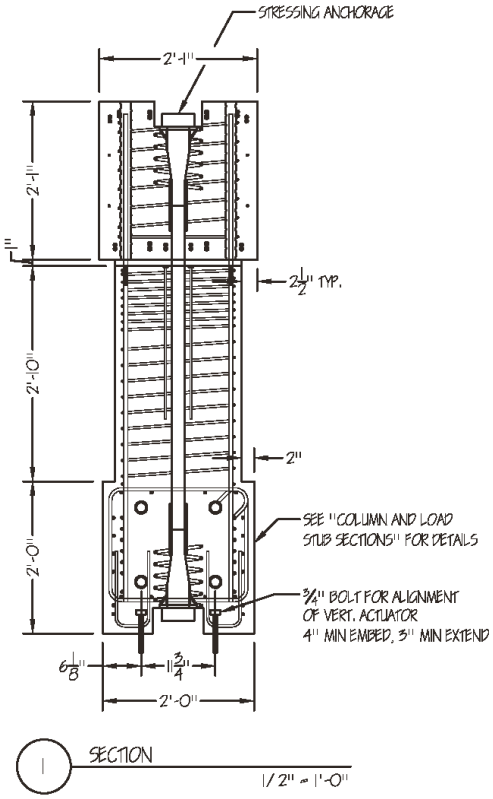

1 SECTION
1/2" = 1'-0"

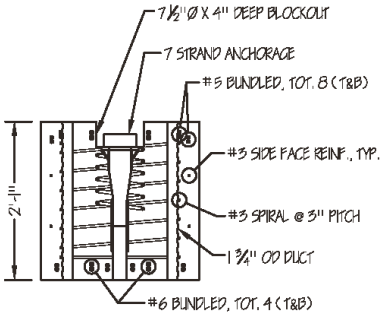

2 BENT CAP SECTION
1/2" = 1'-0"

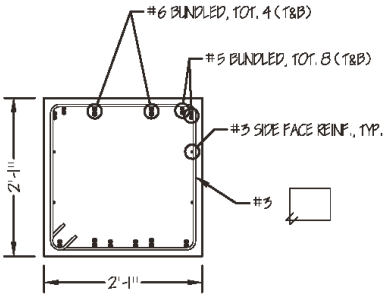

3 BENT CAP SECTION
1/2" = 1'-0"

N.T.S.

UCSD

NCHRP PROJECT 12-74

GENERAL SECTION

DUCTILITY:	SUPER. CONNECTION:	CONNECTION DETAIL:
FULL	NON-INTEGRAL	CONVENTIONAL HYBRID DETAIL

BY:	CHK:	DATE:	SCALE:	SHEET:
MJT		07/29/07	1/2" = 1'-0"	03

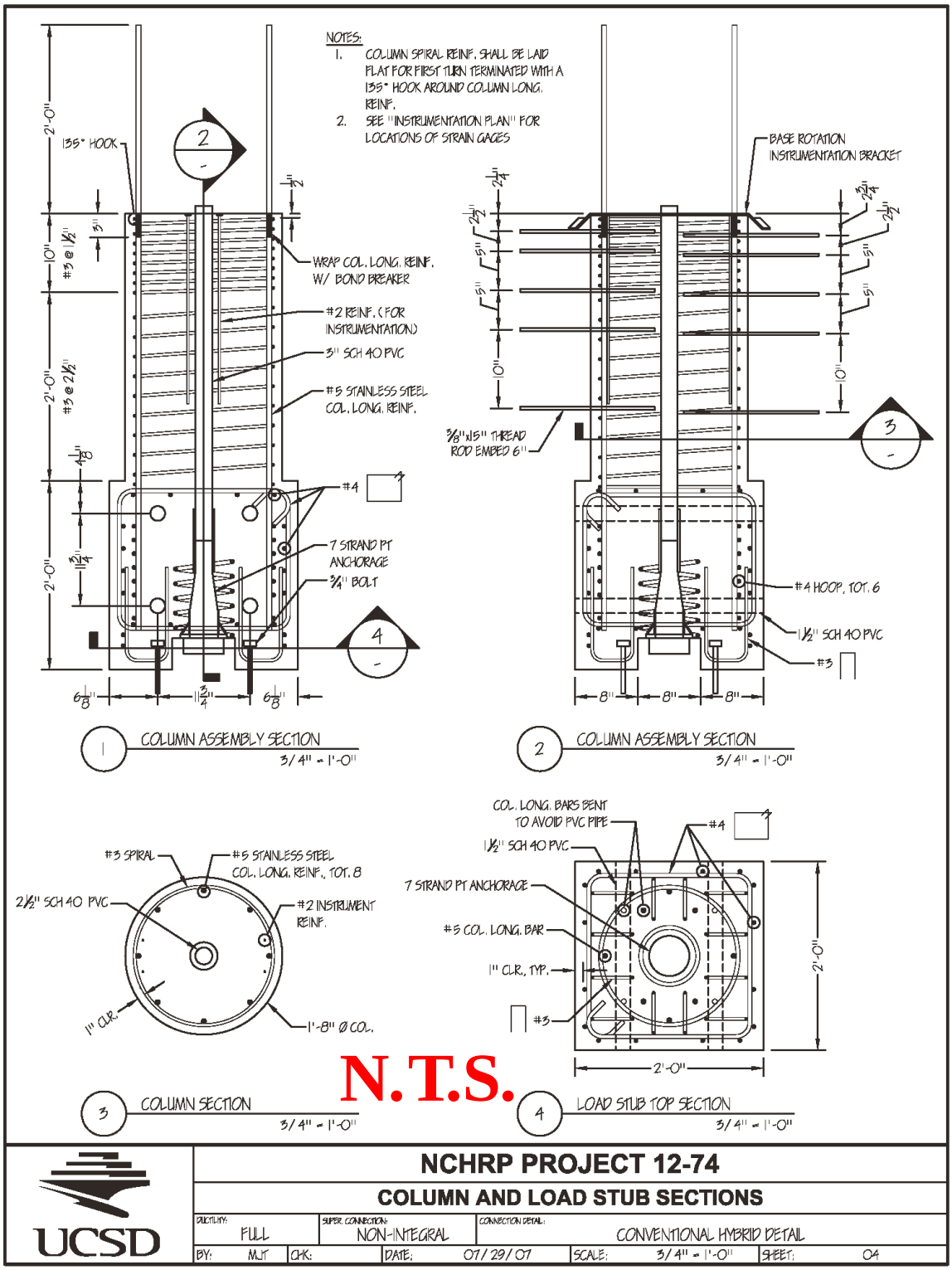
NOTES:
1. COLUMN SPIRAL REINF. SHALL BE LAID FLAT FOR FIRST TURN TERMINATED WITH A 135° HOOK AROUND COLUMN LONG. REINF.
2. SEE "INSTRUMENTATION PLAN" FOR LOCATIONS OF STRAIN GAGES
135° HOOK
WRAP COL. LONG. REINF. W/ BOND BREAKER
#2 REINF. (FOR INSTRUMENTATION)
3" SCH 40 PVC
#5 STAINLESS STEEL COL. LONG. REINF.
#4
7 STRAND PT ANCHORAGE
3/4" BOLT
#3 @ 1½"
#3 @ 2½"
2'-0"
10"
3"
1/2"
4 1/8"
11 3/4"
6 1/8"
BASE ROTATION INSTRUMENTATION BRACKET
3/8"x15" THREAD ROD EMBED 6"
#4 HOOP, TOT. 6
1½" SCH 40 PVC
#3
2 1/4"
2 1/2"
5"
8"
1 COLUMN ASSEMBLY SECTION
3/4" = 1'-0"
2 COLUMN ASSEMBLY SECTION
3/4" = 1'-0"
#3 SPIRAL
#5 STAINLESS STEEL COL. LONG. REINF., TOT. 8
2½" SCH 40 PVC
#2 INSTRUMENT REINF.
1" CLR.
1'-8" Ø COL.
COL. LONG. BARS BENT TO AVOID PVC PIPE
7 STRAND PT ANCHORAGE
#5 COL. LONG. BAR
1" CLR., TYP.
3 COLUMN SECTION
3/4" = 1'-0"
4 LOAD STUB TOP SECTION
3/4" = 1'-0"
N.T.S.
UCSD
NCHRP PROJECT 12-74
COLUMN AND LOAD STUB SECTIONS
DUCTILITY: FULL
SUPER. CONNECTION: NON-INTEGRAL
CONNECTION DETAIL: CONVENTIONAL HYBRID DETAIL
BY: MJT
CK:
DATE: 07/29/07
SCALE: 3/4" = 1'-0"
SHEET: 04

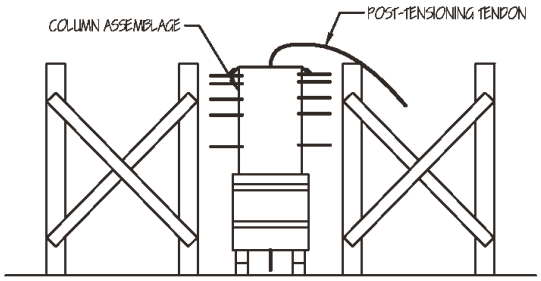

CONSTRUCTION STAGE ACTIVITIES:

1. SET COLUMN ASSEMBLAGE ON SUPPORTS
2. THREAD POST-TENSIONING TENDON THROUGH COLUMN AND SET IN DEAD END ACHORAGE
3. CONSTRUCT BENT CAP SUPPORT STRUCTURE

STAGE 1

1/4" = 1'-0"

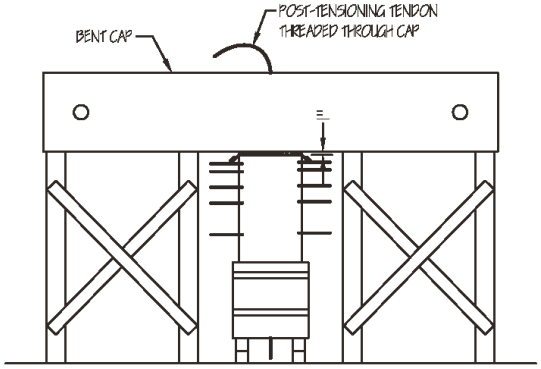

CONSTRUCTION STAGE ACTIVITIES:

1. SET BENT CAP ON SUPPORT STRUCTURE
2. THREAD POST-TENSIONING TENDON THROUGH BENT CAP
3. FORM AROUND BEDDING LAYER
4. GROUT BEDDING LAYER AND GROUTED DUCTS PER GROUTING PROCEDURE

STAGE 2

1/4" = 1'-0"

N.T.S.

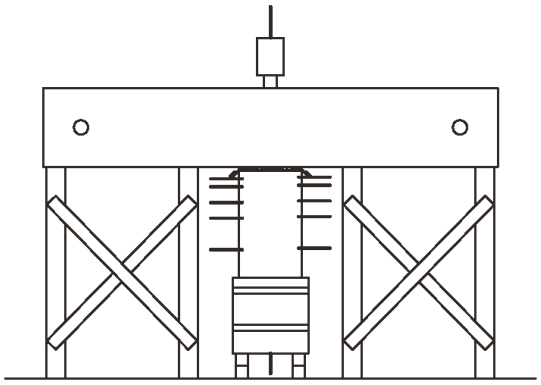

CONSTRUCTION STAGE ACTIVITIES:

1. ALLOW GROUT TO SET PER GROUT PROCEDURE
2. POST-TENSION TENDONS TO SPECIFIED LOAD
3. CUT EXCESS TENDON FROM BOTH ANCHORAGES

STAGE 3

1/4" = 1'-0"

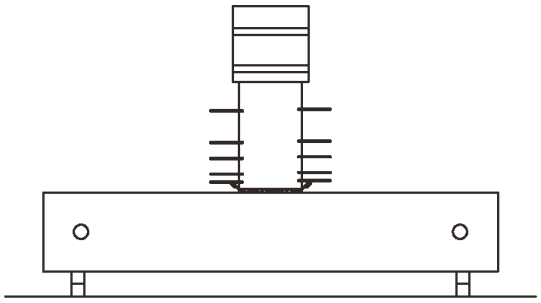

CONSTRUCTION STAGE ACTIVITIES:

1. INVERT SPECIMEN PER "SPECIMEN INVERSION PROCEDURE"
2. MOVE SPECIMEN TO TEST SETUP
3. PAINT SPECIMEN
4. ATTACH ACTUATORS

STAGE 4

1/4" = 1'-0"

UCSD

NCHRP PROJECT 12-74

ERECTION PROCEDURE

DUCTILITY:	SUPER. CONNECTION:	CONNECTION DETAIL:
FULL	NON-INTEGRAL	CONVENTIONAL HYBRID DETAIL

BY:	CHK:	DATE:	SCALE:	SHEET:
MJT		07/29/07	1/4" = 1'-0"	05

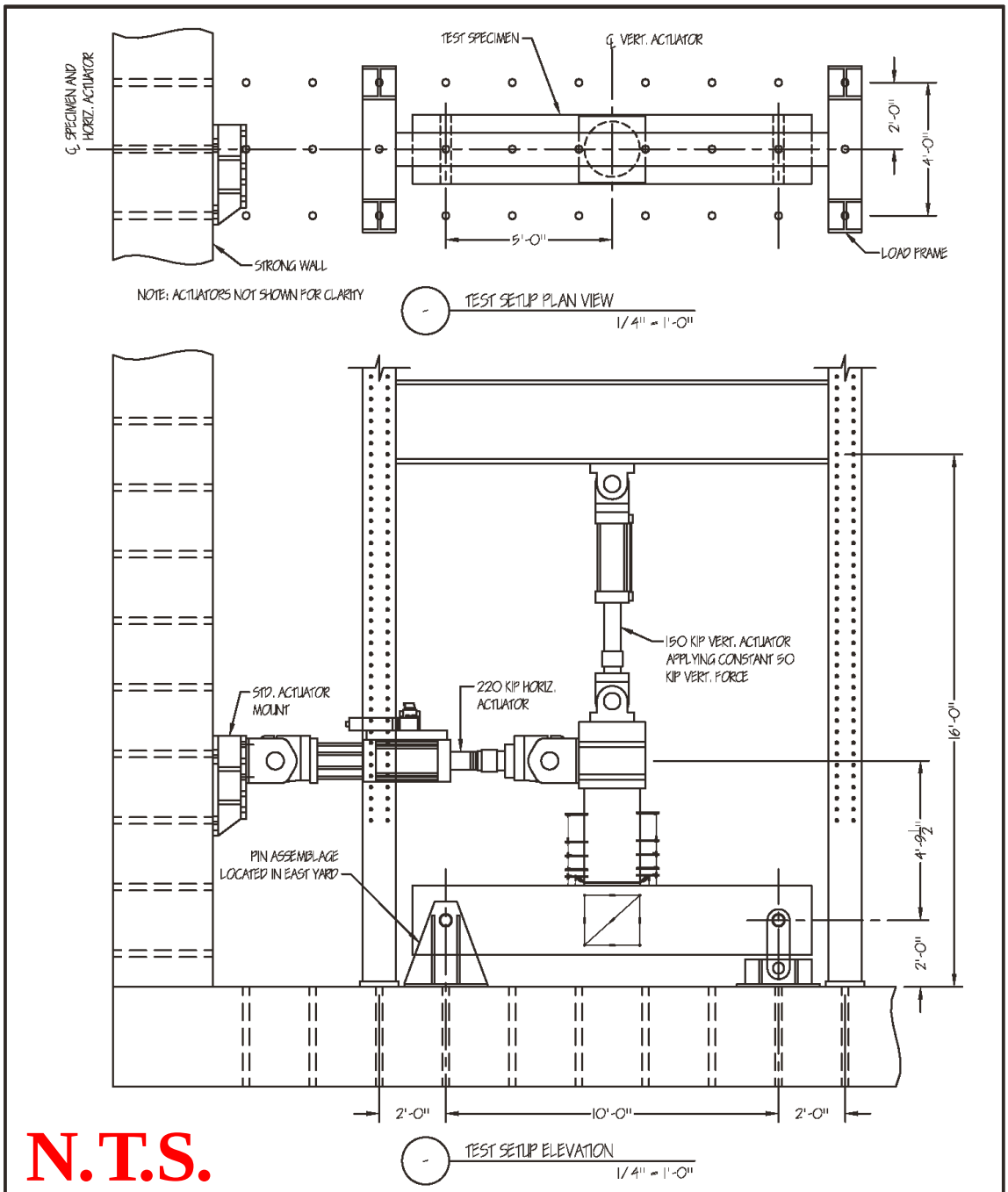

UCSD

NCHRP PROJECT 12-74

TEST SETUP OVERVIEW

DUCTILITY:	SUPER. CONNECTION:	CONNECTION DETAIL:
FULL	NON-INTEGRAL	CONVENTIONAL HYBRID DETAIL

BY:	CHK:	DATE:	SCALE:	SHEET:
MJT		07/29/07	1/4" = 1'-0"	06

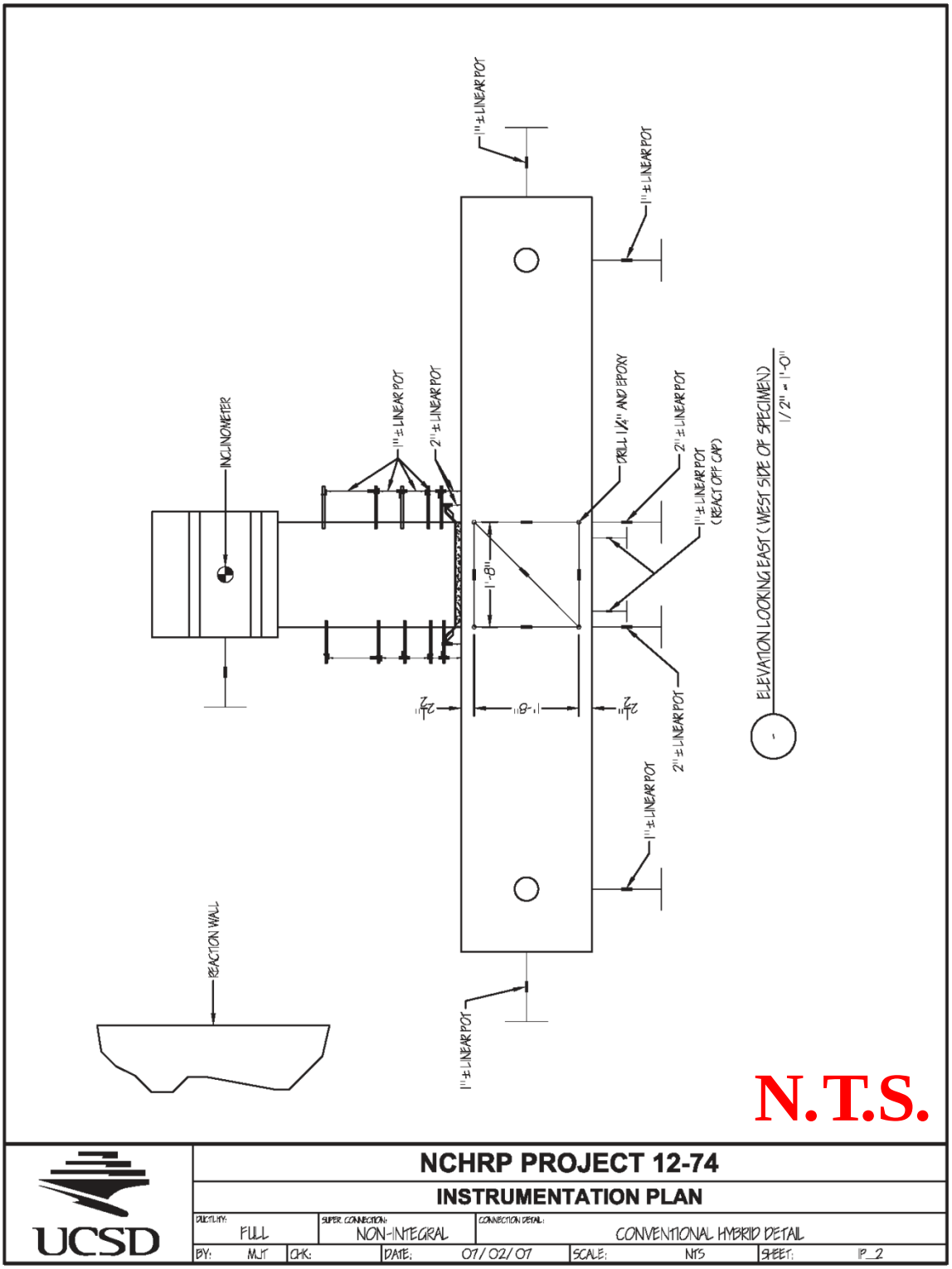
1" ± LINEAR POT
1" ± LINEAR POT
INCLINOMETER
1" ± LINEAR POT
2" ± LINEAR POT
DRILL 1½" AND EPOXY
2" ± LINEAR POT
1" ± LINEAR POT
(REACT OFF CAP)
1'-8"
2½"
1'-8"
2½"
2" ± LINEAR POT
1" ± LINEAR POT
REACTION WALL
1" ± LINEAR POT
ELEVATION LOOKING EAST (WEST SIDE OF SPECIMEN)
1/2" = 1'-0"
1
N.T.S.
UCSD
NCHRP PROJECT 12-74
INSTRUMENTATION PLAN
FACILITY: FULL
SUPER. CONNECTION: NON-INTEGRAL
CONNECTION DETAIL: CONVENTIONAL HYBRID DETAIL
BY: MJT
CHK:
DATE: 07/02/07
SCALE: NTS
SHEET: IP_2

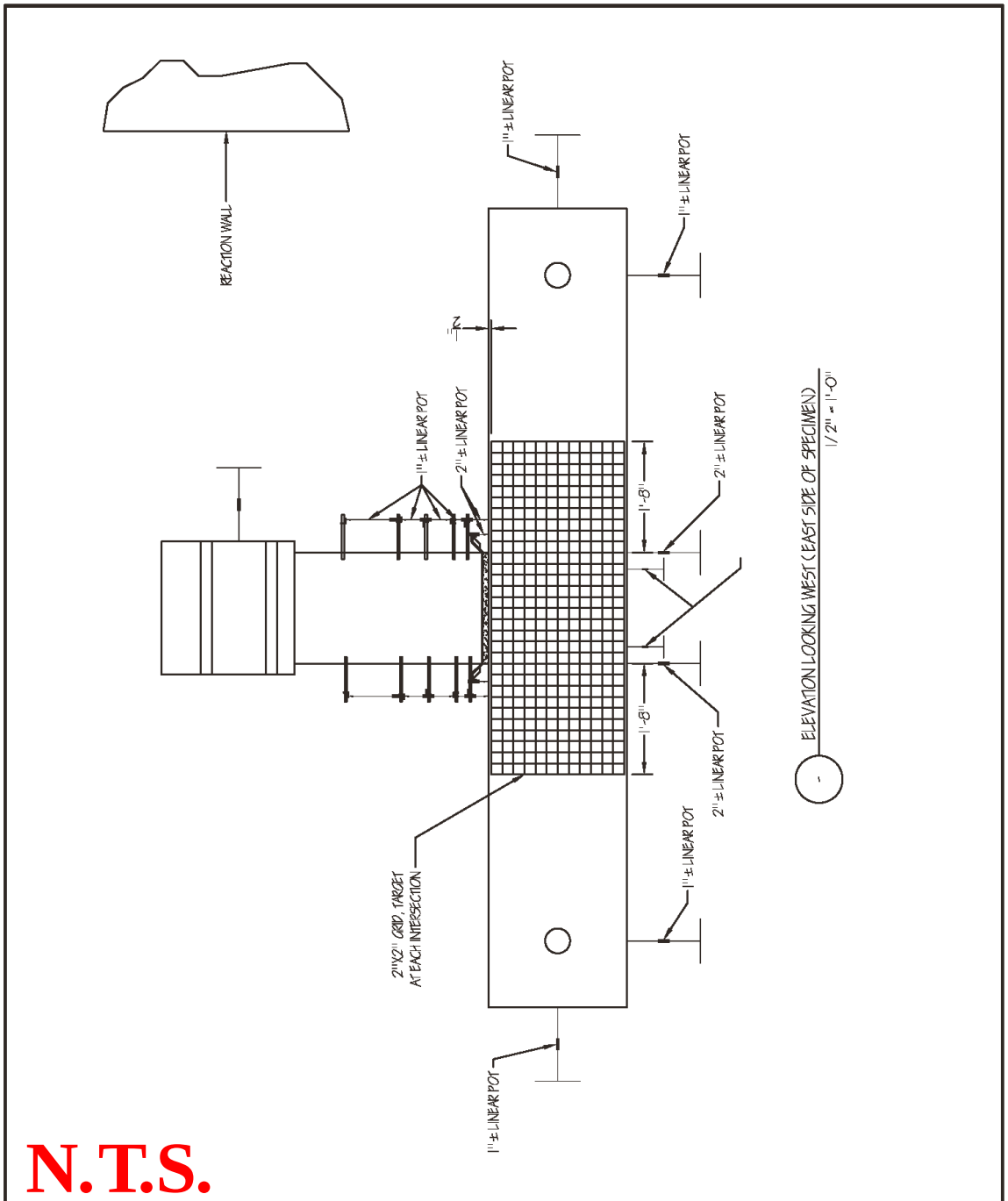

N.T.S.

UCSD

NCHRP PROJECT 12-74

INSTRUMENTATION PLAN

DUCTILITY:	SUPER. CONNECTION:	CONNECTION DETAIL:
FULL	NON-INTEGRAL	CONVENTIONAL HYBRID DETAIL

BY:	CHK:	DATE:	SCALE:	SHEET:
MJT		07/02/07	NTS	IP_2

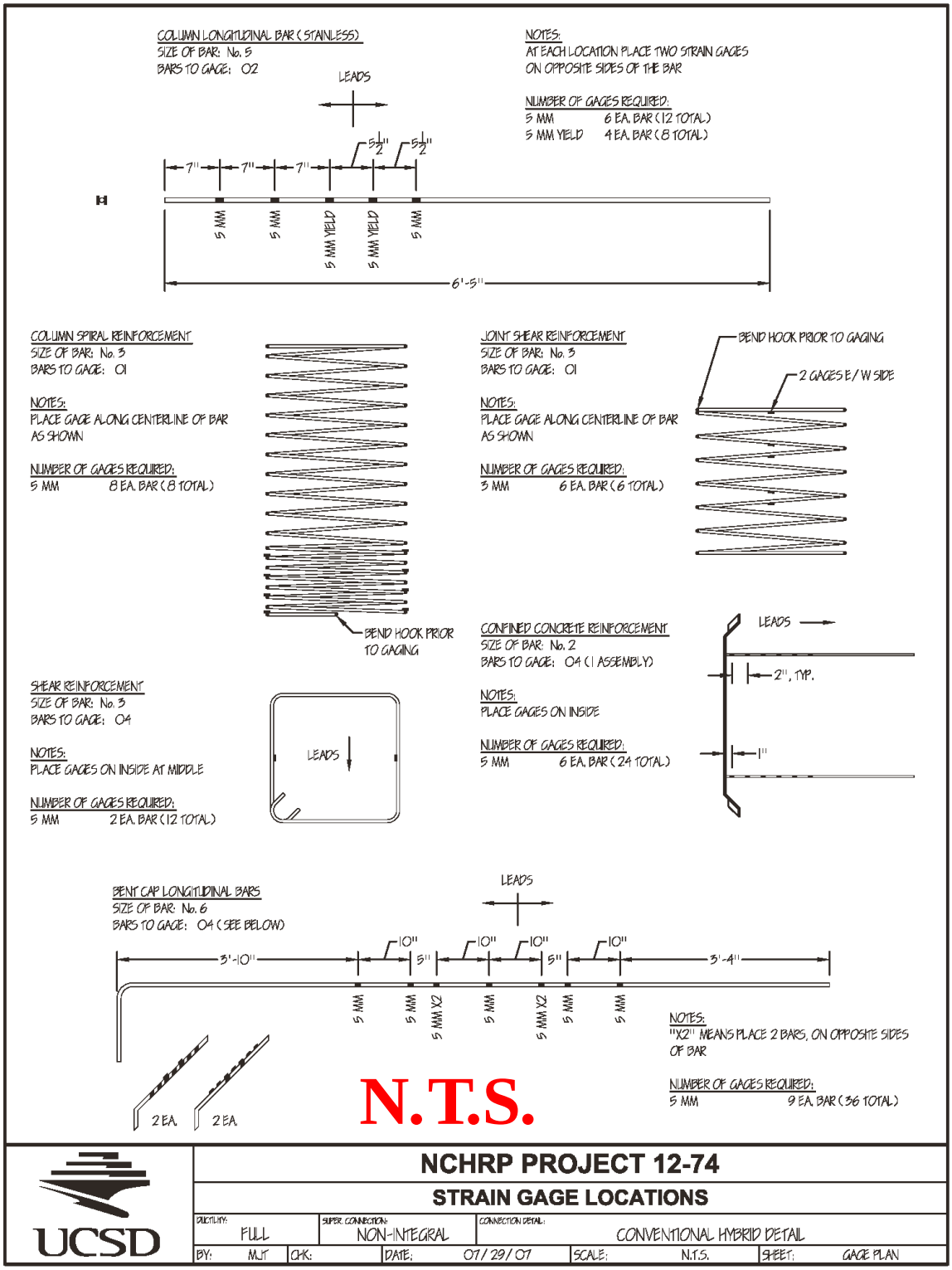
COLUMN LONGITUDINAL BAR (STAINLESS)
SIZE OF BAR: No. 5
BARS TO GAGE: 02
NOTES:
AT EACH LOCATION PLACE TWO STRAIN GAGES ON OPPOSITE SIDES OF THE BAR
NUMBER OF GAGES REQUIRED:
5 MM 6 EA. BAR (12 TOTAL)
5 MM YIELD 4 EA. BAR (8 TOTAL)
LEADS
7"
7"
7"
5 1/2"
5 1/2"
5 MM
5 MM
5 MM YIELD
5 MM YIELD
5 MM
6'-5"
COLUMN SPIRAL REINFORCEMENT
SIZE OF BAR: No. 3
BARS TO GAGE: 01
NOTES:
PLACE GAGE ALONG CENTERLINE OF BAR AS SHOWN
NUMBER OF GAGES REQUIRED:
5 MM 8 EA. BAR (8 TOTAL)
BEND HOOK PRIOR TO GAGING
JOINT SHEAR REINFORCEMENT
SIZE OF BAR: No. 3
BARS TO GAGE: 01
NOTES:
PLACE GAGE ALONG CENTERLINE OF BAR AS SHOWN
NUMBER OF GAGES REQUIRED:
5 MM 6 EA. BAR (6 TOTAL)
BEND HOOK PRIOR TO GAGING
2 GAGES E/W SIDE
SHEAR REINFORCEMENT
SIZE OF BAR: No. 3
BARS TO GAGE: 04
NOTES:
PLACE GAGES ON INSIDE AT MIDDLE
NUMBER OF GAGES REQUIRED:
5 MM 2 EA. BAR (12 TOTAL)
LEADS
CONFINED CONCRETE REINFORCEMENT
SIZE OF BAR: No. 2
BARS TO GAGE: 04 (1 ASSEMBLY)
NOTES:
PLACE GAGES ON INSIDE
NUMBER OF GAGES REQUIRED:
5 MM 6 EA. BAR (24 TOTAL)
LEADS
2", TYP.
1"
BENT CAP LONGITUDINAL BARS
SIZE OF BAR: No. 6
BARS TO GAGE: 04 (SEE BELOW)
LEADS
3'-10"
10"
5"
10"
10"
5"
10"
3'-4"
5 MM
5 MM
5 MM X2
5 MM
5 MM X2
5 MM
5 MM
2 EA.
2 EA.
NOTES:
"X2" MEANS PLACE 2 BARS, ON OPPOSITE SIDES OF BAR
NUMBER OF GAGES REQUIRED:
5 MM 9 EA. BAR (36 TOTAL)
N.T.S.
UCSD
NCHRP PROJECT 12-74
STRAIN GAGE LOCATIONS
DUCTILITY: FULL
SUPER. CONNECTION: NON-INTEGRAL
CONNECTION DETAIL: CONVENTIONAL HYBRID DETAIL
BY: MJT
CHK:
DATE: 07/29/07
SCALE: N.T.S.
SHEET: GAGE PLAN

Appendix B Concrete Filled Pipe Specimen Drawings

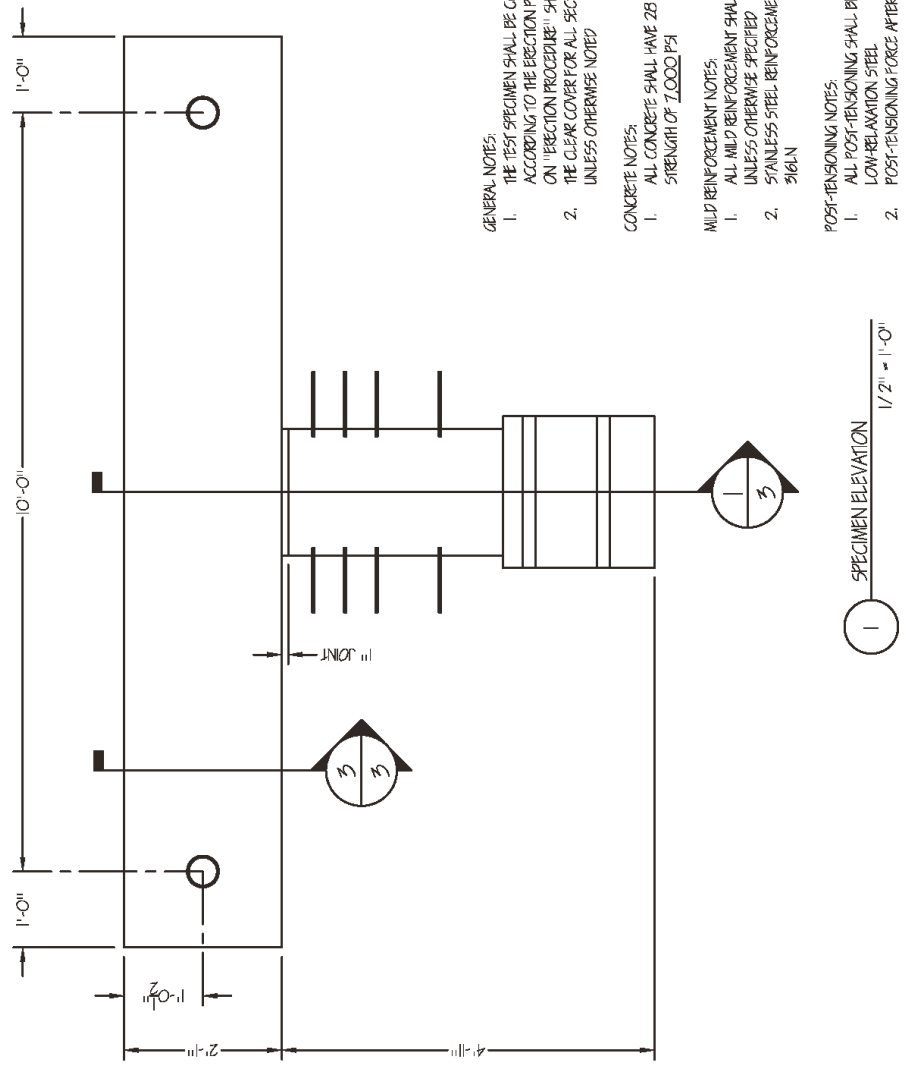

GENERAL NOTES:
1. THE TEST SPECIMEN SHALL BE CONSTRUCTED ACCORDING TO THE ERECTION PROCEDURE PRESENTED ON "ERECTION PROCEDURE" SHEET
2. THE CLEAR COVER FOR ALL SECTIONS SHALL BE 1" UNLESS OTHERWISE NOTED

CONCRETE NOTES:
1. ALL CONCRETE SHALL HAVE 28 DAY COMPRESSIVE STRENGTH OF 7,000 PSI

MILD REINFORCEMENT NOTES:
1. ALL MILD REINFORCEMENT SHALL BE A706 GRADE 60 UNLESS OTHERWISE SPECIFIED
2. STAINLESS STEEL REINFORCEMENT SHALL BE TYPE 316LN

POST-TENSIONING NOTES:
1. ALL POST-TENSIONING SHALL BE A416 GRADE 270 LOW-RELAXATION STEEL
2. POST-TENSIONING FORCE AFTER IMMEDIATE LOSSES SHALL BE 152 KIPS

STEEL NOTES:
1. STEEL SHELL SHALL BE A572 GRADE 50

N.T.S.

APPROVED FOR PRODUCTION

UCSD

NCHRP PROJECT 12-74					
SPECIMEN ELEVATION					
DUCTILITY: FULL	SUPER. CONNECTION: NON-INTEGRAL	CONNECTION DETAIL: HYBRID SPECIMEN 2 - CONCRETE FILLED STEEL TUBE			
BY: MJT	CHK:	DATE: 01/08/08	SCALE: 1/2" = 1'-0"	SHEET: 01	

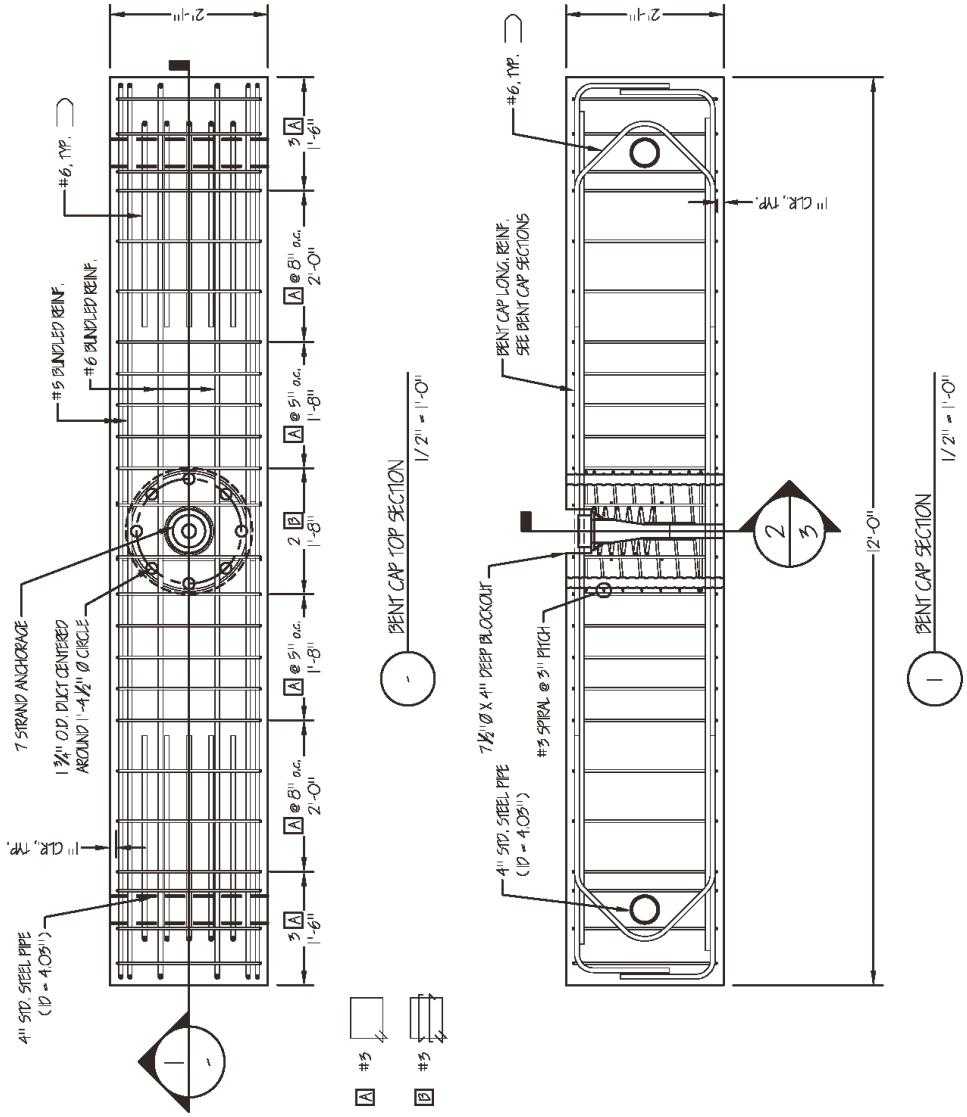

N.T.S.

APPROVED FOR PRODUCTION

UCSD

NCHRP PROJECT 12-74

BENT CAP DETAILS

DUCTILITY:	SUPER. CONNECTION:	CONNECTION DETAIL:
FULL	NON-INTEGRAL	HYBRID SPECIMEN 2 - CONCRETE FILLED STEEL TUBE

BY:	CHK:	DATE:	SCALE:	SHEET:
MJT		01/08/08	1/2" = 1'-0"	02

y

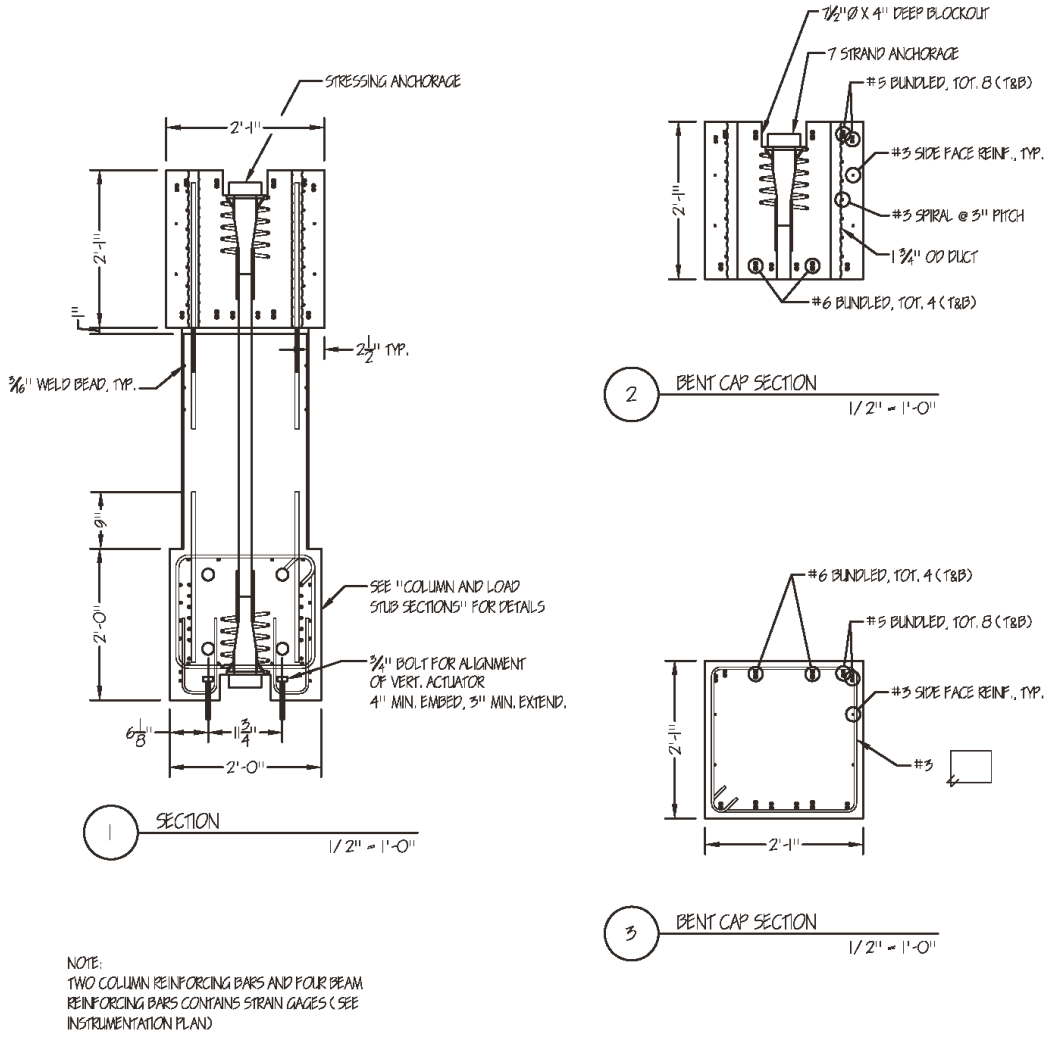

NOTE:
TWO COLUMN REINFORCING BARS AND FOUR BEAM REINFORCING BARS CONTAINS STRAIN GAGES (SEE INSTRUMENTATION PLAN)

N.T.S.

APPROVED FOR PRODUCTION

UCSD

NCHRP PROJECT 12-74

GENERAL SECTION

DUCTILITY:	SUPER. CONNECTION:	CONNECTION DETAIL:
FULL	NON-INTEGRAL	HYBRID SPECIMEN 2 - CONCRETE FILLED STEEL TUBE

BY:	CHK:	DATE:	SCALE:	SHEET:
MJT		01/08/08	1/2" = 1'-0"	03

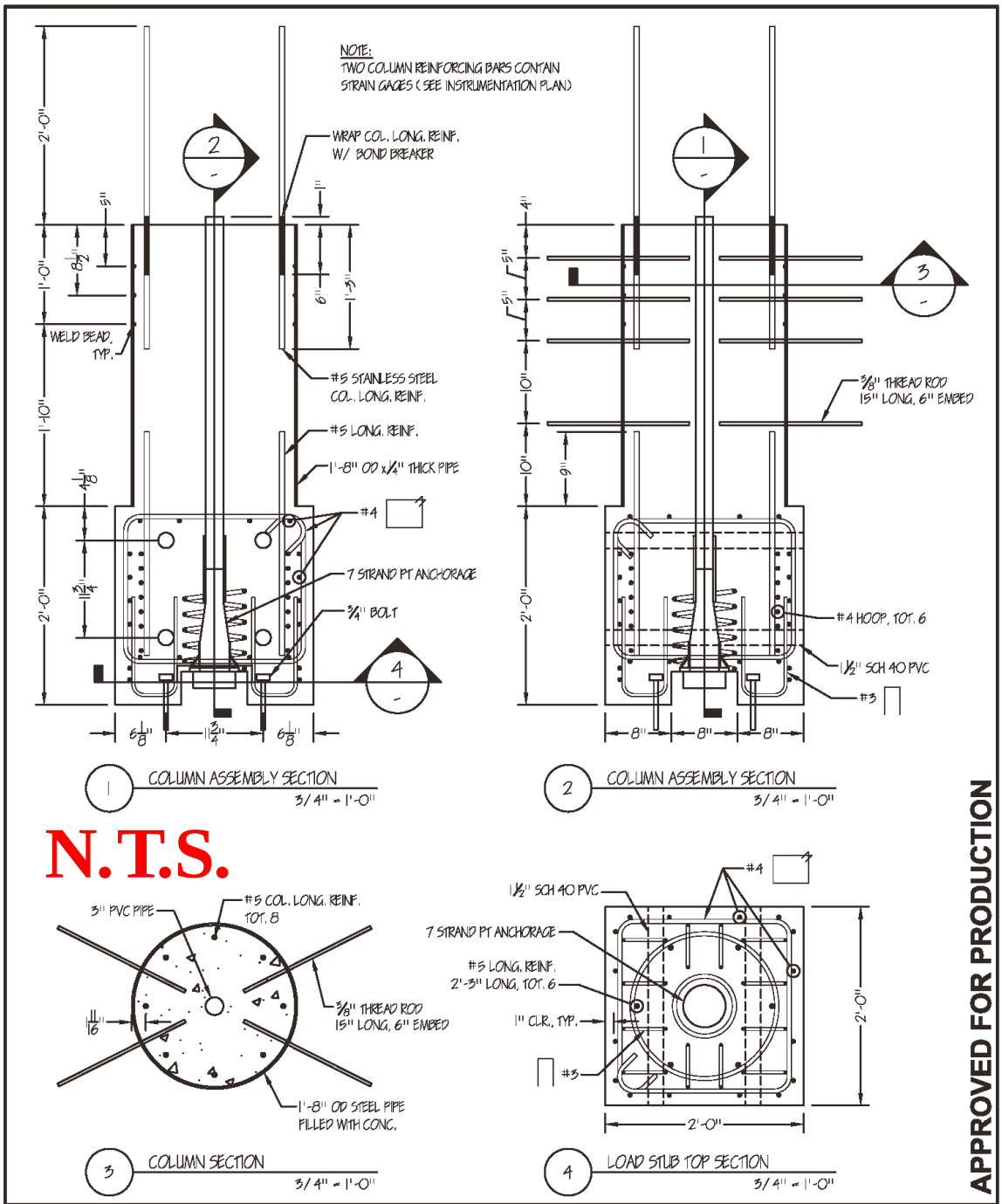
NOTE:
TWO COLUMN REINFORCING BARS CONTAIN STRAIN GAGES (SEE INSTRUMENTATION PLAN)
WRAP COL. LONG. REINF. W/ BOND BREAKER
WELD BEAD, TYP.
#5 STAINLESS STEEL COL. LONG. REINF.
#5 LONG. REINF.
1'-8" OD x 1/4" THICK PIPE
#4
7 STRAND PT ANCHORAGE
3/4" BOLT
3/8" THREAD ROD 15" LONG, 6" EMBED
#4 HOOP, TOT. 6
1 1/2" SCH 40 PVC
#3
COLUMN ASSEMBLY SECTION
3/4" = 1'-0"
COLUMN ASSEMBLY SECTION
3/4" = 1'-0"
N.T.S.
3" PVC PIPE
#5 COL. LONG. REINF. TOT. 8
3/8" THREAD ROD 15" LONG, 6" EMBED
1'-8" OD STEEL PIPE FILLED WITH CONC.
COLUMN SECTION
3/4" = 1'-0"
1 1/2" SCH 40 PVC
#4
7 STRAND PT ANCHORAGE
#5 LONG. REINF. 2'-3" LONG, TOT. 6
1" CLR., TYP.
#3
LOAD STUB TOP SECTION
3/4" = 1'-0"
APPROVED FOR PRODUCTION
UCSD
NCHRP PROJECT 12-74
COLUMN AND LOAD STUB SECTIONS
DUCTILITY: FULL
SUPER. CONNECTION: NON-INTEGRAL
CONNECTION DETAIL: HYBRID SPECIMEN 2 - CONCRETE FILLED STEEL TUBE
BY: MJT
CHK:
DATE: 01/08/08
SCALE: 3/4" = 1'-0"
SHEET: 04

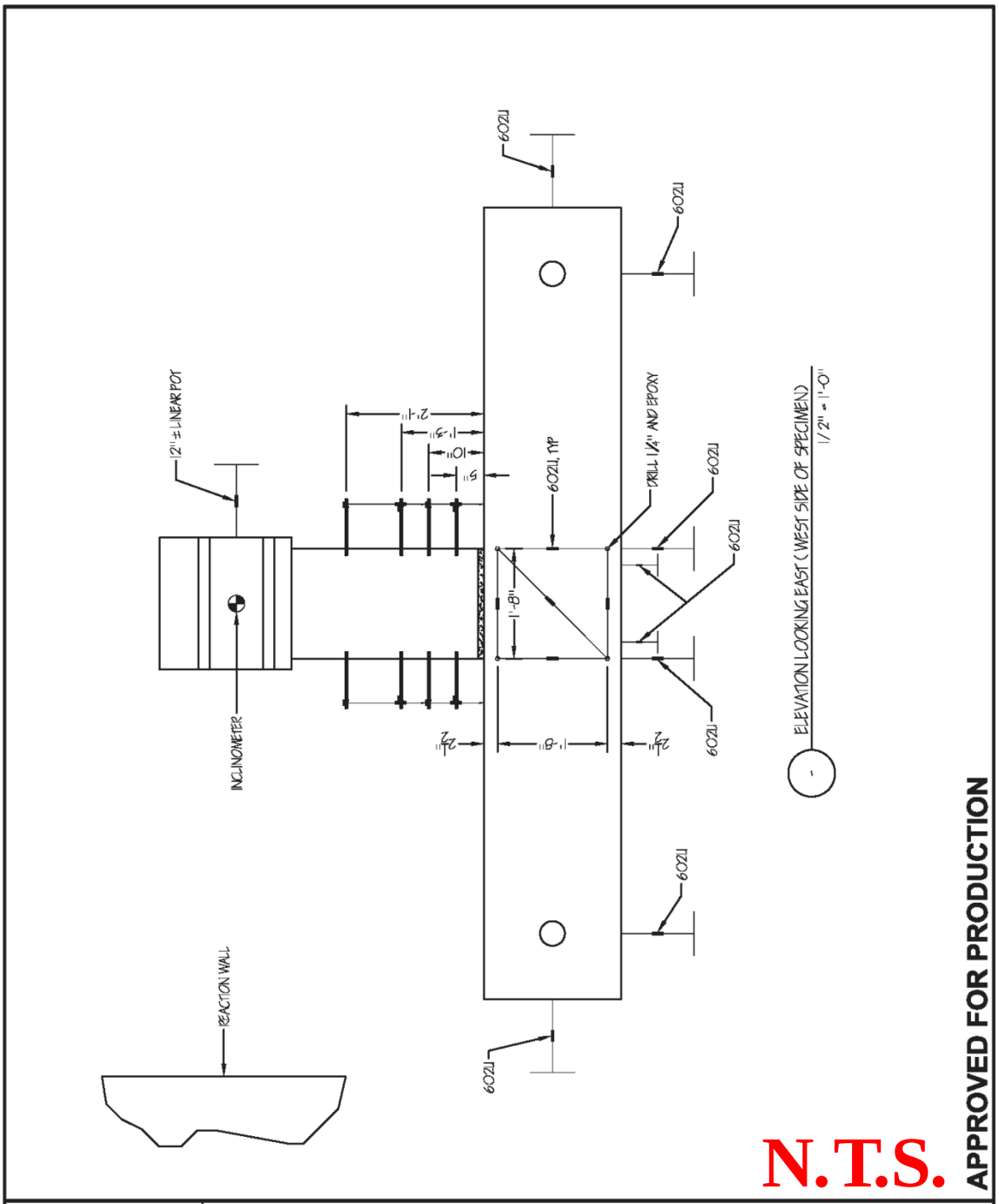
12" ± LINEAR POT
INCLINOMETER
REACTION WALL
2'-1"
1'-3"
10"
5"
6021
6021, TYP
DRILL 1/2" AND EPOXY
1'-8"
2 1/2"
1'-8"
2 1/2"
6021
6021
6021
6021
6021
ELEVATION LOOKING EAST (WEST SIDE OF SPECIMEN)
1/2" = 1'-0"
1
N.T.S.
APPROVED FOR PRODUCTION
UCSD
NCHRP PROJECT 12-74
INSTRUMENTATION PLAN 2
DUCTILITY: FULL
SUPER. CONNECTION: NON-INTEGRAL
CONNECTION DETAIL: HYBRID SPECIMEN 2 - CONCRETE FILLED STEEL TUBE
BY: MJT
CHK:
DATE: 01/08/08
SCALE: NTS
SHEET: 07

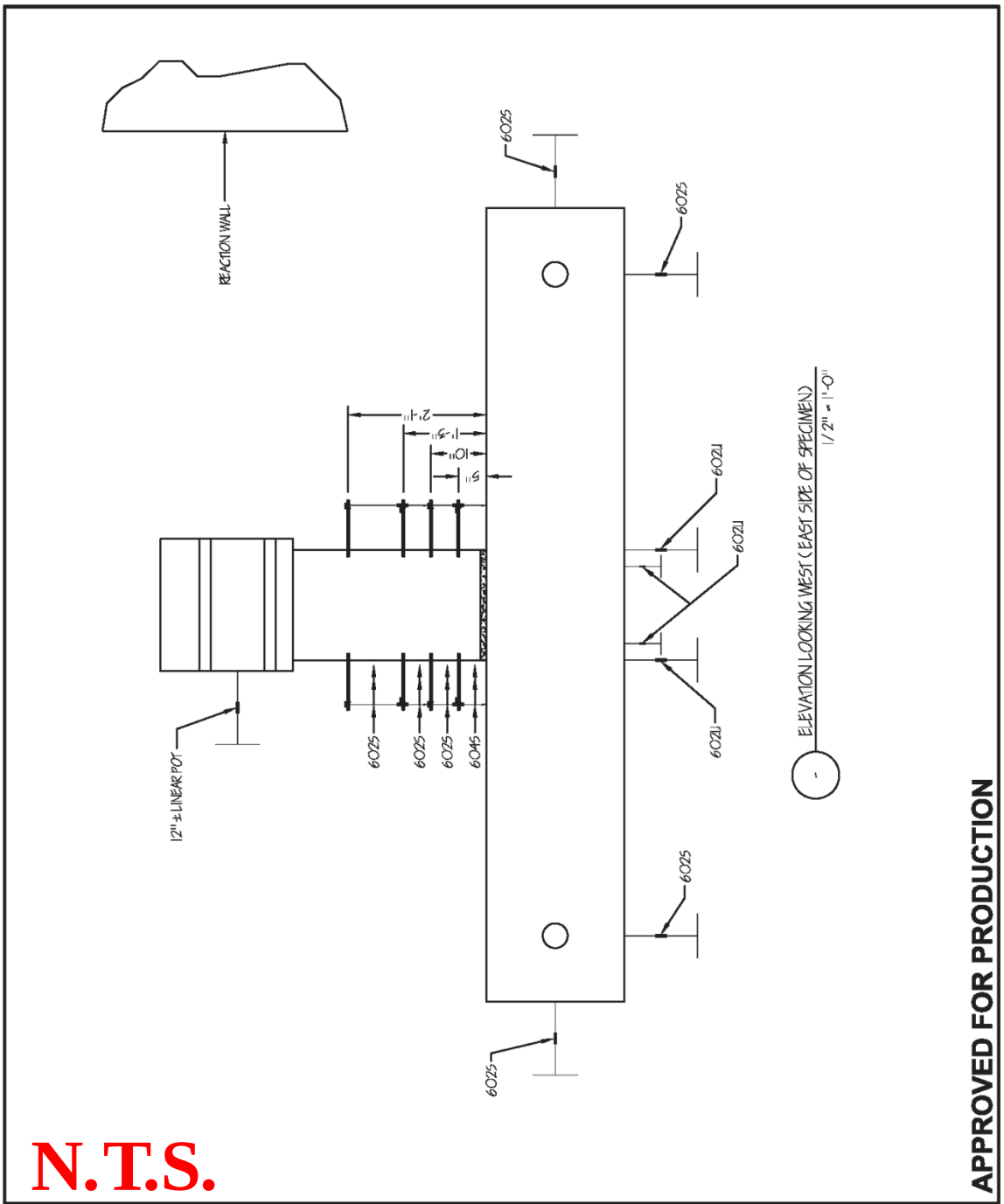

N.T.S.

UCSD

NCHRP PROJECT 12-74

INSTRUMENTATION PLAN 3

DUCTILITY:	SUPER. CONNECTION:	CONNECTION DETAIL:
FULL	NON-INTEGRAL	HYBRID SPECIMEN 2 - CONCRETE FILLED STEEL TUBE

BY:	CHK:	DATE:	SCALE:	SHEET:
MJT		01/08/08	NTS	08

COLUMN LONGITUDINAL BAR (STAINLESS)
SIZE OF BAR: No. 5
BARS TO GAGE: 04

NOTES:
AT EACH LOCATION PLACE TWO STRAIN GAGES ON OPPOSITE SIDES OF THE BAR

NUMBER OF GAGES REQUIRED:
5 MM 6 EA. BAR (12 TOTAL)
5 MM YIELD 6 EA. BAR (12 TOTAL)

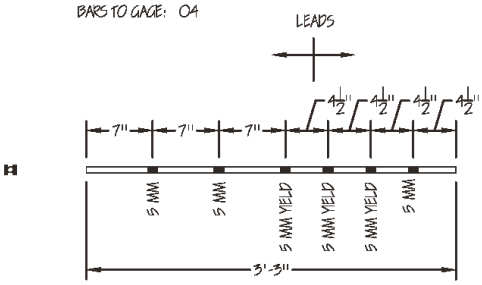

JOINT SHEAR REINFORCEMENT
SIZE OF BAR: No. 3
BARS TO GAGE: 02

NOTES:
PLACE GAGE ALONG CENTERLINE OF BAR AS SHOWN

NUMBER OF GAGES REQUIRED:
3 MM 6 EA. BAR (6 TOTAL)

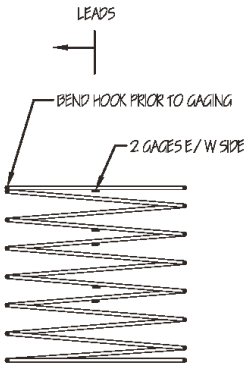

BENT CAP LONGITUDINAL BARS
SIZE OF BAR: No. 6
BARS TO GAGE: 08

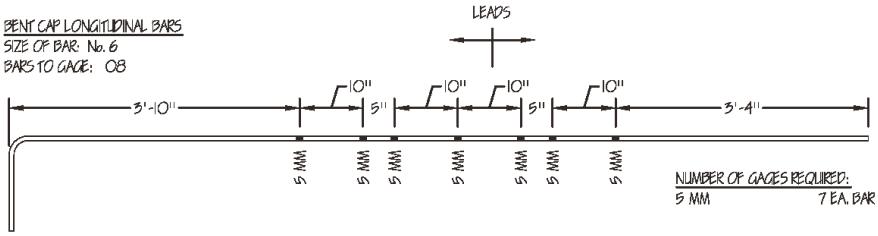

NUMBER OF GAGES REQUIRED:
5 MM 7 EA. BAR (28 TOTAL)

N.T.S.

APPROVED FOR PRODUCTION

UCSD

NCHRP PROJECT 12-74					
STRAIN GAGING PLAN					
DUCTILITY: FULL	SUPER. CONNECTION: NON-INTEGRAL	CONNECTION DETAIL: HYBRID SPECIMEN 2 - CONCRETE FILLED STEEL TUBE			
BY: MJT	CHK:	DATE: 01/08/08	SCALE: NTS	SHEET: 09	

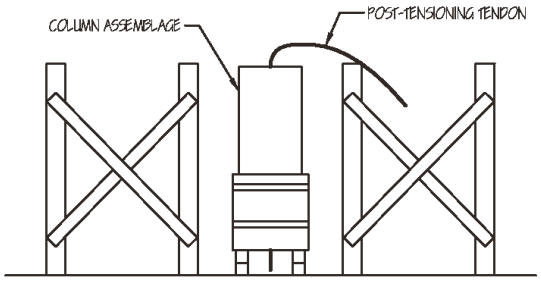

CONSTRUCTION STAGE ACTIVITIES:

1. SET COLUMN ASSEMBLAGE ON SUPPORTS
2. THREAD POST-TENSIONING TENDON THROUGH COLUMN AND SET IN DEAD END ACHORAGE
3. CONSTRUCT BENT CAP SUPPORT STRUCTURE

STAGE 1

1/4" = 1'-0"

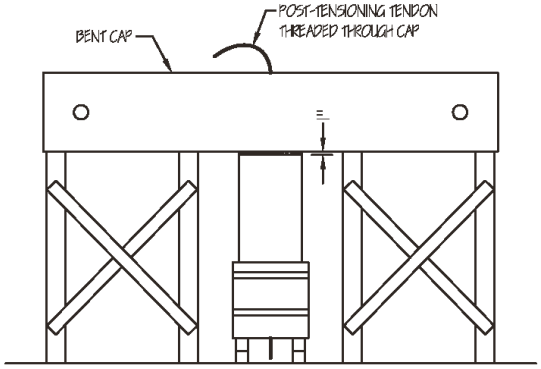

CONSTRUCTION STAGE ACTIVITIES:

1. SET BENT CAP ON SUPPORT STRUCTURE
2. THREAD POST-TENSIONING TENDON THROUGH BENT CAP
3. FORM AROUND BEDDING LAYER
4. GROUT BEDDING LAYER AND GROUTED DUCTS PER GROUTING PROCEDURE

STAGE 2

1/4" = 1'-0"

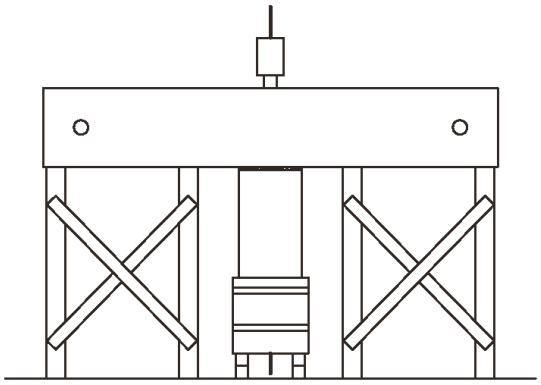

CONSTRUCTION STAGE ACTIVITIES:

1. ALLOW GROUT TO SET PER GROUT PROCEDURE
2. POST-TENSION TENDONS TO SPECIFIED LOAD
3. CUT EXCESS TENDON FROM BOTH ANCHORAGES

STAGE 3

1/4" = 1'-0"

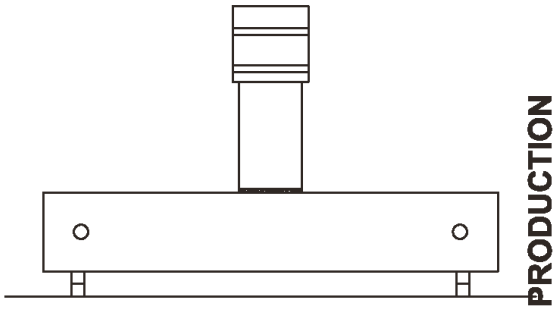

CONSTRUCTION STAGE ACTIVITIES:

1. INVERT SPECIMEN PER "SPECIMEN INVERSION PROCEDURE"
2. MOVE SPECIMEN TO TEST SETUP
3. PAINT SPECIMEN
4. ATTACH ACTUATORS

STAGE 4

1/4" = 1'-0"

N.T.S.

APPROVED FOR PRODUCTION

UCSD

NCHRP PROJECT 12-74

ERECTION PROCEDURE

DUCTILITY:	SUPER. CONNECTION:	CONNECTION DETAIL:
FULL	NON-INTEGRAL	HYBRID SPECIMEN 2 - CONCRETE FILLED STEEL TUBE

BY:	CHK:	DATE:	SCALE:	SHEET:
MJT		01/08/08	1/4" = 1'-0"	10

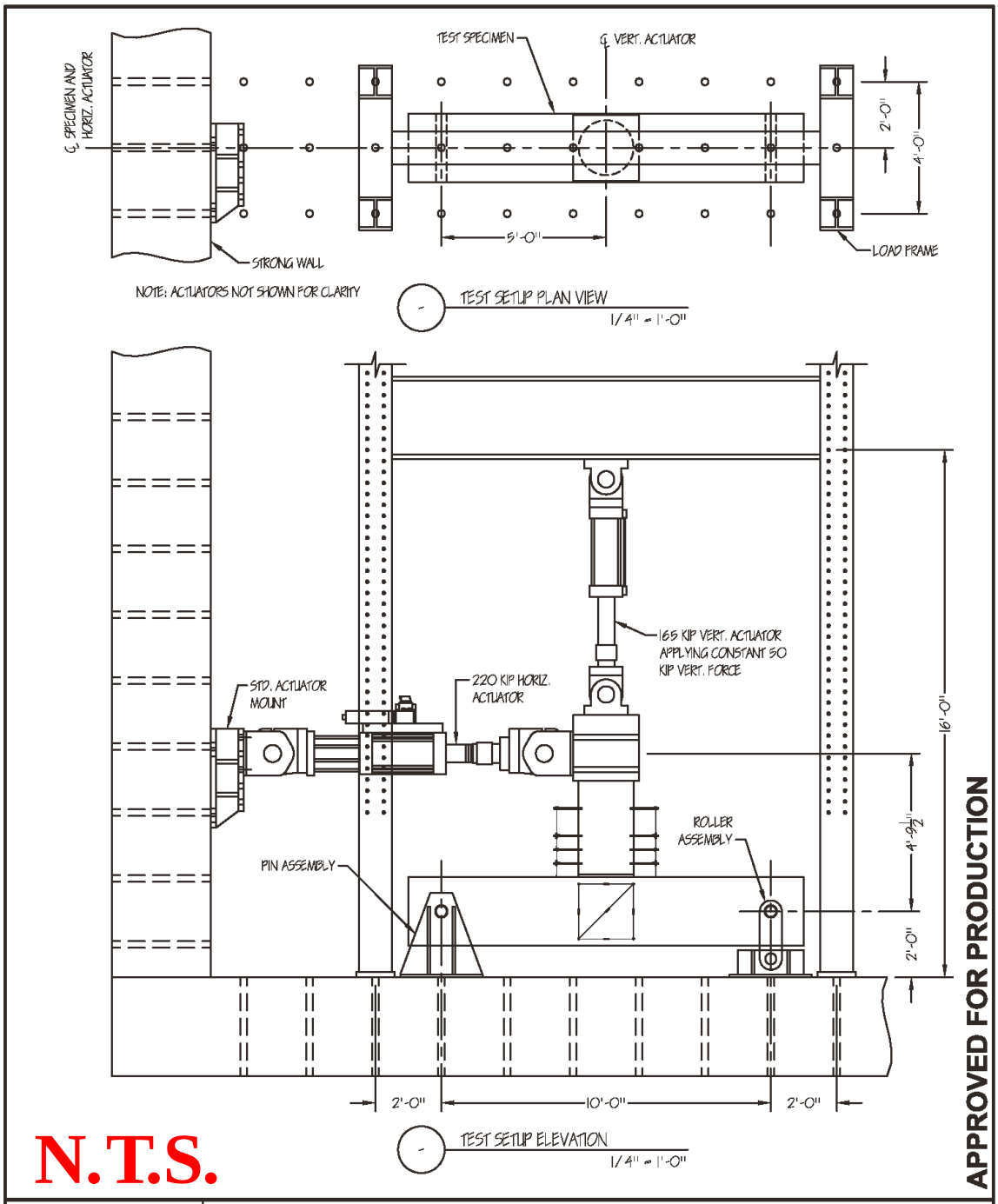

UCSD

NCHRP PROJECT 12-74

TEST SETUP OVERVIEW

DUCTILITY:	SUPER. CONNECTION:	CONNECTION DETAIL:
FULL	NON-INTEGRAL	HYBRID SPECIMEN 2 - CONCRETE FILLED STEEL TUBE

BY:	CHK:	DATE:	SCALE:	SHEET:
MJT		01/08/08	1/4" = 1'-0"	11

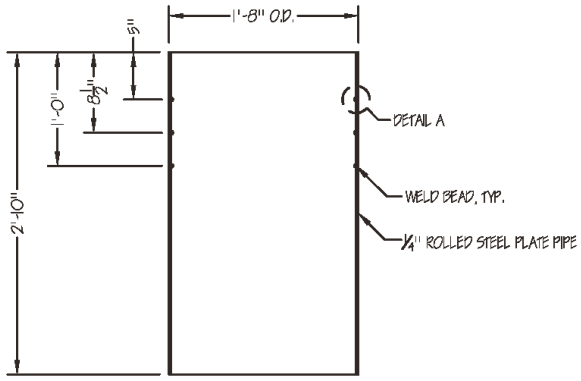

1 STEEL PIPE LONG SECTION
3/4" = 1'-0"

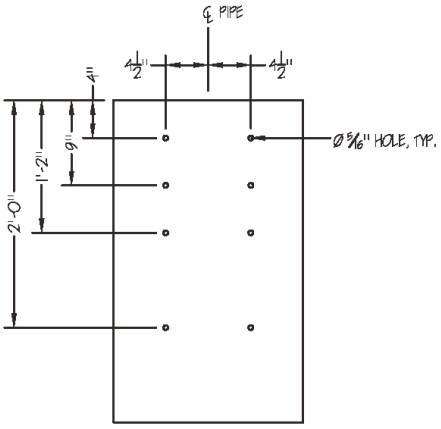

1 STEEL PIPE HOLE LOCATIONS
3/4" = 1'-0"

NOTES:

1. ROLLED STEEL PLATE PIPE SHALL BE A572 GRADE 50 AND WELDING SHALL BE COMPLETE JOINT PENETRATION.
2. ALL WELDING SHALL BE USING E70 ELECTRODE.
3. LOCATIONS OF WELD BEAD GIVEN TO CENTER OF BEAD.
4. WELD BEAD SHALL BE PLACED AROUND ENTIRE INNER CIRCUMFERENCE.
5. A TOTAL OF 2 PIPE SECTIONS SHALL BE FABRICATED.

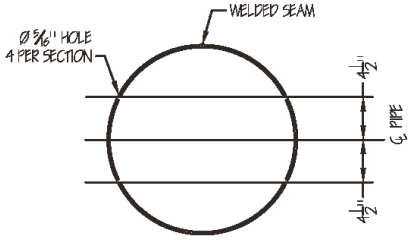

1 STEEL PIPE SECTION
3/4" = 1'-0"

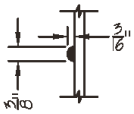

A WELD BEAD DETAIL
1/4" = 1"

N.T.S.

APPROVED FOR PRODUCTION

UCSD

NCHRP PROJECT 12-74

COLUMN PIPE DETAIL

DUCTILITY:	SUPER. CONNECTION:	CONNECTION DETAIL:
FULL	NON-INTEGRAL	HYBRID SPECIMEN 2 - CONCRETE FILLED STEEL TUBE

BY:	CHK:	DATE:	SCALE:	SHEET:
MJT		01/08/08	AS SHOWN	12

Appendix C Dual Shell Specimen Drawings

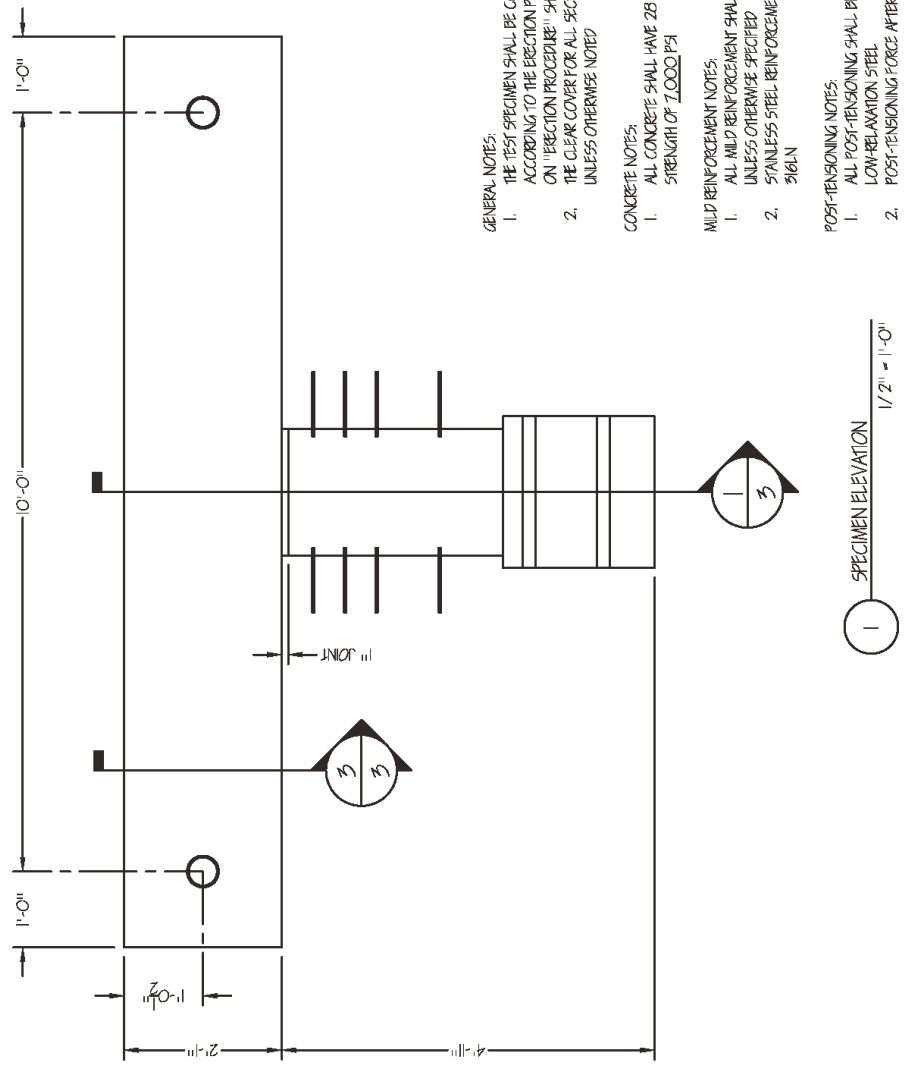

GENERAL NOTES:
1. THE TEST SPECIMEN SHALL BE CONSTRUCTED ACCORDING TO THE ERECTION PROCEDURE PRESENTED ON "ERECTION PROCEDURE" SHEET
2. THE CLEAR COVER FOR ALL SECTIONS SHALL BE 1" UNLESS OTHERWISE NOTED

CONCRETE NOTES:
1. ALL CONCRETE SHALL HAVE 28 DAY COMPRESSIVE STRENGTH OF 7,000 PSI

MILD REINFORCEMENT NOTES:
1. ALL MILD REINFORCEMENT SHALL BE A706 GRADE 60 UNLESS OTHERWISE SPECIFIED
2. STAINLESS STEEL REINFORCEMENT SHALL BE TYPE 316LN

POST-TENSIONING NOTES:
1. ALL POST-TENSIONING SHALL BE A416 GRADE 270 LOW-RELAXATION STEEL
2. POST-TENSIONING FORCE AFTER IMMEDIATE LOSSES SHALL BE 152 KIPS

STEEL NOTES:
1. STEEL SHELL SHALL BE A572 GRADE 50

N.T.S.

APPROVED FOR PRODUCTION

UCSD

NCHRP PROJECT 12-74					
SPECIMEN ELEVATION					
DUCTILITY: FULL	SUPER. CONNECTION: NON-INTEGRAL	CONNECTION DETAIL: HYBRID SPECIMEN 3 - DUAL SHELL COLUMN			
BY: MJT	CHK:	DATE: 01/08/08	SCALE: 1/2" = 1'-0"	SHEET: 01	

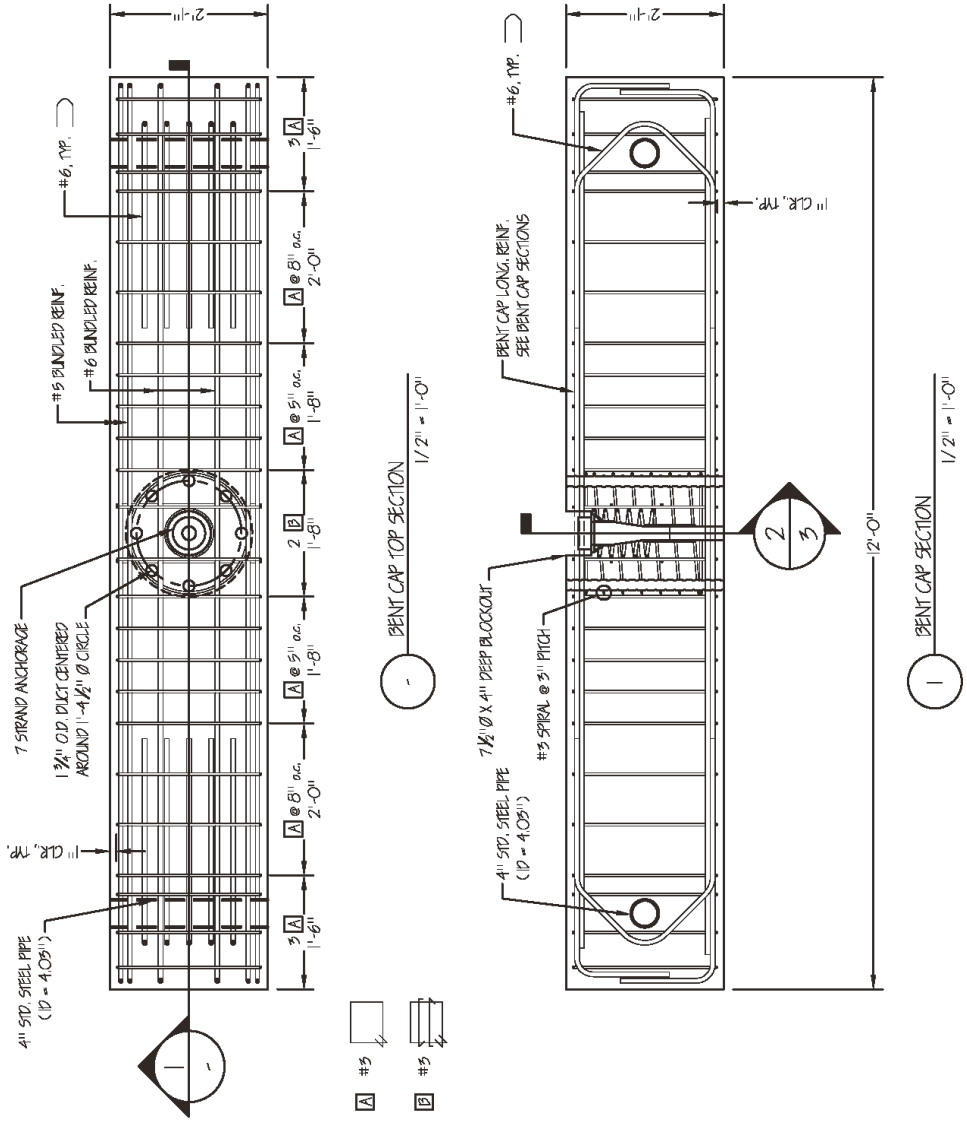

N.T.S.

APPROVED FOR PRODUCTION

UCSD

NCHRP PROJECT 12-74

BENT CAP DETAILS

DUCTILITY:	SUPER. CONNECTION:	CONNECTION DETAIL:
FULL	NON-INTEGRAL	HYBRID SPECIMEN 3 - DUAL SHELL COLUMN

BY:	CHK:	DATE:	SCALE:	SHEET:
MJT		01/08/08	1/2" = 1'-0"	02

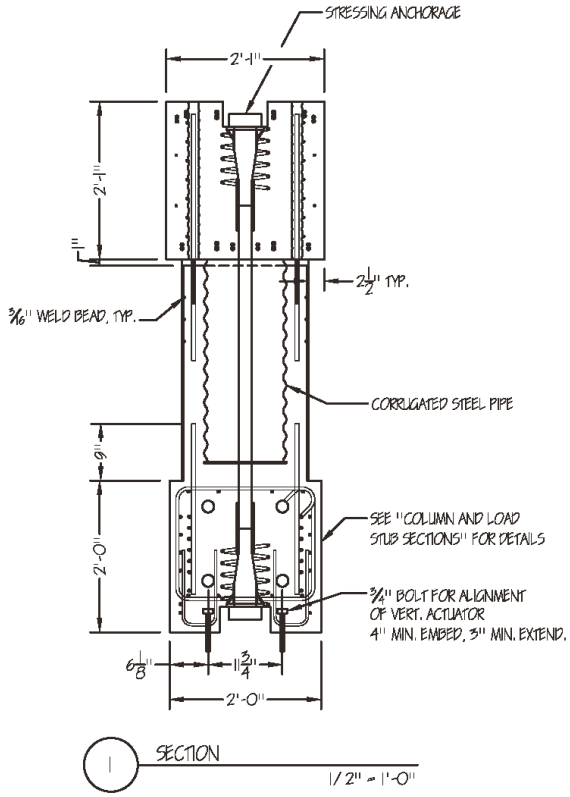

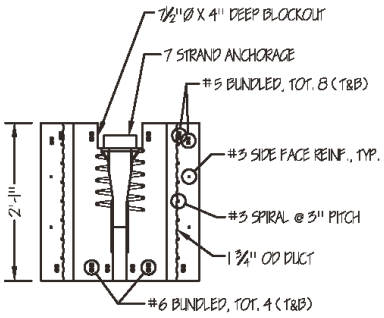

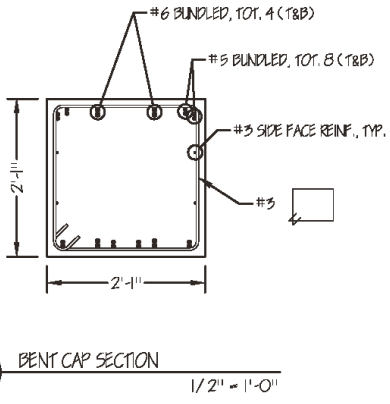

NOTE:
TWO COLUMN REINFORCING BARS AND FOUR BEAM REINFORCING BARS CONTAINS STRAIN GAGES (SEE INSTRUMENTATION PLAN)

N.T.S.

APPROVED FOR PRODUCTION

UCSD

NCHRP PROJECT 12-74

GENERAL SECTION

DUCTILITY:	SUPER. CONNECTION:	CONNECTION DETAIL:
FULL	NON-INTEGRAL	HYBRID SPECIMEN 3 - DUAL SHELL COLUMN

BY:	CHK:	DATE:	SCALE:	SHEET:
MJT		01/08/08	1/2" = 1'-0"	03

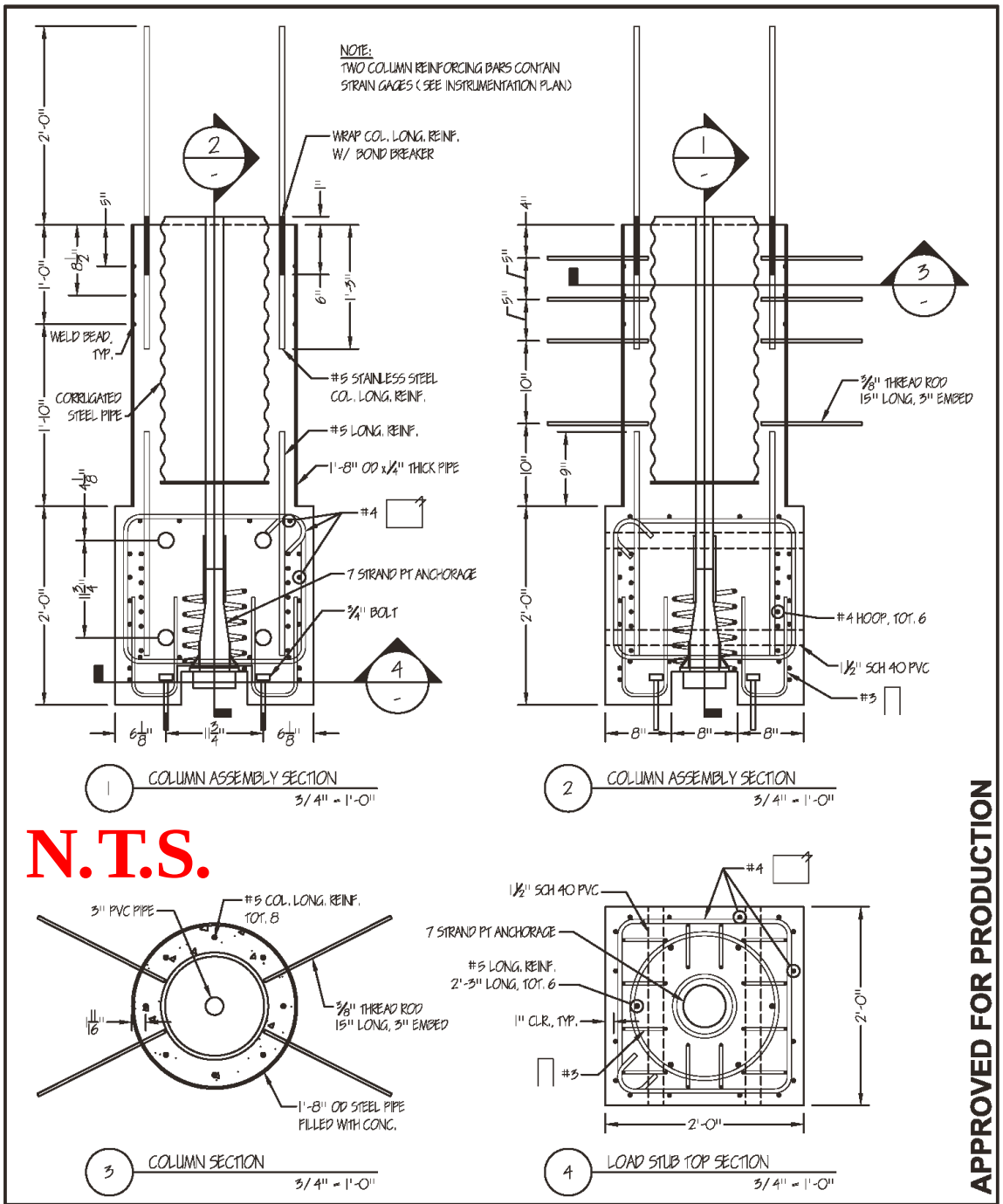
NOTE:
TWO COLUMN REINFORCING BARS CONTAIN STRAIN GAGES (SEE INSTRUMENTATION PLAN)
WRAP COL. LONG. REINF. W/ BOND BREAKER
WELD BEAD, TYP.
CORRUGATED STEEL PIPE
#5 STAINLESS STEEL COL. LONG. REINF.
#5 LONG. REINF.
1'-8" OD x 1/4" THICK PIPE
#4
7 STRAND PT ANCHORAGE
3/4" BOLT
3/8" THREAD ROD 15" LONG, 3" EMBED
#4 HOOP, TOT. 6
1 1/2" SCH 40 PVC
#3
COLUMN ASSEMBLY SECTION
3/4" = 1'-0"
COLUMN ASSEMBLY SECTION
3/4" = 1'-0"
N.T.S.
3" PVC PIPE
#5 COL. LONG. REINF. TOT. 8
3/8" THREAD ROD 15" LONG, 3" EMBED
1'-8" OD STEEL PIPE FILLED WITH CONC.
1 1/2" SCH 40 PVC
7 STRAND PT ANCHORAGE
#5 LONG. REINF. 2'-3" LONG, TOT. 6
1" CLR., TYP.
COLUMN SECTION
3/4" = 1'-0"
LOAD STUB TOP SECTION
3/4" = 1'-0"
APPROVED FOR PRODUCTION
UCSD
NCHRP PROJECT 12-74
COLUMN AND LOAD STUB SECTIONS
DUCTILITY: FULL
SUPER. CONNECTION: NON-INTEGRAL
CONNECTION DETAIL: HYBRID SPECIMEN 3 - DUAL SHELL COLUMN
BY: MJT
CHK:
DATE: 01/08/08
SCALE: 3/4" = 1'-0"
SHEET: 04

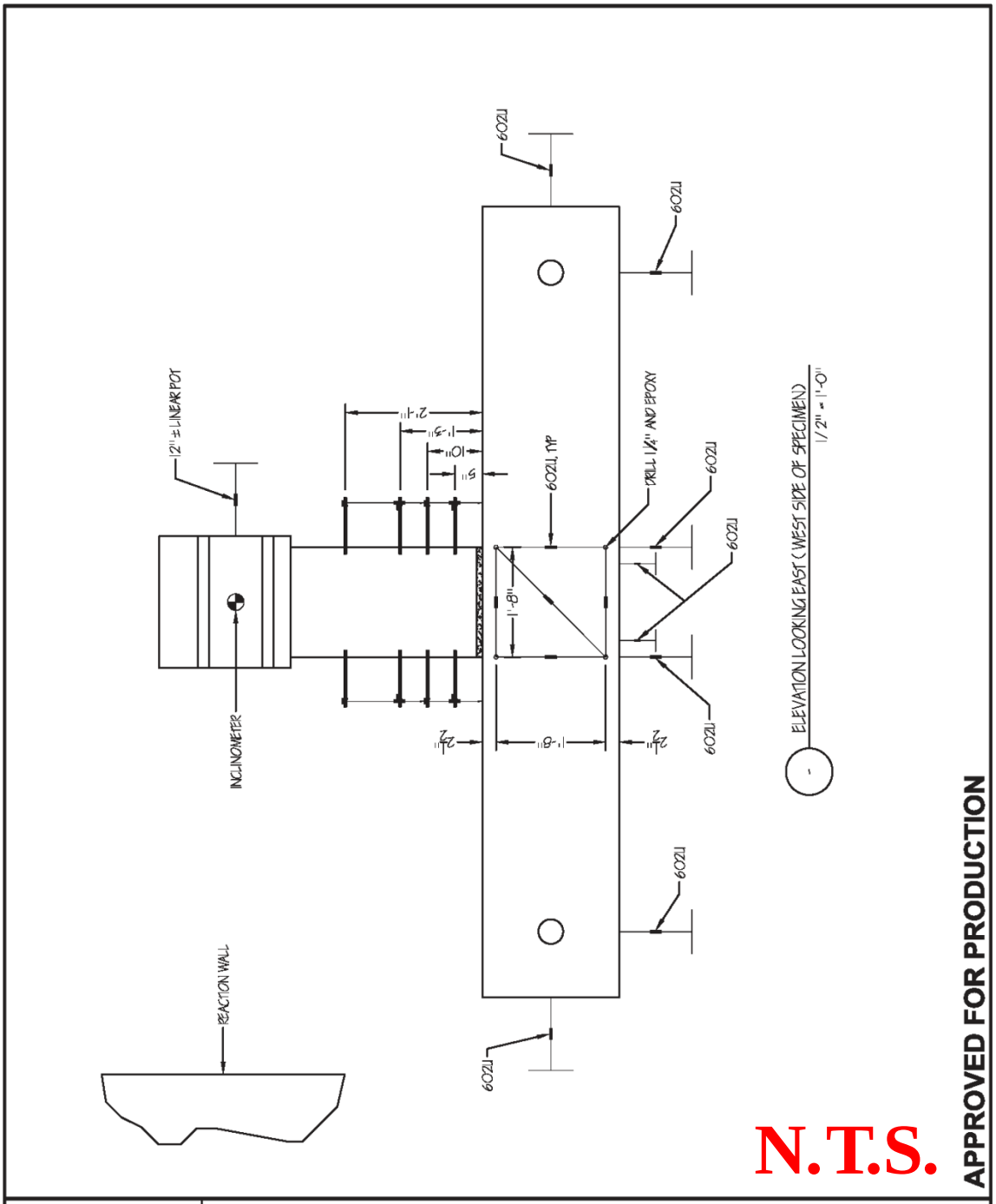

UCSD	NCHRP PROJECT 12-74				
	INSTRUMENTATION PLAN 2				
	DUCTILITY: FULL	SUPER. CONNECTION: NON-INTEGRAL	CONNECTION DETAIL: HYBRID SPECIMEN 3 - DUAL SHELL COLUMN		
	BY: MJT	CHK:	DATE: 11/08/07	SCALE: NTS	SHEET: 07

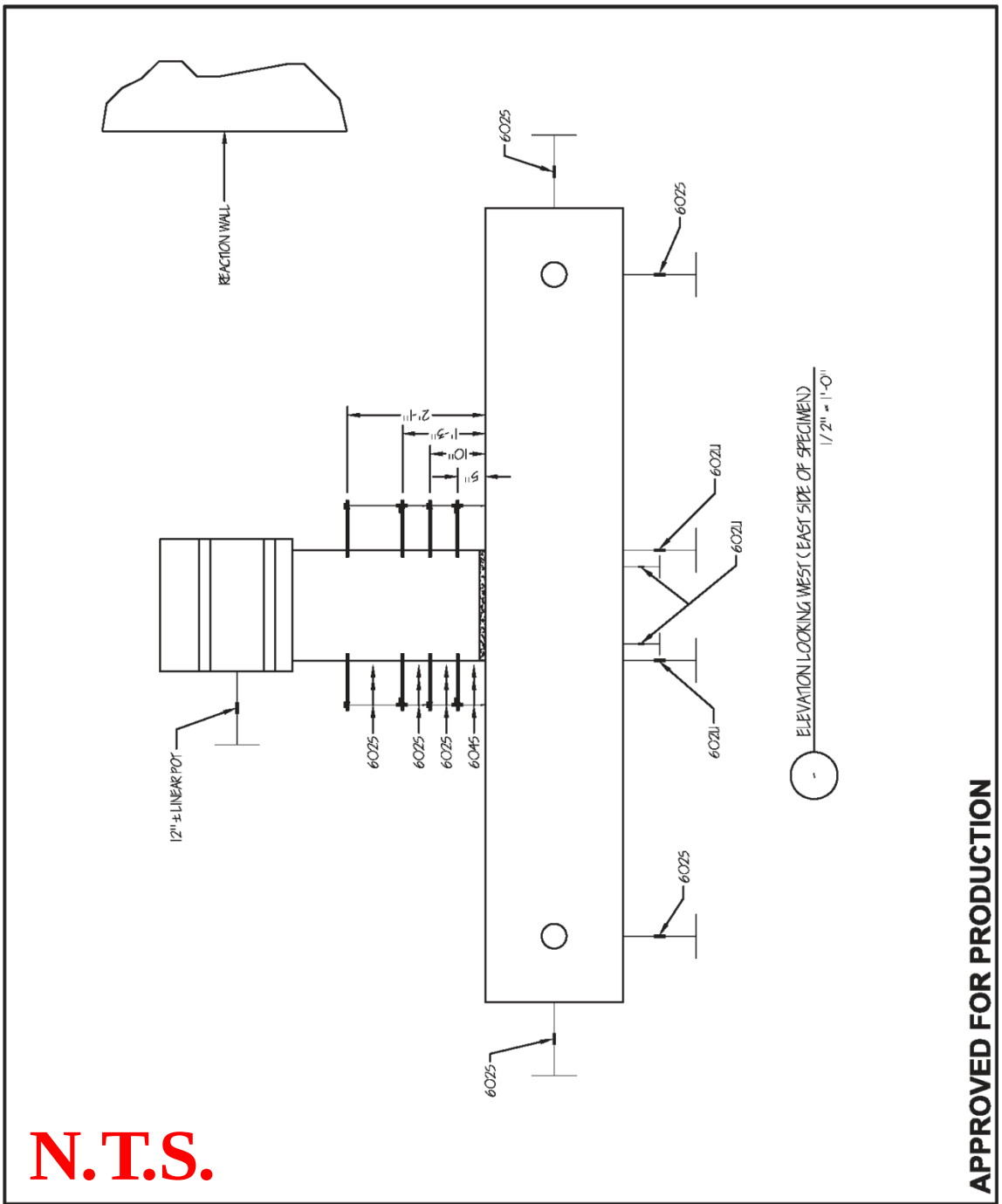

N.T.S.

UCSD

NCHRP PROJECT 12-74

INSTRUMENTATION PLAN 3

FACILITY:	SUPER. CONNECTION:	CONNECTION DETAIL:
FULL	NON-INTEGRAL	HYBRID SPECIMEN 3 - DUAL SHELL COLUMN

BY:	CHK:	DATE:	SCALE:	SHEET:
MJT		11/08/07	NTS	08

COLUMN LONGITUDINAL BAR (STAINLESS)
SIZE OF BAR: No. 5
BARS TO GAGE: 04

NOTES:
AT EACH LOCATION PLACE TWO STRAIN GAGES ON OPPOSITE SIDES OF THE BAR

NUMBER OF GAGES REQUIRED:
5 MM 6 EA. BAR (12 TOTAL)
5 MM YIELD 6 EA. BAR (12 TOTAL)

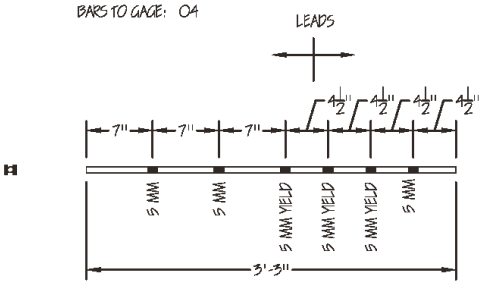

JOINT SHEAR REINFORCEMENT
SIZE OF BAR: No. 3
BARS TO GAGE: 02

NOTES:
PLACE GAGE ALONG CENTERLINE OF BAR AS SHOWN

NUMBER OF GAGES REQUIRED:
3 MM 6 EA. BAR (6 TOTAL)

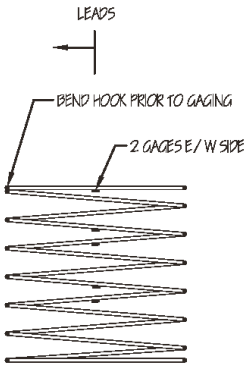

BENT CAP LONGITUDINAL BARS
SIZE OF BAR: No. 6
BARS TO GAGE: 08

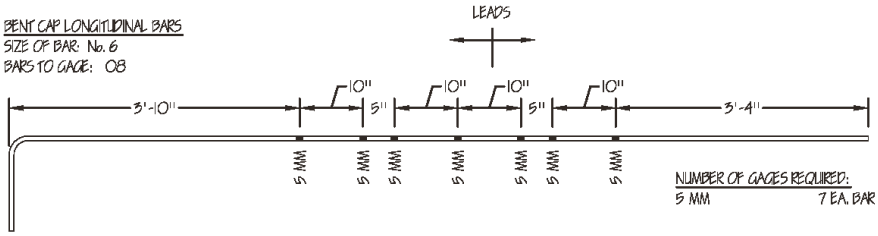

NUMBER OF GAGES REQUIRED:
5 MM 7 EA. BAR (28 TOTAL)

N.T.S.

APPROVED FOR PRODUCTION

UCSD

NCHRP PROJECT 12-74					
STRAIN GAGING PLAN					
DUCTILITY: FULL	SUPER. CONNECTION: NON-INTEGRAL	CONNECTION DETAIL: HYBRID SPECIMEN 3 - DUAL SHELL COLUMN			
BY: MJT	CHK:	DATE: 11/08/07	SCALE: NTS	SHEET: 09	

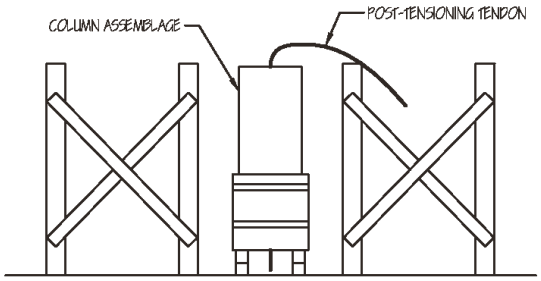

CONSTRUCTION STAGE ACTIVITIES:

1. SET COLUMN ASSEMBLAGE ON SUPPORTS
2. THREAD POST-TENSIONING TENDON THROUGH COLUMN AND SET IN DEAD END ACHORAGE
3. CONSTRUCT BENT CAP SUPPORT STRUCTURE

STAGE 1

1/4" = 1'-0"

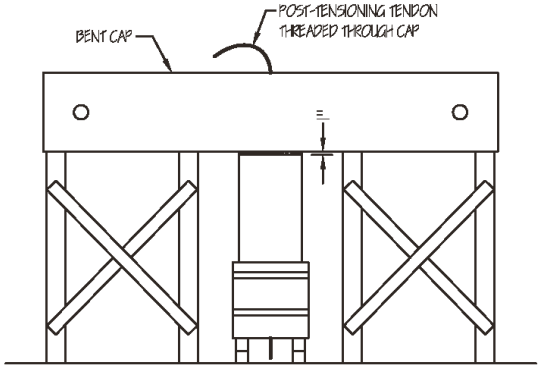

CONSTRUCTION STAGE ACTIVITIES:

1. SET BENT CAP ON SUPPORT STRUCTURE
2. THREAD POST-TENSIONING TENDON THROUGH BENT CAP
3. FORM AROUND BEDDING LAYER
4. GROUT BEDDING LAYER AND GROUTED DUCTS PER GROUTING PROCEDURE

STAGE 2

1/4" = 1'-0"

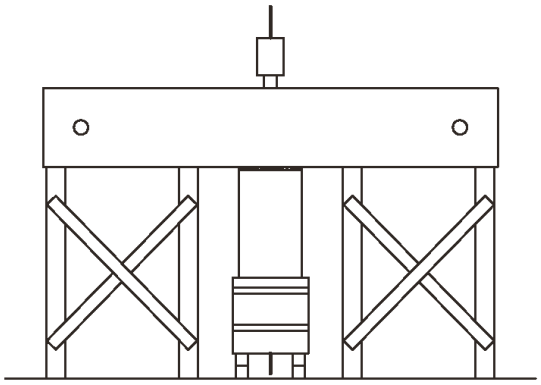

CONSTRUCTION STAGE ACTIVITIES:

1. ALLOW GROUT TO SET PER GROUT PROCEDURE
2. POST-TENSION TENDONS TO SPECIFIED LOAD
3. CUT EXCESS TENDON FROM BOTH ANCHORAGES

STAGE 3

1/4" = 1'-0"

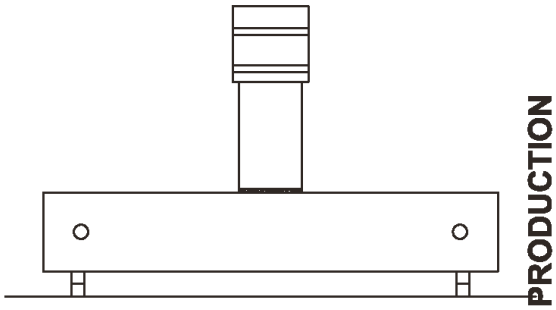

CONSTRUCTION STAGE ACTIVITIES:

1. INVERT SPECIMEN PER "SPECIMEN INVERSION PROCEDURE"
2. MOVE SPECIMEN TO TEST SETUP
3. PAINT SPECIMEN
4. ATTACH ACTUATORS

STAGE 4

1/4" = 1'-0"

N.T.S.

APPROVED FOR PRODUCTION

UCSD

NCHRP PROJECT 12-74

ERECTION PROCEDURE

DUCTILITY:	SUPER. CONNECTION:	CONNECTION DETAIL:
FULL	NON-INTEGRAL	HYBRID SPECIMEN 3 - DUAL SHELL COLUMN

BY:	CHK:	DATE:	SCALE:	SHEET:
MJT		11/08/07	1/4" = 1'-0"	10

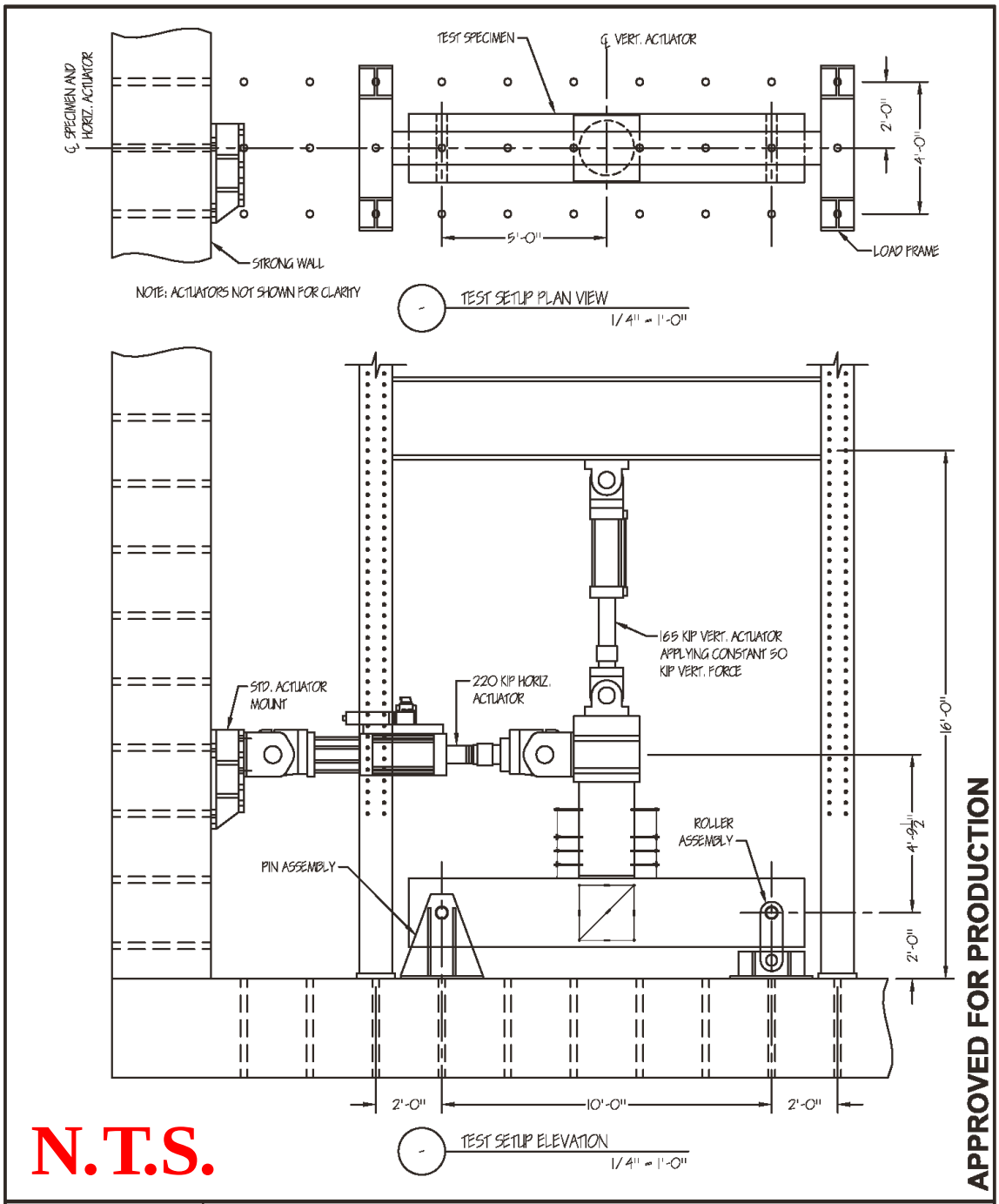

UCSD

NCHRP PROJECT 12-74

TEST SETUP OVERVIEW

DUCTILITY:	SUPER. CONNECTION:	CONNECTION DETAIL:
FULL	NON-INTEGRAL	HYBRID SPECIMEN 3 - DUAL SHELL COLUMN

BY:	CHK:	DATE:	SCALE:	SHEET:
MJT		11/08/07	1/4" = 1'-0"	11

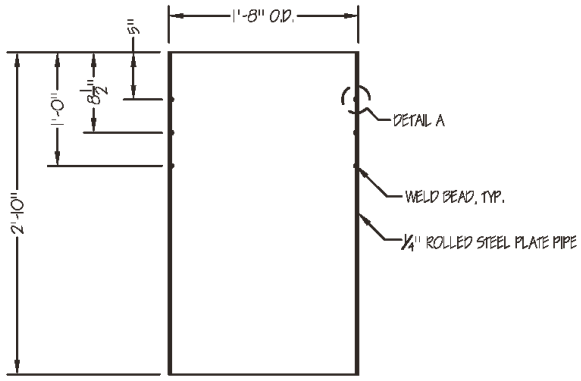

1 STEEL PIPE LONG SECTION
3/4" = 1'-0"

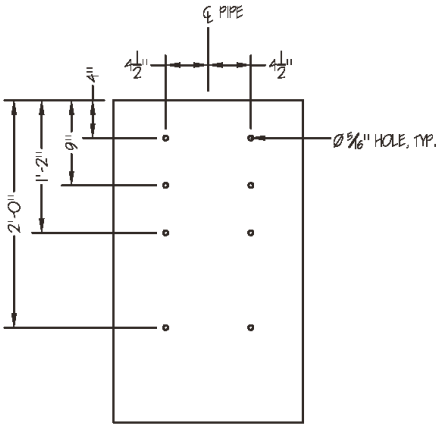

1 STEEL PIPE HOLE LOCATIONS
3/4" = 1'-0"

NOTES:

1. ROLLED STEEL PLATE PIPE SHALL BE A572 GRADE 50 AND WELDING SHALL BE COMPLETE JOINT PENETRATION.
2. ALL WELDING SHALL BE USING E70 ELECTRODE.
3. LOCATIONS OF WELD BEAD GIVEN TO CENTER OF BEAD.
4. WELD BEAD SHALL BE PLACED AROUND ENTIRE INNER CIRCUMFERENCE.
5. A TOTAL OF 2 PIPE SECTIONS SHALL BE FABRICATED.

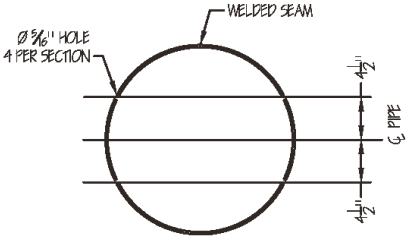

1 STEEL PIPE SECTION
3/4" = 1'-0"

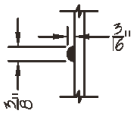

A WELD BEAD DETAIL
1/4" = 1"

N.T.S.

APPROVED FOR PRODUCTION

UCSD

NCHRP PROJECT 12-74

COLUMN PIPE DETAIL

DUCTILITY:	SUPER. CONNECTION:	CONNECTION DETAIL:
FULL	NON-INTEGRAL	HYBRID SPECIMEN 3 - DUAL SHELL COLUMN

BY:	CHK:	DATE:	SCALE:	SHEET:
MJT		11/08/07	AS SHOWN	12

University of California, San Diego

Department of Structural Engineering

Structural Systems Research Project

NCHRP 12-74 Integral System Final Report

By

Matthew J. Tobolski, Ph.D., P.E.

Graduate Student Researcher

José I. Restrepo, Ph.D.

Professor of Structural Engineering

Report Submitted to the National Cooperative Highway Research Program Under Contract No.
NCHRP Project 12-74

Department of Structural Engineering

University of California, San Diego

La Jolla, California 92093-0085

November 2009

DISCLAIMER

The opinions and conclusions expressed or implied in this report are those of the research agency. They are not necessarily those of the Transportation Research Board, the National Research Council, the Federal Highway Administration, the American Association of State Highway and Transportation Officials, or the individual states participating in the National Cooperative Highway Research Program.

EXECUTIVE SUMMARY

Throughout the United States and abroad, there are numerous bridge structures in need of structural repair or replacement to rectify deficiencies or enhance the operational performance of transportation networks. With the ever increasing congestion and a public desire to minimize the impact of highway construction, accelerated bridge construction practices are becoming more prevalent. Precast concrete bridge systems offer many advantages over traditional cast-in-place methods and can help to meet the public desire to minimize the impacts of bridge construction. Precast concrete systems can accelerate construction, reduce environmental impacts, improve construction safety and provide structures that are more durable. Due to limited knowledge of the performance of precast systems in seismic events, their usage in regions susceptible to earthquake shaking has been limited especially in high seismic regions.

The potential implementation of precast concrete systems in regions subjected to high seismic actions requires the development of integral precast connections. In order to reduce seismically induced displacement demands, designers often rely on framing action between the superstructure and substructure. Developing integral behavior using precast systems while minimizing the required on site cast-in-place connections is cumbersome. There is a clear need to develop and validate an integral connection detail which minimizes the required on-site casting of cementitious materials as a means to accelerate bridge construction. In addition, the developed detail needs to be constructible and cost effective to promote the use throughout the nation's seismic regions.

This report presents the findings of an extensive research program conducted under the National Highway Cooperative Highway Research Program (NCHRP) Project 12-74, "Development of Precast Bent Cap Systems for Seismic Regions." The current report specifically details the research efforts associated with the development and validation of a promising integral, precast concrete bridge system. The proposed detail draws on many bridge systems and details that have been previously constructed in the United States and abroad. This detail relies on the splicing of precast concrete girders through the precast bent cap using post-tensioning. In developing this connection type, the research team considered the commonly used precast segmental superstructure type and also the precast, post-tensioned splice girder. This investigated detail was developed with significant collaboration with industry in an attempt to develop a cost-effective, constructible detail.

This report is divided into four chapters. Chapter 1 provides an introduction to the use of precast bent cap systems and a discussion of previous research and construction projects using integral, precast concrete connection concepts. Chapter 2 provides an in depth discussion of the connection detail considered in this investigation, the associated target performance objectives and the prototype structure used for the development of the testing program. Chapter 3 provides a summary of the test specimen and loading, outlines the construction activities and describes the overall testing program. Chapter 4 presents the results of the experimental and analytical efforts, provides a discussion of the observed performance and presents general design recommendations developed through this research effort.

ACKNOWLEDGEMENTS

This research project was sponsored by the American Association of State Highway and Transportation Officials, in cooperation with the Federal Highway Administration, and was conducted in the National Cooperative Highway Research Program (NCHRP) under Project 12-74 “Development of Precast Bent Cap Systems for Seismic Regions”, which is administered by the Transportation Research Board of the National Research Council. This financial support is greatly acknowledged.

The authors would like to acknowledge the dedicated efforts and valuable comments of the NCHRP 12-74 Research Team, including: Dr. Eric Matsumoto (Co-PI), Mary Lou Ralls, Steve Mislinski, Jon Grafton and Dr. Nigel Priestley. In addition, the efforts of the NCHRP 12-74 Technical Advisory Group are greatly appreciated, including: Dr. Reid Castrodale, Bill Spence, Scott Harrigan, Lucian Bodgan, Daniel Tassin and Robert Gulyas. The insightful comments and guidance of the NCHRP 12-74 Project Panel are also greatly appreciated.

The experimental efforts described herein could not have been performed if not for the dedicated and skillful efforts of the staff at the Charles Lee Powell Structural Research Laboratories at the University of California, San Diego. The following individuals are acknowledged: Andrew Gunthardt, Paul Greco, Dr. Chris Latham, Bob Parks and John Ward.

Industry support has greatly contributed to the success of this research program. Material donations were provided by Dywidag Systems International (post-tensioning hardware and strand).

TABLE OF CONTENTS

LIST OF FIGURES

LIST OF TABLES

NOTATIONS

C	Compression force acting at the joint, kip
d_{ss}	Total depth of superstructure, inches
M_a	Applied moment demand, kip-ft
M_{DL}	Dead load moment, kip-ft
M_n	Nominal moment capacity, kip-ft
$M^o{}_S$	Overstrength seismic moment demand on superstructure, kip-ft
T_{pse}	Post-tensioning force after short and long-term losses (end of service), kip
$T_{PT,b}$	Force in lower post-tensioning ducts, kip
$T_{PT,t}$	Force in upper post-tensioning ducts, kip
T_s	Force in deck reinforcement, kip
V_a	Applied shear demand, kip
V_{cap}	Shear friction capacity at joint, kip
φ_u	Ultimate curvature capacity, inches^{-1}
θ_u	Ultimate rotation capacity, radians
μ	Shear friction coefficient

Chapter 1 Introduction

Throughout the United States, there are a great number of bridges that are in need of repair or replacement to rectify structural deficiencies and/or to meet the operational needs of a region (ASCE, 2009). According to the U.S. Department of Transportation (2007), approximately 25% of the United States bridges are classified as either structurally deficient or functionally obsolete. This means that over 150,000 bridges throughout the United States are classified as deficient in some manner. Figure 1.1 provides a graphical overview of the number of structurally deficient and functionally obsolete bridges throughout the United States along with the seismic design category for Site Class D soil. Clearly, a significant number of bridges requiring repair or replacement are located in regions requiring some level of seismic design. There is a clear need to develop innovative, seismically resistant approaches to replace these deficient structures while minimizing the impacts to the public, environment and workers.

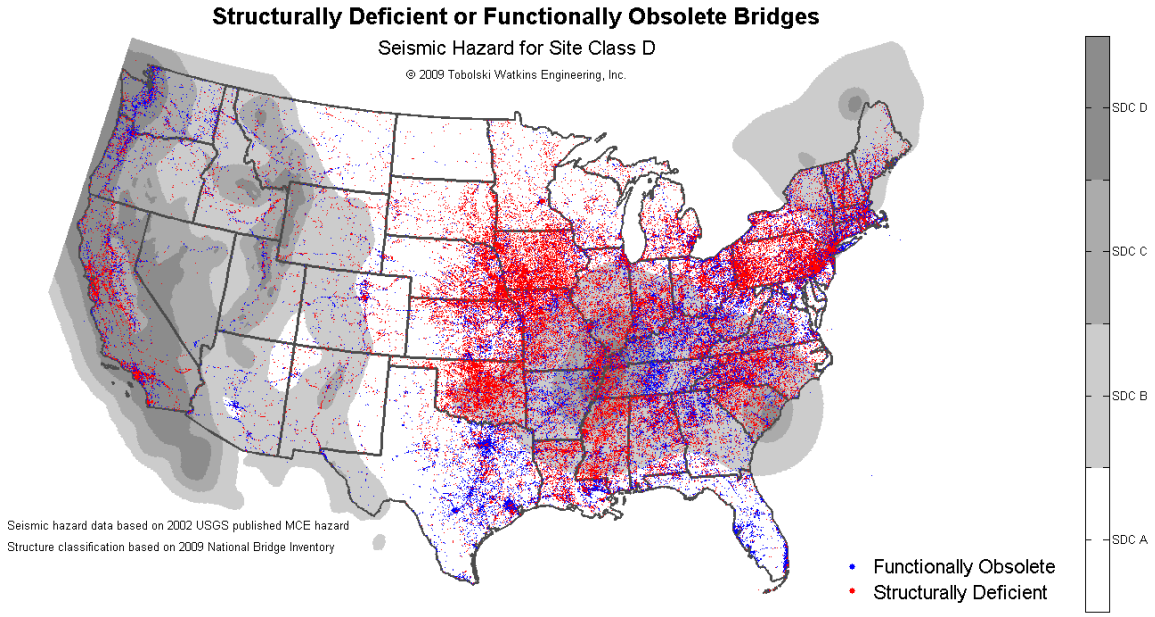

Figure 1.1 Structurally Deficient and Functionally Obsolete Bridges Overlapping the US Seismic Hazard Map for Site Class D Soil

Many of the deficient or obsolete bridges serve as key links in local and national transportation networks with severe impacts associated with bridge closures. With bridges located in urban regions, the potential impacts to a large population are obvious. However, the impacts in rural regions can be as significant as many times local bridges serve as the only convenient means of getting from one point to another without significant detours.

The potential impacts of bridge construction to the public are apparent, whether through traffic delays or potential local impacts on the economy. In addition, lengthy on-site bridge construction projects put construction workers at increased risk. Reducing construction time therefore can serve to reduce the impacts on the public, on workers and on the environment. The use of precast concrete solutions for accelerating bridge construction can also enhance the quality of the end product through fabrication in a more controlled environment.

However, the jointed nature of precast concrete has limited its use in high seismic regions due to uncertainties in seismic response when precast elements serve as elements in the lateral force resisting system (Tobolski, et al., 2006). Due to the promising nature of precast construction for accelerated bridge construction, there has been significant interest in its use in all regions of seismicity. The National Cooperative Highway Research Program (NCHRP) funded Project 12-74 to investigate the development of seismically reliable precast concrete bent cap systems as a means to accelerate bridge construction throughout the United States. This report presents the results of a portion of NCHRP Project 12-74 focused on the investigation of a promising girder-to-bent cap connection for seismic resistance.

1.1 Overview

Previous research conducted as a part of NCHRP 12-74 focused on the column-to-bent cap connections aimed at validating connection details for non-integral bridge systems. For a non-integral system, the connection between the superstructure and substructure is intended to be pinned such that in the longitudinal direction the inelastic action is focused at the base of the columns (see Figure 1.2a). The detail investigate in this report is an integral detail in which framing action is intended between the superstructure and substructure (see Figure 1.2b). For high seismic regions, it is often desirable to use an integral detail such that the imposed seismic displacement demands are reduced. Providing integral response for cast-in-place systems is relatively simple as all connections are made with monolithic concrete pours producing reliable connections. For precast systems, achieving integral response while meeting accelerated construction goals is more complicated due to inherent jointed nature of precast construction.

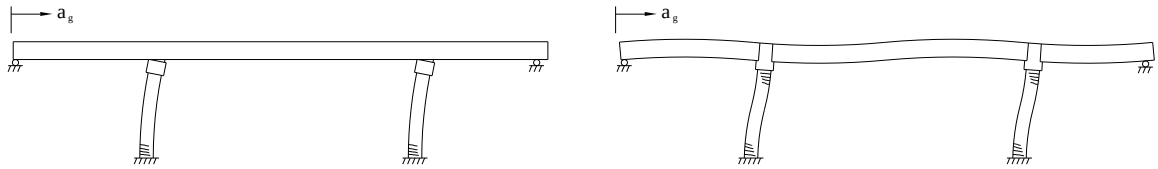

Figure 1.2 System response for a) non-integral systems and b) integral systems

A review of previous precast, integral system details for high seismic applications indicated a common requirement for site cast concrete connections. Figure 1.3 provides an image of a connection detail used on the San Mateo-Hayward bridge in northern California. This connection detail can be classified as a partially precast bent cap as the majority of the bent cap was cast on site. In comparison to cast-in-place construction, this detail proved to accelerate construction significantly. However, the significant amount of onsite casting of concrete was considered undesirable during the development of the connection detail investigated in this report.

Figure 1.3 San Mateo-Hayward bent cap during construction

While there has not been significant usage in high seismic regions in the United States, the use of precast segmental construction has many of the desirable characteristics sought in the development of the connection detail in this report. Precast, balanced cantilever segmental construction has historically used cast-in-place pier segments through which primary longitudinal post-tensioning runs. The splicing of segments through a pier segment was the driving force in the development of the detail investigated herein. The goal of the detail is to require only a minimal amount of site casting of cementitious material. In the detail presented herein, the goal is to splice the post-tensioning through the bent cap with a closure joint constructed of grout between the bent cap and girder (see Figure 1.4). To minimize the construction footprint, this detail was also developed considering the use of strong back systems to support all girders from the top down minimizing the need for the construction of temporary falsework. The system being investigated was aimed at meeting an array of performance objectives, from accelerated construction to reliable seismic performance.

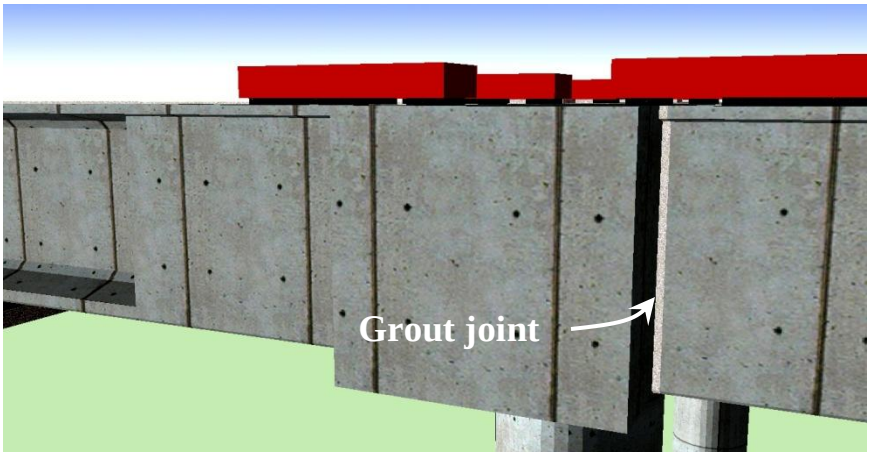

Figure 1.4 Proposed precast bent and girder detail

1.2 Background

In recent years, experimental and analytical efforts have been conducted relating to the use of integral precast superstructure systems for high seismic applications. Research has been conducted on precast girder systems, as well as precast segmental systems.

A large-scale investigation on the use of precast girder systems in an integral manner was conducted at the University of California, San Diego (Holombo, et al., 1998). This study focused on the longitudinal seismic response of two different precast girder specimens that are spliced though a cast-in-place concrete bent cap. The first specimen used precast bulb-tee girders, which are continuous through the bent cap and spliced away from the bent cap joint (Figure 1.5). The second specimen used precast bathtub girders, which are discontinuous at the bent cap joint and splice through the cast-in-place bent cap (Figure 1.6). The seismic response of these systems was investigated through the lateral load testing of a 40% scale portion of a prototype bridge representative of a typical California structure. The aim of this project was to confirm the overall structural design would provide essentially elastic superstructure response with inelasticity in the system mainly focused in specially detailed column hinges.

Longitudinal post-tensioning was present in both details with a profile developed primarily based on service load demands. Therefore, longitudinal post-tensioning was run high across the bent cap to maximize the negative flexural capacity across the cap. Positive continuity was made using pretensioning strand extensions spliced within the cast in place bent cap.

Figure 1.5 Bulb-tee girder specimen (Holombo, et al., 1998)

Figure 1.6 Bathtub girder specimen (Holombo, et al., 1998)

Experimental results confirmed the intended longitudinal response mechanism with essentially elastic superstructure response. The overall system exhibited adequate inelastic displacement capacity provided mainly by the flexural hinging in the reinforced concrete column. Due to the use of transverse post-tensioning in the bent cap, the researchers recommended that the bulb-tee girders located adjacent to the column be designed for two-thirds of the overstrength seismic moment whereas for the bathtub girder system, the researchers recommended that the webs adjacent to the column be designed for 55% of the overstrength seismic moment. This

recommendation varies from the provisions of the AASHTO Guide Specification for LRFD Seismic Bridge Design, which requires the effective area for superstructure flexural resistance be based on a 45-degree projection from the bottom of bent cap (AASHTO, 2009). The main reason for the increase in distribution of seismic moment at the bent cap is the enhancement of the torsional distribution mechanism in the cap through post-tensioning.

Although not identical in details, precast segmental bridges have similarities in terms of connection details when compared with the fully precast bridge system considered in the current research program. Both systems have distinct discontinuities between precast segments, which are required to transfer vertical shear demand as well as resist imposed flexural moment demands. Therefore, research related to the seismic response of precast segmental bridge structures is relevant. A multi-phased research program was conducted at the University of California, San Diego. Phase I was targeted at the investigation of mid-span segment joint response with flexurally dominated loading, i.e. high moment-low shear, whereas Phase II was targeted at the pier segment joint response, i.e. high moment-high shear (Megally, et al., 2002; Megally, et al., 2003). This research effort investigated the use of bonded versus unbonded post-tensioning in the superstructure. Response from these experimental efforts indicated that precast segmental details have large rotation capacity with failure controlled by either rupture of longitudinal post-tensioning or crushing of concrete. The use of unbonded post-tensioning produce a noticeably more ductile response as compared to fully bonded post-tensioning. Negligible shear slip at segment joints was recorded during testing.

Phase III of the University of California, San Diego research project was a large scale system test to investigate overall longitudinal seismic response of a precast segmental bridge system (Burnell, et al., 2005; Megally, et al., 2003; Megally, et al., 2002). An overview of the experimental specimen is shown in Figure 1.7. Initial stages of testing were designed to maintain zero joint opening up to a displacement ductility of 4. Following this target, additional vertical load was added and post-tensioning reduced to allow flexural joint opening. During testing, all observed joint openings reversed and closed upon removal of lateral loading. Ultimate failure of the system was controlled by the column substructure system, thus the superstructure was known to have reserve capacity.

Figure 1.7 Precast segmental system test

Phase I-III focused on the local response of segmental bridge joints under potential seismic loading conditions. The influence of the seismic joint opening on overall system response was investigated in more detail in a subsequent analytical phase (Veletzos, et al., 2006). A preliminary stage of this effort was the detailed calibration of segment non-linear models for inclusion in large bridge models. The efforts of Phase I and II were used in the development of these models. Two bridge models were developed similar to recently constructed precast segmental bridges in California to investigate the influence of joint stress condition due to time-dependent effects and vertical accelerations. Analytical results indicated that the stress condition on the joint could play a role in the extent of seismic joint opening. Additionally, vertical ground motion effects were shown to be significant especially for long span structures. The shorter span length structure was 300 feet in length, which is significantly greater than any structure constructed with precast girders. Time dependent effects should be considered by analysis at the end of construction and end of service life as these are the controlling limits.

While these projects did not investigate the bridge details considered in the current project, they did provide results that are of interest:

- Superstructure joint opening in large-scale bridge tests closed
- Capacity designed superstructures will remain essentially elastic
- Negligible shear slip between segments is observed under seismic testing
- Flexural opening due to vertical acceleration is more prominent on spans larger than those supported by precast girder construction

1.3 Objectives

The aim of the NCHRP 12-74 project is to develop systems and connection details that show promise for widespread implementation across the United States. Therefore, these systems and details must have adequate performance when subjected to service and extreme loading, be cost effective, durable, constructible and be aesthetically pleasing. The development of an integral detail constructed using precast concrete members intended for use in seismic regions presents unique challenges due to the jointed nature of the system and importance of these connections for seismic resistance. The detail that has been developed was the result of significant discussions and design reviews resulting in what is believed to be a reliable system, which can meet the accelerated bridge construction goals.

The overall concept of the integral system investigated herein is straightforward: provide a reliable flexural connection by splicing precast girders through the bent cap using post-tensioning. However, this detail could have variations in exact details used at the joint region. The intent of the testing program developed and executed was to investigate a specific variation of the detail that is severely loaded, i.e. a worst case loading. The reason the detail investigated is considered a worst case scenario is because the connection relies completely on the development of a stable shear friction mechanism to transfer vertical shear between the girder and bent cap. Another possible detail would utilize a permanent embedded strong back, which would provide a secondary means of shear transfer across the joint, i.e. a fully redundant shear transfer mechanism. Both concepts are reliable connection details expected to provide the requisite seismic performance.

1.4 Scope of Report

This report focuses on the analytical and experimental conducted on the integral bent cap connection detail developed under NCHRP Project 12-74. This report is divided into the following sections:

- Chapter 1: Introduction
    - Provides a discussion of relevant background to the project and connection detail considered
    - Discusses the objectives of the experimental program performed
- Chapter 2: Connection Detail Investigated and Analysis
    - Provides an in depth discussion of the detail investigated
    - Outlines the target performance objectives for the integral system

    - Presents the prototype structural design
- Chapter 3: Experimental Basis and Specimen Design
    - Provides a summary of the development of the test specimen based on the prototype structure
    - Presents the experimental specimen design and construction activities
    - Describes the testing program
- Chapter 4: Experimental Results
    - Presents the results of experimental testing and processed data
    - Provides a discussion of the observed structural performance and associated design recommendations

Chapter 2 Connection Detail Investigated and Analysis

This Chapter presents the integral connection detail investigated, the prototype bridge structure and associated structural analysis and predictions.

2.1 Connection Detail

2.1.1 Description

An initial step in this research program was the development of an appropriate integral connection detail and prototype structure for development of a realistic test specimen. The integral detail was developed with significant interaction within the research group, industry and the NCHRP 12-74 Panel.

Based on design objectives and input from the project Panel, the goal of the integral bridge detail was to develop a structural system that can be constructed in an accelerated manner, minimizing the use of site-cast concrete and providing a streamlined appearance for visual appeal. The resulting structure was developed using a similar mentality as a span-by-span constructed, precast segmental bridge. In this structure, precast girders are spliced through the bent cap using post-tensioning steel similar to the splicing of precast segmental segments with continuity post-tensioning following placement of all segments.

Figure 2.1 provides a section view of the typical connections showing the splicing of precast concrete girders through the bent cap member. In this system, the closure joint between the bent cap and precast girder is achieved using a 2-inch grout joint. Post-tensioning ducts are spliced in blockouts within the precast girder prior to grouting of the closure joint. Similar to a precast segmental superstructure, transfer of vertical shear is achieved through a shear friction mechanism developed through the presence effective post-tensioning force.

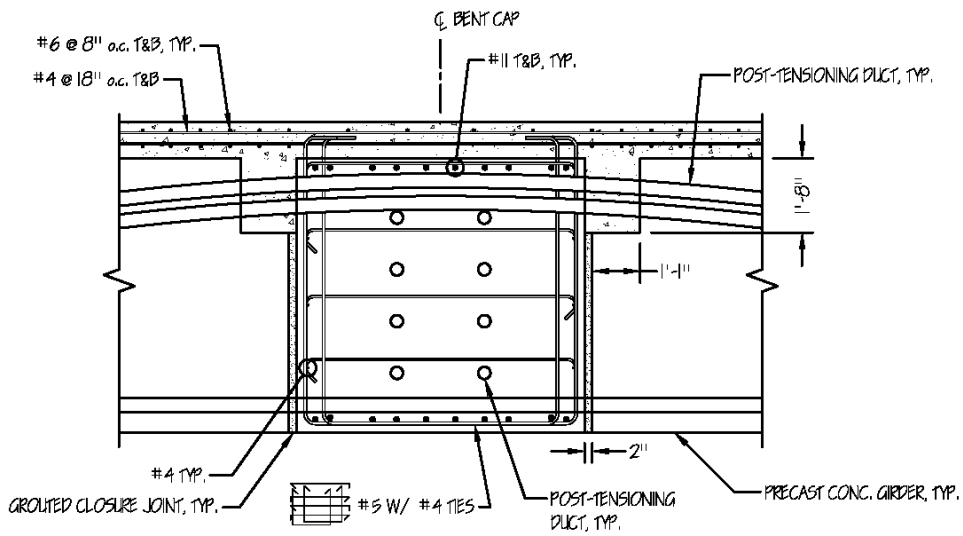

Figure 2.1 Prototype bridge bent cap transverse section

The vertical shear capacity of the system is a function of the compression force across the joint (see Figure 2.2). Therefore, the capacity is a function of the effective post-tensioning force, in addition to the increase in compression due to applied moment demands. For design purposes, the recommended method for determining the compression force is to consider only the effective post-tensioning force in the tendons at the end of service (considering short term and long term losses). The vertical shear capacity is equal to the effective compression force multiplied by a shear coefficient. For design purposes, this coefficient may be conservatively equal to 0.60 based on an assumed smooth joint between the grout and precast members.

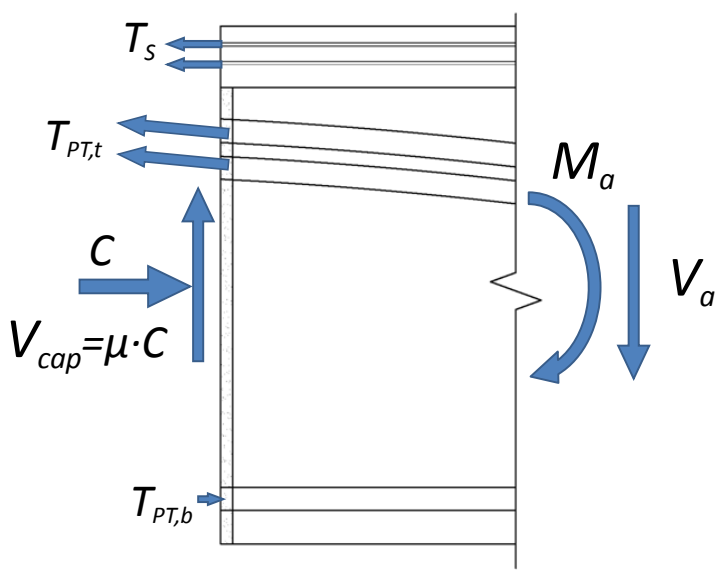

Figure 2.2 Girder shear friction mechanism

2.1.2 Performance Objectives

A rational design approach must be considered in the analysis, design and detailing of this integral connection to ensure reliable seismic performance is achieved. The overall seismic performance objectives for this system are:

- Operational Performance Objectives
    - Superstructure responses elastically under service load conditions
    - No shear slip between girder and bent cap that would affect rideability
- Life Safety Performance Objectives
    - Essentially elastic superstructure response under design level seismic
    - Collapse prevented under maximum considered earthquake with inelastic mechanism from column flexural plastic hinging
    - Ensure adequate superstructure rotation capacity to accommodate potential relative settlement

The Operational Performance Objectives are satisfied through superstructure design considering construction staging and time-dependent effects. The first two Life Safety Performance Objectives are satisfied through a capacity design approach, considering also the potential for vertical ground excitation. The third Life Safety Performance Objective is accommodated through proper detailing of the superstructure and subsequent validation through experimental testing as performed herein.

Development of Superstructure Design Forces

Traditional capacity design approaches should be used when designing the superstructure for seismic loading (see Figure 2.3). Overstrength seismic demands based on a selected earthquake resisting system must be considered to ensure the superstructure responds in an essentially elastic manner (AASHTO, 2009). In the event that either the positive or the negative flexural capacity is significantly greater than the other, it is permissible to allow for a redistribution of up to 30% of the seismic moment demand (Priestley, et al., 1996). Additionally, the combination of horizontal and vertical seismic demand should be considered to ensure acceptable joint response is achieved.

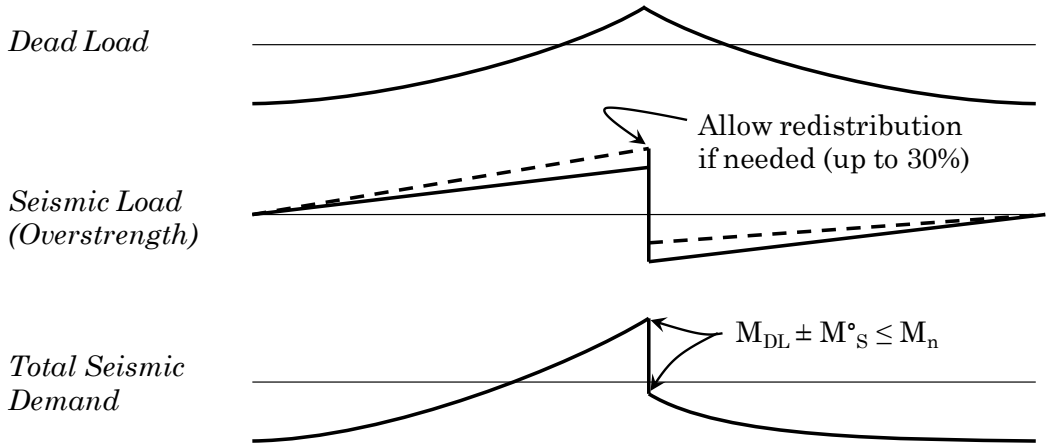

Figure 2.3 Superstructure demand and capacity protection

While capacity design approaches can provide for a rational superstructure design when subjected to lateral seismic loading, there are shortcomings relating to the seismic design for considering vertical loading. As a vertical mechanism is not developed in the column, the effects of flexural hinging in the column must be added to the vertical seismic demands on an elastic basis. Previous research has shown the sensitivity of jointed superstructures to vertical seismic demands (Veletzos, 2007). Vertical demand analysis is recommended by AASHTO (2009) and Caltrans (2006) for bridges located near faults with significant shortcomings in the development of demands. Caltrans requires the consideration of uniform 0.25g acceleration for structures with design rock acceleration equal to or greater than 0.6g. AASHTO does not address the development of vertical acceleration demands but states that vertical motion should be considered for near source events. A more rigorous procedure for the development of input seismic demands is required for this structure type.

Research conducted by Bozorgnia and Campbell (2004) determined that the vertical acceleration spectrum, as compared to horizontal demand spectrum, is sensitive to the period, fault distance and soil type. This study provided results as a ratio of vertical spectral demand to horizontal spectral demand at each period (termed the V/H ratio). The V/H ratio was found to be much less sensitive to earthquake magnitude and fault mechanism. A procedure for the development of an appropriate vertical design spectrum is presented in the article, which can be used for design of this integral system. Vertical seismic demand can increase the flexural design moment in the superstructure, but more importantly, can increase the vertical shear demand at the joint, which relies on a shear friction mechanism.

For the consideration of vertical shear effects, a vertical response spectrum analysis is recommended using either a site-specific vertical design spectrum or a spectrum developed through the procedure presented by Bozorgnia and Campbell (2004). The vertical seismic demands should be added to the demands developed through the commonly used capacity design procedure for lateral seismic demands to develop the total seismic demand on the superstructure.

Superstructure Design

For the integral connection considered, the key response of the bridge will be focused at the joint between the precast girder and precast bent cap. Flexural moment and shear capacity across the joint is provided by the presence of post-tensioning which runs through both the top and bottom of the joint. The top post-tensioning tendons are stressed and must be designed to provide adequate negative flexural resistance for strength and extreme event load cases. Additionally, as these are the stressed tendons they must also be designed to provide adequate effective post-tensioning to develop the required vertical shear capacity across the joint. The unstressed bottom continuity tendon is intended to enhance the positive flexural capacity across the joint and provide some level of resistance to joint opening under lower level lateral loading.

Design of the post-tensioning force should be based on service, strength and extreme event load cases in accordance with AASHTO provisions (2007). For service level design, it is important to consider the development of stresses in the structure between composite and non-composite actions due to construction staging. Negative flexural moment capacity can be determined using traditional AASHTO equations for concrete design. However, for positive flexural capacity, simplified equations do not adequately predict the capacity of the system at the joint due to the presence of unstressed post-tensioning tendons. The positive flexural capacity should be determined through strain compatibility. Away from the bent cap-to-girder joint, traditional flexural design approaches can be implemented.

At the joint, the shear transfer is accommodated through a shear friction mechanism. It is recommended that the effective post-tensioning force at the end of service life should be considered in this shear transfer mechanism multiplied by a friction coefficient equal to 0.6 (conservatively assumed smooth surface). The effective post-tensioning force and associated shear friction capacity shall be greater than the total vertical shear demand from strength or extreme event load cases. Due to the importance of this shear mechanism and variation in traditional shear capacity, it is appropriate to consider additional conservatism in the developed capacity.

For shear design in the girder near the joint, the potential for joint opening must be considered in determining the spacing and size of shear reinforcement. The potential for joint opening dictates the need to consider a reduced shear depth relative to the shear transfer mechanism. The total vertical shear demand must be developed within the neutral axis depth when subjected to opening moments. The neutral axis depth should be determined through a strain compatibility analysis, such as moment curvature analysis, to ensure a realistic estimation of the neutral axis depth is achieved. This shear distribution length assumes a strut mechanism develops with approximately a 45-degree angle. The area of shear reinforcement within that region must be capable of resisting the maximum vertical shear load calculated in the girder.

Superstructure Detailing

Although the design approach is to produce essentially elastic response in the superstructure, the girder ends should be detailed considering the potential for inelastic actions including joint opening and yielding at the joint caused by potential relative settlement or vertical flexural demands in excess of design demands. As the joint opens from positive flexural demand, the effective shear depth reduces significantly. It is essential to ensure the shear reinforcement in the girder is designed to resist the applied vertical shear demand develops within the required distance. Testing performed and summarized in this report utilized traditional bent shear reinforcement in the girder, which did not perform as desired under larger joint rotations. For detailing at the joint region, it is recommended that shear bars be detailed such that the full development of the bar occurs near the end of the bar. The use of headed reinforcing bars within a distance equal to one-half the structure depth is recommended (see Figure 2.4).

The performance of the grout used in the closure joint is essential to the performance of this system. The grout material used within the joint should have a compressive strength greater than the girder and bent cap to ensure the grout is not a localized weak spot in the flexural capacity. Additionally, to ensure the integrity of the grout joint is maintained during larger rotation demands, a fiber reinforced grout should be used. The use a polypropylene fiber reinforced grout material is beneficial due to the increase in toughness of the material and enhancement in overall joint integrity. While cracking in the grout matrix may occur, the presence of fibers will serve to resist unrestrained cracking and in turn hold the joint together. If no fibers are used in this vertical joint, once cracking occurs the joint material may simply fall out and cause a significant reduction in the superstructure capacity at the joint.

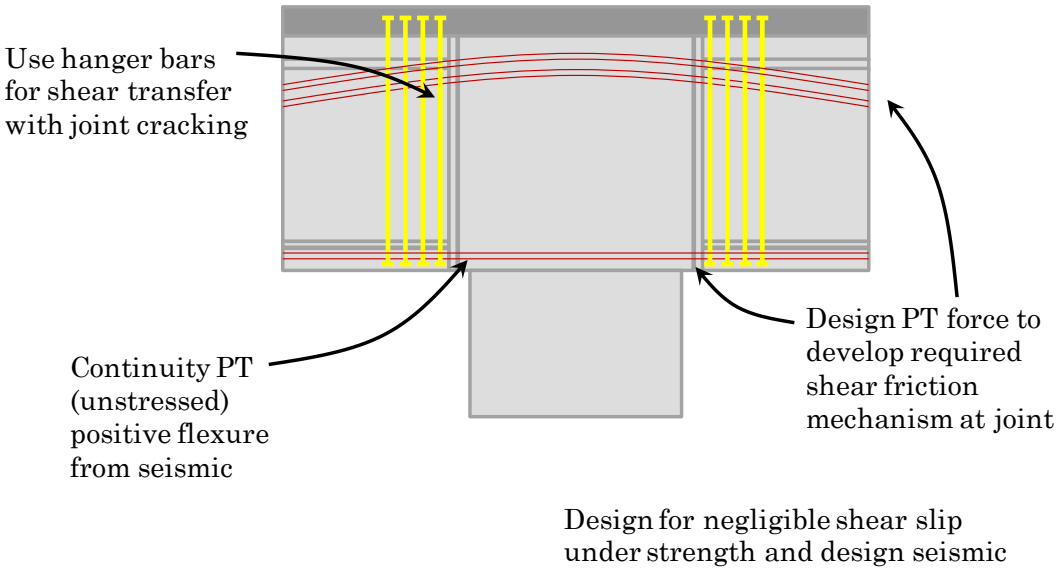

Figure 2.4 Connection detailing considerations

Relative Settlement

A potential hazard during strong ground shaking is the relative settlement between adjacent bents. Modern seismic design codes aim at reducing this hazard, but for ordinary bridges may not properly address the potential for settlement due to lateral spreading, liquefaction or dynamic soil compaction. It is important to ensure that the proposed detail can accommodate geometrically imposed deformations without significant loss in capacity or collapse. In this system, deformations associated with relative settlement are expected to be focused at the bent cap-to-girder connections, thus these should be able to accommodate some level of inelastic rotation. The potential hazards associated with relative settlement between bents are not specific to this precast system. In fact, the similar seismic hazards should be considered for traditional cast-in-place concrete bridges. To ensure a satisfactory level of safety is provided by this bridge structure, it was deemed important to explicitly consider the potential relative settlement in the development of this experimental program.

Although capacity design provisions are used in the design of the superstructure, this design approach cannot preclude the development of flexural hinges in the girders if relative settlement occurs. Similar to the need to consider vertical flexural demand, potential relative settlement demands cannot be tied to a mechanism of inelastic action in the column as is traditionally considered. While relative settlement may impose significant inelastic demands on the superstructure requiring eventual structural replacement, the need to satisfy Life Safety

Performance Objectives and provide a means for emergency traffic requires that the girders stay in place with residual load carrying capacity.

To provide an enhanced level of negative rotation capacity, it is recommended that closed hoop reinforcement be used at the bottom flange of the girder to provide a level of enhanced confinement. The experimental program conducted investigated the potential rotation capacity to provide an enhanced level of understanding of the ultimate performance of the system detail.

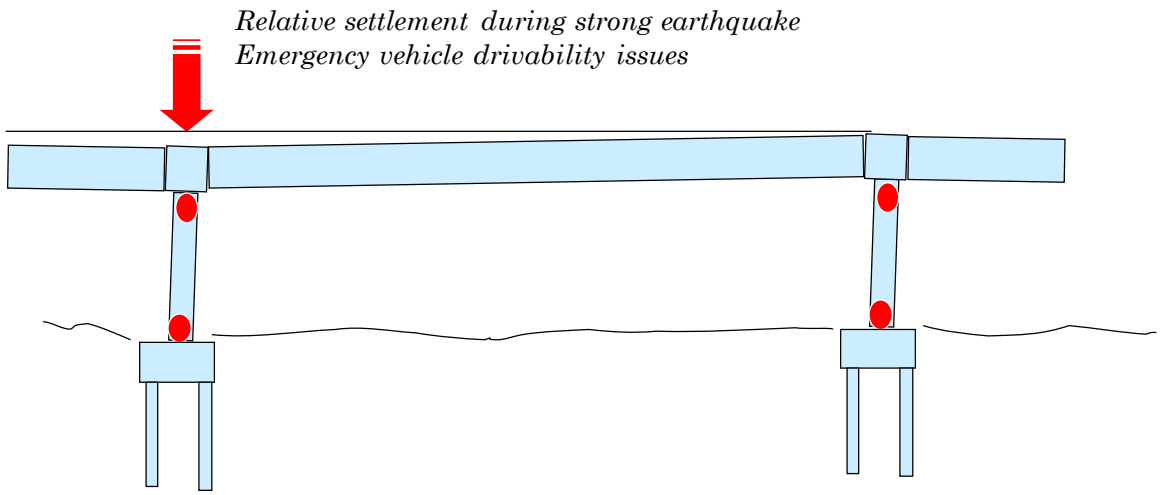

Figure 2.5 Superstructure relative settlement considerations

2.2 Prototype Structure

Based on the selected connection detail, a prototype structure was selected and designed in coordination with the NCHRP 12-74 Panel to represent a typical bridge structure seen in high seismic regions of the United States.

2.2.1 Prototype Bridge Description

The prototype bridge selected and designed was a four-span, integral bridge with three, two-column bents, see Figure 2.6. The span arrangement for the prototype system was based on the goal of providing a balanced span configuration, thus the back span lengths are approximately 80% of the central span lengths. The central spans had spans lengths equal to 140 feet whereas the back spans had span lengths equal to 110 feet. The structural width was selected based on an assumed design to maintain three lanes for traffic with standard shoulders. Six precast, pretensioned girders were used and post-tensioned through the bent cap for continuity. For aesthetic reasons, the bottom of girder elevation was maintained equal to the bottom of bent cap

elevation. The aim of this design feature was to develop a visually appealing structure and eliminate the use of a drop cap system.

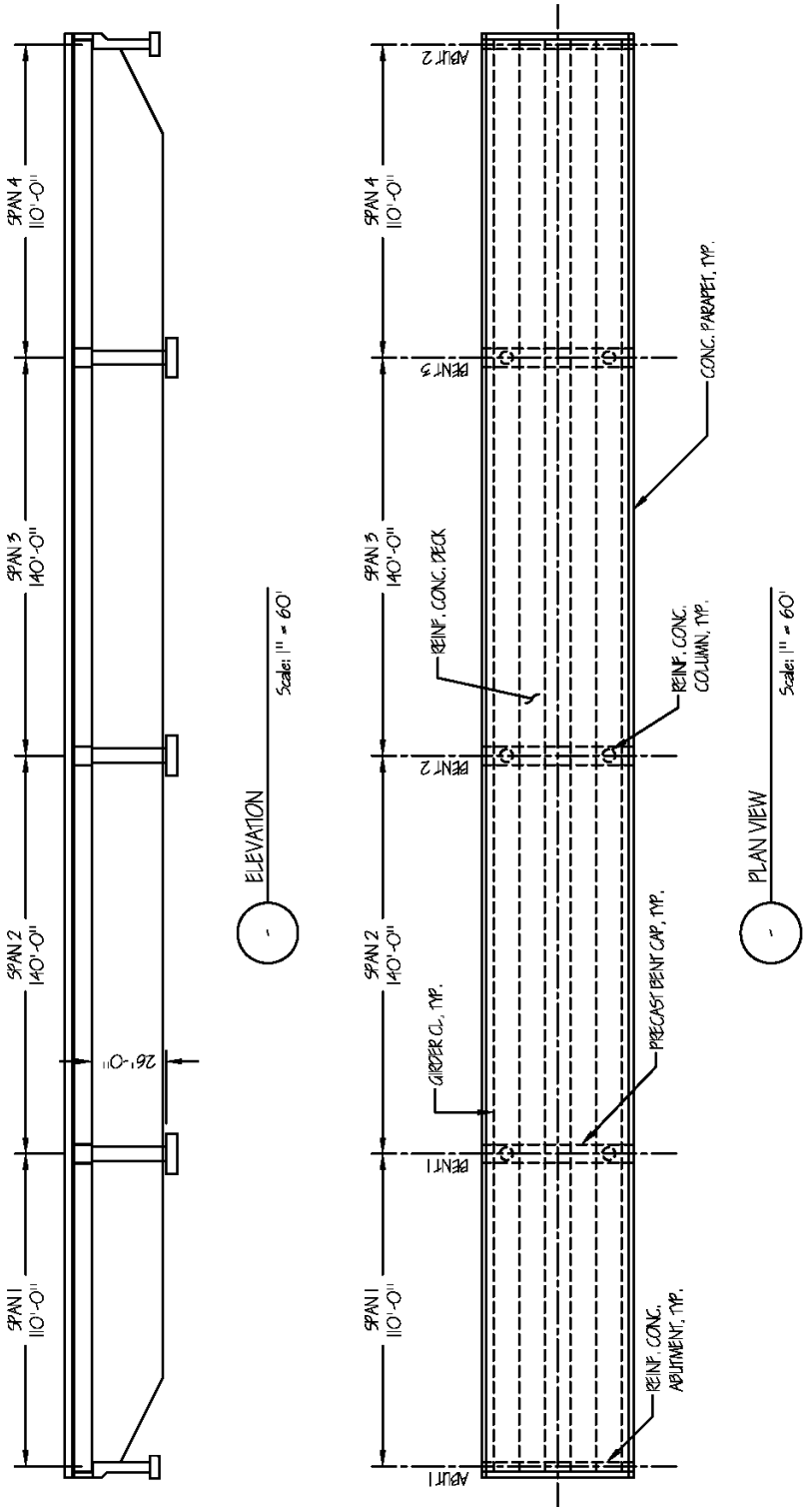

Figure 2.6 Prototype bridge general plan and elevation (not to scale)

Typical sections for the bridge are shown in Figure 2.7. The girders used consisted of precast I-girders with end blocks at the bents and back span supports. The girder sections selected were based on the Washington Department of Transportation standard details for post-tensioned girders. The section selected was the W74PTG precast, post-tensioned girder. End blocks are required at each bent to facilitate the splicing of post-tensioning ducts within the girder webs. The girders were designed with pretensioning to prevent cracking under their own dead weight an minimize deformations along the length of the beam for constructability.

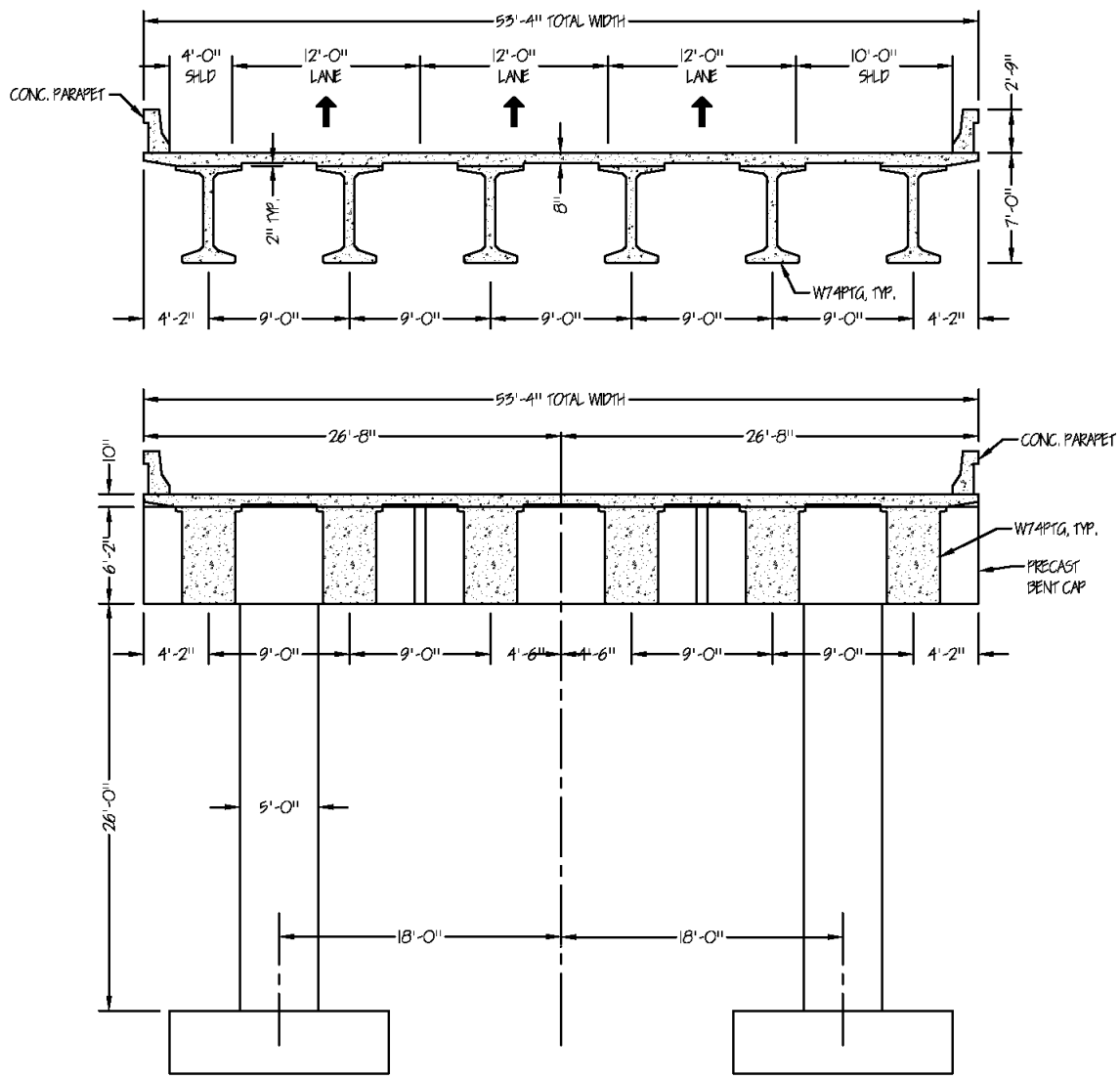

Figure 2.7 Prototype bridge general sections

The plan view of the bent cap reinforcing is shown in Figure 2.8. From this figure, the continuity of the girder post-tensioning ducts is noted. With the placement of the girders, it is important to

consider the required joint shear reinforcement in the precast bent cap, as there is potential interference with the post-tensioning ducts. All joint detailing was performed in accordance with the provisions of the AASHTO Guide Specification for LRFD Seismic Bridge Design. Torsionl design of the precast bent cap was completed using torsional shear friction mechanism presented in the PCI Bridge Design Manual (Precast Prestressed Concrete Institute, 2003).

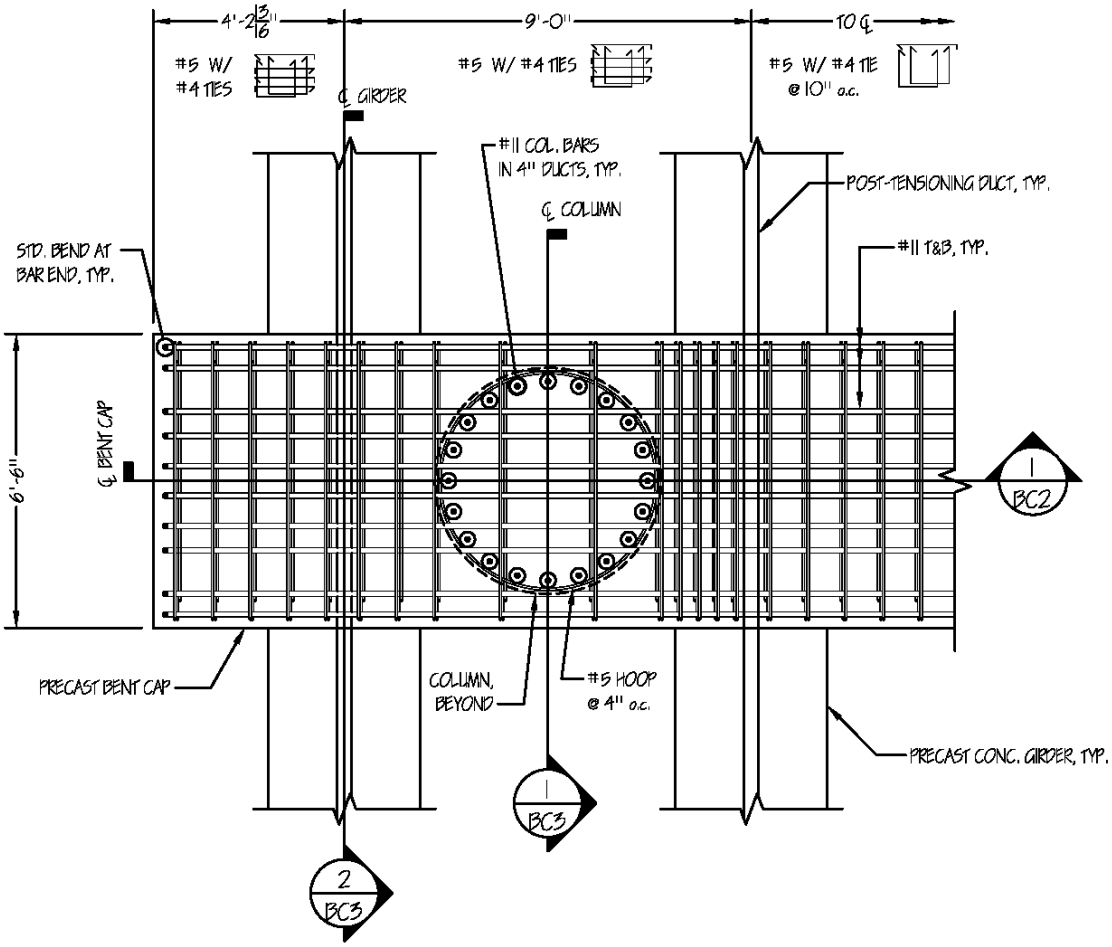

Figure 2.8 Prototype bridge bent cap reinforcement plan

For high seismic regions, especially on structures with longer span lengths, the cross-sectional dimension of the bent cap may become significant resulting in a relatively heavy member. The weight of the precast bent cap may become larger than the girders, which would require the use of a larger crane for erection. In the prototype bridge structure, a precast segmental bent cap was selected to reduce the require pick weights. Post-tensioning was run along the length if the bent cap to provide continuity in the member, see Figure 2.9.

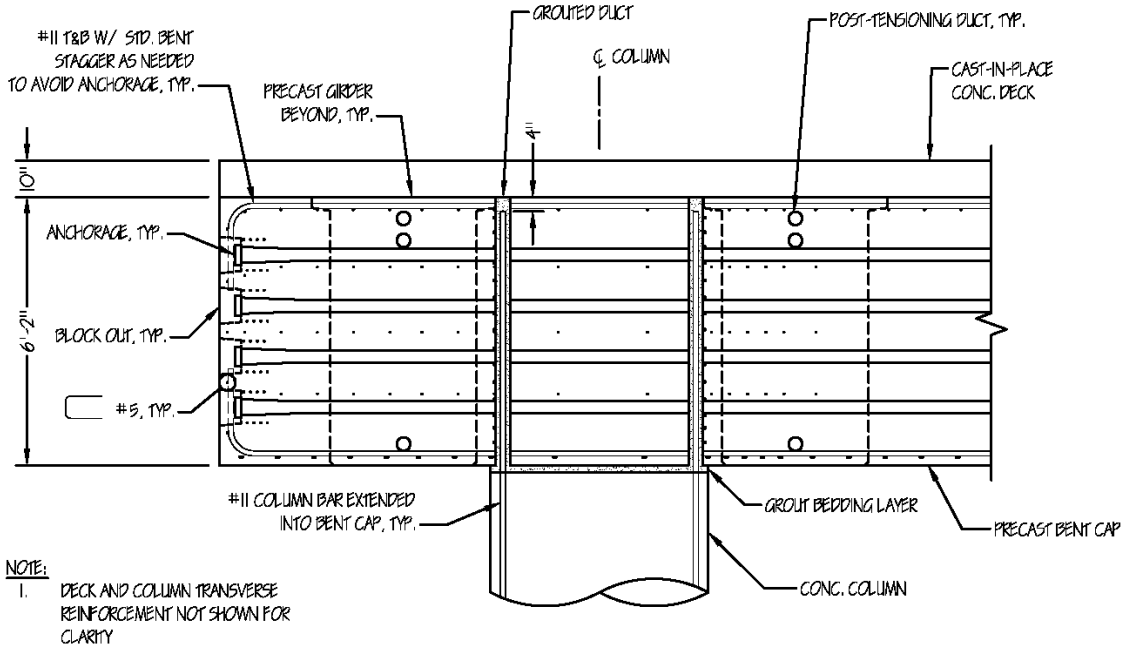

Figure 2.9 Prototype bridge bent cap section

2.2.2 Prototype Construction Sequence

The construction sequence considered for the precast bent cap is shown in Figure 2.10. Due to the long spans associated with the prototype structure, the girder depth dictated a similarly deep bent cap. The resulting geometric dimensions of the cap were significant enough to cause concern regarding potential shipping and erection complications. To remedy these concerns, a precast segmented bent cap was considered. The first bent cap segments placed are those over the column which can be supported by way of friction collars or shims. Following the casting of the selected bent cap-to-column connection, the middle segment can be places using a strong back system to minimize the impacts below and required falsework. Transverse post-tensioning is used to provide flexural and shear strength throughout the cap, especially across the closure joint. The post-tensioning ducts must be spliced and the closure joint cast with concrete.

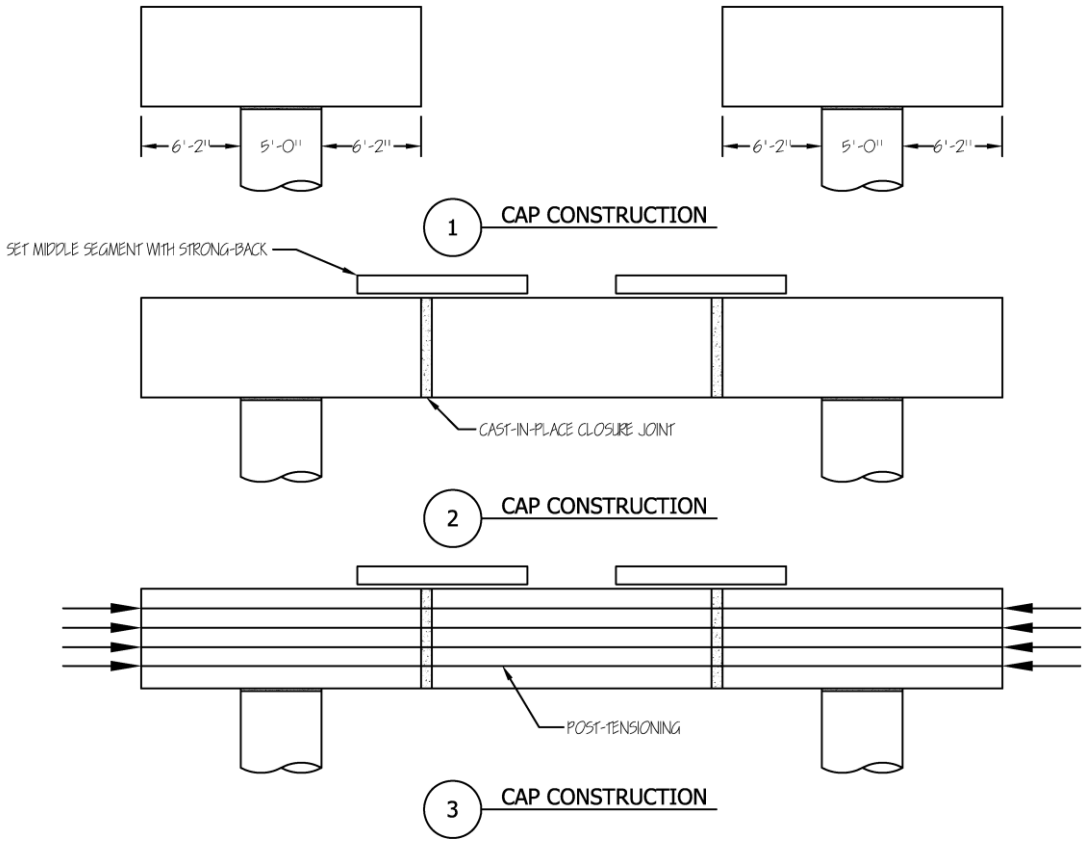

Figure 2.10 Bent cap construction sequence

Figure 2.11 shows a rendering of a potential strong-back support for a segmental bent cap system. Once all segments are in place, the post-tensioning ducts are spliced and the closure joint poured to provide continuity.

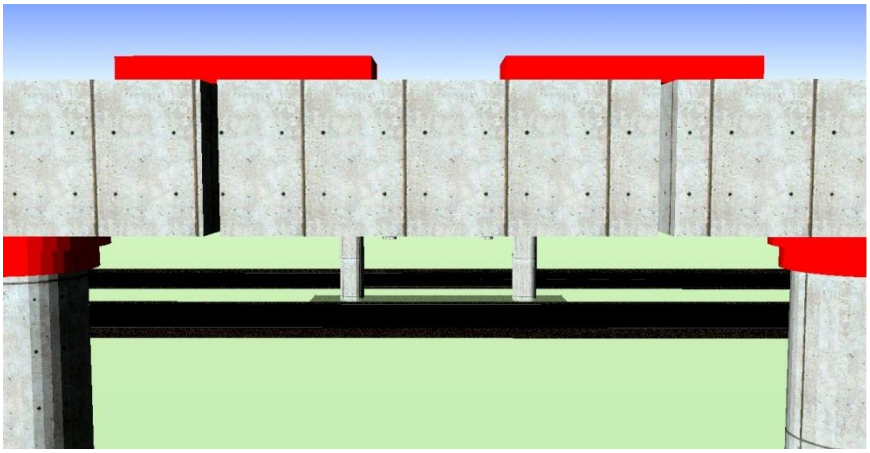

Figure 2.11 Bent cap strong-back rendering

Figure 2.12 shows the main construction sequences for longitudinal members. Once the bent cap segments are set and have sufficient strength, longitudinal girders can be placed. These girders are set using a strong back detail, which reacts off of the bent cap to minimize the construction footprint and minimize the need for temporary falsework. A closure joint of two inches on both ends of the girder was specified to allow for construction tolerances between bents. Additional tolerances can be achieved; however, increasing the closure joint would require a modification to the considered joint material and the use of concrete would be required. In addition to the use of concrete, reinforcement would be required to be placed on site in the joint region for shear and flexural development. The bottom headed reinforcing bars in the girder would need to be extended into the joint to develop the requisite joint force transfer mechanism.

For this prototype, once the girders are placed the post-tensioning ducts are spliced within blockouts in the girder ends. The closure joint is then formed and cast using a high strength, non-shrink grout with a volume fraction of fiber reinforcement of 0.2%. The first stage post-tensioning follows the casting of the closure joint with the stressing and grouting of the middle post-tensioning tendon. The bottom tendon is also set and not stressed but grouted after placement. This bottom tendon is the unstressed continuity tendon aimed at reducing the level of joint opening due to positive flexural demands.

The deck is the cast reacting all casting activities off the in place precast girders. Once the deck is cast and has reached sufficient strength, the final stage of post-tensioning occurs with the stressing of the top tendon. Following this stressing, the structure has sufficient strength for operation and the remaining construction items are completed (parapets, overlay, etc.).

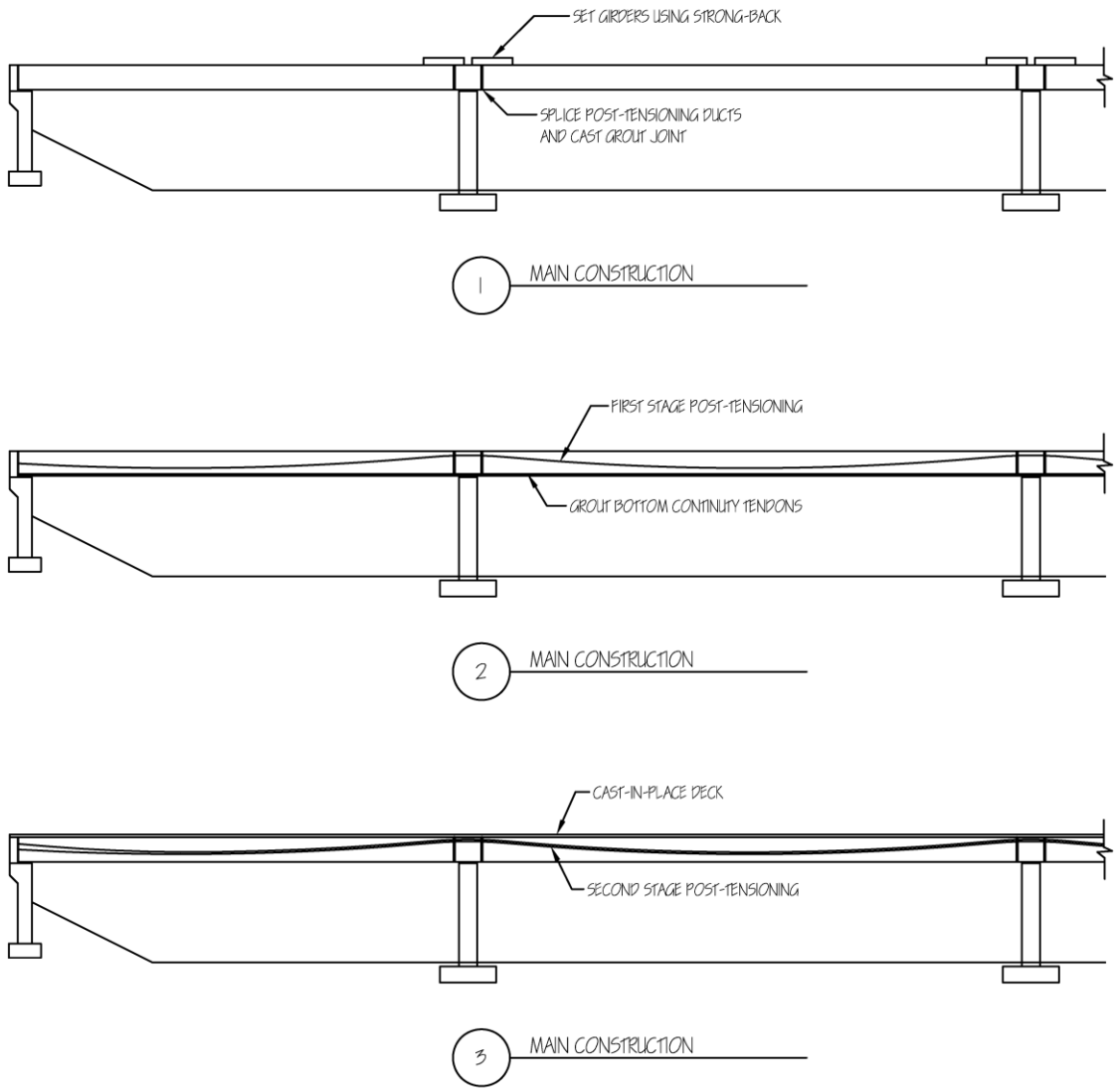

Figure 2.12 Prototype construction sequence

2.2.3 Strong-back Detail

During the development of the integral connection detail, significant attention was paid to the constructability of the detail to promote implementation in practice. To ensure the selected detail was constructible, the full potential construction sequence and accumulation of stresses was considered to ensure this detail could be built with minimal impact to surrounding areas in a rapid and efficient manner. A key consideration during the development of this detail was the manner in which the girders will be supported during construction. The method presented, and recommended, consists of the use of a strong-back system to support the bridge girder off the bent cap during construction. A rendering of this system is provided in Figure 2.13. From this

figure, the advantages of a strong-back system are apparent with the girder being supported without impact below the structure. This reduction in construction footprint is highly advantageous for structures in congested urban regions, environmentally sensitive regions or water crossings. The use of strong-back systems is discussed in depth in NCHRP Report 517, which discusses methods for increasing span ranges when using precast, prestressed concrete girders (Castrodale, et al., 2004).

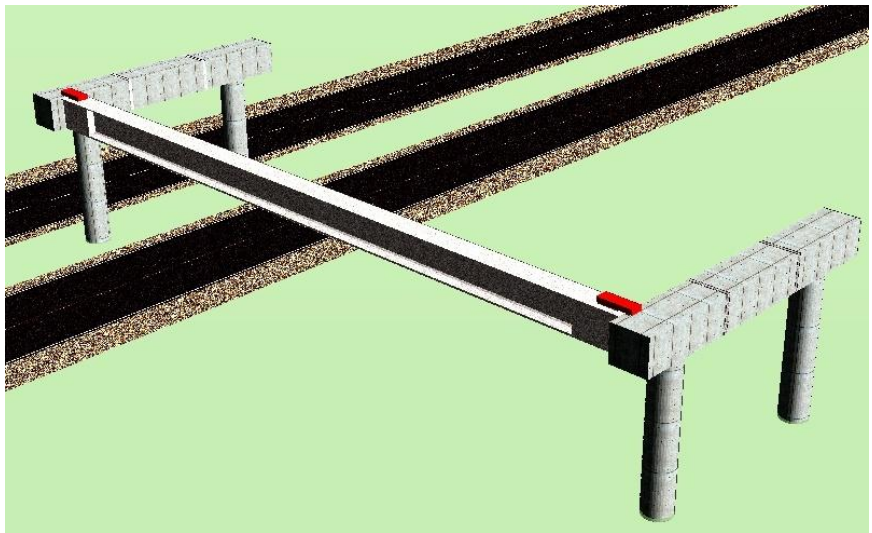

Figure 2.13 Girder temporary strong back system

The strong back system considered in this project was a temporary system that is removed following the first stage of post-tensioning. In this system, the strong back is required to resist vertical shear demands across the joint associated with the dead weight of the girder prior to the presence of an effective post-tensioning force. Following the grouting of the closure joint and first stage post-tensioning, there is enough effective post-tensioning in place to resist vertical shear demands and flexural demands associated with the dead weight of the girder and the wet weight and construction activities associated with casting of the deck.

Other strong back systems are possible, including the use of a permanent strong back system that remains in place for the life of the structure. For many structures, it may be cost-effective to embed a permanent strong back into the girder system as opposed to using temporary systems. In this case, there is an added level of redundancy through an alternative load path for vertical shear resistance in the event of complete rupture of all post-tensioning in the bridge.

2.2.4 Prototype Bridge Design

The design of the prototype bridge was completed in accordance with the AASHTO LRFD Bridge Design Specifications (Fourth Edition) and the AASHTO Guide Specifications for LRFD Seismic Bridge Design (First Edition).

The selection of initial member sizing was based on conventional design practices and span range tables for girder systems used. The 74-inch deep Washington Department of Transportation post-tensioning beam was selected using recommended span limits published for these girders. This girder section was selected over a bulb-tee due to the increased bottom flange area desirable for negative flexural demands at the bent cap. The design was refined through the application of LRFD design requirements, as needed. To minimize the neutral axis depth, a design 28-day compressive strength of 9 ksi was used for the prototype structure.

Post-tensioning in the girders was designed such that the ultimate, extreme event and service limit states were satisfied. The design of the post-tensioning was governed by the Strength I limit state with the seismic demands being of a similar magnitude. Two stages of post-tensioning were specified with the first stage occurring prior to the deck casting and the second stage occurring after the deck casting. Service level performance of the structure was considered in the prototype design through a construction staging analysis explicitly considering the development of stresses in the system at various stages.

For seismic design, the prototype bridge was considered non-essential and designed to meet the life safety requires as defined by the AASHTO Guide Specification for LRFD Seismic Bridge Design. The specified mechanism of inelastic deformation in the longitudinal direction consists of flexural plastic hinge formation at both top and bottom of columns and knock off backwalls. Additionally, the superstructure-to-bent cap joint was allowed to open during seismic excitations so long as the response is essentially elastic. Transverse mechanism involved the development of flexural plastic hinging at both top and bottom of columns and shearing of sacrificial shear keys at the abutments.

The design acceleration response spectrum (ARS) was developed in accordance with the AASHTO Guide Specification for LRFD Seismic Bridge Design. The ARS curve incorporated 5% damping and was developed using a one-second acceleration of 0.80 g, a 0.2-second acceleration of 1.50 g and site coefficients for Site Class D Soil. The resulting peak rock acceleration for the prototype design for the study site is 0.60 g. The input seismic demand and site classification result in a bridge subject to seismic design category (SDC) D requirements.

This ARS curve is representative of a site located in a high seismic region, such as Southern California. The imposed demand levels required a seismic demand analysis, displacement capacity analysis with pushover, capacity design provisions and SDC D detailing. Due to the assumed site location, the bridge was considered to be located within 6 miles of a fault. Therefore, vertical ground motion was considered with a magnitude of 0.80 g of vertical excitation.

The structural system was modeled in the computer analysis program, SAP2000 for service, strength and seismic design. Modeling procedures for seismic analysis were performed based on the provisions of the AASHTO Guide Specification for LRFD Seismic Bridge Design. Effective section properties were modeled to consider the expected dynamic behavior of the bridge system, including column inelasticity. Dynamic analyses indicated the dominant transverse period of vibration is equal to 0.73 seconds and the dominant longitudinal period of vibration is equal to 0.69 seconds. The longitudinal analysis considered the effects of the backwall stiffness in accordance with the provisions of the AASHTO Guide Specification. The resulting displacement demands in the longitudinal and transverse directions are 6.8 inches and 7.5 inches, respectively.

In order to determine the displacement capacity of the system, an inertial pushover analysis was conducted in both the longitudinal and transverse directions. In the longitudinal direction, the bent cap-to-girder joint was allowed to open during seismic excitation. This decision was made based on extensive discussions with the research team and project Panel. It was decided that allowing the bridge to flex and open at the joint is acceptable so long as the joint responds in an essentially elastic manner.

To consider the potential joint opening, a superstructure moment-rotation hinge was modeled at the face of the bent cap. For the prototype design, these hinges were based on moment-curvature analyses of the superstructure and an assumed equivalent plastic hinge length. The original design considered an effective hinge length equal to one foot; however, a more realistic length is equal to approximately one-half the structure depth. Through allowing the superstructure joint to hinge, a redistribution of seismic moment demand is expected due to the reduction in stiffness following hinging. The prototype design resulted in seismic moment redistribution approximately 20%. The observed response from analysis indicated that the system is expected to respond in an essentially elastic manner.

In the longitudinal direction, the displacement capacity determined via pushover analysis is 11.0 inches, which results in a demand-to-capacity ratio of 0.62. The results of the longitudinal pushover analysis indicated that positive joint opening is expected but without appreciable

rotation demand. The response of the joint is classified as essentially elastic as the calculated rotations are only slightly greater than the elastic rotation. For the transverse displacement capacity, overturning effects were considered in determining the column inelastic response. The transverse displacement capacity determined via pushover analysis was 10.6 inches, which results in a demand-to-capacity ratio of 0.71. Ductility demands for both directions were approximately equal to 5, well below the limit of 8 for multicolumn bents.

Capacity design principles were applied to the design of the superstructure to ensure that the seismic overstrength demands can be resisted in a nominally elastic manner. Column transverse reinforcement was designed based on overstrength demands imposed by transverse response. Flexural and shear demands on the cap beam were based on the demands developed with flexural hinging of the columns at overstrength demands. Design of bent cap reinforcement was based on overstrength demands in addition to the longitudinal and transverse force-transfer mechanisms assumed in the AASHTO Guide Specification for LRFD Seismic Bridge Design.

2.2.5 Scaling of Prototype

Geometry and demands were used from this prototype structure to define the geometry and reinforcing requirements in the test specimens. Based on the laws of similitude, scale factors shown in Table 2.1 were used.

Table 2.1 Specimen scale factors

Length/Displacement	0.500
Force	0.250
Moment	0.125

Demands were scaled based on the aforementioned scaling principles. Reinforcing sizes were also scaled using the same principles to best represent the reinforcing arrangement in the full-scale prototype. Detailing of the system was performed based on the actual specimen size, reinforcing and demands as opposed to purely scaling the prototype system.

2.3 Capacity Predictions

It is important to accurately predict the flexural capacity of the system in terms of shear capacity, moment capacity and rotation capacity. Additionally, it is important to provide a means to estimate the force-deformation response of the system in the event that inelastic actions are expected.

2.3.1 Shear Capacity

The prediction of shear strength at the joint is a relatively simple procedure with existing design recommendations already in place (AASHTO, 2007). The transfer of vertical shear forces across the grout closure joint is accommodated through a shear friction mechanism. Neglecting the influence of any reinforcing or post-tensioning steel or cohesion across the joint, the shear friction capacity is directly related to the effective compression force acting across the joint. As the overall integrity of the system relies heavily on the shear friction capacity, a conservative estimate of the shear friction capacity is recommended.

$$V_{cap} = \mu T_{pse} \qquad 2\text{-}1$$

The friction coefficient recommended for design is equal to 0.60 considering a concrete-to-concrete surface that is not intentionally roughened (AASHTO, 2007). Although the end of the girder is intentionally roughened to promote bond between the girder and joint, the face of the bent cap is not roughened. Roughening of both the bent cap and girder may result in the introduction of tensile strains within the closure joint. By roughening only one face, the overall integrity of the joint is expected to be greater with cracking focused at the face of the bent cap.

While the prediction of the shear strength is relatively simple, the prediction of shear stiffness and deformation capacity is not as simple when considering potential for actual relative slip between the girder and bent cap. The desire to understand the deformation capacity based on shear transfer at the joint is a driving factor for the experimental program.

2.3.2 Moment-Rotation Response

The flexural capacity of the joint in the negative direction can be adequately predicted using common prestressed concrete design equations such as those presented in the AASHTO LRFD Bridge Design Specifications (2007). However, in the positive flexural direction the presence of unstressed post-tensioning tendons is not adequately accounted for in these common equations. In light of this, the flexural moment capacity in the positive direction should be determined using a strain compatibility approach.

Moment-curvature analysis programs are commonly used in the seismic design of bridges to estimate the flexural response of bridge columns. Many commonly available programs can readily consider any sectional geometry and reinforcing pattern. Therefore, the use of moment-curvature programs to predict both the positive and negative flexural capacities is desirable for this considered detail. As moment-curvature analysis methods are based on strain compatibility

approaches, they are best suited for the calculation of the positive flexural capacity and will also provide more refined estimates of the negative capacity.

Although it is not required for common bridge design based on capacity design approaches, it is important to estimate the moment-rotation response of the tested specimen to determine the accuracy of inelastic prediction techniques. The prediction of the moment-rotation response envelope can be performed using the results of a moment-curvature analysis. However, to predict the desired moment-rotation response, the curvature must be multiplied by an effective hinge length to account for the distribution of inelastic actions including penetration of strains into the girder and bent cap. Over the years, many methods to relate curvature to rotation through an effective plastic hinge length have been developed (Hines, 2002). A reasonable assumption for plastic hinge length in a column, which can be extended to the flexurally dominated superstructure system, is that the average plastic hinge length can be approximated as one-half the column diameter, or in this case superstructure depth (Priestley, et al., 1984). For the analyses conducted herein, the assumption of an effective plastic hinge length equal to one-half the overall superstructure depth at the joint will be used. Therefore, the ultimate rotation capacity of the superstructure can be approximated as:

$$\theta_u \cong \varphi_u \frac{d_{ss}}{2} \qquad \text{2-2}$$

Chapter 3 Experimental Basis and Specimen Design

The experimental program for the integral unit was developed to validate the seismic response of the system by subjecting the system to simulated seismic rotation demands. Additionally, this program was aimed at confirming the design assumptions used in the design of the prototype bridge system. This section describes the basis for the experimental program including an overview of the prototype system design. Additionally, design details associated with the specimen are provided.

3.1 Testing Setup

3.1.1 Development of Test Specimen

The main goal of the experimental effort is to determine the response of the girder-to-bent cap joint when subjected to simulated seismic demands. To satisfy this goal, a portion of the prototype structure was extracted for experimental testing. The test specimen selected for testing consists of a girder, deck and reaction block. This specimen is based on an extracted portion of the prototype bridge, as shown in Figure 3.1. The scaled length of the girder used in the experimental program is 31 feet in length, which is representative of 0.46 times the central span length.

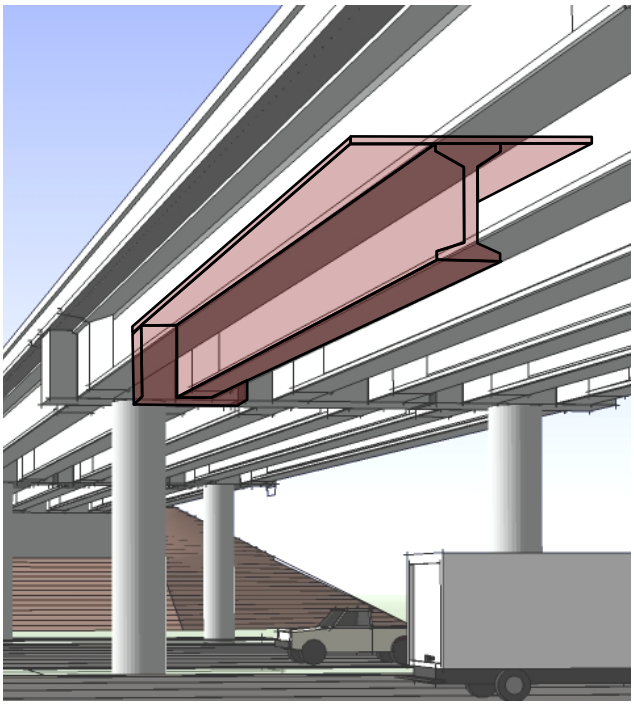

Figure 3.1 Test specimen

The bent cap is represented by a large reaction block in the testing of the specimen. The flexibility of the bent cap can be neglected in experimental efforts as the deformation from this member can be considered in analytical modeling. The extracted portion of the prototype bridge will provide sufficient information regarding moment-rotation response of the joint and shear transfer across the joint. These two items are the major unknowns with the performance of this integral bridge detail.

3.1.2 Testing Setup

The testing setup, prior to installation of the vertical actuators, is shown in Figure 3.2. A series of three hydraulic actuators are connected to the girder in order to apply simulated loadings to the girder and more specifically, at the girder-to-bent cap joint region.

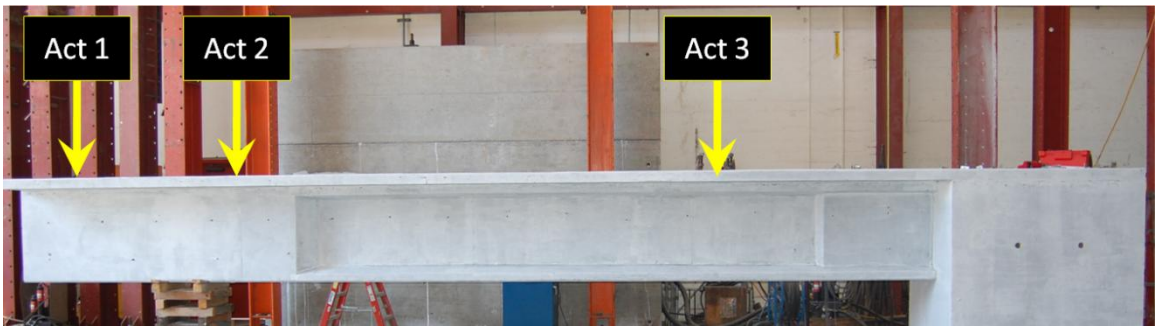

Figure 3.2 Testing setup

This testing setup was developed to provide a means to apply simulated flexural and shear demands based on the prototype structural analysis. During simulated seismic loading, the flexural inflection point will vary due to the superposition of dead load and seismic load demands. To properly impose the correct flexural moment demands onto the test specimen, Actuator 1 and Actuator 2 apply a fixed end moment and vertical shear demands based on developed loading equations. Actuator 3 is located to apply a constant downward shear load during all testing to properly simulate the expected vertical shear demand across the joint under all loading cases.

The shear and moment demands imposed from the testing setup, as compared to the scaled prototype demands, are shown in Figure 3.3 through Figure 3.5. As is apparent from these figures, the applied vertical shear demand and moment demand across the joint matches the scaled prototype demands extremely well. The equations developed for actuator control are based on the observed relationships in the prototype structure and match the scaled demands at all seismic loading levels.

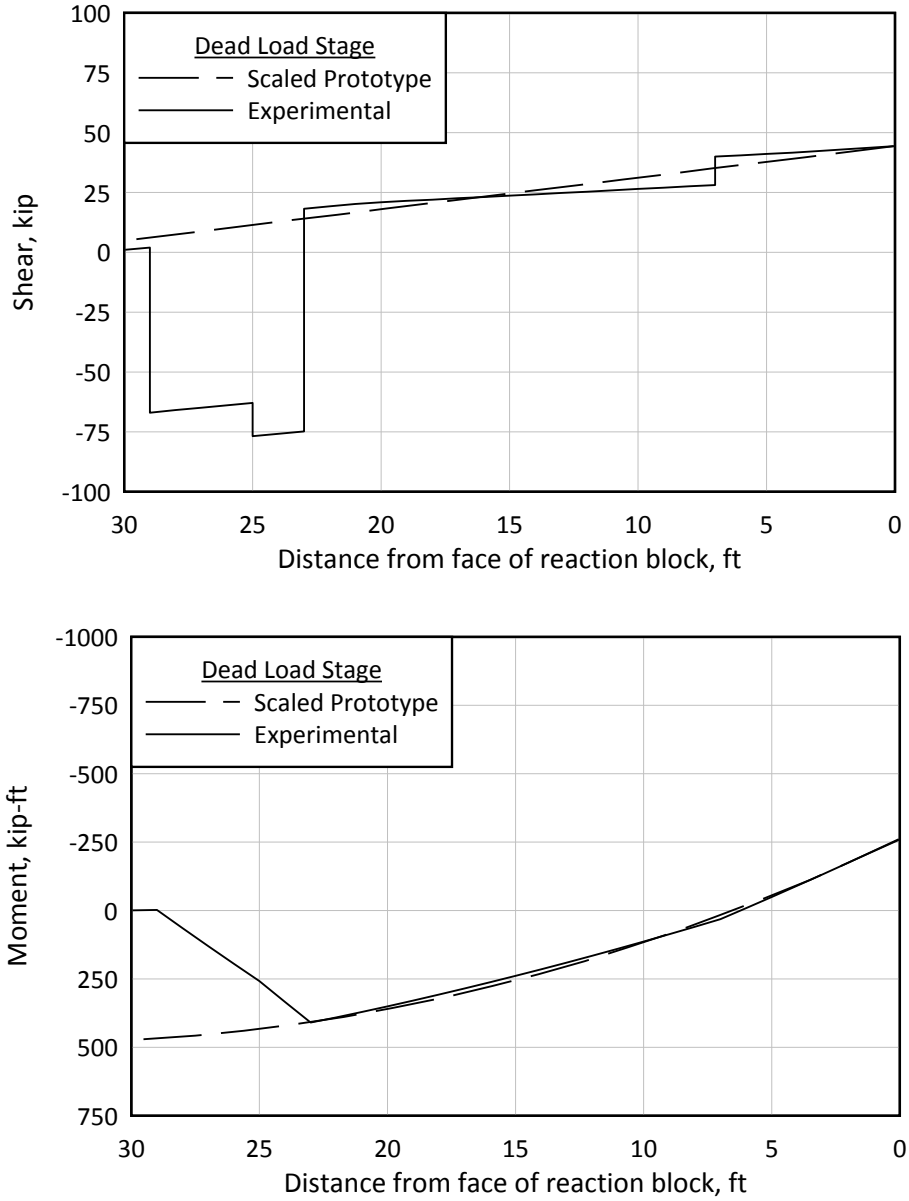

Figure 3.3 Scaled prototype demands compared to test demands – dead load

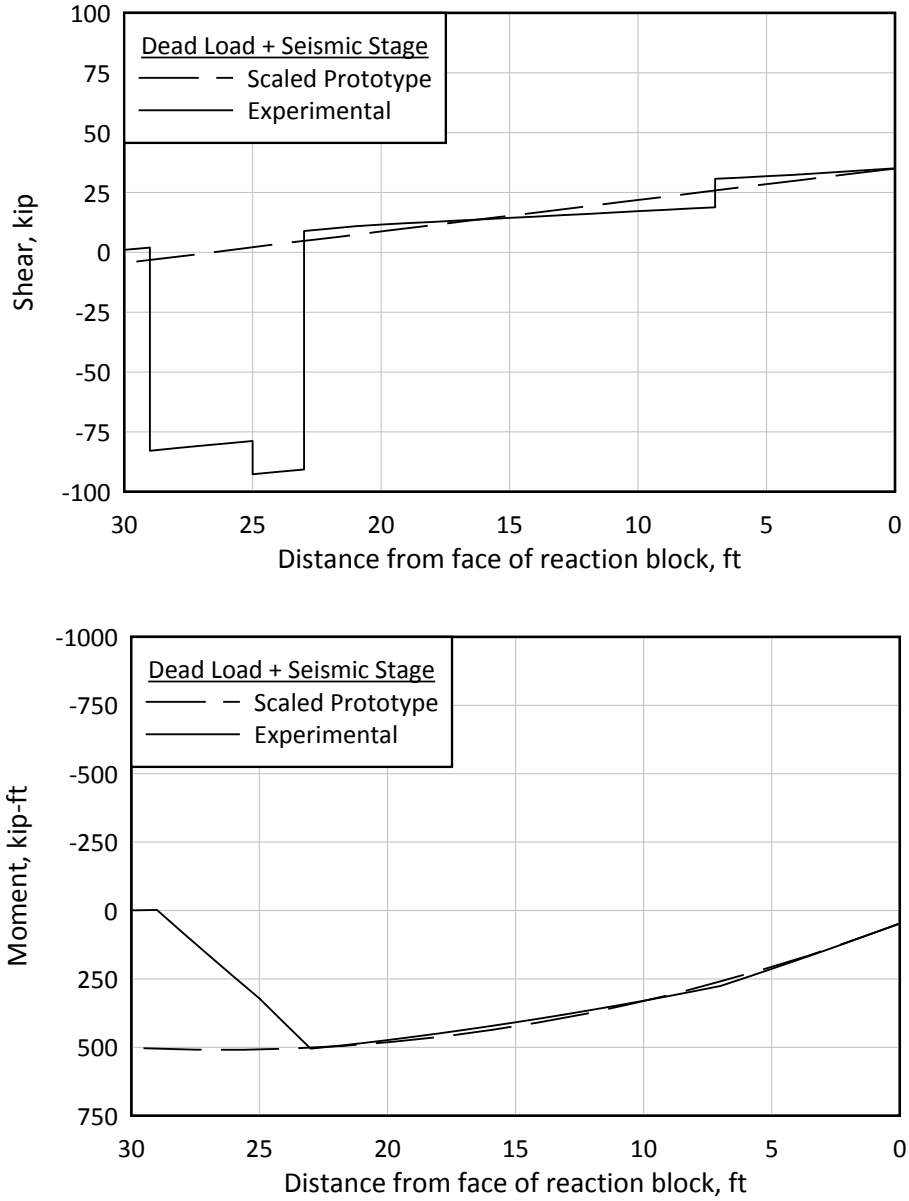

Figure 3.4 Scaled prototype demands compared to test demands – dead load + seismic

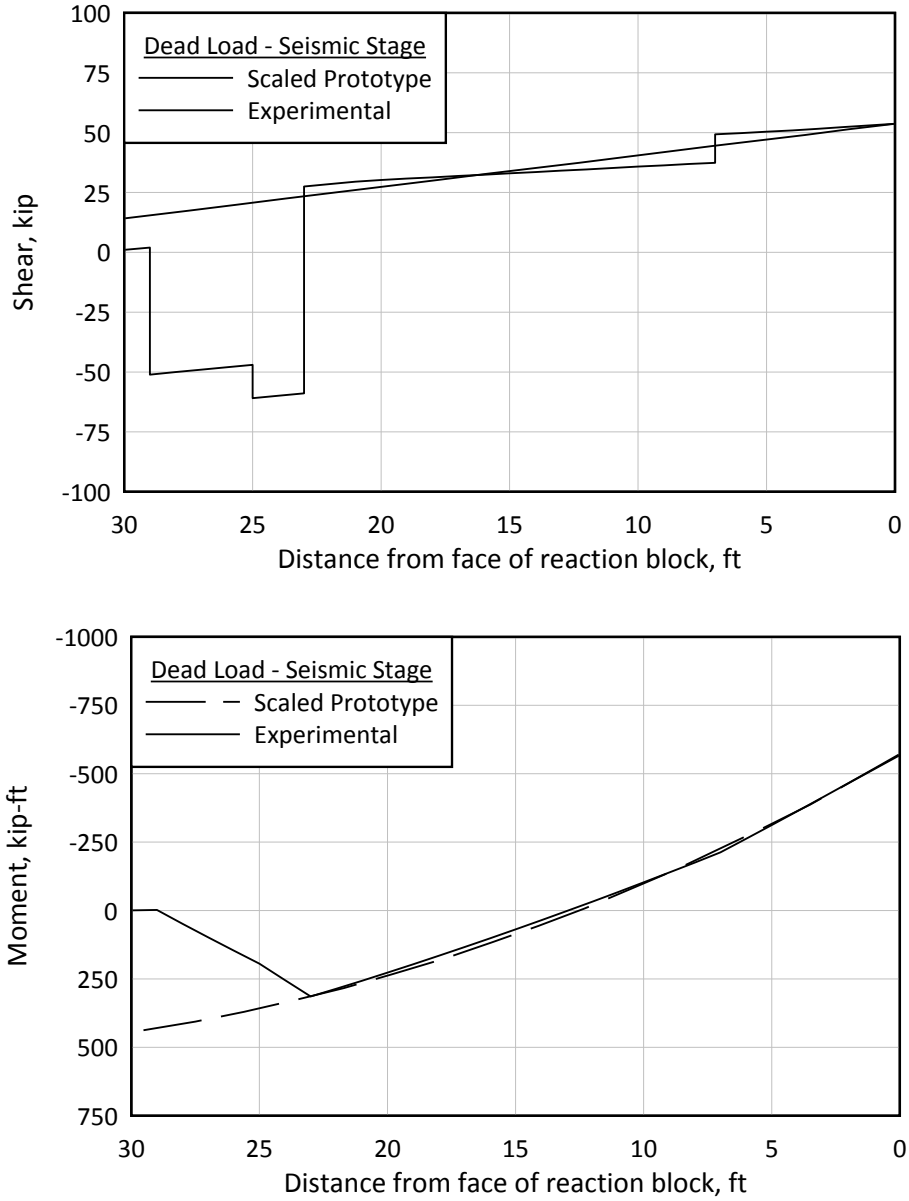

Figure 3.5 Scaled prototype demands compared to test demands – dead load - seismic

3.2 Design Details

Based on the prototype specimen, and in accordance with Section 3.1.1, the prototype specimen was designed and detailed. The specific details of the test unit are provided in this section.

3.2.1 Specimen Details

The entire drawing set for the test specimen is provided in Appendix A. There are three main components of the test unit: 1) the girder, 2) the reaction block and 3) the deck. The overall

geometric footprint of the entire combined test specimen is 37 feet long, 4.5 feet wide and 6.42 feet tall. A general elevation of the complete test unit is shown in Figure 3.6. The general dimensions of the individual components are:

- Girder 31 feet long, 37 inches tall and 20 inches wide
- Reaction Block 6 feet long, 54 inches wide and 6 feet tall
- Deck 4 inches thick with 1 inch haunch over girder

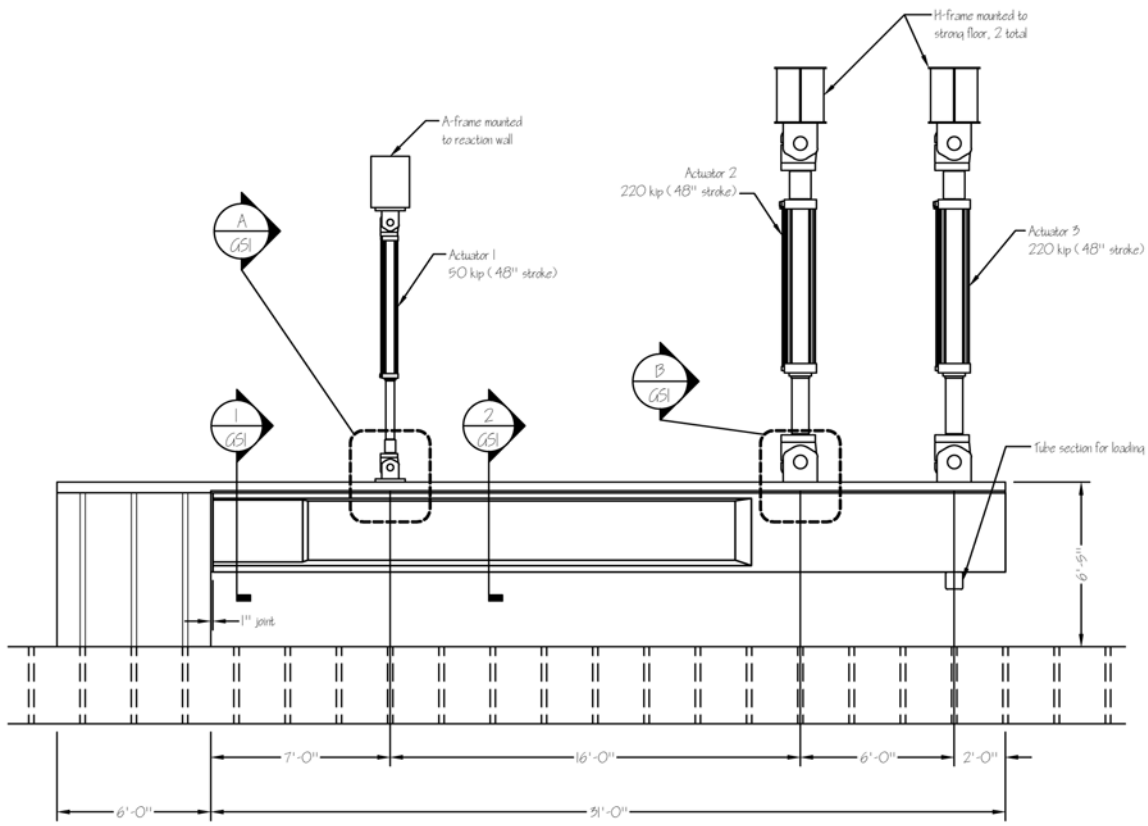

Figure 3.6 Specimen test setup elevation looking east

Over the majority of the length, the concrete girder is an I-shaped section with standard web width equal to 5 inches (see Figure 3.7a). At the end of the girder near the reaction block, the web width flares to 10 inches to accommodate the blockout for splicing of post-tensioning ducts (see Figure 3.7b). The girder is reinforced with four No. 4 reinforcing bars at the bottom flange without any pretensioning. The prototype structure used pretensioning in combination with post-tensioning to provide flexural strength. However, this specimen was constructed at the University of California, San Diego laboratories without pretensioning equipment. Mild reinforcement was used in lieu of pretensioning as the main region of interest during testing is the joint region, which

would not have developed pretensioning in the prototype structure as well. The use of mild reinforcement over the main portion of the girder will not affect the structural response parameters of interest. However, the use of mild reinforcement as opposed to pretensioning will result in additional cracking over the main portion of the girder. The deck is reinforced with the same reinforcing pattern as the prototype specimen with scaled reinforcing sizes and spacing.

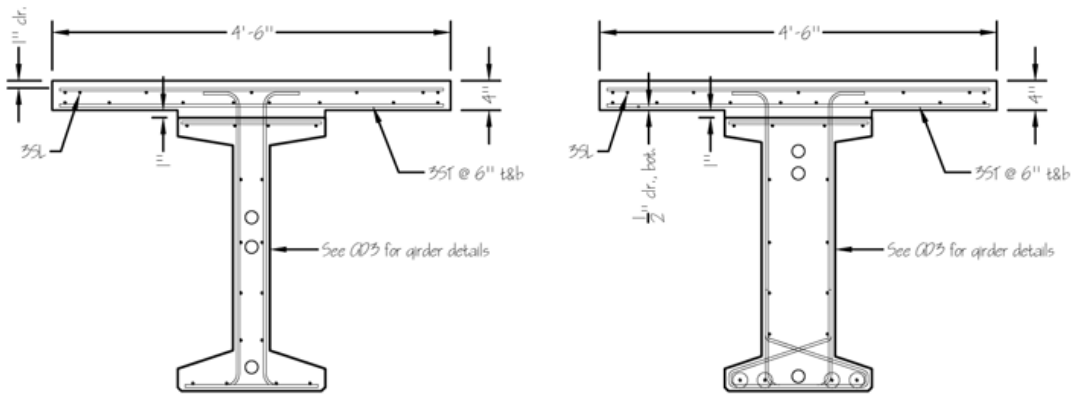

Figure 3.7 Girder section a) at main span b) at reaction block

The general exterior dimensions of the concrete girder are shown in Figure 3.8. From this figure it is observed that the web width varies over the length of the specimen. At the reaction block and for the first 3.5 feet, the width is equal to 10 inches. Over the main portion of the girder the width is equal to 5 inches. As the girder approaches the connection points for Actuators 1 and 2 the web width increases to 20 inches to accommodate the connection of these actuators and provide stable force transfer into the unit.

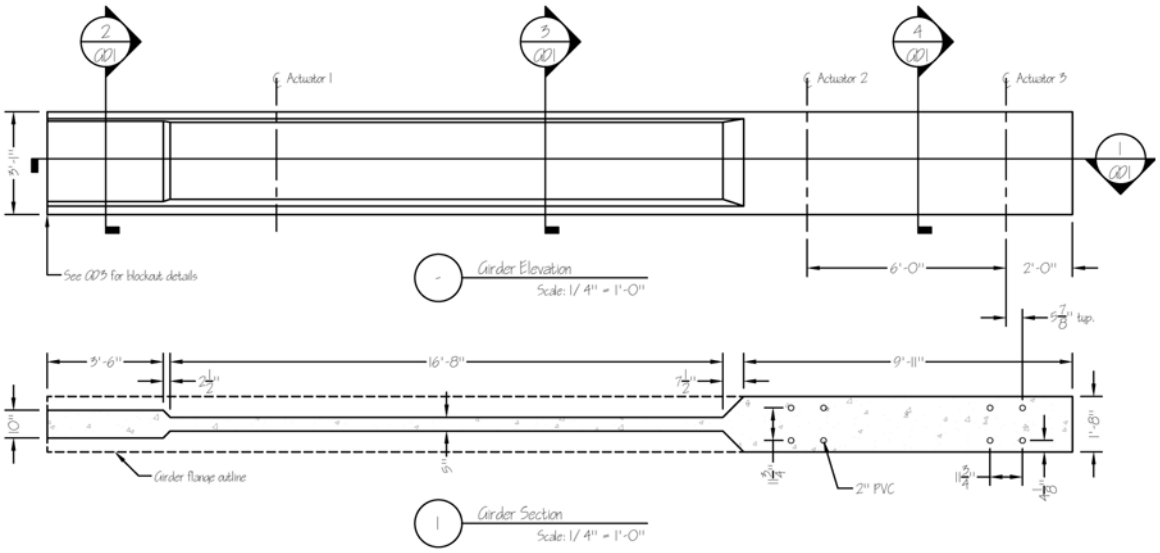

Figure 3.8 Girder dimensions

The overall girder transverse reinforcement is shown in Figure 3.9 along with the general girder post-tensioning profile. The transverse reinforcement was design and detailed based on the actual applied shear demands from testing. The post-tensioning profile was designed to be similar to the prototype specimen near the reaction block. At the free end of the girder, the effective location of the post-tensioning force was slightly higher due to spreading requirements at the anchorage.

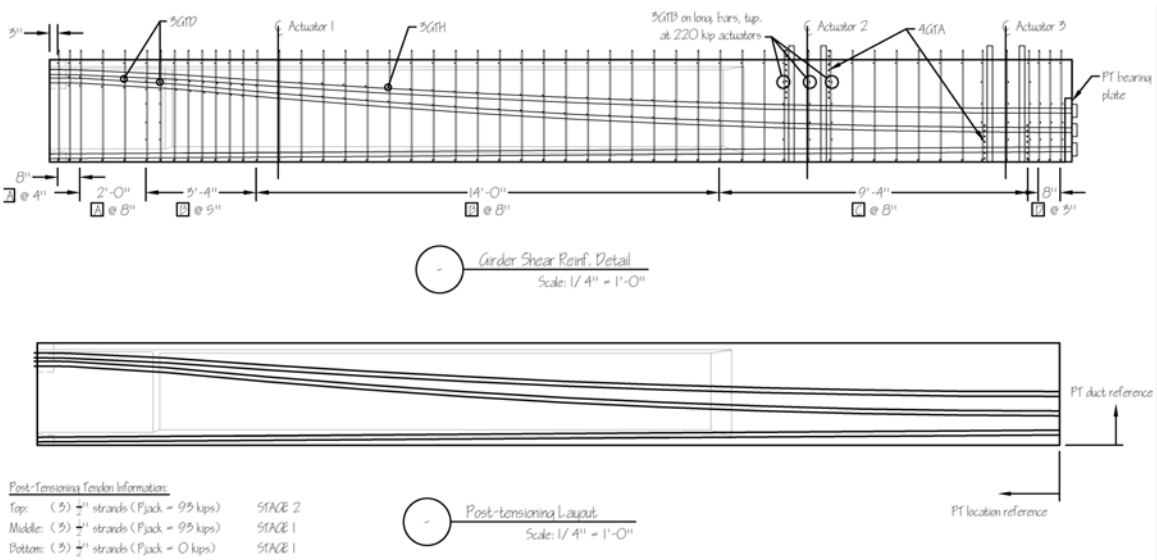

Figure 3.9 Girder reinforcement and post-tensioning profile

3.2.2 Construction Sequence

The construction of the experimental specimen was aimed at inducing similar stresses into the system as with the prototype bridge. Figure 3.10 depicts the construction sequence for the test specimen. The girder and reaction block were designed to be cast on the floor at the University of California, San Diego laboratory. Unlike the prototype structure, pretensioning was not specified due to the cost and complexity associated with this activity. The main area of concern for this test is at the joint between the girder and bent cap and the pretensioning would not be developed at this location. Thus, the removal of pretensioning strands and replacement with mild reinforcement will not affect the experimental results of interest.

Instead of fabricating a strong back system for the specimen, the girder was temporarily supported from the base as a cost savings measure. This does not influence the accumulation of stresses in the system with any significance. The post-tensioning ducts are then spliced and the closure joint cast. Similar to the prototype bridge, a high strength, non-shrink grout is specified for the closure joint with a volumetric fraction of polypropylene fibers of 0.2%. The first stage of post-tensioning requires the stressing of the middle tendon and the setting and grouting of the bottom unstressed continuity tendon.

Once the post-tensioning grout achieves sufficient strength, the temporary support at the bent cap location is removed similar to the removal of the strong back system. Deck falsework is construction to react off the girder such that the deck casting operation induces similar stresses into the non-composite beam as with the prototype bridge. Once the deck has reached strength, the formwork is removed and the final stage of post-tensioning occurs. The final stage post-tensioning involves stressing of the top tendon to provide the system with the required strength.

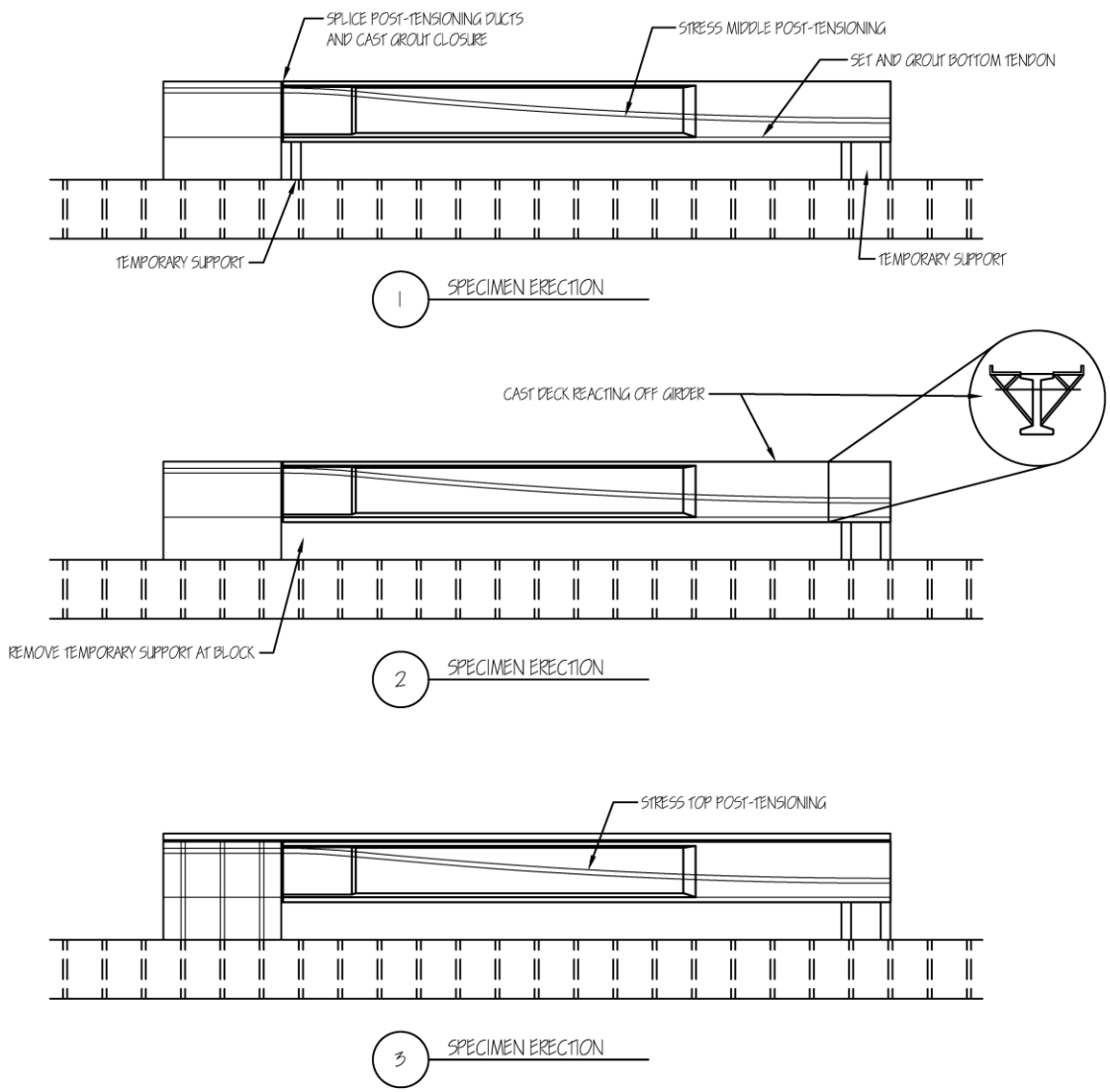

Figure 3.10 Test specimen construction sequence

3.2.3 Load Protocol

For this system, the first stage of loading consisted of relieving the reaction from the temporary support installed between actuator 1 and actuator 2. The goal of this stage was to relieve the reaction while minimizing the associated displacement. Actuators 2 and 3 are set to force control with zero force. Actuator 1 is controlled in manual displacement control and applying upward displacements until the load on the temporary support tower is relieved.

The next stage of loading is designed to apply the simulated dead loading. Actuator 1 was controlled in displacement control and applied upward displacements until a specified force was

reached. Actuators 2 and 3 were slaved to Actuator 1 in force control to apply moment and shear profiles as shown in the prototype specimen section.

For all additional stages, Actuator 1 was controlled in displacement until either a specified force or joint rotation limit was reached. A modified equation relating the force in Actuators 2 and 3 to the force in Actuator 1 was used. This new loading equation is based on the seismic flexural and shear demand profiles determined via analysis of the prototype structure.

Following the application of the simulated dead loading, 100 cycles of essentially elastic loading were imposed on the system primarily in the negative flexural direction. This loading was intended to investigate the potential response of the system under in service and ultimate loading. The system was loaded initially in the negative flexural direction until the system was nearing the expected limit of proportionality. Following this, the system was loaded to 90% of the initial dead load demand. This was repeated for 100 cycles in continuous operation.

The next stage of loading is simulated seismic demands. The loading was controlled while operating Actuator 1 in displacement control set to hold when a specified joint rotation limit was reached. The rotation targets were initially specified using the linear potentiometers at the joint. However, it became apparent during testing that these calculated rotations were not correct during increasing displacements due to cracking at potentiometer target supports and spalling of concrete. The actual achieved rotations were reassessed based on more reliable inclinometer readings, which match better the observed rotations during testing. The actual loading protocol used during the seismic cycle is shown in Figure 3.11. A comparison between the original target joint rotations and the realized rotations during the third cycle are shown in Table 3.1. As a main goal of large joint rotation cycles is to determine the overall rotation capacity of the connection due to relative settlement potential, the use of a reversed cyclic loading protocol is a highly severe case. This is because relative settlement demands on the connection will only occur in one loading direction and not reverse. This protocol likely caused a reduction in the actual ultimate rotation capacity when subjected to loading in a single direction. Another driving factor in the development of this testing protocol was the desire to determine the inelastic rotation response in the event of superstructure inelasticity.

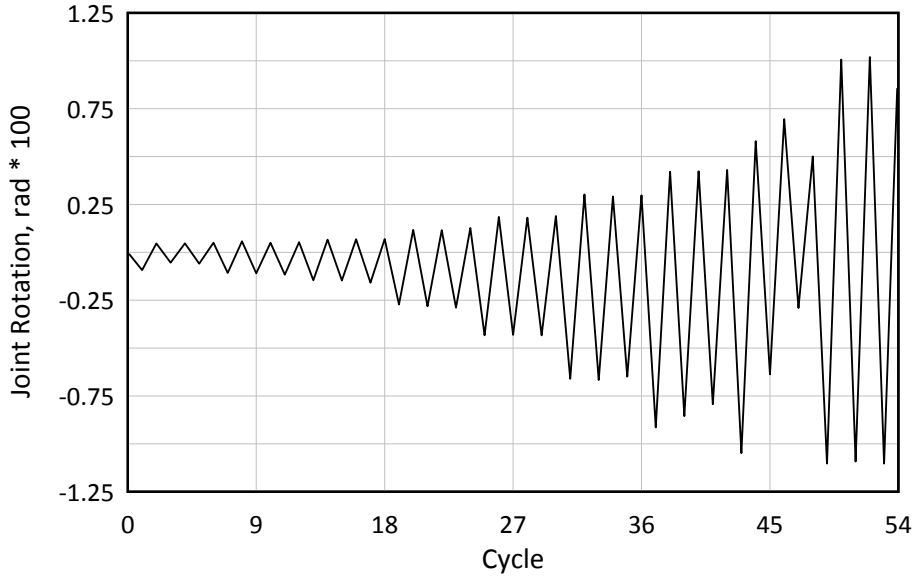

Figure 3.11 Realized loading protocol

Table 3.1 Target joint rotation versus realized joint rotation at 3rd cycle

Stage Identifier	***Target Joint Rotation, %***	*Actual Joint Rotation, %*	***Target Joint Rotation, %***	*Actual Joint Rotation, %*
Stage 1	**-0.02**	-0.06	**0.02**	0.05
Stage 2	**-0.04**	-0.12	**0.04**	0.05
Stage 3	**-0.06**	-0.16	**0.06**	0.07
Stage 4	**-0.10**	-0.29	**0.10**	0.13
Stage 5	**-0.15**	-0.43	**0.15**	0.19
Stage 6	**-0.25**	-0.65	**0.25**	0.30
Stage 7	**-0.38**	-0.79	**0.38**	0.43
Stage 8	**-0.50**	-0.29	**0.50**	0.50
Stage 9	**-1.00**	-1.10	**1.00**	1.03

3.2.4 Instrumentation

The test specimen was instrumented to capture the major response characteristics of the specimen when subjected to applied loadings. This instrumentation includes strain gages mounted on rebar and post-tensioning and external gages mounted onto the specimen.

External instrumentation consists of linear potentiometers, string potentiometers and inclinometers mounted on the exterior of the specimen. A summary of external instrumentation is shown in Figure 3.12. Linear potentiometers are placed to capture opening of the joint, slip between the girder and reaction block and estimated rotation of the girder at the joint. String potentiometers are installed to capture the displacement of the specimen at the actuator locations. Inclinometers are installed to capture to rotation of the reaction block and girder at the joint. A summary of the external instrumentation categories is provided:

- SP series String potentiometers to record displacement at actuators
- Bot series Linear potentiometers for bottom of joint displacement (E: east, W: west)
- Top series Linear potentiometers for top of joint displacement (E: east, W: west)
- Slip series Linear potentiometers for shear slip at joint (E: east, W: west)
- Inc series Inclinometer on face of girder near joint (E: east, W: west)
- RBInc series Inclinometer mounted on reaction block

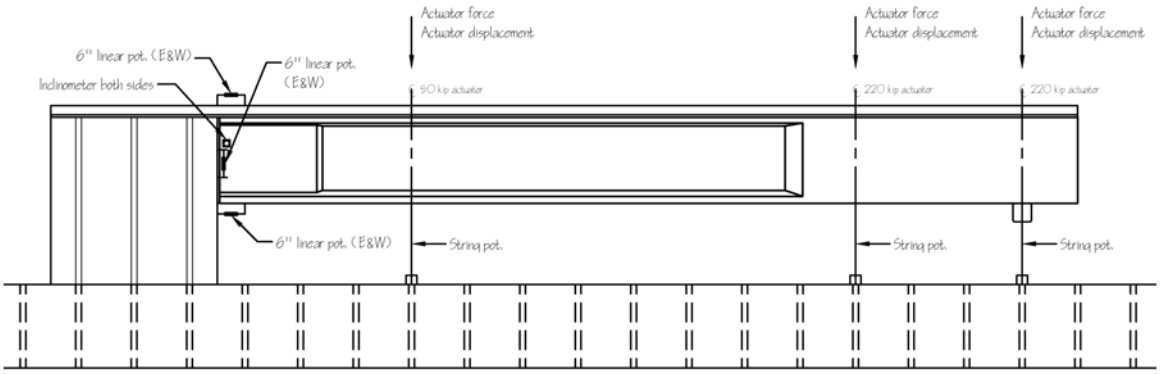

Figure 3.12 External instrumentation configuration

Strain gages were installed on deck longitudinal reinforcement, girder longitudinal reinforcement at the base and girder shear reinforcement. The general locations of these strain gages is shown in Figure 3.13. A summary of the strain gage categories based on labels is provided:

- DR series Deck longitudinal rebar in center
- DRO series Deck longitudinal rebar at outside
- GL series Girder longitudinal rebar
- GS series Girder shear rebar (T: top, B: bottom)
- PT series Post-tensioning strands (B: bottom, M: middle, T: top)

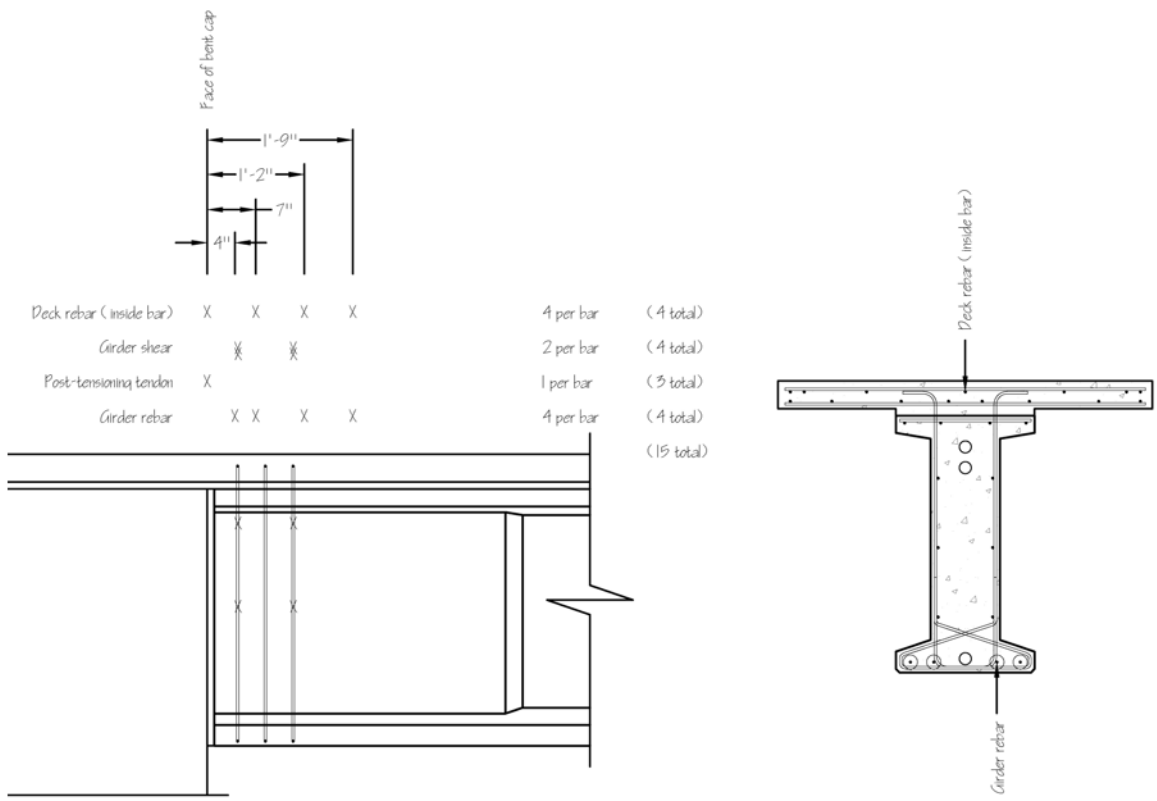

Figure 3.13 Strain gage layout

3.3 Fabrication and Assembly

This section describes the process of section fabrication and assembly.

3.3.1 Component Fabrication and Erection

The integral test specimen was fabricated and constructed at the University of California, San Diego Charles Lee Powell Structural Systems Laboratory. Labor for construction activities was provided by a combination of subcontracted construction firms and lab staff. The majority of construction activities related to fabrication of the steel reinforcement cages were performed by a local steel fabrication company. The majority of construction activities related to building formwork were performed by a local construction company experienced in bridge construction. All post-tensioning activities were performed by a post-tensioning manufacturer and contractor. Casting of concrete and all activities related to erection of members were performed by lab staff.

The first stage of fabrication consisted of the construction of the reinforcing cages for the girder and reaction block. The girder reinforcing cage can be seen in the foreground of Figure 3.14

whereas the reaction block cage can been seen in the background. The girder reinforcing cage was tied on the lab floor including the installation of the post-tensioning ducts. The formwork for the girder was then constructed leaving one sidewall off to the side. The reinforcing cage was then lifted onto the formwork as shown in Figure 3.15. Once installed in the formwork, the final position of the post-tensioning ducts and other reinforcing bars were checked and shifted as required.

Figure 3.14 Girder rebar cage during fabrication

Figure 3.15 Girder rebar cage installed in formwork

Figure 3.16 provides a view of the girder reinforcing cage installed in the formwork after both sidewalls were installed. From this view, the congestion issues related to the post-tensioning duct within the web can be observed. The scaling of this specimen does not provide significant access for pencil vibrators in the duct. To ensure that adequate consolidation would be achieved during fabrication, a form vibrator was used in regions with limited pencil vibrator access. In addition, a superplasticized concrete mix was used to enhance flowability during casting. Following the installation of the reinforcing cage, form ties were installed at regular intervals along the length of the girder, as shown in Figure 3.17. The girder formwork prior to casting of concrete is shown in Figure 3.18 with an overall view of both the girder and reaction blocks prior to casting shown in Figure 3.19.

Figure 3.16 Girder rebar cage installed in formwork

Figure 3.17 Installation of form ties

Figure 3.18 Completed girder formwork with rebar cage installed

Figure 3.19 Completed specimen formwork prior to casting

Concrete for the girder and reaction block were cast using a bucket attached to the overhead crane in the laboratory. The girder was cast first to ensure the maximum flowability of the concrete mixture was obtained during the casting of the member with limited vibrator access. During casting of the girder, an external form vibrator was attached to the formwork near the location at which concrete was being poured. This vibrator was moved around the formwork as concrete was placed in different locations and was used on both sides of the formwork. At the end regions where more sufficient vibrator access was provided, traditional pencil vibrators were used. Figure 3.21 provides a photo following the completion of the concrete casting activities with the girder and reaction block.

Figure 3.20 Casting of girder

Figure 3.21 Specimen after casting of concrete

The girder and reaction block were cast on a Friday morning and allowed to harden over the weekend. The concrete compressive strength was determined by breaking a single cylinder to ensure the girder had strength greater than 3 ksi. The concrete break data indicated a compressive strength in excess of 3.5 ksi, therefore the formwork was removed and the specimens could be safely handled in the lab. The girder following removal from formwork is shown in Figure 3.22. Inspection of the girder indicated only one region of minor concrete segregation over a small portion of the bottom flange of the girder (approximately 4 inches in length). This region was patched by lab staff following placement on temporary supports.

Figure 3.22 Girder following removal of formwork

The girder was moved away from the reaction block to facilitate the construction of two temporary support towers. Following the completion of these towers, the girder was lifted and placed on these temporary towers in line with the reaction block (Figure 3.23). Using previous measurements on the lab floor, the girder was placed to ensure proper alignment with the reaction block and future actuators. The girder was leveled on the temporary supports and subsequently secured using chains to provide stability during construction activities.

Figure 3.23 Lifting of girder for placement with reaction block

Figure 3.24 Girder on falsework for closure pour and post-tensioning

During placement and alignment, the girder was placed to maintain an approximate 1 inch closure joint between the reaction block and girder. This joint is shown in Figure 3.25. Additionally, the alignment was checked to ensure the post-tensioning ducts were properly aligned, see Figure 3.26. The careful activities carried out during the placement of the girder resulted in a system in which the post-tensioning ducts and closure joint were properly aligned with no noticeable variations. The post-tensioning ducts were then jointed using industrial adhesive tape, which was applied by hand. The scaled specimen made the joining of these ducts slightly cumbersome, as hand access was tight. However, the splicing of these ducts was performed without any major complications.

Figure 3.25 Closure joint prior to forming casting grout

Figure 3.26 Post-tensioning duct a) prior to splice and b) after slice

The girder formwork was modified and reused as the closure joint formwork by drilling new holes in the form and reusing the original form tie holes in the girder, see Figure 3.27. After installation of the side forms, the bottom of the joint was closed using a single piece of plywood. A drain hole was placed in the bottom of the form to allow for draining of excess water used to moisten the faces of the reaction block and girder prior to grouting. The edges of the formwork were sealed using a commercially available sealant and allowed to set prior to grouting. Grout material was mixed on the laboratory floor and lifted onto the top of the specimen. The grout was

then gravity fed into the closure joint, as shown in Figure 3.28. The grout material was Masterflow 928 high strength, non-shrink grout containing a 0.2% volume fraction of polypropylene fibers. This grout matrix was mixed to be flowable based on manufacturer's recommended water content and considering the presence of the fibers. The relatively low volume fraction of fibers did not greatly affect the flowability of the matrix. No noticeable leakage was observed during the grouting activities. The top of the grout closure joint following grouting is shown in Figure 3.29. The grouting activities were completed without any observed complications.

Figure 3.27 Closure joint formwork installed

Figure 3.28 Gravity flow grouting of closure joint

Figure 3.29 Top of closure joint following casting

Formwork was removed from the girder the following day. The resulting closure joint is shown in Figure 3.30. Observations after removal of the formwork indicated no observable voids in the closure joint and overall a very successful grouting operation. The grout was allowed to cure for 3 days prior to the first stage post-tensioning. The first portion of the post-tensioning operation

consisted of setting the wedges for the bottom tendons. Each strand was stressed to approximately 5% GUTS to allow for sufficient seating of the wedge on the live end. The middle tendon was then stressed to a target stress of 75% GUTS. Each strand was individually stressed, as shown in Figure 3.31 using a monostrand jack. Both the bottom and middle ducts were then grouted using SikaGrout 300PT(Sika, 2009). Following two days of curing in the post-tensioning grout, the temporary support near the reaction block was removed simulating the removal of the strong back in the prototype structure (see Figure 3.32). The post-tensioning force in the middle tendon at this stage provides a sufficient shear friction mechanism in the system for casting of the deck and associated construction activities.

Figure 3.30 Closure joint after removal of formwork

Figure 3.31 First stage post-tensioning of middle tendon

Figure 3.32 Specimen following first stage post-tensioning and removal of end support

Formwork for the reinforced concrete deck was constructed to react off the girder as is customary in precast concrete bridge construction, as shown in Figure 3.33. The construction of the deck formwork utilized the existing holes in the girder from the form ties to secure the forms in place. With the formwork in place, the deck reinforcing cage was fabricated as shown in Figure 3.34. The entire specimen, prior to casting of the reinforced concrete deck, is shown in Figure 3.35. As is apparent from this figure, a significant portion of the shear load of the wet concrete matrix will be carried across the closure joint using a shear friction mechanism developed by the middle tendon post-tensioning.

Figure 3.33 Deck formwork installed on girder

Figure 3.34 Installed deck reinforcement

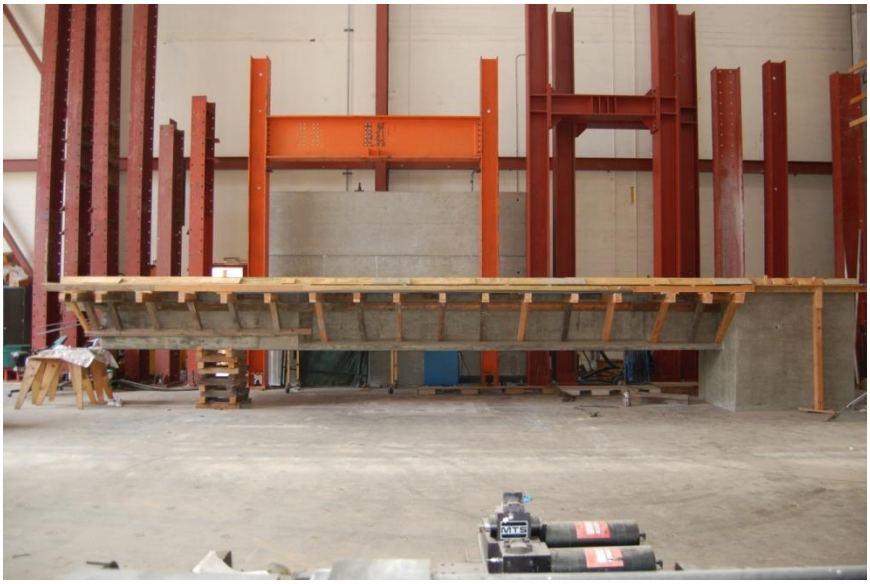

Figure 3.35 Specimen prior to casting concrete deck

Similar to casting of the deck and reaction block, the deck was cast using a bucket attached to the overhead crane. The finished deck following casting is shown in Figure 3.36. In this figure, the alignment bolts for Actuator 3 can be seen. The deck concrete was cast on a Friday and allowed to cure over the weekend. The formwork was then removed resulting in the specimen as shown in Figure 3.37. The deck was cast without any complications nor any noticeable defects.

Figure 3.36 Concrete deck after casting of concrete

Figure 3.37 Specimen following removal of deck formwork

The top post-tensioning tendon was stressed approximately 6 days following the casting of the deck. This tendon was stressed to 75% GUTS similar to the middle tendon. Additionally, each strand in the tendon was individually stressed using a monostrand jack. Following post-tensioning, the duct was grouted using SikaGrout 300PT and allowed to cure. The specimen was then painted white to aid in the identification of cracking during testing, Figure 3.38. Loading frames and external instrumentation were subsequently installed on the specimen, in addition to the installation of vertical actuators in preparation of testing (see Figure 3.39).

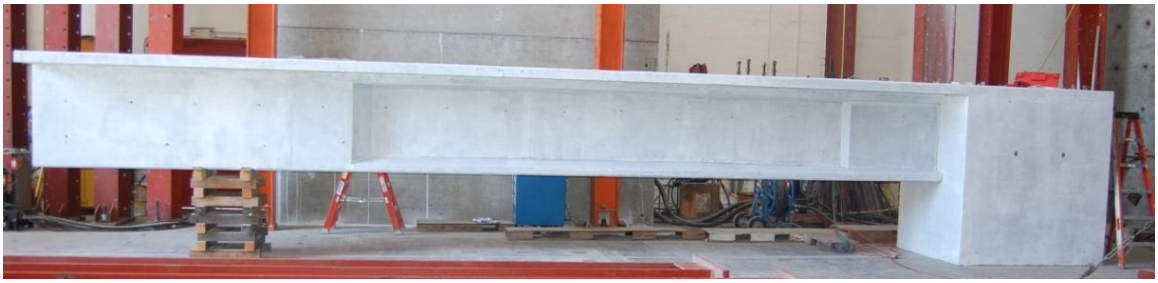

Figure 3.38 Specimen after painting

Figure 3.39 Installation of loading frames

3.3.2 Post-Tensioning

During the post-tensioning operation, readings from strain gages mounted on individual strands were collected. Figure 3.40 shows strain readings collected from the middle strands during the first stage of post-tensioning. The initial effective post-tensioning stress in the tendon based on average strain readings less than an hour after stressing indicates a resulting stress of approximately 67% GUTS. However, readings from the first 300 hours indicate a steady loss in effective post-tensioning force resulting in a stress of approximately 54% GUTS.

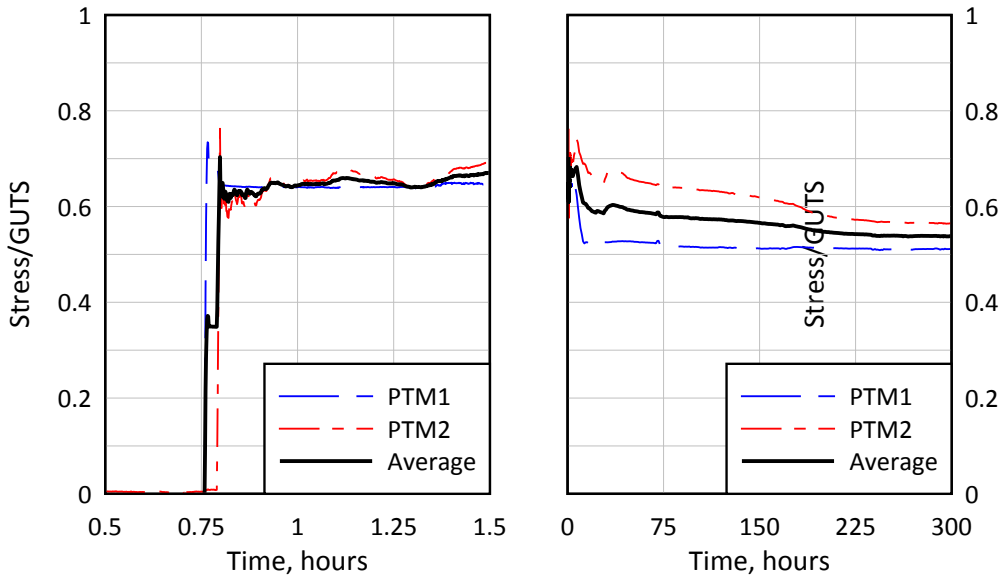

Figure 3.40 Middle post-tensioning strain history for stage 1 tensioning

Strain readings from the second stage of post-tensioning are provided in Figure 3.41. These results indicate that the strain readings in gage PTM1 did not increases during the second stage post-tensioning. However, readings from PTM2 indicate an increase in strain in this strand during the second stage of post-tensioning. Following the second stage post-tensioning, the readings in gage PTM2 decreased. The resulting average stress in the middle post-tensioning tendon approximately 300 hours after the second stage post-tensioning is approximately 61% GUTS.

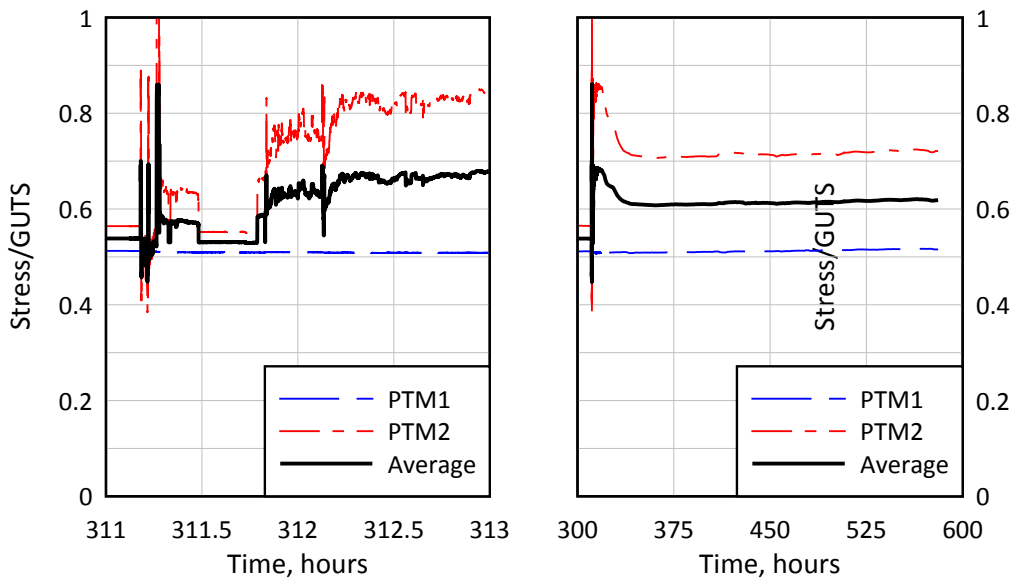

Figure 3.41 Middle post-tensioning strain history for stage 2 tensioning

Strain readings from the bottom post-tensioning during the first stage of post-tensioning are shown in Figure 3.42. The goal of this stage of post-tensioning in the bottom tendon was to ensure the wedges were adequately set. From these readings, the effective post-tensioning stress immediately following the stressing operation was equal to approximately 3.5% GUTS. Over the first 300 hours, the average stress increased in one strand and decreased in another resulting in an effective post-tensioning stress equal to approximately 5.1%.

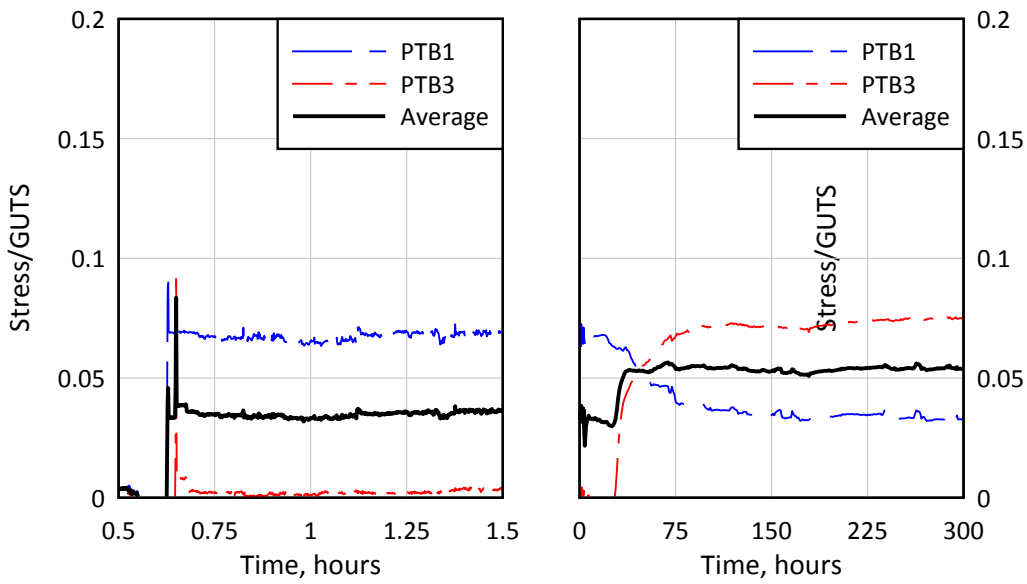

Figure 3.42 Bottom post-tensioning strain history for stage 1 tensioning

The second stage of post-tensioning strain readings are shown in Figure 3.43. These readings indicate that no observable increase in stress occurred during the second stage post-tensioning operation. However, over the 300 hours following the second stage post-tensioning, the stress in both gages gradually increased. This indicates there was a general increase in positive flexure at the joint likely caused by creep and shrinkage in the concrete due to the second stage of post-tensioning. It is believed that the majority of this time dependent response relates to the early age at stressing of the concrete deck.

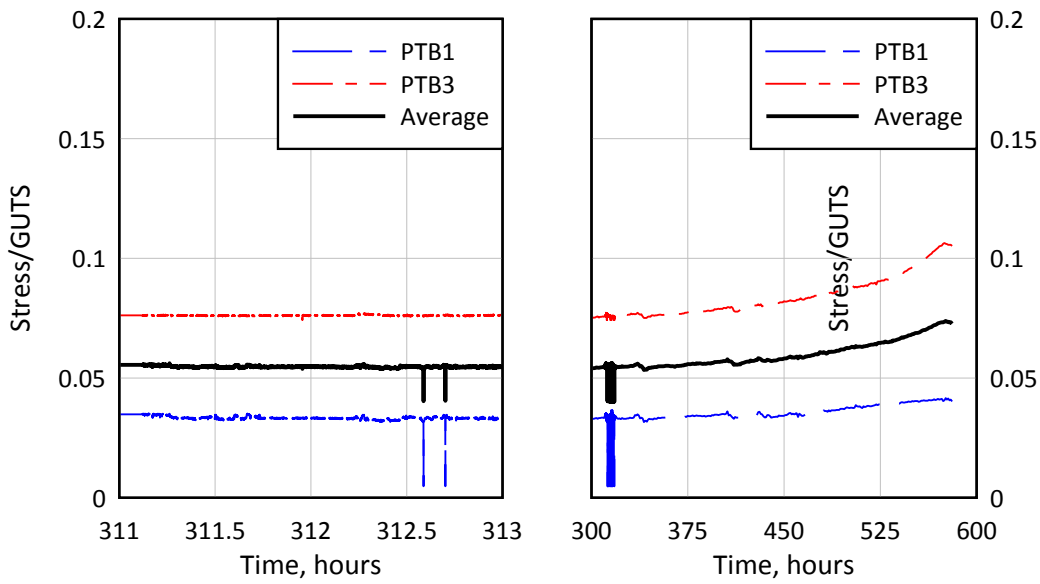

Figure 3.43 Bottom post-tensioning strain history for stage 2 tensioning

3.4 Material Properties

Material properties for rebar, post-tensioning and cementitious materials are provided in the following section.

3.4.1 Mild Reinforcement

All mild reinforcement used in these specimens conforms to the specifications of ASTM A706. Stress-strain test results from uniaxial tension tests for coupon samples from the girder and deck reinforcing bars are provided in Figure 3.44. The yield and ultimate strengths for each bar type is provided in Table 3.2.

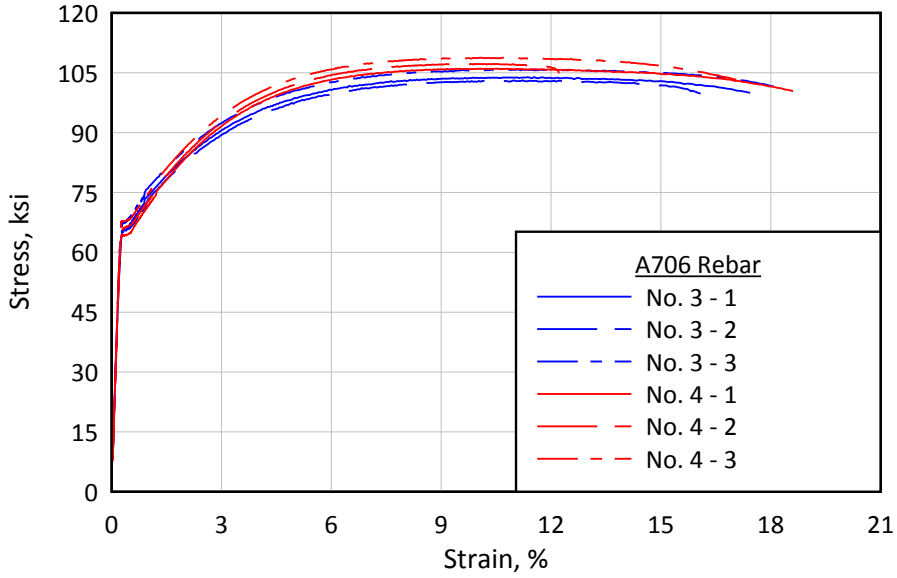

Figure 3.44 Rebar stress-strain curves

Table 3.2 A706 rebar strength and deformability

Bar Description	*Size*	*Yield, ksi*	*Ultimate, ksi*	*Uniform Strain*
Girder longitudinal	#4	68.2	108.7	10.9%
Girder shear	#3	67.1	105.8	12.1%
Deck longitudinal	#3	67.1	105.8	12.1%

3.4.2 Post-Tensioning

Coupon testing of post-tensioning strands were not completed by the University of California, San Diego laboratory. Testing data was provided by the post-tensioning strand supplier from this lot of material. The summary of data collected from these tests is provided in Table 3.3.

Table 3.3 Post-tensioning strength and deformability

Specimen	*Yield, ksi*	*Ultimate, ksi*	*Elongation*
Specimen 1	258.7	279.5	6.1%
Specimen 2	260.2	282.3	5.2%
Specimen 3	259.3	283.6	5.4%
Specimen 4	260.1	285.2	5.4%
AVERAGE	**259.6**	**282.6**	**5.5%**

3.4.3 Cementitious Materials

The reaction block and girder were fabricated with normal weight concrete developed to achieve a target compressive strength of 8 ksi at 28 days with early aging properties. The mix design was developed using a nominal ½ inch maximum aggregate size with a superplasticizer to provide enhanced flowability into the congested girder.

The deck was fabricated with normal weight concrete developed to achieve a target compressive strength of 4 ksi at 28 days with early aging properties. This mix design was developed using a nominal ½ maximum aggregate size.

The cementitious grout selected for use at the closure joint was Masterflow 928 (BASF, 2006) grout with the addition of polypropylene fibers. The grout material is a prepackaged hydraulic cement-based mineral-aggregate high strength, non-shrink grout with an extended working time. The grout material is developed to meet the requirements of ASTM C 1107, Standard Specification for Packaged Dry, Hydraulic-Cement Grout (Non-shrink)), Grades B and C, and the Army Corps of Engineers' CRD C 621, Specification for Non-Shrink Grout, Grades B and C. The polypropylene fibers were approximately ¾" in length and added to the grout matrix at a 0.20% volume fraction.

The cementitious grout selected for use in the tendons was SikaGrout 300PT (Sika, 2009). The grout material is a non-shrink, cementitious grout with a unique 2-stage shrinkage compensating mechanism. The matrix is design with a special blend of shrinkage-reducing and plasticizing/water-reducing agents which results in a material that compensates for shrinkage in both the plastic and hardened states.

Compression strengths for cementitious materials were established through cylinder testing at the day of test (DOT). Results from compression testing for both concrete and grout materials are

listed in Table 3.4. The values presented are based on the average compressive strength of three specimens tested.

Table 3.4 Cementitious material strengths

Material Description	*Age at DOT*	*Strength, ksi*
Girder and reaction block concrete	41 days	8.40
Deck concrete	27 days	5.58
Closure joint grout	37 days	9.55
Bottom and middle duct grout	34 days	10.92
Top duct grout	21 days	8.82

Chapter 4 Experimental Results and Recommendations

The experimental results collected during testing are presented in this section including observations made during testing and post-processing of recorded data.

4.1 Observations During Testing

The following section summarizes the observations made during testing. Observations and photographs were taken at the final cycle at a given force or displacement. Recordings were made at the final cycle in both push and pull directions for a given loading case. Cracks were marked using colored markers corresponding to a given loading case or direction. Green crack markings represent cracks observed following the application of simulated dead loading. Black crack markings represent cracks observed following the elastic force cycles. Blue markings represent cracks observed following cycles to negative joint rotation whereas red markings represent cracks observed following cycles to positive joint rotation.

The test unit prior to testing is shown in Figure 4.1. For the purposes of damage descriptions, references with be made to north, south, east and west. These directions are shown in the figure. North is associated with the direction nearest the reaction block whereas south is associated with the direction nearest actuators 1 and 2. East and west can be inferred from standard practice.

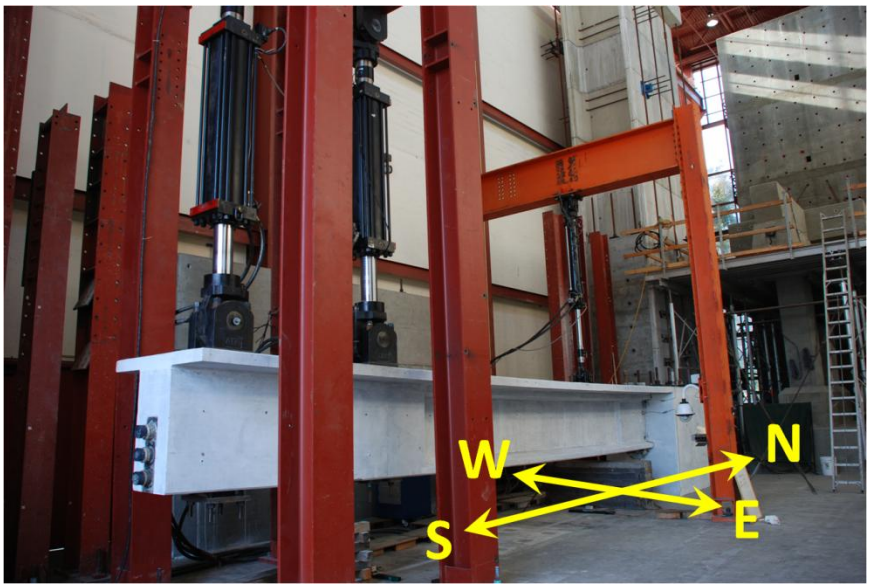

Figure 4.1 Test unit prior to testing

Application of Simulated Dead Loading

At the application of the simulated dead loading, flexural cracks were observed in the reinforced concrete deck. The observed crack widths were less than 0.005 inches. Figure 4.2 shows the east side of the deck with a flexural crack running full depth through the concrete deck. Figure 4.3 shows a view of the top of deck depicting the location of flexural cracking. Three discontinuous cracks were observed in the deck.

Figure 4.2 Side view of deck crack at application of dead load

Figure 4.3 Top view of deck at application of dead load

Elastic Loading Cycles (100th Cycle)

Elastic cycles were focused mainly on the application of additional negative flexural moment demands due to predominance of negative flexural demand expected in service. These load cycles produced flexural demands nearing the point of noticeable nonlinearity in the hysteretic response to investigate system response and degradation potential in the elastic range. The top of deck can be seen in Figure 4.3. Additional flexural cracks were observed up to 41 inches from the joint region. These cracks were well distributed with a maximum observed crack width in the deck at the joint of less than 0.005 inches.

Additionally, a splitting crack was observed in the top of deck that is caused by the development and strain penetration of the post-tensioning tendon as the strains increase with joint opening. This crack width was less than 0.005 inches.

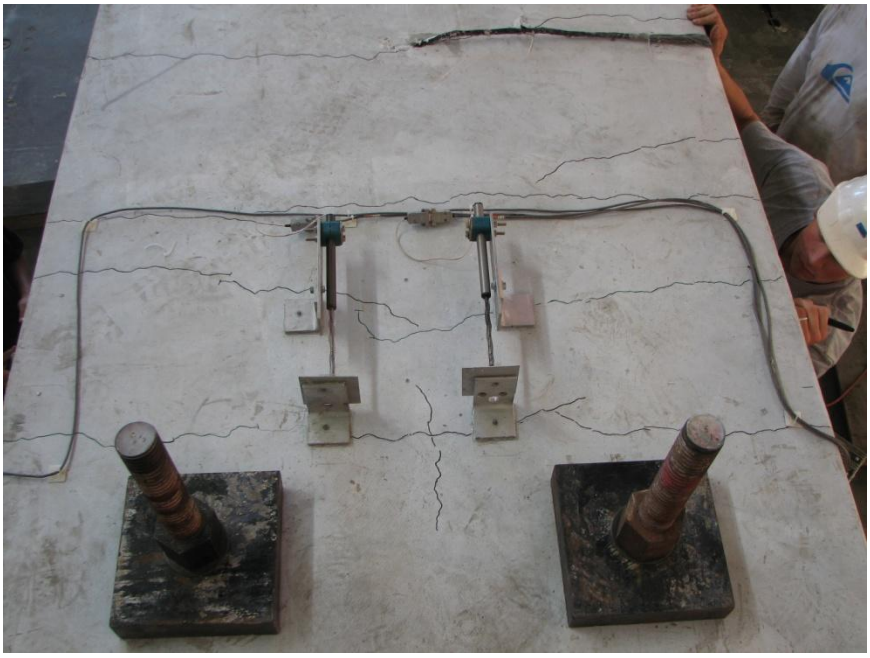

Figure 4.4 Top view of deck after elastic load cycling

The east side of the girder is shown in Figure 4.5. Flexural cracks were observed in the top of the girder extending up to 9 inches from the top of girder. Flexural cracking in the girder was observed up to 37 inches from the joint. A close up view of the top of girder at the joint is shown in Figure 4.6. Maximum joint cracking was observed to be approximately 0.01 inches as opposed to cracking in the deck of less than 0.005 inches. This indicates that the flexural joint opening at the closure joint interface is distributed between two cracks in the deck.

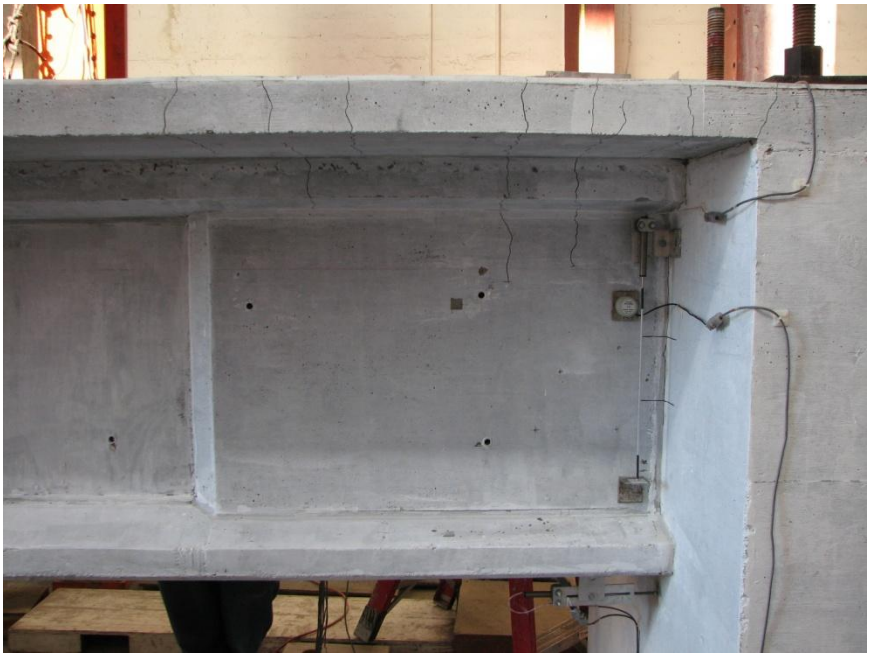

Figure 4.5 East view of girder after elastic cycling

Figure 4.6 East view of top of girder after elastic cycling

-0.06% Joint Rotation (3rd Cycle)

The top of deck view is provided in Figure 4.7. Additional flexural cracks were observed in the deck away from the joint region. The maximum observed crack width across the joint in the deck

was slightly less than 0.02 inches. Flexural cracks in the deck continue to be well distributed along the length of the deck.

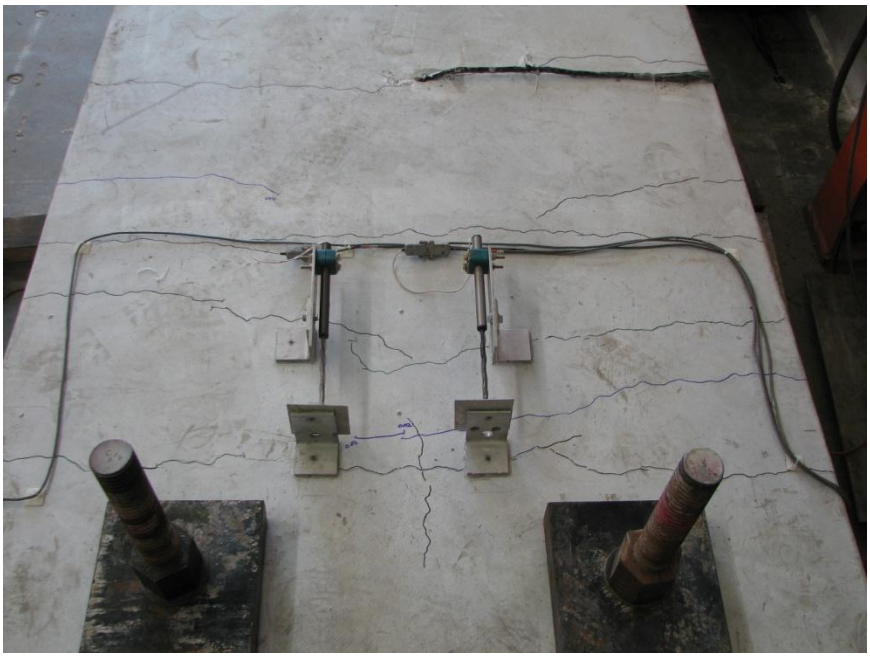

Figure 4.7 Top view of deck at -0.06% joint rotation

The east side of the girder is shown in Figure 4.8. One existing flexural crack extended to approximately mid-depth of the girder with a slight inclination indicating a potential transition to diagonal tension cracking. A new flexural crack was observed approximately 23 inches from the joint that transitioned into a diagonal tension crack extending to approximately mid-depth of the girder. A diagonal tension crack was also observed at the transition from the end block to standard girder section appearing only in the web.

Similar crack patterns were observed on the west side of the girder, as shown in Figure 4.9. Diagonal tension crack extensions did not extend as deep into the girder as did those observed on the east side of the girder.

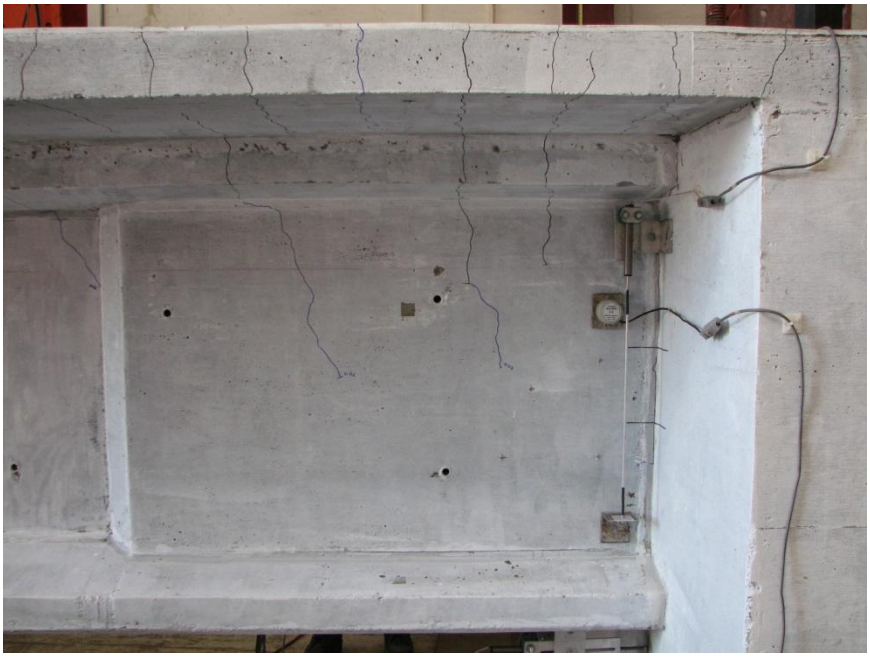

Figure 4.8 East view of girder at -0.06% joint rotation

Figure 4.9 West view of girder at -0.06% joint rotation

+0.05% Joint Rotation (3rd Cycle)

During this cycle, cracking was observed at the bottom of the joint extending approximately to the bottom of the web, see Figure 4.10. The measured crack width was less than 0.005 inches. Additionally, positive flexural cracking was observed along the length of the girder and auditory observations indicated distributed flexural cracking was occurring as loading was applied. In the actual bridge system, this flexural cracking would not be expected due to the use of pretensioning. However, for ease of construction mild reinforcement was used in place of post-tensioning as the key region of concern is the joint and not the main portion of the girder. An example of the observed cracking near actuators 1 and 2 is shown in Figure 4.11.

Figure 4.10 West view of closure joint at +0.05% joint rotation

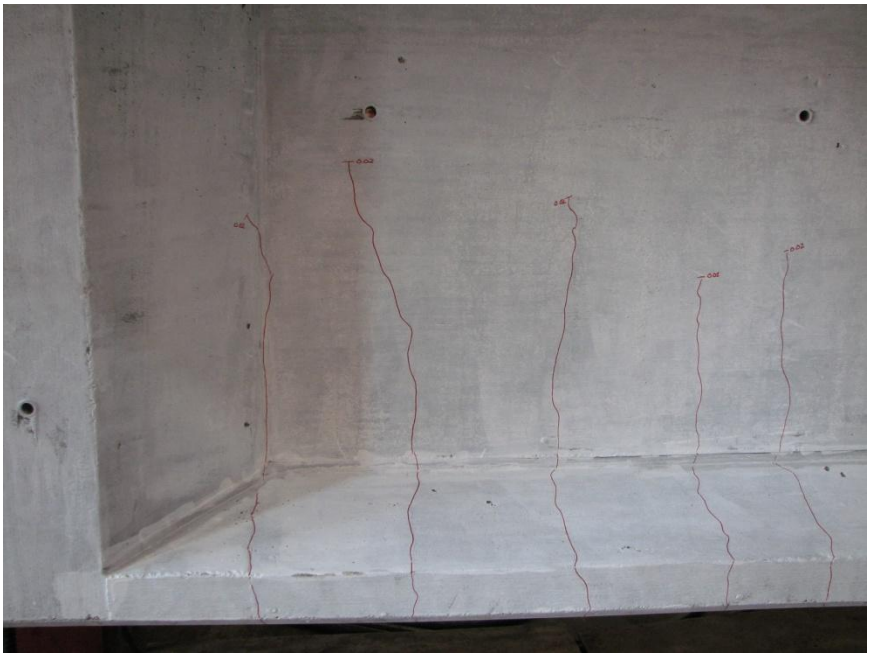

Figure 4.11 Girder cracking near actuator 2 at +0.05% joint rotation

Figure 4.12 View of bottom flange at +0.05% joint rotation

-0.12% Joint Rotation (3rd Cycle)

The top of deck at this load cycle is shown in Figure 4.13. Minor additional cracking was observed with slight flexural crack extensions noted. The measured maximum crack with in the

deck at the joint was 0.02 inches. Diagonal tension crack extensions were observed in the west side of the girder to approximately mid-depth of the girder, see Figure 4.14. Additional minor extensions were also observed on the east side of the girder, as shown in Figure 4.15.

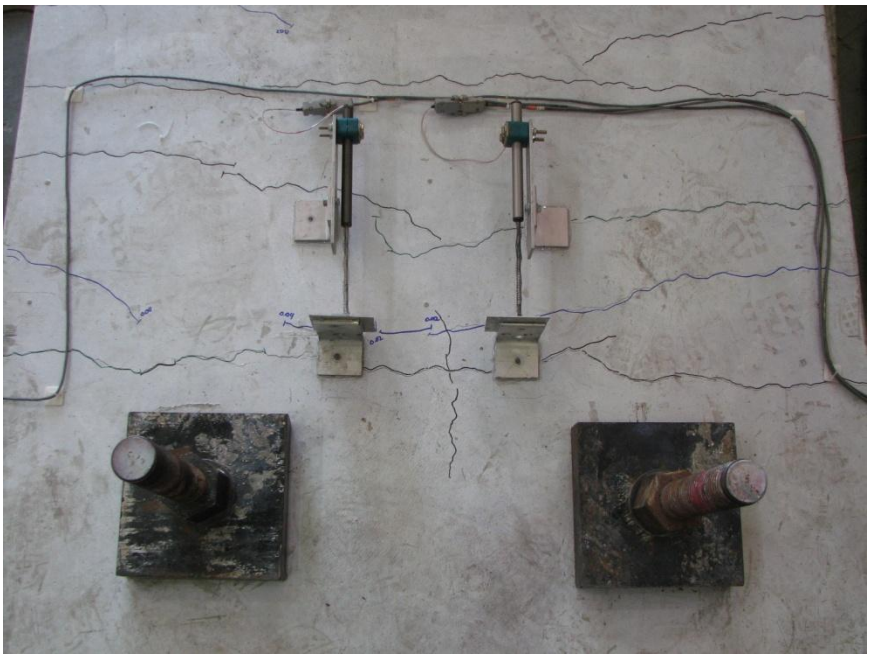

Figure 4.13 Top view of deck at -0.12% joint rotation

Figure 4.14 West side of girder at -0.12% joint rotation

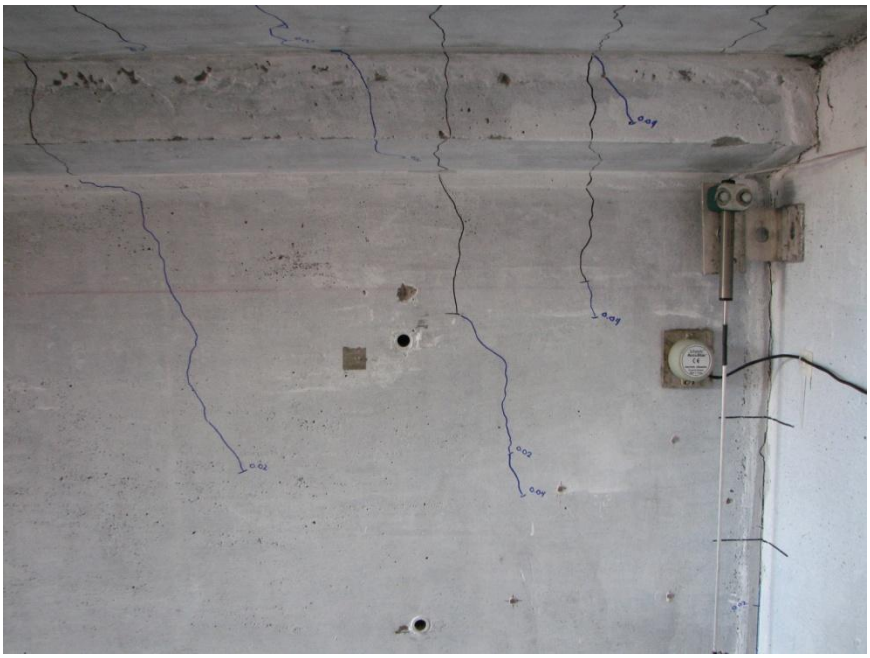

Figure 4.15 East side of girder at -0.12% joint rotation

+0.05% Joint Rotation (3rd Cycle)

The bottom of the east side of the joint is shown in Figure 4.16. The bottom of joint flexural crack was not observed to increase in dimension with a measured crack with equaling less than 0.005 inches. Cracking in the main portion of the girder had minor extensions along the length with no new flexural cracks observed.

Figure 4.16 East view of closure joint at +0.05% joint rotation

-0.16% Joint Rotation (3rd Cycle)

A close up of the flexural crack in the deck at the joint is shown in Figure 4.17. The maximum dimension of the crack was measured to equal approximately 0.03 inches. The overall deck crack pattern is shown in Figure 4.18. Additional distributed flexural cracking was observed up to approximately 7 feet from the joint. Observed cracking remained well distributed throughout the deck. Figure 4.19 shows that flexural cracking in the deck extended throughout the deck for the majority of the observed distributed cracks.

Additionally, extensions in the diagonal tension cracking were observed on both sides of the girder. Cracking extended past the mid-depth point of the girder. The previous diagonal tension crack at the end block transition extended to approximately mid-depth of the girder with an additional diagonal tension crack forming approximately 5 inches further from the joint.

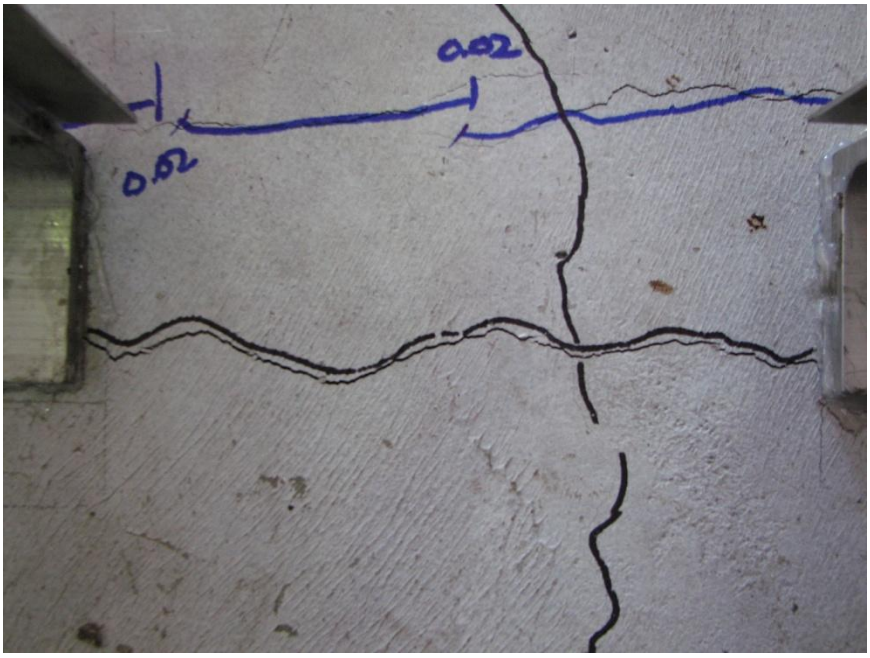

Figure 4.17 Close up of deck crack at -0.16% joint rotation

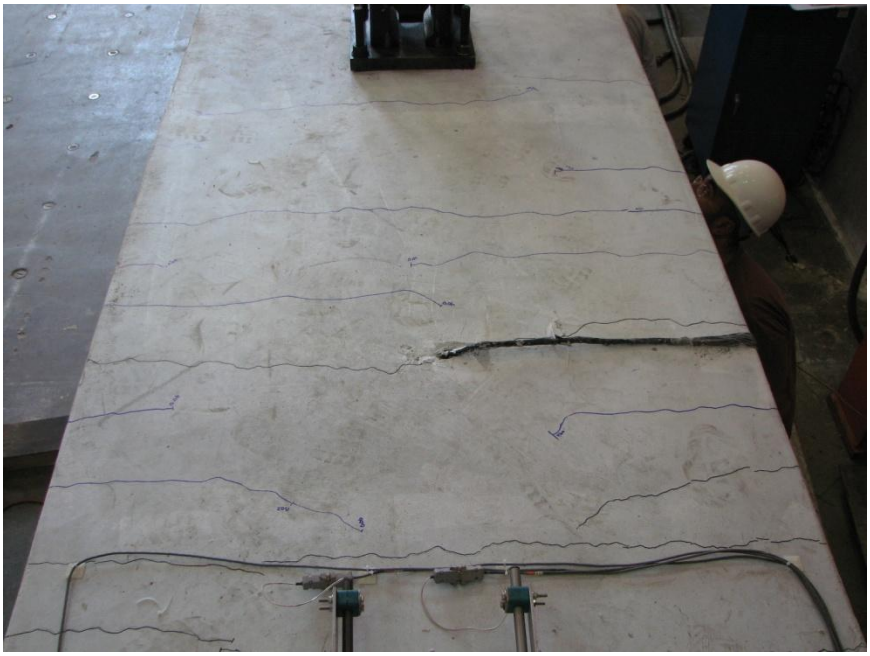

Figure 4.18 Top of deck at -0.16% joint rotation

Figure 4.19 Underside of east deck overhang at -0.16% joint rotation

+0.07% Joint Rotation (3rd Cycle)

The east side of the girder at this cycle is shown in Figure 4.20. A few additional flexural cracks were observed in the main portion of the girder in additional to vertical extensions of existing flexural cracks. Additionally, a flexural crack was observed in the end block portion of the girder approximately 30 inches from the joint. The maximum measured crack width in the bottom of the joint was approximately 0.03 inches.

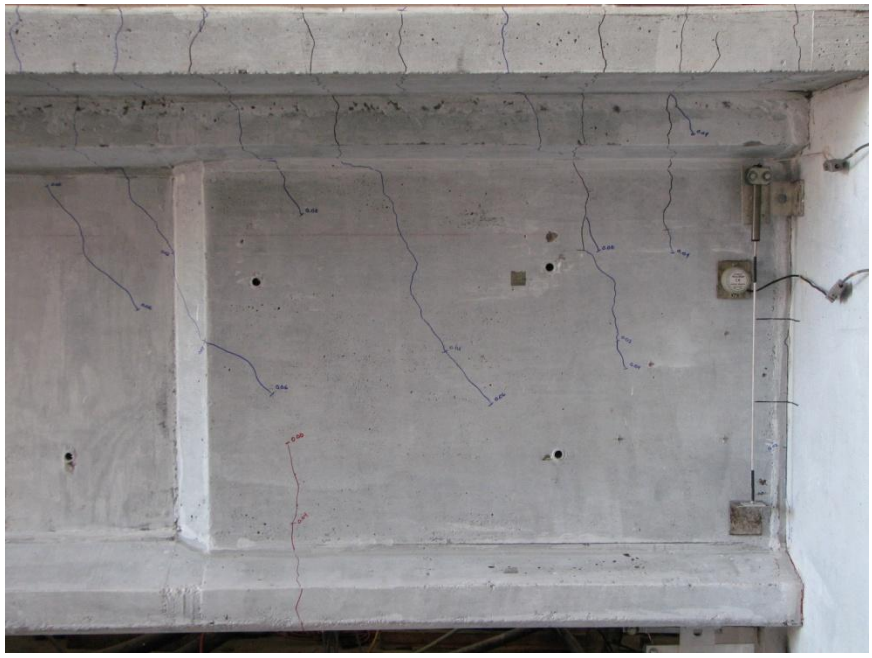

Figure 4.20 East side of girder at +0.07% joint rotation

-0.29% Joint Rotation (3rd Cycle)

The east view of the girder at this cycle is shown in Figure 4.21. Continued diagonal extensions of existing cracks are observed for the majority of the existing cracks on the east side of girder. These existing cracks have extended to approximately three-quarters of the depth of the girder. Similar crack extensions are observed on the west side of the girder, as shown in Figure 4.22. However, these cracks have extended only slightly past the mid-depth of the girder. Four new diagonal tension cracks were observed in the west side of the girder in the main portion of the girder just past the end block transition.

The measured flexural crack width at the top of the girder joint was approximately 0.08 inches. However, this crack was distributed to two flexural cracks in the deck each with a measured width of approximately 0.04 inches.

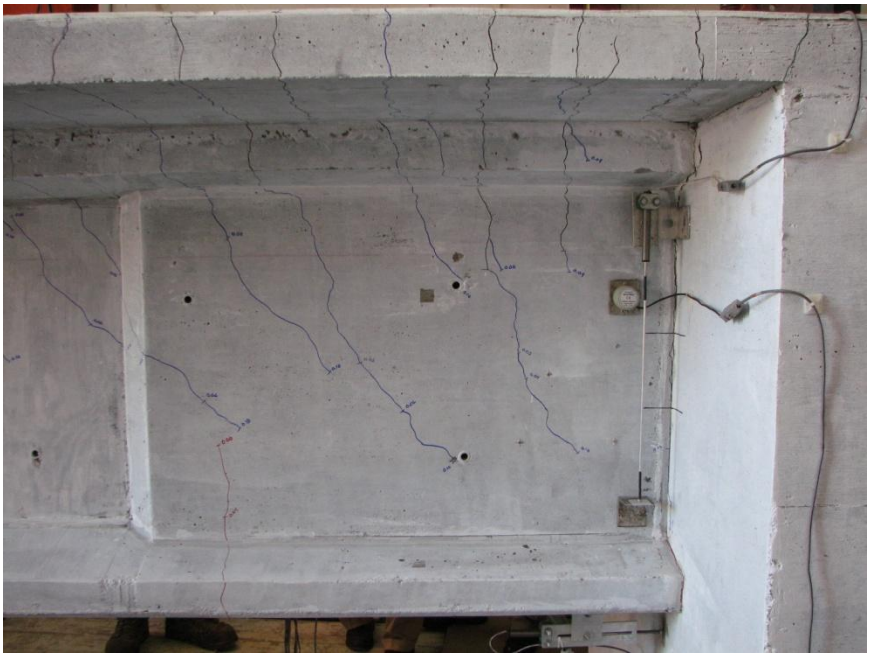

Figure 4.21 East side of girder at -0.29% joint rotation

Figure 4.22 West side of girder at -0.29% joint rotation

Figure 4.23 Underside view of east deck overhang at joint at -0.29% joint rotation

+0.13% Joint Rotation (3rd Cycle)

An additional flexural crack was observed on the east side of the girder in the end block as shown in Figure 4.24. This crack was approximately 20 inches from the joint and was approximately the same length as the existing crack. The measured crack width at the base of the joint was approximately 0.03 inches.

Figure 4.24 East side of girder at +0.13% joint rotation

-0.43% Joint Rotation (3rd Cycle)

Only minor increases in cracks were observed in the girder with no new cracks observed. The top of the girder joint is shown in Figure 4.25. From this photo, it is apparent that the flexural crack in the joint is spread to two cracks (one at the joint and one approximately 2 inches from the joint). The maximum measured crack with of the joint was approximately 0.08 inches.

Figure 4.25 Underside view of east deck overhang at joint at -0.43% joint rotation

+0.19% Joint Rotation (3rd Cycle)

No additional cracks were observed in the girder during this loading cycle. The bottom of the joint is shown in Figure 4.26. The flexural crack is confined to one crack between the grout and reaction block with a measured crack width of approximately 0.07 inches.

Figure 4.26 East view of closure joint at +0.19% joint rotation

-0.65% Joint Rotation (3rd Cycle)

The east side of the girder and deck is shown in Figure 4.27. The observed cracking indicates a continued increase in the dimension of cracks in both the joint and deck. The measured crack width in the girder joint was approximately 0.10 inches. The measured crack widths in the top of deck cracks were approximately equal to 0.07 inches.

Additionally, in Figure 4.27 a horizontal crack is observed between the top of girder and haunch extending approximately 6 inches from the joint. This crack is the result of vertical shear at the end of the girder with inadequately anchored shear reinforcement. The use of traditional bridge details with bent bars for shear reinforcement did not adequately anchor the bars within the depth of the deck and resulted in this cracking. For applications of this bridge system, the use of headed reinforcing bars is highly recommended as a means to enhance the anchorage of the shear reinforcement and prevent this observed response.

A diagonal shear crack was also observed at the top of the girder at the joint on the west side, as shown in Figure 4.28. The observed crack width was appreciable and would be reduced using headed reinforcing bars to better resist the applied shear loading.

Figure 4.27 East side of girder/deck at joint at -0.65% joint rotation

Figure 4.28 West side of girder/deck at joint at -0.65% joint rotation

+0.30% Joint Rotation (3rd Cycle)

Another view of the horizontal crack between the top of girder and haunch is shown in Figure 4.28. The observed crack with was approximately the same as for the negative cycle. Although

there a reduction in vertical shear across the joint, the opening of the joint during positive loading causes the shear transfer to occur mainly at the top of girder and deck. The measured bottom of joint crack width was approximately equal to 0.12 inches.

Figure 4.29 East side of girder/deck at joint at +0.30% joint rotation

-0.79% Joint Rotation (3rd Cycle)

Crack widths at the joint continued to open during this cycle, as shown in Figure 4.30 and Figure 4.31. The measured crack width at the top of girder was approximately 0.16 inches with two deck cracks at approximately 0.08 inches. The horizontal crack between the top of girder and haunch on the east side displayed an increase in dimension. Additionally, the diagonal shear crack on the west side showed increasing dimension with a maximum width of approximately 0.07 inches.

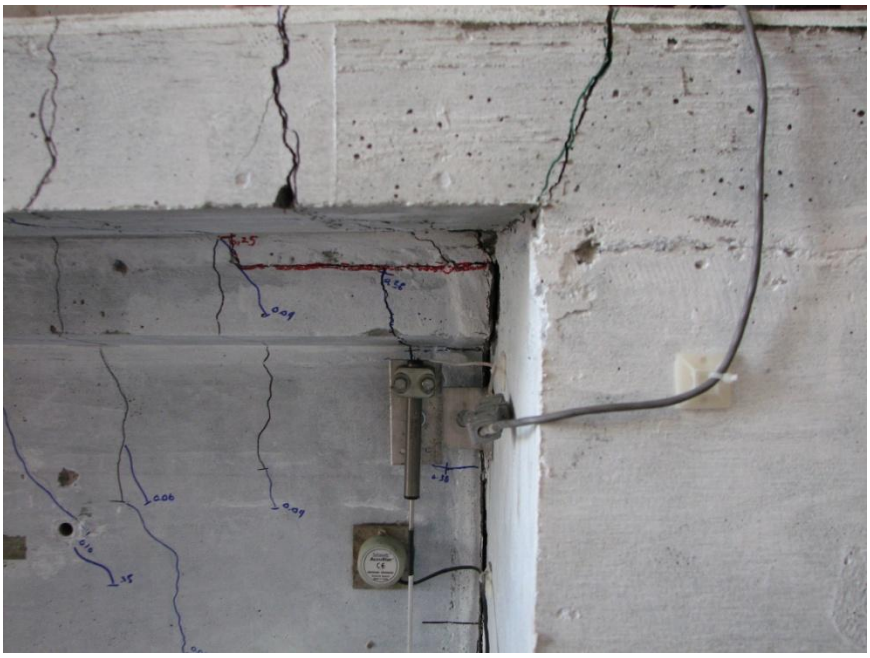

Figure 4.30 East side of girder/deck at joint at -0.79% joint rotation

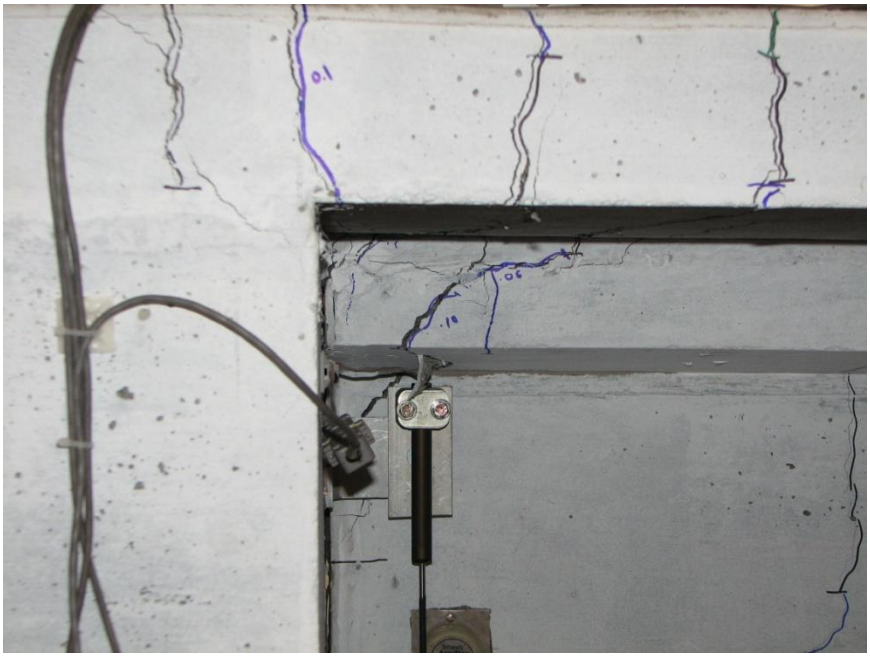

Figure 4.31 West side of girder/deck at joint at -0.79% joint rotation

+0.43% Joint Rotation (3rd Cycle)

The maximum measured crack width of the west side of the joint was approximately 0.18 inches. On the east side of the joint, an additional crack was observed at the interface between the joint

and girder. Up until this point, all joint cracking was observed to occur between the joint and reaction block. The east side joint displayed two cracks whereas the west side joint still maintained only one crack (see Figure 4.32 and Figure 4.33).

Figure 4.32 West view of closure joint at +0.43% joint rotation

Figure 4.33 East view of closure joint at +0.43% joint rotation

-0.29% Joint Rotation (3rd Cycle)

Up until this loading cycle, all displacement-controlled cycles were controlled by the joint rotation calculated using the linear potentiometers on the top and bottom of the joint. However, it was observed during the end of this cycle that there was noticeable spalling at the base of the reaction block causing inaccurate readings (see Figure 4.34). This spalling, and resulting error in the control rotation, resulted in the third cycle achieving an actual joint rotation of -0.29% based on inclinometer readings. The maximum recorded joint rotation during the first cycle, based on inclinometer readings, was -1.05%.

During this load cycle, noticeable shear slip between the girder and reaction block was observed as shown in Figure 4.36. This slip was observed to be approximately 0.25 inches based on visual observations during testing.

Figure 4.34 Observed damage and spalling of reaction block at -0.29% joint rotation

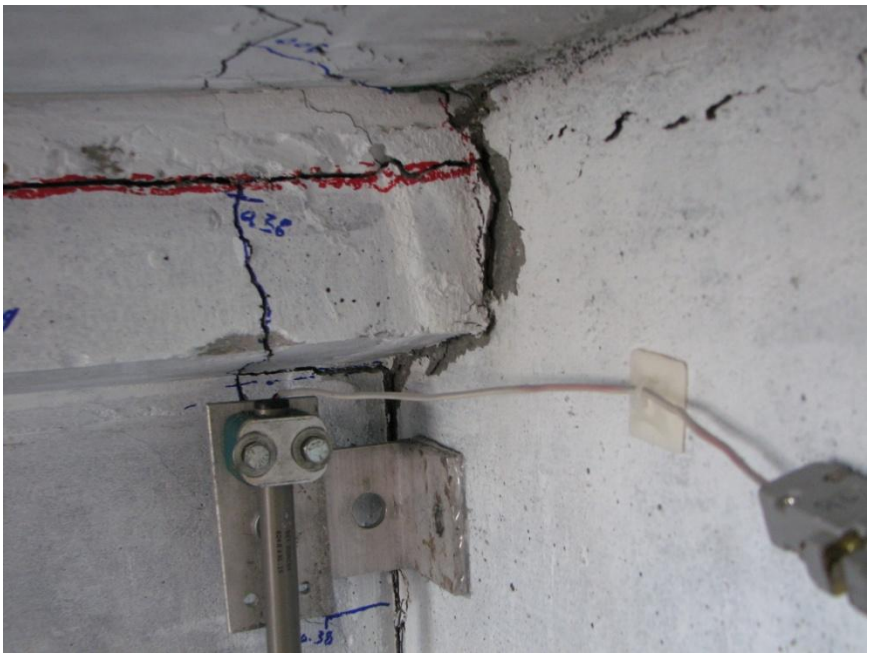

Figure 4.35 East view of top of girder at joint at -0.29% joint rotation

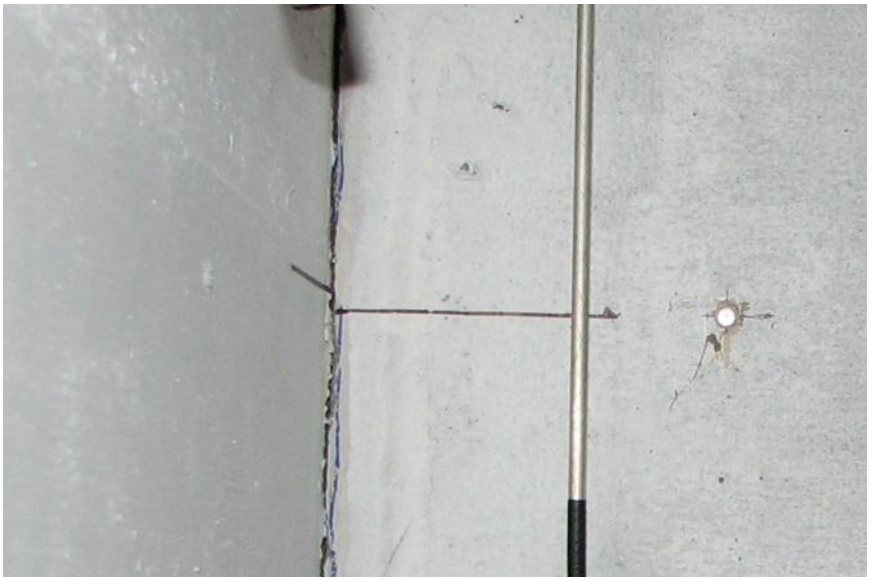

Figure 4.36 Noticeable shear slip at -0.29% joint rotation

+0.50% Joint Rotation (3rd Cycle)

The horizontal crack between the top of girder and haunch continued to increase in dimension as shown in Figure 4.37. This cracking resulted in a portion of the observed vertical shear slip observed during the negative drift cycle. Additionally, the observed diagonal tension crack at the top of the west side of the girder continued to open with an additional horizontal crack extending

along the haunch observed during this cycle as shown in Figure 4.38. The bottom of joint opening continued to increase on both the girder and reaction block sides of the grout (Figure 4.39).

Figure 4.37 East view of top of girder at joint at +0.50% joint rotation

Figure 4.38 West view of top of girder at joint at +0.50% joint rotation

Figure 4.39 East view of closure joint at +0.50% joint rotation

-1.10% Joint Rotation (3rd Cycle)

Figure 4.40 shows the east side of the girder at the joint region. The horizontal crack continued to open due to poor development of the shear reinforcement into the deck. Additionally, a vertical crack was observed in the top flange that became horizontal at the web to flange interface. This crack has an appreciable width and, combined with the crack at the haunch interface, is the cause of the observed shear slip between the girder and reaction block.

The diagonal shear crack and horizontal crack at the haunch on the west side of the girder are shown in Figure 4.41. Significant crack widths are apparent from this figure indicating significant slip of the girder shear reinforcement and inadequate anchorage. This response will be significantly reduced through the use of well anchored shear reinforcement such as headed reinforcement.

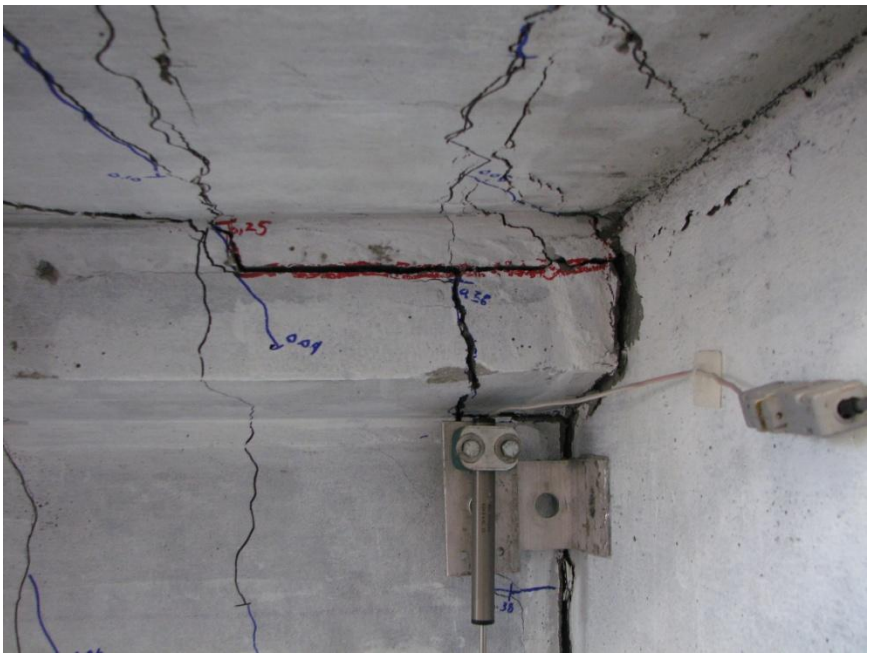

Figure 4.40 East view of top of girder at joint at -1.10% joint rotation

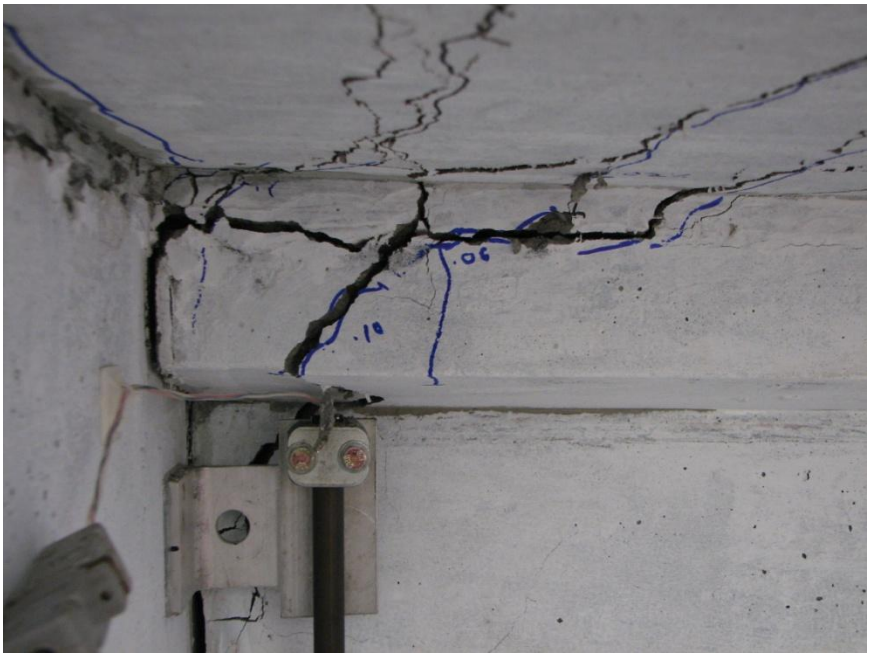

Figure 4.41 West view of top of girder at joint at -1.10% joint rotation

Figure 4.42 shown the bottom of the girder and joint during this loading cycle. Noticeable incipient spalling of concrete in the bottom flange was observed during this cycle. However, although the concrete is exhibiting incipient spalling, the joint grout material appears to be in tact with no signs of spalling.

Figure 4.42 East view of closure joint at -1.10% joint rotation

An overall view of the east side of the girder is shown in Figure 4.43. From this view the localized shear slip is noticeable as the deck exhibits a kind near the joint region to accommodate this vertical slip. The overall view of the top of deck is shown in Figure 4.44. The localized large crack width at the joint is apparent in this photo. However, all other crack widths are significantly less than that joint crack.

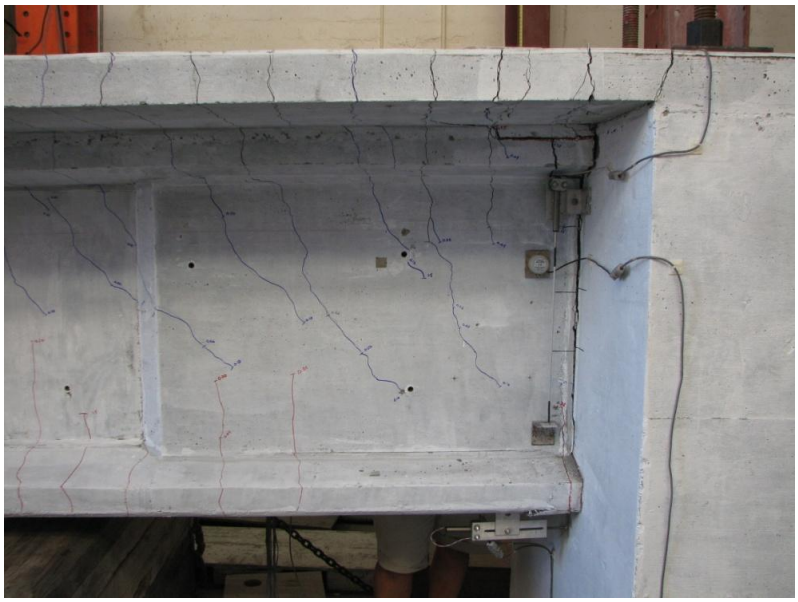

Figure 4.43 East side of girder at -1.10% joint rotation

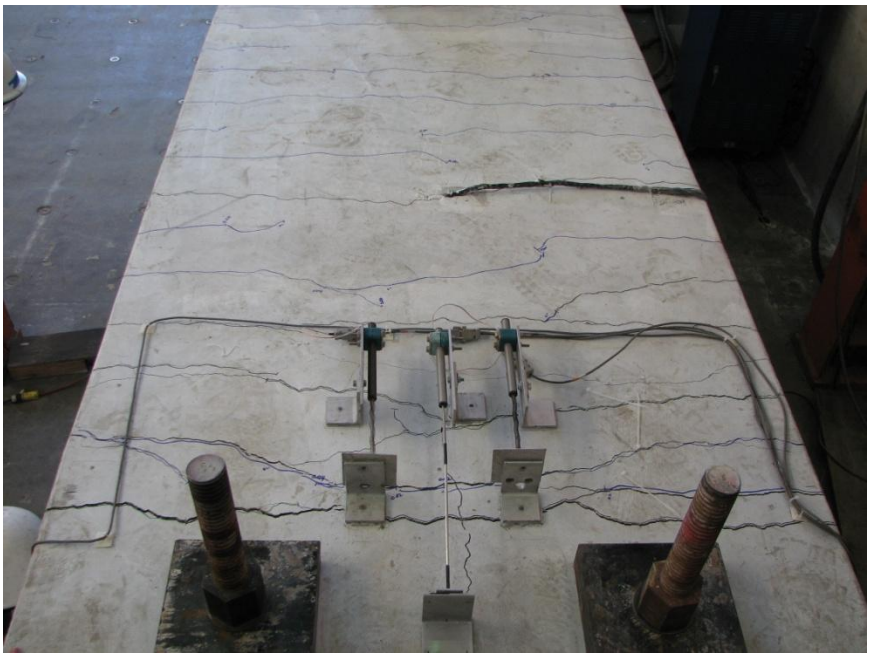

Figure 4.44 Top of deck at -1.10% joint rotation

+1.03% Joint Rotation (3rd cycle)

The overall view of the specimen at this cycle is shown in Figure 4.45. Significant system deformation is apparent from this photo. The east side of the girder at the joint is shown in Figure 4.46. No additional cracking is observed minus the continued increase in the crack widths at the bottom of the joint and at the top of girder to haunch interface. A close up of the bottom portion of the joint is shown in Figure 4.47. From this figure, it is apparent that the majority of the joint rotation is accommodated by the crack between the grout and reaction block, with the girder to grout crack having a significantly smaller dimension. Shear slip between the girder and reaction block is still apparent and increasing at this load cycle; however, it is observed to be of a smaller magnitude as compared to the negative cycle.

Figure 4.45 East view of entire specimen at +1.03% joint rotation

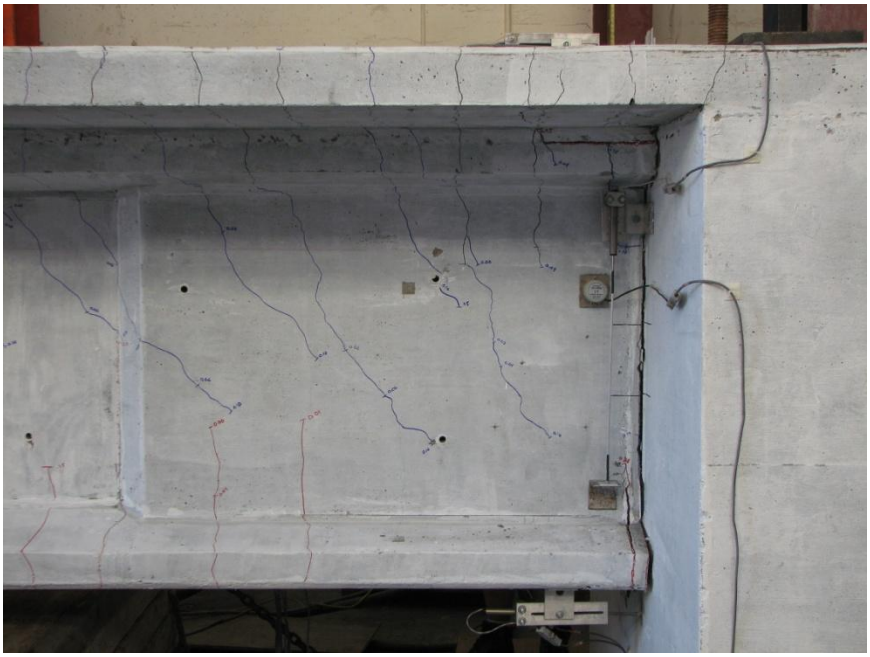

Figure 4.46 East side of girder at +1.03% joint rotation

Figure 4.47 East view of closure joint at +1.03% joint rotation

Figure 4.48 Noticeable shear slip at +1.03% joint rotation

After Failure

The system underwent three cycles to approximately ±1% joint rotation without failure. On the cycle to -1.5% joint rotation, both of the top tendons exhibited fracture at approximately -1.3% joint rotation as noted through auditory observations. Subsequent to this failure, the system was loaded in the positive direction to fail the bottom tendon. The bottom tendon fractured at approximate 1.2% joint rotation resulting in the damage shown in Figure 4.49. By forcibly fracturing all post-tensioning in this system, there was no longer a stable mechanism to resist vertical shear loads as the transfer across the joint relies of a shear friction mechanism. After failure of the tendon, the girder displaced downward and activated a secondary load transfer mechanism through the deck rebar.

Figure 4.49 East side of girder after failing all post-tensioning

A view from the bottom of the deck is shown in Figure 4.50. Following stabilization of the unit, unsound concrete was systematically removed from the deck to reveal that there was no sound concrete remaining in the deck near the joint region. Upon removal of the unsound concrete, Figure 4.51 was obtained showing the straightening of the bent shear reinforcement. This straightening effect confirms the previously stated belief that the shear reinforcement was poorly anchored in the deck. The use of headed bars or another form of well anchored reinforcement is expected to alleviate the observed separation between the girder and deck.

Figure 4.50 East side of deck after failing all post-tensioning

Figure 4.51 Evidence of bent shear reinforcement straightening after testing

4.2 Experimental Results

Data collected during testing from instrumentation is presented and discussed in the following section.

4.2.1 Global Response

Moment-Rotation Response

The recorded moment-rotation response at the joint is shown in Figure 4.52 for the 100 cycles of elastic loading. This response indicates there is no noticeable degradation in stiffness or strength within this loading range. These loading cycles confirm the elastic response of the joint region when subjected to loading within the service load range. Figure 4.53 overlays the elastic loading cyclic response over the lower level seismic response to provide a visual comparison of the relative elastic demand compared with the section capacity. The joint rotation in these plots are based on a zero rotation at the beginning of elastic loading and do not include the original rotation imposed during the application of simulated dead loading. The moment-rotation predication is also shown on Figure 4.53. The predicted response indicates the system was loaded in the negative direction just prior to a predicted reduction in the stiffness of the system.

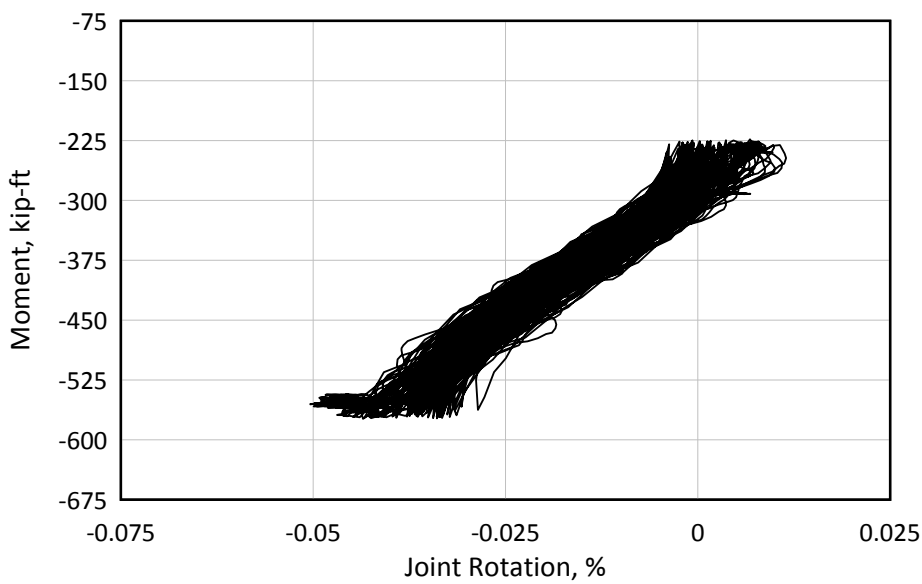

Figure 4.52 Moment-rotation response during 100 cycles of elastic loading

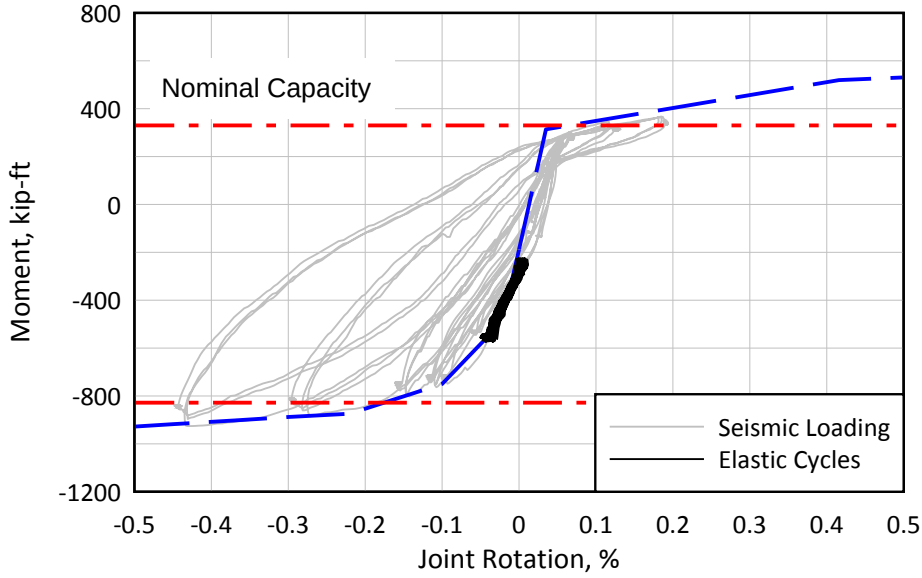

Figure 4.53 Moment-rotation response at low level seismic and elastic loading

The complete moment-rotation hysteretic response is shown in Figure 4.54. This plot indicates that there is appreciable energy dissipation capacity in the negative flexural direction with significantly less in the positive direction. This response characteristic is expected as the negative flexural direction has a significantly greater amount of mild reinforcement present, which is expected to yield and dissipate seismic energy under increasing load cycles. Under increasing levels of rotation demand at the joint, a noticeable reduction in the negative flexural stiffness is observed. This is caused by the yielding of mild reinforcement in the concrete deck, which decreases the effective stiffness of the reinforcement. In the positive flexural direction, the reduction in post-yield stiffness under increasing cycles is not as significant as in the negative direction.

The moment-rotation predicted envelope is also shown in Figure 4.54. The predicted response shows good agreement with the recorded results assuming an effective plastic hinge length equal to one-half times the superstructure depth including deck (42 inches). Although the envelope captures the inelastic response with accuracy, the ultimate rotation capacity is over-predicted. The observed failure of the system occurred at approximately 1.3% drift in both the positive and negative directions. However, the predicted failures in the positive and negative directions were at joint rotations equal to 1.46% and -1.69%, respectively. The error in ultimate rotation is approximately 12% in the positive direction and 30% in the negative direction. Both the prediction and observed failure was controlled by fracture of the post-tensioning tendons. The

failure strain in the post-tensioning tendon was equal to 0.03 in/in as per the AASHTO Guide Specification for LRFD Seismic Bridge Design (AASHTO, 2009). The over-estimation of the ultimate rotation is caused by the observed kinking action in the tendon due to shear slip under large rotations. The recommended modification to the shear reinforcement detailing at the girder end is expected to alleviate much of this issue and thus result in an increase in the ultimate rotation capacity of the connection. Even with the reduction in ultimate rotation capacity due to kinking action, the ultimate rotation capacity results in a system that can safely undergo relative settlements between adjacent bents in excess of one foot for a 100 foot long structure. This level of geometric demand is greater than would be expected in a properly designed bridge structure.

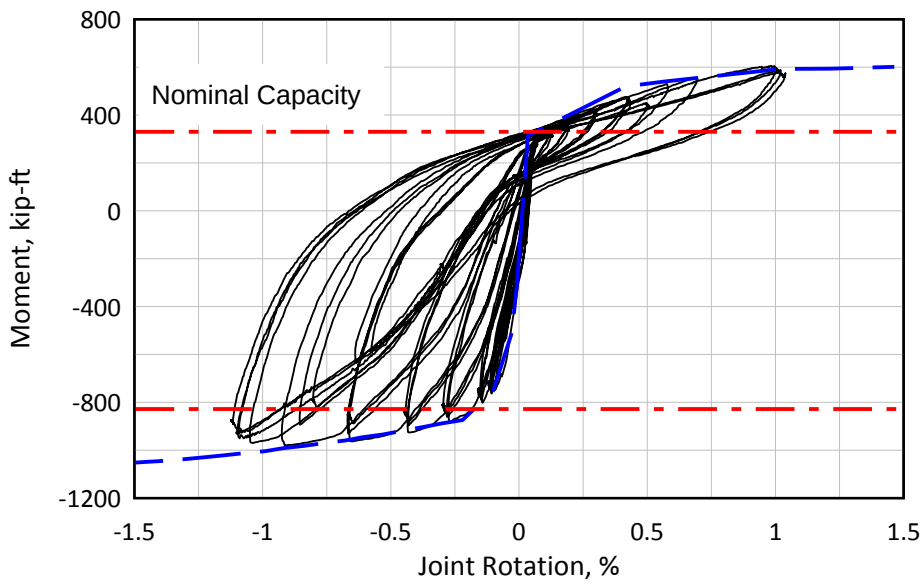

Figure 4.54 Moment-rotation response during seismic loading

The simplified nominal section capacity is also shown on the moment-rotation plots. This capacity prediction provides a relatively accurate prediction of the nominal capacity in both positive and negative directions. The negative flexural capacity was predicted using standard design equations in the AASHTO LRFD Bridge Design Specifications. This calculated capacity shows excellent agreement with the capacity determined using a strain compatibility method. For the positive flexural direction, the capacity was calculated using a moment-curvature program that considers strain compatibility across the section. The rationale for using a strain compatibility approach is due to the presence of unstressed post-tensioning in the bottom of the girder. In addition, it was observed that the moment-rotation prediction is highly sensitive to the tensile strength of the concrete, which is not accounted for in traditional design equations. While the use

of simplified capacity equations for positive flexural capacity will be conservative, it is recommended to also perform a capacity calculation using strain compatibility to determine a better estimate of the connection capacity.

The moment-rotation response under lower level joint rotations is shown in Figure 4.55. From this plot it is apparent that the predicated moment-rotation envelope also provides an adequate level of accuracy under lower level rotations. It is important to note that the effect of tension stiffening was removed from the prediction due to the cyclic loading that was performed. Tension stiffening behavior is expected when a specimen is subjected to monotonically increasing deformation without cycling. For any capacity predictions under seismic loading for systems which may experience prior cycling or cracking, the effects of tension stiffening should be neglected.

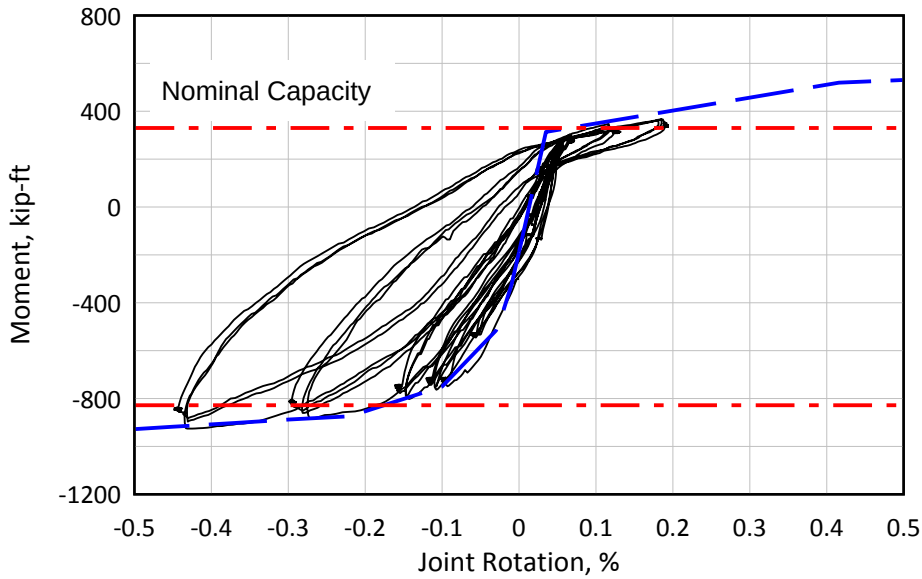

Figure 4.55 Moment-rotation response up to -0.43% / +0.19% joint rotation

Original Test Rotation Control Channel

During the majority of the testing, target joint rotation was defined based on the calculated rotation from linear potentiometers mounted at the top and bottom of the girder at the joint. During later stages of testing, it became apparent that this calculated channel was not producing valid results due to location of cracking in the top deck and the observed damage to the reaction block. Cracking was observed in the top deck that progressed underneath the mounting hardware resulting in inaccurate calculation of joint rotation. Additionally, the development spalling of a

portion of concrete from the reaction block resulted in the gross miscalculation of rotation during the stages prior to spalling.

Figure 4.56 provides a comparison between the calculated rotation and the rotation obtained using inclinometers mounted on the girder near the joint. From this plot, it is observed that the calculated rotation is slightly less than the rotation from the inclinometers in the positive direction. In the negative rotation direction, the calculated rotations are approximately one-half of the rotation from the inclinometers for the majority of loading. As this calculated rotation is less than the actual rotation calculated from inclinometers, the actual rotation achieved during a given target rotation is significantly greater than intended in the negative direction. This is consistent with the information provided in Section 3.2.3.The drifting of calculated rotation is due to the initiation of spalling at the reaction block which caused the miscalculation of drift.

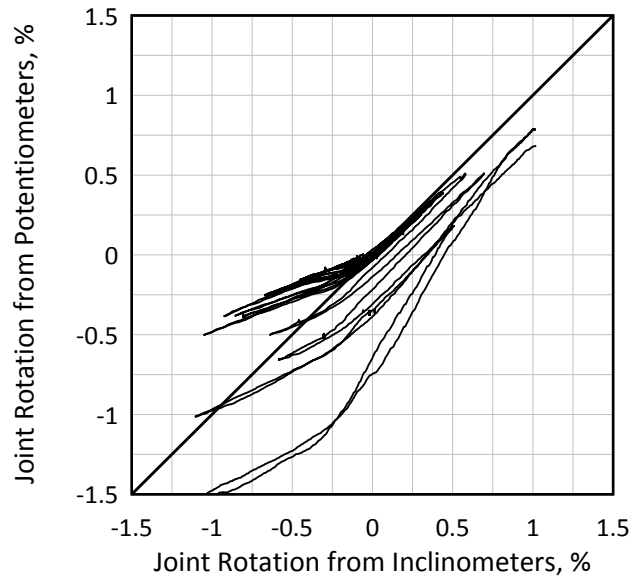

Figure 4.56 Inclinometer rotation versus potentiometer rotation

Reaction Block Rotation

The recorded reaction block rotation history compared with the joint rotation is shown in Figure 4.57. From this plot, it is apparent that there is a general positive trend in reaction block rotation with increasing joint rotation. This trend is expected based on the loading of the system and supporting strong floor. However, the maximum rotation is in general less than 5% of the recorded joint rotation. The rotation associated with the reaction block is removed from the

recorded inclinometer readings to provide the actual relative rotation between the girder and reaction block.

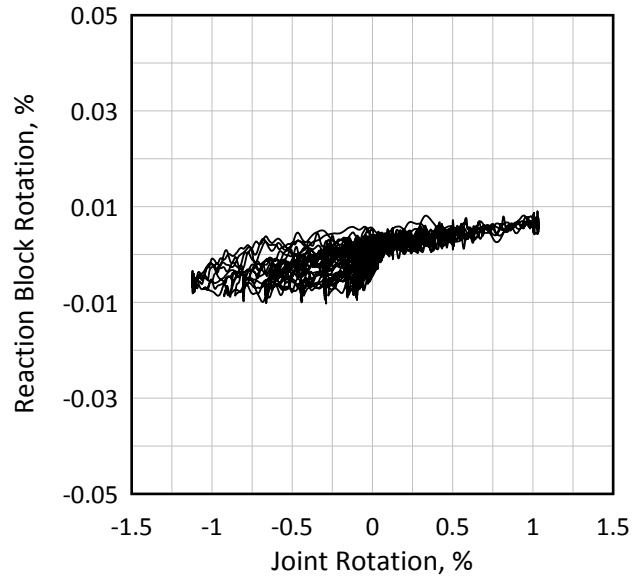

Figure 4.57 Reaction block rotation

Bottom Joint Opening

Figure 4.58 shows the bottom of joint deformation recorded using the eastern external linear potentiometer. During testing, the accumulation of damage on the reaction block resulted in erroneous data recordings from the western external linear potentiometer. Results from this instrumentation indicate a linearly increasing joint opening under increasing positive joint rotation. This response characteristic is expected as a significant portion of the positive joint rotation is facilitated by the

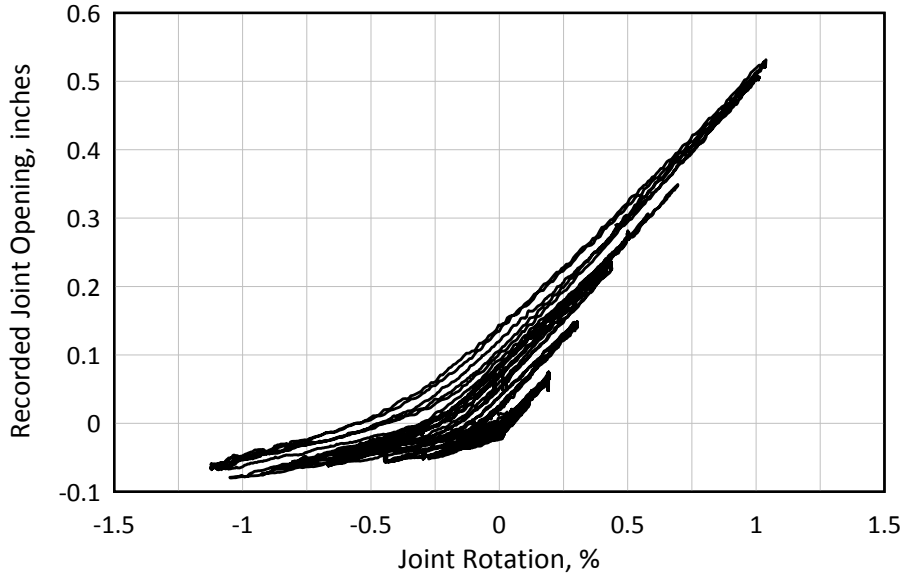

Figure 4.58 Bottom joint opening – east potentiometer

Girder Shear Slip

The girder shear slip history during the 100 simulated elastic cycles is shown in Figure 4.59. Results from this loading indicate that the maximum relative slip between the girder and reaction block is less than four-hundredths of an inch during the entirety of the loading. Interestingly, these results indicate that during the elastic loading cycles, the girder also slipped upwards during many cycles. This recorded response does not match the expected response as downward shear loading is applied to the system during all stages. The relatively minor differential movement between the girder and reaction block is not considered a significant response characteristic and is not expected to cause adverse impacts in structural response or functionality of a bridge structure.

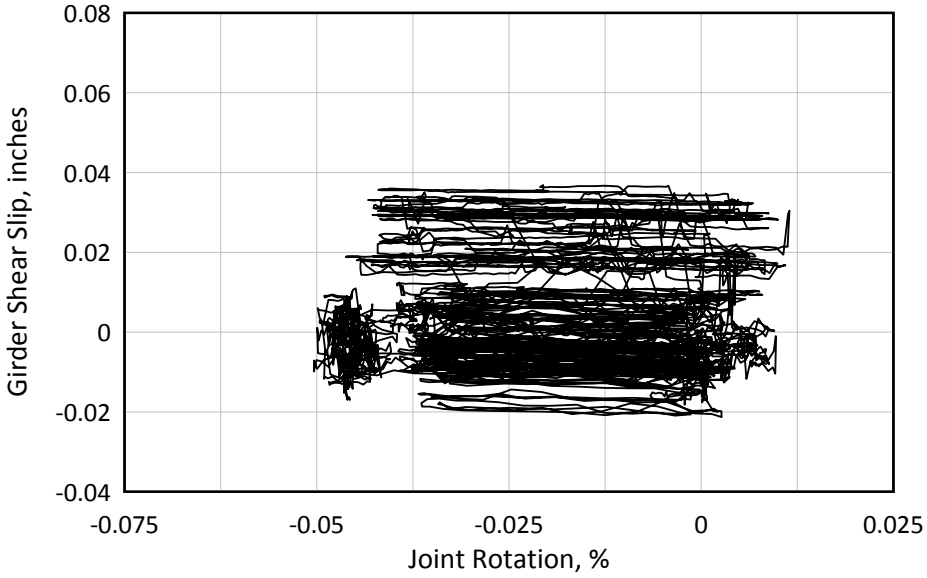

Figure 4.59 Girder shear slip during 100 cycles of elastic loading

Figure 4.60 shows the recorded girder shear slip history during the seismic loading stages. During all loadings cycles below approximately -0.6% joint rotation have less than five-hundredths of an inch slip. As applied joint rotations increased, the recorded drifts continued to increase. Review of the recorded results indicate that during the larger joint rotations cycles, the positive loading cycles have less slip as compared to the negative cycles. This trend is expected due to the decrease in applied shear loading during the positive cycles.

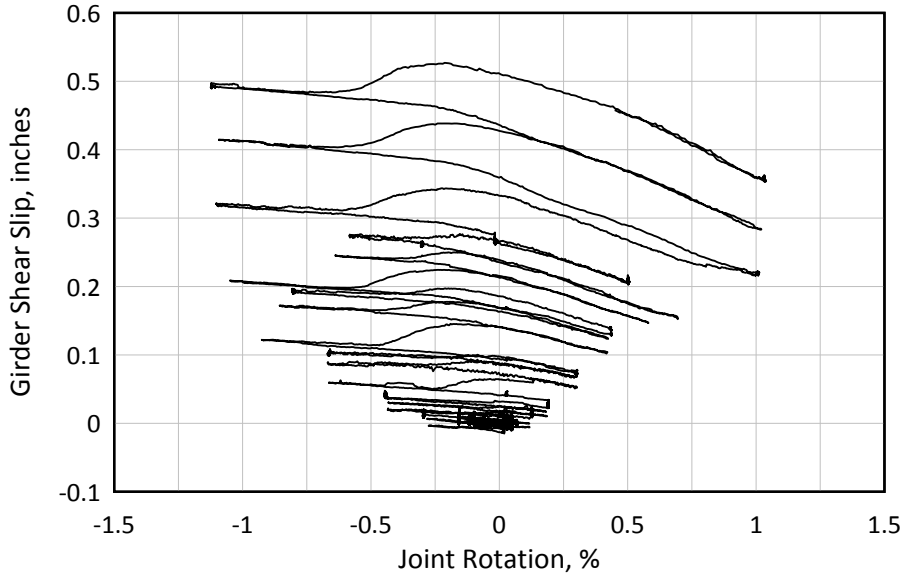

Figure 4.60 Observed girder shear slip

Observations made during testing indicate a significant portion of the observed shear slip is likely due to the separation between the girder and deck. This separation is caused by the inadequately anchored shear reinforcement in the girder, which cannot develop the required shear within the deck. The use of headed reinforcing bars is expected to greatly reduce the observed shear slip by fully anchoring the shear reinforcement within the reinforced concrete deck. As shown in Figure 4.61, the observed horizontal cracking between the deck and girder provided a length of embedded shear reinforcement that was less than the required development length. Therefore, although the shear strength of the system was maintained, there was continued slip of the bar during repeated cycles of testing. To mitigate this issue, the use of well-anchored shear reinforcement in the deck is recommended.

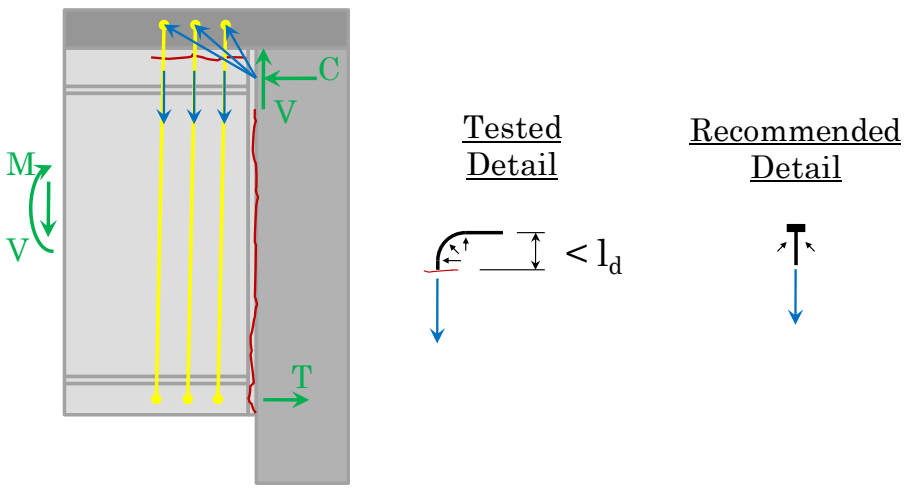

Figure 4.61 Girder shear slip mechanism

4.2.2 Displacement Profile

The recorded displacement profile from the first cycle at each stage is shown in Figure 4.62. The displacement at the reaction block is taken as the relative slip between the girder and reaction block. This figure indicates that for negative loading, the overall response is dominated by the joint end rotation due to the fairly constant slope in the displacement profile. For the positive loading cycles, the profile indicates that there is a significantly influence of the girder end rotation. However, there is also noticeable additional deformation in the system based on the slightly non-linear profile. This indicates that there are appreciable deformations in the girder which correlates with the observed flexural cracking of the girder.

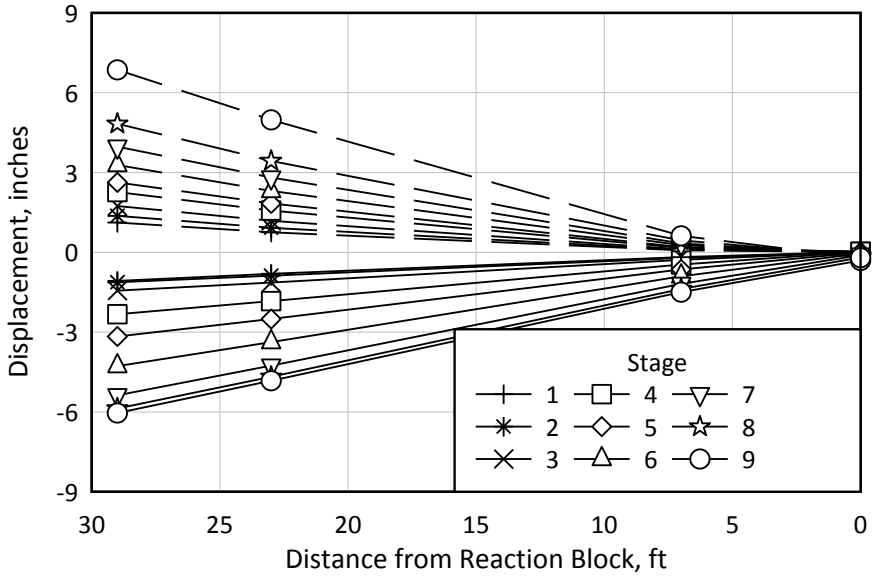

Figure 4.62 Girder displacement profile

4.2.3 Strain Gage Histories

A number of strain gages are mounted on various pieces of reinforcing steel throughout the specimen. Many of these gages were damaged during fabrication, erection and testing thus many readings are not show herein. Additionally, many plots have incomplete data due to damage or malfunctioning gages. This section provides information on the strain histories recorded by various gages.

Deck Reinforcement

Strain histories for gages mounted on the middle deck reinforcing bar are shown in Figure 4.63 through Figure 4.65. It is observed that the bar yields during the first seismic loading cycle for the bar located at the joint (DR1). This correlates with the observations made during testing including the presence of a noticeable crack in the deck at the joint location. The recorded strain history indicates significant strain concentration occurred at the joint location during negative loading cycles. During positive loading cycles, the compressive strains imposed at the joint were insufficient to ever impose negative straining in the bar.

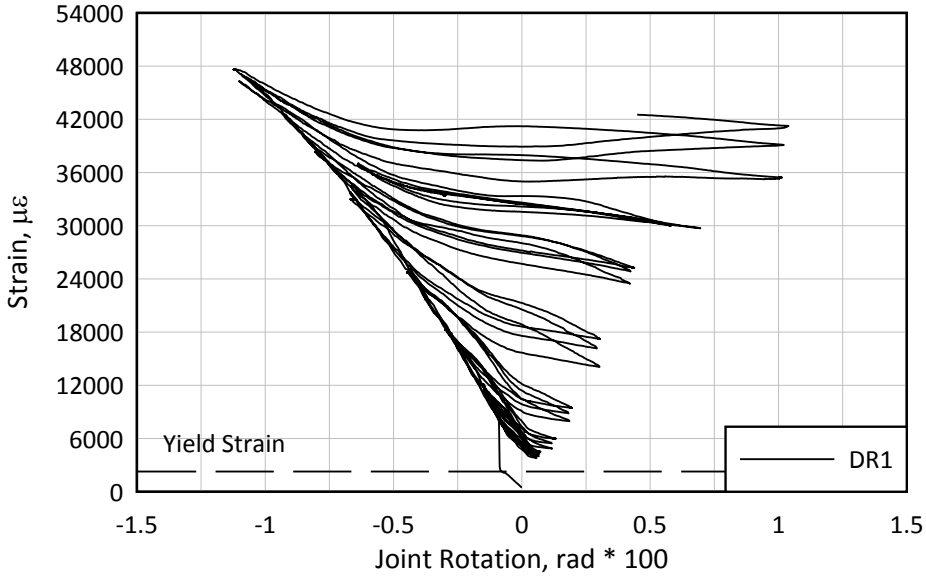

Figure 4.63 Deck middle rebar strain history – DR1

Recordings from the gages 7 inches and 14 inches away from the joint (DR2 and DR3) show significantly lower strain readings as compared to the gage located at the joint. Only minor yielding of the reinforcing bar was recorded at the location 14 inches from the joint whereas appreciable yielding was observed 7 inches from the joint.

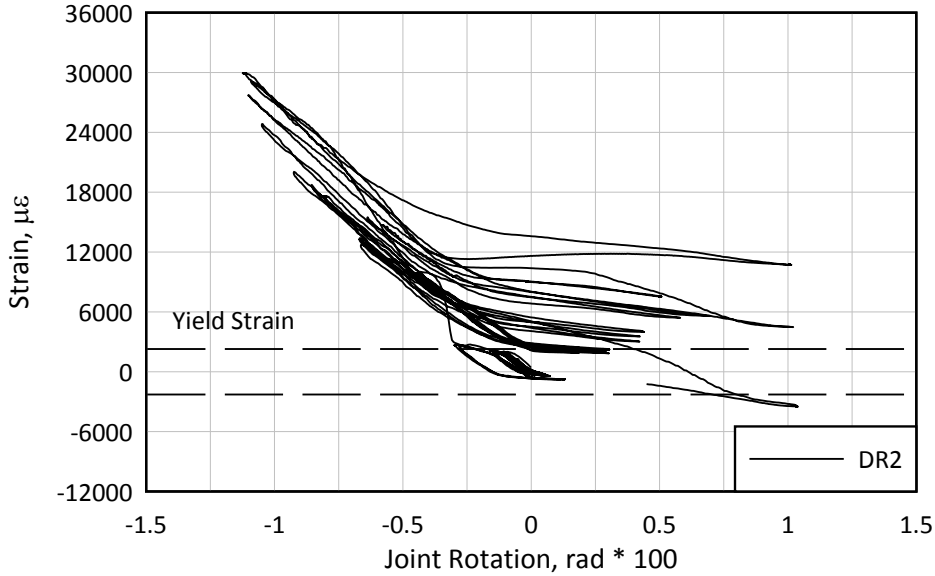

Figure 4.64 Deck middle rebar strain history – DR2

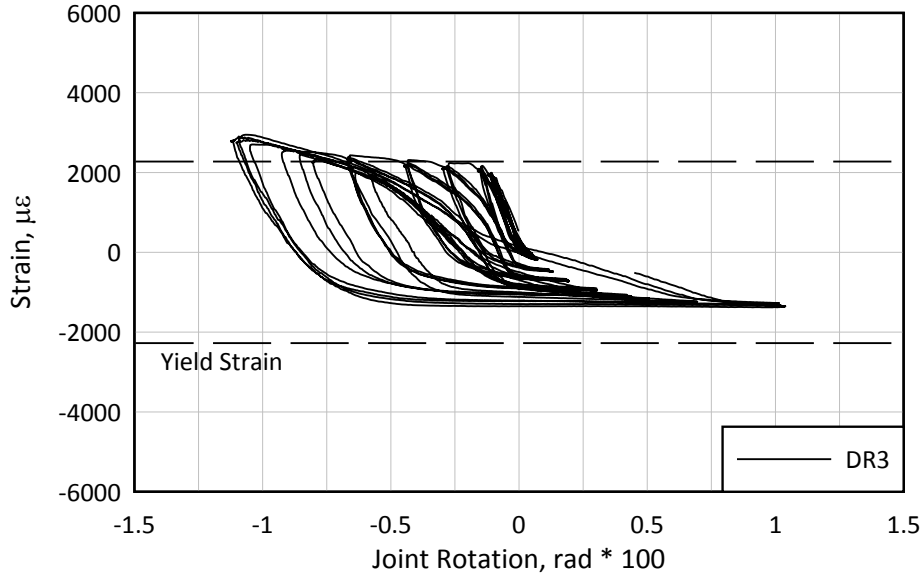

Figure 4.65 Deck middle rebar strain history – DR3

Similar to the middle deck reinforcing bar, the outer bar also exhibited significant yielding. The bar at this location did not yield until after the completion of the first seismic cycles, after the observed yielding at the middle bar. Similar to the middle bar, this bar experienced no negative straining during seismic testing. Recordings indicate that the strain in the outer bar at the joint are less than those in the middle bar for the majority of the testing.

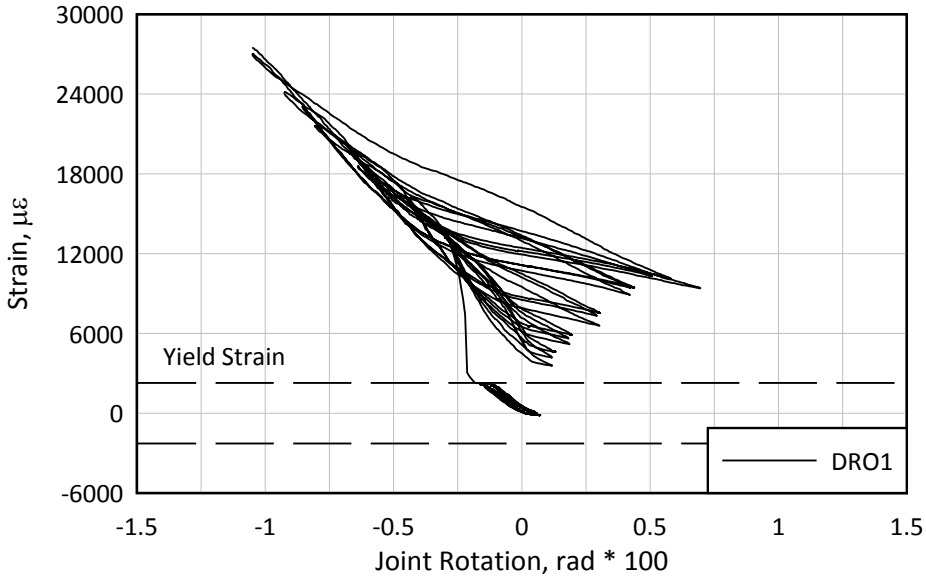

Figure 4.66 Deck outside rebar strain history – DRO1

The outside bar experienced yielding at both the location 7 inches from the joint and the location 14 inches from the joint. The larger strains recorded at the outer bar as compared to the middle bar are likely caused by the flexural cracking of the deck which was observed along the length of the girder during seismic testing.

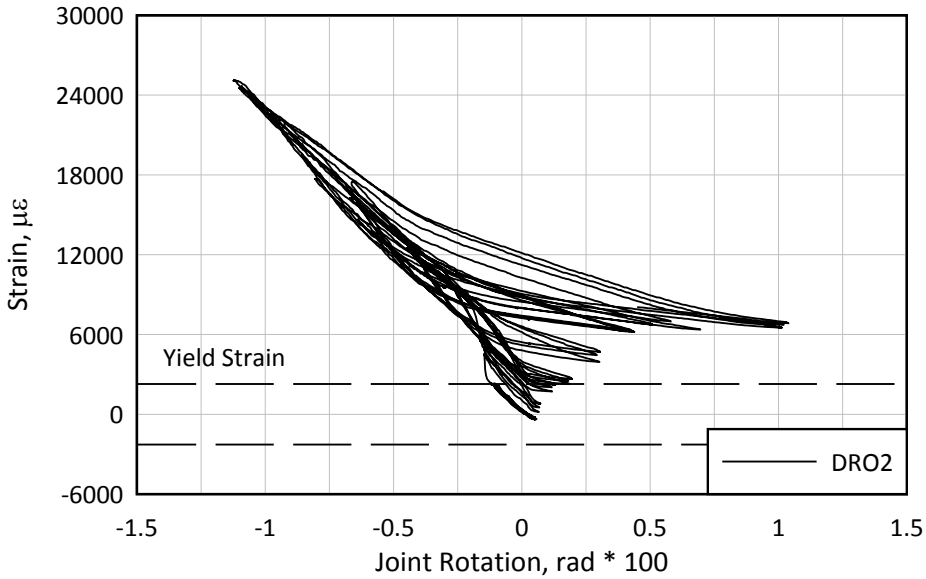

Figure 4.67 Deck outside rebar strain history – DRO2

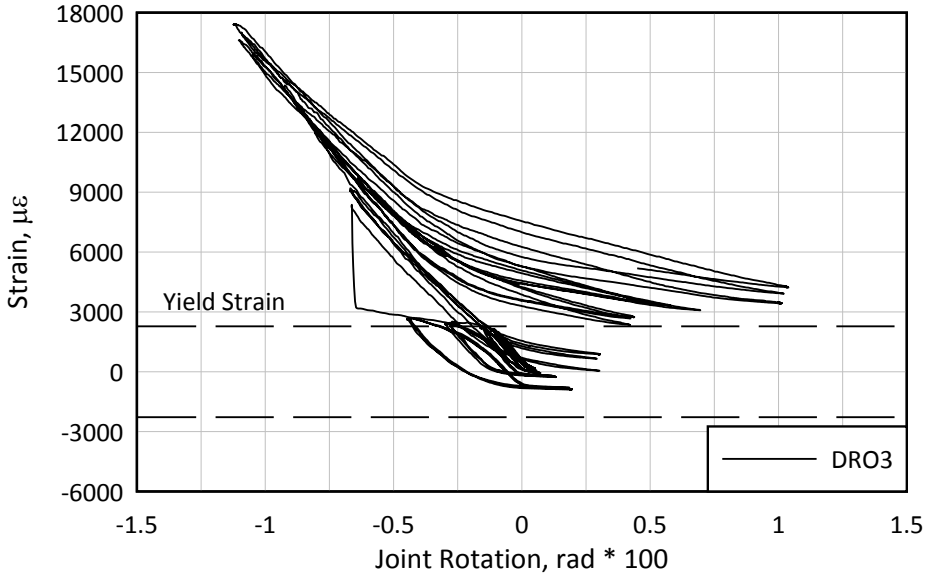

Figure 4.68 Deck outside rebar strain history – DRO3

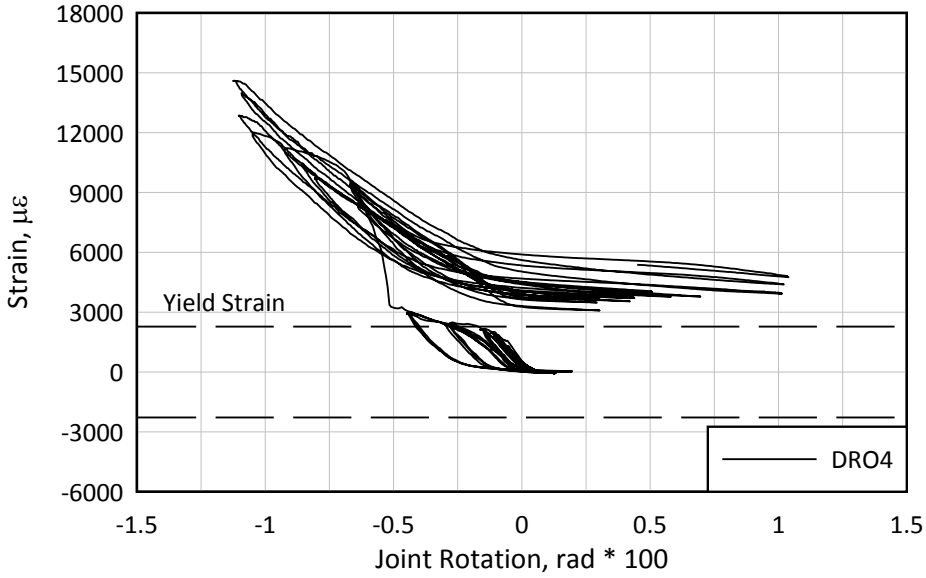

Figure 4.69 Deck outside rebar strain history – DRO4

Girder Longitudinal

Strain histories for gages mounted along the longitudinal bar at the bottom of the girder are shown in Figure 4.70 through Figure 4.73. These recorded histories indicate that the headed reinforcing bar experiences both tensile and compressive strains during the entirety of the seismic testing. No yielding of the reinforcing bars were observed based on the recorded strain histories. The maximum compressive strains in the reinforcing bar are observed to decrease as the distance from the joint increases. However, tensile strains in the reinforcing bars are observed to increase with increasing distance due to the increase in positive moment demand away from the joint region.

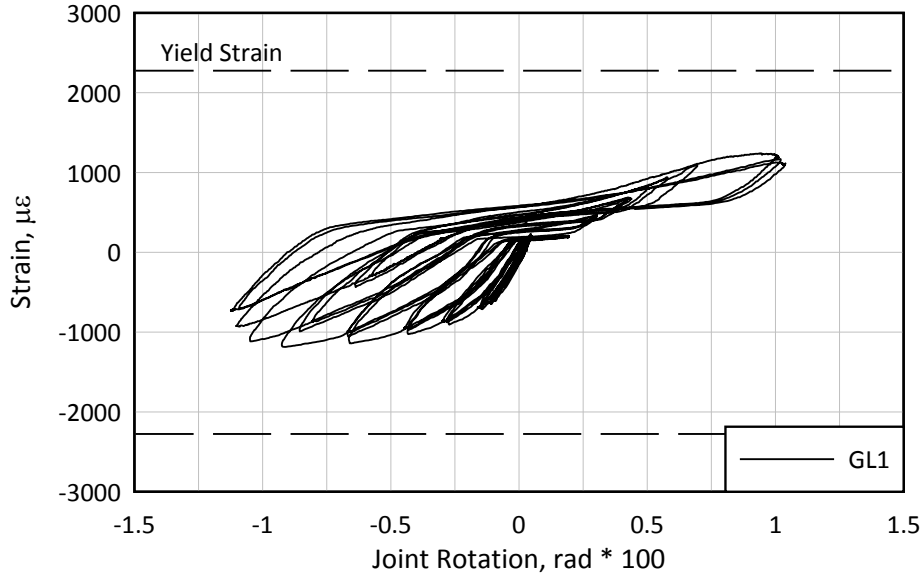

Figure 4.70 Girder longitudinal rebar strain history – GL1

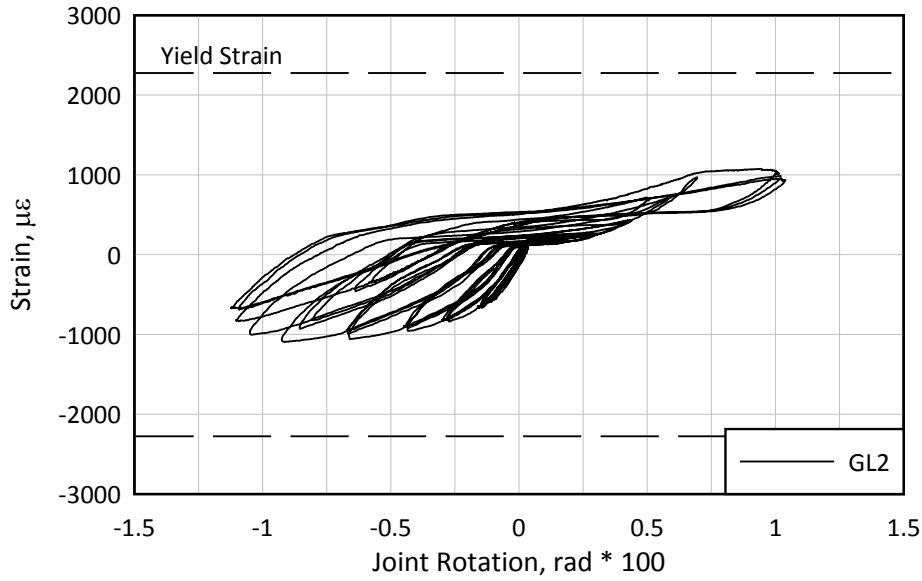

Figure 4.71 Girder longitudinal rebar strain history – GL2

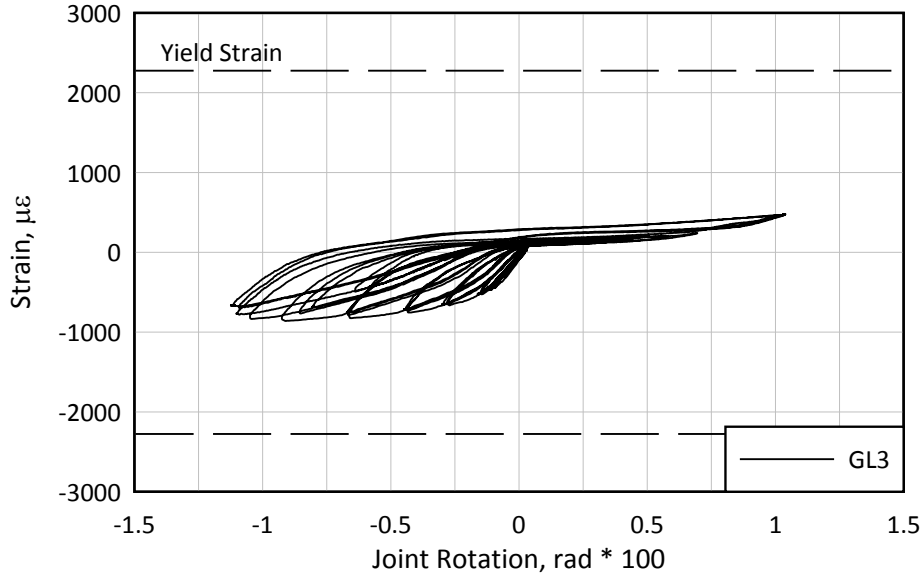

Figure 4.72 Girder longitudinal rebar strain history – GL3

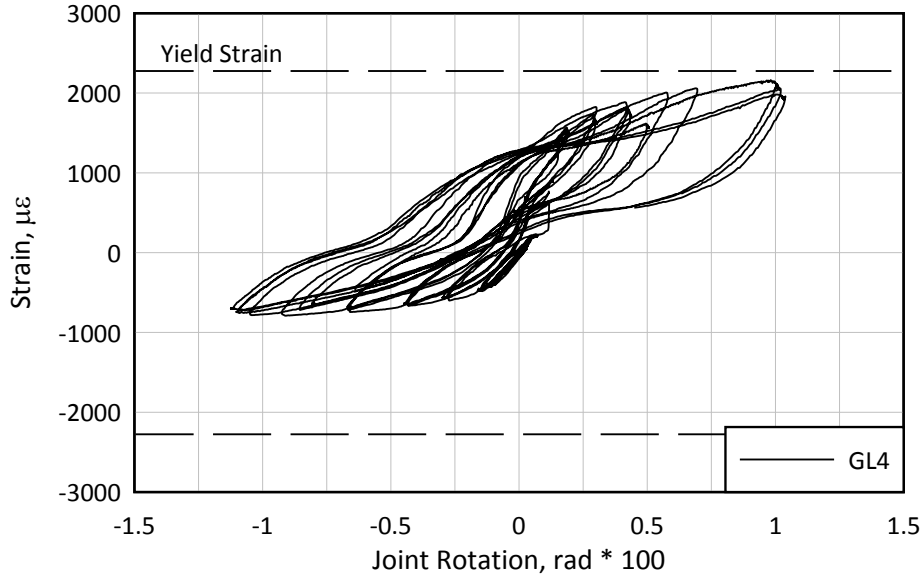

Figure 4.73 Girder longitudinal rebar strain history – GL4

Girder Shear

Strain gage histories from the shear reinforcement are provided in Figure 4.74 through Figure 4.77. These recorded measurements indicate that the strain in the shear reinforcement is well below yield for all loading cycles.

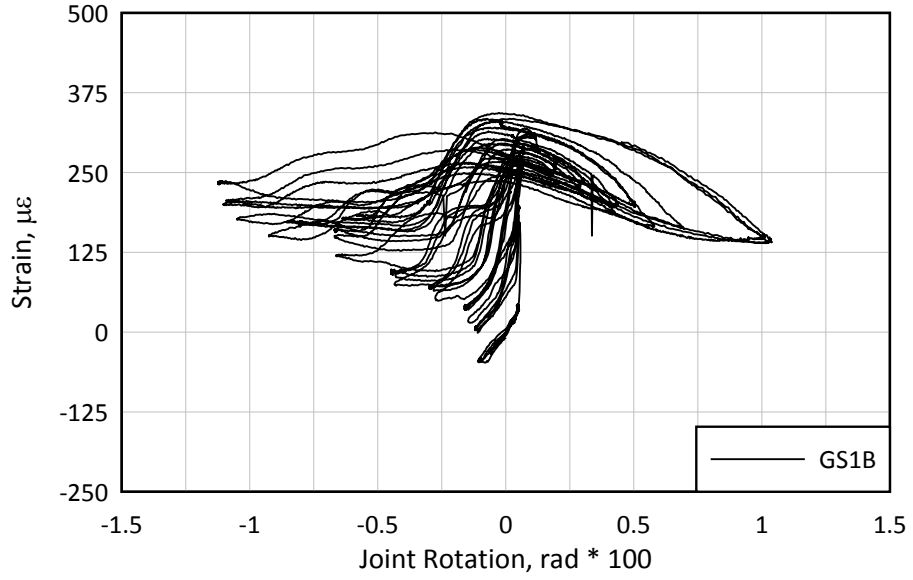

Figure 4.74 Girder shear rebar strain history – GS1B

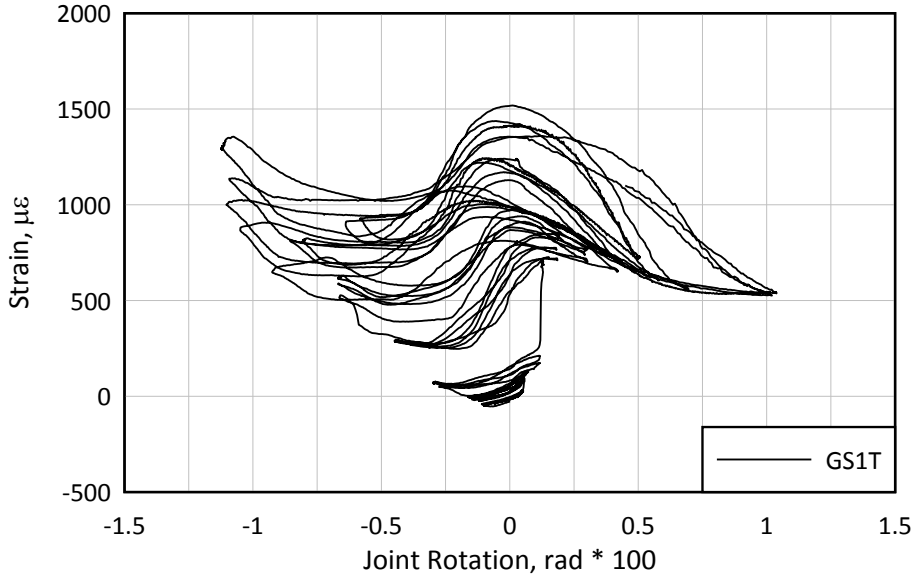

Figure 4.75 Girder shear rebar strain history – GS1T

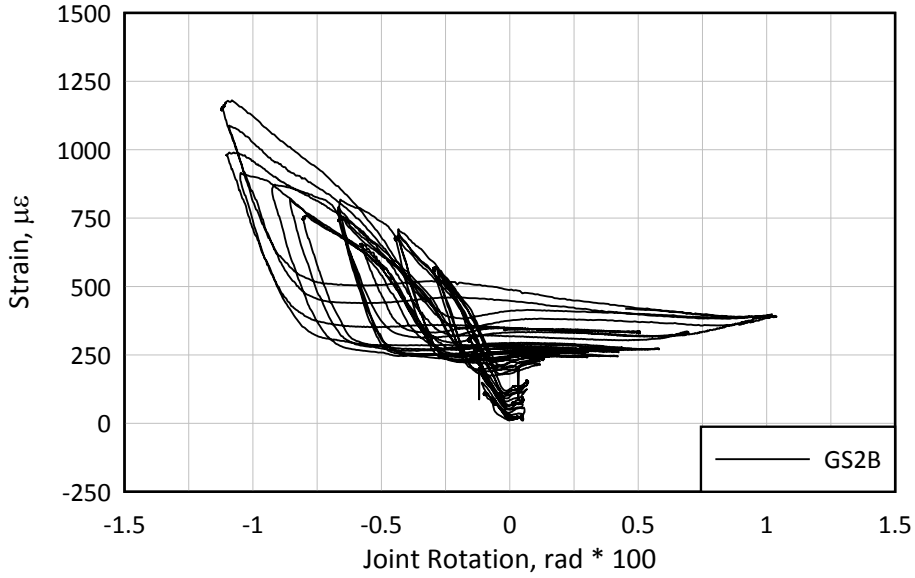

Figure 4.76 Girder shear rebar strain history – GS2B

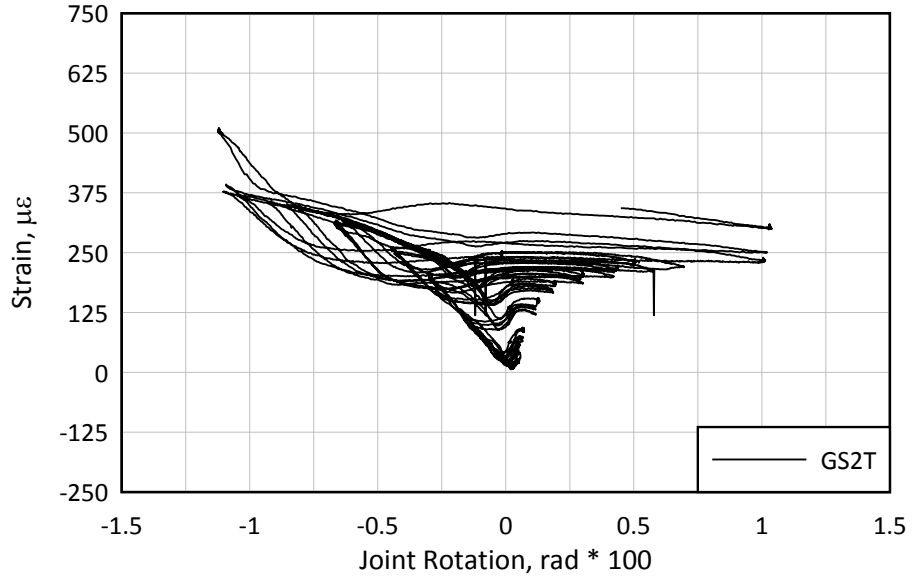

Figure 4.77 Girder shear rebar strain history – GS2T

Post-Tensioning

Strain histories for function gages mounted to post-tensioning strands are shown in Figure 4.78 and Figure 4.79. All strain gages mounted to strands in the top tendon malfunctioned during the stressing operation. Additionally, two of the three gages mounted on both the middle and bottom

strands malfunctioned prior to seismic testing. The functioning strain gage mounted on a strand in the bottom tendon malfunctioned prior to the end of testing, but provides sufficient information during the majority of testing. During the recorded testing up to 0.75% joint rotation, the strain readings are below the yield strain of the strand. However, these readings are approaching the tensile yield strain during positive loading cycles. The post-tensioning strands do not experience significant compressive strains during testing and are mainly subjected to tensile loading during the positive loading cycles.

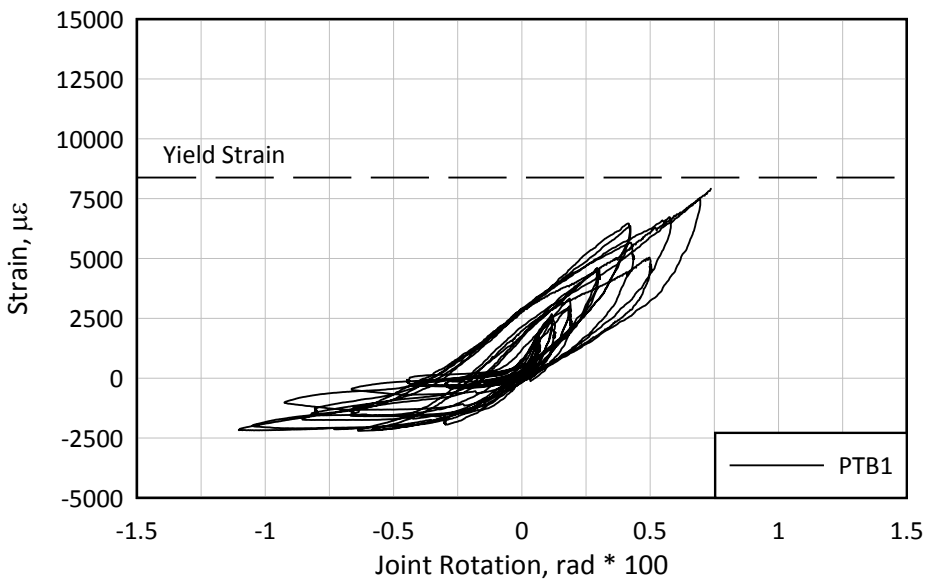

Figure 4.78 Bottom post-tensioning strain history – PTB1

Strain readings from the strand located in the middle tendon provide less information as compared to the bottom due to failure prior to reaching -0.50% joint rotation.

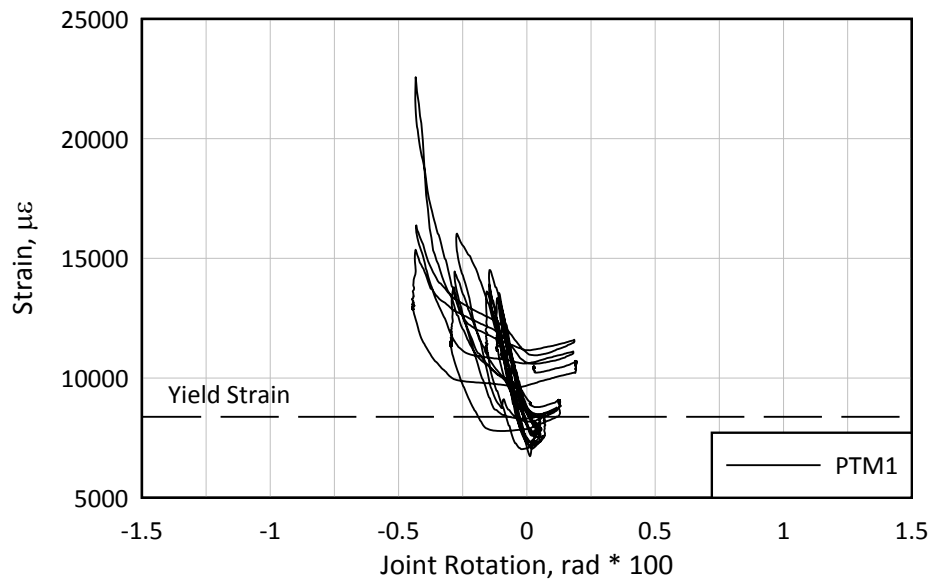

Figure 4.79 Middle post-tensioning strain history – PTM1

4.2.4 Strain Profiles

Strain gage readings at peak responses in both push and pull directions were used to generate strain profiles for various elements. These profiles were generated for peak points in the loading cycles for the first cycles in both push and pull directions.

Deck Longitudinal Profiles

Longitudinal strain profiles from the middle and outside deck reinforcement are shown in Figure 4.80 and Figure 4.81. As is expected, for both the inside and outside reinforcing bars, the largest strain measurements are recorded at the joint location and reduce with increasing distance from the joint. The recorded strain profile during the positive moment cycles, with large tensile strains, is the result of tensile yielding of the reinforcing bars during negative loading. The lack of noticeable compressive strains correlates with the observed performance with residual crack openings in the deck following post-yield negative response. The magnitude of strain in the outer bars is significantly less than that in the middle bar during positive loading indicating less significant residual straining of the bar due to tensile loading.

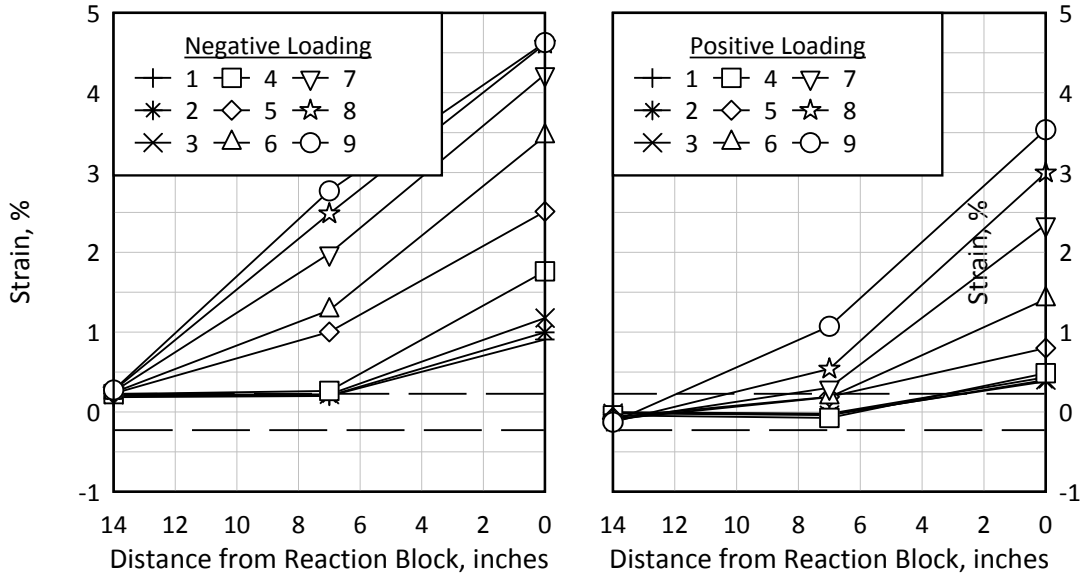

Figure 4.80 Middle deck rebar longitudinal strain profile

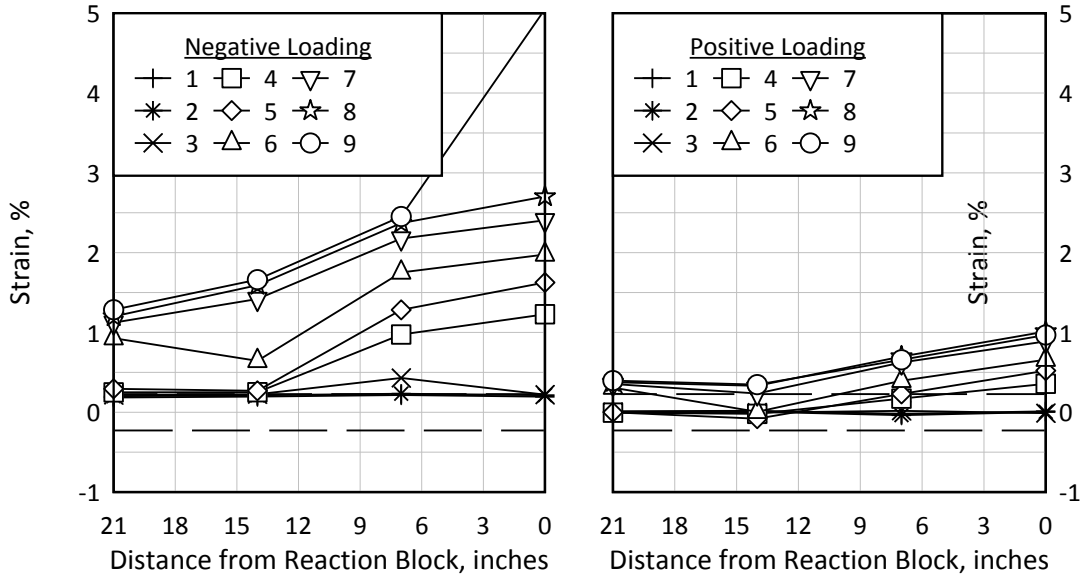

Figure 4.81 Outer deck rebar longitudinal strain profile

Deck Transverse Profiles

Transverse strain profiles for the deck reinforcement at the joint, 7 inches from the joint and 14 inches from the joint are shown in Figure 4.82 through Figure 4.84. The transverse profile at the joint indicates that the middle of the deck experiences more significant tension strains, which is

the expected response due to shear lag in the deck. The main girder connection at the center of the deck will result in more pronounced flexural response in the center of the deck due to a more direct load path. Flexural response further from the girder will have a less pronounced response due to the shear lag response required to develop forces away from the girder. As the distance from the joint increases, the transverse profile exhibits a flatter response indicating a more even distribution of forces within the deck. As the distance from the connection increases, the shear lag mechanism begins to stabilize and results in a more constant sectional response.

The observed response 14 inches from the joint indicates a significant tensile response at the outside reinforcing bar. This response does not correlate with fundamental mechanics, but is believed to be caused by a flexural crack crossing the location of the strain gage and resulting in the concentrated tension strain observed.

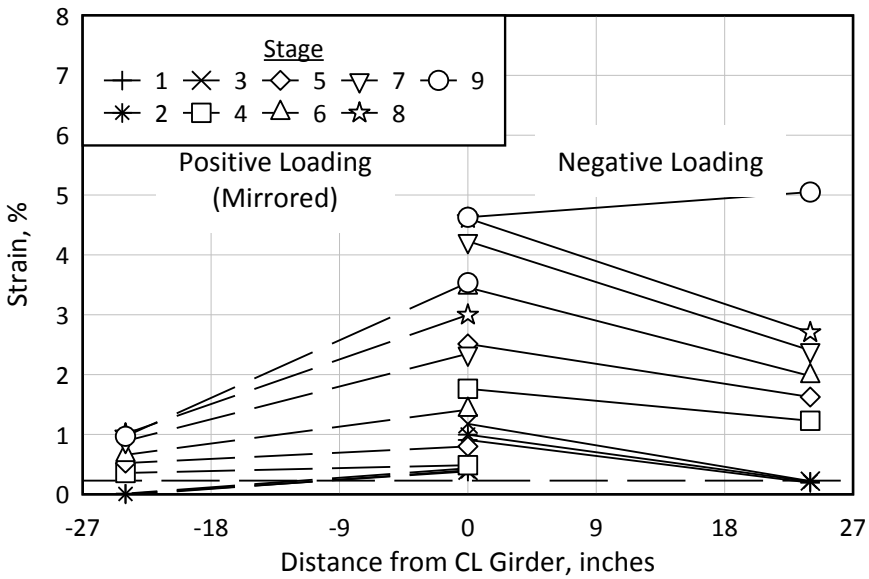

Figure 4.82 Deck transverse strain profile at joint

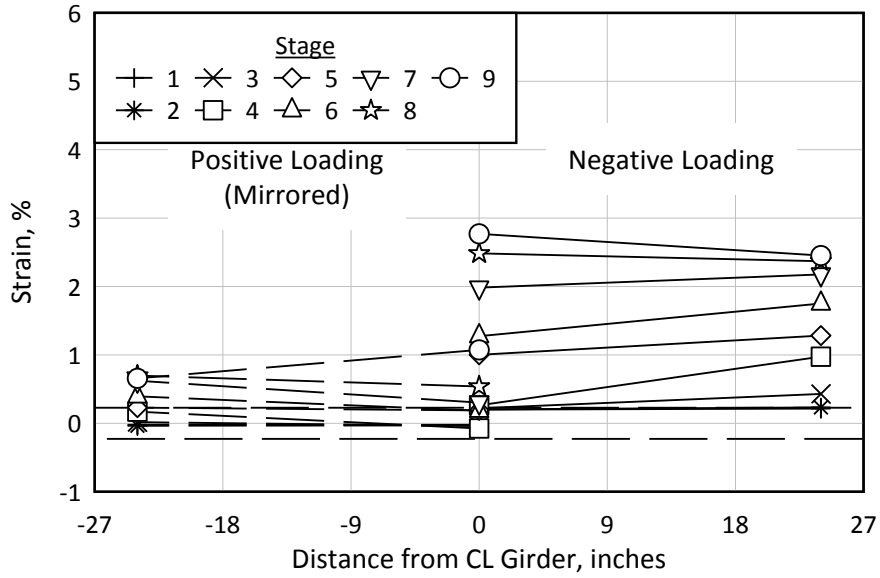

Figure 4.83 Deck transverse strain profile 7 inches from joint

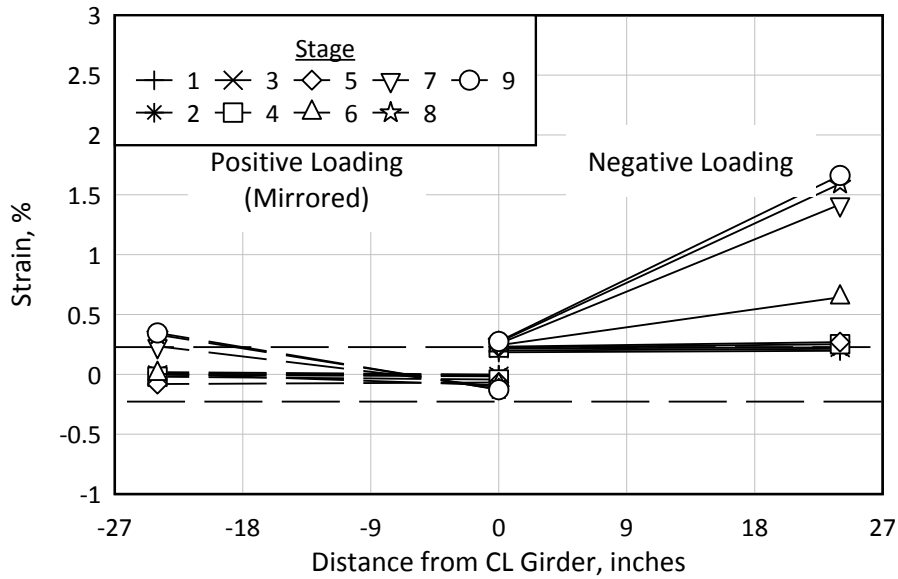

Figure 4.84 Deck transverse strain profile 14 inches from joint

Girder Longitudinal Profile

Strain profiles for the girder longitudinal reinforcement is shown in Figure 4.85. During negative loading, the response observed in this figure matches well with expected behavior. The largest compressive strains are observed at the joint where the flexural moment demand is largest. The

use of headed reinforcing bars will result in a more direct transverse of compressive strain into the rebar and does not require any development length to achieve appreciable compressive strain. Under positive flexural demands, the observed response again correlates well with expected response. The larger tensile strains observed at the joint are expected to be caused by the bond-slip response of the bottom post-tensioning tendon under increasing strain. At increasing distances from the joint over the first 14 inches, the strain reduces due to the development of the post-tensioning tendon into the girder. At increasing distances past 14 inches, the recorded strains begin increasing because of the increasing positive flexural moment demand further from the joint.

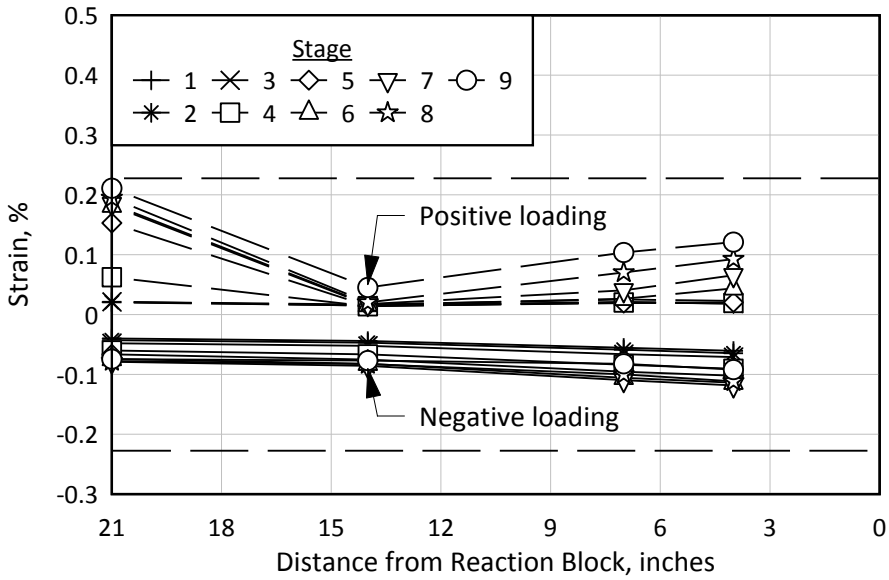

Figure 4.85 Girder longitudinal strain profile

4.3 Summary of Specimen Response

The integral specimen was designed and detailed to represent a portion of the integral prototype bridge structure designed as a part of the NCHRP 12-74 project. The specimen is intended to represent a typical connection between a girder and bent cap in the prototype bridge. General dimensions from this specimen were developed based on a geometric scale factor of 0.50. The response of the girder-to-bent cap connection was determined to be the major source of uncertainty in the performance of this system. Other general performance characteristics of the overall bridge system are expected to be similar to commonly accepted characteristics, such as bent cap response and substructure performance. The goal of the integral test specimen is to

experimentally determine the moment-rotation response of the system and investigate the shear transfer mechanism of the system.

Fabrication of the precast components took place within the University of California, San Diego Charles Lee Powell Structural Systems Laboratory by industry contractors, with the assistance of lab personnel. During the fabrication of the specimen, input from the contractors was solicited to determine if there were any major complications in the fabrication effort. The largest issue that was raised was related to the vibrator access at the main portion of the girder due to the presence of post-tensioning ducts in the web. This complication was compounded by the scaling of the specimen, which provided limited access to the web and flange below the ducts. Form vibrators were using during casting to ensure adequate consolidation was achieved below the ducts.

Observations during testing indicate that during elastic loading cycles the system performs in an essentially elastic manner. Under increasing imposed joint rotations, the system response in a manner consistent with predictions up to approximately 0.6% joint rotations. The majority of lateral deformation as accommodated through the localized joint opening in both the positive and negative flexural directions. Observed response indicated tensile yielding of deck reinforcement based on the presence of deck flexural cracking. Flexural response appears stable past 1% joint rotation in both positive and negative flexural directions. Minimal slip between the girder and reaction block was noted up to 0.6% joint rotation, after which increasing rotation resulted in increasing slip. Observed slip between the girder and bent cap was caused by the inadequate anchorage of bent cap shear reinforcement at the girder end as evinced by horizontal and shear cracking near the top of the girder.

Data collected during testing was post-processed and reviewed to provide additional insight into the response of the unit. The moment-rotation hysteretic response indicated there is stable response up to approximately 1% joint rotation. During the elastic loading cycles, negligible slip between the girder and reaction block and negligible reduction in stiffness in the system was observed. During large rotation cycles, more appreciable energy dissipation is noted in the negative flexural direction, which is expected due to the larger amount of mild reinforcement present in the concrete deck. Failures of the unit occurred during both the push and pull directions while approaching the 1.5% joint rotation level. The recorded response of the system indicates that the system responds in an essentially elastic manner under low amplitude rotations and has adequate post-yield deformation capacity.

The predicted moment-rotation response of the system provided a reasonable estimate of the system response. However, the ultimate rotation capacity predicted was overestimated in both

positive and negative directions. The ultimate failure of the system during testing, due to fracture of post-tensioning tendons, occurred at approximately 1.3% joint rotation in both the positive and negative directions. The predicated rotation capacity was overestimated by approximately 12% in the positive flexural direction and 30% in the negative flexural direction. The over-estimation of the ultimate rotation capacity was the result of kinking action in the post-tensioning tendons due to increasing shear slip between the girder and reaction block under increasing rotation demands. The recommended modifications to the shear detailing in the girder will serve to reduce the shear slip and as a result also decrease the kinking action in the tendons thereby increasing the ultimate rotation capacity.

Results from the experimental program that the capacity predictions and overall response can be adequately predicted with moment-curvature analyses. The consideration of an effective plastic hinge length equal to one-half the overall structure depth was appropriate for the system investigated. The ultimate deformation capacity was over-predicted, likely caused by the cyclic fracture of the post-tensioning tendons. Seismic design of the investigate bridge system should be based on a capacity design methodology where the total seismic demand on the superstructure should be limited to the nominal capacity as calculated using moment-curvature analysis. The system has adequate inelastic deformation capacity to accommodate potential seismic events greater than the design basis event providing confidence in the satisfaction of life safety performance objectives in real construction. Additionally, the system displays adequate ultimate rotation capacity to accommodate potential differential seismic settlements between bents.

4.3.1 Conclusions

Based on experimental observations and readings related to the response of the integral specimen, the following conclusions can be made:

- Operational Performance Objectives
    - Superstructure responded elastically under service load conditions
    - No shear slip between girder and bent cap was observed that would affect rideability under elastic loading
- Life Safety Performance Objectives
    - Superstructure response essentially elastic under design level seismic
    - Collapse can be prevented under maximum considered earthquake with inelastic mechanism from column flexural plastic hinging
    - Over +/- 1.0% superstructure rotation capacity to accommodate potential relative settlement

- General Conclusions
    - Design predictions provide reasonable estimates of the observed moment-rotation response
    - Ultimate failure of system occurs during loading cycles to 1.5% superstructure rotation slightly prior to reaching target joint rotation
    - Flexural yielding during negative seismic loading cycles results in residual cracking in the reinforced concrete deck and subsequent residual joint rotations similar to what is expected in any reinforced concrete deck system
    - Appreciably more energy dissipation was observed during negative flexural loading as compared to positive due to the presence of distributed mild reinforcement in the deck
    - A horizontal crack between the girder and deck developed at -0.65% joint rotation which resulted in the beginning of noticeable shear slip between girder and reaction block
    - Standard shear reinforcement details resulted in increasing separation between the deck and girder as the bent bar began to straighten out during testing

4.4 Design Recommendations

Based on the results obtained from experimental and analytical efforts, the following recommendations are provided for the design of the integral precast system investigated:

- Service and Strength Loading
    - Under service load cases, do not permit any tensile strains in the closure joint
    - Ensure the effective post-tensioning force is capable of resisting the maximum factored shear demand across the joint assuming a friction factor equal to 0.6
    - Use conventional methods or strain compatibility methods to determine the negative flexural capacity of the superstructure at the joint
    - Use strain compatibility procedures to determine the positive flexural capacity of the superstructure at the joint neglecting the contribution of concrete tensile capacity to provide a conservative estimate of the positive moment capacity
- Seismic Loading
    - Design the superstructure to remain essentially elastic when subjected to seismic loading through capacity design approaches and consideration of vertical demand

    - Distribute overstrength seismic moment demand from the mechanism of inelastic action (i.e. column plastic hinging) into the girders based on the AASHTO provisions for any bent cap configuration (AASHTO, 2009)
    - Consider vertical seismic demands for structures located near faults using site specific vertical hazard or the recommendations of Bozorgnia et al. (2004)
    - To predict the moment-rotation response of the superstructure connection, assume an effective plastic hinge length equal to one-half the overall superstructure depth
- Connection detailing
    - Use hanger bars, such as headed reinforcement, as shear reinforcement in the girder at the joint to ensure an appropriate force transfer mechanism can develop as joint opening occurs
    - Use polypropylene fiber reinforced, high strength, non-shrink grout at the closure joint with a 0.2% volume fraction of fibers

REFERENCES

AASHTO Guide Specifications for LRFD Seismic Bridge Design, 1st Edition [Report]. - Washington, DC : [s.n.], 2009.

AASHTO LRFD Bridge Design Specifications, 4th Edition [Report]. - Washington, DC : [s.n.], 2007.

AASHTO Recommended Guide Specifications for LRFD Seismic Bridge Design [Report]. - Washington, D.C. : [s.n.], 2007.

Almer K and Sanders D Seismic Performance of Precast U-girders Integrally Connected to a Cast-in-Place Substructure [Conference] // Proceedings of the 2008 FHWA Accelerated Bridge Construction - Highways for Life. - Baltimore, MD : [s.n.], 2008.

ASCE Report Card for America's Infrastructure [Online]. - 2009. - May 10, 2009. - http://www.infrastructurereportcard.org/.

BASF Masterflow 928 Product Data [Book]. - 2006.

Bozorgnia Y. and Campbell K.W. The Vertical-to-Horizontal Response Spectral Ratio and Tentative Procedures for Developing Simplified V/H Vertical Design Spectra [Journal] // Journal of Earthquake Engineering, Vol. 8, No. 2. - 2004. - pp. 175-207.

Burnell K.P. [et al.] Seismic Testing of Precast Segmental Bridge Systems: Phase III, Bridge Systems Tests [Report] : SSRP 2005/01. - [s.l.] : University of California, San Diego, 2005.

Caltrans Seismic Design Criteria, Version 1.4 [Report]. - Sacramento, CA : [s.n.], 2006.

Castrodale Reid W and White Christopher D NCHRP Report 517, Extending Span Ranges of Precast Prestressed Concrete Girders [Report]. - Washington, D.C. : National Cooperative Highway Research Program, 2004.

FHWA 2007 FHWA Seismic Accelerated Bridge Construction Workshop Outcomes and Follow-up Activities [Report]. - [s.l.] : FHWA, 2007.

Hines E.M. Seismic Performance of Hollow Rectangular Reinforced Concrete Bridge Piers with Confined Corner Elements [Report] : Ph.D. Dissertation. - La Jolla, CA : University of California, San Diego, 2002.

Holombo Jay, Priestley M.J. Nigel and Seible Frieder Longitudinal Seismic Response of Precast Spliced-Girder Bridges [Report] : SSRP 98/05. - [s.l.] : University of California, San Diego, 1998.

MATLAB MATLAB 2009a (V7.8) User's Manuel. - 2009.

Megally S., Seible F. and Dowell R.K. Seismic Performance of Precast Segmental Bridges: Segment-to-Segment Joints Subjected to High Flexural Moments and Shears [Journal] // PCI Journal. - 2003. - 2 : Vol. 48. - pp. 80-96.

Megally S.H. [et al.] Seismic Performance of Precast Segmental Bridge Superstructures [Report] : SSRP 2001/24. - [s.l.] : University of California, San Diego, 2002.

Paulay T and Priestley M J N Seismic Design of Reinforced Concrete and Masonry Buildings [Book]. - New York : John Wiley and Sons, 1992.

Precast Prestressed Concrete Institute PCI Bridge Design Manual [Report]. - Chicago, IL : Precast Prestressed Concrete Institute, 2003.

Priestley M J N, Seible F and Calvi G M Seismic Design and Retrofit of Bridges [Book]. - New York, NY : John Wiley and Sons, 1996.

Priestley M.J.N. and Park R. Strength and Ductility of Bridge Substructures [Report] : RRU Bulliten 71. - Wellington, New Zealand : Road Research Unit, National Roads Board, 1984.

Priestley M.J.N., Seible F. and Calvi G.M. Seismic Design and Retrofit of Bridges [Book]. - New York, NY : John Wiley & Sons, Inc, 1996.

Sika SikaGrout 300PT Product Data [Report]. - 2009.

Tobolski M.J. [et al.] Development of Precast Bent Cap Concepts [Report] : SSRP 06/10. - La Jolla, CA : University of California, San Diego, 2006.

U.S. DOT, Research and Innovative Technology Administration, Bureau of Transportation Statistics Transportation Statistics Annual Report 2007 [Report]. - Washington, D.C. : [s.n.], 2007.

Veletzos M.J. The Seismic Response of Precast Segmental Superstructures with Bonded Tendons [Report] : PhD Thesis. - La Jolla, CA : University of California, San Diego, 2007.

Veletzos M.J., Restrepo J.I. and Seible F. Seismic Response of Precast Segmental Bridge Superstructures [Report] : SSRP 2006/18. - 2006 : University of California, San Diego, 2006.

Appendix A Specimen Drawings

GENERAL NOTES:

1. These plans provide the general plans and construction sequence for the NCHRP Integral Specimen. Any questions or concerns regarding dimensions, details, erection or any other means and methods of construction shall be directed to:
   Matthew Tobolski
   858-822-8517
2. Dimensions are shown to the nearest one-sixteenth of an inch

MATERIALS:

STRUCTRUAL STEEL
- Plate Sections -ASTM Designation A36

REINFORCING STEEL
- ASTM Designation A 706 Grade 60
- Headed bars shall be HRC Headed Bars or Equivalent

PRESTRESSING STEEL
- Uncoated seven wire, low-relaxation strand, ASTM Designation A 416, Grade 270
- Uncoated high-strength steel bar, ASTM Designation A 722

CONCRETE
- All concrete shall be $\frac{3}{8}$" maximum aggregate size
- Girder, reaction block, f'c=7,000 psi, slump 7"-9"
- Deck, f'c=4,000 psi, slump 4"-6"
- All concrete shall have mix design and previous fresh and mechanical properties submitted to researcher prior to order

GROUT
- All grout shall be non-shrink and shall have a minimum compressive strength of 10,000 psi after 28 days
- Grout shall have polypropelyne fibers per volume fraction
- Contact researcher for volumetric proportion

CONCRETE NOTES:

1. All reinforcing bars shall have the following minimum cover:
   Girder $\frac{1}{2}$"
   Slab $\frac{1}{2}$" bottom, 1" top
   Reaction block 1"
2. Proposed lifting inserts shall be submitted to research prior to selection for approval including product specifications and locations of inserts
3. Inserts for forms, ties, etc. shall be submitted to researcher prior to selection including product specifications and locations of inserts
4. All inserts shall be set prior to placement of concrete unless otherwise authorized by researcher
5. All concrete surfaces shall be finished to provide clean, smooth finished surface and shall be free of discolorations or stains

UCSD	NCHRP PROJECT 12-74				
	GENERAL NOTES				
VISUAL SCALE: 0 $\frac{1}{4}$" $\frac{1}{2}$" 1"	DUCTILITY: FULL	SUPER. CONNECTION: INTEGRAL	CONNECTION DETAIL: INTEGRAL COMPONENET TEST		
	BY: MJT	CHK:	DATE: 06/30/09	SCALE: N.T.S.	SHEET: GN

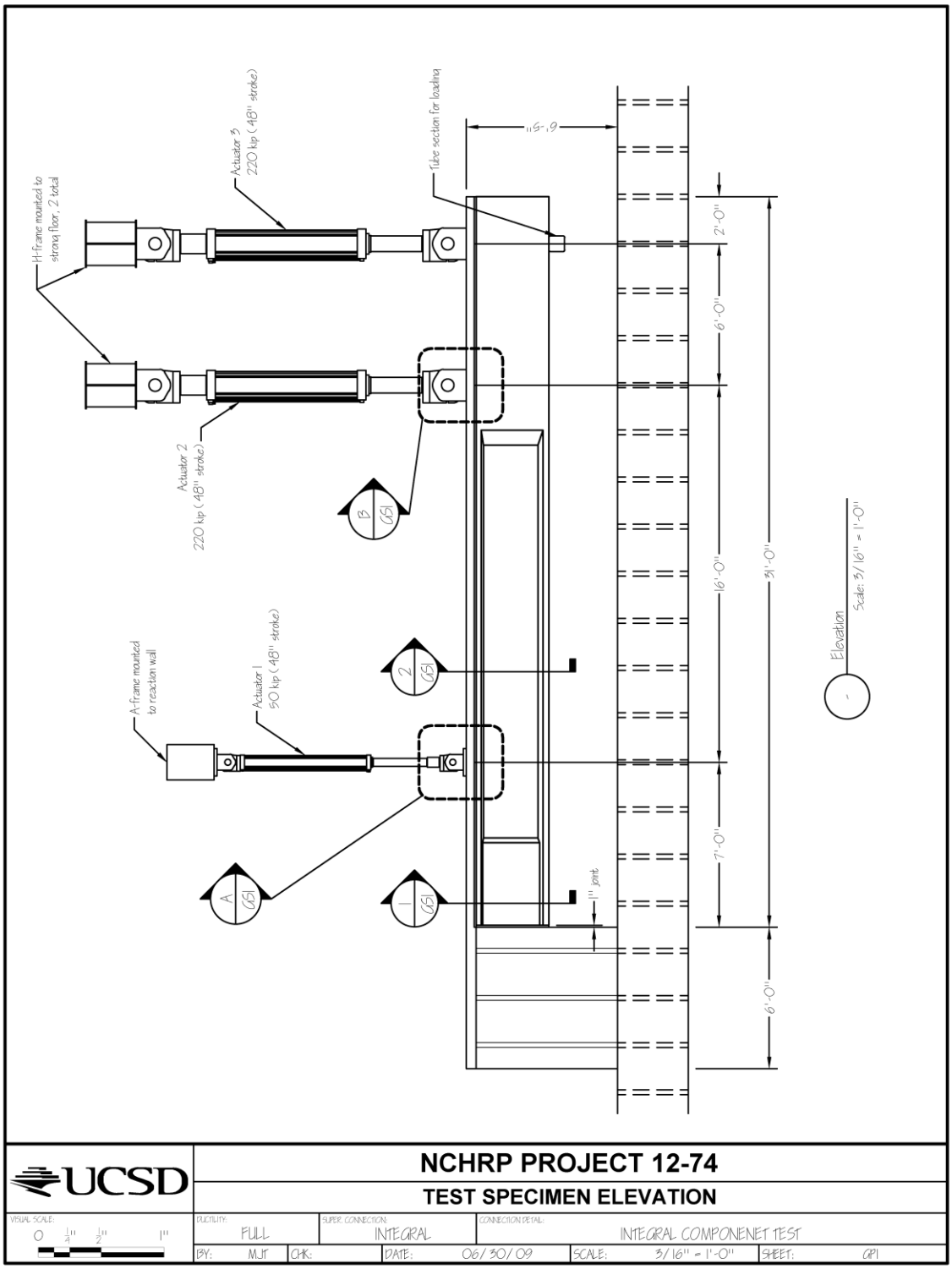
H-frame mounted to strong floor, 2 total
Actuator 3
220 kip (48" stroke)
Tube section for loading
115.9
2'-0"
6'-0"
16'-0"
31'-0"
7'-0"
6'-0"
Actuator 2
220 kip (48" stroke)
B
GS1
A-frame mounted to reaction wall
Actuator 1
50 kip (48" stroke)
2
GS1
A
GS1
1
GS1
1" joint
Elevation
Scale: 3/16" = 1'-0"
UCSD
NCHRP PROJECT 12-74
TEST SPECIMEN ELEVATION
VISUAL SCALE:
0 1/4" 1/2" 1"
FUCTILITY: FULL
SUPER. CONNECTION: INTEGRAL
CONNECTION DETAIL: INTEGRAL COMPONENET TEST
BY: MJT
CHK:
DATE: 06/30/09
SCALE: 3/16" = 1'-0"
SHEET: GP1

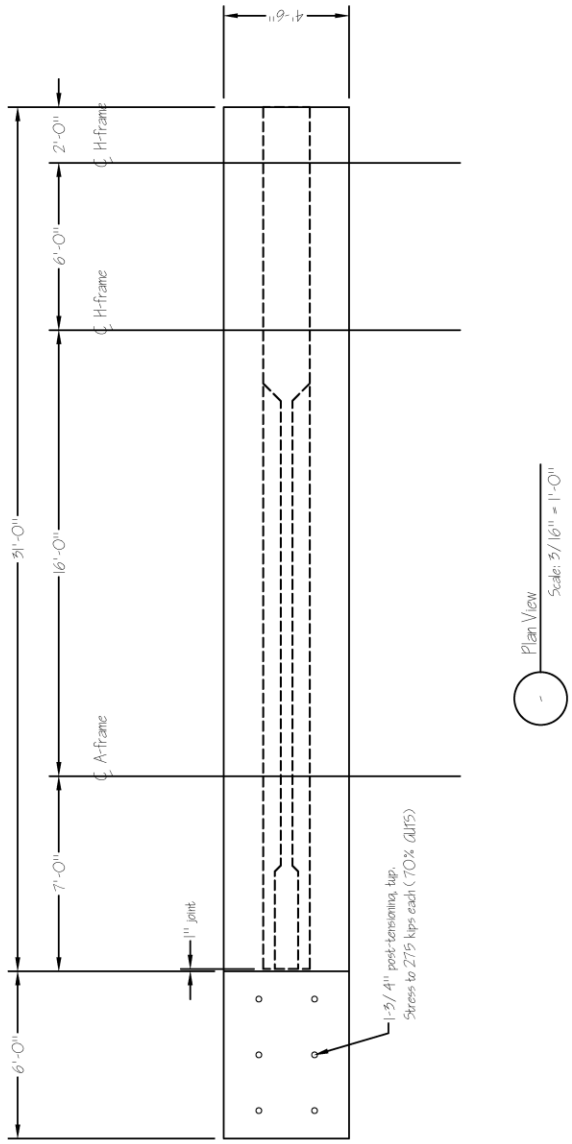

UCSD

NCHRP PROJECT 12-74

TEST SPECIMEN GENERAL PLAN

VISUAL SCALE:	DUCTILITY:	SUPER. CONNECTION:	CONNECTION DETAIL:			
0 1/4" 1/2" 1"	FULL	INTEGRAL	INTEGRAL COMPONENET TEST			
BY: MJT	CHK:	DATE: 06/30/09	SCALE: 3/16" = 1'-0"	SHEET: GP2		

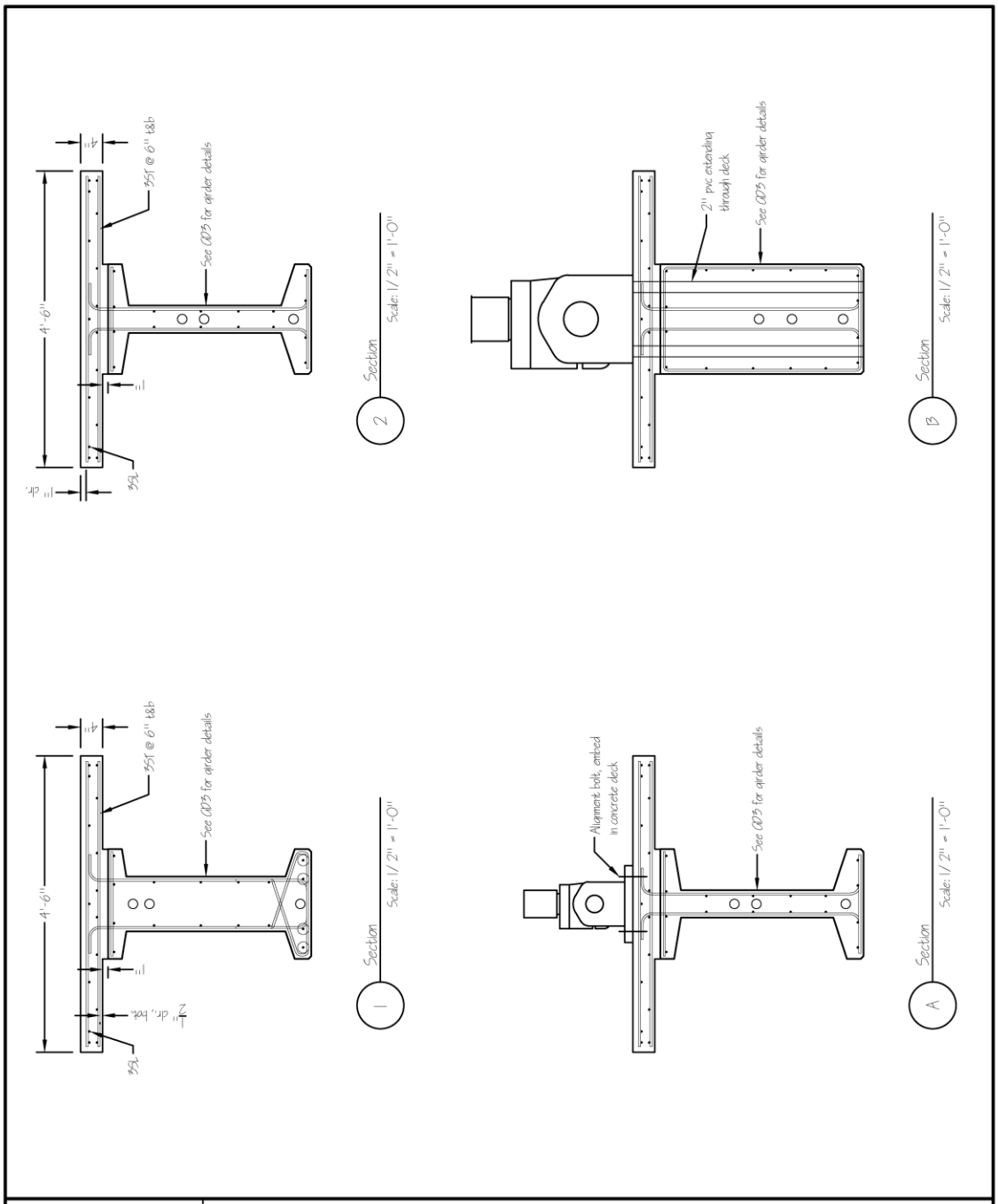

UCSD

NCHRP PROJECT 12-74

TEST SPECIMEN GENERAL SECTIONS

VISUAL SCALE:	FUCTILITY:	SUPER. CONNECTION:	CONNECTION DETAIL:			
0 1/4" 1/2" 1"	FULL	INTEGRAL	INTEGRAL COMPONENT TEST			
	BY: MJT	CHK:	DATE: 06/30/09	SCALE: 1/2" = 1'-0"	SHEET: 061	

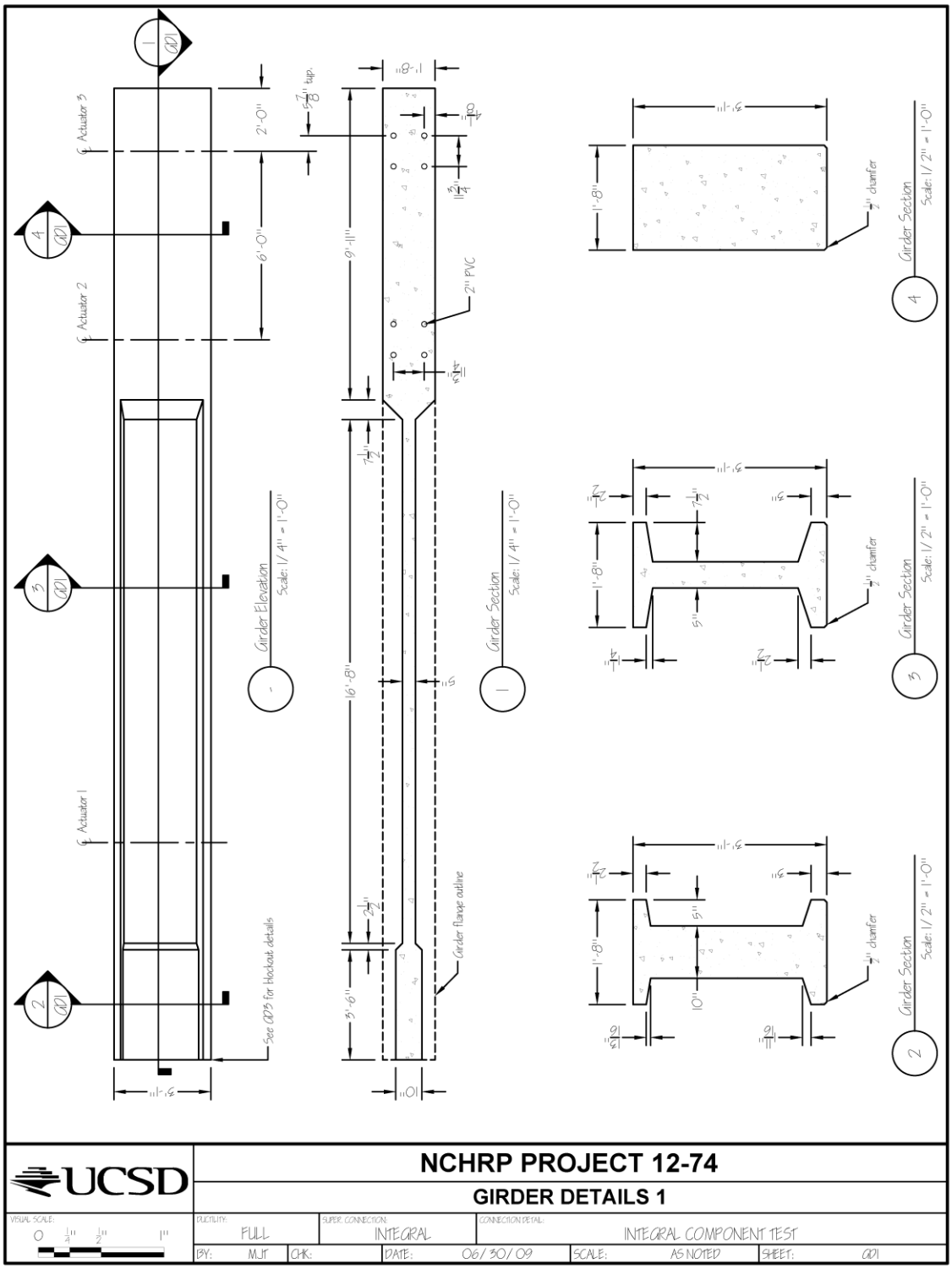
Girder Elevation
Scale: 1/4" = 1'-0"
Girder Section
Scale: 1/4" = 1'-0"
Girder Section
Scale: 1/2" = 1'-0"
Girder Section
Scale: 1/2" = 1'-0"
Girder Section
Scale: 1/2" = 1'-0"
Actuator 1
Actuator 2
Actuator 3
2" PVC
Girder flange outline
See 0D3 for blockout details
1/2" chamfer
UCSD
NCHRP PROJECT 12-74
GIRDER DETAILS 1
VISUAL SCALE:
FULL
INTEGRAL
INTEGRAL COMPONENT TEST
BY: MJT
CHK:
DATE: 06/30/09
SCALE: AS NOTED
SHEET: 0D1

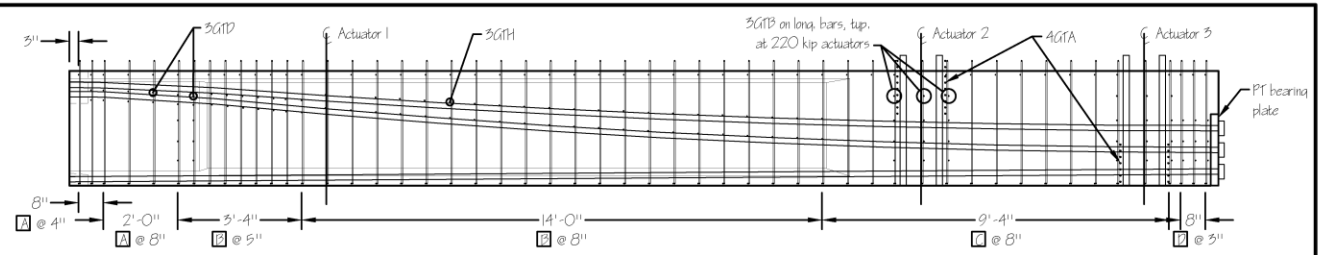

Girder Shear Reinf. Detail
Scale: 1/ 4" = 1'-0"

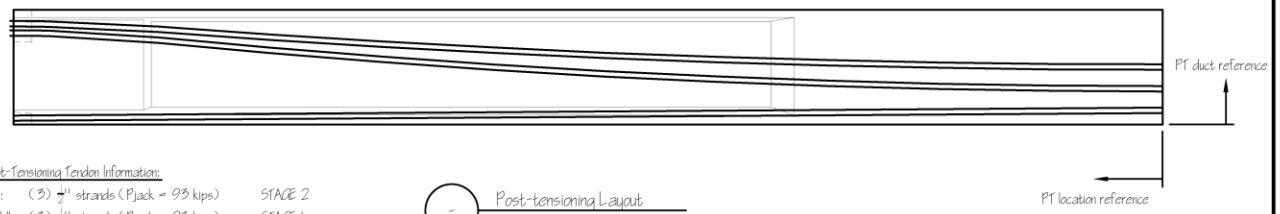

Post-Tensioning Tendon Information:

Top:	(3) $\frac{1}{2}$" strands (Pjack = 93 kips)	STAGE 2
Middle:	(3) $\frac{1}{2}$" strands (Pjack = 93 kips)	STAGE 1
Bottom:	(3) $\frac{1}{2}$" strands (Pjack = 0 kips)	STAGE 1

Post-tensioning Layout
Scale: 1/ 4" = 1'-0"

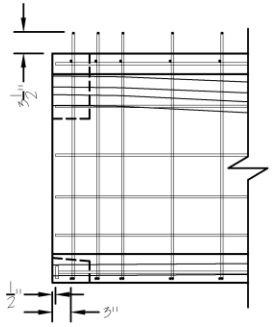

Girder Section at Bent Cap
Scale: 1/ 2" = 1'-0"

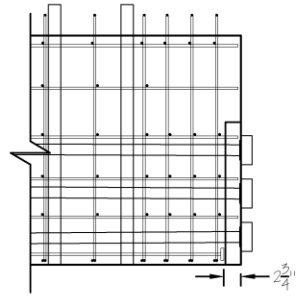

Girder Section at Anchorage
Scale: 1/ 2" = 1'-0"

CENTER OF POST-TENSIONING DUCTS

Location (feet)	Bottom (inches)	Middle (inches)	Top (inches)
0	4 - 1/2	11 - 1/2	18 - 1/2
3	4 - 1/4	11 - 11/16	18 - 5/8
6	4	12 - 1/4	19 - 1/8
9	3 - 3/4	13 - 1/4	19 - 7/8
12	3 - 9/16	14 - 5/8	20 - 15/16
15	3 - 5/16	16 - 5/16	22 - 1/4
18	3 - 1/16	18 - 7/16	23 - 15/16
21	2 - 13/16	21	25 - 7/8
24	2 - 9/16	23 - 7/8	28 - 1/8
27	2 - 5/16	27 - 3/16	30 - 11/16
30	2 - 1/16	29 - 3/8	32 - 3/8
30'-11"	2	29 - 1/2	32 - 1/2

UCSD

NCHRP PROJECT 12-74

GIRDER DETAILS 2

VISUAL SCALE: 0 $\frac{1}{4}$" $\frac{1}{2}$" 1"

QUALITY: FULL

SUPPS CONNECTION: INTEGRAL

CONDITIONS FOR: INTEGRAL COMPONENT TEST

BY: MJF

CHK:

DATE: 06/30/09

SCALE: AS NOTED

SHEET: GD2

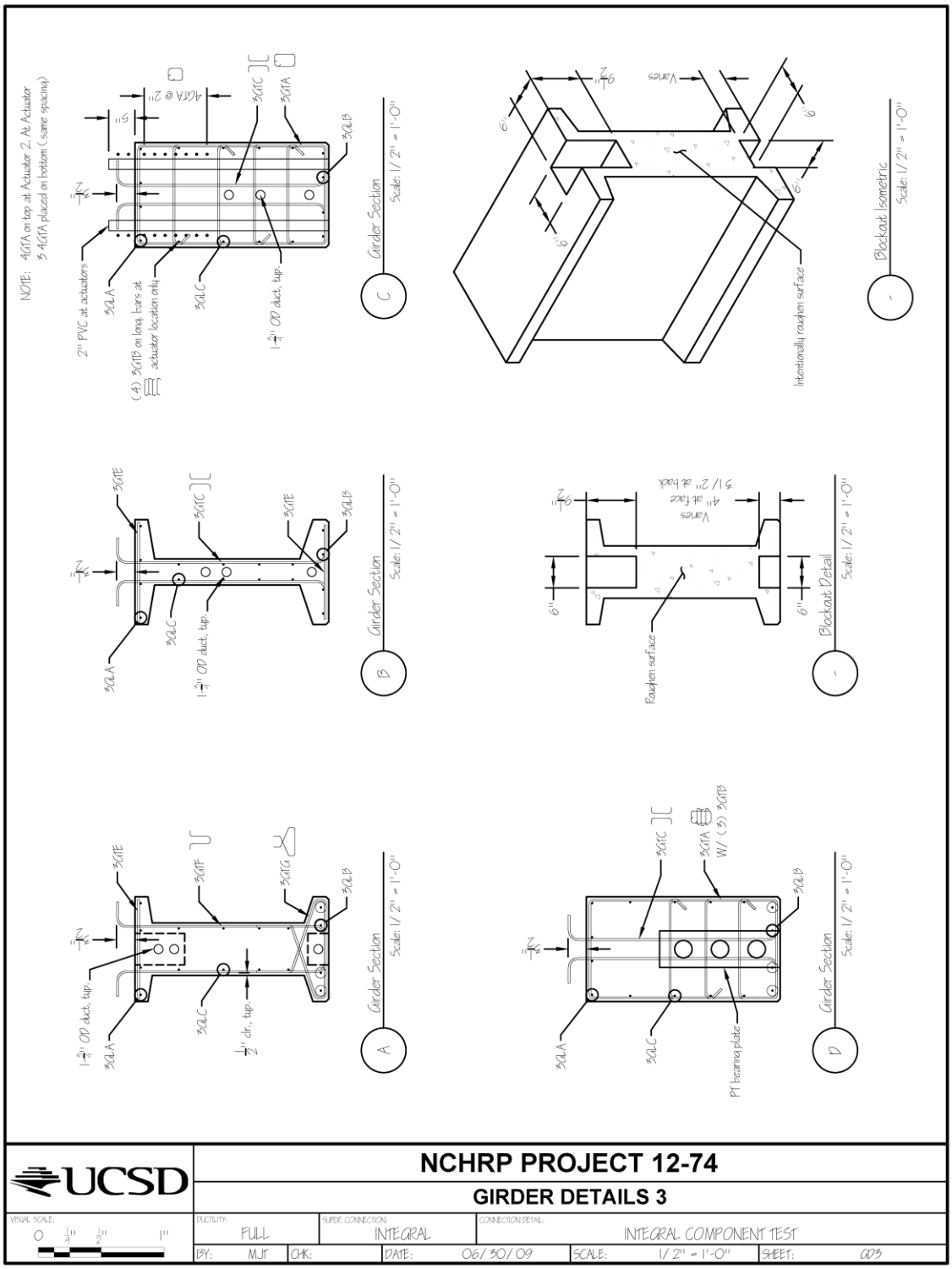
NOTE: 4G17A on top at Actuator 2, At Actuator 3 4G17A placed on bottom (same spacing)
2" PVC at actuators
3GLA
(4) 3G17B on long bars at actuator location only
3GLC
1-3/4" OD duct, typ.
4G17A @ 2"
5"
3G17C
3G17A
3GLB
Girder Section
Scale: 1/2" = 1'-0"
C
Intentionally roughen surface
Vanes
9 1/2"
6"
Blockout Isometric
Scale: 1/2" = 1'-0"
1
3GTE
3G17C
3GLA
3GLC
1-3/4" OD duct, typ.
Girder Section
Scale: 1/2" = 1'-0"
B
Roughen surface
Vanes
4" at face
5 1/2" at back
Blockout Detail
Scale: 1/2" = 1'-0"
1
3GTE
3GTF
3G17G
1-3/4" OD duct, typ.
3GLA
3GLC
1/2" clr., typ.
Girder Section
Scale: 1/2" = 1'-0"
A
3G17C
3G17A
W/ (5) 3G17B
3GLA
3GLC
PT bearing plate
Girder Section
Scale: 1/2" = 1'-0"
D
UCSD
NCHRP PROJECT 12-74
GIRDER DETAILS 3
VISUAL SCALE:
0 1/4" 1/2" 1"
DUCTILITY: FULL
SUPER. CONNECTION: INTEGRAL
CONNECTION DETAIL: INTEGRAL COMPONENT TEST
BY: MJT
CHK:
DATE: 06/30/09
SCALE: 1/2" = 1'-0"
SHEET: 003

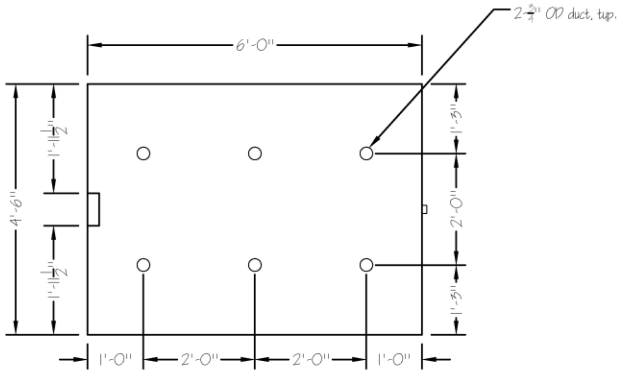

Reaction Block Plan View
Scale: 3/8" 1'-0"

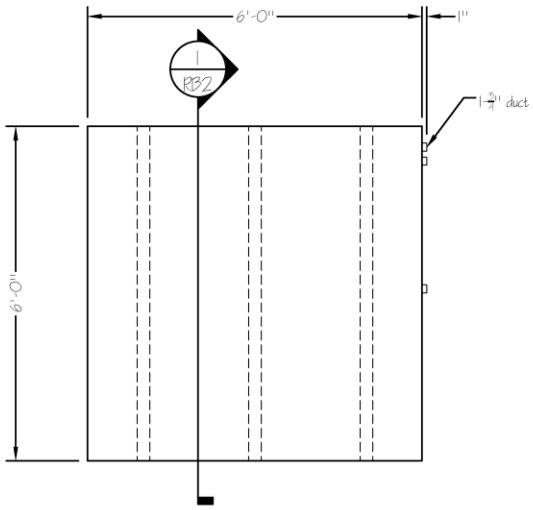

Reaction Block Front Elevation
Scale: 3/8" 1'-0"

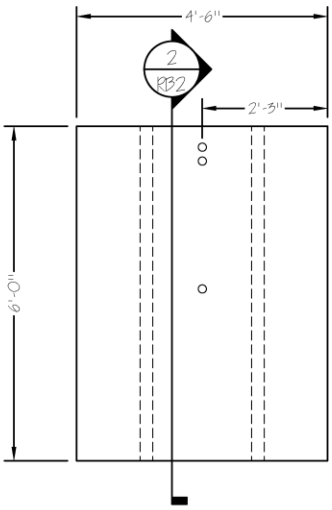

Reaction Block Side Elevation
Scale: 3/8" 1'-0"

UCSD

NCHRP PROJECT 12-74

REACTION BLOCK DETAILS 1

VISUAL SCALE:	DUCTILITY:	SUPER. CONNECTION:	CONNECTION DETAIL:			
0 1/4" 1/2" 1"	FULL	INTEGRAL	INTEGRAL COMPONENT TEST			
BY: MJT	CHK:	DATE: 06/30/09	SCALE: 3/8" = 1'-0"	SHEET: RB1		

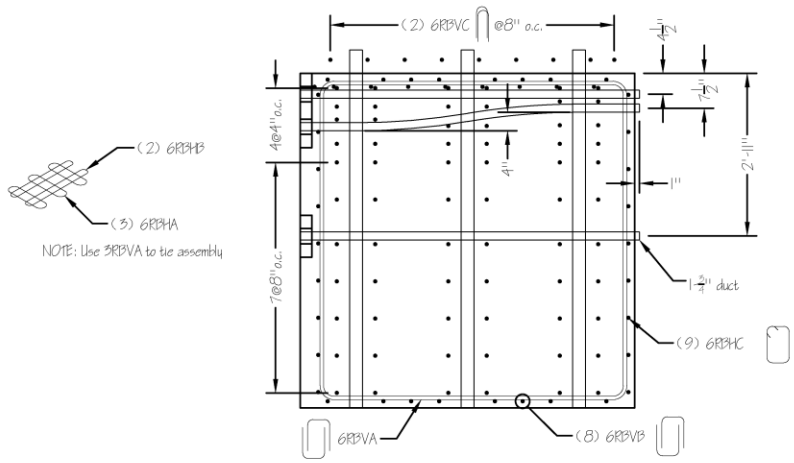

1 Reaction Block Section
Scale: 3/8" 1'-0"

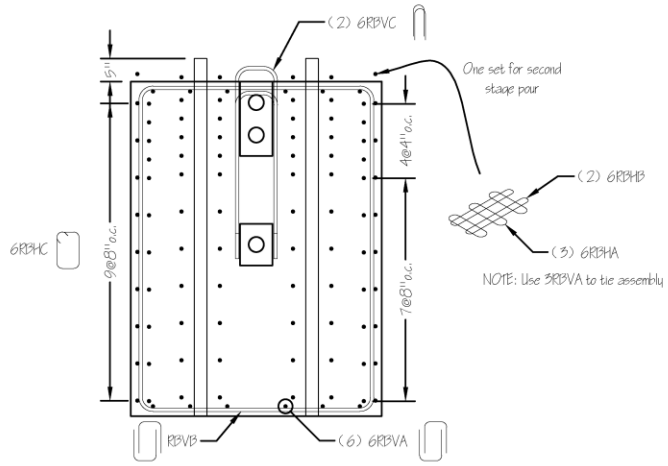

2 Reaction Block Section
Scale: 3/8" 1'-0"

UCSD	NCHRP PROJECT 12-74				
	REACTION BLOCK DETAILS 2				
VISUAL SCALE: 0 1/4" 1/2" 1"	FUCILITY: FULL	SUPER. CONNECTION: INTEGRAL	CONNECTION DETAIL: INTEGRAL COMPONENT TEST		
	BY: MJT	CHK:	DATE: 06/30/09	SCALE: 3/8" = 1'-0"	SHEET: RB2

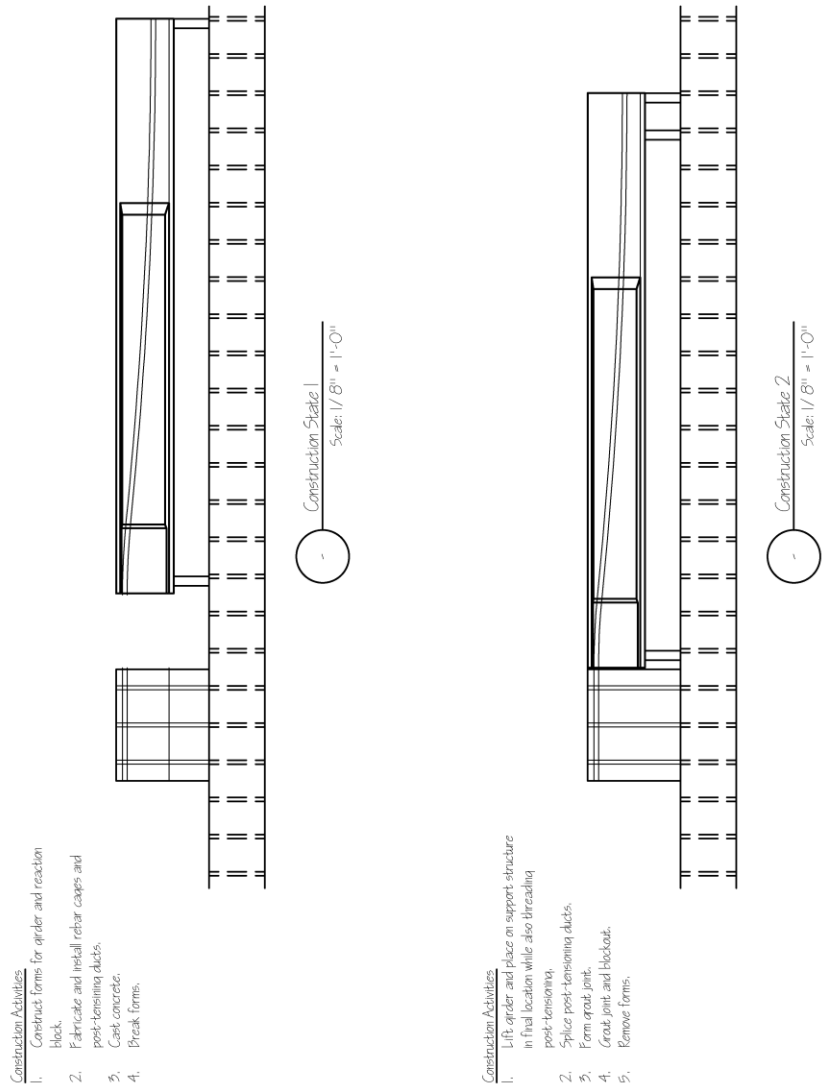

UCSD

NCHRP PROJECT 12-74

CONSTRUCTION STAGING 1

VISUAL SCALE: 0 1/4" 1/2" 1"	DUCTILITY: FULL	SUPER. CONNECTION: INTEGRAL	CONNECTION DETAIL: INTEGRAL COMPONENT TEST		
BY: MJT	CHK:	DATE: 06/30/09	SCALE: 1/8" = 1'-0"	SHEET: CS1	

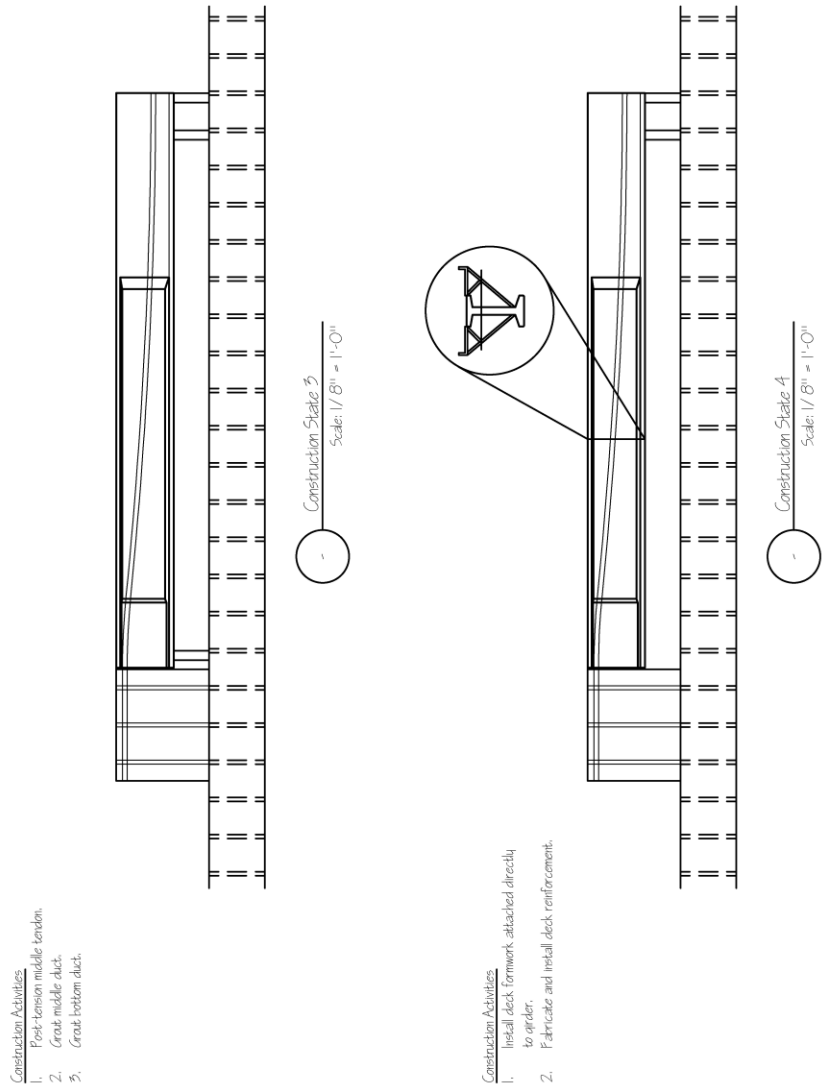

UCSD

NCHRP PROJECT 12-74

CONSTRUCTION STAGING 2

VISUAL SCALE:	DUCTILITY:	SUPER. CONNECTION:	CONNECTION DETAIL:		
0 1/4" 1/2" 1"	FULL	INTEGRAL	INTEGRAL COMPONENT TEST		
BY: MJT	CHK:	DATE: 06/30/09	SCALE: 1/8" = 1'-0"	SHEET: CS2	

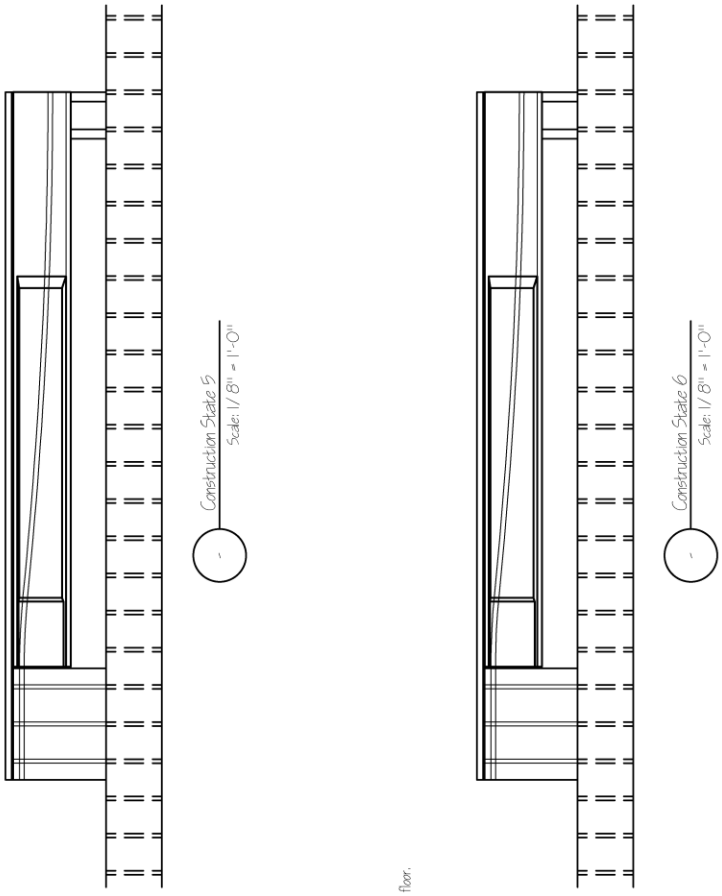

UCSD

NCHRP PROJECT 12-74

CONSTRUCTION STAGING 3

VISUAL SCALE: 0 1/4" 1/2" 1"	DUCTILITY: FULL	SUPER. CONNECTION: INTEGRAL	CONNECTION DETAIL: INTEGRAL COMPONENT TEST		
	BY: MJT	CHK:	DATE: 06/30/09	SCALE: 1/8" = 1'-0"	SHEET: CS3

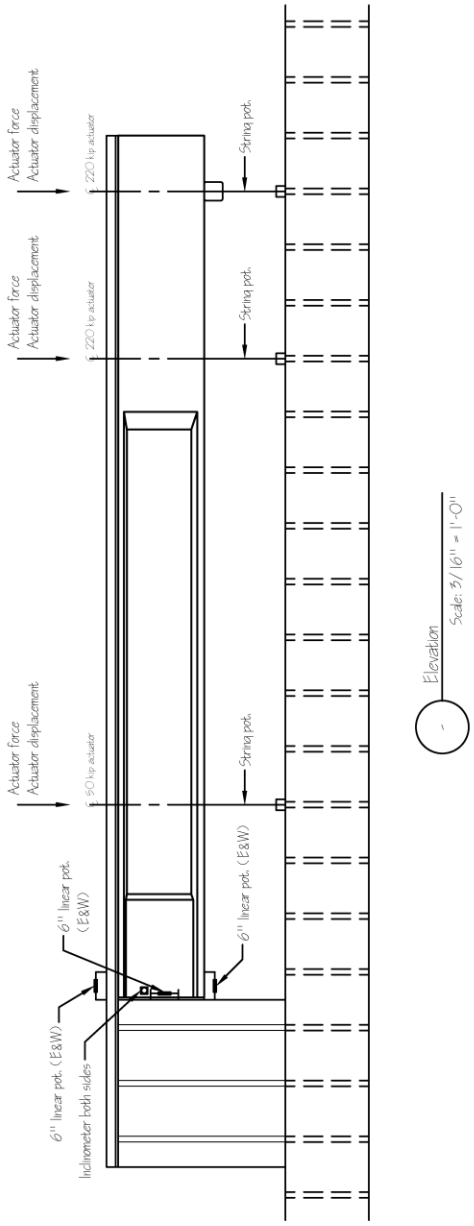

UCSD

NCHRP PROJECT 12-74

INSTRUMENTATION PLAN 1

VISUAL SCALE:	FUCILITY:	SUPER. CONNECTION:	CONNECTION DETAIL:			
0 1/4" 1/2" 1"	FULL	INTEGRAL	INTEGRAL COMPONENET TEST			
	BY: MJT	CHK:	DATE: 06/30/09	SCALE: AS NOTED	SHEET: IP1	

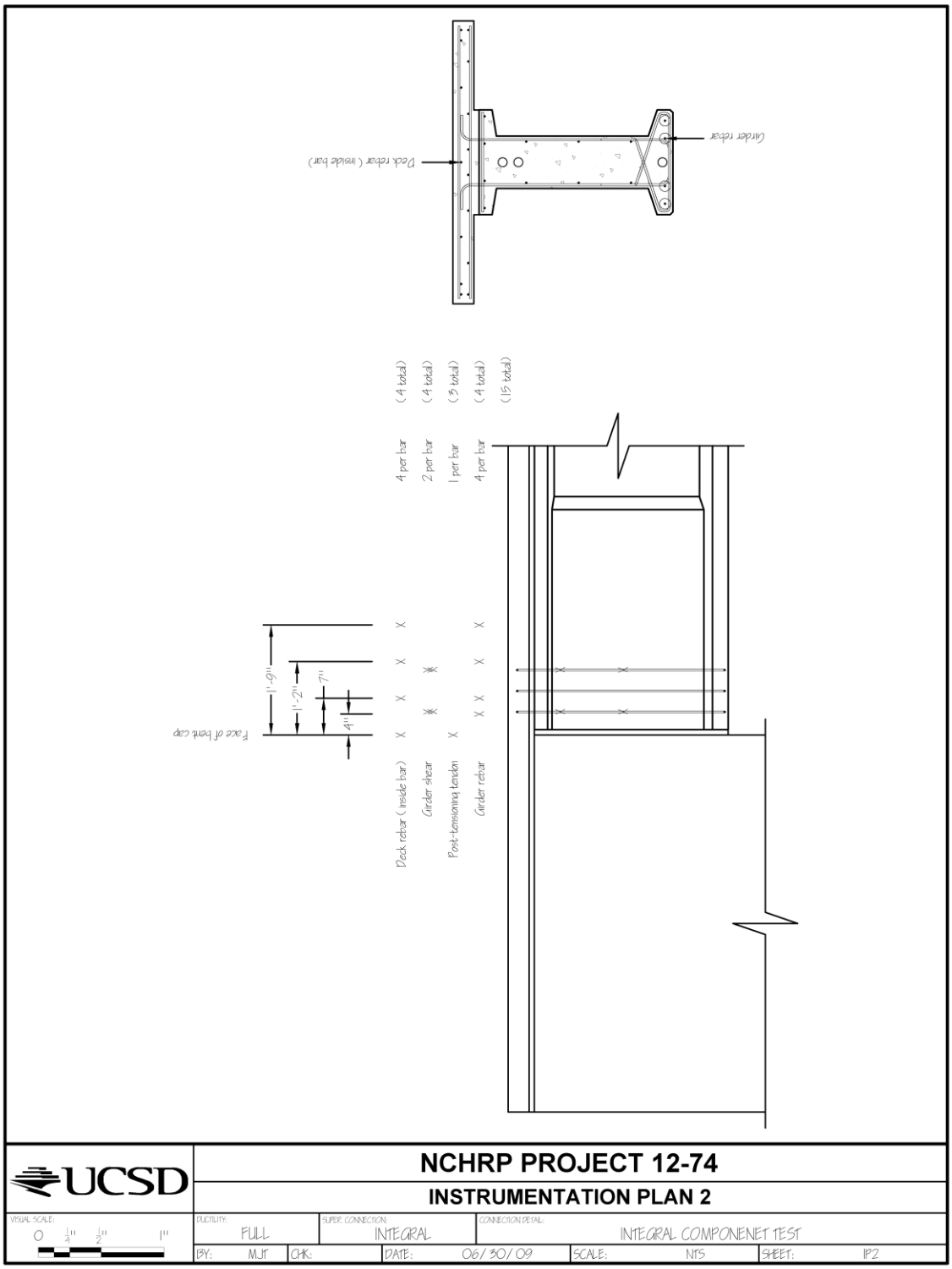

UCSD

NCHRP PROJECT 12-74

INSTRUMENTATION PLAN 2

VISUAL SCALE:	FACILITY:	SUPER. CONNECTION:	CONNECTION DETAIL:			
0 1/4" 1/2" 1"	FULL	INTEGRAL	INTEGRAL COMPONENET TEST			
	BY: MJT	CHK:	DATE: 06/30/09	SCALE: NTS	SHEET: IP2	

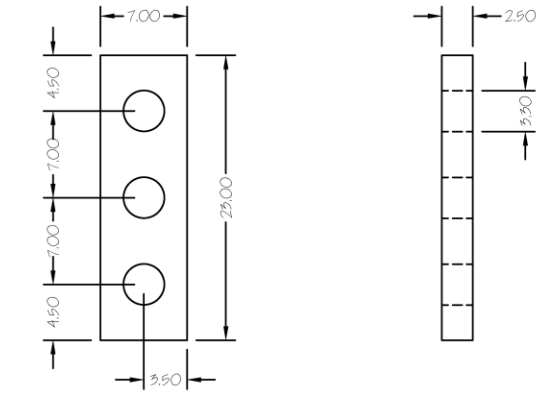

Bearing Plate 1

Scale: 1" = 1'-0"

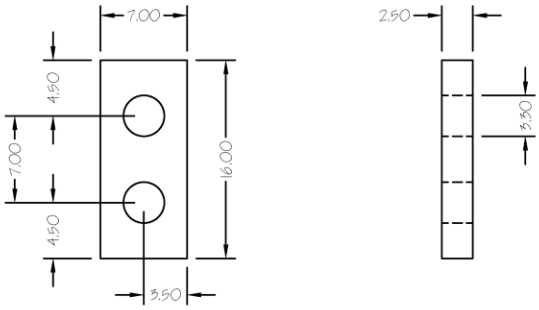

Bearing Plate 2

Scale: 1" = 1'-0"

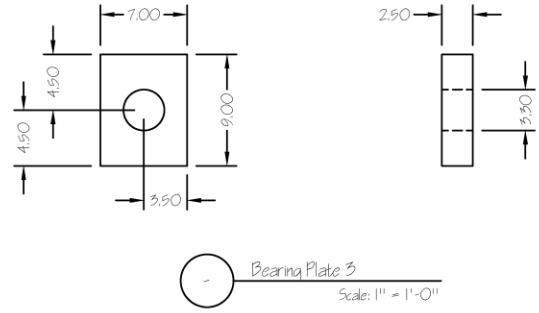

Bearing Plate 3

Scale: 1" = 1'-0"

Plate shall be A36 steel

UCSD	NCHRP PROJECT 12-74					
	BEARING PLATE FABRICATION DRAWINGS					
VISUAL SCALE: 0 1/4" 1/2" 1"	DUCTILITY: FULL	SUPER. CONNECTION: INTEGRAL	CONNECTION DETAIL: INTEGRAL COMPONENT TEST			
	BY: MJT	CHK:	DATE: 06/30/09	SCALE: AS NOTED	SHEET: BP1	

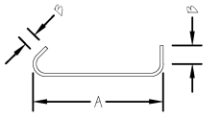

BAR ID	A	B	C	QTY
3G1B	1'-7"	2¼"	-	50
3G1D	0'-9"	2¼"	-	25
3G1H	0'-4"	2¼"	-	60

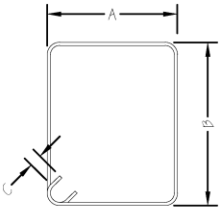

BAR ID	A	B	C	QTY
3G1A	1'-7"	3'-0"	2¼"	20
6RB1HA	0'-9"	3'-11"	3"	45
6RB1HB	0'-9"	5'-2"	3"	30
6RB1HC	4'-4"	5'-7½"	3"	12
4G1A	1'-4"	1'-4"	3"	25

BAR ID	A	B	C	QTY
3G1C	0'-7"	3'-4"	5"	120

HRC headed bar, or similar

BAR ID	A	B	C	QTY
3G1B	18'-6"	-	-	16

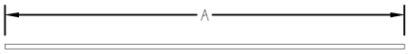

BAR ID	A	B	C	QTY
3S1	4'-4"	-	-	175
3S1	21'-6"	-	-	40
3G1E	1'-7"	-	-	90
3G1A	17'-6"	-	-	16
3G1C	17'-6"	-	-	20
3RB1VA	5'-6"	-	-	8

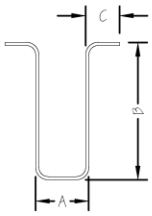

BAR ID	A	B	C	QTY
3G1F	0'-9"	3'-4"	5"	10

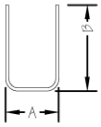

BAR ID	A	B	C	QTY
6RB1VC	0'-9"	3'-0"	-	40
6RB1VA	5'-6"	4'-2"	-	24
6RB1VB	4'-2½"	4'-2"	-	24

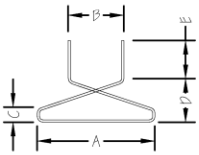

BAR ID	A	B	C	D	E	QTY
3G1G	1'-7"	0'-9"	2⅝"	7"	6¼"	10

NOTES:

1. All reinforcement shall be A706 Gr 60
2. All bend dimensions are to outside of bend

UCSD

NCHRP PROJECT 12-74

REBAR SCHEDULE

VISUAL SCALE: 0 ¼" ½" 1"

FACILITY:	SUPER. CONNECTION:	CONNECTION DETAIL:
FULL	INTEGRAL	INTEGRAL COMPONENT TEST

BY:	CHK:	DATE:	SCALE:	SHEET:
MJT		06/30/09	NTS	REBAR